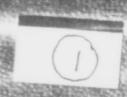
AD-A274 800



TITANIUM 92

SCIENCE AND TECHNOLOGY

VOLUMEIII

TIC SELECTE JAN 10 1994

This document has been approved for public release and sale; its distribution is unlimited

Edited by F.H. FROES and I.L. CAPLAN

TITANIUM '92

SCIENCE AND TECHNOLOGY

VOLUME III

94-00278

94 1 5 094

TITANIUM '92 SCIENCE AND TECHNOLOGY

VOLUME III

Proceedings of a Symposium sponsored by the Titanium Committee of the Minerals, Metals & Materials Structural Metals Division

Held at the Seventh World Titanium Conference June 29 - July 2, 1992 in San Diego, California

Edited by F.H. FROES and I.L. CAPLAN

A Publication of TMS

Minerals • Metals • Materials

A STATE OF THE STA

Accesi	on For)	
NTIS	CRA&I	70	
DTIC	TAB	Ġ	1
	ounced	ر_:	1
Justific	cation		
By So Distrib	ed as	3 Vol	· sol
Α	(Vd) hadina	e di M	
Dist	Avaii . Spe		
A-1	2/		

A Publication of The Minerals, Metals & Mater: ale Society
420 Commonwealth Drive
Warrendale, Pennsylvania 15086
(412) 776-9000

The Minerals, Metals & Materials Society is not responsible for statements or opinions and is absolved of liability due to misuse of information contained in this publication.

Printed in the United States of America Library of Congress Catalog Number 93-78482 ISBN Number 0-87339-222-1

Authorization to photocopy items for internal or personal use, or the internal or personal use of specific clients, is granted by The Minerals, Metals & Materials Society for users registered with the Copyright Clearance Center (CCC) Transactional Reporting Service, provided that the base fee of \$3.00 per copy is paid directly to Copyright Clearance Center, 27 Congress Street, Salem, Massachusetts 01970. For those organizations that have been granted a photocopy license by Copyright Clearance Center, a separate system of payment has been arranged.



© 1993

If you are interested in purchasing a copy of this book, or if you would like to receive the latest TMS publications catalog, please telephone 1-800-759-4867.

TABLE OF CONTENTS

VOLUME III

VOLUME I	
SURFACES, ENVIRONMENTAL EFFECTS, PROTECTION	
Protective Coatings for Titanium Aluminide Intermetallics	1
Results on Nitriding Titanium and TiAl6V4 with a New Thermochemical Treatment Under High Gas Pressure	9
Metallurgy of the Ti-N System: Heat-Treatment of Titanium Mono-Nitride1,989 YU. Sohn, J.P. Bars, and E. Etchessahar	9
The Electroplating of Titanium From NaCl-KCl Fused Salt	7
The Strengthening of Friction Unit Parts Produced of Titanium Alloys by Explosive Coatings	5
Surface Hardening of Ti-6Al-4V Alloy by Electrochemical Hydrogenation	9
Sputter Ion Plating on Ti6AI4V and Ti(CP) - Preparation and Properties of Oxidation and Resistant Wear Coatings	7
Reliable Operation and Environmental Compatibility in Cold Forming Process with Adapted Ceramic Coatings2,027 D.A. Keller, R. Hauert, and J. Reissner	7
The Oxidation of High Temperature Titanium Alloys	5
Environmental Influence on Fatigue Crack Growth Performance of Ti-1100 at Elevated Temperatures	3
Investigation of Properties of α-Titanium Alloys in a Gaseous Hydrogen Medium	9
Hydrogen Assisted Stress Cracking of Titanium Alloys	5
Microstructure Transformation and Cracking of Titanium Alloys Under Contact Loading	5
Effects of Oxygen and Iron on the Environmental and Mechanical Properties of Unalloyed Titanium2,073 R.W. Judy, Jr., I.L. Caplan, and F.D. Bogar	3

Same Regularities of Alloying Elements Effect on α-Base Titanium Alloys Embrittlement in Air and Corrosive Environment
Hydrogen Absorption of Titanium in Offshore Related Environments Under Cathodic Charging
Enhancing Corrosion Resistance of the Ti-3Al-8V-6Cr-4Zr-4Mo (Beta-C™) Alloy for Industrial Applications
Electrochemical Behavior of Titanium Implanted with Molybdenum and Tantalum Ions
The Effect of Beta-Stabilizers on Low Cycle Life Sensitivity of α-Base Titanium Alloys to Chloride Solutions
Electrochemical Behavior of TiN Coated Titanium in a Hydrochloric Acid Solution
Structural Characterization of Plasma Nitrided Titanium Alloys
Properties of Surface Oxides on Titanium and Some Titanium Alloys2,135 N. Frey, T. Buchillier, VD. Lê, and S.G. Steinemann
A New Corrosion-Resistant Titanium Alloy Ti-3AR
with Higher Strength2,143 Y.J. Hu, X.Z. Cai, and G.Z. Liu
The Optimization of Descaling Oxide Skin of Ti-2.5 Cu Alloy2,149 X.Z. Cai, Y.Q. Zhang, P.Q. Li, and H.H. Zheng
Corrosion Behavior of Ti-Ni-(Pd, Ru)-Cr Alloys in Hydrochloric Acid2,157 K. Ueda, Y. Sugizaki, and H. Satoh
Thin N*/H2O Ion Beam Treated Titanium Layers as Diffusion
Barrier for Hydrogen2,163 B. Kempf
Ripple Load Degradation in Titanium Alloys
Oxidation Characteristics of Beta-21S in Air in the Temperature Range 600 to 800° C
Mechanical Properties of Coated Beta-21S After Exposures to Air at 700 and 800° C
The Detection of Crevice Corrosion in Titanium and Its Alloys
Through the Use of Potential Monitoring
The Influence of Hydrogen on the Mechanical Properties
of Timetal 21S

Hydrogen Environment Embrittlement of Beta Titanium Alloys2,209 L.M. Young and R.P. Gangloff
A Study on the Anodic Behavior of Titanium and Some Ti Alloys in Hot Acid NaCl Solution
RAW MATERIALS, MELTING, RECYCLING AND PRIMARY PROCESSING
Raw Materials, Melting, Recycling and Primary Processing (Critical Review)
Estimating Domestic Titanium Requirements for the 90's
Leaching of Ilmenite with Sulfuric Acid-Thiourea Solutions
HID and HDI Dissolution During Titanium Melting Processes
DOSS, an Industrial Process for Removing Oxygen from Titanium Turnings Scrap
Preparation and Characterization of Extra-Low Oxygen Titanium
High Intensity Magnetic Removal of Paramagnetic Material from Recycle Titanium Turnings2,281 R. Young
Titanium Sponge Automatic Sorting
The Effects of Plasma Cold-Hearth Melting on the Production of Titanium Alloy Ingots
Recent Improvements in the Economics of Plasma Melting
Thermochemical Analysis of Kroll Process for Titanium Sponge Production
A New Method to Produce Segregation-Free Ingot of Ti-6AI-6V-2Sn by VAR2,317 H. Hayakawa, N. Fukada, M. Koizumi and H.G. Suzuki
Large Scale Statistically Based Exception Reporting in Vacuum Arc Melting
Electroslag Remelting of Titanium

C.H. Entrekin and H.R. Harker
Thermal Modelling of Solidification and Cooling of an Electron Beam Melted Titanium Ingot
Investigation of Heat-Exchange in the Electrode Tip of the Non-Consumable Electrode Vacuum Arc Furnace for Melting Titanium2,355 K. Rüdinger, KE. Piper, H. Schnecke, and P. Schüler
Production Titanium Plasma Cold Hearth Melting
Electrorefining Titanium - The Process Capability2,371 H.W. Rosenberg and J.E. Green
Potentialities of Electroslag Reme!*ing as Applied for Production of High-Quality Titanium Ingots
Developing a New Continuous Process for Making Titanium
Induction Slag Process for Producing Titanium by Reduction of Calcium Fluorotitanate
Industrial Production of Spongy Titanium of Low Hardness and Prevention of Gas-Saturated Inclusions
Temperature Measurements of Surface and Evaporated Species of Molten Titanium in Thermal Plasma
Five-Tonne Titanium Ingots Produced by Skull Melting
Oxygen Contamination of Titanium Sponge in the Kroll-Process2,423 S.V. Aleksandrovsky, A.A. Zakharevich, and A.I. Guliakin
Arc-Slag Remelting of Titanium and Titanium Alloys
Electrowinning of Titanium from Sulfuric Acid Titanium Solutions2,439 S.L. Bribiesca, E.S. Contreras, and F.J. Tavera
Characteristics of Niobium-Aluminum Master Alloy for Production of Advanced Titanium Alloys
Titanium Alloy Hearth Melt Technology
Industrial Production of High Purity Titanium by the Improved Iodide Process

METAL MATRIX COMPOSITES

Titanium Based Composites (Critical Review)	2,467
Continuously Reinforced Titanium Based MMC's Produced by the Matrix Coated Fibre Process	2,479
M. Hagiwara, S. Emura, J. Takahashi, Y. Kawabe, and N. Arimoto	2,487
Selective Reinforcement of Investment Cast Titanium Components Via Bicasting	2,495
Titanium/Ceramic Composites Produced by Laser Processing	2,503
Advanced Powder Metal Titanium Alloy Matrix Composites Reinforced with Ceramic and Intermetallic Particles	2,511
Combustion Synthesis of TiC-Al ₂ O ₃ -Ti Ceramic-Metal Copmosite Materials: An Initial Phenomenological Examination	2,519
Micromodelling and Methodology of Assessment of Fibre Reinforced Titanium Metal Matrix Composites Using Fracture Mechanics Parameters	2,529
Micromechanical Prediction of the Thermal Stresses in Sigma Fiber (SiC)/β-21S Titanium Composite: Effect of Coefficient of Thermal Expansion of the Coating	2,537
Fiber-Matrix Interfacial Behavior in SiC-Titanium Alloy Composites I. Roman, S. Krishnamurthy, and D.B. Miracle	2,545
Fiber/Matrix Interface Structure and Fracture Behavior in Continuous SCS-6™Reinforced Ti-15-3-3-3	2,553
Interfacial Reaction Kinetics in α- and β- Titanium Based Metal Matrix Composites	2,561
The Use of Pushout Testing to Investigate the Interfacial Mechanical Properties in Ti-SiC Monofilament Composites	2,569
Micromechanisms of Damage in Fibre Reinforced Titanium Based Metal Matrix Composites	2,577
The Forging Characteristics of Two Ti-6Al-4V-Based Particulate Composites	2,585

Metal Matrix Composites	2,593
S.W. Schwenker, D.J. Evans, and D. Eylon	
Cyclic Fatigue Resistance of Fibre Reinforced Titanium Metal Matrix Composites at Ambient and Elevated Temperatures	2,601
Deformation Mechanisms in a Ti-Alloy/SiC Metal Matrix Composite B.S. Majumdar, G.M. Newaz, F.W. Brust, and J.R. Ellis	2,609
Microstructural Property Correlation in a Unidirectional SiC (SCS-6) Fiber-Reinforced Ti-24Al-11Nb Composite	2,617
Microstructure of Unidirectional SiC/Ti-24Al-11Nb Composite Deformed in Tension, Fatigue and Creep	2,625
SiC Fibre/Ti-Based Composites: Processing, Microstructure and Interface Properties	2,633
Metal-Ceramic Composite Layer Formation on Titanium Surfaces Through Laser Treatment	2,641
Interfacial Properties and Fatigue Crack Propagation in Continuously Reinforced Ti/SiC Metal Matrix Composites	2,649
NON-AEROSPACE APPLICATIONS	
New Development in Application of Titanium as an Ecological Metal:	2 659
Non-Aerospace Application/Environment and Development	2,000
K. Sakai Application of Near Beta Titanium Alloys for Turbine Blades A. Takemura, Y. Ashida, H. Ohyama, A. Morita, S. Hattori, K. Tani,	2,673
K. Sakai Application of Near Beta Titanium Alloys for Turbine Blades	2,673 2,681
K. Sakai Application of Near Beta Titanium Alloys for Turbine Blades	2,673 2,681
K. Sakai Application of Near Beta Titanium Alloys for Turbine Blades	2,681 2,689 2,697

Improved Water Brake2,721
S.L. Opet, Jr., and D.F. Peters
Production of Titanium 6AI-4V ELI Electronic Bottles
for the Curv III Submersible
M.E. Wells and J.A. Sasse
Corrosion Behavior of Timetal-21S for Non-Aerospace Applications2,737 J.S. Grauman
Anodizing Mechanisms in High Purity Titanium2,743 H.W. Rosenberg and M.S. Cooper
A Ti-5%Ni Alloy Electrode for Production of Electrolytic
Manganese Dioxide
Development of Endosseous Implants on the Base of Titanium Alloys
with Improved Functionality2,757
J. Breme, W. Schulte, and K. Donath
Development of a new Casting Technology for Dental Applications
Using Titanium
H. Brauner, U. Holzwarth, and U. Zwicker
Superplastic Forming of Ti-6Al-4V Denture Base
The Use of Titanium Chelate in Agriculture2,779 ML. Huang, XD. Tang, and L. Liu
A New Low Cost Titanium Alloy
Titanium Tubing Experience in Utility Condensers
INSPECTION, NDE,
QUALITY ASSURANCE, DEFECTS
Quality Assurance for Titanium Critical Applications
Laser Ultrasonics for Large Metal Structures
Ultrasonic Noise and Its Influence on Flaw Detection
in Aircraft Engine Alloys
Confirmation Test Methods for Titanium Tube Damage
of Steam Surface Condenser
Analyzing High Purity Titanium
Radioautography Investigation of the Distribution Regularities (Carbon) in Ingots as Well as Forgings of Pseudo-Alpha-Titanium Alloys

Ultrasonic Inspection of Titanium Billets
The Role of Melt Related Defects in Fatigue Failures of Ti-Al-4V2,867 K.R. Clark, A.B. Dillard, B.C. Hendrix, J.K. Tien, and T. Denda
AEROSPACE APPLICATIONS
Application of Ti Alloys in the European Aerospace Industry
Titanium Application in Aviation Industry of China2,891 C. Li and J. Ma
Ultra High Strength Titanium Alloy for Fasteners
Applications of Titanium Aluminides in Gas Turbine
Engine Components
The Titanium Investment Casting Technology
Timetal·1100 Sheet Properties
Rolls-Royce's Wide Chord Fan Blade - The Next Generation2,931 G.A. Fitzpatrick and J.M. Cundy
ADDENDUM
Pressure Welding Process Window for Ti-6Al-4V
Subject Index2,949
Author Index2,973

SURFACES, ENVIRONMENTAL EFFECTS, PROTECTION

PROTECTIVE COATINGS FOR TITANIUM ALUMINIDE INTERMETALLICS

R.L. McCarron and J.C. Schaeffer, GE Aircraft Engines; G.H. Meier and D. Berztiss, University of Pittsburgh; R.A. Perkins and J. Cullinan, Lockheed Missiles and Space Company

Abstract

Advanced titanium aluminide intermetallics are being developed for applications where service temperatures are in the range 650°C to 900°C. The usefulness of these alloys may be limited by oxidation and by oxygen-induced embrittlement. Successful application of these materials requires that the kinetics of oxidation for the base alloys are parabolic and that coatings are available for environmental protection of alpha-2 alloys above 700°C and gamma alloys above 815°C. Results of an ongoing program to meet these requirements for gamma alloys are presented.

Introduction

Gamma titanium aluminide (γ-TiAl or gamma) alloys are being developed for application in aircraft gas turbine engines. Potential applications include: components in the compressor, turbine, and exhaust sections of the engine. Gamma alloys have a higher specific strength and specific modulus than nickelbase alloys like Alloy 718 and Rene'41 which are currently used in these applications. These properties translate into better fuel efficiency through weight savings if γ-TiAl alloys substitute for nickel or cobalt-base alloys. General Electric Aircraft Engines (GEAE) is carrying out a program to develop a coating for environmental protection of gamma alloys at temperatures above 700°C. This program is sponsored by the Naval Air Warfare Center at Warminster, PA. Researchers at the University of Pittsburgh and Lockheed Missiles and Space Co. (LMSC) are partners with GEAE in this research. This paper reviews results from this ongoing program.

Titanium '92 Science and Technology Edited by F.H. Froes and I. Caplan The Minerals, Metals & Materials Society, 1993

Alloy Selection

A gamma allcy with a nominal composition of Ti-47Al-2Cr-4Ta (47-2-4)¹ was selected as the substrate alloy for use in this program. The isothermal oxidation behavior of this alloy has been measured by Meier at 800, 900, and 1000°C². Results are shown in Figure 1. The ultimate tensile strength as a function of temperature for this alloy is shown in Figure 2. Work is still in progress to determine the susceptibility of the 47-2-4 alloy to environmental attack by high velocity cyclic oxidation/hot corrosion, hot salt stress corrosion cracking, and surface hardening due to interstitial dissolution. It seems prudent to assume that a coating will be required for environmental protection in most applications.

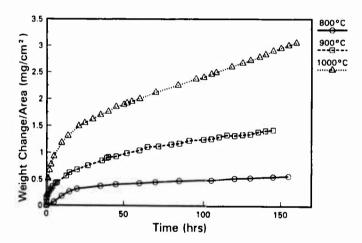


Figure 1 - Isothermal oxidation results for the Ti-47Al-2Cr-4Ta alloy at several temperatures.

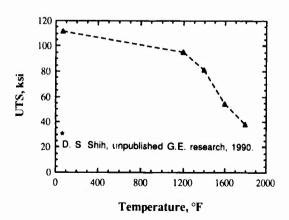


Figure 2 - Ultimate tensile strength as a function of temperature for the Ti-47Al-2Cr-4Ta alloy. *

1,972

Coating Selection

The ideal coating for γ -TiAl should form an adherent alumina scale similar to that on coated superalloys. The composition should be adjusted so that thermal expansion mismatch and interdiffusion are minimized. Work done at the University of Pittsburgh and LMSC identified compositions in the Ti-Cr-Al system that meet these goals^{3,4}. Applying Wagner's analysis⁵ for the transition from internal to external oxidation these workers determined that a third element must be added to γ -TiAl alloys in order to form alumina scales over a wide range of temperatures and compositions.

Chromium was selected as the best third element. A detailed study of the oxidation behavior of alloys in the Ti-Cr-Al system was made at 800, 1100, and 1300°C. An oxide map showing the boundary of compositions which will form a continuous alumina scale with no transient oxide in air at each temperature is shown in Figure 3. A composition boundary for alloy melting is also shown. As temperature is reduced, both the Al and Cr contents of the alloys must be increased to form alumina scales. Alloys that can form alumina in air at all temperatures from 800°C to the melting point must have compositions lying above the 800°C oxide map boundary in Figure 3.

Coating/Process Development

Coating development is based upon compositions in the Ti-Cr-Al system and includes evaluation of several processes for coating application. Eight compositions of bulk TiCrAl alloys were selected based upon the 800°C boundary

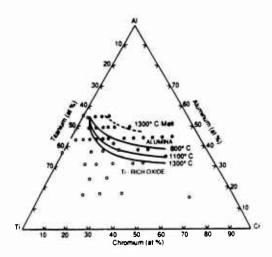


Figure 3 - Oxide map showing the composition of alloys in the Ti-Cr-Al system which form protective alumina scales in air at 800°C, 1100°C and 1300°C. The compositions where incipient melting occurs at 1300°C are also indicated on the map.

in Figure 3. The alloy compositions are plotted on Figure 4. Also included in Figure 4 is an approximation of the selected gamma alloy composition, Ti-47Al-2Cr-4Ta, denoted by the star.⁶

The program consists of three tasks. Under Task 1 the bulk TiCrAl alloys were prepared in the laboratory and then evaluated for oxidation resistance, mechanical behavior, thermal stability and thermal expansion properties. Based upon Task 1 results several coating compositions were identified for coating of the gamma alloy in Task 2. Task 2 is partly a coating process study where slurry fusion, low pressure plasma spray, high velocity oxygen fuel spraying and sputtering were evaluated as methods for applying the TiCrAl coatings to the gamma alloy. Specimens of the coated gamma alloy were then evaluated in oxidation between 760° and 1000°C. Tasks 1 and 2 are now complete.

Task 3 will include a fine tuning of the best TiCrAl coating composition and process where specimens will be evaluated in rigorous environmental tests which closely simulate engine conditions. Finally, the effect of the coating and application process on tensile (R.T. and 760°C in air) and creep properties (760°C and 1000°C in air) of the gamma alloy will be evaluated.

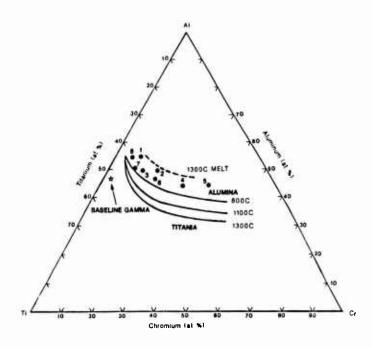


Figure 4 - Oxide map for the Ti-Cr-Al system showing compositions of the eight bulk TiCrAl alloys and the baseline gamma alloy.

Summary of Preliminary Results

Following is a summary of the key results on the program to date:

- (1) TiCrAl alloys with Cr contents from 6-35 atom percent and Al contents from 47-55 atom percent form thin alumina scales in air at temperatures between 760 and 1000°C. An example is shown in Figure 5 where a thin continuous alumina scale is observed on alloy #8 after 1578 hours of cyclic oxidation at 1000°C in air.
- (2) Bulk TiCrAl alloys have excellent cyclic oxidation resistance at 900 and 1000°C, similar to coatings used on Ni-base alloys. The data in Figure 6 illustrate this point, where a higher Kp value represents more rapid oxidation. Data from this program show that the gap in the oxidation resistance between the camma alloy and a Ni-25Al alloy (nickel-base alumina former) is bridged by the TiCrAl alloy.
- (3) Results of diffusion couple studies show that the TiCrAl alloys exhibit limited interdiffusion with the gamma alloy substrate containing Cr and Ta at 1000°C. This behavior is shown in Figure 7 for TiCrAl alloy #6 on the Ti-47Al-2Cr-4Ta substrate after 256 hours of exposure at 1000°C. The Cr rich precipitates in the gamma alloy suggest that the major atom movement is chromium from the coating into the substrate. If the depth of Cr diffusion is equated to the depth of precipitation, then it is estimated that the maximum interdiffusion after 5000 hours would be about 25μm.

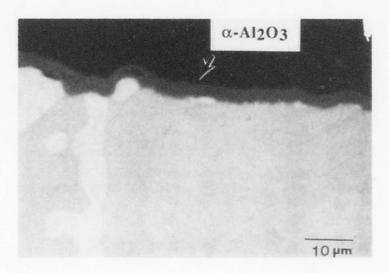


Figure 5 - Micrograph of alloy #8 (Ti-55Al-6Cr) after 1578 Hr. of cyclic oxidation at 1000°C. The scale is a thin continuous layer of alumina.

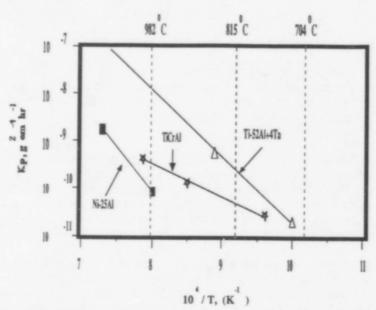


Figure 6 - Plot of the parabolic rate constant, K_p, vs the reciprocal of the absolute temperature for a gamma alloy (in 0₂), a TiCrAl alloy and Ni-25Al⁷ (the latter two in air).

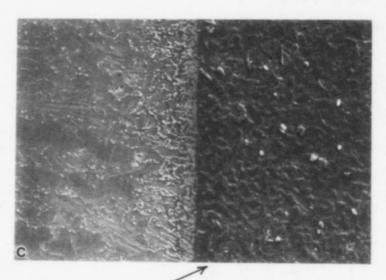


Figure 7 - Micrograph of alloy #6 (Ti-47Al-18Cr) diffusion bonded to the Ti-47Al-2Cr-4Ta alloy after 256 hours at 1000°C.

(4) Measurements have shown that bulk TiCrAl alloys have larger mean expansion coefficients than gamma alloys. The thermal expansion mismatch, $\Delta\alpha$, has been calculated to be less than 10% in the temperature range where gamma alloys will be used. This degree of mismatch should not cause failure at the coating/substrate interface because the thermal stresses produced are less than the fracture strength of either the coating or substrate.

(5) Formation of TiCrAl coatings on the gamma substrate has been demonstrated using:

Sputtering

- Low Pressure Plasma Spraying
- High Velocity Oxygen Fuel Spraying

Slurry Fusion

- (6) Thermodynamic analysis indicates the feasibility of producing TiCrAl coatings with the pack cementation process.
- (7) The best TiCrAl coatings to date have been applied by sputtering. The microstructure of the sputtered alloy #4 (Ti-44Al-28Cr) coating on the gamma alloy substrate is shown in Figure 8.

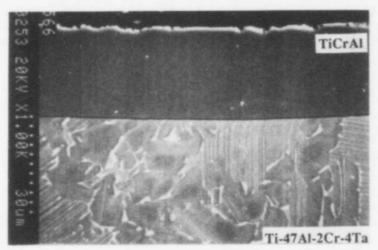


Figure 8 - Micrograph of alloy #4 (Ti-44Al-28Cr) sputtered onto the Ti-47Al-2Cr-4Ta gamma substrate. Little reaction or interdiffusion occurs at the coating/substrate interface as a result of the coating process.

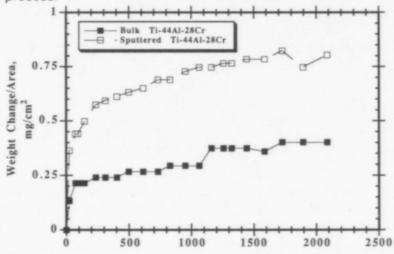


Figure 9 - Cyclic oxidation kinetics for a gamma alloy coated with alloy #4 (Ti-44Al-28Cr) are similar to those observed for bulk alloy #4.

(8) Isothermal and cyclic oxidation testing of sputtered coatings have produced encouraging results. Cyclic results at 900°C in air are illustrated in Figure 9 for the alloy #4 (Ti-44Al-28Cr) in bulk form and sputtered onto the gamma substrate. Note that the weight change is exceedingly small for times over 2000 hours and that the coating is behaving the same as the bulk alloy.

Summary

Research to date has shown that a range of alloy compositions in the Ti-Cr-Al system form protective alumina scales in the temperature range 760 to 1000°C in air. These alloys can be applied as a coating on a gamma alloy and provide excellent oxidation protection via the formation of a thin adherent film of α -Al₂0₃. The final phase of this research program will evaluate the effects of the coating and the application process on the mechanical properties of the base gamma alloy.

References

- D.S. Shih, S.C. Huang, G.K. Scarr, H. Jang and J.C. Chesnutt, in symposium proceedings "Microstructure/Property Relationships in Titanium Alloys and Titanium Aluminides", eds. R. Boyer and Y.K. Kim, TMS-AIME 1991.
- G.H. Meier, unpublished results from a GEAE funded research program at the University of Pittsburgh, August 5, 1991.
- R.A. Perkins and G.H. Meier, "Oxidation Resistant Aluminides for Metal Matrix Composites", Proceedings of the Advanced Materials Institute, Golden, Colorado, 1989, p. 92.
- Perkins et. al., "Formation of Alumina on Niobium and Titanium Alloys," in Oxidation of High Temperature Intermetallics, T. Grobstein and J. Doychak eds., TMS, 1989.
- 5. C. Wagner, Z. Elektro chem., 63 772, (1959)
- Meier et.al., "High Temperature Coatings for Gamma Titanium Aluminide Intermetallics", Interim Report #1 on Navy Contract N62269-90-C-0287, June 1991.
- F.S. Pettit, "Oxidation Mechan sm for Nickel-Aluminum Alloys at Temperatures Between 900 and 1300°C, Trans. AIME, vol. 239, 1967, p. 1297-1305.

RESULTS ON NITRIDING TITANIUM AND TIA16V4 WITH A

NEW THERMOCHEMICAL TREATMENT UNDER HIGH GAS PRESSURE

F. Preisser, P. Minarski Leybold Durferrit GmbH Rodenbacher Chaussee 2-4 D 6450 Hanau Germany

Introduction

The outstanding mechanical properties of titanium have led to a great increase in the field of application. However, one of the disadvantages that prohibit further increase in applicability of titanium is the unsatisfactory resistance to wear due to the relatively low surface hardness /1/.

In order to increase the surface hardness, in addition to technical alloy measures, it is possible to employ carbon or nitrogen just as for the hardening of steel. Because of the extreme hardness of the compound TiN, attempts are still being made to generate this compound on the titanium surface and to anchor it firmly in the base material by means of suitable measures. This is opposed by the high affinity of titanium for oxygen, which makes a normal thermochemical surface treatment impossible, e.g. gas nitriding or gas nitrocarburizing. This work describes the first successful developmental steps in high-pressure nitriding, a process for the nitriding of titanium by means of a thermochemical reaction.

Titanium '92 Science and Technology Edited by F.H. Froes and I. Caplan The Minerals, Metals & Materials Society, 1993 During recent decades reports have been published on some processes which are also used productively on a small scale. Table I gives a survey of these processes, and compares them with the process newly developed by Leybold Durferrit GmbH, the high-pressure nitriding process.

| Surface Nitriding Processes

Process	Charac- teristic			
PVD	coating	300-500 degC		
Plasma-Spraying	coating	MICULATA	300-500 degC	
Plasma-Nitriding	diffusion	plaeme	700-800 degC	
Salt-Bath-Nitriding	diffusion	eelt	800 degC	
Laser-Nitriding	alloying	melt	> 72	
Pressure-Nitriding TIDUNIT®	diffusion	000	800-800 degC	

Table 1: Processes for surface hardening of titanium

All of the processes mentioned - with the exception of the salt bath process - have une point in common, that in order to overcome the oxide layer barrier they must be preceded by costly, preliminary cleaning operations (pickling, sputtering).

An intensive evaluation of the literature relating to the subject, "High-pressure nitriding, of metals", and initial spot checks, on which /2/ and/3/ report, gave indications that a treatment of titanium in gas under increased pressure can also offer advantages with respect to the speed of handling and the depassivation of the surface.

The high-pressure nitriding of titanium materials is marked by the use of gas (nitrogen, ammonia, or nitrogen-ammonia mixtures) as transfer medium. This process can be employed in the temperature range of 600-800°C, and is classed as a diffusion-controlled process.

Fig. 1 reproduces the processing sequence followed in high-pressure nitriding. The processing steps are listed on the center axis. After a step where the parts are degreased in alkaline soap not shown in Figure 1, the parts are placed on normal charge carriers similar to those also used in the vacuum heat treatment, and the plant is charged. In order to generate a low oxygen partial pressure, the plant is then evacuated to 10-2 mbar. After heating of the plant to nitriding temperature, the actual nitriding process is initiated by filling of the plant with the process gas to pressures between 5 and 50 bar. As process gas, nitrogen, ammonia, or mixtures can be considered.

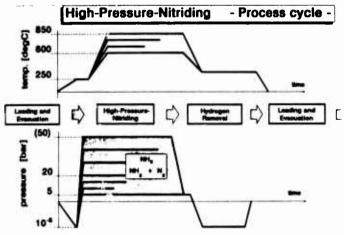


Fig. 1: Processing sequence in high-pressure nitriding

When No is used, nitride layers of different thicknesses are built up depending on the pressure, as reported in /2, 3/, however these layers are in all not adequate. A lowering of the temperature below 800°C is not possible in N2. An intensification is possible in ammonia when the hydrogen that has diffused in is removed again by an annealing process in vacuum. At atmospheric pressure, increases in hardness are attained on the surface of pure titanium when the treatment temperature lies higher than 900°C. The high temperatures result in an influence on the base metal which can not be tolerated for technical applications. Through an increase in pressure - just as when nitrogen is used - an improved nitriding effect must be expected. At the present time, an NH3 pressure of 12 bar can be built up in the plant. Higher pressures can be attained with ammonianitrogen mixtures. The nitriding treatment is concluded by cooling of the charges and release of pressure in the plant. In order to dehydrate the parts, a tempering treatment can follow at temperatures between 300 and 400°C in vacuum at 10^{-2} mbar.

Our own studies

Procedure

In order to test the process, flat test specimens of pure titanium (3.7035) and of the alloy TiAl6V4 (3.7165) were nitrided for metallographic studies. The surfaces of the test specimens were precision-ground.

The experiments were carried out in the temperature range of 600 to 900°C. The treatment time varied between 1 and 4 hours. As described above, and proceeding from the results of /2, 3/, the medium used was ammonia at a pressure of 12 bar. Following the nitriding treatment, the test samples were tempered at 300°C in vacuum for 4 hours.

Results an discussion

After a nitriding treatment at 850°C for 4 hours, pure titanium forms a lustrous gold layer almost 20 µm thick. By means of SIMS (secondary ion mass spectroscopy) it has been possible to establish that the uppermost layer consists of TiN. Slight impurities with carbon and oxygen decrease rapidly after sputtering off of the uppermost atomic layers. The cause for the carbon contamination is the graphite lining of the furnace. Under the TiN layer, a layer of Ti2N formsof approximately equal thickness which is converted into a zone where nitrogen is dissolved in the titanium. From the hardness indentations, the steady decrease in hardness is illustrated as the base material is approached. Qualitatively, the same surface structure applies for the titanium alloy, TiAl6V4. Here, however, the layer thicknesses are considerably less. The cause for this is the formation of stable aluminium oxides on the surface which are not reduced under the conditions given.

Under the covering layers of TiN and Ti2N, a layer of globularly formed α -titanium grains can be recognized which must be attributed to the κ -stabilizing effect of the nitrogen. The structure of the base material is not affected. Although hydrogen diffuses into the titanium when ammonia is used, and hydrides form at the grain boundaries, these can no longer be detected metallographically after an optimized tempering treatment in a vacuum.

Titanium

high-pressure-nitrided: 12 bar NH3

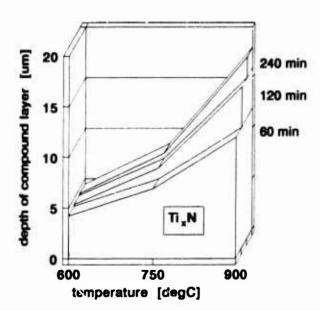


Fig. 2 Effect of various temperatures and times on the compound layer of pressure-nitrided titanium

Fig. 2, where pure titanium is used as an example, show how the formation of the surface layers on pure titanium depends on the treatment temperature and on the time. After a treatment time as short as 60 minutes at 600°C, more than 90% of the layer thickness has been attained in comparison with a treatment of 4 hours.

It is ovbious that with "high-pressure nitriding" a rapid and efficient reduction of the surface is attained, which together with the high density of the medium and the associated high availability of diffusible nitrogen results in a considerable shortening of the process time.

The courses of hardening in Fig. 3 for different treatment temperatures show that in every case a hardness of about 1000 HV is attained in the temperature range of interest. This value does not give the true hardness of the surface layer because influences of the base material must not be ruled out in the measurement process employed.

Hardness of Titanium high-pressure-nitrided: 12 bar NH3

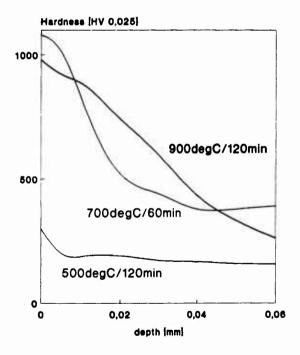


Fig. 3: Hardness of titanium

The studies of TiAl6V4 (Fig. 4) likewise showed that after a relatively short treatment time the layer build-up is almost completed. In contrast to pure titanium, the layer thickness at high temperatures increases only moderately with time. The reason for this is likewise to be found in the aluminium oxide coating on the surface, which can only be converted to suboxides and reduced in the temperature range starting at about 1100°C. The hardness (Fig. 5) likewise lies in the range of 1000 HV when treatment temperatures are selected above 750°C, whereby the hardness values of the surface can be seriously falsified by the base material.

TIAL 6 V4

Hardness of TiAl6V4 high-pressure-nitrided: 12 bar NH3

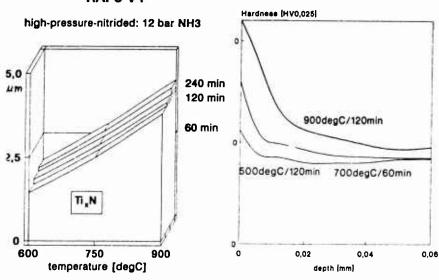


Fig. 4: Effect of various Fig. 5: Hardness of TiAl6V4
temperature on the
compound layer thickness
of pressure-nitrided
TiAl6V4

Applications engineering

On the basis of the encouraging results, applications engineering experiments were carried out on parts. In these experiments, additional, far-reaching advantages are found referring to the geometry of the part. Fig. 6 gives an overwiew of parts made of titanium which were surface-refined by high-pressure nitriding from the sectors

- medical technology
- automobile construction (racing)
- machine construction
- dental engineering
- precision mechanics.

All parts represented were nitrided in the temperature range of 650 to 950°C depending on specification.



Fig. 6: High-pressure nitrided series parts

With the processes known in the past, it is almost impossible to generate uniform surface layers, especially on complicated partgeometries. However, by nitriding under high pressure, even points where accessibility is difficult such as, for example, narrow, deep holes and blind holes, undercuts, threads, etc. can be nitrided perfectly and at no additional expense.

Summary

High-pressure nitriding opens up new possibilities for the use of titanium alloys. It was shown that through employment of this process a thermochemical treatment of titanium is possible even at temperatures below the transition temperature. The process gas at a high density causes the rapid build-up of a TiN layer without the material having to be pretreated for reduction of the surface. It is possible to attain uniform nitriding of evenparts with an extremely unfavorable geometry at no additional expense for the charging.

References

- /1/ K.H. Kramer, "Anwendungsgebiete von Titan", Metall, 43 Vol. 2, (1989)
- /2/ F. Hoffmann, P. Mayr, P. Minarski and F. Preisser, "Nitrieren/Nitrocarburieren bei erhöhtem Druck", <u>Härterei-Technische Mitteilungen</u>, 46 Vol. 6, (1991), 354 - 360
- 73/ T. Bell, H.W. Bergmann, I. Lanagan, P.H. Morton and A.M. Staines, "Surface Engineering of Titanium with Nitrogen", Surface Engineering, 2 Vol. 2, (1986)

METALLURGY OF THE TI-N SYSTEM:

HEAT TREATMENT OF TITANIUM MONO-NITRIDE

Yong-Un SOHN, *** J.P BARS*, E. ETCHESSAHAR*,

M. HARMELIN** and J. DEBUIGNE*

*Laboratoire de Métallurgie et Physico-Chimie des Matériaux
U.R.A.-CNRS 254, I.N.S.A., 20, avenue des Buttes de Coësmes
F. 35043 RENNES CEDEX - FRANCE

**C.E.C.M./C.N.R.S., 15, rue Georges Urbain
F. 94407 VITRY sur SEINE - FRANCE

***Present address: Korea Institute of Energy and Ressources, 71-2 Jang-Dong, Yoosung-gu, Daejon, Korea

Abstract

The nitriding reaction of formation of Ti-N alloys is studied, Microhardness measurements are used for the mechanical characterization of the alloys ; and D.S.C., D.T.A. and X-ray diffraction and metallography for the physical characterization. The phase transformation quenched $\delta \rightarrow \delta'$ is complete for the composition 33.8±0.5 at.% N. The enthalpy of reaction being $\Delta H = -64~Jg^{-1}$. The δ' phase undergoes peritectoïd decomposition at 800 ±10°C according to the reaction $\delta' \Leftrightarrow \epsilon + \delta$. A partial Ti-N equilibrium diagram is proposed.

Introduction

The transformation of the quenched δ -TiN0.5 phase into a δ '-TiN0.5 phase by low temperature annealing was first shown by Lobier and Marcon [1]. The different works on the Ti-N phase diagram are summarized in the critical review of Wriedt and Murray [2]. They [2] suggest that the upper limit of stability of the δ ' phase is 800°C , where it coexists with ϵ -Ti2N and δ -TiNx in a peritectoid equilibrium. The δ ' phase has a narrow homogeneity range around 37.5 at %N. This subnitride, derived from the δ -f.c.c. phase by ordering of the nitrogen vacancies along the c axis, has a tetragonal symmetry, space group I41/amd, a = 4.1493 Å, c=8.7858 Å [3]. It may be represented as a superposition of two f.c.c. lattices. Lengauer and Ettmayer [4] have shown, firstly, that quenched δ -TiN0.5 is transformed into δ '-TiN0.5 at 700°C in 180 min, then transforms slowly into the ϵ phase, and secondly, that the δ ' phase appears to be metastable. In recent work [5], the present authors made the same observation and indicated that the δ ' phase appears within the limits TiN0.5-TiN06. The number and the diversity of the proposals relating to the homogeneity range of δ ' have led us to undertake a deeper study of this phase.

Experimental procedures

"Clean" techniques were used (pure gas, laboratory vessels perfectly out-gassed, ultrahigh vacuum, non-reactive sample holders). The base metal used was pure titanium, supplied by Cezus. The principal impurities (in 10-6 atomic fraction) were as follows:

Titunium '92 Science and Technology Edited by F.H. Froes and I. Caplan The Minerals, Metals & Materials Society, 1993

280 carbon; less than 200 nitrogen; 900 - 1800 oxygen; 10 - 200 aluminium; 15 - 60 vanadium; 50 chromium; 150 - 250 iron; 60 nickel; 25 zirconium. The nitrogen gas used, supplied by Air Liquid, had a purity better than 99.9999%. Two types of TiNx homogeneous bulk samples were produced by nitrogen diffusion. After nitriding at 1300°C, the plates 45x10x0.4 mm³ were homogenized at 1300°C for 600h. These treatments were carried out by r.f. induction heating, the samples being kept inside a cylindrical reaction vessel of nitrided zirconium. The strip bulk samples were obtained by direct heating, using the Joule effect, of titanium strips measuring 150x10x0.12 mm³. The main aim of the experimental procedure was to load the titanium strip with nitrogen, over a known length and in an homogeneous manner, by introducing a definite quantity of nitrogen into the reaction vessel. This preparation was based on similar work on Zr-O alloys [6]. After all the nitrogen necessary for the reaction had been consumed, pure argon was introduced (105 Pa) to carry out homogenizing annealing for 485 h [7]. The homogeneous length was 100 mm. The concentration determined by the definite quantity of nitrogen gas introduced in the reaction vessel was compared with that obtained by X-ray diffraction according to the law of variation of the lattice parameter in δ -TiN_x[5]. Some samples were analysed by the method of complete hot oxidation of TiNx into TiO2.

For the DSC and DTA thermal studies, the samples were placed in cylindrical copper or platinum crucibles which were then crimped to render them gas tight, this operation being carried out in a glove-box under argon. The alloys obtained underwent isothermal annealing at 750° and 950°C. Finally each sample was studied by x-ray diffraction, microhardness and optical microscopy.

Kinetics of the nitriding reaction

The kinetics of the mass increase Δm (fig.1) of the samples follow a law of the parabolic type. In the expression of the form $\Delta m^x = Kt$, a mean value of x = 1.9 is obtained, instead of 2 for a strictly parabolic law. In the temperature range 1410 -1500°C, the following expression is obtained for the kinetic constant : $K = 1.49 \times 10^{-6} \exp$ (-275 kJ/RT) mg² cm⁻⁴ s⁻¹.

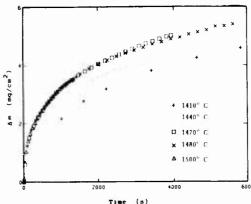


Figure 1 - Mass increase as a function of Time

Vickers microhardness

The results are given in Table 1.

TABLE 1. - Values of vickers microhardness (HV100 = kg.mm-2)

Concen- tration	Temp. (*C)	Phases	lattice parameter	Vickers microhar (load 100 g	
at.% (TiN _z ,x=)	Duration (h)		(nm)	HV ₁₀₀ *	Kg/m²
29.5	1400°C,492h	8	-		2300
(x=0.42)		(8+a)		(±300	Kg/m²)
32.7 (x=0.47)	800°C, 24h 800°C,401h	•	a=0.4945 c=0.3035	(±300	1890
33.7 (x=0.51)	930°C, 23h 750°C, 24h		-	(±600	2510
34.5 (x=0.53)	620°C,0.5h 920°C,0.5h		a=0.4146 c=0.8792	(±400	3130
37.8 (x=0.61)	850°C, 24h 750°C, 24h 750°C,744h	8	a=0.4219	(±400	3210
39.0 (x=0.62)	1300°C,492h	8	a=0.4222	(±400	2970
39.0 (x=0.62)	950°C, 24h	8	n=0.4223	(±400	3130
39.0 (x=0.62)	950°C, 24h 750°C, 48h	1	a=0,4219	{+400	3130
40.0 (x=0.67)	750°C, 24H	8	a=0,4226	(±400	3050

The test load of 100g was chosen in the load range in which the Meyer Law is followed (the slope of the corresponding straight line is about 2 with a correlation coefficient = 0.99). The microhardness depends on nitrogen concentration but is little influenced by heat treatment. By order of decreasing microhardness, the results were ar follows:

 δ phase > δ phase > ϵ phase > α phase

DSC results.

Three alloys of composition 33.8, 34.7 and 35.3 at.% N, all being singlephase δ -TiN_x after quenching , were studied. Figure 2 shows an exemple of DSC curves for the alloy of 33.8 at % N, an exothermal transformation appears only for the first heating cycle.

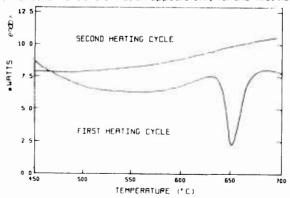


Figure 2 - DSC curves AT 2.5° C min⁻¹ for the alloy of 33.8 at. % N, first and second heating cycles

Table 2 gives the experimental results. With the increase in the nitrogen concentration in these alloys, it will be noticed that for the transition quenched $\delta \to \delta'$ there is an increase in the transformation starting temperature ($\Delta T = 50\,^{\rm o}$ C) and a decrease in exothermal effect. The final structural is single-phase δ' for the alloy of 33.8 at % N and becomes two-phase ($\delta + \delta'$) for higher concentrations. Kinetic problems for the formation of the δ' phase appear at 35.3 at.% N, an exothermal transformation appears for the first and second heating cycles.

TABLE 2. - DSC results at 1.25 and 2.5°C min-1 for the four alloys

Alloy Initial at "" N phase		Heating Transition excle quenched δ • δ and rate			Linal phase	Parameters nm:		
		number Cmin	°C.	θ _M "C	H. T	All Jg		
118	quenched δ	1.25	630	651	680	4(1	۵	a = 0.4142 + 0.880
118	quenched δ	1.1.25	590	615	650	64	ð	a = 0.4142 + 0.8814
34.7	quenched δ	1-1-25	640	661	680	31	8 + 8	$\delta = 0.415 c = 0.880$ $\delta = 0.422$
35.3	quenched δ	1-1-25 2-1-25 3-1-25	600 600		725 700	4	8'+8	$\delta' a = 0.416 c \approx 0.876$ $\delta a \approx 0.4221$

 $[\]theta$, $\theta_{\rm M}$ and $\theta_{\rm I}$ are the initial, maximum and final temperatures of the DSC peak respectively. ΔH is the transition enthalpy

If Kissinger's method is applied to these results obtained at only two rates, the activation energy of the transformation is evaluated as 114 \pm 1 kJ mol-1.

DTA results.

In order to pursue our investigation at higher temperatures, two alloys were studied by DTA, one of 34.7 at % N, the other of 35.3 at.% N. The heat cycle rates were identical within \pm 3°C min⁻¹. Figure 3 shows DTA curves and Table 3 gives the results.

TABLE 3 - DTA results for alloys of 34 and 35.3 at % N

Concentration at ⁰ n N :	Quenched 8 . 8			8' →1 +8			1+0+0		
	θ,	$\theta_{\rm M}$	θ_i	$\boldsymbol{\theta}_{i}$	$\theta_{\rm M}$	θ_{i}	θ	$\theta_{\rm M}$	$\theta_{\rm r}$
34.7	700	730	790	800	905	9 1	800	740	635
15 3	650	720	780	780	830	850		40.0	

 $[\]theta$, θ_M and θ_t are the initial, maximum and final temperatures of the DTA peaks respectively

34.7 at.% N alloy: On heating an exothermic peak spreading from 700 to 790°C corresponding to the transition quenched $\delta \to \delta'$, can be seen, along with an endothermic peak from 800 to 913°C corresponding to transition into the two-phase domain $\delta + \epsilon$. On cooling, only one exothermic peak is observed from 800 to 635°. It corresponds to the reappareance of the δ' phase.

35.3 at.% N alloy: On heating two successive peaks can be seen, but they are of smaller amplitude than those of the preceding alloy. On cooling no peak is observed.

The transition of quenched $\delta \to \delta'$ appears, for the three alloys as an irreversible exothermic phenomenon. The δ' phase, thus, has a lower free energy than the quenched phase. The quenched $\delta \to \delta'$ transition is complete for 33.8 at % N, whereas it is incomplete for higher concentrations. The decrease in the transition peaks in DSC and DTA with the increase in concentration shows that the proportions of the δ and δ' phases are certainly functions of the concentration. The peritectic corresponding to the reaction $\delta' \Leftrightarrow \epsilon + \delta$ can be drawn at $800 \pm 10\,^{\circ}\text{C}$.

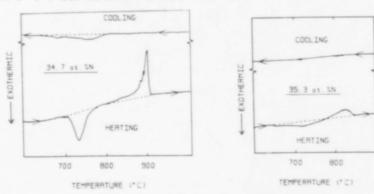


Figure 3 - DTA heating and cooling curves

Sectural and metallographic study, phase equilibrium at 750 and 950°C

The equilibrium of the δ , δ ', ϵ and α phases were studied during heat treatments under ultrahigh vacuum.

Isotherm 750° C, TT1, 48 h.

The graph temperature vs concentration (fig.4) shows the experimental results. The proportion of transformation quenched $\delta \to \delta'$ varies linearly with concentration in the concentration range 33.8-38 at.% N. Two micrographs (fig. 5 and 6) show the δ' phase in two alloys.

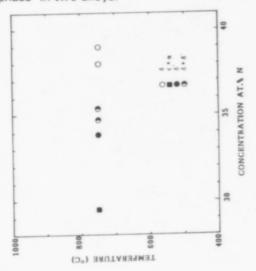




Figure 4 - Phase diagram after annealing at 750° (TT1). Figure 5 - 33.8 at.% N alloy after annealing at 750°C. Surface examination of the sample, which is completely δ' phase, active under polarized light (Very fine needles are formed along several preferred directions)

1 993

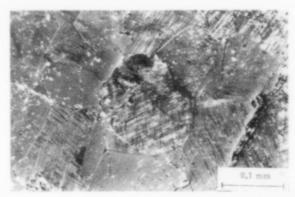


Figure 6 - Alloy of 35.3 at.%N after annealing at 750°C for 48h. Inside the primary grains of the δ phase, the δ ' phase, active under polarized light, has developed as very fine needles along preferred directions. The grains are not all occupied by the δ ' phase.

Isotherm 950°C, TT2, 24h.

The structural state of the samples annealed at 950°C after quenching, gives information on the different phases present at this temperature (Figure 7 and Figure 8) : at 29.5 at. % N, ϵ and α ;

at 33.8 at. % N, ϵ and δ ;

from 35.3 at. % N and above, δ .

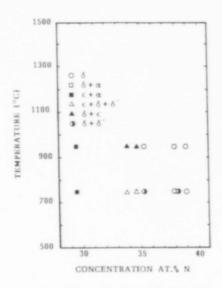




Figure 7 - Phase diagram for isotherms 950°C (TT2) and 750°C (TT3)

Figure 8 - 34.7 at % N alloy after annealing at 950°C, surface examination of the sample, Micrographic structure is in a state of granular reorganization ε + δ along the previous δ ' needles.

Isotherm 750°C, TT3

This series of heat treatment cycles (950°C for 24h, with a rapid return to ambient conditions followed by annealing at 750°C for about 330h) gives information on the structure at 750°C, of equilibrated alloys $\delta + \varepsilon$ of known characteristics (fig 7).

The different phases present are as follows:

35.3 at. % N to about 38.3 at. % N: the samples are two-phase δ + δ ', and beyond this limit the samples are single phase δ ;

33.8 to 34.7 at. % N: the samples are three-phase $\varepsilon + \delta + \delta'$ with a majority of ε ; 29.5 at. % N: they are two-phase $\varepsilon + \alpha$ with majority of ε .

In no case has a structural state with a majority of δ' been observed.

Comparing the structural results of the two cycles of heat treatment carried out at 750° C, for samples having the same concentration, the phases obtained are different. The proportions of δ' vary according to the original structure and remain constant (about 15%) after heat treatment of type TT3.

The fact that a three-phase domain $\epsilon + \delta + \delta'$ is found for an annealing time of 330 h at 750°C reveals an important kinetic problem [4]. Formation of ϵ from δ is a reconstructive transformation associated with nucleation problems probably due to the generation of interfaces of high interfacial energy. These factors greatly slow down the low-temperature transformation rates.

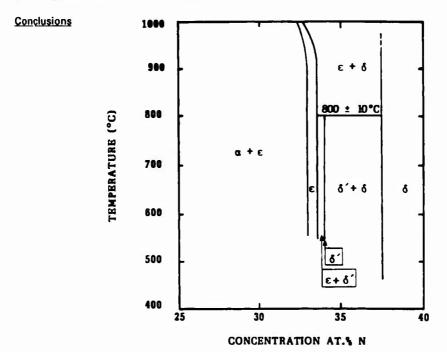


Figure 9 - Partial Ti-N diagram

Fig(9) gives the partial TI-N diagram corresponding to the present results. The δ' phase, which is an equilibrium phase, splits up on a peritector at 800°C \pm 10°C according to the reaction $\delta' \Leftrightarrow \epsilon + \delta$. For temperature under 800°C, the δ' phase separates two-phase regions : the first, $\epsilon + \delta'$, is located between 33 and 33.8 at % N, the second, $\delta' + \delta$, between 33.8 and 38 at. % N. The only important disagreement with Arbuzov's diagram [8] concerns the position of the δ' phase, which he situates at 37.5 at. % N and which we find at 33.8 \pm 0.5 at. % N.

References

- 1. G. Lobier and J. Marcon, C.R. Acad. Sci., Ser. C, 268 (1969), 1132-1135.
- 2. H.A. Wriedt and J.L. Murray, Bull. Alloy Phase Diagrams, 8(4) (1987), 378-412.
- A.N. Christensen, A. Alamo and J.P. Landesman, <u>Acta Crystallogr.</u>, C41 (1985), 1009-1011.
- 4. W. Lengauer and P. Ettmayer, High Temp. High Pressures, 19(1987) 673-676.
- E. Etchessahar, J.P. Bars and J. Debuigne, <u>J. Less-Common Met.</u>, 134 (1987), 123-129.
- 6. E. Gebhardt at al., J. Nucl. Mater., 4(3) (1961), 241-254.
- 7. Y.U. Sohn, <u>Thesis</u>, Rennes, November 27, 1989, no. Identification National 891 ISAR 0006.
- M.P. Arbuzov, S. Ya. Golub and B.V. Khayenko, <u>inorg. Met.</u> 13 (10) (1977, 1434-1437.

THE ELECTROPLATING OF TITANIUM

FROM NaCI-KCI FUSED SALT

Shuzhen Duan, Ying Kong, Zhiyu Qiao, Xuefan Gu.
University of Science and Technology Beijing, Beijing 100083, China.

ABSTRACT

The electrochemical reduction and electrodeposition process of titanium metal from NaCl-KCl molten salt have been studied by cyclic voltammetry and chronoamperometry. It has been confirmed that the reduction of Ti subchlorides are stepwise as: $Ti^{3+} + e = Ti^{2+}$, $Ti^{2+} + 2e = Ti$ and electrochemically reversible. The diffusion of titanium ions is rate-controlling. The deposits of Ti have been found to partially diffuse into Pt or Fe substrates.

The electrodeposition of Ti metal undergoes instantaneous three dimensional nucleation nucleation and growth of hemispherical nuclei controlled by diffusion of ions in the melt. It could be used to optimise electroplating process of titanium. On this basis, high quality titanium coatings have been obtained by using the high frequency pulse potentiostatic technique.

Titanium '92 Science and Technology Edited by F.H. Froes and I. Caplan The Minerals, Metals & Materials Society, 1993

INTRODUCTION

Titanium and its alleys are widely used as important materials due to their high melting point, low specific gravity, corrosion resistance and high strength. Electroplating of titanium onto various substrates may offer combined properties of Ti and substrate materials. Hence the electroplating of Ti is an efficient method to more effectively utilize Ti metal. Recent studies have dealt with electrodeposition of Ti from molten salts because Ti could not be deposited from aqueous solutions. Electrodeposition processes in molten salts are generally rate—controlled by diffusion of ions and result in dendritic deposits. The practical experience of molten salt electroplating shows: Due to the influence of concentration polarization, the irregular profile produced is unavoidable in molten salts electroplating under constant current density⁽¹⁾. In molten salt electroplating, it is hard to find the complex smoothing and leveling agents which may be used to control the quality of coated layers. Thus, operation under charge—transfer (kinetic) control, or control of initial stage of nucleation and growth may be a prerequisite for obtaining coherent deposits of Ti metal⁽⁴⁾.

The present investigation was undertaken to determine how far cathodic reduction of Ti ions occurs, and to characterize the nature of electrodeposition of Ti metal from NaCl-KCl(1:1mol%) molten salt by cyclic voltammetry and chronoamperometry. Based on these studies, it is easy to find out the relation of the forms and properties of titanium deposits prepared under well defined electrochemical conditions, and use this to optimise the properties of electroplate.

EXPERIMENTAL

Experiments were performed in a stainless steel cell. The NaCl and KCl salts used were of analytical purity. The electrolyte NaCl-KCl (1:1mol%) was contained in an inner alumina crucible and dehydrated under vacuum prior to use as temperature was gradually raised to 480°C, then the mixture continued to be melted at 720°C under an argon atmosphere. It was followed by preelectrolysis using a graphite rod electrode until the residual current was less than 0.5mA/cm². Titanium subchlorides were prepared by the reaction of Ti metal with liquid titanium tetrachloride in a NaCl melt at 700°C.

The potentiostatic circuit consisted of a three-electrode system, Potentiaostat SHD-1. XY and an recorder. The reference electrode was Ag/AgCl-(NaCl-KCl)(1) which was shielded from the electrolyte by a porcelain sheath. The working electrode was a Pt flag or a pure iron sheet, and the counter electrode was a graphite rod. A Pt wire and low carbon steel wire were used as working electrode, pure titanium sheet as a counter electrode, and a Ti wire as reference electrode during chronoamperometric experiments. Because of disproportionation of Ti subchlorides, electrochemical measurements should be carried out after the establishment of equilibrium between Ti metal, Ti2+ and Ti3+, which was determined by measuring the electrode potential⁽¹⁾ $E_{\tau_i^{1+}/\tau_i^{1+}}$ vs. Ag/Ag(I) reference potential.

In electroplating, the working electrode is made of low carbon steel wire, the coun-

ter electrode is a pure titanium plate, and the reference electrode is of a pure titanium wire. A Mo rod was used as an indicating electrode, an Ag/AgCl for the reference electrode, for measuring the average valance of the system. The low carbon steel rod used as the substrate of electroplating must be polished in a stepwise fashion using metallographical sand—paper of different grades.

The electrolyte NaCL: KCL (1:1 mol) containing low-valance titanium salt, (under sat. Ti sponge conditions) is maintained for 4 hours to achieve equilibrium. When the average valance falls below 2.35, the electroplating can proceed. At this point, the electrolyte contains 4.4 wt% TiCl₂ and 2.0 wt% TiCl₃.

RESULTS AND DISCUSSION

The Study of Electrochemical Process

Fig.1 represents typical voltammogram obtained after addition of Ti subchlorides to the NaCl-KCl melt. There are two reduction waves (a,b) and three reoxidation waves (c, d, and e) when the potential scan is reversed.

Peak potentials E_{p}^{a} and E_{p}^{b} , and half-peak potentials $E_{p/2}^{a}$ and $E_{p/2}^{b}$, are virtually unchanged with increasing scan rate ν , indicating that both reduction processes are reversible⁽²⁻³⁾. The cathodic current peaks I_{p}^{a} and I_{p}^{b} increase linearly with an increase in (scan rate)^{$\frac{1}{2}$} at various concentrations as shown in Fig. 2. Both reduction processes are diffusion—controlled⁽⁴⁾.

A half-peak potential for a soluble product under reversible condition is given by the equation:

$$E_{n/2} - E_n = 2.20RT / nF \tag{1}$$

According to equation (1), electron numbers n_a and n_b of electrode reactions for Ti^{2+} and Ti^{3+} , respectively, were calculated as $n_a = 1.27$ and $n_b = 2.07$. The results show that cathodic reduction of Ti subchlorides undergoes two steps: $Ti^{3+} + e = Ti^{2+}$ and $Ti^{2+} + 2e = Ti$. The deposition titanium metal can dissolve into the Pt substrate and form a Ti - Pt alloy. (5).

Typical current-time transients obtained for electrodeposition of Ti onto Pt electrode is presented in fig.3. The currents did not simply decay with time, but increased again after rapidly decreasing. This is characterisitic of nucleation and growth of nuclei.

The I VS. $t^{\frac{1}{2}}$ relationship corresponding to rising sections of current-time profiles under various overpotentials shows linear dependence with increasing slopes(fig.4). It obeys the kinetic equation for instantaneous nucleaction^(6,7) followed by growth of three dimensional nuclei under ions mass-transfer control:

$$i = ZF\pi N_0 (2DC)^{\frac{3}{2}} M^{\frac{1}{2}} l^{\frac{1}{2}} / \rho^{\frac{1}{2}}$$
 (2)

where ZF is the molar charge of depositing species, D is its diffusion coefficient, C its concentration in mol cm⁻³, M its molecular weight and ρ its density. Hence, the electrodeposition of Ti onto Pt electrode presents instantaneous nucleation features.

The slopes of $I - t^{\frac{1}{2}}$ lines increases with increasing overpotentials a...d indicates that nucleation rate and nucleation densities are very sensitive to the magnitude of overpotentials, Nucleation densities increase with increasing overpotential, and the crystallites become finer.

This chronoamperommetry study reveals that electrodeposition of titanium undergoes an initial stage of nucleation and growth of nuclei under proper overpotentials. Therefore, it is possible to obtain the maximum nuclei density by controlling overpotentials in order to produce a coherent, dense and adherent deposit of Ti metal.

The Electroplating of Titanium

a. Constant Potential Electroplating

The constant potential electroplating means an over potential is continuously maintained during the process of electroplating. The results from investigating of electrodeposition show that it is the same for the Ti deposition as that for other metals, and that a critical nucleation overpotential exists. The constant potential must be higher than the critical nucleation potential.

The metallograph shows that if the overpotential is under constant potential electroplating, a branch style crystal is observed. If it is cleaned by dilute sulphuric acid, the loose branch style crystals will be lost, in which only a thin uniform layer near the substrate is left, as shown in Figure 5. The thickness of the coated layer abtained from the process of constant potential method is rather thin $(5 \sim 6\mu)$.

b. Pulse Potential Electroplating

Two types of pulse electroplating have been used. One is with low frequency pulse, or in other words, the time interval for nucleation is about several seconds. The other is with higher frequency, that is 10^{-2} - 10^{-4} sec.for nucleation.

1. Low Frequency Pulse Electroplating

After each nucleation, the potential on electrode drops to zero (relative to Ti reference electrode), hence no nucleation occurs on the electrode, about 20mA Jissolving current is proceeded, the concentration of Ti ions on the surface of electrode is increased, this will be benificial to the nucleation for the next pulse. After the pulse sustains a period, the layer near the substrate with partial branch style crystal components evidently reduces, and the rate of covering is increased clearly (Fig.6). In low frequency pulse electroplating, when $\eta_1 = -350$ to -500mv, t = 2sec. or 3sec, $\eta_2 = 0$, the time for on and off ratio $t_1/t_2 = 2:1$ or 1:1, and after several pulses, the coated layer on the substrate has rather good cohesion and high covering rate.

2. Higher Frequency Pulse Electroplating

Many papers indicate that pulse electroplating can produce high quality coating which are much better than these from direct current electroplating. Not only is the crystallization of the coating fine, the grain of crystal small, and the holes on the coating reduced, but also impurities in the coating largely reduced. Thus, the purity of the layer

is enhanced, and corrosion resistance is improved.

In our experiments, square—wave voltage pulses are used, in which t_1 and t_2 are all in the range of 10^{-2} – 10^{-4} sec.. Fig. 7 shows that the good covering rate and fine structure of the coating can be obtained near the substrate under conditions of: $\eta_1 = -350 \sim -500$ mv, $\eta_2 = 0$, $t_1 = 10^{-2}$ – 10^{-4} sec, and an on / off ratio $t_1 / t_2 = 1$:1: or 2:1.

The Characteristics of Coating

The covering rate of a coating is the criteria of the quality of the layer. Fig.8, which corresponds to Fig.7 represent the topographs of coatings. These pictures show that the grain sizes on the surface are uniform, no holes are present and a better covering rate was achieved. The energy spectrum obtained from a scanning electromicroscope indicated that the coating is pure Ti metal. (Figure 9).

CONCLUSIONS

- 1. The electrolytic reduction process of titanium ions in NaCl-KCl melt, at 720°C, has been studied by cyclic voltammetry. The results indicate that the cathodic reduction of Ti(|||) and Ti(|||) are Ti(|||) +e = Ti(|||) and Ti(|||) +2e = Ti, and both reductions are diffusion controlled.
- 2.The electrocrystallization of titanium has been studied by chronoamperometry. The chronoamperogram showed that the deposition process of Ti involves instantaneous three dimensional nucleation followed by growth of nuclei contolled by diffusion of ions in the melt.
- 3. The method of constant potential or the method of pulse electroplating can produce a fine structure Ti coating on low carbon steel substrate for NaCl-KCl (1:1 molar radio) molten salt system under 700°C. The stability of the experiment, the uniformity of the coating, and the covering rate obtained by the pulse electroplating are better than those associated with the constant potential method. Fine structure crystals can be achieved at the beginning stage of nucleation in NaCl-KCl-4%TiCl₂-2.2% TiCl₃ at 700°C under the following two sets of conditions.

a.low frequency

 $\eta_1 = -350$ mv ~ -500 mv, $\eta_2 = 0$, $t_1 = 2-3$ sec, and $t_2 / t_1 = 1:1$ or 1:2. b.higher frequency

 $\eta_1 = -350 \text{mv} \sim -500 \text{mv}, \quad \eta_2 = 0, \quad t_1 = 10^{-2} - 10^{-4} \text{ sec, and } t_2 / t_1 = 1:1 \text{ or } 1:2.$

REFERENCES

- (1) Qiao Zhi yu, Li Guo Xun, Rare Metals, No.3, 1980, P88
- (2) F.R.clayton, G.Mamantov, D.L. Manning, J.Electrochem. Soc., vol.120, No.9, 1973, 1193-1199
- (3) R.S.Nicholson and I.Shoun, Analytical chemistry, vol.46, No.4, 1964, 706-723
- (4) P.Delahay, New Instrumental Metals in Electrochemistry Interscience, New york 1954
- (5) Yang Yi Qin, Rare Metals, vol.1, No.1, 1982, 38-44

- (6) G.J.Hills, et al, Electrochem Acta, 19, 1974, 657-670
- (7) F.Lantelme and J.Chevalet, J. Electroanal. Chem., 121, 1981, 311-327
- (8) S. Duan, G. Zhao, Rare Metal, No5, 1987, P376.
- (9)K.I. Popov et al, Surface Technology, 6, 287~300(1978).

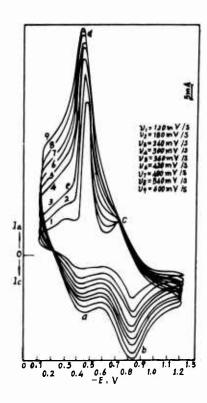


Fig.1. Typical Voltammogram obtained using a Pt electrode ($A = 0.24cm^2$)

T i C 1₂ = 0 . 7 0 % w t ,

TiCl₃ = 0.44%wt.

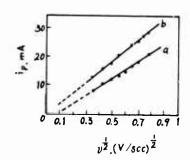


Fig.2. Plots I_p^a , $I_p^b - v^{1/2}$ (Pt electrode)

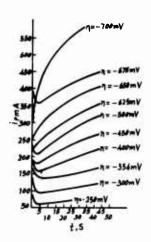


Fig. 3. Chronoamperograms for the reduction of titanium ions in NaCl-KCl at 700°C (TiCl₂ 4.0%wt, TiCl₃ 2.2%wt, Pt electrode, S=0.016cm, vs. Ti⁺²/Ti⁺³)

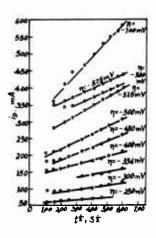


Fig.4. I_p vs. t^{1/2} plots for the growth of titanium nuclei on a Pt electrode.

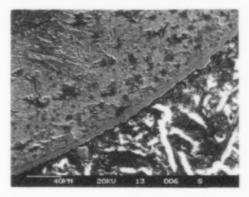


Fig. 5. Transverse section of Ti coating (375x), constant potential electroplating. $\eta_1 = -300 \text{mv}$, t = 10 min.

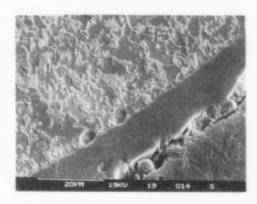


Fig.6. Transverse section of Ti coating (1400x) Low frequency pulse electroplating. $\eta_1 = -400 \text{mv}$, $\eta_2 = 0$. $t_1 = 3 \text{ sec}$, $t_2 = 1 \text{ sec}$.

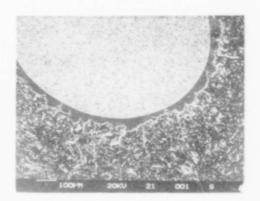


Fig.7. Transverse section of Ti coating (100x) High frequency eletroplating $\eta_1 = -350 \text{mv}$, $\eta_2 = 0$, $t_1 = 3 \times 10^{-4} \text{sec}$, $t_2 = 2 \times 10^{-4} \text{sec}$. Electroplating time 30 min.

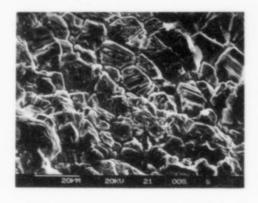


Fig.8. Topograph of coating (1100x)

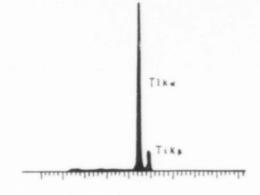


Fig.9 Energy spectrum of the coating surface

THE STRENGTHENING OF FRICTION UNIT PARTS PRODUCED

OF TITANIUM ALLOYS BY EXPLOSIVE COATINGS

Vitaliy Goldfine, Irshat Galeev, Victor Ignatov, Stal Ushkov

Central Researcgh Institute of Structural Materials

Sankt-Petersburg, 193167, Russia

Abstract

The paper deals with tensile properties increasing methods by oxide coatings the results of selection crating composition, based in ${\rm Al}_2{\rm O}_3$. The features of coating formation, their structural, phase and stressed state are established.

The explosive oxide coatings are applied to increase the life of shaft and seals, support and stop pump beartigs gears, engines and other products of titanium alloys.

Introduction

The titanium alloys are known to have low inherent tribotechnical characteristics limited by the sensitivity of the titanium to friction contact adhesion. There exist several methods to increase the wear resistance of the titanium alloys. The paper deals with the tribotechnical characteristics of the explosive oxide coatings applied on the specimens of the titanium alloys. The aluminium oxide coatings are charactrized by a high wear resistance, corrosion resistance and can be applied in various friction units, operating in agressive media.

The coatings of 0,3 - 0,5 mm in thickness were applied by the explosive spraying performed on explosive facilities "Prometey". The distance of spraying is 150 - 160 mm. The spraying was performed on the specimen surface, pretreated by an abrasive-jet method up to $R_z = 20 - 30 \, \mu$ m. To increase the cohesion strength of the oxide coating Cr_2O_3 and TiO_2 were added to the coating (up to 10 % by weight) electrocorund ($\mathcal{A}-Al_2O_3$) of particles ranging spraying coating. It was established that the chromium and the titanium additions reduce the porosity of the oxide coatings and increase the hardness. The cooling rate of the coating material ranges to $10^7 - 10^5$ grad/s and because of this at the time of crystalization a non-equilibrium $\mathcal{X}-Al_2O_3$ phase is formed in the coating. The \mathcal{A} -ray structural studies show that the oxide coatings with maximum cohesion strength contain up to 95 % of $\mathcal{X}-Al_2O_3$, the balance is $\mathcal{X}-Al_2O_3$. The chromium oxides in the form of an individual phase isn't observed in the coating. When spraying the chromium oxide dissolves in Al_2O_3 and the spectrum analysis of electron-paramagnetic resonance indicates,

Titanium '92 Science and Technology Edited by F.H. Froes and I. Caplan The Minerals, Metals & Materials Society, 1993 that the dissolution occurs in $\mathcal{A}-\text{Al}_2\text{O}_3$, preferentially. The chromium oxide at the spraying is reduced partially to a metallic chromium. The titanium oxide in the form of rutile and brukite modifications were observed in the coating, applied by the spraying of the appropriate mixture.

The microhardness of the coatings loaded by 50 g changes in the range of 10 - 13 GPa. The adhesion strength of the coating was evaluated by pin method in dependence of the spraying parameters. It amounts to 35 - 40 MPa for the $\mathrm{Al_2O_3}$ + $\mathrm{Cr_2O_3}$ coatings 30 - 32 MPa for the $\mathrm{Al_2O_3}$ + $\mathrm{TiO_2}$ coatings. The tribotechnical properties were studied on precision friction machine. The friction on the machine is established between the end surface of the three columns of 5 mm in diameter and the end of the ring with diameter of 52 x 32. The following homogeneous friction pairs were investigated: explosive coatings 1) $\mathrm{Al_2O_3}$ + $\mathrm{Cr_2O_3}$; 2) $\mathrm{Al_2O_3}$ + $\mathrm{TiO_2}$; 3) $\mathrm{Al_2O_3}$ (Table 1). The wear resistrence in the range of the three columns of 5 mm in diameter and the end of the ring with diameter of 52 x 32.

Table 1 The test results obtained on precision friction machine with friction rate of 0,25 m/s and friction length of 5 km

The material of coating	Friction parameter lubrication pressure,	Friction coefficient	Wear criteria I x 10°, 1/MPa	
Al ₂ O ₃ Al ₂ O ₃ + Cr ₂ O ₃ Al ₂ O ₃ + TiO ₂ Al ₂ O ₃ + TiO ₂ Al ₂ O ₃ + Cr ₂ O ₃	Water 5.0 Water 1.0 Water 2.0 Water 10.0 Water 20.0 Dry 2.0 friction	0.26 - 0.87 0.06 - 0.30 0.06 - 0.19 0.43 - 0.60 0.27 - 0.55 0.37 - 0.81	0.54 0.23 0.18 0.17 0.14 1.80	

tance, friction coefficient and working surface condition were used as the criterions of estimation of the capacity for work with friction. The wear resistance was evaluated by direct measurements of the wear by vertical comparator with scale division of 0.1 $\mu\rm m$. The relative wear criteria, I $_{\rm o}$, is obtained by the formular:

$$I_0 = \frac{\Delta h}{Q \cdot L}$$
,

where h is a linear wear, sm,

q is a pressure, MPa,

L is a friction length, sm.

The tests on the precision friction machine indicate that the explosive coatings based on ${\rm Al}_2{\rm O}_3$ modified by ${\rm Cr}_2{\rm O}_3$ and ${\rm TiO}_2$ additions are characterized by a higher carrying capacity and wear resistance compared to the coatings of the pure ${\rm Al}_2{\rm O}_3$. It is of note, that after the tests the friction surfaces of the specimens were operable, have no surface damanges and a roughness of the surface was improved approaching to that of the polished surface. The Figure 1 shows the data of the relative wear resistance of the explosive coatings and oxidized titanium specimens of the Ti + 5 % Al alloys. It is obvious that the explosive coatings not the common thermal oxidizing allow to rise the tribotechnical properties of the parts of the friction units of the titanium alloys appreciably and to expand the application range of the titanium alloys in the machinebuilding.

The developed coatings were applied to increase the surface life of the products with the friction units in the form of sliding ball-bearings and movable seals and also to harden the seals of the fifting gates. They provide the surface life up to 60 000 hours, the pressure up to 20 MPa, the friction

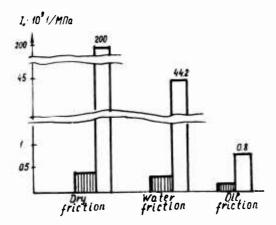


Figure 1 The comparative wear resistance of the explosive coatings and of the oxidized titanium in the homogeneous friction pairs.

rate up to 60 m/s.

SURFACE HARDENING OF Ti-6Al-4V ALLOY BY ELECTROCHEMICAL HYDROGENATION

Tair I Wu
Department of Materials Engineering, Tatung Institute of Technology
Taipei, Taiwan 10451, R.O.C.

Pee Yew Lee and Jiann Kuo Wu Department of Marine Engineering, Materials Program National Taiwan Ocean University Keelung, Taiwan 20224, R.O.C.

Abstract

Surface hardening of Ti-6Al-4V alloy can be performed by electrolytic charging in an acid and a basic solution, with or without subsequent solution treatment, and followed by dehydrogenation to obtain equiaxed a grains in transformed β matrix. Surface hardnesses of the processed specimens show better than that of the mill-annealed specimen. The depth of hardened layer depends on the processing parameters.

Introduction

The absorption of hydrogen cause serious damage in titanium alloys, but proper usage of hydrogen as a temporary alloying element can bring surprising beneficial for some materials. By adding an adequate amount of hydrogen to some titanium alloys, the forging and superplastic forming temperature of which can be lowered (1, 2), the microstructure of which can be modified (1-6), which has been adopted by aerospace industry to refine the coarse and dendritic microstructure thus to improve the mechanical properties of titanium casting parts (7-9). This developed technique route to modify microstructures of titanium net-shape products which are impossible to achieve by using conventional thermomechanical treatment. Thermal charging is not the only way to hydrogenate Ti-6Al-4V alloy. In this study, hydrogenation was carried out to improve surface hardness by various aqueous cathodic polarization. Comparisons of microstructure and hardness changes between various processing parameters are reported.

Experimental Procedures

Material

The material used in this study was received in the mill-annealed conditions. The chemical composition is analyzed and given in the Table 1. Round bar stock with 13mm in diameter were firstly β -solution treated at 1000°C in a vacuum of 2×10^{-4} Pa and furnace cooled to room temperature. Specimens were cut from the treated bar to 3mm in thickness.

Thermochemical Processing

Titanium '92 Science and Technology Edited by F.H. Froes and I. Caplan The Minerals, Metals & Materials Society, 1993

Thermochemical treatment and processing parameters are shown in Figure 1 and Table 2. The processing parameters were grouped from S1 to respectively. S13 to S16 had been performed earlier at our laboratory and the experimental results had been published (10, 11), which are listed here for the comparison. Specimens were ground with 320 grade abrasive paper, ultrasonic cleaned, cathodically charged with 1mA/cm2, at 15°C in 1N NaOH and 1N H₂SO₄ for 24 and 48 hours with or without 1g/liter thio-urea, respectively; then they were removed from the electrolyte, cleaned with deionized water, acetone and dried with pressurized air. The specimens were subsequently dehydrogenated in a tubular furnace in an argon atmosphere to 760°C. The furnace was them pumped to a vacuum of 2×10⁻⁴ Pa and the temperature was held at 760°C for 1 hour. Then the power was turned off, the vacuum system was kept running during furnace cooling to room temperature. To compare the effects of low temperature annealing on grain refinement, specimens with 48 hours charging (S9-S12) were subjected in an air furnace at 200°C for 3 hours and followed by forced air convection, then they were placed in a vacuum furnace to perform the same dehydrogenation treatment.

Microscopy

Specimens prepared for metallographic observations were ground down to 1000 grade SiC paper, polished with $1\mu m$ Al₂O₃ powder and them etched with Kroll's reagent.

Microhardness

The microhardness tests were conducted with a Matsuzawa MXT50 digital microhardness tester under a load of 100g.

Results and Discussion

Typical microstructures of mill-annealed Ti-6Al-4V alloy are shown in Figure 2. Figure 3 shows the optical micrographs of β -solution treated specimen with grain size more than 2mm. Figure 4 shows the cross sections of the microstructure after various cathodic charging and following different heat treatments. The detailed processes and refined layers are summarized in Tables 2 and 3. Equiaxed a grain layer is observed near the surface. The thicker and more uniform refined layer is found after the cathodic charging in 1N H₂SO₄ or longer time in 1N NaOH with promoter, due to the higher hydrogen permeation rate. A typical surface microstructure of the processed specimen is shown in Figure 5 (a). Some poor surface refined conditions were performed in alkaline solution, of which a typical photomicrograph is shown in Figure 5 (b). Phillips et al. (12, 13) reported the hydrogen absorption rate in titanium was extremely low in alkaline solutions, and the thicker hydride layer can be found in acid solutions. The thicker refined layer of titanium alloy (S4, S8, S13-16) in acid solution with promoter can be emphasized as the higher absorption rate of hydrogen. The refined layer of specimen (S1-S8) show higher thickness than those (S9-S12) with low temperature annealing treatment, and also show higher hardness than those (S13-S16) with high temperature annealing treatment. The thinner or less hard surface layer can be explained as that hydrogen diffuses in the alloy and cause a less concentration of hydrogen near the surface. The depth of the hardened surface layer depends on the charging current density, charging time, temperature, pH of solution, promoter and subsequent heat treatment.

Conclusion

Surface hardening of Ti-6Al-4V alloy can be achieved by electrochemical charging, subsequent solution treatment, followed by dehydrogenation to

obtain an equiaxed σ grain in transformed β matrix. The hardness and depth of the surface layer depends on the processing parameters.

Acknowledgements

The authors are grateful for financial support of this research by the National Science Council under Grant No. NSC 81-0405-E019-04.

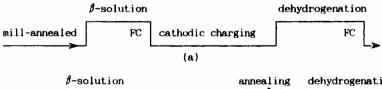
References

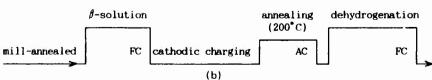
- H.Kimura and O.Izumi, eds., Titanium'80, Science and Technology (Warrendale, PA, TMS-AIME, 1980), 2478.
- D. F. Hasson and C. H. Hamilton, eds., Advanced Processing Methods for Titanium (Warrendale, PA, TMS-AIME, 1982), 115.
- J. M. Capus and D. L. Dyke, eds., Progress in Powder Metallurgy, vol. 37 (Princeton, NJ, MPIF, 1982), 289.
- F.H. Froes and D. Eylon, eds., Titanium Net Shape Technology (Warrendale, PA, TMS-AIME, 1984), 145.
- A. W. Thompson and N. R. Moody, eds., Hydrogen Effects on Materials Behavior (Warrendale, PA, TMS-AIME, 1990), 273.
- Behavior (Warrendale, PA, TMS-AIME, 1990), 273.

 6. F. H. Froes et al., "Thermochemical Processing of Titanium Alloy," JOM, 42(3) (1990), 26-27.
- G. Lutjering et al., eds., Titanium Science and Technology (Oberursel, West Germany, DGM, 1985), 2107.
- 8. C. V. White et al., eds, High Integrity Castings (Metals Park, OH, ASM International, 1988), 3.
- 9. C. F. Yolton and F. H. Froes, U.S. patent 4,219,357, Aug. 26, 1980.
- T.I. Wu and J.K. Wu, "Surface Hardening of Ti-6Al-4V Alloy by Hydrogenation," Scripta Met. et Mat., 25, (1991), 2335-2338.
- 11. T. I. Wu et al., "Surface Modification of Ti-6Al-4V Alloy by Electrochemical Hydrogenation at 353K," Tatung Journal, 21, (1991), 195-200.
- 12. I. I. Phillips et al., "Hydride Formation during Cathodic Polarization of Ti-I. Effect of Current Density on Kinetics of Growth and Composition of Hydride," Corrosion Science, 12, (1972), 855-866.
- 13. I. I. Phillips et al., "Hydride Formation during Cathodic Polarization of Ti-II. Effect of Temperature and pH of Solution on Hydride Growth," Corrosion Science, 14, (1974), 533-542.

TABLE I. CHEMICAL COMPOSITION OF THE AS-RECEIVED ALLOY (wt%)

İ	Al	V	С	Fe	0	N	Н	Ti
	6.48	4.27	0.044	0.204	0.16	0.012	0.0079	balance





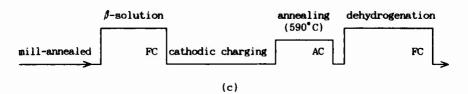


Figure 1. schematic diagram of designed thermochemical treatment (a) without annealing, (b) with 200°C annealing and (c) with 590°C annealing

TABLE II. THERMOCHEMICAL PROCESSING PARAMETERS PERFORMED IN THIS STUDY

Specimen No.	\$\beta\text{-Solution} \text{Treatment} (\cdot C/hrs)	Cathodic Charging (solution/°C/hrs mAcm ⁻² /promoter)	Annealing (°C/hrs)	Vacuum Dehydrogenation (*C/hrs)
			(C/ILS)	
S1	1000/0.5	NaOH/15/24/1/X		760/0.5
S2	1000/0.5	NaOH/15/24/1/P		760/0.5
S 3	1000/0.5	H ₂ SO ₄ /15/24/1/X		760/0.5
S4	1000/0.5	H ₂ SO ₄ /15/24/1/P		760/0.5
S5	1000/0.5	NaOH/15/48/1/X		760/0.5
S6	1000/0.5	NaOH/15/48/1/P		760/0.5
S7	1000/0.5	H ₂ SO ₄ /15/48/1/X		760/0.5
S8	1000/0.5	H ₂ SO ₄ /15/48/1/P		760/0.5
S9	1000/0.5	NaOH/15/48/1/X	200/3	760/0.5
S10	1000/0.5	NaOH/15/48/1/P	200/3	760/0.5
S11	1000/0.5	H ₂ SO ₄ /15/48/1/X	200/3	760/0.5
S12	1000/0.5	H ₂ SO ₄ /15/48/1/P	200/3	760/0.5
S13	1000/0.5	H ₂ SO ₄ /15/24/50/P*	590/1	760/2
S14	1000/0.5	H ₂ SO ₄ /80/24/50/P*	590/1	760/2
S15	1000/0.5	H ₂ SO ₄ /15/48/50/P*	590/1	760/2
S16	1000/0.5	H ₂ SO ₄ /80/48/50/P*	590/1	760/2

X-without promoter, P-with promoter of 1g/l, P*-with promoter of 5g/l

TABLE III. HARDNESS AND DEPTH OF REFINEMENT FOR VARIOUS PROCESSING

Treatment	Hardness (HV)			Depth of Grain Refinement (#m)	
	Refined Layer	Core	Surface		
mill-annealed		- 330			
β-solution		305	305		
S1	340	280	320	*	
S2	370	280	330	*	
S3	380	280	320	*	
S4	380	280	380	100	
S5	370	280	320	50	
S6	370	280	350	50	
S7	400	280	390	50	
S8	410	280	390	150	
S9	370	280	330	*	
S10	370	280	340	*	
S11	390	280	370	*	
S12	400	280	380	50	
S13	340	290	340	150	
S14	340	320	340	200	
S15	340	320	340	230	
S16	340	320	340	250	

^{*} Refined layer is undetectable due to very thin

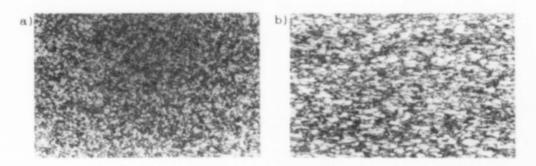


Figure 2. Microstructure of the mill-annealed alloy (a) transverse, (b) longitudinal section

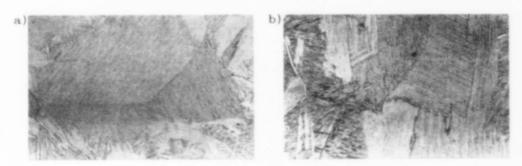
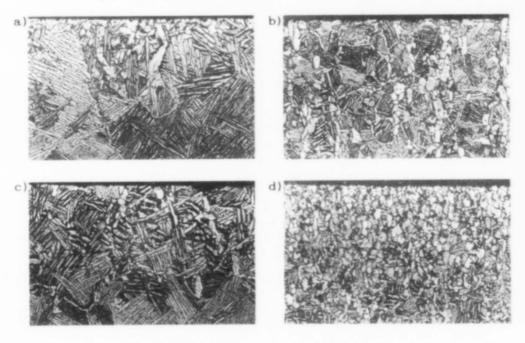
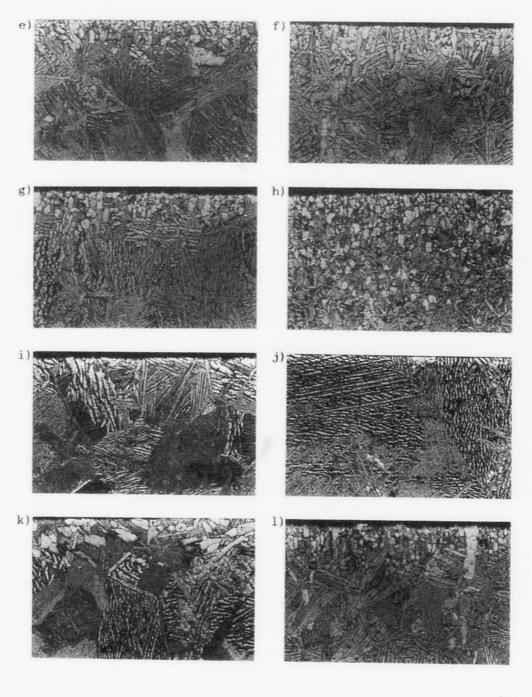


Figure 3. Microstructure of the β -solution treated alloy (a) surface, (b) cross section



80µm



80µm

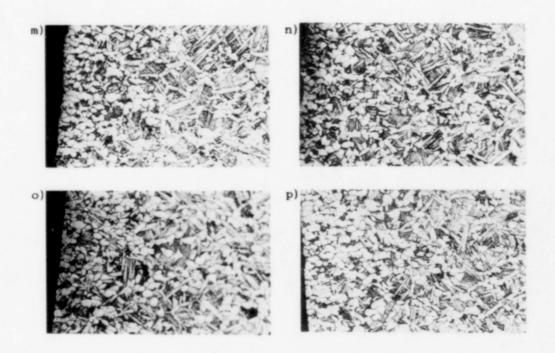


Figure 4. Microphotographs of cross section after TCP (a)S1, (b)S2, (c)S3, (d)S4, (e)S5, (f)S6, (g)S7, (h)S8, (i)S9, (j)S10, (k)S11, (1)S12, (m)S13, (n)S14, (o)S15, (p)S16

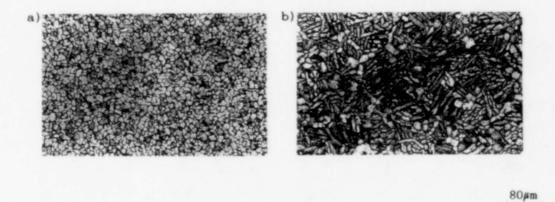


Figure 5. Surface microphotographs after TCP (a) typical refined equiaxed α phase, (b) coarse acicular α phase

Sputter ion plating on Ti6Al4V and Ti (cp) - Preparation and properties of

oxidation and wear resistant coatings

- M. Meyer; R. Suchentrunk, H. Franz; MBB-Deutsche Aerospace,
- P. O. Box 801109, D-8000 Munich 80, Germany
- W. Herr ; E. Broszeit; Institute of Materials Science, Technical University Darmstadt, Grafenstraße 2, D-6100 Darmstadt, Germany

ABSTRACT

For high temperature applications, the common titanium alloys are coated in order to avoid surface embrittlement and crack initiation as a consequence of oxygen penetration and dissolution. Sputter ion plating as a versatile deposition technique was applied. Titanium Ti6Al4V and Ti(cp) were coated with Al, Ni, NiCr, Cr and Cr $_2$ N. Nickel and aluminium form titanium intermetallics rapidly, while chromium and Cr $_2$ N do not. Crack propagation during 3 point bending tests was observed on differently coated Ti6Al4V in the SEM. The results provide information on the mechanical behaviour of the thin layers. The wear tests in a plate-on-cylinder tribometer show a large decrease of wear if the titanium plates were coated by a PVD/galvanic deposition.

Introduction

With respect to high temperature applications most of the common titanium based alloys have to be surface treated. The uncoated surface is sealed by a natural or anodized oxide layer, which protects the titanium base material sufficiently at low temperatures < 400°C. But at high temperatures > 600°C oxygen diffuses quite fast into titanium and favours the enrichment of the brittle α -phase in the α + β alloys 1). This embrittlement of the surface initiates cracks (see Fig. 5c) and is detrimental to the base material, especially for thin-walled structural elements. Even at low temperatures the wear of titanium, e.g. fretting, is severe. Fretting phenomenena have been reduced by surface coating 2 , 4). Furthermore the environmental attack from erosion 3 and hot salt corrosion call for appropiate coatings.

It is difficult to surface coat titanium alloys by means of electrodeposition. In this paper the magnetron sputter ion plating is applied to coat thin layers on titanium Ti6Al4V and Ti (cp).

Sputter ion plating is well suited to depositing thin adherent layers on any kind of substrate material. The intensive ion bombardement cleans the titanium surface and intermixes it with coating material. The ion bombardement during the deposition leads to dense coatings.

Tilanium '92 Science and Technology Edited by F.H. Froes and I. Caplan The Minerals, Metals & Moterials Society, 1993

Preparation of coatings

The titanium materials were precleaned in acid etch (HF-HNO $_3$) and placed into the sputter chamber (Leybold 2700 P2), followed by an intensive ion etching of the substrates at 1400V. Thin adherent layers, gradient layers of Ni, NiCr, Al, Cr and Cr $_2$ N were plated on titanium. The preparation of the binary compound Cr $_2$ N was insitu-monitored by optical emission spectrometry $_5$ 1. Nitrogen was introduced as a reactive gas during the deposition.

Before galvanic thickening up to 30 μ m in sulfamate nickel, the sputtered specimens were cathodically degreased and pretreated with nickel strike with a current density of 2,5 A/dm².

Results

Coating analysis

Weight gain measurements, AES concentration profiles as well as α -case etching and hardness measurements on the metallographic cross-sections after different exposure times at high temperatures in air provide a first check of the feasibility and compatibility of the coating. The overall incorporation of oxygen refers to the weight gain. The AES-profiles show the interdiffusion of the layer material and oxygen penetration in the substrate. The formation of intermetallic compounds are detected by AES.

Ni, NiCr and Al-layers

A high interdiffusion and the formation of Ti-intermetallic of a 7 μm NiCr layer after 12 h at 700°C in air is shown in Fig.1. Chromimum diffuses to the layer surface and is sacrified by oxydation. It is likely that the formation of the intermetallics is the reason for this chromium shift and not its oxidation at the surface. Because after annealing in vacuum the same shift is found but without any surface oxidation. The rapid formation of the intermetallic can be estimated from the fact that two thirds of the 7 μm NiCr layer have been displaced after 2 h annealing time at 700°C. No oxygen diffusion is detected by means of AES in the intermetallic layer.

The same annealing of sputtercoated aluminium on titanium Ti6Al4V merely shows the formation of the TiAl intermetallic compound and a solid solution of aluminium in the titanium substrate material. The top of the surface is sealed by a thin $\mathrm{Al}_2\mathrm{O}_3$ layer. No oxygen penetration through the intermetallic could be detected by means of AES. A detailed study on phases and diffusion coefficients in titanium is given in the literature 6). Although the oxygen penetration and weight gain after short time annealing was measured to be low, the formation of intermetallics may embrittle the surface. Thus nickel and aluminium coatings are suggested to be applied beyond $400^{\circ}\mathrm{C}$.

- Electrodeposited nickel on sputtered Ni- and NiCr-layers Nickel and nickel-chromium sputtercoatings were thickened by electrodeposited nickel. Because of the columnar structure of the sputtered nickel layers (Fig. 2a), the scratch tests show that they were quite weak to bear the thick (30 μm) electrodeposited layer (compare Fig. 2b). As pointed out in Fig. 3, the critical load for flacking off the layersystem is greatly enhanced if NiCr as an intermediate layer is sputtered. The cross-section in Fig. 2b shows a dense nickel-chromium sputter layer, nearly completely impermeable for the nickel electrolytes. The few microscopic spots which show the electrodeposited nickel penetrating through the intermediate layer do not show any drawbacks - neither for the electrodeposition process nor for the properties of the layer system.

- Cr- and Cr $_2$ N-layers As chromium does not form intermetallic compounds with titanium (which can be concluded from Fig. 1), thin chromium and chromium nitride layers (3 μ m) were sputtered.

Fig. 4 shows the AES concentration profile a 3 μm thin Cr_2N coating which is only oxydized to one third after 79 h at 700°C in air. It seems from the AES-concentration profiles that the incorporated oxygen shifts the nitrogen from chromium into titanium. Unfortunately the determination of nitrogen is only ambiguously determined by means of AES, because titanium and nitrogen have similar excitation characteristics. The diffusion of nitrogen into titanium can be detrimental as nitrogen also raises the amount of the brittle α -phase. But fortunately an enhanced diffusion of nitrogen into titanium cannot be concluded from the corresponding α -case etching, which shows an ultimately small α -phase rim zone (see Fig. 5a).

The long time exposure (up to 630 h in air, 700°C) of a thin (3 μm) sputtered pure chromium layer on Ti6Al4V show no oxygen penetration in titanium by means of AES. But in this case the chromium has reacted almost completely to chromium oxide. After an annealing time of 184 h at 700°C in air, the α -case rim zone beneath a 3 μm chromium nitride layer has a depth of 12 μm , and beneath a 3 μm chromium layer a 50 μm α -case zone is formed, as shown in Fig. 5. The weight gain of chromium and chromium nitride (Cr₂N) layers remains below 0,3 mg/cm² over long periods of time (up to 160 h). From this it may be concluded that chromium and chromium nitride are well suited as oxidation resistant layers. The good mechanical and wear properties of Cr₂N on titanium materials Ti6Al4V and Ti(cp) have been reported recently 7).

In contrast to most of the sputtercoated nitride layer, Cr_2N has been deposited up to 30 μm in thickness without any flake off. This seems to be important if complexly shaped tools with less accessible surfaces are coated: the accessible parts have to bear thick coating in order to ensure that the less accessible parts are coated entirely. As chromium nitride layers are less hard but more ductile they are superior to titanium nitride layers 5).

Loading tests

Crack initiation and propagation in the layer by stress loading is an essential criteria for the feasibility of the corresponding layer/substrate combination. With respect to the application the coated specimens are tested in the SEM by using a 3 point bending equipment. During the loading, the surface of the specimen is investigated in the SEM, at the same time the stress strain diagram is recorded. The load (stress) and the strain at which the first cracks are detected is registered.

Fig. 6 - 9 show the stress-strain diagrams and the different crack progress behaviours of the four different thin films. The σ - ϵ diagrams are the diagrams of the substrate Ti6Al4V and not of the thin films. The different strains at which the first cracks appear and the SEM pictures of the crack progress give information of the mechanical behaviour of the thin film.

A comparison of an unannealed and an annealed Cr/Cr_2N coating shows that the latter fails at a smaller strain. The ultimate stress of the coating on the Ti6Al4V substrate for the annealed layer is 200 MPa and for the unannealed one 410 MPa. The crack propagation of the annealed film is in comparison to the unannealed one rectilinear and brittle. It has been pointed out recently 7 ; that the adhesion, crystallinity and wear properties of the annealed and unannealed Cr_2N -layers differ widely.

By a comparison of the NiCr- with the Cr/NiCr-film the first one cracks at a substrate stress of 170 MPa and the last one at 340 MPa. If the above mentioned films are electrodeposited with a 40 µm thick Ni-layer and loaded, up to a load of 1200 MPa no cracks are seen. A micrograph of the cross-section after loading shows that the NiCr film is detached from the substrate while the Cr/NiCr film is undamaged.

The X-ray diffraction and texture investigations show that the temperature treatment of the Cr/Cr₂N film reduce cristallinity and texture. The NiCr film has a well defined (111)-texture, which means a great anisotropy in depth of the film. The galvanic Ni-layers have a very small texture.

Mechanical properties and year behaviour

The hardness and the adhesion (scratch test) of the layer systems Ni(sputter/Ni(galvanic) and Ni $_{80}$ Cr $_{20}$ /Ni(galvanic) have been tested (Fig. 3). The measured hardness corresponds to the hardness of electrodeposited nickel. Due to the columnar structure of the sputtered nickel layers this intermediate coating is too weak to bear the electrodeposited nickel. As an additional chromium intermediate sputtered layer reduces delaminations (see last chapter), this was also considered in the wear tests. They were performed in a plate-on-cylinder tribometer with the following conditions:

Load: F = 100 N Velocity: v = 0.04 m/sec Cylinder material: x 155 CrMoV12 1 Room temperature: T = 20 \pm 2°C Humidity: 50 \pm 3 %

The wear volumina of the coated plates were determined. They were decreased by a factor 5 or 10 compared with the uncoated titanium materials Ti(cp) or Ti6Al4V as shown in Fig. 10. A significant difference in the tribological behaviour orignating from the different sputtered intermediate layers NiCr and Cr/NiCr could not be found. The profiles of the traces were analysed and indicate no adhesive wear with slight material transfer to the cylinder. This was in contrast to the uncoated titanium plates.

Ackknowledgement

This work was supported by the Federal Ministry of Research and Technology under Grant 13N5731.

Literature

- A. M. Chaze; C. Coddet; G. Beranger Dissolution of oxygen in the metallic phase during high temperature oxidation of titanium and some alloys Proceedings of the sixth world conference on titanium, France 1988, p. 1765
- M. Thoma
 Influence on fretting fatigue behaviour of Ti6Al4V by coatings,
 Proceedings of the sixth world conference on titanium, France 1988,
 p. 1877

- P.M. Finnerty; P.A. Mackett; D.G. Teer; K. Luing Thick refractory metal coating for high temperature erosion protection of T318 alloy IPAT, May 1991, Brussels, to be published
- 4) K.H. Kloos; E. Broszeit; Th. Roth; B.O. Schweighöfer Schwingungsverschleißeigenschaften von ionenplattierten metallischen Schutzschichten auf Ti6Al4V Verschleiß- und Korrosionsschutz durch ionen- und plasmagestützte Vakuumbeschichtungstechnologien, 2. Internat. Tagung der THD 11./12. März 1986, p. 271
- H. Benien; J. Maushart; M. Meyer; R. Suchentrunk
 D.C. magnetron sputtering of oxidation-resistant chromium and CrN films monitored by optical emission spectrometry
 Material Science and Engineering A 139 (1991), p. 126 131
- 6) G.D. Rieck; G.F. Bastin; F.J.J. van Loo Reaction diffusion between two metals including titanium and niobium Plansee seminar, Reutte, 24. - 28.6.1968
- 7) W.Herr; B. Mathes; E. Broszeit; M. Meyer; R. Suchentrunk Fundamental properties and tribological wear behaviour of sputtered Cr-CrN coatings on light weight metals International conf. of metallurgical coatings and thin film San Diego, 6. - 10. April 1992

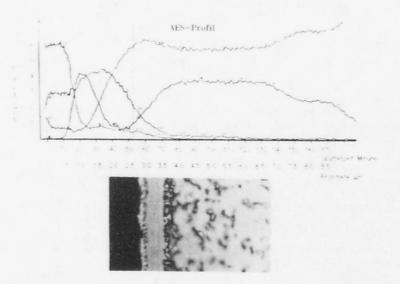


Fig. 1: AES-concentration profile of a Ni(80wt%) Cr(20wt%) sputter layer on titanium Ti6Al4V after annealing 12 h, 700°C in air

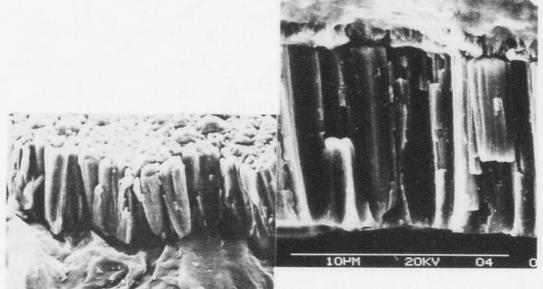


Fig. 2a: Columnar structure of sputtered pure nickel on titanium Ti6Al4V

Fig. 2b: Sputtered NiCr electrodeposited with nickel on titanium Ti6Al4V

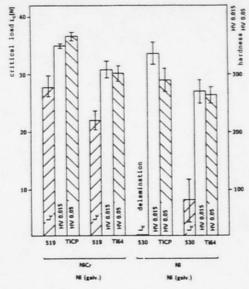


Fig. 3: Layer systems by PVD/galvanic on Ti6Al4V and Ti(cp)

 hardness of the nickel layers (electrodeposited)

 critical load of the scratch test (loss of adhesion)

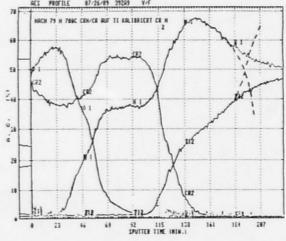


Fig. 4: AES-concentration profile of a 0,2 μm Cr/3 μm Cr₂N-layer on titanium after 79 h, 700°C in air

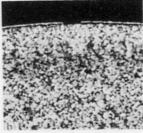


Fig. 5: α -case etch on Ti6Al4V: (a) \rightarrow Cr (0,2 μ m)/CrN (3 μ m) after oxidation at 700°C for 168 h in air (α -zone, 12-14 μ m); (b) 2,5 μ m chromium after oxidation at 700°C for 168 h in air (α -zone, 40 μ m); (c) uncoated, after oxidation at 700°C for 184 h in air (α -zone, 170 μ m)

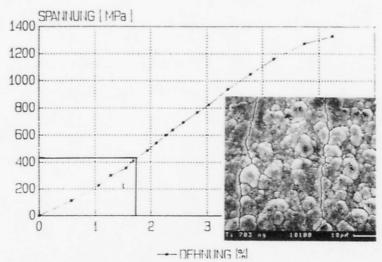


Fig. 6: Stress-strain diagram of the substrate Ti6Al4V with indication of the strain where the first cracks in the layers are registered; layer: 2 µm Cr/14 µm Cr₂N, SEM picture at 706 MPa

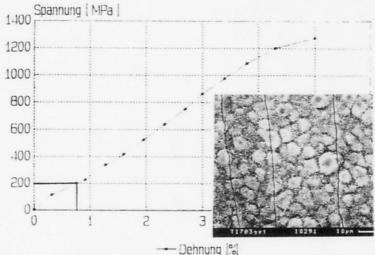


Fig. 7: Stress-strain diagram of the substrate Ti6Al4V with indication of the strain where the first cracks in the layers are registered; layer: 2 μm Cr/14 μm Cr₂N (annealed), SEM picture at 750 MPa

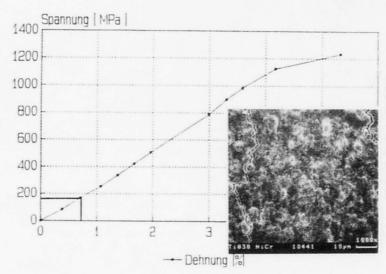


Fig. 8: Stress-strain diagram of the substrate Ti6Al4V with indication of the strain where the first cracks in the layers are registered; layer: 10 µm NiCr, SEM picture at 850 MPa

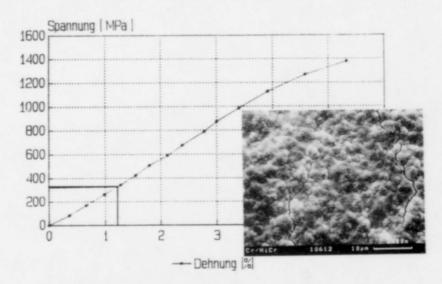


Fig. 9: Stress-strain diagram of the substrate Ti6Al4V with indication of the strain where the first cracks in the layers are registered; layer: 2 µm Cr/6 µm NiCr, SEM picture at 750 MPa

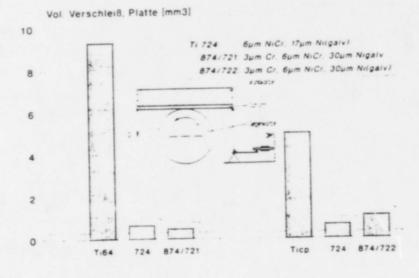


Fig. 10: Wear (volume mm³) of different coated and uncoated Ti6Al4V and Ti(cp) plates (plate-on-cylinder tribometer)

RELIABLE OPERATION AND ENVIRONMENTAL COMPATIBILITY IN COLD FORMING PROCESS WITH ADAPTED CERAMIC COATINGS

D.A. Keller*, R. Hauert** and J. Reissner*.

- * Institute for Forming Technology, ETH Zürich, Switzerland.
- ** Federal Materials Testing and Research Institute, Dübendorf, Switzerland.

1. INTRODUCTION

Ceramic coated tools are characterised by long endurances and, for appropriate design of the coatings and choice of a suitable topography for effective lubrication, also by particularly good emergency running properties and resistance to cold welding. The advantage of coated tools lies in the separation of the tribological functions. A more specific design of the tools can be made than has so far been possible: the ceramic-like layer has the function of protecting the tool from wear, cold welding and corrosion. The function of the base material is only to provide support. This relaxes the conflict between the requirements for supportstrength and wear resistance.

A running in phase in the normal sense is avoided so that the tribological conditions remain

practically constant from the very beginning.

Associated ecological aspects of the use of ceramic coated tools are provided by improvements in terms of the increase of the endurances and the possibility of recoating valuable tools [2], the achievable shaped part qualities and accuracies, the reduction in the amount of lubricant required and the use of rapidly biodegradable lubricants [3]. A major consequent reduction in costs and increase in productivity attest the resulting economic benefit.

2 EXPERIMENTAL

2.1 Test Materials and Test Performance

The tests were performed on sheet strip: of CrNi steel X 5 CrNi 18 9. The following results were obtained in investigations of the frictional behaviour of 3C surfaces, whereby various drawing edges were used. The tests concern ceramic coated tools with titanium carbide (TiC) or titanium nitride (TiN) as coating material. The coatings were applied as multilayer laminates using the LP-CVD technique (Low Pressure-Chemical Vapour Deposition). The properties of these edges were compared with those of aluminum bronze (Jnoxida), with uncoated edges of the tool steel X 155 CrVMo 12 1 and ADLC coated edges (Amorphous Diamond-Like Carbon) in strip-drawing test with single deflection of 90 degrees [4].

An undiluted rape oil (100% modified), various mineral oils and different drawing emulsions were used as intermediate materials, which differed in viscosity and composition.

2.2 Evaluation of the Topographies

The topographies of the tools and of the workpieces are investigated in the scanning electron microscope (SEM) and atomic force microscope (AFM) and with a laser-optics surface-measuring device.

Titanium '92 Science and Technology Edited by F.H. Froes and I. Caplan The Minerals, Metals & Mat : ials Society, 1993 Since all roughness parameters according to DIN only apply for mechanically measured surfaces, comparative measurements were made with a mechanical surface measurement device for the examples of TiN and TiC coated tools. For laser-optical measurements of surface roughness, depending on the surface condition and as a result of the considerably greater lateral resolution, values are measured which are a factor of 4 respectively 2.5 times greater than those measured using mechanical scanning [3].

2.3 Chemical Analysis of the Tool Surfaces

In tribological processes the condition of the outer atomic layer is of major importance in that the wetting behaviour of the lubricant and the adhesion behaviour of the form material to the tool

surface are determined by the chemical behaviour of this outer atomic layer.

The chemical composition as a function of the distance from the interface tool-workpiece, and particularly of the condition and thickness of the tool surface oxide layer, is determined using AES (Auger Electron Spectrometry) and ESCA (Electron Spectrometry for Chemical Analysis). The measuring depth of AES lies between 0,5 and 2 nanometers (2 to 6 atomic layers). When measuring a depth profile several atomic layers are removed between successive measurements by means of argon ion bombardment (ion etching). The identification of the chemical condition of the measured elements is made by comparison with Auger signal forms obtained from reference measurements [5].

3. RESULTS

The surface roughening of the workpiece, caused by the forming process, may have the following effects depending on the tool material employed [1]:

Case A: Tool material harder than the workpiece material: Grains exposed from the workpiece surface tend to exhibit cold welding on the tool as a result of the intensive contact and hence can be torn from the workpiece surface, Fig. 1.

Case B: Tool material softer than the workpiece material:

Grains exposed from the workpiece surface can penetrate into the tool. The consequence is a scratching of the tool surface with abrasive transfer of tool material onto the deep-drawing part. The tool geometry is lost.

Case C: The hardnesses of tool and workpiece material are insignificant:
In the last case the grains exposed from the tool surface are removed from the effective gap without having the opportunity to affect the lubrication system: This applies, for example, to hydrodynamic friction.

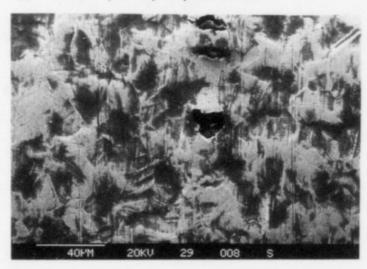


Fig. 1: 3D-Sheet surface (X 5 CrNi 18 9) after sliding on a TiN-coated tool: Torn out grains leave holes behind.

3.1 Effect of the Tool on the Lubrication System

3.1.1 Effect of Surface Topography

Investigation of uncoated tools

Cold welding presents a serious problem, particularly in the forming of CrNi steels. So far the successful solution lay in the use of high-strength bronze alloys as tool materials. However the endurances of such tools are relatively short as a result of the abrasive wear of the deformation-induced martensite [1]. Fig. 2 shows a aluminum-bronze tool after use. Mechanism B can be deduced from the width of the scratches (up to $10~\mu m$). Support for this hypothesis is provided by the analysis of the grain size distribution of the form material employed. A mean grain diameter of about $15~\mu m$ is obtained.

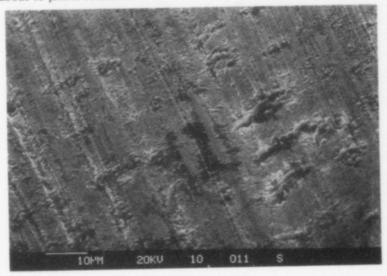


Fig. 2: Scratched surface of aluminum-bronze tool.

When using the tool steel X 155 CrVMo 12 1 major cold weld points [3], of adhesive type, are formed within extremely short times.

Ti CTi N Ti

Fig. 3: TiN coating contaminated with aluminum (Al cold welds).

2,029

As a result of the extreme hardness of the protecting layer there is no abrasion of the tool, so that the conditions according to case A are satisfied. Nevertheless there is generally no danger of cold welding, since the tendency to adhesion between the metallic form material and the ceramic-type protecting layer is very slight. However this statement should be limited in that an important role is played by the topography of the surface layer and its definition in terms of the specific function. Account must also be taken of the separating medium, normally the deep drawing oil, of the process temperature and of the surrounding atmosphere.

As shown in Fig. 3, massiv contamination of the layer is observed for undefined topographies with uncontrolled running in behaviour and for inappropriate layer-substrate combinations or conditions. This applies particularly at high loading levels and where lubrication is inadequate. In Fig. 4 this corresponds to inadmissible behaviour during manufacturing, such as shown by curve 1 for aluminum and curve 2 for austenitic steel as form material. For this reason high-performance ceramics must allways be used with surfaces having appropriate

frictional properties.

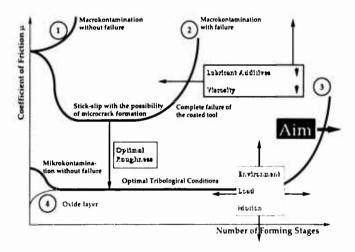


Fig. 4: Schematic representation of the coefficient of friction for coated tools with different topographies, as a function of the number of strokes and other factors.

The risk of cold welding is reduced by mecanical reworking of the coating surface, provided that a surface topography can be generated with suitable frictional properties [3], as shown in Fig. 4, curve 3 and Fig. 5. However small depressions typically caused by growth or substrate irregularities (average depth of 0,5 to 1,5 µm, measured in the AFM) can provide initiation points for cold welding under extreme conditions, such as inadequate lubrication, dry running, or the deformation of CrNi steels or Aluminum, as shown in Fig. 6. On the other hand, under normal to extreme conditions of mixed lubrication, these depressions act as lubricant pockets and show extremely favourable properties from the point of view of lubrication (micro squeeze currents [6]). Under extreme loading conditions the depressions lead to the following processes:

- The tearing out of individual grains from the form material, Fig. 1.

embedding of these grains in the depressions of the coating material with anchoring in the notched base of the depressions, Fig. 6.

deposition (cold welding) of further form material on the embedded grain, Fig. 7.

Tests have shown that the coefficient of friction is somewhat reduced during the phase in which small workpiece particles are cold welded onto the coating surface. With the growth of contamination islands, primarily in the direction of drawing, the coefficient of friction increases again [3].

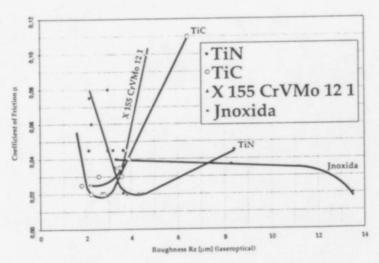


Fig. 5: Coefficient of friction μ as a function of R_z (determined with laser optics) and the edge material.



Fig. 6: TiN-coated tool surface partially contaminated with CrNi steel (microscopic cold welding) with insufficient lubrication up to dry running. The contamination apears to grow particularly from the lubrication pockets in the micro to nanometer range.

From a certain critical size of the contamination islands, the following mechanisms are effective, depending on the specific form material:

Very pronounced contamination of the drawing dies for the forming of soft and "sticky" materials, such as aluminum alloys:

The contamination increases steadily as a result of workpiece abrasion. In this process the coating is not destroyed since the workhardening of the form material is not as strong as for CrNi steels. Clearly visible scratches are formed on the workpiece [2].

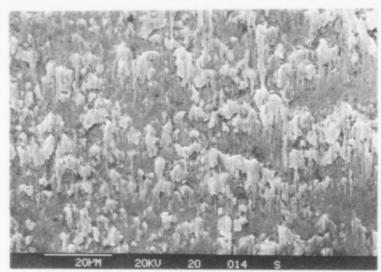


Fig. 7: Workpiece particles (X 5 CrNi 18 9) which are growing together to islands in the drawing direction on a TiN-coating during dry sliding.

The low elastic modulus and the large number of slip systems in aluminum (FCC lattice) permit internal locking in the irregular depressions. Macroscopic cold welds then gradually appear as a result of the high reactivity of aluminum.

Breaking out of individual islands while generating high local shear stress levels, with the possibility of microcrack formation in the ceramic coating: Progressive microscopic roughening in the course of the manufacturing cycles; first locally but then extending to include the entire effective surface in the form of wear tracks.

For austenitic materials the internal locking is only observed at higher loading levels, which, as mentioned above, can lead to failure of the coating, Fig. 8.

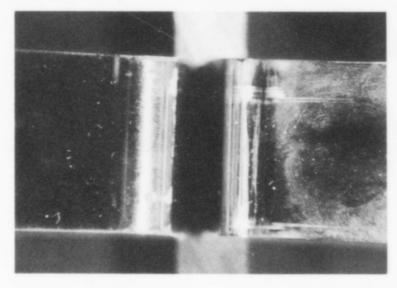


Fig. 8: TiN-coated edges after dry running on CrNi steel sheet. The left-hand one is contaminated with workpiece material. For the right-hand edge the contamination was etched off with aqua regia, whereby the coating was also partially etched away.

When the TiC or TiN coatings suffer spalling, and hence no longer provide continous protection, failure of the tool progresses more or less rapidly. This occurs preferentially in the form of wear tracks, whereby mechanisms of self-destruction by detached coating particles are also effective.

The ADLC-coated tools were characterised by low values of the coefficient of friction (μ < 0,015) and surfaces practically free of contamination, even under extreme conditions. However wear tracks were formed as a result of tribo-oxidation wear. For these types of coated tools inadequate or dry lubrication leads to early failure of the tool. In this respect a higher level of safety is provided with TiC and TiN-coated tools.

- Particularly favourable behaviour is observed especially when the islands of contamination can be more easily pushed off. At the same time the lower shear stresses reduce the danger of cold welding and microcrack formation:

These favourable frictional conditions can be achieved for functional topographies when the boundary layer region of the coating system permits reproducible substructures on the nanometer scale [7]. In this case the coefficient of friction is hardly dependent on the number of forming stages, as shown in the strip drawing tests. In addition such composite-layer tools are characterised by excellent emergency operation properties.

3.1.2 Oxidation of the Surface

For short periods of time the surfaces reach high temperatures, resulting in a thin TiO₂ layer which covers the entire surface, Fig. 9. The TiO₂, which has a positive effect on the friction [8], curve 4 in Fig. 4, is already present on the surface of TiN and TiC after mechanical reworking. However at this stage the boundary layer is not uniformly continuous. The polarity of TiO₂ and a possible hydration of the outermost layer in normal environments result in an improvement of the wetting of the surface with polar lubricants (natural esters). This arises from the possibility of the formation of hydrogen bonds. The consequence is a low coefficient of friction and a reduction in the tendency of cold welding, Fig. 10.

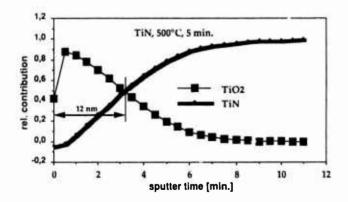


Fig. 9: Depth profile of a TiN coating oxidised for 5 minutes at 500 C.

In addition steep gradients and sharp edges in the topography, which serve, under frictional conditions as initiation points for cold welding, are also "smoothed" by the oxidation [7]. This was shown by AFM analysis. This is observed particularly for TiN, which exhibits preferently columnar growth. For TiC this is not of the same importance since TiC already has fewer steep gradients and sharp edges in the original condition, as a result of its nub growth and smaller grains. Nevertheless oxidation also leads here to a reduction in the tendency to cold welding.

Due to the weak bonding and low hardness (< 1800 HV) of this starting layer it is partly sheared off from the tool by the tribological loading. However it has been observed that a layer of TiO2, only a few nanometers thick remains, and is sufficient to maintain the advantages

achieved. At points where the tribological loading leads to exposere of the highly reactive underlying coating material, there is generally a regeneration of the TiO₂ film with oxygen. Hence the advantages in terms of reduced coefficient of friction and tendency to contamination are maintained.

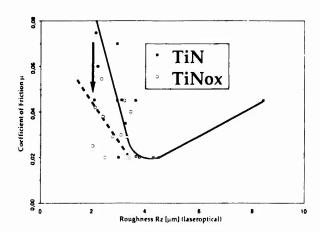


Fig. 10: Coefficient of friction μ as a function of R_z (determined by laser optics) for TiN-coated edges and those with continuous oxide layers (TiN*).

4 CONCLUSIONS

The lubrication system can be influenced not only in terms of tool surface, lubricant and workpiece, but also be optimised specifically for the required values.

Thin ceramic-type coatings are of particular importance provided that, from the point of view of tribological parameters, topography, layer design and composition of the ceramic coatings can be varied practically independently of one another.

A TiO₂ layer produced from the start by oxidation of the TiC-TiN reduces the coefficient of friction and the tendency to microscopic cold welding. This results in suppression of macroscopic cold welding or delays it so that the occurrence of layer spalling is also moved to later times.

5 REFERENCES

- [1] : Keller, D.A.; Hora, P.; Groth, H.P. and Reissner, J.: Environmentally Compatible Deep Drawing under Extreme Conditions. Rohre, Bleche, Profile 9-1991 (in German).
- [2] : Keller, K. and Koch, F.: Coated Forming Tools for Extreme and Very Extreme Sheet Forming. DFB-Kolloquium, Werkzeugtechnik in der Blechbearbeitung, 26. und 27. Februar 1991 (in German).
- [3] : Keller, D.A. and Reissner, J.: Economical and Environmental Effects on the Tribological System. Zürcher Tagung '91: "Der Umformbetrieb von morgen", 27. September 1991 (in German).
- [4] : Meier, B.: The Transfer of Strip Coefficients of Friction to Actual Deep-Drawing Parts.
 Tribologie und Schmierungstechnik, 35. Jahrgang 6/1988 (in German).
- [5] : Briggs, D. and Seah M.P.: Practical Surface Analysis. John Wiley & Sons Ltd.
- [6] Reissner, J.: Friction Condition in Lubricated Deep Drawing Process.3. Int. Colloqu., Jan 12- 14, 1982 Esslingen, Vol.1.
- [7] : Keller, D.A., Hauert, R. and Reissner, J.: Ceramic Coatings in cold Forming Processes. Nordtrib '92, Finland. 8.-11.6.1992 Helsinki, Vol. 1, p. 3.
- [8] : Woydt, M. C.: Resistant. Maschinenmarkt Würzburg 96 (1990) 38 (in German).

Oxidation of High Temperature Titanium Alloys

T.J.Johnson, M.H.Loretto, M.W.Kearns*

Interdisciplinary Research Centre in Materials for High Performance Applications, The University of Birmingham, Edgbaston, Birmingham, B15 2TT, UK.

* I.M.I Titanium Ltd, PO Box 704, Witton, Birmingham, B6 7RU, UK.

Abstract

The oxidation behaviour of commercially pure titanium has been compared with that of a conventional high temperature titanium alloy and an α_2 titanium aluminide. Isothermal oxidation tests have been performed on IM1125, IM1834 and "Super α_2 " over the temperature range 600 to 900°C. The development, compositions and morphologies of the various scales produced have been examined using X-ray diffraction, Auger electron spectroscopy and analytical electron microscopy to establish the nature of the oxides formed and the chemical partitioning which occurs in both the substrate and the scale. Microhardness measurements have been used to determine the depth of penetration of oxygen into the alloys during oxidation. Preliminary results from oxidation trials on Ti-48A1-2Nb-2Mn are also presented. The observations show that the oxidation rate is a complex function of oxidation temperature and alloy composition. It appears that oxidation is controlled by the kinetics of competing mechanisms rather than by minimum energy considerations.

Titanium '92 Science and Technology Edited by F.H. Froes and I. Caplan The Minerals, Metals & Materials Society, 1993

Introduction

The use of conventional titanium alloys is limited to temperature regimes below about 600° C because of their oxidation behaviour which proceeds via the inward diffusion of oxygen to produce thick oxide scales, and results in a pronounced degradation in mechanical properties associated with the dissolution of oxygen in the titanium matrix. Oxygen is soluble in α -titanium up to 34 atomic% and is α -stabilising which leads to severe embrittlement in the oxygen-enriched surface layer of the material.

Whilst it is known that various alloying additions to pure titanium have a beneficial effect on its overall rate oxidation it would seem that the basic mechanism remains the same with both oxide scales and α -case being formed simultaneously. It is obvious that in order to effect a further increase in the high temperature capabilities of titanium alloys, either through compositional control or by some method of coating, it will be essential to gain a better understanding of the role of the individual alloying elements on the oxidation behaviour of these materials.

Titanium aluminide materials have potential for high temperature applications and are superior to titanium alloys in terms of oxidation resistance [1]. The use of aluminides may however also be limited by their poor resistance to oxidation above about 600° C (α , -alloys) and 900° C (γ -alloys) [2]. The basic principles of loss of structural material by oxide scale formation and surface embrittlement apply equally to the oxidation of the titanium aluminides. Scales produced are heterogeneous mixtures of TiO, and Al,O,, and again additional elements such as Nb have a beneficial effect on the rate of oxidation [3].

The aim of the present study is to compare high temperature oxidation studies of IMI834, "Super α ," and Ti-48Al-2Nb-2Mn with that of commercially pure titanium and more clearly define the behaviour of their key alloying additions.

Experimental Details

Specimens of IMI125, IMI834 and Super a, were prepared in the form of 10mm diameter discs of 1mm thickness. These were mechanically polished to 800 grit SiC paper and degreased prior to oxidation. The specimens were then isothermally exposed in air at temperatures from 600 to 900°C for 100h, using a Stanton Redcroft Thermobalance. Morphological studies of the oxides were carried out using a Cambridge scanning electron microscope (SEM), Auger analysis (AES), X-ray photoelectron spectroscopy (XPS), and X-ray diffraction (XRD) studies were also done on these specimens and on samples of spalled oxides. Table I shows alloy compositions. Cross-sections of oxidised specimens were prepared for microhardness traverses and oxide thickness measurement by SEM examination. Transmission electron microscopy (TEM) was carried out on cross-sectional specimens of oxidised material produced by glueing together two disc specimens of 1.5mm thickness using an epoxy resin. These were then sectioned to produce a rectangular specimen of 3mm x 3mm x 10mm, which was carefully filed down until small enough to be encapsulated in a thin walled brass tube of 3mm outside diameter. Sections of 0.3mm thickness were cut from the specimen and were mechanically polished to 100-150µm before being dimpled to less than 50µm using an SBT Precision Dimpling Instrument. The thin discs were finally ion milled for TEM examination which was carried out on either a JEOL 4000FX or a Philips CM20.

TABLE 1 Composition of the alloys

Material	Composition (wt %)
IMI125	Ti - 0.13 O ₂
IMI834	Ti -5.8Al - 4Sn - 3.5Zr - 0.7Nb - 0.5Mo - 0.35Si.
Super $\alpha_{_2}$	Ti - 14A1 - 20Nb - 3.2V - 2Mo.
48-2-2	Ti - 48Al - 2Nb - 2Mn. 2,036

Results

Figure 1 shows weight gain data for commercial purity Ti (IM1125), IM1834, Super α , and Ti-48Al-2Nb-2Mn, which include corrections due to buoyancy effects. Double logarithmic plots of this data allow evaluation of n, the exponent for oxidation according to the equation:

$$\Delta W^n = Kt + C \tag{1}$$

where ΔW is weight gain (mgcm²), K is the constant of oxidation, t is time and C an integration constant.

IMI125 shows parabolic kinetics at low temperatures after extended times, and at high temperatures, but linear kinetics at intermediate conditions. Discontinuous curves are indicative of para-linear behaviour which is usually associated with the repeated cracking and spalling of scale followed by rapid oxidation. IMI 834 exhibits a low linear rate of oxidation after exposure at 700°C, but rates tend towards parabolic at 800-900°C. Super α_i is found to have a low linear rate of oxidation at 600°C, at 700°C a linear rate prevails up to 20h after which kinetics tend towards parabolic. Parabolic behaviour is found at 800-900°C. Ti-48Al-2Nb-2Mn has a low linear rate of oxidation at 800°C, and cubic oxidation rates at 900°C.

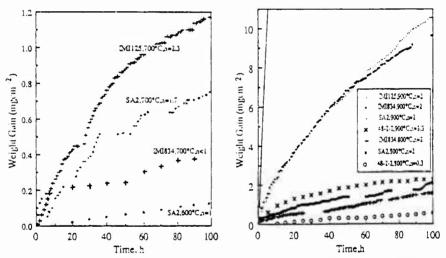


Figure 1. Isothermal Oxidation Curves of Weight Gain (ΔW) versus Time (t) for IMI125, IMI834, Super α_s and 48-2-2

In general the results obtained between 600°C and 900°C show the beneficial effect of alloying on the oxidation resistance of titanium although overall weight gains are higher for Super α_i than for IM1834. For both alloys the temperature range over which parabolic kinetics are observed is extended towards higher temperatures when compared with unalloyed titanium. The initial oxidation rate (less than 10h), for IM1834 at 700°C however is actually faster than that of IM1125. The observed reversion of IM1125 to parabolic kinetics at 900°C is attributed to the densification of the scale adjacent to the substrate, thus the diffusion of oxygen through the scale rather than along micro-cracks and porosity, becomes rate controlling.

SEM and Auger Spectroscopy of oxide scales

SEM observation of oxidised pure titanium, figures 2 and 3, show that the porous scale, formed at 700°C, develops into a uniformly stratified scale after oxidation at 800°C. The stratification begins to disappear at 900°C by sintering and densification of the scale adjacent to the metal substrate. The surface oxide grains are quite angular and faceted after oxidation at 900°C. Scales at all temperatures have very poor adherence.

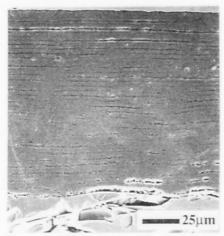


Figure 2. SEM micrograph of oxide on IMI125 after 100h at 800°C.

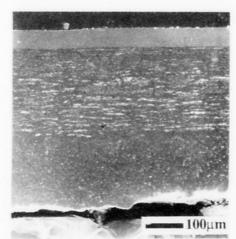


Figure 3. SEM micrograph of oxide on IMI125 after 100h at 900°C.

Fine needle-like oxide crystals are formed on the surface of IMI834 after oxidation at 600°C, which develop into faceted columnar grains at higher oxidation temperatures. At 900°C the oxide scale, figure 4, comprises a coarse grained surface layer of approximately 7μm, a compact but stratified oxide of about 55μm and a thin porous layer at the metal:oxide interface. The oxide remains reasonably adherent up to 800°C, above this the deep yellow outer oxide readily spalls to reveal a dark blue/grey adherent oxide. X-ray diffraction (XRD) of the scale formed at 600°C found only "TiO₂". Scale formed at 900°C was found to be a mixed oxide of "TiO₂"and "Al₂O₃". It should be noted that these oxides are likley to be doped with alloying elements, however their concentration is below the limit of detectability in the techniques used here.

Auger Electron Spectroscopy (AES) and X-ray Photoelectron Spectroscopy (XPS) of IMI834 have been used to analyse the oxide scale and the metal:oxide interface. Both Al₂O₃ and SiO₂ were detected in a predominantly TiO₂ oxide scale. It would appear that there is a very thin layer of Al₂O₃ on the surface of the scale, of the order 150Å. An AES depth profile, figure 6, showed that a possible layer of SiO₂ is removed after etching for approximately 4 minutes, which suggests that the thickness of the layer is about 0.15µm [4]. Al₂O₃ and SiO₂ are found in small concentrations throughout, and analysis of the fractured scale suggests that there is some concentration of Al₂O₃ along the cracks and that SiO₂ is found in greatest concentration at the metal:oxide interface.

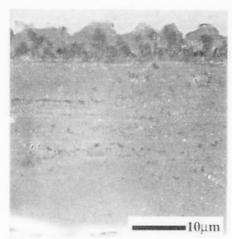


Figure 4. SEM micrograph of oxide on IMI834 after 100h at 900°C.

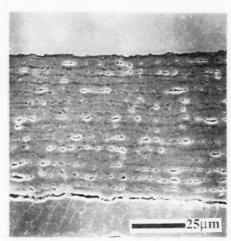


Figure 5. SEM micrograph of oxide on Super α, after 100h at 900°C.

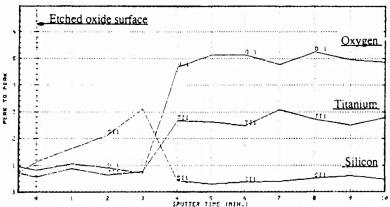


Figure 6. AES Profile through surface of scale formed on IMI834 after 100h at 900°C.

The oxide formed on Super α , remains adherent up to 900°C. This oxide, Figure 5, consists of uniformly thick layers in which grains are rounded and equiaxed. The total thickness of the oxide is ~75 μ m. Beneath this layered oxide, adjacent to the metal substrate, there is a dark, thin, adherent oxide. XRD analysis of the specimen detects TiO, with only small amounts of Al₂O, AES showed that the scale formed at 900°C consists of TiO₂ and Al₂O, with trace amounts of Nb and V. A depth profile through approximately 0.5 μ m of the scale from the surface showed very little change in composition except for an apparent reduction in the V signal after etching the surface.

Oxide thickness measured by SE.4 examination of cross-section specimens, shows that scales formed on the alloys are not only considerably thinner than those formed under equivalent conditions on titanium, but are also more compact and stratification is less distinct thus preventing easy access of oxygen to the metal surface and diffusion-controlled kinetics are maintained. Alpha-case depths above $6(0)^{\circ}$ C, are also considerably thinner in the alloys than in the unalloyed material. Below 800° C there is negligible difference between the two alloys. There is however, a rapid increase in the aipha-case on IMI834 above 800° C, which is likely to be caused by the loss of scale adherence, hence permitting the rapid ingress of oxygen to the exposed surface. The scale thickness on Super α_2 increases with respect to that of IMI834 above 800° C, but remains strongly adherent even after oxidation at 900° C.

Cross sectional TEM of oxidised samples

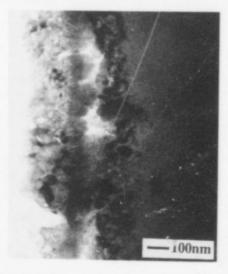
Cross-sectional TEM has been carried out on specimens of IMI125 and IMI834 oxidised at 600°C for 100 h, figure 7. Measurements of the scale thickness and the appearance of distinct oxide layers is consistent with SEM observations. The alloy scale consists of a compact layer about 2nm thick, which is found next to the substrate, a more porous layer of 50nm and a coarse surface oxide of about 150nm. EDX has not shown any major differences in composition in the oxide on IMI 834.

Selected area diffraction of the scales gives a series of ring patterns, which have been indexed and identified as TiO_2 . No cross sectional specimen of Super α_2 has been produced as yet but extensive further work is planned.

Measurement of oxygen penetration depth from hardness profiles

Hardness measurements have been made on oxidised samples which were cross sectioned after oxidation at 600 and 900° C. Assuming that oxygen concentration is directly related to hardness of the material, hardness profiles reflect the relative oxidation rates of the alloys at the different temperatures. The penetration is greatest in IM1125, and least in Super α_{i} . At lower temperatures the behaviour is not as systematic, as pointed out from the weight gain observations, and

it appears that short circuit diffusion paths influence oxidation at these lower temperatures. Diffusion coefficients for volume diffusion of oxygen in the matrix materials are presented in the form of an Arrhenius relation in figure 8.



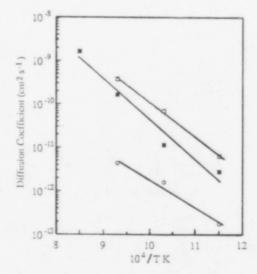


Figure 7. TEM micrograph of cross-section oxide on IMI834 after 100h at 600°C.

Figure 8. Diffusion coefficient for oxygen in IMI125, IMI834 and Super α,.

Discussion

The interpretation of the results obtained in this work is not straightforward and it is clear that not only are different factors important at different temperatures but it is also clear that kinetic factors are involved as well as minimum energy considerations. The fact that there are changes of mechanisms with change of temperature is well illustrated by the weight gain experiments where the relative rates of the samples changes between 600 and 900°C. This immediately raises difficulties in determining the activation energies of the processes which are rate-controlling as will be discussed below.

The importance of factors, other than minimum energy considerations is apparent from the Auger observations where it has been found that alumina is formed in the oxide both on IMI834 and on Super α . It has been found that the concentration of Al needs to be above about 57-59 at% before a continuous Al₂O₃ scale is oxidised from Ti alloys [5]. The Al contents of the alloys investigated here are well below this and Al is present in small concentrations throughout the scales on both of the alloys, in the form of α -Al₂O₃. The presence of Al must therefore involve a mechanism other than that dictated by the relative activity of Ti and Al. If, as seems likely, Ti is indeed oxidised first to form TiO,, or some sub oxide, there will be an increase in the Al concentration at the oxide metal interface, unless the Al diffuses away from this interface into the body of the metal. If Al is simply incorporated into the advancing oxide, there could be significant build up of Al in the oxide. Subsequent oxidation of the Al would lead to the formation of Al₂O₃ and this would lead to a reduction in the oxidation rate in IMI834 and Super α, as compared with that in IMI125, as observed. In addition the formation of Al₂O₂ could slow the oxidation rate down to such an extent that the diffusion of oxygen into the body of the metal could now be controlled by the rate of arrival of oxygen at the metal-oxide interface and this would influence the oxygen penetration depth as measured using hardness measurements.

On the basis of the Wagner-Hauffe theory of mass transport in oxides Al3-cations present in the anion deficient TiO_{2-x} lattice should increase the number of oxygen vacancies and thus cause an increase in the rate of oxygen transport through the oxide. This however, is not observed experimentally and it should be noted that the presence of pentavalent cations in the alloy readliy compensate for this effect. Other mechanisms must be operative as mentioned above; an effect of Al occupying interstitial positions in the TiO₂[6], or simply the trapping of diffusing

oxygen atoms by the Al atoms, would result in the reduction in the rate of oxidation.

The Auger analysis of oxidised Super α_i detected trace amounts of Nb and V in the TiO₂+ Al₂O₃ scale, however it is not obvious that such small concentrations could have a significant effect on the oxidation rate. The Wagner-Hauffe theory predicts that the substitution of Nbth and Vth into the TiO₂ lattice would cause a reduction in the number of oxygen vacancies and hence a reduced rate of oxidation. Again since this effect is very small and easily compensated by other alloying elements, some other mechanism of reducing the oxygen flux must be operative. Nb₂O₃ scale formed on Nb is very porous and offers little resistance to oxidation, however it is the most stable of the Nb oxides in this system, and can form complex oxides with TiO₃ and Al₃O₃[3]. These compounds being relatively dense are more protective, than the porous TiO₂-Al₂O₃ scale.

In contrast to the activity argument for the formation of Al₂O₃, the concentration of SiO₄ at the metal:oxide interface on IM1834 is not surprising since the free enthalpy of formation of SiO₄ is smaller than that of TiO₄. The presence of smaller concentrations of SiO₄ detected throughout the scale is consistent with cation diffusion towards the oxygen:oxide interface. Si is thought to play an important role in the prevention of oxygen dissolution into the metallic substrate [7], although the mechanism for this is not clear. It would appear however, that its presence at the interface has a detrimental effect on the adherence of the scale at the higher temperatures. This is in agreement with the findings of [8] who report that small concentrations (less than 0.5 wt %), teduce scale adhesion when compared to pure Ti. The Pilling-Bedworth ratio of SiO₄ (1.88-2.15) is significantly larger than that of TiO₄ (1.73); this difference in molecular volume between the two oxides and the metal will cause an increase in stress at the interface.

Cracking and spalling of the oxide make it very difficult to determine the rate controlling factors that govern oxidation from measurements of the oxide thickness. The data collected in the present work has shown that over some ranges of temperature the oxidation, as measured by weight gain is parabolic. Since the weight gain is due to oxygen which has diffused to form both oxide and oxygen-rich surface layers it is a measure of the total rate of oxygen take-up. The temperature dependence of the weight gain, when the kinetics are diffusion-controlled (ie. when the gain is parabolic with time) could be used to determine the activation energy over that limited temperature range. Unfortunately the data obtained do not show smooth parabolic weight gain over a sufficient temperature range to allow such an analysis.

It is tempting to consider whether the hardness data, which measures the oxygen penetration into the samples can be used instead to determine the rate controlling factors. On the assumption that the rate controlling factor is the diffusion of oxygen through the alloy, and that the diffusion of oxygen through the growing oxide does not influence the rate of penetration, the diffusivity of oxygen in the alloy can be measured from the hardness measurements. Thus the diffusion distance at each temperature is given by $x = \sqrt[3]{Dt}$ so that D can be obtained as a function of temperature. Figure 6 shows a plot of D against $10^{\circ}/T$ which allows the determination of D_o and Q defined in the equation

$$D = D_a \exp(-Q/RT)$$
 (2)

Values of D_a and Q obtained from these results, on the assumption there is a singly activated event controlling oxygen penetration in the metal, are presented in Table II.

TABLE II Diffusion Coefficients and Activation Energies from hardness profiles (Hv)

Material	Q, kJ mole 1	D _o , cm ² sec ¹
IMI125	155	1.4x10 ²
IMI834	180	1.0 x 10 ¹
Super α.	121	4.6 x 10°

The values of D_a and Q obtained for IMI125 and for IMI834 are comparable with published data [9] and appear to be physically reasonable. The data obtained for Super α_a , however, give values of Q and D_a which do not seem to be physically reasonable. Earlier analysis has shown [10] that very low values of D_a are not compatible with singly activated events. Various suggestions have been put forward to account for such low values but from the present viewpoint it is reasonable to conclude that equation (2) does not appear to describe diffusion through Super α_a .

The oxidation behaviour of titanium alloys at high temperatures and the role of additional elements is complex. Further work is required to understand all contributing factors, a fact reflected in the wide divergence in reported data. It may not be appropriate to use a simple Arrhenius relationship to characterise the kinetics; a more detailed examination of all the mechanisms of diffusion involved in the oxidation process is necessary. The improvement in oxidation rate of the alloys over that of pure titanium may be attributed in part, to the improvement in the barrier properties of the scale. Cation diffusion through the scale seems a likely mechanism of reducing the flux of oxygen to the metal interface. An important factor in scale adherence is the build up of stresses at the metal-oxide interface; the influence of alloying additions concentrated in this region on oxide spalling characteristics merits further investigation. Furthermore, additional cross-sectional TEM examination is considered important to the understanding of the oxidation behaviour of these materials.

Acknowledgements

The authors would like to thank Professor J.F. Knott, Head of the School of Metallurgy and Materials, for the provision of laboratory facilities and, IMI Titanium and SERC for their financial support. Dr Charles Youne: of The Interface Analysis Centre, Bristol University is also gratefully acknowledged for the provision of Auger facilities and for many useful discussions.

References

- 1. M. W. Kearns, "High Temperature Oxidation of Binary and Ternary Titanium Aluminides", (Paper presented at Conference"Production and Applications of Less Common Metals", Hangzhov, China, 8 November, 1982).
- 2. H. A. Lipsit, "Titanium Aluminides-An Overview", <u>High Temperature Ordered Intermetallic Alloys</u>, Mater. Res.Soc. Symp. Proc., 39, (1989), 351-357.
- 3. G. Welsh and A. I. Kahveci, "Oxidation Behaviour of Titanium Aluminide Alloys", Oxidation of High-Temperature Intermetallics, (Cleveland, OH: The Minerals, Metals and Materials Society, 1989), 207-218.
- 4. C. M. Younes and T. J. Johnson, Unpublished work.
- 5. G. H. Meier and D. Appolonia, "Oxidation of Ti-Based Alloys", Oxidation of High Temperature Intermetallics. (Cleveland, OH: The Minerals, Metals and Materials Society, 1989), 185-193.
- 6. K. S. Forland, Acta Chem. Scand., 20, (1966), 2573.
- 7. A. M. Chaze and C. Coddet, Journal of Materials Science, 22, (1987), 1206-1214.
- 8. A. M. Chaze and C. Coddet, Oxidation of Metals, 28,1/2, (1987),61-71.
- 9. Z. Lui and G. Welsh, Met. Trans. A, 19A, (1988), 1121-1125.
- 10. R. P. Agarwala, S. P. Murarka, M. S. Anand, Acta Met., 12, (1964), 871-874.

ENVIRONMENTAL INFLUENCE ON THE FATIGUE CRACK GROWTH

PERFORMANCE OF TI-1100 AT ELEVATED TEMPERATURES

R. Foerch, A. Madsen and H. Ghonem

Mechanics of Solids Laboratory
Department of Mechanical Engineering and Applied Mechanics
University of Rhode Island, Kingston, RI 02881 (USA).

Abstract

The high temperature fatigue crack growth behavior of Ti-1100 is investigated for different loading frequencies in both air and vacuum environments. Two types of time-dependent damage mechanisms have been identified: oxidation and creep effects. It is concluded that the effect of oxidation on the crack growth acceleration is rapid and constant in relation to the frequencies tested and only weakly dependent on cycle time. Creep effects, on the other hand, are dominant at low frequencies in both air and vacuum and found to be loading-rate dependent. The degree of contribution of each of these two damage modes during the steady state growth region has been determined by examining the frequency response of the exponent and coefficient parameters of a Paris-type equation.

INTRODUCTION

A new silicon bearing near alpha titanium alloy, Ti-1100, was developed by TIMET to provide an optimum level of creep and fatigue performance at temperatures up to 593°C. The nominal chemical composition of this alloy is: Ti-6A1-2.8Sn-4Zr-0.4Mo-0.4SSi-0.070-<0.03Fe. The work of Bania [1,2] describes in details the microstructure characteristics of this alloy and elaborates on its uniaxial mechanical properties. Ghonem and Foerch [3] have studied the effect of loading frequency on fatigue crack growth behavior of Ti-1100 at 593°C. In their work, the influence of low and high frequency was examined in both air and vacuum environment. While the results have established an influence of environment on the crack tip damage, it did not examine the synergism of time dependent effects due to elevated temperature crack propagation in the pure cyclic and creep-fatigue regimes. This paper will attempt to explore the interrelated effects of these regimes in order to identify the boundary of each corresponding damage mechanism.

EXPERIMENTAL PROCEDURE

Fatique crack growth tests were performed in air and high vacuum (5x10⁻⁸ Torr, 6.6x10⁻⁶ Pa) at both room (23°C) and elevated temperatures (593°C). Loading frequencies examined in this work have varied from 30 Hz to 0.0031 Hz in air, and 10 Hz to 0.0031 Hz in vacuum. All tests utilized compact tension specimens machined with the crack front perpendicular to the rolling direction (L-T). Crack length was measured remotely using the direct current potential drop method. Crack closure was measured in all air tests. In vacuum, however, no closure was measured except the case of 0.5Hz, room temperature test. To establish material properties for analysis of the fatigue crack growth data, tensile tests under variable strain rates were performed. All the test specimens generated during the experimental portion of this work were examined extensively using SEM and optical techniques.

EXPERIMENTAL RESULTS

The average prior- β grain size was = 550 μ m and the average aligned alpha colony size was =40 μ m as determined by linear intercept. Transmission Electron Microscopy revealed almost no beta phase layer between the alpha plates or even at colony boundaries. In addition although the material was air cooled

Titanium '92 Science and Technology Edited by F. H. Froes and I. Caplan The Minerals, Metals & Materials Society, 1993 from the forging temperature and received an 8 hour aging treatment at 593°C, neither precipitates of Ti₃Al nor silicides were apparent in this condition.

The results from the tensile tests at strain rates of 10^{-2} , 10^{-4} and 10^6 1/s and 593°C showed almost no strain rate sensitivity for the yield stress, values being 490 MPa at 10^{-2} 1/s, 505 MPa at 10^4 1/s, and 480 MPa at 10^{-6} 1/s. Serrated yielding was observed in the 10^{-2} and 10^{-4} strain rate conditions. In addition, work by Bania [2] shows a plateau in the test temperature vs. yield stress curve indicating that the yield stress has a lack of temperature dependence for the temperature range 300-550°C. This combination of features is often cited as indicative of dynamic strain aging, a process linked to both silicon and oxygen content in other titanium alloys [4].

Experimental data from crack growth tests carried out in air environment are shown in Figure 1. Results from vacuum tests are shown separately in Figure 2. Examination of this data supports observations made in Ref. [3] that in this alloy a significant frequency and temperature influence on crack growth rate exists in both air and vacuum environments. Comparison of the air and vacuum results also shows a general improvement in fatigue crack resistance in vacuum at all loading frequencies at both room and elevated temperatures. Note, however, that the improvement in vacuum is

most pronounced at lower ΔK , while the effect decreases as ΔK increases.

The data for some high temperature tests, especially in vacuum, show a knee in the FCGR curves at low values of ΔK similar to that frequently observed in other materials at elevated temperature and which is attributed to a change in crack growth mechanism [3,5,6]. At high values of ΔK there is an increase in slope and a convergence of all curves to a single line indicative of the approaching K_{IC} value where environment and creep components are of lesser consequence. Such changes in growth behavior are traditionally labeled as stages I, II, and III, for microstructurally sensitive growth at low ΔK , linear Paris Law steady state growth, and nearly unstable fracture regions respectively.

The stage I to II knee is seen to be most pronounced at elevated temperature in the 10 Hz, 0.5Hz, and 0.05 Hz vacuum tests and also in air tests run with frequencies less than 0.05 Hz, while the knee is relatively absent in air and vacuum at 23°C. One should recognize, however, that the change from stage I to stage II need not be accompanied by a noticeable knee in the curve as is shown by Yoder [7] and this is indeed the case in this material under certain conditions as discussed in Ref. [8]. It is also observed that, within the stage II steady state behavior, there is a consistent change in slope of the curves, such that the Paris Law exponent decreased with increased cycle time and with increased temperature in both air and vacuum environments. These results are consistent with damage effects produced by combined environmental embrittlement and creep deformation.

Temperature effects for the group of tests run at 10Hz are presented in Figure 3 as crack growth rate versus ($\Delta K/\sigma_{ys}E$). When loading is represented as CTOD accounting for yield and modulus changes, there is only a small enhancement of environmental effect when considering a change in temperature from 23°C-650°C.

Crack closure is shown in Figure 4 as the ratio of $\Delta K_{eff}/\Delta K_{nom}$ versus ΔK_{nom} , where the

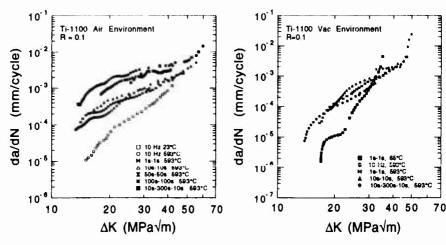
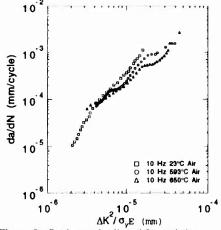


Figure 1: Crack growth rate versus ΔK for some tests in air environment.

Figure 2: Crack growth rate versus ΔK for tests in vacuum environment



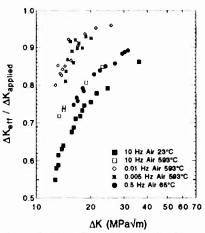


Figure 3: Crack growth adjusted for variation in modulus and yield due to temperature change.

Figure 4: Crack closure ic rels for air and room temperature tests.

subscripts eff and nom indicate effective and nominal, respectively. In previous work on Ti-1100 under variable loading frequencies it was noted that closure was significant at low ΔK loadings, particularly at room temperature [3]. The effect of closure on a da/dN vs. ΔK plot is to decrease the slope of the FCGR curve, especially in the stage I region. In addition, under decreasing frequencies, where the knee is most evident, the closure levels are found to be much reduced, not significantly altering the shape of the growth curve. The results from the 0.5Hz 23°C vacuum test shows a level of closure which is very similar to but slightly less than that of the 10Hz, 23°C air test.

The fracture morphologies seen in Ti-1100 under the test conditions run in the present

investigation are classified as follows:

1) At low ΔK , in air and vacuum, growth takes place in a cyclic cleavage process largely along the basal plane, with furrows connecting the cleaved planes [21-23]. Cleavage is promoted by the widmanstatten microstructure in which the alpha phase platelets have the same crystallographic orientation within a colony. Fracture surfaces from test run in air and vacuum displaying the quasi-cleavage fracture morphology are shown in Figure 5. It can be seen in Figure 5a that the cleavage process in air is much more glassy in nature than cleavage features in vacuum which has less distinct with a highly textured, ruptured appearance in places.

2) Stage-II propagation in air is characterized by a striated growth (Figure 5c). In air environment, the striations are clearly defined and measurements of striation spacing accurately represent the crack growth rate. The local crack growth direction indicated by the striations was seen to vary a great deal showing that the local crack growth is often quite different from the macroscopic growth direction. In vacuum, a striation-like morphology was observed as vague ripple patterns which are discontinuous along their length, and often do not have a constant step distance between two lines, see Figure 5d.

3) High ΔK loading at low frequencies and elevated temperature yields intergranular prior- β grain boundary fracture [3]. Air and vacuum intergranular modes display the same rough texture appearance. Intergranular fracture was seen to begin at a higher frequency in vacuum tests than in air with mixed transand intergranular fracture in vacuum at 0.05Hz while in air at the same frequency, fracture is fully transgranular. Fully intergranular fracture in air was not observed until a very high ΔK level in the 0.005Hz test, the percentage of intergranular fracture in the 0.05Hz vacuum tests specimen being approximately equal to the 0.005Hz air test. Five minute hold time at maximum load gave fully intergranular fracture in both air and vacuum environments over the entire range of ΔK tested.

ANALYSIS AND DISCUSSION

Environmental effects: Environmental influence on FGC of metallic materials at elevated temperatures has been seen to manifest itself by one or a combination of the following mechanisms:

(i) Short range stress directed diffusional mechanism where a brittle oxide layer is formed at the crack tip and subsequently fractured by the cyclic process [9]. (ii) Long range stress directed diffusional mechanisms which may include a multi-layer stable oxide growth or large depth of penetration by oxygen effectively creating a boundary layer of modified alloy in the region of the crack tip [10]. (iii) Adsorption

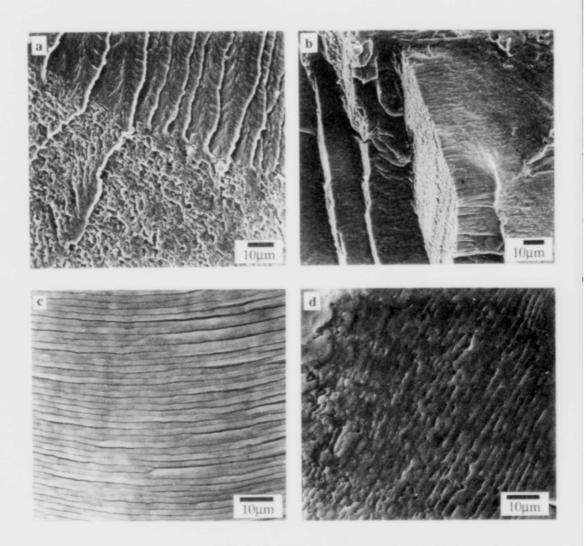


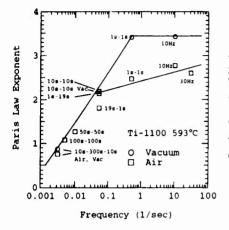
Figure 5: Fracture surface morphologies in both air and vacuum. (a) Difference in cleavage appearance in air (upper right) and vacuum (lower left). (b) Intersecting cleavage planes with striated plane in vacuum. (c) Appearance of striations in air. (d) Appearance of striations in vacuum.

processes requiring the formation of a complete monolayer on the fresh crack surface which lowers the energy required to form new crack surface and which limits rewelding and reversibility of slip [11].

(iv) Oxide induced crack closure mechanisms.

From the comparison given in Fig. 3, the short range brittle oxide mechanism described above is not evident in the present results, since it would be expected that a temperature increase from 23° C to 650° C would promote oxide formation through enhancement of diffusion, but bulk yield and modulus changes were found to be sufficient to consolidate the growth rate curves. It could be argued that 10Hz is too high a frequency to allow environmental effects to influence the crack growth process. This is, however, contrary to the observation that environmental effects are seen when comparing vacuum and air results at 593° C at 10Hz. Likewise, the oxide induced closure mechanism was not found to play a significant role in fatigue crack growth behavior of this alloy. The lack of spalled oxide traces on the fracture surface, lack of enhanced oxide coloration in the low Δ K growth region, and closure trends between room and elevated temperatures with closure levels being highest in room temperature, and decreasing with cycle time at elevated temperature [3] support this conclusion.

The fact that an environmental effect exists but is weakly temperature-dependent lends credence to a mechanism like (ii) and (iii) above where the environmental effect is through a fast, stress induced, non-Arrehnius type of diffusion, and/or through an adsorption mechanism. These two



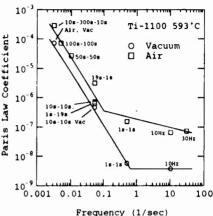


Figure 6: Relationship between Paris Law exponent and cyclic frequency.

Figure 7: Relationship between Paris Law coefficient and cyclic frequency.

mechanisms are difficult to separate, but in either case the environmental effect appears to "saturate" even at a frequency of 10Hz.

Closure Effects: As mentioned earlier, closure measurements in vacuum have not been obtained except for the case of 0.5Hz at room temperature. However, at elevated temperature, indirect evidence exists that closure may be responsible for the appearance of distinct knees in the vacuum crack growth rate curves. In air, the existence of knees are found to be the result of a combination of crack closure and some transient effects and not due to a change from stage I to stage II growth mechanisms. This conclusion was reached as a result of constant ∆K tests carried out at low ∆K (≈ 7 MPa√m) for which da/dN values fell on the line extended from the stage II region curve. Furthermore, on the basis of fracture surface analysis, the position of the apparent knee in air was found to be at a much lower ΔK value than that at which the transition from quasi-cleavage to striations occurs. The existence of knees as an indicator of transition from stage I to stage II growth is discussed in the work of Yoder [7] in which the sharpness of the knee is directly related to the narrowness of the distribution of aligned alpha colony sizes in the microstructure. The existence of knees in vacuum could, however, be explained on the basis of the enhanced crack tip closure observed in vacuum. Here the sharper knee in the 10Hz vacuum test compared to that of the 0.05Hz in vacuum agrees with the trend towards higher closure levels with increasing frequency as has been observed in air tests [3]. Furthermore, the observation that the onset of formation of striation in vacuum coincides with the appearance of the knee could be caused by a closure mechanism which changes abruptly when the fracture mode changes from quasi-cleavage to a striated-like mode.

Frequency Effects: The FCGR results from 593°C in vacuum indicate clearly a frequency effect which is independent of the environment. The results from air tests, in which environmental effects are expected to play a role, display trends similar to those of vacuum tests, while showing an overall higher crack growth rate for a given condition. This behavior could, in a simple approach, be expressed by employing a Paris-type equation that would incorporate both the frequency effect seen in vacuum and the environmental effect seen in air into the coefficient, C, and exponent, m, of this equation which is written as:

$$da/dN = C(593^{\circ}C, freq, env) \Delta K^{m}(593^{\circ}C, f, env)$$

By applying this equation to all test conditions at elevated temperature, one obtains relationships between the exponent, m, and coefficient, C, and the test frequency as shown in Figs. 6 and 7. It is seen that in air and vacuum tests there is a dependence on cyclic frequency for both parameters; in particular for air environment at frequencies below 0.05 Hz and in vacuum below 0.5 Hz. The nature and magnitude of frequency effect for both conditions below these transitional frequencies is very similar and, assuming that no oxidation effects are present in vacuum, it can be concluded that creep related effects dictate the response of crack growth to frequency. Additionally, the effect of unsymmetric

rather than the total. Conversely, the 0.05 Hz condition with fast loading (1s-19s) correlates based on the total cycle time. Loading rate can therefore be associated with creep-fatigue damage, while

environment effects are based on total exposure time.

Environment effects are seen to be most significant at frequencies above 1 Hz, where there is a large difference in both the coefficient and the exponent. This does not mean that the effect of environment decreases with increasing cycle time, but rather that another time-dependent process, such as creep, becomes the controlling factor at lower frequencies. At frequencies lower than the transitional frequencies of this material, the Paris exponent decreases rapidly as a logarithm of frequency and is independent of environment. Meanwhile, at these frequencies, the coefficient parameters from the air tests show a constant scaling compared to the vacuum results. This scale value, which can be taken as a direct measure of the environmental effect, results in about a three-fold crack growth rate increase between vacuum and air tests. It is significant that this scale factor is practically independent of cycle time, indicating a mechanism of environmental effect which is fast with respect to the test frequencies while remaining constant in magnitude. The coefficient is seen to have a low order time dependence at frequencies higher than the transitional frequency in air environment, while the vacuum tests are independent of frequency before creep is activated.

CONCLUSIONS

The effects of the environment on the fatigue crack growth of the titanium alloy, Ti-1100, found in the study can be summarized as follows:

 The primary effect of the environment is to increase the fatigue crack growth rate, but the effect is not large. This effect was found to be constant and rapid in relation to the frequencies tested and is weakly dependent on cycle time.

2. An effect of environment was found to be an increase in the Paris law exponent and a decrease in

the Paris law coefficient when going from the vacuum to air environment.

3. Viscoplasticity has a dominant effect in controlling fatigue crack growth behavior at 593°C at low frequencies. The effect manifests itself as a shift towards higher ΔK in the transition from quasicleavage to striation dominated transgranular growth and as a change from transgranular to intergranular fracture mode. Paris law parameters in stage II growth are largely determined by the extent of viscoplastic response.

4. A significant secondary effect of environment is seen as a reduction of viscoplastic response in air compared to vacuum such that, for example, intergranular growth is evident in vacuum at higher

cyclic frequencies than in air.

An additional effect of environment is an apparent change in crack closure with the possibility of a
greater degree of closure in vacuum.

Acknowledgment: The financial support of this work is provided jointly by TIMET, Henderson, Nevada and USAF Office of Scientific Research, Bolling AF Base under grant AFOSR-89-0285. The authors acknowledge the valuable discussions with Dr. P. Bania of TIMET.

REFERENCES

 P.J. Bania, "Ti-1100: in Sixth World Conference on Titanium, Part II, Cannes, France, 6-9 June 1988, ed. P. Lacombe, R. Tricot, G. B'eranger, 825-830. Les editions de physique, Les Ulis Cedex, France (1988).

P.J. Bania Journal of Metals, V 40, Number 3 (1988) 20-22.

3. H. Ghonem, R. Foerch, Materials Science and Engineering, V A138, (1991) 69-81.

- M.R. Winstone, R.D. Rawlings, and D.R.F. West, Journal of Less-Common Metals, V 31, (1973) 143-150.
- H.W. Liu, J.J. McGowan, AFWAL-TR-81-4036, Air Force Materials Laboratory, Wright-Patterson Air Force Base, OH (1981).
- A.S. Krausz, K. Krausz, Fracture Kinetics of Crack Growth, Mechanical Behavior of Materials, V 1, Kluwer Academic Publishers, The Netherlands, (1988).
- G.R. Yoder, L.A. Cooley and T.W. Crooker, Engineering Fracture Mechanics, V 11 (1979) 805-816.

8. H. Ghonem and D. Zheng, Material Science and Engineering, V 135, (1992),

9. R. Foerch, A. Madsen and H. Ghonem, Metallurgical Transaction, to be published (1992)

10. T. Ericson, Canadian Metallurgical Quarterly, V 18 (1979) 177-195.

 G.R. Yoder, L.A. Cooley, and T.W. Crooker, Metallurgical Transactions, V 8A (1977) 1737-1743.

INVESTIGATION OF PROPERTIES OF LITANIUM ALLOYS

IN A GESEOUS HYDROGEN MEDIUM

Victor Sytshikov, Lubov Rtitsheva, S. Ushkov, V. Durjagin, A. Repechenko

The Central Research Institute of Structural Materials "Prometey" Sankt-Petersburg, Russia, 193167

Abstract

The tensile tests of \mathcal{J} -titanium alloys in hydrogen gas showed that the decrease of tensile static properties regardless of test temperature occures. The low cycle endurance test of alloys in hydrogen gas showed that medium effect is observed at stresses higher than $0.6\,\mathrm{G}_{\mathrm{B}}$; it is correlated to increased hydrogen content on surface fracture of the sample and fracture surface fracture appearance.

The conformities of hydrogen-metal interaction, hydrogen-titanium, in particular, and the hydrogen embrittlement of the metals are of great importance due to the prospects of hydrogen power plants development.

The hydrogen effect on the tensile properties of the titanium and titanium alloys was studyed on a prehidrogenated material in general, when the concentration relations were put to the first line and the accepted hydrogen content in materials or structures was determined.

A general approach to the development of the titanium structure keeping the safety under the hydrogen attack can be formulated as follows: the standard hydrogen content of thin semiproducts can deviate to a sense of an increase, and that of thick semiproduct can be corrected to a sense of reduction as compared to a critical hydrogen content, if an middle thick semiproducts (25 mm).

The tensile properties of the titanium alloys operating of testing in a gaseous hydrogen at elevated pressures and temperatures, especially, are less investigated. This work shows the tensile properties of the α -titanium alloy under uniaxial tension in a gaseous hydrogen medium as a function of a test temperature and hydrogen pressure at low cycle fatigue tests. The tests were carried out on the specimens in IIT-3B and IIT-7M titanium alloys, whose chemical composition meets the requirements of the GOST 19807-74. The IIT-7M alloy, alloyed by 2,5% Zr and by about 2,0% Al is commercially pure α -alloy, where hydride mechanism of hydrogen embrittlement is activated. The IIT-3B alloy contains about 4,0% Al and about 2% V and is a betized α -alloy, whose structure contains 2-3% of the α -phase. Because of this either the hydride hydrogen embrittlement or the embrittlement of the second type, characteristic of the alloy at low rate of applied stresses,

Titanium '92 Science and Technology Edited by F.H. Froes and I. Caplan The Minerals, Metals & Materials Society, 1993 occurs.

The procedure impurity content (Fe,Si,C,N,O) etc of the alloy as typical to the commercial materials.

The gaseous hydrogen of A grade in accordance with the GOST 3022-80 was ap- ied as plied as a hydrogen medium, air was applied as a reference medium. The tests were carried out in accordance with the procedure and using facilities of the Physico-Mechanical Institute of AS Ukraine. These procedures allow to investigate a structural material behaviour in an aggressive media of elevatedparameters.

The tensile tests were carried out on the 5-fold cylindrical specimens of 5 mm gauge section diameter at 20-300°C and at 1MPA and 40 MPa operating hydrogen pressure. The tensile properties of the IIT-7M alloy as a function of the tensile strain rate which varies in 0,1-100 mm/min range were investigated. The information of the tensile properties as a function of temperature and rate in the hydrogen medium is required for ,firstly, correct evaluation of their properties and secondly, to account for a possible hydrogen effect. The minimum strength of the alloy in the hydrogen was observed at 0,1 mm/min, the tensile properties as a function of temperatures of the alloy were evaluated at the rate. The hydrogen effect results in some reduction of the tensile properties of the material, especially, at 40 MPa hydrogen pressure. The increase of ductility is observed, the relative elongation values in the hydrogen is 27-30%, and in the air - 19-21%. Figure 1 shows the test results of IIT-3B and IIT-7M alloy.

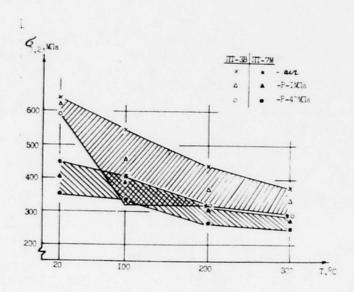


Figure 1 Test temperature and hydrogen pressure effects on the tensile properties of the IIT-3B and IIT-7M alloys at 0,1 mm/min uniaxial tensile rate.

The strength of IIT-3B alloy in the hydrogen is reduced by 8--39~% as compared to air, the maximum reduction (39%) was observed at 100°C . The strength of the IIT-7M alloy in the hydrogen as compared to air is reduced by 15--43%, the maximum reduction is observed at room temperature. The hydrogen effect on ductility characteristics is small. The date analysis shows that the

test medium influences the IIT-3B alloys more as compared to the IIT-7M alloy which is undoubtly related to their structural features. The higest effect of the medium was observed at $100^{\circ}C$ (the strength was decreased up to 39%), which implies that under tension the occlusion mechanism is activated. On the contrary, the hydrogen effect on the IIT-7M alloy is utmost at room temperature. The indirect method indicating the test medium effect on the titanium properties is related to a scanning electron microscopy. A fracture surface of the specimens after tensile tests was investigated with the "Stereoscan-150", the scanning electron microscope. It seemed that all the fracture surfaces of the IIT-3B alloy tested in air and in hydrogen are characterized by a ductile fracture of a dimple relief. However, on the fracture surfaces of the specimens tested in hydrogen small secondary cracks were observed, they are clearly seen at large magnification (Figure 2). The

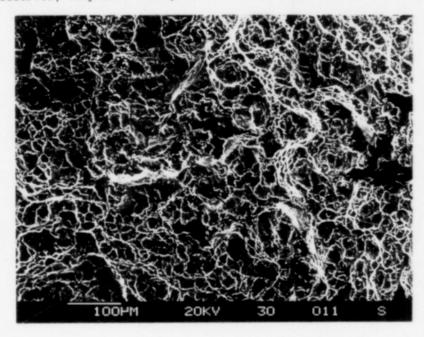


Figure 2 Fracture surfaces of the specimens in IIT-3B alloy after tensile tests in the hydrogen medium at 300°C.

low cycle fatigue tests with an applied frequency of pulsing load equal to 6 cycles/min were carried out at an ambient temperature in the hydrogen medium on the specimens with stress concentrators (χ = 2,8-3,0). The strength of the notched specimens in the IIT-3B and IIT-7M alloys of 100 MPa and 90 MPa, respectively, was determined prior to low cycle fatigue tests. The low cycle fatigue tests were performed under the three cyclic load values equivalent to 0,40B, 0,60B and 0,450B (OB for the IIT-3B alloy). The test indicated (Figure 3) that the low cycle life time of the IIT-3B alloy tended to reduce under the two levels of amplitude range of the cyclic load, corresponding to 0,70B and 0,60B (Oc = 80 MPa, Oc = 65 MPA). At lower cyclic load value (Oc = 50 MPa) there is non-exsitance of the hydrogen effect on the low cycle fatigue. This is of great importance for the structures and systems operating in the hydrogen medium, i.e.at loads equal to or lower than 0,450B the χ -titanium alloys can safely operate in the hydrogen medium.

The investigation of the fracture surfaces with the "Stereoscan-150" electron scanning-myc roscope indicated the existance of appreciable difference

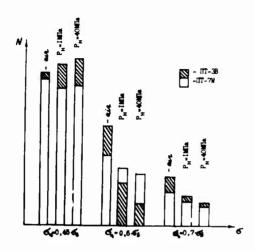


Figure 3 The effect of the hydrogen on the low cycle fatigue of IIT-3B and IIT-7M alloys.

of the fracture surface microstructure of the specimens tested in air and in hydrogen. The specimens tested at $\bigcirc_{\rm C}$ = 65 MPa characterized by the utmost effect of the hydrogen were investigated. The both test types (in air and in hydrogen) are characterized by the similar fracture type: crack initiation zone, fatigue striations, shear, ductile dimple after fracture. However, the fracture surfaces of the specimens in the IIT-3B alloy tested in the gaseous hydrogen medium the fraction of brittle constituents is increased appreciably i.e. fractures of the shear type, many secondary cracks (over up to 60% of the fracture area) (Figure 4). The base fracture types of the fracture surfaces of the specimens tested in air are a fatigue zone and ductile afterfracture.

The random evaluation of the hydrogen content of the specimens tested in the hydrogen medium (Table 1)showed the hydrogen content gradient across the section. The hydrogen content was determined by a spectral method laverwise across the thickness of the specimen.

It is of note the existance of "grey" colour on the fracture surface of the specimens tested in the gaseous hydrogen medium, which is characteristic of the specimens, the hydrogen embrittlement effect of which is activated during specimen testing. The phenomena seems to indicate a formation of a thin hydride film on a juvenile surface of the specimens at the time of a crack opening in the hydrogen medium. This is indicated by the above data.

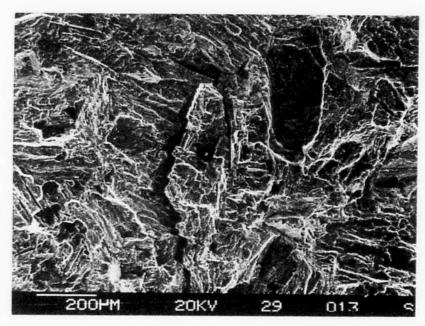


Figure 4 The fracture surfaces of the specimens in IIT-3B alloy after low cycle life time tests in the gaseous hydrogen medium.

Table 1 A layerwise hydrogen content of the specimens in IIT-3B alloys after the low cycle tests

The test medium	The distance from a surface, mm				
	0,05-0,08	0,10-0,13	0,20		
air	0,01 - 0,07	0,015 - 0,016	0,005 - 0,013		
hydrogen, 1 MPa	gen, 0,05 -0,02 0,013 0,05 0,017 0,10 0,009		0,013 0,017 0,007		
hydrogen, 40 MPa	0,10 0,10	0,33 0,02	0,018 0,017		

Conclusion

1. The mechanical proper ties of the Δ -titanium IIT-7M and IIT-3B alloys evaluated in the gaseous hydrogen medium are reduced with hydrogen pressure increase and at P = 40 MPa the mean reduction of the materials strength is 20% in respect with the original value. The ductility parameters of the alloys in the gaseous hydrogen mediam are less deduced. The increase of the test temperature up to 300°C doesn't effect on the established relations for the IIT-7M alloy, while those of the IIT-3B alloy are slightly reinforced which is induced, perhaps, by the 2 - 3% β -phase in its structure. 2. The low cycle life time tests of the both alloys in the gaseous hydrogen medium indicate that the hydrogen effect appears only at 0,6°B cyclic load

amplitude range and higher: for example, at 5c = 0.70B the life time to failure of the 117-7M alloy by about 35% and of 117-3B alloy by about 50%. On the fracture surfaces of the specimens in the 117-3B alloy tested in the hydrogen under the increase of the brittle constituents, the shear fracture and many secondary cracks are observed.

3. The results of the investigation allow to recomend the application of the α -titanium alloys as a structural material for vessels and tanks to keep

the saseous hydrogen.

However, to provide a higher safety the selection of the strength ratio as a function of stress values is to be made more carefully and with their increasing.

HYDROGEN ASSISTED STRESS CRACKING OF TITANIUM ALLOYS

I.Azkarate, A.Recio, A.Del Barrio.

INASMET. Bº Igara - 20009 SAN SEBASTIAN (SPAIN)

ABSTRACT

The behaviour of Titanium Grades 2, 5 and 12 alloys under hydrogen assisted stress cracking conditions has been studied by means of the slow strain rate technique. Tests have been performed in air and synthetic sea water while hydrogen was potentiostatically produced on the specimen surface during the test. Measurements of elongation, reduction of area, maximum load and true stress at fracture as well as metallographic and fractographic studies have been carried out in order to assess the loss of ductility of the studied alloys. Hydride penetration and cracking with a slight loss of ductility was observed for Ti Gr-12 when the highest cathodic potential was applied. Ti Gr-5 did show a significant loss of ductility, but no hydriding or cracking was detected. The best behaviour against hydrogen assisted stress cracking was shown by Ti Gr-2 samples; although a thick hydride layer grew on the specimen surface and some lateral cracking appeared when -1500 mV (SCE) polarization was applied to the specimen. However, no loss of ductility was observed.

KEYWORDS

Titanium, cracking, hydrogen.

INTRODUCTION

Titanium and its alloys are increasingly being used in conditions where a high corrosion resistance is required. Moreover, its good mechanical properties/density ratio make these materials very attractive for applications in which reduced weight is an important consideration. Unalloyed titanium is successfully being used in marine and certain chemical industry equipments because of its excellent corrosion resistance due to the high stability, adherency and protective character of the titanium oxide. Titanium behaves satisfactorily as long as the media is oxidizing or slightly reducing. There is a risk of hydriding and embrittlement if the reducing character of the environment increases, the titanium is galvanically coupled to some less noble material, or some special situation occurs where hydrogen is formed on the material surface.

EXPERIMENTAL

Hot rolled and annealed 6 mm, thick Titanium Grades 2, 5 and 12 plates were studied in the present work. Their chemical composition and mechanical properties are given in Tables I and II. Metallographic samples were prepared and optically studied. Their microstructure is formed by equiaxed alpha grains in the case of Ti Gr-2, slightly elongated alpha grains with intergranular beta for Ti Gr-5, and elongated alpha grains with intergranular transformed beta for Ti Gr-12.

Titanium '92 Science and Technology Edited by F.H. Froes and t. Caplan The Minerals, Metals & Materials Society, 1993 Three mm diameter round transverse tensile specimens were machined and finished with 600 grade emery paper. Slow strain rate tests in air and synthetic sea water were $_{\rm F}$ erformed at room temperature in a K & H CERT 2000 electromechanical tensile testing machine. Hydrogen was cathodically produced on the specimen surface using a Wenking LT 78 potentiostat. The specimen was located in a methacrylate cell together with the reference (SCE) and counter (graphite) electrodes. Three different potentials were used: the corrosion potential -1000 and-1500 mV (SCE). Strain rates used were in the range of 10° - 10^{7} s¹. All testing conditions are given in Table III.

Maximum load, elongation, true stress at fracture and reduction of area were the parameters measured to assess the loss of ductility. In order to quantify the hydriding of the alloys under different testing conditions, samples from the specimens' gauge lengths were analyzed using an automatic LECO RHIE hydrogen analyzer.

RESULTS

The results obtained in the SSRT tests are summarized in Figures 1, 2 and 3 where maximum load, elongation, true stress at fracture and reduction of area are plotted versus applied polarization for each material and strain rate. Hydrogen analysis results are summarized in Table IV.

Ti Gr-2 has shown no loss of ductility as a function of the cathodic potential for any of the strain rates used $(1.5 \times 10^6, 3 \times 10^7, 2.4 \times 10^7 \, s^4)$, and no clear trend in the measured parameters was noticed (Figure 1). Hydrogen analysis show that appreciable hydriding does not occur until the -1500 mV potential is applied to the specimen. This is in agreement with what is observed in the metallographic studies where no hydrides are detected until the highest cathodic polarization is used. In this case superficial hydriding and some lateral secondary cracks near the surface are present for all the strain rates used. Secondary cracking is more severe, as expected, in the specimen tested at the lower strain rate; some of this cracks can be observed in Figure 4. Specimen fracture surfaces were studied by means of the scanning electron microscope. The fracture mode was ductile for all test conditions, even when the highest cathodic potential was applied to the specimen. The fracture surface was primarily ductile and only some minute brittle areas have been observed at crack initiation sites.

Sensitivity to the hydrogen assisted stress cracking has been more evident for Ti Gr-12. It suffered some loss of ductility mainly manifested in the reduction of area and consequently in the true stress at fracture. (Figure 2). As in the case of Ti Gr-2, metallographic studies and hydrogen analysis show no significant hydriding until the highest cathodic potential is applied to the specimen. Figure 5 show photomicrographs of specimens tested at $2 \times 10^7 \, \mathrm{s}^3$ strain rate. Considerable hydriding with significant diffusion towards the bulk material and extensive secondary cracking along the gauge length of the specimens is seen. The fracture mode observed from SEM studies is ductile for all testing conditions except when -1500 mV (SCE) polarization is used, in which case a more brittle fracture mode is detected at the crack initiation site (Figure 6).

Finally, Ti Gr-5 has been the alloy that has sustained the greatest loss in ductility as manifested in the values of elongation, reduction of area and stress at fracture for specimens tested at the highest cathodic polarization (Figure 3). Unlike Ti Gr-2 and Ti Gr-12 alloys, no hydride formation nor secondary cracking has been observed in the metallographic study, but chemical analysis show that Ti Gr-5 specimens tested in the -1500 mV polarization condition have also experienced significant hydrogen uptake. The fracture surface mode observed in SEM studies was ductile for all test conditions, except for the specimen polarized at -1500 mV, which revealed a large area exhibiting a brittle fracture mode (Figure 7).

DISCUSSION

The resistance of titanium grades 2, 5 and 12 to stress corrosion cracking in synthetic sea water is shown to be excellent since no secondary cracks or losses in ductility have been observed in tests performed with different strain rates at the corrosion potential. When cathodic polarization of -1.5 V is used to produce hydrogen on the specimen surface during the test, the behaviour of the alloys studied changes.

In fact it has been observed that hydrogen produced on the Ti Gr-2 specimen surface forms a hydride layer of 40 mm and also secondary cracks of up to 70 mm. In Ti Gr-12, hydrogen diffused into the

material forming hydrides to a maximum depth of 120µm, and secondary cracks of 200µm have been observed. On the other hand, no hydrides nor secondary cracks were detected in Ti Gr-5, but chemical analysis show that the hydrogen content has also increased for this material.

The different behaviour of these alloys seems to be associated with the different penetrability and solubility of hydrogen in each alloy, and can be explained based on the following considerations: 1. The beta phase content is negligible for Ti Gr-2, approximately 3 volume % for Ti Gr-12 (1), and 15% for Ti Gr-5 (2). 2. The solubility of hydrogen in alpha titanium increases from 30-45 ppm at room temperature (3, 4) to 1500 ppm (6,72 at.%) at the eutectic (300°C); at this temperature the solubility in the beta phase is 13200 ppm (39 at.%) (5). 3. The diffusivity of hydrogen in alpha titanium is considerably lower than in the beta phase. Phillips et al. (6) found that alpha titanium's diffusion coeficient over the temperature range 25 to 100°C is given by:

 $D_a = 6 \times 10^2 \times exp (-14400 \pm 800/RT) cm^2 \times s^{-1}$

Which yields a value of 3.2×10^{-12} cm² x s⁻¹ at 25°C, too low for any appreciable diffusion to be observed.

On the other hand, Holman et al. (7) determined the diffusion coefficient in a beta titanium alloy over the temperature range 20 to 500°C as:

 $D_6 = 1.58 \times 10^{-3} \times \exp(-5140 \pm 300/RT) \text{ cm}^2 \times \text{s}^{-1}$

Given a value of 3.3×10^{-7} cm² x s⁻¹ at 25°C, it is 10^5 times higher than in the alpha phase.

Therefore the superficial hydride layer formed on the Ti Gr-2 specimen can be explained by the low solubility and diffusivity of hydrogen in this all alpha alloy. In the case of Ti Gr-12, the small amount of beta phase channels hydrogen towards the bulk material increasing its penetration; but when saturation of hydrogen is reached, hydrides precipitate in the alpha phase along the grain boundary. This can be seen in Figure 8. Hydrides precipitate in the alpha phase along the intergranular beta phase. Finally, titanium Gr-5 has a higher beta phase content that appears to be enough to dissolve all hydrogen that has diffused into the material without forming hydride precipitates.

Loss of ductility exhibited by Ti Gr-12 and Ti Gr-5 is likely to occur by a different mechanism for each alloy. For Ti Gr-12, the formation of a brittle hydrogen rich phase (hydride) is responsible for the cracking and loss of ductility. For Ti Gr-5, its higher beta phase content admits more hydrogen entering the material by interstitial solid solution without forming hydrides. When hydrogen content reaches a certain level, lattice decohesion occurs with a brittle rupture.

CONCLUSIONS

- No SCC was indicated for any Titanium alloys tested in seawater at or noble to a potential of 1000 mV.
- Hydriding of Titanium Grades 2, 5 and 12 strained in sea water does not occur when cathodically polarized at or noble to potentials of -1000 mV (SCE).
- Titanium Grade 12 suffers hydride cracking and some loss of ductility when slowly strained and polarized at -1500 mV (SCE).
- Titanium Grade 5 suffers a significant loss of ductility when slowly strained and polarized at -1500 mV (SCE).
- Titanium Grade 2 suffers superficial hydriding and some cracking but no loss of ductility when cathodically polarized at -1500 mV.
- Beta phase content appears play a fundamental role in the hydriding and loss of ductility of titanium alloys while strained and cathodically polarized

REFERENCES

- (1) N.R.Moody, S.L.Robinson, F.A.Grenlich. Hydrogen Effects on Ti Code 12. Properties and Microstructure. SANDIA Report. SAND 85-8203. Department of Energy. U.S.
- (2) A.Gysler, G.Lütjering. Influence of Test Temperature and Microstructure on the Tensile Properties of Titanium Alloys. Metallurgical Transactions. Vol.13A 1982, p.1435
- (3) R.S.Vitt, K.Ono. Metallurgical Transactions. Vol. 2. 1971, p.608.
- (4) R.W.Schutz, J.S.Grauman. Determination of Cathodic Potential Limits for Prevention of Titanium Tube Hydride Embrittlement in Saltwater. Corrosion 89. Paper Nr. 110.

- (5) A.San Martin, F.D.Manchester. Phase of Binary Titanium Alloys. J.L.Murray Ed.ASM. Metals Park. Ohio. (1987). 123.
- (6) I.I.Phillips, P.Poole, L.L.Shreir. Hydride Formation during Cathodic Polarization of Ti-II. Effect of Temperature and pH Solution on Hydride Growth. Corrosion Science. Vol.14. 1974, p.533.
- (7) W.R.Holman, R.W.Craw, T.Paredes Jr. Hydrogen Diffusion in a Beta Titanium Alloy. Transactions of the Metallurgical Society of AIME. Vol. 233. 1965.

Table I. Chemical composition of materials tested (Weight %)

			•		Element					
Alloy	N	С	н	Fe	0	Al	V	Мо	Ni	Ti
Ti Gr-2	0.0032	0.005	0.0030	0.048	0.126			1.1	-	Bal
Ti Gr-5	0.011	0.020	0.0083	0.18	0.144	6.4	3.8		-	Bal
Ti Gr-12	0.017	0.010	0.0021	0.11	0.15	-	Ţ-	0.26	0.66	Bal

Table II. Tensile properties of materials tested (transverse)

Alloy	Y.S. 0.2% (MPa)	U.T.S. (MPa)	E (%)
Ti Gr-2	430	499	31
Ti Gr-5	988	1030	12.6
Ti Gr-12	484	587	20

Table III. Slow Strain Rate Tests conditions

Environment: Air

Sea water (ASTM D-1141)

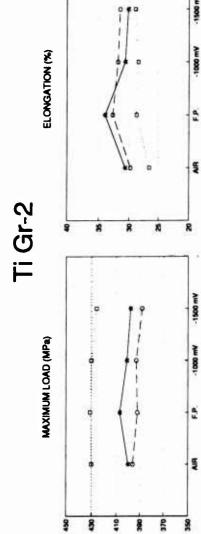
25°C

Temperature: Potentials:

Corrosion Potential, -1000 and -1500 mV (SCE)

 1.5×10^6 , 3×10^7 , 2.4×10^{-7} s⁻¹ (Ti Gr-2) Strain rates: 3 x 10⁷, 2 x 10⁻⁷ s⁻¹ (Ti Gr-5 and 12)

Table IV	V. Total hydrogen content of specia	mens tested.
Alloy	Impressed Potential	Hydrogen content (ppm)
	None	20
Ti Gr-2	-1000 mV	39
	-1500 mV	232
	None	23
Ti Gr-12	-1000 mV	60
	-1500 mV	320
	None	69
Ti Gr-5	-1000 mV	104
	-1500 mV	253



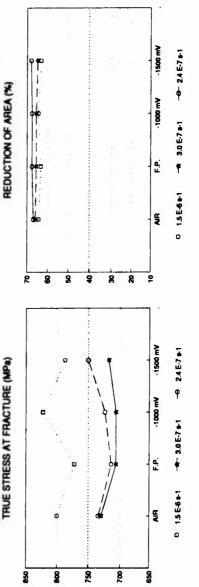


Fig 1.Results of SSRT tests for Ti Gr2

-0 24E781

U 15E-6+1 -- 30E-7+1

-0 2.4 E-7 s-1

4 306.741

14851 0

Ti Gr-12

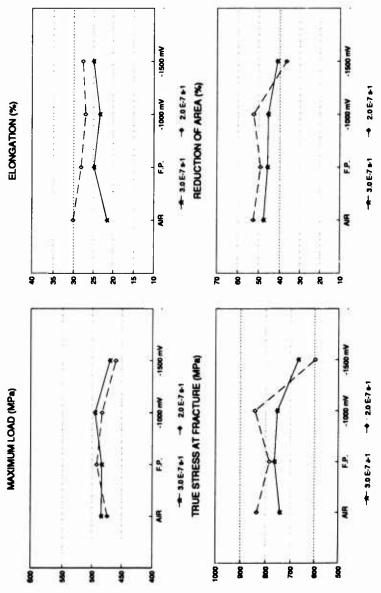


Fig.2. Results of SSRT tests for Ti Gr-12

Ti Gr-5

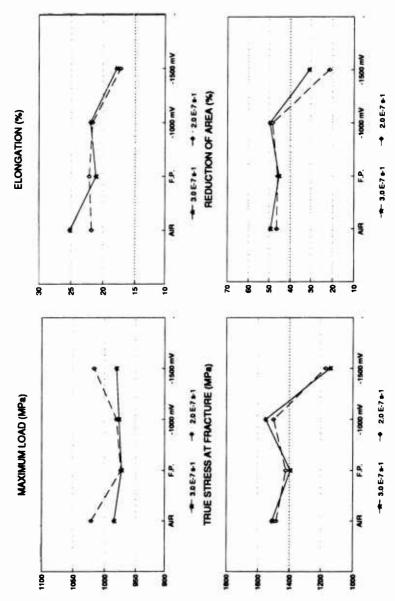


Fig. 3. Results of SSRT tests for Ti Gr-5

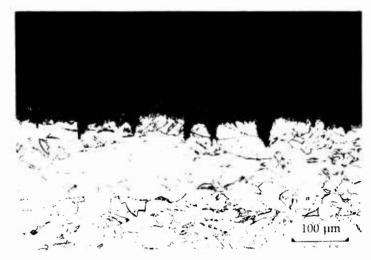


Fig. 4. Optical micrograph showing lateral secondary cracks starting in the hydride layer in Ti Gr-2 tested at 2.4 x10 7 s⁻¹ strain rate with -1500 mV (SCE) cathodic polarization

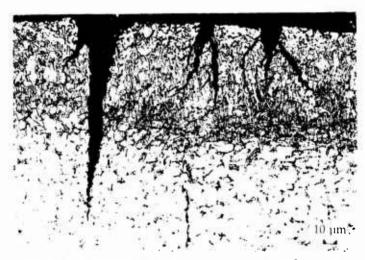


Fig. 5. Optical micrograph of Ti Gr-12 tested at 2 $\times 10^7$ s⁻¹ strain rate with -1500 mV (SCE) cathodic polarization.

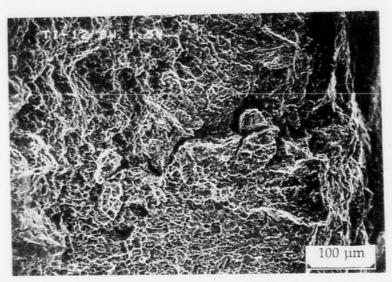


Fig.6. SEM micrograph of the fracture surface of Ti Gr-12 tested at 2 x 10^7 s⁻¹ strain rate with -1500 mV (SCE) cathodic polarization showing brittle fracture mode.

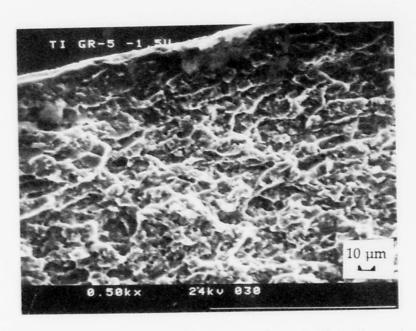


Fig.7. SEM micrograph of the fracture surface of TI Gr-5 specimen tested at 2 x 10^{-7} s⁻¹ strain rate with -1500 mV (SCE) cathodic polarization showing a brittle mode

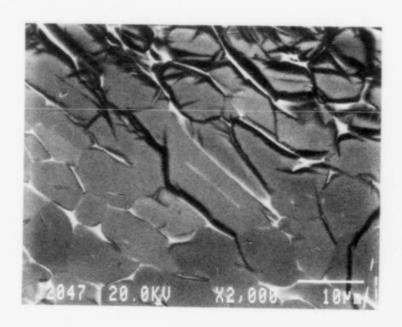


Fig.8. Backscattered electron image of Ti Gr-12 specimen tested with -1500 mV (SCE) cathodic polarization showing hydride precipitates (dark) ocurring in the alpha phase (grey) along the intergranular beta (bright)

MICROSTRUCTURE TRANSFORMATION AND CRACKING

OF TITANIUM ALLOYS UNDER CONTACT LOADING

P. Blanchard, S. Fayeulle, A.B. Vannes, L. Vincent

Ecole Centrale de Lyon Laboratoire Matériaux-Mécanique Physique URA CNRS 447 69131 ECULLY Cedex, FRANCE

Abstract

Small displacement amplitude friction tests were used to analyse the change in properties of several titanium alloys submitted to contact loading in air. Superficial layers of the alloys have been characterized by optical and scanning electron microscopy. Depending on the amplitude of the displacement, partial slip or gross slip occured in the interface. During partial slip, cracks initiated and propagated. Mechanisms for crack behaviour are described in terms of fatigue properties. Gross slip led to debris formation. A new structure called Tribologically Transformed Structure (TTS) was detected in the superficial layers. The debris particles generated from the transformed areas and were quickly oxidized once in the interface. The influence of several test parameters on the thickness of the TTS was analysed. The role of the TTS on the wear behaviour and the influence of various properties of the titanium alloys are discussed.

Introduction

When surfaces are in contact, very damaging phenomena occur if oscillatory displacements of small amplitude are imposed. Fretting wear resulting from these displacements has been observed for many years (1-3) and two main damages have been described for numerous metals and alloys: cracking and particle detachment (4,5). These two mechanisms are strongly dependent on the friction conditions: so far, the role of two parameters has been emphasized: the normal load acting on the samples and the imposed displacement (4,6). When the normal load (respectively the imposed displacement) is decreasing (respectively increasing), the main damages observed on the samples are progressively changing from cracking to detachment of particles. This has been described using the concept of fretting map recently proposed (6,7): material response fretting

Titanium '92
Science and Technology
Edited by F.H. Froes and I. Caplan
The Minerals, Metals & Materials Society, 1993

map (MRFM) (6) have been defined to represent the various damages (Non Degradation: ND, Cracking: C, Particle Detachment: PD) observed as a function of the test parameters (Normal load and amplitude of displacement).

Cracking and particle detachment have been observed on titanium alloys which are often used in applications involving fretting problems. Their possible role on decrease of fatigue strength and fatigue life has been previously studied (8-11). The mechanism of detachment of particles has been carefully analysed (12). It has been shown that a tribological transformed structure (TTS) is achieved in the superficial layers of sample during fretting tests. The TTS is very hard and is made of ultrafine equiaxed grains of α -phase. It is not oxidized. Particles are detached from the TTS in which numerous cracks have been observed.

In this paper, we present new results relating to the TTS and the cracking mechanisms. Relations between damages and material properties are investigated.

Experimental

Fretting tests were conducted using a tension compression hydraulic machine where reciprocating movement of a given amplitude was imposed to one sample (4). The normal load was applied to the other one. The experimental conditions were:

normal load: from 300 to 500 N

amplitude displacement: from ±15 to ±50 μm

frequency = 1 Hz

Tests were done in air at room temperature. Test samples were 10x10x10 mm³ parallelepipeds. Curved samples (sphere of radius R = 0.5 m) on nearly flat (R = 30 m) contacts were used, giving contact area of about 1 mm large. The surfaces were polished with diamond paste (3 μ m) and alumina (0.5 μ m) and cleaned with ethanol before testing. Materials were $\alpha+\beta-\text{Ti}6A14V$ (hot forged), Ti15V3A13Cr3Sn (called TV15CA), $\alpha+\beta-\text{Ti}6A15Zr$ and $\alpha+\beta-\text{Ti}5A14Cr$ titanium alloys slid against themselves. TV15CA alloy was used with two different stuctures α and β . After testing, the samples were cut (cross sectional cut parallel to the sliding direction) and polished for optical and electron microscopy. The different phases were revealed by etching with (H₂O + 1% (HNO₃-HF)) reagent.

Results and discussion

Cracking

When the actual displacement at the interface is small (imposed displacement smaller than $25~\mu m$ in our tests for titanium alloys), sticking can be achieved in the center of the contact area. In this case, cracks are observed at the location of the maximum tensile stresses. This has been widely studied for aluminium alloys (6) where cracks are easily produced as soon as Hertzian contact pressure is equal to 80~MPa.

In the case of hot-forged Ti6Al4V alloy, Hertzian pressure leading to cracks initiation and propagation has to be greater than 280 MPa. Below this value, no degradation of the surfaces is seen in the optical microscope (Non Degradation domain of the MRFM). But cracks can be detected for lower contact pressure (110 MPa) if the Ti6Al4V alloy has been heat treated in order to decrease the endurance limit from 600 to 300 MPa. An example of 100 μm long cracks observed on heat treated Ti6Al4V is shown in figure 1. These results on Ti6Al4V and the comparison with the case of aluminium alloys (6) reveal that a major parameter for crack initiation and propagation is the endurance limit σ_d : the stresses due to contact (i.e. stresses σ_{XX} due to the normal and the tangential forces) have to be greater than σ_d for cracks to initiate. This shows that the classical fatigue approach can be very useful to analyse fretting fatigue.



Figure 1- Cross section view of cracks in heat treated Ti6Al4V alloy (fretting conditions: P = 110 MPa, $D = \pm 25 \mu m$, 50000 cycles)

Particle detachment

When sliding occurs in the interface, TTS is observed in the superficial layers as shown in figure 2 (α -TV15CA). The TTS has been detected on all kind of titanium alloys (12) and also on other materials (5). It is always very hard (more than 1000 HV50) and made of the most stable phase (α -phase for Ti alloys), whatever the initial structure.

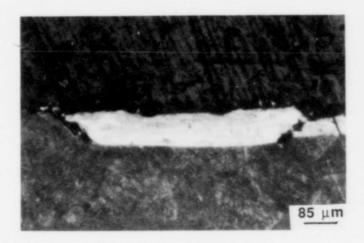


Figure 2 - Optical view (cross section view) of the superficial layer of α -TV15CA alloy ($\pm 50~\mu m$, 50000~cycles)

The thickness of the TTS depends on the alloy and on friction parameters. The variation of the thickness is given as a function of the number of cycles on figure 3 and as a function of the amplitude of displacement on figure 4 (on this figure, the actual displacement is equal to the imposed displacement minus the displacement corresponding to clastic deformation of the device). A maximum value of the thickness was observed for each alloy. It was obtained very quickly (less than 1000 cycles) and as soon as the actual displacement was equal to 50 μ m. The same TTS has been observed for the various titanium alloys (12). Nevertheless, the properties of the alloys can be used to discuss about some TTS characteristics. The formation of the TTS (transformation from β to α phase and formation of ultrafine grains) has been explained by deformation induced mechanisms and is not related to increase of temperature (12).

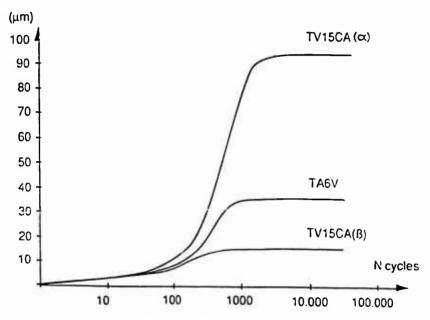


Figure 3 - Variation of the thickness of the TTS versus number of cycles amplitude = $\pm 50 \mu m$

The formation of TTS is much more difficult for β alloys and figure 5 shows that for α or $\alpha+\beta$ alloys, the thickness of the TTS can be correlated with the temperature of the β -transus: the higher the β -transus temperature, the thinner the TTS. This reveals that the formation of the TTS is easier when the energy of recrystallization is lower

For a given alloy, the thickness of the TTS does not depend on the size of the initial grains: tests performed with quenched and tempered Ti6Al4V alloy (acicular small grains) gave the same thickness than the hot-forged Ti6Al4V alloy with bigger grains.

But this size influences the shape of the boundary between the TTS and the initial material. If the initial grains are very small $(\alpha-TV15CA)$, the boundary appears straight in the optical microscope (figure 2). On the contrary, for hot forged Ti6Al4V, the boundary of the TTS follows that of the initial grains and appears as a broken line: this can be explained by the fact that the transformation depends on the crystallographical orientation of the initial grains.

The shape of the boundary may influence the possible initiation of cracks in the bulk material (notch effect) and can thus change the friction behaviour.

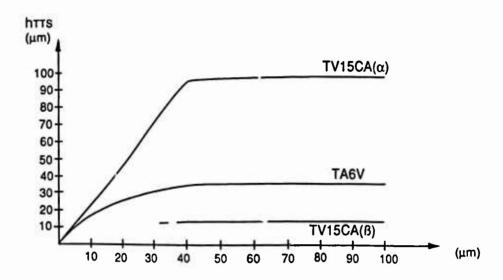


Figure 4 - Variation of the thickness of the TTS versus amplitude of displacement

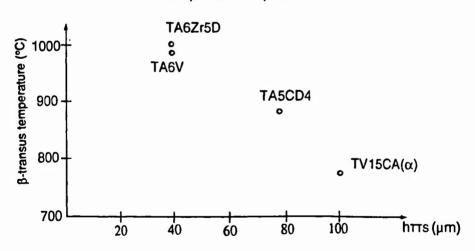


Figure 5 - Variation of the thickness of the TTS versus the β -transus temperature for various α and $\alpha+\beta$ alloys (±50 μ m, 50000 cycles)

The thickness of the TTS is also a major parameter for the friction behaviour because it determines the thickness of the third body layer in the interface. Indeed, particles are detached only from TTS. Numerous cracks were observed in the TTS. These cracks initiated always from the surface and propagated inside TTS or at the interface TTS/ initial material as seen on figure 6. Cracks were seen as soon as after 100 cycles and led to the detachment of big particles (figure 7). These particles were crushed and oxidized in the contact area to give the third body layer. This third body was highly adherent to surfaces and

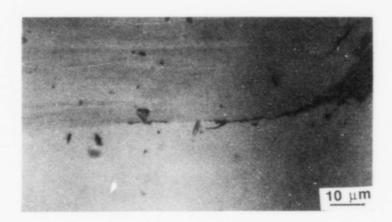


Figure 6 - Optical view of cracks in the TTS on α-TV15CA alloy (±50 μm, 50000 cycles)



Figure 7 - Optical view of big debris particles detached from the TTS on α-TV15CA alloy (±50 μm, 1000 cycles)

For Ti6Al4V or α -TV15CA alloys, the TTS was thick and so was the debris layer. Thus, stresses transmitted to the bulk were lowered, the material was protected and no more damage occur in the bulk alloy. On the contrary, if the layer was too thin, e. g. for β -TV15CA, cracks initiated and propagated below the TTS because the tangential stresses transmitted to the surface through the debris layer remained higher than σ_d .

In order to choose an alloy for a fretting application, this study shows that material response fretting maps (MRFM) can provide valuable informations (figure 8). If particle detachment occurs (i.e. if samples are tested with friction conditions corresponding to the PD domain of the material response fretting map), properties of the initial alloy such as KIC are not very useful since the same new structure, the TTS, is always detected, whatever the initial alloy. Nevertheless, the thickness of the TTS depends on the alloy. It can be very thin and this gives small

amount of detached particles. In the MRFM, this case corresponds to the shaded area of the PD domain near the C domain. In this area, chances for cracks initiation are not equal to zero. Consequently, the use of an alloy giving thick TTS is recommended if friction conditions are such that the working point of the alloy is located in the shaded domain. When fretting conditions are such that the alloys are tested in C or ND domain of the MRFM, then fatigue properties are a useful guideline for the choice.

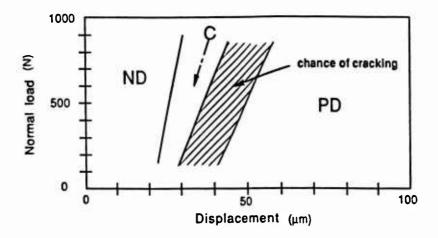


Figure 8 - Material Response Fretting Map (MRFM) for titanium alloys: ND = no degradation, C = cracking, PD = particle detachment.

Conclusion

Fretting wear behaviour of various titanium alloys has been presented. Two main kinds of damage have been observed:

- cracking when partial sticking is achieved in the contact area

- particle detachment if gross sliding takes place.

This has been represented using material response fretting map where the damage domains are given as a function of the test parameters.

Cracking can be related to classical fatigue studies. Particularly, the endurance limit σ_d determines the possibility for cracks to initiate and propagate.

Particle detachment occurs after the transformation of the superticial layer to form the TTS. The thickness and shape of this TTS depends on:

- the fretting test conditions (number of cycles, amplitude of displacement)
- . the initial structure of the alloy
- . the β-transus temperature

the size and orientation of the initial grains.

To understand completely the particle detachment process and thus the friction behaviour after this detachment, we would now have to analyse the properties of the TTS itself.

References

1. R.B. Waterhouse, Fretting Corrosion, Pergamon Press, Oxford, 1972

- 2. R.C. Bill, J. Lubr. Technol, 105 (1983), 230
- 3. Y. Berthier, C. Colombié, L. Vincent, and M. Godet, ASME Jour. Tribology, 7 (1988)
- 4. P. Blanchard, C. Colombié, V. Pellerin, S. Fayeulle, and L. Vincent, Metal. Trans. A
- 22 (1991) 1535
- 5. S. Fayeulle, A.B. Vannes, and L. Vincent, <u>Proc. 17th Leeds-Lyon Conf.</u> Eds. D. Dowson, M. Godet To be published
- 6. Z.R. Zhou, S. Fayeulle, and L. Vincent, to be published in Wear (1992)
- 7. O. Vingsbo, and S. Soderberg, Wear 126 (1988) 131
- 8. D.W. Hoeppner, and G.L. Goss, Wear, 24 (1973) 61-70
- 9. D. Godfrey, Nat. Advis. Comm. Aeronaut. Rep. 1009, 1951
- 10. S.F. Wayne, H. Novotny, and S.L. Rice, in <u>Titanium 80</u> Ed. H. Kimura (AIME, New York 1980) 1295
- 11. D.W. Hoeppner, and G.L. Goss, Wear, 24 (1973) 61-70
- 12. S. Fayeulle, P. Blanchard, and L. Vincen, to be published in <u>Tribology</u> <u>Transactions</u> (1992)

EFFECTS OF OXYGEN AND IRON ON THE ENVIRONMENTAL AND

MECHANICAL PROPERTIES OF UNALLOYED TITANIUM

R. W. Judy, Jr.*, I. L. Caplan**, and F. D. Bogar*

*Naval Research Laboratory, Washington, DC 20375-5000 **Naval Surface Warfare Center-Annapolis Detachment, Annapolis, MD 21402-1198

Abstract

Unalloyed titanium is being widely used in machinery and piping for applications involving large, thick components and the seawater environment. It has been shown that oxygen has a strong effect on the resistance of most titanium products, including unalloyed titanium, to environmental cracking, and strong effects on the mechanical properties, as well. In evaluating the suitability of materials for service in particular environments, it is important to consider the entire gamut of properties of candidate materials. This paper reports the result of experimental determinations of the stress corrosion cracking performance of unalloyed titanium with oxygen content varying between 0.10 and 0.26 weight percent, with two levels of iron, 0.06 percent and 0.18 percent. These properties were measured using wedge-opening loaded specimens in static load frames. To assist in understanding the SCC data, values of J_{IC} were determined in standard specimens; this helped establish the distinction between environmental crack growth and mechanically-driven crack growth.

Titanium '92 Science and Technology Edited by F.H. Froes and I. Caplon The Minerals, Matals & Materials Society, 1993

Introduction

Unalloyed titanium is used in many commercial and other applications where the three necessary conditions for potential stress corrosion cracking (SCC) are present: tensile stresses, small defects due to fabrication, and aqueous environments. Oxygen is the principal addition to unalloyed titanium in order to increase the strength. Oxygen additions, however, also decrease the fracture toughness and the resistance to SCC at the same time. Iron which can be present in tramp amounts or can be added intentionally for strength or producibility, also is thought to affect these properties. The existing body of information to quantify these effects is sparse (1,2); the purpose of this work was to systematically investigate the mechanical properties and environmental cracking resistance of unalloyed titanium to provide such information.

Materials and Procedures

The materials for this investigation were ten rolled plates of unalloyed titanium, 25 mm thick. The nominal oxygen contents were 0.10, 0.13, 0.17, 0.20 and 0.26 weight percent, and a sample of each oxygen content was produced having nominal iron content of 0.06 and 0.17 percent. The plates were produced as small double-melted 45 kg laboratory heats by TIMET, and were rolled unidirectionally to final thickness. The materials were arbitrarily assigned a letter code, as is shown in Table 1. Microstructures of all the plates are shown in figure 1. A distinct trend for the grain size to decrease with increasing oxygen is apparent, as is a tendency for those samples with higher iron content to have smaller grains than their counterparts with the same nominal oxygen content and lower iron. Standard tensile, fracture toughness, and SCC tests were conducted for each plate. Results of the tensile tests, along with the ingot chemistries, are given in Table 1. Fracture resistance tests utilizing the J-Integral method were also conducted for each sample of material with a standard 1-T compact tension specimen oriented in the TL direction, i.e., the orientation such that crack propagation is expected in a plane parallel to the rolling direction and perpendicular to the plate surface. Unloading compliance techniques were used for detection of crack growth, and values of J were computed by the method outlined in reference (3).

Stress corrosion cracking tests to determine the threshold stress intensity for SCC (K_{ISCC}), using wedge-opening-loaded (WOL) specimens were carried out for each material in the TL orientation. Pin-loaded WOL specimens were loaded in static load frames using a 3.5% NaCl in distilled water solution as the environment.

UNALLOYED TITANIUM

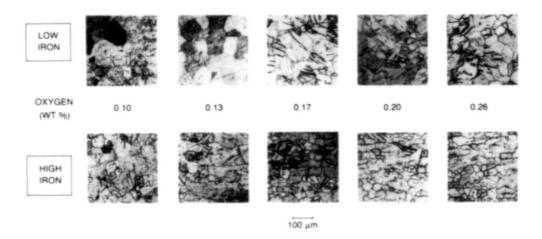


Figure 1 - Microstructures of ten samples of unalloyed titanium. The samples were all rolled to 25 mm plate in a single direction.

Measurements of time, applied load and crack-mouth-opening were recorded by a system utilizing a personal computer, so that the onset of crack growth could be easily identified and crack-growth rate data could be easily computed. The minimum exposure time was 150 hours, and most tests ran for more than 180 hours. In these tests, bracketing techniques (between points of no crack growth and crack growth) were used to define the threshold stress intensity for SCC. When SCC was found to be present, the value was noted KISCC; when no crack growth was associated with the test, the threshold value was noted as Ksw. To obtain as much data as possible from each specimen, the fatigue crack was extended into undamaged material following each load exposure, so that as many as seven experiments could be run with a single specimen. Computations of K for these specimens were made on the basis of crack lengths measured after the specimen was broken and loads recorded by the load cell during the test. In pin-loaded specimens, the stress intensity field increases slightly with crack extension; this is in contrast to cantilever bend specimens where K increases very rapidly with crack extension. In materials where SCC was present, the maximum load prior to crack growth was used to compute K for bracketing purposes. Many samples did not exhibit SCC and were very ductile. Successive loadings to higher K values, which is a normal part of the test, only caused more extensive yielding, crack blunting, etc., as would be expected. Under such circumstances, the K term has little meaning. For this reason, the point of deviation from linearity on the loaddisplacement diagram was taken as the load value for computing K when there was no crack growth.

Additional experiments were conducted with bolt-loaded WOL specimens; in these specimens the K gradient decreases rapidly with crack extension. A single specimen of each material, cut in the TL orientation, was loaded to an applied K at least 10 MPa \checkmark m above the K_{ISCC} or Ksw value. The test duration was 500 hours; and a computer-based data acquisition system was used to record load readings from instrumented bolts during the tests. Values of K_{SW} and K_{ISCC} were computed from measured values of final crack lengths and loads. Experiments were conducted even when gross yielding was expected at the initial loading, on the premise that environmental effects which might take place at such extreme conditions could be missed in other tests.

Results Results of the mechanical property tests and the SCC tests are summarized in Table 1 below:

Table I. Properties of Unalloyed Titanium

CODE	OXYGEN (%)	IRON (%)	YS (MPa)	UTS (MPa)	EL (%)	PIN K _{SW} (MPa √m)	BOLT K _{SW} (MPa √m)
Α	0.097	0.062	263	392	45	77*	36*
В	0.095	0.170	287	410	45	86*	43*
С	0.134	0.058	326	443	42	82*	40*
D	0.128	0.170	346	463	44	93*	48*
E	0.186	0.061	417	524	35	84*	58*
F	0.164	0.171	393	518	34	90*	56*
G	0.200	0.072	435	561	30	65	62
Н	0.192	0.182	455	549	27	75	61
I	0.259	0.072	460	579	29	47	57
j	0.265	0.188	467	621	29	53	47

^{*} No SCC crack growth

Effects of oxygen content on the mechanical properties of the samples of unalloyed titanium were quite pronounced on both yield strength and ultimate tensile strength, while the effects of the iron content were more subtle. As expected, both yield and ultimate strength values increased sharply

with increasing oxygen (figure 2). There was a consistent trend for the yield strength in the direction transverse to rolling to be higher than yield strength measured in the direction parallel to rolling, but the ultimate strengths were the same for both orientations. Values of yield strength for materials having high iron were slightly higher than their counterparts for materials having low iron and the same oxygen content. The difference was slight, and there is some room for doubt that it is statistically significant.

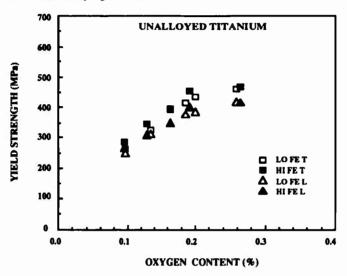


Figure 2 - Effect of oxygen and iron content on the yield strength of unalloyed titanium.

Fracture test results showed little or no dependence of J_{IC} (or Kj, the value of stress intensity computed from J_{IC}) on either oxygen content or on tensile properties. It is noted that the materials were extraordinarily ductile, and in some cases there was no crack growth. Valid J_{IC} numbers could not be computed for most of the specimens because of the lack of crack growth; in addition, the specimens failed the crack front straightness criteria. Tests were usually terminated because the displacement gages reached the end of their travel. Values are reported in terms of Kj to facilitate comparison with SCC data; these should be considered "lower bound" values and used only to observe trends, rather than as absolute values. The values shown here grossly underestimate the resistance of the materials to crack extension from purely mechanical causes. There were two exceptions, both at the highest values of oxygen (>0.19%) in the high iron content materials. Sample J, which was earlier described as having a different microstructure than the others, failed in a brittle manner, with a valid K_{IC} value of 38 MPa \checkmark m (35 ksi \checkmark in.). It is noted that the tensile ductility in this material was reasonably high. The fracture test specimen of sample H exhibited crack growth of sufficient length that a J-R curve could be constructed, but the specimen failed the crack front straightness test, since there was extreme tunnelling of the crack front.

Results of SCC tests using pin-loaded WOL specimens showed that the materials having nominal oxygen contents greater than 0.19% had some degree of sensitivity to SCC; these were materials coded G,H,I, and J in Table 1. The remaining materials were immune to SCC. Values of K_{ISCC} and K_{SW} are plotted vs oxygen content in figure 3. Note in figure 3 that, with decreasing oxygen, the values of K_{SW} measured in pin-loaded specimens reach a peak and then decrease. This is because the failure point is determined by plastic flow rather than by environmental effects as as the oxygen content decreases, the yield strength also decreases. Samples having high iron content consistently have higher K_{SW} values than those with lower iron.

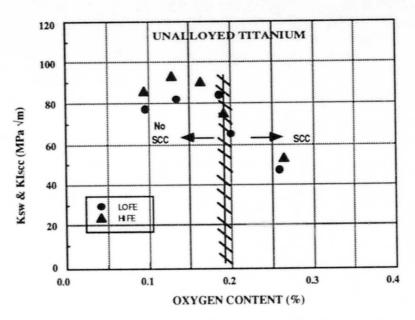


Figure 3 - Variation of K_{SW} and K_{ISCC} with oxygen content. Note that the samples having higher iron content have slightly higher values of K_{ISCC} than their counterparts.

UNALLOYED TITANIUM

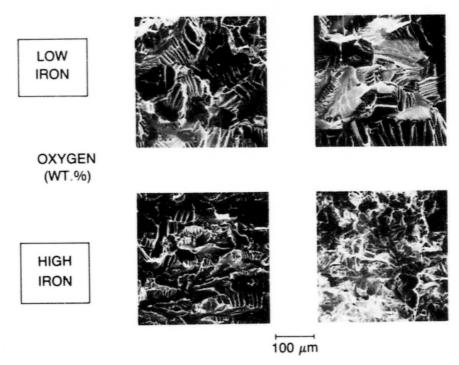


Figure 4 - Fractographs of the materials showing evidence of SCC.

In the sensitive materials, the crack growth was very rapid. The microcracking mode is shown in the photomontage of figure 4. The specimen of material J, which had high iron and 0.26% oxygen, broke in a brittle manner after a small increment of crack growth. Specimens of the other three materials exhibited small increments of crack growth, which were arrested in a short

time. In alloys G, H, and I, the fractures were characteristically very flat facets (quasi-cleavage) inclined at different angles, separated by regions of ductile fracture (fluting). This behavior was noticed in earlier work involving cast unalloyed titanium (2). This supports the concept that the SCC cracks propagate in these alloys by the formation of the quasi-cleavage facets, while the macroscopic crack growth rate is controlled by the ductile failure of material separating the facets. Therefore, even though the K gradient is positive in the pin-loaded WOL specimens, there was insufficient energy to drive the cracks after crack growth began in these three samples. This is because the crack fronts were probably quite diffuse rather than being a single straight front as is modeled by mechanics. In specimens loaded such that the K gradient is much steeper, i.e., cantilever specimens, the specimens would fail at the first small increment of crack growth, and the measured values of K_{ISCC} would probably be slightly lower. Sample J was different in that the fracture toughness was distinctly lower than in the other materials, and after a small increment of SCC crack growth, the specimen fractured completely. The fracture face of the SCC specimen consisted of a small area fraction of quasi-cleavage and more in-plane ductile fracture than was observed in the other specimens.

Values of $K_{\rm ISCC}$ determined with pin-loaded specimens are compared to values determined with bolt-loaded WOL specimens and values of Kj, as a finction of oxygen content in figure 5. The data trends show that both types of WOL specimen give identical values of $K_{\rm ISCC}$, within experimental scatter, when the materials are sensitive to SCC. When there is no SCC, the much lower values of apparent $K_{\rm ISCC}$ are measured with bolt loaded specimens. Values of Kj are much higher than either of these, except for the one point which was a valid $K_{\rm IC}$ value. These observations are a function of the time at load, i.e., the time available for plastic flow at the crack tip to allow load relaxation. Experiments with materials having higher values of strength and lower fracture toughness would probably cause all of these values to become nearly coincident.

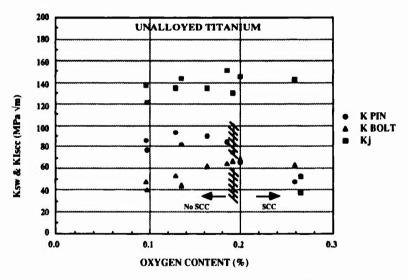


Figure 5 - Comparison of the SCC and fracture properties of unalloyed titanium materials with oxygen content.

The same data are presented as a function of yield strength in figure 6, and show the same general trends. In figure 6, the two lines divide the chart into regions where crack growth would occur under elastic conditions (labelled "PLANE STRAIN") and where plastic deformation is expected prior to crack growth (labelled "PLASTIC"), and a transition region between. The values of K_{ISCC} that fall in either the transition or plane strain region can be analyzed by fracture mechanics; those that fall in the plastic region are not amenable to analysis by linear elastic methods. The ratio lines represent K/YS of 0.145 for the lower bound and 0.10 for the upper

bound, using the metric scales shown here. The origin of the upper limit is Hahn and Rosenfield's (4,5) work which showed that at this ratio of K/YS for 25 mm thick material, a flat plate containing a through-thickness flaw would require yield level loading for crack extension. Data measured with bolt-loaded specimens without any SCC approximate that line very closely, which supports the contention that the differences between the three values of stress-intensity are time-dependent. Furthermore, the effects of strain rate on fracture resistance are such that K increases with increasing strain rate; conversely, unalloyed titanium is very much subject to creep deformation.

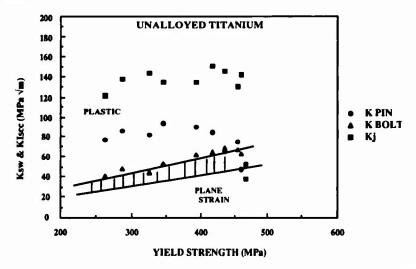


Figure 6 - Variation of K_{SW} and K_{ISCC} measured with pin-loaded- and with bolt-loaded-WOL specimens with yield strength. Only the four points at the highest strengths had SCC. Also shown are lower bound values of J_{IC} measured using 25 mm thick specimens.

Samples of alloys I and J oriented in the LT direction, i.e., with the crack propagation perpendicular to the rolling direction were tested in the pin-loaded configuration. Very little crack propagation was noted in alloy J when it was loaded above the KISCC determined in the TL orientation. Cracks propagated out of plane in alloy I at values of applied initial K roughly corresponding to KISCC, and quickly arrested.

Data concerning the effects of oxygen content on SCC of unalloyed titanium taken in this work are compared to the existing data taken from the literature in figure 7; both rolled plate and cast materials are considered. The data form a continuum showing that the critical oxygen content is 0.19 weight percent. Reference 2 is earlier work performed by the authors with mostly cast materials using the same experimental equipment and techniques. The data of reference 1 were taken with 12 mm thick specimens; hence the point at 0.12 % oxygen is below the other points because of differences in constraint to crack tip plastic flow in specimens of different thicknesses.

Summary

Experimental determinations of the susceptibility of unalloyed titanium to SCC in salt water resulted in the following conclusions:

- Alloys having oxygen content of 0.19 weight percent or higher are sensitive to SCC while those with lower oxygen are immune.
- Oxygen content has a strong effect on the strength properties of unalloyed titanium, while small variations in iron content have a very small effect.

- Apparent insensitivity of fracture properties, measured in terms of J Integral parameters, to
 oxygen content is an artifact of the specimen size relative to the ductility of the material; the
 small specimens grossly underestimate the resistance of the material to crack extension.
- For materials not sensitive to SCC, the trends of fracture behavior measured with small specimens reflect the dependence of the plastic flow processes on loading rate, and are not a measure of the intrinsic fracture resistance of the material.

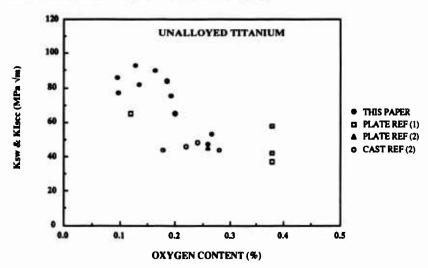


Figure 7 - Comparison of data measured in this work with other data for both rolled plate and cast materials. The data show that at about 0.19 weight percent oxygen or less, unalloyed titanium is not sensitive to SCC.

Acknowledgement: The materials for this investigation were provided gratis by TIMET; the authors wish to thank Dr. Paul Bania of the Henderson Technical Laboratory. Mr. H.I. Jones conducted the J Integral tests; his assistance is gratefully acknowledged.

References

- 1. R.F. Curtis, R.R. Boyer, and J.C. Williams, "Relationship Between Composition, Microstructure, and Stress Corrosion Cracking in Salt Solution in Titanium Alloys", Transactions of the ASM, Vol 62, p 457, 1969
- 2. R.W. Judy, Jr., B.B. Rath, and I.L. Caplan, "Stress Corrosion Cracking of Pure Titanium as Influenced by Oxygen Content", Proceedings of the Sixth World Conference on Titanium, Vol IV, p 1747, 1988
- 3. ASTM Standard E 813-88, Standard Test Method for JIc, A Measure of Fracture Toughness, American Society of Testing and Materials, Philadelphia, PA, 1988
- 4. G.T. Hahn and A.R. Rosenfield, "Sources of Fracture Toughness: The Relation Between K_{IC} and the Ordinary Tensile Properties of Metals," ASTM STP 432, American Society for Testing and Materials, Philadelphia, 1968, pp. 5-32
- 5. G.T. Hahn and A.R. Rosenfield, "Plastic Flow in the Locale of Notches and Cracks in Fe-3Si Steel Under Conditions Approaching Plane Strain," Ship Structures Committee Report SSC-191, U.S. Coast Guard, Washington DC, Nov 1968

SAME REGULARITIES OF ALLOYING ELEMENTS EFFECT ON &-BASE TITANIUM

ALLOYS EMBRITTLEMENT IN AIR AND CORROSIVE ENVIRONMENT

Stal Ushkov, Andrey Igolkin

Central Research Institute of Structural Materials "Prometey" Sankt-Petersburg, 193167, Russia

Abstract

A consideration is given for some common features of the effect of alloy composition on the susceptibility to brittle behaviour of d-base titanium alloys in air and corrosive media, sea water in particular. SCC embrittlement is regarded as an early form of the ordinary brittle degradation due to alloying additions. The effects of alpha stabilizers and eutectoid beta stabilizers provoking the phenomenon as well as the opposite action of isomorphous beta stabilizers are explained in terms of d-solid solution stability aspects as well as electronic structure changes. Some analogies of other metallic system are provided.

Introduction

High strength α -base titanium alloys are recognized as very effective materials in manufacturing various stressed marine constructions /1,2/. These exclusively demandable applications require special care relative to the chemical composition and structure which are generally different from those for airospace titanium alloys since one of the main problem here is in preventing stress corrosion cracking SCC embrittlement. This phenomenon has been discovered for about three decades ago /3/ and a lot of papers concerning the subject has been publishing /4-8 etc./. It seems now that in the light of the knowledge accumulated it is possible to envisage the problem of α -base titanium alloys embrittlement in corrosive environment and air together. In this paper we attempted to do it.

Main Theses

General View

High loaded constructions made of titanium alloys are mostly exploited in media which substantially do not affect them in terms of the general as well as macroscopically local corrosion losses. It distinguishes titanium and its alloys among other structural materials including stainless steels. In order to induce SCC embrittlement of titanium alloys it is necessary to rupture mechanically the protective surface oxide film which is to be done by means of plastic deformation of the substrate. SCC susceptibility may be evaluated

Titanium '92 Science and Technology Edited by F.H. Froes and I. Caplan The Minerals, Metals & Materials Society, 1993 by various testing procedures, the criterion being the techique should show different results in air (vacuum) and corrosive environments. The influence of alloying additions will be considered in view of the following sheme:

chemical composition — structure — property.

Considerations of the Transgranular Embrittlement

It is known that pure titanium displays no susceptibility to SCC which is caused mainly by alpha stabilizing additions such as oxygen or aluminium. These elements provide a great hardening effect and lead to the plasticity losses as well. But SCC embrittlement (in chloride solutions for example) are usually appeared under the content of the elements mentioned which are quite tolerable in air (see Figure 1).

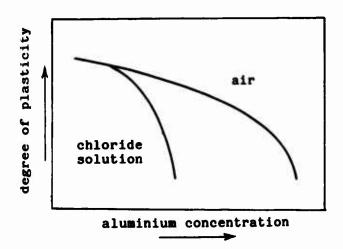


Figure 1 Scheme of the effect of aluminium additions of the embrittlement of titanium alloys in air and 3.5 % NaCl aq.sol.

The same is true for the effect of eutectoid beta stabilizers /9/. A significant embrittlement of Ti-Al alloys in air is associated with the visible d_2 -phase (Ti_3Al) precipitations whereas SCC susceptibility may appear under the absence of any detectable secondary precipitates. Only oblique analyses (magnetic and electrical resistance testing for example) seems to be capable to catch out some weak structural changings under ~1.0 wt.% Al and ~5.0 wt.% Al to be regarded as certain d_2 -phase prototipes formation (ordering) /10/. Thus the emergence of SCC susceptibility of d_2 -base titanium alloys due to the alloying is associated with the same structural changes which being is its more pronounced forms (under higher component content) would lead to the ordinary loss of plasticity.

Many investigators emphasized the fact that ${\bf d}$ -base titanium alloys transgranular SCC embrittlement was related with the changes in the plastic deformation character- from cell-like to co-planar /11 etc./. The same relationship is very characteristic for SCC of austenitic stainless steels and other structural alloys, whereas the crystallographic slipping system may be kept unchangable. The electrochemical interaction presumably takes place along the emerging slipping steps formed due to co-planar slipping /12/ but the following appears to be of importance as well . The co-planarity of the slipping may be envisaged as some form of restriction of the plastic defor-

mation under the submicroscopical level. But it is the localization (nonuniformity) of the elastic-plastic material response to loading which is generally accepted as the cause of brittle behaviour without the corrosive factors affectioning.

The transgranular SCC of \ll -base titanium alloys is associated eith the formation of basic (1000) or near basic $\{10\overline{17}\}$ cleavage fracture planes. That SCC peculiarity attracted great attention in due time /13/ and it has been noted the strange curcumstance that near basic cleavage plane is characteristic for brittle fracture of high aluminium titanium alloys in air when impact tested /6/.

It is known that so intrinsic for transgranular SCC embrittlement cleavage plane is encountered in a great variety of cases of d-base titanium as well as zirconium alloys embrittlement in various media including air and vacuum (see Table 1).

Table 1 The cases of the basic (near balic) cleavage fracture planes

Material	Environment or loading conditions	Failure cleavage plane	Reference
		{10 1 7 } {10 1 8 }	/6,14/
"	Hg,Cd	{10 1 7} (0001)	/15/
- 11 -	slow strain rate testing (air)	12 ⁰ from (0001)	/16/
Ti-8Al, Ti ₃ Al	impact testing (air)	(00 <u>0</u> 1) {1017}	/6/
Ti-6Al-4V high cycle fatigue testings in air and vacuum		{10 1 7}	/17,18/
Zn	Hg	(0001)	/19/

Therefore, there are a series of important moments to be common for transgranular embrittlement of α -base titanium alloys in air and corrosive environments.

Constitutional Diagrams and Titanium Alloys Brittle Behaviour

The effective way to mitigate SCC embrittlement of $\boldsymbol{\alpha}$ -base titanium alloys is isomorphous beta stabilizers (Mo, V, Ta, Nb) additioning /6/. The mechanism of the effect is little studied but is related with the presence of beta stabilizing elements in $\boldsymbol{\alpha}$ -solid solution /20/. Striking fact is that isomorphous beta stabilizers have been found as useful alloying elements in supressing various forms of titanium alloys embrittlement - the slow strain rate brittleness /21/, intergranular embrittlement /10/ as well as SCC susceptibility in many environments. These elements reportedly mitigate formation of laves phase in chromium containing titanium alloys /22/. Thus these elements are distinguished among other alloying additions by its favourable effect on titanium alloy. What attracts attention is that in its first approach the constitutional diagrams of titanium with all these ele-

ments are quite alike and simple ones (see Figure 2).

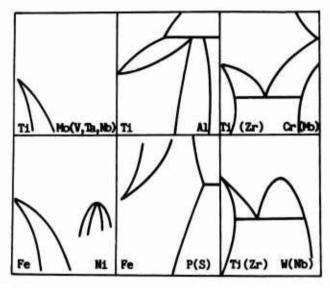


Figure 2 Schematical image of the left corner of some constitutional diagrams.

It is interesting to note also the resemblance between constitutional diagrams of Ti-Mo (V, Ta, Nb) and Fe-Ni. The c. fect of nickel is known as unique one in suppressing low temperature embrittlement of ferrous alloys. As contrary to d-stabilizing elements (aluminium, oxygen, interstitials for iron to be known as embrittling species for the systems) the isomorphous beta stabilizers and nickel are able to decrease the & -lattice stability temperature without obvious intermetallic formations (see Figure 2). It may be suggested that for metallic systems there probably exists some positive correlation between the effect of alloying elements on the matrix phase polymorhous temperature and its influence on the embrittlement. It appears that by lowering the phase stability temperature the elements (for example isomorphous beta stabilizers for titanium and nickel for iron) are lowering the temperature field to be intrinsic for the phase delamination processes. The later may include ordering, segregation or compound formation reactions etc., which are caused by the presence of some low-soluble additions or contaminants. This way the neutralization of the embrittling elements is making. For Ti-Al alloys the isomorphous teta stabilizers seemingly suppress d2-phase formation making the alloys less susceptible to SCC embrittlement. The correlation considered above is probably analogous one for the following tendency being intrinsic for unalloyed metals - the higher its melting point the higher its low-temperature brittle-ductile threshold (which is caused by contaminants). This correlation for unalloyed matals is related with the increase in the valent electron localization degree for high melting elements i.e. with the increase of the covalent component of interatomic bond /23/. As for isomorphous beta stabilizers and nickel their presence correspondingly in α -solid solutions of titanium alloys and steels causes the increase in the metallic component of interatomic bond /24,25/. The experimental studies also showed that titanium alloying by alpha stabilizers led to the increase in the covalent component of the bonding /10,26/. Thus the effect of alloying element invisaged is related with the changes in the electronic structure. Not going further in the consideration we are to note here that

isomorphous beta stabilizers for titanium and nickel for iron as well as renium for tungsten (well known "renium effect" is meant) are occupied relatively siniour positions in the periodic system displaying themselves as more multivalent elements. It should be noted that the more equilibrium conditions provided the Ti-Mo (V) systems are not free from any nonvariatable transformations (see Figure 2). The fact of the compounds formation for zirconium analogous systems urges to suggest for similar interaction for titanium systems (see Figure 2) to take place. Therefore it is the degree of realization of a transformation which is of importance in the context. The effect of various alloying elements on α -base titanium alloys embrittlement in air and corrosive environments should be envisaged taking into account some microstructure changes which are also of importance. But we suggest that microstructure parameters keeping the same the effect is determined by matrix solid solution characteristics.

Conclusion

1. There are some substantial points to be common for α -base titanium alloys embrittlement in corrosive midia (SCC) and air. Although the SCC embrittlement is necessitated by the electrochemical interaction it relates with the same structural and phenomenological changings due to alloying elements which are responsible for the ordinary transition to brittle behaviour.

2. There probably exists a positive correlation between the effect of alloying elements on the polymorphous temperature and their influence on embrittlements in air and corrosive invironments, which may be related with electronic structure changes. Isomorphous beta stabilizers are capable to neutralize the embrittling effect of alpha-stabilizers and eutectoid beta stabilizers by lowering α -solid solution delamination temperature.

References

- 1. Boris Chechulin et al., "<u>Titanovye Splavy v Mashinostroenii</u>", (Moskow); Mashinostroenie, 1977), 249.
- 2. H.G.Suzuki et al., "The Development of High Pressure, Proof, Vessel, for 10 km Submarine Esploration", Sixth World Conference on Titanium, ed.P.Lacombe et al., (France, 1988), 477-482.
- 3. B.F.Brown, "A New Stress-Corrosion Cracking Test Procedure for High Strength Alloys", Materials Research & Standards ,6,(1966)(3).
- 4. L.S.Moroz, I.N.Razuvaeva, S.S.Ushkov, "Osobennosti Vliania Aluminia na Mehanicheskie Svoistva Titana", Novyi Constructsionnii Material-Titan, (1972), 109-114.
- 5. I.R.Lane, J.L.Cavallare, "Metallurgical and Mechanical Aspects of the Sea-Water Stress Corrosion of Titanium", Applications Related Phenomena in Titanium Alloys, ASTM STP 432, (1968),147-169.
- 6. M.J.Blackburn, J.A.Feeney, T.R.Beck, "Stress-Corrosion Cracking of Titanium Alloys", Advan.Cor.Sci.Technol.,3(1973),67-292.
- 7. R.E.Oxtis, R.R.Boyer, J.C.Williams, "Relationship Between Composition, Microstructure and Stress Corrosion Cracking (in Salt Solution) in Titanium Alloys", Trans.of the ASM, 62 (1969),457-469.
- 8. R.W. Judy, R.B. Rath and I.L. Caplan, "Stress Corrosion Cracking of Pure Titanium as Influenced by Oxygen Content", Sixth World Conference on Titanium, ed.P. Lacombe et al. (France, 1988), 1747-1752.

- 9. A.I. Igolkin, (Cand. Tech. Sci. Thesis, Leningrad, 1991).
- 10. S.S. Ushkov, (Doct. Tech. Sci. Thesis, Russia, Leningrad, 1983).
- 11. J.Williams, G.Leutjering, "The Effect of Slip Length and Slip Character on the Properties of Titanium Alloys", <u>Titanium. Science and Technology</u>, (New-York) 1 (1980), 671-681.
- 12. J.C.Scully, D.T.Powell, "The Stress Corrosion Cracking Mechanism of d-Titanium Alloys at Room Temperature", Corr.Sci.10(1979),719-731.
- 13. R.H.Wanhill, "A Consideration of Cleavage in Alpha Titanium", Acta Met. 21 (1973),1251-1259.
- 14. B.Cox, "Stress Corrosion Cracking of Zircaloy-2 in Neutral Aqueous Chloride Solutions at 25 gC", <u>Corrosion</u> 29 (4) (1973),157-166.
- 15. D.N.Fager, W.F.Spurr, "Solid Cadmium Embrittlement of Titanium Alloys", Corrosion, 24 (10) (1970), 409-419.
- 16.S.M.Ward-Clase, "Austained Load Failure of Ti-4Al-4Mo in Air and 3.5% Sodium Chloride Solution", <u>Titanium</u>, <u>Science and Tech.</u>,ed.G.Lütjering et al. (FRG, 1984), 1749-2759.
- 17. M.Peters, A.Gysler, G.Lütjering, "Influence of Texture on Fatigue Properties of Ti-Al-V Alloys", Metal.Trans., 15A(8)(1984), 1597-1604.
- 18. D.F. Neal. P.A. Blenkinsop, "Internal Fatigue Origins in & +3 Titanium Alloys", Acta Metal., 24(1)(1976), 59-68.
- 19. Embrittlement of Engineering Alloys, ed.by C.L.Briant and S.K.Banerji, Academic Press, (1983).
- 20. S.S.Ushkov, Yu.D.Hesin, L.A.Ivanova, A.I.Igolkin (to be published these Proceedings).
- 21. L.S.Moroz et al., <u>Titan i Ego Splavy</u> (Russia, Leningrad, Sudpromgiz, 1960)515.
- 22.S.G.Glazunov, V.N.Moiseev, <u>Konstructsionye Titanovye Splavy</u> (Moskow, Russia, Metallurgia, 1974),368.
- 23. V.G.Gluschenko, "O Prirode Hladnolomkosti Perehodnyh Metallov", Metall. <u>i Term.Pbrab.</u>, 4(1982),2-4.
- 24. O.P.Nasimov, A.A.Ilin, "Electronnoe Stroenie, Fazovaia Stabilnost i Svoistva Titanovyh Splavov", v sb.Electr.str. i F-H-Svoistva Tugopl. Soed. 4 Spl., Ukraine, Kiev: Naukova Dymka (1980), 258-263.
- 25. T.D.Nakorneev, "Vlianie Ligiruschih Elementov na Viasko-Hrypkii Perehod v Splavah Geleza", (Cand.Techn.Sci.Thesis, Tumen, 1974).
- 26. E.W.Collings, The Physical Metallurgy of Titanium Alloys, ASM, OH 44073.

HYDROGEN ABSORPTION OF TITANIUM IN OFFSHORE RELATED ENVIRONMENTS UNDER CATHODIC CHARGING

Liv Lunde, Rolf Nyborg and Werner Wilhelmsen

Institutt for energiteknikk N-2007 Kieller, Norway

Abstract

Titanium alloys of Grade 2, 5, 9, 12 and Beta-C have been exposed for periods up to two years with cathodic polarization in deaerated artificial seawater at temperatures between 20 and 80 °C. All alloys except Grade 12 had low hydrogen absorption at -1050 mV vs. Ag/AgCl. Titanium Grade 12 had a hydrogen absorption 3-20 times higher than the other alloys, and is not recommended for use in applications where the material is exposed to cathodic protection. The high absorption rate was related to the nickel content of this alloy. The alpha-beta high-strength alloys Grade 5 (6Al-4V) and Grade 9 (3Al-2.5V) showed about the same hydrogen absorption as unalloyed titanium Grade 2. The high-strength beta alloy Beta-C had generally somewhat higher hydrogen absorption than unalloyed titanium, but lower than Grade 12.

The hydrogen absorption in titanium Grade 12 was considerably lower at -700 mV than at -1050 mV vs. Ag/AgCl. In the other alloys the hydrogen absorption was low at both these potentials. The hydrogen absorption in deaerated seawater was about the same at 20 °C and 80 °C. The reason for this is that surface films containing carbonates form at higher temperatures, and these films seem to protect against hydrogen absorption. This effect is even stronger in water containing carbon dioxide, where carbonate films form at lower temperatures.

Introduction

Titanium has an excellent corrosion resistance in seawater, and has been widely used for seawater cooled heat exchangers for the last twenty years. There is a growing interest for titanium also in other offshore applications, where titanium often will be coupled to other materials and may also be exposed to cathodic protection systems. In some of these applications the low weight-to-strength ratio makes titanium especially attractive, particularly in combination with its low modulus of elasticity. A 400 m long titanium drilling riser is currently being evaluated for a tension leg platform in the North Sea, and a titanium stress joint has been in service at 500 m water depth in the Gulf of Mexico. Here the titanium components are large diameter (~30 inch) tubes of high strength titanium with thick wall (1 inch). This type of applications requires the use of high-strength titanium alloys of the alpha-beta or beta type.

Titanium '92 Science and Technology Edited by F.H. Froes and I. Caplan The Minerals, Metals & Materials Society, 1993 Titanium alloys absorb hydrogen at low potentials, and when the solubility limit is exceeded hydrides will form. The hydrides are brittle and in extreme cases hydrides may lead to deterioration or fracture of the component. The behaviour of alpha titanium alloys in seawater is apparently well documented, while little information is available on the hydrogen absorption behaviour of high strength alloys. It is often difficult to use hydrogen absorption data because hydrogen analyses have been applied without differentiation between hydride films at the surface and hydrogen absorbed in the bulk material. It is mainly precipitated hydrides in the interior of the metal that will endanger the service life of a component, while thin hydride films at the surface have less practical implications.

The most important factors for hydrogen absorption in titanium are pH, electrochemical potential, temperature and alloy composition. Rules of thumb given for seawater service of alpha titanium alloys are not always reliable, and they can not be applied for beta or alpha-beta alloys. Information relevant to conditions on the hydrocarbon side of oil and gas production or transport equipment is lacking. Experience from oil refineries shows that coupling to carbon steel has led to hydrogen absorption in environments containing hydrogen sulphide. An important question is whether the small H_2S amounts present in North Sea hydrocarbons (<100 ppm) are enough to trigger hydrogen absorption.

The objective of the present work was to investigate hydrogen absorption on the seawater side in titanium components coupled to other metals exposed to cathodic protection and on the hydrocarbon side of titanium components coupled to carbon steel. The experiments were a part of an EEC funded project within the EURAM programme (1). The project was based on a cooperation between research institutions in four European contries, including Inasmet, Spain, Technical Research Institute of Finland, Imperial College, England and Institutt for energiteknikk, Norway. The aim of the Norwegian studies was to investigate hydrogen absorption without mechanical loading, while work in Finland and Spain was concentrated on the influence of cathodic protection on stress corrosion cracking and corrosion fatigue in artificial seawater. The British studies were aimed at the role of hydrides in the cracking of titanium alloys.

Experimental

Hydrogen absorption studies were performed with the following titanium alloys: Ti Grade 2 (CP Ti), Grade 5 (6Al-4V), Grade 9 (3Al-2.5V), Grade 12 (0.8Ni-0.3Mo) and Beta-C. In some of the experiments new experimental alloys supplied by TIMET (Beta-21S) and Sumitomo (0.05Pd-0.3Co) were included. The composition and mechanical properties of the alloys are given in Table I. Flat specimens with thickness 3 mm and surface area about 5 cm² were exposed to synthetic seawater according to ASTM D-1141 in glass cells with automatic pH and temperature control. The electrolyte was replaced at regular intervals. The specimens were ground and then pickled in a HNO3-HF-H2O solution before the experiment. Experiments were performed at 20, 40, 60 and 80 °C. The solution was flushed with either N₂ CO₂, or CO₂ with 50 ppm H₂S in order to simulate either produced water (hydrocarbon environment with CO₂) or seawater at large depths where the oxygen content is low. The pH of the solution was kept at 4.0 in most experiments, while a few experiments were performed with higher pH values. The potential of the specimens was kept at either -700 mV vs. Ag/AgCl (corresponding to galvanic coupling to carbon steel) or -1050 mV vs. Ag/AgCl (corresponding to a structure with cathodic protection). Exposure times were from 20 to 700 days. The specimens were examined for hydride precipitation by metallography, and the hydrogen content of both exposed and unexposed specimens was measured by TIMET by vacuum extraction and mass spectrometry.

Table I. Chemical composition and mechanical properties of the investigated alloys. Data from certificate for all alloys except Grade 9.

	Alloy							
Composition %	2	5	9	12	0.05Pd-0.3Co	Beta-C	Beta-21S	
N	0.008	0.01	0.02	0.003	0.05	0.017		
С	0.025	0.02	0.18	0.016	0.10	0.2		
Fe	0.05	0.22	0.25	0.12	0.07	0.08		
0	0.19	0.125	0.15	0.14	0.20	0.077		
Al		6.2	2.5-3.5			3.3	3	
V	Ì	4.0	2-3			8.0		
Other				Mo 0.28	Pd 0.03-0.07	Mo 4.0	Mo 15	
				Ni 0.87	,Co 0.2-0.7	Zr 3.9	Nb 2.6	
						Cr 6.4	Si 0.2	
H * ppm	70	60	80	50	50	140	90	
Mechanical pro	perties							
YP MPa	418	986	560	400		834		
UTS MPa	527	1034	655	600		862		
Elongation %	26	13	29	23		21		

^{*} Measured by TIMET for this project

Results

The amount of absorbed hydrogen in the different titanium alloys exposed to artificial seawater with CO_2 at 80 °C, pH 4.0 and -1050 mV vs. Ag/AgCl is shown in Figure 1. The hydrogen data are given as absorbed hydrogen in μ g per mm² surface area of the specimen. This parameter gives values for absorbed hydrogen independent of the thickness of the material. Hydrogen values in ppm of the bulk material are less informative and do not take into account that most

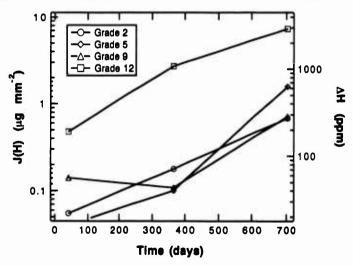


Figure 1. Hydrogen absorption in titanium as function of exposure time. Exposure in artificial seawater with CO₂ at 80 °C, -1050 mV vs. Ag/AgCl and pH 4.0.

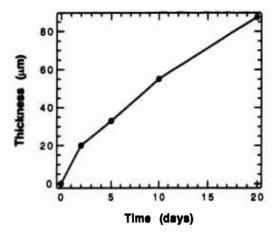


Figure 2. Thickness of hydride layer in titanium
Grade 12 as function of exposure time.
Exposure in artificial seawater with CO₂ at
80 °C, -1050 mV vs. Ag/AgCl and pH 4.0.

of the absorbed hydrogen is accumulated in a thin surface layer. However, as many previously reported hydrogen data have been given in ppm, an approximate scale for the hydrogen content in ppm in a 3 mm thick plate exposed on both sides is also given in the figure. The hydrogen content in ppm will be different for other thicknesses.

Figure 1 shows that the hydrogen absorption does not slow down even after long exposure times. In fact, the hydrogen values after two years are more than twice the values after one year for all alloys. The figure also shows that Ti Grade 12, which contains nickel and molybdenum, absorbs 3-20 times more hydrogen than Grade 2, 5 and 9. Grade 12 showed

considerable hydride formation, while very little hydrides were found in the other alloys. The thickness of the hydride layer in Ti Grade 12 specimens tested at 80 °C, pH 4.0 and -1050 mV vs. Ag/AgCl is shown as function of exposure time in Figure 2. The figure shows that an appreciable hydride layer can be observed already after two days' exposure. The thickness of the layer increases approximately proportionally with the square root of the exposure time.

Experiments with abraded and pickled specimens tested with nitrogen flushing at 20 °C showed that abraded specimens had considerably higher hydrogen absorption than pickled specimens after 40 days' exposure. After 120 days' exposure the difference between pickled and abraded specimens was much smaller, and the initial surface condition seems to be less important.

The effect of temperature on the hydrogen absorption in the different alloys is shown in Figure 3. In the experiments with nitrogen flushing the hydrogen absorption increases markedly from 20 °C to 40 °C and then decreases from 40 to 80 °C. In experiments with $\rm CO_2$ flushing the hydrogen absorption decreases from 20 to 40 °C and then remains about the same up to 80 °C. Grade 12 has the highest hydrogen absorption at all temperatures, while Beta-C also absorbs much hydrogen at 20 and 40 °C.

The hydrogen absorption in Ti Grade 12 after one year exposure in synthetic seawater with CO_2 flushing at 80 °C and pH 4.0 was about seven times higher at -1050 mV than at -700 mV vs. Ag/AgCl. For the other alloys the hydrogen absorption was much lower, with almost no difference between -700 and -1050 mV vs. Ag/AgCl. An experiment with CO_2 + 50 ppm H_2S as flushing gas with pH 6.5 resulted in similar or somewhat lower hydrogen uptake than pure CO_2 and pH 4.0. A few experiments with different pH values were performed with nitrogen flushing at 80 °C and -1050 mV vs. Ag/AgCl. Grade 12 specimens tested at pH 13 showed no hydride precipitation, while pH 6.2 resulted in formation of some hydrides. Specimens exposed at pH 4.0 under the same conditions showed a thick hydride layer at the surface and hydride needles deep into the metal.

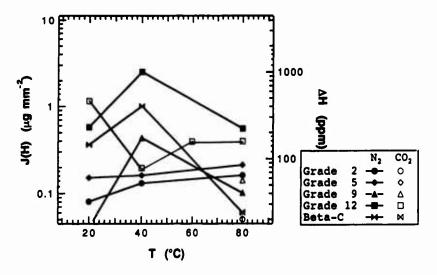


Figure 3. Hydrogen absorption in titanium as function of temperature. 40 days' exposure in artificial seawater at -1050 mV vs. Ag/AgCl and pH 4.0.

Discussion

Effect of temperature and water chemistry

Hydrogen absorption in titanium has traditionally been considered to be a problem only at temperatures above 80 °C, where the diffusion rate of hydrogen becomes significant (2). The present experiments in synthetic seawater with nitrogen flushing show that the hydrogen absorption increases from 20 to 40 °C, but then decreases from 40 to 80 °C. With CO₂ flushing the hydrogen absorption decreases already from 20 to 40 °C. The surface films on titanium seem to be more important for the total hydrogen absorption than the effect of temperature on diffusion. An X-ray energy dispersive analysis of the surface of specimens exposed with nitrogen flushing at 80 °C showed the presence of calcium that has been deposited on the surface, probably as CaCO₁. Carbonate scales form easily at high temperature because the solubility of calcium carbonate decreases with increasing temperature. Natural seawater contains enough carbonate ions to get this effect. When the water contains carbon dioxide, the content of carbonate ions is larger and carbonate scales are more easily formed at low temperature. This accounts for the observed effect of CO₂ on the hydrogen absorption. The effect of carbonate films on hydrogen absorption of titanium in seawater may have important practical consequences, as this might result in negligible hydrogen absorption in cases where this otherwise could be a problem.

Previous investigations of grade 2 titanium in natural seawater showed small differences in hydrogen absorption between 25 and 50 °C, while exposure at 80 °C gave a marked increase in hydride layer thickness (3). These results were obtained at pH 2 and are not relevant for normal seawater exposure. Another study reported a higher hydrogen absorption in 3 months at 25 °C compared to two months at 100 °C (4). This is more in line with the present findings.

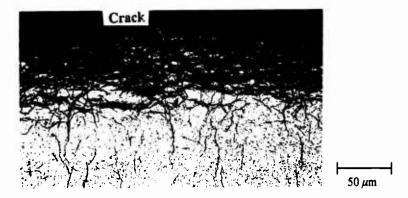


Figure 4. Hydride layer with crack on titanium Grade 12 after 40 days' exposure in artificial seawater with CO₂ at 80 °C and pH 4.0.

In order to judge the detrimental effect of hydrogen it is necessary to have information on the distribution of hydrides as well as the total hydrogen content. Hydrides oriented perpendicular to the loading direction can be dangerous even with reasonably low total hydrogen contents. This is clearly demonstrated in Figure 4 where surface cracks starting from hydrides can act as stress risers by introducing a stress concentration factor.

Dense surface hydride layers were observed in Grade 2 specimens exposed with nitrogen flushing at 20 °C and almost no hydrides at 80 °C, although the hydrogen content was about the same at the two temperatures. In Grade 12 specimens exposed with CO_2 flushing, dense surface hydrides with thickness 5-30 μ m were observed in specimens exposed at 20 °C, while specimens exposed at 80 °C also showed hydride needles up to 300 μ m deep into the metal. Specimens exposed at 40 and 60 °C had thicker surface hydride layers with up to 60 μ m depth. This may seem surprising since the hydrogen absorption was highest at 20 °C, as shown by the open points in Figure 3. However, the hydride layer at 20 °C was very dense because very little of the absorbed hydrogen had diffused into the bulk metal. These observations illustrate that the diffusion of hydrogen from the surface and deeper into the metal increases with temperature, but this is not the limiting factor for the hydrogen absorption.

The hydrogen absorption increases with decreasing pH. The experiments with pH 4 represent accelerated conditions compared to neutral seawater. Flushing with $CO_2 + 50$ ppm H_2S at pH 6.5 gave similar or somewhat lower hydrogen uptake than pure CO_2 at pH 4.0. This does not exclude a detrimental effect of H_2S on hydrogen absorption, but it seems that the small amounts of hydrogen sulphide in the North Sea fields (<100 ppm) do not cause any dramatic changes in the hydrogen absorption for the hydrocarbon side of titanium components coupled to carbon steel.

Effect of alloying elements

Titanium Grade 12 absorbed much more hydrogen than the other alloys (3-20 times more), and was the only alloy with extensive hydride formation. Small amounts of nickel are known to cause increased hydrogen absorption in titanium alloys (5), and it is likely that the 0.8 % nickel in Grade 12 accounts for the increased hydrogen absorption. This was verified by Ti Grade 2 specimens with small amounts of nickel electrodeposited on the surface. These specimens

developed a severe hydride attack after only 20 days' exposure, while no hydrides were found in parallel specimens without nickel. A few experiments with the alloy Ti 0.05Pd-0.3Co showed two to three times higher hydrogen absorption than for unalloyed titanium Grade 2. The palladium content is probably responsible for this, but the cobalt content may also contribute.

The high-strength beta alloy Beta-C showed generally somewhat higher hydrogen absorption than unalloyed titanium, but lower than Grade 12. The alloy Beta-21S was also tested and had about the same hydrogen absorption as Beta-C. Both the solubility and the diffusion rate of hydrogen are several times higher in the beta alloys than in the alpha alloys, and no hydrides were ever found in the beta alloys.

The alpha-beta high-strength alloys Grade 5 (6Al-4V) and Grade 9 (3Al-2.5V) had about the same hydrogen absorption as unalloyed titanium Grade 2. However, Grade 9 had higher hydrogen absorption in a pickled specimen at 40 °C and an abraded specimen at 20 °C. No hydrides were found in the alpha-beta alloys, except for the abraded Grade 9 specimen mentioned above, where a $100 \, \mu \text{m}$ thick hydride layer was found after 40 days' exposure.

Effect of potential

The hydrogen absorption in titanium Grade 12 was considerably lower at -700 mV than at -1050 mV vs. Ag/AgCl. In the other alloys the hydrogen absorption was low at both these potentials. This together with the beneficial effect of CO₂ indicates that hydrogen absorption should not be a problem on the hydrocarbon side of titanium components coupled to carbon steel, where the potential is typically -700 mV vs. Ag/AgCl. On the seawater side, a titanium component coupled to a structure with cathodic protection will have a potential of about -1050 mV vs. Ag/AgCl. At this potential significant hydrogen absorption can occur in titanium Grade 12. Previous investigations have indicated that hydrogen absorption occurs in natural seawater only when titanium has a potential lower than about -0.7 V vs. SCE, with significant hydrogen absorption between -0.8 and -1.0 V vs. SCE (6, 7). Other investigators have found significant hydriding of titanium in neutral seawater only at potentials lower than -1.2 V vs. SCE, and they have suggested -1.0 V vs. SCE as a limit for avoiding significant hydriding below 45 °C (8).

Conclusions

Exposure of titanium alloys of Grade 2, 5, 9, 12 and Beta-C in deaerated artificial seawater at -1050 mV vs. Ag/AgCl showed a low but significant hydrogen absorption in all alloys except Grade 12. The exposure at pH 4 represents accelerated conditions compared to neutral seawater. The hydrogen absorption did not slow down even after two years. Titanium Grade 12 had a hydrogen absorption 3-20 times higher than the other alloys and extensive hydride formation. This alloy should not be recommended for use in applications where the material is exposed to cathodic protection. The high absorption rate of Grade 12 is related to the nickel content. The alpha-beta high-strength alloys Grade 5 (6Al-4V) and Grade 9 (3Al-2.5V) showed about the same hydrogen absorption as unalloyed titanium Grade 2. The high-strength beta alloy Beta-C had somewhat higher hydrogen absorption than unalloyed titanium, but lower than Grade 12. No hydrides were found in the Beta-C alloy. The results indicate that these high-strength alloys are at least as good as unalloyed titanium regarding hydrogen absorption.

The hydrogen absorption in deaerated seawater was about the same at 20 °C and 80 °C, while it was higher at 40 °C. The reason for this is that surface films containing carbonates start to form between 40 °C and 80 °C. These films seem to protect against hydrogen absorption. This

effect is even stronger in water containing carbon dioxide, where the hydrogen absorption decreases from 20 to 40 °C because carbonate film formation start at lower temperatures.

The hydrogen absorption is initially much higher at abraded surfaces than at pickled surfaces, but the differences in original surface conditions become less important after longer exposure times. The hydrogen absorption in titanium Grade 12 was considerably lower at -700 mV vs. Ag/AgCl than at -1050 mV vs. Ag/AgCl. This together with the beneficial effect of CO_2 indicates that hydrogen absorption should not be a problem on the hydrocarbon side of titanium components even with small contents of H_2S , while some hydrogen absorption may occur on the seawater side of titanium components coupled to a structure with cathodic protection.

Acknowledgment

The present experiments have been financed by the Royal Norwegian Council of Scientific and Industrial Research, Phillips Petroleum, Saga Petroleum, Statoil, Proserv and Institutt for energiteknikk. Their permission to publish this work is gratefully acknowledged. Thanks are also extended to TIMET who has performed all the hydrogen analyses free of charge.

References

- EURAM Contract No. MAIE/0056/C: "Environment Sensitive Cracking of Titanium in Offshore Equipment" (Commission of the European Communities, Brussels, 1988).
- W.H. Cubberly et al., eds., <u>Metals Handbook</u>, vol. 2 (Metals Park, OH: American Society for Metals, 1987), 669-706.
- J. I. Lee, P. Chung and C. H. Tsai, "A Study of Hydriding of Titanium in Seawater under Cathodic Polarization" (Paper presented at CORROSION/86, Houston, Texas, 17-21 March 1986, Paper No. 259).
- T. Fukuzuka et al., "Corrosion Problems and Their Preventions of MSF Desalination Plant Constructed with Titanium Tube" (Paper presented at International Congress on Desalination and Water Re-use, Nice, France, October 1979), Vol. II, 389-398.
- L.A. Charlot, "Investigation of Galvanically Induced Hydriding of Titanium in Saline Solutions" (US Department of the Interior, Research and Development Progress Report No. 624, 1970).
- 6. L. C. Covington, "The influence of Surface Condition and Environment on the Hydriding of Titanium", Corrosion, 35 (8) (1979), 378-382.
- H. Sato et al., "Hydrogen Pickup by Titanium Held Cathodic in Seawater" (Paper presented at 2nd International Congress on Hydrogen in Metals, 6-11 June 1977, Paris, France).
- R. W. Schutz and J. S. Grauman, "Determination of Cathodic Potential Limits for Prevention of Titanium Tube Hydride Embrittlement in Salt Water" (Paper presented at CORROSION/89, New Orleans, Louisiana, April 1989, Paper No. 110).

ENHANCING CORROSION RESISTANCE OF THE Ti-3Al-8V-6Cr-4Zr-4Mo $(Beta\text{-}C^{TM}) \text{ ALLOY FOR INDUSTRIAL APPLICATIONS}$

R. W. Schutz and M. Xiao RMI Titanium Company

Abstract

Enhancement of Beta-C™ titanium with 0.04 - 0.10 wt.% Pd or Ru dramatically expands the alloy's resistance to hot reducing acids, and to stress and crevice corrosion in high temperature deaerated, reducing, and/or sour brine media. High resistance to hydrogen absorption with sustained exposure to hot dilute reducing acids or high temperature caustic solutions also resulted, contrasting behavior in conventional titanium alloys. These positive effects appear to stem from formation of a more protective passive oxide film, and not cathodic depolarization traditionally achieved by precious metal additions to titanium. These improvements in corrosion and hydrogen resistance in reducing acidic media have direct positive implications for application of enhanced Beta-C titanium alloys in hypersaline geothermal brine wells, deep sour gas wells, and even chemical and organic compound synthesis processes.

Introduction

Beta-C titanium is characterized as an ageable beta titanium alloy which offers a unique, attractive combination of high strength, low density and modulus, and elevated corrosion resistance. This attractive suite of properties has been successfully exploited for production tubular applications in hypersaline geothermal brine extraction wells in the Salton Sea(1), and is driving current interest in this alloy for production tubulars, casings, and ancillary well equipment in deep sour gas wells(2). Service experience and laboratory testing, however, have revealed subtle limitations in crevice and stress corrosion resistance above ~185°C in both sweet and sour brines.

These corrosion performance windows can be expanded to a significant extent by the minor addition of a platinum group metal (i.e. Pd, Ru, Pt, Ir, Rh) to this alloy. Significant improvement in crevice, stress, and/or reducing acid corrosion resistance have been demonstrated in alpha(3,4), alpha-beta (3,4), and beta titanium alloys(2,5) with minor precious metal additions. This paper examines the scope of corrosion performance benefits derived by enhancing the Beta-C titanium alloy with either Pd or Ru within the 0.04 - 0.10 wt.% range. Enhanced beta alloy passivity and resistance to crevice and pitting corrosion, hydrogen absorption, and stress corrosion cracking were evaluated via laboratory tests in hot environments ranging from oxidizing to reducing and acidic to alkaline. Performance of this improved alloy is compared to that of the standard Beta-C alloy and is discussed in terms of potential industrial applications.

Titanium '92 Science and Technology Edited by F.H. Froes and I. Caplan The Minerals, Metals & Materials Society, 1993

Experimental

Test Materials

Corrosion testing was performed on three versions of the Beta-C alloy (Ti-3Al-8V-6Cr-4Zr-4Mo): standard Beta-C, Pd-enhanced Beta-C, and Ru-enhanced Beta-C. The actual composition of the sheet and pipe product forms evaluated are outlined in Table I. The 1.8 mm sheet stock was tested in the hot-rolled and solution-treat (816°C-30Min-AC) or "ST" condition (~827 MPa), and in the 50% cold-rolled and solution-treat + age (816°C-30Min-AC + 579°C-24Hrs-AC) or "STA" condition (~965 MPa YS), and was exposed in the ground and pickled surface condition. The mill-produced 73 mm OD x 5.5 - 6.8 mm wall pipe samples used for stress corrosion testing were cold-pilgered and solution-treat + aged to a yield strength of ~952 MPa, with a machined and pickled surface.

Test Methods and Media

General corrosion testing consisted of simple weight loss immersion exposures (1-3 days) of specimens in boiling solutions of HCl, 10% HNO₃, and 10% FeCl₃; and higher temperature solutions of molybdate-inhibited HCl, 10% formic and acetic acids, and 20% NaOH. Although most solutions were left unchanged during testing, solutions were refreshed every 24 hours and 14 days during the HNO₃ and NaOH test exposures, respectively.

Table I. Composition of Beta Titanium Alloy Product Forms Tested

Alloy	Standar	d Beta-C	Pd-Enhanced Beta-C		Ru-Enhanced Beta-C	
Product Form	1.8 mm sheet	73 mm OD pipe	1.8 mm sheet	73 mm OD pipe	1.8 mm sheet	
%A1 (%V)	3.5 (8.1)	3.3 (7.8)	2.7 (7.8)	3.1 (7.9)	3.0 (8.1)	
%Cr (%Zr)	5.8 (3.8)	6.2 (3.8)	6.0 (4.0)	6.0 (4.0)	6.1 (3.9)	
%Mo (%O)	3.9 (0.09)	4.0 (0.08)	4.1 (0.08)	4.2 (0.08)	4.2 (0.09)	
%Pd (%Ru)			0.045	0.062	(0.086)	

Anodic/cathodic polarization characteristics of the sheet samples were determined in deaerated (argon sparged) 20% NaCl (pH 0.5) at 90°C via potentiodynamic scanning at 0.5 mV/sec. The anodic repassivation pitting potential of the sheet material was measured in boiling 5% NaCl (pH 3.5) via the galvanostatic method utilizing a constant current density of +200 mA/cm².

Crevice corrosion resistance was evaluated using bolted assemblies of interspaced metal sheet (38 mm x 38 mm x 1.8 mm) and 1 mm Teflon® sheet spacers, bolted together with a torque of 30 - 50 mm*kg. Each assembly incorporated five metal samples and created multiple metal-Teflon and metal-metal crevices(2). Test solutions included deaerated concentrated NaCl, NaBr, and CaCl, brines at 232°C, a sour brine consisting of 20% NaCl + 1 gpl sulfur + 1.4 MPa H₂S at 100-276°C, and highly oxidizing (pH 1-2) 20% NaCl brines at 90°C. Exposure period was 30 days.

Hydrogen absorption was evaluated by two methods. One method involved hydrogen absorption as a by-product of general corrosion in dilute boiling HCl solutions. Sheet specimens were removed every 14 days, annealed at 232°C for 24 hours to homogenize internal hydrogen, and lightly re-pickled in HF/HNO₃ solution to clean surfaces before re-exposure. The second method utilized a galvanic couple between Beta-C titanium and carbon steel sheets

(1:1 surface area ratio) exposed to a deaerated 46% NaBr brine at 232°C for 500 hours. The hot vacuum extraction method was used to measure sample hydrogen content before and after exposure.

Stress corrosion cracking (SCC) susceptibility was also assessed via two methods on the two pipe products tested (Table I). C-rings, prepared according to ASTM G-38, were stressed to 95% yield strength and exposed for 30 days to the deaerated, concentrated NaCl, NaBr, and CaCl₂ brines at 232°C. Slow strain rate (SSR) testing was also performed on L-direction pipe samples in hot sour brine at a strain rate of 4 x 10⁻⁶ sec⁻¹, using failure criteria described elsewhere (5). SSR and some C-ring (3-6 mo.) testing was conducted in a sour brine consisting of deaerated 20% NaCl with 1 gpl sulfur and pressurized with 6.9 MPa $\rm H_2S$ and 3.4 MPa $\rm CO_2$ at 175 - 300°C.

Results/Discussion

Acid Resistance

Corrosion rate profiles for the modified Beta-C alloys in boiling HCl media are presented in Figure 1. The dramatic extension of corrosion resistance into the higher acid concentration range is obvious when the Beta-C alloy is enhanced with Ru and Pd. The Pd imparts, by far, the greatest beneficial influence, with the benefit of Ru judged to be roughly midway between the standard and Pdenhanced alloys. The metallurgical condition of each alloy (i.e. ST vs. STA) appears to have a relatively minor effect on reducing acid resistance. The ST condition in the Pd-enhanced alloy did improve resistance at very high acid levels (>6%), whereas the STA condition exhibited improved resistance below 1.5% HCl in the standard alloy.

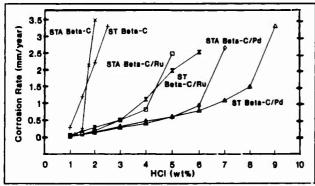


Figure 1 Corrosion rate profiles for beta alloys in boiling HCl solution.

The beneficial influence of Pd is similarly observed in inhibited high temperature reducing acids, as shown in Figure 2. Exposure to the mildly reducing organic acid media, 10% acetic 10% formic acids. at 232°C produced rates of 0.04 and 0.18 mm/yr., respectively, for standard Beta-C. The Pd-enhanced alloy comparison,

exhibited nil corrosion. Table II provides comparative corrosion rate data in two hot oxidizing acid solutions. No apparent influence of Pd or Ru, or metallurgical condition was observed. As expected, the beta alloys were not as resistant as unalloyed titanium under hot, highly oxidizing nitric acid conditions, but were more resistant than the Ti-6Al-4V alloy due to its higher aluminum content.

Caustic Resistance

As with most titanium alloys, these beta alloys exhibit only minor corrosion rates in hot 20% NaOH media with relatively little, if any, effect of Pd or Ru on Beta-C alloy corrosion rate in this media. The factor that often limits use of titanium alloys in hot, highly alkaline media is continued, excessive

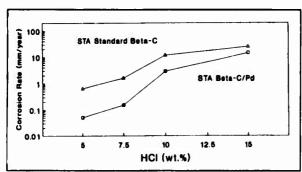


Figure 2 Effect of acid concentration on beta alloy corrosion rate in 4.5% Na₂MoO₄-inhibited HCl solutions at 204°C.

hydrogen absorption and eventual em brittlement resulting from finite corrosion. Standard Beta-C exhibits significant increases in hydrogen level at boiling (107°C), but does show excessive absorption at 149°C as shown in Figure 3. In contrast, the two enhanced alloys experienced n o significant changes in hydrogen content after six weeks' exposure at 149° and 177°C. Since it had influence on corrosion

rate, the precious metal alloy addition probably increased or modified the oxide surface film barrier to thwart absorption of atomic hydrogen. In fact, a green chromium-rich surface scale was detected on both enhanced alloys, but not on standard Beta-C after exposure. This possible influencing factor and the ability of the film to resist hydrogen pickup warrants further testing in longer exposures and also in flowing caustic solutions.

Table II. Corrosion Rate of Standard and Enhanced Beta-C™ in Various High Temperature Acidic Solutions

ALLOY	CONDITION	10% HNO, (mm/yr)	10% FeCl, (mm/yr)
Std. Beta-C	ST and STA	0.18	0 00
Beta-C/Pd	ST and STA	0.15	0.00
Beta-C/Ru	ST and STA	0.17	0.01

Electrochemical Traits

Alloy corrosion potentials in hot acidic NaCl brine are listed in Table III. The more noble (positive) corrosion potentials of the enhanced alloys are apparent in the deaerated and aerated solutions, especially with the Pd alloy. As expected, these values correlate with alloy resistance in HCl (Fig. 1).

Table III. Corrosion Potential of Standard and Enhanced Beta-C Alloys In Acidic 20% NaCl Brine at 90°C (volts vs. Ag/AgCl)

ALLOY	CONDITION	DEAERATED (pH 0.5)	AERATED (pH 0.5)	w/1500 ppm FeCl, (pH 2)		
Std Beta-C	ST	-0.60	+0.10	+0.64		
Std Beta-C	STA	-0.58	+0.10	+0.64		
Beta-C/Pd	ST	-0.17	+0.15	+0.64		
Beta-C/Pd	STA	-0.19	+0.14	+0.64		
Beta-C/Ru	ST	-0.40	+0.11	+0.64		
Beta-C/Ru	STA	-0.40	+0.11	+0.64		

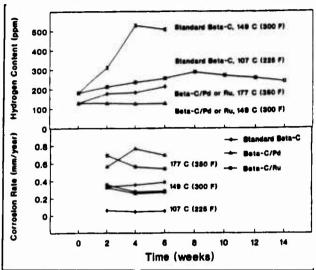


Figure 3 Corrosion rate and hydrogen content of beta alloys exposed to high temperature 20% NaOH solutions.

difference in allov corrosion potential i s observed when FeCl, added. is regardless metallurgical condition. indicating that the Pd or Ru imparts no cathodic influence in highly oxidizing environments.

Other alloy polarization characteristics are outlined in Table IV. Anodic passive current density was exceptionally low for the Pdenhanced Beta-C in conditions, both suggesting formation of an especially protective

oxide film compared to the other two alloys. Cathodic Tafel slope values, however, are all fairly similar, indicating little influence of Pd, Ru, or metallurgical condition on cathodic kinetics. Overall, this suggests that the greater nobility and resistance of Pd-enhanced Beta-C in reducing acids results from formation of a more protective oxide film, unlike the cathodic depolarization mechanism classically associated with alpha and alpha-beta titanium alloys(4). Both anodic pitting and repassivation (protection) potential values for each alloy also proved to be similar (Table IV). Again, no significant influence of precious metal or metallurgical condition is noted. Anodic pitting values fall between those for the Gr. 2 and 5 Ti alloys.

Table IV. Other Beta Alloy Polarization Characteristics (Volts vs. Ag/AgCl)

ALLOY	CONDI- TION	CATHODIC TAFEL SLOPE•	ANODIC BREAK- DOWN POTENTIAL (V)*	ANODIC REPASS. POT'L (V)**
Std Beta-C	ST	0.09	3.0	3.0
Std Beta-C	STA	0.09	3.2	3.3
Beta-C/Pd	ST	0.12	3.1	3.3
Beta-C/Pd	STA	0.12	3.5	3.3
Beta-C/Ru	ST	0.08	3.1	3.5
Beta-C/Ru	STA	0.08	3.6	3.4

^{* -} Deaerated 20% NaCl, pH 0.5, 90°C

^{** -} Boiling 5% NaCl, pH 3.5

Crevice Corrosion Resistance

Approximate temperature thresholds for crevice corrosion for these beta alloys are indicated in Figure 4 in deaerated sweet and sour 20% NaCl brines. Note

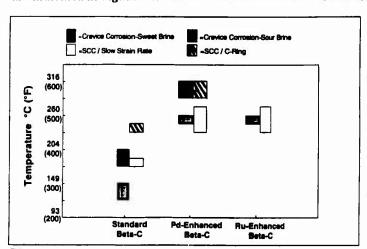


Figure 4 Approximate temperature thresholds for crevice corrosion and stress corrosion cracking of beta alloys in deaerated sweet and sour NaCl brines.

that both Pd Ru an d additions elevate temperature thresholds by approximately 100°C over the standard allov in either brine. Resistance to crevice attack even within tight (worst-Teflon case) sheet-tometal crevices is observed with these enhanced alloys t o temperatures high 88 246° - 260°C the sour

brine, and even higher in sweet brines. Thresholds for the less severe metal-to-metal crevices tested were much higher. Results for ST and STA conditions were similar in all cases. A similar beneficial effect of Pd-enhancement was noted in the deaerated 44% CaCl₂ brine exposures. Although the standard (STA) alloy also resisted attack in the deaerated 26% NaCl and 46% NaBr brines, Teflon to metal crevice corrosion was observed in the CaCl₂ brine at 232°C(2). Crevice testing in low pH 1-2 oxidizing NaCl brine (containing FeCl₃ or Cl₂ sat.) revealed severe crevice attack for all three beta alloys at 90°C. The ST samples consistently displayed more extensive attack in all alloys, with borderline attack noted with STA samples at pH 2. Thus, although the Pd and Ru alloy addition offers no real benefit in hot highly-oxidizing acidic brines, it is of obvious benefit in hot, reducing acidic brines.

Hydrogen Absorption

Galvanic coupling tests between these beta alloys and carbon steel (1:1 area ratio) in deaerated 46% NaBr brine at 232°C failed to reveal any significant hydrogen uptake after 500 hours, regardless of metallurgical condition. The boiling 2 and 3% HCl acid exposures on the Pd-enhanced Beta-C also produced no significant hydrogen absorption over the 16 week exposure period (see Fig. 5). The standard alloy, in contrast, experienced continued, substantial absorption and eventual embrittlement in the boiling 1.2% HCl exposure. Despite the finite corrosion rate in these reducing acids, the Beta-C/Pd remained passive and appeared to maintain an oxide film which resisted atomic hydrogen produced by corrosion. Standard Beta-C became active, and could not sustain a hydrogen barrier film. These test results, combined with the hot caustic test data (see Fig. 3), suggest that Pd and Ru enhancement dramatically improves Beta-C's resistance to hydrogen absorption.

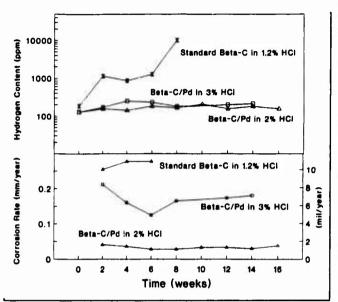


Figure 5 Absorption of hydrogen with exposure time for beta alloys in dilute boiling HCl media.

Resistance Stress Corrosion Figure also presents approximate temperature thresholds for STA) beta allov SCC in deaerated sweet and sour brines derived from SSR and Cring tests. Note SCC that thresholds are raised the on order of 55°C by Pd or Ru alloy enhancement in either brine. Although SSR thresholds generally 5 5 ° C about more conservative (lower) than the C-ring results, a similar

improvement in SCC threshold is observed with either test method. Further details of Beta-C alloy SCC test procedure and data can be found elsewhere(5). The benefit of Pd alloy addition was similarly revealed in C-ring exposures in 44% CaCi₂ brine at 232°C. Standard Beta-C (STA) pipe cracked, whereas the Beta-C/Pd (STA) pipe was fully resistant. Both alloys resisted SCC in concentrated NaCl and NaBr brines in similar testing at 232°C.

Conclusions and Applications

Pd-or Ru-enhancement of Beta-C titanium significantly expands the alloy's resistance to hot reducing acids, and stress and crevice corrosion in high temperature deaerated, reducing and/or sour brine media. With useful temperature limits to at least 230-260°C, these enhanced Beta-C alloys become improved and ideal candidates for high strength production tubulars and ancillary downhole components for hypersaline geothermal brine well(1) and deep sour gas well (2) service. The improved corrosion and hydrogen resistance noted in hot dilute organic and inorganic reducing acids may be attractive for chemical and organic compound synthesis processes, where titanium Grades 7 and 12 may experience continued hydrogen absorption with time. A similar benefit over alpha and alpha/beta alloys in resisting hydrogen absorption is also indicated in high temperature alkaline solutions and merits further evaluation for hot caustic service. These improvements appear to stem from formation of a more protective oxide film, and not cathodic depolarization normally associated with precious metal additions to titanium. Alloy metallurgical conditions tested had little effect on overall alloy corrosion performance. Alloy performance under oxidizing conditions was also not significantly influenced by Pd or Ru enhancement.

References

- W. W. Love, et. al., "The Use of Ti-38644 Titanium for Downhole Production Casing in Geothermal Wells," <u>Sixth World Conference on Titanium Proceedings</u>, Cannes, June 6-9, 1988, Société Française de Métallurgie, Les Ulis Cedex, France, pp. 443-448.
- D. R. Klink and R. W. Schutz, "Engineering Incentives for Utilizing Ti-3Al-8V-6Cr-4Zr-4Mo Titanium Tubulars in Highly Aggressive Deep Sour Gas Wells," Paper No. 63, presented at NACE Corrosion '92, Nashville, TN, Apr. 27 - May 1, 1992.
- Y. Shida, et. al., "Method of Improving the Resistance of Ti-based Alloys to Corrosion in Deep Well Environments," U.S. Patent #4,859,514, Aug. 22, 1989.
- N. D. Tomashov, et. al., "Corrosion and Passivity of the Cathode-Modified Titanium-Based Alloys," <u>Titanium and Titanium Alloys - Scientific and Technological Aspects</u>, Vol. 2, Plenum Press, NY, pp. 915-924, 1982.
- R. W. Schutz, M. Xiao and T. A. Bednarowicz, "Stress Corrosion Behavior of the Ti-3Al-8V-6Cr-4Zr-4Mo Titanium Under Deep Sour Gas Well Conditions," Paper No. 51, presented at NACE Corrosion '92, Nashville, TN, April 27-May 1, 1992.

ELECTROCHEMICAL BEHAVIOR OF TITANIUM IMPLANTED

WITH MOLYBDENUM AND TANTALUM IONS

Yasuaki Sugizaki, Tatsuya Yasunaga, and Hiroshi Satoh

Materials Research Laboratory, KOBE STEEL, LTD. Takatsukadai, Nishiku, Kobe, 651-22 Japan

Abstract

Electrochemical behaviors of titanium implanted with molybdenum ions or tantalum ions or a combination of the two have been investigated in a sulfuric acid solution, as a function of fluences. The metallographically polished surfaces of titanium were exposed to molybdenum or tantalum ion beams in fluence range of 1×10^{16} to 3×10^{17} ions/cm². Potentiodynamic polarization curves of the implanted specimens were measured in a boiling 10wt% sulfuric acid solution. The implanted surfaces were also characterized by means of Auger electron spectroscopy with an argon bombardment.

Electrochemical measurements have revealed that molybdenum implantation significantly promotes the passivation of titanium with an increase of fluences and the corrosion potentials resided in the passive region at fluences above $5 \times 10^{16} \, \mathrm{ions/cm^2}$. Tantalum implantation was effective in reducing the critical current densities for passivation and passive current densities. These effects were smeared at fluences above $7 \times 10^{16} \, \mathrm{ions/cm^2}$, which was due to decreasing the concentration of the implanted species by self-sputtering effect. The polarization curves for the co-implanted specimens exhibited more stable passive behaviors with low passive current densities. It was concluded that excellent corrosion resistance of titanium was achieved by complementary effects of molybdenum and tantalum implantation.

Titanium '92 Science and Technology Edited by F.H. Froes and I. Caplan The Minerals, Metals & Materials Society, 1993

Introduction

lon implantation is widely regarded as a versatile process to offer the capability in surface modification of materials. In the process, the desired surface properties of materials, such as the wear resistance or corrosion resistance are enhanced without affecting physical and mechanical stabilities of the bulk. Recently, a number of investigator have demonstrated that ion implantation has been successfully used to improve the corrosion resistance of metals[1]. The beneficial effect of surface alloying using ion implantation has been first demonstrated by Ashworth et al.[2]. Chromium implantation achieved to improve the corrosion resistance of iron as well as bulk alloying such as stainless steel. Ferber et al.[3] have presented that the corrosion rate was altered by ion implantation with ion species, because of inhibiting the hydrogen evolution reaction. implantation have been also applied for improving the corrosion resistance titanium[4,5,6]. Surface alloying using palladium or platinum implantation has been found to promote the passivation of titanium and provide long-term corrosion resistance in reducing acids. It is well-known that addition of small amount of palladium into titanium causes reduction of the corrosion rate in extreme conditions[7]. It has been also demonstrated that palladium implantation achieved a marked improvement in the resistance of titanium to either crevice corrosion in hot chloride solutions.

In the present work, we have employed molybdenum and tantalum implantation in an attempt to improve the corrosion resistance of titanium in reducing acids and examined the combined effect of co-implantation with both of the two. In order to establish the clear picture of the effect, potentiodynamic polarization curves have been measured as a function of fluence in the range of 1×10^{16} to $3 \times 10^{17} ions/cm^2$. The implanted surfaces have been also characterized by using Auger electron spectroscopy analysis.

Experimental Procedure

Commercially pure titanium (purity; 99.5%) was used as the substrate in the present study. The specimens with dimension 25x25x1mm were polished metallographically with 1µm diamond paste and carefully rinsed before ion implantation. The polished surfaces were exposed to molybdenum and tantalum ion beams in a vacuum of $3x10^{-5}Pa$. The implantation energy was 50keV for molybdenum ions and 45keV for tantalum ions. Specimens(A) were implanted with molybdenum ions at fluence range of $1x10^{16}$ and $3x10^{17}ions/cm^2$, and specimens(B) with tantalum ions at fluences of between $1x10^{16}$ and $1x10^{17}ions/cm^2$. Combined implantation with molybdenum and tantalum ions into specimens(C) was carried out in the same fluence range for molybdenum and tantalum implantation. The temperatures of the specimens were kept below 100^{0} C during implantation by intimate contact with a water cooled holder.

The compositional depth profiles for the implanted surfaces were determined by means of a sequential Auger electron spectroscopy (AES) technique with argon ion bombardment. An argon sputter gun was operated at a 3kV potential wish a 25mA beam current, which corresponded to an etch rate of approximate 55 A/min for titanium.

Potentiodynamic polarization measurement has been performed for the implanted surfaces in a boiling 10wt% sulfuric acid solution. The anodic and cathodic potential scanning with a sweep rate of 40mV/min were started from the corrosion potentials after keeping for three minutes under open-circuit condition. All the potentials were measured with respect to a Ag/AgCl electrode and a platinum sheet was used as a counterelectrode.

Results and Discussion

Prior to electrochemical measurements, AES analysis was carried out implanted specimen. The typical compositional depth profiles for specimens(A),(B) and (C) are shown in figure 1. In the specimen(A), 3x100 1 ions/cm2 fluence of molybdenum species at asymmetrically distributed around a peak at the depth of 70A. This depth was the estimated value of 220A from TRIM simulation[8]. coincided with Self-sputtering effect, which caused removal of the implanted species from fluences. This was true for the surface, was enhanced at such higher tantalum implantation. The profile of implanted tantalum species showed the asymmetric distribution around a concentration peak. It was conspicuosly caused by elimination of implnated species at fluences above 7x10¹⁶ions/cm². profile for the co-implanted specimens is shown in figure 1(c), where tantalum ions were subsequently implanted into the molybdenum implanted that the molybdenum concentration was specimen. It was presented considerably reduced by tantalum implantation, of which sputtering effect is more effective in removal of the surface species.

Corrosion properties were studied by measurements of potentiodynamic polarization curves. Figure 2 shows the result obtained from the tantalum implanted specimens(A). The curve obtained from the unimplanted was also shown for comparison. The corrosion potentials of the tantalum implanted specimens were gradually shifted to the less noble side in the first ten minutes during immersion. The curves shown in figure 2 were obtained after the first three minutes immersion. The corrosion potentials were slightly shifted in the noble direction with fluence up to $5x10^{16}ions/cm^2$, in accompanied with suppression of the critical current densities. At higher fluences, the critical current densities increased and the curves became closer to the unimplanted. This was due to the removal effect of sputtering introduced by tantalum implantation at higher fluences. The tantalum

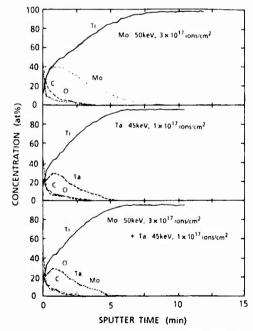


Figure 1 - Compositional depth profiles of the specimen implanted with (a)molybdenum, (b)tantalum and (c)combination of these species, obtained by a sequential AES analysis.

SUPTTERING RATE : 55A/min

implantation at relatively lower fluences was effective in anodic current densities in the active and passive region of titanium.

Figure 3(a) and (b) shows the anodic and cathodic polarization curves the molybdenum implanted specimens(B), respectively. At fluences below 5x1016 ions/cm2, the polarization behaviors were found to be almost the same the unimplanted, showing the active dissolution followed by passivation. At such fluences, the active-passive transition region became with an increase of fluences and the corrosion potentials were

10 1

POTENTIAL (V vs Ag/AgCI)

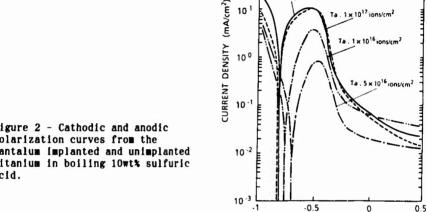
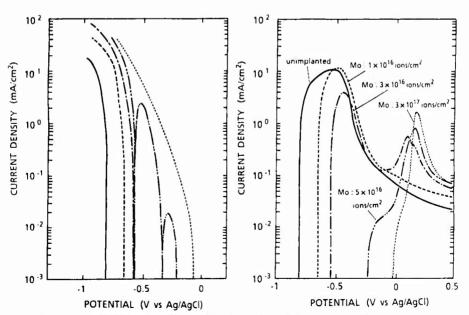


Figure 2 - Cathodic and anodic polarization curves from the tantalum implanted and unimplanted titanium in boiling 10wt% sulfuric acid.



(a)Cathodic and (b)anodic polarization curves from molybdenum implanted and unimplanted titanium in boiling 10wt% sulfuric acid.

shifted to the critical potential for passivation. The corrosion potential at fluence of 5x1016 ions/cm2 was resided in the passive region of titanium. Upon decreasing the potential from the corrosion potential, the polarization curve exhibited the alternative current densities as shown in figure 4(a). The cathodic current density, which had a peak at -0.25V, appeared in the region of between -0.2V and -0.4V before reaching activation. The active dissolution followed in the further less noble potential region and then the cathodic current density rose again due to the hydrogen evolution reaction. This behavior could be interpreted as a result that molybdenum implantation introduced the shift of the mixed potential in the modified surface to that of pure molybdenum and, hence partial anodic and cathodic polarization curves intersected at the three potentials. At fluences of 1x1017 ions/cm2, no net active-passive transition region was observed as can be seen figure 3. Molybdenum implantation at fluences above this introduced the complete passive behavior of titanium. The second active peaks due to active dissolution of implanted molybdenum species were appeared in the vicinity of 0.1V, corresponded to the corrosion potential of pure molybdenum. These results from molybdenum implantation were in agreement with that of molybdenum alloying addition to titanium[9].

The polarization curves for specimens(C), co-implanted with tantalum and molybdenum ions, were shown in figure 4 and 5, respectively. corresponded curves for molybdenum implanted specimens were superimposed. In figure 4, the fluence of molybdenum implantation was fixed at and tantalum ions were implanted additionally at various fluences. The corrosion potentials were slightly shifted from the molybdenum implanted However, the critical current densities were significantly decreased with tantalum fluence. The second-active peak, which was due to dissolution of molybdenum was disappeared for co-impliated specimens(C) and the current densities in passive region were suppressed gradually with tantalum fluences. For molybdenum implantation with higher fluences, the corrosion potentials were resided in vicinity of OV and the cathodic and displayed the stable passive corrosion behavior. curves additional tantalum implantation reduced the passive current densities in conjunction with reduction of the second-peaks. The passive behavior with lower passive current was obtained at tantalum fluence of 5x1016ions/cm2. The current densities in the passive region with such tantalum fluence was

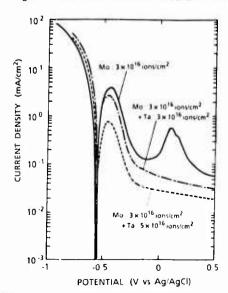


Figure 4 - Polarization curves from titanium co-implanted with molybdenum and tantalum ions, where fluence of molybdenum implantation is fixed at $3x10^{16}$ ions/cm².

reduced by approximate one order. For higher tantalum fluence, the anodic curves were not varied from the stable behavior and the cathodic curves were alternated. This is thought to be caused by eliminating the implanted species from modified surfaces, which was introduced by sputtering effect at higher tantalum fluence.

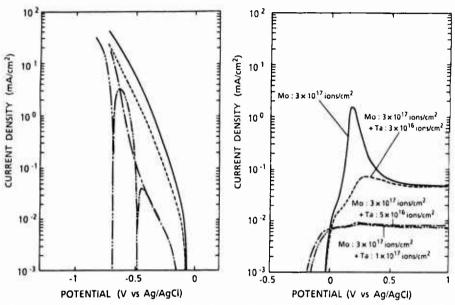


Figure 5 - (a) Cathodic and (b)anodic polarization curves from titanium coimplanted with molybdenum and tantalum ions, where fluence of molybdenum implantation is fixed at $3x10^{17}ions/cm^2$.

conclusion

It has been demonstrated in the present work that the electrochemical behavior of titanium is significantly affected by implantation with molybdenum, tantalum and a combination of these species. Tantalum implantation effectively suppressed dissolution of titanium in active and passive regions. Molybdenum implantation promoted the passivation of titanium through shifting the corrosion potential. Titanium co-implanted with tantalum and molybdenum ions exhibited complete passive behavior with extremely low passive current densities, as a consequence of the combined effect of these implantation. However, it was noted that the combined effect was smeared at higher fluence through the removal by sputtering.

Acknowledgement

This work was conducted in the program: "Advanced Material-Processing and Machining System", consigned to AMMTRA from NEDO, which is carried out under the Large-Scale Project enforced by the Agency of Industrial Science and Technology.

- [1] For example, H.Ferber and G.K.Wolf, Materials Science and Engineering, 90 (1987) 213.
- [2] V.Ashworth, W.A.Grant, R.P.M.Procter and T.C.Wellington, Corrosion Sci., 16 (1976) 393.
- [3] H.Ferber, A.Kasten, E.K.Wolf, W.J.Lorenz, H.Schweickert and H.Folger, Corrosion Sci., 20 (1980) 117.
 [4] G.K.Hubler and E.McCafferty, Corrosion Sci., 20 (1980) 103.
- [5] P.Munn and G.K.Wolf, Nucl. Instrum. Meth., B7/8 (1985) 205.
- [6] B.D.Lichter, N.G.Thomson, B.R.Appleton and E.J.Kelly, Ion Implantation into Metals, edt. V.Ashworth, W.A.Grant and R.P.M.Procter, Pergamon Press, New York (1983) p97.
- [7] P.Munn and G.K.Wolf, Mater. Sci. Eng., 69 (1985) 303.
 [8] J.F.Ziegler, J.P.Biersack and U.Littmark, The Stopping and Range of Ions in Solids vol.1, edt. J.F.Ziegler, Pergamon Press, New York(1985).
- [9] J.C.Griess, Jr., Corrosion NACE, 24 (1968) 96.

THE EFFECT OF BETA STABILIZERS ON LOW CYCLE LIFE SENSITIVITY

OF &-BASE TITANIUM ALLOYS TO CHLORIDE SOLUTIONS

Stal Ushkov, Andrey Igolkin, Yuliy Hesin, L.A.Ivanova

Central Research Institute of Structural Materials "Prometey"

Sankt-Petersburg, 193167, Russia

Abstract

A systematic study was undertaken to clarify the effects of beta stabilizing elements on SCC susceptibility of α -base titanium alloys in 3.5 % NaCl aq. sol. which was evaluated by low cycle fatigue testings. It has been corroborated that eutectoid beta stabilizers (Fe, Cr) are provoking SCC susceptibility whereas the reverse is true for isomorphous ones (Mo, V). However the effects of beta stabilizers were found to relate with their concentrations in α -solid solution to be in great dependance of certain hot processing peculiarities.

Introduction

It is well known that some $\rlap/$ -base titanium alloys are sensitive to stress corrosion cracking (SCC) in chloride solutions /1/. For Ti-Al alloys the phenomenon was found to originate from either the ordering of $\rlap/$ -solid 30-lution or the dispertion precipitation of Ti_3Al coherent particles $\rlap/$ -phase) /2/. These processes are stipulated by high aluminium content as well as other alpha stabilizers and occur during aging at about 500°C. Much less is known relative to the effect of beta stabilizing elements. As generally accepted isomorphous beta stabilizers (Mo, V,Ta,Nb) unlike eutectoid beta stabilizers (Cr, Co, Mn, Fe etc.) are capable to mitigate or even suppress SCC /1,2/. However some experimental results are questioning the rule. This study was aimed to clarify the effect of beta stabilizers on SCC in 3.5 per cent sodium chloride aqueous solution.

Experimental Procedure

Titanium alloys containing various amounts of beta stabilizing elements (Mo, V, W, Fe, CR) with 6 wt. per cent aluminium as a constant addition were double-arc vacuum melted into ingots of 10 kg weight, which were further forged to 20 mm diameter rods. Some large sized Ti-6Al-2Mo forgings have also been investigated. Admitting that SCC in its strict meaning is to be evaluated by the fracture toughness test we nevertheless have chosen other method by measuring low cycle fatigue life in air and 3.5 % NaCl aq.sol. Cost saving considerations and practical value of the fatigue testing re-

Titanium '92 Science and Technology Edited by F.H. Froes and I. Caplan The Minerals, Metals & Materials Society, 1993 sults as well as their correlation to the fracture toughness test results altogether have determined that choice.

Fatigue tests were performed by the axial tensile cyclic loading of notched specimens (5 mm of diameter, stress concentration coefficient ~3,6) with 1 cycle per minute frequency under the nominal stress amplitude of 0.7 of the yield strength. The ratio of life to fracture in 3.5 % NaCl aq. sol. and air was taken as a measure of SCC susceptibility. X-ray microspectroscopy studies were carried out using Superzond 733 unit with 15 kv accelerating voltage. Electrochemical measurements were performed by detecting potential on the previously oxidized samples in 3.5 % NaCl aq.sol. during bending.

Results

It has been found that isomorphous beta stabilizers additions (Mo,V) improved SCC resistance of the alloys investigated whereas eutectoid beta stabilizers (Cr. Fe) decreased sharply the characteristic (see Figure 1). There

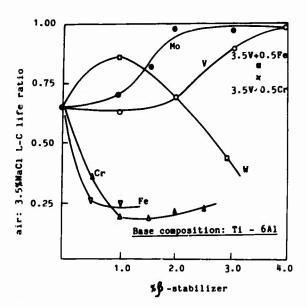


Figure 1 Effect of beta stabilizers on the low cycle fatigue life susceptibility to 3.5 % NaCl aq. sol.

seemingly exists some amount of isomorphous beta stabilizers for the given aluminium content to be critical in respect of SCC suppressing. Having been introduced together eutectoid and isomorphous beta stabilizers mitigated their actions reciprocally. Quasi-isomorphous beta stabilizer tungsten was found to produce more complex effect. Electrochemical experiments have revealed the displacement of potential in the negative direction which was much more significant in case of eutectoid beta stabilizers compared with isomorphous ones (see Figure 2). Interesting results have been obtained when studying the effect of cooling rate on SCC susceptibility. The experiment was in heating the alloys at the temperature of above beta trunsus (1000-1050°C depending on the chemical composition) followed by water quenching, air cooling, furnace cooling and step furnace cooling (500, 100, 3.0 and 0.3 grade/min rate respectively) down to 650°C. Then aging at 500°C for

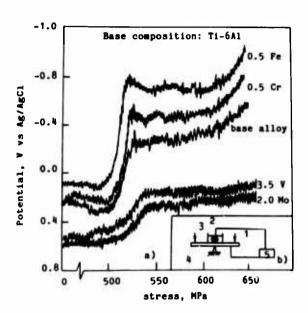


Figure 2 a) Effect of continiously imposed stress on the electrochemical potential in 3.5 % NaCl aq.sol. b) Principal scheme of the experiment. 1 - sample, 2 - 3.5 % NaCl aq.sol., 3 - loading, 4 - electrode, 5 - potentiometer.

100 hours was given in order to provoke & -solid solution ordering. As may be seen from Figure 3 the fast cooling made the alloys containing isomorphous beta stabilizers substantially immune to SCC whereas quite opposite effect was observed in case of the eutectoid beta stabilizers. However, as the cooling rate decreased the effect of various beta stabilizers was less profound and SCC susceptibility for all alloys investigated was close enough at the lowest cooling rate. Microstructural changings as influenced by the rate variations are shown in Figure 4. X-ray microspectroscopy have revealed a great deal of alloying elements redestribution in case of the low cooling rates (see Figure 5). As cooling rate decreases the d -phase becomes more depleting for beta stabilizers as well as enriching for alpha stabilizers. The influence of annealing temperature on the low cycle fatigue life in the corrosive environment with and without molybdenum alloying additions is shown in Figure 6. There exists a significant drop of the property when the alloy was heated high in $(\mathbf{d} + \mathbf{\beta})$ - field followed by aging provoking \mathbf{d} -solid solution ordering reaction. The fatigue life in air was found to be little affected by the annealing temperature variations. Also Figure 6 displays data for Ti-6Al alloy for comparition. Table 1 shows results of testing of two large-sized Ti-6Al-2Mo bars which were different in that one of its was beta processed whereas another was processed at the temperatures below beta transus during final stages of forging. Shown in Figure 7 micrographs were made by secondary electron microscopy technique. The black and white contrast produced is a result of alloying element redistribution.

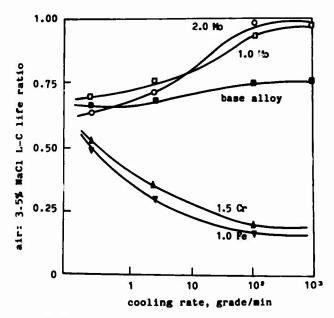


Figure 3 Effect of cooling rate on the fatigue life susceptibility to 3.5 % NaCl aq.sol.

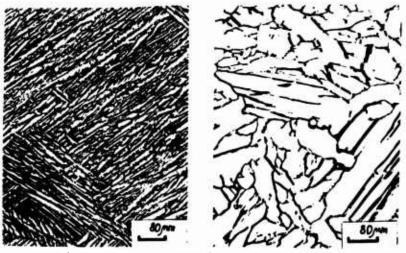


Figure 4 Microstructures of Ti-6Al-1,5 Mo alloy after beta annealing followed by cooling with the rate of 100 grade/min(a) and 0.3 grade/min (b).

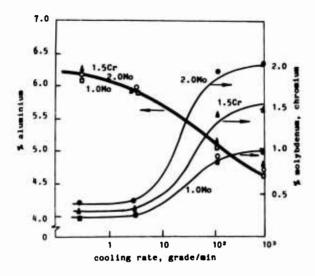


Figure 5 Effect of cooling rate after beta heating on the alloying elements content in & -phase.

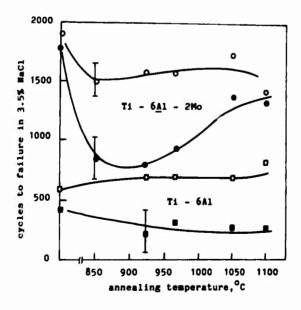


Figure 6 Effect of temperature on the low cycle fatigue life in 3.5 % NaCl aq. sol.q,o - as annealed condition; ■, • - after aging for 500°C during 100h.

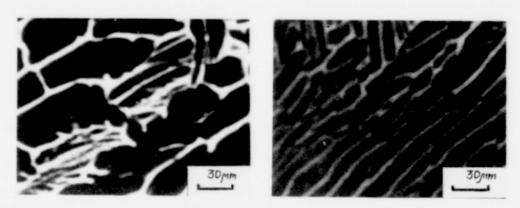


Figure 7 Microstructural images of forging No 1(a) and No 2(b) (see Table 1).

Table 1 The mechanical properties of some Ti-6Al-2Mo forgings

	Final forging temperature,		YTS, MPa	EL %	RA %	KCU joule m ²	Number of cycles to failure	
						m<	In air	n 3.5% NaCl
1	1000-1020 $(4+\beta)$ -processing	876	851	12.3	27.5	55	1870	380
2	1040-1060 (\$ - pro- cessing)	896	823	12.2	29.7	64	2030	1640

Discussion

The results obtained have corroborated the fact that the additions of isomorphous beta stabilizers (molybdenum and vanadium in particular) to \mathcal{A} -base titanium alloys made them less sensitibe or even devoid of SCC. In contrast to that eutectoid beta stabilizers were found as greatly enhancing SCC susceptibility. It is well known that quasy equilibrium conditions provided beta stabilizers tend to enrich β -phase at the expence of depleting \mathcal{A} -phase. Because of it the lowering of cooling rate from β -field heating made \mathcal{A} -solid solution substantially depriving of beta stabilizers. The structure changes corresponding the rate variations were almost the same for alloys containing isomorphous as well as eutectoid beta stabilizers - the coarsening of \mathcal{A} -platelets with the cooling rate decreasing. Therefore the effect of beta stabilizers in respect of SCC susceptibility relates with their content in \mathcal{A} -phase.

A slight enrichment of $\mathcal A$ -phase by alpha stabilizers should also be taken into consideration. It should be noted here that certain aging procedure is necessary to provoke SCC. The mechanism of beta stabilizers influence on SCC is probably related with electrochemical processes (see Figure 2). The results suggest that during manufacturing of $\mathcal A$ -base titanium alloys products the substantial supersaturation of $\mathcal A$ -solid solution should be provided if practically unsesceptible to SCC material is to be produced.

Summary

The experimental results obtained have corroborated the general rule that eutectoid and isomorphous beta stabilizers produce quite different effect on SCC susceptibility (including low cycle fatigue life susceptibility to 3.5 % NaCl aq.sol.) - enhancing and eliminating, respectively. The results also showed that the effect of beta stabilizers is dependent of its content in α -phase (besides other factors). Thus in order to obtain maximum effect from isomorphous beta stabilizers additions in respect of suppressing SCC susceptibility the supersaturation of α -solid solution for these element is to be provided. In particular long-term exposures high in $(\alpha + \beta)$ -field should be removed because of α -solid solution depletion of isomorphous beta stabilizers.

Acknowledgement

Authors wish to express much gratitude to Dr.Scherbinin V.F. for his creative participating in electrochemical studies.

References

- 1. Igor Gorynin, Boris Chechulin, <u>Titan v Mashinostroenii</u>, (Russia, Moscow, Mashinostroenie, 1990).
- 2. M.J.Blackburn, J.A.Feeney and T.R.Beck, "Stress Corrosion Cracking of Titanium Alloys", Advan.Cor.Sci.Technol.3 (1977).
- 3. R.A.Wood, J.D.Boyd, R.I.Jaffee, "The Effects of Alloy Composition on the Salt-Water Stress Corrosion Susceptibility of Ti-Al Base Alloys", <u>Titanium</u>, <u>Science and Technology</u>, 4,Plenum Press.,(New-York London, 1973), 2639-2654.
- 4. S.S.Ushkov, A.I.Igolkin, "Some Reguliarities of Alloying Elements Effect of &-Base Titanium Alloys Embrittlement in Air and Corrosive Environment", (to be published this proceeding).

Electrochemical Behavior of TiN Coated Titanium in a

Hydrochloric Acid Solution

T. Yashiki*, Y. Sugizaki**, H. Towari** and H. Satoh**

*Steel Casting & Forging Plant Takasago,
KOBE STEEL, LTD. Shinhama, Arai-Cho, Takasago, 676 Japan
**Materials Research Laboratory, KOBE STEEL, LTD.
Takatsukadai, Nisi-ku, Kobe, 655-22 Japan

Abstract

Electrochemical behaviors of titanium coated with TiN in a boiling 5% HCl solutionhave been investigated. The metallographically polished surfaces have been coated with TiN 1μ m in thickness by using a reactive RF sputtering method. The specimens coated under various conditions were measured using potentiodynamic polarization curves and were characterized by X-ray diffraction(XRD) and X-ray photoelectron spectroscopy(XPS) techniques.

It was found that TiN films remarkably inhibited the active dissolution of titanium, and the coating conditions affected the electrochemical behavior of titanium coated with TiN. The bias voltages, which were applied to the specimens during coating, could significantly affect the crystal orientation and composition of TiN films. The preferred orientation of (111) was exhibited as the bias voltage applied and the anodic current density was decreased accompanied by the orientation.

Titanium '92 Science and Technology Edited by F.H. Froes and I. Caplan The Minerals, Metals & Materials Society, 1993

Introduction

It has been demonstrated that titanium has superior corrosion resistance to oxidizing acids and chloride solutions in the service environment. In a non-oxidizing acid such as hydrochloric acid and sulfuric acid, titanium may corrode under conditions of high concentration and temperature.

A number of investigations have been made in an attempt to improve the corrosion resistance of titanium by alloying it with paladium ¹⁾, nickel and molybdenum ²⁾. It has also been reported that corrosion resistance of titanium was improved with thermal oxidation ²⁾, and coating with PdO/TiO₂ ⁴⁾.

The coating of various kinds of ceramics by CVD(Chemical Vapor Deposition) and PVD(Physical Vapor Deposition) techniques is expected to increase the corrosion resistance of titanium. It has already been recognized that the corrosion resistance of steel and stainless steel using these techniques^{a)}.

The corrosion behaviors of metals coated with ceramics have been reported in related to process conditions. There are seldom reports correlating corrosion resistance with film characteristics (for example crystal orientation, film composition).

In the present work, we prepared TiN coated titanium by using a reactive RF sputtering method, and investigated the corrosion behaviors of the specimens by using electrochemical polarization measurements. TiN was chosen as test films because of its chemical stability and its good adherence to titanium substrate.

Experimental Procedures

Commercially pure titanium (ASTM Grade 3) was used as test material. Before coating, the substrates with dimension $36\times18\times1\text{nm}$ were polished with emery paper 6400 followed by rinsing and degreasing. Pre-bombardment was carried out in an argon atmosphere of about 2.7Pa for 5 minutes, and then the vacuum chamber was evacuated to a vacuum of $8\times10^{-4}\text{Pa}$. The coatings were formed by the reactive RF sputtering method in an Ar-N atmosphere of about 2.7 $\times10^{-1}\text{Pa}$. Commercially pure titanium (ASTM Grade 1) was used as a target material. As shown in table 1, two process parameters, nitrogen flow rate and bias voltage, were varied. The film thickness was controlled about $1\,\mu$ m.

The anodic polarization curves of these specimens were measured potentiodynamically in a boiling 5% HCl solution. The sweep rate was 0.05V/min. The potential was measured with reference to a Ag/AgCl

Table | Process condition

Paramete	r 	Condition
Nitrogen f	low rate	7.5~19.2SCCM
Bias volta	ge	0~-150V
Process po	мег	2000W
Pressure	Pre-bombardment	2.7Pa
	Coating	$2.7 \times 10^{-1} Pa$
Pre-bombar	dment time	5 min

electrode and a platinum sheet was used as the counter electrode. The crystal orientation and composition of films were characterized

by X-ray diffraction(XRD), we also carried out X-ray photoelectron spectroscopy(XPS) to examine the film compositions of near surface layer of TiN films, which electrolysed at constant potentials in a boiling 5% HCl solution.

Results and discussion

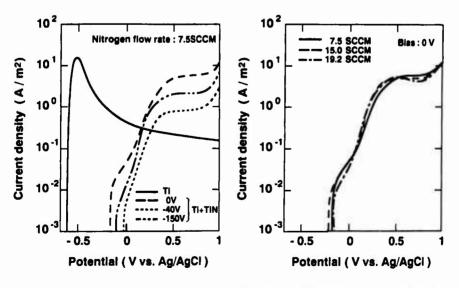
We controlled the film thickness at about 1 μ m and confirmed that the influenceof the pin hole was negligible at such thickness by measurement of the anodic polarization curves of titanium coated with TiN and glass coated with TiN.

Potentiodynamic polarization measurement has been made for the specimens deposited at various bias voltages in order to understand the effects of bias voltage.

Figure 1 shows the anodic polarization curves of titanium and TiN coated titanium which were deposited at various bias voltages (0 \sim 150 $\rm V$). The corrosion potential of the specimens coated with TiN the passive region of titanium, and as a consequence, the active-passive transition region disappeared. The potentials were shifted in the noble direction with the bias voltage in conjunction with a decrease of anodic current density.

Figure 2 shows the anodic polarization curves of TiN coated titanium which was deposited under various nitrogen flow rates (7.5~19.2SCCM). The variation of nitrogen flow rate during coating slightly affects polarization behavior in comparison with the specimens coated at various bias voltages.

As can be seen in figure 1 and 2, as the potential increased, the anodic current density of specimens rapidly increased, and then the anodic current density was saturated when the potential was in the



anodic polarization curves.

Figure 1 - influence of bias voltage on Figure 2 - influence of nitrogen flow rate on anodic polarization curves.

vicinity of 0.5V.

In order to understand these behaviors, an XPS analysis was carried out for the specimens, which were electrolyzed at a potential of 0 and 0.5 V. The compositional depth profiles obtained from the near surface layers are presented in figure 3. The compositional depth profile of the specimen which was electrolized at 0V was hardly changed from the unelectrolized specimen. For the specimen electrolized at a of 0.5 V, the depth profile was significantly changed, oxigen displaced nitrogen in the near layer surface of TiN.

The rapid increase of anodic current density, then, is due to the decomposition reaction of the TiN, while the region of constant current density is due to the forming of TiO, film at the surface of the TiN film.

We evaluate "corrosion current density" which was defined as the anodic current density at the corrosion potential+0.05V and "decomposition current density" which was defined as the anodic current density at 0.5V.

Figure 4 shows the corrosion current density and the decomposition current density of the specimens coated as a function of the nitrogen flow rate and the bias voltage. As the nitrogen flow rate increased, the corrosion current density decreased, while the decomposition current density slightly decreased. It was found that the corrosion current density and decomposition current density significantly decreased when bias was applied. However, the change of these current densities was not observed at various bias voltages. It was found that deposition with bias was most effective in decreasing the corrosion current density and the decomposition current density.

In order to further understand the dependence of these current densities on the process conditions, the crystal prientation and the lattice parameters of the TiN films were determined by XRD. Figure 5 shows the XRD result obtained from the specimens coated at various bias voltages. The intensity of the (200) peak decreased as the bias voltage increased, and the intensity of the (111) peak relatively increased.

Figure 6 shows the intensity ratio 1(200)/1(111) and the lattice parameters of TiN films deposited at various bias voltages. It is well known the lattice parameter was proportional to the composition of TiN.

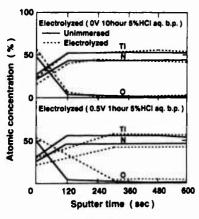


Figure 3 - Depth profiles of unimmersed and electrolyzed titanium coated with TIN obtained by sequential XPS analysis.

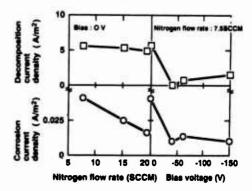


Figure 4 - Influence of nitrogen flow rate and bias voltage on anodic polarization curves.

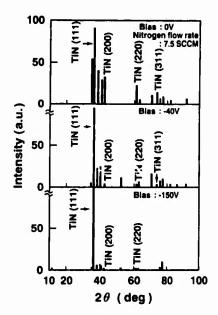


Figure 5 - X-ray diffraction patterns of titanium coated with TIN at various blas voltages.

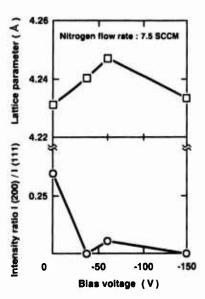


Figure 6 - Influence of bias voltage on X-ray diffraction patterns and lattice parameter of TiN film.

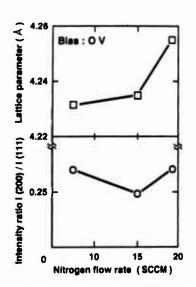


Figure 7 - Influence of nitrogen flow rate on X-ray diffraction patterns and lattice parameter of TiN films.

The lattice parameters were calculated from the peak positions of each crystal plane. The preferred orientation of (111) was suddenly exhibited when the bias voltage was applied. The lattice parameters increased as the bias voltage increased in the range of between 0V and -60V, and decreased at -150 V. The intensity ratio I(200)/I(ii1) in figure 6 varied in correlation with the variation of the anodic current density as a function of the bias voltage in figure 4. It was found that TiN films with the (111) preferred orientation were significantly effective in decreasing the anodic current density.

Figure 7 shows the intensity ratio and the lattice parameters of TiN films deposited under various nitrogen flow rates without bias voltage. Although no influence of the nitrogen flow rate on the preferred orientation of TiN film was observed, the lattice parameter increased with the increasing nitrogen flowrate. Compositional change of nitrogen in TiN film is comparable with that of anodic current densities. The increase of the lattice parameter(nitrogen content) was found to suppress the current densities without bias voltage. It was noted that the bias voltage applied during deposition had influence on the properties of TiN films. The preferred orientation appearing in TiN film had a stronger correlation to the behavior of the anodic current densities than to the change of the lattice parameter. The anodic current densities decreased with the increase of nitrogen flow rate through the increase of lattice parameters, when no bias voltage was applied during deposition.

Okamoto et al. ⁶⁾ proposed that the crystal planes having large atomic densities were more corrosion resistant than the planes having small atomic densities. The (111) plane of TiN, which had a fcc crystal structure, then, was more corrosion resistant than other crystal planes.

However, D. Wang et al. 47 reported that the TiN films which exhibited a preferred orientation of (200) deposited by reactive ion plating were more corrosion resistant than the (111) oriented films in 0.5N Na₂SO₄.

In our investigation, the TiN films which exhibited a preferred orientation of (111) had more excellent corrosion resistance than the (200) oriented films in 5% HCl. We conside the activation energy of corrosion reactions of each crystal plane to be different in various corrosion environments. In our investigation's environments (boiled 5% HCl), the activation energy of the (111) plane might be larger than that of the (200) plane.

Conclusions

It was found that TiN films remarkably inhibited the active dissolution of titanium and the coating conditions affected the electrochemical behavior of TiN coated titanium. The bias voltages could significantly affect the crystal orientation and composition of TiN films. The preferred orientation of (111) was exhibited as the applied bias voltage and the anodic current densities decreased together with the orientation. The preferred orientation of (111) was a more dominant factor governing the decrease of anodic current density than the composition of TiN.

References

- 1. M. Stern and H. Wissenberg, "The Influence of Noble Metal Alloy Additions on the Electrochemical and Corrosion Behavior of Titanium," J. Electrochem. Soc., 106(1959), 759-764.
- 2. Annual Book of ASTM Standards (1985) Sec. 2, B265 p. 174, B337 p. 203, B338 p. 209, B348 p. 218, B363 p. 265, B381 p. 292
- 3. Chuk-ching Ma and E. Peres Jr., "Corrosion Resistance of Anodized and Unanodised Titanium," <u>Industry and Engineering Chem!stry</u>, 43(3)(1951), 675-679.
- 4. T. Fukuzuka, K. Shimogori, H. Satoh and F. Kamikubo, "Protection of Titanium Against Crevice Corrosion by Coating with Palladium Oxide," Titanium 80 Science and Technology, Proc. 4th Int'l Conf. on Ti, ed. by H. Kimura and O. Izumi, Kyoto, (1980), 2631-2638.
- 5. For Example, Y. Massiani J. Crousier and L. Fedrizzi, et al., "Study of the Behavior in Acidic Solution of Titanium and TiN Coatings Obtained by Cathodic Sputtering, "Surface and Coatings Technology, 33(1987), 309-317.
 6. G. Okamoto, et al., "Application of Transition State Method to the Heterogeneous Reaction on Hydrogen Electrode, "Sci. Paper Inst. Phys. Chem. Res., 29(1936), 223-251.
- 7.D. Wang, H. Murata and T. Oki, "Orientation, Morphology and Properties of TiN Films Deposited by Reactive Ion Plating," Hyomen Gijutsu, 41(4)(1990), 382-387.

STRUCTURAL CHARACTERIZATION OF

PLASMA NITRIDED TITANIUM ALLOYS

M. Salehi*, T. Bell[†], and P. H. Morton[†]

*Department of Materials Engineering, Isfahan University of Technology, Isfahan, Iran

†School of Metallurgy and Materials, University of Birmingham, Birmingham, B15 2TT, England

Abstract

Plasma nitriding technique has been employed to improve the surface quality of titanium alloys. The technique represents a plasma assisted thermochemichal treatment process in which glow discharge nitrogen is allowed to diffuse into the surface of the titanium component to form a ${\rm Ti}_{\rm x}$ -Ny surface layer. The structure and composition of the plasma nitrided titanium have been investigated by means of metallographic examination and X-ray diffraction analysis. Plasma nitriding of titanium alloys resulted in the formation of a duplex compound layer, consisting of an outermost golden δ -TiN layer lying on the top of a lower layer of compound, having a silvery appearance and consisting of δ -TiN + ϵ -Ti₂N. This observation that the inner compound layer is two phased is reported for the first time.

Titanium '92 Science and Technology Edited by F.H. Froes and I. Caplan The Minerals, Metals & Materials Society, 1993

Introduction

In recent years, several methods of surface alloying with nitrogen have been used and successfully employed to produce titanium surfaces with lower friction and minimal wear in sliding. In particular, the benificial effect of glow discharge nitriding on the tribological properties of sliding surfaces of titanium components has been observed in several studies⁽¹⁻⁶⁾.

In the plasma nitriding of unalloyed titanium, the phases present will be governed by the Ti-N binary system(7) (Fig. 1). When Ti 6Al 4V is nitrided the reactions must be generally similar, although the equilibria will be modified by the presence of aluminium and vanadium. At the beginning of the plasma nitriding process, high energy nitrogen ions react with titanium on the surface to form an outer layer of the highest nitride, 8-TiN. This layer prevents any further high energy nitrogen ions which strike the surface from reacting directly with titanium atoms to form further titanium nitride. Growth of the layer takes place by inward diffusion of nitrogen into the substrate, together replenishment by fresh nitrogen atoms arriving at the surface. As diffusion progresses lower nitrides may be formed, and in particular tetragonal ε -Ti₂N is likely to be formed below the δ -TiN layer. As pointed out by Rennhack et al⁽⁸⁾ the formation of ϵ -Ti₂N depends upon the rate at which nitrogen arrives at the δ -TiN/ ϵ -Ti₂N interface and the rate at which it leaves the ϵ -Ti₂N/ α -Ti. The thickness of each layer will depend on the rate of nitrogen diffusion through the layer relative to the diffusion rates in adjacent layers, on the range of composition which the phase in question can exist, and on the rate at which it can be consumed by the metal of the previous layer. Once the reaction has proceeded sufficiently far to allow the setting up of a steady state, the rate of absorption of nitrogen by the metal will be controlled by the slowest transfer process of the whole sequence, i.e. diffusion of nitrogen through the δ-TiN layer.

In the present investigation, experiments were first carried out to establish the relationship between the nitrided structure and the nitriding conditions. The influence of nitriding temperature on the nitrided structures was studied, and the optimum nitriding temperature has been established to obtain the highest surface quality.

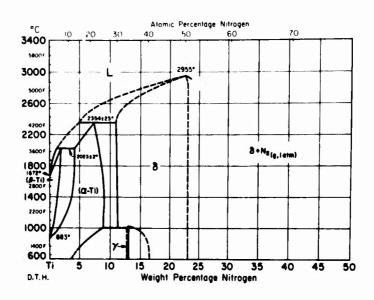


Figure 1. The phase diagram of binary system Ti-N(7).

Plasma Nitriding Procedure

Ti 6Al 4V disc shaped specimen was surface finished by grinding to an average roughness of $1.3 \,\mu\text{m}$, and was then cleaned ultrasonically in successive rinses of trichloroethylene, acetone and ethanol. The surface finished and cleaned substrate was then subjected to a glow discharge in a Klockner Ionon GmbH plasma unit (Fig. 2) by application of a potential difference of several hundred volts between the chamber (anode) and the specimen (cathode) in a gas mixture of $25.1 \, \text{kN} - 74.9 \, \text{kH}$ at a pressure of 5 mbar. The equipment, developed and designed as a fully computerised industrial system, consists of a DC 40 kw power supply, a computer control unit, a gas mixing device, a stainless steel cold wall vacuum furnace and a vacuum pump system. Plasma heat treatments were conducted at temperatures of 700°C, 750°C, 850°C, and 950°C for a period of 20 hours.

Special jigging arrangements were made in order to minimise any non-uniformity of surface properties due to an uneven amount of sputtering at the edges and centre of the face of the specimen. To achieve this, every other specimen was placed between a set of specially designed and constructed reset jigs. For effective temperature control, the whole system was placed on a titanium supporting block to minimise any radiation effects from the bottom of the furnace support, eleminating any edge effect.

The temperature was measured with a sheathed thermocouple which was introduced into the furnace through a thermo lead-in. The specimens were arranged on the bottom of the chamber and the thermo-lead-in was incorporated in the bottom. The tip of the thermocouple insulator was inserted in a hole 10 mm deep drilled into a dummy specimen. This is less than the recommended depth of 30 mm but was necessitated by the limited height of the specimen used.

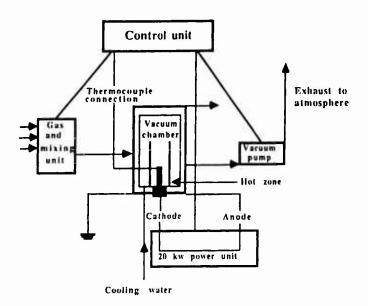


Figure 2. Schamatic representation of a glow discharge heat treatment plant.

Phase Identification Techniques

The structure and composition of the surface treated titanium were studied by means of optical metallography and X-ray diffraction.

Cross section of untreated and treated specimens were prepared for the light optical microstructral investigation by appropriate sectioning, hot mounting in conductive bakelite and mechanical polishing on grinding papers, 6 µm diamond paste and 0.3 µm colloidal silica in distilled water. The samples were then degreased in trichloroethylene and ultrasonically rinsed in methanol. To preserve the compound layer and to avoid mechanical damage during sectioning the specimen surface was covered by hard setting Araldite before sectioning.

Polished and etched microstructures were studied and recorded using the Neophot 21 optical microscope. The optical microscope was fitted with a plate camera for taking micrographs.

X-ray diffraction patterns of the surface treated titanium specimens were recorded using Cu K_α radiations in a Philips X-ray diffractometer. A step scanning mode with 0.01 step width at a counting time of 3 seconds was used and diffraction angle values could be read with an accuracy of +0.01°. The interpretation of the X-ray results was undertaken using the powder X-ray file index. The as-treated specimens were tested on the surface without any additional preparation. Some of the plasma nitrided specimens were in addition polished lightly with 0.3 μ m colloidal silica in distilled water in order to expose the inner lighter layer to more X-rays, where appropriate.

Results

The cross section of a plasma nitrided sample normally reveals a duplex compound layer above a nitrogen enriched diffusion zone which lies above the core material. The outer part of the compound layer has the typical golden colour of titanium nitride (TiN). Within the compound layer and directly below the golden layer, a second layer with lighter colour could be observed (Fig. 3), which will be referred to as the inner compound layer.

Plasma nitriding at temperature of 700° C yielded only a very thin compound layer without a diffusion zone (Fig. 3a). With plasma nitriding carried out at 750° C (Fig. 3b) and 850° C (Fig. 3c) a diffusion zone appeared in addition to the compound layer. Diffusion of nitrogen into the substrate has caused the formation of an α -case, which is considerable thicker at 850° C than at 750° C treatments. It can be seen that the nitride layer achieved by treating at 850° C is more toothed which will certainly improve the bonding of the layer. At a treatment temperature of 700° C the lowest layer thickness of less than 1 μ m was found. Compound layers produced at 950° C (Fig. 3d) of up to 18μ m were thicker than those produced at 750° C and 850° C (2.0 and 4.5μ m respectively).

A semiquantitative idea of the variation in the amounts of phases present was obtained by comparing the intensities of the diffraction lines which do not overlap but are sufficiently intense (Fig. 4). It should be noted that, although the intensities of diffraction lines of a given phase are not a precise measurement of the quantity of that phase in any mixture of the phases, the intensity values can be used as an indication of the relative amount of each phase. For plasma nitriding at 700°C, the structure of the Ti-N layer is predominantly \varepsilon-Ti_2N (Fig. 4a). This phase exists only in a very narrow composition range centred at 33 at. %N (Fig. 1). At temperature of 700°C reflections from the TiN(111) start to appear. From Figure 5b it can also be seen that the intensity of the diffraction line belonging to the TiN(111) increases at 750°C. In contrast, the intensity of the diffraction line belonging to Ti₂N(210) decreases at this temperature. For treatments of 850°C and 950°C (Fig. 4) a mixture of Ti₂N(112) and TiN(200) is formed. A careful examination of these patterns also shows that the intensity of the diffraction lines belonging to Ti₂N(210) and TiN(200) increase with temperature whereas those belonging to Ti₂N(111) and Ti₂N(022) decrease with temperature. Using these results, together with those from metallographic examinations (Fig. 3), the phase constituents in

compound layer were identified. The outer (golden) and inner (light) parts of compound layer were identified as single phase TiN and a two phase layer of $TiN + Ti_2N$ respectively.

At the start of plasma nitriding the surface region will have transformed to $\alpha + \beta$ with grain growth occurring. However, as nitriding proceeds, the β phase phase becomes a coarse-grained α -phase, consisting of α -grains in a matrix of transformed β having a Widmastatten α -structure. Plasma nitrided samples at 950°C show larger α grains than those treated at 700°C, 750°C and 850°C due to the grain growth that accompanies annealing at higher temperatures (Fig. 3).

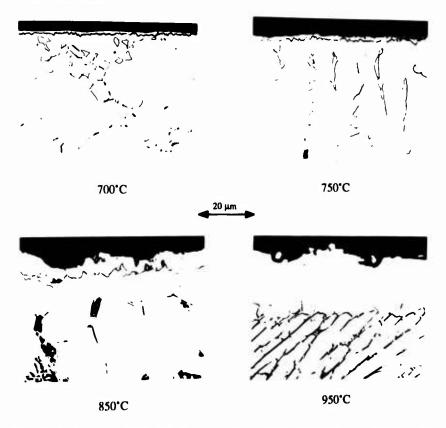


Figure 3. Optical micrographs showing the variation of the compound layer thickness with nitriding temperature. 20 hrs, 5mbar. x1000.

Discussion

Compound layer: The X-ray diffraction patterns of the plasma nitrided titanium were studied to identify the phases present in the compound layer. In agreement with the binary system, patterns revealed the presence of δ -TiN on all of the surfaces studied (Fig. 4) and this is the phase which gives plasma nitrided titanium alloys their characteristic golden colour. At 700°C and 750°C, δ -TiN is only shown by a small reflection from (111). However, this was in contrast to the TiN produced at 850°C and 950°C, which had strong textures with (200) and (220), Figure 4.

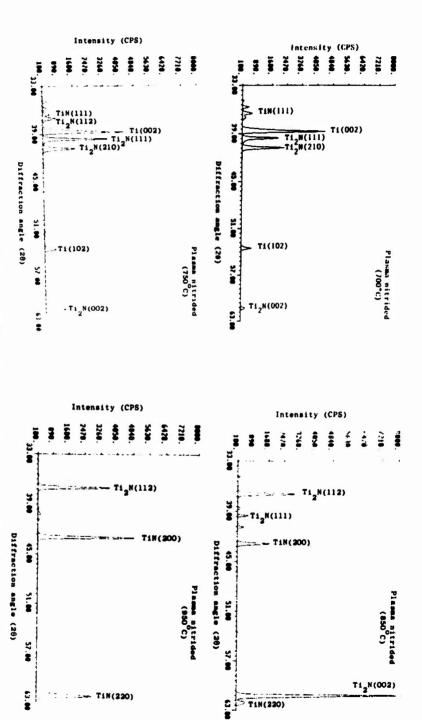


Figure 4. X-ray diffraction patterns of plasma nitrided Ti 6Al 4V surfaces.

The presence of ε -Ti₂N was also confirmed by X-ray diffraction patterns (Fig. 4). These patterns suggested that the ε -Ti₂N phase produced at 700°C and 750°C had fairly random textures, (111), (210), and (002). At 750°C reflection from the (112) phase also starts to appear. From Figure 4 it can be seen that the intensity of reflection from the (112) phase increases with temperature. In contrast, the intensity of the diffraction lines (210) at 850°C and (210) and (111) at 950°C have disappeared.

It should be noted that the reflections from α-Ti diminished with increasing temperature, i.e. with increasing compound layer thickness, indicating that the Ti(002) and Ti(102) diffraction lines at temperatures of 700°C and 750°C belong to the substrate.

Microstructural examination revealed a duplex compound layer consisting of an outermost golden layer lying on the top of a layer with a silvery appearance (Fig. 3). In order to identify the constitution of each compound layer, further X-ray diffraction analysis was performed on the plasma nitrided titanium following removal of the thin golden layer. The XRD pattern produced a persistent TiN peak in spite of the removal of outermost layer. The analysis of these pattern confirms the presence of δ -TiN layers not only in the outermost surface but also in the $(\delta$ -TiN + ϵ -Ti2N) inner compound layer. This observation of a two-phase inner compound layer is in conflict with the results of Lanagan(9) who found that the inner compound layer is a single phase. A feature of particular interest is the formation of ϵ -Ti2N precipitates at δ -TiN grain boundaries in the inner compound layer matrix. It is assumed that transformation temperatures in Ti-N phase diagrams (Fig. 1) have been affected by the presence of aluminium and vanadium. According to this phase diagram the compound layer is formed as single phase TiN at the nitriding temperature. As one progresses from the outside to the inside of this layer, the nitrogen content reduces progressively, and the ϵ -Ti2N phase has precipitated from low nitrogen δ -TiN phase during slow cooling.

<u>TiN/Ti₂N</u>: A number of investigators^(4,10,11), have reported that the fraction of δ-TiN in the compound layer increases with treatment temperature. Bragnaza et al⁽¹⁰⁾ found that the ratio of δ-TiN to ε-Ti₂N is constant independent at diffusion time, but increased with temperature. This is in agreement with the X-ray diffraction results of the present investigation where the ratio of TiN/Ti₂N is found to increase steadily with increasing temperature (Fig. 4). Figure 4d illustrates the rapid rise in the intensity of the TiN(200) and TiN(220) lines at a temperature of 950°C. This indicates that although the thickness of the monolayer δ-TiN increases very little with temperature, the proportion of δ-TiN in the (δ-TiN + ε-Ti₂N) layer increases very rapidly as temperature is raised i.e. the quantity of δ-TiN in (δ-TiN + ε-Ti₂N) increases at a much faster rate than that of the δ-TiN uppermost layer.

The majority of reports on plasma nitriding titanium have been considered the inner compound layer as a single phase, ε -Ti₂N(9.12), and its texture has not been studied in any detail. In the present study, the inner compound layer has been considered as a two-phase structure, and both the texture and fraction of TiN/Ti₂N are likely to have an effect on the hardness and and load bearing capacity of the inner compound layer. In this work, the compound layer of plasma nitrided surface at 700°C had a predominant ε -Ti₂N phase with a small fraction of δ -TiN.

Alpha stabilised diffusion layer: Below the compound layer is an α -stabilised diffusion layer which is very much thicker in comparison with the layers above it (Fig. 3). In this diffusion layer the nitrogen is in solution and acts as a stabiliser of the α -phase caused by the higher solubility of this phase for nitrogen. Before the titanium nitride layer has formed, the reaction rate is probably controlled by the rate of diffusion of nitrogen in α -Ti, which even at temperatures above the transformation temperature of the pure material, will be present in the nitrogen contaminated region. As one progresses from the outside to the inside of this layer, the nitrogen content diminishes progressively to that of the matrix and the proportion of β -phase increases correspondingly.

Core structure: Plasma nitriding also influences the microstructure in the core sections. It can be seen that little change had taken place in the structure of Ti 6Al 4V after plasma nitriding at

700°C. Treating at temperatures of 750°C produced nearly similar structures, and the structure consists of equiaxed α phase and β phase at grain boundaries. Treatment at 850°C caused a substantial proportion of the structure to transform to the β phase, which is revealed at room temperature as regions of transformed β between α grains. After plasma nitriding at 950°C the core structure consists almost entirely of the transformed β in the form of coarse, plate-like α grains (light) and intergranular β phase (dark). It can be suggested from this that the plasma nitriding temperature during treatment may have been slightly above the β transus i.e. higher than 950°C.

Conclusion

Plasma nitriding of Ti 6Al 4V in the temperature range of 700°C to 950°C results in the formation of a duplex compound layer, consisting of an outermost golden δ -TiN layer lying on the top of a lower layer of compound, having a silvery appearance and consisting of δ -TiN + ϵ -Ti2N. This observation that the inner compound layer is two-phased is reported for the first time. Previous reports on plasma nitrided titanium have considered that the inner compound layer is a single phase, ϵ -Ti2N. Beneath the compound layer lies an α -stabilised diffusion layer which is very much thicker in comparison with the layers above it.

References

- 1. T. Bell, H.W. Bergmann, J. Lanagan, P.H. Morton, and A.M. Staines, <u>Surface Engineering</u>, 2 (2) (1986), 133.
- 2. D. Treheux, and L. Nincent, <u>Proceeding of 5th International Conf. on Titanium</u>, Munich, F.R. Germany, (1984), 2187.
- 3. E. Rolinski, Surface Engineering, 2 (1) (1986), 35.
- 4. J. Lanagan, P.H. Morton, and T. Bell, <u>Designing with Titanium</u>, The Inst. of Metals, (1986), 136.
- 5. M. Miyagi, Y. Sato, T. Mizuno, and S. Sawada, <u>Proceeding of 4th International Conf. on Titanium</u>, 4 (1980), 2867.
- 6. M. Salehi, (Ph.D Thesis, University of Birmingham, 1990).
- 7. T. Lyman et al. eds., Metals Handbook, 8th Edition, vol. 8 (Metals Park, OH: American Society for Metals, 1973), 322.
- 8. E.H. Rennhack, W.C. Coons, and R.A. Perkins, <u>Trans. Met. Soc. AIME</u>, 87 (1968), 343.
- 8. J. Lanagan, (Ph.D. Thesis, University of Birmingham, 1989).
- 9. K.T. Rie and T. Lampe, <u>Proceeding Conf. Heat Treatment '84</u>, Institute of Metals, London, (1984).
- 10. C. Bragnaza, H. Stussi, and S. Veprek, J. Nuclear Materials, 87 (1979), 331.
- 11. K.T. Rie, T. Lampe, St. Eisenberg, Surface Engineering, 1 (3) (1985), 198.

PROPERTIES OF SURFACE OXIDES ON TITANIUM AND SOME TITANIUM ALLOYS

N. Frey*, T. Buchillier**, V.-D. Le, and S.G. Steinemann

Institut de physique expérimentale, Université de Lausanne, CH 1015 Lausanne-Dorigny, Switzerland

Abstract

Surface oxides formed spontaneously and by anodic oxidation on cp titanium and Ti alloys are examined for their conductivity by dc and ac measurements, electrochemical polarization resistance and ellipsometry for film thickness. Foreign elements are usually incorporated in the oxide which is also x-ray amorphous; even with defects, the oxide retains insulating properties and full corrosion resistance.

- * Present adress: Ecole Polytechnique Fédérale de Lausanne, DMX-LMCH, MX-C Ecublens, CH 1015 Lausanne
- **Now: Institut de Radiophysique Appliquée, Centre Universitaire, CH 1015 Lausanne

This study was supported in part by Schweizerischer Nationalfonds zur Förderung der wissenschaftlichen Forschung under National Program No. 19 "Materials for Tomorrow".

Titanium '92 Science and Technology Edited by F.H. Froes and I. Caplan The Minerals, Metals & Materials Society, 1993

Introduction

The physical properties of surface films formed spontaneously, or by anodic oxidation on titanium are of interest in relation to the stability of the metal in corrosive environment. Examination of these surface films by x-ray photoelectron spectroscopy and microanalysis shows that foreign atoms are occluded in the oxide following any chemical attack, e.g. the anions chlorine, fluorine, phosphate after electropolishing, pickling, anodizing, and the cations Al, V, Mo, etc. resulting from oxidation of the base metal [1]. Their concentrations are several %, i.e. orders of magnitude higher than typical doping levels in the n-type semiconductor. The color of the surface oxide should darken and the electrical resistivity should drastically fall. That is not observed.

Nevertheless, it is true that electrical, optical and mechanical properties of these films vary with the electrolyte to which they are exposed, its pH and temperature, growth rate and thickness, and surface preparation. A great number of procedures for anodic oxidation of Ti are shown in a review of early work by Aladjem [2]. This author concludes that (i) anodic films on that metal are rarely, if ever, pure and stoechiometric TiO₂ but contain also elements other than titanium and oxygen, and that (ii) the films may be amorphous or consist of any of the known modifications of TiO₂ or mixtures thereof. Such variability suggests that the diffusion mechanism controlling oxide growth is important. Inward anionic diffusion dominates for the Ti/TiO₂ system in the case of thermal oxidation [3] and for low-temperature anodic oxidation [4,5]. For very small growth rates, Wiesler et al. [6] find an epitaxial relation between the metal and a rutile and an anatase phase what is a rather strong indication that oxides are formed at the metal/oxide interface. Such ordered structures do not necessarily exist at higher growth rates used normally.

In this work, the electrical resistivity of surface films is obtained by direct and electrochemical methods. Surface oxides grown under conditions of industrial surface treatments are studied.

Material and surface preparation

Oxides grown on cpTi and several alloys (alpha-beta Ti6Al4V, Ti6Al7Nb, Ti5Al2.5Fe; beta-type Ti15Mo5Zr3Al) are examined. The surfaces are prepared by:

(i) mechanical grinding on abrasive (SiC) paper to grit 4000,

(ii) electropolishing in methyl alcohol + ethylene glycol/perchloric acid [7] or H_2SO_4/HF base electrolyte (proprietary recipe),

(iii) anodic oxidation in 10% phosphoric acid under current limitation and preset maximum voltage. Growth rate is 20Å/s, at a current density of 5-10 mA/cm².

The thickness of the anodic oxide was measured by ellipsometry. The optical constants for the metal and oxide as given by Musa and Neal [8] were used. The results agree well with faradaic rates measured during growth. The oxide thickness is:

t in Å = 30 for electropolished samples, $103 + 22 \cdot V(\text{cell})$ for ground and anodized samples, $34 + 17 \cdot V(\text{cell})$ for evaporated and anodized Ti. The first figure corresponds to the "natural" oxide film as measured by XPS, or equals the intercept at zero potential.

Crystalline oxide films above 500Å can be detected by x-ray diffraction. But peaks were not found. The anodic oxides grown in a phosphoric acid electrolyte and at high rates are x-ray amorphous.

Resistivity and polarization experiments

Two types of experiments, "dry" and "wet", were done to characterize the surface films.

Dc and ac resistivity of surface oxides

The direct, or "dry" resistance measurement is done by contacting the oxide with a 70/30% Hg-In amalgam (fig. 1). The liquid contact wets and is ohmic. Slow current-potential scans and impedance measurements for 1E-2 to 1E+5 Hz are performed. An electrochemical interface 1286 and frequency response analyser 1250 (SOLARTRON) and 8500 digital plotter (ENERTEC SCHLUMBERGER) is used.

The current-potential plots show linear behaviour for about 100mV (fig. 2). A non-linear variation beyond that span results from band-bending [9,10]. At still higher field strength (above 1E+6V/cm) breakthrough occurs (fig. 2, at right).

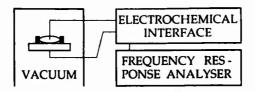
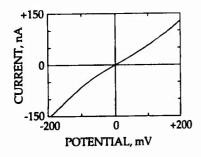


Figure 1 - Measurement of oxide film properties by direct contact.



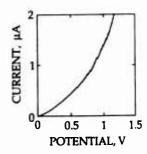


Figure 2 - Slow current-potential scan for an oxide film formed at 40V on electropolished cpTi.

The impedance measurements are done with an amplitude of 100mV and less. The results of figure 3 are obtained for an anodized surface (film of thickness 910Å).

Young [4] admits that the constitution of the surface oxides is not uniform and suggests a model with RC circuits in series. The slope of impedance is then not -1 per decade of frequency. Present results are best interpreted by a single RC circuit and a time constant τ . It is:

$$R = r \frac{d}{A}$$
 $C = \varepsilon_0 \varepsilon_0 \frac{A}{d}$ and $\tau = RC$ (1)

with ρ specific resistivity, d thickness of film, A area of electrode, ϵ the dielectric constant.

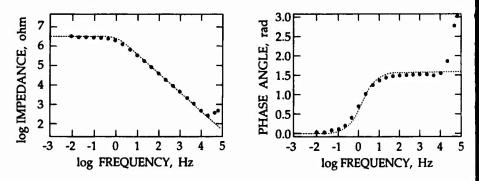


Figure 3 - Impedance curve for an oxide film formed at 40V. The fit for a simple RC circuit is added.

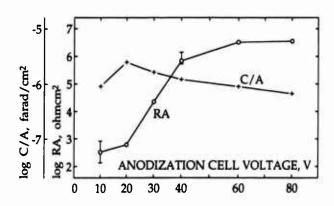


Figure 4 - Resistance and capacitance of anodic films formed at various cell voltages on electropolished cpTi.

Marquardt's method, the standard of nonlinear least-square routines, is used to model the data. ϵ , ρ and τ , also constants in Young's theory can be extracted by such a fit. Results are shown in fig. 4. The time constants vary from a fraction of ms to some s. The contribution to such changes is small for the capacitance and the dielectric constant is 100-120 (uncertainties exist for films formed at 10V). But the specific resistivity depends on thickness of the surface oxide; ρ is 1.2E+8 ohmcm for d = 240Å(10V) and above 1E+11 ohmcm for films of 1000Å and more. Defects in the oxide might cause this variation, but it is remarked that the width of the space charge layer is about the same as the thickness of the thin surface oxide.

Polarization resistance measurements for titanium and Ti alloys

The electrochemical, or "wet" resistance measurement is done in aerated 3% NaCl solution. Currents are very small and the galvanostatic method is preferable (fig. 5).

The (electrochemical) polarization resistance is related to the corrosion current density j through

$$R_{p} = \frac{b_{an}b_{ca}}{2.3(b_{an}+b_{ca})} \frac{1}{j} = k \frac{1}{j_{corr}}$$
 (2)

where the b's are the Tafel constants of anodic and cathodic reactions [12]. The kinetic coefficient k is 5E-2V for $b_{an} = \infty$ (anodic process is limited for the stable oxide) and $b_{ca} = 0.1V/\text{decade}$ for oxygen reduction and electronic conduction.

Results of measurements for different surface preparations and for two metals are shown in fig. 6. Data for chosen surface treatments and other metals are further given in the table.

It is surprising to find that the polarization resistance, i.e. the corrosion resistance, of alloys is higher than that of cp Ti. The structureless state and the many valency defects in the oxide even seem favourable.

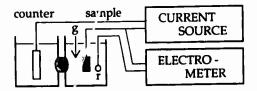


Figure 5 - Polarization resistance measurement by galvanostatic method. Two compartments contain the cathode and sample (anode); g is gas inlet (oxygen) and r the reference electrode.

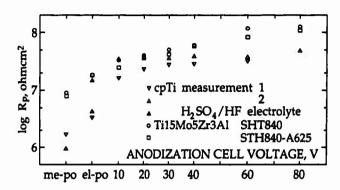


Figure 6 - Polarization resistance for oxides of different thickness and on different substrates; me-po is mechanically polished and el-po is electrolytically polished.

Table - Polarization resistance and resting potential of mechanically ground and electropolished Ti and its alloys.

	mechanica	mechanically ground		electropolished		
	rest. pot.	pol. resist.	rest.pot.	pol. resist.		
cpTi	230/210	0.96/1.7	80/140	4.4/3.4		
_		110	15			
Ti6Al4V	-20	3.1	100	3.6		
Ti5Al2.5Fe	-10	1.6	90	2.7		
Ti6Al7Nb	30	1.9	130	2.4		
TiMoZrAl SHT840	<i>7</i> 0	9.1	130	19		
SHT740A625	40	8.0	100	18		
Unit	mV(SCE)	Mohmcm ²	mV(SCE)	Mohmcm ²		

Discussion

The impedance of the surface oxides refers to a bulk property. For the thicker films, the dielectric constant is high and compares with that of crystalline rutile. The short range ordering in the amorphous oxide apparently retains configurations of the particular solid. The specific resistivity however is low for the anodic films, compared to rutile with $\rho=1E+15$ ohmcm and more. The difference has certainly to do with the occlusion of foreign atoms but is not a doping in proper sense.

The polarization resistance has the same dimension as the bulk resistance (see formulas 1 and 2). The mechanisms behind the two measurements however are not the same. R_p is 10-30 times larger than RA, thus equal to the inverse of the kinetic coefficient in formula (2). The coefficient is related to the electron transfer at the film-electrolyte interface, thus to an apparent current density in $R_p = \Delta E/\Delta j$, while the (direct) resistance is connected with the electron conduction in the film. But this electronic current flows for the reduction process in the electrolyte.

The incorporation of foreign elements during anodic growth of titanium oxide is apparently a normal process and can not be suppressed. The insulator character of the films nevertheless is essentially preserved, as show these experiments.

References

- 1. P.-A. Mäusli, S.G. Steinemann and J.P. Simpson, "Properties of Surface Oxides on Titanium and some Titanium Alloys", <u>Proc. 6th World Conf. Titanium</u>, ed. P. Lacombe, R. Tricot and G. Béranger (Les Ulis: les éditions de physique, 1988), 1759-1764
- 2. S. Aladjem, "Review-Anodic Oxidation of Titanium and its Alloys", <u>I. Mat. Sci.</u>, 8 (1973), 688-704.
- 3. M. Leseur and B. Pieraggi, "Structure of Metal-Oxide Interfaces", <u>I. de Physique</u> Colloque, 46 (1985), C4: 135-140.
- 4. J.A. Davies et al., "The Migration of Metal and Oxygen during Anodic Film Formation", J. Electrochem. Soc., 112 (1965), 675-680.
- 5. J.P.S. Pringle, "The Anodic Oxidation of Superimposed Metallic Layers: Theory", Electrochimica Acta, 25 (1980), 1423-1437.
- 6. D.G. Wiesler et al., "Structure and Epitaxy of Anodic TiO₂/Ti(1120)", <u>Surface Science</u>, 268 (1992), 57-72.
- 7. R. Osadchuk, W.P. Koster, and J.F. Kahles, "Recommended Techniques for Polishing Titanium for Metallographic Examination", <u>Metal Progress</u>, October 1953, 129-240.
- 8. A.H. Musa and W.E.J. Neal, "Optical Properties of Bulk Titanium and Thermally Grown Oxide Films on Titanium using Ellipsometry", <u>Surf. Technol.</u>, 11 (1980), 323-332.
- 9. N. Sato, "An Overview on the Passivity of Metals", Corr. Sci. 31 (1990), 1-19.
- 10. H.O. Finklea, "Titanium Dioxide (TiO₂) and Strontium Titanate (SrTiO₄)", <u>Semiconductor electrodes</u>, ed. H.O. Finklea, studies in physical and theoretical chemistry 55 (Amsterdam: Elsevier, 1988), 43-145.
- 11. L. Young, Anodic Oxide Films, Trans. Faraday Soc. 51, 1955, 1250-1256.
- 12. M.G. Fontana and N.D. Greene, <u>Corrosion Engineering</u> (New York: McGraw Hill Book Comp., 1967), 344.

A new corrosion-resistant titanium alloy Ti-3AR with higher strength

Hu Yaojun Cai Xuezhang Liu Guozhong

Northwest Inst. for Nonferrous Metal Res. P.O.Box 71. Baoii. Shaanxi. P.R.China 721014

Introduction

Ti-3AR (Ti-Al-Mo-Ni) is a new corrosion-resistant titanium alloy with higher strength, which have been developed by Northwest Institute for nonferrous metal research, China. Ti-3AR possesses excellent corrsion-resistance and higher strength, which is higher 30-40% than that of Ti-12 (Ti-0.3Mo-0.8Ni), and its resistance to uniform corrosion, crevice corrosion, pitting corrosion is as good as Ti-12. Ti-3AR is generally used in annealed condition, with higher strength and elongation, s> 720MPa, 63900 > 480MPa, 5>18%. Ti-3AR possesses better hot and cold workability, can be easily forged, extruded, rolled, cold formed and welded, it can be produce into plate, sheet, bar, tube, wire etc. The aluminium contant of Ti-3AR contributes to its strength and hot resistance, the molybdenum and nickel content impart corrosion-resistance in acid environments. It can be used for marine engineering and chemical industry, especifically a future for the alloy is forecas in high temperature, high pressure applications. It's mechanical properties and corrosion-resistant properties in acid have been studied in this work. Ti-12 is used for comparative materials.

Experimental procedure

Ti-3AR used in this study is plate of 12mm and 2mm thickness, which were prepared by 2 times of melting in vacuum are furnace, followed Forging, rolling, annearing for a hour at 700°C and air colding. The speciments of $2 \times 20 \times 30$ mm and $\Phi15.9 \times$ 2mm used as corrosion tests and electrochemical tests, respectively. Corrosion tests were performed in nitric, chioric. Suiphric acid solution at various concentration and temperature. The speciments were immersed in 20~50% HNO solutions, 1.5~15% HCl solutions, 1.5~30% H₂SO₄ solutions, at room, 60°C, boil temperature for 1274, 298, 48hr, respectively. After immersion the weight losses of these speciments were measured and average corrosion rates were estimated by following equation (1):

Corrosion rate = $(k \times w) / (A \times T \times D)$

Corrosion rate: mm/y K: constant, 8.76×10 W: weight losses, grain T: immersed times, hours

A: all area of speciment, cm2

D: density, 4.5g / cm²

electrochemical tests were done with M351. The corrosion potential and polarization curve of Ti-3AR were measured in same solution as immersion tests. Saturated calomed electrode (SCE) were used as a reference electrode. Scanning rate is equal to 50mv/min.

> Titonium '92 Science and Technology Edited by F.H. Froes and I. Caplan
> The Minerals, Metals & Materials Society, 1993

Results and disussion

mechanical properties

Table 1 shows tensile properties at room temperature and 250°C and impact toughness of Ti-3AR. It has higher strength which is higher $30 \sim 40\%$ than Ti-12 (Ti-0.3Mo-0.8Ni) and better plasticity, toughness, $\sigma_b > 720$ MPa, $\sigma_b^{330} > 480$ MPa, 5% > 18, $a_E > 1000$ KJ/ m^2 .

Table 1 mechanical properties of Ti-3AR

	plate			sheet	
		RT	350 C	RT	3500
UTS	M Pa	720	480	810	500
YS	M Pa	640	400	760	
EL	%	19	18	19	24
A _E	KJ/m²	1100			

Corrosion rates

in HNO, solution

Table 2 and Fig.1, Fig.2 show the affects of HNO, concentration and temperature on the corrosion rates of Ti-3AR and Ti-12. from table 2, it is clear that corrosion rate of Ti-3AR is small, HNO, concentration affects light to corrosion rate, which increases with temperature. The relationship between the corrosion rate and HNO, concentration, between the corrosion rate and temperature were replotted in Fig.1 and Fig.2.

The surface oxide film formed and became yellow, yellowish—brown, blue, etc, on the Ti-3AR immeased in HNO, solutions, which protect titanium from corrosion.

Table 2 corrosion rates in HNO,

temperature	concentration %	corresion rates (mm / y)			
t		Ti-3AR	Ti-12		
	20	0.001	0.001		
RT	35	0.001	0.001		
	50	0.001	0.061		
	20	0.02	0.01		
60 C	35	0.04	0.01		
	50	0.02	0.01		
BT	20	0.1	0.1		

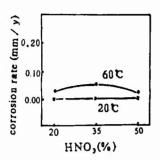


Fig.1 relationship between corrosion rate and HNO, concentration

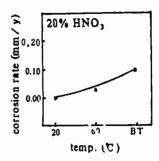


Fig.2 affect of temp. ou corrosion rate.

in H280, solution

Table 3 and Fig.3 show the corrosion rate of Ti-3AR and Ti-12 in $\rm H_2SO_4$ solution at room , 60°C and boile temperature. The concentration and temperature affect considerably corrosion rate, which increase with the concentration and temperature. Ti-3AR was subject to active corrosion over 10% $\rm H_2SO_4$ solution. The corrosion rate rises 2.5mm/y in 30% $\rm H_2SO_4$ solution, white precipitate $\rm Ti_2(SO_4)_3$ occurs and hydrogen is deaerated, the solution become purple black because of production of Ti³⁺. The reaction of Ti with $\rm H_2SO_4$ can be expressed:

$$Ti+H_2SO_4 = TiSO_4+H_2\uparrow$$

 $Ti+H_2SO_4 = Ti_2(SO_4)_2+H_2\uparrow$

Ti2+ is unstable and can be oxides to Ti2+.

Table 3 general corrosion rate in H₂SO₄

temperature T	concentration	corresion rates (mm/y)		
	*	Ti-3AR	TI-12	
	5	0.001	0.001	
RT	10	0.1	0.3	
	30	2.5*	_	
	1.5	0.005	0.003	
50 C	5	5.5*	5.9°	
	10	4.9°	8.4*	
DT	1.5	2.2*	8.3*	

* The solution became purple black and white precipitant occures.

in HCl solution

Table 4 and Fig.4 indicate that corrosion rate of Ti-3AR and Ti-12 in HCl solution at room, $60\,^\circ$ C, boile temperature. The temperature and concentration of HCl solution influence evidently on corrosion rate, which increases with temperature and concentration. They both have smaller corrosion rate in 10% HCl at room temperature, however, it is 5.5mm/y in 10% HCl solution at $60\,^\circ$ C (Table 4) and white precipitate TiCl, produces, the solution become purple black. If the concentration is reduced, the corrosion rate is smaller at higher temperature, too, e.g. corrosion rate is equal to $0.04\,\mathrm{mm}$ /y in 1.5HCl solution at boile temperature.

temperature U	concentration	corresion rates (mm/y)		
	%	Ti-3AR	Ti-12	
	5	0.001	0.001	
RT	10	0.1	0.1	
	15	1.5	1.0	
	1.5	0.001	0.001	
60 C	5	0.2	0.5	
	10	5.5*	7.4*	
BT	1.5	0.04	0.07	

Table 4 general corrosion rate in HCl

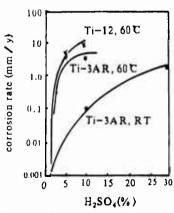


Fig.3 relationship between corrosion rate and the concentration

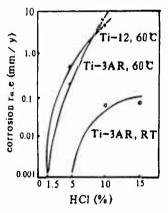


Fig.4 corrosion rate in HCl solution

^{*} The solution became purple black and white precipitant occures.

Electrochemical character

The corrosion potential and polarization curves of Ti-3AR were measured in 5% HCl and 10% H₂SO₄solution at room temperature, which are shown in Fig.5.

The anodic polarization shows active dissolution, passivation and corrosion potential. From the polarization curve the critical current density for passivation ic and passive current density ip were obtained, in 5% HCl solution, ic $\approx 10\mu A/cm^2$, ip $\approx 10\mu A/cm^2$, Ecorr ≈ -0.02 VSCE, in 10% H₂SO₄ solution, ic $\approx 50\mu A/cm^2$, ip $\approx 13\mu A/cm^2$, Ecorr ≈ -0.55 VSCE.

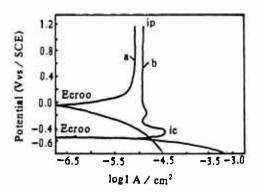


Fig.5 polarization curve of Ti-3AR

a in 5% HCl,

b in 10% H,SO.

Conclusions

- 1. Ti-3AR is a new corrosion resistant titanium alloy with higher strength, placticity, workability and excellent corrosion resistant, $\sigma_b > 720 \text{MPa}$, $\sigma_b^{330 \text{C}} > 480 \text{MPa}$, $\delta_5 > 18\%$, $a_K > 1000 \text{KJ/mm}^2$.
- 2. Ti-3AR possesses excellent corrosion resistant in 5% $\rm H_2SO_4$, 10% HCl at room temperature, in 1.5% $\rm H_2SO_4$, 5% HCl at 60°C, in 1.5% HCl at boile temperature and 20 \sim 50% HNO₃ at room \sim boile temperature.

References

- 1. ASTM G1-72, 10,1979
- 2. Xin Xiangje, The corrosion, protection and application of titanium, 1988

The optimisation of descaling oxied skin of Ti-2.5Cu alloy

Cai Xuezhang, Zhang yuqin, Li pingquan, Zheng heihan

Northwest Institute for nonferrous metal Research

P.O Box 71

Bao a Shanxi 721014

P.R China

Abstract

Ti-2.5Cu alloy easily picks up hydrogen in the descaling bath of molten alkaline mixture of Sodium hydroxied and Nitrate. In order to optimize the condition under which the amount of hydrogen pick up of the alloy will be minimum, temperature and composition of the bath as well as time of descaling was varied and the effect of these parameters on the amount of hydrogen pickup, metal loss and surface quality has been modeled and the optimization of descaling conditions has been made. Depending on practice of production and requirement of surface quality of products, the modifying descaling condition can be easy optimized.

Introduction

The oxide skin of Ti-alloy formed at above 600°C is hardly removed by pickling method[1], generally it is removed by molten alkali bath. Due to hydrogen absorption of Ti and Ti-alloy in the alkaline bath, usually oxygenant is added into the bath. For example, NaNO₁ is added into the molten-NaOH bath, to prevent hydrogen pickup, increasing flowability of the molten alkali and decreasing the dangerous degree of fire. This type of the alkaline bath is designate as an oxidizing bath, is now popularly used in the practical production of Ti and Ti-alloy products, and it usually includes three kinds of high temperature (454-537°C), intermediate temperature (371-454°C) and low temperature (190-218°C) types [2], the first one is mainly used for removing oxide skin of products produced by hot working and heat treatment, the second one is used for removing oxide skin and a solided layer of lubricating glass, and the third one is used for removing oxide skin of the Ti-alloy having age hardening reaction[2], also, the reductive or the electrolytic type of bath is favourable to remove the layer of lubricative graphite or grease, and oxide skin etc.

The present work is aimed at the hydrogen absorption of the hot rolled and annealed Ti-2.5Cu alloy sheet during descaling oxide skin in the alkaline bath, the investigation on the amount of added NaNO, temperature, corrosion rate etc has been conducted. The relationship between the hydrogen pickup and its influencing factors have been investigated and the mathematic mode related to descaling parameters of the sheet in the

molten NaOH bath have been established.

Experiment

The 0.7mm and 1.2mm thickness sheets of Ti-2.5Cu alloy used in the work are annealed at 790°C / 30 A.C. The alloy chemical composition is listed in Table 1.

Titanium '92 Science and Technology Edited by F.H. Froes and I. Capton The Minerals, Metals & Materials Society, 1993

Table 1 The Ti-2.5Cu alloy composition

Element (wt%)		Fe 0 118	Si 0.014	C 0.012	N 0.02		H 0.002
(W1%)	2.38	0.118	0.014	0.012	0.02	0.12	0.002

The NaNO₃ oxygenant, its amount varies within 5-25 Wt%, is added into the molten NaOH bath with temperature varying range of 425-520°C, and descaling time varies from 2 to 25 minutes. The specimens descaled under the conditions above mentioned are pickled for 3-5 minutes in a 5%HF, 25%-35% HNO₃ and 60-70% H₂O(in volume).

The hydrogen absorption and the weight loss of the sheets is determined, and the descaled and pickled sheet surface is observed at low magnification of optical microscope.

Results

The effect of NaNO₃ content

The hydrogen content and the weight loss of sheet descaled at 460°C / 10 minutus (A) and 490°C / 5 minutes (B) in the bath containing various NaNO3 content is listed in Table 2.

Table 2 The hydrogen content (0.7mm thickness) and the weight loss (1.2mm thickness) of the descaled sheet

NaNO ₃ content in the bath (wt%)	in the	n content e sheet t%)	weight loss of the sheet (g / cm ²)		
	A	В	A	В	
5	0.042	> 0.039		0.0155	
10	0.019	0.0268	0.0093	0.00871	
15	0.0062	0.0054	0.0074	0.0064	
20	0.0067	0.0062	0.0051	0.00593	
25	0.0071	0.0067	0.0067	0.00567	

As data in table 2, the hydrogen content and the weight loss both increased with decreasing NaNo₃ content. when the NaNO₃ content is below 10wt%, the hydrogen absorption increased drastically, gets above 170ppm under A and 248ppm under B; and the weight loss also increases drastically, gets above 0.0087g/cm²or over under A or B. While the NaNO₃ content go to and over 15wt%, the hydrogen content and the weight loss obviously dropped to the level corresponding with that(hydrogen content must be less than 100ppm) stipulated as the related standard. In view of the surface state of the descaled and pickled sheet, the best condition is also that under 15wt% NaNO₃.

Temperature effect

Fig 1 shows that hydrogen content and weight loss of 1.2mm thickness sheet (a), (b). and hydrogen content of 0.7mm thickness sheet (c).

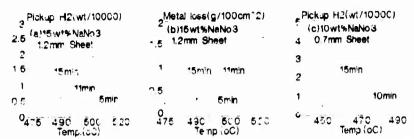


Fig1 Temperature effect on hydrogen absorption and weight loss of the descaled and pickled sheets.

As for 1.2mm thickness sheet, under the condition of descaling time of 5-15 minutes and 15wt% NaNO₃ in the bath, the descaling temperature must be limited below 490°C for 15 minutes and below, Fig 1 (a), so that to prevent that the hydrogen content in the sheets exceeds the stipulated value (less than 100 ppm). As to 0.7mm thickness sheets, under 10wt% NaNO₃, the descaling temperature must be limited below 470°C for 10 minutes and below, Fig 1 (c). As to the weight loss of 1.2mm thickness sheet, the descaling temperature also must be limited below 475°C to keep a lower level of the metal loss, Fig 1 (b). Considering the descalling effect and surface state of the descaled and pickled sheets, and controlling hydrogen content below 100 ppm, the descaling temperature and time is selected as high and long respectively as possible.

The effect of descaling time

As to 0.7mm thickness sheet, under the conditions of 430°C, 460°C and 490°C, and 10wt%, 15wt% and 20wt% NaNO₃ respectively in the bath, the time effect on the hydrogen content of the sheets after descaling and pickling shown in Fig 2. With regard to the hydrogen absorption, when the NaNO₃ content is over 15wt%, the descaling time can be lasted to 20 minutes and over for 430°C, 15 minutes for 460°C, and below 5 minutes for 490°C, and then the hydrogen content in the sheets maintained below 100ppm, see Fig 2(b),(c). But under 10wt% NaNO₃, the descaling time must be dropped below 15 minutes for 430°C, 12 minutes for 460and 2 minutes for 490°C, see Fig 2(a).

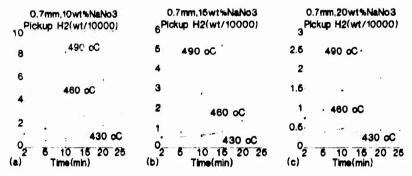


Fig 2 The descaling time effect on the hydrogen absorption of the 0.7mm thickness sheet.

In view of the descaling effect and surface state, as to 1.2mm thickness sheets, it is expected for descaling at a higher temperature and shorter time, for example, 490°C and 2 minutes, but it is difficult to realize such conditions for bigger batch of sheets to be descaled. So the better way is to use less low temperature and less long time, e.g 475°C

and 15 minutes. As for 0.7mm thickness sheet, the proper time of descaling(10-15 minutes under 460°C and 10-15 wt% NaNO₃) should be selected as the same reason as for 1.2mm thickness sheet.

The effect of sheet thickness

Just as above discussed, the different temperatures and times are required for descaling of different thickness sheets, i, e, 0.7mm and 1.2mm as shown in Fig 3(a) (b). Under 490°C, the hydrogen content of 0.7mm thickness sheets is consistantly higher than that of 1.2mm thickness sheets by 20ppm, and the difference of the hydrogen content increases with lasting of the descaling time, espeially under 10wt% NaNO₃, Fig3(b). Under 460°C, the hydrogen content of 0.7mm and 1.2mm thickness sheets is near the same until the time lasting to 15 mimutes, and then the difference between them increased drastically, see Fig 3(a). While under 10wt% NaNO₃, the difference of the hydrogen content between them appears early at the descaling time about 5 minutes, see Fig 3 (b).

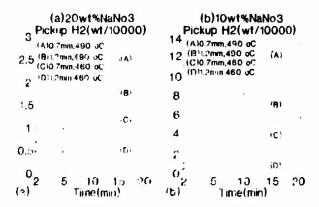


Fig3 The hydrogen content of the descaled sheet with different thickness

Discussing and mathematically modelling

On the oxidation of Ti and Ti-alloys at the elevated temperature, the surface layer is TiO₂, subsurface layer is TiO, the ratio of their value is 1.7[3], resulting in a large stress between the surface and subsurface layers, and thus leading to turn the surface layer of TiO₂ into a porrous and loose state. As descaling in the bath with high temperature, the oxide skin of the surface layer is further broken due to the difference of thormo expansion between oxidizing layer and matrix, and it is easy for permeating of the molten alkali into the oxide skin TiO of the subsurface layer, which is further oxidized into TiO₂ by the oxygen released from oxidizer as NaNO₃, and thus entire oxide skin is broken. Except for this mechanical references reaction of TiO₂with the molten alkali [4] takes place:

Na₂TiO₃produced during the reaction() sediament or removing from the surface by water quenching and picking the fact that, the matrix is bared in the bath, the chemical reaction of matrix with the molten alkali appears:

2NaOH + Ti >NaTiO₂+ H₂ ↑ (2) Because of the affinity of Titanium with hydrogen, it is easy to form hydrogenized Ti[5]. Besides, the solubility of hydrogen in a-Ti depends upon the partial pressure of hydrogen, temperature and the added element and inclusion content in the alloy expresses as following:

 $P = KC^{2} exp\left(\frac{Q}{nT}\right) \tag{3}$

In which, C—hydrogen solubility, Q—solution heat, K—constant related alloy composition, P—partial pressure of hydrogen, R—gas constant, and T—temperature.Q and k value doesn't vary as hydrogen concentration and temperature, and it varies as crystal structure and phase composition of the alloy. The solubility of hydrogen in α-Ti within 20°C—300°C obeyed following the relation[6]:

$$C = 8.60 \times 10^4 \text{e x p}(-2.52 \times 10^3 / \text{T})$$
 (4)

In which. C—hydrogen concentration (ppm), T—temperature (k). From that, the hydrogen solubility is about 20ppm in room temperature, and over 1000ppm at 300°C. For this reason, once the hydrogen has been produced in the bath, as formula(2), and will be absorbed by the matrix of Ti and Ti-alloys. The hydrogen, which is absorbed by α -Ti matrix under the bath with temperature more than 400°C, is precipitated in form of the hydrogenated Ti when the temperature of α -Ti alloy dropped down to room temperature. The hydrogenated Ti is precipitated in aciculate shape, that resulting in brittle break, in 1.2mm thickness sheet of Ti-2.5Cu alloy contained 280ppm hydrogen, which is absorbed under the descaling condition of the bath with 15 wt% NaNO₃ and at 500°C, therefore, in order to prevent from hydrogen absorption of the sheets descaling in the bath, first, the NaNO₃ oxidizer should be added into the bath, and the reaction takes place as following:

$$2NaOH + Ti + O_2 > Na_2TiO_1 + H_2O$$
 (5)

Second, the temperature and time should properly be choiced, so that preventing the reaction as formula(2), as far as possible, because it is difficult to stop completely the reaction(2) under the condition of practical descaling at large quantities due to non-uniformity of oxide skin of the sheet and temperature distribution in the bath, and thus it isn't able to ensure chemical reaction of descaling at the same pace. That means it is sure for producing hydrogen at more or less amount as formula(2). So it is effective method for adding NaNO₃ into the bath to prevent the sheets from hydrogen pickup. In order to further understanding the relationship between hydrogen absorption and descaling parameters and make them optimizing, the mathematical model, which described the influencing regularity of temperature, time and NaNO₃ content on hydrogen absorption of 0.7mm thickness sheets descaled in the bath, has been established on basis of experiment data treated by computer. Considering descaling efficiency in practical production, the range of NaNO₃ content, temperature and time is 10-20wt%, 430-490°C and 2-25 minutes respectively. Considering the effect of NaNO₃ content on the hydrogen absorption, the mathematical model can be described as exponent function:

$$C_{H} = A_{1}e \times p(B_{1} / C_{N})$$
 (6)

In which, C_H —hydrogen content in the sheets(wt%), C_N —NaNO₃content in the bath(wt%), A₁and B₁——coefficien: related with descaling temperature and time, and material state. the corresponding values of A₁and B₁in the model formula (6) is listed in Table 3.

Table 3 The values of A₁ and B₁ in Model [6]

Temperature (°C')	Time (min)	$\begin{array}{c} A_1 \\ (\times 10^{-3}) \end{array}$	B
400		2 2102	1 4000
430	10	2.5183	1.4807
	15	1.4553	3.9052
	20	1.0386	5.4696
	265	0.7421	6.8456
460	5	3.6075	1.4487
	10	2.8942	1.8891
	15	1.7778	5.9072
	20	1.9202	6.3989
490	2	1.6379	3.7020
	5	2.6263	3.3890
	10	3.3414	5.4996
	15	6.1638	5.2621

Fig 4 shows that the curves ploted as the calculated results according to Model(6).

(a)430 oC 3 Pickup H2/wt/10000	(b)460 aC Pickup H2(wt/10000)	(c)490 oC Pickup H2(wt/10000)
2.6 (A/10nin. 2 (C) (B/15min. 1.6 (D)25min	6 (A15min. (B)10min. (C)15min. (C)15min. (D)20min.	(D) (A)2min. (B)6min. 8 (C)10min (D)15min
(B) (A) (b) (1	2 1 (B) 0 (A) 21 9 11 13 15 17 19 21 (b) NaNo3(wf%)	4 2 (B) 0 (A) 9 (1 13 16 17 19 21 (J) NeNo3(w(S)

Fig 4 Effect of NaNO, content as model (6)

Considering the effect of descaling time, the mathematical model have been obtained by means of linear regression as following

As for the bath with 430°C:
$$C_H = A_2 t^{B_2}$$
 (7-1)
As for descaling in the bath with 460°C or 490°C:

 $C_H = A_2 \exp(B_2 t)$ (7-2) t— descaling time, A_2 , B_2 —coefficient relating with temperature and NaNO₃ content of the bath and materials. The former (7-1) is a power function and the latter (7-2) is an exponent function. The values of A_2 , B_2 are listed in Table 4. Table 4 The value of A₂, B₃ in model (7-1) and (7-2)

Temperature (じ)	NaNO, content (wt%)	$\begin{array}{c} A_2 \\ (\times 10^{-3}) \end{array}$	B ₂
430	10	0.09532	1.762886
	15	1.02707	0.65812
	20	1.87021	0.27595
460	10	2.19366	0.16238
	15	3.34387	0.06998
	20	2.53338	0.06713
490	10	7.89623	0.17789
	15	3.38501	0.19102
	20	3.39954	0.13562

Fig 5 shows the curve of Model(7-1), (7-2). It can be seen that under $NaNO_3$ content over .5wt% and 430°C temperature, the curves are near straight line, so the model(7-1) is a power function with a small exponent (B_2) .

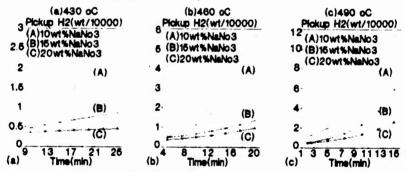


Fig.5 Efffect of time as model (7)

Under higher temperature, the hydrogen absorption rate is more sensitive to descaling time, because of reaction rate between oxide skin and molten alkali is also speeded up. So the model(7-2) is an exponent function. Finally, the model of the effect of temperature on the Hydrogen absorption is expressed as Hyperbola function:

$$\frac{1}{C_N - K} = A_3 + B_3(\frac{1}{T}) \tag{8}$$

In which, K—criginal Hydrogen content in the sheets before descaling (about 0.002ppm), T-batic temperature (C). A₃, B₃-coefficient relating with NaNO₃ content and time of bath descaling and material. A₃ and B₃ values are listed in Table 5.

Table 5 A. B. values in Model (8) A, NaNO. time В, (wt%) (mixutes) 10 10 -1946.40959637.0 15 -680.57338090.8 15 10 -3446.421614054.0 15 -2217.481098474.0 2645046.0 20 10 -5317.1015 -3209.841597990.0 The curves shown in Fig 6 exhibit clear the variation of hydrogen content with descaling temperature.

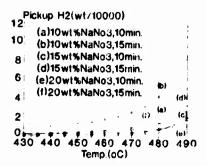


Fig 6 The effect of temperature on hydrogen absorption as model (8)

Comparing these mathematic models obtained in the present work, i.e model formula (6), (7-1), (7-2) and (8) with (3) and (4) being in work (5,6), rather defferent functions between them can be seen. In fact, the hydrogen concentration (C_H) in the functions [5] and [6] is the saturated solutility, but the hydrogen in model functions of the present work is nonsaturated. These models described the beginning situation of hydrogen absorption under the jointed effect of various factors in descaling bath.

Conclusion

(1) The descaling oxide skin formed during annealing of Ti-2.5Cu alloy sheet in the molten alkaline bath, the hydrogen absorption is mainly influenced by adding NaNO₃ content, temperature and time.

(2) According to criterion of hydrogen content allowed in the sheet, metal loss, sheet surface appearency and descaling efficiency, the proper range of descaling parameters, i.e. NaNO₃ content of 10-20wt% in the bath, temperature of 430-490°C and time of 5-20 minutes of descaling, can be selected.

(3) The established model function between the hydrogen absorption and descaling parameters can be used for optimization of descaling technology in the bath.

Reference

- (1) Lester F.Spencel, "Descaling Tianium and Titanium Alloys", Metal Finishing, 66(8), 1968, P52
- (2) Nathanlel Hall, ed., Metal Finishing Guidebook & Directory (Metals and Plastic pub. INC, Hackcusack, USA, 1978), P151
- (3) Tr. Sovesh Po Metallokhim Metalloved. i Primenene Titana i ego Splovov ,(in Russian) 16, 1965, P143
- (4) E.I.Vydro et al, "Ob Okislitei'nykh Shchelochnykh Rasplavakh dlya Udaleniya Okaliny s Titana", Zash. Met. (in Russian) 14(2), 1978
- (5) V.N. Eremenko, <u>Titan i ego Splavov</u> (in Russian) (Akademii. Nauk Ukranskoi CCR 1955), P79
- (6) Ronold S.Vitt, Kanji Ono, "Hgdrogen Solubility in Alpha Titanium", Met. Trans 12A(2), 1971, P608
- (7) P.F.A.BilMer, "Pickling Titanium in Hgdroflnoric-Nitric Acid", Metal Finishing, 68(11), 1970, P64

Corrosion Behavior of Ti-Ni-(Pd, Ru)-Cr Alloys in Hydrochloric Acid

Keiji Ueda , Yasuaki Sugizaki and Hiroshi Satoh

Material Research Laboratory KOBE STEEL, LTD.

Takatsukadai, Nishiku Kobe, 651-22 JAPAN

ABSTRACT

General and crevice corrosion behavior of titanium alloys(Ti-Ni-(Pd.Ru)-Cr and Ti-Cr) have been examined in comparision with unalloyed titanium. Specimens, prepared by unconsumable arc melting in an argon atomsphere, were subjected to conventional corrosion tests in boiling hydrochloric acids and chloride solutions. Electrochemical properties of the alloys were also measured in order to understand the influence of chromium addition on the corrosion behaviors. The results indicated that chromium additions to titanium and Ti-Ni-Pd-Ru alloy affected the corrosion behaviors. Excellent improvement in general and crevice corrosion resistance was achieved by addition of chromium with Ni, Pd and Ru.

However, single addition of chromium significantly deteriorated corrosion resistance in hydrochloric acids. The corrosion kinetics for these alloys were discussed in term of the compositional change during corrosion process. An excellent corrosion resistance of Ti-Ni-Pd-Ru-Cr alloy was considered to be originated by accelerated dissolution of titanium at initial stage of corrosion, which resulted in enrichment of Pd and Ru in the corroded surface region.

Introduction

Titanium exhibits supreme corrosion behavior in the most environments due to the presence of the stable passive film on the surface. For this reason it is widely utilized in chemical industry as construction materials. (1) However, in aggressive reducing environments or concentrated chloride solution, titanium is susceptible to sever general corrosion and crevice corrosion. (2) (3) A number of investigations have been made on effect of some alloying elements to improve the corrosion resistance of titanium in such environments. According to the result reported by Stern (4) (8), improvement in corrosion resistance of titanium was successfully achieved by small additions of noble metals such as Pt and Pd, which promote its passivation in reducing environments(hyrochloric acids). The resistance to crevice corrosion was noticeably improved by addition of these elements. It has also demonstrated that alloying with Ni and Mo improves corrosion resistance in acidic chloride media. (7) (8) Utilization of these titanium based alloys in the practical fields are limited by cost or mechanical properties and fablicability. (8) (18) Recently, the needs of titanium alloys, which is low-costed and has excellent fablicability have arose in chemical industrial fields. We already observed, reduction of the corrosion rate of titanium by small addition of Ni, Pd, Ru in boiling HCl solutions. (11) Furtermore, corrosion resistance was improved by addition chromium to this alloy, is particularly interesting. Because, single addition of chromium to titanium has deteriorated corrosion registance exists among the single addition of chromium and composite addition of chromium to Ti-(Ni-Pd-Ru) alloy.

> Titanium '92 Science and Technology Edited by F.H. Froes and I. Caplan The Minerals, Metals & Materials Society, 1993

Experimental procedures

1. Preparation of specimens

Titanium alloy buttons weighting 100g were prepared by nonconsumable arc melting in an argon atmosphere. Each button was turned over and remeited six times to produce homogeneity. The alloys were further homogenized at 850°C and cold rolled to 2mm thick sheet. Their chemical compositions are given in Table 1.

Table I Chemical compositions of titanium alloys (wt%)

		-				
alloys	Ni	Pd	Ru	Cr	0	Fe
Ti-Ni-Pd-Ru	0.41	0.01	0. 02	_	0.06	0. 03
Ti-Ni-Pd-Ru-Cr	0.41	0.01	0.02	0.14	0.06	0.03
Ti-Cr	_	_	_	0.16	0.06	0.03
c. p. Ti (ASTM Gr. 2)	_	-	_	_	0.06	0.05
Ti-Pd (ASTM Gr. 7)	_	0.16	_	_	0.06	0.03

N. H : <0.01wt%

2. Immersion test for Corrosion

In order to examine the corrosion resistance of the alloys to general and crevice corrosion in hydrochrolic acids and chloride solutions, conventional methods have been employed. The specimes for the immersion tests were abraded by wet silicon carbide emery before the immersion. Each specimens were taken out from the glass flask after 24 hours immersion. The average corrosion rate was determined from the corrosion weight loss. The multi-crevice technique was employed to examine the corrosion resistance of the alloys to crevice corrosion. The specimens for multi-crevice corrosion test were seted up by bolting a PTFE(Teflon) spacer, having 16 grooves on the containing face, to the titanium sheet by using titanium fastenners. The cervice corrosion tests were performed in a boiling 42% MgCl₂(142°C) solution. The specimens were taken out of the solution after immersion for 100 hours, and the occurrence of crevice corrosion was checked by surface observation using a microscope.

4. Electrochemical measurement

In order to understand the influence of alloying additions with chromium, electrochemical behaviors of the alloys were examined by measurement of potentiodynamic polarization curves. The electrochemical cell was consist of 1 liter flask with inlets for the working and counter electrode of a plutinum sheet. All the potentials were measured with respect to a Ag/AgCl reference electrode. Electrochemical measurements were performed by the following methods. The corrosion potential and potentiodynamic polarization curves of each alloys were measured in a boiling 10% HCl solution. The potential scanning with a sweep rate of 50mV/min were started from the corrosion potentials after keeping for ten minutes under open-circuit condision. For comparisoin between the alloys in ease for passivation, the corrosion potentials were measured in boiling 10%HCl solutions with various contents of oxidizing agency Fe^{3*}. Durability reached to break down of passivity for each alloys was obtained by monitoring the decay of the potentials after polarizated at +0.2V for 2 minuits.

Following experiments were carried out to obtain further information on the corrosion behavior by the following; corrosion potential (Ecor.)-time variations and compositional change of addition elements resulting from corroson.

Result and Discussion

1. Immersion test

The corrosion rates of alloys in boiling HCl solutions are shown in Fig. 1. The measured corrosion rates of all the alloys increased with HCl concentration. The corrosion rate of Ti-Cr alloy was larger than pure titanium. Single addition of chromium has deteriorated corrosion resistance of titanium in HCl solutions. On the other hand, The addition of Ni, Pd, Ru reduces the corrosion rate of titanium by almost two orders of magunitude, further improvement in corrosion resistance was achieved by addition of chromium of with Ni, Pd, Ru.

The probabilities for occurrence of crevice corrosion are shown in Table 2. For pure titanium, crevice corrosion occured with the probability of 100 %, while additin of Ni, Pd, Ru to titanium considerably suppessed crevice corrosion. No crevice corrosion occurrence was observed on the alloys added with chromium and Ni, Pd, Ru. Significant difference in corrosion resistance exists among the single addition chromium and composite addition of chromium to Ti-Ni-Pd-Ru alloy. Electrochemical measurements and surface characterization were carried out to obtained the detailed account of the influence of chromium addition.

2. Polarizaition curves

Fig. 2 presents the potentiodynamic polarization curves obtained with the alloys in a boiling 10%HCl solution. The corrosion potential of each alloys are more noble than that of pure titanium. In Ti-Cr alloy, the critical current density for passivation was higher than that of pure titanim. This was in agreement with the results of immersion test in such environment. It was considered that chromium addition caused to shift sightly the corrosion potential of titanium in the noble direction, resulted in increase of exchange current at the corrosion potential. On the contrary, chromium addition with Ni, Pd and Ru was found to more effective in passivity. In this alloy, no active-passive transition region was observed and the corrosion potential was more noble than that of the alloy added with Ni, Pd and Ru, which promoted passivation of titanium.

3. Passivation Fe³⁺ ion concentration

Fig. 3 shows the depedence of the corrosion potentials on the concentration of oxidizing agency Fe³⁺ in a boiling 10%HCl solution. Each alloys has steep increase of the corrosion potential at certain Fe3+ concentration, which exhibited ease to passivation in such environment. Pure titanium exhibited potential in up to active dissolution Fe3+ ion cocentration of 10ppm, and then the corrosion potential shifted abruptly to the passivation region at 30ppm, and steadies at approximately +0.08V indicating the passivation. This suggested that the critical Fe3+ ion concentration for passivation of c.p. Ti is 22ppm. The critical concentrations for Ti-Cr, Ti-Ni-Pd-Ru and Ti-Ni-Pd-Ru-Cr were 24, 6.2 and 2.7ppm, respectively. Chromium addition to pure titanium or Ti-Ni-Pd-Ru alloy shifted the corrosion potential in the noble direction, leading to alternative influences in the different based alloys. Chromium addition

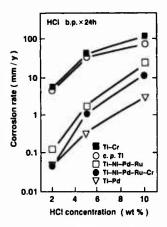


Fig.1 Influence of HCl concentration on corrosion rate of titanium alloys

Table I Probability of crevice corrosion occurrence of titanium alloys

alloys	Probability of crevice corrosion occurrence (%)
TI-NI-Pd-Ru	18.9
TI-NI-Pd-Ru-Cr	0
Ti-Cr	62.4
c.p.Ti (ASTM G2)	100
Ti-Pd (ASTM G7)	0

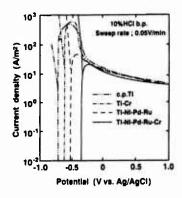


Fig. 2 Polarization curves of titanium alloys

caused enhancement of active dissolution through the increasing of exchange current. However, enhanced passivation was taken place by chromium addition with Ni,Pd and Ru, and the corrosion potential was resided in the passivation of titanium.

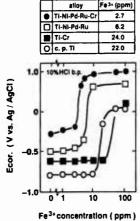


Fig.3 Effect of Fe³⁺ content of corrosion potential of titanium alloys

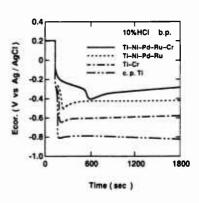


Fig.4 Potential decay curves of titanium alloys

4. Measurments of durabilities to depassivation

The potential decay curves for the alloys are shown in Fig. 4. These curves were obtained under open-circuit condition after holding the potential at +0.2V for 2 minutes. The corrosion potentials were decreased toward the less-noble potentials with immersion time. In pure titanium, the potential was immediately shifted to less-noble after the polarizating and reached to the saturation at -0.83V. The decay curve of Ti-Cr alloy was similar to that of pure titanium, but the potential was saturated at -0.56V. On the other hand, alloys added with Ni, Pd, Ru and with Ni, Pd, Ru, Cr were found to the potentials for in passivation after sufficient immersion. It was noted that the potentials were gradually shifted to the active dissolution region and reversibly increased to reside in the passive region, the result from these measurements, indicated that the improvement of corrosion resistance of titanium introduced by chromium addition with Ni, Pd and Ru through the enhancement of passivity.

5. Corrosion potential (Ecor.) - time variations

The corrosion potentials of the alloys at various immersion time in a boiling 10%HCl solution are shown in Fig. 5. The corrosion potential of pure titanium showed a noble potential of about -0.36 V at an early stage of immersion, but the potential shifted abruptly to the less noble side after about 2.5min, and steadled at -0.76 V. The corrosion potential of Ti-Ni-Pd-Ru allow was noble in early stage of immersion. and then, became less-noble with a prolonged immersion, and showed noble again after immersion of 20 minutes. The similar behavior was obtained in Ti-Ni-Pd-Ru-Cr alloy. Ti-Ni-Pd-Ru-Cr alloy remained active for early stage to become passive. This behavior

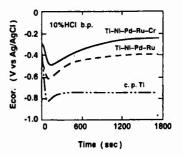
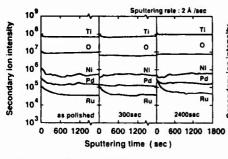


Fig.5 Corrosion potential change of titanium alloys with immersion time

was interpreted by enrichment of alloying elements during initial immersion stage.

However, reversibly changing the potential in Ti-Ni-Pd-Ru-Cr alloy was occurred in

However, reversibly changing the potential in Ti-Ni-Pd-Ru-Cr alloy was occurred in the earlier initial stage than that of Ti-Ni-Pd-Ru alloy and the saturated potential was more



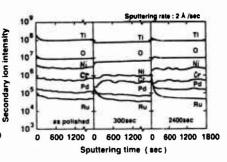


Fig. 6 depth profile of Ti-Ni-Pd-Ru alloys immersed in boiling 10%HCl

Fig.7 depth profile of Ti-Ni-Pd-Ru-Cr alloys immersed in boiling 10%HCl

noble than Ti-Cr alloy. This result was comparable with the potential decay behavior, as can be seen in Fig. 4. Consequently, the chemical composition of surface on titanium was changed with immersion time in a boiling HCl solution.

6. Chemical composition of corroded surfaces

The compositional depth profiles of alloy elements were determined by using secondary ion micro spectroscopy (SIMS) technique with sequential argon sputtering. Figure 6 shows the profiles for Ti-Ni-Pd-Ru alloy obtained after immersion with various time. Figure 7 is for Ti-Ni-Pd-Ru-Cr alloy. Concetration of Pd and Ru in the surface region increased in both alloys with immersion time. However, Pd and Ru enrichment in the surface region was more accelerated by chromium addition to Ti-Ni-Pd-Ru alloy. The difference between both alloys in enrichment of Pd and Ru, became clear at a prolonged immersion time. This result suggested enrichment of Pd and Ru on surface of titanium accelerated by the preferential dissolution of titanium by addition of Cr on Ti-Ni-Pd-Ru alloy.

Conclusion

An effect of Chromium addition to Ti-(Ni-Pd-Ru) alloy on the behavior has been investigated by conventional immesion tests and characterization of electrochemical properties. The obtained results are summarized as follows:

- (1) The corrosion resistance of titanium is deteriorated by single addition of chromium in boiling HCl solutions. However the addition of Ni, Pd, Ru reduces the general corrosion rate of titanium, further improvement was achived by addition chromium with Ni, Pd and Ru.
- (2) Passivity was enhanced by addition chromium to Ti-(Ni-Pd-Ru) alloy. Furthermore, formed passive film was greatly toughened in reducing acids.
- (3) The corrosion kinetic of Ti-(Ni-Pd-Ru)-Cr alloy was concluded that the enrichment of Pd and Ru on the surface was enhanced by acceleration of the preferential dissolution of titanium by addition of chromium

References

- 1) R.W. Schultz and L.C. Convington, "Effect of Oxide Films on the Corrosion Resistance of
- Titanium, NACE, 37, 10, (1981), 585-591
 II. Satoh et al., "Effect of Gasket Materials on Corrosion of Titanium", Titanium Science 2) II. Satoh et al., Technology, edited by G. Lutjering, U. Zwicker, W. Bunk, 4, (1984), 2633-2639
- 3) P. Mckey and B. Mitton, Corrosion, 41, 1, 52, (1985)
- 4) M. Stern and H. Wissenberg, "The Influence of Noble Metal Alloy Additions on the Electrochemical And Corrosion Behavior of Titanium", J. Electrochemical Society, 106, (1959), 755-764
- 5) M. Stern and C. R. Bishop, "The Corrosion Behavior of Titanium-Palladium Alloy" Trans ASM, 52. (1960), 239-256
- 6) J.C. Gries, Jr., Corrosion, 24, (1968), 96
- 7) L. C. Convington and H. R. Palmer, Technical Report of TIMET (1974)
- 8) R.S.Glass, Effect of Intermetallic TiaNi on The Electrochemistry of TICODE-12 in Hydrochroric Acid", Elerochmica Acta. 28, (1983), 1507-1513
- 9) K. Taki, "An Excellent Corrosion Resistance Titanium Alloy-TICOREX", Titanium Zirconium JAPAN, 36, 1, (1988), 29-33
- 10) S. Kitayama, Y. Shida, "The effect of Addition of Alloying Elements on the Crevice Corrosion Resistance of Titanium in Not Salt Solutions", Journal of The Iron and Steel Institute of JAPAN, 77, 9, (1991), 1495-1502
- 11) K. Ueda et al., "Corrosion resistance of titanium alloy contaning chromium (Ti-Ni-Pd-Cr) Current Advances in Materials and Processes, Report of the ISIJ Meeting, 4, (1991), 1741.

Thin N₂/H₂O Ion Beam Treated Titanium Layers as Diffusion Barrier for Hydrogen

B.Kempf

Deutsche Bundespost TELEKOM, Forschungsinstitut beim FTZ Am Kavalleriesand 3, D-6100, Darmstadt, Germany

A new method to passivate titanium against indiffusion of hydrogen is demonstrated. Nitrogen ion beaming of Ti in presence of a low H₂O background pressure leads to formation of a titaniumoxinitride layer, which works as a diffusion barrier. Diffusion is studied by the method of layer lift off provoked by generation of strain at an Ti-InP interface.

1. Introduction

TiN is well-known in surface science and engineering for its great hardness and chemical stability. In addition it is applied as a diffusion barrier in semiconductor contact - and interconnection technology where it helps to avoid unwanted intermetallic mixing (1, 2). Once et al. (3) have shown recently that thin TiN films deposited by an activated reactive evaporation (ARE) process can supress hydrogen outdiffusion in stainless steel, a procedure with important consequences for future ultra high vacuum technology.

Usually thin TiN layers are deposited either by reactive sputtering or by reactive evaporation in a low pressure nitrogen atmosphere. However, the application of both methods to semiconductor technology is limited. In the former case the all angle impingement of the sputtered material is not compatible with lift off processes for patterning contact pads and fine interconnection lines. In the latter case the high substrate temperature required for TiN formation may be detrimental to the electrical properties of semiconductor and contact. These insufficiencies are circumvented by the method introduced in the present paper:

It is demonstrated, that simple N₂⁺/H₂O ion beam treatment can passivate the surface of a thin Ti-layer to prevent indiffusion of hydrogen at least up to a temperature of

Science and Technology
Edited by F.H. Froes and I. Caplan
The Minerals, Metals & Materials Society, 1993

350°C. Such a thin surface layer consisting of non stoichiometric titaniumoxinitride was already shown to be responsible for the extremely low etch rate when ion beam etching titanium with a N_2^*/H_2O gas mixture (4). The condition for diffusion barrier formation and the mechanism which suppresses hydrogen indiffusion are discussed. The importance of nitrogen is elucidated by comparison with experiments of hydrogen indiffusion into Ar $^*/H_2O$ treated and naturally oxidized titanium layers.

2. Experimental procedures

Titanium layers with thicknesses in the range of 100 to 300 nm are evaporated by e-gun in a turbomolecular pumped stainless steel chamber. Before coating the wafer the base pressure of the system (p = $5 \cdot 10^{-7}$ torr) is further lowered by preevaporation of titanium against the chamber wall. Chemomechanically polished (100)-InP wafers are choosen as substrate material. InP fullfills the demand for an easily cleaveable smooth substrate, which shows no interfacial reaction with titanium up to a temperature of 350°C. Ion beaming of the titanium films is done in a second vacuum system of similar performance and base pressure. It is equipped with a Kaufmann-type ion gun (MIM TLA 5.5 II Technics GmbH, Europe). The etch gas (N2 or Ar) is admitted through the gun, while the H2O gas is fed directly into the etch chamber providing a non ionised background atmosphere. At working conditions the N_2 (Ar)-pressure amounts to 1.10^{-3} torr in the gun, to 4.10^{-5} torr in the chamber. The H₂O-gas flow is adjusted to reach a partial pressure of 1·10⁻⁵ torr. Throughout the experiments etching is done with an ion beam current density between 0.5 and 1 mA/cm² and an ion energy of 1000 eV. The samples to be etched are fixed with photoresist on a watercooled stage, wich is rotated by 2 rpm. The angle of ion beam incidence is fixed at 11.5°. 3 types of samples are tested for their behaviour against hydrogen indiffusion:

- 1) naturally oxidized titanium
- 2) titanium ion beam treated with Ar*/H2O
- 3) titanium ion beam treated with N2*/H2O

The process sequence consists of heating up the samples in a neutral hydrogen stream at a rate of $280^{\rm O}/{\rm min}$, holding the temperature at a level of $330^{\rm O}{\rm C}$ for times t_L up to 10 min and cooling down to room temperature at a rate of $140^{\rm O}/{\rm min}$. The temperature – time variation is accomplished by a programmable temperature controller. Simultaneously the surface state of the titanium layer is monitored via the intensity of the reflected light of a 633nm He-Ne laser (Fig.1).

3. Experimental results and discussion

As revealed by X-ray diffraction the evaporated titanium layers crystalize in the hexagonal α -phase with a strong texture having the base plane parallel to the InP (100) surface. SEM pictures of the films show a columnar structure, which is often also found in the case of TiN coatings. The coarse grain boundaries of such a structure, leading directely into the interior, are excellent fast diffusion paths and have to be stuffed for a good barrier function. This can be done by oxidation (5,6).

In the present work the problem is solved by ion beaming of titanium with N_2^\star/H_2O , a low temperature process which does not interfere with lift off technology. In this process nitridation of the sample is done simultaneously by ion beam implantation and absorption of nitrogen coming from the N_2 background atmosphere. Oxidation is performed via chemisorption of water on the sample's surface. Since the sample is thermally coupled to a watercooled stage the sticking-coefficients for water and nitrogen are high, especially in that part of the surface where titanium atoms are uncovered by physical sputtering of incoming nitrogen ions. As the heat of formation of TiN and TiO₂ is similar and negative, competition between N_2 and H_2O in forming a surface layer is expected. In a simplified picture build up of non stoichiometric titaniumoxinitride seams feasible. An enrichment of nitrogen and an easy formation of TiN within the penetration depth of the nitrogen ion beam are expected. This process is promoted by the fact that primary molecular N_2^\star -ions dissociate immediately at the surface into twice the number of highly reactive N atoms .

To show the combined role of N_2 and H_2O for the formation of a barrier some titanium layers have been ion beamed with Ar^{2}/H_2O instead of N_2^{2}/H_2O . In the case of Ar^{2}/H_2O treatment a dynamical balance is reached between preferential sputtering of oxygen and the reoxidation of titanium and it's partly reduced oxides (TiO, Ti₂O₃) by impinging water molecules.

To prove hydrogen indiffusion, a phase transition in the system Ti-H is exploited. Strain thereby generated at the Ti-InP interface leads to blisters at the sample's surface. According to the phase diagram (7, 8) Fig (2) titanium can, depending on it's temperature, disolve up to 8 at% hydrogen in it's hexagonal α -phase. During cooling down the sample from a point in the α -region the phase boundary is crossed into a two phase region ($\alpha + \gamma$) where the γ -phase is of a body centered cubic lattice type. Fig (3) shows a blistered titanium layer on InP after hydrogenation and cooling down. The sudd'n change of the titanium surface from mirrorlike reflection to diffuse scattering allows the exact determination of the transition temperature via reflection.

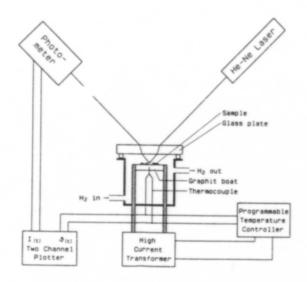


Figure 1 - Experimental set-up for the study of hydrogenation behaviour of titanium films on InP-substrates.

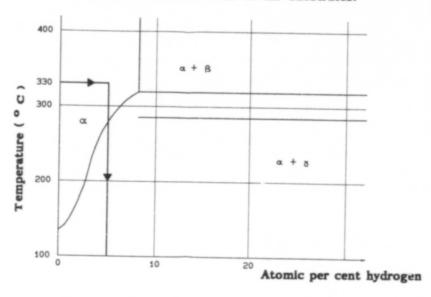


Figure 2 - Ti - H phase diagram (detail).

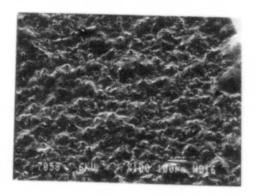


Figure 3 - Blistered titanium layer on InP substrat

Fig (4) shows transition temperatures for different holding times for the case of naturally oxidized and $Ar^{+}/H_{2}O$ ion etched samples. The holding temperature was fixed at 330° C. The increase of the transition temperature with increasing holding time is a consequence of the α /(α + γ)-phase boundary. The different behaviour of unetched and $Ar^{+}/H_{2}O$ etched samples is due to different velocity of hydrogen indiffusion. The presence of additional diffusion paths due to lattice vacancies in the latter case makes H_{2} indiffusion faster.

The behaviour of N_2^+/H_2O ion etched samples proved to be completely different. They don't blister across the surface when treated with neutral hydrogen. Obviously the generated surface layer acts as a diffusion barrier. This assumption is supported by the fact that samples cleaved after ion beam etching show blistering effects starting at freshly opened Ti side wall areas. Fig (5)

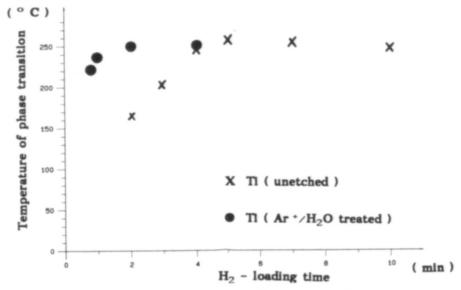


Figure 4 - Influence of hydrogen loading time on the phase transition of titanium.

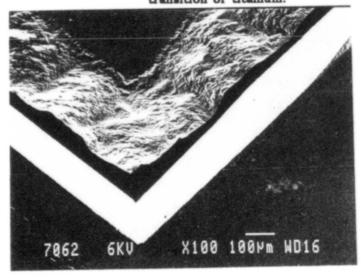


Figure 5 - N_2^+/H_2^-O ion etched sample after hydrogenation.

4. Conclusions

Ion beaming of titanium with N_2^+/H_2O creates a surface layer which prevents hydrogen indiffusion. The barrier function was tested at 330°C. The upper limit of 350°C for H_2 diffusion experiments is not governed by the thermal stability of the barrier layer but by the start of an intermetallic reaction at the Ti-InP interface, which strengthens adhesion and prevents blistering even in the case of Ar^+/H_2O treated samples.

References

- W.J.Garceau, P.R.Fournier, and G.K.Herb, "TiN as Diffusion Barrier in the Ti-Pt-Au Beam-Lead Metal System," Thin Solid Films, 60 (1979),237-247.
- C.Y.Ting, "TiN formed by Evaporation as a Diffusion Barrier between Al and Si,"
 J. Vac. Sci. Technol., 21 (1982),14-18.
- K.Onoe et al., "Outgasing Properties and Microstructures of Ti-N Films" J.Vac. Soc. Jpn., 34 (1991),420-426.
- 4 .B.Kempf et al., "N₂/H₂O: A New Mixture for Deep Groove Ion Beam Etching of Long Wavelength Quaternary Mushroom Typ Laser Structures,) (Paper presented at the SSDM 90, Sendai / Japan, August 22-24,1990)
- W.Sinke, G.P.A.Frijlink, and F.W.Saris, "Oxygen in Titaniumnitride Diffusion Barrier," Appl.Phys.Lett., 47 (1985),471-473.
- J.O.Olowolafe et al., "Effects of Oxygen in TiN_x on the Diffusion of Cu in Cu/TiN/Al and Cu/TiN_x /Si Structures," Appl.Phys.Lett., 58 (1991),469-471.
- 7. A.D.McQuillan, Proc.Roy.Soc., A204 (1950), 309.
- 8. G.A.Lenning, C.M.Craighead, and R.I.Jaffee, Trans.AIME 200 (1954) 367.

Ripple Load Degradation in Titanium Alloys

P.S. Pao, R.A. Bayles, S.J. Gill, D.A. Meyn and G.R. Yoder*

Naval Research Laboratory Washington, DC 20375-5000

Abstract

The influence of ripple loads (small amplitude cyclic loads superimposed on a large sustained load) on the stress-corrosion cracking (SCC) resistance of various titanium alloys has been investigated. It has been found that the extent of ripple load degradation in a 3.5% NaCl aqueous environment varies with the material's inherent resistance to SCC. For instance, the application of small ripple loads to SCC-resistant materials, such as beta-annealed Ti-6Al-4V and all beta alloy Ti-15V-3Cr-3Al-3Sn, causes a large degradation that is manifested by a significant reduction in time-to-failure and threshold stress intensity. However, ripple loads appear to cause relatively little or no damage to the less SCC-resistant materials such as recrystallization-annealed Ti-6Al-4V and duplex-annealed Ti-8Al-1Mo-1V. This apparent contrast between SCC and ripple-load cracking susceptibilities can be reconciled with the recently developed predictive framework for ripple-load degradation.

Introduction

Ripple loading refers to the superposition of relatively small amplitude cyclic load perturbations on a much larger static load. (Ripple loading usually assumes a stress ratio, R \geq 0.90.) This contrasts with the stress-corrosion cracking (SCC) phenomenon, which assumes a constant load condition. The presence of small amplitude load perturbations can have significant effects on the SCC resistance of materials and is described as the "ripple effect" by Speidel [1]. Recent work on steels, titanium alloys, and aluminum alloys has suggested that these ripple loads can significantly reduce the apparent SCC threshold and can shorten the life of a structure [2-5]. Parkins [6,7] has observed that small fluctuating loads may produce SCC at significantly lower stresses than those required to produce SCC under purely static loads. Komai et al. [8-10], in a series of investigations, have found that small vibratory stresses can considerably decrease the apparent SCC threshold and refer to this phenomenon as "dynamic" stress-corrosion cracking. Thus, a design solely based on the static KlSCC, without a proper consideration of the ripple-load effect, may be nonconservative.

Not all materials, however, are susceptible to ripple load degradation. Generally speaking, SCC-resistant alloys are more likely to exhibit ripple load degradation while the SCC-susceptible alloys are less likely. For instance, Crooker et al. [2] demonstrated, using a ripple load equal to 10 per cent of the maximum applied load, a 60 per cent degradation from the static K_{ISCC} level in the case of an HY-130 steel, yet absolutely no degradation in the case of a 4340 steel.

* Office of Naval Research, Arlington, VA 22217

Titanium '92 Science and Technology Edited by F.H. Froes and I. Caplan The Minerals, Metals & Materials Society, 1993 The purpose of this paper is to show that various titanium alloys, particularly the SCC-resistant alloys such as beta-annealed Ti-GAI-4V and beta Ti-15V-3Cr-3AI-3Sn, may exhibit substantial degradation due to the ripple-load effect (RLE), and to demonstrate that the sensitivity of a specific material to ripple-load degradation, or the lack thereof, is predictable. Critical conditions for ripple load cracking and a methodology for quantitative prediction can be obtained if the ripple-load effect is considered in terms of the interface between corrosion fatigue and stress-corrosion cracking. A new ripple load cracking threshold, K_{IRLC}, which marks the onset of ripple load crack growth, has been devised and is offered as a design parameter to represent the upper bound of the design limit.

Materials and Experimental Procedures

Titanium alloys included in this study were rolled plates of beta- and recrystallizationannealed Ti-6Al-4V, beta- and duplex-annealed Ti-8Al-1Mo-1V and Ti-15V-3Cr-3Al-3Sn. The chemical compositions are given in Table I. Specific heat treatments and mechanical properties are available from previous publications [4,11].

To simulate a ripple-load condition and to measure threshold levels of stress-intensity range directly, precracked specimens were cyclically loaded at room temperature in a 3.5% NaCl solution with a stress ratio (minimum: maximum) of R = 0.90 (10% ripple loading), a haversine waveform, and a cyclic frequency of 5 Hz. SCC thresholds were determined in the 3.5% NaCl solution using slow-strain rate tests with a loading rate of 10-4 MPa\m/m/s. Crack lengths were determined using a compliance related CMOD technique. Details of the experimental procedures have been published elsewhere [2-5].

Table I Chemical Compositions (wt%)

Material	Al	V	Мо	Cr	Sn	Fe	O	С	н
Ti-6Al-4V	6.7	4.3			-	0.1	0.20	0.03	0.006
Ti-8Al-1Mo-1V	7.8	1.1	1.0	-	-	0.07	0.11	0.03	0.0046
Ti-15V-3Cr-3Al-3Sn	2.8	14.1	-	2.5	2.4	-	0.13	-	0.015

Results and Discussion

(A) Analysis of the Ripple Load Effect

In the present investigation, the authors treat ripple-load cracking (RLC) as a high stress ratio corrosion fatigue phenomenon. The critical conditions and the predictive methodology for ripple load effects involve the interface between SCC and corrosion fatigue behavior. In this study, our attention was focused on the regime below $K_{\rm ISCC}$ where propagation of existing cracks and failure are not expected under a constant load condition. Thus, in the presence of small ripples superimposed on a large sustained load, the maximum stress intensity in the ripple load cycle, $K_{\rm max}^{\rm RL}$, was equal to or less than $K_{\rm ISCC}$. That is, the first condition for ripple load cracking can be set as:

$$K_{\text{max}}^{\text{RL}} \leq K_{\text{ISCC}}$$
 (1)

On the other hand, from corrosion fatigue considerations, crack propagation is not going to take place during ripple loading unless the applied stress intensity range, ΔK^{RL} , in the ripple cycle

equals or exceeds the threshold stress intensity range, ΔK_{th} , or:

$$\Delta K_{th} \leq \Delta K^{RL}$$
 (2)

or
$$\Delta K_{th}/(1-R) \leq K_{max}^{RL}$$
 (2a)

Here, a new parameter, KIRLC, the ripple load cracking threshold below which ripple load cracking will not occur, can be defined as:

$$K_{IRLC} = \Delta K_{th} / (1-R)$$
 (3)

This new ripple load cracking threshold, K_{IRLC} , is conceptually similar to that of the SCC threshold, K_{ISCC} , under the sustained load. Like K_{ISCC} , K_{IRLC} for a given material is affected by the test environment and temperature. Also, as shown in Relation (3), K_{IRLC} is influenced by the stress ratio as well.

Combining (1), (2a), and (3), the conditions for a material to exhibit ripple load cracking are:

$$K_{IRLC} \le K_{max}^{RL} \le K_{ISCC}$$
 (4)

Relation (4) is schematically illustrated in Fig. 1. The shaded region, whose upper bound is the SCC threshold, K_{ISCC}, and whose lower bound is the ripple load cracking threshold, K_{IRLC}, defines a "window of susceptibility" in which the ripple load effect would be anticipated. The wider the window the more susceptible the material is to ripple load cracking. In the extreme case where K_{IRLC} approaches K_{ISCC}, the susceptibility window is closed and no ripple load effect is expected. The ripple load cracking time-to-failure curve, for a particular structural geometry, can be predicted from a simple piecewise numerical integration of the corrosion-fatigue crack growth rate curve. This predicted ripple load cracking time-to-failure curve can be verified with actual data from stress-corrosion cracking tests conducted under sustained loading.

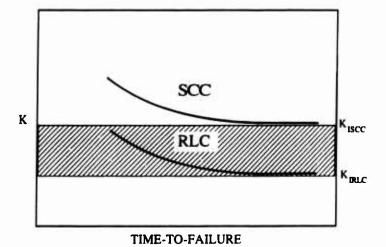


Fig. 1 Schematic showing the ripple load effect and the "window of susceptibility."

If one considers the difference between $K_{\mbox{IRLC}}$ and $K_{\mbox{ISCC}}$, then the maximum extent of ripple load degradation can be defined as:

% degradation =
$$(1 - K_{IRLC} / K_{ISCC}) \times 100$$
 (5)

(B) Ripple Load Cracking in Titanium Alloys

(i) Ti-6Al-4V

Figure 3 shows the ripple load degradation of the RA Ti-6Al-4V, which is less SCC resistant than the BA Ti-6Al-4V. The ripple load cracking threshold was determined to be around 39 MPa $^{\prime}$ m, which is about 9% lower than the static K_{ISCC}. The lower degree of RLC susceptibility is partly due to the low static K_{ISCC} of this alloy, which defines the upper bound of the susceptibility window.

(ii) Ti-8Al-1Mo-1V

The predicted ripple load cracking curves for BA and DA Ti-8Al-1Mo-1V are shown in Figs. 4 and 5. Following the trend established for Ti-6Al-4V, the moderately SCC-resistant BA Ti-8Al-1Mo-1V exhibits a larger degree of ripple load degradation (19%) while the less SCC-resistant DA Ti-8Al-1Mo-1V demonstrates no ripple load degradation.

(iii) Ti-15V-3Cr-3Al-3Sn

Ti-15V-3Cr-3Al-3Sn is a beta titanium alloy with good resistance to salt water stress-corrosion cracking. However, as shown in Fig. 6, when this alloy experiences ripple loading in an SCC environment, cracking can occur at stress intensities as much as 72% below the apparent K_{ISCC}.

The ripple load cracking susceptibility and the extent of ripple load degradation of the five alloys studied are summarized in Table II. Table II clearly demonstrates that materials which exhibit greater SCC resistance under static load conditions are far more susceptible to ripple load degradation. Without exception, highly SCC-resistant alloys are more prone to ripple load degradation than less SCC resistant alloys. The two most highly SCC-resistant alloys, BA Ti-6Al-4V and beta Ti-15V-3Cr-3Al-3Sn, with their KISCC levels of about 60 MPaVm, experience reductions of more than 50% in apparent KISCC when they are subjected to ripple load conditions. The two moderately SCC-resistant alloys, RA Ti-6Al-4V and BA Ti-8Al-1Mo-1V, both with KISCC levels of about 43 MPaVm, are less susceptible to ripple load degradation. DA Ti-8Al-1Mo-1V, the least SCC-resistant alloy in the group, with a KISCC of about 25 MPaVm, exhibits no ripple load degradation. The significance of this finding is obvious, at least phenomenologically, as a structure designed to the high KISCC of a highly SCC-resistant material may fail if ripple load conditions exist. To circumvent this problem, it is suggested that the ripple load cracking threshold, KIRLC, should be considered along with the static KISCC to determine allowable stress and inspection intervals.

Ripple load cracking characteristics can be affected by mechanical and environmental parameters. However, many of these are not adequately understood. The size of the ripple can

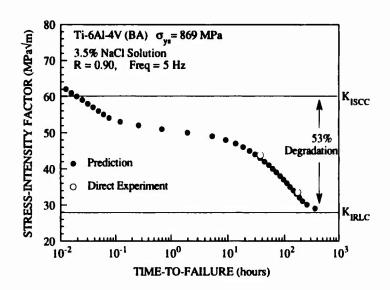


Fig. 2 Ripple load response in beta-annealed Ti-6Al-4V.

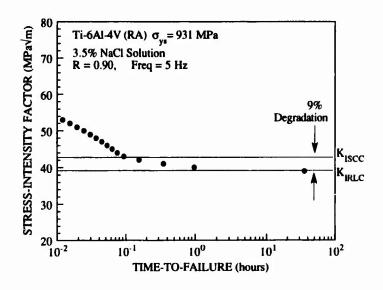


Fig. 3 Fadicted ripple load response in recrystallization-annealed Ti-6Al-4V.

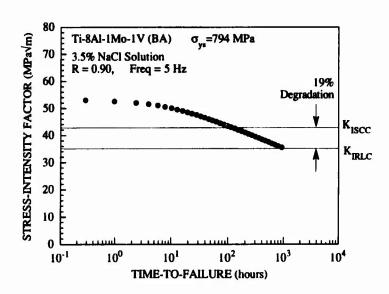


Fig. 4 Predicted ripple load response in beta-annealed Ti-8Al-1Mo-1V.

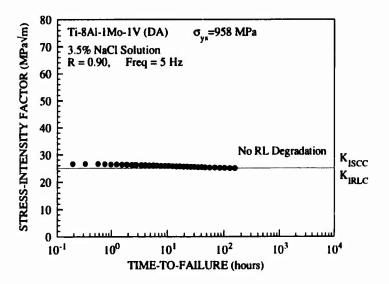


Fig. 5 Predicted ripple load response in duplex-annealed Ti-8Al-1Mo-1V.

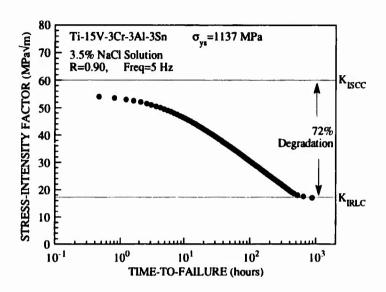


Fig. 6 Predicted ripple load response in Ti-15V-3Cr-3Al-3Sn.

Table II Summary of SCC and RLC Properties

Material	SCC Resistance	RLC Susceptibility	K _{ISCC} (MF	K _{IRLC} 'a√m)	RL Degradation
BA Ti-6Al-4V	High	High	60	28	53 %
RA Ti-6Al-4V	Moderate	Low	43	39	9 %
BA Ti-8Al-1Mo-1V	Moderate	Moderate	43	35	19 %
DA Ti-8Al-1Mo-1V	Low	None	25	25	0 %
Ti-15V-3Cr-3Al-3Sn	High	High	60	17	72 %

significantly influence the ripple load cracking phenomenon [3]. Extremely small ripple loads (less than 2.5% of the sustained load) were found to have no damaging effect on 5Ni-Cr-Mo-V steel. Temperature and load frequency, which are known to affect corrosion fatigue crack growth kinetics in titanium alloys, should also influence ripple load cracking.

Finally, a few words are in order regarding the material selection process. Even though materials with superior SCC resistance exhibit more ripple load degradation, there are indications that their K_{IRLC} values are still equivalent to or better than those for less SCC-resistant materials. Thus, SCC-resistant materials may still be the materials of choice even in the presence of ripple loading. However, in such instances, the ripple load cracking threshold, K_{IRLC} , should be used to maintain conservativism in the design of structural components.

Conclusions

- 1. Ripple-loading can significantly reduce the apparent SCC threshold and the time-to-failure for highly SCC-resistant alloys such as beta annealed Ti-6Al-4V and beta Ti-15V-3Cr-3Al-3Sn while having no damaging effect on SCC-prone alloys such as duplex annealed Ti-8Al-1Mo-1V.
- 2. A new parameter, K_{IRLC} , the threshold stress intensity factor below which ripple load cracking will not occur, is identified and recommended as a design consideration if ripple load conditions are suspected.
- 3. The "window" for ripple load cracking susceptibility is bounded at the top by $K_{\mbox{IRLC}}$ and at the bottom by $K_{\mbox{IRLC}}$. Alloys more susceptible to ripple load cracking will exhibit larger windows.

Acknowledgements

The support of this work by the Office of Naval Research is gratefully acknowledged, as are discussions with Dr. A. J. Sedriks, ONR Scientific Officer. The authors are also grateful to Dr. R. R. Boyer of Boeing for providing the Ti-15V-3Cr-3Al-3Sn plate used in this study.

References

- 1. M.O. Speidel, Corrosion Fatigue of Steam Turbine Blade Materials, (New York, NY: Pergamon, 1983), p. 1.
- T.W. Crooker, J.A. Hauser II and R.A. Bayles, Environmental Degradation of Engineering Materials, (University Park, PA: Pennsylvania State University Press, 1987), p. 521.
- P.S. Pao, R.A. Bayles and G.R. Yoder, Trans. ASME, J. Eng. Matls Tech., Series H, 113, 125 (1991).
- 4. G.R. Yoder, P.S. Pao, and R.A. Bayles, Scripta Met., 24, 2285 (1990).
- 5. P.S. Pao, S.J. Olli, R.A. Bayles, and O.R. Yoder, Scripta Met., 24, 2085(1991).
- 6. R.N. Parkins, B.S. Greenwell, Metal Sci., 8/9 1977: p. 405.
- 7. R.N. Parkins, P.M. Singh, Corrosion, 46, 485(1990).
- 8. K. Komai and K. Minoshima, JSME Int. J., Ser. I, 32 1(1989).
- 9. K. Komai, K. Minoshima, and Y. Nishide, JSME Int. J., 30, 401(1987).
- K. Endo, K. Komai, and K. Minoshima, Materials, Experimentation and Design in Fatigue, (Westburry House, 1981), p. 77.
- 11. G.R. Yoder, L.A. Cooley, and T.W. Crooker, Eng. Fracture Mechanics, 11, 805(1979).

OXIDATION CHARACTERISTICS OF BETA-21S IN AIR

IN THE TEMPERATURE RANGE 600 TO 800°C

T. A. Wallace*, K. E. Wiedemann**, and R. K. Clark*

*NASA Langley Research Center Mail Stop 194, Hampton, Virginia 23665-5225

**Analytical Services and Materials, Inc. 107 Research Drive, Hampton, Virginia 23666 Abstract

The metastable β -Ti alloy Beta-2iS, Ti-15Mo-2.7Nb-3Al-.2Si (weight percent), has been proposed as a candidate for use in metal matrix composites in future hypersonic vehicles. The present study investigated the oxidation behavior of Beta-21S over the temperature range 600 to 800°C. Oxidation weight gain was evaluated using thermogravimetric analysis. Oxidized specimens were evaluated using x-ray diffraction techniques, scanning electron microscopy, energy dispersive x-ray analysis, and electron microprobe analysis to identify oxidation products and evaluate oxidation damage to the alloy.

Introduction

Current designs for future hypersonic vehicles call for the use of titanium-matrix composites for many components, consituting as much as fifty percent of the structural weight. This will require a titanium alloy which has good oxidation resistance, is easily producible as foil, and has good high temperature properties in the temperature range 600 to 800°C. This has required the development of new titanium alloys with an acceptable balance of these properties. One alloy developed for use in this application is the metastable β -Ti alloy Beta-21S, Ti-15Mo-2.7Nb-3Al-.2Si (wt. %).

The purpose of the present study was to characterize the oxidation behavior of Beta-21S in the temperature range 600 to 800°C. Oxidation weight gain was determined by oxidizing samples in air using thermogravimetric analysis (TGA). Selected samples were analyzed metallographically to characterize the oxide composition and morphology and the microstructural changes in the metal.

Experimental Procedures

Specimens and Materials. The as-received Beta-21S material was produced from a triple m. o' ingot by forging to a 12.7 cm (5 inch) slab, hot rolling to a nominal thickness of 0.406 cm (0.160 inch), and cold rolling to 0.051 cm (0.02 inch) thickness

Titanium '92 Science and Technology Edited by F.H. Froes and I. Caplan The Minerols, Metals & Materials Society, 1993 using intermediate vacuum anneal steps. The chemical analysis of the Beta-21S materials in weight percent was 15.8 Mo, 2.95 Al, 2.88 Nb, 0.23 Si, 0.026 C, 0.114 O, and 0.005 N with the balance being Ti.

Thermogravimetric analysis (TGA) samples were machined to a width of 1 cm, and a length of 1.5 cm with a 0.16 cm diameter hole through the thickness at one end for suspending the sample during the test. Sample surfaces were ground to a uniform finish using silicon carbide paper through 1200 grit. Samples were first detergent cleaned, then ultrasonically cleaned in acetone and ethyl alcohol, and finally air dried. The dimensions of finished samples were measured to the nearest 0.0001 inch and weights were recorded before and after exposure to the nearest 0.01 mg.

Oxidation Tests. Oxidation tests were conducted in high purity air (true hydrocarbon content less than 0.1 ppm) from 600 to 800°C for times up to 100 hr. The sample weight change was recorded continuously during exposure using a Cahn C2000 microbalance with an accuracy of 1 μ g. Samples were suspended by quartz fibers in a mullite tube inside a vertical tubular furnace, and the temperature was monitored continuously with an R-type thermocouple located just below the suspended specimen. A low flow of air (1 cc/sec) through the mullite tube was maintained during the test. Duplicate or triplicate tests were performed at each temperature.

Characterization Studies. Specimens were examined before and after oxidation using scanning electron microscopy (SEM), energy dispersive X-ray spectroscopy (EDS), and X-ray diffraction (XRD) to characterize the microstructure and identify oxide phases. The distribution and morphology of the oxide phases were determined by examining cross-sectioned specimens using SEM, EDS, and electron microprobe analysis. These specimens were cross-sectioned after mounting in epoxy, then polished and lightly etched using Kroll's reagent (2 % HNO₃, 1 % HF), and finally coated with a thin layer of gold to minimize charging.

Results

Oxidation Kinetics. Table 1 summarizes the results for the oxidation exposures of Beta-21S over the temperature range 600 to 800° C. The total weight gains were obtained from comparing initial and final specimen weights. Analysis of the weight gain data obtained from the TGA showed that the weight gain increased parabolically with respect to the time of exposure, as would be expected for a titanium alloy in this temperature range (1). This means that the weight gain can be expressed as $w^2 = k_p t$ where w is the weight gain per unit area, k_p is the parabolic rate coefficient, and t is the time of exposure. Calculated values of k_p for Beta-21S are presented in table 1.

Figure 1 is an Arrhenius plot of the parabolic rate coefficients calculated for Beta-21S. The activation energy for oxidation was calculated to be 41.2 kcal/mol from the parabolic rate coefficients. Also shown for reference is data for commercially pure (c.p.) titanium (2), and the Ti₃Al-based alloy Ti-14Al-21Nb (wt %) (3). This analysis shows that over the temperature range investigated, Beta-21S has better oxidation resistance than c.p. titanium but oxidizes more rapidly than Ti-14Al-21Nb.

Oxidation Products. The results from XRD analysis of as-received and oxidized Beta-21S specimens are shown in table 2. The as-received material consisted exclusively of β -Ti, while some α -Ti was identified after all oxidation exposures. TiO₂ (rutile)

Table 1. Thermogravimetric Analysis Results For Beta-21S

Exposure Conditions		Total Weight	Parabolic Rate	
Temp,°C	Time,hr	Gain, mg/cm²	Coefficient mg²/cm⁴/hr	
600	72.5	0.204	0.000575	
650	70.8	0.364	0.00187	
700	71.8	0.762	0.00801	
700	111.5	1.01	0.00922	
750	24.1	0.809	0.0271	
800	29.8	1.55	0.0808	
800	100.1	2.92	0.0852	

was the primary oxide identified after exposure at all temperatures examined. Trace amounts of Al₂O₃ were also identified after exposure at temperatures above 600°C.

Figure 2 is an SEM micrograph of the cross-section of a specimen exposed 100 hr at 800°C. The surface oxide consists of two regions; a discontinuous top layer, and a relatively thick compact (void-free) layer. EDS analysis of the top layer showed the presence of Ti, Al, and O; while analysis of the middle layer showed the presence of Ti, O, and a small amount of Nb. Combined with the XRD analysis results (table 2), these scans suggest that the surface oxide is primarily TiO₂, with a mixture of Al₂O₃ and TiO₂ at the surface.

Table 2. Oxide Composition Of Beta-21S From XRD

		Measured Intensities1		
Exposure	β-Ti	α-Ti	TiO ₂	Al ₂ O ₃
as-received	vs	-	-	
600°C, 72.5 hr	VS	VS	W	•
700°C, 71.8 hr	S	S	VS	W
800°C, 29.8 hr	W	W	VS	W
800°C, 100.1 hr	W	W	VS	\mathbf{W}

¹ VS=very strong, S=strong, W=weak

The oxidation of titanium alloys, however, is known to proceed by the dual processes of oxygen dissolution and oxide formation. The total weight gain, therefore, represents the sum of the oxygen consumed in the formation of the surface oxide and the

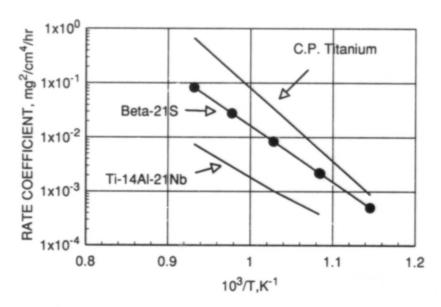


Figure 1 - Arrhenius Plot of Oxidation Rates for Beta-21S

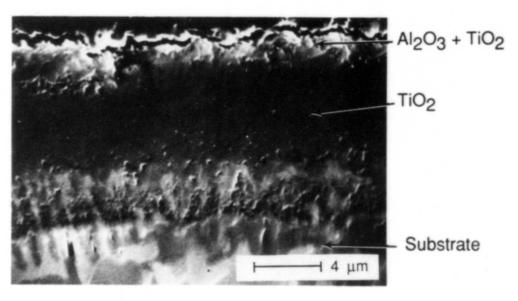


Figure 2 -SEM Micrograph of Beta-21S Exposed at $800^{\circ}\mathrm{C}$ for $100~\mathrm{hr}$

oxygen that diffuses into the metal. Metallurgical analysis of the oxidized specimens is necessary to allocate the total weight gain between these two processes.

Measurement of oxide thicknesses can be used to estimate the amount of oxygen consumed in oxide formation. Since the oxide on Beta-21S has been shown to be primarily TiO₂, the oxide thickness can be used to estimate a weight gain per unit area using the theoretical density of oxygen in TiO₂ (1.7 g/cm³). Subtracting this weight from the total measured oxygen weight gain also allows an estimation of the amount of oxygen that has diffused into the substrate.

The results of this analysis for several oxidized Beta-21S specimens are presented in table 3. These results show that there is measureable weight gain due to oxide formation. Comparison with the total weight gain data, however, shows that oxide formation only accounts for 70 percent of the total oxygen reacting with the metal. This means that there is also an appreciable amount of the oxygen diffusing into the metal.

Table 3. Results of Oxide Thickness Measurements for Beta-21S

Exposure Condition		Oxide Thickness,	Weight Gain, mg/cm ²	
Temperature, °C	Time, hr	μm	Oxide	Metal
600	72.5	0.84	0.14	0.061
700	71.8	3.2	0.54	0.22
800	29.8	5.8	0.99	0.56

¹ VS=very strong, S=strong, W=weak

Metallurgical examination of the oxidized Beta-21S specimens should confirm the fact that oxygen diffusion is occuring since oxygen is a known α -Ti stabilizer and should produce some microstructural changes. Figure 3 shows the resulting microstructure after various oxidation exposures. Figure 3(a) shows the microstructure after exposure at 800°C for 30 hr, (b) 800°C for 100 hr, (c) 700°C for 70.8 hr, and (d) 600°C for 72.5 hr. All specimens consist of a mixture of α -Ti and β -Ti, with an increase in the tendency to form Widmanstatten α -Ti as the temperature is decreased. Separation of the effects of oxygen and thermal exposure in this temperature range is difficult, however, since the β -Ti transus for Beta-21S is roughly 815°C (4).

Close examination of these cross-sections, however, does indicate an increased concentration of α -Ti near the metal surface, particularly after exposures at 700°C and 800°C. Figure 4 plots the fraction percent α -Ti (calculated using the point count method: ASTM E562) as a function of distance from the oxide-metal interface for specimen exposed 30 h and 100 hr at 800°C. For the specimen exposed for 30 hr there is approximately 50 percent α -Ti at the specimen surface decreasing to a constant value of approximately 10 percent 100 μ m from the oxide-metal interface. After

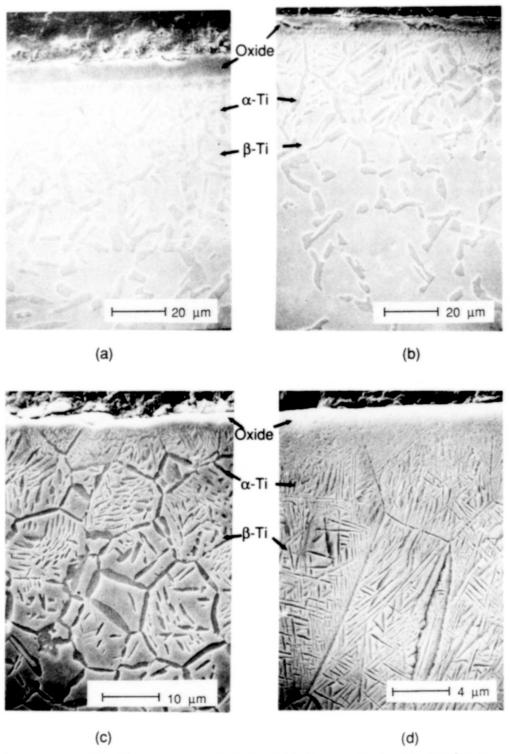


Figure 3 - SEM Micrograph of Beta-21S Exposed at (a) 800°C for 30 hr, (b) 800°C for 100 hr, (c) 700°C for 72 hr, and (d) 600°C for 72.5 hr.

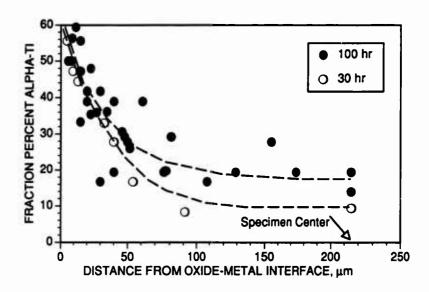


Figure 4 - Fraction Percent α -Ti as a Functions of Distance from the Oxide-Metal Interface for Beta-21S Exposed at 800°C.

100 hr exposure at 800°C, however, the percentage of α -Ti is higher throughout the entire specimen, decreasing to about 20 percent α -Ti at the center of the specimen. Although percent α -Ti is not a direct measurement of oxygen content, the increased levels of α -Ti near the surface do indicate that there is a concentration gradient of oxygen into the metal, extending across the entire specimen after longer term exposures.

Discussion

The oxidation behavior of Beta-21S, like that of other titanium alloys, is difficult to define precisely due to the number and complexity of operative oxidation mechanisms. For instance, for c.p. titanium it has been shown that oxidation proceeds by simultaneous growth of a surface oxide of TiO₂ and oxygen dissolution into the metal. At low temperatures (below 650°C) the oxidation rate is controlled by the growth rate of the TiO₂, producing an activation energy between 25.4 kcal/mol and 27.4 kcal/mol. At higher temperatures, the activation energy changes to that required for diffusion of oxygen into the metal (2,5).

Analysis of the oxidation kinetics and metallurgical characterization for Beta-21S, however, does allow some important insights. For instance, if the surface oxide layer of TiO₂ that forms on Beta-21S was rate controlling, the activation energy should be similar to that for c.p. titanium and other titanium alloys. The activation energy for the oxidation of Beta-21S, however, was calculated from the parabolic rate coefficient to be 41.2 kcal/mol. This indicates that oxide formation does not control the oxidation

kinetics, and suggests that oxygen dissolution into the metal also must be considered.

The fact that measureable oxygen dissolution occurs is confirmed by metallurgical examination of the oxidized Beta-21S specimens. Figure 3 and figure 4 indicates that there there is an increase in the percent of α -Ti near the specimen surface after oxidation exposure, suggesting the presence of an oxygen concentration gradient in the metal. In fact, after 100 hr exposure at 800°C, the percent alpha is increased even at the center of the specimen, suggesting that oxygen has diffused throughout the entire specimen thickness.

This analysis of the oxidation behavior of Beta-21S has shown that, although oxidation rates for that alloy are lower than that for other titanium alloys, there are still measureable oxidation weight gains in the investigged temperature range. While some of this weight gain is due to oxide formation, an appreciable amount of this oxygen weight gain is due to oxygen diffusing into the metal. The increase in amount of α -Ti as a result of this oxygen diffusion could have significant effects on the mechanical properties of Beta-21S.

Conclusions

Analysis of the oxidation behavior of Beta-21S over the temperature range 600 to 800°C shows that it does have better oxidation resistance than c.p. titanium, but poorer resistance that titanium aluminides. While Beta-21S forms a compact layer of TiO_2 , the data suggests that oxygen dissolution into metal is appreciable. Examination of the microstructures after exposure showed an increase in the amount of α -Ti with length of exposure, which should be linked directly with the diffusion of oxygen into the metal. This means that in the temperature range 600 to 800°C, exposure to air may severely degrade the mechanical properties of Beta-21S.

References

- 1. Kofstad, P.; Anderson, P. B.; and Krudtaa, O. J.; Oxidation of Titanium in the Temperature Range 800-1200°C. J. Less-Common Metals, vol. 3, no. 2, Apr. 1961, pp. 89-97.
- 2. Unnam, J.; Shenoy, R. N.; and Clark, R. K.; Oxidation of Commercial Purity Titanium. Oxidation of Metals, vol. 26, Nos. 3/4, 1986, pp. 231-252.
- Sankaran, S. N.; Clark, R. K.; Unnam, J.; and Wiedemann, K. E.: Oxidation Characteristics of Ti-14Al-21Nb Alloy. NASA-TP 3012, 1990.
- 4. Bania, P. J.: Beta-21S: A High Temperature Metastable Beta Titanium Alloy. Proceedings of the 1990 International Conference on Titanium Products and Applications, Titanium Development Association, 1990.
- Stringer, J.: The Oxidation of Titanium in Oxygen at High Temperatures. Acta Metallurgica, vol. 8, Nov. 1960, pp. 758-766.

MECHANICAL PROPERTIES OF COATED TITANIUM BETA-21S AFTER EXPOSURES TO AIR AT 700 AND 800°C

K. E. Wiedemann Analytical Services and Materials, Inc. 107 Research Drive, Hampton, VA 23666

R. K. Bird, T. A. Wallace, R. K. Clark NASA Langley Research Center, Hampton, VA 23665-5225

Abstract

Mechanical properties of Beta-21S (Ti-15Mo-3Al-2.7Nb-0.2Si, wt%) with glass, aluminide, and glass-on-aluminide coatings less than 3-μm thick were studied. Coatings were deposited by sol-gel processing or electron-beam evaporation onto 4.5-mil (113-μm) thick Beta-21S sheet. Tensile test specimens were machined after oxidizing in air at 700 or 800°C. Plastic elongation was the most severely degraded of the tensile properties; the glass-on-aluminide coatings were the most effective in preventing degradation. Significant roles were played by oxygen trapped as oxides in the coating, and reactions between the coatings and the Beta-21S alloy.

Introduction

Surface oxide formation and oxygen dissolution (to form oxygen interstitials in the alloy) are concurrent oxidation processes in titanium alloys. At low temperatures, oxide formation is the dominant process and the oxide that forms is protective, corrosion resistant, and inert to many forms of chemical attack. At higher temperatures (> 400°C) oxygen dissolution increases in importance because it comes to dominate the oxidation kinetics (ref 1 & 2), gives rise to interstitial hardening, and stabilizes the alpha phase. The latter factors have a considerable influence on the mechanical properties of the alloy including tensile strength, ductility, and elastic modulus. Ductility is the first and most seriously affected of these properties, and its loss is a sign that oxygen interstitials have formed.

The role of nitrogen, during oxidizing exposures in air, is currently uncertain: nitrogen is known to behave similarly to oxygen and with similar effects on the ductility of the alloy, but whether it reacts with titanium alloys in the presence of oxygen is not clear. In any case, to prevent embrittlement of the alloy, interstitials of both elements must be kept from forming, and this can be accomplished with coatings by two approaches: 1) by blocking transport across the coating or 2) by trapping these elements as oxides or nitrides within the coating.

Beta-21S (Ti-15Mo-3Al-2.7Nb-0.2Si, wt%) is a metastable beta-titanium alloy and is considered, on the basis of fabricability, strength, density, and oxidation resistance, to be a promising candidate for aerospace applications. The oxidation resistance of Beta-21S is significantly better than Ti-15V-3Cr-3Sn-3Al and a little better than commercial-purity (cp) titanium (ref 3).

Science and Technology Edited by F.H. Froes and I. Caplan The Minerals, Metals & Materials Society, 1993

Table I. Chemical Analyses of the Titanium Beta 21-S Material

Sample	Fe	Мо	Al	Nb	Si	С	0	N	Н
Ingot, Top*	0.088	16.8	3.18	3.00	0.16	0.018	0.127	0.005	_
Ingot, Bottom*									
As-Received Sheet	0.130†	15.3	2.90†	2.97†	0.16†	0.035‡	0.148‡	0.038‡	103 ppm§

- * Ingot chemistry reported by TIMET for Heat G-1664
- † By direct-current plasma (DCP)
- 1 By combustion thermal-conductivity
- § By vacuum hot extraction

Beta-21S is now being evaluated for use in hypersonic-vehicle airframes as a composite-matrix material. This would involve frequent short-duration exposures to air at 816°C (1500°F) where oxidation occurs rapidly (ref 4). The need for coating Beta-21S when used in this environment is evident, and it is of interest to learn which coating strategies will be most successful. Glass coatings, which block transport across the coating, are representative of one strategy, and aluminide coatings, which trap oxygen by forming aluminum oxide, represent a second strategy. In this paper, the effect of glass and aluminide coatings, singly and in combination, on the oxidation and mechanical properties of Beta-21S is reported.

Procedure

Mill-annealed, 4.5-mil Beta-21S sheet (see chemical analyses in Table I) was cut into 1.5×5-in. panels with the longer dimension parallel to the rolling direction of the sheet. The panels were cleaned with a detergent, rinsed with acetone followed by methanol, blotted dry, and baked for 30 min at 90°C.

The aluminide coatings were formed by depositing 1 μ m of aluminum by electron-beam evaporation, and converting it to TiAl₃ by annealing for 8 h at 621°C in a vacuum furnace. This heat treatment produced in the alloy a basket-weave alpha-plus-beta microstructure.

The glass coatings were silicophosphates applied by a sol-gel process (ref 5) and cured for a total time of 40 min at 650°C. The process produced in the alloy a very fine, strongly oriented alpha-plus-beta microstructure.

The glass-on-aluminide coatings were formed by applying glass coatings to completed aluminide coatings. The resulting microstructure of the alloy was identical to that of the aluminide coated material.

Continuous thermal exposures were conducted in air at atmospheric pressure by introducing the specimens into furnaces preheated to the test temperature, and by air cooling at the end of the test exposure to minimize the time at temperatures where the omega phase might form.

After exposure, three tensile-test specimens were cut from each panel and machined to the specifications of ASTM Standard E8 (ref 6): the width of the reduced section was 0.250 in. and the length was 1.25 in.

The specimens were loaded at room temperature in tension until failure occurred. Back-to-back extensometers with a 1.000 in. gage length were used to measure strain. For

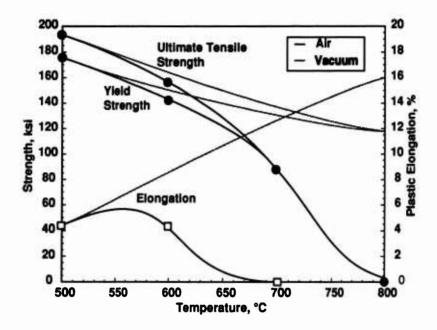


Figure 1. – Room-temperature mechanical property data for uncoated Beta-21S after 12 h exposure to air at the indicated temperature. The vacuum data (ref 3) shows the effect of thermal exposure, and the difference between air and vacuum shows the effect of oxidation.

determining yield, an 0.005 in./min cross-head-deflection rate was used until 5% total strain when the cross-head-deflection rate was increased to 0.05 in./min for the remainder of the test. Yield strengths were determined by the 0.2% offset method and elastic moduli by linear regression over the portion of the stress-strain curve between 0 and 0.5% total strain. Metallurgical specimens were prepared by sectioning the exposed foils and mounting them in a thermosetting medium. The metallurgical specimens were attack-polished using Kroll's reagent and a coloidal-silica slurry.

Results and Discussion

Reduced oxygen-weight gains and retained mechanical properties are benefits that a coating system is expected to provide. In a general sense, these two are related, but the degree of correlation depends on the coating type and the alloy's thermal stability. If the coating actively forms oxides, large weight gains may not imply degradation of properties. If the alloy's thermal stability is poor, changes unrelated to oxidation may be observed in the mechanical properties.

Oxidation Effects on Uncoated Beta-21S

Uncoated Beta-21S was tested to establish a baseline for evaluating the coatings and for distinguishing between oxidation and thermal exposure effects. In figure 1 are the room temperature ultimate tensile strengths (UTS), yield strengths (YS), and plastic elongations for 4.5-mil sheet, initially in the beta-annealed condition, after 12 h in air

2.187

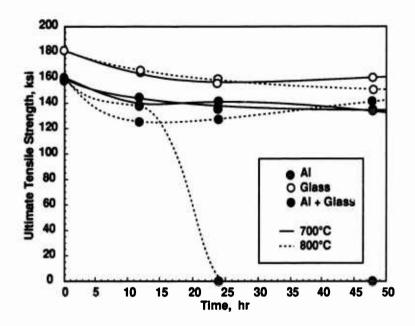


Figure 2. – Room temperature ultimate tensile strengths for coated 4.5-mil Beta-21S sheet after air exposures.

(this study) or 10 h in vacuum (ref 3).

At 500°C, the agreement between the vacuum and air data showed that oxidation in this exposure was not significant. At 600°C, the UTS and YS were almost equal for the vacuum and air exposures, but the difference in plastic elongation indicates a significant loss of ductility caused by oxidation. There was a complete loss of ductility and a considerable reduction in UTS and YS at 700°C due to oxidation. At 800°C, the material exposed in air was very fragile: all specimens broke while being prepared for testing.

Effect of Coatings on Ultimate Tensile Strength

Except for cases of complete coating failure, the UTS of coated Beta-21S was relatively insensitive to oxidizing exposure (see figure 2). A small decrease in UTS, seen in all coated material during the first few hours of exposure, was an aging response associated with changes observed in the microstructure.

The UTS of the glass-coated material was consistently higher than the UTS of aluminide-coated or glass-on-aluminide-coated material. This was attributed to the very fine, highly oriented alpha-plus-beta microstructure of the glass-coated material.

The only serious loss of strength was in the aluminide-coated material at 800°C after 24 and 48 h where the material proved to be very fragile: all of the specimens broke while being prepared for testing.

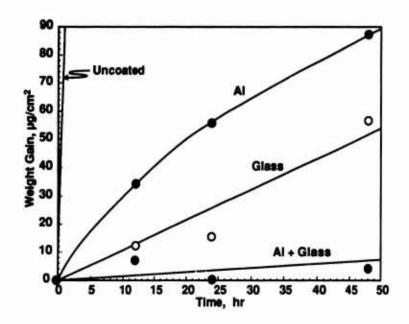


Figure 3. - Oxygen weight gained during 700°C air exposures of coated Beta-21S.

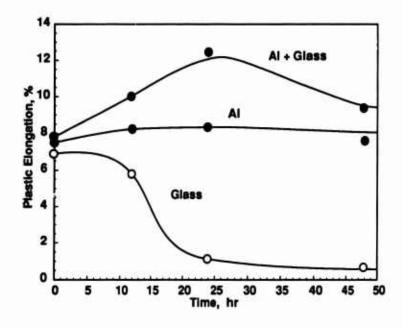


Figure 4. - Room-temperature ductility after 700°C air exposures of coated Beta-21S.

Weight Gains and Plastic Elongation at 700°C

The oxygen-weight gains at this temperature for all coated materials were small (see figure 3). All of the coated material showed significantly less weight gain than the uncoated material: after 12 h there was at least an order of magnitude difference. The low weight gains imply that all of the coatings were effective in limiting the entry of oxygen (and nitrogen) from the atmosphere.

While the precise dependence of plastic elongation on oxygen weight gain had not been established for 4.5-mil Beta-21S sheet, prior experience indicated that weight gains of less than 70 μ g/cm² should only have a minor effect. Consequently, it was expected that the ductility of all the coated material at 700°C would not be excessively degraded. In fact the plastic elongation of material with aluminide or glass-on-aluminide coatings were consistently high, but the plastic elongation of material with glass coatings steadily declined (see figure 4). This decline was attributed to oxygen interstitials generated by reactions between the oxygen-rich glass and the titanium alloy.

Weight Gains and Plastic Elongation at 800°C

The oxygen-weight gains for the glass and glass-on-aluminide coatings exposed at 800°C were small, but the weight gain for the aluminide coating, after an initial lag, closely paralleled the weight gain of the uncoated material (see figure 5). This suggested that the glass and glass-on-aluminide coatings were effective at this temperature, but that the aluminide coating was not protective. The glass-on-aluminide coating did very well: even after 48 h the oxygen-weight gain was less than 35 μ g/cm². If it is assumed that this represents oxygen permeation through the 1.5- μ m-thick glass layer, the oxygen-weight gain corresponds to an oxygen diffusivity of roughly 2.4×10^{-14} cm²/sec, which is within an order of magnitude of the oxygen self-diffusion coefficient for fused quartz $(3.5 \times 10^{-15} \text{ cm}^2/\text{sec}, \text{ ref 7})$.

The plastic elongations (see figure 6) confirmed, for the most part, the pattern of oxidation damage observed in the oxygen-weight gains. However, the ductility of the aluminide coated material after 12 h is surprisingly high in light of its very large weight gain. This leads to the conclusion that most of the weight gain went into oxide formation, and that the portion that went into interstitial formation was actually quite low.

The ductility of the glass coated material was lower it should have been according to oxygen-weight gains. This suggested that more interstitials were formed than weight gain could account for. It was surmised that where the glass and alloy were in direct contact, that the glass underwent a reduction reaction due to the high affinity of the alloy for oxygen. The oxygen from the glass then entered the alloy as interstitials contributing to the degradation of mechanical properties. The plastic elongations of the glass-on-aluminide coated material were much better than that of the other coated materials, and comparable to those of Beta-21S vacuum annealed at this temperature (ca 16%, ref 3). This was attributed to the more complete exclusion of interstitials by the glass-on-aluminide coating.

The amount of interstitials can be inferred, under special conditions, from the volume fraction of alpha in the microstructure. At 800°C, which is just below the beta transus of this alloy, there would only be a small amount of alpha in the microstructure if no

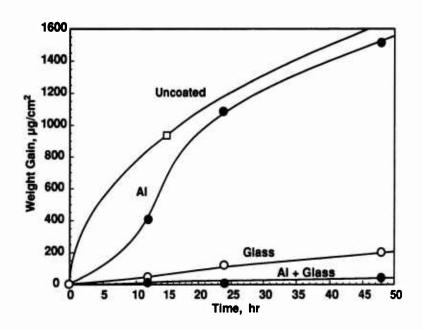


Figure 5. - Oxygen weight gained during 800°C air exposures of coated Beta-21S.

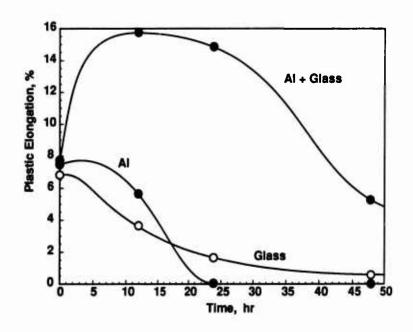


Figure 6. - Room-temperature ductility after 800°C air exposures of coated Beta-21S.

interstitials were present. The volume fraction of alpha for the glass-coated material after 12 h at 800°C was 21 vol%; for the aluminide-coated material it was 10 vol%; and for the glass-on-aluminide-coated material it was 7 vol% (ref 8). The glass-on-aluminide-coated material has the lowest volume fraction of alpha and the best residual ductility which, taken together, indicate that this material has the fewest interstitials.

Concluding Remarks

The results reported in this paper demonstrate the potential for practical coating systems for the Beta-21S titanium alloy that are very thin ($< 3 - \mu m$ thick), exclude oxygen from the alloy, and prevent unacceptable degradation of the mechanical properties. It is possible that such coatings may find application in titanium alloy aerospace structures which are subject to high temperatures in service.

It was shown that uncoated Beta-21S, 4.5-mil sheet was embrittled at 700 and 800°C after only 12 h of exposure, but embrittlement was prevented by glass, aluminide and glass-on-aluminide coatings less than 3- μ m thick. The glass-on-aluminide coating was the most successful with greater than 15% plastic elongation retained after 24 h at 800°C in air.

References

- J. Stringer, "The Oxidation of Titanium in Oxygen at High Temperatures," Acta Met., vol 8, 1960, pp 758-766.
- P. Kofstad, High Temperature Corrosion, Elsevier Applied Science, London, 1988, pp. 289-299.
- P. J. Bania and W. M. Parris, "Beta-21S: A High Temperature Metastable Beta Titanium Alloy," Titanium 1990, Products and Applications, Proceedings of the Technical Program from the 1990 International Conference, vol II, Titanium Development Association.
- T. A. Wallace, R. K. Clark, K. E. Wiedemann, "Oxidation of Beta-21S in Air in the Temperature Range 600 to 800°C," Proceedings of the Seventh World Conference on Titanium. TMS Titanium Development Association, 1992.
- K. E. Wiedemann, P. J. Taylor, R. K. Clark, T. A. Wallace, "Thin Coatings for Protecting Titanium Aluminides in High-Temperature Oxidizing Environments," Environmental Effects on Advanced Materials, Eds. R. H. Jones and R. E. Ricker, The Minerals, Metals, and Materials Society, Warrendale, PA, 1991, pp 107-121.
- E8-85b, "Tension Testing of Metallic Materials," 1986 Annual Book of ASTM Standards, vol 03.01, American Society for Testing and Materials, 1986, pp 124-145.
- P. Kofstad, "Nonstoichiometry, Diffusion, and Electrochemical Conductivity in Binary Metal Oxides," Wiley-Interscience, New York, 1972, pp 348-355.
- K. E. Wiedemann, T. A. Wallace, R. K. Clark, "Mechanical Properties of Coated Titanium Beta-21S after Exposure to Air at 700 and 800°C," NASA Technical Memorandum 104220, June 1992.

THE DETECTION OF CREVICE CORROSION IN TITANIUM AND

ITS ALLOYS THROUGH THE USE OF POTENTIAL MONITORING

D. D. Bergman and J. S. Grauman

TIMET
P.O. Box 2128
Henderson, NV 89009

Abstract

Conventional laboratory crevice corrosion testing requires approximately thirty days and is a simple go/no go test which does not indicate crevice corrosion incubation time and propagation. This study focuses on the effectiveness of electrochemical potential monitoring to detect the onset and propagation of crevice corrosion for several titanium alloys in chloride environments. Utilizing this technique, crevice corrosion initiation is detected immediately, thus, in most cases allowing a shorter test period. This technique may well be suited for field as well as laboratory applications. Crevice corrosion incubation periods and corresponding electrochemical potential behavior are investigated along with the effect of crevice to uncreviced surface area ratio. Under freely corroding conditions, which better simulate in-service conditions, the relationship between the corrosion potential (Ecorr) and crevice corrosion initiation and propagation was readily determined. Corresponding crevice corrosion initiation and steady-state propagation surface morphology were also examined.

Introduction

The titanium industry has traditionally relied on a thirty day go/no go freely corroding crevice test assembly in chloride environments at 90°C and above. The primary goal was to provide information on maximum safe operating temperature at a given chloride level and pH. There have been several studies of potential-time behavior of freely corroding crevice and free surface (uncreviced) specimens of unalloyed titanium, however, to date alloyed titanium behavior has not been studied. M. Kobayshi, et al.2, observed a steady-state potential of -465 mV SHE after 40 days in a boiling, 6 wt.% NaCl bulk solution with a crevice specimen containing an NaCl crystal sealant and a crevice/uncreviced ratio of 1:1. The initiation/propagation potential criteria, however, was not explored. P. Mckay, et al.3, reported approximately -300 mV SHE as a steady-state potential at 150°C, 1.6 wt.% NaCl solution, and a crevice/uncreviced ratio of 1:4. Incubation periods to a steady-state potential were reported in generally 10 to 15 hours at 150°C, and 20 to 30 hours at 95°C.

Titanium '92 Science and Technology Edited by F.H. Froes and I. Caplan The Minerals, Metals & Materials Society, 1993

A study of current-time behavior of a freely corroding crevice and free surface specimens was initially reported by T. S. Lee 4 for stainless steel. A crevice corrosion cell based on the concept of a galvanic couple consisting of a crevice anode and a boldly exposed comparably large cathode (typically anode/cathode ratio 1:90) with provisions for measurement of a current between the two was used. Lee observed that an increase in current did not correspond to crevice initiation as determined visually. Utilization of this technique in the present study has shown that a current increase was consistent with crevice surface oxidation, on ASTM grade 2 titanium, after a two day immersion. However, several studies of similar galvanic coupling of grade 2 in chloride solutions, including the one by P. Mckay, et al.3, reported that after the galvanic current reached a maximum (25-75 hours) it continuously decreased with time, eventually reaching a low constant value, although crevice propagation continued. This current decrease could be attributed to an increasing potential balance between such galvanically coupled specimens.

It is important to establish a practical method to detect the onset of crevice corrosion and propagation so that meaningful predictions of crevice corrosion behavior of alloyed and unalloyed titanium may be made. This investigation has shown that laboratory potential monitoring is a relatively simple method for quantifying the initiation and propagation stages of crevice corrosion.

Experimental

<u>Materials/Apparatus</u>. The compositions of all the alloys used in this study are listed in Table I. Titanium specimens were from mill and laboratory produced sheet, with standard annealing treatments ranging from 788°C for the alpha and near alpha alloys, to 843°C anneal for the beta alloys. Specimen sheet gage varied from .76 to 1.52mm. Titanium specimens were tested in the as-pickled surface condition. Specimen preparation and test technique are described elsewhere. All test solutions were prepared with distilled/deionized water and reagent grade chemicals.

A high temperature Ag/AgCl reference electrode was used for all potential measurements. Corrosion potential measurements were made using a Triplett Corporation 3360 electrometer.

Table I. - Nominal Composition of Titanium Test Alloys

	Composition (Wt. %)							
Alloy	0	н	Fe	Al	Mo	V	Cr	Other
ASTM Grade 1 Ti	0.06	.005	0.02	_	_	-	_	-
ASTM Grade 2 Ti	0.10	.005	0.15	-	-	-	-	-
TIMETAL . 38644	0.09	-	<0.03	3.0	4.0	8.0	6.0	4.02r
TIMETAL . 21S	0.13	-	0.15	3.0	15.0	-		2.7Nb,0.2Si

<u>Procedure.</u> The standard test condition consisted of testing a crevice assembly with a 4:1 crevice/uncreviced surface area ratio in a 5 wt.% NaCl solution at pH 2, 93°C, and natural aeration.

A crevice was formed by compressing the test specimen between two Teflon sheets (torqued to 1.8 N.m) utilizing two plates of grade 7 titanium and grade 2 titanium bolts wrapped with Teflon tape to ensure electrical insulation. The crevice specimens were assembled under the bulk chloride solution (without oxidizers) to avoid conditions of inconsistent wetting of the creviced surfaces. The standard creviced area was 6.45 cm² and the

external uncreviced area was 1.61 cm², thus, achieving a 4:1 crevice/uncreviced surface area ratio. The 1:3 and 1:90 crevice/uncreviced surface area ratios utilized a creviced area of 1.94 cm² and the external uncreviced area was 6.45 cm² and 174.19 cm². A Teflon insulated grade 2 titanium wire was resistance welded to the uncreviced area for monitoring purposes. Post test evaluations of crevice specimens required a light (5-8 sec) sandblasting per ASTM G 46, to remove the tenacious corrosion product scale and facilitate examination of the crevice surface.

Results

Potential Monitoring Reproducibility. To determine potential indication reproducibility, ten (each) titanium grade 1 and 2 creviced specimens were tested under standard conditions, as defined in the experimental section. Crevice specimen potentials were recorded at 3 to 24 hour intervals and certain corresponding creviced surfaces examined in 10 to 100 mV variations. In addition, specimens at matching potentials were compared. Crevice initiation was defined to begin when crevice pits were first detectable at 8% magnification. Crevice propagation was defined to begin when a steady-state potential was first reached after initiation had occurred. When a potential lower than -360 mV (Ag/AgCl) was recorded crevice corrosion initiation had occurred on all specimens observed. When a potential higher than -290 mV was recorded crevice initiation has not occurred on any of the specimens observed. At potentials ranging from -290 to -360 mV crevice initiation was observed on some of the specimens, whereas others only exhibited a thicker oxide film, typical by its variety of colors (blue, violet, etc.). Specimens examined at potentials varying by 5-10 mV exhibited comparable surface morphology. After crevice initiated a steady-state potential of -440 mV with approximately 40 mV daily fluctuation was reached on all specimens, and corresponding severe crevice corrosion was noted.

Unalloyed Titanium

The corrosion potential/time behavior as presented in Figures 1, 2 and Table II illustrates the sensitivity of the potential monitoring technique, in distinguishing the slight differences in crevice corrosion resistance between grade 2 and grade 1 under all tested conditions. The small differences in crevice corrosion severity between the grades was in agreement with minimum incubation periods for crevice initiation. Initiation and propagation potentials were clearly defined by a significant drop in potential.

Addition of oxidizers, and a larger crevice to uncreviced ratio accelerated incubation periods for initiation and propagation, which was consistent with crevice corrosion severity. Changes in incubation periods for initiation and propagation were also adequately reflected by changes in pH. Initiation and propagation potentials remained generally constant with changes in pH and crevice to uncreviced ratio. However, a significant increase in potentials was observed with the addition of ferric chloride.

Alloyed Titanium

Results as presented in Figure 3 and Table II clearly indicate the superior crevice corrosion resistance of TIMETAL.21S. Limitation of crevice corrosion could not be detected in TIMETAL.21S, despite lowering the

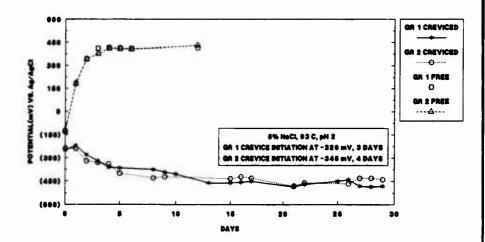


Figure 1 - Average crevice vs. free surface potential for titanium grades 1 and 2 at pH 2.

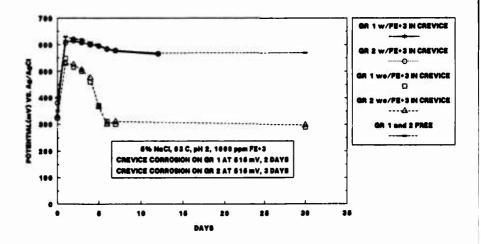


Figure 2 - Average crevice vs. free surface potential for titanium grades 1 and 2 in an oxidizing media.

solution pH to 0.2. Instead, passivation of the creviced specimen occurred under all testing conditions. TIMETAL.38644, however, which crevice corroded in these low pH solutions was readily detected using potential monitoring. Unusual repassivation cycling was detected after crevice corrosion initiation. The cycling amplitude appeared to diminish with crevice corrosion propagation.

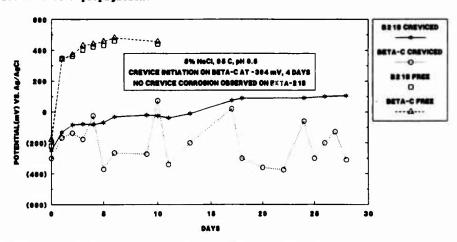


Figure 3 - Average crevice vs. free surface potential for titanium grades 1 and 2 at pH 0.5.

Table II. - Results Summary

			Initiation		Propagation	
	Variations of	Crevice/Uncreviced	Potential	Time	Potential	Time
Alloy	Standard Solution1	RALIO	(mV)	(Days)	(mV)	(Days)
Ti Grade 1	None	4/1	-320	3	-440 to -485	10
	Air Sparging	4/1	-320	2	-440 to -485	6
	Pe+3 (1000 ppm) ²	4/1	+515	2	+330 to +300	6
	pH 5	4/1	-320	6	-440 to -460	17
	None	1/3	-330	1	-430 to -480	4
	None	1/90	-300	1	-270 to -460	5
Ti Grade 2	None	4/1	-345	4	-440 to -480	10
	Air Sparging	4/1	-345	3	-440 to -485	
	Fe+3 (1000 ppm)2	4/1	+505	3	+330 to +300	6
	pH 5	4/1	-345	7	-420 to -450	17
TIMETAL. 38644	95°C, pH 1	4/1	-304	15	Repassivation Cycles -304 to +60	n 1*
	95°C, рн 0.5	4/1	-370	5	Repassivation Cycles -370 to +73	n 5*
TIMETAL•218	95°C. mH 1	4/1	Did Not Cre	/ice		
**********	95°C, pH 0.5	4/1	Did Not Cre	rice		
	98°C, pH 0.2	4/1	Did Not Cre	rice		

^{*}Between cycles after initiation.

istandard Solution: 5% NaCl, 93°C, pH 2, Natural Aeration. 2Crevices were assembled in standard solution (without $Fe^{\pm 3}$).

Discussion

Unalloyed Titanium

Corrosion Behavior: Critical potentials recorded for crevice initiation and propagation remained generally constant with solution parameter variations and crevice/uncreviced surface area ratio. The only exception was the addition of a high potency oxidizer - ferric chloride, which increased the corrosion potential (Ecorr) significantly. In turn, crevice initiation and propagation potentials, which consist of a mixed crevice and uncreviced (Ecorr) potential, increased considerably. In addition, the higher 1:90, crevice/uncreviced surface ratio had a minor effect on increasing crevice initiation potential (and near initiation potential) due to the larger uncreviced area initially raising the overall potential (mixed crevice and uncreviced potential). However, upon propagation, the more severe crevice corrosion due to the ratio effect, decreased the propagation potential to -500 mV. In contrast, minimum incubation periods to initiation and steady-state propagation varied considerably with solution parameters, and the overall crevice corrosion severity varied accordingly.

<u>Grade Composition Effect</u>: Grade 1 and 2 consistently varied by approximately one day in minimum incubation periods to initiation. The difference in crevice corrosion severity after a 30 day test was not always detectable, thus it is not surprising that these grades are considered to have similar crevice corrosion resistance. It is apparent, therefore, that potential monitoring provides for a more subtle difference in crevice corrosion resistance.

The somewhat better crevice corrosion resistance of grade 2 is believed to be due to its higher iron content, .10-.15 wt.\$, in comparison to 0.02-0.04 wt.\$ for grade 1. It is possible that minute amounts of ferric ions are present in the crevice liquid boundary layer, during the early stages of corrosion, thus enhancing passivation. Concentrations of 100 ppm ferric ions (Fe^{+3}) are known to significantly reduce the general corrosion rate of unalloyed titanium in HCl solutions. Such high concentrations of ferric ions are probably not attained in the crevice, but significant concentrations are possible considering the limited crevice volume.

Oxidizers and Crevice/Uncreviced Ratio Effects: Data on the effect of oxygen concentration on the crevice corrosion of unalloyed titanium are inconsistent, with some studies reporting an increase in susceptibility with increasing concentration^{5,6} and other reporting the opposite⁷. This investigation clearly defined the increase in susceptibility with increasing oxygen concentration, by showing a repeated acceleration of initiation and propagation incubation periods. Overall, the effect of 1000 ppm Fe⁺³ in the bulk solution was similar to that of higher oxygen concentration in accelerating crevice corrosion. These cationic oxidizers act as cathodic depolarizers, and thus accelerate cathodic reduction kinetics, which in turn increases the anodic crevice reaction. These oxidizers will not diffuse into the positively charged active crevice to effect passivation due to similar charge repulsion. On the other hand, certain anionic oxidizing species, such as ClO3 and others can migrate into the anodic crevice due to dissimilar charge attraction and inhibit crevice attack.

A crevice (anode) to uncreviced (cathode) surface area ratio larger than or equal to 1:3 had a more pronounced effect on accelerating crevice corrosion than was observed by the addition of oxidizers to a 4:1 ratio. The value of the galvanic current flowing from the anodic crevice is determined by the balance between the anodic reaction in the crevice and cathodic depolarization of the external uncreviced titanium surface. The couple potential at any time is limited by the degree of the cathodic depolarization kinetics as mentioned before, which would depend on oxygen/oxidizer concentration, uncreviced surface area, and solution conductivity at the temperature of interest. Thus, the mechanism of accelerated crevice corrosion is similar for both a larger uncreviced to crevice surface area and the addition of oxygen/oxidizers in their effect on the controlling cathodic depolarization kinetics of the external uncreviced titanium surface. It is important to note that at any ratio of crevice/uncreviced greater than or equal to 1:3, the crevice corrosion accelerating effect was similar in a 5 wt. % NaCl, pH 2, 93°C solution. Thus, at this ratio and solution, the maximum degree of anodic polarization was produced.

Alloyed Titanium

Corrosion Behavior: Alloyed titanium has shown remarkable repassivation cycling, which has not been reported in the literature previously, after crevice initiated, with some decrease in cycling amplitude as propagation approached steady state. Repassivation cycling could be attributed to certain alloying elements such as molybdenum, chromium and vanadium. These elements detected in the crevice corrosion products are believed to be present in the crevice liquid boundary layer as oxidizing species, enhancing passivation. Concentrations of 100 ppm Mo⁺⁶, Cr⁺⁶, and V⁺⁵ ions have shown to significantly reduce the general corrosion rate of unalloyed titanium in HCl solutions. Since these elements inhibiting effect is temporary, it is believed that their oxidation states are lower than otherwise will be in the bulk solution. More research, beyond the scope of this study, is necessary to conclusively establish their role.

Summary

The results illustrated that measuring corrosion potential/time profiles provided a relatively simple means of detecting the onset and propagation of crevice corrosion on titanium. Tests concluded upon crevice initiation provided satisfactory crevice corrosion resistance data by allowing comparison of incubation periods to initiation, thus a shorter test period was required. The reproducibility of potential measured and the extent of crevice corrosion observed suggests that this technique provides a realtime signal for monitoring crevice corrosion.

Critical crevice potentials recorded for unalloyed titanium creviced specimens remained generally constant regardless of solution pH, and crevice/uncreviced surface area ratio variations. However, the addition of potent oxidizers such as ferric chloride increased critical potentials significantly.

Alloyed titanium has shown an unusual repassivation cycling after crevice corrosion initiation. Critical crevice potentials remained generally constant with solution pH variations.

Conclusions

The research performed during this laboratory examination has led to the following conclusions:

- It was feasible to correlate potential measured with severity of attack, indicating initiation and propagation of crevice corrosion. Initiation data, alone, provided satisfactory results, and thus a shorter test period was required.
- This technique distinguished between subtle differences in crevice corrosion resistance.
- Addition of oxidizers, and change in crevice/uncreviced ratios, were adequately reflected by changes in electrode potential. Thus, shifts from the corrosion potential (Ecorr) in the active and noble directions denoted increasing and decreasing crevice corrosion attack, respectively.
- The newly developed titanium alloy, Beta-21S, has proven to possess superior crevice corrosion resistance to pH levels as low as 0.2.

References

- 1. "Guidelines for Corrosion Testing of Titanium," <u>Industrial Application of Titanium and Eirconium</u>, ASTM STP 728, ed. E. W. Rleefish (Philadelphia, PA: American Society for Testing and Materials, 1981), 59-70.
- H. Kimura, and O. Izumi eds., <u>Titanium '80 Science and Technology</u>,
 Vol. 4 (Warrendale, PA: The Metallurgical Society, 1980), 2613.
- 3. P. Mckay and D. B. Mitton, "An Electrochemical Invesigation of Localized Corrosion on Titanium in Chloride Environments," <u>Corrosion</u>, (1) (1985), 52-62.
- 4. "A Method for Quantifying the Initiation and Propagation Stages of Crevice Corrosion," <u>Electrochemical Corrosion Testing ASTM STP 727</u>, eds. Florian Mansfeld and Ugo Bertocci (Philadelphia, PA: American Society for Testing and Materials, 1981, 43-68.
- 5. J. C. Griess, "Crevice Corrosion of Titanium in Aqueous Salt Solutions," Corrosion, 4 (1967), 96-102.
- 6. "Crevice Corrosion in Titanium," High Temperature High Pressure Electrochemistry Aqueous Solutions, eds. D. Jones, J. Slater, and R. Staehle (Houston, TX: National Association of Corrosion Engineers, 1976), 479-490.
- 7. P. B. Needham et al., "Corrosion Studies in High Temperature, Hypersaline Geothermal Brines," Corrosion, 59 (1979), 50-59.

THE INFLUENCE OF HYDROGEN ON THE MECHANICAL PROPERTIES OF TIMETAL 21S

George A. Young Jr. and John R. Scully

Department of Materials Science and Engineering The University of Virginia Charlottesville, VA 22903

Abstract

The effects of internal hydrogen on the room temperature mechanical properties of the peak aged beta titanium alloy, TIMETAL 21S, are quantified as functions of stress and strain state in Bridgman notched tensile bars. Electrochemical precharging of hydrogen into previously aged material is employed to preserve a fully aged microstructure. Hydrogen effects are de-coupled from aqueous embrittlement phenomena via mechanical testing of pre-charged material in air. Maximum longitudinal stress and plastic strain at maximum load decrease with increasing hydrogen concentrations ranging from 10-3000 ppm. Fracture path is shown to be a function of hydrogen concentration and level of constraint. Intergranular separation is attributed to high levels of hydrogen and constraint and possibly to abundant α precipitation on grain boundaries. X-ray diffraction analysis of the failed notched regions detected no evidence of hydride formation in the subsurface α phase.

Introduction

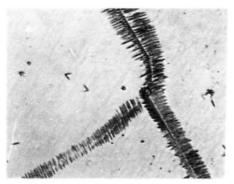
Critical aerospace, petrochemical, and marine applications demand high strength. formable materials which are resistant to corrosion, stress corrosion, and hydrogen embrittlement. Modern & titanium alloys are candidates for many such applications due to their excellent strength, toughness, formability, and resistance to general corrosion [1-5]. Furthermore, titanium's compact surface oxide film limits hydrogen entry and the underlying B matrix has a high solubility for hydrogen [6-7]. However, both model binary beta titanium alloys as well as early developmental \(\theta\) alloys (Ti-13V-11Cr-3Al) can be susceptible to hydrogen embrittlement [8-15]. Hydrogen has also been implicated as the embrittling species in aqueous environmentally assisted cracking (EAC) of α - β and B alloys [16-20]. Factors supporting a hydrogen embrittlement mechanism for TIMETAL 21S in aqueous solutions include a) electrochemical conditions at the crack tip which favor hydrogen production b) a loading rate dependency and c) discontinuous crack Current understanding of the controlling hydrogen embrittlement mechanisms in peak aged, β-titanium alloys is insufficient to enable critical, damage tolerant applications [21]. The present research seeks to define the effects of a range of internal hydrogen concentrations on the room temperature mechanical properties of the peak aged \(\theta\)-titanium alloy, TIMETAL 21S.

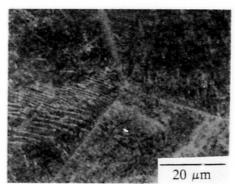
Experimental

Solution annealed and cross-rolled TIMETAL 21S plate, nominally 10 mm thick was received from TIMET. The solution annealed condition was 871 °C for 8 hours followed by an air cool. Heat treatment of as-received plate consisted of an 8 hour age in air at 538° C, followed by an air cool, as recommended by the vendor. One hour and

Titanium 92 Science and Technology Edited by F.H. Froes and I. Caplan The Minerals, Metals & Materials Society, 1993 eight hour aged microstructures are shown in Figure 1. Note that α precipitates nucleate preferentially on β grain boundaries after the 1 hour age but the α - β distribution has homogenized after 8 hours. Hardness for the eight hour, "peak aged" condition was approximately R_c 42 +/-1.2. Yield strengths corresponding to this aging condition are approximately 1205-1380 MPa [4,22].

Figure 1. Optical Micrographs of TIMETAL 21S aged at 538 °C for a)1hr and b)8hrs a) b)





Aged plate was machined into circumferentially notched tensile bars. Electrochemical pre-charging of hydrogen was conducted at 90° C, in a solution of 10ml sulfuric acid, 1000ml H $_2\text{O}$ and 0.8g sodium pyrophosphate. Machined specimens were cathodically polarized to 10 mA/cm^2 to promote hydrogen uptake and to provide cathodic protection [23]. Results of the hydrogen charging operations are summarized in Table I, as analyzed by thermal emission methods (LECO). It is important to note that egress of hydrogen while the specimen is exposed to air is significantly impeded for titanium due to the formation of an oxide film permeation barrier upon removal of specimens from the charging bath.

Table I. Summary of charging times and resulting hydrogen concentrations.

Charging Time	Total Hydrogen Concentration	Comment
As-received	50-100 ppm	"Low Hydrogen"
24 Hours	950-1750 ppm	"Medium hydrogen"
64 Hours	1900-3600 ppm	"High Hydrogen"

The effects of constraint on the failure stress and strain were investigated by employing Bridgman-type, circumferentially notched tensile bars to develop differing levels of net section triaxial constraint [24]. Constraint levels from 0.52 (0.33 = uniaxial tension) to 1.03 (2.5 = sharp notch) were investigated. Degree of embrittlement was quantified by determining the maximum longitudinal stress developed at the centerline of the notched region and the effective plastic strain across the notch diameter at maximum load [24-26]. Following the procedure of Hancock et. al. [25], maximum load

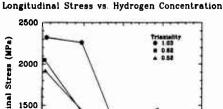
was used as the comparison point since uncharged bars failed after achieving a maximum load as well as experiencing a load decrease, while hydrogen charged bars consistently failed at maximum load.

Results/Discussion

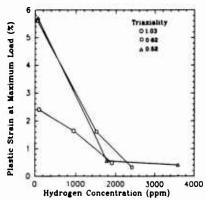
Mechanical Testing

For each constraint level investigated, hydrogen decreases the longitudinal stress developed at the centerline of the notch at maximum load and the effective plastic strain across the notch diameter. Both stress and strain decrease with increasing hydrogen concentration as shown in Figure 2. The hydrogen concentrations reported here were obtained from a section of each tensile bar near the notch and as such represent an average concentration for the volume of metal tested.

Figure 2. Effect of hydrogen on the a) stress and b) strain developed at maximum load for aged β 21S at room temperature. a) b)



Plastic Strain vs. Hydrogen Concentration



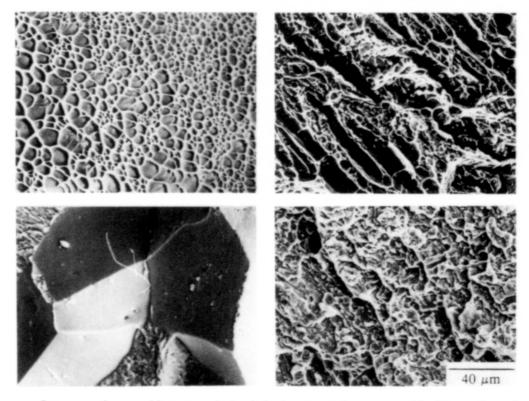
Maximum Longitudinal Stress (MPa) 1000 500 1000 2000 3000 4000 Hydrogen Concentration (ppm)

Interpretation of Fracture Paths

Four distinct fracture modes were observed as a function of hydrogen concentration and constraint as shown in Figure 3. Ductile fracture of uncharged specimens appear to follow void initiation, growth, and coalescence mechanisms. Large, equiaxed voids are often seen at globular (silicide-phosphide-type) inclusions which are connected by areas of finer voids oriented approximately 45° to the tensile axis. As hydrogen and constraint are increased to the "medium" levels investigated here, a second fracture mode (Transgranular 1) is triggered. This fracture mode, although containing regions which appear microscopically ductile, occurs with significantly less plasticity than uncharged specimens. The tearing features suggest that ductile separation of the α/β interfaces has occurred along with some trans-plate fracture. Hydrogen may segregate to these interfaces as a consequence of coherency strains or it may simply embrittle the surrounding & matrix. At similar constraint levels but higher hydrogen concentrations, the microscopic ductile tearing features disappear and a transgranular fracture mode containing small flat regions joined by ledges results (Transgranular 2). During this fracture process, the increased hydrogen content may embrittle the $\beta + \alpha$ structure to a

degree which precludes ductile tearing of α - β interfaces. Instead, transgranular fracture of the α and β phases results with very limited plasticity. Both transgranular modes might be expected with sufficient dissolved hydrogen based on the literature which reports a transgranular fracture appearance for both solutionized and aged Ti-15-3 as well as Ti-13-11-3 at room temperature [12,27]. Moreover, for both solutionized and aged Ti-15-3 and "aged and partially resolutionized by dissolved hydrogen" β 21S, the ductile to brittle transition temperature inherent to bcc metals is observed to increase above room temperature with dissolved hydrogen [27-28]. Such "lower shelf" behavior has apparently been achieved in the present study at 25 °C.

Figure 3. Fracture modes observed in peak aged TIMETAL 21S subjected to differing levels of hydrogen concentration and constraint. From top left clockwise, microvoid rupture, ductile tearing of α - β interfaces, transgranular fracture, intergranular fracture.



Intergranular cracking, seen in both hydrogen and aqueous chloride testing of aged TIMETAL 21S [19] appears to occur only at a high degree of triaxiality and hydrogen concentration. Preferential α precipitation at β grain boundaries (Figure 1) may provide a continuous path for localized hydriding and subsequent fracture. Although bulk hydriding of the α phase was not detected, it is possible that local hydriding of the α phase occurred at α/β interfaces [29]. Alpha titanium has a relatively small hydrogen solubility (approximately 80 ppm at 90°C) [30] and stress assisted hydriding in α and α - β alloys is well established [31,32]. Hydrogen accumulation at α/β interfaces, which serve either as trap sites or sites for local strain induced hydriding, could result in subsequent fracture along α - β interfaces. This multiple stage process is consistent with the intergranular crack bursting phenomena associated with a time for hydrogen accumulation [19]. Moreover, if the continuous grain boundary α is removed (as in TIMETAL 15-3 which does not exhibit preferential α precipitation along β grain

boundaries) β -titanium alloys may be resistant to EAC in aqueous chloride environments [19]. The absence of intergranular cracking of high hydrogen, high constraint notched tensile specimens of aged TIMETAL 15-3 will be confirmed in future work. While intergranular fracture processes may involve local hydriding of the preferentially nucleated, grain boundary α phase or trapping at α/β interfaces, it is important to note that overall hydrogen embrittlement of β titanium alloys is not contingent on bulk α hydriding as shown by the hydrogen embrittlement of solutionized β -Ti alloys [8-12].

Inspection of Table II reveals seemingly contradictory information. intergranular fracture mode occurs near the edge of the specimen where the triaxial stress is lowest according to Bridgman's analysis [24-26]. In contrast, a fracture mode apparently requiring intermediate fracture energy (transgranular) is observed near the specimen centerline. However, these results are consistent with a hydrogen concentration profile which decreases from edge to center. Such a concentration profile was verified through determinations of the B lattice parameter at various depths from the precharged surface. These results imply a hydrogen diffusion coefficient below 1.3 x 10⁻⁶ cm²/sec at 90 °C for aged TIMETAL 21S since a diffusion coefficient above this value would ensure completely uniform charging across the notch diameter in 24 hours, assuming diffusion controlled ingress. Holman et al., obtained the following relationship for hydrogen diffusion in solutionized Ti-13V-11Cr-3Al: $D = 1.58 \times 10^{-3} \exp(-5140 \pm$ 300 cal/mole / RT) [33]. This relationship yields a diffusion coefficient of 1.9x10⁻⁶ to 8.4x10⁻⁷ cm²/sec at 90 °C. Holman's result is in good agreement with Adler's work on the solution annealed β -Ti alloy Ti-8Mo-8V-2Fe-3Al which reported D = $\delta \pm 2 \times 10^{-7}$ cm²/sec at 25 °C [34]. It is clear from the present work that TIMETAL 21S has an apparent diffusion coefficient including a trapping effect of α precipitates, dislocation density, and other sites, which is significantly lower than solution annealed β -Ti alloys.

Table II. Fracture modes of a) near the edge and b) near the center of peak aged, notched, TIMETAL 21S tensile bars at room temperature.

a)	Degree of Constraint				
H Conc. (wt. ppm)	0.52	0.62	1.03		
Low (50-100)	Microvoid Rupture	Microvoid Rupture	Microvoid Rupture		
Medium (950-1750)	Transgranular 2 /Intergranular	Transgranular 2 /Intergranular	Transgranular 2 /Intergranular		
High (1900-3600)	Transgranular 2	Intergranular/ Transgranular 2	Intergranular/* Transgranular 2		
b)	Degree of Constraint				
H Conc. (wt. ppm)	0.52	0.62	1.03		
Low (50-100)	Microvoid Rupture	Microvoid + Transgranular 1	Microvoid Rupture		
Medium (950-1750)	Microvoid + Transgranular 1	Transgranular 1 + Microvoid	Transgranular 1°		
High (1900-3600)	Transgranular 2°	Transgranular 1	Transgranular 1		

^{*} Denotes case which is shown in Figure 3.

Despite, the non-uniform hydrogen concentration profile, the results shown in Table 2 point to the possibility of a critical stress - hydrogen concentration failure criterion. Although, the stress at the notch surface of the high constraint tensile bar is lower than the stress at the centerline by a factor of 0.59, the hydrogen concentration is appreciably greater. It is interesting to note that rising load fracture mechanics testing on β 21S in 3.5% NaCl produced discontinuous crack jumps of distances equal to two β grains (\approx 200 μ m) over time periods of several hours suggestive of diffusion controlled hydrogen transport in the fracture process zones [19]. The radial depth of the intergranular zone shown here was approximately 900 μ m after charging for 64 hours. Both results independently imply an apparent diffusion coefficient below 10^{4} cm²/second. Together, these results suggest that intergranular cracking is no longer favorable when a high hydrogen concentration does not exist in the fracture process zone over a distance equal to a multiple number of grains.

X-ray Diffraction Studies

Analysis of x-ray diffraction (XRD) data from peak aged TIMETAL indicates a B phase lattice parameter of 0.325 nm for uncharged material (\approx 75 ± 25 ppm), 0.328 for 24 hour charging (≈1400 ± 400 ppm) and 0.331 nm for 64 hour charging (≈2600 ± 800 ppm). Paton et al. correlated lattice parameter to hydrogen concentration in solution annealed Ti-18 Mo [35]. They obtained 0.328 and 0.331 nm at 1000 and 2100 ppm. respectively, in good agreement with the data presented here. No evidence of hydriding of the B phase was found. Regarding the possibility of hydriding of the a precipitate, xray diffraction analysis was conducted on (a) specimen surfaces, (b) several micrometers beneath the specimen surface, and (c) at a position as near as possible to the centerline of notched region of the high constraint, high hydrogen condition. The latter two conditions were achieved by surface grinding and sectioning, respectively. Neither a nor B phase hydride formation were detected at either (a), (b) or (c). Instead, peaks coinciding with the a phase are observed, except for immediately at the charged surface where neither the α phase nor its corresponding hydride are observed. Electron microscopic examination revealed that selective elimination of the α phase was due to spalling of the near surface a precipitates. Such spalling would be expected based on the volume change which occurs on hydriding [8,36]. To confirm the notion that surface a could be hydrided under the electrochemical conditions used here, commercially pure Ti was charged under identical conditions used for β 21S. Hydride formation was indeed confirmed by XRD. To summarize, our current findings suggest that hydriding of a precipitates occurs at the free surface but that hydriding of a large volume fraction of the subsurface α does not occur due to partitioning of hydrogen to the β phase.

Conclusions

Peak aged TIMETAL 21S is embrittled by hydrogen concentrations well below those required to hydride the β phase. Fracture path is a function of both level of constraint and hydrogen concentration. Approximate ranking of fracture modes from toughest to most brittle is: microvoid rupture, transgranular tearing of α - β interfaces, transgranular fracture through the α - β microstructure, and intergranular fracture. Intergranular fracture was only produced at the highest constraint and hydrogen concentrations. Preferential α precipitation on β grain boundaries is suggested to have a detrimental role on HEAC since transgranular cleavage cracking is more typically observed for solutionized β . Alpha precipitates within the β matrix may hydride locally at α/β interfaces although no evidence of this was detected. Alternatively the α/β interface may serve as a trap site whose strength increases with increasing hydrogen concentration due to increased coherency strain. The resulting intergranular fracture

morphology in the case of high hydrogen-high constraint, tensile specimens is similar to that observed in 3.5% NaCl at -600 mV, suggesting a hydrogen assisted mechanism for the latter.

Acknowledgements

This research was supported by the Office of Naval Research (Grant N00014-91-J-4164) with Dr. A. John Sedricks as Scientific Monitor and by the Virginia Center for Electrochemical Science and Engineering at the University of Virginia. Material was donated by the Titanium Metals Corporation. The authors wish to acknowledge the helpful discussions with L.M. Young, R.P. Gangloff, D.G. Kolman, and B.P. Somerday.

References

- [1] H. G. Nelson, "Hydrogen Environment Effects on Advanced Alloys and Composites in Aerospace Structures", in <u>First Thermal Structures Conference</u>, E. Thornton, ed., Nov 13-15, The University of Virginia, Charlottesville, VA 22903, pp. 301-311 (1990).
- [2] P.J. Bania, G.A. Lenning and J. A. Hall, "Development and Properties of Ti-15V-3Cr-3Sn-3Al (Ti-15-3)", in <u>Beta Titanium Alloys in the 80's</u>, R.R. Boyer and H.W. Rosenberg eds., TMS-AIME, Warrendale, PA, pp. 209-229, (1983).
- [3] A.G. Hicks and H. W. Rosenberg, "Ti-15-3 Foil Properties and Applications", in <u>Beta Titanium Alloys in the 80's</u>, R.R. Boyer and H.W. Rosenberg eds., TMS-AIME, Warrendale, PA, pp. 231-238, (1983).
- [4] P.J. Bania and W.M. Parris, "BETA-21S: A High Temperature Metastable Beta Titanium Alloy", presented at the Titanium Development Association International Conference, Orlando, FL (1990).
- [5] T.W. Duerig and J.C. Williams, "Overview: Microstructure and Properties of Beta Titanium Alloys", in <u>Beta Titanium Alloys in the 80's</u>, R.R. Boyer and H.W. Rosenberg, eds., TMS-AIME, Warrendale, PA, pp. 19-67, (1983).
- [6] R.W. Schutz and D.E. Thomas, "Corrosion of Titanium and Titanium Alloys", in Metals Handbook, 9th edition, Vol. 13, ASM International, Metals Park, Ohio 44073, pp.669-706, (1987).
- [7] A.D. McQuillan, "An Experimental and Thermodynamic Investigation of the Hydrogen-Titanium System", *Proceedings of the Royal Society of London.*, Vol. A204, pp. 309-323 (1950).
- [8] D.S. Shih, and H.K. Birnbaum, "Evidence of FCC Titanium Hydride Formation in β Titanium Alloy: An X-Ray Diffraction Study", Scripta Met., Vol 20, pp 1261-1264, (1986).
- [9] J.J. DeLuccia, "Electrolytic Hydrogen in Beta Titanium", Report No. NADC-76207-30, Naval Air Development Center, Warminster, PA 1976.
- [10] J.S. Grauman, "A New High Strength, Corrosion Resistant Titanium Alloy", (Paper presented at the Titanium Development Association International Conference, Orlando, FL 1990).
- [11] W.W. Gerberich et al., "Hydrogen in α/β and all β Titanium Systems", <u>Hydrogen Effects in Metals</u>, I.M. Bernstein and A.W. Thompson eds, TMS-AIME, Warrendale, PA, pp. 731-745 (1981).
- [12] K. Nakasa and J. Liu, "Bending Strength of Hydrogen Charged Ti-13V-11Cr-3Al Alloy", K. Koshiya translator, J. Japan Inst. Metals, Vol. 55, No. 9, pp. 922-927, (1991).
- [13] N.E. Paton and O. Buck, in <u>Effect of Hydrogen Behavior of Materials</u>. I.M. Bernstein and A.W.Thompson, eds., TMS-AIME, Warrendale, PA, pp. 83-89, (1975).
- [14] N.E. Paton, R.A. Spurling and C.G. Rhodes, in <u>Hydrogen Effects in Metals</u>, I.M.Bernstein and A.W.Thompson, eds., TMS-AIME, Warrendale, PA, pp.269-279, (1981).
- [15] J.E. Costa, D. Banerjee, and J.C. Williams, "Hydrogen Effects in \$-Titanium

Alloys", in <u>Beta Titanium Alloys in the 80's</u>, R.R. Boyer and H.W. Rosenberg, eds., TMS-AIME, Warrendale, PA, pp. 69-84, (1983).

[16] D.E. Thomas and S.R. Seagle, "Stress Corrosion Cracking Behavior of Ti-38-6-44 in Sour Gas Environments", <u>Titanium Science and Technology</u>, Vol. 4, G.Lutjering, U.

Zwicker, and W. Bunk, eds., pp. 2533-2540, (1984).

[17] M.J. Blackburn and W.H. Smyrl, "Stress Corrosion and Hydrogen Embrittlement", Titanium Science and Technology, R.I. Jaffee and H.M. Burte, eds., New York, NY, pp. 2577-2609, (1973).

[18] H.G. Nelson, "Aqueous Chloride Stress Corrosion Cracking of Titanium - A Comparison with Environmental Hydrogen Embrittlement", Hydrogen in Metals, I.M.

Bernstein and A.W. Thompson, eds., pp. 445-464, (1973).

[19] L.M. Young and R.P. Gangloff, "Hydrogen Environment Embrittlement of Beta Titanium Alloys", to be published in <u>Proceedings of the Seventh World Conference on Titanium</u>, F.H. Froes, ed., TMS-AIME, Warrendale, PA (1992).

[20] D.N. Fager and W.F. Spurr, "Some Characteristics of Aqueous Stress Corrosion in

Titanium Alloys", Trans. ASM, Vol. 61, (1968).

[21] R.P. Gangloff and J.R. Scully, "Mechanisms for the Environmental Cracking Resistance of High Strength Titanium Alloys", Proposal No. MS-DOD/ONR-4956-91, University of Virginia, Charlottesville, VA, (1991).

[22] L.M. Young, Unpublished Research, The University of Virginia, (1992).

[23] Z.A. Foroulis, "Factors Influencing Absorption of Hydrogen in Titanium from Aqueous Electrolytic Solutions", <u>Titanium 80. Science and Technology</u>, H. Kimura and O. Izumi eds., TMS-AIME, Kyoto, Japan, pp. 2705-2711 (1980).

[36] J. Liu and K. Nakasa, "Surface Peeling of Ti-6Al-4V Alloy Specimens during Hydrogen Charging", J. Japan Inst. Metals, Vol. 54, No. 11, pp. 1261-1269, (1990).

[24] P.W. Bridgman, Studies in Large Plastic Flow and Fracture, McGraw-Hill Book Company, Inc., New York, NY, (1952).

[25] J.W. Hancock and A.C. Mackenzie, "On the Mechanisms of Ductile Failure in High-Strength Steels Subjected to Multi-Axial Stress-States", *J.Mech. Phys. Solids*, Vol. 24, pp. 147-169, Pergamon Press, (1976).

[26] A.C. Mackenzie, J.W. Hancock, and D.K. Brown, "On the Influence of Stress on Ductile Failure Initiation in High Strength Steels", *Engineering Fracture Mechanics*, Vol. 9, pp. 167-188, (1977).

[27] K. Nakasa, Personal Communication, 1 September 92.

[28] R. Lederich, McDonnell Douglas Corp., Personal Communication, September 1992.

[29] D.N. Williams, "The Hydrogen Embrittlement of Titanium Alloys", J. Inst. Met., Vol. 91, pp. 147-152, (1962).

[30] R.S. Vitt and K. Ono, "Hydrogen Solubility in Alpha Titanium", Met. Trans., Vol. 2, (1971).

[31] H. Margolin, "Stress, Hydrogen Segregation, and Fracture in α - β Titanium Alloys", *Met. Trans*, Vol. 7A, pp. 1233-1235, (1976).

[32] J.D. Boyd, "Precipitation of Hydrides in Titanium Alloys", *Trans. ASM*, pp. 977-988, (1969).

[33] W.R. Holman, R.W. Crawford, and F. Paredes, Jr., "Hydrogen Diffusion in a Beta Titanium Alloy", Trans. AIME, Vol. 22, pp. 1836-1939, (1965).

[34] P.N. Adler and R.L. Schulte, "Stress Induced Hydrogen Migration in β Phase Titanium", Scripta Met., Vol. 12, pp. 669-672, (1978).

[35] N.E. Paton, O. Buck, and J.C. Williams, "The Effect of Hydrogen on the Strength, Modulus and Lattice Parameter of a Ti-Mo Alloy", *Scripta Met.*, Vol. 9, pp. 687-691, (1975).

HYDROGEN ENVIRONMENT EMBRITTLEMENT OF BETA TITANIUM ALLOYS

Lisa M. Young and Richard P. Gangloff

Department of Materials Science and Engineering
University of Virginia
Charlottesville, VA 22903-2442

ABSTRACT

The environment assisted cracking (EAC) resistance of two peak aged metastable β -titanium alloys, Beta 21S and Ti-15-3, is characterized by a fracture mechanics resistance-curve method. Rising load experiments in aqueous 3.5% NaCl at -600 mV_{ace} show that Beta 21S is susceptible to environmental cracking. Relative to a moist air crack initiation toughness (plane strain $K_{\rm IC}$) of 67 MPa/m with transgranular fracture, the threshold for stable crack growth ($K_{\rm TH}$) in chloride is as low as 38 MPa/m and fracture occurs by intergranular separation. The reduction from $K_{\rm IC}$ to $K_{\rm TH}$ mildly depends on loading rate; $K_{\rm TH}$ for Beta 21S appears to be minimized at crack tip strain rates between 10^{-5} sec⁻¹ and 10^{-4} sec⁻¹; cracking in chloride is discontinuous in this regime. In contrast the moist air initiation toughness of Ti-15-3 is lower (58 MPa/m) than that of Beta 21S, but is unaffected by exposure to NaCl at several loading rates where $K_{\rm TH}$ equals $K_{\rm IC}$. The reduced EAC resistance of Beta 21S, compared to Ti-15-3, is attributed to abundant α precipitation at β grain boundaries, and perhaps to higher yield strength for the former alloy. The mechanistic contributions of localized dissolution, film rupture and hydrogen embritlement are not determined, however, the latter is suspected for EAC of Beta 21S.

INTRODUCTION

High strength β -titanium alloys are susceptible to brittle environment assisted cracking (EAC) in ambient temperature halide ion solutions. Fracture mechanics experiments demonstrate that early developmental alloys (Ti-11.5Mo-6Zr-4.5Sn and Ti-13V-11Cr-3Al; wt%) and binary model compositions (Ti-Mo), stressed in NaCl and KCl solutions, exhibit stable crack growth at stress intensities (K) well below the plane strain fracture toughness, $K_{\rm KC}$ [1-3]. Environmental fracture progresses by intergranular separation and transgranular "cleavage" or "quasi-cleavage"; the cleavage plane is {1.0} [2]. Cracking in neutral NaCl is exacerbated at intermediate loading rates (crack tip strain rates) and applied electrode potentials (near -600 mV_{SCE}), by increased yield strength (σ_{yz}) , and by cathodic polarization with H₂S addition [1,3-6]. Relative to steels and α/β -titanium alloys, environmental cracking in β -titanium alloys is poorly characterized and understood.

It is reasonable to attribute cracking of β -titanium alloys in aqueous electrolytes to hydrogen embrittlement (hydrogen environment assisted cracking, HEAC) because of the extreme hydrogen susceptibility of high strength body-centered cubic steels [7], because both gaseous hydrogen and cathodically precharged hydrogen embrittle β -titanium alloys [8,9], and by analogy with HEAC in α/β -titanium alloys [10]. The HEAC mechanism for β -titanium alloys in neutral chloride involves: (a) development of an occluded crack electrochemistry, (b) coupled crack surface dissolution, passive film formation and cathodic H production, (c) film rupture, (d) hydrogen absorption and diffusion into the crack tip process zone, (e) segregation at microstructural trap sites, and (f) hydrogen assisted microcracking, probably

Titanium '92 Science and Technology Edited by F.H. Froes and I. Caplan The Minerals, Metals & Materials Society, 1993 by decohesion, localized plasticity or hydride mechanisms. The crack surface passive film should play a central role in HEAC, with a sound film blocking hydrogen production and/or uptake. Many factors; including alloy composition, microstructure, applied electrode potential, bulk electrolyte composition, slip deformation mode, and dynamic cyclic strain; could compromise the passive film and enhance the uptake of embrittling hydrogen.

Research was initiated to investigate surface passivity and localized dissolution in addition to hydrogen production, uptake, trapping and embrittlement in the crack tip region of high strength β -titanium alloys in aqueous marine environments [11]. The objective of the work reported here is to characterize the EAC behavior of two modern β -titanium alloys, subjected to dynamic straining to destabilize crack tip passivity, and employing advanced fracture mechanics methods.

EXPERIMENTAL PROCEDURE

Two alloys, Beta 21S (Ti-15Mo-2.7Nb-3Al-0.2Si-0.15 O; wt%) and Ti-15-3 (Ti-15V-3Cr-3Al-3Sn; wt%), were obtained as 10.2 and 9.5 mm thick hot rolled plate, respectively, in the solution treated conditions (871°C for 8 hours and 816°C for 30 minutes, respectively). Oversized blanks of each alloy were peak aged at 538°C for 8 hours. The resultant microstructures are homogeneous and isotropic in all directions, and consist of fine α platelets in a β matrix of 100 μ m diameter grains, as illustrated for Beta 21S in Fig. 1. The optical microstructure of Ti-15-3 is identical to that shown in Fig. 1, with the exception of differences in grain or near-grain boundary α precipitation (see Discussion). Each alloy is presumed to be stable with regard to ω and β ' precipitation. Measured yield strengths from replicate specimens of this aging condition are 1380 MPa (R_c 42.5 \pm 1.3) for Beta 21S and 1315 MPa (R_c 36.9 \pm 1.3) for Ti-15-3.

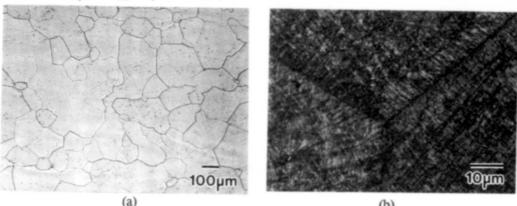


Figure 1: Optical micrographs of Beta 21S in the: (a) as-received solution annealed and (b) peak aged conditions.

EAC resistance was characterized with a slowly rising load fracture mechanics method applied to the fully rotating single edge precracked specimen (SEN; nominal crack length = 17.8 mm, thickness = 5.08 mm, width = 38.1 mm) [12-14]. A servohydraulic machine was employed for fatigue precracking (load control with K_{max} less than 30 MPa/m) and rising load cracking (actuator displacement control). Specimens were precracked in the aqueous environment, then fractured under rising load. Crack length was monitored using a computer-automated direct current (applied current = 2 to 4 amperes) potential difference (DCPD) method, including current polarity switching to eliminate thermal voltages and a reference probe pair to account for temperature and current variations during prolonged

experiments [15]. Measured voltages were related to crack length through Johnson's analytical equation for the SEN specimen. Applied stress intensity was calculated from load and crack length with a standard elastic solution [16], and plotted as a function of crack extension increment (Δa). The threshold K for crack growth initiation ($K_{\rm IC}$ in air and $K_{\rm TH}$ for aggressive environments) was calculated from the applied load at the first change in the slope of the initially linear electrical potential versus load record; Δa is assumed to equal zero prior to this point [17]. While ASTM Standard E399 was not adhered to for $K_{\rm IC}$ [18], crack initiation occurred under plane strain constraint based on the J-integral approach (thickness and ligament > 25 $J_{\rm initiation}/\sigma_{yz}$) [12,13,19]. Since small scale yielding was maintained for all cases, the contribution of $J_{\rm plastic}$ to K was negligible and assumed to equal zero. Environmental effects on crack propagation under increasing K are indicated by the slope of the K- Δa data. Shear walls, present after initiation, indicate that the crack propagated under mixed plane strain and plane stress.

Fracture experiments were conducted in either moist air or 0.6M (3.5 wt%) NaCl at fixed electrode potential, near-neutral pH of 7, and 25°C. The central portion of the edge cracked specimen was immersed in flowing (60 ml/min) chloride (pH 8, 23°C) in a sealed plexiglass chamber. The specimen was maintained at constant potential by a Wenking potentiostat in conjunction with a Ag/AgCl reference electrode and two platinum counter electrodes, each isolated to minimize solution contamination.

RESULTS

Ti-15-3 is resistant to EAC during rising load at various slow displacement rates; these conditions promote HEAC in ferritic and martensitic steels exposed to NaCl [7]. K- Δ a results are presented in Fig. 2. For benign moist air, the initiation toughness (K_{IC}) of Ti-15-3 is 57 and 59 MPa/m based on replicate experiments. For aqueous chloride at a fixed potential of -600 mV_{sce}, K_{TH} ranges from 61 to 65 MPa/m, independent of actuator displacement rate varying between 25 and 0.25 μ m/min. The chloride environment does not degrade the crack initiation toughness. For each environment, some stable crack extension is observed (dK/d Δ a > 0), however, this tearing resistance is not environmentally influenced. The difference in dK/d Δ a is larger for the replicate air tests compared to the aqueous environmental effect; actuator displacement rate does not affect the EAC propagation resistance of Ti-15-3.

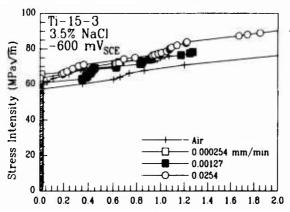


Figure 2: Rising load stress intensity versus crack extension data for Ti-15-3 in moist air and deaerated 3.5% NaCl (-600 mV_{see}) as a function of loading rate.

 $\Delta a (mm)$

The variability of the crack propagation results for moist air may be related to subtle inaccuracies in defining the electrical potential corresponding to crack initiation. The problem is that crack tip plastic deformation, microvoid damage and macrocrack growth can contribute to voltage increases. Discontinuous crack bursts were indicated by measured DCPD, but only for the aqueous environment and not moist air.

Environment did not influence the microscopic fracture morphology for Ti-15-3. Typical scanning electron fractographs of the crack initiation region, adjacent to the fatigue precrack, are presented in Fig. 3 for air and aqueous NaCl. For each case, the crack surface is mainly populated by transgranular features indicative of microvoid-based cracking, as confirmed by high magnification observation. Scattered facets are present, indicating limited intergranular microvoid rupture; intergranular EAC is not likely for Ti-15-3 because similar facets are observed for cracking in NaCl, moist air and ultra-high vacuum.

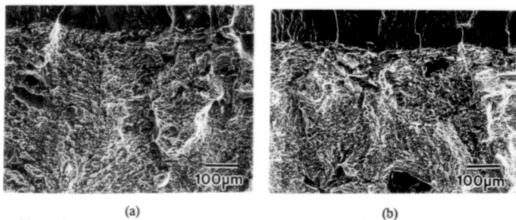


Figure 3: SEM fractographs of the fatigue precrack (top) and rising load fracture toughness crack surfaces in Ti-15-3: (a) air; (b) deaerated 3.5% NaCl.

In contrast to Ti-15-3, Beta 21S is embrittled by aqueous chloride at -600 mV_{∞ e}, as shown by the K- Δ a data in Fig. 4. While K_{IC} is high (66 and 68 MPa/m) for moist air, K_{TH} values range from 38 to 51 MPa/m for Beta 21S in NaCl at -600 mV_{∞ e}. The macroscopic

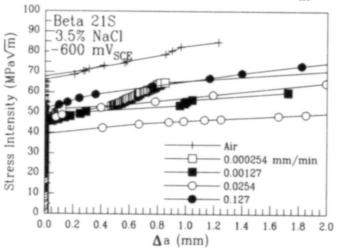


Figure 4: Rising load stress intensity versus crack extension data for Beta 21S in moist air and deaerated 3.5% NaCl (-600 mV_{sce}) as a function of loading rate.

crack growth resistances (average $dK/d\Delta a$) are similar for each environment. Aqueous NaCl caused a dramatic fracture mode transition. The fractographs in Fig. 5 show that, while the air crack appears to involve intergranular microvoid fracture (with limited tear-free facets), the chloride case is almost entirely intergranular with little evidence of resolvable localized plasticity.

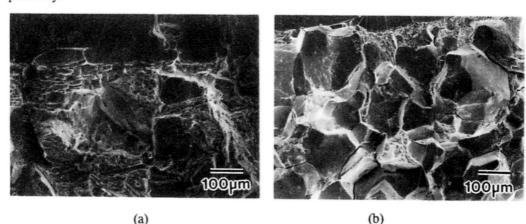


Figure 5: SEM fractographs of the fatigue precrack (top) and rising load fracture toughness crack surfaces in Beta 21S: (a) air; (b) deaerated 3.5% NaCl.

Actuator displacement rate mildly affects K_{TH} for EAC of Beta 21S in NaCl. Whille obscured by variability for replicate experiments at 25.4 μ m/min and a recently measured high value ($K_{TH} = 52$ MPa/m) at 12.7 μ m/min, K_{TH} appears to be broadly minimized at displacement rates between 0.6 and 6 μ m/min. Additional experiments are in progress to define the strain rate dependence of HEAC. Recent results suggest that K_{TH} equals K_{IC} at high loading rates and that crack growth is not observed for static loading (24 hours) at K levels up to 60 MPa/m. Crack bursts were observed for Beta 21S in NaCl, but only for the two slowest loading rates. Bursts were large (50 to 300 μ m) and occurred at about five hour intervals. Discontinuous cracking, below 20 μ m bursts, would not be resolved by DCPD.

DISCUSSION

Fracture Toughness: Moist Air The moist air fracture toughnesses of Ti-15-3 ($K_{IC} = 57$ to 59 MPa/m) and Beta 21S ($K_{IC} = 66$ to 68 MPa/m) are comparable to values reported for β-titanium alloys at similar yield strengths [20-22]. This agreement suggests that the DCPD-based K- Δ a approach accurately characterizes plane strain fracture toughness in spite of small specimen thickness compared to the requirement of Standard E399 [18].

The fracture toughness of Beta 21S is superior to that of Ti-15-3, particularly considering the higher yield strength of the former. This is curious because cracking of Beta 21S in air appears to involve grain boundary microvoiding. Beta 21S contains substantial α precipitates at or near β grain boundaries, a microstructure that is not observed for Ti-15-3. Lee et al. and Froes et al. report that K_{IC} is degraded by grain boundary α [21,22]. Localized plastic deformation in low strength α results in strain concentration and microvoid nucleation at α/β interfaces near β grain boundaries. The fracture toughness of Beta 21S may be further improved by processing to eliminate α precipitates at β grain boundaries.

Environmental Cracking Resistance K_{TH} for HEAC of the 1350 MPa yield strength level of tempered martensitic steels in aqueous chloride varies between 12 MPa/m and 38 MPa/m, but typically equals 25 MPa/m, depending on metallurgical and mechanical variables [7].

The EAC resistances of high strength Beta 21S and particularly Ti-15-3 are good compared to such steels, consistent with previous results [23]. Ti-15-3 may be embrittled by more aggressive hydrogen producing environments, for example acidified NaCl with sulfide addition and cathodic polarization [1,5-7]. Additional experiments are in progress and include longer exposure times, a range of loading rates and applied electrode potentials, in addition to low amplitude ripple loading [24].

The rising load EAC results do not, in isolation, define the embrittlement mechanism for the β -titanium alloys; this is being examined in parallel studies [8,24,25]. Two points are notable. Intermittent crack bursts, over distances greatly in excess of the crack tip process zone and on the order of one to five grain diameters, suggests HEAC with a strong role of grain boundary traps. Intergranular cracking is a classic damage mechanism for hydrogen embrittled steels [7]. The extent to which predissolved hydrogen degrades $K_{\rm IC}$ during rising loading and produces intergranular cracking is being determined for comparison with the EAC behavior of Beta 21S and Ti-15-3 in NaCl [25].

It is important to understand the different EAC sensitivities of Ti-15-3 and Beta 21S. Assuming HEAC, the resistance of Ti-15-3 may be explained by yield strength. Modeling and experiment show that lower strength steels are less susceptible to HEAC, particularly for NaCl and strengths below 1500 MPa [7]. The expected yield strengths of Beta 21S and Ti-15-3 are 1210 MPa and 1010 MPa, respectively, for the eight hour age at 538°C [23,26], suggesting better HEAC resistance for Ti-15-3. Gagg and Toloui report that Ti-15-3, aged at 510°C for six hours (ultimate tensile trength = 1260 MPa and $\sigma_{ye} \approx 1200$ MPa), is embrittled during slow strain rate loading of smooth tensile specimens in several chloride solutions [5]. These σ_{ye} values are substantially less than the measured strengths of the two alloys studied here; the reason is undetermined. A strong yield strength effect on K_{TH} is not likely because of the small measured strength difference between Beta 21S and Ti-15-3. Additional work is, however, required because of the unexpectedly high values of σ_{ye} .

The relative HEAC behaviors of Ti-15-3 and Beta 21S are not explained by occluded crack solution hydrogen production and uptake [11]. Cr and V solute in the β phase of Ti-15-3 should dissolve and hydrolyze at -600 mV_{sce} to produce a more acid crack tip pH compared to Beta 21S which contains Mo and Nb. Mo should promote crack tip passivity and hinder hydrogen uptake. These hypothesis are not consistent with the measured HEAC resistances of the two alloys.

It is reasonable to speculate that Beta 21S is sensitive to intergranular EAC in NaCl because of extensive α precipitation at or near beta grain boundaries. This microstructure was not observed for Ti-15-3, as demonstrated by interrupted aging (2 hours at 538°C); Fig. 6. Whether very fine α is present at Ti-15-3 boundaries must be determined by electron microscopy. Gagg and Toloui did not report the microstructure or the solution treatment conditions of Ti-15-3 that was embrittled by NaCl [5]. The Beta 21S microstructure may be environment sensitive because a brittle continuous hydride film forms in hcp α -titanium and at α/β interfaces [1,27,28]. Intergranular cracking may also be traced to hydrogen trapping at α/β interfaces, to localized plastic deformation in the soft α that produces stress/strain concentrations that interact with embrittling hydrogen, or to local dissolution of α . Either cold rolling of Beta 21S prior to aging, or restricted recovery and recrystallization during hot rolling and solution treatment, should provide distributed intragranular nucleation sites for α precipitates, apart from β grain boundaries [29]. The more homogeneous microstructure should be resistant to HEAC [1].

EAC and HEAC depend on strain rate. For NaCl, embrittlement is maximum at an intermediate strain rate of order 6 x 10^{-6} sec⁻¹ for β Ti-15-3 and 2 x 10^{-3} sec⁻¹ for α/β Ti-6Al-4V [1,5,10,30]. For Beta 21S in NaCl, the mild minimum in K_{TH} (Fig. 3) occurs at an

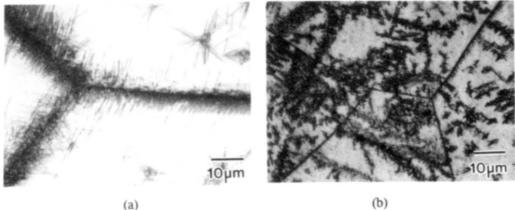


Figure 6: Optical micrographs of underaged (a) Beta 21S and (b) Ti-15-3.

estimated crack tip strain rate of between 10^{-5} and 10^{-4} sec⁻¹, corresponding to actuator displacement rates of 0.6 and $6 \mu m/min$ and constant loading rates of 15 and 150 N/min. It is not possible to quantitatively compare smooth specimen and crack tip strain rates because the former is typically not measured or maintained constant [5]. Crack tip strain rate varies with distance into the process zone and is not accurately known [31]. (The above strain rates were calculated at a distance of one blunted crack tip opening displacement ahead of the crack tip.) From the HEAC perspective, embritlement may be most severe at the strain rate that balances surface film destabilization and hydrogen uptake (promoted by increased rate) with the time necessary for hydrogen diffusion into the crack tip process zone (promoted by decreased rate). The kinetics of each process are not defined.

CONCLUSIONS

- The threshold stress intensity for stable crack propagation in Beta 21S is significantly reduced by simultaneous slow loading and exposure to aqueous NaCl at -600 mV_{sce}. Cracking in chloride is intergranular compared to grain boundary and transgranular microvoid processes for moist air, and is possibly by hydrogen embrittlement.
- The crack initiation fracture toughness and microscopic fracture processes of Ti-15-3
 are unaffected by chloride environment exposure for several slow constant actuator
 displacement rates.
- 3. The EAC susceptibility of Beta 21S and the resistance of Ti-15-3 are explained by copious α precipitation at β grain boundaries and the high yield strength of the former alloy.
- The chloride environmental cracking thresholds of Ti-15-3 and Beta 21S are superior to the behavior of tempered martensitic steels at equal yield strength.
- Dynamic loading rate affects EAC in Beta 21S; K_{TH} for crack growth in NaCl may be minimized at a crack tip strain rate between 10⁻⁵ and 10⁻⁴ sec⁻¹.

ACKNOWLEDGEMENTS

This research was supported by the Office of Naval Research (Grant N00014-91-J-4164) with Dr. A. John Sedriks as Scientific Officer, and by the Virginia CIT Center for Electrochemical Science and Engineering at the University of Virginia. Material was donated by the Titanium Metals Corporation. This support is gratefully acknowledged, as are informative discussions with Dr. J.R. Scully and Messrs G.A. Young and D.G. Kolman.

REFERENCES

- M.J. Blackburn, J.A. Feeney, and T.R. Beck, in <u>Advances in Corrosion Science and Technology</u>, M.G. Fontana and R.W. Staehle, eds., Vol. 3, Plenum Publishing, NY, NY, pp. 67-292, 1972.
- 2. D.N. Fager and W.F. Spurr, Trans. ASM, Vol. 61, pp. 283-292, 1968.
- 3. J.A. Feeney and M.J. Blackburn, Met. Trans., Vol. 1, pp. 3309-3323, 1970.
- Corrosion: Metals Handbook, Vol. 13, Edition 9, ASM International, Metals Park, OH, pp. 483-485, 1987.
- 5. C. Gagg and B. Toloui, in Sixth World Conference on Titanium, pp. 545-550, 1988.
- D.E. Thomas and S.R. Seagle, in <u>Titanium Science and Technology</u>, Vol. 4, G. Lutjering, U. Zwicker and W. Bunk, eds., pp. 2533-2540, 1984.
- R.P Gangloff, in <u>Corrosion Prevention and Control</u>, M. Levy and S. Isserow, eds., US Army Laboratory Command, Watertown, MA, pp. 64-111, 1986.
- N.E. Paton, R.A. Spurling and C.G. Rhodes, in <u>Hydrogen Effects in Metals</u>, I.M. Bernstein and A.W. Thompson, eds., TMS-AIME, Warrendale, PA, pp. 269-279, 1981.
- W.W. Gerberich, N.R. Moody and C.L. Jensen, in <u>Hydrogen Effects in Metals</u>, I.M. Bernstein and A.W. Thompson, eds., TMS-AIME, Warrendale, PA, pp. 731-745, 1981.
- H.B. Nelson, in <u>Hydrogen in Metals</u>, I.M. Bernstein and A.W. Thompson, eds., ASM International, Metals Park, OH, pp. 445-464, 1974.
- R.P. Gangloff and J.R. Scully, "Mechanisms for the Environmental Cracking Resistance of High Strength Titanium Alloys", Proposal MS-DOD/ONR-4956-91, University of Virginia, Charlottesville, VA, 1991.
- D.R. Anderson and J.P. Gudas, in <u>Environment Sensitive Fracture: Evaluation and Comparison of Test Methods</u>, ASTM STP 821, S.W. Dean, E.N. Pugh and G.M. Ugiansky, eds., ASTM, Philadelphia, PA, pp. 98-113, 1984.
- E.M. Hackett, P.J. Moran and J.P. Gudas, in <u>Fracture Mechanics: Seventeenth Volume. ASTM STP 905</u>,
 J.H. Underwood, et al., eds., ASTM, Philadelphia, PA, pp. 512-541, 1986.
- 14. R.A. Mayville, T.J. Warren and P.D. Hilton, Trans. ASME, Vol. 109, pp. 188-193, 1987.
- J.K. Donald and J. Ruschau, in <u>Fatigue Crack Measurement: Techniques and Applications</u>, K.J. Marsh, R.A. Smith and R.O. Ritchie, eds., EMAS, Ltd., West Midlands, UK, pp. 11-37, 1991.
- 16. H. Tada, P.C. Paris and G.R. Irwin, The Handbook, Del Research Corp., St. Louis, MO, p. 2.11, 1985.
- 17. P. Doig and K.R. Abbott, J. Test. Eval., Vol. 12, pp. 297-304, 1984.
- "Standard Test Method for Plane Strain Fracture Toughness of Metallic Materials", ASTM Standard E399-90, Annual Book of ASTM Standards, Vol. 03.01, ASTM, Philadelphia, PA, pp. 506-536, 1992.
- "Standard Test Method for J_{IC}, A Measure of Fracture Toughness", ASTM Standard E813-89, <u>Annual Book of ASTM Standards</u>, Vol. 03.01, ASTM, Philadelphia, PA, pp. 732-746, 1992.
- 20. R.R. Boyer, J. Metals, March, pp. 61-65, 1980.
- C.S. Lee, S.J. Kim, C.G. Park and Y.W. Chang, "Effect of Microstructural Variation on the Mechanical Properties of Ti-10V-2Fe-3Al", Unpublished Research, 1992.
- F.H. Froes, J.C. Chesnutt, C.G. Rhodes and J.C. Williams, in <u>Toughness and Fracture Behavior of Titanium</u>, ASTM STP 651, ASTM, Philadelphia, PA, pp. 115-153, 1978.
- P.J. Bania, G.A. Lenning, and J.A. Hall, in <u>Beta Titanium Alloys in the 80's</u>, R.R. Boyer and H.W. Rosenberg, eds., TMS-AIME, Warrendale, PA, pp. 209-229, 1983.
- L.M. Young, "Marine Environmental Cracking of High Strength Beta Titanium Alloys", MS Thesis, University of Virginia, Charlottesville, VA, in preparation, 1992.
- 25. G.R. Young and J.R. Scully, Unpublished Research, University of Virginia, Charlotterville, VA, 1992.
- P.J. Bania and W.M. Parris, "Beta-21S: A High Temperature Metastable Beta Titanium Alloy", presented at the 1990 TDA International Conference, Orlando, FI, 1990.
- T.W. Duerig and J.C. Williams, in <u>Beta Titanium Alloys in the 80's</u>, R.R. Boyer and H.W. Rosenberg, eds., TMS-AIME, Warrendale, PA, pp. 19-67, 1983.
- J.E. Costa, D. Banerjee and J.C. Williams, in <u>Beta Titanium Alloys in the 80's</u>, R.R. Boyer and H.W. Rosenberg, eds., TMS-AIME, Warrendale, PA, pp. 69-84, 1983.
- J.C. Williams, in <u>Titanium Science and Technology</u>, R.I. Jaffee and H.M. Burte, eds., TMS-AIME, New York, pp. 1433-1494, 1973.
- 30. J.A. Muskovitz and R.M. Pelloux, Corrosion, Vol. 35, pp. 509-514, 1979.
- W.W. Gerberich and S. Chen, in <u>Environment Induced Cracking of Metals</u>, R.P. Gangloff and M.B. Ives, eds., NACE, Houston, TX, pp. 167-187, 1990.

A Study on the Anodic Behavior of Titanium And

Some Ti Alloys in Hot Acid NaCl Solution Yongxin Zhao

China Environmental Protection Co. Beijing 100081, P. R. China

> Fuxing Gan, Iau-an Yao Wuhan University Hubei 430072, P. R. China

Abstract

The anodic behavior of Ti and Ti alloys (Ti-0.3Mo-0.8Ni, Ti-6Al-4V and Ti-0.2Pd) in hot acid NaCl solution was studied. By investigating the effects of pH, Cl ions, temperature, Ti(II) and Ti(IV) ions as well as dissolved oxygen on anodic behavior of Ti, we obtained three experimental equations relating critical passivation current density (i_m) to pH, Cl and temperature (T) respectively as follows:

dlog $i_m/dpH = -1.5$; dlog $i_m/dlog(Cl^-) = 1.0$; log $i_m = A - 4.29 \times 10^3/T$.

According to the experimental results, a mechanism for active dissolution-passivation of Ti in this solution has been suggested.

Introduction

A considerable amount of work has been done on the anodic behavior of Ti and Ti alloys in strong acid solutions of HCl, H₂SO₄, etc. and several dissolution-passivation mechanisms of Ti have been estabilished in terms of their experiments(1-8). However, there are a few investigations about the anodic behavior of Ti and Ti alloys in hot acid NaCl solutions. For this reason, this note, using electrochemical methods, was undertaken in order to study in more detail on the anodic behavior of Ti alloys and the effects of some factors in hot acid NaCl solution. On the bases of results, an anodic dissolution-passivation mechanism of Ti in this solution has been proposed. All of which would provide bases for titanium alloys used in chemical industry, desalination of seawater and long-term disposals nuclear fuel wastes, etc.

Experimental

The electrodes used for the experiments were made from commercial-purity Ti alloy coupons. Their compositions are

Titanium '92 Science and Technology Edited by F.H. Froes and 1. Caplan The Minerals, Metals & Materials Society, 1993 shown in Table 1. The electrodes were fabricated in 0.7cm diam and embeded in PTFE cylinders. After polished in sequence with nos. 1 to 6 emery paper, the electrodes were washed with distilled water and degreased with acetone. The solution was dearated with prepurified nitrogen for at lest 1 hour before an experiment ran. In order to be measured the typical activation passivation curves, the electrodes were activated in HF +HNO₃ + lactic acid for 1 minute, then were washed quickly with double-distilled water and were introduced into the dearated solution. Unless otherwise noted, the temperature of the solution was maintained at 100 ± 0.5°C and a condenser tube was

Table 1. The compositions of Titanium alloy coupons

wt%	Al	٧	Mo	Ni	Pd	Fe	Si	C	N	Н	0	Ti
Ti		_	_	_	_	.14	.04	.02	.01	.002	.12	bal.
TC4	6.20	4.05		<u>-</u>		.15	.04	.02	.03	.006	.13	bal.
Ti-12	_	_	0.26	0.78	_	.10	.05	.02	.02	.005	.45	bal
Ti-0.2P	d -	-	-	-	0.20	.15	.05	.03	.03	.005	.19	bal

annexed to the cell to keep the water loss for the solution evaporation. The anodic behavior curves were determined by potentiodynamic measurements with a scanning rate of 20 mv/min. from the corrosion potential which was achieved for about two hours. All electrode potentials (E) were measured against an external saturated calomel electrode (SCE) at room temperature and it was 87mv against internal 0.1N KCl Ag/AgCl reference electrode at 100°C.

Results and Discussion

1. The Anodic Characteristic of Ti.
Fig. 1 is the anodic polarization curve of Ti in pH = 1.2
NaCl solution. It has a typical active-passive shape. When E<
-600mv, Ti is at active state and when -600mv<E<-450mv, Ti is at an active-passive transition region. The primary passivation

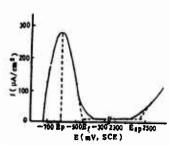


Fig.1 Anodic polarization curve of Ti in NaCl+HCl solution. T=100°C, pH=1.2, (Cl⁻)=1.3M

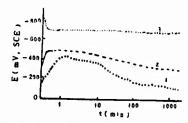


Fig. 2 Ti curves of E_{corr} vs. time T=106°C, pH=1.5 saturated NaCl. 1. Non-polished electrode.

 Electrode exposed to air for 30 min. after polished.

Electrode defilmed by the etchins solution.

potential E_p is -602mv. As E>-450mv, Ti is at a total passivation region. E_f =-450mv is Flade potential. And when E>2400mv, the current increases again. The perpassive potential potential E_{sp} is 2460mv. Because the pitting potential of Ti in chlorine acid is so high even though at 100°C it is more than 5V (9), the anodic reaction at the perpassive region is mainly chloring or oxygen discharged reaction.

2. Self-passivation Behavior.

The corrosion potential-time curves of Ti in the test solution are shown in Fig 2,3. Fig 2 indicates the passivation film of Ti, which had formed at air for a half hour, can deter the corrosion of pH=1.5 boiling saturated NaCl solution and Ti cannot be activated. As Fig.3 shows, the higher pH value, the more tendence of Ti self-passivation increase. When pH>2.0, the corrosion potentials can quickly go into the passive region even though the electrodes were activated in etching solution for removing the passive film. Meanwhile, as the acidity of the solution increases (pH<1.5), Ti is difficult to become self-passivation.

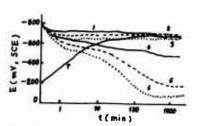
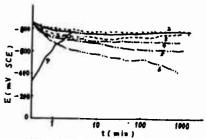
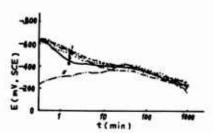


Fig.3 Ti curves of E_{Corr} vs time (C1-)=1.3M, T=100°C 1-6. defilmed electrodes. 7. non-defilmed electrode. 1,7.pH=1.0; 2.pH=1.2; 3.pH=1.5: 4.pH=1.8; 5.pH=2.0; 6.pH=2.2



Pig.4 TC₄ curves of E_{corr} vs time the condition as in Pig.3



Pig.5 Ti-12 curves of E_{COTT} vs. time. T=100°C NaCl+HCi 1,5. pH=0.7 saturated NaCl solution; 2.pH=1.0 Cl⁻=1.3M; 3. pH=1.5 Cl⁻=1.3M 4. pH=1.0 Cl⁻=2.7M

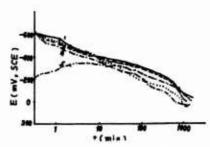


Fig. 6 Ti=0.2Pd curves of E_{COTT} vs time. the condition as in Fig. 5.

The E - t curves of TG4, we would see in Fig 4, are similar to those of Ti except that the active corrosion potential of TC4 is more negative than that of Ti. However, as shown in Fig 5, 6, the corrosion potentials of Ti-l2 and Ti-0.2Pd quickly shift toward positive and attain E > -400mv in just a few minutes. Even though in the strong acid (pH=0.7, measured in 100°C) saturated NaCl solution, their corrosion potentials never steadily go into the active state of Ti. Therefore, the self-passivation ability of Ti-l2 and Ti-0.2Pd is far greater than that of Ti and TC4.

- 3. The Effects of Some Factors on Anodic Behavior of Ti.
- (1). Acidity: Our former studies on the anodic polarization curves of Ti in various pH solutions has revealed that (10) the primary passive potentials ($E_{\rm p}$) become slightly more negative and the critical current densities ($i_{\rm m}$) become smaller with increasing pH values. Results are given in Fig. 7a, in which logarithmic critical current densities are plotted as a function of pH in HCl+NaCl solution. It shows an approximately straight line. The slope of the line is -1.5, which is more negative than references (3, 7) described in the ambient temperature solutions.
- (2). Chloride ions: There are a number of inconsistencies about the effects of chloride ions on the corrosion behavior of titanium (2,3,11-15). It is our former experimental confirmation that the active dissolution of Ti increased with increase in the concentration of chloride ions (10,16). Fig. 7b is logarithmic relation of critical current of Ti and chloride ion concentration. It also manifests a similarly straight line, of which slope is about 1.0. It indicates that the chloride ions on this condition promote corrosion of Ti.
- (3). Temperature: The experiments revealed that, as the temperature increases, titanium can more easily go from passi-

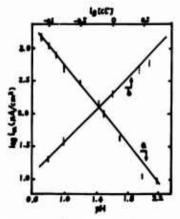


Fig.7 a. Ti curve of logim vs. pH. T=100°C, (Cl⁻)=1.3M. b. Ti curve of logim vs. log(Cl⁻). pH=1.2

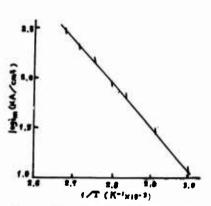


Fig.8 Ti curve of logim vs. 1/T. pH=1.0, (Cl⁻)=1.3M

vation state into activation region as well as increase the critical current densities. Fig 8 shows that $\log i_m$ vs. 1/T discloses very well a linear function. In accord with Arrhenius Law: $\log i_m = A - E/RT$, we could obtain an apparent active energy $E = 8.21 \times 10^4$ J/mol (19.7 Kcal/mol) of anodic procedures of titanium in this solution.

- (4). Dissolved oxygen: Our former note, using Ti disk electrode, has shown (10) that, in the absolutely dearated solutions, the anodic curves are not relative with the disk speeds, but in the non-dearated solutions, the critical currents decrease with the rotation speeds increase. Only as w > 3000rpm, the anodic curves overlapped. It displays that the dissolved oxygen is beneficial to Ti passive film formation.
- (5). Ti(III) and Ti(IV) ions: Although many articles are discordant with regard to the trivalent and the tetravalent ions present (3, 5-7, 11). our results have shown (10), Ti(II) ions are olay oxidized at a passive Ti surface to form Ti(IV) ions in this solution and don't promote dissolution of Ti. The trivalent ions oxidization reaction, which is diffusion-controlled, is first order with respect to the concentration of Ti(III) ions and the rate constant for the oxidation is 1.21 x 10⁴ μA/cm²M. And as the presence of Ti(IV) ions, the anodic currents decrease because Ti(IV) ions are reduced at an active state Ti electrode to form Ti(III) ions in solutions and only act as cathodic de-polarization. The reduction reaction is also first order with respect to the concentration of Ti(IV) ions and the rate constant for the reduction is 6.87x10⁴ μA/cm²M.

4. The Anodic Behavior of the Alloys.

The steady active-passive curves of TC_4 in the study on the anodic behavior of TC_4 have also obtained. Only difference from Ti is that the corrosion potential and primary passiva-

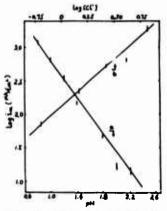
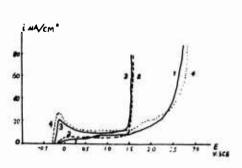


Fig. 9 a. TC₄ curve of logi_m vs pH. T=100°C, (Cl⁻)=1.3M; b. TC₄ curve of logi_m vs log(Cl⁻). pH=1.2, T=100°C



Pig.10 Anodic polarization curves of Ti-12 and Ti-0.2Pd at 100°C 1,2--pH=1.2 H₂SO₄; 3,4--pH=1.2 (C1")=1.3M HC1+NaC1. 2,3--Ti-12; 1,4--Ti-0.2Pd.

tion potentials of TC4 are much more negative than those of Ti, meanwhile the primary passivation current densities of TC4 are greater than those of Ti at the same condition, which means that TC4 is inferior to Ti for anti-corrosion in this solution and it is contrary to Frayret studied in hydrochloric acid (8). By the study, we have obtained two similarly straight lines about the effects of pH and Cl⁻ ions too, as shown in Fig 9, $dlogi_m/dlog(Cl^-) = 1.0$ and $dlogi_m/dpH = -1.5$. That also denotes H⁺ and Cl⁻ ions intensifying corrosion of TC4 in this solution.

For the electrochemical behavior of Ti-12 and Ti-0.2Pd alloys, as above this note, the two alloys corrosive potentials quickly go into the passive state potential of Ti. The region of anodic dissolution therefore is absent on the anodic curves, as shown in Fig 10. Furthermore, Fig 11. shows that the cathodic curves for the two alloys are from 400 to 450mv more noble than that of Ti and TC4 owing to a considerable decrease of hydrogen overvoltage. So the steady-state potentials of the two alloys are definitely in the range where Ti is completely passivated. In Fig 10, we could see the anodic current densities of Ti-12 at 1420mv in both NaCl+HCl and H₂SO₄ solutions rise greatly, which is different from Ti-0.2Pd and Ti. It probably corresponds to a lower oxygen overvoltage on Ti-12 surface than on the other alloys.

5. Anodic Activation-passivation Mechanism.

According to previous descriptions and our former investigation on the films of Ti in the same solutions(10, 17) as well as the results of this note, we believe that the abodic dissolution of Ti in hot acid NaCl solution constitutes three parallel procedures: anodic dissolution, passivation and chemical dissolution of passive film. The probable procedures as following:

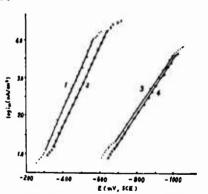


Fig.11 Cathodic polarization curves of Ti alloys in pH-1.5, (Cl⁻)=1.3M, NaCl-HCl. 1. Ti-0.2Pd; 2. Ti-12; 3. pure Ti; 4. TC₄.

$$Ti + H_2O = Ti(OH)_{ad} + H^+ + e$$
 (1)

$$Ti(OH)_{ad} + H_2O = (Ti(OH)_2)_{ad} + H^+ + e$$
 (2)

$$(\text{Ti}(OH)_2)_{ad} + H^+ \xrightarrow{I_S} (\text{Ti}(OH))^{2+} + H_{2O} + e$$
 (3)

$$(Ti(OH))^{2+} + H^{+} + Cl^{-} = TiCl^{2+} + H_{2}O$$
 (4)

(B). Passivation:

After (Ti(OH)2)ad is produced in Eq. (2),

$$(Ti(OH)_2)ad \xrightarrow{If} TiOOH + H^+ + e$$
 (5)

$$TiOOH + H_2O = TiO(OH)_2 + H^+ + e$$
 (6)

$$TiO(OH)_2 = TiO_2 + H_2O$$
 (7)

(C). Chemical dissolution of passivation film:

$$TiO_2 + H^+ = (TiO(OH))_{ad}^+$$
 (8)

$$(\text{TiO}(OH))_{ad}^{+} + Cl^{-} \xrightarrow{B} (\text{TiO}(OH)Cl)_{ad}$$
 (9)

$$(TiO(OH)Cl)_{ad} + H^+ = (TiOCl)^+ + H_2O$$
 (10)

$$(\text{TiOCl})^+ + 4\text{Cl}^- = (\text{TiOCl}_5)^{3-}$$
 (11)

This mechnism has mainly two different points from former proposed. First, it is considered the effects of H⁺ and Cl⁻ ions in active dissolution procedure. Second, it is assumed that the absorption of H⁺ and Cl⁻ ions in the passive film dissolution is Temkin absorption.

Assume I_S to be the current density of the active-state dissolution, I_f to be the current density of the passive film formation and B to be chemical dissolution of the passive film. Consequently, by simply deducing, we can obtain stationary dynamic equation as following (17):

$$I = (I_g + I_f)/(1 + SI_f/B)$$
 (12)

where S represents the passive film aera formed by consuming one coulomb current capacity.

At primary passivation potential $B_{\rm p}$, it can be believed $I_{\rm s}\gg I_{\rm f}$ and $SI_{\rm f}/B\gg I_{\rm f}$, that means the active-state current density is far more than the current density of the passive film formation and the passive film formation rate is far more than the passive film dissolution rate. Consequently, Eq.(12) can be simplified to:

$$I_{m} = I_{s}B/SI_{f}$$
 (13)

If assume that Eq.(8) and Eq.(9) are Temkin absorption, and because Eq.(8) is at a quasi-equilibrium state, we can easily deduce the expression (17):

$$BK_{Q} = (K_{8}/K_{-8})^{(1-r)}(H^{+})^{(1-r)}(C1^{-})$$
 (14)

where K_9 , K_8 and K_{-8} are Eq.(9) and Eq.(8) rate constants respectively and r is absorption summetry factor of which usual value is 0.2-0.8.

Because Eq.(3) and Eq.(5) are parallel anodic reactions, So:

$$I_8/I_f = K_3(H^+)\exp(\alpha_3FE/RT)/K_5\exp(\alpha_5FE/RT)$$

$$= K_3K_5^{-1}(H^+)\exp((\alpha_3-\alpha_5)FE/RT)$$
(15)

where K₃ and K₅ are Eq.(3) and Eq.(5) rate constants.

By using Eq.(14) and Eq.(15) inserted into Eq.(13), then
the critical current density is given by Eq.(16):

$$I_{m} = K_{3}K_{5}^{-1}K_{9}(K_{8}/K_{-8})^{(1-r)}S^{-1}(H^{+})^{2-r}(Cl^{-})exp((\alpha_{3}-\alpha_{5})FE/RT)$$
(16)

For usually r = 0.5, Eq. (16) gives the results:

 $dlogI_m/dpH = -dlogI_m/dlog(H^+) = -1.5$ (17)

 $dlog I_m/dlog(Cl^-) = 1.0$ (18)

Eq.(17) and Eq.(18) agree with the experimental results. It illustrates the assumption mechanism is reasonable.

Conclusion

(1). pH, Cl⁻ ions, temperature and dissolved oxygen have obvious effects on the anodic behavior of Ti in hot acid NaCl solution. The Ti(II) ions do not effect the activation and the passivation of Ti, and the Ti(IV) ions only act as cathodic depolarization for Ti. As to these factors, the three experienced equations have been obtained: $dlogI_m/dpH = -1.5$,

 $dlogI_m/dlog(Cl^-) = 1.0$, $logI_m = A - 4.29 \times 10^3/T$.

(2). The TCA alloy has the similar anodic behavior to pure Ti, but it is inferior to pure Ti for corrosion resistance in this studied condition. The Ti-12 and Ti-0.2Pd alloys don't reveal the typical active-passive behavior ewing to the shift of the stead-state potentials by a great decrease in hydrogen overvoltage to the potential region where Ti is completely passive. Thus, They can act as the best corrosion-resistant alloys in this solution.

(3). The activation-passivation mechanism of Ti in this solution is from Eq. (1) to Eq. (11) reactions.

References

R. D. Armstrong, J. A. Harrison, H. R. Thirsk, et al., J. Electrochem. Soc., 117 (1970), 1003.
 J. C. Griess, Jr., Corrosion, 24 (1968), 96.
 N. T. Tomas and K. Nobe, J. Electrochem. Soc., 116 (1969)

- 116 (1969), 1748; 119 (1972), 1450. 4. A. Caprani and J. P. Frayret, Electrochim. Acta, 24 (1979),
 - 835; 26 (1981), 1783; 27 (1982), 391.
- 5. D. Sinigaglia, et al., Werkst. Korros., 24 (1973), 1027. 6. N. D. Tomashov, et al., Zashch. Met., 26 (1990), 127. 7. E. J. Kelly, J. Electrochem. Soc., 126 (1979), 2064.
- 8. J. P. Frayret, A. Caprani, et al, Corrosion, 41 (1985), 656; 40 (1984), 14.

 9. T. R. Beck, J. Electrochem. Soc., 120 (1973), 1310-24.

 10. F. X. Gan, Y. X. Zhao and L. A. Yao, J. Chinese Soc. of Corrosion and Protection, 10 (1990), 307.

- 11. M. Levy, Corrosion, 23 (1967), 236.

 12. Watanabe Takashi, Naito Hiromitsu, et al, J. Japan Inst. of Metals, 50 (1986), 734.

 13. I. F. Shekun, et al, Electrokhimiya, 26 (1990), 754.

 14. F. Mansfeld, et al, Corrosion, 42 (1986), 249.

 15. Akiro Takamura, Corrosion, 23 (1967) 306.

 16. L. A. Yao, F. X. Gan, Y. X. Zhao, et al, Corrosion, 47 (1901) 420

(1991), 420.

17. Y. X. Zhao, "The Study on Corrosion Behavior of Ti Alloys in Hot Acid NaCl Solutions" (M.S. degree dissertation, Wuhan University, 1988),p44-53.

RAW MATERIALS, MELTING, RECYCLING AND PRIMARY PROCESSING

CRITICAL REVIEW: RAW MATERIALS, MELTING, RECYCLING

AND PRIMARY PROCESSING

P. J. Bania

TIMET
P.O. Box 2128
Henderson, Nevada 89009

Abstract

This paper will review some of the developments in the areas of sponge production, melting, recycling and primary processing since the last conference four years ago. As many of the developments in this general area are proprietary, it is difficult to present an all-encompassing viewpoint. Nonetheless, there are still many areas which can be discussed in an open format, and as many of these as possible will be addressed.

Introduction

Examining the world titanium industry over the past four years and comparing it to the prior twenty-five to thirty years, one readily concludes that the past few years have seen more change in the industry than any comparable period. For example:

- a) The political developments in Russia have brought the world's largest capacity producer much closer to the world market than ever before. The need for hard currency in this region of the world will undoubtedly bring a substantial amount of sponge and/or mill product to the market at very competitive prices.
- b) The economic recession in the Western World has taken a heavy toll on the titanium industry. For example, in 1991 U.S. shipments suffered the largest percentage drop from the prior year (34.2%) in over 30 years. (See Table I).
- c) RMI Titanium Co. closed its 24 M-lb/yr sponge facility in early 1992 after over 35 years of operation. This reduces the U.S. sponge capacity from 67 M-lbs/yr in 1991 to 46 M-lbs/yr, a 31.3% decline.
- d) TIMET announced an agreement to join Union Titanium Sponge Corporation (UTSC, a Japanese consortium) in the construction of a 22 M-lbs/yr vacuum distillation facility at TIMET's Henderson, NV sponge plant. This facility, which will be operational in early 1993, will be the only U.S. vacuum distillation facility. TIMET plans to idle a comparable amount of its current leached sponge

Titanium '92 Science and Technology Edited by F.H. Froes and I. Caplan The Minerals, Metals & Materials Society, 1993 capacity when the distilled sponge production begins.

e) After 40 years of almost exclusively relying on vacuum arc melting, cold hearth melting, either plasma or electron beam, has emerged as a viable production melt practice. This new melt practice is already qualified for premium rotating grade applications in gas turbine applications.

These changes are certainly dramatic in an industry which usually undergoes evolutionary rather than revolutionary changes. Coupled with other related developments, it is easy to argue that the face of the worldwide titanium industry will continue to change far more rapidly than past history would suggest.

TABLE I. - U.S. Industry Mill Product Shipments by Year and Sected by Percentage Change from Prior Year

	-	•			
	Shipments	1 Year		Shipments	1 Year
Year	(H-Lhe)	Charge	Year	(H-Lba)	Change
1981	0.3		1958	3.3	- 60.76
1952	0.8	150.04	1991	34.2	- 34.2%
1953	2.2	340.0%	1962	36.6	- 28.24
1954	2.6	18.29	1971	22.5	- 22.45
1955	3.6	46.25	1983	31.9	- 12.8%
1956	0.1	113.20	1960	23.8	- 12.85
1957	8.4	3.79	1975	31.3	- 10.39
1958	3.3	- 60.75	1986	41.7	- 9.78
1959	7.8	136.45	1970	29.0	- 9.10
1960	9.2	17.99	1963	10.6	- 0.54
1961	11.4	23.9%	1976	28.8	- 8.04
1962	11.0	3.50	1981	\$1.0	- 5.99
1963	10.8	- 0.55	1990	52.0	- 5.6%
1964	15.4	42.65	1967	27.3	- 2.5%
1965	18.7	21.49	1951	0.2	-
1966	28.0	49.74	1985	46.2	1.69
1967	27.3	- 2.5%	1962	11.0	3.59
1968	23.6	- 12.8%	1957	8.4	3.74
1969	31.9	34.0%	1987	44.6	7.06
1970	29.0	- 9.15	1977	30.9	7.34
1971	22.5	- 22.49	1989	55.1	10.9%
1972	28.3	13.49	1979	46.2	11.19
1973	29.0	14.69	1908	49.7	11.49
1974	34.9	20.3%	1972	28.3	12.49
1975	31.3	- 10.34	1973	29.0	14.64
1976	20.6	- 8.0%	1980	54.2	17.34
1977	30.9	7.34	1960	9.2	17.9%
1978	41.6	34.44	1954	2.6	16.24
1979	46.2	11.19	1974	34.9	20.3%
1980	54.2	17.36	1965	18.7	21.40
1981	\$1.0	- 8.94	1961	11.4	23.9%
1982	36.6	- 28.29	1969	31.9	34.0%
1963	31.9	- 12.00	1978	41.6	34.6%
1904	45.4	42.30	1984	45.4	42.3%
1985	46.2	1.89	1964	18.4	42.69
1986	41.7	- 9.78	1955	3.6	46.20
1987	44.6	7.04	1966	28.0	49.70
1980	49.7	11.46	1956	8.1	113.20
1909	55.1	10.90	1959	7.8	136.49
1990	52.0	- 5.60	1982	0.5	150.04
1991	34.2	- 34.29	1983	2.2	340.0%

Source: U.S. Bureau of Hines

Raw Materials

Production/Capacity Statistics. Table II provides a summary of world sponge capacity from 1981-1991. Overall, world-wide capacity changed very little over that span, ranging from 227 M-lbs in 1981 to 263 M-lbs in 1984 and 1990 - a modest 15% change over the entire period. However, the pie-chart in Figure 1s shows the 1990 breakdown by country, with Figure 1b showing the projected breakdown for 1992. As noted earlier, Russia has the largest capacity, with Japan ranked second and the U.S. third, even further behind Japan with the closing of the RMI sponge plant. Given the current economic environment in the titanium industry, it is difficult to project much of any substantial increase in capacity over the short term. The only

						/11
TABLE	II.	-	World	Sponge	Capacity	, (1 /

Capacity (m-1bs)	'81	182	'83	184	185	186	87	'88	189	'90	'91
U.S.	61.0	67.0	67.0	67.0	65.0	61.0	56.0	58.0	64.0	67.0	67.0
Japan	60.0	71.0	75.0	75.0	69.0	69.0	51.0	51.0	59.5	63.5	63.5
Europe	8.0	11.0	11.0	11.0	11.0	11.0	11.0	11.0	11.0	11.0	11.0
Subtotal	129.0	149.0	153.0	153.0	145.0	141.0	118.0	120.0	134.5	141.5	141.5
Russia (C.I.S.)	92.0	100.0	100.0	104.0	106.0	106.0	110.0	110.0	115.0	115.0	115.0
China	6.0	6.0	6.0	6.0	6.0	6.0	6.0	6.0	6.0	6.0	6.0
Total	227.0	255.0	259.0	263.0	257.0	253.0	234.0	236.0	255.5	262.5	262.5

Sources: (1) Titanium Statistical Review: 1981-1990 Published by U.S. Titanium Development Association (1991 Values Estimated).

added capacity known by the author to be under construction at this time (other than the TIMET distillation facility) is the 24-cell, roughly 7 M-lb capacity, electrolytic plant being constructed in Terni, Italy by Ginatta Torino Titanium. It should be noted, however, that RMI discontinued its operation of a single Ginatta pilot cell in 1991.

WORLD SPONGE CAPACITY

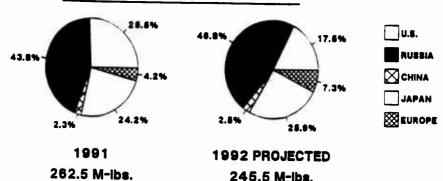


Figure 1a and 1b - Percentage Breakdown of World Sponge Capacity.

Tables III and IV list the sponge production statistics as a percentage of overall capacity for the U.S. and Japan respectively. This data shows the historical "boom-bust" cycle that has plagued the titanium industry for so long (See also Table I). In the U.S., sponge production as a function of capacity ranged from 41.6% to 86.9% while Japanese capacity utilization ranged from 31.1% to 91.2%.

Since the aerospace industry (military plus commercial) typically accounts for well over half of titanium consumption, it is generally felt that expansion into non-aerospace (industrial) markets will lessen the cyclical

	TABLE	III.	-	U.S.	Production	Statistics (1))
--	-------	------	---	------	------------	----------------	---

54.7

91.2

37.1

52.2

23.3

31.1

Sponge Production

? of Capacity

	'81	*82	<u>'83</u>	184	185	'86	187	'88	189	90	191(2)
Sponge Production (m-lbs)	-	1-1	27.9	48.7	46.5	34.8	39.4	49.1	55.6	54.4	29.5
I of Capacity	-	-	41.6	72.7	71.5	57.0	70.4	84.6	86.9	81.2	44.0
Ingot Production (m-lbs)	92.4	53.1	52.9	80.0	70.8	70.2	74.4	85.7	91.0	81.1	54.9
Z of Capacity	92.5	45.2	43.7	57.1	50.6	50.1	50.6	58.3	61.9	54.2	37.1
Scrap Consumed (m-1bs)	29.6	17.0	20.3	31.1	29.4	33.0	36.1	39.8	38.8	33.0	25.1
I of Ingot Production	32.0	32.0	38.4	38.9	37.3	47.0	48.5	46.4	42.6	40.7	45.7
TABLE IV Japane	se Prod	uction_	Statist	lcs (1)							
	181	182	'83	184	185	'86	187	188	189	'90	'91

Sources: (1) Titanium Statistical Review: 1981-1990 Published by U.S. Titanium Development Association and (2) 1991 Mineral Industry Surveys, U.S. Bureau of Mines. February 28, 1992.

33.9

45.2

49.1

71.2

32.1

46.5

22.2

43.5

36.1

70.7

47.0

79.0

56.5

89.0

nature of the industry. Much effort is being expended to develop such markets. For example, the automotive market is considered a strong candidate for a new industrial market for titanium.¹⁻⁵ Since cost is overwhelmingly the key driver in this market, special low cost titanium alloys have been developed for this market. Daido has developed a free-machining alloy grade to help reduce the high machining costs in connecting rod manufacture. TIMET has developed a low cost substitute for Ti-6Al-4V for use in exhaust valves and/or connecting rods. Such efforts hopefully will not only lead to applications in the automotive arena but also in other non-aerospace applications as well.

Ultra-High Purity Titanium. Although it is very small compared to the conventional markets for titanium sponge, there is a steadily increasing market for ultra-high purity titanium for use on integrated circuits for the electronics industry. Within this market segment, purity levels are often referred to as 4-9's (99.99%), 4-9's, 7 (99.997), 5-9's (99.99%) etc... but only metallics are considered in this figure. For example, a 4-9's product has less than 100 ppm (total) of all tramp metallics (Fe, Ni, Cr, Al, V, Mn...) but could contain several hundred ppm of interstitials such as oxygen, nitrogen, etc. Currently, the market for this product is moving from about 99.993 (4-9's, 3) towards a 5-9's product. While the U.S. market is only roughly in the 15,000 to 20,000 lbs/yr range, the ultra-high purity product commands a significantly higher price than conventional sponge.

The high purity product is most often produced by a molten salt electrorefining similar to the process cited by the U.S. Bureau of Mines. 8,9 Special attention is paid to all processing steps thru melting in order to reduce tramp contamination. Some recent patents 10,11 relating to improved production methods have been issued during the last few years.

Melting

Cold Hearth Helting: Arguably the most dramatic progress in the melting arena over the last several years has been the emergence of the cold hearth melting process as a production tool. There are two types of cold hearth furnaces currently being used - those which use electron beam guns for melting (EB) and those which use plasma torches (Plasma). Table V lists some of the pro's and con's of each type of furnace. Perhaps the most significant drawback to the EB furnace is the evaporative loss of high vapor pressure elements such as aluminum and chromium. On the other hand, the plasma process has limited hydrogen removal capability and a more turbulent pool. Also shown in this table is the poorer melting power efficiency of these processes compared to VAR, establishing these processes as higher cost melting practices. However, both processes appear to be very effective in their primary function - removing potential defects.

TABLE V. - Comparison of Melting Systems

	E.B.	Plasma	
	Cold Hearth	Cold Hearth	VAR
Evaporative Loss	Yes	No	No
Hydrogen Removal	Yes	Limited	Yes
Power Consumption (KWH/kg)	2.4	3.0	1.0
Loose Feed Capability	Yes	Yes	Limited
Sponge Feed Capability	Limited	100%	100%
Furnace Cost/Lb Capacity	Highest	High	Moderate
Maintenance Cost	High	High	Moderate
HDI Removal	Yes	Yes	No
LDI Removal	Very Good	Very Good	Limited

Although several production "in-spec" heats of Ti-6Al-4V were produced by 1988, 12 it was the tragic United 232 incident at Sioux City in July of 1989 that significantly accelerated efforts to employ this process on a production basis. The initiation site for the crack which ultimately led to the fan disc failure in the United 232 incident was found to be associated with an undissolved burnt sponge particle, otherwise known as a Type I low density inclusion (LDI). Such burned sponge particles, when high enough in nitrogen content, do not melt during the melting process and hence must be dissolved by the molten pool. For a given particle size, there is a critical residence time in the molten pool (at a given temperature) which must be exceeded before the particle will be dissolved. The advantage, and hence utility, of the cold hearth melting process is that the time material spends in the hearth - known as residence time - is independent of power supplied to the hearth. Thus, as opposed to VAR melting, residence time in the molten pool is theoretically infinitely variable. It is felt that the cold hearth process should be capable of dissolving or trapping "all" potential LDI formers. In addition, the hearth has been shown to be essentially 100% effective 13,14 in trapping other high melting, high density defects (such as tungsten particles) known as HDI's (high density inclusions). Because of the well established benefits of this process in terms of "eliminating" LDI's and HDI's some engine producers are now specifying hearth melted material for critical component manufacture.

As would be expected with such a relatively new process, there are still some unanswered questions regarding cold hearth melting:

- a) Does hearth melting remove 100% of LDI's and, if so, can designers actually take advantage of this? This leads to a related issue about NDI and the ability to verify a "defect free" condition.
- b) Is there a difference between plasma vs. EB melted quality?
- c) Is it necessary to VAR after hearth melting? Today, all hearth melted material is subsequently VAR processed.
- d) What about the economics of hearth melting in general (hearth vs. VAR) and EB vs plasma?

Since most rotating gas turbine engine components are designed on the basis of low cycle fatigue and operate at very high stresses (hence have relatively small critical flaw sizes), the clean ingot technology could have a major impact on the design/service life of such components. However, airframe structures which generally operate at lower stresses and are designed for crack growth (ie. damage tolerance) are less likely to be affected by such technology. As a result, the large engine producers (principally GE) have spearheaded the efforts to bring this process to a full production status. They have incorporated this melting process into their specifications and continue to work on improvements and a better understanding of the process.

An example of the on-going efforts is the current A.F. sponsored program¹⁴ being conducted by G.E. to "establish the hearth melt 'only' processes and procedures for preparation of premium quality alloys for gas turbine engine components". Today all hearth melted material is given a final VAR step. The A.F./G.E. program is evaluating elimination of the final VAR melt step.

One of the principle techniques to be used in the A.F./G.E. program will be to seed the ingots with a high number of artificial seeds (nitrided sponge particles) and subsequently ultrasonically inspect (UI) the product as billet and bar. It should be noted that the product can only be pronounced as 'clean' as the UI capability. From a conservative design standpoint, one could only assume a defect size equivalent to (or slightly below) that to which the material can be inspected. This has brought to bear a considerable amount of effort into improved UI capability.

It is also important to note that cold hearth melting is being applied to non-aerospace or non-premium grade product. In such cases, hearth melting is strictly driven by economics wherein low cost forms of scrap are recycled thru the hearth, typically at a much faster melt rate than premium grade product. In these instances, up to 100% scrap (such as turnings) can be recycled.

<u>Fine Sponge</u>. At the 1988 International Conference, J. Hall¹⁵ reported on a U.S. Patent¹⁶ which disclosed the method of rendering sponge particles "finer" than normal in order to facilitate the dissolution of undesirable LDI formers. There are two key variables in determining the time required for dissolution of a particle:

- a) Particle size
- Dissolution rate (dependent on molten pool temperature, chemistry, stirring...)

The fine sponge process takes advantage of a smaller particle size to promote particle dissolution. By shearing and screening processes, the largest sponge particle, and hence potential LDI former, can be substantially reduced. TIMET implemented the fine sponge process for VAR in 1988 by reducing the maximum sponge particle size from about 8mm dia. to 3.4mm dia. This change in particle size has contributed to roughly an 8-fold reduction in LDI incidence rate. Such an improvement was demonstrated over a production run of over 5 million pounds of product.

A logical extension of this development could be the combining of the cold hearth melting process with the fine sponge approach. The benefit might not only be greater assurance of LDI dissolution but also economic savings. The finer particles will require less residence time and hence a faster melt rate could be used. Using the relationships cited by Hall¹⁵, wherein the time to dissolve a cylindrical particle is proportional to the square of its radius, halving of the particle size reduces the dissolution time by a factor of four.

Computer Modelling of VAR and Hearth Melting. The vacuum arc remelting processes is very complex. There are many variables which can affect ingot quality from the standpoint of homogeneity, and soundness. Such variables can also affect product yield thru their impact on grain structure and surface quality. It is usually difficult and very expensive to adequately quantify the effects of the numerous melting variables such as voltage, current, stirring, etc... In order to more efficiently evaluate these effects, computer modelling of the VAR process has been developed. Such a model is discussed by J. R. Faber 17 in a recent publication. Faber begins by showing the correlation of the model vs. prior published data in predicting molten pool depths as a function of melt rate (power). He then shows the excellent correlation between actual thermal measurements on an instrumented crucible wall during a production VAR melt vs. the model predictions. Having established the validity of the model, he then goes on to show how the model can be used to predict segregation tendency in a difficult to melt alloy (Ti-10V-2Fe-3A1) by combining the Tiller Equation 18 with the model's predicted temperature gradients and solidification rates. By the Tiller Equation, it is shown that dendritic freezing and microsegregation are avoided when:

$$\frac{GD_L}{V} \ge ie, -MC(\frac{1-k}{k})$$

where G = thermal gradient at the liquid interface; D_L = diffusivity of the solute (Fe in the case of Ti-10V-2Fe-3Al) in the liquid; V = freezing velocity of the interface. These values on the left-hand side of the equation are melting variables (D_L is affected by stirring). The variables on the right-hand side are a function of the solute element of interest: M = slope of the liquidus at the melting point; C = solute content in the liquid away from the interface and k = partitioning coefficient (ratio of solidus content vs. liquidus content). By rearranging the terms,

Tiller Factor = $\frac{GD_L k}{VMC(1-k)}$ < 1 ,

Paber uses the Tiller factor to determine if segregation can be avoided (ie. segregation is avoided if the Tiller factor is less than one).

Since the melting variables can be calculated by the model, and the material variables can be approximated from binary phase diagrams, one can use the model to predict the impact of melting variables on segregation tendency and thereby design a suitable melt practice which avoids the segregation.

Such modelling can be used to solve a variety of melting problems. For example, post-melt thermal gradients can be altered by melt practice in such a way so as to minimize or eliminate cracking of brittle ingots such as alpha-two or gamma titanium aluminides. Also, the modelling process can be used to predict residence time/temperature profiles for dissolution of burned sponge particles which can lead to low density inclusions (LDI's).

The modelling technique can also be used to study hearth melting as well. It is clearly a very powerful and useful tool which will continue to evolve as demands on melting quality become more stringent.

Scrap Recycle

<u>DOSS Process</u>. RMI Titanium Co. (J. L. Fisher) discloses a "process for deoxidizing refractory metals such as titanium which contain less than about one percent oxygen" in two recent patents^{19,20}. The process is referred to as the DOSS (<u>De-Qxidation</u> in the <u>Solid State</u>) process. It is intended to be used on section sizes less than about 4.7mm (.185") in thickness, typically for powder, chips, turnings, sheet or foil. The process consists essentially of the following steps:

- a) Placing the "high" oxygen material (typically .2 to .3% oxygen) in a container with about one tenth by weight as much deoxidizer plus carrier. The preferred deoxidizer is calcium and the preferred carrier is sodium. The calcium to sodium ratio is about 1:4 to 1:10.
- b) Heating the combined substances to roughly 900°C to 1000°C under vacuum or inert gas for 2 to 12 hrs.
- c) Distilling off the carrier (optional)
- d) After cooling the product to room temperature, crushing if necessary then acid leaching, rinsing and drying.

The patents cite examples wherein samples originally containing .2 to .3% oxygen are reduced to about .025 to .055% levels. Thus, oxygen is commonly lowered by roughly 65% to slightly over 90% in some cases.

A similar process for oxygen removal from "bulk" titanium is also shown by Okabe ${\rm etal}^{21}$ in which they employed calcium plus ${\rm CaCl}_2$ flux. They reported reductions in oxygen from 800 to 1200 ppm down to less than 100 ppm (30 to 90 ppm) by exposing small cross-section titanium samples to the Ca + CaCl $_2$ mixture in the temperature range of 900°C to 1000°C for 24 to 60 hrs. This process is essentially that cited by Rostron 22 in 1958. In that case,

Rostron was using the calcium deoxidation as a second reduction step following a primary step which was incapable of removing enough oxygen. The utility of these deoxidation processes is, as usual, driven by economics. If the cost of titanium scrap (eg. turnings) plus the cost of deoxidation is less than that of virgin materials (sponge + master alloy), then the process can be viable. This assumes, of course, that the deoxidized material can be melted and processed on an equivalent cost basis as the virgin material.

Primary Processing

<u>Processing Windows</u>. One of the key's to producing a high quality mill product such as aerospace quality billet or bar is the ability to produce a fine uniform macrostructure as early in the conversion process as possible. Since an as-cast ingot contains not only very coarse grains but also a wide range of grain sizes and morphologies, it is usually a primary objective of the early ingot conversion steps to induce recrystallization in order to refine the grain size and produce a uniform grain size. Failure to do so properly can result in unacceptable product containing undesirable defects such as strain induced porosity (S.I.P.), continuous grain boundary alpha, blocky alpha, etc..

In order to provide for complete and uniform recrystallization, processing windows²³ such as that shown schematically in Figure 2 are being used. While it is readily apparent in this figure that work conducted below the beta transus is very effective in driving complete recrystallization, one does not always have that option available. For example, metastable beta alloys and beta rich alpha-beta alloys have such low beta transus values and high flow stresses at the subtransus temperatures, it is often impossible to effectively use subtransus work to drive recrystallization. Even in alloys with higher beta transus values, section size requirements often preclude the use of subtransus work. In such cases, work above the beta transus temperature must be used to drive recrystallization.

The schematic in Figure 2 shows that, for a given amount of work, there is an optimum combination of work temperature and anneal temperature in order to provide complete recrystallization. Usually, it is desirable to drive recrystallization at as low a temperature as possible in order to keep grain size as fine as possible.

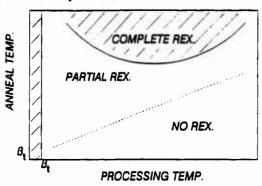


Figure 2 - Schematic representation of a Processing Window for a given amount of applied strain (work).

This philosophy of properly controlling thermomechanical processing (TMP) variables to control recrystallization is not limited to ingot conversion practices. A recent patent by Bhowal²⁴ et al. discloses a similar concept used in the production of fine grained titanium forgings. By this method, isothermally beta forged components are held in the isothermal dies for a sufficient time to allow recrystallization to occur.

The Next Four Years ..

Driven by product quality and/or production cost demands, and with work currently directed in these areas, it seems rather straightforward to predict some of the areas where significant progress will be made over the next four years:

- a) Low Cost Sponge Production. It has long been a goal within the industry to reduce production costs by employing a continuous sponge making process instead of the current batch processes. Recent patents²⁵⁻²⁷ in this area suggest that substantial progress will be made over the next few years, although implementation of a production facility would appear to be several years away.
- b) Improved Ultrasonic Inspection. With the improved quality derived from efforts such as cold hearth melting and "fine sponge", there is now tremendous pressure on the non-destructive inspection community to improve overall capability. It is difficult from a design standpoint to take advantage of "clean" material unless there is a method of verifying its quality. We can expect not only improvements in the inspection instrumentation itself, but also enhancements in the materials inspectability thru controlled thermomechanical processing.
- c) Cold hearth melting will see a significant advancement in the development and implementation of sensors specifically designed for the process. Sensors which can measure molten pool temperature and depth (volume) will be used to verify residence time in the hearth. Also, particularly for the E.B. systems, real time analytical sensors will determine pool chemistries in order to be able to adjust alloy content to accommodate evaporative losses.
- d) <u>Metal Matrix Composites</u>. With the extensive research now on-going relative to metal-matrix composites, especially very high temperature composites, novel methods are emerging^{28,29} for production of low cost foils as well as low cost methods of coating fibers directly. The viability of many advanced engines and airframe structures seems to be intimately linked to development of these advanced composites.

All things considered, the next four years appear to be shaping up as a period of adjustment to the recent changes, highlighted by progress resulting from the changes.

References

- Sommer, A. et al., "Titanium in Motorsports Racing", <u>Designing With Titanium</u>, Proceeding of International Conference, The Institute of Metals, London, July 1986.
- Toyama, K. and Kuwayama, T., "Trial Production and Strength Assessment of Titanium Alloy Connecting Rods", The Sumitomo Search No. 39, September 1989.

- Sherman, A., "Titanium Coil Springs for Automotive Suspension Systems", SAE Technical Paper Series No. 800481, February 1980.
- Mushaike, M. et al., "Development of Titanium Alloy Valve Spring Retainers", SAE Technical Paper Series No. 910428, March 1991.
- Cochran, C. N., et al., "Automotive Materials Decision: Energy, Economics and Other Issues", SAE Technical Paper Series No. 820149, February 1982.
- Kimura, A. et al., "A Free Machining Titanium Alloy For Connecting Rods", SAE Technical Paper Series No. 910425.
- Hutt, A. J. et al., "A New Low Cost Titanium Alloy", <u>Proceedings</u> of the Seventh World Titanium Conference (San Diego), TMS-AIME, 1992.
- Nettle, J. R. et al., "Electrorefining Titanium Metal", Bureau of Mines Report of Investigations 5315, (1957).
- Baker, D. H., and Nettle, J. R., "Titanium Electrorefining: Cathode Studies and Deep Bath Deposition", Bureau of Mines Report of Investigations 5481, (1959).
- Shimotori, K. et al., "Highly Pure Titanium and Method for Producing the Same", U.S. Patent No. 4,793,854, December 1988.
- Shimatori, K. et al., "Highly Pure Titanium", U.S. Patent No. 4,891,066, January 1990.
- Entrekin, C. H. and Harker, H. R., "Recent Developments in Electron Beam Hearth Refining", <u>Proceedings: Sixth World Conference on Titanium</u>, Les Editions de Physique, France, (1988).
- Chinnis, W. R., "Plasma Cold Hearth Melting of Titanium in a Production Furnace", <u>Titanium 1990: Products and Applications</u> (International Conference Proceedings), published by Titanium Development Association, (1990).
- Buttrill, W. H., et al., "Manufacturing Technology for Premium Quality Titanium Alloys for Gas Turbine Engine Rotating Components", Interim Report No. 5, U.S.A.F. Contract F-33615-88-C-5418, September 1991.
- Hall, J. A., "Recent Advances in Titanium Processes, Alloys and Products", <u>Proceedings: Sixth World Conference on Titanium</u>, Les Editions de Physique, France, 1988.
- Bania, P. J., "Production of Titanium Articles That Are Free From Low Density Inclusions", U.S. Patent No. 4,678,506, July 1987.
- Faber, J. R., "Some Aspects of the Modelling of the VAR Process", <u>Titanium 1990: Products and Applications</u> (International Conference Proceedings), published by Titanium Development Association, (1990).
- Tiller, W. A., "The Redistribution of Solutes Atoms During the Solidification of Metals", <u>Acta Metallurgica</u>, Vol. 1, July 1953.

- Pisher, R. L., "Deoxidation of Titanium and Similar Metals Using a Deoxidant in a Molten Metal Carrier", U.S. Patent No. 4,923,531, May 1990.
- Fisher, R. L., "Deoxidation of a Refractory Metal", U.S. Patent No. 5,022,935, June 1991.
- Okabe, T. H., et al., "Preparation of Extra Low Oxygen Titanium by the Calcium Halide Flux Deoxidation Process", <u>Titanium 1990: Products and Applications</u> (International Conference Proceedings), published by Titanium Development Association, 1990.
- Rostron, D. W., "Method of Thermally Reducing Titanium Dioxide", U.S. Patent No. 2,834,667, May 1958.
- Weiss, I. et al., "Grain Size Control in Near Beta Ti-10V-2Fe-3Al Alloy", <u>Strength of Netals and Alloys</u>, Proceedings of Seventh International Conference, ed. by H. J. McQueen et al., Pergamon Press, (1985).
- Bhowal, R. P. et al., "Fine Grain Titanium Forgings and a Method for Their Production", U.S. Patent No. 5 026,520, June 1991.
- Okudaira, S. et al., "Method for Producing Titanium Alloy", U.S. Patent No. 4,902,341, February 1990.
- Toraut, D. E., "Indution Slag Reduction Process for Making Titanium", U.S. Patent No. 4,985,069, January 1991.
- Kametani, H. and Hidenori, S. "Nethod for Manufacturing Titanium Powder or Titanium Composite Powder", U.S. Patent No. 5,032,176, July 1991.
- MiOguchi, T. et al., "Cont/nuous Thin Sheet of TiAl Intermetallic Compound and Process for Froducing Same", U.S. Patent No. 5,028,277, July 1991.
- Regan, R., "T.I. Cold Folling Gamma Titanium Aluminide", <u>American Metal Market</u>; Focus: Edvanced Materials, January 29, 1992.

Estimating Domestic Titanium Requirements

For the 90's

Richard L. Fisher RMI Titanium Company 1000 Warren Avenue, Niles, Ohio, USA

Abstract

The U.S. Bureau of Mines publishes quarterly reviews of production statistics for titanium. Data obtained from this Mineral Industry Survey has been compiled into a titanium raw materials model. This model is based upon data developed over the past three decades. Mill shape production rates are used to estimate end product and scrap generation rates. Average market growth rates were computed using five year increments. Future market growth rate has been estimated by regression analysis of this data. Comparisons are made between anticipated sponge metal needs and installed sponge capacity. Trends in scrap inventory levels are predicted from the model. This paper discusses the development of this model at RMI Titanium Company and presents one potential market growth scenario based upon a historical market growth estimate.

Introduction

Commercial titanium production began in 1948. Demand for products manufactured from titanium has been cyclic and varies in a cycle approximately ten years in length.

The greatest demand for titanium is in aerospace applications. Alloys of the metal are particularly well suited for use in the engines and airframes of modern jet aircraft. Periodic increases in the demand for titanium have occurred during the build up of commercial airliner fleets and acquisition of large numbers of modern jet aircraft by the military. A second major market area makes use of titanium's excellent corrosion resistance in a variety of industrial applications.

Demand for titanium for industrial applications has increased steadily since 1965 when this market area experienced rapid growth from a base level of about three-quarters of a million pounds per year. Since 1967, industrial markets have shown an average growth rate of about 2.6% per year. Two significant "accelerated" demand cycles occurred as a result of shortages which occurred during the late 1970's and 1980's. These "growth spikes" both occurred when large demands in aerospace markets triggered raw materials shortages and extended delivery times for mill product shapes. Expansions of sponge production capacity during the late 70's and 80's satisfied these short term raw materials requirements.

Titanium '92 Science and Technology Edited by F.H. Froes and I. Caplan The Minerals, Metals & Materials Society, 1993 The U.S. Bureau of Mines has published an excellent review covering distribution of titanium raw materials, ingot, mill products and scrap for the 1960's.(1) This review contains production and inventory statistics compiled from reports issued quarterly by the U.S. Department of Commerce.(2) A study detailing scrap utilization in titanium production was contained in a report published in 1975. (3)

Similar data summaries covering periods from 1978 Grough 1991 were published by the Bureau of Mines and complied by the Titanium Development Association (TDA). (4) Data estimating titanium utilization (buy to fly ratios) for aerospace applications was obtained from a study published in 1983 for the Federal Emergency Management Agency. (5)

In 1985, data from all available sources was compiled into a computer model which was used to track and predict changes in domestic scrap supplies. (6) The original Bureau of Mines tabular model was used as a basis to upgrade the original scrap model to reflect current market distributions. In early 1991, this model was modified to provide capabilities for estimating market trends, raw materials needs, and scrap inventories. The model can be used to estimate mill products requirements and raw materials needs for a range of aerospace and industrial market growth assumptions.

Development of the Model

The RMI Titanium Company raw materials model was based upon a titanium scrap flow diagram developed in 1975. A tabular summary of data covering the period from 1960 through 1969 is included as Table I. This summary provides an excellent review of production data, but does not include scrap inventory data for the period.

Information compiled by the TDA was used to expand this tabulation to include data for the period from 1978 to 1984. (2) Other sources were used to develop data for periods between 1970 and 1977. Data published by the Bureau of Mines in reviews are annualized and posted into the model quarterly. (4)

Lag times were built into the model to account for shipping and conversion schedules. Mill products shipped in 1983 are assumed to be converted into final products and scrap during 1984. In the original version of the model, predictions of scrap usage were estimated from five year running averages of historical data. Similar techniques were used to generate estimates for imports and exports. Prediction of future mill product needs were based upon marketing estimates.

Additional categories have been added to the original Bureau of Mines data table to handle more input and recycle loops. Discrete categories were added for sponge capacity, sponge imports, scrap import and export data and scrap recycle to the system from used end products. Conversion ratios for mill products are estimated from a ratio of aerospace to industrial markets. The original model was useful for predicting trend changes in scrap inventory, either increases or decreases in level. See Figure 1. Changes in scrap inventories could be directly associated with future scrap availability, price and sponge production needs.

TABLE I. Titanium Scrap, 1960-69 (Tons)

	1960	1961	1962	1960 1961 1962 1963 1964 1965 1966 1967 1968 1969 Total	1964	1965	1966	1967	1968	1969	Total	
Lav metal supply:								20 00		76. 06		
Sponge consumption	2,487	166'9	1,136	6,565	11,131	17, 105	179,61	700,02	16,43/	471 '07	162,01	2
Scrap consumption	2,527	2,501	3,160	2,235	2,877	3,303	4,857	5,822	4,701	7,566	39,54	ر م
Total rac metal supply	8.014	9,492	10,296	11,100	14,008	15,408	765,45	25,884	18,938	27,690	165,36	Ł
Inear production!	8.297	9.371	10,400	11,138	13,964	15,294	24,253	25,960	19,234	28,490	166,40	=
Topon continue for	7.978	8.878	9,773	10,506	13,501	14.694	22,317	25,386	18,323	27,082	158,43	•
Mill shapes productions	5.071	5,147	6,521	6,112	7,708	9,358	13,996	13,634	11,900	15,80	95,38	=
Resignated percent to Eabricated products 25.0 26.3 27.6 28.9 30.4 31.9 33.5 35.2 36.9 38.8 33.1	25.0	25.0 26.3	27.6	28.9	30.4	31.9	33.5	35.2	36.9	38.8	33.	_
Pabricated products production3	1,268	1,354	1,800	1,766	2,343	2,985	4,689	4,799	4,391	6,185	31,58	외
Scrap supply:									-			
Inger production minus mill shapes production. 3,226 4,224 3,879 5,026 6,256 5,936 10,257 12,326 7,334 12,550 71,014	3,226	4,224	3,879	5,026	6,256	5,936	10,257	12,326	7,334	12,550	2,1,0	*
Mill shapes minus fabricated products (previous									200		77 73	9
year)4	207,2	203	3,733	2,408 3,803 3,793 4,721 4,348 3,340 4,343 4,340 3,340 8,833 1,249 59,890		2		\\\\\\\\\\\\\\\\\\\\\\\\\\\\\\\\\\\\\\		2027	73.00	21:
Total acrap supply	100	2,027	7/01/	7,74	10,004	11,30	10,00	41,033	10, 103	,,,		•
Yearend scrap stocks ⁵	ž	£	ž	ž	Ş			17/ 4 9/5 4 9/8 4 4 76 4 17/	4.4	77/7	<u>.</u>	ı
Scrap consumption:								-				
Titanium recycle	2,527	2,501	3,160	2,235	2,877	5.50	2	2,522	41/01	, ,	Ž:	1
Steel production:						-						
Direct alloying and deoxidizing	930	972	1,076	630 972 1,076 1,305 1,525 1,800 2,100 2,500 2,900 3,447 1,0,23	1,525	3	3;	2,700	3,4	1	707	ח מ
Exports	879	200	212	1,261	1,817	2,132	1,/33	1,429	2,130	, œ,	70,0	2
Perrotitanium production (contained								}			-	5
titanium)7	986	716	280	739	11.15	1.180	1.369	(8)	1.099	1133	7.7	313
Total steel production	2,455	2,574	2,474	3,325	4,493	5,112	5,402	4,714	6,755	7	1,1	9
Aluminum-base hardeners (contained titanium)	933	1,115	1,569	933 1,115 1,569 2,170 1,586 1,002 793 682 700 668 11,218	1,586	1,00	793	985	<u>8</u>	3	11,2	20
Monrecoverable metal losses (estimated at					13							
25 percent of ingot production)*	2,075	2,343	2,600	2,785	3,487	3,824	6,064	6,490	4,809	7,122	41.5	21
Total scrap consumption	7,990	6,533	9,803	110,515	12,443	13,241	17,116	17,708	16,965	22,800	137.1	2
*Estimated. MA Not available.												

Includes imported sponge and alloy addition.

The data

include some offgrade sponge.

The percent of mill products which became fabricated products was estimated at 25 percent for 1959-60. After 1960, yield is assumed to increase at the rate of 5 percent per year.

Includes minor amounts of castings.

Hill shapes production for 1959 was 3,211 tons, and estimated fabricated products production was 803 tons.

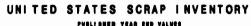
Scrap stocks held by ingot and mill shapes producers.
*Data for years 1960-63 obtained from American Iron and Steel Institute Annual Statistical Report 1961 and 1963.

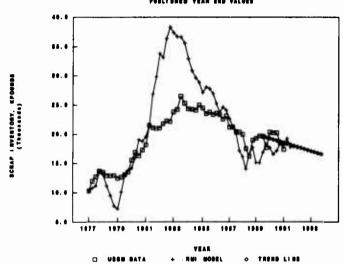
Includes minor amounts from ilmenite-magnetite slags.

The hardeners contain 5 to 10 percent titanium; 10 percent was used in calculating the titanium content to compensate for titanium scrap consumed for direct alloying of casting alloys.

^{*}General shrinkages from missegregation, grinder dust, pickling, etc. See section on nonrecoverable losses for explanation.

Figure 1 - Original Scrap Inventory Model





Improvement of the Model

In late 1990, an internal review of domestic scrap markets was completed. (6) This review showed that scrap inventories would begin increasing during 1991. The study also indicated that a market turndown might occur during the next year. See Figure 3. Since industry market estimates for 1991 showed continuing high demand, the significance of this trend was not realized. The unusual results were inconsistent with accepted market projections. The model was expanded to include better forecasting capabilities for mill product market needs. Data was obtained for historical market growth for the period from 1960 through 1990. This data was averaged in five year intervals.

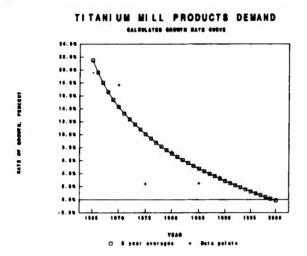
These averages were evaluated statistically to generate a best fit equation. This equation was logarithmic and of the form:

$$y = 0.38247 - 0.1040794 * Ln (x)$$
 (1)

where x equals the time increment in years from a base year, 1960. This equation is shown graphically in figure 2 together with the actual data points.

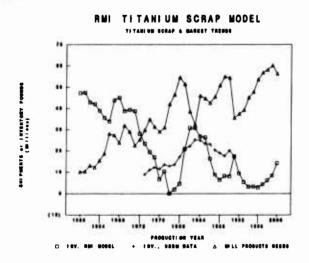
Evaluation of historical market growth data by strict mathematical methods infers that traditional markets have matured. Periodic spikes in demand have been the result of high growth rates caused by short term demand for military aircraft and wide bodied commercial jets. An average market growth rate for the 1990's estimated from historical growth rates is estimated to be 1.43%.

Figure 2: Historical Titanium Market Growth Rate Curve



The raw materials model was updated in early 1991 during an economic study of scrap usage and availability. The model predicted the domestic mill products market, including castings, would be approximately 36.5 million pounds in 1991. Data from this evaluation is shown graphically in Figure 3.

Figure 3 - Raw Materials Model Estimates, February 1991



This estimate was based upon a titanium market growth rate of 3.0% for the 1990's. This value was consistent with average growth rates during the 1980 era. The goal

of the study was to estimate scrap availability rather than to predict mill product shipments during 1991. Therefore, little significance was given to the market estimate until later in the year when the mill products markets deteriorated. It was recognized that the raw materials model had predictive power and could be used to estimate future raw materials needs for various market growth assumptions.

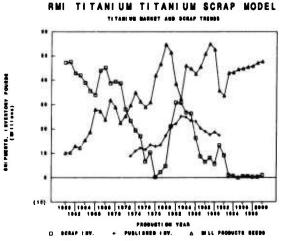
Market data for the period between 1960 and 1991 was separated into the discrete market areas of commercial aviation, military aviation and industrial applications. These markets areas were adjusted by applying individual growth rates. Growth was adjusted to the average 1.43% value obtained from statistical evaluation of historical growth data. These major market areas were adjusted as shown in Table II.

Table II - Assumed Growth Rates for Titanium Markets
Historical Statistical Evaluation

Market <u>Area</u>	Share %	Growth <u>%</u>
Commercial Aerospace	59%	2.00%
Military Aerospace	18%	-1.30%
ndustrial Applications	24%	2.05%
Weighted Average		1.43%

These values were then used in the model to estimate titanium requirements for the decade ending in the year 2000. Sponge requirements and scrap inputs were computed based upon estimated final product needs. A tabular summary of this model is included as Table III. These results are shown graphically in Figure 4.

Figure 4 - Mill Products Estimate for the 1990's with Derived Growth Rate



Conclusions

Titanium market growth rates can be estimated from an evaluation of historical data. Evaluations indicate that traditional markets have matured and the rate of market growth in these areas will continue to decrease during the next decade. Reductions in military aerospace spending and a severe economic recession caused an abrupt drop in demand for titanium in 1991.

Use of industry indicators such as inventories, backlogs, and estimated market growth rates permit estimations of raw materials needs to be made. Evaluation from this model indicate that the domestic industry can support a scrap recycle level up to about 43 percent of ingot production. United States sponge capacity appears to be adequate to supply estimated domestic market needs through the late 1990's.

Future increases in market growth rate depend upon the development of new uses for titanium. This growth potential is most likely in industrial applications. Moderate growth in this area will not drastically impact future mill products needs. Conversion yield for mill shapes into end products is high for most industrial applications. Since market growth is really in end products, mill shape needs will grow more slowly for industrial uses than for aerospace or defense applications.

Raw materials models are easily modified to reflect any projected market growth rate estimate. A model of this type provides a convenient tool for predicting raw materials needs and for forecasting market trends.

References

- 1. Gray, J.J and Mcliroy, P., "Utilization of Secondary Titanium-An Economical-Statistical Evauation", Bureau of Mines Information Circular, United States Department of Interior, (1970)
- Staff, Bureau of Mines, "Titanium Quarterly Reviews", Mineral Industry Surveys, United States Department of Interior, (1975 - 1992)
- 3. Wood, R.A., "The Titanium Industry in the Mid-1970's",(Report MCIC-75-26, Battelle Columbus Laboratories, 1975)
- Staff, Titanium Development Association, "Titanium 1985", TDA Statistical Review, 1978 - 1985, (1986)
- 5. National Materials Advisory Board Panel, "Titanium: Past, Present, and Future", (Report, NMAB-392, Federal Emergency Management Agency, 1983)
- Fisher, R.L., "An Evaluation of the Titanium Scrap System", (Report, R&TD Report #689, RMI Company, Unpublished Research Report, 1987)

pode
7
Herlah
į
5
Panel
7
≡
Ž

1801 - 3800 DATE									:	
25 - ext - 22					٦	(Kpounds)				
HISTORICAL GROWTH MODEL	Ē	Ĭ	-	Ĭ	-	=	1	Ī		2002
						8		8	2	2
Copecity mod	2	2	2.2	2.5	2	20.00	20.0%	20.2	78.9%	78.9%
Rest Motel Supply: Sormy usage	¥.7	2 . S	43.5%	48.7%	48.0%	44.24	12.4%	***	12.00	40.0%
į	20.465	27.041	38,788	35,600	2007	26,000	25,25	3	20.00	87.88
Spenge Imports	- 200	•								
Spenge Consumption	700,055	20.073	200	26.625	20.00	26.576	87.000	20.675	*1.00	41.20
Sorap Consumption	25,653	20,55	20,000	20.02	20.00	20.00	20,10	20.00	26.00	200
Manther affley engepty	2.00.2	3,283	8,782	3,867				4.112	4.467	4.417
Total Rew metal cuppity	67.74	86.238	2.3	3	70.464	78.67	72.010	72.867	74.767	75.74
Inget Production	84.746	*	98,124	84.378		1987	8	70.466	72.00	72.68
Inget Consumption	20,284	101,48	20,28	25.8	1	-	***	2	7	72.48
Mill Products Objensets	26,38	2	1000	43,147	2.1	44.78	4	£748	47,141	67.78
% mill predeats converted that shapes	×6.8	25.85	37.18	F. P.	76.K	F. 12	31.0%	20.00	21.0%	2
Febricated Products production	10112	11024	1000	1	13867	14878	14816	16461	14616	-
Estimated product demand	18778	- - -	12000	- - - - -	-	13867	LL SEL	1484	18636	10001
Shortfell/Customer Inventory Lovel	7,676	6.22.0	2,000	3,412	3,776	4,100	4,316	4,140	3,881	3,866
Market Growth Rate	-11.0%	A. 0.	4.0.0	£.	2.0%	3.9%	3.0%	4.0%	4.0%	2.4
										1.65%
	*	\$	43.80	25.28	44	44.86	*	46.16	***	47.84
North Pagety.	•	1	1883	1	186	1986	1887	-		2007
Off-grade Spenge (10 to 5% of Pred)	-	2	į	1678	- 726	1788	1780	178	-	1676
Inget minus mil chapes production	-	1	2314	200	22		20000	20042	1	28714
Mill Shapes miles Fabrisated Shapes	į	2	23844	2002		i	•	200	2118	1
Greations year)										
	•	1	1	1	1	1	į	į	1	•
Recycled and products, (15 yr 20)	7.1	3,882		8.618		7.817		-	-	
	000,000		200,00	67.873	200	71.68	71,000	2	26.78	78.786
Borge Consumption:										
Thesian Resysted to products	1	1			8		31000	***	20000	****
Sheel Production:										
Direct after and decaddring	į	į	•	•	į	ł	i	į	-	=
	200,2	3.5	=	=	# E	=	11,000	= . = .	2.0	# E
Other Alloying, Superalloys etc	218	2188	2100	2188	218	2188	218	218	210	2100
Total steel predection	22188	22168	22100	22788	22000	22000	22000	22000	23868	20100
Honroseverable metal leases	14457	1000	178-00	1718	17861	17746	-	18147	-	1
(artificated at 20% of raw meterlate)										
Total sorap commercion	84.878	79,467	1146	800,000	70,221	70,048	71,000	79,767	70,782	73,646
	17,881	10,000						-		
Computed Sorap Invantory Lovel	13,387	162,0	1,004	786	Ī	2	613	Ř	*	1,070
Year	-	1	1885	1861	1 000	188	1887	-	386	
									-	

LEACHING OF ILMENITE WITH SULFURIC ACID-THIOUREA SOLUTIONS

Francisco J. Tavera, Sandra L. Bribiesca, Eugenia S. Contreras

Instituto de Investigaciones Metalúrgicas
Universidad Michoacana de San Nicolás de Hidalgo
Morelia, Mich., 58000 México.

ABSTRACT

The dissolution of ilmenite in sulfuric acid-thiourea solutions has been examined experimentally under controlled acid concentration, particle size and temperature conditions. The temperature range of the experiments was 303 - 353 K. The reaction --system was analyzed under acid concentration of 0.1, 0.5, 1.0 --and 2.0 N. Particle size varied between 38 and 250 microns. Experiments have shown that the rate of dissolution increased with --increasing temperature, acid concentration and specific ore surface. The arrhenius activation energy was found to be 32.3 KJ --per mole. The experimental work has shown that the addition of --thiourea in the leachant increases, markedly, the recovery of titanium and the rate of ilmenite dissolution as compared with sulfuric acid-ilmenite leaching systems.

Titanium '92 Science and Tachnology Edited by F.H. Froes and I. Caplan The Minerals, Metals & Materials Society, 1993

INTRODUCTION

Ilmenite is an important source of titanium in the world --

which can be treated for metal extraction and for pigmento too. Extensive studies on the dissolution of ilmenite in acid media - have been conducted to determine the behaviour of leaching systems. In general, experimental results have shown that the rate-of ilmenite dissolution in acid media is increased with increasing acid concentration and temperature

It has been observed that the reactivity of ilmenite in sulfuric acid media increases as the natural weathering of the ore is increased (1). Experimental results have shown that the rate of a

acid media increases as the natural weathering of the ore is increased (1). Experimental results have shown that the rate of - ilmenite dissolution in sulfuric acid and hydrochloric acid is - strongly affected when acid concentration increases from 0.03 to 1.0 M and temperature increases from 313 to 363 K (2).

It was observed the dissolution behaviour of ilmenite in sulfuric acid leachants where acid concentration varied between 4.7 to -- 12.5 M and temperature was varied in the range 338 to 358 K (3); it was pointed out that the reaction was indicated to be controlled by a chemical process at the mineral surface.

The effect of temperature, particle size, stirring speed and accid concentration on the rate of dissolution of ilmenite in sulfuric acid media was studied (4); it has been found that the --leaching of ilmenite at temperature between 361 and 388 K is described by a surface chemical reaction limiting.

(5); the kinetic data of the leaching of ilmenite-hematite has -been explained in terms of a complex geometrical relationship.

The leaching of powdered ilmenite ore with highly concentrated -hydrochloric acid was studied (6), where acid concentration was-varied between 11.3 to 11.6 M, over the temperature range 303 to 333K. At temperature of 303 to 323 K, the leaching of ilmenite -has been explained in terms of a surface chemical reaction. At -temperatures of 323 to 333 K, the rates were limited by difu---ssion of dissolved metal ions through a residual layer of the --ore.

Leaching of ilmenite was studied at temperatures between 323 to-

353 K in hydrochloric solutions (7); it was found that the rateof dissolution was initially rapid, then declined, apparently -due to the polymerization and transport of dissolved titanium -within the porous solid.

The present experimental work has been intented to study the effect of addition of thiourea in the dissolution behaviour of $i\underline{l}$ menite in sulfuric acid media.

EXPERIMENTAL

Materials.

the ilmenite sand used in this study was obtained from the Mi--- choacán shore (México). This sand has 11.5 wt % of TiO₂. The chemicals used in this work are of analytical grade.

Apparatus and Procedure.

Sand particles less than 38 microns were prepared by grinding of the original sand. The experiments were carried out in a glass reactor in a cosnstant temperature bath. The glass reactor was sealed from the atmosphere by means of a glass cover which had four openings in order to fit a vapour condenser, an air lance,a thermometer and a sampling tube.

Leaching experiments were conducted in the temperature range 303 to 353 K.

The glass reactor was filled with 500 ml of sulfuric acid-thiourea solution, with the desired acid concentration, and heateduntil the experimental temperature was reached; at this point 2grams of ilmenite sand were added into the reaction system and the experiment began. Leaching solutions contained 10 grams of thiourea per liter.

The kinetics of the experiment was followed by taking samples of 5 ml from the experimental solution at given periods of time. Experimental samples were analized in triplicate by both X-Ray - fluorescence analysis (KEVEX 7000-77) and atomic absorption spectrometry (Perkin-Elmer). Leaching solid residues were examined - by X-Ray diffraction techniques (Philips).

RESULTS AND CONCLUSIONS.

The dissolution of ilmenite in sulfuric acid has been represented as the equation:

$$FeTiO_3 + 4H^+ = Ti^{+2}O + Fe^{+2} + 2 H_2O$$
 (1)

and the oxidation of the ferrous specie,

$$Fe^{+2} + H^{+} + \frac{1}{4} O_{2} = Fe^{+3} + \frac{1}{2} H_{2}O$$
 (2)

Thiourea has been used for metal extraction in the leaching of some materials, to produce a metal-thiourea specie in solution in acid media (8-10). Thus, the addition of thiourea in the present reaction system can be represented as follows:

Fe Ti
$$O_3$$
 + 2 SC $(NH_2)_2$ + 4 H⁺ = Ti O (SC $(NH_2)_2$)⁺¹ + Fe⁺³+ 2H₂O (3)

Which indicates that the increase in acid concentration will increase the amount of titanium in solution.

Figure 1 shows the fraction of leached titanium plotted as a --function of the experimental time. As it can be noted, dissolu-tion rate increases clearly as the concentration of sulfuric a-cid is increased.

Figures 2(a) and 2(b), shows the rate of reaction for the ilmenite dissolution plotted as a function the acid concentration. The experimental data have shown that the dissolution rate of ilmenite in sulfuric acid-thiourea media follows an exponential parettern with respect to the change in the acid concentration. It can be seen that the rate of dissolution remains in a relative low value when acid concentration is low, however when acid concentration increases the rate of reaction for the ilmenite dissolution increases suddenly; this behaviour is more evident as temperature increases.

The reaction rate for the ilmenite dissolution under the present experimental conditions can be expresed as follows:

$$T = 353 \text{ K: } LnK = 2.5 \text{ C} - 1.03$$

 $T = 323 \text{ K: } LnK = 2.8 \text{ C} - 4.35$

The most important feature in the present experimental results - is that the addition of thiourea in the leaching solution re---sults in an increase in the ilmenite dissolution rate and high - titanium recovery in solution compared with ilmenite leaching -- systems in sulfuric acid solution (4); this effect is shown in - Figure 3.

Effect of Particle Size.

The effect of particle size on the rate of dissolution of ilmenite in sulfuric acid thiourea solution was analized at 353 K and sulfuric acid concentration 2.0 N. Figure 4 shows the experimental results for five different ilmenite particle size, 38, 100,-127, 166 and 250 microns used here. It can be seen that the rate of dissolution of ilmenite in the present experimental solutions is affected by size of the particles. The recovery of titanium in solution and the rate of dissolution of ilmenite increase asparticle size decreases. Figure 5 shows the rate constant of leaching plotted as a function of particle size; it can be seen ---that there is an exponential behaviour of the reaction system. This fact is in according with the increase of the specific area of the mineral.

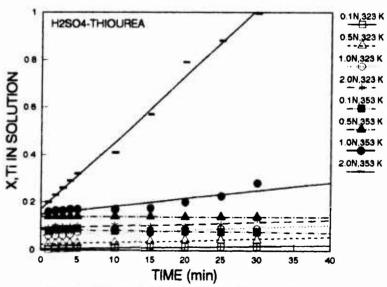
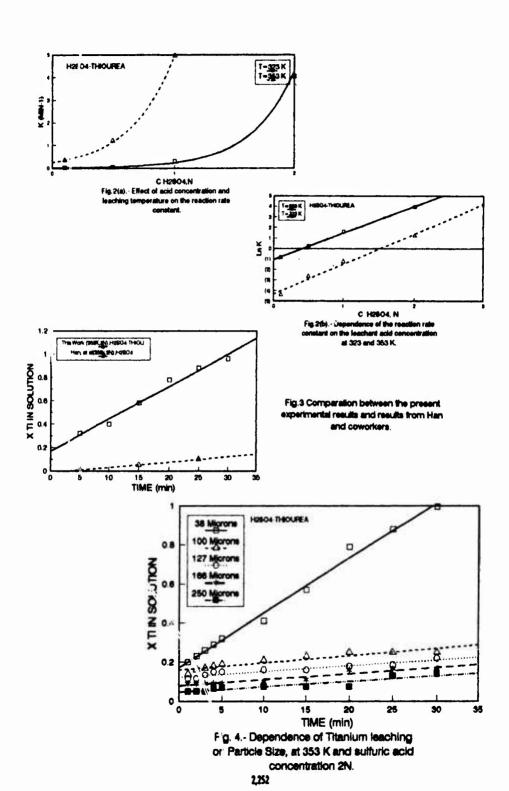
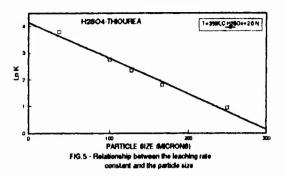


Fig.1.- Effect of acid concentration on the mole fraction of leached titanium at 323 and 353 K





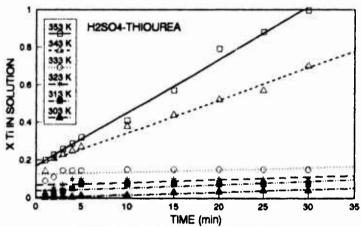


Fig. 6.- Titanium leaching dependence from experimental temperature. C H2SO4 2 N.

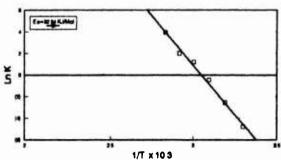


Fig. 7.- Arrhenius plot for the dissolution of Irmenite in Sulphuric Acid-Thioures solutions

Effect of Temperature.

Ilmenite particles, 38 microns were leached in sulfuric acid --thiourea solutions, H₂SO₄ 2.0 N, at 303, 313, 323, 333, 343 and353 K. It has been observed that the dissolution of ilmenite in
the present leaching system is very much affected by temperature
as it can be seen in Figure 6, where the fraction of dissolved titanium is presented the experimental observations have shown that the ilmenite rate of dissolution increases very markedly as
the experimental temperature is increased.

The leaching results obtained for six different temperature areplotted in Figure 7 as the Arrhenius relationship; the apparentactivation energy value of 32:2 KJ per mole was calculated.

CONCLUSIONS.

The leaching of ilmenite sands in sulfuric acid media containing additions of thiourea has been experimentally analized in terms-of the effect of sulfuric acid concentration, particle size and-temperature. The following conclusions can be derived based on -the experimental results.

- The rate of dissolution of ilmenite in the experimental lea-chants increases as temperature and acid concentration increase as and as particle size decreases.
- 2. The apparent activation energy is 32.2 KJ per mole.
- 3. The rate of dissolution of ilmenite in sulfuric acid-thiourea solutions is higher than the dissolution rate of ilmenite in sulfuric acid solutions, as it has been compared with recent experimental data.

ACKNOWLEDGMENT

The authors wish to thank Dr. Juan Serrato who collected and provided the natural ilmenite ore. Also, thanks are due to Mr. Gerrardo Rosas for his help during the chemical analysis of the experimental samples.

REFERENCES

- B. Judd and E.R. Palmer: Proc. Aust. Inst. Min. Metall, 1973, No. 247, Pp. 23-33.
- M. Imahashi and N. Takamatsu: Bull. Chem. Soc. Jpn., 1976, -- Vol. 49, pp. 1549-53.
- A.F.M. Barton and S.R. McConnel: J. Chem. Soc. Faraday Trans.
 I., 1979, Vol. 75, pp. 971-83.
- 4. K.N. Han, T. Rubcumintara and M.C. Fuerstenau: Met. Trans B., 1987, Vol. 18B, pp. 325-330.
- 5. M.E. Wadsworth: Light Metals, 1976, Vol. I, p. 481.
- 6. T. Hisashi: Bull. Chem Soc. Jpn., 1982, Vol. 55, pp. 1934-38.
- J.F. Duncan and J.B. Metson: New Zealand J. Sci., 1982, Vol. 25, pp. 103-09.
- E. Becker, E. Knothe and J. Lobel: Hidrometallurgy, Vol. 2, -1983.
- 9. R. Groenewald: Hidrometallurgy, Vol. 1, 1976.
- 10. F. J. Tavera: El Relox y La Rosa, Univ. Michoacana, No. 1, -1990.

HID AND HDI DISSOLUTION DURING TITANIUM MELTING PROCESSES

A. Mitchell and D.W. Tripp

Department of Metals And Materials Engineering
University of British Columbia
6350 Stores Road
Vancouver, B.C. V6T 1Z4

ABSTRACT

The computed temperature profiles which exist in the feed material and liquid metal pools during Vacuum Arc Remelting (VAR), Electron Beam (EB) and Plasma Arc (PA) melting indicate that, for the majority of cases, the removal of both HID and HDI material (including alloy additions) is a diffusion/solution process. The rates of these processes depend critically on the process, and on the dissolving component. The practical aspects of process operation in regard to defect-free material are discussed particularly as the procedures relate to the thermal regime. We conclude that defect-free alloys are a realistic aim and that the observed dissolution rates, combined with buoyancy mechansims require hearth melting for full defect removal.

INTRODUCTION

Titanium alloys do not contain inclusions from the same mechanisms as those found in steels or superalloys, since the requisite thermochemical conditions for their precipitation do not exist. The term "inclusion" in the context of titanium refers instead to what in steel terminology would be an exogenous inclusion, (i.e., a particle which has been trapped in the melt by accidental interaction with an external source of contamination). Although titanium alloys have the reputation of being excellent solvents for almost any material, the solution processes take a finite time. Should this time be less than the process time at high temperature, the particle will survive to become a potential source of concern in the mechanical behaviour of the alloy

in service. In practice, the inclusions which we observe fall into two categories;

- "High Interstitial Defects" (HID)
 - "High Density Inclusions" (HDI)

We will consider these two categories separately in the discussion below.

High Interstitial Defects

At a relatively early stage in the progress of titanium use it was observed that the material could contain small areas of alpha-stabilized alloy, usually associated with cracks or porosity and with a hardness considerably in excess of the bulk material or the alpha-phase of the bulk alloy. Subsequent analysis of these areas showed that they contained high contents of nitrogen, oxygen and carbon in various combinations(1,2,3). In the time frame of that work, it was

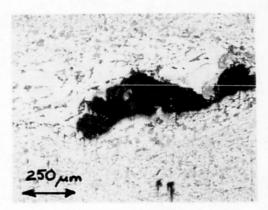


Figure 1.: Typical Hard-α Defect

Titanium '92
Science and Technology
Edited by F.H. Froes and I. Caplan
The Minerals, Metals & Materials Society, 1993

concluded that the origin of the particles was in contaminated titanium sponge. Subsequent studies have shown that the particles may come from many sources(4) including recycled scrap and the melting process itself. Further studies(5) have also shown that the VAR process has only a limited capacity for dissolving the particles, partly because of the inherent dissolution rate and partly because of the finite risk of a particle path "short-circuiting" the process whilst trapped in a convective flow. The particles have various physical forms depending on their origin but generally are of the form shown in Figure 1., with dimensions ranging between 1 and 50 mm depending on the degree of deformation during working.

The dissolution process for the particles in liquid titanium alloys has been studied by several workers(5,6,7) all of whom comment on the fact that it is a diffusion controlled process since the melting point of the particles is above the process temperature for almost all of the exposure in VAR. The diffusion process is evidently quite complicated since the particles can lose or gain alloy elements at the same time as the dissolution process is proceeding; a factor that greatly complicates the identification of their origin. The dissolution process is found to follow the expected Arrhenius relationship for thermal activation, leading to a strong temperature dependence of the dissolution rate. Clearly a major factor in the survival of the particles in VAR is that the ingot pool in the process contains very little superheat and the exposure time of the particle to high temperature can be quite limited.

The rate of dissolution is difficult to measure with any accuracy since the experiment necessarily requires a definition of the composition and physical form of the particle. In this and previous work the dissolving particle has been assumed to be equivalent to the "burnt sponge" composition, made synthetically by nitriding sponge under controlled conditions. There is indirect evidence from production trials that particles that contain higher contents of oxygen than the synthetic burnt sponge dissolve faster than the high nitrogen particles, which would also be in agreement with the relation between the Ti - N and Ti - O phase diagrams. If this is the case then the dissolution rates used in these studies represent worse case rates.

The experimental results which have been obtained by dissolution studies of pure, monolithic TiN appear to give approximately the same dissolution rates as have been observed for artificially-nitrided sponge particles(6), and which correlate well with the assumption that it is a diffusion-controlled process in which the particle rapidly becomes isothermal with the surrounding titanium alloy and subsequently dissolves by the diffusion of nitrogen into the bulk alloy. The contents of nitrogen in typical HID material seldom exceed 8wt%, but since the addition of even small amounts of nitrogen to titanium causes a substantial increase in the melting point, it is unlikely that any HID composition will melt in the VAR ingot pool and hence all of the particles will be removed by dissolution, rather than by melting. It is also worthy of note that in the case of HID (and also of HDI) the contribution of the dissolved elements from the inclusion material to the bulk

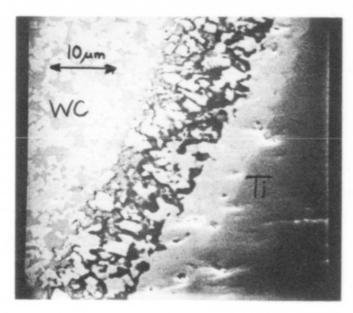


Figure 2A: WC/Ti boundary (map master)

analysis is extremely small and we cannot, therefore, obtain useful information about the dissolution process from the bulk analyses of the alloy before and after melting.

High Density Inclusions

The most common sources of high density inclusions arise in contaminated scrap and are predominantly chips from tool bits used in machining parts or ingots. Modern methods of scrap preparation and inspection have essentially eliminated this problem in premium grade titanium alloys, but the problem is still of general interest in the manufacture of CP titanium where the scrap preparation and also the melting methods may not be as rigorous as those applied in the aerospace industry. The most general types of HDI material which are found are tool-bits consisting of Co-bonded WC, or monolithic WC, and also welding electrode tips consisting of W with some small

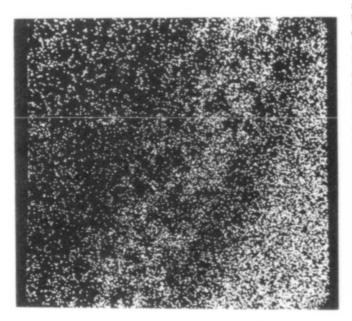


Figure 2B: Ti X-Ray Map of HDI Shown in Figure 2A

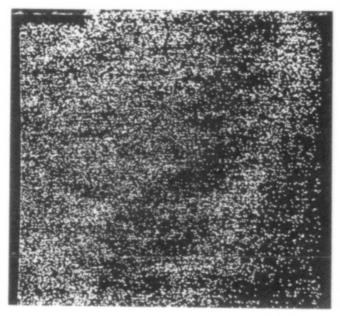


Figure 2C: W X-Ray Map of HDI Shown in Figure 2A

addition of thoria. The latter material behaves in the same way as the case of Nb considered below, but the dissolution of the tool-bits is an interesting process involving both diffusion and dissolution. The particle/alloy boundary has the form shown in Figure. 2 during the dissolution step, in which we can see two distinct layers between the bonded WC and the liquid alloy. These layers correspond to the phases that are to be expected from the system Ti-W-C(8), namely TiC(s) + Ti-W(l) alloy and a Ti-C-W(1) alloy. In the case of the cobaltbonded structure, the Co bond is replaced very quickly at the start of the particle-alloy contact, by liquid Ti alloy. After less than 60 seconds of contact time at 1800 C there was no detectable Co content in a Co bonded tool-bit of 1mm cube dimensions. The carbide bonding process involves sufficient particle-particle contact that the structure remains intact even after the extraction of the infiltrated cobalt, and the dissolution process in the liquid alloy consists of the diffusion reactions of the multilayer structure shown in Figure 2. Experimentally, the dissolution rate of Co-bonded WC at 1700 C was found to be in the range 0.03 - 0.05 g cm⁻²min⁻¹. Since the available time at high temperature in the ingot pool is very small (the 1 mm cube falling in the centre would reach the liquidus of a typical 800 mm dia. CPTi ingot in 1 sec), the HDI particles are seldom changed significantly by the melting process, and their absence in the final product can only be assured by raw material preparation and/or hearth melting.

A general problem still remains in relation to the dissolution processes which are required in the formation of an alloy containing high density, high melting-point elements. With the advent of more alloys in this category, particularly the beta-alloys, this problem will become more acute. The technique which has been used successfully for many years for in-

troducing alloy elements such as Mo or V is that of first forming a master alloy with aluminium through various types of aluminothermic reduction. This method is entirely satisfactory for those alloys in which we can tolerate the necessary levels of Al (i.e. the alloys with significant alpha fraction). It is however not possible to use it for the beta- or near-beta alloys. In this latter case we have a very significant practical difficulty to dissolve the alloy elements and to homogenize the alloy during melting. (It should be noted that solid-

state diffusion processes would require unreasonably long times at high temperature to provide the homogenization of any of the inclusion types studied.)

Although the practical aspects of this problem have been known for some time, the dissolution rates have not been studied. However, if we assume that the particle would have only a very small relative velocity in the liquid, we may estimate the dissolution rates from a simple diffusion calculation (Appendix 1). The result demonstrates clearly the practical difficulty of making such an alloy, since the diffusion times required are well beyond the capability of a single VAR melt. We also see that this process is temperature sensitive, as would be expected, and that from the point of view of accelerating the dissolution process elevated temperature is more effective than extended time. In the following work we have chosen the example of Nb to illustrate the solution process as it applies to the VAR system. Figure 3 illustrates two cases of melting conditions for Nb 50 wt% Ti alloy, in which Nb particles in the electrode were observed to be in the one case preserved and in the other case to be dissolved.

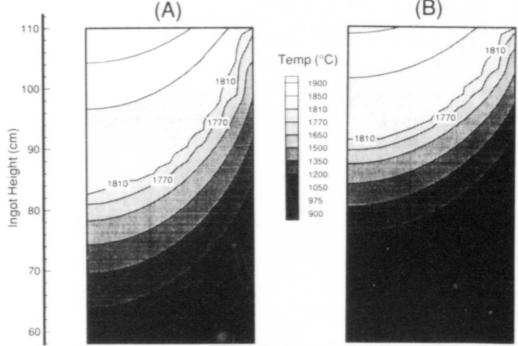


Figure 3: Computed Pool Profiles of Niobium Titanium Ingots Melted Using the VAR Process. Ingot Diameter is 52 cm. In (A) the Melt Rate was 6 kg/min and Particles 1000 µm in Diameter Were Dissolved. In (B) the Melt Rate was 2.8 kg/min and the Particles Survived.

Stoke's Law was used to calculate the times taken for a 1000 µm particle to fall to the liquidus. In the case of ingot 2 (Figure 3B), in which the particles survived, a particle would have take 0.63 seconds to settle through a stagnant liquid. In ingot 1 (Figure 3A), where no niobium particles were found, a similar particle takes almost 0.9 seconds to do the same. According to Appendix 1, neither of these times allow for the complete dissolution of a niobium particle at the temperatures indicated in Figure 3. Consequently some factor associated with the higher melt rate and the higher temperatures present in ingot one must explain the removal of niobium particles from that ingot.

DISCUSSION

The removal of HID from the melting system rests on two essential features; the elimination of "short - circuit" paths, and the application of a sufficient time/temperature parameter for dissolution. As has been pointed out in the literature, a fundamental weakness of the VAR system is the intrinsic presence of a direct link from the electrode to the ingot pool, leading to the conclusion that VAR will not be able to provide the inprinciple guarantee of HID removal. It is this factor which has lead to the advent of hearth melting, either by electron beam or plasma, but even in these processes it is still necessary to pay detailed attention in the furnace design to the prevention of the short-circuit mechanism.

The work detailed above offers an indication of the time/temperature relationship required to dissolve HID and it is notable that although the ingot pool in the VAR process does not provide a large superheated volume, the droplets falling from the electrode may be highly superheated for the short time of transit across the arc. In this case, the removal of HID would be a function of the electrode diameter since the current density is an inverse function of the electrode diameter. As a result then, we would expect to find a higher occurrence rate of HID in larger ingots, all other factors being equal. We can consider that the arc in the VAR process moves from point to point on the electrode surface and is located at any one time on the individual cone of liquid metal which is the precursor of droplet formation. We may calculate the temperature rise in the local area of the arc assuming this set of conditions, as shown in Appendix 2, and find that in this case the temperature will reach a superheat of more than 1000 K in the time the arc will be located on the metal cone, as suggested by high-speed video recording of arc behaviour(9). Should the metal cone contain an HID particle, this superheat will not cause its decomposition to a lower level of nitrogen (Figure 4) but will greatly decrease the time required for its solution in the alloy. The fraction of metal which passes through the process postulated above is still a matter for conjecture, but is highly unlikely to be 100% of the electrode weight. The arc-superheating effect would therefore be a potential contributor the the overall removal scheme for HID, but

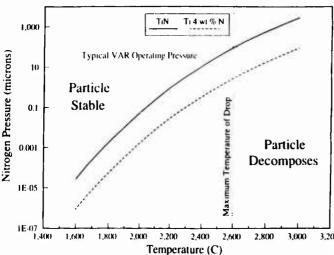


Figure 4: Equilibrium Diagram for the Reaction $TiN(s) \Leftrightarrow Ti(1) + \frac{1}{2}N_2(g)$ Showing Regions of Particle Stability and Decomposition

could not be relied upon for complete removal of the particles.

A second feature of HID removal which has not been widely discussed in the literature concerns the bulk density. Although the inclusions are termed HID, the density of the high nitrogen particles is greater than the density of the equivalent alloy, provided that their porosity is low. We can expect, therefore, in practice that some of the particles will sink in the alloy, whilst others 3,200 (with porosity) will float. This factor makes an accurate calculation of the dissolution time extremely difficult.

The dissolution of HDI material is clearly more simple to quantify than HID, since the relative density is such that the particles will always sink in the alloy. The solution rate can probably be approximated quite satisfactorily by the use of a diffusion model operating isothermally in a situation with no relative velocity between the particle and the bulk liquid. We see from the results of this study that quite long times are required for the dissolution process and that it would, therefore, be of advantage to either manufacture master alloys containing sufficient Ti to accelerate the process, or to use a primary process (such as ISM) which will permit sufficient solution time. Given the uncertainties of particle trajectories in the VAR pool it is unlikely that even multiple VAR will consistently guarantee zero HDI occurrence in the beta alloys.

A common theme in the above discussion of both HID and HDI removal is the uncertainty in predicting the mechanism in the VAR process due to the possibility that the particles can "short-circuit" the process so as to have only a very short residence time in the high temperature region. It has become clear from commercial practice that whilst we can take steps to minimize this possibility, and indeed bring the defect incidence to an extremely low level, there is no variant of the VAR system which will guarantee the complete removal of the particles under all circumstances. Although this factor has been the subject of intensive discussion in relation to aero-engine rotating-part quality alloys, it has not been widely noted that the problem is equally pressing in the case of heat exchanger tubing for nuclear or desalination purposes. The solution proposed for the aerospace case is that of hearth melting(9), which has been developed to the point at which it has become not only a technical competitor for triple VAR, but also an economic one. However, the need for a solution to the HID/HDI problem in the other applications indicated above will require the same measures,

leading to the conclusion that most of the titanium melting technology will follow the same route as the more specialized aerospace alloy application. The behaviour of HDI in the hearth processes is quite well established(10) and evidently follows the expected gravity separation, since the high negative buoyancy forces which worked against the VAR process are very advantageous in this case, the HDI particles being collected in the forepart of the hearth system in a predictably quantitative manner. The removal of HID by the various hearth systems presently in use has been well established as a practical result but the precise mechanisms of removal are not well defined. Some solution of HID certainly takes place, but the role of additional mechanisms such as gravity separation has not been quantified. It is clear, however, that the hearth systems are capable of removing even high levels of HDI and HID from contaminated feed material and should be used in preference to multiple VAR melting in all cases where the absence of these particles is essential.

ACKNOWLEDGMENTS

The authors would like to thank the National Sciences and Engineering Research Council of Canada for their financial support in the production of this paper. In addition, the assistance of various people and organizations in the titanium industry is greatly appreciated.

REFERENCES

- F.W. Wood, "Elimination of Low Density Inclusions in Titanium Alloy Ingots", (AFML-TR-69-47, April, 1969).
- F.W. Wood, R.L. Carpernter, "Improvement of Titanium Alloy Ingot Consolidation", (AFML-TR-72-46, May 1972).
- J.L. Henry, S.D. Hill, W.E. Anable, et. al., "Source and Control of Nitride Inclusions in Titanium", (United States Bureau of Mines Report on Investigations 7933, 1974).
- C.E. Shamblen, "Titanium Alloy Melt Related Defect Sources", (Technical Information Series, No. R89AEB141, January 1989, General Electric Aircraft Engines, EMTL, Cincinnati, Ohio).
- P.J. Bania, "Production of Titanium Articles Free From Low Density Inclusions", US Patent Number 4678506, July 7, 1987.
- T.K. Redden, "Dissolution Rate of Titanium Nitride in Titanium Melts", (General Electric Co. Technical Memorandum No. TM-85-127, March 1985.)
- R.N. Jarrett, "Removal of Defects From Titanium Alloys with Electron Beam Cold Hearth Refining", (Paper Presented at Electron Beam Remelting and Refining, State of the Art, 1986 Conference, November 1986), 332-346.
- E. Rudy, "Constitution of Ternary Titanium-Tungsten-Carbon Alloys", Journal of the Less Common Metals, (33), 1973, 245-273.
- F.J. Zanner, R.L. Will anson, R.P. Harrison, "Vacuum Arc Remelting of Alloy 718", (Paper presented at Superalloy 718: Metadurgy and Applications Meeting, Pittsburgh, Pennsylvania, June 1989), 17-32.
- C.H. Entrekin, "The Removal of High Density Inclusions by the Hearth Remelting Process", (Paper Presented at Electron Beam Remelting and Refining, State of the Art, 1985 Conference, November 1985), Part I, 40-47.

APPENDIX 1

The dissolution rate of an isothermal sphere of niobium in an infinite bath of isothermal titanium can be calculated empirically using the empirical relationships determined by Steinberger et. al.(A1).

The amount of solute material diffusing into the bath is expressed as:

$$N_{Nb} = k_{Nb} \left(C_{Nb}^{\bullet} - C_{Nb}^{Bulk} \right). \tag{A1}$$

where N_{Nb} = dissolution molar flux of niobium, C_{Nb}^{\bullet} = the interfacial concentration of niobium (i.e. the licuidus concentration) and C_{Nb}^{Bulk} is the bulk concentration of niobium in the liquid. k_{Nb} represents the mass transfer coefficient.

For convective mass transport of niobium from a dissolving sphere to the bulk of a titanium bath, the correlation which includes both natural and forced convection is:

$$Sh = 2 + \underbrace{0.0254(Gr \cdot Sc)^{1/3}Sc^{0.244}}_{Nonaral Convection} + \underbrace{0.347(Re \cdot \sqrt{Sc})^{0.62}}_{Forced Convection}$$
(A2),

where $Sh=k_{Nb}d/D_{Nb-Ti}$, $Gr=\rho_{Ti}^2\beta_mg\Delta xd^3/\mu^2$, $Sc=\mu/\rho_{Nb}D_{Nb-Ti}$ and $Re=\rho_{Ti}u_{rel}d/\mu$. The velocity in the equation for the Reynolds number (Re) is given by Stoke's Law as $u_{rel}=gd^2(\rho_{Nb}-\rho_{Ti})/18\mu$.

The diffusion constant D_{Nb-Ti} is not well known, nor is the viscosity μ . For the purposes of these calculations, D_{Nb-Ti} has been taken to be 2 x 10^{-5} cm²/sec and the viscosity has been set to that of liquid steel or 0.064 poise.

Using equation A2, the mass transfer coefficient can be easily calculated. The mass flux from a dissolving sphere is given as

$$\frac{dN_{Nb}}{dt} = \frac{1}{2} \frac{\rho_{Nb}}{MW_{Nb}} \frac{d(d)}{dt} = k_{Nb} C_{Nb}^*$$
 (A3).

By suitable integration this equation can be used to determine the time for dissolution for particles of various initial diameters. This can be seen in Figure A1.

In the above formulation, the only parameter that varies with temperature is the liquidus concentration of niobium. The diffusion coefficient D_{Nb-Ti} and the viscosity μ are both assumed to be independent of temperature. This is certainly not the case in actual dissolution where both the diffusion coefficient and the viscosity are likely to be very strongly dependent on temperature.

With these considerations, Figure A1 represents a "worst-case-scenario". At higher temperatures, the dissolution rates are likely to be much higher than those indicated in figure A1.

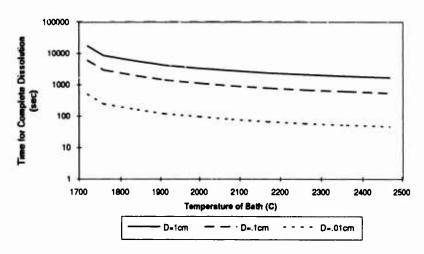


Figure A1: Complete Dissolution Time vs Temperature for Niobium Spheres Dissolving in Liquid
Titanium.

APPENDIX 2

Let us assume that a drop forming on the surface of a melting electrode is conical in shape with a base of 0.015 m (15 mm) in diameter and a height of 0.01 m (10 mm). A simple heat balance allows for the calculation of the maximum temperature attained by the drop during melting. The governing heat transfer equation is:

$$\dot{q}_{p} = -\rho V C_{p} \frac{dT}{dt} \tag{A4}.$$

Equation A4 can be easily solved to give:

$$\Delta T = \frac{q_p^*}{\rho V C_n} \tag{A5}.$$

Assuming that no heat is lost due to either radiation or convection and that the only source of heat is that applied to the cone by the arc and that for the time the arc spends on each drop site, its entire energy is deposited on the surface of the cone we can calculate the temperature change. In the case of titanium melting, the electrode voltage drop is about 6 V and the melting current is 10,000 A (for an 0.8 m diameter electrode). Thus the energy transferred to the drop site is approximately 60,000 W. Using an average density of 4540 kg/m^3 , a cone volume of $5.89 \times 10^{-7} \text{ m}^3$, a heat capacity of 655.1 J/kg and a typical arc dwell time of 0.030 seconds (30 milliseconds), a change in temperature of 1,027 C is calculated using equation A5.

References

- A1. R.L. Steinberger and R.E. Treybal: "Mass Transfer from a Solid Soluble Sphere to a Flowing Liquid Stream", Journal of A.I.Ch.E₄, 6 (2) (1960), 227-232.
- A2. S.A. Argyropoulos and R.I.L. Guthrie, "Dissolution Kinetics of Ferroalloys in Steelmaking", (Paper Presented at 65th Steelmaking Conference, ISS-AIME, Pittsburgh Pennsylvania, 1982), 156-167.
- A3. L. Gourtsoyannis, R.I.L. Guthrie and G.A. Ratz: "The Dissolution of Ferromolybdenum, Ferroniobium and Rare Earth (Lanthanide) Silicide in Cast Iron and Steel Melts", (Paper presented at the 42nd Electric Furnace Conference, Toronto, 1984), 119-132.

DOSS, AN INDUSTRIAL PROCESS FOR REMOVING

OXYGEN FROM TITANIUM TURNINGS SCRAP

Richard L. Fisher and Stan R. Seagle

RMI Titanium Company
1000 Warren Avenue, Niles, Ohio, USA

Abstract

A process called DOSS has been developed for removing oxygen from titanium and other reactive and refractory metals. The process involves heating scrap turnings at about 925°C in the presence of calcium. The turnings are then leached with dilute acid to remove excess calcium and calcium oxide. DOSS has been successfully used to treat powder, thin sheet and scrap turnings. The first commercial application of the technology was for removal of oxygen from titanium turnings scrap. The process has been successfully scaled up to treat 1200 to 1400 kilogram lots of scrap in existing sponge reduction equipment. Oxygen content of turnings was reduced from 0.25% to values as low as 0.04%. Tests conducted on metal samples produced from ingots melted with DOSS treated scrap in an electron beam melting furnace were similar to those rolled from ingot melted from untreated scrap.

Introduction

Titanium mill products are used in a wide range of aerospace and industrial applications requiring high quality metal products. The high cost of virgin materials has provided impetus for the development of new processes for recycling scrap. As the titanium industry matured, virgin sponge and alloying metals have been displaced by scrap in melting processes. In the United States, scrap recycle now averages between thirty-five and forty-five percent of ingot production.

RMI Titanium Company has developed a new process, DOSS, an acronym for DeOxidation in the Solid State. This process can be used to upgrade the quality of scrap. The process utilizes calcium vapor to remove oxygen from machine turnings and other metal scrap. Deoxidation of titanium with calcium has been studied by various researchers [1] and can be expressed by equations (1) and (2).

$$Ca(g) + O (mass\% in Ti) = CaO (s)$$
 (1)

$$K_1 = a_{CaO}/a_{Ca} h_O = a_{CaO}/a_{CaO} f_O(mass\% O)$$
 (2)

where a denotes the activity of component / relative to the pure substance; h_o , the activity of oxygen relative to 1 mass% O; (mass% O) the mass% of oxygen in the solid metal and \int_O is the activity coefficient of oxygen relative to 1 mass% O.

Titanium '92 Science and Technology Edited by F.H. Froes and J. Caplan The Minerals, Metals & Materials Society, 1993 Because the oxygen content is low, oxygen in the metal obeys Henry's law and \int_0 is unity. As the reaction progresses, a layer of liquid calcium and calcium oxide form on the surfaces of the turnings. As the reaction approaches equilibrium, a approaches unity. The solubility of oxygen in the Ca-O system has been estimated to be small from the phase diagrams developed by Fischbach.(2) The value of a can be estimated from equation (3) and Raoult's law.

$$a_{ca} = 1 - X_{o}$$
 (in Ca) (3)

From evaluation of these equations, an equilibrium limit for mass% oxygen in titanium of 0.035 to 0.045 mass% has been predicted by Ono et al. within a range of practical operating temperatures from 1273 to 1373° K. (3)

This reaction can be used to lower the oxygen content in titanium scrap turnings generated by the aerospace industry. Treated turnings can be blended with clean turnings containing higher levels of oxygen to achieve specified oxygen contents in ingot. Low oxygen turnings can serve as a direct replacement for sponge as a "sweetener" for titanium ingots melted from scrap.

This paper reviews development of the DOSS process at RMI Titanium Company.

Laboratory Scale Development

The DOSS process was developed as a result of experiments designed to produce titanium powder from titanium dioxide. In these experiments, titanium dioxide was reduced using titanium powder and a sodium-calcium sludge, ggwview of experimental results indicated that solutions of calcium in liquid sodium were effective in reducing oxygen to very low levels in titanium powder. Residual oxygen content in the treated powder was lower than levels documented for a similar process used to produce titanium powder by a multiple step reduction of titanium dioxide with calcium.(4) It was projected that high oxygen levels in titanium scrap turnings and powders could also be reduced by similar treatment. Laboratory experiments were conducted to verify this concept.

The oxygen content in samples of titanium, 6% aluminum, 4% vanadium scrap was reduced from an initial level of 0.22% to less than 0.04% (400 ppm). Experiments were conducted with other titanium alloys. Oxygen was also removed when samples of zirconium and hafnium scrap were treated.(5) Data for oxygen removal from these elements are given in Table I.

Table I - Oxygen Removal from Group IVA Elements

Element, Alloy, Form	Initial O ₂ , ppm	Final O ₂ , ppm	Time Hours
itanium, pure, chips	2010	400	4-6
litanium, 6-4, chips	2540	280	4-6 4-6 5-6
Titanium, 6242, chips	2200	350	5-6
Zirconium, pure, chips	1900	480	5 5
Hafnium, pure, chips	650	230	5

Tests were done at temperatures between 900 and 1000°C.

Oxygen removal was also evaluated for Group VA elements. Data obtained for elements in Group VA are given in Table II. Oxygen was reduced in vanadium, niobium and tantalum at temperatures between 900 and 1000 °C.

Table II - Oxygen Removal from Group VA Elements

Element, Alloy, Form	Initial O ₂ , ppm	Final O ₂ , ppm	Time Hours
Vanadium, pure, chips	3000	230	5
Niobium, pure, powder	690	260	5
Tantalum, pure, powder	3700	730	5

Experiments were conducted to evaluate removal of oxygen from the elements in Group VIA. The results of these evaluations are summarized in Table III. Significant oxygen reduction was possible when chromium and molybdenum were treated. Less removal was obtained when tungsten powder was deoxidized.

Table III - Oxygen Removal from Group VIA Elements

Element, Alloy, Form	Initial O ₂ , ppm	Final O₂, ppm	Time Hours
Chromium, pure, powder	2400	820	5
Tungsten, pure, powder	1600	1200	5
Tuliustell. Dule. Downell			

Pilot Plant Development

Pilot plant experiments were done in an eighteen inch diameter, stainless steel retort. The retort was heated in an electrical resistance furnace. Initial experiments utilized 2.27 kilogram batches of 6-4 titanium alloy turnings. A sodium-chicum mixture which contained approximately 25 percent calcium was mixed with dry scrap turnings in a dry box. A covered crucible containing the charge was transferred into the retort. The retort was sealed and purged with argon. The furnace was heated to a temperature of 950°C and maintained for 7 to 9 hours. Sodium distilled from the charge and collected in an external condenser. About 70 percent of the initial oxygen was removed after the turnings were leached in dilute acid solution.

Table IV - DOSS Pilot Plant Results, Sodium - 25% Calcium

Rur #	Weight Kgms	Time Hours	Oxygen %, Start	Oxygen %, Final	Calcium %
1	4.50	5	0.278	0.093	0.008
2	11.4	6	0.278	0.082	0.026
3	9.09	5.5	0.259	0.064	N/D

Results of experiments conducted at temperatures from 900 to 950°C in which sodium-calcium mixtures were used to remove oxygen from scrap are given in Table IV. These tests demonstrated that the process could be scaled up by a factor of 50

with only small loss of efficiency. During these tests, distillation of sodium from the retort resulted in safety and handling problems. In order to minimize the safety problems identified during the initial pilot tests, pure calcium metal was substituted for sodium-calcium mixtures. Blends of turnings and calcium metal were heated in an inert atmosphere. Pure calcium removed oxygen from scrap turnings adequately and sodium metal was eliminated from the process. Results from tests in which calcium replaced sodium-calcium mixtures are given below.(6)

Table V - DOSS Pilot Plant Results, Pure Calcium Metal

Run #	Weight Kgm	Time Hours	Oxygen %, Start	Oxygen %, Final	Calcium %
1	2.27	5	0.204	0.056	0.005
2	4.55	7	0.204	0.057	0.025
3	11.36	7	0.225	0.053	0.032
4	22.73	7	0.225	0.055	0.045
5	45.45	6	0.222	0.045	0.033

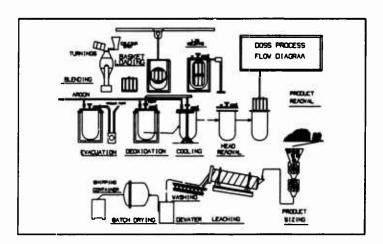
These pilot plant tests verified that the DOSS process could be scaled up in volume.

Commercial Scale Development

Successful pilot plant trials prompted a scale up into reduction plant equipment. This scale up was designed to use as much existing sponge reduction equipment as possible. Reduction furnaces, retorts, vacuum systems, leaching equipment and drying ovens were used in DOSS process designs. The process is shown as a flow diagram in Figure 1. In order to avoid contaminating reduction retorts used for the process, an internal basket system was designed. Scrap baskets held the charge and minimized difficulties during removal of the scrap.

After heating, the normally loose, free flowing chips formed dense masses that sintered together. Pneumatic rock drills used for removing mixtures of salt and titanium sponge from retorts were unsuitable for removing the sintered mass formed during DOSS treatment. An internal liner system was designed in the form of segmented baskets. Baskets were designed to stack around a central pipe support. This pipe was also used to align two baskets stacked one above the other. These baskets were separated into eight pie shaped sections. Each compartment was designed to hold about 150 pounds of scrap. In the original design, removable mesh dividers were used to hold chips within the baskets. These screens were also used to separate the charge into wedge sections that were easier to remove and crush.

Figure 1 - DOSS Process Flow Sheet



Two demonstration runs were made in early 1991. In the first scale up experiment, 227 kilograms of turnings were placed into a conical basket. The clean alloy chips were blended with calcium shot and placed into the basket. The basket was transferred into the bottom of a reduction retort. A lid was welded to the top of this retort. The retort assembly was evacuated and refilled with argon gas under pressure. After leak tests were completed, the retort assembly was transferred into a gas fired furnace and heated to approximately 925°C. A positive argon pressure was maintained for the 12 hour heating cycle. The retort was then cooled to room temperature.

The retort lid was then removed and the basket was lifted from the retort. The scrap charge had compacted to about one-third it's original volume. Eight wedge shaped sections were removed from the baskets as dense, sintered masses. These wedges were sheared into smaller pieces and crushed with a small hammer mill. The crushed turnings were leached with dilute hydrochloric acid in rotary mixers to remove residual calcium compounds. Data from the analysis of these chips verified good oxygen removal and are detailed in Table VI.

Table VI - Results of DOSS Plant Scale Demonstration Tests

Sample	Weight Kilograms	Oxygen %	Nitrogen %	Carbon %	Calcium %
First Trial: Before Tre	227 eatment	0.258	0.016	0.025	N/D
After Treat		0.077	0.014	0.062	N/D
Second Tr					
Before Tre		0.215	0.016	0.025	<0.001
After Treat	ment	0.065	0.015	0.062	0.035

In a second experiment, two segmented baskets were stacked into the reduction retort. This purpose of this experiment was to demonstrate the process for commercial quantities of scrap. The two baskets were loaded with a total of 2200 pounds of six aluminum, four vanadium (6-4) alloy turnings. These turnings were blended with three percent calcium shot. The scrap baskets were placed into the retort and stacked around a central pipe hub. The treatment cycle was completed using procedures similar to those used for the first demonstration trial. The reaction retort was maintained at a temperature between 900 and 925°C for 14 hours with an argon atmosphere. Results of the second commercial trial were also successful. Oxygen removal was slightly better than the results obtained in the first scale up experiment. Analytical results from these tests are also documented in Table VI.

These experiments proved that the DOSS process could be scaled up to treat commercial quantities of scrap turnings in regular sponge production equipment. Operating problem areas were identified during these trials. A carefully planned engineering effort was initiated to find practical solutions to these problems.

Process Problems Identified During Scale Up

1. Carbon Contamination:

Problem:

Residual oils and greases were found on "clean" turnings. Residual carbon content of the treated turnings was increased during the heat treatments required for good oxygen removal.

Solution:

A heated evacuation cycle was added to the process to aid in removal of most of the residual oils by vacuum distillation.

2. Acetylene Formation:

Problem:

Acetylene gas was formed when reactors were opened in moist air. High concentrations of this gas were measured after retorts were opened. Some gas were also present during scrap removal and sizing.

Solution:

Gas formation was controlled by minimizing calcium usage. A ratio of 1.5% calcium was adequate to remove oxygen. Removal of excess oils also reduced gas formation. A high volume ventilation system was specified for basket removal and crushing areas.

Current Program Status

The DOSS process was operated as a semi-works from December, 1991 through February, 1992. Capacity was increased to a level of about 9.1 metric tons per month. Technicians and plant personnel operated the process and produced low oxygen turnings for electron beam melting applications. These semi-commercial operations were terminated in late February, 1992 when RMI Company closed its sponge reduction plant. Commercial use of the process is expected to be further defined in late 1992. Analyses from typical scrap batches processed during semi-works operations are given in Table VII.

Table VII - Typical Analysis of Deoxidized Turnings; DOSS Semi-Works

Sample	Weight Kilograms	Oxygen %	Nitrogen %	Carbon %	Calcium %
Before I	ooss	0.240	0.016	0.025	<0.002
Lot #1,	4,600	0.053	0.015	0.041	0.0183
Lot #2,	3,100	0.055	0.015	0.040	0.0320
Lot #3.	5,600	0.037	0.016	0.036	0.0132
Lot #4.	2,300	0.040	0.016	0.036	0.0150
Lot #5.	5,300	0.055	0.013	0.035	0.0060

Although the oxygen content of this scrap was successfully reduced, small quantities of calcium remained in the turnings. Uncertainty existed about the impact of this residual calcium on metal products produced from scrap treated by this process. There is no known history of problems from residual oxides or compounds after melting of sponge which contains residual salts of sodium or magnesium. Evaluations were undertaken to identify any potential adverse effects caused by residual calcium compounds in ingot produced from DOSS treated scrap.

Samples were taken from an electrode melted from low oxygen tumings treated during the initial DOSS demonstration runs. Samples of this ingot were evaluated by standard gas analysis and spark source mass spectrographic methods. Results of these tests were compared with Ingot samples melted from untreated alloy turnings. Both electrodes were melted in an electron beam furnace. Residual calcium compounds left during oxygen removal were eliminated during ingot melting. Examination of "as cast" samples showed only minor structural differences between samples from the two ingots sources. After rolling these samples into sheet, only minor differences could be found between the two samples. Data obtained from analysis of these samples are included in Tables VIII and IX.

Table VIII - Comparison of Trace Element Analyses, EB Melted DOSS
Treated and Untreated Turning Scrap

Impurity Element, Spark Source Mass Spectrometry	Untreated Scrap, ppm	DOSS Treated Scrap, ppm
Antimony, Sb	5.1	<0.15
Tin, Sn	45	2.4
Copper, Cu	31	53
Nickel, Ni	67	470
Iron, Fe	~2100	~1600
Calcium, Ca	3.3	0.89
Chlorine, CI	21	1.3
Sulfur, S	15	9.7
Silicon, Si	285	325

Table IX - Comparison of Gaseous Element Analyses

Leco Gas Analyses	ppm	ppm
Oxygen, O	2330	1250
Nitrogen, N	120	120
Carbon, C	300	700

Summary

The DOSS process removes 70 to 75% of the oxygen from titanium turnings. The process can be used to remove oxygen from Group IVA, VA and VIA elements. The practical operating temperatures of the process is approximately 950°C. At this temperature, the diffusion rate of oxygen is a major rate controlling step. Due to this limition, the DOSS process has been found to be most effective for removing oxygen from thin sheet, powders or machine turnings.

The process has been successfully scaled up from bench scale to 1.2 metric ton batches. Commercial quantities of low oxygen scrap turnings have been produced in a semi-works operation. Treated scrap has proven to be well suited for recycle into hearth melting processes.

The metallurgy of sheet samples made from ingots melted from DOSS treated turnings is not measurably different from samples obtained from untreated scrap ingots. Residual calcium compounds are removed during ingot melting.

References

- 1. H. Niiyama, et. al., "Deoxidation Equilibrium of Solid Titanium, Zirconium, and Niobium with Calcium", *Journal of Less-Common Metals*, 169, (1991), 209-216
- 2. K. Ono, T. Olshi and S. Miyazaki, "Thermodynamic Properites of Oxygen in the Alpha and Beta Titanium-Oxygen Alloys at 800-1200°C, "Titanium Science & Technology, 4(1985), 2657
- 3. H. Fischbach, Steel Res., 56(1989), 431
- 4. G. Buttner, H.G. Domazer, and H. Eggert, U.S. Patent 4,373,947, February 15, 1983, Assigned to Th. Goldschmidt AG, Essen, Fed. Rep. of Germany
- 5. R. L. Fisher, "Deoxidation of Titanium and Similar Metals Using a Deoxidant in a Molten, Metal Carrier", U.S. Patent 4,923,531, May 8, 1990, Assigned to RMI Company, Niles, Ohio
- R. L. Fisher, "Deoxidation of A Refractory Metal", U.S. Patent 5,022,935, June 11, 1991, Assigned to RMI Titanium Company, Niles, Ohio

PREPARATION AND CHARACTERIZATION OF

EXTRA-LOW-OXYGEN TITANIUM

T.H.Okabe, M.Nakamura, T.Ueki, T.Oishi and K.Ono

Department of Metallurgy, Kyoto University, Yoshida Honmachi, Sakyo-ku, Kyoto 606, JAPAN

Abstract

Removal of oxygen in titanium by reaction with chemically active calcium dissolved in CaCl₂ was examined at temperatures between 1173 and 1473K with the purpose of obtaining extra-low-oxygen titanium. CaCl₂ was used as a flux to facilitate the reaction by decreasing the activity of the by-product CaO. Titanium wires and small pieces of titanium

were deoxidized to 20 - 60 mass ppm oxygen by use of calcium-saturated CaCl₂.

Trace element analysis, micro Vickers hardness measurements, and electrical resistivity measurements were carried out to characterize the deoxidized titanium. Titanium with a high residual resistivity ratio ($\rho_{299}/\rho_{4.2}=100$) was produced by the deoxidation of electrolytically refined titanium. The "ideal resistivities", or hypothetical resistivities of pure titanium, at 77 and 298K were determined to be 40 and 440 n Ω m, respectively. The influence of oxygen on resistivity at 4.2K was also measured by using titanium containing 30 and 500 mass ppmO, and was determined to be 88 n Ω m/at%O.

As an alternate method for deoxidation, titanium wire was immersed into molten CaCl₂. Titanium and carbon electrodes acted as cathode and anode, respectively, using an external DC source. By this procedure, it is believed that the calcium potential in CaCl2 increased at the titanium surface. Oxygen dissolved in the salt bath through deoxidation of titanium reacted at the carbon anode to form CO (or CO₂) gas and was removed from the system. The titanium samples in the salt were deoxidized by the electrolytically-produced calcium, and oxygen in titanium was lowered to below the 20 mass ppm level whereas the

carbon concentration was increased to some extent.

Introduction

Over the past several years, the demand for high purity titanium for use in electronic materials has increased. For applications such as target materials for semiconductor use, 4 to 5N (excluding gaseous elements) high purity Kroll tranium has been mainly employed. More recently, for electronic materials use, titanium is purified further by using method of the iodide process(1) or electrolytic refining(2). The level of purity of titanium produced in these ways is between 5 and 6N (excluding gaseous elements), with the major impurity of 6N titanium being oxygen at about 100 mass ppm.

Among the known purification processes (e.g. electrolysis in molten salts, electron beam floating zone melting, electro-transport, and degassing in ultra high vacuum), no effective methods other than electrolytic refining and iodide refining have been developed for oxygen removal to a level below 100 mass ppm. Even if low oxygen titanium is successfully produced using these optimized methods, contamination by oxygen is inevitable during

subsequent processing, such as during electron beam melting.

Oxygen removal directly from titanium-oxygen solid solution to a level below 50

Titonium '92 Science and Technology
Edited by F.H. Froes and I. Caplan
The Minerals, Metals & Materials Society, 1993 mass ppm is deemed to be very difficult because titanium has a strong affinity for oxygen. For this reason the conventional titanium refining process is based on reaction of oxygen free titanium compounds in a gas-tight system. From a thermodynamic view point, external gettering used for solid state refining is one of the most promising methods for direct deoxidation of titanium⁽³⁾. This method can be applied during final deoxidation of titanium products as a surface deoxidation treatment following machining.

This paper reports the results of an experimental investigation directed towards the preparation of extra-low-oxygen titanium by using the calcium saturated CaCl₂ flux deoxidation method.⁽³⁾⁽⁴⁾ As an alternative, an electrochemical deoxidation technique.⁽⁵⁾ was applied for producing oxygen-tree-titanium. Characterization of the resulting degree of purity was made by trace element analyses, micro Vickers hardness measurements, and

electrical resistivity measurements.

Calcium-Halide Flux Deoxidation Process

Principle

It is well known that a large amount of oxygen dissolves in titanium to form an interstitial solid solution. The maximum solubility of oxygen in hexagonal close-packed titanium (α -Ti) is about 33mol%. (6) The oxygen solubility in the high temperature bcc phase (β -phase) is much lower (about 2mol% at 1273K) and the α - β transformation temperature

increases sharply with increasing oxygen content.

In this study, titanium deoxidation by reaction with a chemically active element, namely calcium dissolved in CaCl₂ through surface contact, was examined in the temperature range 1273 to 1473K, to obtain low oxygen-containing titanium. Calcium is thought to be the most effective deoxidation agent not only because it has an extremely strong affinity for oxygen but because it has a high vapor pressure around 1273K (P_{Ca}=1.9kPa)⁽⁷⁾ and can diffuse into CaCl₂. Furthermore the maximum solubility of calcium in titanium is reported to be only about 60 mass ppm at 1273K.⁽⁸⁾ CaCl₂ was used as a flux to contain the deoxidation agent calcium and in addition, to facilitate the reaction by diluting the reaction product CaO, i.e., decreasing the activity of the by-product CaO.

Since details of the principle of calcium-halide flux deoxidation of titanium are reported elsewhere⁽³⁾, only a brief outline will be given here. Titanium-oxygen solid solution can be deoxidized by calcium to a lower oxygen level by the following reaction:

$$O(in Ti) + Ca(in flux) = CaO(in flux)$$
 (1)

Co-existence of calcium and the by-product, CaO, fixes the equilibrium oxygen partial pressure, and hence, the amount of residual oxygen in titanium is thermodynamically determined. The deoxidation limit of titanium is given by Equation (2) at temperature T.

[%O] =
$$(a_{CaO}/a_{Ca})(1/f_O)\exp(\Delta G^o/RT)$$
 (2)

where ΔG° is the standard free energy change of Equation (1), $a_{C_0 O}$ and a_{C_0} are the activities

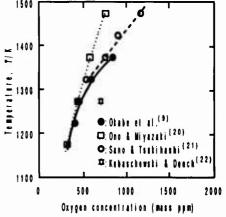


Figure 1 - Equilibrium oxygen concentration in Ti under Ca-CaO existence. (9)

of CaO and calcium, respectively, and f_0 is the activity coefficient of oxygen in solid titanium. When determining the partial pressure of oxygen in β -solid titanium, the authors measured the equilibrium oxygen concentration in titanium coexisting with calcium and CaO at temperatures between 1173K and 1373K. Based on these obtained data, and the condition that the activity of the by-product CaO is unity, the predicted deoxidation limit of titanium by using pure calcium at 1273K is about 500 mass ppm as shown in Fig.1. The authors also discussed the feasibility of preparation of low oxygen-containing titanium by decreasing the activity of the by-product CaO using various calcium—halide fluxes in the presence of calcium metal. After consideration of several factors in choosing a flux and the process parameters for deoxidation, CaCl₂ was decided to be the most suitable among many halide

2.274

fluxes around 1300K⁽³⁾. CaCl₂ used as a flux dissolves a large amount of CaO (about 20 mol% at 1273K ⁽¹⁰⁾), while the solubility of CaCl₂ in calcium is less than 5 mol%⁽¹¹⁾. Therefore, it is expected that the CaO by-product of deoxidation will be dissolved by the calcium-saturated CaCl₂ flux, and that the deoxidation limit will be lowered as the activity of CaO (refer to Equation (2)) is decreased. For example, Equation (2) shows that when the activity of CaO in the flux is decreased to a level of 0.01 in the presence of calcium, the deoxidation limit is lowered to the 5 mass ppm level at 1273K.

Experimental

Fig.2 shows the arrangement of the reaction tube used for titanium deoxidation in this study. Ten to fifteen titanium samples (about 0.1 - 2g each) were placed on a titanium dish within a titanium cup, which was filled with about 20g of CaCl₂. The CaCl₂ used in this study was reagent grade anhy-drous CaCl₂ (99.9%) in powder form, dried at 800K for more than 200ks. Several kinds of titanium pieces and wires with different oxygen concentration and configuration were used as starting materials. The cup containing the titanium sample and CaCl2 was sealed in a stainless steel tube with 5g of calcium granules, as shown in Fig.2. To avoid contamination of the sample by impurities in calcium (mainly CaO and nitrogen), calcium was isolated from the samples and flux, and supplied to the flux in vapor form.

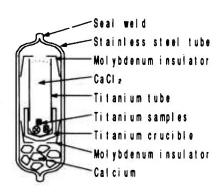


Figure 2 – Schematic illustration of the reaction tube.

The assembled sealed tube was heated in an electric furnace to a temperature between 1173 and 1473K. The holding time was between 86.4ks and 260ks, after which, the reaction tube was taken out from the furnace and quenched in water. The amount of time necessary to reach equilibrium was determined in previous work(9). In some experiments, for the purpose of annealing, the reaction container was cooled in the furnace, or quenched and then heated again to 1073K for 10ks to remove defects in the samples which would interfere in resistivity measurements. After heat treatment, the calcium-saturated fused salt in the titanium cup was removed by leaching with (1+1) acetic acid, and the resulting titanium samples were carefully cleaned in warm HCl aqueous solution followed by water, alcohol and acetone, and then allowed to dry.

Oxygen and nitrogen analyses of the samples were made using an inert gas fusion infrared absorption method (LECO TC-336 analyzer). For oxygen and nitrogen extraction, 0.1g of titanium sample enclosed in 1g of platinum foil was dropped into a graphite crucible and held at a temperature above 2800K. Electrical resistivity measurements were carried out on samples in wire-form which were immersed in liquid helium, liquid nitrogen, and water kept at 298K. The conventional four probe direct current technique was adopted. Micro Vickers hardness measurements using a 500 g load were carried out at room temperature on the chemically polished surfaces of cross sectioned samples. Trace element analysis of titanium was carried out utilizing glow discharge mass spectroscopy(GDMS), and in the case of calcium, the values were cross checked by using flameless atomic absorption spectroscopy.

Results and Discussion

Oxygen and nitrogen analysis Some representative analytical oxygen and nitrogen concentrations in titanium before and after experiments are listed in Table I.

By using Ca-CaCl₂ flux, titanium samples were deoxidized to a level below 50 mass ppm, and in some experiments the oxygen contents in titanium were lowered to less than 20 mass ppm. The final oxygen concentrations were essentially independent of the initial oxygen concentrations under these experimental conditions. The reaction periods appear to be sufficient to reach equilibrium, and thus, the deoxidation limit in these experiments may be determined from the activity of CaO in the flux. It is believed that, in this study, the amount of

CaO derived from deoxidation of titanium was small in comparison to the level of CaO impurity in CaCl₂. For further deoxidation, it seems necessary to refine the CaCl₂ for CaO elimination.

Table I Results of titanium deoxidation by the calcium-halide flux deoxidation method.

Exp. condition		en conc. s ppm)	Nitrogen o		ickers hardness (kgf/mm²)	RRR (\rho 298 / \rho 4. 2)
Temperature / Holding time	Initial	After exp.	Initial	After exp	. After exp.	After exp.
1273K / 86ks	900÷	80	100	130	103	17
1273K / 90ks	130° 130° 200	16 17 23	10 10 20	41 34 52	85 79	100 100
1373K / 86ks	110*	37	5	48	86	120
1373K / 40ks	130° 130°	35 22	10 10	49 45	93	95

* : Electrolytically refined titanium. + : Commercial grade titanium.

Nitrogen concentrations in the samples were independent of the experimental conditions, and increased from the initial values by about 40 mass ppm, in all cases. This increment seems to be caused by residual nitrogen in the reaction tube and/or the presence of nitrogen in the CaCl₂ and calcium, since no nitrogen gas elimination was done preceding the sealing of the sample in the reaction tube.

Micro Vickers hardness measurements The micro Vickers hardness value of electrolytically refined titanium was 80-90 kgf/mm² following deoxidation. Typical hardness

values are also listed in Table I.

17 as shown in Table I.

Trace elements analysis Results of GDMS indicate that calcium, chromium and nickel concentrations remained unchanged with the deoxidation treatment. The calcium concentration of the deoxidized samples were cross checked by using an atomic absorption method: the analyzed values ranged from 0.8 to 1.2 mass ppm. Detailed analysis of trace metal impurities in titanium before and after deoxidation are provided in a previous work.⁽⁴⁾ Residual resistivity ratio measurements The resistivity ratios, $\rho_{298}/\rho_{4.2}$ (=RRR) and ρ_{298}/ρ_{77} , are fairly accurate, since values do not include error associated with size measurements. The RRR values increased in all cases following deoxidation treatment. It is worth noting that the RRR value for electrolytically refined titanium wire reached a magnitude of hundred after deoxidation, while that for commercial grade titanium wire showed only about

In general, the resistivity of titanium at temperature T, ρ_T , can be put in the form

$$\rho_{\rm T} = \rho_{\rm i,T} + \rho_0 + \Delta_{\rm T,C} \tag{3}$$

where $\rho_{i,T}$ is the "ideal resistivity" due to scattering of electrons by thermal vibration, ρ_0 is the residual resistivity at absolute zero (0 K) determined by impurities and lattice defects, and $\Delta_{T,C}$ is the deviation from Matthiessen's rule (DMR). The residual resistivity, ρ_0 , is essentially equal to the resistivity at 4.2K, $\rho_{4,2}$, in the case of titanium because $\rho_{i,T} + \Delta_{T,C}$ is negligible compared to ρ_0 .

Assuming that Matthiessen's rule can be applied, that is, $\Delta_{T,C}$ in Equation (3) is zero,

values measu: able with high accuracy can be expressed as follows;

$$\rho_{77} / \rho_{298} = (\rho_{i,77} + \rho_0) / (\rho_{i,298} + \rho_0)$$
 (4)

$$\rho_{4.2} / \rho_{298} = (\rho_{i,4.2} + \rho_0) / (\rho_{i,298} + \rho_0). \quad (5)$$

The relationship between ρ_{77}/ρ_{298} and $\rho_{4.2}/\rho_{298}$ can be obtained by eliminating ρ_0 from Equations (4) and (5) as follows,

$$\rho_{77}/\rho_{298} = A \rho_{4.2}/\rho_{298} + B$$
 (6)

where A and B are $(\rho_{i,298}-\rho_{i,77})/(\rho_{i,298}-\rho_{i,4.2})$ and $(\rho_{i,77}-\rho_{i,4.2})/(\rho_{i,298}-\rho_{i,4.2})$, respectively. The

values A and B in Equation (6) are constant, and independent of impurity concentration. Consequently, if Matthiessen's rule can be applied to titanium which contains dilute impurities, every pair of measured values (ρ_{77}/ρ_{298}) and $\rho_{4.2}/\rho_{298}$ for the samples should fall on a straight line expressed by Equation (6), even though ρ_0 of these samples may be very large. Also the values, ρ_{77}/ρ_{298} and $\rho_{4.2}/\rho_{298}$, should approach the values, B and 0, respectively, as

the purity of titanium increases (viz. ρ_0

approaches 0).

In Fig.3, measured values of ρ_{77}/ρ_{298} are plotted against $\rho_{4.2}/\rho_{298}$ for deoxidized titanium wires as well as for as-received titanium wires. The measured values for deoxidized samples fall on a straight line, but those for as-received titanium wires, especially for samples with high ρ_0 (high oxygen \sim concentration), deviate from the straight line. This result indicates that the effect of oxygen on the term $\Delta_{T,C}$ in Equation (3) cannot be neglected, and that Matthiessen's rule cannot be applied to titanium with high oxygen concentration. From the 24 pairs of measured values for deoxidized titanium wires, the constants (Equation (7)), A and B were calculated using the least square approximation, and are depicted by the solid line in Fig 3.

$$\rho_{77}/\rho_{298} = 0.951 \ \rho_{4.2}/\rho_{298} + 0.0918 \ (7)$$

The sum of A and B in Equation (6) should theoretically be one, whereas the measured value in Equation (7) is 1.04.

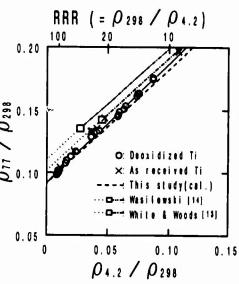


Figure 3 – Relationship between ρ_{77}/ρ_{298} and $\rho_{4.2}/\rho_{298}$ for deoxidized titanium wires. (4)

This 4 percent discrepancy is somewhat large and cannot be attributed solely to experimental error, and seems to be due to DMR of samples with some impurities in addition to oxygen. That is to say, not only oxygen but also other impurities contribute to DMR for titanium to some extent. For a more rigid discussion concerning DMR, titanium purified further to a lower ρ_0 value is needed, and effect of hydrogen on resistivity must also be considered (12). Ideal resistivities of titanium In Table II, the ideal resistivities at 77 and 298K were calculated by using deoxidized samples on the assumption that $\Delta_{T,C}$ in Equation (3) is negligible for samples with RRR of about one hundred. The data obtained by White and Woods (13) and by Wasilewski (14) are also listed for comparison. By using the values in Table II, the constants A and B in Equation (6) can be calculated. Calculated relationships between ρ_{77}/ρ_{298} and $\rho_{4,2}/\rho_{298}$ are illustrated in Fig.3 along with their respective literature value (1). The dashed line in Fig.3 is calculated using the values in Table II obtained in this study. There is a large discrepancy between the three calculated lines, probably due to DMR. That is, in the calculation of $\rho_{1,T}$ in Equation (3) using a sample with large ρ_0 , it is unavoidable that there is contribution of $\Delta_{T,C}$ to $\rho_{1,T}$. Therefore, it seems necessary to use as low residual resistivity as possible to minimize the interference by DMR in the determination of the ideal resistivity.

Table II Ideal resistivity of titanium at 298 and 77K.

	$(n\Omega m)$	$(\hat{\mathbf{n}} \hat{\boldsymbol{\Omega}} \hat{\mathbf{n}})$	ρ (nΩm)	Note	Ref.
White & Woods	437*	44.5*	19. 7	ρ., 270 = 390 nΩm	13
Vasilevski	461*	50. 9	13. 1	$\rho_{1,474} = 414 \text{ n}\Omega\text{m}$	14
G. Elssner et al.	430			210 ppmO, 20 ppmN	17
This study	440	40	4.6	30 ppm0, 50 ppmN	4

Influence of oxygen on electrical resistivity The contribution by oxygen to the resistivity of titanium, $\Delta \rho/c$, determined in this study, as well as from the literatures, is given in Table III.(15-19) The calculated value, 88 n Ω m/mol Ω 0, using the data for electrolytically refined high purity titanium, which contained 28,17,22 and 500 mass opm oxygen is in fairly good agreement with the reported data.

Table III Contribution of oxygen to the resistivity of titanium at several temperatures for various oxygen concentration ranges. $\rho_{\rm T}$ is the resistivity with lowest oxygen concentration at the measured temperature.

and To Section	$\Delta \rho / c$ (n Ω m/mol%0)	T (K)	$ ho_{\mathrm{T}}$ (n Ω m)	Oxygen conc. range (mol%0)	Ref.
Ames & McQuillian	113	293	470	- 1.5	15
Vasi levski	123	273	427	0.13 - 10	16
Elssner et al.	82	298	430	0.063 - 1.0	17
Komatsu et al.	101	77	60.6	0.890 - 3.2	18
Baur & Lehr	103	20. 4	2. 68	0.009 - 0.32	19
This study	88	4.2	4. 60	0.009 - 0.15	4

An Electrochemical Deoxidation Technique

Principle

In the calcium-halide flux deoxidation process mentioned above, there exist strict limitations on the purity of flux and the initial oxygen content of the titanium used, since the ultimate limit of deoxidation is dependent on the amount of oxygen present as an impurity in the flux and on the amount of CaO produced during deoxidation.

An alternate method for deoxidation, expressed schematically in Fig.4, is characterized by both production of calcium deoxidant from the flux and by effective removal of O²-(mainly present as CaO in the flux) dissolved in the flux by means of an electrochemical technique. (5) The deoxidation reaction given in Eq.(1') is thus facilitated. By the method developed in this study, titanium in the vicinity of the titanium cathode is deoxidized by calcium which is produced electrochemically on the surface of the cathode according to Eq.(8). According to the cathodic reaction, O²- species in the flux, present as impurities or as the deoxidation product CaO, are continuously transported for reaction at the carbon anode, and oxygen in the flux is removed from the system as CO (or CO₂) gas by the anodic reaction expressed in Eq.(9).

$$O (in Ti) + Ca (in flux) = Ca2+ (in flux) + O2- (in flux) (1')$$

$$Ca2+ (in flux) + 2e- = Ca (on Ti cathode : in flux) (8)$$

$$O2- (in flux) + C (carbon anode) = CO (gas) + 2e- (9)$$

Unlike the calcium-halide flux deoxidation process, metallic calcium is not necessary as a deoxidant since the activity of calcium near the cathode can be increased by controlling the applied voltage between the titanium cathode and carbon anode, such that deoxidation is effected. In some cases, calcium can even be precipitated on the cathode. That is, this electrochemical method has another advantage in that elimination of impurities originating

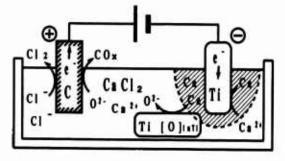


Figure 4 - Deoxidation of titanium using an electrochemical technique.

2.27

from metallic calcium deoxidant is not a concern.

Experimental

A schematic illustration of the apparatus used in the electrochemical deoxidation method is shown in Fig.5. CaCl₂ flux which had been previously dehydrated at 473K under vacuum was heated to 1173K. A titanium cathode and glassy carbon anode were then inserted into the molten CaCl₂ flux. Deoxidation of titanium cathodes consisting of titanium samples of various oxygen concentrations (200-1400 mass ppmO) was effected using an applied voltage between 2 and 6V for a time greater than 18ks. The titanium samples obtained were subjected to oxygen, nitrogen and carbon analyses using LECO analyzers. For the purpose of increasing the accuracy of the oxygen and nitrogen analyses, 1g of platinum foil containing 4.5±1.0µg oxygen was used as an extraction bath for each 0.1g titanium sample.

Results and Discussion

Some representative results of the experiments are listed in Table IV. Deoxidation of titanium was performed effectively. Titanium samples were successively deoxidized to a level below 50 mass ppmO during a reaction period of several hours. Among the deoxidized samples, some oxygen-free-titanium samples were obtained, that is, titanium containing oxygen below the detection limit(about 10 mass ppmO) of analysis was produced.

The carbon concentration was considerably increased after reaction (Exp.no.49) By implementing a titanium partition wall with bored holes between the cathode and anode (Exp.no.17), or by regulating the applied voltage between electrodes (Exp.no.46,44,21),

the increase in carbon was lowered.

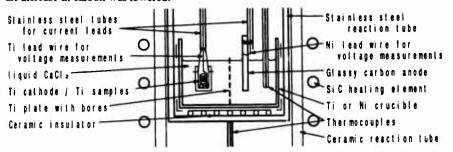


Figure 5 - Schematic illustration of the apparatus used in the electrochemical deoxidation method.

Table IV Results of titanium deoxidation using an electrochemical technique.

Exp.	Experimental conditions	Oxygen conc. (mass ppm)			gen conc. ppm)	Carbon conc. (mass ppm)		
no.		Initial	Afer exp.	Initial	Afer exp.	Initial	Afer exp.	
49	1223K / 22ks 3.5V / 1.8A	900 1400	<10 <10	40 20	40 20	30 50	900 670	
17*	1173K / 23ks 4.0V / 1.8A	900	60	20	20	30	60	
46	1223K / 22ks 3. 0V / 0. 27A	140 1400	100 60	<10 20	<10 20	20 50	20 50	
44	1223K / 22ks 2.8V / 0.50A	900	50	40	40	50	60	
21	1173K / 27ks 2.8V / 0.40A	900 1400	<10 100	20 20	20 50	30 50	30 70	

^{* :} Ti plate with bored holes was implemented between electrodes.

Conclusions

Titanium in the form of wires and small pieces was deoxidized to a level of 20 - 60 mass ppm oxygen by use of calcium-saturated CaCl₂ flux at 1273K. The micro Vickers hardness value of electrolytically refined titanium was 80-90 kgf/mm² following deoxidation. The calcium concentration in titanium remained unchanged.

Resistivity measurements were carried out at 4.2, 77 and 298K on titanium wires. Deviation from Matthiessen's rule was observed for titanium samples with high residual resistivity. By deoxidizing electrolytically refined titanium wire, titanium with a high residual resistivity ratio ($\rho_{298}/\rho_{4,2}=100$) was produced, and the ideal resistivities at 77 and 298K were determined to be 40 and 440 n Ω m, respectively. The contribution by oxygen to resistivity at 4.2K was also measured by using titanium samples obtained in this study, and determined to be 88 n Ω m/mol%O.

An alternate method for removing oxygen dissolved in titanium was also developed. Titanium containing several hundred mass ppm oxygen could be deoxidized to a level below the detection limit of oxygen analysis (about 10ppm) by using the electrochemical technique.

Acknowledgments

The authors wish to express their sincere appreciation to Mr.M.Maeno for his invaluable experimental assistance, and to Mr.E.Nishimura (Nippon Mining Co. Ltd.), Dr. Y. Yoshimura (Osaka Titanium Co. Ltd.) and Mr. T. Ueda (Mitsubishi Kasei Ltd.) for sample preparation and analyses. Last, but not least, the authors are very grateful to Dr.K. Yoshiki-Gravelsins, Dr.H. Wada and Dr.H. Numakura (Kyoto Univ.) for stimulating discussions and suggestions throughout the progress of the work. Some analyses of titanium were done at Osaka Titanium Ltd., KOBELCO Research Institute, Inc. and Mitsubishi Kasei Ltd, and these are gratefully acknowledged.

References

- 1. T.Ishigami, H.Ishihara and K.Shimotori, Toshiba Review, 161 (1987) 38-41.
- 2. E.Nishimura, M.Kuroki and N.Kikuchi, Japanese Patent, H02-213490, (24Aug. 1990).
- 3. T.H.Okabe, R.O.Suzuki, T.Oishi and K.Ono, Testu-to-hagane, 77(1991)93-99.
- 4. T.H.Okabe, T.Oishi and K.Ono, J.Alloys and Compounds(J.Less-Common Metals), (1992) in process of publication.
- 5. M.Nakamura, T.Ueki, T.H.Okabe, T.Oishi and K.Ono, Proceedings of Annual Meeting of the Japan Institute of Metals, (October, 1991)581.
- 6. J.L.Murray and H.A. Wriedt, Binary Alloy Phase Diagrams 2nd Edition, ed. T.B. Massalski (Materials Park, Ohio: ASM International, 1990) 2924-2927.
- 7. I. Barin, O. Knacke and O. Kubaschewski, "Thermochemical Properties of Inorganic Substances Supplement", (Springer Verlag, Berlin, 1977).
- 8. I.Obinata, Y.Takeuchi and S.Saikawa, <u>Trans. Amer. Soc. Met.</u>, 52 (1960)1072-1083.
- 9. T.H.Okabe, R.O.Suzuki, T.Oishi and K.Ono, Mater. Trans. JIM, 32(1991)485-488.
- 10. D.A. Wentz, I. Johnson and R.D. Wolson, Phase Diagrams for Ceramists, ed. by
- M.K.Reser(1975),p.394 [The American Ceramic Society, Ohio].
- 11. E.D.Eastman, D.D.Cubicciotti, and C.D.Thurmond, <u>Chemistry and Metallurgy of Miscellaneous Materials</u>, ed. by L.L.Quill, McGraw-Hill, New York, (1950) Paper 2, p.10.
- 12. S.Komatsu, M.Ikeda, T.Oda, K.Asayama, T.Sugimoto and K.Kamei, Journal of the Mining and Materials Processing Institute of Japan, 107(1991)887-893.

 13. G.K.White and S.B. Woods, Phil.Trans.Roy.Soc., A251(1959)273-302.

 14. R.J. Wasilewski, Trans.Met.Soc.AIME, 224(1962)5-7.

- 15. S.L.Ames and A.D.McQuillan, Acta Met., 4(1956)619-626.
- 16. R.J. Wasilewski, <u>Trans. Met. Soc. AIME</u>, 224(1962)8-12.
- 17. G.Elssner, U.Krohn and O.Ruano, Z.Metallkde., 67(1976)311-317.
 18. S.Komatsu, M.Ikeda and K.Inoue, 76th Proceedings of Keikinzokugakkai, (1989).57-58.
- 19. G.Baur and P.Lehr, <u>J.Less-Common</u>. Met.,69(1980)203-218.
- 20. K.Ono and S.Miyazaki, J.Japan Inst. Metals, 49(1985)871-875.
- 21. N.Sano and F.Tukihashi, Report No.2, 69th Committee of Japan Society for Promotion of Science, (28 November, 1989),31-32.
- 22. O.Kubaschewski and W.A.Dench, J.Inst.Metals, 82(1953-54), 87-91.

HIGH INTENSITY MAGNETIC REMOVAL OF PARAMAGNETIC

MATERIAL FROM RECYCLE TITANIUM TURNINGS

Ronald Young

Oregon Metallurgical Corporation, Albany, Oregon - U.S.A.

Abstract

Oregon Metallurgical Corporation has recycled titanium turnings since 1964 as an integral raw material in production of titanium ingots. The primary objective, after having removed tramp material, has been to remove high density inclusions. This objective has been accomplished.

However, contamination with stainless steel and high nickel alloys has been an ever increasing problem. Gravimetric and conventional magnetic separation systems are not adequate to remove these contaminates to an acceptable level as there is more than one type and/or size of contamination causing the input material to have varying magnetic susceptibility.

To address this problem, Oregon Metallurgical Corporation has added to its material processing system a high intensity magnetic separation device that is capable of separation by paramagnetic properties.

Titanium '92 Science and Technology Edited by F.H. Froes and J. Captan The Minerals, Metals & Materials Society, 1993

Introduction

The cost of titanium sponge and alloy additions for titanium ingot production has always driven manufacturers of titanium ingots to utilize an ever increasing percentage of recycle titanium turnings as an alternative source of raw materials. This paper will demonstrate one way to utilize an optimum amount of titanium turnings in melting titanium ingots.

Background

For the first twenty years of titanium turnings recycling, the market was dominated by the use of recycle turnings as feedstock for ingot production. During that time, users emphasized the need for clean, segregated turnings relatively free of contaminants. The determining factor for use was that tramp contaminants could not impact the chemistry of the ingot. In the last few years, the increased use of titanium for alloying additions has shifted both emphasis and demand. Now, the volume use of recycle turnings is for alloying additions where the emphasis on low contamination is not as critical. This affects recycling for titanium usage two ways, a greater amount of the "clean" material is being applied to non-titanium usage and less emphasis is being made at the source to keep turnings segregated.

Turnings are generated in machine shops in place at end users operations, as well as independent machine shops supplying parts to end users. In the United States, most of these are supporting the aerospace industry. In aircraft engine manufacturing operations, non-magnetic contaminants would be superalloys utilized in the hot sections of the engines. Operations supporting airframe manufacturing would use high strength steels, while machine shops supporting industrial markets may have corrosion resistant alloys.

When machined titanium turnings are first received, they are processed through a system designed to remove a wide variety of contaminants, ranging from oil, dirt, rags, paper cups, bottles, and even nut shells, to non-titanium metallics such as steels and carbide tool bits. (1) A series of mineral processing techniques are used to remove these contaminants, including crushing, washing, drying, screening and gravimetric and magnetic separation.

Established processes utilizing size, gravimetric and magnetic separation techniques have been shown adequate at removing high density contaminants such as WC tooling as well as W, Nb, and Mo, and those materials with magnetic characteristics. Conventional magnetic separation using a combination of electro-permanent, magnetic equipment consisting of plate magnets with cross belts and/or drum or pulley magnets using gravitational and/or centrifugal force are very effective at removal of tramp materials and other strongly magnetic contaminants. Gravimetric separation techniques are effective for density separation where the product is of uniform size, or where sufficient difference in density exists.

However, the most difficult contaminants to identify and economically remove have been the metallic contaminants that are similar in geometry and appearance and are in the size range of the titanium turning, but do not have sufficient difference in density from titanium to allow separation. Such turnings would include stainless steel and high nickel alloys⁽⁹⁾.

While gravimetric and conventional magnetic separation works well to remove high density and strongly magnetic contaminants, neither has been effective for removal of material with small, but positive magnetic susceptibility. Alloy additions in various elements dramatically alter magnetic susceptibility thereby creating separation difficulties.

Although separation through paramagnetic property differences has been accomplished under controlled laboratory tests, the concept was not thought to be feasible at an economic production rate. $^{(5)}$

Discussion

Under ideal conditions, turnings generated from a titanium part, with the exception of interstitials, will have metallic levels identical to that of the originating ingot. Thus, Ti-6Al-4V turnings will have 6% Al and 4% V unless contaminated by another alloy. The alloy systems that are typically found as a cross contaminant, other than titanium alloys, are from Fe, Cr, Ni based systems. Thus in this evaluation, the tramp levels of Fe, Cr, and Ni are examined.

The information presented in this paper has been extracted from production data on over 1,000,000 pounds of Ti-6Al-4V turnings. All lots were processed under identical operating parameters. Upon completion of standard operations, the lots were sampled and analyzed for chemistry. Lots found to contain a high degree of contamination were then run through the high intensity magnetic system and reanalyzed. The lots were selected to show the typical types of paramagnetic material contamination that occurs and the effectiveness of a high intensity magnetic system in removing contaminants with paramagnetic properties.

Each lot represents one truck load of purchased recycle material. The lot is broken down into sublots for ease in processing. Variations between sublots may and very often does occur, due to the method of accumulation and the types of machining operations where the turnings are generated.

Final Product Evaluation

Tables I through III will demonstrate the degree of removal of various paramagnetic materials and the results in three different categories; high Fe contamination, high Ni contamination and low contamination levels.

1. High Fe Contamination

Table I shows high contamination with well over 2% Fe, as well as elevated Cr and Ni. All three of these elements were dramatically reduced by about 90%. Now, all of the product turnings are usable for titanium ingot production.

However, with this high degree of contamination, 6.92% of the input material was removed. Although this removed paramagnetic material is worthless for use in producing titanium ingots, it does have a value as a by-product.

2. High Ni Contamination

Table II shows high contamination of Ni up to almost 1%. After removal of paramagnetics, the Ni was reduced by over 85%, the Fe by about 40% and the Cr by about 75%. Paramagnetic removal was 5.82% of the input weight.

Low Contamination Levels

Table III shows a lot with low enough levels of contamination that it could have been used in ingot production as it was. However, it was processed through a high intensity magnetic separator to demonstrate the effective removal of paramagnetic material even at low levels. The amount of paramagnetic material removed was .52%.

After tabulation and review of the contaminated lots, they could have been separated into three categories based on the type of contaminant. They are:

- Material that has a high level of Fe contamination with moderate levels of Cr and Ni contamination.
- Material that has a high level of Ni contamination with moderate levels of Cr and Ni contamination.
- 3. Material that has moderate levels of contamination in Fe, Cr, and Ni.

The results of analysis before and after paramagnetic separation are presented in the following Figures.

Figure 1 - Fe Contamination

The plot of Fe analysis before and after paramagnetic separation shows a very distinct separation of the three categories of contaminants. The high Fe contaminant lots show a very flat curve indicating that the effectiveness of the separation is not dependent upon the amount of contaminant. All of the lots reported in this group, as shown by the Y intercept, have after Fe levels similar to those found in ingot product.

Figure 2 - Cr Contamination

In this plot of Cr contamination, there is greater definition between the lots with high Ni contaminants and the lots having moderate contamination with Fe, Cr and Ni.

Figure 3 - Ni Contamination

Finally, the graph of Ni removal distinctly shows the higher Ni contaminant lots.

The results reported on these three graphs show that the parameters utilized in the paramagnetic separator step are very efficient at removing high Fe contaminants such as stainless steels. For these types of material, the magnetic system is very efficient at separation and is not dependent upon the amount of contaminant present. For high Ni, contaminants (alloys such as Inconel 718) the magnetic system is capable of separating contaminants from titanium turnings. However, reducing contaminants to low levels may require several runs through the system to be effective. Finally, contaminants from Fe, Cr, and Ni alloys without a characteristically high Ni or Fe content are not effectively removed by this system.

Conclusion

A high intensity magnetic separator can effectively remove contaminates with paramagnetic properties from titanium turnings. The use of a high intensity magnetic separator in a production line has enabled Oregon Metallurgical Corporation to take titanium turnings previously good only for steel additive, and convert them into a high-grade additive in production of titanium ingots. While it has been shown particularly effective at removing specific contaminants, additional work is necessary to determine optimum operating parameters needed to remove each contaminant group found.

References

- K. H. Kramer, K. Hulse, E. Detemple, J. Berggreen, "Titanium Science and Technology" Proceedings of the Fifth International Conference on Titanium, 217
- J. Berggreen, "Titanium Science and Technology" Proceedings of the Fifth International Conference on Titanium, 241
- J. P. Laughlin, Proceedings of the Sixth World Conference on Titanium, 627
- J. B. Dresty, Jr., "Titanium Science and Technology" Proceedings of the Fifth International Conference on Titanium, 225
- J. P. Laughlin, Proceedings of the Technical Program from the 1986 International Conference, TDA, 879

TABLE I HIGH PE CONTAMINATION

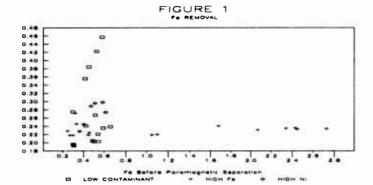
BEFORE PARAMAGNETIC REMOVAL				AFTER PARAMAGNETIC REMOVA					
SUBLOT	A PE	• CR	NI	SUBLOT	A FE	• CR	NI		
-1	2.43	.610	. 295	-1	.236	.038	.021		
-2	2.73	. 687	.338	-2	.234	.038	.022		
-3	2.34	. 59	.281	-3	.235	.036	.022		

TABLE 11 HIGH NI CONTAMINATION

BEFORE PARAMAGNETIC REMOVAL				AFTER PARAMAGNETIC REMOVAL			
SUBLOT	A FE	• CR	NI	SUBLOT	A FE	_ CR	NI.
-1	.515	. 265	.711	-1	.296	.063	.098
-2	.475	. 239	.640	-2	.289	.059	.084
-3	.587	.353	.971	-3	.298	.072	.122

TABLE III LOW CONTAMINATION LEVELS

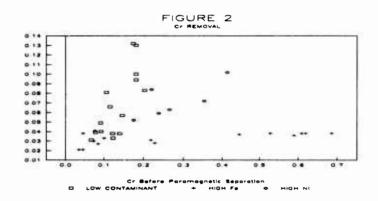
	BEFORE PARAMAGNETIC REMOVAL				AFTER PARAMAGNETIC REMOVAL			
SUBLOT	A FE	• CR	NI	SUBLOT	A FE	• CR	A NI	
-1	.298	.045	.058	-1	.218	.021	.017	
-2	.449	.085	.136	-2	.219	.027	.033	
-3	.270	.035	.033	-3	.218	.021	.014	

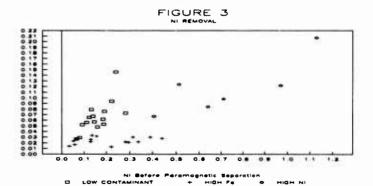


Fe Atter Poromografic Separation

Cr Alter Paramegnetic Separation

M Mar Paramagnetic Separation





TITANIUM SPONGE AUTOMATIC SORTING

A.N.Petrunko, V.M.Malshin, A.D.Kulkov U.S.Levin, E.D. Samusik, A.A.Golubev Titanium Institute, Ukraine Association "Titanium", Russia

Abstract

A semiproduction experimental complex for sorting of titanium sponge of fraction -12+2 mm has been developed and put into operation. The main methods applied in automated sorting of titanium sponge are thermoelectric and photometric ones. Their joint use permits effective removal of defective particles from titanium sponge.

Introduction

One of the important problems in titanium sponge production is the removal of defective inclusions and titanium sponge particles having an enhanced content of impurity elements. This operation is implemented manually by a visual ispection of crushed titanium sponge flow on a moving belt. The method of a visual control is subjective and insufficiently reliable. The realization of automated sorting on the basis of objective signs of separating quality and off-grade particles is an important direction of enhancing titanium sponge lots quality guarantee.

Automated sorting of lump materials consists in rapid determination of any physical properties of sponge material relative to its quality indices. The methods of sorting widely used: photometric, radiometric, electromagnetic, X-ray radiometric.

Optical Properties

For titanium sponge having acquired distinct and various colou ring enhanced impurity contents, the main separation sign is its optical properties in visible and adjoining spectrum region. The results of measurement of defective titanium sponge surface optical properties, given in a number of works, can not be considered valid since the measurements have been performed without taking into account the effect of shading from pores on the particle surface. This can vary greatly due to the in-

Titanium '92 Science and Technology Edited by F.H. Froes and I. Captan The Minerals, Metals & Materials Society, 1993 tensity of reflected light flux under measurement. The investigations of spectral characteristics of good quality and defective titanium sponge surface reflections in ultraviolet and visible bands of wavelength (220+830 nm) have been studied. Titanium sponge specimen special characteristics were obtained, taking into account the effect of shading pores, geometric location in relation to source and detector of radiation/relation of reflecting power to impurity element content. Spectral characteristics of the following species of titanium sponge defective samples have been investigated: burnt-white, white-yellow, orange, brown and grey colours; oxydized - blue-violet, blue, different tints of yellow and temper colours; slimed - dark and grey colours; with chlorides film-having distinct salt inclusions of white colour; iron-rich.

The investigation of influence of different factors on the results of measurement of coefficient of reflection for surface of defective and quality titanium sponge particles in an initial state (without application of special preparation) has been completed. The results of measurement of coefficient of reflec tion are mostly influenced by porosity. Measurement signal can vary in several ways, depending on the location at the particle surface. Therefore, the measurement of absolute magnitudes of coefficients of reflection directly from titanium sponge particles surface does not result in exact information. The measurements of the ratio of coefficients of reflection at two wavelengths are more optimum. This ratio shows the most abrupt change in a wavelength range of 250 to 500 nm. The coefficient of reflection in this range changes between 1.5 to 2.5 times. The spectral characteristics of coefficient of reflection in this range for defective particles show a marked difference from the spectral characteristics of quality titanium. This difference amounts to 10-50% of the value under measurement depending on defect species.

On the basis of analysis of spectral characteristics, the optimum conditions revealing the difference between defective titanium sponge particles and quality ones have been found. Burnt oxydized, slimed and underseparated defective titanium sponge particles are better seen in ultraviolet range of spectrum. Burnt oxydized, and enriched with iron defective titanium sponge particles also can be revealed in a visible range of spectrum.

Thermoelectrical Properties

Because of the complexity of creating conditions for effective sorting all of the defective varities by optical properties, other physical properties of titanium sponge were studied as well. There is a definite relationship between titanium electrical properties (coefficient of thermo-emf, electrical resistance, contact potential difference) and its structure, phase, elemental composition and hardness. Coefficient of thermo-emf is the most sensitive to changes in elemental and phase composition and hardness of titanium sponge. A linear relationship between coefficient of thermo-emf and hardness of titanium sponge in the range of 80-300 HB has been experimentally determined.

A 5 kg sample (about 20000 pieces of tit lium sponge) has been sorted out by coefficient of thermo-emf by means of a laborato ry measuring device. Initial titanium sponge obtained 0.5% particles with slime and those enriched with iron. In sorted titanium sponge defective particles were absent. Microstructure of sorted titanium sponge is represented by \mathcal{A} -solid solution. The results of sorting are given in Table I.

Table I Sorting of Scull Titanium Sponge of Fraction
-12 +5 mm by Coefficient of Thermo-emf

Material	Coef- fici- ent of	f= Yield,	Hard- ness,	Impurities content, %					2.1
	temf, mu V/K	нв		Рe	0	N	Si	Ni	Cr
	(-4)+8 6.5 + 8 +4.0+6.5		208 123 170		0.20 0.08 0.17	0.01		0.02	0.01

Particles enriched with iron and containing slime inclusions were easily separated from the quality portion of titanium sponge. When coefficient of thermoemf is changed within the limits of 4+8 mu V/K, impurity content in titanium sponge particles correlates with the magnitudes of coefficient, although such particles do not show significant visual differences.

More than 95% of the titanium sponge particles having the coefficient of thermo-emf below 4 mu V/K also did not show significant visual differences from acceptable quality commercially pure titanium particles. The metallographic investigation, however, has shown that such titanium sponge has structure with distinctive signs of contaminated titanium: platelikeness, polyhedron bands, intermetallide and carbide inclusions having a microhardness above 500 kg/mm². The investigations have shown that thermoelectric sorting enables the separation of not only some varities of defective particles but also the isolation of quality titanium sponge particles from the product qualified as the grade TG-Tv.

Magnetic Properties

The investigations of titanium sponge magnetic properties have been also studied. Averaged magnetic susceptibility of commercially pure titanium amounts to (3.2+4.0).10-6cm³/g. For individual particles having simultaneously high iron and oxygen content magnetic susceptibility can be an order higher due to the presence of ferromagnetic phases. The devices are known to sort low-intensity magnetic materials having a magnetic susceptibility above 10.10-6cm³/g. These devices are not designed for sorting of titanium sponge. Nevertheless, during pilot magnetic separation of titanium sponge in the separator 229PSE, iron content in sorted product was lowered by 0.03-0.11% in comparison with the initial one. The best results were obtained for

sorting of titanium sponge with a narrow size fraction, -4+2 mm, using a laboratory magnetic separator of improved design, the sensitivity of which is enhanced up to 1.10-6 cm³/g (Table II).

Table II The Results of Testing of Magnetic Separator of Improved Design

Material	Yield.	Impurities content,%					
	%	Fe	Si	Ni	Cr		
Initial	-	0.69	0.042	0.015	0.080		
Magnetic(with defective particles	3) 27.5	1.40	0.070	0.019	0.156		
Industrial product	48.9	0.57	0.038	0.016	0.058		
Free from magnetic fraction (pure)	23.6	0.10	0.020	0.009	0.040		

Implementation of Technologies

The investigations have shown that magnetic separation can result in a positive effect when purifying titanium sponge from particles having an enhanced impurities content. On the basis of the fulfilled investigations of physical properties and the evaluation of the possibility of using them for automatic sorting, photometric, thermoelectric and magnetic methods of tita nium sponge sorting as well as the corresponding engineering for the realization of them have been developed.

Specification for prototypes of photometric and thermoelectric separators is given in Table III. Titanium Institute, jointly with other organizations, has developed the sorting complex for automated sorting of titanium sponge of fraction -12+2 mm, and the corresponding sorting technology. The complex is installed in a titanium and magnesium integrated plant and is comprised of three photometric separators for fractions -12+8, -8+4,-1+2, respectively, two thermoelectric separators for fractions -12+8, -8+4 mm, and electromagnetic roll separator for fraction -4+2 mm, auxil iary equipment and an automatic control system. Titanium sponge of fractions -12+8, -8+4 mm enters thermoseparators. A quality part of sponge is fed to photoseparators. A non-quality part from thermoseparators enters directly a non quality product collector without further sorting. Titanium sponge of fraction -4+2 mm is sorted by photoseparator and electromagnetic separator. The flow sheet of sorting of titanium sponge of fraction -12+2 mm is given in Fig.1. The sorting complex allows removal of titanium sponge particles differing in their surface reflecting power from those of quality titanium, and with a probability of 80%, removal of particles inde-

pendent of their outside appearance having an enhanced conten of impurity elements (nitrogen, oxygen, iron and others).

Table III Specification of Photometric and Thermoelectric Separators

Name of specification item		Thermoelectric separator
Particle size of material under sorting, mm	- 12+2	-12+4
Separator capacity, kg/h - fraction -12+2 mm - fraction -8+4 mm - fraction -4+2 mm	180 75 20	120 6 0
Prabability of removal, % - defective particles - particles with enhanced con- tent of impurity elements - quality material	95-99 20	80 20
Quantity of isolated spectrum areas	2	
Consumed power, kVA	0.460	13
Overall size	1800x1800x1500	1950x1800x1940
Mass, kg	7 50	970

The capacity of a pilot complex amounts to 150+180 kg/h. The complex, in comparison with a manual sorting, permits reduction of impurity element content, enhance uniformity and reliability of titanium sponge quality guarantee by the use of sponge particle control for optical and thermoelectric properties. The joint use of thermoelectric and photometric separators is an effective technique of removing defective particles. This permits extraction of metal from low-grade titanium TG-Tv designed for using in ferrous metallurgy. When sorting the grade TG-Tv having an initial hardness of 170 HB, 49% titanium sponge having a hardness of 120 HB have been extracted.

At present, works on further improvement of titanium sponge auto mated control with a view of sorting it and evaluating the quality are under way.

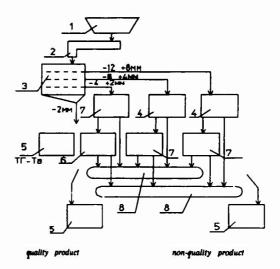


Figure 1. Flow sheet of sorting of titanium sponge of fraction -12 + 2 mm

- 1 hopper; 2 tray feeder; 3 vibrating acreen; 4 thermoelectric separator;
- 5 bucket; 6 electromagnetic roll separator; 7 photometric separator; 8 conveyer.

THE EFFECTS OF PLASMA COLD-HEARTH MELTING

ON THE PRODUCTION OF TITANIUM ALLOY INGOTS

J. W. Sears*, J. M. Young** and M. Kearns***

*ManLabs, A Division of Alcan Aluminium Corporation
21 Erie Street, Cambridge, Massachusetts
02139 U. S. A.

**IRC in Materials for High Performance Applications
The University of Birmingham
Edgbaston, Birmingham B15 2TT, United Kingdom

***IMI Titanium Limited
P.O. Box 704 Witton
Birmingham B6 7UR, United Kingdom

ABSTRACT

As part of the foundation programme at the Interdisciplinary Research Centre (IRC) in Materials for High Performance Applications at The University of Birmingham several Ti Alloys have been plasma melted and cast into ingots. Plasma cold-hearth melting (PACH) has been evaluated to determine its effect on the chemistry, microstructure, homogeneity and macrostructure of the as cast ingot. Ti alloys including CP-Ti (Grade 4), IMI-318 (Ti-6-4), IMI-834, super-α₂, and γ-Ti, have been plasma melted and cast into 100 mm or 150 mm ingots up to 500 mm long. Elemental compacts, master alloy compacts and previously vacuum-arc melted (VAR) material has been used as feed stock. Plasma-VAR, VAR-plasma and plasma-plasma melting schemes have been used to produce Ti alloy ingots. These ingots have been examined as discussed above and compared to commercially available material. The details of this analysis will be provided.

INTRODUCTION

The use of Plasma-Arc Cold-Hearth (PACH) melting of Titanium has reached production scale in the last few years and furnaces capable of melting and casting ingots up to 5000 kg are now in use¹. A PACH furnace operates in much the same way as an Electron-Beam Cold-Hearth (EBCH) furnace, except transferred-arc plasma torches are used in place of electron beam guns, and melting takes place under an atmospheric pressure of inert gas rather than in vacuum². The feed material for these furnaces may include loose sponge, compacted material, recycled scrap or ingot.

The IRC PACH furnace, a schematic of which is shown in figures 1, melts and casts ingots of high performance materials. Titanium alloys have been the principal materials of interest in the programme, but several nickel and iron alloys have also been melted for evaluation. The furnace, supplied by Retech, Inc., Ukiah, CA, is powered by two 150 kW transferred-arc plasma torches. The plasma torch located over the hearth melts the feedstock and the plasma torch over the crucible hot tops the ingot that is being formed. Feed material can consist of ingots or compacts. Most of the ingots melted for this study have been previously cast in the furnace from compact feedstock, but VAR material has also been used. Titanium alloy compacts, supplied from IMI Titanium Ltd., were made by pressing together master alloys or the

Science and Technology
Edited by F.H. Frees and 1. Caplan
The Minerals, Metals & Materials Society, 1993

alloy elements (Ti portion being sponge). A more detailed description of the furnace has been given elsewhere ³.

Helium is used as the plasma gas but the furnace is backfilled and continuously purged with Ar to maintain a positive pressure; both gases are vented to the outside of the building. Helium consumption has been measured to be about 40 slpm for each plasma torch. Gas recirculation, an option with a plasma furnace, was not considered economical due to the low He consumption rates.

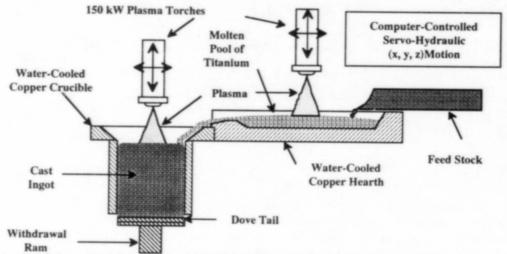


Figure 1: Schematic drawing of the IRC PACH furnace showing the component parts.

Furnace Operation

The normal operation of the IRC PACH furnace begins with loading ingots or compacts in to the feed chamber. While the furnace is open, each torch is inspected for wear and water leaks, as well as the hearth and crucible assemblies. The torch start up positions and torch patterns are checked by watching each torch as it is stepped through the motion sequence, as discussed by M. E. Schlienger⁴. The furnace doors (melt chamber, feeder and withdrawal chambers) are then bolted shut and the furnace is evacuated by a roots-blower mechanical-vane vacuum pump combination. The pump down time depends on the type of feed stock, amount of time the chamber was open and the amount of maintenance that was carried on during the last change over (water exposure). Normally, a pump down is performed overnight to achieve < 20 μ bar pressure in the chamber.

Prior to furnace start up, the exit gas analysers (O_2 , H_2 , H_2O) are warmed up by passing He gas through them. Initially a five minute leak up rate (LUR) is performed to determine the furnace integrity. An acceptable LUR value is $< 5 \,\mu bar / min$, otherwise, the system is examined to find and repair leaks. After a satisfactory LUR is obtained, the furnace is back-filled with Ar to $105 \,kPa$. The exit gas analysis system is then used to measure O_2 , H_2 and H_2O contents as Ar is purged through the furnace. The level of these gases should be $< 10 \,\nu ppm$ for O_2 and O_2 and O_3 and O_4 and O_3 prior to melting. During operation O_3 and O_4 levels increase due to moisture in the feed stock (particularly Ti sponge) or from residual moisture on the furnace walls. As shown in figure 2, each of the exit gas levels are originally within startup specifications, but as the melting proceeds, the furnace heats up the walls and feed material, releasing O_4 into the furnace atmosphere which reacts with the Ti, liberating O_4 into the furnace chamber. O_4 levels as high as O_4 0 vppm have been observed but have had little effect on the interstitial pickup of O_4 in the cast ingot, as discussed later. The O_4 0 reading rises slightly during the first part of the run, then begins to drop off as moisture is removed from the feedstock

and chamber walls. In order to reduce the initial moisture in the system, longer pump downs can be used, the chamber walls can be heated during pumping and continuous operation could be carried out.

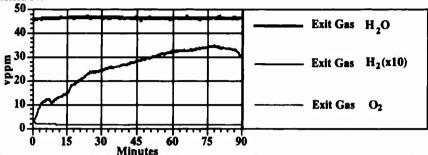


Figure 2: Analysis of the gas exiting from the plasma furnace during the casting of a 150 mm ingot of Super - α_2 , (Note, H₂ levels are x 10).

The melting operation begins after the exit gas requirements are obtained. Helium gas and water are supplied to the torches. Adequate flows satisfy interlocks for the power supplies, allowing them to be energised. Each torch is then tested electrically by raising it about 100 mm then pressing the start button. With the power supplies saturated, a small voltage drop should be observed, indicating satisfactory pilot-arc ignition and no insulation break-down. Upon successful completion of the pilot-arc, the torches are returned to their start-up position and the power supplies are turned off.

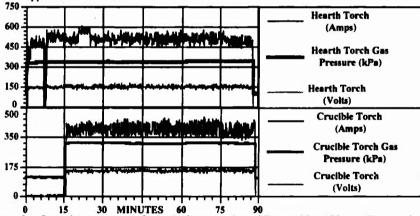


Figure 3: Operating parameters for both plasma torches while remelting 100 mm diameter ingot of Super - α_2 into the 150 mm diameter crucible.

Initiation of the melting process begins by again energising the power supplies and selecting a setting of 50%. Depressing the start button establishes an arc between a graphite starter block and the torch electrode. Current is adjusted to about 350 amps prior to pressing the sequence button. Under computer control, through servo-hydraulics, the torch moves from the start-up block over the material in the hearth in an oblong type pattern. The current is then raised to about 500 amps to obtain a stable arc and maintain proper heat input to establish a molten pool in the hearth. When a molten pool is established, material may be fed into the hearth. The torch then moves in a sequence of separate patterns, a crossing pattern to melt the feed material, an oblong pattern to keep the hearth bath molten and a sweeping motion to move the material out of

the hearth into the crucible. Enough material has to be cast into the crucible in order to cast a dove tail shape to lock on the withdrawal ram.

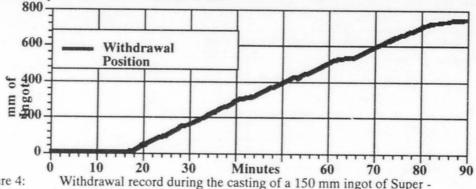


Figure 4: Withdrawal record during the casting of a 150 mm ingot of Super - α₂ indicating a melt rate ~ 1 kg/min.

With sufficient material covering the dovetail, the crucible torch is started in a similar fashion to the hearth torch. The crucible torch pattern is a circular motion over the ingot surface in the withdrawal crucible at a current level of about 400 amp (depending on the alloy being melted). Data from a super- α_2 melt, shown in figure 3, displays the operation described above. The crucible torch is also used to clear the notch between the hearth and crucible. A stirring coil applies an electromagnetic field around the crucible, interacting with the current passing through the plasma to the ingot surface (Bxj) causing the molten metal to rotate around the plasma impingement area. The stirring coil is programmed to reverse directions of the field periodically to ensure a more uniform microstructure. Concurrently, a withdrawal velocity is selected to match the melt rate of the system. Superimposed on the withdrawal velocity is a dither motion to prevent sticking in the crucible. Stirring, withdrawal velocity and dither are all computer-controlled functions. The importance of withdrawal control has been discussed elsewhere⁵. Withdrawal velocities of about (12.5 mm / min) have been obtained for a cast of 150 mm diameter ingot of super - α_2 (Figure 4). Note that it took almost 18 minutes to establish a melt pool and cast a dove-tail.

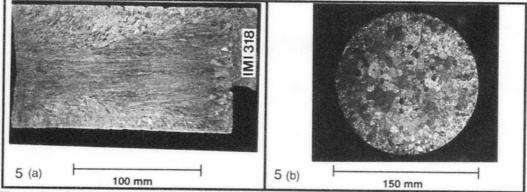


Figure 5 a) Macrographs from a 100 mm diameter IMI-318 ingot - axial direction, and b) 150 mm diameter IMI-318 ingot - radial direction.

Ingot Production

Commercially Pure-Ti (Grade 4), IMI-318, IMI-834, γ -Ti and super α_2 -Ti have been plasma melted and cast into 100 mm or 150 mm diameter ingots for macrostructural and chemical analysis. The plasma melted γ -Ti and super α_2 -Ti ingots will be thermomechanically processed and then tested to compare them with the commercially available material 6,7,8. Further studies

will involve processing these plasma melted Ti aluminide alloys by the powder metallurgy (PM) and sprayforming routes^{9,10}.

The raw materials for this programme included VAR ingot, Ti sponge, master alloys and elements. The Cp-Ti trials were conducted using VAR ingot. The IMI-318 compacts were composed of Al/V master alloy, Al shot, TiO₂, Ti sponge (Mg reduced) and Fe wire. For the IMI-834 programme, compacts were comprised from DTL granules (Na sponge), Zr sponge, Nb/Al/Si/Ti and Al/Si master alloys, Super Pure (Sp) Al, Sn, Mo and C powder. The aluminide compacts consisted of DTL granules, Nb/Al master alloy, Mn flakes and Sp Al for gamma-Ti and the super- α_2 master alloy compact contained Ti sponge, DTL granules, Nb/Al, V/Al, Al/Si master alloys, Sp Al and Mo powder while the super- α_2 elemental compact had Ti sponge, DTL granules, V/Al master alloy, Nb swarf, Sp Al, Mo and Si powder.

Initial Trials Cp-Ti & IMI-318

Commissioning trials were undertaken using ingots of CP-Ti. Initial results show little change in the oxygen and nitrogen concentrations during plasma melting and good O₂ homogeneity. Similar chemistry results were obtained from an ingot of IMI-318 melted from sponge compacts, as discussed before³. Macrostructural examination of the IMI-318 ingots revealed the presence of equiaxed grains on the exterior edge of the ingot, while the grains towards the centre were elongated in the axial direction (Figure 5(a)) and equiaxed in the radial direction (Figure 5(b)). This is typical of the microstructure to be expected, where the finer equiaxed grains are formed from the high thermal gradient present when in contact with the crucible wall and the elongated central grains grow more slowly in the core where the thermal gradient is lower. Ingot surfaces in general were good, the best comparable with VAR. Porosity was found through out the IMI-318 ingot, similar to IMI-834 ingots and will be discussed later.

Table #1, Specifications and Chemistry results from IM1-834 melting programme.

IMI-8.	34	Al	Sm	Zr	Nb	Мо	Si	C	02	N ₂
		5.5 -	3.7 -	3.3 -	0.65 -	0.45 -	0.28 -	0.04 -	0.075 -	<0.01
SPECIFICA	TIONS	5.95	4.2	4.0	0.75	0.57	0.44	0.08	0.150	
					·					
SINGLE	Т	5.83	3.77	3.65	0.67	0.52	0.32	0.04	0.083	0.001
PLASMA	M	6.15	4.11	6.06	0.72	0.50	0.33	0.04	0.083	0.003
MELT #23	В	5.74	4.09	3.25	0.73	0.52	0.34	0.03	0.090	0.003
	T 70.0		1 4 04	2.00		T 0.40	0.24	1 0 04		
VAR	T-C	5.84	4.06	3.78	0.72	0.52	0.34	0.04		
MELT	T-MR	5.84	4.07	3.78	0.72	0.52	0.34	0.04		
OF	M-C	5.82	4.06	3.77	0.72	0.51	0.33	0.04	ļ	
SINGLE	M-MR	5.83	4.06	3.77	0.72	0.51	0.34	0.04		
PLASMA	B-C	5.89	4.00	3.41	0.71	0.52	0.32	0.04	L	
MELT #23	B-MR	5.98	4.01	3.68	0.71	0.53	0.32	0.04		
m 1 1 1/4 m			1 00	2 44		0.63	0.11	0.04	1 0 120	0046
Triple VAR	T	5.80	4.00	3.45	0.71	0.53	0.33	0.06	0.130	.0045
#34709	В	5.73	3.99_	3.60	0.70	0.52	0.35	0.06	0.130	.0040
MELT #31	T-C	5.85	4.03	3.63	0.71	0.53	0.34	0.06		
SINGLE	T-MR	5.81	4.03	3.60	0.71	0.53	0.35	0.06		
PLASMA	M-C	5.81	4.01	3.56	0.70	0.53	0.36	0.06		
OF VAR	M-MR	5.87	4.02	3.48	0.71	0.53	0.33	0.06		
MELT	B-C	5.87	3.99	3.68	0.69	0.52	0.36	0.06		
#34709	B-MR	5.80	3.99	3.63	0.69	0.52	0.37	0.06		
MELT #32	T-C	5.99	4.04	3.84	0.72	0.52	0.34	0.04	<u> </u>	
DOUBLE	T-MR	5.96	4.04	4.73	0.73	0.53	0.32	0.04		
PLASMA	M-C	5.85	4.02	3.86	0.71	0.50	0.32	0.04		
MELT	M-MR	5.90	4.06	3.79	0.72	0.50	0.31	0.04		
OF	B-C	5.56	3.98	3.43	0.71	0.51	0.31	0.05		
COMPACTS	B-MR	5.63	3.99	3.38	0.72	0.52	0.30	0.05		

T-C -TOP Centre of Ingot, T-MR - TOP Mid Radius of Ingot, M-C - MIDDLE Centre of Ingot, M-MR - TOP Mid Radius of Ingot, B-C - BOTTOM Centre of Ingot, B-MR - TOP Mid Radius of Ingot

IMI-834 Melting

A programme for evaluation of IMI-834 ingots included single plasma-melt from compacts, plasma-melting of compacts followed by another plasma-melt (double plasma), plasma-melting of compacts followed by a VAR melt, a triple-melted VAR followed by a plasma melt, and triple VAR. The chemistries of the various IMI-834 ingots produced are given in Table 1, along with the alloy specification. As can be seen from the values in the table, plasma melting produced homogeneous ingots with in-spec. chemistries in most cases. In Melt # 23 a high Zr concentration was found, most likely due to incomplete melting of the Zr sponge. A double plasma-melt (Melt # 32) shows good homogeneity, and compares well with triple-melted VAR and the plasma-VAR combinations. Notice that the C concentration in Melt #31 (plasma melted VAR) is consistently higher than the VAR remelt of Melt #23 or any of the other ingots produced using plasma as a primary melt. It has been pointed out that a small C buildup is normal for VAR, therefore, C in the compacts was mixed at a low level (0.04%) to allow for this pickup¹¹. Chemistry irregularities observed in single melted ingots can be attributed to the dwell time in the molten pool which is small because of the size of the IRC plasma hearth.

Macrostructures of IMI-834 ingot cross sections in figure 6 show that the grain size of the double plasma ingot (c) is much finer than the plasma-VAR ingot, (a) and similar to the VAR-plasma (b) suggesting that a plasma-melt has a favourable effect on reducing grain size for this alloy. This could have a favourable effect in the subsequent processing of the alloy. In all cases for plasma-melted IMI-834, ingot surfaces were very good.

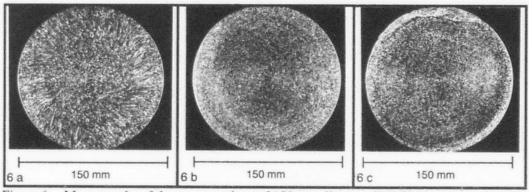


Figure 6 Macrographs of the cross-sections of 150 mm diameter IMI-834 ingots produced by a) VAR of a single plasma, b) plasma melt of a triple VAR and c) double plasma.

Porosity was found in the plasma-melted ingots of IMI-318 and IMI-834, as mentioned earlier. An example of the porosity observed in a 100 mm diameter double plasma-melted ingot of IMI-834, is shown in Figure 7 (b). Similar porosity had been found before in the IMI-318 plasma-melted ingots as mentioned before. As shown in Figure 7 (a), porosity was also found in a plasma-VAR IMI-834 ingot. There was concern that this porosity was due to gas entrapment introduced during the plasma-melting of these ingots. Gas analysis was performed on several plasma-melted specimens; IMI-318, IMI-834, Ti-48-2-2 and Super- α_2 . The results of the Ar gas analysis, performed at INCO Alloys Ltd., Hereford, U. K., were found to be less than detectable.

An additional test was performed to determine the source of the porosity. Samples from double plasma-melted and plasma-VAR ingots (Figures 7 (a) and (b)) were each HIP'd at 965°C at 100 MPa for 1h. As shown in figures 7 (c) and (d), after the Hipping operation, no porosity can be observed. These samples were then vacuum annealed at 1200°C for 16h, again no porosity was observed (Figures 7 (e) and (f)). Since inert gases are insoluble in Ti, the vacuum

anneal should have allowed the compressed gas to reopen the pores which were closed during Hipping. This is similar to the Thermally Induced Porosity (TIP) checks for gas porosity carried out on gas atomised Ni-based superalloys. Since no porosity was observed in the vacuum annealed condition, it is concluded that the pores must have originated from interdendritic solidification shrinkage.

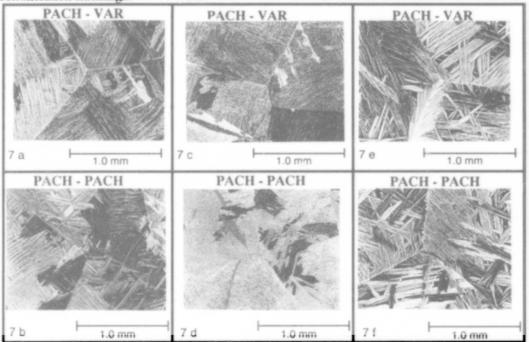


Figure 7 Micrographs of IMI-834: a) As cast (PACH - VAR), b) As cast (PACH - PACH), c) HIP at 965°C - 100 MPa - 1h (PACH - VAR), d) HIP @ 965°C - 100 MPa - 1h (PACH - PACH), e) Vacuum Anneal at 1200°C - 16h (PACH - VAR), f) Vacuum Anneal at 1200°C - 16h (PACH - PACH).

Super-a2-Melting

Super α_2 -Ti ingots produced by plasma melting exhibited a fine uniform grain structure in the radial cross section and grains that were somewhat elongated in the lengitudinal direction, as shown before². The ingot surfaces were excellent. The plasma melted ingot structure is more refined than that of VAR for this alloy, for these sizes of ingots. In the main, this can be attributed to the solidification control of the plasma torch hot topping the ingot in the withdrawal crucible, but may be also in part due to the size of the ingot (100 mm diameter) and the low melt rate (1 kg/min).

Table 2: Blend levels and chemical composition of plasma melted Super- α_2 (wt%).

Super a2	Al	Nb	v	Мо	02	N ₂	H ₂	
BLEND LEVEL		14.2	20.0	3.2	2.0	0.0600		
MELT #29	TOP	14.4	19.0	3.18	1.93	0.065	0.0040	0.0010
SINGLE PLASMA	MID	14.2	19.1	3.17	1.90	0.065	0.0035	0.0010
FROM COMPACTS	BOT	14.3	19.3	3.14	1.92	0.065	0.0035	0.0015

TOP -TOP Centre OF Ingot, MID- MIDDLE Centre OF Ingot, BOT- BOTTOM Centre OF Ingot

Overall, chemistry results for the super α_2 -Ti were very good, as shown in Table 2. Even in a single plasma-melt good homogeneity can be observed. It should also be pointed out that the interstitial content of H_2 and N_2 were excellent and only a 50 ppm pickup of O_2 was measured.

These results were obtained with the furnace exit gas containing 2 to 3 vppm O_2 , 45 vppm H_2O and up to 350 vppm H₂.

Gamma - Ti (48-2-2) Melting

FROM COMPACTS

Ingots of y-Ti were produced by plasma melting Ti sponge and master alloy compacts. As in the super α₂-Ti ingots, the chemistries were very good. Again, with relatively high H₂ levels (400 vppm) in the chamber atmosphere, the interstitial H₂ content was barely detectable. Minimal O₂ pickup was observed, even in the double plasma melted ingots, as shown in Table 3.

Table 3: Blend levels and chemical composition of plasma melted Ti- 48-2-2 (wt%).

11-48A1-2ND-2MB		AL	ND	MB	U ₂	N2	H2
BLEND LEVEL		34.2	5.0	2.51	0.060		
MELT #27	TOP	34.8	4.99	2.96	0.065	0.0030	0.001
SINGLE MELT	MID	34.9	5.11	2.85	0.065	0.0035	<.001
FROM COMPACTS	BOT	35.2	5.08	2.69	0.070	0.0040	<.001
MELT #38	TOP	35.4	5.16	2.80	0.075	0.0040	0.001
DOUBLE MELT	MID	24.9	5.08	2.83	0.070	0.0035	< 001

35.2 TOP -TOP Centre OF Ingot, MID-MIDDLE Centre OF Ingot, BOT-BOTTOM Centre OF Ingot

BOT

Conclusions

5.05

0.0040

<.001

0.085

PACH has shown to be a valuable tool in producing complex Ti alloys such as IMI-834. Results to date indicate that PACH, under the conditions employed does not introduce inert gas porosity. Chemical control and homogeneity were found to be very good in the PACH material. Preliminary results also suggest that PACH has the added benefit of producing ingot material with smaller grain size than VAR, which could be important in structural development during subsequent thermomechanical processing.

Acknowledgements

The authors would like to thank the SERC for providing funds through a foundation grant with the IRC at The University of Birmingham, Edgbaston, England. The assistance of the IRC staff, especially T. Perry and R. Skeldon, made this project possible. Many thanks to the people at IMI Titanium for their contributions of time and materials.

- M. P. Schlienger, private conversation with author, Retech, Inc., December, 1991.
- J. W. Sears, "Current Processes for the Cold-Wall Melting of Titanium," Journal of Metals, Vol. 42, No. 3, March, 1990, p. 17-21.
- 3 J. W. Sears, "Clean Melting Techniques for the Production of Titanium Alloy Powders and Spray Deposits", Advances in Powder Metallurgy - 1991, Editors: L. F. Pease III and R. J. Sansoucy, MPIF, Princeton, N.J., Vol.6, p. 335-346.
- M. E. Schlienger, "Computer Control of Plasma Torches in Plasma Melting," Proceedings of the 1989 Vacuum Metallurgy Conference, Pittsburgh, PA, May., 1989, p.27-30
- M. E. Schlienger and D. Malley, "Control Considerations in Cold Hearth Withdrawal," Electron Beam Melting and Refining - State of the Art 1989, Ed. R. Bakish, Bakish Materials Corp., Englewood, NJ, p. 175-184, Oct. 29-31, 1989.
- R. V. Ramanujan, et al, "The Influence of Heat Treatment on the Microstructure of Plasma-Melted y-Based Titanium Aluminides," this conference
- Z. Chen, et al, "The Influence of Thermomechanical Processing on the Microstructure and Properties of Plasma-Melted Ti Aluminides," this conference.
- M. L. H. Wise, et. al, "The Influence of HIP'ing and Forging on the Microstructure and Properties of Plasma-Melted y-Based Titanium Aluminides," this conference.
- J. W. Sears, et. al, "Spray Forming of Ti-Aluminide-Based Alloys," this conference.
- 10 J. W. Sears, "Titanium Spray Formed Structures," Proceedings of the 1992 PM Congress, by MPFI, San Francisco, CA., June 21-26, 1992.
- 11 P. Blenkinsop, private conversation with author, IMI Titanium Ltd.

Recent Improvements in the Economics of Plasma Melting

R. C. Eschenbach, M.E. Schlienger and R. E. Haun Retech, Inc.

Abstract: In recent years, plasma melting has become an important technique in the production of titanium and its alloys. Continuing development work has enabled improvements in the econimics of plasma melting which are applicable to production operations.

Background: Improvements in plasma processes for melting reactive and refractory metals have substantially affected both the cost of melting and the properties of the melted metal.

Economic factors discussed below include melt rate, power cost, consumables, yield and raw material cost. The melt rate achievable has a strong effect on the cost of melting. Labor costs are almost independent of melt rate; thus doubling the melt rate reduces the labor cost per pound almost a factor of two. Increasing the melt rate usually also reduces the specific power cost. Consumables include plasma gas consumption, torch replacement parts and maintenance of furnace equipment. Final product yield depends on surface finish, chemistry uniformity, shrinkage porosity, evaporation loss and ingot shape. Raw material costs can be reduced if the process permits achieving product quality standards while feeding lower cost material, e.g. dirtier material.

Quality factors also affect economics of the total process, even if they may not change melting cost per pound. A reduced grain size

> Titanium '92 Science and Tachnology Edited by F.H. Froes and 1. Caplan The Minerals, Metals & Materials Society, 1993

or greater freedom from inclusions affects down-stream processing cost and customer acceptability, thus changes in these are also important.

Technology Improvements Since 1986: One of the most striking improvements in the rate of melting titanium was the substitution of helium for argon as the plasma torch gas. This was first tried at Oregon Metallurgical Corporation in their PASER (Plasma Arc Single Electrode Remelt) furnace, made by Retech. Data on the effects of arc gas, pressure and current in a lab-size furnace were presented at the 1986 Pittsburgh Vacuum Metallurgy Conference(1). When melting titanium at pressures near atmospheric, the melt rate with helium was about twice that with argon at the same torch current and standoff. The difference between argon and helium in specific power to melt is less than for the melt rate, since arc voltage is greater in helium than in argon.

Subsequent to the 1986 study, additional work on the effect of furnace pressure on melt rate showed that reducing the furnace pressure from 1100 millibar to 200 millibar, in helium at constant current, reduced the melt rate when standoff was held constant, but increased the melt rate when voltage (and thus power) was held constant⁽²⁾. Data from the two papers is replotted in figure 1.

It is believed that the pronounced difference between helium and argon in melt rate results from the factor of ten ratio in molecular weights; helium's low molecular weight results in much higher thermal conductivity and decreased radiation loss. This low molecular weight also results in a higher torch gas flow rate with helium at similar pressure and geometry.

At the 1987 Electron Beam meeting in Reno (3), successful use of a gas recirculation system for the RP-250T torch was reported. Using a makeup flow rate of 6%, the cost of the helium flowing through the melt torch was reduced from \$134/hr (48 Nm³/hr x \$2.82/Nm³) to \$8/hr. The melt rate was 198 kg/hr and the power to the melt torch was 270 kW (290 kW including power supply losses). Thus power cost to melt at \$.10/kWh was 14.8¢/kg. Gas cost would have been 68¢/kg without recirculation and only 4.1¢/kg with recycle and 6% makeup. Table 1 below gives data for production size furnaces on the importance of gas cost with respect to power cost as affected by recycling.

TABLE 1 - GAS RECYCLE ECONOMICS

	CONSOLIDATION MELT	HEARTH MELTING
NUMBER OF TORCHES	1	3
MELT RATE kg/hr	700	700
TOTAL POWER, kW	800	2000
TOTAL GAS FLOW RATE Nm ³ /hr	70	210
MAKEUP FLOW RATE Nm ³ /hr	2.1	6.3
GAS COST/POWER COST* - NO RECYCLE EUR. / U.S.	7.0/3.5	8.4/4.2
GAS COST/POWER COST* - RECYCLE** EUR./U.S. * Assuming 1Nm ³ He costs 80 x 1 kWh in Eur. U.S.	0.2/0.1 ope, 40 x 1 kWh	0.25/0.12 n in

Subsequent work with a number of production systems has shown that the makeup rate for such systems averages 2% to 3%. However, if feed stock has perceptible moisture or contains hydrided scrap, the hydrogen concentration in the recycle gas can build up to levels where hydrogen content of the ingot is too high. Then, addition of hydrogen removal equipment to the gas recycle system is desirable. Figure 2 shows the elements of a helium recycle system which removes particulates, hydrogen and water.

Electrode lifetime with hollow electrodes has been increased by some refinements in electrode configuration and gas injection geometry. Lifetime for the production size RP-600T are typically 200 to 300 hours at 2500 to 3000 amperes. Lifetime with the pilot-size RP-250T at 1200 to 1500 amperes was initially 15 to 20 hours, but has been increased to at least 80 hours. Similar refinements of the RP-75T electrode have increased its life from 8 hours to more than 30 hours, occasionally 75 hours.

^{**}Assuming 3% makeup

The yield of forgeable ingot from plasma hearth melted material depends on surface smoothness (laps or variations in ingot diameter may have to be machined), presence of solidification voids (sometimes found on the centerline about half an ingot radius below the top surface if power is shut off abruptly) evaporation losses and on whether any ingots are rejected for being outside chemical or inclusion specifications.

An investigation carried out jointly by Pratt & Whitney Division of UTC and Retech (4) brought out important parameters for achieving smooth surfaces. The work showed that surface quality with helium was much better than with argon. Subsequent production experience has show that surface finish of withdrawn ingots can be comparable with the best practice with stationary cast ingots (as in VAR). The 1990 program (4) showed that selection of optimum parameters resulted in an rms roughness of only 125 micrometers.

Shrinkage voids have been found on axis about half the ingot radius below the top surface when casting has been abruptly stopped and the ingot torch current has been simultaneously abruptly changed to zero. However, a hot-top achieved by reducing the power of the ingot torch more gradually (i.e. two minutes for an eight inch diameter ingot) prevents void formation. Such voids obviously increase yield loss.

Plasma melting was noted prior to 1986 as a low evaporation loss process (5). Development and production tests confirm that even multi-hearth plasma melting results in evaporation loss rates for titanium alloys of less than 1%. The low evaporation rate both has a direct effect on production cost, and constitutes a "hidden" economic factor that can have a significant impact on process development cost.

In general, it is difficult to gauge alloy losses that occur in a vacuum melt. This difficulty is compounded as the alloy system becomes more complex and the constituent requirements are tightened. Typically multiple melts are required for each alloy in order to determine the appropriate amount of "sweetening" to account for process losses of the volatile constituents. In addition, melting techniques must often be carefully designed and meticulously followed, since even relatively small deviations from steady state may result in compositional inhomogeneities.

Since plasma melting occurs at significantly higher pressures, the loss of volatile constituents is drastically reduced. For most titanium and zirconium alloys, the composition of the ingot accurately reflects the composition of the raw materials fed. Plasma's positive pressure capabilities allow the successful production of such materials as niobium aluminides. Plasma's ability to produce one of a kind melts, in spec, has been repeatedly demonstrated. This represents a significant cost saving when trying to bring a new alloy to market.

Since compositional control is de-coupled from molten metal residence times, process fluctuations due to such items as variations in feed rate have little or no effect on the compositional integrity of the produced ingot. As a result generic melt practices may be successfully used for a wide variety of alloys. This factor in conjunction with the ease of attaining in spec chemistry provides a significant economic advantage in situations where a diverse alloy mix and one of a kind "specials" are expected.

Using electromagnetic stirring in conjunction with plasma melted ingot withdrawal results in finer grains in the ingot. Benefits include less tendency to crack during forging operations, i.e. higher yield. In addition, improvements in homogeneity and microalloying have been reported.

Current practice for rotating grade titanium alloys uses cold-hearth melted (either plasma or electron beam) ingots which are subsequently melted once in a consumable electrode furnace. A significant cost saving is achievable if the VAR step can be omitted. As noted above, reducing the hydrogen content in the gas recirculation system permits making single process ingots which fully meet all specs and which represent a substantial improvement over the prior three-step VAR process in freedom from inclusions, reduced grain size and improved micro-homogeneity (i.e. no freckles).

WHAT LIES AHEAD: Further improvements in plasma processing of reactive and refractory metals are expected. Several possibilities have been verified at development scale, but only a small amount of production experience has been gained. Four primary items are listed here.

Round cornered slabs have been made by plasma, and offer the possibility of reduction in down-stream processing cost and yield improvement.

Powder made from alloys melted in plasma and bottom-poured may permit significant broadening of available alloy chemistries, due to the characteristics of rapidly solidified metals. Even with conventional chemistries, improvements in alloy cleanliness are attainable.

Extension to nickel-base alloys should permit the same advantages of fine grain and good micro-homogeneity shown for titanium alloys.

Hollow rounds have now been made with plasma, following the electron beam example, and should offer some cost advantages when making tubular shapes.

REFERENCES

- 1.) R. C. Eschenbach, "Lab Scale Plasma Melting Furnace," 1986 Vacuum Metallurgy Conf. on Specialty Metals Melting and Processing, Pittsburgh, PA, June 9-11, 1986
- 2.) R. E. Haun, R. A. Lampson "The Effect of Chamber Pressure on Melt Rate in Plasma Arc Melting," 1991 Vacuum Metallurgy Conf., Pittsburgh, PA, September 9-10, 1991
- 3.) M. P. Schlienger, R. C. Eschenbach, "Recent Developments in Plasma Melting of Reactive and Refractory Metals," Electron Beam Melting & Refining, Reno, Nevada, November 8-10, 1987
- 4.) D. R. Malley, R. C. Eschenbach, M.E. Schlienger, "Control of Plasma Hearth Melted Ingot Surfaces," 10th ICVM, Beijing, China, June 11-15, 1990
- 5.) R. C. Eschenbach, G. Herman, "Plasma Melting of Reactive Metals," Vacuum Metallurgy Conf. on Specialty Metals Melting & Processing, Pittsburgh, PA, June 11-13, 1984

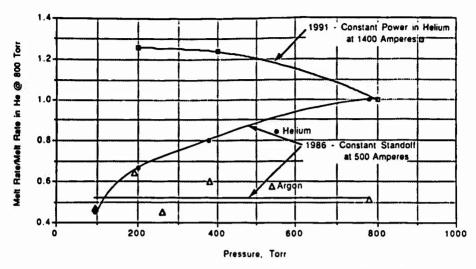


Figure 1: Effect of Furnace Pressure on Melt Rate

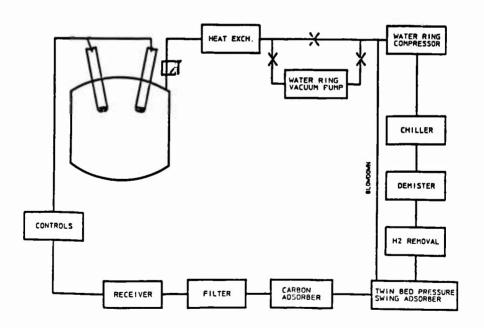


FIGURE 2: ELEMENTS OF A HELIUM RECIRCULATION SYSTEM

THERMOCHEMICAL ANALYSIS OF KROLL PROCESS FOR TITANIUM SPONGE PRODUCTION

Ch.RVS Nagesh, K.V.Rama Rao and Ch.Sridhar Rao

Defence Metallurgical Research Laboratory, Kanchanbagh post, HYDERABAD - 500258, India

ABSTRACT

Kroll process is practiced for commercial production of titanium metal. However, the reaction kinetics of the process are not adequately known. In this work thermochemical aspects of the process have been investigated. The reaction temperatures and profiles as a function of TiCl4 feed rate have been determined. The predictions on the rate constants for intrinsic rate and growth rate have been made.

INTRODUCTION

Bulk of titanium sponge in the world over is produced by magnesium reduction of TiCl4 i.e, by Kroll Process [1]. In this process pure liquid magnesium contained in a clean argon filled reactor, reacts with continuously fed TiCl4. The reaction product MgCl2 being denser than magnesium moves away from the reaction surface and is subsequently taken out of the reactor. Titanium metal is deposited as a spongy mass which in the course of reaction also descends down the reactor.

Titanium '92 Science and Technology Edited by F.H. Froes and I. Caplan The Minerals, Metals & Materials Society, 1993 The reaction process is very complex as it involves many chemical reactions associated with gaseous, liquid and solid phases. Attempts have been made by many investigators [2] to understand the reaction kinetics and mechanism. Studies on the kinetics of the fast reactions of this type are limited. However, studies relating to reduction process, heat transfer, structure and quality of sponge have been reported [3-11]. In this paper an attempt has been made to study the effect of the heat generation and its transfer on the kinetics of the process. A rate expression for the process has been proposed.

KINETICS OF REDUCTION:

For the purpose of evaluation of intrinsic kinetics the three rate controlling factors viz (1) mass transfer of TiCl4 in the vapour phase(Kg), (ii) chemical surface reaction(Ks) and (iii) exchange through the external solid surface (Ke) are considered. The suitable expression for the rates and rate constants available from the literature have been used [2,12]. The dependence of these rate constants on temperature and temperature gradients have been accounted. The chemical reaction rate constant has been estimated from the initial reaction periods at low feed rates of TiCl4. The overall rate constant (Ko) is determined assuming that the rate controlling factors (resistances) are in series, ie.

$$\frac{1}{K_0} = \frac{1}{K_0} + \frac{1}{K_0} + \frac{1}{K_c}$$

For the nucleation and growth rates kinetics associated with constant feed rate of TiCl4 period has been considered and a rate expression and a rate constant (K) have been derived [13] and determined from the experimental results. The rate equation adopted is

On integration we have,

$$-\ln(1-x) = \frac{bKC_b}{\ln_0 h_0} \frac{t^2}{2}$$

TEMPERATURE PROFILES

Heat generated at the surface of magnesium due to reaction between TiCl4 and Mg is conducted always through the product mass. Convection and radiation heat transfer also takes place due to high temperature and temperature gradients and relative flow of liquids. In this analysis however, only heat conduction is considered and results of rise in surface temperature is taken for all calculations i.e. for estimation of mass transfer rate constant, surface reaction rate constant and exchange rate constant.

HEAT CONDUCTION CALCULATIONS:

The unsteady state heat conduction equation in cylindrical co-ordinates is written as

 $K\left(\frac{\partial T}{\partial x^{L}} + \frac{1}{h}\frac{\partial T}{\partial x} + \frac{\partial T}{\partial z^{L}}\right) + \hat{q} = \int C \frac{\partial T}{\partial z}$

This equation is solved subject to the convective boundary condition,

on the side walls of the cylinder and the initial condition T=830C everywhere. Here 1 and 1 are the direction cosines of the normal to the surface, k is the thermal conductivity, \dot{q} the heat source term, p density and c is the specific heat of the material and T the temperature, r and z are the spatial co-ordinates and t is the time.

Following the usual way [14], the differential equation is put in the matrix form as

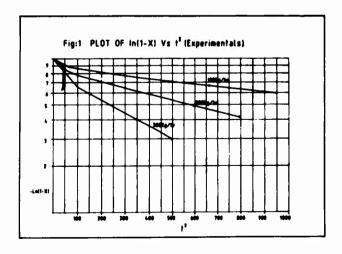
where T is the matrix of nodal temperatures and T is the matrix of nodal temperature derivatives. K is the symmetric matrix of heat conduction coefficients and K' the symmetric matrix of constant heat capacity coefficients and P is the vector of known quantities. Expressing the above differential equations in finite difference form, we have

$$(K + \frac{2}{4}K')T_{n+1} = (\frac{2}{4}K'-K)T_n + P_{n+1} + P_n$$

The above equation is solved for the nodal temperature, T at time level n+1 with the knowledge of temperature at time level n. Bull DPS 6/850 computer at DMRL was used for calculating the temperatures at various points of the cross-section of the reactor.

DISCUSSION:

The conversion of magnesium with time is shown in Fig-1 It is seen that $\ln(1-x)$ where x is fraction of conversion for magnesium, has a linear relationship with t indicating generally the rate of metal (sponge) formation that is mainly follows growth kinetics. The rate constant K_{pq}^{-4} determined from the slope of the line was calculated at $0.23-1.179 \times 10^{-4}$ in the TiCl4 feed rate range of 120 to 300 kg/hr. The values of K_{pq} are shown in Table.1. The values of Kg,Ks,Ke and Ko determined from the temperature based relationship are also given in Table-1.



REACTION RATE CONSTANTS

Table-1

Flowrate of TiCl ₄ Kg/hr		CAL	EXPERIMENTAL				
	Tempera *(oture Kg Cm/Sec	Ks Cm/Sec	Ke Cm/Sec	Ko Cm/Sec	$\left[\frac{\mathrm{Ko}^2}{\mathrm{ho}}\right]$ = Kr $\mathrm{Cm/Sec}^2$	Kr Cm/Sec2
120	940	0 1134	0 0721	0 662	0 0413	0 28×10	0 23×10
200	1103	0 1191	0 744	0 855	0 091	1 38×10 4	0 536×10
300	1360	0 1253	5 163	1 047	0 1091	1 98×10	1 177×10

The rate equatio - In [1-x]= 497.22 $\left[\frac{\text{Ko}}{\text{ho}}\right]^2$ t^2 WHE::E Ko is overal reaction rate constant (Cm/Sec) t (time:sec) and x Conversion of Magnesium(fraction)

Figure 2 shows the temperature profiles determined from the calculations. The relation between K_and Ko is determined to be

$$K_{R} = \frac{K_{o}^{2}}{h_{o}}$$

$$-\ln(1-x) = K_n \left(\frac{k_0}{h_0}\right)^2 t^2$$

where Kn is a constant. The value of Kn is determined as 497.2 and t is time in seconds. The expression is found valid for nearly 70% conversion of magnesium. Further conversion of magnesium is determined purely by magnesium transparent rate. As in the last stages of reaction period the rate is likely to be very low and hence no significant conversion is expected. However, further work is considered necessary to determine the effect of temperature gradient across and along the mass and velocity

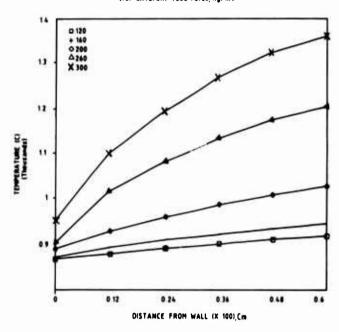


Fig:2 TEMPERATURE PROFILES
(for different feed rates, Kg/hr)

profiles of the reacting species on conversion of magnesium and the progress of the reaction.

CONCLUSION

By finite element analysis the temperature of magnesium surface as function of TiCl4 feed rate has been predicted. The predicted temperatures were used to determine the intrinsic reaction rate constants. A rate equation for the estimation of conversion of magnesium from the intrinsic rate constants has been proposed.

ACKNOWLEDGMENT

The authors express their gratitude to Sri R.B.Subramanyam, Director(P) for the cooperation extended for carrying out these studies. They are also extremely grateful to Sri SLN Acharyulu, Director DMRL for providing necessary encouragement and support to the study.

REFERENCES

- 1. W.J.Kroll, Journal of the Electrochemical Society, 78, 1940, pp 35-47
- V.A.Garmata et al, "The metallurgy of titanium", Translation division, Wright Patterson Airforce Base, Ohio, NOv., 1970
- R.A.Sandler et al, "Secondary structure of titanium sponge produced by magnesiothermic reduction of the lower chlorides", Izv., Vuz., Tsventnaya, Metallurgiya, 1970
- V.V.Vlasov et al, 'The effect of the rate of magnesiothermic production of titanium sponge on its structure', Tsventye Metally, 1966
- V.A.Likhterman et al, 'Investigations of the structure of the forms of titanium sponge', Sov. Non Ferrous Met., Res., 12,(2), 1984.
- V.A.Likhterman, R.A.Sandler, A.A.Zakharevich; Tsvent Met.,(3), 62-64, 1985
- 7. V.A.Likhterman, Izv. VUZ Trvetn Metals, (2),33-38, 1984
- S.V, Aleksandrovskii et al, 'Effect of structural characteristics of titanium sponge on its quality', Sov. J. Non Ferrous Met., Res., 10, (4), 1982
- A.A.Zakharevich et al 'Effect of titanium tetrachloride input rate on the structure and quality of titanium sponge', Sov. J.Nonferrous Met., 26, (7), 1985.
- S.V.Aleksandrovskii et al, 'A study of fine structure of titanium sponge', Izv. Akad. Nauk. SSSR Met (6), 67-70,1982.
- 11. M.S.B.Chandra Sekhar et al, Temperature profiles in batch reactor for production of titanium sponge by Kroll process, proceedings of the second international conference on titanium products and applications, Walt Disney World village, Florida, USA, Sept/Oct, 1990.
- Szkeley and Themelis ,'Rate Phenemenz in Process Metallurgy' John Wiley & Sons Inc., NewYork, 1971.
- 13. To be published
- S.S.Rao, 'The finite element method in engineering', 2nd edn., Pergamon Press, Oxford, OX3, OBW, England, 1989.

NOMENCLATURE

b : stoichiometric constant of the reaction

K : conversion rate constant

A : cross-sectional area of the reactor

t : time in seconds

Ni : number of moles of magnesium at any instant

C : molar volume of TiCl4

? : density

h : initial magnesium level inside the rector

A New Method to Produce Segregation-free Ingot

of Ti-6Al-6V-2Sn by VAR

Hiroshi Hayakawa¹⁾, Nobuo Fukada²⁾, Masaaki Koizumi³⁾ and Hirowo G. Suzuki⁴⁾

1) Formerly Nippon Steel Corporation, Stainless Steel and Titanium Lab., Now Pacific Metals Co., Ohtemachi, Chiyodaku, Tokyo, 100 Japan. 2) Formerly Toho Titanium Co., Now Sankyo Diamond Industrial Co., Hongo, Ebina, Kanagawa, 243-04 Japan. 3) Toho Titanium Co., Chigasaki, Chigasakisi, Kanagawa, 253 Japan. 4) Nippon Steel Corporation, Iron & Steel Labs., 20-1 Shintomi, Futtu, Chiba, 299-12 Japan.

Abstract

The solidification structures and segregation of the VAR cast ingot of Ti-6Al-6V-2Sn alloy were investigated by using a new etching technique with a high concentration of hydrofluoric acid. Segregation of Fe and Cu is remarkable in the zone of equiaxed grains in the center of ingot. To minimize segregation, the authors propose a VAR procedure of casting at a faster solidification rate and a greater temperature gradient by the use of a consumable electrode tapered to the stick during hot topping.

Titanium '92 Science and Technology Edited by F.H. Froes and I. Captan The Minerals, Metals & Materials Society, 1993

Introduction

To improve the quality and reliability of titanium alloy products, efforts have been made to reduce the irregularity and defects in solidification structure of the cast ingots (1.2.3). For the general purpose alloy Ti-6Al-4V, however, there are only a few studies on the solidification structure covering all the ranges of mill cast ingots (4.5). The authors have reported the solidification structures in alpha+beta type titanium alloy ingots produced by the vacuum arc consumable electrode remelting method (VAR)(6). This paper clarifies the cast structure of Ti-6Al-6V-2Sn (Ti662) alloy by a new etching technique and segregation of Fe and Cu by computerized X-ray microanalyser (CMA), and proposes a new method to reduce segregation.

Experimental Procedure

Test material and processing conditions: The starting material was an ingot of a highly β flecks sensitive commercial alloy of Ti662, 5.85%Λ1, 5.62%V, 1.95%Sn, 0.72%Cu, 0.69%Fe, 0.005%C, 0.005%N, 0.16%O and H<0.001%. The ingot was about 3970 kg with 750 mm ♦ and 2000 mm in length. The test material was twice VAR melted by hot top technique⁽⁷⁾ in which the melting rate is reduced 90 min before melt end. The melting rate was changed from 23 to 16 kg/min. The ingot was cut for examination as shown in Fig.1. CMA analysis and macrostructure observation were focused to hatched areas: Top (T), Middle (M) and Bottom (B).

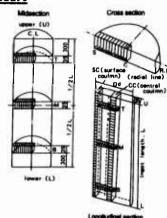


Fig. 1 Sampling positions in ingot.

Observation of cast (C) and solidification (S) structure, and shrinkage cavities: Specimen surfaces were finished by mechanical grinding and immersed for etching; the etchants and etching conditions are shown in Table 1. The structures were revealed by immersion in a solution (HF: HNO3: H2O = 1:1:1 to 40) for at least 5 min at room temperature. For S-structures, etch pits were formed by the difference in chemical compositional variation during the solidification of the melt. The difference between the C- and S- structures was revealed in a greater amount of water and longer etching time in the former. Shrinkage cavities were revealed by a high precision automatic ultrasonic flaw detector as described elsewhere⁽¹⁾.

Objective structure Etchant Etching condition

Microstructure (as-cast) HNO₃: 15ml, HF: 15 ml, H₂O 600 ml > 5 min at R.T.

Macrostructure (solidification) HNO₃: 15ml, HF: 15 ml, H₂O: 15 ml < 5 min at R.T.

Table 1 Etching technique.

Quantification of segregation: Samples for chemical analysis were taken from the longitudinal and cross sections of the ingot, as shown in Fig.1. The elemental segregation in these samples were investigated with $CMA^{(9)}$. In the analysis, Al, V, Sn, Fe and Cu were analyzed at 250 x 250 points over the area of 10 x 10 mm² and the picture element of 40 x 40

um². Differential thermal analysis (DTA) was applied to the samples T, M and B taken from the central column of the ingot⁽⁶⁾. Temperature distribution in the ingot during solidification and cooling was calculated⁽⁶⁾ by the difference calculus⁽¹⁰⁾, assuming that the solidification temperature⁽¹¹⁾ was 1600°C and the liquid alloy of 2000°C ⁽¹²⁾ was cooled in a water cooled copper mold.

Experimental Results

Cast structures of longitudinal sections of ingot: Figure 2 shows the C-structure on the vertical section and the close-up of the B zones. The C-structure in Figs. 2a) and b) is characterized by the three zones: CH; rapidly cooled equiaxed grains (chilled layer) contacting the bottom and side surfaces of the mold, CO; columnar grains growing from the CH-structure to the center of melt, EA; equiaxed grains in the central zone, as shown in Fig.3a).

Solidification lines on longitudinal sections of ingot: On the longitudinal section of the ingot in Fig.2b), parallel and equal interval etch pit lines are observed perpendicular to the growth direction of columnar grains of the C-structures. This shows selective etching of parts in the compositional variation and the resultant linear loci of solidification line. The features of the Sstructure can be summarized as follows: CH; the Slines of etch pits formed on the ingot surface in a shell form with a slope of about 20° toward the surface(6), CO; the etch pit lines intersecting vertical to the growth direction of columnar grains as the Slines of solid-liquid phase, and EA; no etch pit line in the equiaxed grain of the central zone and random distribution of pits. The S-lines can be divided into two parts as shown Fig.3b): the conventional and the hot top melting. The difference of energy supplied to melt in the two techniques leads to the slope changes of 20 to 60° in the S-lines towards the surface of the ingot (6). CMA analysis of Fe and Cu distributions reveals microscopic segregation stripes of Fe and Cu as in Figs.4b) and c). The etch pit lines in Fig.4a) correspond to the Fe and Cu enrichment.

Shrinkage cavity lines on longitudinal sections of cast ingot: The distribution of shrinkage cavities on the longitudinal section of the ingot is shown in Fig.2c). Shrinkage cavity lines of several mm interval intersect perpendicular to the columnar grains. These intervals and forms correspond to the microscopic segregation stripes in Figs. 4b) and c); and to the etch pit lines in Fig.2 b) or Fig. 4 a). The shrinkage cavity lines are not

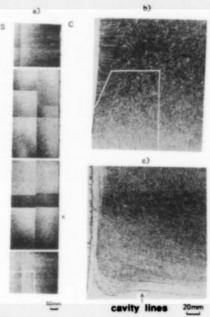
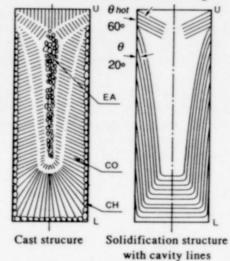


Fig. 2 Macro- and micro-structure on the midsection of the ingot.



on the midsection of ingot.

CH: chilled layer CO: columnar structure EA: equiaxed structure

Fig. 3 Schematics of as cast and solidification structure.

clear in the CH- than the CO-structure. The EA-structure shows no cavity line with irregular distribution of rough shrinkage cavities. The CO-structure has a number of spherical or elliptical cavities of about 20 µm diameter. The EA-structure shows complicated conical and polyhedral cavities of about 100 µm long⁽⁶⁾.

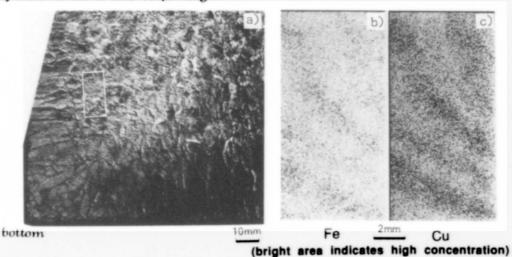


Fig. 4 Segregation of Fe and Cu along solidification fronts in ingot bottom corner.

Melt pool depth and solidification curve:

The X marks in Figs. 2a) indicate the boundary between the CO- and EA-structures and indicate the bottom of the melt pool which is about 1440 mm below the top of ingot. Figure 5 depicts the solidification curve at 1600°C and the profile of melt pool in VAR ingot(6). The curves were obtained by calculating the isotherm of 1600°C solidification temperature with an interval of 6 min after melting of the ingot by the difference method. Solidification of the melt in contact with the water cooled copper mold proceeds along the shell-like solidification lines. The measured and calculated melt pool depth are as high as about 2/3 of the ingot height. These isothermal solidification profiles are similar to the contours of etch pits and shrinkage cavity lines in the CO-structure.

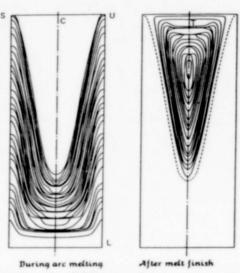


Fig. 5 Simulation of solidification front movement during and after VAR melting.

Segregation: Chemical analysis was carried out over the left half on the longitudinal section of the ingot. The analysis of Al and Fe shown in Fig.6 indicates no segregation of Al and Fe in the surface layer. The same is true for Cu, V and Sn. Along the center line, on the other hand, Fe gradually increases from B to T. The same was true for V and Cu. The high concentrations of Fe, Cu and V occur in the top of ingot center as shown by hatching in Fig.6. The long conical zone (70mm dia. x 500mm) is the central zone of the EA-structure. This EA-conical zone corresponds to macroscopic V-shape segregation (β flecks). No segregation of Al as well as Sn is observed in the center zone. Figure 7 gives the distribution of Al, V, Sn, Fe and Cu of T, M and B samples taken from the center zone of the cast ingot. They are divided into two groups in terms of the coexisting elements. One is Al and Sn, and the other is V, Fe and Cu.

The distributions of elements in the former and the latter are reversed. The trend is especially strong in T and M zones in comparison with B zone. The β flecks existing in the macroscopically segregated T zone of the ingot forms several mm masses. Also Fe and Cu were enriched to the amount of 2.1 and 2.2, respectively due to the segregation ratio⁽⁶⁾. This result means that the equilibrium distribution coefficient Ks is smaller than the unit in Fe and Cu. The results of the measurement of beta transus, T_{β} by DTA in this zone indicated that T_{β} (=700°C) of T zone of the cast ingot was about 50°C lower than that of B zone (=747°C)⁽⁶⁾.

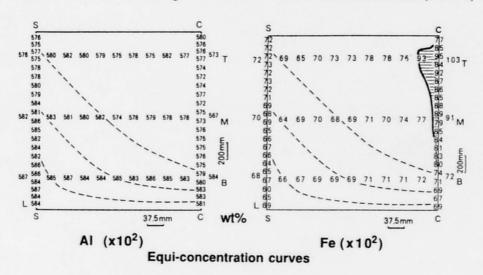
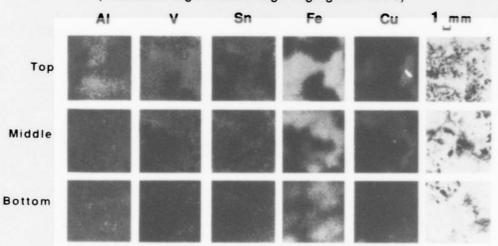


Fig. 6 Elemental segregation of Al and Fe on the midsection of ingot. (Shadowed region shows high segregation of Fe)



(bright area indicates high concentration)
Fig. 7 CMA color mapping of elemental distributions and optical micrographs in T, M, and B of ingot.

Discussion

Solidification Phenomena during VAR

a) The Stage from Start to End of Arc Melting(CH- and CO-structure area). The overheating degree is defined as the difference between the high melt pool temperature and solidification

temperature. In the solid-liquid interface, 2000°C liquid phase and 1600°C solidification phase come into contact, and the temperature gradient is sharp. The compositions Fe, Cu and V with Ks<1 are enriched to the liquid phase in the interface, and subsequent solidification takes place with clusters such as Fe and Cu being nucleus. In this way, a shell-like solidification layers with a certain thickness is successively formed as shown in Fig.8. In other words, the solidification proceeds intermittently. Solidification proceeds toward the melt pool at nearly constant intervals until arc stops. This results in banded compositional variation.

b) Melt Pool Solidification (EA-structure area).

After arc stops, the regular solidification lines described above do not occur as shown in Fig.8, because the degree of overheating is smaller in the melt pool. On the other hand, solidification takes place with the enriched zone being coagulated because of the enriched beta phase stabilizing elements. In the center of molten pool heat convection promotes dendrite growth with segrgating elements on the front. Consequently large melt traps are formed in interdendrites leading to β flecks.

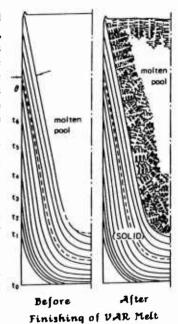


Fig. 8 Schematic of solidification structure formation in VAR.

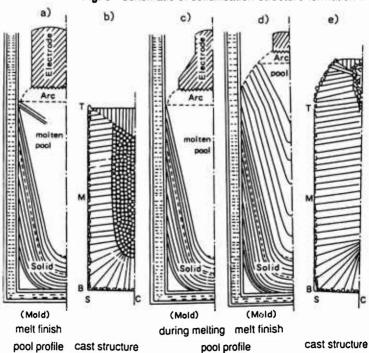


Fig. 9 Comparison of solidification behavior and cast structurre between conventional and new tapered electrode methods in hot top VAR melting.

Measures for Reducing Macroscopic Segregation: Some papers reported that it is important to keep the melt pool depth shallow to improve the ingot quality^(13, 14, 15, 16, 17). The present structural observation for minimizing the segregation of VAR ingot leads to the following two basic counter measures: (1) To make temperature gradient greater, and accordingly to make solidification rate faster, and (2) To make heat radiation from the mold faster. The melt pool depth is made shallow by these two measures, which well coincide with the proposals insisted by R.T. Adams et al^(16, 17), by using smaller diameter ingots. Fig. 9 compares the solidification behavior and solidification structure between the conventional electrode and the present tapered electrode methods in hot top VAR melting. The conventional method tends to form deep pool as shown in Fig. 9. For minimum segregation, the authors have developed the tapered electrode method (Fig. 9c). The end of consumable electrode is tapered to the stick. Melting with the tapered electrode reduces the pool size during melting (Fig. 9d). On the melt finish solidification progresses rapidly without formation of melt traps in interdendrite region and prevents β flecks.

- (1) The end of consumable electrode shall be conically tapered to the stick, and the diameter of the electrode shall be made smaller at the time of final melting to make the pool size smaller.
- (2) A given current density shall be maintained until the conical top of electrode is melted and the melt shall be agitated to make the component elements in the melt pool homogeneous.
- (3) Heat radiation rate shall be made faster by using the adequate materials for the side and bottom of the mold to improve cooling rate.

Conclusions

This study dealt with the analysis of the cast structure of Ti662 ingot produced by the commercial vacuum arc consumable electrode remelting method. The key results are summarized as follows:

- (1) Etching in a new solution (hydrofluoric acid: nitric acid: water = 1: 1: 1 to 40) for several minutes reveals the details of cast and solidification structure.
- (2) The cast structure consists of a chilled layer in the outer surface, columnar grains in the intermediate zone and equiaxed grains in the central zone of the ingot.
- (3) Solidification lines appear as dotted lines of etch pits, suggesting the elemental distribution at the solidification front which is perpendicular to the growth direction of columnar grains as a result of intermittent solidification.
- (4) Segregation of Fe and Cu is remarkable in the equiaxed structure zone. In CH- and CO zones, no beta flecks occurs.
- (5) Segregation of Fe and Cu is reduced by casting at a faster solidification and a greater temperature gradient and by using a consumable electrode tapered to the stick than the hot topping of VAR.

REFERENCES

- H.Ichihashi: <u>Present Aspects of Titanium Materials Research in Japan</u>, ISIJ, Tokyo, (1989),
- H.B.Bomberger and F.H.Froes: <u>Titanium Technology</u>, ed. F. H. Froes, D. Eylon, H.B.Bomberger, (1985), 25.
- 3. V.V.Tetyukhin et al.: <u>Titanium and Titanium Alloys</u>, ed. J.C.Williams and A.F.Belov, Plenum Press, New York, (1982),141.
- 4. VI.Dobatkin et al: Slitki Titanovykh Splavov (Ingots of Titanium Alloys), Moscow, (1966),96.
- V.V.Tetyukin, V.N.Kurapov and Y.P.Deniso. <u>Titanium and Titanium Alloys</u>, Plenum Press, New York, (1982),141.
- 6. H.Hayakawa et al: ISIJ International, 31(1991), 775.
- H. Siraisi, Y. Kondou and A. Kanai: <u>Present Aspects of Titanium Materials Research in Japan</u>, ISIJ, Tokyo, (1989), 12.

- 8. K.Kawasima, T.Utagawa and M.Hatta: J. N.D.I., 37-2A(1988), 150.
- 9. I. Taguchi and H. Hamada: Anal. Sci., 1(1985), 144.
- 10.K.Chihara and G.Usui: Nippon Kokan Tech. Rep., 36(1966), 10
- 11. A.Mitchell, D.Mitchell and D.Tripp: 8th ICVM Vol.2, Linz, Austria, (1985),1269.
- 12. H. Ichihasi et al.: Tetsu-to-Hagane, 72(1986),579.
- 13.H.Ichihasi: Present Aspects of Titanium Materials Research in Japan, ISIJ, Tokyo, (1989), 16.
- 14. V.I. Dobatkin and M.I. Musatov: <u>Titanium Science and Technology</u>, Plenum Press, New York, (1973),319.
- 15.H.D.Broby and S.A.David: <u>The Science and Technology and Application of Titanium</u>, eds. R.I.Jaffee and N.E.Promisel, Pergamon Press, (1970), 21.
- 16.R.T.Adams and H.W.Rosenberg: <u>Titanium and Titanium Alloys</u>, eds. J.C.Williams and A.F.Belov, Prenum Press, (1982),127.
- 17. W.A. Tiller, J. W. Jackson, J. W. Rutter and B. Chalmers: Acta Metall., 1(1953), 428.

LARGE SCALE STATISTICALLY BASED EXCEPTION

REPORTING IN VACUUM ARC MELTING

Warren George

Oregon Metallurgical Corporation P.O. Box 580 Albany, Oregon 97321

Abstract

Much discussion has been made of the potential benefits of using SPC concepts to discern between random variation within the process capability, and non-random or special cause variation. Most approaches to practical application of these concepts involve small numbers of key product variables which are tracked using manual intervention in the capture, extraction, posting, or interpretation of result data.

Oregon Netallurgical Corporation, on its computer controlled VAR furnaces, has been applying a strategy called Large Scale Statistically Based Exception Reporting which differs somewhat from the traditional approach as described above. The chief differences are in the volume of tracked variables, up to 550 per melt cycle; the type of variables, many are related to equipment performance or productivity rather than product; and the methods by which the furnace control software automatically extracts the tracked variables from raw data and warns of exceptions without manual intervention being required.

The experience that has been gained in the six years that this system has been in use shows that there are important factors to be considered for developing and using such systems but that the results can be surprisingly effective, not only in reducing process variation, but in improved maintenance procedures, faster troubleshooting, and in achieving greater production efficiency.

Titanium '92 Science and Technology Edited by F.H. Froes and I. Caplan The Minerals, Metals & Materials Society, 1993

Introduction and Background

Oregon Metallurgical Corporation (OREMET) operates five VAR furnaces built by RETECH of Ukiah, California. These furnaces are used primarily for vacuum melting of titanium and titanium alloys. Conversion of these furnaces to computer controls was begun in 1981. The capability for Large Scale Statistically Based Exception Reporting was added in 1985.

The key control hardware components for each furnace consist of three computers and their ancillary equipment as well as a manual backup control system.

All analog measurements and loop control are accomplished with a Hewlett Packard 2250 operating at just over 5 cycles per second. In addition to 60 analog values, the 2250 monitors the on/off status of some 140 devices and switches.

A Hewlett Packard 9920 on each furnace acts as a supervisory controller and is responsible for the operator interface as well as data handling and short term data storage on a local hard disk.

Control of certain pumps, valves and relays is performed through a Westinghouse PC700 which takes instructions from the 2250, the 9920, and manual switches or pushbuttons.

A manual backup system is provided such that the furnace operator can complete an in-progress melt should a failure occur in the computer control system. Such failures have been very rare.

An additional HP 9920, the "department master", is connected to each of the furnace control 9920's in a manner that the master 9920 can read the data temporarily archived by each furnace 9920 on its own hard disk. The master computer extracts data for analysis and long term archival, and provides various utilities and peripherals for graphical and mathematical examination. It is the master computer that maintains the standards for the exception reporting system and compares new values against the standards, printing a list of exceptions on a per melt basis.

The furnace 9920's also share a speech unit which announces key events and alarms.

Each furnace 9920 receives all accumulated data from its companion 2250 at about one second intervals, performs additional calculations based on the data, updates the operator display monitor, and routes events and alarms to the printer, speech system, and monitor depending upon priority tables. In addition, all events and alarms are recorded to hard disk files no matter what the priority. Readings from eight major signals are extracted for logging to the hard disk at 0.975 second intervals and a reading from all 60 analog variables is extracted every 20.085 seconds. In addition, certain process summary data is maintained in memory until the end of the melt when a summary report is printed out for inclusion in the QC file.

At the end of each melt the master computer is triggered to automatically transcribe the portions of the data which apply to each particular melt from the temporary files on the furnace hard disk, to permanent files on a larger, centralized hard disk.

The automatic profile control of arc current, arc voltage, and stirring coil current is accomplished through pre-prepared procedures. Based on the procedure number and melt type, the 9920 loads the appropriate control file from disk. The procedure appears as instruction code values in the 2250 and as step by step instruction text on the operator's screen. Each step in the procedure is described by specific instructions (such as ramp, step, hold for time, hold until weight achieved, etc.) which are chained together to form a complete procedure.

Implementation and Operation

The methods chosen for detecting exceptional conditions utilize the simple to do the obvious. From the raw data for each melt, a large set of summary statistics is generated. Over time, the computer keeps track of the mean and standard deviation for each of these calculated variables by groups of similar melts. At the end of each new melt, the computer prints out on an exception report, any value outside the "plus and minus three sigma" limits as compared to previous melts in its standard group.

Two assumptions were inherent in the selection of these methods to discern abnormal conditions. 1) The variables would be randomly and normally distributed. 2) At the start of data collection, each variable was depicting a "correct" or "normal" state.

A wide range of summary variables were selected for inclusion. Hundreds were already available within the system and more were identified and easily programmed into the system. In general, raw data for each melt was summarized into averages, standard deviations, maximums and minimums, net changes, counts, time between events, ratios, and other appropriate characterizing variables. Some values are computed for the entire melt as a whole, others for each procedure step or only for specific procedure steps as appropriate. Depending upon the melt type and number of procedure steps, up to 550 variables per melt were initially included. That number has since been increased.

To get the system started, data was accumulated for a brief period of time. Then the computer generated the "standards" for each variable within each standard grouping by computing the mean and standard deviation of the accumulated observations. A second pass through the data was automatically made in order to remove outliers which we would have wanted to be reported as exceptions, from the population mean and standard deviation calculations.

The number of exceptions reported for a melt varies significantly but is typically in the range of 5 to 15. A process control engineer reads the 'xceptions as an aid in seeing generally how the equipment is running and whether unusual process conditions have occurred. At the discretion of the engineer, who takes into account such things as the importance of the variable and the strength of the exception as measured in units of "sigma", some exceptions are identified for further investigation.

Results

Numerous examples are available of exceptions which have been investigated and yielded some useful or interesting result. A few are given below.

- a) A slight, but statistically significant increase in the time taken for the roughing pumps on a particular furnace to evacuate the furnace to a preset level resulted in the discovery of a broken valve spring in one pump.
- b) Warnings of a gradual increase over a number of days in the voltage applied to a hydraulic servo valve in order to achieve ram drive was first misdiagnosed as a valve problem until the hydraulic motor froze up solid.
- c) Inexplicable fluctuations in average melt rate at constant measured current led to a decision to replace the existing current measurement shunts with new devices based on different technology. These new devices have exhibited superior consistency and accuracy.
- d) One specific melt with a higher than normal melt efficiency (weight melted per unit of electrical energy) was investigated and after studying all available information, a hypothesis was reached that a chunk of electrode had fallen into the pool at a particular point during the final melt. The ingot was diverted to internal conversion and the inclusion found in the area predicted.
- e) An increase in the standard deviation of current readings from one of four 10,000 amp rectifiers on one furnace was traced, with some difficulty, to a fuse on one phase in that rectifier, which would conduct at low current as from test meters but would open under load. The result of this condition was that

the other two phases were operating far beyond their design limit in order to make up for the lost phase. Had the exception system not provided the clue, this condition would have continued unnoticed until the rectifier failed.

- f) A drastic increase in the standard deviation of readings from a pressure transducer on a hydraulic cylinder holding a critical connection together as part of the high current path, caused that furnace to be immediately removed from service until the difficulty could be understood and corrected. The design was such that the oil in the cylinder was kept up to pressure by a regulator and prevented from escaping by a check valve. Only after extensive investigation was it determined that in fact, the pressure would be EXPECTED to fluctuate with the temperature changes caused by changes in current settings but we had never before seen the pressure rise above the setting of the regulator. After questioning many people about how the sudden change in the pressure behavior could have occurred, an off-shift millwright divulged that immediately before the last melt, he had fixed a hydraulic leak, near the cylinder, which had been present since the furnace was new.
- g) An investigation of a triple VAR ingot with multiple type I alpha defects in a particular location, led to the accidental discovery that the ratio of the vacuum readings from two different types of sensors could be used as an effective but very inexpensive residual gas analyzer. This helped to confirm that an air leak had occurred briefly during this final melt. The leak was so slight that furnace pressure rose by only a few microns.

Difficulties

While the exception system has substantially proven its capability for early problem detection, fast troubleshooting diagnostics, process verification, sensor calibration, and as computer system watchdog, certain difficulties have been apparent as well.

The design assumption that all tracked variables would be normally and randomly distributed has prevented us from well characterizing a portion of the variables. Most typical of these variables are the standard deviations of large sets of readings. The distributions of these standard deviation variables from melt to melt are typically very skewed. The result of this is that melt variables which are "smoother" than normal generally do not generate exceptions.

Another difficulty which has been exposed is that reading the exception report, especially with the large number and types of variables involved, requires extensive knowledge of the process physics and a full understanding of literally hundreds of system devices and how they are connected. This has limited direct use of the exception system to a very small number of people.

One additional fault of the system is probably a result of faulty expectation rather than attributable to system fault. Where it was dreamed that the system would require no effort to maintain and keep standards up-to-date, it has become evident that maintaining the standards to keep up with a dynamic environment does take some degree of diligence.

Future Plans

Based on the results of large scale exception reporting, OREMET's expectation of the future is that these kinds of tools will and should become commonplace within our company and within the industry. OREMET's own plans for development include the following.

Where the existing program identifies exceptions only after the process is complete, it would be better to report exceptions as near to real-time as possible.

The ability to handle non-normal distributions will increase the number of variables for which the frequency distribution is accurately modeled.

The true capability of large scale exception reporting will be obtained by combining exception systems with expert systems which can assist in interpreting the meaning and probable cause of various combinations of exceptions.

Acknowledgements

I would like to thank Steve Stocks and Dan Taylor who made the initial decision to develop the control system and have given full and necessary backing to the project, and Bill Glassmire and Lloyd Skogstad who were indispensable in their roles with software development and instrumentation respectively.

Also, the project would not have been successful without the exceptional capabilities of the Hewlett Packard products utilized, and the support of those products by Hewlett Packard.

Electroslag Remelting of Titanium

Alok Choudhury, Harald Scholz und Norbert Ludwig

LEYBOLD DURFERRIT GmbH Rueckinger Str. 12 6455 Erlensee/Germany

Abstract

The electroslag remelting process is a well known technique for melting tool steels, superalloys etc. Up to now, some investigations in the USA and the former USSR have shown that this technique can also be used for melting titanium. However, the ESR process has not experienced a real breakthrough for titanium production because of quality reasons.

In order to assess the potential of the ESR process, investigations were carried out with titanium sponge in a new equipment concept. Apart from that, new slag systems based on calcium fluoride were tested. The paper describes the experimental procedure as well as the resulting quality, such as oxygen and nitrogen content of the remelted material.

Introduction

Titanium metal as an engineering material came into use in the 1950's in the USA in response to the critical demands for low density, high strength material for aircraft and emerging space technologies. The titanium industry was mostly interested in the aircraft, especially military aircraft, and space market, where the cost was not a primary criterion for the selection of the material. However, times have changed now. The consumption of titanium in the aircraft and space industry has been stagnant for the last five years. The titanium industry must, therefore, look for markets other than the aerospace industry.

Titanium '92 Science and Technology Edited by F.H. Froes and I. Captan The Minerals, Metals & Materials Society, 1993

Non-Aerospace Applications of Titanium

Titanium has an excellent resistance to corrosion in most environments. Accordingly, a number of materials being used today in such applications can be totally or partly replaced by titanium. A recent study carried out by Charles River Associates /1/ shows a variety of materials against which titanium has a relative advantage (Fig. 1):

- Cupronickels (90/10 and 70/30)

- 316 stainless steel

- Super-ferritic stainless steel

- Super-austenitic stainless steel

- Dupley stainless

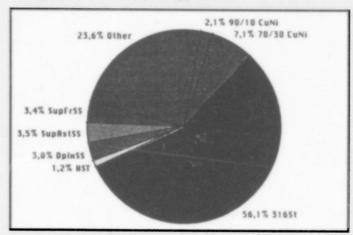
- Duplex stainless steel Hastelloy C-276

Competing Material with Titanium

- Cupronickels (90/10 and 70/30)
- Super-Ferritic Stainless
- Super-Austenitic Stainless
- **Duplex Stainless**
- AISI 316 Stainless
- Hastalloy C-276

Fig. 1: Material Competing with Titanium

Fig. 2 shows the portion of the market of competing materials which can be potentially replaced by titanium. It is evident that titanium can gain a sizable market just by replacing the stainless steel grades in non-aerospace applications.



Source: Charles River Associates,

Fig. 2: Weight Percent of Materials in Uses Potentially Available for Titanium Substitution

Fig. 3 shows that titanium may compete with high performance stainless steel at lower sponge prices and by reducing the thickness or by a combination of both. In the case of standard stainless steel grade 316, a substantial reduction of thickness is required. In this figure, only the cost for titanium sponge has been considered. Another important factor determining the titanium price is the cost of melting and fabrication of the final product.

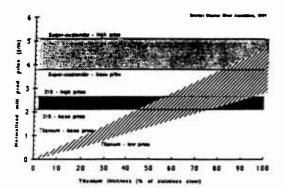


Fig. 3: Cost Effectiveness of Titanium Compared with Stainless Steels as a Function of Thick-

For effectively competing with stainless steel grade 316 it will be necessary to reduce the cost of the complete route of fabrication (Fig. 4).

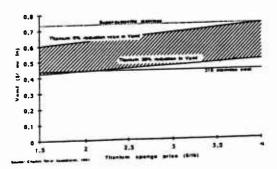


Fig. 4: Combinations of Sponge Price and Reduction in Mill Product (VAMF) can make Titanium cost effective with Super-Austenitic and 316 Stainless Steels

Fig. 4 demonstrates titanium in competition with super-austenitic stainless steel as well as with 316 stainless steel grade. It is evident that with a 30 % reduction in the cost of melting and further fabrication (VAMF = value added for melting and primary fabrication) with a simulaneous reduction of the sponge price, the cost of titanium comes very close to that of Grade 316 stainless. The question is how to lower the cost of melting and further fabrication. The present production route for titanium sheet products is as follows (Fig. 5): consumable vacuum arc remelting, at least twice forging to slab or square surface conditioning

- rolling

Production Route for Titenium

- Consumable Vacuum Arc Remelting at least Twice
 - Forging to Slab or Square
- Surface Conditioning
- Rolling to Desired Dimensions

Production Route for Titanium Sheet Fig. 5:

As vacuum arc remelting can only produce round ingots, a forging sequence with subsequent surface conditioning must be introduced into the production route in order to get rollable material. Appreciable cost savings are, therefore, only possible by direct remelting to slabs or squares with subsequent rolling without any forging. This can be realized with electroslag remelting (ESR) of titanium.

Electroslag Remelting of Titanium

Consolidation of titanium sponge by the ESR process was started in the early 1960's, especially in the former USSR /2/ but also in the USA /3/. It has been reported, that the former USSR is melting titanium with the ESR process on a production scale. In the Western World this technology has not experienced a technological breakthrough until now. LEYBOLD DURFERRIT GmbH has carried out tests in order to determine the metallurgical parameters required to achieve optimum results with respect to ingot quality.

Titanium is a reactive metal with high affinity for oxygen and nitrogen. Apart from that, titanium reacts with almost all oxides at high temperature. Bearing this in mind, the electroslag remelting of titanium must fulfill the following parameters:

- turnace atmosphere must be free from oxygen and nitrogen, eg. an inertgas atmosphere must

- be secured
- slag must be free from oxides, which can be reduced by titanium

In order to assure a 100 % inertgas furnace atmosphere the usual ESR-furnace with a hood is not suitable. The ESR-unit must be a closed chamber installation. The conception of such an ESR-plant is not new. LEYBOLD DURFERRIT GmbH has already built such furnaces for electroslag remelting under pressure (PESR). Fig. 6 shows schematically a PESR-furnace, which can work also under vacuum or inertgas atmosphere. The present experimental work was carried out with such a laboratory scale PESR-furnace equiped with a pumping set for prior evacuation of the furnace chamber.

- Electrode leed drive system.
- Bail screw
- Movable turnace support frame
- Furnace lifting system,
- 5 Load cell system,
- Ejectroge ram Electrode
- 8 Water lacket
- 9 Slag pool.
- 10 Ingot.
- 11 Mold assembly,
- 12 Quick flange . 13 Vacuum-/pressure chamber
- 14 Alloy feeder.
- 15 Coaxial power cables.
- 16 Ram guioing system,
- 17 Maintenance platform

12 10

Fig. 6: Pressure/VAC-ESR Installation

Common ESR slags are based on CaF_2 , CaO and Al_2O_3 , sometimes with additions of MgO and/or SiO_2 depending on the alloy grade to be remelted. For titanium remelting, slags containing Al_2O_3 , CaO, MgO and SiO_2 cannot be used, as they are sources of undesired contaminations in titanium. According to the published literature, the most suitable slag for titanium remelting is pure calcium fluoride. The present work was, therefore, started with technically pure CaF_2 .

Tab. 1 shows the remelting parameters of the three experiments.

		Melt No. 1	Melt No. 2	Melt No. 3	Melt No. 4
Electrode diameter	mm	110	110	110	110
Electrode length	mm	850	1000	1000	800
Electrode weight	kg	25,8	29,8	29,8	34,0
Mold diameter	mm	170	170	170	170
Current	kA	4	3,8	3,8	3,8
Power	kW	135	100	100	115
Melt rate	kg/h	19,0	52,6	54,2	40,7

Before starting the remelting process, the furnace chamber was evacuated to a pressure of approx. 2 x 10^{-2} mbar and subsequently backfilled with argon of a purity of 99,99 % to a pressure of approx. 1000 mbar. The first melt was carried out with pure CaF_2 , whereas in the other melts some additions were made to the CaF_2 slag. It is evident from Table 1 that the melt rate of the first melt is much slower despite much higher power consumption.

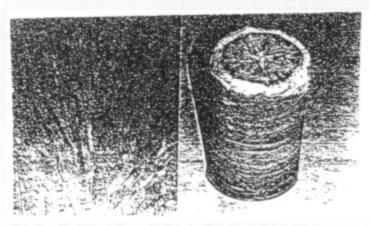


Fig. 7: Titanium Ingot and Primary Structure of the Ingot

Fig. 7 shows the titanium-ingot and the primary structure of the ingot. The macrostructure is dense and free from any oxides. The chemical composition of the ingots, with respect to gas and carbon contents, is listed in Table 2.

<u>Tab. 2.</u> Chemical composition of the ingot, in respect of gas- and carbon-content

Element	- Lu	Ingot No.	<u>.</u>		g n l	Ingot No.	6		l n	Ingot No.	o. 3		l n g	Ingot No.	o		ASTM-Speci- fication for Titanium Grade 1	÷ _
	Electrode	В	Σ	T	Electrode	8	2	-	Electrode	В	2	_	T Electrode	В	2	1		
C (ppm)	80-150	20	60	60	60-100	100	60	60	06-08	80		60	80	70	70	7.0	max. 1000	Q
(wdd) O	006-009	200 650	650		600 700-1300 1300 1050 800 500-1300 1200	1300	1050	800	500-1300	1200		006	006	700	909	900	тах. 1800	Q
(mdd) N	100-150 180 170 170	180	170	170	80-160	180	170	140	180 170 140 70-160 140	140		160	120	100	100 100	100	тах. 300	
(mdd) H	76-94	25	24	24	34.42	35	30	26	36-41	28	-	27	24	18	12	15	max. 150	٥
F (ppm)		09	9	09	•	60	60	60			_	,				•		
											·							

It can be seen from Table 2, that there is an overall decrease in the concentration of carbon and hydrogen in the remelted ingot. In the case of nitrogen, the remelted materials show a little higher concentration than in the electrode. There is no additional oxygen pick-up during remelting. It must be mentioned that the values of oxygen and nitrogen content in the electrodes are probably not representative of the whole electrode. It is evident, that all values are within the ASTM-specification for Grade 1 titanium (CP).

Conclusions

Electroslag remelting is an efficient process for the consolidation of titanium.
 It appears that a single melt will be sufficient for further working.
 With proper process control, any additional pick up of undesired elements, like oxygen and nitrogen, can be completely avoided.

Literature

- / 1 / Firoze E. Katrak, I.S. Servi and I.C. Agarwal "Non-Aerospace Applications, Titanium Sole Opportunity for Growth" Metal Bulletin Monthly, August 1991, pp. 28 to 33
- / 2 / S.M. Gurewich and Co-workers "Properties of Technical Grade Titanium and OT4-Alloys Produced by Electroslag Melting" Automatic Welding (1963), Vol. 16, pp. 20 to 21
- / 3 / C.E. Armentront and R.H. Natziger "Development Electroslag Melting of Titanium" Trans American Foundrymen's Society 77 (1969), pp. 353 to 359

State of the Art in

Electron Beam Melting of Titanium

C. H. ENTREKIN and H. R. HARKER
Axel Johnson Metals, Inc.
P. O. Box 529
Exton, PA, 19341 U.S.A.
(215 Welsh Pool Road, Lionville, PA, 19353 U.S.A.)

Abstract

The electron beam cold hearth melting (EBCHM) process has developed into a premier refining tool for both aerospace and industrial titanium applications. Hearth refined titanium has now been specified in critical jet engine components. Improved levels of quality control are obtained by maintaining close control over such operating parameters as electron beam energy distribution, condensate management, and chemical homogeneity. Advances have been made in near net shape castings of preforms (semi's) for the direct rolling of as-cast titanium slabs.

"MaxiMelt," the world's largest electron beam cold hearth furnace (3300 kW - 915 mm diameter ingots) has recently been commissioned at Axel Johnson Metals, Inc. Start up and qualification programs for this new furnace are discussed.

Introduction

Since the time of the Sixth World Conference on Titanium, numerous developments have occurred in the Electron Beam Cold Beam Hearth Refining (EBCHR) process for titanium. During the Sixth World Conference, some of the initial work on "in-spec" alloy electrodes and near net shape casting was presented. Developments were also reported in the areas of on-line chemistry and intelligent materials processing. (1)

During the last four years, the EBCHR process has continued its steady evolution into a premier refining tool for both industrial and aerospace titanium applications. This paper is intended to review the current status of high-volume commercial products such as large slabs and refined alloy electrodes. It will also present a brief history and current status of the world's largest operational electron beam furnace, MaxiMelt, which was built and commissioned during the last four years.

New developments in controls, instrumentation, and operating practices are continuing to occur. This paper will also highlight these areas for future growth.

Titanium '92 Science and Technology Edited by F.H. Froes and I. Caplan The Minerals, Metals & Materials Society, 1993

Cast Titanium Slabs

One of the first titanium products produced in commercial volumes by EBCHR was cast slabs. These slabs represented an early form of near net shape casting since they avoided the forging or cogging step required to convert a round ingot into a rectangular slab suitable for flat rolling. These products have steadily gained acceptance in nearly all flat rolled markets and millions of pounds are produced yearly.

Mold Development

A 150 x 965 mm (6 x 38 inch) slab mold was first used by Axel Johnson Metals (AJM) in 1983. These slabs were intended for direct rolling to plate or coil. Maximum slab weight was about 2.5 MT (5,400 lbs.), although the practical limitation was about 2.2 MT (4,800 lbs.) due to certain size restrictions for cross-rolling at some rolling mills. The maximum as-cast weight in the mold was limited by the size of the casting chamber and therefore limited coil applications due to economic reasons.

In an effort to provide more weight, a 305 x 1120 mm (12 x 44 inch) slab mold was introduced in 1985. These slabs weighed up to 5.7 MT (12,500 lbs.) and made the rolling of coils more economical. The 305 mm (12 inch) thickness also permitted greater rolling reductions for heavier gauge plates. The cross-section of the product was limited at the time not by a particular metallurgical reason but by the physical capabilities of the original Axel Johnson Metals electron beam furnace.

In 1991, the commissioning of the second EB furnace at AJM allowed the opportunity to install a 150 x 1270 mm (6 x 50 inch) slab mold in addition to the continuing use of the older two sizes. The maximum length of the cast slabs was also increased from 3,780 mm (149 inches) to 4,700 mm (185 inches). These wider and longer products opened new opportunities for direct coil rolling as weights of the conditioned slabs exceeded 4.1 MT (9,000 lbs.).

The goal of a 4.5 MT (10,000 lb.) conditioned thin slab for direct coil rolling was achieved in 1992 with the installation of a 178 x 1270 mm (7 x 50 inch) mold. Examples of these new slabs are seen in Figure 1.

Heavy slab evolution also progressed with the purchase and installation of the current jumbo mold for 305×1575 mm (12×62 inch) slabs. These slabs, with weights up to 9.1 MT (20,000 lbs.) were developed to avoid the necessity of cross-rolling for wide coils and to provide extra weight for heavy plates.

Surface Conditioning

Conditioning practices for the as-cast slabs have also evolved over the years. The first cast slabs were machined on the major surfaces using a horizontal planer to a surface finish of about 4.4 μ m (175 microinches) RMS. Most rolling practices at the time included an intermediate break-down stage at about 75 mm (3 inches) with the opportunity to inspect and grind any residual surface defects.

As the applications for the slabs broadened, new conditioning practices were also developed. Some demanding applications such as the direct rolling of hot band from 305 mm (12 inch) slabs required a better surface finish than $4.4~\mu m$ (175 microinches) since the opportunity for an intermediate inspection and conditioning had been eliminated. For these cases, a "precision machined" surface finish was developed. This machining practice involved planing a $1.3~\mu m$ (50 microinch) RMS surface on the major surfaces, the sides, and the edges. The precision machining, combined with dye penetrant inspection greatly improved the surface quality and the finished yield of the products.

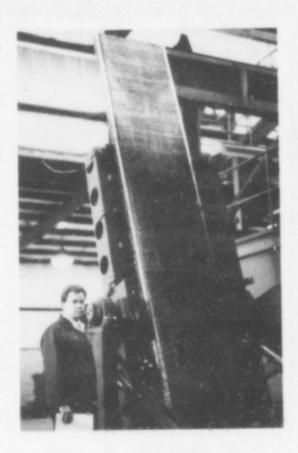


Figure 1. As-cast thin titanium slab.

To further enhance as-rolled surface quality, belt sanding was introduced as an option in early 1991. A typical belt sanded surface is similar in roughness to a "precision machined" surface. Belt sanding can be used independently of or in conjunction with machining.

Today, surface conditioning can be tailored for specific customers and their processing requirements. A wide variety of conditioning options are available and are routinely delivered.

The Clean Alloy Titanium Program

Electron Beam Cold Hearth Refining has been used for many years to remove high density inclusions (HDI) from titanium scrap. The inclusions such as tungsten welding electrode tips, molybdenum or tantalum fasteners, or tungsten carbide tool bit pieces sink into the skull of solid and mushy titanium contained in the cold water cooled copper hearth as the liquid metal flows over the hearth. (2) In 1984 General Electric Aircraft Engines approached Axel Johnson Metals to investigate the removal of low density inclusions (primarily titanium nitrides) by EBCHR using AJM's 2 megawatt furnace. The subsequent development efforts included many melting trials in which the furnace geometry and melting parameters were varied and tested by melting feedstock which had been seeded with known high interstial defect (HID) formers. This work resulted in a commercial process to produce "clean titanium alloy" as reported at the 1988 titanium conference, Figure 2. (1)

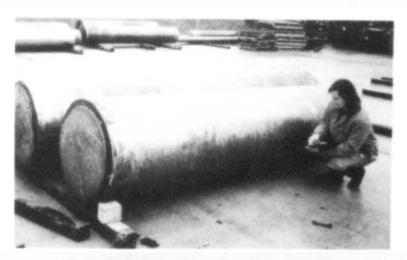


Figure 2. Hearth-refined alloy titanium ingots for aerospace application.

The "clean titanium" EBCHR process has grown commercially since 1988 extending to advanced alloys such as Ti-17 as well as to Ti-6Al-2Sn-4Zr-2Mo. The process is being more widely accepted following the FAA report on the titanium industry after the Sioux City DC-10 crash. (3) Much has been learned about optimizing the process by using special furnace geometries, heat and flow patterns, and sensors. The EBCHR process has recently been joined commercially by a plasma torch heated hearth melting process (PAM). (4)

Over 2,700 MT (6 million lbs.) of hearth refined "clean titanium" has been produced to date. In response to this increased demand, a new 3.3 megawatt EBCHR furnace has been built and qualified at AJM's Morgantown, PA, USA facility. (5) All indications are that hearth refining (EB or Plasma) will be used to process most titanium alloys for premium quality aerospace applications in the future.

MaxiMelt

The capacity of the 2 megawatt EBCHR furnace which AJM brought on stream in 1983 had been reached by 1988. It was time to design a new furnace. A market review indicated the need to scale up the existing furnace by about 50%. The resulting design featured 3.3 megawatts of power with three 600 kW and two 750 kW EB runs, six 50,000 liter/sec diffusion pumps, and a larger ingot and slab casting capacity. New mold sizes included a 508 x 1524 x 4699 mm (20 inch x 60 inch x 185 inch) mold for titanium slabs weighing 16.4 MT (36,000 lb.) and a 914 mm diameter x 4699 mm (36 inch dia. x 185 inch) mold for titanium ingots weighing up to 13.6 MT (30,000 lb.). (5)

The overall layout of the furnace uses two melt chambers so that while one chamber is in production, the other chamber can be cleaned out and maintained, Figure 3. The power lid can be easily switched from one chamber to the other as can the pumping, feeding, and casting systems. The melting chambers are large enough, 4m (13 foot) diameter, to allow a large patented "C" shaped refining hearth geometry and spray baffle to be optimized for producing hearth refined "clean" titanium, Figure 4. (6) A computerized beam energy distribution system is utilized to provide maximum flexibility and memory recall of preset distribution programs.

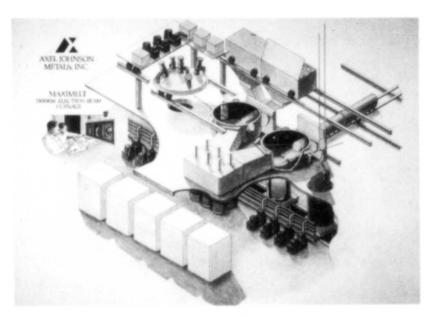


Figure 3. Schematic drawing of 3.3 megawatt, dual chamber MaxiMelt electron beam furnace.

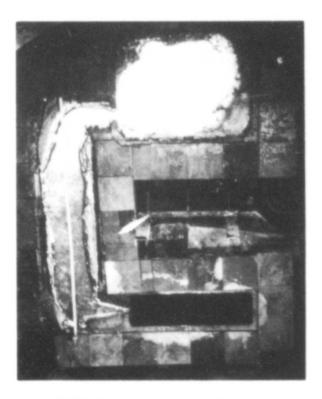


Figure 4. Overhead view of "C" shaped hearth and mold geometry containing solidified titanium skull. Melt zone is at top of photo, refining hearth is on left side; empty slab mold is at bottom.

AJM acted as general contractor for this installation using Retech, Inc., for mechanical components and Innotech, Inc., for power supplies and controls for the Von Ardenne electron beam guns purchased from Bakish Materials Corporation. Local contractors erected the furnace. Assembly of the furnace started in January, 1990 after one year of engineering and fabrication. The first ingot was cast in September, 1990 with commercial operation following immediately, Figure 5.

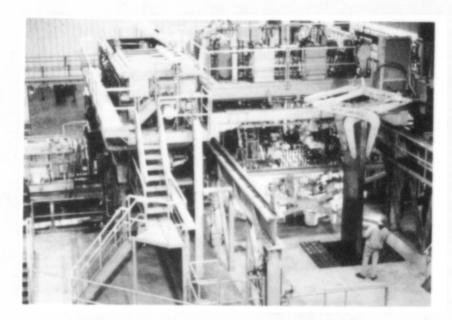


Figure 5. Side view of MaxiMelt dual chamber furnace.

The "MaxiMelt" or "B" furnace was designed for a nominal 4500 MT (10 million lbs.) per year capacity (varies with product mix) which together with the smaller "A" furnace provides a nominal 6800 MT/year (15 million lbs./year) of EBCHR capacity in the AJM melt shop.

New Developments

On-Line Chemistry Control

During the Sixth World Titanium Conference and at subsequent events, a system for online, real time chemical analysis based on energy dispersive x-ray (EDX) spectroscopy was described. (1) This system had worked well during laboratory trials and there was reason to believe it would also be successful in an industrial environment. Unfortunately, several problems were experienced which greatly retard d the further development of the system. These problems included the high number of back scattered and secondary electrons which are present in large industrial furnaces and the small fluctuations in beam focus and location caused by small (approximately $5~\mu m$) pressure changes in the furnace atmosphere. Development of the EDX system was suspended in 1990 in favor of a twin wavelength spectroscopy system being developed at Forschungsgesellschaft fur Elektronenstrahl und Plasmatechnik mbH (FEP), a former division of the Manfred Von Ardenne Institute in Dresden, Germany. The twin wavelength x-ray monitoring system (TXM) measures the intensity at two pre-selected wavelengths in the x-ray spectrum. One wavelength is a characteristic wavelength of the element of interest, such as Al or Cr, and the second wavelength is part of the background, or bremsstrahlung, radiation. The ratio of the intensity at these wavelengths can be correlated to the chemistry of the molten pool using a package of custom software. The system was described in more detail by N. Schiller in a paper at the 1991 Reno EB Conference. (7)

Axel Johnson Metals has joined with FEP and Bakish Materials Corporation to continue the development and installation of the first industrial TXM system. These three organizations have also executed a commercial agreement for the marketing and distribution of similar systems.

Condensate Control

The term "condensate" is usually given to all types of deposits which form on the internal walls and structures of the vacuum chamber in an EB furnace. The management of condensate has been an issue since the early days of electron beam melting.

Although often described by the same term, "condensate" really takes two primary morphologies. The first type is the classical form in which evaporating species leave the molten bath in the gaseous state and travel to cooler structures within the vacuum chamber where they condense to a solid coating.

The second type of deposit is not related to evaporation from the molten bath. This type of deposit would be more accurately described as "spatter" since it results from the ballistic transfer of small liquid and solid pieces of the raw material from the melt zone to the walls and overhead screen. This type of deposit is most commonly caused by the explosive release of trapped gases and chlorides from titanium sponge which has not been vacuum distilled.

Various strategies have been developed over the years for dealing with both true condensate and spatter. The most common and most successful strategies have been to provide an overhead screen and other similar places to collect and retain the deposits and to control the selection of raw materials charged into the furnace. Advances have been made in recent years in such areas as screen design and construction, the installation of vertical spray shields, and the usage of higher proportions of vacuum distilled sponge. These changes, while certainly helpful, have been gradual in nature. Efforts are now underway to identify and implement breakthrough technologies to provide a major improvement in condensate management. Techniques now being studied include dynamic removal of the deposits between ingots by thermal shock, vibration, and melting. Furnace operation at increased pressure (100 μ m) is being investigated to attempt to reduce evaporation along with carefully programmed electron beam energy distribution and liquid metal surface temperature monitoring. The interior geometry of the furnaces is being evaluated and modified to minimize the area of condensing surfaces close to the liquid metal including such developments as low profile hearth and mold configurations. Melting techniques are also being developed to continually recycle (reflux) spray deposits from sponge as they occur in the melt area.

Conclusion

Electron Beam Cold Hearth Refining has experienced substantial growth over the past four years in capacity, quality, and commercial acceptance. Many applications such as hollow ingot casting, improved scrap recycle techniques, and more efficient sponge melting are to be expected in the next four years.

References

- Entrekin, C.H. and Harker, H.R., "Recent Developments in Electron Beam Hearth Refining." <u>Proceedings of the Sixth World Conference on Titanium</u> (ed. P. Lacombe, R. Tricot, and G. Beranger), Les Editions de Physique, Paris (1988), pp. 615-619.
- Entrekin, C.H., "The Removal of High Density Inclusions by the Hearth Refining Process." Proceedings of the Conference Electron Beam Melting and Refining - State of the Art 1985 (ed. R. Bakish) Bakish Materials Corp., Englewood, NJ (1985), pp. 40-47.
- Koenig, R.J., et al., "Titanium Rotating Components Review Team Report," U.S. Federal Aviation Administration, Engine and Propeller Directorate (December 14, 1990).
- Chinnis, William R., "Plasma Cold Hearth Melting of Titanium in a Production Furnace." <u>Proceedings of the Conference Electron Beam Melting and Refining - State of the Art 1990</u> (ed. R. Bakish), Bakish Materials Corp., Englewood, NJ (1990), pp. 128-134.
- Tilmont, S.M. and Harker, H.R., "MaxiMelt Axel Johnson Metals' New Electron Beam Furnace." <u>Proceedings of the Conference Electron Beam Melting and Refining - State of the Art 1990</u> (ed. R. Bakish) Bakish Materials Corp., Englewood, NJ (1990) pp. 135-145.
- Harker, H.R. and Entrekin, C.H., "Cold Hearth Refining," <u>U.S. Patent No. Re</u> 32.932, May 30, 1989.
- Schiller, S. and Schiller N., "On-Line Compositional Control in Electron Beam Melting." <u>Proceedings of the Conference Electron Beam Melting and Refining -State of the Art 1991</u> (ed. R. Bakish) Bakish Materials Corp., Englewood, NJ (1991), pp. 67-74.

THERMAL MODELLING OF SOLIDIFICATION AND COOLING OF AN ELECTRON

BEAM MELTED TITANIUM INGOT

J.P. Bellot, A. Jardy and D. Ablitzer

Laboratoire de Science et Génie des Matériaux Métalliques URA CNRS 159 Ecole des Mines de Nancy, Parc de Saurupt, F-54042 Nancy Cedex - France

Abstract

Electron beam remelting ("drip melting" or "cold hearth refining") is a technique which is frequently used for the production of titanium alloys. In order to describe the thermal behaviour of the remelted ingot, a mathematical model has been used. The model, which involves a numerical solution of the heat transfer equation in the ingot during its growth, calculates the temperature distribution in the ingot, the profile of the melt pool, the overall heat balance and the weight losses due to evaporation of liquid metal, for all stages of the remelting operation. The results of melt simulations are presented and discussed. The effect of variations in the operating parameters (melting rate, gun power, beam focusing) is described.

Introduction

Over the last decade, the increasing demand for high purity ultra-clean titanium and titanium alloys has led to a growing interest in the electron beam remelting process (1). Two remelting processes, employing one or more electron guns, are in use today:

- the discontinuous "Drip Melting" technique, in which a primary ingot is melted by the electron beam(s), the resulting metal droplets forming a secondary ingot which solidifies in a water-cooled copper crucible,
- the continuous "Electron Beam Cold Hearth Refining (EBCHR)" process, involving a
 purification and inclusion separation stage in a cold hearth furnace before ingot
 formation.

The present paper treats this secondary ingot formation stage, which is common to both processes. Mathematical modelling represents a powerful tool for analyzing and optimizing the process, which involves numerous interdependent physical phenomena, and where an experimental approach is difficult, due to the high temperatures attained. The study carried out at the School of Mines in Nancy, which is presented here, is based on the development of a thermal model of the secondary ingot and its application to the remelting of titanium.

Titanium '92 Science and Technology Edited by F.H. Froes and I. Caplan The Minerals, Metals & Materials Society, 1993

Presentation of the model

The model, which draws strongly on the simulation of the consumable electrode vacuum arc remelting process recently developed in Nancy (2,3) and based on the pioneering work of Ballantyne and Mitchell (4), involves the numerical solution of the heat transfer equation in the ingot, with appropriate boundary conditions.

Assumptions

The geometry is axisymmetrical. This assumption reduces the problem to two spatial dimensions, r and z.

The ingot build-up during melting is simulated by adding a certain quantity of metal to the top of the ingot at time intervals determined by the rate of filling of the mould.

Heat balance equation

Taking into account the above assumptions, this equation is written:

$$\rho \operatorname{Cp}^* \frac{\partial T}{\partial t} = \frac{1}{r} \frac{\partial}{\partial r} \left(r \operatorname{F} \lambda \frac{\partial T}{\partial r} \right) + \frac{\partial}{\partial z} \left(\operatorname{F} \lambda \frac{\partial T}{\partial z} \right) \tag{1}$$

where T represents the temperature, t the time, ρ the density and λ the thermal conductivity.

The model takes account of turbulent movement in the liquid pool by multiplying the thermal conductivity by a factor F, equal to 1 in the solid ingot. The value of F in the liquid pool is an adjustable parameter in the model.

The dissipation of latent heat during solidification and the $\beta \to \alpha$ transition is taken into account by using an equivalent specific heat Cp*, the specific heat being increased by a fraction of the latent heat during the phase transformation.

Boundary condition at the ingot top

As far as boundary conditions are concerned, the main difference between this model and VAR modelling is the boundary condition at the top of the ingot. During E.B. remelting, heat transfer at the free surface of the melt pool is a complex phenomenon involving:

- the direct energy input from the electron beams,
- radiation from the free surface to the furnace walls,
- the heat of volatilization of the metal and impurities,
- the enthalpy supplied by the liquid droplets which feed the melt pool.

At the point of impact of the beam, the kinetic energy of the electrons is converted to heat energy, but the backscattered electrons are responsible for high losses, whose value, which depends on the metal bombarded and the angle of incidence of the beam, represents between 30 and 50 % of the incident energy in the case of titanium. The notation Peff will be used below to represent the effective thermal power supplied to the free surface.

The electron beam, which produces a spot of about one centimetre in diameter, sweeps the surface of the liquid metal, combining a rotational movement about the axis of symmetry with a radial movement perpendicular to the axis. During the passage of the beam, the temperature of the liquid rises sharply, then decreases again. Tripp and Mitchell (5) have shown that, for a sweeping frequency greater than 50 Hz, the thermal cycles become

sufficiently close together for the surface temperature to tend towards a quasi-stationary state. In order to take account in the model of the accuracy and flexibility of the electron gun control, the distribution of the heat energy imposed on the pool surface has been defined by the sum of two terms:

- a uniform flux density.
- a flux density with a Gaussian distribution curve, with standard deviation σ and centered on a radius r_c.

The contribution of each of these terms is determined by their ratio α . Thus, σ , r_c and α represent three degrees of freedom which have enabled the simulation of widely different thermal energy distributions. The energy flux density supplied by the electron beams can therefore be described in the form :

$$\phi_{EB}(r) = P_{eff}\left(\frac{\alpha}{\pi R^2} + (1 - \alpha) \frac{\exp\left(-\left(\frac{r - r_c}{\sigma}\right)^2/2\right)}{\int_0^R 2 \pi r \exp\left(-\left(\frac{r - r_c}{\sigma}\right)^2/2\right) dr}\right)$$
(2)

where R is the radius of the crucible.

The molten metal surface radiates to the furnace walls, whose mean temperature is equal to T_{fur} . The heat flux density dissipated by radiation at the free surface is therefore to a first approximation:

$$\varphi_{r} = \varepsilon \, \sigma' \, (T^{4} - T_{fur}^{4}) \tag{3}$$

where ε is the emissivity of the liquid metal and σ' is the Stefan-Boltzmann constant.

The presence of a high vacuum (of the order of 10^{-4} mm Hg) in the furnace enhances volatilization of the metal. According to Langmuir's law (6), the weight flux density of evaporated titanium J_{Ti} is thus expressed:

$$J_{Ti} = P^{o}_{Ti} \sqrt{\frac{M_{Ti}}{2 \pi R T}}$$
 (4)

where M_{Ti} represents the molecular weight of titanium, P^o_{Ti} its saturating vapour pressure at the surface temperature T and R is the perfect gas constant.

The heat flux density due to volatilization is thus given by:

$$\varphi_{v} = J_{T_{v}} L_{-} \tag{5}$$

where Ly is the enthalpy of evaporation of liquid mamili

Because of their low concentrations, the heat of the impurities makes a negligible contribution to the overall thermal balance fractly, as described above, the heat input associated with the addition of metal at the top of the largest is also taken into account.

The situation at the top of the ingot used in the model corresponds to a Neumann condition:

where ϕ represents the total energy flux density supplied to the free surface.

Numerical solution

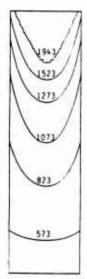
A finite volume numerical method was chosen to solve the heat equation in the time intervals between two additions of molten metal. In order to ensure good numerical stability, the alternating direction implicit (A.D.I.) procedure was employed. This numerical technique is based on the tridiagonal matrix solution algorithm. The mesh size employed is typically 20 x 100 nodes, with time increments of about 1 second.

Results obtained with the model

The model calculates the temperature distribution in the ingot at any instant during the remelting operation. The shape and volume of the melt pool are thus obtained from the "melting temperature" isotherm. Figure 1 shows an example of the temperature distribution in a titanium ingot at the end of melting, for the operating parameters given in table I.

Table I - Operating conditions for the reference melt

Crucible radius (m)	0.4
Melting rate (kg/h)	550
Total ingot weight (kg)	6200
Effective thermal power Peff (kW)	400
Fraction of power distributed uniformly a	1



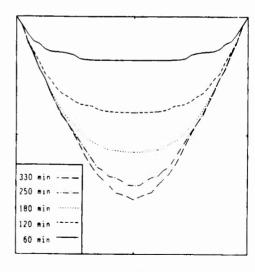


Figure 1 - Temperature distribution (K) in the ingot at the end of the reference melt.

Figure 2 - Shape and depth of the melt pool at different stages of the reference melt.

For this same melt, figure 2 shows the shape of the melt pool calculated at different stages. The depth and volume of the melt pool increase at the beginning of melting and attain a constant value corresponding to a quasi-stationary regime in the upper part of the ingot. In particular, the shape of the melt pool then remains unchanged. The large volume attained $(V = 0.13 \text{ m}^3)$ and the thermal gradients between the surface of the liquid metal (maximum temperature 2139 K) and the solidification front (melting temperature 1943 K) suggest that the natural thermal convection currents are strong and highly turbulent. The value of the multiplying factor F must therefore be high. For this simulation, it was taken to be F = 8.

The determination of the overall heat balance at any instant during melting makes it possible to compare the different thermal contributions, and to verify the internal coherency of the model. The diagram in figure 3 shows the energy balance calculated at the end of remelting, for the operating conditions given in table I.

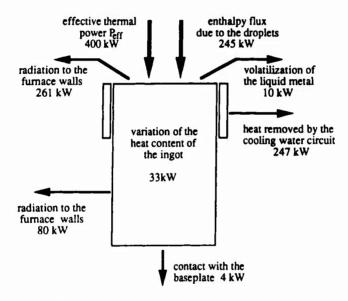


Figure 3 - Thermal balance of the ingot at the end of the reference melt.

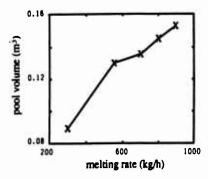
The model also enables calculation, at any stage of remelting, of the weight losses due to titanium evaporation, and thus of the total losses during the operation.

Application of the model

The model constitutes an efficient tool for analyzing the influence of the operating parameters on the thermal characteristics of the process. Different titanium remelting operations have been simulated, with separate variations in melting rate, gun power and incident energy distribution, compared to the reference test.

Figure 4 shows the variation of the final melt pool volume with the melting rate. When the melting rate increases, the heat contained in the liquid metal droplets cannot be dissipated sufficiently rapidly in the ingot, and the volume of the melt pool increases. These results are in agreement with the well established behaviour in vacuum arc remelting (2,4), where both numerical calculations and experimental observations reveal that the depth of the melt pool increases with melting rate. For a complete remelting operation (whose duration is inversely proportional to the melt rate), figure 5 shows that the titanium losses due to volatilization are

considerably increased at low melting speeds, requiring frequent recovery of the metal condensed on the furnace walls and on the E.B. gun protection shields.



200 600 1000 melting rate (kg/h)

Figure 4 - Influence of melting rate on the final melt pool volume.

Figure 5 - Influence of melting rate on the total titanium losses.

Raising the effective thermal power input at the top of the ingot markedly affects the degree of superheating in the liquid metal, and contributes to the increase both in the melt pool volume (figure 6) and the titanium losses due to volatilization (figure 7).

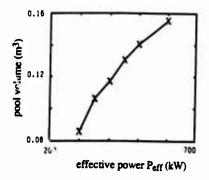


Figure 6 - Influence of the effective power on the Sinal melt pool volume.

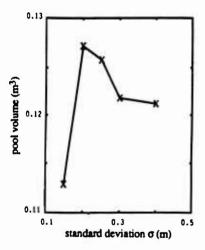
Figure 7 - Influence of the effective power on the total titanium losses.

The melting rate and the effective thermal power imposed on the ingot surface are two parameters which can be varied during an E.B. remelting operation. In order to reduce titanium losses by volatilization, the operator can work with both a high melting rate and a low thermal input at the ingot surface. By comparing two simulations, table II illustrates the extent to which metal losses can be reduced, without appreciably modifying the shape and depth of the melt pool. The independence of the two operating parameters, melting rate and heat input imposed at the liquid metal surface, represents a major advantage of the E.B. remelting process over the "competitor" VAR technique.

Table II - Reduction of titanium losses by adjustment of the operating conditions

Melting rate (kg/h)	P _{eff} (kW)	Maximum superheat (K)	Final melt pool volume (m ³)	Total melt duration (min)	Total losses (kg)
550	400	196	0.130	700	46.5
800	300	100	0.126	465	11.0

Figures 8 and 9 illustrate the effect of focusing the thermal power of the guns on the final melt pool volume and on the metal losses due to volatilization. When the power distribution is centered on the symmetry axis and strongly focused, the radiation from the metal surface and the cooling at the crucible walls lead to a drop in temperature at the periphery sufficient to form a broad ring of solidified metal, thus reducing the volume of the melt pool. The maximum temperatures attained at the center of the ingot are very high (superheat greater than 500 K for $\sigma = 0.15$ m), leading to heavy metal evaporation.



300 (200) See 200 (200) (20

Figure 8 - Influence of focusing the electron beams on the final melt pool volume.

$$(r_c = 0 \text{ m}, \alpha = 0)$$

Figure 9 - Influence of focusing the electron beams on the total titanium losses.

($r_c = 0 \text{ m. } \alpha = 0$)

Furthermore, for sufficiently low melt rates and specific localizations of the electron beam power, certain unusual temperature distributions and melt pool shapes can be obtained. Thus, when the power is focused on the edge of the molten metal surface, a "raft" of solid appears at the center of the melt pool (figure 10). According to Mitchell (7), a similar phenomenon has been observed in practice for appropriate gun procedures, and has been used to obtain ingots with a very fine grain structure.

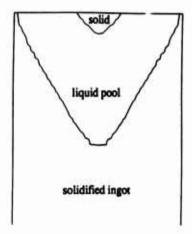


Figure 10 - Shape of the melt pool at the end of melting when the E.B. power is localized at the periphery.

Conclusions

A thermal model of the secondary ingot formation stage, common to both the Drip Melting and E.B.C.H.R. processes, has been developed at the Nancy School of Mines and used to simulate the remelting of titanium. Particular attention has been paid to the thermal conditions at the top of the ingot, taking into account the radiation from the free surface to the furnace walls and the heat of volatilization of the metal.

This mathematical model calculates the temperature distribution in the ingot at any instant during remelting, and consequently defines the shape and volume of the melt pool. It has been used to study the influence of the operating conditions on the melt pool volume and the metal losses due to volatilization.

References

- 1. R.Balish, "The State of the Art in Electron Beam Melting and Refining", <u>J. O. M.</u>, 1991, n° 5: 42-44.
- 2. L. Falk et al., "Thermal Modelling of Vacuum Arc Remelting of Titanium or Zirconium Alloys", <u>Mathematical Modelling of Materials Processing Operations</u>, eds. J. Szekely et al., (Warrendale, PA: The Metallurgical Society, 1987), 1041-1054.
- 3. A. Jardy, L. Falk and D. Ablitzer, "Energy Exchanges During Vacuum Arc Remelting", Ironmaking and Steelmaking, in print.
- 4. A.S. Ballantyne and A. Mitchell, "Modelling of Ingot Thermal Fields in Consumable Electrode Remelting Processes", Ironmaking and Steelmaking, 1977, n° 4: 222-239.
- 5. D. Tripp and A. Mitchell, "The Hot Spot Problem in EB Melting of Alloys", E.B.M.R. State of the Art 1987, ed. R. Bakish, (1987), 23-40.
- 6. I. Langmuir, "The Vapor Pressure of Metallic Tungsten", Phys. Rev., 2 (1913), 330-342.
- 7. A. Mitchell, (Communication made at E.B. Workshop, Tours, France, april 1991).

Investigation of Heat-Exchange in the Electrode-Tip of the

Non-Consumable Electrode Vacuum Arc Furnace for Melting Titanium

Klaus Rüdinger *), Karl-Erich Piper, Harald Schnecke **), Peter Schüler

Thyssen Edelstahlwerke AG Oberschlesienstraße 16 D-4150 Krefeld 1, Germany

Abstract

The water-cooled copper tip of the rotating non-consumable electrode of the vacuum arc remelt furnace is highly charged by temperature, which results in distortion of the tip shape and its internal water cooling system, followed by decreased service life.

During melting time the temperature gradient has been determined at different measuring points on the tip and its cooling water for different melting currents and for varied electrode positions. Test results show characteristic data for the melt history and point the way to process improvements.

Introduction

The melting technology by consumable electrode in vacuum arc furnace is mainly used for all kinds of melting titanium. That's why melting conditions like molten pool volume, distance from pool level to crucible edge and degassing conditions vary greatly. Input of small scrap for primary melting is limited.

Primary melting by using the non-consumable electrode vacuum arc melting process with continuous feeding of raw materials allows high scrap and chip feed rates. Combined with cold hearth melting a better control and dissolution of harmful contaminations is possible (1,2,3).

The non-consumable rotating electrode is moved over all areas of the molten pool during melting, whereby the water-cooled copper tip is in a continuous motion relative to the arc between the electrode and the molten pool. This allows the melting of continuously fed raw material. The electrode tip is a prominent part of the equipment. It is exposed to high temperature and distortion which greatly influence the service life.

- *) now University of Duisburg
- **) now Arnold Company, Kempen

Titanium '92 Science and Technology Edited by F.H. Froes and I. Caplan The Minerals, Metals & Materials Society, 1993 Objective of this investigation is to determine the correlation between melting condition, energy exchange and temperature influence on the tip of the non-consumable electrode.

Experimental procedure

The temperature distribution in the wall of the copper tips of the electrode has been measured by mostly four thermocouples which were fit in different distances from the tip surface located as shown in Figure 1.

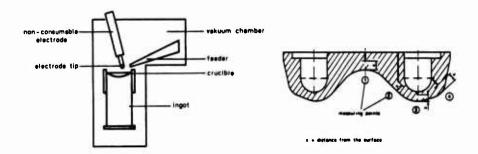


Figure 1: Schematical diagramm of the furnace and location of the measuring points in the electrode tip

The smallest possible distance between the single measuring point and the tip surface is 3 mm. The bundled thermocouple wires have been situated within the inner water tube over the whole length of the electrode up to a mercury collector, where the measured voltage is deducted from the rotacing electrode. This allows an undisturbed measurement of the temperature in the electrode tip during the whole melting time.

All signals are recorded by a process computer. The cyclus of measuring is between 2 and 600 s, providing information about short time processes, like the influence of electrode revolution on time-temperature profiles at each of the electrode tip thermocouple locations.

Investigations have been carried out on heats of c.p. titanium and titanium alloys, mainly Ti6Al4V. The ingot diameter varies between 500 and 750 mm, the ingot weight between 3000 and 6000 kg. The raw materials consists of sponge, alloying additions and feedstock scrap including chips.

Results and discussion

Time depending operation characteristics.

The melting current for a typical melt process during a melting time of about 6 h is shown in Figure 2.

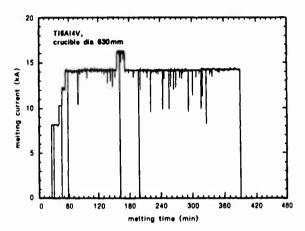


Figure 2: Melting current during melting time

At the beginning, the melting current is increased in several steps from 8 to 10, 12, 14 kA and after 2 h for a period of 15 min to 16 kA. Besides this, the diagram shows some interruptions of melting current only for some seconds, which mostly correspond to extremely high voltage fluxuations amplitudes as shown in Figure 3.

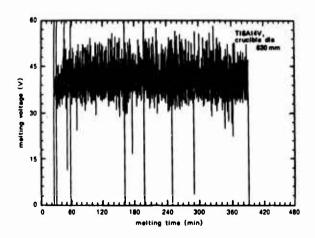


Figure 3: Melting voltage during melting time

The melting voltage is in a close correlation with the distance of the electrode from the molten pool surface. Figure 4 shows the superimposing influences of the permanent changing position of the electrode tip over the molten pool and the adapted distance to it which is automatically kept by the control system, operating in the voltage control mode.

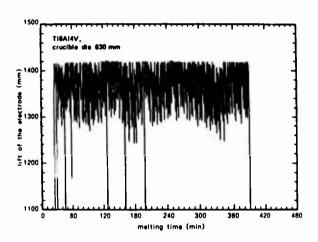


Figure 4: Lift of the electrode during melting time

The flow of cooling water in the electrode decreases about 1 % only during the melting-time and the temperature of the cooling water slightly varies. The temperature between incoming and outgoing cooling water of the electrode differs constantly at 4 $^{\circ}$ C.

The copper wall of the electrode tip however is much more influenced by variations of temperature. The absolute temperature depends very much on the distance of the measuring point from the tip surface as well as on its position within the tip. While the maximum value of the temperature in the tip center (Figure 1, measuring point 1) reaches 120 °C with a relative low spread (Figure 5), the temperature on top of the tip increases to 400 °C and even more (Figure 1, measuring point 3) with an extensive spread as shown in Figure 6.

When the melting starts and the amperage is increased step by step, the temperature in the tip rises, too. Short time interruption of melting current causes an immediate drop of the temperature in the electrode tip close to $20\,^{\circ}\mathrm{C}$.

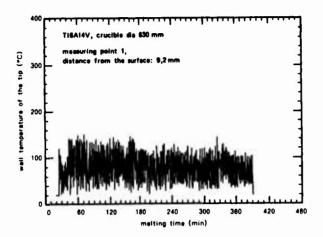


Figure 5: Wall temperature in electrode tip (measuring point 1) during melting time

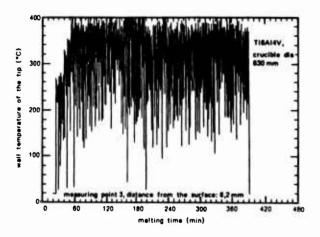


Figure 6: Wall temperature in the electrode tip (measuring point 3) during melting time

Correlation of electrical power and heat flow.

The simultaneous data logging of melting current and voltage permits calculation of the electrical power directly as their product. Much of the electrical power is transformed into heat of which an indication is found in the temperature level of the cooling water of the electrode. A higher melting rate increases the heat charge of the electrode and also the heat flow, which is led away by the cooling water as shown in Figure 7.

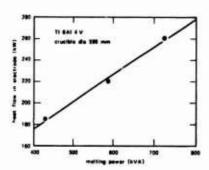


Figure 7: Heat flow in the electrode in as influenced by the melting power

Occurrences in the electrode tip.

The electrode tip is mechanically and thermal highly charged by the mostly unavoidable touching of the melting material which creates an attack of the tip surface. Even more destructive is the distortion of the electrode tip. It narrows the cooling water ducts, can cause cracks and limits its service life.

<u>Temperature gradient</u>. The measuring point 1 has been situated in the center of the tip, just below the inner water tube, where the cooling water streams out. The other measuring points, 2, 3 and 4, are situated in the area of the wandering source of the arc. Because of their short distance trom the molten pool surface they are subjected to extreme conditions. The flow rate of cooling water in this area is very high and the temperature changes rapidly.

For getting a better recorded short time information the course of temperature and the position of the electrode have been expanded and limited to 4 min only as shown in Figure 8.

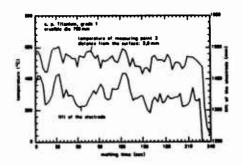


Figure 8: Course of wall temperature and lift of the electrode during melting time (measuring point 3)

It clearly shows the dependence of the course of temperature upon the electrode distance from the molten pool. If the arc is interrupted and the electrode pulls back, the wall temperature of the electrode tip will cool quickly by about 40°C. The rotation of the electrode doesn't induce a cyclic temperature variation as supposed. It is impossible to establish such an effect even by more stretching the recording, not even for the smallest possible distance of 3 mm between the measuring point and the tip surface.

The courses of temperature of measuring point 1 and 2 are similar to the measuring point 3, only the amplitudes are diminished. All test results of measuring point 4 are remarkable because of their reflected image to all other points. There are grounds for the assumption that this is caused by the wandering of the arc from the inner side to the outside of the pad of the electrode tip.

<u>Influence of electrode position and melting amperage</u>. Independent of measuring point and melting amperage there is a scattering of the various tip wall temperatures, which increase with increasing amperages between 8 and 16 kA as shown in figure 9 for a time range between 5 and 10 min. It shows the high alternating temperature loading of the tip.

If the continous electrode rotation is stopped for a few seconds, the temperature in the electrode tip will remain nearly constant.

The angularly mounted electrode directed assymetricly to the crucible doesn't influence the temperature in the electrode. The thermal strain of the electrode tip is nearly constant over the whole molten pool surface independent of the crucible diameter between 500 and 750 mm.

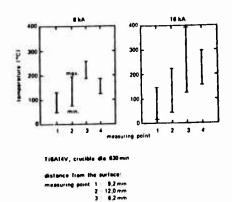


Figure 9: Influence of melting current on the wall temperature of the electrode tip

An essential reason for the permanent temperature variation in the electrode tip is probably the turbulent molten pool surface, which changes continuously when raw materials are charged. If the charged material is melted down and dissolved completely and the feeding of raw materials is interrupted, the measured temperatures in the electrode tip will be much more uniform even if the electrode moves.

On condition that the local course of temperature is quasi-stationary the temperature of the copper tip at its inner water cooled surface make infer an amount of 70 to 90. C by lineary extra polation. The outer surface reaches 500, 560 and 640. C at melting currents of 10, 14 and 16 kA. A further increase of melting current exceeding 16 kA should be avoided in view of the service life of the copper tip of the electrode.

Electrode cooling. Safe and effective cooling is important for a favourable service life of the electrode tip. There have been established several design changes to optimize the stream of water and the heat exchange at the tip. The buckling behaviour at the radiussed shape of the tip cannot be prevented completely. However, the internal water pressure can be slightly diminished and the stream of water can be increased.

Conclusion

The measured data show the correlation between electrical efficiency and heating stream as well as the influence of melting current on the temperature gradient in the tip of non-consumable electrode under different conditions.

Temperature measurements in the electrode tip show a higher thermal strain of the electrode tip with the increasing melting current. The temperature of the outer surface reaches 540. C when raising the melting current up to 16 kA. A further improved water cooling of the internal wall decreases its temperature only by 10 to $\frac{10}{2}$ C, which is nearly equal to the reduction of its outside temperature. A thinner wall of the tip could be more effective if its stability and secure life remained unchanged.

References

- M. Schlienger, Melting Systems for Production of Titanium Ingots and Castings, fitanium Science and Technology, Proceedings of the 5th Int. Coef. on Sitanium, Vol. 1 (Deutsche Geseilschaft Sir Metallkunde e.V., Oberaise), 1985, 15-35.
- K. Rüdinger, fitanschrott als Robstoff zum Schmeizen von fitan, Metall, 12 (1988), 177-180.
- k. Rudinger, K. F. Fiper and H. Schnecke, <u>Experience of Vacuum</u> Arc Notting with Non-Consumable and <u>Consumable Electrode</u>, Titanium Science and <u>Technology</u>, Proc. of the 5th Int. Conf. on Titanium, vol. 1 (Deutsche Gesellschaft für Metallkunde e.V., Oberursel, 1985), 115-121.

PRODUCTION TITAMIUM PLASKA COLD BEARTH MELTING

W.R. Chinnis W.H. Buttrill
Teledyne Allvac G.E. Aircraft Engines

ABSTRACT

Cold hearth melting is a technique now being used for production of titanium alloys. This method provides elimination of harmful inclusions that occasionally occur with conventional melting techniques. Several production titanium cold hearth furnaces are now operating, including a plasma cold hearth furnace at Teledyne Allvac. Defect seeding experiments have proven this furnace's capability to remove the two types of inclusions found in titanium alloys . Evaluation of plasma cold hearth plus single VAR has demonstrated chemical uniformity, structure, and mechanical properties equivalent to conventionally produced material. Control of as-plasma melted hydrogen content has been achieved with catalytic oxidation of hydrogen in the recycled gas An Air Force sponsored program is presently investigating cold hearth single melt titanium for premium grade applications.

INTRODUCTION

A significant problem of titanium alloys used in critical applications is the occasional occurrence of high density and hard alpha inclusions. Catastrophic jet engine failures have been directly attributed to the undetected presence of such defects in titanium components. Cold hearth melting is a technique designed to produce the highest quality titanium alloys free of these inclusions. A process consisting of cold hearth melting plus single vacuum arc remelting (VAR) is quickly gaining acceptance as superior to conventional double or triple VAR. In addition, an Air Force sponsored program is presently evaluating a cold hearth single melt process for premium quality titanium.

Cold hearth furnaces use either electron beam guns or plasma torches as the heat source. At least four producers are now cold hearth melting titanium alloys at various qualification stages. One of these producers, Teledyne

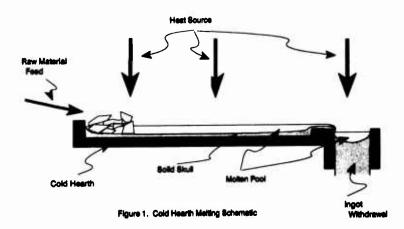
Titcnium '92 Science and Technicogy Edited by F.H. Froes and I. Caplan The Minerals, Metals & Materials Society, †993 Allvac, is operating a plasma cold hearth furnace and is supplying cold hearth plus single VAR for premium grade applications. Teledyne is also participating in the cold hearth single melt program.

This report describes plasma cold hearth melting in general, as well as specific evaluations and experience with the Teledyne Allvac furnace. Both the plasma cold hearth plus single VAR and the plasma cold hearth single melt processes are discussed.

DEFECTS AND COLD MEARTM MELTING

Two types of inclusions occur in titanium alloys: high density inclusions (HDIs) and type I hard alpha defects. HDIs are particles of significantly higher density than titanium; commonly molybdenum, tantalum, tungsten, and tungsten carbide, and are introduced through contamination of raw materials used for ingot production. Hard alpha defects are titanium particles or regions with high concentrations of the interstitial alpha stabilizers nitrogen, oxygen, or carbon. At least 28 potential sources of hard alpha defects in conventional melt processing have been identified. The most troublesome defects are high in nitrogen and result from titanium burning in air during raw material manufacture, handling, or melting. Due to the nature of conventional melting processes and limitations in inspection techniques, both high density inclusions and hard alpha defects can find their way into finished titanium components.

Cold hearth melting offers the ability to eliminate these inclusions. Raw materials are fed into one end of a water cooled copper hearth where they are melted (Figure 1). The molten metal is heated further as it flows across the hearth and is deposited in an ingot mold at the other end. Plasma torches or electron beam guns may be used as the heat source. A solid titanium skull forms between the liquid pool and the copper hearth. Any HDI fed in with the raw materials will sink to the bottom of the pool and become trapped in the skull. If a type I alpha defect fed in is denser than the liquid, it will be removed in a similar manner. If the defect is less dense, it will be carried along with the flow and must be dissolved before reaching the ingot. Pool superheat, pool volume, and melt rate are critical, therefore, as they directly affect this dissolution.



PLASMA COLD MEARTH MELTING

Multiple high powered transferred arc plasma torches are used as the heat source in several presently operating cold hearth furnaces. In the Teledyne Allvac furnace, four torches rated at 750 KW each are used. Helium, used as the plasma gas, is fed through each torch at a rate of 2,800 SLM. A nominally 3,000 amp arc is transferred from a water cooled copper anode contained within each torch to the material to be heated. The atmosphere used in the furnace is pure helium at a pressure of 830 torr. Energy distribution over the molten pools is accomplished by automated three axis motion of the plasma torches. The plasma gas is continuously recycled.

Selective losses of high vapor pressure alloy elements such as aluminum are virtually nonexistent in plasma furnaces of this type, leading to excellent chemical uniformity. Raw material flexibility is also good, with the ability to directly melt 100 percent titanium sponge, either acid leached or vacuum distilled, as well as any percentage of a wide range of revert types. Low evaporation losses, efficient feeding methods, and skull recycling give high raw material to ingot yields.

Ingots with diameters up to 760 mm and weights up to 7,700 kg are routinely produced in commercial plasma cold hearth furnaces. Vacuum locks are commonly used to permit multiple ingots to be cast without opening the furnace chamber.

PROCESS CONTROLS

Typical process monitoring and control is applied to plasma cold hearth furnaces. This includes establishing setpoints and/or limits for all significant measurable parameters, and continuously monitoring and recording these parameters for quality assurance. The typical parameters include voltage, amperage, gas flow, and movement pattern for each torch; ingot withdrawal position and rate; and furnace atmosphere oxygen, hydrogen, and water content.

Direct measurement of the critical parameters of pool temperature and volume is very desirable, but technically difficult to achieve. Considerable research in pool temperature measurement is being conducted both by cold hearth melters and titanium end users. Spot and imaging radiation pyrometry is being investigated in wavelength ranges from approximately 0.8 to 6.0 microns. The difficulties in applying this technique are many, and include unknown emissivity of liquid titanium and it alloys, attenuation of the radiation from dust in the furnace atmosphere and on the furnace windows, and extraneous radiation from the plasma plume. Partial or complete solutions to these problems are being found and preliminary results at Teledyne Allvac have shown the capability to measure hearth pool temperature with a reproducibility from the beginning to the end of a 16 hour heat of \pm 15 degrees(C).

Hearth pool surface dimensions are currently being measured on production furnaces. True pool volume would also require that pool depth be measured. A joint Department of Energy and industry consortium is presently being formed to investigate non-contacting laser acoustic molten metal depth sensing technology.²

SEEDED BEAT EXPERIMENTS

Demonstration of the claimed inclusion elimination capabilities of production cold hearth furnaces is important to gain industry acceptance of the process in general as well as application specific approvals of each furnace. The most accurate proof of this capability is to compare the frequency of inclusions in the product of the furnaces to that of conventional triple VAR. The frequency of hard alpha inclusions detected in triple VAR product is approximately 1.5 per 100 heats. Demonstrating a statistically significant improvement in a frequency this low requires the melting of a large number of heats. It is impractical for a melter to develop this kind of a database on a furnace before being able to supply product. An interim step is to use a seeded heat.

In a seeded heat, a large number of known inclusion sources are mixed with standard raw materials and melted. The resultant ingot is then processed to bar and evaluated to determine defect survival. A reasonable goal for such an experiment is a zero survival rate. The results can also be compared to similar experiments conducted in triple VAR. In one such trial with a full scale Ti-17 (Ti-5Al-2Sn-2Zr-4Mo-4Cr) heat, melted in 1983-1984, eight percent of nominally 0.25 inch diameter nitrided sponge seeds survived triple VAR. It is generally agreed that VAR provides very ineffective removal mechanisms for high density inclusions.

Several seeded heats have been produced in the Teledyne Allvac plasma cold hearth furnace. Table I gives the typical seeds and seeding densities of the raw materials used in these heats. The heats weighed approximately 4,000 pounds each. The inclusion sources were added to titanium sponge and alloy elements which were compacted and fed as in standard practice. After cold hearth melting (no VAR), the ingots were hot worked to bar less than two inches in diameter with at least 97 percent alpha-beta work (to ensure cracking of any hard alpha site). Ultrasonic and X-ray inspections of the bar were performed to detect surviving inclusions. The results of these seeded heats demonstrated zero survival of the inclusion sources.

Table I. Typical Inclusion Source Seeding of Experimental Heats

HARD ALPHA SOURCE	RATE	HDI SOURCE	RATE
Nitrided (8% N, 1/4") Nitrided (2% N, 1/4") Burned (1/4" - 1")	1/5 lbs 1/5 lbs 1/5 lbs 1/5 lbs 1/10 lbs	WC (-3/8" to +1/4") WC (-1/4" to +8 mesh) WC (-8 to +14 mesh) WC (-14 to +20 mesh) WC (-20 to +40 mesh) WC (-40 to +60 mesh) MO Wire (.04" by 1/4") HO Angular (1/4") Ta Angular (1/4") W Angular (1/4")	.74 lb .50 lb .30 lb .20 lb .16 lb .10 lb 1/20 lbs 1/100 lbs 1/10s

PLASMA COLD BEARTH PLUS SINGLE VAR PRODUCT EVALUATION

Chemical Uniformity

The chemical uniformity of the plasma cold hearth melted product is of great interest to confirm the lack of significant selective evaporation of the alloy elements and to demonstrate good general process control. Table II contains chemical uniformity information for four typical plasma plus single VAR ingots. These ingots, approximately 5,000 kg each, were processed to billet and checked for chemistry at three to five locations from surface to center at three to five equally spaced locations along their length. The average given in the table is that of the nine to twenty-five samples; the variability given is the difference between the highest and lowest values. No measurable evaporation loss is observed, which if present would appear most strongly in lowered and variable aluminum content. Overall chemical uniformity is comparable to that of conventionally produced ingots. Nitrogen and copper analysis showed no significant air or hearth contamination.

TABLE II. PLASMA + SINGLE VAR CHEMICAL UNIFORMITY

	A	1	v		r		0	
HEAT	AVG	VAR	AVG	VAR	AVG	VAR	AVG	VAR
AR89	6.35	0.33	4.06	0.22	0.22	0.06	0.18	0.0
AW54	6.42	0.16	4.08	0.27	0.17	0.07	0.18	0.00
AW55	6.36	0.21	4.05	0.22	0.17	0.07	0.17	0.0
AW57	6.37	0.20	4.06	0.35	0.16	0.06	0.17	0.0
Std. Prod.	6.34	0.18	4.04	0.23	0.19	0.06	0.17	0.0
Spec. Aim	€.30		4.20		0.15		0.17	

AVG - Average of samples

VAR - Variation, difference between highest and lowest of samples

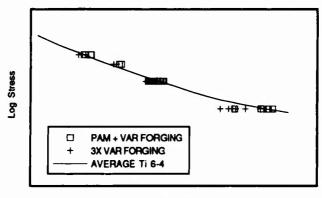
Billet and Bar Inspection

Over 150 heats and 700,000 kg of 660 and 760 mm diameter ingot have been produced in the Teledyne Allvac furnace to date. Billet and bar macrostructure, microstructure, and mechanical property evaluations of this material have shown equivalent results to material produced by conventional processing. No inclusions have been found during ultrasonic inspection of this material.

Part Forging Evaluation

The Wyman Gordon Co. recently conducted a forging evaluation of plasma cold hearth plus single VAR material.⁵ A commercial engine Ti-6Al-4V fan disk

configuration was chosen. The forging was produced from Teledyne Allvac billet using the same forging parameters as those previously used for triple VAR billet. Wyman Gordon's evaluation plan duplicated that required to qualify the part for new production. It included evaluations of chemistry, microstructure, tensile, fatigue (Figure 2), and fracture toughness properties. GEAE reviewed the data package and compared it to typical Ti-6Al-4V material, to the original qualification, and to the 50th and 200th cut-up evaluations of this part. The data in all cases except one was statistically indistinguishable. The only exception was fracture toughness; it was 34 MPa lower than average and is traceable to a near maximum oxygen content of this particular heat. All of the properties including fracture toughness met specification minimums.



Log Life

Figure 2. Ti-6Al-4V Low Cycle Fatigue (Room Temperature, Smooth Bar)

PLASMA COLD BEARTH SINGLE NELT DEVELOPMENT

The development issues associated with the introduction of an industry acceptable plasma cold hearth single melt (no VAR) can be grouped into three general categories: chemistry control, product integrity, and product yield.

Single Welt Chemistry Control

An original concern of "hearth only" processing was the degree of chemical homogeneity that could be achieved without subsequent VAR melting. Chemical variation of the first single melt Ti-17 heat produced at Teledyne Allvac was very low, demonstrating the capability to produce an acceptable chemical profile in a full scale heat. The heat weighed 2,300 kg and was 660 mm in diameter. The metallic elements were within 0.1% of target in each case with a standard deviation generally less than 0.05%.

Hydrogen control is also an important chemistry issue. Hydrogen is evolved in practically all titanium melting operations. This comes both from hydrogen in the raw materials and from reduction of residual water in the melt chamber and raw materials. In vacuum melting operations, the hydrogen partial pressure of the melt atmosphere is maintained very low by continuous pumping, and ingot levels of less than 20 ppm are readily obtained. In

plasma melting with a recycled plasma gas, the evolved hydrogen quickly builds up in the atmosphere and reaches equilibrium with the molten metal, at which point no more hydrogen is removed. To address this problem, Teledyne Allvac installed a catalytic reactor for removal of hydrogen from the recycled gas stream. Oxygen is mixed with the hydrogen bearing gas exiting the melt chamber and the mixture is passed over a catalyst bed where oxidation takes place. The resultant water vapor is removed in a molecular sieve dryer. A hydrogen excess is maintained in the reaction to prevent an oxygen breakthrough. Figure 3 shows the relationship obtained between the hydrogen content exiting the furnace and that of the resultant ingot. These results correlate closely with reported equilibrium data. 4 Ti-17 single melt heat had a hydrogen content of approximately 225 ppm at billet, without the use of the hydrogen removal system. The second such heat had an average of 80 ppm at billet with first generation operation of the system. Later heats have shown levels of less than 30 ppm to be achievable with appropriate controls.

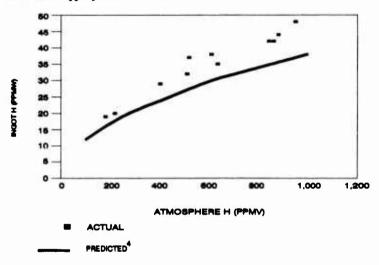


Figure 3. Plasma Cold Hearth Hydrogen Control

Single Nelt Product Integrity

Billet integrity may be adversely affected by the presence of inclusions or by the presence of clean voids which may or may not be gas filled. The effective elimination of inclusions in the Teledyne Allvac furnace has been demonstrated as discussed earlier. By elimination of the final VAR process, the potential introduction of inclusions during that process is eliminated. The occurrence of clean voids, although not widely observed, is still a concern. Since the plasma process takes place under one atmosphere of inert gas, it seems conceivable that a mechanically entrapped gas bubble could be formed at a solid/liquid/gas interface, such as can occur near the ingot edge. Since the solubility of helium in titanium is negligible, this is the only reasonable mechanism that has been proposed for forming such a gas filled void. Evacuated voids caused by solidification shrinkage are also possible and are probably more likely to occur than gas filled ones. Evacuated voids are generally not considered to be a problem as they tend

to heal during hot working.

A frequency of occurrence of clean voids in plasma cold hearth single melt material has not been measured because of the small amount of material produced to date. Further investigation will be required into this issue and adequate process controls will be established to avoid the potential problem.

Single Welt Product Yield

Yield in the single melt process is impacted by several factors. The surface condition of the ingots produced to date is not as good as that produced by VAR melting; however, much development remains to be done in this area. Improvements in both ingot structure and solidification pipe size have been observed in the single melt ingots and these should lead to significant yield improvements.

SUNCARY

Plasma cold hearth melting has the ability to produce high quality titanium alloys free of high density and type I hard alpha inclusions. In early 1990, Teledyne Alivac began operating a production scale furnace of this type. Initial melting has shown the furnace to be reliable and capable of melting a wide variety of raw materials. Evaluation of billet and bar product has shown good chemical uniformity, mechanical properties, microstructure and macrostructure and freedom from defects. Seeded heats have proven the furnace's ability to eliminate high density and type I hard alpha inclusions, a significant improvement over the best of the conventional processes, triple VAR. This furnace is now qualified to supply cold hearth plus single VAR for critical aerospace applications. Issues for introduction of plasma cold hearth single melt are currently being resolved.

REFERENCES

- Clifford E. Shamblen and Gordon B. Hunter, "Titanium Base Alloys Clean Melt Process Development," <u>Proceedings of the 1989 Vacuum Metallurgy Conference on the Melting and Processing of Specialty Materials</u> (Warrendale, PA: Iron and Steel Soc., Inc.), pp3-11
- "Cooperative Research and Development Agreement between EG&G Idaho, Inc. and General Electric Company," (EG&G Idaho, November 1991), Appendix 1 p1
- W.H. Buttrill, G.B. Hunter, and C.E. Shamblen, "Interim Technical Report No. 5," <u>Manufacturing Technology for Premium Quality Titanium Alloys for Gas Turbine Engine Rotating Components</u>, (Report R91AEB507, GE Aircraft Engines, 1991), p41
- V.A. Shapovalov et al., "Interaction of Hydrogen with Holten Titanium and Its Alloys," <u>Probl. Spets. Elektrometall.</u>, 1983, Vol. 19, pp59-62
- W.H. Everett, Wyman Gordon Co., letter report to W.H. Buttrill, GERE, 11/26/91
- M. Geibel, GEAE Materials Applications Engineering, letter report to W.H. Everett, Wyman Gordon Co., 12/17/91

ELECTROREFINING TITANIUM - THE PROCESS CAPABILITY

H W Rosenberg and J E Green The ALTA Group Fombell, Pa 16123

Abstract

Electrorefined titanium emerged as an item of commerce during the late 1980s. Pioneered by the U. S. Bureau of Mines station in Boulder City Nev. in the 1950s and 1960s, the titanium electrorefining process essentially remained a laboratory scale practice until 1985 when the ALTA Group was founded for the sole purpose of producing ultra-high purity titanium for electronic applications. Now, seven years and five design iterations later, the process capability is heading toward 99.999%, 5N, purity in total metallics and 4N purity in total gases. The current process capability is examined.

Introduction

A process for electrorefining titanium was pioneered in the 1950's and 1960's at the U S Bureau of Mines station in Boulder City Nevada. Electrolytic titanium was produced on the research scale until 1985 when The ALTA Group formed with the express purpose of producing high purity electrorefined titanium on a commercial scale. The first ALTA cell design was derived from first principles and immediately established new standards for metal purity and productivity.

Each cell design was a learning experience. The fifth design generation brought the original design concept to new highs in efficiency and quality. Along with that progress, the market has demanded higher and higher purities. ALTA's 1985 product was typically better than 99.995% pure on a metallic basis. The first electron beam melts using electrorefined crystal were completed in early 1986. Beginning in 1988, the second through fifth design iterations occurred in successive years. Product produced in 1988 was typically 99.997% pure in metallics. The original cells were abandoned in 1990. In 1990 ALTA also added electron beam melting capability inhouse. It became possible for the first time to institute an effective statistical process

Titanium '92 Science and Technology Edited by F.H. Froes and J. Caplan The Minerals, Metals & Materials Society, 1993 control program. What follows is an over view of the titanium ingot purity situation as it existed in 1990 - 1991. Process capability will be the common theme.

Process capability is the inherent reproducibility of a process in terms of some measurement or attribute. Process capability is commonly used to define a manufacturing processes in terms of their statistics. A process is said to be in control when its residual variance arises through random chance alone. No assignable causes that produce process variation are acting when a process is in control. Under these conditions it is possible to calculate meaningful process capability indices which may or may not be related to commercial specifications. Various indices have been developed that relate process capability for a process in control to commercial specifications for the product manufactured. Meeting a specification, however, is not the same thing as being in control. Few processes are always in control.

Residual process variation is often, but not always, normally distributed with Gaussian statistics. When the residual variation is non-normal, the standard errors from repeated sample lots will themselves, in the limit, tend to be normally distributed and be useful for Gaussian based statistical analyses. In many cases it is possible to find transformations that produce approximately normal distributions in small populations. Valid statistical treatments are possible.

Relating a specification to a process usually begins in terms of the mean and standard deviation of the process when it is in control. One common standard in the electronic industry requires that 99.7% of a measured product fall within specification limits. This is the familiar plus/minus three standard deviations from the mean standard. Two standard deviations may be used in less demanding situations. In the electronics industry, however, Motorola and others have taken the lead in driving toward quality standards where six standard deviations, or six sigma, is the goal. For a perspective, see how many handbooks of mathematics and statistics you can find that give values that far from the mean? At last report, Motorola had not achieved all of their goals but by shooting high they had achieved impressive gains with large and dramatic cost savings.

On another plane, in the electronic industry, semiconductor devices routinely require silicon and other materials having total impurities less one part per million or even less than one part per billion in the case of alpha emitters. And such purities have been available for quite some time in a number of materials. When counting atoms, five sigma is equivalent to about one-third impurity atom per million and six sigma is equivalent to about one impurity atom per billion.

Five sigma is not yet here for titanium, at least on a routine commercial basis. Only since 1985 has 4.5 sigma titanium (about 30 ppm total metallic impurities) been a commercial guarantee. Titanium with less than 10 ppm total metallic impurities, about 4.75 sigma, is now available commercially in limited quantities. That progress came through improved understanding of the underlying factors that include, physics (e.g. instrumentation and its use), chemistry (e.g. electromotive series for electrolysis) and human factors (e.g. developing and following effective standard operating and statistical process control procedures). With understanding, comes control. Improved process capability is the natural result.

This doesn't happen overnight. An appropriate string of metaphors might be, birth (seminal concepts and lab scale experience), growth (initial manufacturing scale experience) and maturity (implementation of SPC with well defined process

capabilities). Ultra-high purity titanium appears to be in late adolescence in such a sequence.

Fused salt electrolysis followed by electron beam melting is used to produce titanium ingot typically having about 10 - 15 ppm total metallic impurities with total gases of about 300 ppm or less. Issues encountered at The ALTA Group in defining overall process capability for ultra-high purity titanium are the subject of this paper.

Results and Discussion

Ingot Oxygen

Oxygen is the principal overall impurity in electrorefined titanium. Once a production run of electrorefined titanium crystal is harvested there is little more that can be done to reduce its oxygen content. The melting process most suited for preserving crystal purity is an electron beam. It is commonly used for just that reason. Since the vapor pressure of itanium monoxide is about the same as that for the metal (1 - 3), crystal oxygen going into electron beam melting should correlate closely with ingot oxygen out. It is this feature that forms one basis for Statistical Process Control, SPC, of ultrahigh purity ingot oxygen.

Ingot characterizations began as soon as electron beam melting began in-house. Twenty-nine heats were involved in this initial phase and two significant issues were encountered: 1) characterization problems related to crystal lot oxygen variability patterns and 2) control of contamination. These same issues attend sponge production but with different levels of criteria of course. With those issues coming under better control, it became possible to address process capability in terms of ingot oxygen. The next 42 production ingots were melted under SPC procedures designed to better predict final ingot oxygen. These were then compared with the original 29 heats.

The comparison involved least squares fits between the apparent oxygen averages for crystal being melted and the resulting average ingot oxygen levels. Results, assuming residual intrinsic variation can be represented by a normal distribution, are given in Table 1.

Ideally, and r^2 should equal 1.00 while the intercept and standard error of estimate should equal zero. The slope would ideally equal unity if electron beam melting neither subtracts nor adds oxygen under all conditions. Those perfect worlds do not exist. Nevertheless the initial results after SPC was implemented went a long way. Whereas before SPC the

Table 1	ECC . CODO	A 1 '1' D 1'		in Electronic Grade Ti
I anie i	HITECT OF SPECO	n Anility in Predic	t Indati iyyden i	IN HISCHMONIC LIPSON II

Series	N	Slope	Intercept	Std Error of Est	r ²
Before SPC	29	0.15	248	.29	0.009
After SPC	42	1.24	87	.08	0.850

"random variance" was 100%, it dropped to 16% (100 x (1 - r²)) afterwards. Before SPC the average ingot formulation estimate was low by 153 ppm oxygen. After SPC that difference dropped to 82 ppm. So SPC had an immediate positive effect on

process control. It became possible for the first time to produce commercial ingots to order at less than 200 ppm exygen.

The residual 15% and 82 ppm are now fair targets to go after. A clue as to direction resides in the raw data: the higher the aim the greater the miss due to random (uncontrolled) causes. Moreover since the low end of the distribution describing impurities must be zero, the data crowding zero bunch up naturally with results skewed to the high side. One might suppose that such behavior arises from the fact that impurities can only enter the process, not leave it. Such a distribution can only have only one tail - to the high side. In such cases, ingot oxygen data may be better treated as belonging to a log normal distribution (4) rather than to a normal one as was assumed for Table 1. It turns out that most metallic impurities in ingot also exhibit a log normal distribution when there is no known assignable cause acting.

Ingot Metallics

Process capabilities for impurities can be rendered in various ways. After logarithmic transformations most impurity distributions approximated normality. Process capability was determened on this basis. In the electronics industry it is common to use ±3 sigma about the mean in describing process capability. That was done here.

The results are summarized in Table 2 which constitutes a survey of process capability under the present state of the art. Three components are involved in that capability, 1) the science of winning high purity titanium from its ores, 2) the process engineering required to do so and finally 3) the human factors embodied in operating the process and creating an effective SPC strategy that the process operators themselves can employ to good effect. The latter is by no means easy. Considerable sophistication is involved and that does not come over night. Table 2 provides some necessary groundwork.

Data from 31 ingots were used to calculate the process statistics after transforming the raw data to their logarithms, calculating the statistics and taking exponents back to ppm. Only the more common impurities were included in the table because frequent detection limits in the data distort interpretations. Certain elements rise significantly above the background, notably Fe and Al. These metals are among the most common mineral forming elements in the earth's crust. They are everywhere in the ambient as dust. They are also common materials of construction. It turned out that Al and Fe each entered the process stream at various points. For a perspective, in a 454 kg ingot, one gram of impurity represents about two ppm. Table 2 represents process capabilities for a number of elements while saying nothing directly about the total metallics. As may be seen, the process capability is skewed with a long tail to the high side, possibly for the reasons discussed above.

In terms of total metallics, Table 3 presents the process statistics after transformation into and out of logarithms. The same data base and methodology was used as for Table 2. Table 3 is a fair representation of the present state of the art. As may be observed, about half of all ingots melted meet a total metallic purity of 99.9986%. The distribution for total metallics is skewed but the number of ingots lying in each interval fit a log normal distribution. Use of a log normal distribution appears to be justified.

Table 2 Process Capability by Element for Ultra-high Purity Titanium Produced by Electrolysis Followed by Electron Beam Melting.

Element	Mean - 3 SD ppm	Mean ppm	Mean +3 SD ppm
Al	0.33	1.3	4.7
Na	0.005	0.02	0.09
Si	0.16	0.52	1.8
K	0.01	0.02	0.03
V	0.12	0.4	1.4
Cr	0.08	0.4	1.7
Mn	0.003	0.02	0.7
Fe	1.5	5.57	20.0
Co	0.0003	0.005	0.1
Ni	0.004	0.04	0.16
Cu	0.19	0.71	2.8
As	0.004	0.03	0.18
Zr	0.5	0.87	1.4
Nb	0.2	0.5	1.1
Mo	0.06	0.14	0.32
Rh	0.002	0.09	0.01
Sn	0.06	0.4	2.5
Sb	0.009	0.08	0.74
Hf	0.008	0.02	0.046
Th	0.0001	0.0003	0.0007
U	0.0002	0.0003	0.0006
Н	1.2	3.2	8
С	9	20	44
N	3.5	10	33
0	94	222	418

Table 3 Process capability in terms of total metallics (56 elements) as calculated from a log normal distribution.

	ppm	% Purity
Mean + 3 SD	32.9	99.9967
Mean + 2 SD	24.7	99.9975
Mean + 1 SD	18.6	99.9981
Mean	14.0	99,9986
Mean - 1 SD	10.6	99,9989
Mean - 2 SD	7.9	99,9992
Mean - 3 SD	6.0	99.9994
Five Sigma	0.3	

The capability shown in Table 3 represents a three fold improvement over four years ago. Some of this improvement came about from procedural and equipment improvements but most of it came from operator training, improved standard operating procedures and the implementation of SPC on the shop floor. ALTA's new goal is another three fold improvement.

Epilog

The trend toward higher overall purity titanium for electronic applications is expected to continue at least into the next century. Further improvements are in progress and new ways of doing certain things may well be needed to meet the ever more stringent electronic materials specifications.

The process capability shown in Table 3 indicates that there is still a long way to go. It remains to bring total gas and metallic impurities to low values simultaneously.

Conclusions

Application of SPC technique is useful in ultra-high purity titanium manufacture.

Residual random errors attending impurity analyses in ingot are normalized by a logarithmic transformation.

About half of today's production of ultra-high purity titanium contains less than about 14 ppm total metallic impurities.

References

- P. W. Gillis, Interactions between gases and condensed phases, in *High Temperature A Tool For The Future*, Stanford Research Institute, Menlo Park Ca, 1956, pp 169 176.
- J. L. Margrave, "Equilibrium considerations for interaction of high temperature materials with their environment", in *High Temperature A Tool For The Future*, Stanford Research Institute, Menlo Park Ca, 1956, pp 87 106.
- 3 H. R. Smith et. al., J of Metals, Feb 1959, p 112
- 4 J. S. Oakland, "Statistical Process Control", Heinemann, London, 1986.

POTENTIALITIES OF ELECTROSLAG REMELTING AS APPLIED

FOR PRODUCTION OF HIGH-QUALITY TITANIUM INGOTS

Radchenko V.N., Tarlov O.V., Maksimov A.P., Dubinsky I.N. and Andrienko S.Yu.

Association of Scientific Instrument-Making and Technology of the Academy of Sciences of Ukraine, Kiev

Abstract

A technology for electroslag remelting of titanium is developed which permits using the active fluxes including metalslag ones, e.g. metallic calcium - calcium fluoride systems. A thermodynamic analysis of the interaction of titanium admixtures with these slag systems is performed. An attempt is made to evaluate behaviour of oxygen under electroslag remelting of titanium using metallic calcium - calcium fluoride flux. A procedure is suggested for calculation of the oxygen distribution by the height of the melted ESR ingot. Technological methods for electroslag remelting of titanium are developed. A conclusion is made that the produced titanium in many cases may be successfully used instead of iodide titanium.

Titanium '92 Science and Technology Edited by F.H. Froes and I. Caplan The Minerals, Metals & Materials Society, 1993 pevelopment of engineering and extension of the spheres of scientific research depend more and more on the use of pure metals and alloys. The existing industrial methods for their production are based on vacuum remelting processes (vacuum arc and electron-beam remelting) which in a number of cases do not provide a necessary purity of metals. At the same time such high-effective methods as iodide refining, distillation and others are characterized by low productivity and high cost \(\int 1, 2 \int 2 \).

Electroslag remelting (ESR) in the atmosphere of inert gas under highly deoxidized fluxes is an alternative to vacuum remelting. Study of ESR under active fluxes including calcium-containing ones has shown wide potentialities of this technological variant for production of top-quality ingots of reactive metals.

Metal-slag fluxes, particularly Ca-CaF₂ systems, provide effective refining of the remelted metals from impurities that possess a considerable thermodynamic affinity to the applied alkali-earth metals (oxygen, nitrogen, phosphorus, sulphur). Besides, intensive evaporation of metallic calcium from slag in the course of melting permits achieving rather low partial pressures of harmful gases (oxygen, nitrogen, hydrogen) in the melting cavity. For example, equilibrium partial oxygen pressure at the temperature of remelting is 10⁻²⁰ – 10⁻²⁵ atm. The latter circumstance allows a contamination-free remelting of titanium possessing high thermodynamic affinity to the above gases.

An attempt is made to evaluate behaviour of oxygen during ESR of titanium under flux of the metallic calcium - calcium fluoride system.

Dissolution of gaseous oxygen in titanium is described by the equations:

$$1/2 \{0_2\} = [0]\tau_i$$
 (I)

$$K_P = \gamma_0 [0]/P_{02}^{1/2}$$
 (2)

$$\Delta G = -RT \ln Kp \tag{3}$$

where γ_0 - coefficient of the oxygen activity; ΓOJ - fraction of total mass of oxygen in titanium, κ ; ρ_0 - partial

pressure of oxygen in the gas phase, MPa; ΔG - variation of the partial mole free energy of oxygen in titanium, kcal/mol.

Results of the experimental determination of AG in titanium-oxygen alloys presented in the work [3] have shown a dependence of AG on the oxygen content in titanium. It is connected with the fact that oxygen solution in titanium even in small concentration deviates considerably from the Henry law.

Since there is no reliable information on the values of the coefficient of oxygen activity in titanium let us introduce the notion of the effective constant of the reaction (I):

$$K'_{P} = K_{P}/\gamma_{0} = [0]/P_{02}^{1/2}$$
 (4)

then

$$\Delta G' = -RT \ln K_P' \tag{5}$$

A dependence presented in Fig.I is obtained on the basis of the experimental data from work [3]. Hyperbola approximation of table values at 2073 K is introduced for determination of the analytical dependence:

$$\Delta G' = -90960,928 - 1829,258/[0] \tag{6}$$

Interaction of oxygen in titanium with calcium dissolved in calcium fluoride is presented as a reaction:

$$\{\mathcal{L}_{\mathbf{a}}\} + [\mathcal{O}]_{\tau_i} = (\mathcal{L}_{\mathbf{a}}\mathcal{O}) \tag{7}$$

which may be obtained by the combination of two following reactions:

$$\{C_{\alpha}\} + \frac{1}{2}\{0\} = (C_{\alpha}0)$$
 (8)

$$1/2 \{0_2\} = [0]\tau_i$$
 (9)

Then

$$\Delta G_7 = \Delta G_8 - \Delta G_9 \tag{10}$$

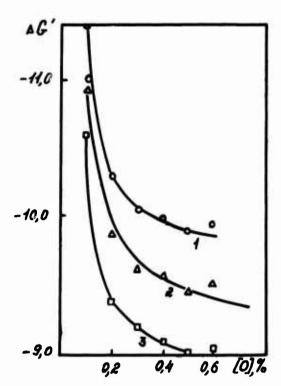


Figure I. Dependence of partial mole Gibbs energy (\(\times \) \(\t

With regard for the dependence (6) and the value aG_{2} = -93050 cal/mol [7] for T = 2073 derive:

$$\Delta G_{7}^{\prime} = -2089,072 + 1629,258 / [0]$$
 (II)

$$K_7' = exp(0.50717 - 0.444097/[0])$$
 (12)

For the reaction (7) write as

$$K_7' = \alpha_{(C_0O)}/(R_a LOI) \tag{13}$$

Since the content of calcium oxide in the slag is incon-

siderable then the expression (I3) may be simplified:

$$K_{r}' = \chi_{(C_{0}0)}/(R_{c_{0}}[0]) \tag{I4}$$

where $X(C_{00})$ - fraction of total mass of CaO in slag; P_{Ca} - pressure of calcium vapour, MPa.

Proceeding from the expressions (I2) and (I4) write as

$$exp(0.50717 - 0.44097/[0]) = X(ca0)/(Pca[0])$$
 (15)

$$P_{C_{\mathbf{a}}} = \alpha_{C_{\mathbf{a}}} P_{\mathbf{a}}^{C_{\mathbf{a}}} \tag{16}$$

where α_{Ca} - calcium activity in the melt $Ca-CaF_2$; $P_0^{Ca} = 53.651-12826,75/T + 0.002T - 14,485 eg T$ - vapour pressure over pure calcium, MPa.

Calcium activity in the slag is determined by the procedure presented in the work [5].

A portion (drop) of titanium of the weight m_{Me} (kg) containing $O_{initial}$ of oxygen, and slag of the weight m_{Σ} (kg) containing (Ca)_{initial},(CaO)_{initial},CaF₂ - the base) interact under electroslag remelting. Transition of a definite quantity of oxygen (Δ [O] %) from the metal drop into slag is described as follows:

$$[0] = [0] \quad \text{initial} \quad -4[0] \tag{17}$$

$$(Ca) = (Ca) initial - \Delta[0] (m_{me}/m_s) (Mco/Mo)$$
 (18)

$$(Ca0) = (Ca0) initial + 4[0] (mme/ms) (Mca0/Mo (19))$$

where \mathcal{M}_{Ca} , \mathcal{M}_{Cao} , \mathcal{M}_{o} - molecular mass of calcium, calcium oxide and oxygen, respectively.

Solving the equation (I5) by the iteration method with regard for the expressions (I7)-(I9) find equilibrium values $[0]_p$, $(C_0O)_p$, $(C_0O)_p$, a portion of metal with exygen concentration $[OJ_p]$ solidifies and does not participate in the reactions any more. A new portion of metal with [OJ] initial is introduced into the slag of composition $(Ca)_p$, $(CaO)_p$ and new equilibrium concentrations are considered. So, it is possible to determine the exygen content in the inget depending on the weight of the remelted metal. Calculations were perfor-

med on microcomputer by a special program which realizes the described algorithm.

Remelting of titanium with oxygen content 0.0I; 0.05; 0.2% is considered. The flux consists of a pure calcium fluoride; the content of calcium oxide in it is assumed as 0.1% which corresponds to the content of this admixture in the most pure flux. The content of calcium in the flux varies from 2.0 to 0.000001% (small values approaching zero). The results of the calculations are presented in Fig. 2.

Proceeding from the above calculations it is possible to conclude as follows: under electroslag remelting it is not possible to obtain the oxygen content in titanium lower than in the consumable electrode. In the case when the initial content of oxygen in the consumable electrodes is small (Fig.2 a,b) the content of oxygen in the metal at the beginning of heat sharply increases, especially when using flux without metallic calcium, then the oxygen content in the ingot falls to the values in the consumable electrodes. Apparently, it is attributed to reduction of the calcium oxide by titanium at the initial period and dissolution of oxygen in titanium. If the flux contains metallic calcium such processes proceed less intensive and restoration of the initial oxygen content is not so fast since in this case the reduction reaction of calcium oxide is retarded.

When the oxygen content in the consumable electrode is increased (Fig. 2 a) then in absence of metallic calcium in the flux the content of oxygen in the ingot remains initial.

If at the initial period of heat the metallic calcium is introduced into the flux then the oxygen content becomes lower and becomes equal to the content of oxygen in the consumable electrode. Apparently, it is connected with the following fact - when the heat starts calcium interacts with titanium oxygen and the more is the flux saturated with the product of the reaction (calcium oxide) the more it hampers the reaction.

Electroslag remelting of titanium has been performed in the mould of 60-I20 mm in dia., ingots of I00-250 mm in height have been produced. Electrodes have been melted from iodide titanium or produced by compaction of the titanium sponge ($T\Gamma$ - 90 and $T\Gamma$ -I20 grades).

Oxygen content in the consumable electrodes has amounted

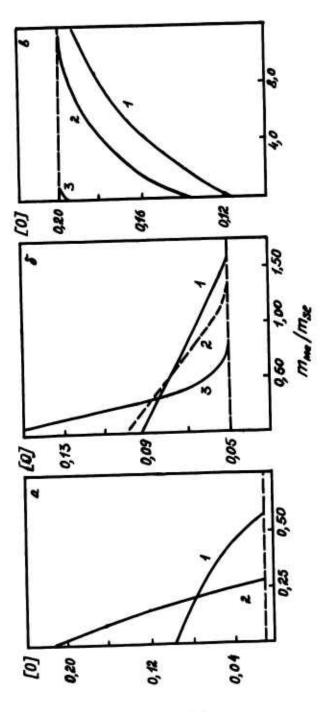


Figure 2. Dependence of the oxygen content in titanium on the relative weight of the melted metal with the oxygen content in the electrode, %: a - 0.01.
0,05, - 0.2 (1-2, 2-1, 3-1 10-5 % (Ga)).

to (%) 0.02 in iodide titanium, 0.04 - in titanium sponge $T\Gamma$ -90 and 0.06 - in titanium sponge $T\Gamma$ -I20.

The oxygen content in the ESR metal in its stable level (start zone being excluded) remains equal to its content in the initial metal. The content of harmful impurities by the height of the ESR ingot of 60 mm in dia. and I50 mm in height remelted from titanium sponge T? -I20 is presented in the table:

Sites of sampling	Fractio	n of tota	l mass	(%)
	H	C	N	0
Top	0.003	0.01	0.005	0.06
Middle	0.004	0.01	0.005	0.06
Bottom	0.005	0.01	0.008	0.08

References

- I. E.M.Savitsky, G.S.Burkhanov, K.B.Povarova et al. Refractory Metals and Alloys (Moscow, Metallurgiya Publishers, 1986) 352.
- V.A.Garmata, B.S.Gulyanitsky, V.Yu.Kramnik et al. Metallurgy of Titanium (Moscow, Metallurgiya Publishers, 1968) 643.
- Reznichenko V.A. and Khalimov F.B. Change of Free Energy in Ti-O System by EDS Method. Processes of Production of Titanium and Its Oxides (Moscow, Nauka Publishers, 1972) 193-197.
- 4. O.I.Kubashevsky and S.B.Olkhov. Metallurgical Thermochemistry. (Moscow, Metallurgiya Publishers, 1982), 290.
- 5. S.V.Terekhov, O.V.Tarlov, V.N.Radchenko et al. "Activity of Components in Slag Systems CaO-CaF₂; Al₂O₃-CaF₂. Ca-CaF₂" Problemy Spetselektrometallurgii 4 (1987), 10-12.

DEVELOPING A NEW CONTINUOUS PROCESS FOR MAKING TITANIUM

René Winand, André Fontana, Luc Segers and Philippe Vernin Université Libre de Bruxelles, Department Metallurgy-Electrochemistry 50 avenue F.D. Roosevelt - B-1050 Brussels - Belgium

Clément Rome, Philippe Dassargues, Bruno Leurquin Cockerill Sambre - 14 Quai d'Ougnée - B-4102 Ougrée - Belgium

ABSTRACT

R. Winand invented a new process to prepare titanium ingot in one step from sodium and titanium tetrachloride. Making use of the two reagents in the gaseous phase and recovering titanium as a liquid on top of a continuous casting mould, sodium chloride is also gaseous, so that titanium is the only condensed material. This process has the following features: it is continuous; the number of intermediate stages are dramatically decreased compared to the Kroll or the Hunter processes; the manpower and the metal inventory are much lower, the energy consumption is decreased while only small amounts of reagents are involved in the reaction at any time so that hazard problems are highly reduced, the metal recovered as an ingot is very pure while the metal not included in the ingot can be sold as a powder, it could also be used to prepare titanium alloys in ingots, or powders of pure titanium or of alloyed titanium including intermetallic compounds. The research started ten years ago at laboratory scale. Since 1987, a pilot capable of 25 kg titanium per hour is operated in the hall for testing prototypes of the Centre de Recherches Industrielles of the Université Libre de Bruxelles. So far, sodium and titanium tetrachloride handling and gas production are under control, giving stable and reproducible constant gas flows. Sodium chloride condensation is also satisfactory. The reaction occurs at high speed and gives the expected high temperatures. However, as it was thought that the heat of reaction is high enough to heat up the reaction chamber, no preheating system was provided. After trying a number of injectors, and also after mathematical modelling, it was shown that preheating is absolutely necessary, otherwise the transient lasts long enough for the reaction chamber to be clogged with partially molten reaction products. Further research including electric resistance preheating showed this method to be unefficient. Despite of that, reactions lasting for two hours were performed, but titanium was recovered as conglomerates of particles instead of a molten pool. Future experiments should make use of other preheating systems.

INTRODUCTION

Owing to its exceptional properties and to the availability of suitable ores, titanium should undergo a wide market expansion. This was not the case so far because the price of the metal is still too high to make it competitive against other materials like for instance stainless steel. Accordingly, except in countries where an industrial strategy for titanium development exists, the uses of this metal and its alloys are restricted mainly to aeronautics, aerospace and chemical industry applications. In fact, there is a need for a new industrial process for making titanium, able to reduce markedly the base metal cost. The Kroll and Hunter processes used today are based on the discontinuous metallothermic reduction of titanium tetrachloride either in one step by magnesium or in two steps by sodium. Despite improvements described in literature [1-3], they involve many operations before getting an ingot suitable for further processing. Attempts to develop alternative processes were up to now largely unsuccessful.

Science and Technology Edited by F.H. Froes and I. Caplan The Minerals, Metals & Materials Society, 1993 This paper is describing the present status of a research aimed at developing a new continuous process [4] for making titanium ingots in one step.

BASIC IDEAS

The general principle of the process is to react, in one step and at atmospheric pressure, gaseous sodium with gaseous titanium tetrachloride. Adiabatic reaction temperature is easily in the range of 2 200-2 400 K, so that the products of the reaction are gaseous sodium chloride and liquid titanium. As titanium is the only condensed constituant, the pure metal should be recovered directly as an ingot (the DITINGOT Process).

Such a process, if successful, has many advantages versus those in use today, mainly because it is continuous and avoids making sponge or powder contaminated with salts as an intermediate. Figure 1 makes this very clear in a synthetic bloc diagram. A Cockerill Sambre industrial evaluation team came to the conclusion that advantages of this new process could be described as follows: The process is continuous, avoids the sponge and the associated operations, and is susceptible of full automation.

Accordingly, the plant can be very compact, reducing investment by a factor of at least two. Energy consumption can also be reduced by at least one third. The processing time and the metal inventory can be drastically reduced by at least 20. The manpower can also be reduced by at least 3. More best quality metal can be produced because no iron contamination can occur in the reactor, and no nitrogen or hydrogen contamination can occur before the ingot solidification due to suppression of any operation on high specific area intermediates, no carbon contamination can occur coming from any vacuum pumping system. Working conditions and environmental protection are also improved because very small amount of reactants are present in the reaction circuit at any time, manual operations during the process are drastically reduced and no handling nor physical treatment of sponge is necessary. All these advantages were due to reduce operating costs by at least twenty percent against conventional processes in use today. The process theoretical feasability was determined on the basis of thermodynamic calculations. Figure 2 shows the results for adiabatic conditions when sodium and TiCl4 are introduced in the reactor at their boiling temperature, as gases. The metallurgical efficiency increases when the percentage of excess sodium increases. Temperature passes however through a maximum, at about 2 400 K, and 25 percent excess sodium. At that point, the metallurgical efficiency is of approximately 91 percent. In practice, some heat loss should be considered in the reaction zone. Further calculations were made for a reactor capable of 25 kg titanium per hour, supposing various heat loss levels in the reactor. Figures 3 and 4 show the favourable influence of such losses (expressed in kW) on the metallurgical efficiency, the reaction temperature remaining well above the titanium melting point. Theoretical optimum conditions could be operating with 10 to 15 percent excess sodium and a reactor heat loss of 20 to 25 kW (for 25 kg Ti/h), resulting in a metallurgical efficiency better than 95 % in the reactor, the rest of titanium being recovered outside, at a lower temperature, as a powder by product. Figure 5 gives an idealized sketch of the process, while figure 6 gives some important figures concerning material balance and power consumption for a 25 kg Ti/h prototype.

EXPERIMENTAL

Small scale laboratory experiments started in 1975 in the Université Libre de Bruxelles (ULB) by Winand, Fontana and Segers, without external funding. Initially, extra heat was provided to the reaction by a d.c. plasma torch but was found deleterious to the metallurgical efficiency in the reactor: argon was diluting the reaction gases, favouring the backward reaction. Further experiments made only use of some external resistance heating. At the end of 1979, a large belgian steel company - Cockerill S.A. - became interested in the project. The initial patent property was transferred to this company and the research went on in the frame of a contract between Université Libre de Bruxelles, Cockerill and IRSIA, a Belgian governmental sponsoring organization. In mid-1980, a new laboratory scale experimental set up was started, capable of 1.5 kg Ti/h. It was possible to feed a reactor with sodium and titanium tetrachloride in gaseous state, to reach the reaction temperature in a very short time, and to produce titanium metal, but it was impossible to achieve thermal autonomy at that scale.

Therefore, it was decided to build a bigger installation able to produce 25 kg Ti/h in the hall for testing prototype of the Centre de Recherches Industrielles (CRI) de l'Université Libre de Bruxelles, at Nivelles, situated at approximately 25 km from Brussels. The experiments started in February 1987, in the form of a research contract between Cockerill Sambre S.A.-ULB and Région Wallonne, the Southern part of Belgium. This last equipment only and some of its experimental results will be described.

The equipment

Feed circuits

Except for sodium special purification problems, sodium and titanium tetrachloride feed circuits were identical. A first part was devoted to loading the reactants to the circuit by either pumping liquid TiCl4 under argon or by manual transfer of sodium ingots. Sodium was melted under argon and transferred through a stainless steel filter to a second vessel. The second part of the feed circuits was a waiting loop where the liquid reactant was kept moving at the approximate flow rate necessary for the reaction. The third part of the feed circuits was made of Inconel 600 evaporator coils included in electric resistance furnaces and of heated transfer lines to the reactor. The third one was fed by opening the waiting loops to start the reaction. TiCl4 was heated up to 400° C and sodium up to 950° C.

Reactor

The reactor was a watercooled vessel with a large lateral opening leading to the salt recovery circuit. The reaction zone included the burner on which the injector was fitted, and a fix-crucible placed to recover titanium. The internal wall of the burner was made of silicon carbide, eventually preheated by electric resistance. After a layer of heat insulator, a sodium cooled coil was inserted in order to maintain the overall shape of the burner during the reaction. The external walls of the burner were made of three titanium sheets placed at three different diameters. Seven different injectors were tried. Each of them provided TiCl4 injection in the center and sodium at the exterior in order to prevent any unreacted TiCl4 from escaping the reaction zone. The fix crucible was made of alumina eventually preheated by electric resistance. It was likely to be replaced by a continuous casting system. A loose cyclindrical metal sheet, which acted as molten salt condensor, was placed inside the vessel, surrounding the burner and the crucible. Molten salt was recovered at its bottom in a large metal crucible.

Salt circuit

At the reactor outlet, a special salt condensor, fitted with metal plates was foreseen. It was followed by three cyclones in series leading finally to a scrubber. This salt circuit proved to be useless because all the salts and the excess sodium were condensed on the loose cylinder inside the reactor during the two hours experiments.

Control room

This room was containing a centralized command pulpit with a synoptic table showing the state of all the valves, pumps and levels of the reactants in their vessels. A centralized data logging system was able to handle more than two hundred measures on a P.C. Twenty measurements were carried out simultaneously and independently of the P.C. allowing permanent visual control.

Safety

The sodium and the titanium tetrachloride vapor feeding circuits were placed in separate small buildings inside the prototype testing hall. The bottom of the sodium building was provided with Graphex Ck 23, while the TiCl4 building was closed and connected to a vertical scrubber placed outside the hall.

EXPERIMENTS

Only the experiments (in total 24) performed with the 25 kg Ti/h equipment will be shortly described.

Experiments without preheating

It was thought initially that preheating of the reaction zone was not necessary, because of the reaction's very high exothermicity. Moreover, as the reactants were introduced as vapors, ignition occured from itself. The burner internal shape was fixed after experiments making use intentionally of too long burners: it was shown that the maximum temperature was reached at a 30 cm distance from the injector nozzle. A narrowed section had to be introduced in the sodium vapor tube to increase the pressure drop and avoiding flow oscillations. The main achievements of these experiments were that sodium and titanium tetrachloride could be securely fed as vapors to the injector in a constant, controllable and reproducible way; that temperatures as high as 2 000 Celcius were effectively obtained in the burner; that large amounts of titanium were recovered in the crucible and in the burner; that no lower valency titanium chlorides were observed and that sodium chloride was mainly condensed on the loose cylinder in the reactor itself.

However, titanium in the crucible was mainly recovered as fine particles with diameters in the range of 2 to 10 micrometers. The inside of the burner itself proved to be clogged in a very short time (ten to fifteen minutes) by sodium chloride and titanium metal conglomerates who changed the burner internal shape and finally the whole reactor zone.

The same results were observed with swirling coaxial and with toroïdal burners.

Experiments with preheating

The first preheating was done by means of an electrical resistance placed like a candle inside the reactor zone and by introducing an electric resistance in the alumina refractory material in the crucible. The maximal temperatures achieved by this method were 800° C in the burner and 1 100° C in the crucible. This proved to be ineffective, so a Kanthal electrical resistance mantel was placed inside the burner walls, behind the silicon carbide.

This allowed preheating of the burner up to 1 100° C. The injector itself was preheated up to 750° C. The experiments performed with this preheating system showed that a maximum temperature of 1 350 to 1 400° C was reached on the external (opposite to the reactor zone) surface of the silicon carbide wall (after 15 to 30 minutes). A tantalum heating mantel was tried, in order to increase the preheating temperature, but it proved unpredictable: it broke usually before the experiment started. In all experiments, the inside of the burner was clogged like in experiments made without preheating, with, however, less sodium chloride in the titanium shapes recovered (see figures 8 to 10).

Concerning titanium recovery, the best results obtained were in the burner, with layers of pure and partially molten titanium and in the crucible, with partly molten titanium particles of about 10 micrometers diameter. The salt condensed on the loose metal sheet in the reactor was mainly sodium chloride and excess sodium but contained approximately half the titanium metal produced as fine powder (2 to 10 micrometers). The metal efficiency in the reaction zone was in the range of 40 to 45 % but not gathered in a satisfactory molten pool. Supplementary experiments were carried out. One of them was made without sodium cooling the burner. The experiment was shortened in order to avoid destroying the burner. However, a maximum temperature of 1 350 Celcius was again observed after 15 minutes. After the experiment, a central egg of pure titanium and layers of titanium were found in the burner. Another experiment was carried out without burner walls, with only the injector and the crucible inside the reactor vessel. Making use of an infrared camera and of an ignition wire, it could be shown that the flame went back from the wire to the injector nozzle, showing the reaction rapidness.

MATHEMATICAL AND PHYSICAL MODELLING

A computer thermal model of the burner was made by BELSIM. On the basis of the measured temperature initial increase, the model showed that a transient time of two hours would be necessary to reach the titanium melting point on burner walls, even if these walls are preheated to 1 100° C. This was due to the sodium cooling, considered as necessary to keep the geometry of the reaction zone. A physical model of the burner and of various injectors was tested at the Von Karman Institute. The vapor mixing proved to be very satisfactory, and can not be considered as a limiting factor. Further mathematical modelling of the reaction was made by Professor J. SZEKELY at MIT. It allowed to determine velocities, temperatures and concentrations in the burner of various injector types. It was shown that the reaction is almost finished when the gases leave the burner, but that the temperature profile is very sensitive to the walls temperature (figure 11).

CONCLUSIONS

The 25 kg Ti/h experimental set up was used for 24 runs lasting up to 2 hours. Some of them rated 35 kg Ti/h for 1 1/2 hour.

It proved satisfactory from the following stand points:

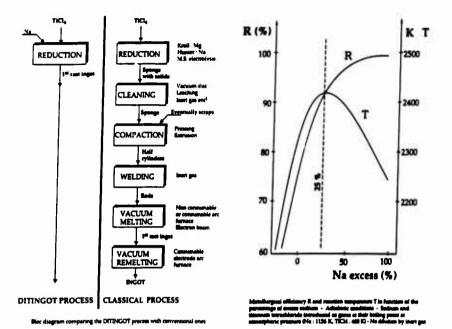
- storage and purification of reactants
- measure and control of reactant flows
- evaporators and injection in the burner
- geometric stability of the burner
- condensation of molten sodium chloride out of the reaction zone

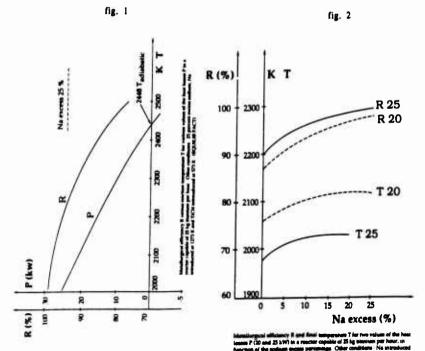
Problems that are still to be solved:

- a satisfactory preheating system to overcome the transient period at the beginning of the reaction to avoid the burner clogging. A temperature higher than the titanium melting point must be reached in the burner. Induction heating seems the most promising, but a plasma torch should also be considered.
- increase the diameter of titanium particles to keep them in the crucible. This point can not be studied if the previous one is not solved.
- realize the continuous casting of titanium.

REFERENCES

- 1- National Materials Advisory Board Report n° 304 Direct reduction processes for the production of titanium metal National Academy of Sciences National Academy of Engineering Washington D.C. (March 1974)
- 2- T. Ikeshima Recent developments in titanium sponge production Proc. 5th Inter. Conf. on Titanium Munich Sept. 10-14 (1984) Ed. : G. Lutjering, U. Zwicker and W. Bunk Deutsche Gesellschaft für Metallkunde Oberursel Germany Tome I, p. 3-14
- 3- T. Tanaka New development in titanium elaboration-sponge, melting and casting Proc. 6th World Conf. on Titanium Cannes June 6-9 (1988) Ed. : P. Lacombe, P. Tricot and G. Beranger Soc. Francaise de Métallurgie Les Editions de Physique France Tome I, p. 11-22
- 4- R. Winand Belgian Pat. 884.108 (31-07-1980); Austrian Pat. 374.502 (15-09-1983); Brazilian Pat. PI 800.4185 (31-05-1988); Canadian Pat. 1.153.210 (06-09-1983); Switzerland Pat. 648.062 (28-02-1985); German Pat. 3.024.697 (18-01-1990); French Pat. 2.461.014 (10-03-1986); British Pat. 2.057.016 (18-01-1984); Italian Pat. 1.131.902 (25-06-1986); Japan Pat. 1.354.037 (24-12-1986); Luxemburg Pat. 82.561 (20-01-1982); Norwegain Pat. 156-495 (30-09-1987); USSR Pat. 1.331-435 (15-08-1987); US Pat. 4.830.665 (16-05-1989)





2,390

fig. 4

fig. 3

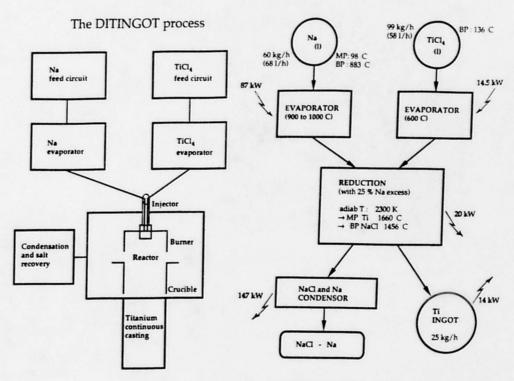
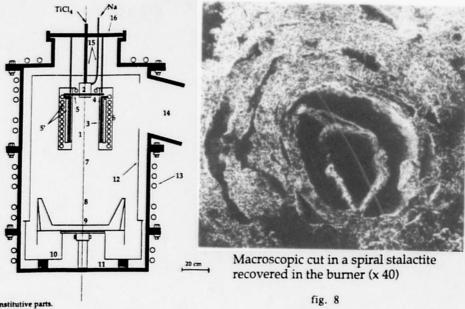


fig. 5 Idealized sketch of the process

fig. 6 Approximate material balance and power consumption for a 25 kg Ti/h prototype.



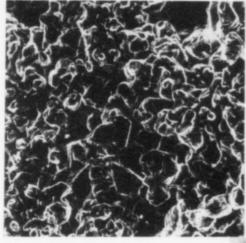
Reactor constitutive parts.

- 1. Inside part of the burner

- 1. Inside part of the burner
 2. Injector
 3. Internal wall of the burner (SiC)
 4. Dead angle of the burner
 5. Upper wall of the burner
 5. Insulation and sodium cooling circuit
 6. Burner external coil
 7. Burner to crucible free space
 8, 9. Upper level and bottom of crucible

- 10. Salt container
 11. Bottom of the reactor
 12. Loose metal sheet
 13. Reactor water cooling coil
 14. Evacuation funnel to condensor
 15. Reactants inlets
 16. Reactor cover

fig. 7

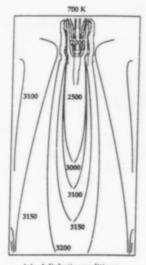


Microscopic cut in a spiral stalactite recovered in the burner (x 200)

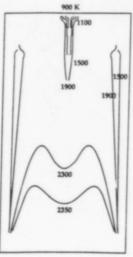
fig. 9



fig. 10 Partly molten and agglomerated titanium particles recovered in the crucible (x3500)



(a) Adiabatic conditions



(b) Walls at 1400 K

fig. 11 Isotherms inside the burner according to mathematical modelling (SZEKELY)

INDUCTION SLAG PROCESS FOR PRODUCING TITANIUM

BY REDUCTION OF CALCIUM FLUOROTITANATE

G. T. Fisher II and D. E. Traut

Albany Research Center, U.S. Bureau of Mines U.S. Department of the Interior 1450 Queen Avenue, SW Albany, Oregon 97321-2198

Abstract

As part of a U.S. Bureau of Mines program to develop a more continuous TI metal process that uses domestic resources, a study was made of the reduction of CaTiF₆ to TI metal using Ca as reductant. Two-stage batch reduction tests carried out at 30-kW power in an induction slag tatch furnace show reaction initiation and completion within 5 min. Techniques were devised to feed this reacted product into an induction slag ingot furnace to produce a TI ingot with 94 pct TI recovery and to separate the TI from the byproduct CaF₂ slag. The latter technique also was applied to investigate a single-step reduction test in which CaTiF₆ and Ca reactants were fed to the ingot furnace to produce TI ingot directly.

Introduction

A process to manufacture pure Ti that would use lower grade, less costly, and more available domestic raw materials, such as limenite (FeTiO₃), has long been sought. A process that is continuous, thus less costly, and uses fewer, simpler process steps would be of great advantage. Early attempts to obtain such an ideal process usually involved a Ti oxide ore such as limenite, and fluoride salts as the Ti extraction agent to produce fluorotitanates and Ti fluorides.

In 1952, Kroli² discussed the advantages and problems of producing TiF₄ and alkali fluorotitanates such as Na₂TiF₆ as alternatives to the chloride route to Ti. The distinct advantage seen by Kroli³ is that O₂ does not displace the fluoride from the Ti as it does from the chloride, making the fluorotitanates somewhat easier to handle. Hunter⁴ found that reduction of Na₂TiF₆ with K produced a product with only 73 wt pct Ti. At about the same time, Welss⁵ attempted to produce Ti by pressing a mbture of K₂TiF₆ and Al or Na into a pencil-shaped electrode, which was reduced by melting in an arc furnace. The product contained 97.5 wt pct Ti and was quite brittle, indicating interstitial contamination.

Most subsequent research (post-1945) emphasized fluorotitanate salt electrolysis in a molten salt bath to form metallic Ti, ⁶⁻⁸ Methods other than electrolysis to obtain metallic Ti, using fluorotitanates as the raw feed material, also have been proposed. These methods include the AITi-Oxy process^{9, 10-12} using Al as a reductant in a Zn bath, as well as methods using Na, ^{5, 13} K, ¹⁴⁻¹⁵, Mg, ¹⁶ and AI^{5, 16-18} as reductants. None of these methods have proved to be commercially successful, and none produce Ti ingot directly.

A simpler, more efficient route to TI metal is by chemical reduction of the fluorotitanate salts to directly form TI ingot. However, molten TI and its alloys are reactive with materials commonly used for containment. An ideal reactor for the reduction of the fluorotitanate salts would provide (1) an enclosure that is nonreactive with the TI and byproducts, (2) a volume with sufficient residence time for completion of

Titanium '92 Science and Technology Edited by F.H. Froes and I. Caplan The Minerals, Metals & Materials Society, 1993 the reaction, (3) input of heat to maintain reaction and maintain the TI and byproducts in the molten state, (4) mixing of the reactants and products to ensure both reactant availability for reaction and product homogeneity, and (5) a method to add more feed and to remove and separate product Ti ingot and byproduct stag to make the process continuous. The induction stag process developed by the Bureau of Mines¹⁹ provides mixing, continuity, and containment, and thus is the ideal reactor. The process was designed specifically for melting Ti scrap and sponge in a water-cooled, segmented crucible by induction heating. In the melting technique, the bottom of the crucible is formed by the cooled Ti ingot, which is continuously withdrawn. The Ti metal route proposed by the Bureau of Mines²⁰⁻²² uniquely applies the induction stag furnace to the reduction of fluorotitenate directly to Ti metal ingot by using a low-cost, domestically available limenite as raw feed material.

A system involving calcium fluorotitanate (CaTIF₆) feed and Ca reductant was chosen for simplicity of chemical species, and in consideration of the volatility of reductant and slag. Calcium has the highest boiling point among the alkali and alkaline-earth elements commonly used for reduction (i.e., Na, K, Mg, and Ca). An additional advantage for the use of Ca in this route was indicated by the thermodynamic work of Mah,²³ Kelley,²⁴ and Kubaschewski,²⁵ and the experimental processing work of Suzuki,²⁶ which showed that Ca has the greatest potential to deoxidize the Ti metal product. A process to deoxidize Ti scrap and powders with Ca in a Na carrier was patented recently by Fisher.²⁷

This paper discusses the reduction of $CaTIF_6$ to Ti metal using Ca metal reductant, with calcium fluoride (CaF_2) as byproduct. Batch-type studies were conducted in an induction stag batch furnace with and without graphite containment crucibles. Continuous production of Ti was tested in an induction stag ingot furnace employing either a two-step process (with reacted feed) or the preferred single-step reduction with Ca metal reductant and $CaTIF_6$ feed.

Experimental Procedures and Results

Process Flowsheet and Chemistry

A process flowsheet for the proposed route to Ti metal²⁰⁻²² is shown in Figure 1. Details of the process unit operations to produce the CaTiF₆ from ilmenite used in the reduction step are presented elsewhere.²¹⁻²² The reduction step is given by--

CaTiF₆ Preparation

To expedite the research effort, a synthetic CaTiF₆ was prepared using pure TiO₂ (anatase) instead of limenite ore for the reduction process studies. The synthesis of the fluorottanate compound is a two-step process.

(a) TiO₂, leached with 48 to 52 pct HF at 338 K, produces an aqueous solution of TiF₄ and is represented by the reaction--

$$TiO_2 + 4HF - TiF_4 + 2H_2O.$$
 (2)

The HF solution first is heated in a water bath to 338 K, then placed in an ice bath to control reaction temperature. TiO₂ is added and the leach solution temperature is maintained at 343 to 353 K by the exothermic reaction and rate of feed of the TiO₂. Unreacted solids are filtered prior to the crystallization step.

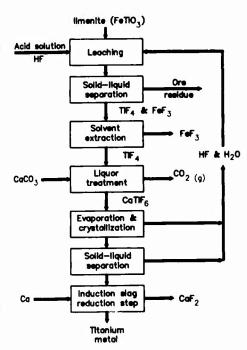


Figure 1 - Process flowsheet of CaTiFs route to Ti.

(b) Calcium carbonate (CaCO₃) then is added to the solution in a water bath at 338 K, after which CaTiF_a precipitates by reactions (3) and/or (4).

$$TiF_A + CaCO_3 + 2HF + H_2O + CaTiF_A + 2H_2O + CO_2.$$
 (4)

The CaTiF₆ siurry is dried overnight at 338 K, and then dried for 3 days at 488 K. The dry powder is crushed and stored in a glovebox or in an oven (373 K) to prevent absorption of moisture. Typical $CaTiF_6$ chemical analyses, shown in Table I, indicate that the $CaTiF_6$ produced to date has not been free from water of hydration. In addition, an O_2 -containing species, $TiOF_2$, also can be present.

Table I Typical CaTIF, Chemical Analyses, weight percent1-2

C	0.0001-0.001	N ₂	0.02
Ca	18.5-20.7	0,	0.78-2
F	45.A-50.5	Si	0.07-0.22
Fe	0.09	Ti	21.1-22.5
Mg	0.15-0.22		

¹Impurity phases detected by X-ray diffraction included CaF₂, TiOF₂, and CaTiF₆*2H₂O.

²Theoretical stoichiometric wt pct for CaTiF₆: 19.85 Ca, 56.44 F. 23.71 Ti.

Differential Thermal Analyses (DTA)

Differential thermal analyses conducted in an atmosphere of flowing argon (Ar) were performed to obtain information on the reaction temperature for the reduction reaction 1. An exothermic reaction was observed at 833 K. Results of X-ray diffraction indicate complete reduction, with a primary phase of CaF₂ and a trace phase of Ti detected. Therefore, with induction heating, a moderate ignition temperature is required by the Ca metal to cause a reaction to occur in induction slag furnace batch reduction tests. In practice, heat from a hot ingot in the ingot furnace would be sufficient to cause complete reduction of the feed material. Therefore, power could be decreased during reactant feeding to avoid volatilization of Ca and then raised to melt the Ti and separate it from the byproduct CaF₂ slag.

Batch Reduction Tests Using Induction Slag Batch Furnace

The induction slag batch furnace was used for batch reduction tests with and without graphite containment crucibles. The furnace contained a 12.7-cm-diameter, 24-segment water-cooled Cu crucible, and power was supplied by a 100-kW, 10,000-Hz motor generator. To minimize the amount of reactants needed, a graphite containment crucible was used for initial tests. The crucible acted as a heat source, being rapidly heated by the induction field. Tests were conducted by placing 100 g CaTiF₆ and 40 g Ca (stoichiometric amount) in a graphite crucible inside of the water-cooled Cu crucible. The system was evacuated to below 50 μ m Hg and backfilled to 69 kPa Ar prior to the run. The reduction of CaTiF₆ took place according to Equation 1. The reduced product contained approximately 17 wt pct Ti as 15 kW were sufficient to initiate a complete reaction. After completion of a test, the charge was allowed to cool for 2 h prior to removal. The reacted product was easily removed from the graphite container and was then ground using a shatter box to prepare a sample for X-ray diffraction and chemical analyses. Typical X-ray diffraction analyses indicated a primary phase of CaF₂ and trace phases (1-10 pct) of Ti, TiC (at higher power levels), CaO, and Ca(OH)₂.

Charges of up to 800 g of CaTIF₆ with stoichlometric amounts of Ca also were reacted without use of a graphite container in the water-cooled Cu crucible. In this case, low-temperature induction heating of the Ca metal was sufficient to initiate the highly exothermic reaction. Power typically was held between 30 and 60 kW. The charge also was allowed to cool for about 2 h prior to removal. As was found in the graphite container tests, X-ray diffraction analyses indicated a primary phase of CaF₂ and trace phases of Ti, CaO, and Ca(OH)₂. The Ti had formed small globules distributed in the CaF₂ slag by-

product. To try to agglomerate these globules, a build-up run was made by consecutively reacting four batches of 400 g CaTiF₆ and 160 g of Ca to yield 2.24 kg of reacted product. This increased the amount of Ti in the crucible, but did not result in more agglomeration.

Ti globules were removed from a reacted mass and melted into a button for chemical analyses by non-consumable arc melting in a water-cooled Cu hearth in an inert atmospher# to determine the Ti product purity. In an initial test, O₂ content of the starting CaTiF₆ powder was 4.5 wt pct, which resulted in contamination of the Ti product (see test 1 in Table II). A second test using CaTiF₆ powder with O₂ content of 0.78 wt pct still resulted in high O₂ content (2.19 wt pct), and the button was extremely brittle. Thus, it is critical to have a CaTiF₆ powder with no O₂ contamination. Chemical analyses of these buttons are shown in Table II. Interstitial contents of Ti sponge (ASTM B299, GP) and unalloyed Ti (Grade 4) are given for comparison.

Table II Chemical Analyses of Ti Buttons (wt pct)

	Ca	F	N ₂	O ₂	С
Test 1 (4.5 wt pct O ₂ in CaTiF ₆)	0.032	0.032	0.08	2.27	0.12
Test 2 (0.78 wt pct O ₂ in CaTiF ₆)	NA	NA	0.05	1.95	NA
Test 3 (40 pct excess Ca)	.01	.12	0.08	1.64	0.05
Test 4 (60 pct excess Ca)	.02	.12	0.11	1.17	0.07
Ti sponge	NS	NS	.02	.15	.03
Unalloyed Ti (grade 4)	NS	NS	.05	.40	.10

NA Not analyzed. NS Not specified.

Thermodynamic information predicted that the Ca would remove O_2 from Ti. Therefore, tests were conducted with 20, 40, and 60 pct excess Ca. Brittle Ti buttons, which were high in O_2 , still resulted, as shown in Table II, although free Ca was present in the slag of the reaction product. Only the 40 and 60 pct excess Ca results are shown.

Reduction Tests in the Induction Slag Indot Furnace

A schematic of the induction slag ingot furnace for the production of Ti ingot from the CaTiF₆ is shown in Figure 2. An initial starting stub of Ti was attached to the water-cooled Cu withdrawal stinger and positioned in the crucible about 7.62 cm from the top. Various diameters of the starting stub were investigated to achieve an adequate slag layer for separation of the byproduct CaF2 slag from the Ti Ingot. An initial amount of CaF, slag (about 700 g) was added on top of the stub. The furnace was evacuated to a pressure less than 50 µm Hg, then backfilled with Ar to 34 kPa. Power initially was turned up to 30 kW to melt the slag. then raised to 50 kW to obtain a molten pool of Ti.

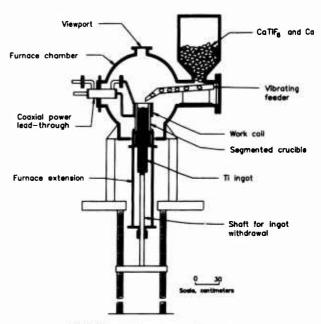


Figure 2 - Induction slag Ingot furnace.

Slag melting was accomplished by conduction of heat from the induction heated Ti ingot. Once a molten pool was established, feeding of the reactants began.

Three methods were examined to react the feed material and separate the byproduct slag from the Ti ingot: (1) feed reactants directly onto molten pool, (2) feed prereduced product from the batch furnace onto a molten pool of Ti in a two-step process, and (3) feed reactants onto the hot, but solidified Ti ingot, with no power until a reduction occurred (to limit Ca volatilization), then turn power to 50 kW to obtain a molten pool of Ti. The third approach was found to be more satisfactory because it avoided Ca loss and was a single-step process.

A 9.53-cm-diameter Ti stub, weighing 5,768 g, was used in the reduction experiment, during which 773 g of reacted product was fed for the two-step reduction process. The majority of the slag remained in the crucible area, and chemical analysis for Ti in the slag was 1 wt pct. Weight gain of the Ti stub was 112 g, with a calculated Ti recovery of 85 pct. Brinell hardness of the top of the ingot increased from 188 HRB to 272 HRB, indicating O_2 contamination, as expected, from the pre-reacted feed. Oxygen content of 0.563 wt pct was measured at the top of the ingot, with a N_2 content of 0.004 wt pct.

One of the problems with this reaction is the excessive amount of CaF₂ slag produced as byproduct. The induction slag ingot furnace had no provision for continuous slag removal. In one run, reacted product was fed to the furnace and resulted in slag build-up in the crucible melting area. The run had to be prematurely terminated after 1.4 kg had been fed. Figure 3 shows the resulting ingot and slag. Therefore, a means of separating slag from the Ti ingot was necessary for continuous operation.

Slag was successfully separated from the ingot during a run (using 2.05 kg of reacted feed) in which a continuous slag layer formed around the stub. A machined Ti starting stub allowed for a 0.48-cm gap between the starting stub and the watercooled Cu crucible, and approximately 1 kg of CaF2 slag was added to the top of the ingot. Power was held low enough to melt the slag and form the desired slag layer, then raised to 70 kW to obtain a molten pool. Reacted product was fed to the pool for about 20 min with no build-up of slag. About 1.4 kg of slag fell to the bottom of the furnace, and the rest appeared as long drips below the Ti stub, as shown in Figure 4. The slag was removed, and the weight gain of the ingot was 325 g, for a Ti yield of The above procedure also was followed for ingot tests using CaTiF₆ and Ca powders for single-step reduction.



Figure 3 - Ti ingot and CaF₂ byproduct showing slag buildup.

Due to the volatilization of Ca, reactants cannot be fed onto a full pool of molten Ti. However, since the reaction temperature is low (<873 K), the power can be turned down (or off) momentarily when reactants are fed onto the stub. Due to the amount of CaF₂ slag produced by the reduction reaction (83 pct of the total mass), it was difficult to re-establish a fully molten pool after the reaction took place. Therefore, an auxiliary directed energy source, such as an Ar plasma torch, is recommended to assist in melting the CaF₂ slag in the reaction/separation zone.

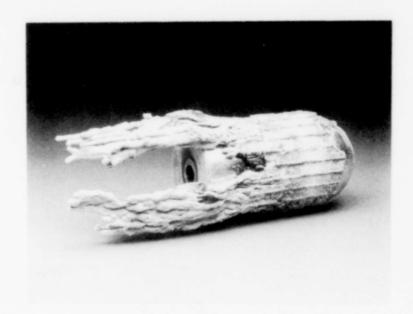


Figure 4 - Separation of CaF2 slag from Ti ingot.

Using the furnace operation procedures described above, $CaTiF_{\epsilon}$ and Ca were fed onto the stub at low temperatures to cause reduction, and then power was increased to form a molten Ti pool and to consolidate the Ti to the ingot and to separate byproduct slag. Titanium recovery of 93 pct was obtained, including complete separation of Ti from slag in a test using 2305 g of reactants to produce 344 g of Ti. Titanium distribution, shown in Table III, was calculated from chemical analyses of the products for Ti. Nearly complete separation of Ti from the byproduct slag reporting to a removable container at the bottom of the furnace enclosure ("slag trap") is shown. Some slag that remained in the crucible was easily removed from the outside surface of the ingot and contained a small amount of Ti.

TABLE III Titanium Distribution and Analyses for CaTiF₆ Reduction Run

	Product	Weight (g)	Ti distribution (pct) from CaTiF ₆ feed ¹	X-ray diffraction
Ti ingo	t	Ingot gain of 344 g	92.85	NA
Slag in	slag trap	1,979	0.09	P=CaF2, BDT=CaO
Slag in	crucible	377	3.23	P = CaF2, BDT = CaO
Furnac	e dust	150	3.81	P=CaF2, T=CaTiF6
NA	Not analyzed.			
P	Primary phase	(40-100 pct).		
T	Trace phase (1-10 pct).		
BDT		ble trace phase (I	ess than 1 pct).	

Conclusions

Ti analysis of starting CaTiF, powder was 22.5 wt pct.

Reduction of $CaTiF_6$ with Ca was investigated in both batch and continuous processes using, respectively, the induction slag batch and ingot furnaces. Reduction and slag separation operations must be performed at different temperatures. Batch reduction tests and DTA results show that the reduction reaction ignition temperature is low (<873 K). In contrast, byproduct slag separation must be accomplished at temperatures above the melting point of CaF_2 (1696 K) using heat from a molten pool of Ti in the induction slag ingot furnace. Byproduct CaF_2 slag separation was obtained, with good Ti recovery to the ingot. However, combining the reduction and slag separation operations into a single-step process at slag separation temperature was unsucessful due to volatilization of Ca metal reductant.

Another problem is the O_2 content of the CaTiF₅ powder produced, which must be lowered from the present 1 wt pct in order to produce Ti ingot of acceptable purity. Use of excess Ca in the reduction step did not lower the O_2 content of the Ti product to acceptable purity.

Another improvement would be a directed heating source, such as a plasma arc torch, to melt the slag since the slag presently is heated only by conduction of heat from the Ti Ingot.

References

- 1. F. H. Hayes et al., "Advances in Titanium Extraction Metallurgy," J. Metals, 36(6) (1984), 70-75.
- W. J. Kroll, "Some Aspects of Titanium Metallurgy," J. Met. Ind., 80 (2 May 1952), 343-345; (9 May 1952), 383-396, 388.
- 3. W. J. Kroll, "Anhydrous Fluorides in Metallurgy," <u>J. Met. Ind.</u>, 83 (31 July 1953), 81-82; (7 August 1953), 101-104; (14 August 1953), 124-126.
- 4. M. A. Hunter, "Metallic Titanium," J. Am. Chem. Soc., 32 (1910), 330-336.
- 5. L. Weiss and H. Kalser, "Metallic Titanium," Z. Anorg. Chem., 65 (1910), 345-402.
- Horizons Titanium Corp., "Preparation of Titanium From Alkali Metal Titanium Double Fluorides," Brit. Pat. 727,088 (30 March 1955).
- 7. E. Wainer and M. E. Sibert, "Production of Metallic Titanium," U.S. Pat. 2,714,575 (2 August 1955).
- 8. M. A. Steinberg and A. A. Topinica, "Production of Titanium by Fused-Salt Electrolysis," U.S. Pat. 2,813,068 (12 November 1957).
- 9. A. J. Myhren et al., "The New Jersey Zinc Company Electrolytic Titanium Pilot Plant," J. Metals, 20(6) (1968), 38-41.
- R. A. Hard and M. A. Prieto, "Process for Making Titanium Metal From Titanium Ore," U.S. Pat. 4,390,365 (28 June 1983).
- 11. J. A. Megy, "Process for Making Zero Valent Titanium From an Alkali Metal Fluorotitanate," U.S. Pat. 4,668,286 (26 May 1987).
- 12. J. A. Megy, "Process for Making Titanium Metal From Titanium Ore," U.S. Pat. 4,468,248 (28 August 1984).
- J. Kamlet, "Process for the Manufacture of Titanium Metal," U.S. Pat. 2,823,991 (18 February 1958).
- 14. S. R. Crane, C. F. Davidson, and D. D. Harbuck, "Titanium Metal Production From Perovskite Using a Sulfate-Fluoride System" (Paper presented at the TMS-AIME Annual Meeting, Phoenix, Arizona, 25-29 January 1988; available upon request from S. R. Crane, Salt Lake Research Center, Bureau of Mines, Salt Lake City, UT).
- 15. P. Gross and D. L. Levi, "Titanium," U.S. Pat, 2,718,464 (20 September 1955).
- 16. Solex Research Corp. of Japan, "Titanium Production," Jpn. Kokai Tokkyo Koho JP 60 17,026 (28 January 1985).
- 17. J. Kamlet, "Titanium-Aluminum Alloys," U.S. Pat. 2,781,261 (12 February 1957).
- 18. J. Kamlet, "Cyclic Process for Manufacture of Titanium-Aluminum Alloys and Regeneration of Intermediates Thereof," U.S. Pat. 2,837,426 (3 June 1958).

- 19. P. G. Cities and R. A. Beall, "Induction Melting of Metals in Cold, Self-Lined Crucibles," U.S. Pat. 3,775,091 (27 November 1973).
- 20. D. E. Traut, "Induction Slag Reduction Process For Making Titanium," U.S. Pat. 4,985,069 (15 January 1991).
- 21. D. E. Traut, D. A. Hansen, and J. I. Palge, "Calcium Fluorotitanate-Induction-Slag Furnace Route to Titanium Metal," <u>Sixth World Conf. on Titanium</u>, Part II, ed. by P. Lacombe, R. Tricot, and G. Beranger (Les Éditions de Physique, France, 1988), 679-684.
- 22. D. E. Traut, D. A. Hansen, and G. T. Fisher II, "Calcium Fluorotitanate-Induction-Slag Furnace Route to Titanium Metal" (Paper presented at the Annual Conference of the Titanium Development Association, Tucson, Arizona, 11-13 October 1989; available upon request from D. E. Traut, Albany Research Center, Bureau of Mines, Albany, OR).
- 23. A.D. Mah et al., "Thermodynamic Properties of Titanium-Oxygen Solutions and Compounds" (Report of Investigations 5316, U.S. Bureau of Mines, 1957), 30-33.
- 24. K. K. Kelley and A. D. Mah, "Metallurgical Thermochemistry of Titanium" (Report of Investigations 5490, U.S. Bureau of Mines, 1959), 15.
- 25. O. Kubaschewski and W. A. Dench, "The Free Energy Diagram of the System Titanium-Oxygen," J. Inst. Met., 82 (1953), 87-91.
- 26. R. O. Suzuki et al., "Preparation of Ti Powders by the Calcium Vapor Reduction of TiO₂ and the Electron Beam Melting," <u>Sbth World Conf. on Titanium</u>, Part II, ed. by P. Lacombe, R. Tricot, and G. Beranger (Les Éditions de Physique, France, 1988), 701-706.
- 27. R. L. Fisher, "Deoxidation of Titanium and Similar Metals Using a Deoxidant in a Molten Metal Carrier," U.S. Pat. 4,923,531 (8 May 1990).

INDUSTRIAL PRODUCTION OF SPONGY PIPANIUM OF LOW HARDNESS AND

PREVENTION OF GAS-SATURATED INCLUSIONS.

A.E. Andreev, A.I. Guliakin, V.M. Malshin, V.S. Lobanov,

V.E.Lugovoy

Titanium Institute, Ukraine Titanium Association, Russia

Abstract

The main factors that define the quality of spongy titanium and allow its production with low hardness and without gas-saturated inclusions are: high level of magnesium and titanium tetrachloride purification, optimization of technological conditions using automated processes control systems, high level of cleanliness in the apparatus, and establishment of strict control at all stages of titanium production.

Introduction

Consequence of interaction with the impurities is considerably more substantial for titanium, than for most structural metals. Contaminated titanium refining presents a complex scientifictechnical problem, which has not yet been introduced into the industrial practice. That is why the quality of primary (spongy) titanium is in the centre of attention since the moment of organizing the industrial production.

Purity of Reactants

Purity of the finished products is, in many respects, defined by the purity of used reagents and the problem of spongy titanium quality is considered as a complex of problems of metal associated manufacturing operations. Influence of each manufacturing stage on the change of spongy titanium hardness is set forth in (1). The technology was developed on the basis of an extensive programme of investigations (2) and includes a matrix of all technical stages of titanium production. Thus, there have been developed apparatus and technology of preparing magnesium as a reducing agent of high purity and transporting it in the moltem form to reduction apparatus (reactor) without the intermediate depressurization (3,4). Such technology is possible thanks to the fact that titanium production is an integrated technolo-

Titanium '92 Science and Technology Edited by F.H. Froes and I. Caplan The Minerals, Metals & Materials Society, 1993 gical cycle with magnesium production. There is also used pure condensate recycled magnesium formed in the process of vacuum separation (5). There have been developed an apparatus and technology for multistage cleaning of titanium tetrachloride that provides its stable quality in spite of use of various types of raw material and carbon reducing agent (6). Titanium tetrachloride is stored under argon atmosphere.

Quality and Process Controls.

Control of technological processes plays an important part in provision of high-quality spongy titanium. Characteristic properties of titanium production are as follows: many stages, variety of controlled and regulated parameters, a large number of simultaneously operating apparatus of the same type, high temperatures at the stages, use of highly reactive dangerous reagents, etc. For magnesium-thermal processes control there is developed an automated system which, by its functional structure, is a hierarchical two-level system (7). At the low level there are solved the problems of automated control or regulation of parameters of reduction or vacuum separation stages. At the upper level there are solved the problems of control common to all shops: treatment of statistical data on carried out cycles, calculation of technological and economic indices, analysis of stability of spongy titanium quality at the given level of technological parameter variations, prediction of cycle termination time, etc. Technical aids for automated systems include: sensors, primary converters, actuating mechanisms, machines of central ized control for electronic computers.

Use of automated systems allows increased reliability and reproducibility of the process conditions; the process is automated and conducted by a specified programm. Extension of reduction and vacuum separation apparatus at all plants (1) positively influenced the quality of spongy titanium produced. At present, the production rate of the apparatus is up to 4t per cycle. Extension of overall dimensions allows an increased yield of sponge of high purity and to decrease the content of such impurities as oxygen (see Table I). Not the least of the factors is the use of high-purity argon, its complementary cleaning of oxygen or nitrogen above heated spongy titanium.

Elimination of Inclusions.

On the whole, the developed technology allows consistent production of quality spongy titanium of less than 90 HB hardness with the high yield reaching 25% of the total output. Besides the requirements for the total level of quality, there must be imposed requirements for the absence in spongy titanium of inclusions (zones) with gas saturation, i.e. nitrogen and oxygen impurities in the form of nitrides or oxynitrides, that may cause failures in the parts of aircraft engines. In order to meet this requirements, at each stage of production there are envisaged the measures preventing the contact of titanium terachloride, molten magnesium, hot reaction mass and heated spongy titanium with air. Measures for the prevention of contaminating titanium with nitrogen or oxygen begin with preparing the apparatus for the process. The main requirements for the

apparatus where titanium is produced, to the pipe lines for titanium tetrachloride, piping arrangement for argon and vacuum lines are air-tightness and operational reliability. They are provided with high quality of components, careful assembly level of organization of assembly/disassembly operations,control of assembly quality. Much attention must be given to incoming control of the quality of reduction apparatus as well as vacuum separation apparatus, current control of quality of assembly welded seams, control of air-tightness of rubber seals in the knock-down structures. As the overall dimensions of apparatus are increased these requirements increase too. One of responsible operations when preparing apparatus before each cycle is control of air-tightness, which is carried out on the specialized stands where the search for leaks in the seams and joints is performed under pressure. Quality of spongy titanium in many respects depends also on reliability and air-tightness of used evacuation system employed. Here necessary measures are undertaken for cutting off vacuum lines from apparatus with heated titanium in case of a sudden failure of the vacuum system.

Table I Quality Indices of Spongy Titanium Produced in Apparatus of Various Cycle Output

Index	Cycle	output,	unit of	measur	ement	
Indox	1.0	1.5	2.3	3.5	4.2	5 .5
Yield of high- purity sponge,%	75	78	79	80	83	85
including: lower than 90 HB from 90 to 120 HB	3 72	8 7 0	12 67	15 65	25 58	32 53
Content of impurities in the mar ketable metal,% - oxygen - nitrogen - iron - hardness, HB	0.048 0.011 0.043 103	0.041 0.013 0.045 100		0.036 0.013 0.046 98	0.035 0.011 0.047 97	0.034 0.010 0.050 97

In industrial practice, there is used the so-called semi-aligned circuit by which assembly of the vacuum separation apparatus is carried out without cooling the reduction apparatus, while the process of vacuum separation is carried out in a specialized furnace. Apparatus design and technological methods prevent the contact of hot reaction mass with atmospheric air during reassembly (2).

In the process of forming the sponge block in the apparatus a considerable part (up to 30%) of impurities entering the reactor and including nitrogen or oxygen are withdrawn from the

process with magnesium dichloride, which is removed in the molten state in the course of reduction process proceeding. The other substantial part of impurities is concentrated in the bottom part of the sponge block, which is then separated during the mechanical treatment of the block. Due to this the probability of contamination of the sponge with gas saturated impurities. Quantitative characteristics of movement of nitrogen or oxygen impurities in magnesium-thermal process show the data of Table II.

Table II Balance of Nitrogen or Oxygen Impurities in Magnesium-Thermal Process

Impurity Input and Removal	quantity of im	purities, kg/t
	Nitrogen (8)	Oxygen (1)
Impurity source 1. From titanium tetrachloride 2. From magnesium: - additionally fed - recycled condensate Magnesium dichloride 4. From argon 5. By adsorption of the air moistum 6. Inleakage into apparatus 7. During grinding Non-controlled sources fotal Impurity Recipient 1. In spongy titanium 2. In magnesium dichloride Total	0.001	0.008 0.219 0.047 0.044 0.001 0.078 0.026 0.060 0.187 0.670 0.563 0.104 0.670

Sponge Handling

In spite of measures undertaken to prevent titanium contamination at all operations, there are carried out strong measures at all subsequent stages of mechanical treatment of spongy titanium blocks right up to completing the commercial lots.

At the manufacturing plants, occasioned incidents of sponge oxydation take place due to various reasons, they are usually associated with the stage of vacuum separation or in the course of mechanical treatment of the sponge. In order to exdude such blocks from the main products, their processing is completed in a separate technological stream and spongy titanium from these blocks nowhere interacts with the main flow of high-quality products.

In the main flow, there is implemented control of the quality of lump material at each stage of crushing and after screening

classification of each fraction is conducted separately. The lumps with defects and all suspect lumps are extracted by their colour attributes. Classifying is carried out by hand on the belt conveyers. Selective control of the absence of lumps with defects is performed when completing the commercial lot. No one lump with a defect is permitted in the lot. This very strict requirement is being consistently fulfilled.

Summary

At every plant, as a result of long-term development and improvement of production and control, a system of sponge titanium quality control has been established including a number of constituent parts: scheme of control, testing and control equipment, staff of testing laboratories, technical control services, worker awareness and training, responsibility and accountability for control, supervision on providing the quality, documents on testing and control of the initial raw material, technological process and commercial products. The whole system is directed at meeting the requirements of state standards and technical conditions for spongy titanium supply. During the last 5 years about 5000 t of spongy titanium the quality of which corresponds to the world level, were supplied to various countries of the world.

The available practical data confirm that spongy titanium moets the most strong requirements to the charge materials used in the air-space engineering. The industrial production of spongy titanium with less than 90 HB hardness was developed since 1974.

References

- 1. Golubev A.A. et al., <u>Titanium, Science and Technology</u>,vol.1 (Oberursel: Deutsche Gesellschaft für Metallkunde E.V., 1985), 103-107.
- 2. Malshin Y.M., Zavadovskaia V.N., Pampushko N.A., <u>Titanium Me</u>tallurgy (M.: Metallurgia, 1991), 208.
- 3. Andreev A.E., Aodiakin V.V., Tkalich V.S., Transactions of Titanium Institute, vol.1 (M.: metallurgia, 1965), 176-184.
- 4. Viharev A.F., <u>Transactions of Pitanium Institute</u>, vol.4 M.: Metallurgia, 1970), 98-104.
- 5. Titarenko A.I. et al., "Experience of Preparing Recycled Condensate for Reduction in Magnesium-Thermic Process of Titanium Production", Non-Ferrous Metals, 9 (1979), 72.
- 6. Baibekov M.K., Popov V.D., Cheprasov I.M., <u>Titanium Tetrachloride Production</u> (M.: Metallurgia, 1987), 128.
- 7, Biriukov V.V., Degtiarik N.S., Skorik V.F., "Automated Control System of the Process of Spongy Titanium Production" Titanium", Non-Ferrous Metallurgy, 1 (1984), 23.
- 8. Malshin V.M., Andreev A.E., Guliakin A.D et al., "Experience of work on Increasing the Quality of Sponge Titanium", Non-Rer-rous Metals; 11 (1978), 65-66.

2.405

TEMPERATURE MEASUREMENTS OF SURFACE AND EVAPORATED SPECIES OF MOLTEN TITANIUM IN THERMAL PLASMA

A. Tomita, T. Nagane, M. Susa and K. Nagata

Department of Metallurgical Engineering, Tokyo Institute of Technology, 2-12-1, Ookayama, Meguro-ku, Tokyo 152 Japan

Abstract

Surface temperature of molten titanium and temperature of titanium vapor in plasma flame were measured by a radiation thermometer and a spectroscope respectively. Titanium was melted by Ar arc plasma with the electric power of about 400W. In order to correct measured temperature, emissivity of molten titanium was determined from temperatures measured by a radiation thermometer and a thermocouple. The portion above 2200K in temperature was limited to the area where plasma flame was directly irradiated. The temperature of molten part except the near-top was constant, around melting point of 1940K. Temperature of titanium vapor was approximately 6500K near the cathode, and 5000K at 1mm above titanium surface.

Introduction

Thermal plasma has been used for melting of refractory or active metals, purifying of metals, refining of metal oxides and so on. These plasma processes include interfacial phenomena between thermal plasma and condensed phases. In order to analyze the reaction at the surface of condensed phase thermodynamically, temperatures of the surface and evaporated species are required.

Ishizuka et al.¹⁾ showed that temperature of melt was about 2100K and 2300K in smelting reduction of ilmenite by Ar-10%H₂ and Ar-20%H₂ plasma respectively. Long et al.²⁾ reported that temperature of melt was 2873K₃ in carbothermic reduction of titanium oxide by Ar plasma. The other studies also presented that temperatures of melts were 2300K to 2900K. In these measurements, a radiation thermometer or a pyrometer were employed. When temperature higher than 2000K are measured by non-contact type thermometers, emissivity of bodies are prerequisite. In the conventional studies, however, emissivity was not discussed sufficiently. Many studies on emissivity were performed for solid metals but very few for liquid metals. Emissivities of liquid metals were previously reported only for iron, cobalt, nickel, chromium and copper.

Evaporated species in plasma flame were conventionally analyzed by a spectroscope. There, however, is considerable difference among plasma gas temperatures obtained by these analyses. For example, plasma gas temperature near cathode of direct current(DC) argon arc plasma was reported to be 10000K to 25000K. This difference is considered to be dependent on experimental conditions, i.e., electric power, arc length, etc.

Titanium '92 Science and Technology Edited by F.H. Froes and I. Caplan The Minerals, Metals & Materials Society, 1993 We report surface temperature and vapor temperature of titanium melted by DC argon arc plasma. Surface temperture of molten titanium is measured by a radiation thermometer. For this measurement, emissivity of molten titanium is determined. Temperature of titanium vapor is determined from the intensity of spectral line of titanium vapor measured by a spectroscope.

Experimental

Melting by DC arc plasma

A DC transfered arc plasma generator was prepared, in which tungsten rod of 3mm in diameter and 50mm in length was used as cathode and water-cooled copper plate of 30mm in diameter and 1mm in thickness as anode, as shown in Figure 1. The chamber was made of cylindrical transparent quartz glass of 50mm in inner diameter and 250mm in length. Argon, which was dehydrated by calcium chloride, and silica gel was introduced into the chamber at the flow rate of 300ml/min.

The sample was a titanium cylinder, about 3g in weight, 8mm in diameter and 13mm in height, and mounted in an alumina tube on copper plate. The alumina tube was 9mm in inner diameter, 17mm in outer diameter, and 8mm in height. It was used to hold the shape of molten titanium.

A radiation thermometer was fixed at a distance of 10cm from the sample and a thermocouple in a glass tube was fixed horizontally near the sample.

DC voltage of about 115V was applied between electrodes. DC arc plasma was ignited by pilot arc sparked from the cathode tip with a high frequency starter. Then the plasma was generated between the tungsten cathode and the titanium sample. While the plasma irradiated the sample, electric current and voltage were about 27A and 15V respectively and electric power was consequently about 400W. Arc length was about 3mm.

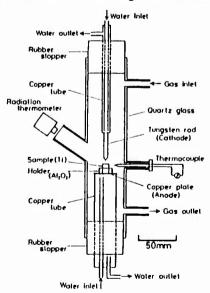


Figure 1. Schematic diagram of plasma generator.

Surface temperature measurement of molten titanium

After confirming that the plasma flame was stable, i.e., are voltage and current were constant, surface temperature was measured by a radiation thermometer in the wavelength of 650nm. The radiation thermometer covered the temperature range of 1173K to 3273K and was able to measure the temperature of the small region of about 0.4mm in diameter.

The upper half of the titanium sample was melted and became hemisphere-shaped, as shown in Figure 2. In the figure, d and $\Delta\theta$ are the distance and the angle between measuring point and the top of molten titanium respectively, ϕ is the angle between bottom of molten part and axis, R is the radius of molten part, h is the height of non-molten part and r is the diameter of sample before melting. The top sometimes was not on the axis.

In order to measure the distribution of surface temperature, the positions of measuring points were represented by $\Delta\theta$. $\Delta\theta$ was calculated from d by the use of equations (1) \sim (4) shown below.

$$V = \pi R^{3} (2-3\cos\phi + \cos^{3}\phi)/3$$
 (1)

$$V = V_0(I_0 - h)/I_0$$
 (2)

$$r = 2R\sin\phi \tag{3}$$

$$d^2 = 2R^2(1 - \cos \Delta \theta) \tag{4}$$

Here V is volume of molten part, V_0 and l_0 are volume and height of sample before melting respectively. d was measured by the use of the circular mark calibrated by a scale in a finder of the radiation thermometer.

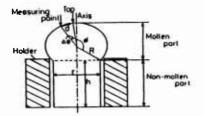


Figure 2. Cross section of melted sample.

Determination of emissivity of molten titanium surface

Determination of the emissivity of a molten titanium surface was performed by measuring the temperature of the same point using both a radiation thermometer and a thermocouple. Figure 3 schematically shows an apparatus for temperature measurement of molten titanium surface by a thermocouple. The thermocouple was W*5Re-W*26Re of 0.25mm in diameter and could measure temperatures below 2623K. The size of hot junction was about 1mm in diameter. A silica tube was used for protection and insulation of the thermocouple.

Determination of emissivity was carried out at a point of solid and liquid coexsiting zone, which was not directly in contact with plasma flame. After the temperature was measured by the radiation thermometer, the hot junction was contacted on surface at the same point. The emissivity (\mathcal{E}) can be determined by substituting the two temperatures measured by the two manners into the equation (5) which was derived from Wien's radiation equation.

(5)

: Temperature measured by thermocouple(True temperature)

S : Temperature measured by radiation thermometer

 ε_s : Emissivity used for the measurement by a radiation thermometer

ε: Emissivity of surface λ: Wavelength for measurement (650nm)

c₂: The 2nd radiation constant(1.4388×10⁻² m·K)

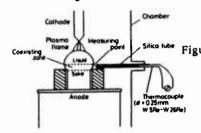


Figure 3. Scheme for temperature measurement of molten titanium surface by a thermocouple.

Temperature measurement of titanium vapor by spectroscope

Figure 4 shows a schematic diagram of an apparatus for spectroscopic analysis. Spectroscopic analysis was carried out through the window of 30mm in diameter. A titanium sample was melted by Ar arc plasma. By the use of a convex lens of 30mm in diameter and 60mm in focal distance, an image of plasma flame enlarged by four times was projected on a screen with a pinhole of 0.9mm in diameter. Only light which passed through the pinhole was analyzed by a spectroscope. The wavelength range of 325nm to 450nm was used for analysis. The analysis was conducted at the four points of 0.75, 1.50, 2.25 and 3.00mm in distance from molten titanium surface along the plasma flame axis, as shown in Figure 5. The analyzing point was chosen by the motion of convex lens.

The temperature of titanium vapor can be determined from the intensity of spectral line by the use of equation (6) shown below.

$$\log(I_n \lambda_n / A_{nm} g_n) = (-5040/T) E_n + Const.$$
 (6)

In : Intens...,

X wavelength

n-to-m tran : Intensity of spectral line n

 $A_{nm}^{"}$: n-to-m transition probability g_n : Statistical weight of excited state n : Arc temperature(vapor temperature)

: Excitation energy

If the local thermal equilibrium(LTE) is realized in the plasma flame, $\log(l_n \lambda_n/A_{nm}g_n)$ is linearly proportional to E_n . Temperature of the titanium vapor therefore can be determined from the slope of the straight line.

Results

Emissivity of molten titanium

The surface temperature of solid and liquid in the coexisting zone has been measured to be around 1830K by a radiation thermometer and 1940K of the melting point by a thermocouple respectively. Because the temperature measured by a thermocouple is considered to be true temperature, emissivity has been calculated by using equation (5). The emissivity of molten titanium is determined to be 0.33.

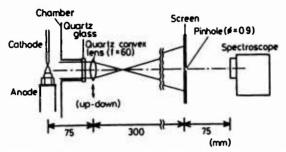


Figure 4. Set up for spectroscopic analysis method.



Figure 5. Measuring points along plasma flame axis for spectroscopic analysis.

Distribution of surface temperature of molten titanium

Figure 6 shows a distribution of surface temperature of molten titanium. For the first measurement, the value of 0.65 was used as the emissivity of molten titanium, since it was previously reported. Temperatures were output digitally by a radiation thermometer. The plots in Figure 6 represent temperatures measured. Different marks of the plots mean different runs to show the magnitude of the reproducibility.

The measured temperatures have been corrected by using 0.33 as emissivity on the basis of Wien's radiation equation. The corrected temperatures are represented by the full line in Figure 6.

The temperature is the highest at the top of the molten titanium and goes downward steeply from the top. The highest temperature is approximately 2800K. Figure 7 schematically shows isotherms on the sample surface. The portion above 2200K in temperature is limited to the area where plasma flame is directly irradiated. The temperature of the molten part except the near-top, is approximately constant, around the melting point of 1940K.

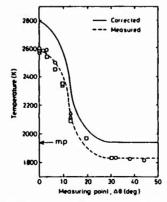


Figure 6. Distribution of surface temprature of molten titanium.

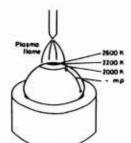


Figure 7. Isotherms on the sample surface.

Temperature distribution of titanium vapor in plasma flame

Figure 8 shows a relationship between $\log(I_0 \lambda_n/A_{\eta m} g_n)$ and E_n for titanium spectral lines. The measurement was carried out in the wavelength range of 372.98nm to 399.86nm. The good linear relationship indicates that LTE is realized in plasma flame. The temperature of titanium vapor can be determined from the slope of the straight line. Figure 9 shows temperatures along the plasma flame axis by this method. The full line represents temperature distribution of titanium vapor. The temperatures are about 6500K and 5000K near the cathode and at 1mm above the surface of molten titanium, respectively. The surface temperature measured by a radiation thermometer is used as the temperature on the surface(at 0mm).

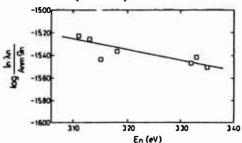


Figure 8. Relationship between intensity of spectral line measured and excitation energy.

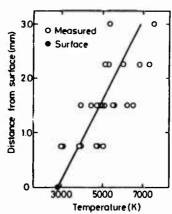


Figure 9. Temperature distribution of titanium vapor along plasma flame axis.

Disscusion

Dependence of emissivity on temperature

Assuming that emissivity of molten titanium is independent of temperature, all temperatures measured have been corrected by use of 0.33 as emissivity. Figure 10 shows the dependence of emissivity of iron, cobalt, nickel and copper on temperature. For these metals, emissivity is almost independent on temperature. It therefore can be considered that titanium also has a similar tendency. This consideration suggests that the assumption is valid.

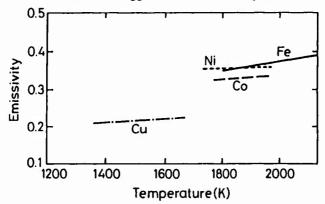


Figure 10. Dependence of emissivity of liquid iron, cobalt, nickel and copper on temperature.

Validity of temperature of titanium vapor in thermal plasma

As shown in Figure 9, the measured temperatures are scattered. The scatter is considered to result from the fluctuation of the plasma flame at the cathode tip.

The temperatures of 6500K to 5000K obtained by the present experiment are much lower than those of above 10000K obtained in previous studies. Nevertheless, the temperatures in the present study are considered to be valid because the electric power of 400W is much smaller than that of a few kilowatts used in previous studies.

Conclusion

Titanium was melted by DC arc plasma. Surface temperature of molten titanium and temperature of titanium vapor were measured by a radiation thermometer and a spectroscope respectively, which lead to the following conclusions:

- On the surface of molten titanium, steep gradient of temperature was formed. The temperature at the molten portion where the plasma flame was directly irradiated was higher than 2200K. The temperature of molten part which was not in direct contact with the plasma flame was approximately constant, around melting point of 1940K.
- LTE was realized in the plasma flame. Temperatures of titanium vapor were about 6500K and 5000K near the cathode and at 1mm above the molten titanium surface, respectively.

Reference

- R.Ishizuka and K.Akashi, "Selective Smelting Reduction of Ilmenite Ore by Ar-H₂ Plasma Arc," J.Japan Inst.Metals, 45(12)(1981), 1229-1235.
- G.W.Long, K.Mimura and K.Taniuchi, "Plasma-Arc Reduction of Titanium Oxide," J.Japan Inst.Light Metals, 31(7)(1981), 462-468.
- 3. K.Ishii, S.Oonishi and M.Sato, "Effect of Melting Condition on Argon Arc Plasma Temperature and Evaporated iron" (Rep. 3rd Meeting on thermal plasma, Iron and steel Inst. Japan, 7 June 1990).
- K.Mimura and M.Nanjo, "Production of Pure Tantalum by Combination Process of Carbon Reduction Smelting and Hydrogen Plasma Arc Melting-Refining," J.Japan Inst. Metals, 52(9)(1988), 843-851.
- 5. A.Sala, Radiant Properties of Materials (US, ISRN, 1986).
- 6. John C.d'Entremont, "Optical Temperture Measurement for Liquid Iron," Transactions of The Metallurgical Society of AIME, 227 (1963), 482-485.
- T.Mori et al., "On the Emissivities of Molten Metals and Iron Alloys," <u>Tetsu-to-Hagane</u>,57(1971),1198-1212.
- T.Makino et al., "Properties of Thermal Radiation of Liquid Transition Metals and Alloys, "Transaction of The Japan Society of Mechanical Engineers: B,50(459)(1984),2655-2660.
- Von Klaus, W.Lange und Hermann Schench in Aachen, "Messung des Spektralen Emissionsgrades von Metallen und Metallegierungen," <u>Archiv fur das Eisenhuttenwesen</u>,39(8)(1968),611-615.
- 10.P. Vervisch, B. Cheron and J.F. Lhuissier, "Spectroscopic Analysis of a TIG Arc Plasma," J. Phys. D: Appl. Phys., 23(1990), 1058-1063.
- Kitamura, K.Shibata and K.Takeda, "Reduction of Oxide in Radio-Frequency Plasma" (Rep. Meeting on thermal plasma, Iron and steel Inst. Japan, 14 May 1990).
- 12.H. Kawaguchi, "The Determination of Temperature of Light Sources for the Spectroscopic Analysis from Spectra," Bunko-Kenkyu, 13(1)(1964), 1-6.
- G.N.Haddad and A.J.D.Farmer, "Temperature Determinations in a Free-Burning Arc: I. Experimental Techniques and Results in Argon," J.Phys.D:Appl.Phys., 17(1984), 1189-1196.
- 14. A.J.D.Farmer and G.N.Haddad, "Local Thermodynamic Equilibrium in Free-Burning Arc in Argon," Appl. Phys. Lett., 45(1)(1984), 24-25.
- 15.J.Nishikawa et al.,eds., Ondo (Japan, Series of Industrial Measure Technique 1,1965),243.

PIVE-TONNE TITANIUM INGOTS

PRODUCED BY SKULL MELTING

M. I. Musatov, A. Sh. Freedman, B. N. Sukhorosov All-Russia Institute of Light Alloys, Moscow, Russia

Abstract

Positive results of vacuum arc skull melting usage in pilotscale production of titanium alloy ingots have become the basis for development of skull furnaces assuring pouring of 5
tonne titanium melt. Results of production technology development aimed at improvement of ingot quality, guaranteed elimination of inclusion-type defects and possibilities for effective usage of feed materials are described in this paper. Additionally, features of a new technique of skull melting, source
material composition, types of recycling scrap, chemical homogeneity of melted metal and thermal conditions of melting are
also discussed. The position of this new technique in the process of ingot production has been determined.

Introduction

Over the past few years, the specialists engaged in melting of titanium alloy ingots, payed their attention to problems of elimination of inclusion-type defects and increasing of fraction of the recycled scrap. These problems have been mainly solved by the development of practices of melting with indirect source of heating, which are alternative to cold-mold vacuum arc consumable electrode melting /1-4/. Among these methods the most developed ones are the following: cold-hearth EBM /2/ and cold-hearth PAM /4/, as well as cold-mold plasma arc melting of charge /1/. From our point of view, the latter one doesnot provide effective elimination of inclusion-type defects.

This paper is focused on solution of the above-mentioned problems using a new type of skull melting wherein the skull, formed in the crucible, can be used as consumable electrode for the subsequent melting. In the laboratory and pilot-scale researches carried out at the earlier stage, interconnection between the process parameters and their effects on ingot quality and technical—and economical indexes have been evaluated. The presented results of the investigation on commercial ingot melting by the above-mentioned method have been described.

Titanium '92 Science and Technology Edited by F.H. Froes and I. Caplan The Minerals, Metals & Materials Society, 1993

Process features

Melting of 4-5 t ingots was carried out in a specially designed skull furnace shown in Fig. 1.

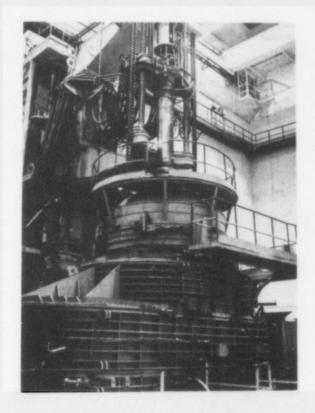


Figure 1 - Appearance of large-capacity skull furnace.

Melting was accomplished by direct-current arc in the metal crucible. The crucible was previously charged and the furnace was evacuated down to 10-1-10-2 mm Hg. Then the electric arc was initiated between the charge and the consumable electrode, i.e. the skull of the previous melting carried out in the same crucible. After complete melting of the consumable electrode the melt was poured out into the mould of the desired form and sizes.

Charge composition

Using this furnace production lots of ingots in commercial titanium and titanium alloy of Ti-6.5Al-2.5Mo-1.5Cr, Ti-6.5Al-3.5Mo, Ti-6.5Al-3.5Mo-1.5Zr, Ti-6Al-3.5Mo-1.5V, Ti-5.5Al-5Mo-5V-1Cr-1Fe systems have been produced. Fig. 2 shows one of the produced ingots.

The content of recycled scrap and primary metals in the charge was determined depending on requirements to alloy to be melted as well as the purity of charge material additions. Various types of bulky casting recycled scrap (templetes, pieces of ingots, "crowns" etc.), forge- and extrusion scrap (rejected for-

gings, waste ends of extrusions, etc.), section rolling scrap (bar-stock and tube chop ends), sheet rolling scrap (side- and flat blanking scrap) and chips were introduced in the charge. Sizes and shapes of the introduced scrap can be varied in a wide range, namely, from samples fractured after mechanical tests to large-sized scrap with linear dimension up to 2 m. This allows use of most of the types of the scrap without fragmentation and decreased metal losses and labour input in preparation of the scrap for recycling.

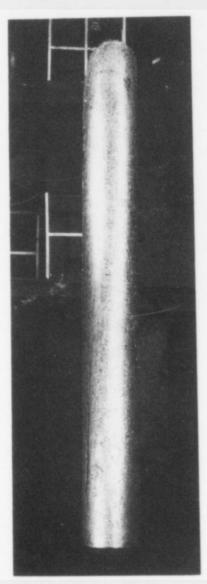


Figure 2 - Appearance of 550 mm dia ingot produced in skull furnace.

As a rule, scrap of the same grade as that of the alloy to be melted was introduced in the charge, but the use of scrap of other alloys is possible due to charge dilution or alloy compensation, if necessary. As primary metals magnesium reduced titanium sponge of ordinary grade, master alloys and pure al-

loy additions were used. Some examples of charges used are shown in Table 1.

Thermal conditions

The most important parameter of melting is electric arc power which is chosen to compensate for thermal losses providing at the same time the maintenance of prescribed quantity of the melt required for pouring. The thermal process of melting can be schematically devided in two-stages - unsteady and quasisteady ones. The initial unsteady stage is remarkable for increase in thermal losses. At this stage the metal bath is formed by melting of the charge placed in the crucible as well as by increase in the melt quantity entering into the bath due to melting of the consumable electrode. At the second quasi-steady stage of melting the thermal loss rate is stabilized and raises insignificantly with increasing melting time.

At this stage, the liquid metal bath in the crucuble is completely formed. By modifying melting parameters, one can choose time for each stage of melting to achieve desired results. When melting commercial titanium alloys, the second stage of melting is absent in most cases. The plot on relative coordinates shown in Fig. 3 demonstrates the thermal losses for such heats.

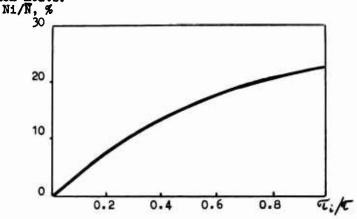


Figure 3 - Curve of crucible thermal losses plotted against average (\overline{N}) input power ($\overline{N}_1/\overline{N}$, %) depending on melting time ($\overline{U}_1/\overline{U}$).

Chemical homogeneity

The ingots produced show a high chemical homogeneity since all volume of the metal in the mould is in melted state before pouring and there is enough time for diffusion processes. As an example, results of analysis of changes in alloying element content through the bulk of the ingot are given in Fig. 4.

The acceptable level of chemical homogeneity of ingots produced during skull melting is confirmed by the results of

TABLE 1 - INITIAL MATERIAL COMPOSITION

Heat number,	Calculated	Content in the charge, kg (%)
alloy	composition,	Primary charge Recycled scrap
01288 VT9	A1 - 6.8 No - 3.6 Zr - 1.8	Sponge - 1396 (40.4) Rings and flashes 400-1100 Alloyage Al-Mo-171 (4.9) mm in size - 1750 (50.6) Zr - 29 (0.8) Chip - 114 (3.3)
01153 VT3-1	Al - 6.6 Mo - 2.4 Gr - 1.5 Pe - 0.4	Sponge - 1776 (35.4) Blades - 1500 (29.9) Alloyage Al-Cr-Mo-227 Casting scrap 750 mm in dimension - 500 (10.0) Al-Mo-48 (1.0), Cr-15 VT1-0 alloy tubes up to (0.3) Al - 48 (1.0) (17.9)
01147 VT22	A1 - 5.4 Mo - 4.9 V - 4.9 Gr - 1.0 Fe - 1.0	Sponge - 1573 (35.6) Bars - 2520 (57.0) Alloyage Al-Mo-V-Cr-Fe - 327 (7.4)

statistical processing of current analysis data for ingot lots. These results compared to those obtained during statistical processing of analysis data for ingots produced by double vacuum arc melting of consumable electrode are shown in Table 2.

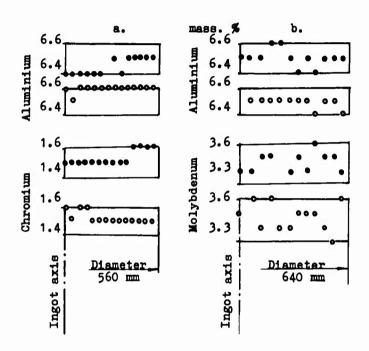


Figure 4 - Distribution of Al and Cr contents in Ti-6.5Al-2.5Mo-1.5Cr ingot (a), and Al and Mo contents in Ti-6.5Al-3.5Mo ingot (b): • middle of ingot; • ingot bottom.

Conditions of skull melting as well as cold hearth melting allow one to keep ingots free from particles with higher density and melting temperature than those of base metal. These particles are trapped in the skull and so their presence in ingots can be avoided. This fact can be confirmed by a wide experience in melting of thousands tonnes of metal. Neither in ingots nor in semis produced from these ingots, such inclusions were detected after strict testing.

As compared to cold hearth melting with indirect source of heating, skull melting technique developed provides the following advantages:

- higher chemical homogeneity of metal;

- the use of large- and small-sized scrap results in lowering of labour input and metal losses during charge preparation;

TABLE II - RESULTS OF STATISTICAL PROCESSING OF CHEMICAL
ANALYSIS DATA OF LOTS OF T1-6.5Al-2.5Mo-1.5Cr
ALLOY INGOTS MELTED BY VARIOUS TECHNIQUES

	Parameters	17	No	Çr	e) E	Si	0
Skull mi	ᆲ	6.0-6.8	101	1.2-1.8	0.30-0.60	1.2-1.8 0.30-0.60 0.23-0.35 1.5 0.45 0.27	0.078-0.13
	ଞ	0.149		0.157	0.080	0.031	0.015
	n	87	87	87	87	87	85
Double mi	In-max	5-8-7-0	2.1-3.0	1-2-1-8	1.2-1.8 0.20-0.60 0.21-0.34 1.5 0.39 0.28	0.21-0.34	0.06-0.15
in the crucible	෪	0.232	0.194	0.137	90.0	0.027	0.019
	a	325	325	325	325	325	394

Symbols: x - arithmetic mean; Gr - standard deviation; n - number of analyses used in the data processing.

- the possibility of melting in a wide range of vapour and gas pressure in the melting zone;

- the simplicity of melting units and techniques ensuring lowering of capital investments and improved reliability.

Summary

The existing development level of this skull melting technique and accumulated experience in ingot production both for critical parts (disks and blades for aircraft engines, highly loaded components of aircraft etc.) and for standard quality parts when using charge with 40-60 % recirculating scrap allow one to consider this technique to be the most effective one for primary melting. Remelting of skull melting ingots carried out in vacuum arc furnace equipped with the mold assures production of sound ingots with acceptable macrostructure.

The skull melting procedure developed is the most effective for production of Ti-base high alloys with refractory metal additions. A great experience in production of titanium alloys containing Mo, Nb and W introduced in the charge as pure elements, but not as components of alloying composition, has shown that the skull melting can assure homogeneous chemical composition of metal and production of inclusion-free ingots.

References

- 1. S. C. Stocks and P. Caputo, <u>Plasma Consolidation of Large Diameter Titanium Electrodes for Single Stick Var Ingot Manufacturing</u> (Proc. of the Sixth World Conference on Titanium, ed. by P. Lacombe, R. Tricot and G. Beranger, Cannes, France, June 6-9, 1988), 573-578.
- 2. R. Bakish, Electron Beam Melting and Refining Entering the Decade of the 90's, Industrial Heating, 57, (5), (1990), 29-34.
- 3. P. Paillers et al., <u>Cold Crucible Induction Melting of Titanium</u> (Proc. of the Sixth World Conference on Titanium, ed. by P. Lacombe, R. Tricot and G. Beranger, Cannes, France, June 6-9, 1988), 583-586.
- 4. J. W. Sears, <u>Current Processes for the Cold-Wall Melting of Titanium</u>, Journal of Metals, 42 (3), (1990), 17-21.

OXYGEN CONTAMINATION OF TITANIUM SPONGE

IN THE KROLL-PROCESS

S.V.Aleksandrovsky, A.A.Zakharevich, A.I.Guliakin Mining Institute, St.Petersburg, Russia

Abstract

Behaviour of oxygen in Kroll-process was investigated at a plant scale with the use of stable isotope ¹⁸O. It was shown that the percent of the oxygen, from each source, passing into titanium sponge from oxygenous compounds is approximately the following for each of raw materials: titanium tetrachloride-80, magnesium-30, circulating condensate-40. More than 13,7% of oxygen entering reactor with all the sources is removed with discharged magnesium chloride, mainly in the first half of the process. Absorption of water vapour and oxygen by the surface of titanium sponge while block dressing leads to increase of titanium hardness by 2-10 HB.

Introduction

Oxygen is known to be one of the most harmful impurities decreasing the quality of titanium sponge and articles made of it. Interaction between titanium and oxygen or oxygenous impurities is determined by high chemical affinity of titanium for oxygen. Thermodynamic calculations show high probability of the reactions between titanium or magnesium oxides and titanium with formation of solid solutions of oxygen in titanium, containing up to 0,1 % of oxygen. According to material balance of main impurities in Kroll-process, 30-40 % of the oxygen sources are unaccounted for. We have investigated behaviour of oxygen during all the stages of Kroll-process at a plant scale. In order to differentiate the role of each source of oxygen stable isotope 180 in the form of gas or water was used.

Experimental Procedures

Oxygen isotope in the form of heavyoxygen water was introduced into titanium tetrachloride and metallic magnesium by bubbling or dispersed inside the reactor containing circulating condensate. To determine the extent of contamination of titanium sponge by oxygen while processing sponge block into final product we have investigated interaction of vaporous ${\rm H_2}^{180}$ or gaseous ${\rm ^{180}_2}$ with metallic titanium having oxidized ("passive") and unoxidized ("active") surface. To control behaviour of oxygen, samples of raw titanium tetrachloride and metallic magnesium, titanium sponge, discharged magnesium chloride and reaction mass were taken. Samples were analysed for total and

Titanium '92 Science and Technology Edited by F.H. Froes and J. Caplan The Minerals, Metals & Materials Society, 1993 stable isotope 18 O content. From results obtained the quantities of absorbed oxygen were calculated. The sensitivity of 18 O analysis was 5^*10^{-6} %.

Results

Oxygen from Titanium Tetrachloride

Studies of behaviour of oxygen, introduced with titanium tetrachloride, show that an increased content of ¹⁸0 has been observed in local samples from upper and lower parts of titanium sponge block and the lowest content - in the centre of the block (Figure 1,A). ¹⁸0 content in discharged magnesium chloride is approximately invariant in first discharges and decreases sharply after the eighth discharge (Figure 2).

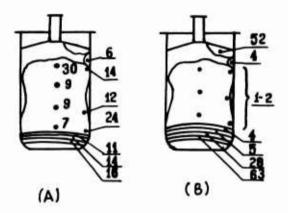


Figure 1 - Distribution of absorbed $^{18}0^{+}10^{4}$ %, in titanium sponge block obtained with the use of: A-titanium tetrachloride, contaminated with $^{18}0$; B-magnesium, contaminated with $^{18}0$.

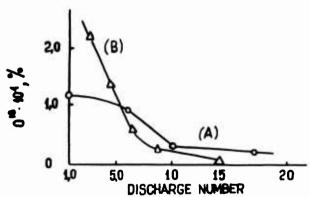


Figure 2 - Content of ¹⁸0 in magnesium chloride discharges.

A - titanium tetrachloride contains ¹⁸0;

B - circulating condensate contains ¹⁸0.

The balance of 18 O in reduction products shows that major part of oxygen from titanium tetrachloride, contained in the form of oxichloride, passes into titanium sponge (Table I). Moreover up to 60 % of 18 O pass into the central part of block and nearly 12 % - into garnissage. About 14 % of oxygen is removed with discharging magnesium chloride. Some part of 18 O passes into metallic magnesium and magnesium chloride remaining in the reaction mass and then passing to circulating condensate.

Table I Distribution of ¹⁸O in the products of magnesium thermic reduction of titanium tetrachloride

Reduction product	Distribution Titanium tetrachloride	of ¹⁸ 0 %, passed Circulating condensate	from Metallic magnesium
Titanium sponge, including:	80,8	40,0	33,0
central part of the block +12-70 mm central part of the	56,4	15,0	7,0
block +0-12 mm garnissage	2,4 12,4	1,5 6,8	2,5 5,5
ground film first layer of	3,4	9,3	9,8
bottom part second layer of	3,4	4,2	6,9
bottom part	2,8	3,2	1,3
Magnesium chloride including:	13,7	55,6	
1-8 discharges 9-17 discharges	11,5 2,2	51,3 4,3	67.0
Circulating condensate including:	5,5	4,4	67,0
magnesium chloride metallic magnesium	1,0 4,5	3,0 1,4	

Oxygen from Magnesium

Oxide compounds, entering the reduction apparatus with metallic magnesium are concentrated in upper part of molten magnesium or precipitated in its bottom after one nour of holding (Table II). When first portions of TiCl4 are charged the distribution of ¹⁸O alters sharply: oxygen content decreases sharply in the upper part of the bath and increases in its central part. After 10 % consumption of magnesium oxygen content in molten magnesium decreases, but magnesium is not completely refined of its oxygen content by the first portions of titanium sponge produced. About 33 % of ¹⁸O passes into titanium sponge from metallic magnesium. More-

About 33 % of 'O passes into titanium sponge from metallic magnesium. Moreover analysis of local samples of titanium sponge (Figure I,B) shows that the maximum content of ¹⁸O has been observed in ground film and first layers of the bottom part. High content of ¹⁸O is also observed in the next layers of bottom part and garnissage. Some quantity of ¹⁸O is also contained in the central part of the block.

Table II Content of ¹⁸0°10⁵ %,in magnesium bath before and in the cource of process

Part of the bath	After holding	After 5 % consumption of magnesium	After 10 % consumption of magnesium
Top Middle Bottom	4,0 1,1 3,0	0,9 3,3 -	0,3 2,6

Oxygen from Recirculated Condencate

When heavyoxygen water is introduced in circulating condensate the $^{18}\mathrm{O}$ distribution in titanium sponge block is about the same as in the case of contamination of raw metallic magnesium. $^{18}\mathrm{O}$ distribution balance shows that about 40 % of $^{18}\mathrm{O}$ pass into titanium sponge and the major part is removed with discharged magnesium chloride (see Table I).

Oxygen from Absorption

In absorption investigations we distinguished two types of titanium sponge surface: unoxidized "active", which exists just after apparatus dismantling and partly while block crushing, and oxidized "passive", which exists while further block dressing (sorting, sets collecting etc.). Studies of moistening of titanium sponge show that metallic titanium with "active" surface absorbs 6-10 times more ¹⁸0 than titanium with "passive" surface (Table III). Vacuum drying of titanium sponge allows the removal of 80 % of absorbed moisture. Experiments carried out with the use of gaseous ¹⁸0 show that annealed titanium sponge absorbs 12-18*10-4 % of oxygen so up to 3-4 molecular layers of oxygen has been absorbed on its surface. It was also shown that intensity of moistening depends on absolute humidity of air, structure of titanium sponge, duration of the process and temperature gradient between metal and environment. So titanium sponge during contact with humid air absorbs considerable quantity of oxygen, sufficient for hardness increase by 2-10 HB.

Table III Absorbed oxygen content, *103%, depending on temperature of drying

Temperature ^O C	Titanium sponge with "passive" surface	Titanium sponge with "active" surface
20	0,4	6,1
50	0,4	4,1
75	0,5	2,8 7,8
100	0,5	7,8
125	1,1	11,8

Discussion

Forming magnesium chloride and structure of titanium sponge block play significant role in distribution of 18 0 in reduction products. Oxide compounds from raw metallic magnesium at the initial stages of the process react with the first portions of titanium sponge and precipitate on the bottom (in the form of ground film and first layer of bottom part) and on the walls (in the

form of garnissage) of reactor. When next portions of titanium tetrachloride are charged, the bottom depositions are stirred up because of the increased temperature gradient and physical disturbances. As a result oxide compounds are transported to the central zone by circulating flows of melt, provoding contamination of the central part of titanium sponge block. The major part of oxide compounds from magnesium is removed with discharged salt at the initial stages of the process. But then the forming block of titanium sponge overlaps all the cross-section of the reactor and acts as a filter. From this time 180 content in discharged magnesium chloride decreases sharply. Oxygenous compounds continuously entering the reactor as a part of raw titanium tetrachloride preferably contaminate the titanium sponge and partly pass into magnesium chloride and metallic magnesium. During the circulation in reduction apparatus, magnesium chloride washs titanium sponge block, wets oxide compounds and removes them from the central zone of reactor. So upper part of the block and garnissage, in contact with surplus magnesium chloride less than central part of the block, contain more oxygen. At the initial stages of process oxygenous compounds, unabsorbed by titanium sponge, are just completely removed from reactor with discharged salt. As mentioned above, after eighth discharge forming block of titanium sponge overlaps all the cross-section of the reactor and prevents removal of oxygenous compounds with discharged magnesium chloride. As a result, lower layers of titanium sponge block are contaminated with ¹⁸O. So the main sources of oxygen contamination of titanium sponge in Kroll-process are raw titanium tetrachloride (up to 80 % of the ^{18}O TiCl4 in the form of oxichloride pass into sponge) and to a lesser extent-metallic magnesium and circulating condensate (from 30 to 40 % of oxide compounds pass into the sponge). Irrespective of source of oxygenous impurities, their behaviour in the Kroll-process may be considered approximately identical. The positive role of magnesium chloride is worthy of note, removing more than 15 % of oxygen, entering reactor from all the sources. Contact of produced titanium sponge with humid air as well as with oxygen of air while block dressing leads to absorption of both water vapour and oxygen by sponge surface up to several molecular layers. As a result final titanium hardness may increase by 2-10 HB.

ARC-SLAG REMELTING OF TITANIUM AND

TITANIUM ALLOYS

- B. E. Paton, B. I. Medovar, V. Ya. Saenko, B. B. Fedorovskii L. B. Medovar, V. V. Shepelev, V. A. Riabinin, J. J. Shutey, Sr.
 - E. O. Paton Electric Welding Institute Kiev, Ukraine Shasta Inc. - Coraopolis, Pennsylvania, USA

The Arc Slag Remelting (ASR) of titanium and titanium alloys has great prospects being a more flexible and less expensive process giving the possibility to manufacture slabs with smooth surface for commercial purity titanium production.

Titanium (we mean by this word not only titanium, but all the alloys on its base), the former structural material for aerospace industry, turns before our eyes into a metal of civil application. This becomes possible just with the end of the cold war when two super powerful states, armed to the teeth, stopped their withstanding. The Soviet Union, one of these super powers, ceased to exist after the August revolution in 1991 (known in the West as the second Russian revolution.) New sovereign states appeared on the ruins of the former great country. The Ukraine is one among them, and we are glad to represent it here together with our American friends from our joint American-Ukrainian company "Shasta-Paton" in Pennsylvania.

The fact that titanium acquires a civil appearance permits us to take a new glance at the whole structure of the titanium industry. The highest and very strict requirements produced to titanium by creators of aerospace engineering, military shipbuilding, armament, ammunition and other military products are sufficiently justified even today. But these requirements can be considerably relaxed if titanium is used now primarily for the creation of different civil engineering installations, various civil constructions, bicycles, cars and other peaceful products. Taking this into consideration, we should do everything to make titanium and its alloys cheaper and quite competitive in comparison with stainless nickel containing steels and alloys. The way to reduce the price lies in the simplifying of the technology. The substitution of the expensive vacuum units for titanium melting by less expensive units using a neutral gas, such as argon, is one way to produce titanium with lower production costs. We suppose not all the participants of this forum are aware that the Ukraine has a great store of titanium raw materials and a titanium industry as well. This industry has survived the period of rapid development and reconstruction of the industrial works on the basis of the newest

> Titanium '92 Science and Technology Edited by F.H. Froes and I. Caplan The Minerals, Metals & Materials Society, 1993

technologies. The question is in the whole production cycle, starting from the mining and separation of raw materials, titanium sponge production and finishing with ready-made products as in rolling stock, tubes, forgings, stamps, castings and welded structures.

In our young independent Ukrainian State, E. O. Paton Electric Welding Institute has been around for more than a half a century. We are very confident that most of those present in this hall can associate the name of Paton Institute first with welding. The military power of the former super state could not have been achieved without welding of titanium and its alloys. The technologies that were created in the Ukraine are submerged arc welding under oxygen free flux and electroslag welding. In addition, the mighty atomic submarines would not have been built if we had not learned in due course to weld between each one run cast propeller blades of several hundred millimeters thickness by electroslag welding. But today the world does not know that a quarter of a century ago the commercial technology of electroslag remelting (ESR) of titanium and its alloys was developed at Paton Institute. Unfortunately, due to rather political than technical reasons, ESR of titanium did not get sufficient applications.

In this way it was opposed by the vacuum arc remelting (VAR). The opponents of ESR had two main reasons against its application in titanium production: an insufficiently high level of metal refining and high specific power consumption in comparison with VAR.

The years passed, but ESR technology was not stagnant. Today it is proven that the quality of ESR titanium and the power consumption can be compared to the results achieved with VAR. Under these conditions such undoubted advantage of ESR over VAR as an excellent ingot surface that does not require roughing or burning-off before further process stage as rolling, pressing, extrusion, piercing, forging - came to the forefront.

Another important advantage of ESR is the possibility of obtaining ingots of any cross-section and, primarily, rectangular ingots, i.e. slabs for sheet rolling mills without obligatory roughing up of VAR ingots having round cross-sections.

Today we would like to attract your attention to our completely new development - Arc-Slag Remelting of titanium and its alloys. From the name itself it is obvious that we speak about a combined process using two heating sources - electric arc and liquid electrically conductive slag.

The most important features of this new process are higher quality of the remelted metal than with conventional ESR, 2-3 times lower specific slag consumption, more than twice lower specific electric power consumption and also the possibility to use low frequency current and direct current along with the alternating current of standard frequency.

The last feature has a decisive meaning for the rapid growth of a new, highly efficient technology, as it can be realized practically in each VAR furnace without alterations.

For the audience's convenience, several figures and tables explaining the main ideas of this report are given below.

We invite everybody to visit us here in America. We also invite potential investors to the Ukraine to develop the titanium industry of our young and completely independent state.

TABLE. MELTING CONDITIONS OF TITANIUM INGOTS

1. ESR N 1	Number		Melting Parameters I(kA)U(v)	Ingot Mass (kg)	Melt Time (min.)	Productivity (kg/h)	Power (KVA)	Electric Power Consumption (KWh per ton)
	N 1	9	37	7.1	4 5	94,6	370	3911,2
2. ESR	ESR N 3	9	36	99	45	87,9	360	4095,5
3. ESR M	4 H	11	;	79	25	153,6	484	3151,0
4. ASR	ASR N 5	7	02	51	10	324,0	490	1512,0
5. VAR*		35	09	0009	300	1200,0	2100	1749,0

*Commercial VAR furnace at a plant in Verchnjaia Sasda (Russia)

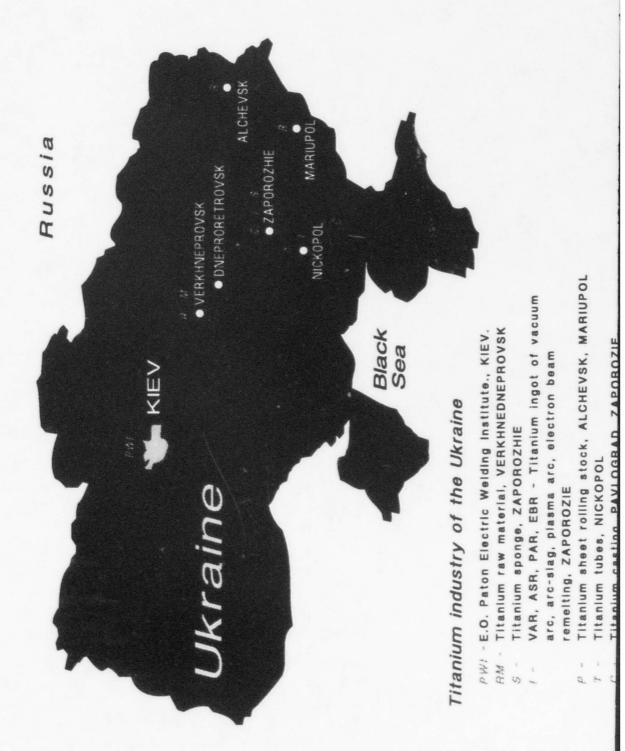




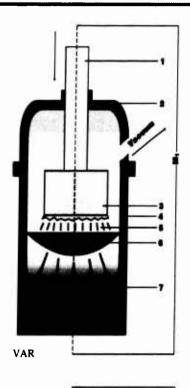
Fig. 1. Titanium Industry of the Ukraine. PWI-E.O.Paton Electric Welding Institute, Kiev RM-titanium raw material, Verkhnedneprovsk

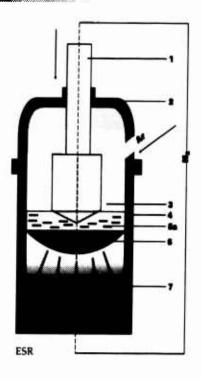
S- titanium sponge, Zaporozhie I- VAR, ASR, PAR, ESR titanium ingot of vacuum-arc arc-slag, plasma-arm, electrone beam remelting Zaporozhie

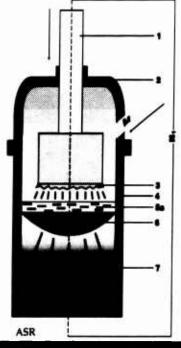
R- titanium sheet rolling stock, Alchevsk, Mariupol

T- titanium tubes, Nickopol

C- titanium castings, Pavlograd, Zaporozhie







Comparison of VAR, ESR and ASR, carried out at VAR furnace

1 — Inventory head

2 — Vacuum chamber

3 — Consumable electrode

4 — Mold

5 — Arc

5a — Slag

6 — Metal pool

7 — Ingot

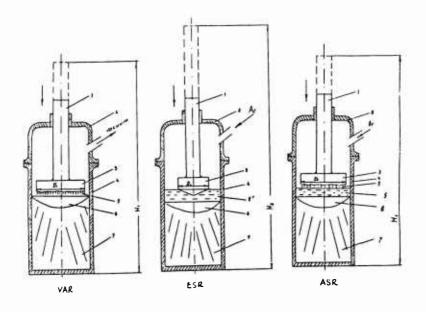


Fig. 2. Scheme of titanium and its alloy ingot melting in vacuum-arc (VAR), electroslag (ESR) and ars-slag furnaces (ASR).

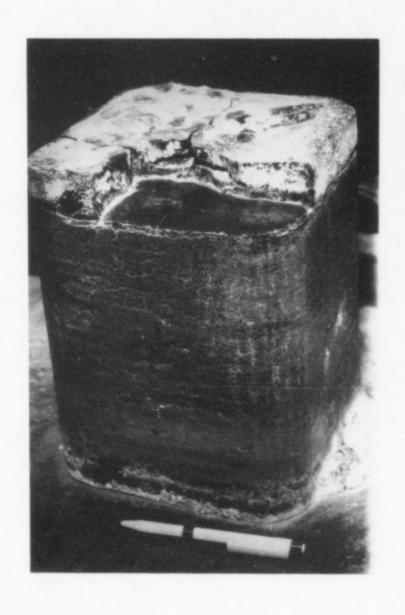


Fig. 3. Surface of ASR titanium ingot.

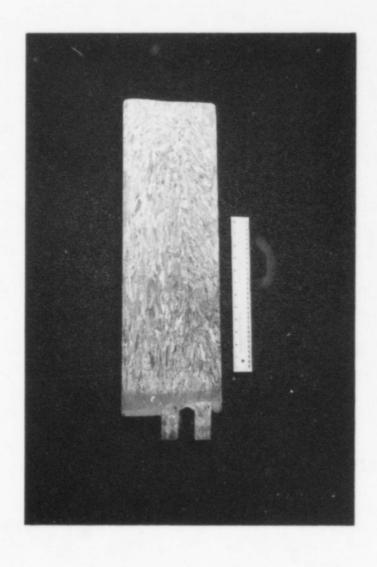


Fig. 4. Macrostructure of ASR titanium ingot.

ELECTROWINNING OF TITANIUM FROM SULFURIC ACID TITANIUM SOLUTIONS

Sandra L. Bribiesca, Eugenia S. Contreras, Francisco J. Tavera

Instituto de Investigaciones Metalúrgicas.

Universidad Michoacana de San Nicolás de Hidalgo.

Morelia, Mich., 58000, México.

ABSTRACT

Electrowinning of titanium from sulfuric acid titanium solutions has been studied at temperatures between 298 and 343 K, sulfuric and concentrations between 0.5 and 3.0 M and current density between 500 and 700 A/m^2 . Experiments have shown that titanium can be efficiently recovered on the cathode however, the recovery efficiency is decreased by iron dissolved in the electrolyte. Acid concentrations and higher current densities werefound to dissolve the stainless steel anode. Thereby increasing the electrolyte iron content. Apparent activation energy has ---been estimated in 26.8 KJ/mole.

INTRODUCTION

Hidrometallurgy, as it applies for extraction of primary materials from their natural resources, becaming important as a result of control over environmental pollution.

The main disadvantage of hydrometallurgical processes is the --high cost in terms of energy requirements and the relatively --long term for process operation.

The present work is carried out in order to study the electrowinning of titanium from weak sulfuric and leaching solutions under high current densitie, and controlled temperature and acid concentration conditions.

EXPERIMENTAL

Experimental materials were prepared by means of chemical reagents. Sulfuric acid solutions were prepared to give the desired acid concentration, i.e. 0.5, 1.0, 2.0 and 3.0 M. Titanium was added to the experimental solutions in such ammount to givea concentration equivalent to 3 Kg/m^3 .

Titanium '92 Science and Technology Edited by F.H. Froes and I. Caplan The Minerals, Metals & Materials Society, 1993 The electrowinning wxperiments were carried out in a temperature controlled electrolitic cell with stainless anode-cathode pair.—Current density values were fixed at values of 500, 600 and 700- A/m^2 . The anode-cathode apacing was cm.

The experiment was followed by taking samples of electrolyte toanalyse the titanium concentration at given periods of time.

RESULTS AND DISCUSSION

In the present work, experiments consisted essentially of -passing an electric current through an electrolytic cell which -contains a sulfuric acid-titanium solution to deposit titanium - on a stainless steel cathode under constant current density. The kinetics of the reaction system is followed by taking electrolyte samples at given periods of time in order to be chemically analyzed.

Figure 1 shows the experimental points and the best fit lines in this work, as the fraction of electrowon titanium as a function-of the experimental time for different current density values — which are imposed. It has been observed that the deposit rate decreases markedly as current density is increased from 500 A/m²—to 700 A/m² which is not in according with such an expected behaviour. During the electrowinning process, the stainless steel anode dissolves into the aqueous phase, and the anode components—in solution increase their concentration as time runs and as current density value is increased. Thus, this peculiar electrowinning behaviour in terms of the titanium recovery on the cathode can be related to the increase in the resistance to titanium—transport to reach the cathode as iron and other anode component concentration increases in the electrolyte.

Figure 2 shows the observed behaviour of titanium during its e-lectrowinning under different sulfuric acid concentrations of electrolyte. In general, the experimental results have shown that
the rate of titanium recovery decreases as the acid concentra--tion increases. This fact is consistent with the transport resis
tance increase as acid concentration in the electrolyte is in--creased.

These experimental data suggest that the rate of titanium recovery on the cathode increases to a maximum value and then it de---creased as acid concentration increases as a result of the competition between conductance and resistance of the electrolyte.

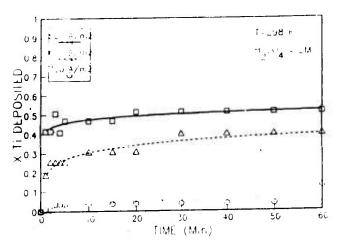


Fig. 1 – Effect of current density on the recovery of litanium at 298 K.

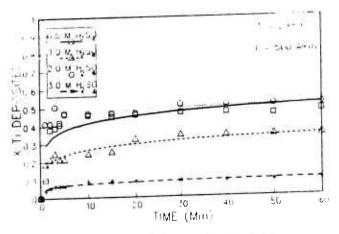


Fig.2. - Acid concentration effect on the recovery of Titanium at 298 K.

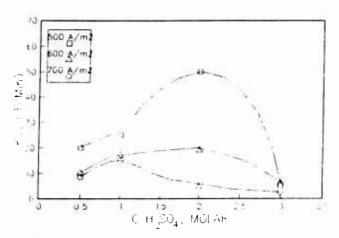


Fig.3.—,Effect of act concentration on the electrowinning rate of litaniam.

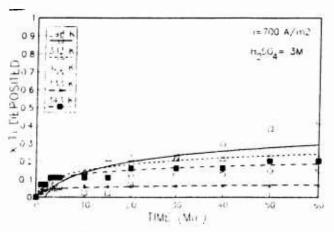


Fig. - Temperature effect on the effects winning of Intamum

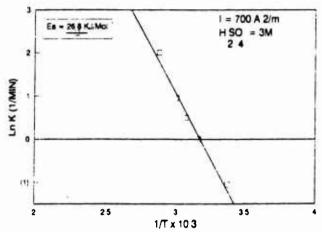


Fig.5.- Arrhenius plot for electrowinning of Titanium.

This behaviour can be seen in Figure 3, where the rate of titanium recovery is plotted as a function of the electrolyte acid concentration. This behaviour is much more clear as the current-density decreases due to the much lower anode dissolution.

The experimental results have shown that under the present process condition the system is not very sensitive to temperature. Figure 4 shows the experimental results plotted as the fraction-of recovered titanium on cathode for each experimental temperature as a function of the experimental time. It can be seen that the general behaviour of the reaction system shows that the annount of titanium on cathode increases as temperature is decreased. From the experimental measurements the rate of titanium recovery is plotted in Figure 5 as the Arrhenius relationship. The apparent activation energy of the process is estimated in 26.8 - KJ/mole.

CONCLUSIONS

Electrowinning of titanium at temperatures between 298 and 343 K, sulfuric acid concentrations between 500 and 700 A/m^2 has shown the following:

- (1) The rate of titanium recovery on cathode increases with decreasing current density and acid concentration due to the decrease in iron concentration in electrolytes.
- (2) The rate of titanium recovery on cathode increase with in--- creasing temperature from 298 to 343 K.
- (3) Apparent activation energy for titanium recovery on cathodehas been estimated in 26.8 KJ/mole.
- (4) The experimental observations suggest that in order to avoid poisonning the electrolyte it is required to use inert anodes, i.e. antimonial lead.

CHARACTERISTICS OF NIOBIUM-ALUMINUM MASTER ALLOY

FOR PRODUCTION OF ADVANCED TITANIUM ALLOYS

Edward A. Loria

Niobium Products Company Inc. Pittsburgh, Pennsylvania A Subsidiary of CBMM, São Paulo, Brazil

Abstract

As a master alloy for niobium bearing titanium aluminides and other advanced titanium alloys, the aluminothermic reduction (ATR) of high-purity niobium oxide to nominal 70Nb-30Al has been produced in the largest single quantity heat (1500 lb.) for consistent quality. The crushed product contained very low dissolved gas content and residual elements. An in-depth analysis and the effect of plasma arc remelting (PAR) of the ATR product was made via optical, SEM, EDS, and X-ray diffraction. The microstructure was dendritic with approximately 67 pct. NbAl3 as the matrix phase and 33 pct. Nb2Al as the second phase per x-ray diffraction, SEM and EDS. Microhardness measurements revealed that the Nb2Al was harder than the NbAl3 phase, (696 vs. 557 VHN). PAR of the ATR product resulted in a much finer structure. cleanliness of both products was very good. Only a small number of inclusions were observed which were cuboidal in shape and EDS analysis revealed that they were rich in Al and Mg, indicating the spinel MgAl204. A demonstration VAR ingot of Ti-24A1-11Nb produced from a compacted electrode of ATR 70Nb-30A1 particles and Ti sponge was split longitudinally through the center and it contained no undissolved particles of this master alloy.

Introduction

The production of niobium bearing titanium aliminides, such as 2411 with 20 wt. pct. Nb, and the Beta 21S alloy, with 3 wt. pct. Nb, should require the addition of consistent quality and higher purity Nb-Al master alloy for blending with high grade Ti sponge for the vacuum arc remelting (VAR) operations. Thus, the degree of cleanliness on hard alpha and inclusions desired by end-users via electron beam cold hearth remelting (EBCHR) and plasma arc remelting (PAR) can be obtained. This paper describes the aluminothermic reduction (ATR) of high purity niobium oxide to nominal 70Nb-30Al in the largest single quantity heats ever produced (1500 lb. at a time) so that a consistent quality level is produced, and it presents an in-depth microstructural analysis of this ATR product and the effect of PAR of the ATR product.

In order to eliminate atmospheric pollution and minimize the impact of cost, CBMM³ has now installed a new semi-continuous autothermic reduction process for producing ferroniobium in a stationary covered reactor that

Titanium '92 Science and Technology Edited by F.H. Froes and I. Caplan The Minerals, Metals & Materials Society, 1993

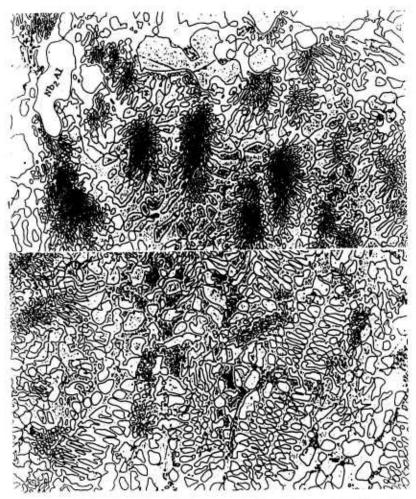


Figure 1. Optical microstructure of ATR 70Nb-30A1 product at X200.

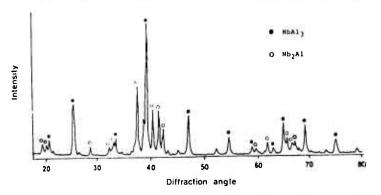
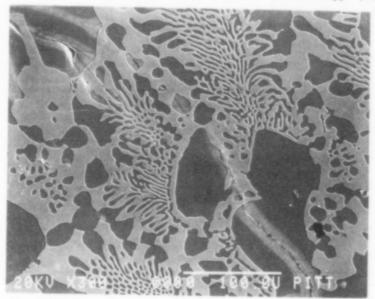


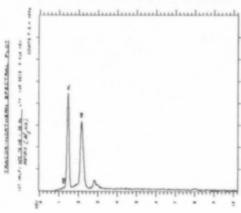
Figure 2. X-ray diffraction patterns of NbAl₃ and Nb₂Al phase in ATR 70Nb-30Al.

resembles a normal electric arc furnace. However, the standard process for making ferroniobium from pyrochlore concentrates is a batch process based on aluminothermic reduction (ATR). The CBMM Araxá facility is the largest in the world in terms of reactor size, quantity of Al powder used and tons of alloy produced by each of six daily reactions (11 tons). ATR Nb-4 to 6 pct. Al feed production of 70Nb-30Al is an extension of this practice. The reduction is accomplished in a smaller reactor and the quality of this ATR product, in terms of interstitials, is dependent upon the Al content; the higher the Al the lower the oxygen content.

Material and Procedure

The crushed ATR product analyzed 69.6 pct. Nb-29.6 pct Al and contained very low dissolved gas content of 45 ppm $\rm O_2$, 55 ppm $\rm N_2$, 10 ppm $\rm H_2$, with the other significant elements being <10 ppm S, <40 ppm P, 0.01 pct. Si, 0.01 pct. C and 0.15 pct. Fe. The overall microstructure after ATR and then after PAR was examined via optical and scanning electron microscopy (SEM). Energy





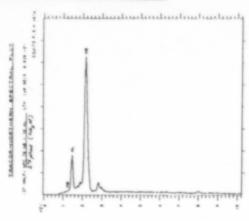


Figure 3. SEM of ATR 70Nb-30Al at X300 and EDS spectral plots of NbAl₃ and Nb₂Al phases.

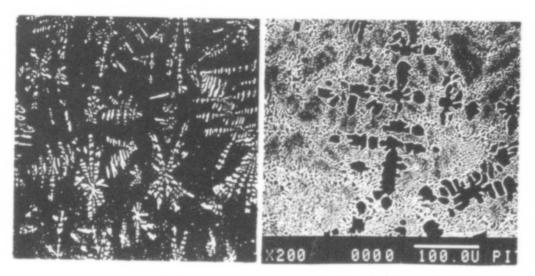


Figure 4. Optical microstructure of ATR 70Nb-30Al after PAR at X150 and SEM at X200.

dispersion spectrometry (EDS) and x-ray diffraction analysis were used to determine the chemical and phase(s) compositions of the matrix and second phase constituents. In addition, the microhardness and volume fraction of the individual microstructural components were determined.

Results

The overall microstructure of ATR 70Nb-30Al is shown in Figure 1. The structure can be described as dendritic and composed of the NbAl $_3$ matrix and interspersed Nb $_2$ Al phase which appeared in a different tone in the original color photomicrographs at 200 and 600x magnification. X-ray diffraction analysis revealed that the dendritic structure was composed of two phases; NbAl $_3$ and Nb $_2$ Al, as seen in the x-ray diffraction pattern of Figure 2. Also, SEM and EDS examination confirmed that the matrix is NbAl $_3$ and the second phase is Nb $_2$ Al, per Figure 3. The percentage of each microstructural component by Quantomet is approximately 67 pct. NbAl $_3$ and 33 pct. Nb $_2$ Al, with \pm 4.2 experimental error. Microhardness measurements indicated that the second phase Nb $_2$ Al is harder than the matrix NbAl $_3$ phase, the respective values being 696 vs. 557 VHN.

The purpose in the PAR processing of a portion of the ATR product was to ascertain if the dendritic structure could be refined by this secondary operation. By combining superheat to eliminate low-density inclusions and melting on a copper hearth to remove high-density inclusions, plasma yields a very clean fine-grained product, and it maintains the chemical composition of the alloy. 5 As seen in Figure 4, the dendritic structure of the ATR product was refined by PAR. In general, the cleanliness of both the ATR and PAR product was very good, only a small number of inclusions were observed. chemical composition and morphology of the inclusions in the ATR product are shown in Figure 5. The inclusions are cuboidal in shape and EDS analysis revealed that they are rich in Al and Mg, maybe forming the spinel MgAl204. Inclusions and gas content would be inherent in the quality of the niobium oxide, the ATR practice and the amount of Al in the ATR product. example, an ATR 90Nb-10Al contains a much higher dissolved gas content of 270 $\mathrm{ppm}\ \mathrm{N}_2$ and 1700 $\mathrm{ppm}\ \mathrm{O}_2$ which could contribute hard alpha and inclusions in the remelting operations that produce advanced Ti alloys.

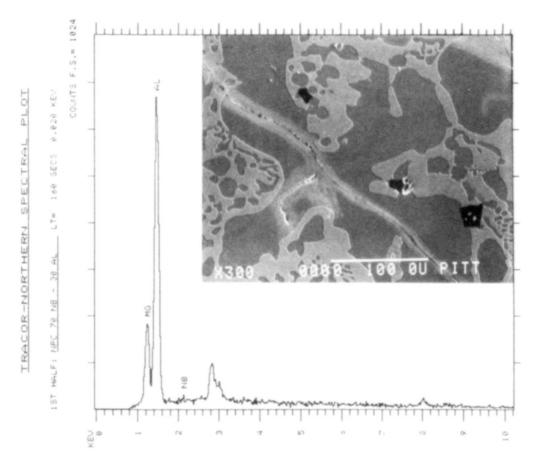


Figure 5. SEM of ATR 70Nb-30Al cuboidal inclusions at X300 and EDS spectral plot revealing Al and Mg content.

The ATR 70Nb-30Al product was ball-milled, without difficulty, to -140+325 mesh powder and is being used as a master alloy addition in the development of Ti-Nb and Nb-Ti alloys. To qualify for Nb-bearing titanium aluminides, a demonstration ingot of nominal 4 in. diameter x 6 in. length of 2411 alloy was cast by VAR of a consumable electrode consisting of the proper particle size relative to the Ti sponge. A macroetch of the longitudinal slice through the center of the ingot is depicted in Figure 6. Any undissolved master alloy particles would act like high-density inclusions or hard alpha particles. In the preparation of this ground/polished surface, they would stand-up as tiny ridges or rough spots felt by hand. Also, the operator did not hear any "clicks" during the surface preparation which would occur if they were present. The macroetch did not reveal any such undissolved particles either visually or under binoculars. It shows the typical elongated grains originating from the starting stub (bottom) and from the water-cooled Cu container, plus the crystallization of smaller, equaaxed grains in the center, upper-half of the VAR ingot.

References

1. R.G. Rowe, Advanced ${\rm Ti}_3{\rm Al}$ -Base Alloy Property Comparison, Synthesis, Processing and Modeling of Advanced Materials, to be published in Conf. Proc. ASM International, Paris, France, September 1991.



Figure 6. Macroetch of longitudinal, center section of 4 in. diam. by 6.25 in. long demonstration ingot of Ti-14Al-2lNb produced by VAR of compacted electrode of Ti-sponge and 70Nb-30Al master alloy. Composition is Ti-16.1Al-20.4Nb-0.15Fe-0.1350₂-0.005N₂-0.013C. Actual size.

- P. J. Bania, Next Generation Titanium Alloys for Elevated Temperature Service, ISIJ International, 31 (8) (1991), pp. 840-847
- R. de Fuccio et al, New CBMM Process Eliminates Pollution, NPC Update (5) (November 1991). To be presented at Infacon 6, Capetown, South Africa, March 1992.
- E.W. Betz and H.S. Moura, New EB Production Furnace High Purity Niobium in Brazil, Electron Beam Melting and Refining, Bakish Conf. Proc., (5) (October 1989).
- W.R. Chinnis and R.C. Eschenbach, Plasma Hearth Melting of Seeded Titanium, Electron Beam Melting and Refining, Bakish Conf. Proc., (4) (November 1988).

TITANIUM ALLOY HEARTH MELT TECHNOLOGY

C.E. Shamblen, W.H. Buttrill, and G.B. Hunter

GE Aircraft Engines 1 Neumann Way Cincinnati, Ohio 45215-6301

Abstract

HM (Hearth Melt) refining of titanium alloys for premium quality gas turbine engine rotating components is now a demonstrated production process. Production of rotating components using the EBM+VAR (Electron Beam Cold Hearth Melt plus Vacuum Arc Remelt) process has been in progress since 1988; the PAM (Plasma Arc Cold Hearth Melt) + VAR process was qualified as having acceptable refining capability in 1991. The need for these Ti alloy HM processes was fully described in a prior publication; it is only summarized here that the necessity is to minimize the probability of premature gas turbine engine component failures caused by melt related inclusions. The refining advantage that the HM processes offer over the prior premium quality triple VAR process is their enhanced capability to eliminate the melt related HID's (high interstitial defects) and HDI's (high density inclusions). This paper considers the initial production introduction of the EBM+VAR process and the qualification of the PAM+VAR process as background technology for the more advanced EBM "only" and PAM "only" processes. These more advanced processes, which involve elimination of the VAR step after hearth melting, are being demonstrated under a USAF ManTech Program (F33615-88-C-5418). The current status of the EBM "only" and PAM "only" process demonstrations is described.

Introduction and Background

Since GEAE's (GE Aircraft Engine's) initial 1989 publication⁽¹⁾ on the development of HM (Hearth Melt) processes for refining Ti alloys, continuous progress has been made toward the introduction and further devolopment of these processes as described herein.

The initial production HM material as indicated in Figure 1 was EBM+VAR Ti-6-4 (Ti-6Al-4V) bar produced using a single hearth process⁽¹⁾. That material demonstrated production capability using the first AJMI (Axel Johnson Metals, Inc.) EBM furnace. Subsequent bar production heats were produced using the first generation dual hearth process; that process was developed to enhance the ability to eliminate melt related inclusions. Advanced dual hearth designs include two major features: a longer hearth length for increased inclusion-elimination residence time, and a shield to prevent ballistic particle transport directly to the ingot mold. The issue

Titanium '92
Science and Technology
Edited by F.H. Fraes and I. Caplan
The Minerals, Metals & Motorials Society, 1993

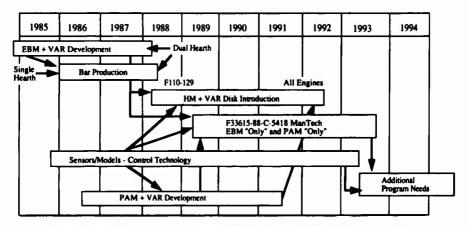


Figure 1 - GEAE Titanium Alloy Hearth Melt Development Strategy:
Hearth Melt + VAR → Hearth Melt Only

of the three remaining possible HID sources in the final VAR process was also addressed in the bar program; added requirements were placed on the VAR process to minimize these possible sources.

PAM+VAR process development was initiated at W-G (the Wyman-Gordon Company) in 1986 and at T-A (Teledyne Allvac) about a year later. T-A's facility has recently been qualified for PAM+VAR production; W-G's qualification efforts have been delayed because of the multiple goals for that facility. Based on T-A's qualification, PAM+VAR entered HM+VAR introduction in 1992.

Concurrent with the HM process development efforts, programs were initiated to develop sensors and models for improved EBM and PAM process control. Significant progress has been made in establishing sensors to monitor the molten pool surface temperature, a critical parameter for the inclusion elimination mechanisms. Development of the advanced molten hearth models for assessment of parameter changes on the inclusion removal mechanisms has been more challenging, but recent progress has been achieved.

All of these combined technologies led to GEAE's decision to introduce the HM+VAR process for production of rotating disk, spool and shaft Ti alloy components in 1988. Typical of any new production process, a few early learning curve issues were encountered, but the process capability has subsequently been established to allow reasonably uneventful HM+VAR production. Production introduction has now expanded to include all military and commercial engines (mid 1992). Approximately two million kg of HM+VAR ingot have been evaluated through the end of 1991; no HID's or HDI's have been found in any of that product produced by qualified sources.

HM "Only" Technical Approach

The major objective of the USAF ManTech Program is to establish new processes that will produce Ti alloy materials which are significantly free of HID's and HDI's while retaining freedom from type II (Al) segregation and beta flecks. Achievement of that objective is being demonstrated using two HM "only" processes, EBM and PAM, to produce two alloy types: Ti-6-4 and an advanced alloy such as Ti-6246 (Ti-6Al-2Sn-4Zr-6Mo) or Ti-17 (Ti-5Al-2Sn-2Zr-4Mo-4Cr).

The potential advantages of the HM "only" processes compared to the triple

VAR and HM+VAR processes are: (1) further cleanliness improvement, (2) finer ingot structure, and (3) reduced costs. The further cleanliness improvement comes from eliminating the three HID sources in the final VAR step of the HM+VAR process. The finer ingot structure produced by the shallower HM ingot pool offers promise to: (1) minimize solidification segregtion, (2) enhance non-destructive (ultrasonic) test capability, and (3) enhance low-cycle fatigue properties. The cost reduction comes from eliminating the final VAR step in the HM+VAR process.

The recently completed Phase I efforts involved producing and evaluating fifteen subscale heats as shown in Table I. While these are designated subscale heats, they ranged in size from 1260 to 4430 kg (432 to 660 mm diameter) and were produced using full scale HM practices. Ti-6-4 and Ti-6246 EBM heats were produced; AJMI already had demonstrated Ti-17 alloy production capability. The PAM heats involved predominantly producing the Ti-6-4 and Ti-17 alloys; T-A preferred gaining experience on Ti-17 since it was the selected Phase II advanced alloy.

Objectives were designated for each heat series as shown in Table I. The 1st and 2nd series heats were used to establish the melt process for each alloy in each melt practice. The major evaluations for these heats involved: (1) monitoring the HM parameters such as heat input, molten pool temperatures, casting rate, etc., (2) evaluating the hearth skull and ingot mold pool profiles, and (3) establishing billet quality and yield. The 3rd series of heats were directed at a proof-of-concept seed-elimination experiment for each alloy in each melt process. Seeds were added to these heats at the industry established seeding level⁽²⁾ using inclusions known to form either HID's or HDI's. The entire ingot was processed to billet and bar to inspect ultrasonically for any surviving seeds for these heats. The 4th series of heats were directed at the economic issue of using lower cost revert input materials.

EBM "Only" Technical Progress

Numerous capability and producibility issues were investigated using the seven EBM "only" heats listed in Table I. All seven heats were produced at AJMI in their first EBM furnace using standard hearth configurations for EBM+VAR production. The ingots were converted to billet or bar for evaluation by the RMI Titanium Company. The major emphases of the evaluations were placed on composition control, billet integrity, and process yield. While EBM refining capability was addressed during EBM+VAR development work, further investigations were needed for better definition of the process limits. EBM process parameters, some requiring special sensor systems or evaluation procedures were monitored for comparison between heats, to assess improved control needs, and for application in advanced process models.

Table I Phase I Subscale Heats

Heat Series/Objective	EBM "Only"		PAM "Only"		
	Ti-6-4	Ti-6246	Ti-6-4	Ti-6246	Ti-17
1st/Process Evaluation	E4-1	E6-1	P4-1W	P6-1W	P7-1T
2nd/Process Evaluation	E4-2	E6-2	P4-2W		P7-2T
3rd/Proof-of-concept	E4-3	E6-3	P4-3T		P7-3T
4th/Revert Material	E4-4		P4-4T		<u></u>

Composition Control

Based on the EBM+VAR development work(1), it was known that EBM "only" ingot composition control would be challenging. The high vacuum required for EBM operation protects the molten metal from atmospheric contamination and reduces the hydrogen content, but it also causes the selective vaporization of high vapor pressure alloy elements, such as Al. As demonstrated by AJMI in commercial EBM+VAR production, achieving composition aims for a given set of EBM process parameters is an empirical process. Although it is difficult to meet composition aims for experimental heats with unusual operating procedures, the "steady-state" portion of each subscale heat was within the specified compositional ranges as shown in Figure 2. Furthermore, the compositional variations were acceptable from center to edge across the billet slices.

Before ingot casting begins, vaporization can excessively deplete Al from the pools as they are being established in the hearths. This material can produce an ingot bottom with a below specification Al content, as shown in Figure 2, resulting in a significant process yield loss. In heats outside the program, and in later program heats, AJMI demonstrated pool formation procedures that prevent this Al depleted region.

After ingot casting stops, beam power is reduced gradually in the ingot mold. Evaluations in this program have shown that this "hot top" practice minimizes voids and segregation in the billet due to shrinkage cavities near the ingot top. Without a hot top practice, the cavities can extend about 200 mm from the ingot top as shown in Figure 3. While the cavities have been essentially eliminated by long duration hot top practices, the resulting Al depletion was unacceptable as shown in Figure 2 for Heat E4-3. A balance between minimizing cavity formation and Al depletion appeared to be achieved in some heats. This practice would minimize the ingot top yield loss. The full scale heats of Phase II will be used to demonstrate whether this balance can be maintained with larger ingot diameters.

Because melt rate is inversely proportional to pool residence time, it directly affects both selective vaporization and inclusion elimination capability. Rough measurements of casting rate, which approximates melt rate, indicated typical process variations of about $\pm 30\%$. While experience has indicated that this is an adequate level of control, improved melt rate monitoring and control practices are being developed.

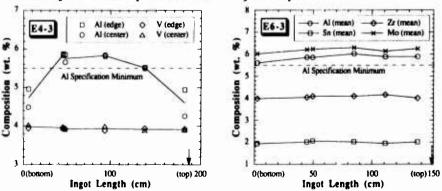


Figure 2. EBM Fillet compositions. Only the central portion of Heat E4-3 has acceptable billet homogeneity; modified procedures in Heat E6-3 achieved acceptable top to bottom homogeneity.

Billet Integrity

No inclusions or segregation were found in the 1st and 2nd series unseeded heats for both alloys. Likewise, no surviving seeds or segregation were found in Heat E4-3 billet and bar, demonstrating full inclusion elimination capability for Ti-6-4. HID's attributed to ten surviving nitrided sponge seeds were found in Heat E6-3. No inclusions were found in similar seeded heats conducted outside of the ManTech program with Ti-17⁽¹⁾, an alloy with similar thermophysical properties to Ti-6246. Investigations indicate that the survival mechanism is related to the solid electrode feedstock preparation used for Heat E6-3; this mechanism did not exist for the compacted particulate feedstock used in the Ti-17 heats. Although this is

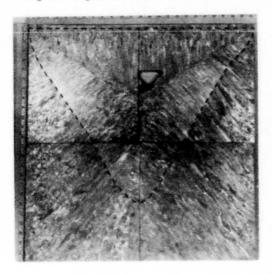


Figure 3. Macroetched axial slice of the E4-4 EBM ingot top. The 470 mm deep pool (outlined) helps to produce a fine billet macrostructure.

a much lower seed survival rate (about 0.4%) than that for the triple VAR process of about 8%⁽¹⁾, work to eliminate this mechanism continues.

Six HID's also were found in Heat E4-4; they were associated with flame-cut VAR crown revert feedstock that is not allowed for current premium quality applications. This is again a much lower incidence than expected for triple VAR, but proves that current restrictions against using such feedstock cannot be relaxed without further development. The HID survival also was associated with HM pour interruptions. As a result, limits and precautionary procedures are being developed for process interruptions.

Vaporized metals in the furnace condense on the cold chamber surfaces to form dense deposits enriched in high vapor pressure elements, in some cases exceeding 50 wt % Al. There is a concern that, without the

subsequent VAR process, deposit pieces that fall into the ingot mold pool could survive to form a segregated region in the EBM "only" ingot. Many such fall-in occurrences were observed, particularly during Heat E4-1, without any associated segregated regions being found in the billet inspections. One cracked segregated region found in billet ultrasonic inspection of Heat E6-3 may have been caused by an unusual deposit from a viewport used only in experimental trials; that possible source has been eliminated. AJMI has demonstrated, and continues developing, practices that greatly reduce occurrences of deposits falling into the ingot mold.

The 152 mm diameter billet macrostructure and microstructure of the subscale heats were equivalent to, or finer than, commercial triple VAR or HM+VAR billet. This is attributed to having less ingot mold pool volume for EBM as shown in Figure 3 than for VAR. Billet structures produced by various conversion practices indicate that additional refinement of billet structure and reduced noise for ultrasonic inspection might be possible.

Process Yield

Based on the subscale results, full scale EBM "only" melting and conversion

yields should be at least equivalent to current commercial experience. Ingot sidewall improvements noted with increasing ingot diameter indicate that full scale ingots can be made with standard EBM "only" procedures that will not require significant sidewall conditioning losses.

PAM "Only" Technical Progress

The PAM approach to melting of Ti alloys is being pursued by several primary titanium suppliers. T-A and W-G have been involved in the USAF ManTech Program and have each melted heats that were planned as a part of the Phase I effort. Eight heats have been melted that ranged in weight from 1475 to 3810 kg. The three heats melted at W-G were 610 mm in diameter and are coded by the letter W in Table I; the five heats melted in T-A were 660 mm diameter and are similarly coded by the letter T. the planned Phase I heats have been melted and evaluated. learned about PAM of Ti alloys. Key capabilities of the process have been identified and key technical issues that are the focus for further efforts toward the implementation of PAM "only" product are being resolved. Space does not allow a full description of all of the pertinent Phase I information; thus, the option was taken to summarize the capabilities and issues identified in the work to date. These capabilities and issues are grouped into the same three broad categories previously discussed in the EBM section: composition control, billet integrity and process yield.

Composition Control

The PAM process evaluations conducted to date under the ManTech Program have shown excellent reproducibility of the raw material composition in the ingot and billet. Chemical analysis of Heat P7-1T was performed at five locations along the billet length, and at the center and surface at each location. The results indicated that all the metallic elements averaged within 0.1 wt% of the target chemistry with a standard deviation of generally less than 0.05 wt%. Earlier program heats that did not achieve the same target accuracy were determined to be the result of the physical characteristics and deblending of the input material blend. In an effort to expand the confidence for reproducibility of composition, a short melt was conducted using billet produced from Heat P6-1W. The short ingot stub produced in this effort was analyzed for chemistry and determined to be within 0.1 wt% of the values previously measured in the billet.

Hydrogen content measured at the billet stage for the early PAM heats have been between 100 and 350 ppm. It has been determined that the PAM furnace atmosphere has a significant influence on the hydrogen content of the ingot produced, and that billet conversion can be expected to add as much as 40 to 50 ppm hydrogen to the product. Significant progress has been achieved in controlling the hydrogen content of PAM "only" material in this program. Heat P7-1T, which was the first PAM Ti-17 heat in the industry, contained approximately 225 ppm hydrogen after billet conversion. This heat and the second PAM Ti-17 heat, P7-2T, were both melted using just sponge and master alloy. Heat P7-2T contained only 60 ppm hydrogen at the ingot stage, and averaged 85 ppm hydrogen as 152 mm diameter billet. The significant change to the PAM process to reduce the heat hydrogen level was to scrub hydrogen from the helium gas atmosphere as it passed through the recirculation system. The subsystem used to scrub hydrogen was operated in a manual mode for Heat P7-2T, and has since been automated.

In summary, efforts conducted under the ManTech program have shown that PAM reproduces input material composition very effectively. With some additional control development and possibly some fine tuning of the

conversion processes, PAM "only" billet will also be capable of meeting the specified hydrogen content.

Billet Integrity

The general subject of billet integrity is broad and includes issues such as: inclusions (HID's and HDI's), voids (both evacuated and gas filled), and structure (micro and macro). T-A has effectively demonstrated total inclusion elimination from Ti-6-4 using PAM; T-A's separate paper discusses the details of these demonstrations.

Clean voids have been observed in PAM billet material evaluated in this Their occurrence has been associated with shrink cavities resulting from an irregularly shaped molten pool pattern in the ingot. The torch pattern over the ingot for Heat P6-1W allowed the solidification of an island in the center of the pool and created shrinkage voids at the bottom left side of the molten pool as shown in Figure 4a. The torch pattern in this instance had been preferentially directed at the edge of the ingot in an attempt to enhance the ingot surface condition. Billet from this heat exhibited clean voids in the location of the shrink porosity. The torch pattern was modified for subsequent heats to yield a typical ingot molten pool as shown in Figure 4b. No clean voids were found in the billet for any other heats in Phase I. The potential for gas filled voids in PAM "only" material exists; however, none have been observed. More direct and definitive approaches to assessment of the level of risk associated with the occurrence of clean voids, both evacuated and gas filled, are being considered. Such approaches could include extensive bar production or extensive large-bar low-cycle fatigue testing.

The macrostructure of PAM "only" converted material is typically finer than that of PAM+VAR or triple VAR material given the same conversion practice. This observed macrostructural refinement is apparently a result of a smaller ingot grain size. No microstructural anomalies have been observed beyond that of the early clean void porosity for PAM "only" billet material, nor are they expected since microstructural features are generally a function of conversion and heat treatment rather than melting.

Process Yield

Process yield has not been fully assessed in the ManTech Program because of

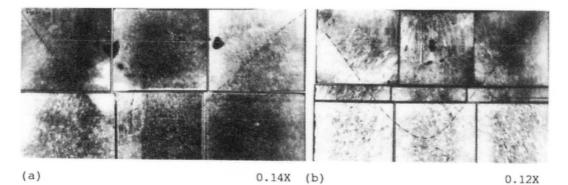


Figure 4. Ingot mold pool profiles for (a) Heat P6-1W and (b) Heat P4-2W. Improper PAM torch patterns (a) can cause ingot microshrink cavities that result in clean voids in the billet. Proper torch patterns (b) eliminate these clean voids.

competing objectives. Specifically, in each heat except the last two, the top of the ingot was not hot topped; it was marked with copper during the final stages of melting and removed prior to conversion for analysis of the steady state molten pool. Removal of the top of the ingot creates a relatively low aspect ratio ingot which is not optimum for yield. The Phase II full scale heats will provide the best opportunity to quantify yields.

Significant features of the process which affect yield and economics can also be identified from the work done on this program. There are almost no losses of raw material in the melting cycle. Given a constant skull weight, the inqut weight resulting from a melt cycle is generally within 1% of the raw material input weight. Present experience shows the surface finish of a PAM "only" ingot is not as good as a PAM+VAR ingot and requires significant conditioning prior to conversion. The shoe required for PAM ingot retraction is also a significant loss to PAM "only" yield. primary yield losses for PAM "only" may be offset to some extent by a reduced molten pool depth at the top of the ingot which will require less cropping during conversion than a PAM+VAR heat. The discussion of product yield is ultimately directed to consideration of process economics. Offsetting the potentially reduced yield in an economic balance will be the avoidance of the cost associated with a subsequent VAR cycle. Further, although it is almost impossible to quantify, the increased product integrity offered by avoiding potential HID occurrence in the final VAR will also be a key economic consideration.

Conclusions

The two million kg of HM+VAR production ingot has demonstrated that hearth melting of Ti alloys is a viable production process; improved freedom from melt related HID's and HDI's has been found in that product compared to current triple VAR material. While most of the HM+VAR production to date has been made by the EBM+VAR process, very encouraging results were obtained for the PAM+VAR process during the qualification demonstrations. Ongoing development efforts directed at HM "only" technology for the EBM and PAM processes have defined issues which must be resolved before these can likewise be considered for production introduction. However, no issues have yet been defined which are not resolvable via reasonable process modifications or enhanced process definition and control.

Acknowledgements

The authors are grateful for the participation of numerous individuals at GEAE and at the subcontractors without whom this work would not have been possible. Gratitude also is extended to the USAF Manufacturing Technology Directorate, Wright Laboratory, for funding this program.

References

- C.E. Shamblen and G.B. Hunter, "Titanium Base Alloys Clean Melt Process Development," <u>Proceedings of the 1989 Vacuum Metallurgy Conference</u>, ed. L.W. Lherbier and J.T. Cordy (Warrendale, PA: Iron and Steel Society, Inc. 1989), 3-11.
- D. Malley and M. Belchak, "Standardizing Defects for Titanium Seeding Experiments," <u>Electron Beam Melting and Refining State of the Art</u> 1990, ed. R. Bakish (Englewood, NJ: Bakish Materials Corporation, 1990), 224-231.
- W.R. Chinnis and W.H. Buttrill, "Teledyne Allvac Plasma Cold Hearth Melting," Seventh World Conference on Titanium, in this publication.

INDUSTRIAL PRODUCTION OF HIGH PURITY TITANIUM

BY THE IMPROVED IODIDE PROCESS

Y. Yoshimura, Y. Shimizu, and Z. Imamura*

Osaka Titanium Co.,Ltd. 1,Higashihama-cho, Amagasaki, Japan 660

* Marusho Electro-heat Co.,Ltd. 26-1, Okada ,Himeji, Japan 670

Abstract

We have produced titanium of 99.999% purity on the 50-100kg per batch scale by the improved iodide process. Unlike the conventional wire filament process on a kilogram scale, we use high purity titanium tube as a deposition substrate. Iodide titanium deposits on an outer surface of the tube, while its inner surface is indirectly heated by a graphite heater. In this way deposition surface area is greatly enlarged by an order of two as compared with the conventional iodide process. A diffusion pump evacuates the inner part of the deposition tube at a pressure bellow 10^{-1} Pa to prevent contamination of titanium from the graphite heater.

1. Introduction

With the rapid increase in the degree of Large-Scale Integration (LSI) in recent years, dimensions of solid state electronic devices are getting smaller and smaller. As a result materials used in such devices require higher purity and strength. Due to the present demand for a remedy to the signal delay caused by the increase in electrode wiring resistivity and electromigration in fine metal interconnects, the focus is now being placed on refractory materials with lower resistance and higher purity, compared to the frequently used polysilicides. Metallic materials with the above properties which can be utilized as electrodes in LSI are molybdenum, tungsten, and titanium or their silicides. Among them titanium is particularly desirable due to its excellent specific strength, workability and corrosion resistance.

However, as an electrode material for semiconductors, titanium metal must be of very high purity. Impurities in titanium which affect the performance of LSI devices are alkaline metals (Na, K), radioactive metals (U,Th), and heavy metals (Fe, Ni, Cr). Impurity contents that are allowable for semiconductor materials are respectively Na, K < 20 ppbw, U, Th < 1 ppbw, and Fe, Ni, Cr < 1 ppmw. One of the typical methods of obtaining high purity titanium is the thermal decomposition of titanium iodides, which was first studied by Van Arkel and de Boer in 1925-1930⁽¹⁾. In the iodide process, the decomposition scheme is described as follows,

Titanium '92 Science and Technology Edited by F.H. Froes and I. Caplan The Minerals, Metals & Materials Society, 1993 A crude titanium reacts with iodine to form a titanium tetraiodide at temperatures of 500-800 K. The thermal decomposition of the titanium tetraiodide proceeds on a deposition substrate which is usually a wire-filament resistively heated at temperatures of 1400 to 1800 K. The iodine liberated returns for further reaction with the crude titanium. A series of reactions involving iodine go on in a cyclic way. Using the above process, high purity titanium can be easily obtained, however, its productivity is very low because of the use of a fine filament as the deposition substrate. Our aim is to develop a new technology for obtaining high purity titanium at high production rates with a lower decomposition temperature.

2. New technology for producing high purity titanium

2-1. Reaction conditions

In the conventional iodide process, titanium tetraiodide is directly decomposed to titanium, which causes high temperature decomposition at 1400-1800 K. On the other hand, titanium refining in our iodide process involves reactions of crude titanium with titanium tetraiodide, thereby synthesizing lower valent titanium iodides, and decomposing the lower valent titanium iodides to high purity titanium. The lower valent titanium iodides, i.e., Til2 and Til3, afford higher synthetic reaction temperatures and lower thermal decomposition temperatures, as compared with titanium tetraiodide. While the reaction mechanisms for the synthesis and decomposition of the lower valent iodides are indistinct, the reactions may be represented by the following equations:

The lower valent titanium iodides are synthesized at about 1000-1200 K. These iodides undergo thermal decomposition more readily than titanium tetraiodide, allowing the thermal decomposition temperature to be lowered to 1400-1500 K. Accordingly, the possibility of thermal decomposition of metal impurities contained in the iodides is more greatly reduced than that at higher decomposition temperatures.

2-2. Improvement of titanium productivity

The rate of titanium deposition is known to be limited by the diffusion of iodine and iodides, i.e.,natural convection in the reaction space (2). Therefore, to attain high titanium productivity, the enlargement of deposition surface area is needed. We used a titanium tube as a deposition substrate instead of a conventional wire filament. Titanium deposits on the outer surface of the tube, while the inner surface was indirectly heated by a graphite heater. The power supply to the tube was not affected by the deposition rate of titanium, and the uniform temperature distribution in the axial direction was attained. By evacuating the heater chamber with an oil diffusion pump, the deposited titanium was free from contamination from the graphite heater. Since the tube permits its diameter and length to be arbitrarily selected, the deposition surface area can be drastically increased in comparison with that of the filament. In addition, the change in the surface area is relatively small as the reaction proceeds, thereby it is easy to maintain the deposition conditions constant.

3.Experimental

3-1. Small scale production of titanium

Preliminary investigation of purification in the iodide process was carried out using a small scale reactor. Figure 1 shows the schematic outline of the apparatus. The reactor made of Inconel tube (250 mm I.D.x1000 mm length) was lined with Ta sheet on its inner surface to prevent corrosive reaction of iodine with Inconel. A titanium tube (43 mm O.D.x 700 mm length) was used as the deposition substrate. The tube was made of 99.998% pure titanium, and its thickness was 1 mm. The tube was heated to 1400 K by a graphite heater installed inside it. The tube was evacuated through a combination of oil diffusion and rotary mechanical pumps to prevent contamination from the graphite heater. About 50 kg of crude titanium was stacked cylindrically in the annular space between the reactor wall and the titanium tube.

Commercial titanium tetraiodide(99.7%) was used as a feeding material without further purification. Titanium tetraiodide was introduced into the reactor which was evacuated and heated to 1-10 Pa and 1150 K, respectively. In this way the titanium tetraiodide reacts with the crude titanium to form lower valent titanium iodides(Til2, Til3). The iodides were transported to the surface of decomposing tube by gas diffusion, and high purity titanium deposited on the outer surface of the tube. By-products(iodine and Til4) again react with the crude titanium to form subiodides. The titanium tetraiodide and subiodide gases repeated these reactions as they traveled up within the reactor and were finally condensed and captured by a trap which was cooled with liquid nitrogen.

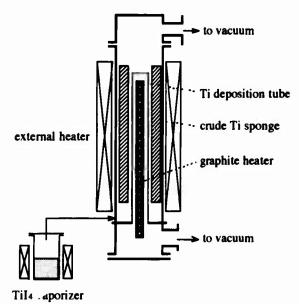


Figure 1 - Schematic outline of the small scale reactor

Starting with the crude titanium sponge of 99.98% purity, the reaction was kept 200 h. We obtained 6.2...g polycrystalline titanium deposit, part of which is shown in Figure 2. Its thickness was about 12 mm and the deposition rate was $1 \mu m/min$. We melt the titanium deposit together with the original substrate by an Ar plasma arc. The analyses of various impurities in the crude

titanium sponge and the titanium deposit are given in table I. Refining effect was prominent especially for Fe, Ni, Al, and O. Carbon contamination from the graphite heater was negligibly small.

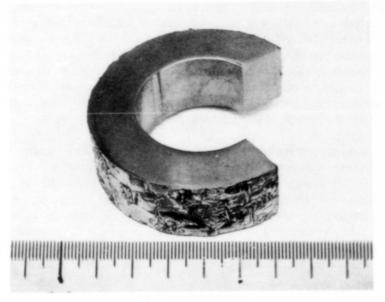


Figure 2 - Titanium deposit produced by the small scale reactor

Table I Typical analysis of crude titanium sponge and deposited titanium

Element	crude Ti sponge(ppm)	deposited Ti(ppm)	
Fe	50	0.5	
Ni	15	0.1	
Cr	8	0.4	
Al	7	1.1	
Si	3	0.4	
Na	< 0.02	< 0.02	
K	< 0.02	< 0.02	
U	< 0.001	< 0.001	
Th	<0.001 <0.00		
C	30	30	
Н	<10 <10		
O	300 80		
N	10	10	

3-2. Large-scale production of titanium

Based on the results of the small scale reactor, we made a design for large scale apparatus with titanium productivity of 50-100 kg/Bt. The flowsheet was similar to that employed for the small

scale. The reactor was made of SUS, whose diameter and height were 500 mm and 2700 mm, respectively. The titanium deposition tube (210 mm O.D.x 2000 mm length) was hung and fixed with its upper flange being sealed. The tube was heated by a graphite heater using a three-phase transformer. The diameter ratio of the reactor and the deposition tube was small, as compared with that of the small scale one. As a result, the temperature of the crude titanium was strongly affected by the heat dissipated from the graphite heater and the temperature gradient from the deposition surface toward the titanium sponge became gradual. As the formation and decomposition of the iodides occur at different temperatures in the same reactor, it is necessary to make steeper temperature gradient toward the radial direction of the deposition tube. We lowered the temperature of outer surface of the reactor by air-cooling.

The titanium sponge was transformed to cylindrical-shape compact by compression and then stacked surrounding the deposition tube annularly. The temperature of the deposition tube, measured by a thermocouple attached to its outer surface, was kept at 1400 K. The surface temperature of the reactor gradually rose up to 1300 K without cooling. Forced air blowing was done to maintain the surface temperature below 1200 K.

We have started carrying out short-period titanium deposition experiments. Figure 3 shows a fraction of the deposited polycrystalline titanium. The experiment was conducted for 190 h, and we obtained 65 kg titanium deposit. The deposition thickness attained to 10-12mm, corresponding to the deposition rate of 0.9-1.1 μ m/min. The deposition rate of the large scale reactor was comparable to that of the small scale one. Preliminary chemical analysis indicated the following levels of impurities: Fe=1; Ni<1; Cr<1; Al<2; C=30; O=80; N=10 ppmw. Gaseous impurity contamination such as oxygen and nitrogen may be caused from leaks in the reactor or desorption of gases from the titanium compact. The longer the deposition period, e.g., 300-400 h, the lower the metallic impurity contents. The proportional ratio of the impurity content of original tube to deposited titanium is expected to come close to negligible, however a complete evaluation has not been made at current stage.



Figure 3 - Titanium deposit produced by the large scale reactor

4. Conclusion

An attempt was made to improve the productivity of high purity titanium by a newly developed iodide process. Unlike the conventional iodide process, we used a high purity titanium tube as a deposition substrate. The deposition surface area was able to be enlarged by an order of two, compared with the conventional wire filament process.

a) small scale reactor

Operation of 200 h produced a 12 mm thickness titanium deposit with a rate of 1 μ m/min. It weighed 6.5 kg. The deposit was observed to contain Fe=0.5 ppmw, Al=1.1 ppmw, O=80 ppmw, Na<0.02 ppmw, etc.

b) large scale reactor

Operation of 190 h produced 65 kg titanium deposit with a thickness of 10-12mm. The deposition rate attains to $0.9-1.1 \,\mu$ m/min. At the present stage we tried a short period operation, however, we can expect more than 100 kg titanium deposit in a period of 300 h.

5. References

- (1) A. E. Van Arkel and J. H. de Boer, Z. anorg. allg. u. Chem., 148(1925), 345
- (2)G. H. Kesler, Trans. A.I.M.E., 218(1960), 197

METAL MATRIX COMPOSITES

Titanium Based Composites T.W.Clyne' and H.M.Flower'

*Department of Materials Science and Metallurgy Cambridge University Cambridge CB2 3QZ, UK

> *Department of Materials Imperial College London SW7 2BP, UK.

Abstract

An overview is given of current work on particulate and fibre reinforced titanium alloys. Composite production methods are surveyed with emphasis on the influence of production method upon the development of the matrix-reinforcement interface. Particular attention is given to interfacial reaction effects, notably with SiC and TiB, and a brief survey of counter measures such as diffusion barrier coatings and close control of processing conditions is presented. The influence of matrix chemistry on these processes is discussed. An outline is given of the effect of coatings and reaction layers on the physical and mechanical behaviour of both the interfacial region and the composite as a whole. The composite properties covered include elastic constants and fracture behaviour.

Introduction

The worldwide interest in developing aerospace structural materials of increased specific strength and stiffness, together with enhanced high temperature strength and creep resistance has led to intensive research into intermetallic compounds on the one hand and metal matrix composites (MMCs) on the other. Titanium plays a key role in both these activities. In the case of MMCs the final microstructure, and hence mechanical properties, is dominated by the processes involved in the creation of the composite material itself and necessitates close control over the starting materials and the processes of production. The key problem lies in the conflicting requirements posed by the need to fully consolidate the metal/ccramic mixture and the avoidance of chemical interaction between the ceramic and metal (which are generally far from being in thermodynamic equilibrium with each other). The former is most easily achieved at elevated temperatures at which the deleterious chemical interaction is promoted. This review examines work on the development of titanium based MMCs since the last World Titanium Conference in Cannes with an emphasis upon the metal-ceramic interface, its reactions and effects on properties.

Titanium '92 Science and Technology Edited by F.H. Froes and I. Caplan The Minerals, Metals & Materials Society, 1993

Ceramic reinforcements

Ceramics are generally characterised by lower density, higher

Table I Selected Properties of Some Titanium Alloys and Ceramics

Materials	Youngs Modulus E(GPa)	Tensile Stress o _{max} (MPa)	Comp. Stress $\sigma_{\text{max}}(\text{MPa})$	Density ρ(g/cm³)	Specific Stiffness E/ρ(GPa.cm³/g)	Coef. of Expansion (x10 ⁻⁶ /°C)
C.P.Ti	105	480	_	4.51	23.6	7.6
T1-6A1-4V	110	925	_	4.65	23.7	9.54
Ti-15-3-3-3	112	850-1400	-	4.76	23.5	9.75
Ti-10-2-3	117	1250	-	4.65	25.2	8.8
TiB,	529	-	666.1	4.53	117.3	6.4
ZrB,	343.3	199	1579	6.10	56.4	5.5
SIC	450	450	1030	3.21	140.2	4.8
TiC	309	467	749	4.92	62.8	7.2
B ₄ C	483	446	2843	2.51	192.4	4.5
BN	85	-2.1	309	2,25	38	7.51
AlN	343.4	_	2060	3.30	104	5.64
Si,N,	385	170	549	3.20	124	2.5
TIN	78.3	-	1270	5.40	14.5	9.3
A1,0;	420	223	2940	4.00	105	8.3

stiffness and lower coefficient of thermal expansion than titanium alloys. Table I (1) compares these properties for a number of titanium alloys and ceramic types. The much higher specific stiffness of most ceramics is evident from this table with TiB₂, SiC and B₄C exhibiting the highest values. Strength levels are generally limited by the low toughness of the ceramics which produces a very high sensitivity to the presence of very small flaws. Application to MMCs is limited by both chemical reactivity and materials availability in appropriate forms, as discussed below.

Ceramic-Metal Interactions

The extreme chemical reactivity of titanium, and the aluminides, with most ceramics (eg.Table II) can result in the formation of chemical reaction product zones at the matrix/ceramic interface as well as modification of matrix chemistry during processing in the solid state.

Table II

Thermodynamic Driving force and Transformation strain for TiChemical Reaction with SiC and TiB,.

Reaction	4 V/V	AG° kJ mole-1	
8Ti + 3SiC→3TiC + Ti,Si,	-4.62	200	
Ti + TiB₂→2TiB	-1.42	220	

Consolidation typically involves temperatures in the range 900-950°C and times up to 1 or 2 hours in which period substantial reaction can take place. Boron, silicon and carbon contained in the ceramics can all produce titanium compounds and nitrogen, oxygen and aluminium exhibit extensive solid solubility in the metal. A number of studies, principally on the Ti-SiC system, have shown that isothermal reaction zone growth follows parabolic of a wide range of ceramic-titanium kinetics. study interactions by Jong et al (1 and 2 (this conference)) has confirmed parabolic kinetics and determined activation energies consistent with transport through the compact segment of reaction zones to be rate controlling. The mechanism of the TiB, to TiB transition is discussed by Prangnell et al (3). This, the work of Jong and parallel work by Clyne et al (4), indicate that TiB. is superior to SiC in terms of reduced rate of zone growth. Many studies have suggested that the zone thickness needs to be maintained at less than lum to avoid serious degradation of the interface strength (eg.4,5). In the light of Jong's work this implies that process temperatures and times lower than those noted above are required to achieve this unless diffusion barrier coatings are employed on the ceramics. Thus control of ceramic composite production route require careful surfaces and examination.

Particulate and In Situ Composites

It is true for MMCs generally that the use of particulate rather than fibre reinforcement lowers the maximum volume fraction of ceramic which can be uniformly distributed in the matrix. This, together with the need for load transfer to the ceramic via the matrix lowers the increases in modulus and strength that can be achieved in particulate MMCs. In the case of titanium based MMCs generally poor interface properties and the greater practical difficulty of coating particles compared to fibres also results in poor toughness (normally higher in particulate MMCs than in continuous fibre reinforced material). For these reasons industrial interest centres on continuous reinforcement. There is interest in particulate reinforcement to increase specific stiffness while retaining the essentially isotropic behaviour of conventional alloys together acceptable toughness for general engineering applications. Work by Clyne and co-workers (4,5) using SiC and TiB, and a titanium matrix has shown that it is possible to process material to near full density with reaction zone thicknesses of the order of 0.1-0.2 mm by extrusion at 900°C of canned cold compacts or by coplasma spray deposition. Jong et al ((2) this conference) have also shown that HIP of a range of ceramics, including SiC and TiB, can be achieved using a B alloy matrix at 700°C and producing reaction zones 0.2 mm or less in thickness. The work by Clyne (4,5) has shown, in agreement with earlier studies, that the modulus and fracture energy of the composite are degraded sharply by heat treatments that thicken the zone to micron dimensions. Fig.1 shows a fall in the modulus of a Ti/SiC composite when reaction is promoted by heat treatment. Furthermore, the stiffness of both as fabricated ($-0.2-0.4\mu m$ reaction layer) and heat treated composites fall as plastic tensile strain is imposed. Such a fall is not observed in compressive loading. This is consistent with the interface opening up readily. This is less evident with Ti/TiB₂. Although it is possible that a difference in reaction mechanism is partly responsible for the greater resistance of the Ti/TiB₂ interface to normal debonding, it seems likely that the stresses from the volume changes (Table II) are at least of some significance particularly as the effect continues to become more pronounced as reaction progresses. Further indications that the reaction in Ti/SiC causes considerable interface damage can be found in thermal measurements. For example, it has been shown (6) that the thermal conductivity of the Ti/SiC composite falls off sharply as reaction proceeds.

Reactive processing, by which the components of the particulate are brought together and chemically combined to produce the particulate is well established v.a the XDT process (see for example (7) and application to titanium aluminides is reviewed by Kumar (8). Because of the reactivity problem there is also interest in the use of ceramics which can be brought into equilibrium with the metal matrix via more conventional processing routes. Loretto and co-workers have investigated TiCtitanium alloy composites produced by a powder route (9). Their work has shown that composites can be successfully produced. The matrix fractures in a ductile mode and particulate fracture occurs through the particles and not at the matrix-particle interfaces. Large changes in the solubility of titanium in TiC, as a function of temperature, can result in the precipitation of titanium particles within the TiC. Such ductile precipitates can be expected to inhibit the propagation of cracks through the particles. Their work also points to the possibility of producing a composite "in situ" by conventional melting and solidification of bulk alloys and exploiting the precipitation of TiC from the melt: cast TiC-Ti and TiC-Ti6%Al4%V were prepared and the feasibility of producing sub-100µm particles was demonstrated (10,11). Small scale experiments in the laboratory of one of the present authors (HMF) (12) have shown that arc melted and cast alloys can be hot forged successfully and that 400 mm long dendritic primary TiC can be broken up into ellipsoidal particles of aspect ratio less than 2:1 mean diameter 20 µm. In samples heat treated to cause precipitation of titanium within the carbide clear evidence of crack arrest at α titanium particles was observed (Fig.2). In all the studies a strong matrix/particle interface was observed with fracture taking place through the particles. In parallel studies Lin and coworkers (13) studied the effects of cooling rate from the melt on carbide size and morphology. Low (5K/s) rates produced coarse (~100µm) globular TiC while rates up to 950K/s produced fine dendritic TiC which exhibited much higher tensile strength and ductility. They also noted that the addition of 6% aluminium inhibited the formation of globular TiC and almost doubled its hardness. This was attributed to solution hardening of the carbide involving Al-C vacancy binding in the highly non-stoichiometric carbide and indicates the importance alloying additions can have on the properties of the particulate as well as the metal matrix.

The work on in situ composites has been extended to silicides although in that case cracking on solidification is observed with a simple titanium base. Alloying to produce a solution

strengthened "near α " base overcomes this problem, refines the silicide eutectic (and alters silicide chemistry (14)) and hot forging breaks up the eutectic colonies in hypoeutectic alloys. With strains in excess of 1 uniform dispersions of fine (~1 μ m thick and <5 μ m wide) silicide plates can be obtained with a volume fraction of 20% and an α grain size <10 μ m (Fig.3). Again fractography indicates excellent particle/matrix cohesion with ductile matrix fracture and crack propagation through the silicides. Such approaches offer the promise of particulate MMCs with the twin advantages that the particulate dispersion is in equilibrium with the metal matrix and the production route is essentially conventional and avoiding high cost powder production and consolidation.

Further refinement in particle size can be achieved by processing routes involving higher cooling rates. Such an approach is being followed by Beaven and co-workers in Germany where a Ti,Al base is being employed with silicon. Early work concentrated on establishing the phase equilibria in this system but recently melt spinning (15) has been employed to refine the eutectic in this candidate Ti,(Al,Si)-Ti,(Si,Al), in situ composite. Rather lower solidification rates of the order of 10 k/s are typical of laser melting of titanium alloy surfaces. Injection of ceramic particulates into the melt pool can be used to create, locally, a composite material. The work of Abboud and West ((16) this conference) shows sub-100 mm titanium diboride particles injected into a titanium matrix. Although the ceramic was in contact with liquid titanium the extent of the chemical interaction with the metal, and the thickness of the resultant rim of TiB around the particles, is limited by the short process time. Injection of SiC has also been reported previously (17).

Fibre Reinforcement

Fibre Coatings. Apart from alumina (which is too reactive to employ in titanium matrices), boron and carbon the only widely available fibre is silicon carbide. It is, therefore, this material which has received the greatest attention in recent years. In the USA this is produced by Textron as the well established $140\,\mu m$ diameter monofilament. For use with titanium matrices the SCS 6 grade is coated with $4\mu\mathrm{m}$ of pyrolytic graphite by chemical vapour deposition (CVD) (18). More recently, in the UK, 100 µm diameter monofilament "sigma" fibre has been produced by BP (BP Metal Composites Ltd)(19), also by CVD, and based on technology bought in from Germany. Fig.4(a) shows a section through a coated sigma fibre with approximately $1\mu m$ layers of carbon and titanium diboride for use with titanium matrices. The relatively tough and compliant graphite protects the fibre while the diboride acts as a diffusion barrier: in this case some needles of TiB, the result of reaction induced by heat treatment, can be seen protruding into the titanium alloy matrix. Sigma fibre exhibits a tensile strength of 3750 MPa, a modulus of 400 GPa and a density of 3.4g/cc. As discussed below, the composite manufacturing processes involve conditions of temperature and time which would produce chemical reaction zones around uncoated fibres and result in significant property degradation. Coatings, as employed on SCS 6 and Sigma are, therefore, essential. Alternative coating materials including TiSi, (20) and Y-Y₂O₃ (21)

(Fig.4(b)) have been investigated in laboratory studies which indicated that these also offer promise as diffusion barriers.

Composite Production. A variety of routes have been used, including (i) foil-fibre-foil lay-up (ii) powder cloth process and (iii) direct matrix deposition onto a fibres and fibre mats. These processes are summarised in (22,23). The foil method, involving the lay-up of fibre arrays, or mats, between thin titanium alloy, or aluminide, sheets carries the advantage of simplicity combined with minimised risk of interstitial element contamination which can occur when finely divided metal powder or spray is employed. Its disadvantages lie in the production of suitably thin gauges of sheet (*fibre diameter), particularly of the aluminides. Alloys such as super a, are available chemically milled to gauge. More recently there has been progress in rolling foil, including super α_2 , to thicknesses comparable to monofilament diameter by hot pack rolling (24) and even by cold foil, including rolling (23), providing a product of improved surface finish and tolerance. Recently a novel variant of (iii) has been developed in which extremely uniform deposition has been obtained by condensation of electron beam evaporated matrices onto sigma fibre (25). Both titanium alloys and aluminides (including TiAl) were successfully deposited in controlled thicknesses from 6 to 65μ m which resulted in fibre volume fractions in consolidated material between 0.19 and 0.8. An example of the latter is shown in Fig. 5. The uniformity of fibre distribution and avoidance of fibre-fibre contact (known to be damaging) is remarkable for such a high fibre content. As in the other process routes vacuum hot pressing (VHP) or hot isostatic pressing (HIP) are required to consolidate the material.

Mechanical Properties. In early examples of monofilament reinforced titanium alloys this reaction resulted in easy fracture in the reaction zone at the matrix/ceramic interface. Longitudinal tensile properties are less affected since the fibre is directly stressed. However, in the transverse direction, in which stress is transmitted to the fibre through the matrix/ceramic interface properties were extremely poor (apparent elastic moduli less than 10% of that of the matrix and tensile strength little greater). The use of coated fibres has produced considerable improvements.

TABLE III
Tensile Properties of Ti-6Al-4V-32 vol% Sigma SiC Composite

	Tensile Strength MPa	Elastic Mcdulus GPa	Elongation %	
Longitudinal	1550	215 (213.4 *)	0.89	
Transverse	550	148 (168.3°)	2.7	

^{*} Predicted by the Eshelby method (26) using $E_{\rm matrix}=115$ GPa, $E_{\rm ribre}=42$ GPa, $v_{\rm metrix}=0.36$ and $v_{\rm ribre}=0.20$.

For example experimental data supplied by BP for a Ti-6Al-4V 32vol% Sigma fibre composite is shown in Table III together with

modulus values predicted by the present authors. Note that the transverse value of E is lower than predicted. This probably reflects the early onset of interfacial debonding, assuming that E was measured from a stress/strain curve (NB it is possible to verify this via ultrasonic stiffness measurement). Confirmation of such debonding is given by measurement of Poisson ratio.

Monitoring of the strains in different directions during loading allows deductions to be made about inelastic deformation mechanisms. It may be noted that the elastic Poisson ratios of the composite can be predicted from stress analysis models (27). example, a Ti-6A1-4V/35%SiC monofilament composite is predicted to have values of 0.23, 0.30 and 0.39 for $\dot{\nu}_{21}$, ν_{12} and v₂₃ respectively. (The fibres are aligned in the 1 direction and the subscript convention is that the first indicates the loading direction and the second the Poisson strain direction.) Experimental data are shown in Fig.6. For the as fabricated composite under axial loading (a), a Poisson ratio close to the elastic value (0.30) is observed up to a strain of about 0.5%, above which it increases. This presumably corresponds to the onset of plastic deformation in the matrix, which is expected to raise the apparent Poisson ratio. Under transverse loading (b), the same specimen again initially shows a value close to that for elastic deformation (~0.23), but inelastic behaviour sets in at a low strain (~0.1%). Beyond this point the value of v_{21} falls sharply. This is consistent with the onset of interfacial damage, since the debonding and opening up of interfaces generates longitudinal extension without the corresponding lateral contraction. Note the large strain to failure (>2%).

Slightly less simple to interpret are the corresponding Poisson plots for the heavily heat treated specimens (having ~5-6 μ m total reaction layer thickness). The axially loaded plot, Fig.6(c), is similar to that of Fig.6(a), but with the expected reduction in ductility and very limited plastic flow in the matrix. The value of υ_1 in the elastic regime seems to be slightly below that predicted, but this could be explained on the basis of the changed properties of the reaction zone region. The transversely loaded curve, (d), however, differs significantly from that for the as-fabricated specimen, having substantially higher values of υ_2 in both regimes. In the elastic region this may also reflect the elastic properties of the reaction zone, but for the inelastic regime the change is presumably due to the reduced capacity of the interface to open up without causing failure of the specimen.

The effect of the development of the interface reaction zone on other properties is presented in Fig.7. The initial increase in frictional sliding shear strength $\tau_{\rm fr}$ was measured (28) by single fibre pushout testing. The observed increase is probably due to a progressive decrease in the thickness of the graphitic layer (29, 30). The relatively sharp increase subsequently may correspond to the interface becoming rather tough, with no remaining graphitic layer. Tensile strength and impact energy measurements are plotted as a function of the thickness of the brittle layer (initial TiB, layer + TiB needles). The observed reduction in ultimate tensile strength with increased reaction

layer thickness can be attributed to the embrittling effect of the layer as noted in other studies (eg.31,32). For the axially loaded specimens, the reduction in the strength of the fibre may also have made a contribution.

Conclusions

The role of ceramic-metal chemical reaction and the development of brittle reaction zones during composite production is critical to the development of composite properties, physical and mechanical. Measurement of fibre pushout stresses, Poisson ratio data as well as more conventional tensile and impact testing are very informative about the state of the interface and the effects of increasing reaction zone thickness. In order to avoid significant property degradation reaction zone thicknesses substantially less than a micron in size are required. This can be achieved via surface coating of the ceramic and/or changes in conditions which avoid extended temperatures of the order of 900°C and above. An alternate, but less well explored route, at least for particulate reinforcement, lies in the creation of the ceramic in situ and in thermodynamic equilibrium with the metal matrix. Such an approach also offers the prospect of a much lower cost product.

References

- 1. E.N.T.Jong, "Particulate-Reinforced Metal Matrix Composites Based on Titanium Alloys" (PhD Thesis, University of London 1992).
- 2. E.N.T.Jong, H.M.Flower and D.R.F.West, "Interfacial Reaction Kinetics in α and β -Titanium Based Metal Matrix Composites", This Conference.
- 3. P.B.Prangnell, A.J.Reeves, T.W.Clyne and M.W.Stobbs, "Comparison of Mechanisms of Interfacial Reaction in Al-SiC and Ti-TiB2 MMC Systems", Proc. 2nd. European Conference on Advanced Materials and Processes, Euromat '91, Edit. T.W.Clyne & P.J.Withers, (Cambridge U.K. Inst. Metals, 1992), 2, 215-229.
- 4. A.J.Reeves, W.M.Stobbs and T.W.Clyne, "The Effect of Interfacial Reaction on the Mechanical Behaviour of Ti Reinforced with SiC and TiB2 Particles", Proc.12th Riso Symp. MMCs. Processing. Microstructure and Properties, Edit. N.Hansen et al, (Riso, Denmark 1991), 631-636.
- 5. A.J.Reeves, H.Dunlop and T.W.Clyne, "The Effect of Interfacial Reaction Layer Thickness on Fracture of Titanium-SiC Particulate Composites", Met.Trans, 23A, (1992), 977-988.
- 6. A.J.Reeves, R.Taylor and T.W.Clyne, "The Effect of Interfacial Reaction on Thermal Properties of Titanium Reinforced with Particulate Sic",
- Mat.Sci.Eng, 141, (1991), 129-138.
- 7. L.Christodoulou and J.M.Brupbacher, "Metal Matrix Composites XDTMMaterials for Aerospace Applications", <u>Materials Edge</u>, Dec. (1990), 29-33.
- 8. S.Sharvan Kumar, "Discontinuously Reinforced Intermetallic Matrix Composites",
- ISI Japan, 31 (10), (1991), 1249-1259.
- M.H.Loretto & D.G.Konitzer, "The Effect of Matrix Reinforcement Reaction on Fracture in Ti-6Al-4V-Base Composites",

Met.Trans, 21A, (1990), 1579-1587.

10. T.P.Johnson, "Ti Metal Matrix Composites by a Casting Route",

(PhD Thesis, University of Birmingham. England. 1990).

J.W.Brooks and M.H.Loretto, "Mechanical T.P.Johnson, Properties of a Titanium Based Metal Matrix Composite Produced by a Casting Route",

Scripta Met, 25 (4), (1991), 785-789.

12. D.C. Johnson. "Assessment of Particulate Reinforced Ti-TiC Composites Produced by Two Process Routes" (MSc Thesis. Composites Centre, Imperial College, London. England. 1989).

13. Y.Lin, R.H.Zee and B.A.Chin, "In Situ Formation of Three Dimensional Tic Reinforcements in Ti-Tic Composites", Met.Trans,

22A, (1991), 859-865.

14. Z. Zhang and H.M. Flower, "The Composition and Lattice parameters of Silicide and Matrix in Cast Ti-Si-Al-Zr Alloys",

Mats.Sci.Tech., 7, (1991), 812-818.
15. M.Es-Souni, R.Wagner and P.A.Beaven. "Microstructure and Phase Relationships in a Rapidly Solidified Dual Phase Alloy Based on Ti3(Al,Si)+Ti5(Si,Al)3", Mats.Sci.Eng. Al51, (1992), 69-

16. J.H.Abboud and D.R.F.West, "In Situ Production of Ti-TiC

Composites by Laser Melting", This Conference.

17. J.H.Abboud and D.R.F.West, "Microstructure of Titanium Injected with SiC Particles by Laser Processing", J.Mat.Sci.

Lett. 10, (1991), 1149-1152. 18. R.Warren and C.H.Anderson, "SiC Fibres and their Potential Use in Composite Materials: part 2", Composites, 15, (1984), 101-111.

19. Sigma Monofilament MMC. (BP Information sheet. Nov.1991).

20. K.Bilba, J.P.Manaud, Y.Le Petitcorps and J.M.Quenisset, "Investigation of Diffusion Barrier Coatings on SiC Monofilaments for Use in Titanium-Based Composites", Mats.Sci.Eng, (1991), 141-144.

21. R.R.Kieschke and T.W.Clyne, "Development of a Diffusion

Barrier for SiC Monofilaments in Titanium", Ibid, 145-149.

22. R.A. Mackay, P.K. Brindley and F.H. Froes, "Continuous Fiber-Reinforced Titanium Aluminide Composites", J. Metals, May, (1991),

23. S.C.Jha, J.A.Forster, A.K.Pandey and R.G.Delagi, "Cold Rolled Titanium Aluminide and Titanium Alloy Foils", ISI Japan, 31 (10), (1991), 1267-1271.

24. C.Bassi, J.A.Peters and J.Wittenauer, "Processing Titanium

Aluminide Foils", <u>J.Metals</u>, Sept, (1989) 18-25. 25. C.M.Ward-Close and P.G.Partridge, "A Fibre Coating Process

for Advanced Metal-Matrix Composites", J.Mat.Sci., 25, (1990), 4315-4323.

26. T.W.Clyne and P.J.Withers, An Introduction to Metal Matrix

Composites, (Cambridge University Press 1992).

27. T.W.Clyne, "A Compressibility-Based Derivation of Simple Expressions for the Transverse Poissons Ratio and Shear Modulus of an Aligned Long Fibre Composite", J.Mat.Sci.Lett, 9, (1990), 336-339.

28. M.C.Watson and T.W.Clyne, "The Use of Single Fibre Pushout Testing to Explore Interfacial Mechanics in SiC Monofilament-Reinforced Ti. Part II: Application of the Test to Composite Material", Acta Met et Mater, 40, (1992), 141-148.

29. C.M.Warwick and J.E.Smith, "Interfacial Reactions in Ti Alloys Reinforced with C/TiB2-Coated SiC Monofilament", Proc.12th Riso Symp. MMCs, Processing, Microstructure and Properties, Edit. N.Hansen et al, Riso, Denmark, (1991), 735-740.

M.C.Watson and T.W.Clyne, "Interfacial Bond Strength Measurements in Monofilament-Reinforced Ti Alloys", Proc. 2nd. European Conference on Advanced Materials and Processes, (Euromat '91, Edit. T.W.Clyne & P.J.Withers, Cambridge U.K. Inst. Metals, (1992), 2, 235-240.

31. A.G.Metcalfe, "Interaction and Fracture of Titanium-Boron Composites", <u>J.Comp.Mats</u>, 1, (1967), 356-365.

32. S.Ochiai and Y.Murakami, "Tensile Strengths of Composites with Brittle Reaction Zones at Interfaces", J.Mat.Sci, 14, (1979), 831-840.

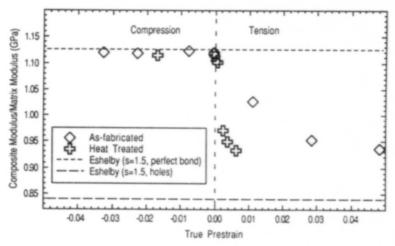


Figure 1. Modulus Degradation on straining of Ti-10%SiC particulate.

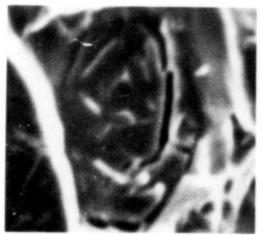


Figure 2. Crack arrest at a particle in TiC in a Ti-TiC composite produced by casting and silicide composite produced by forging.

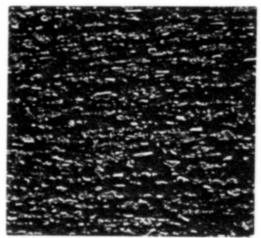
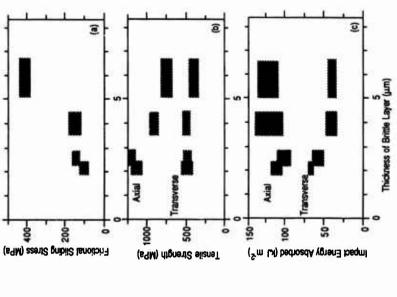
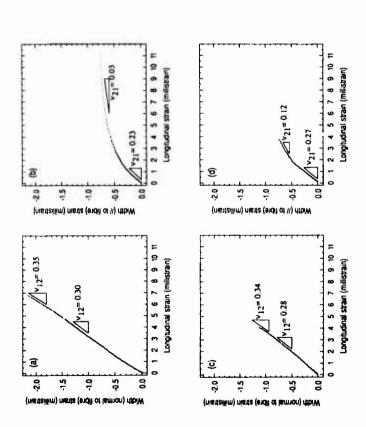


Figure 3. Uniform dispersion in a near alpha Ticasting and forging.

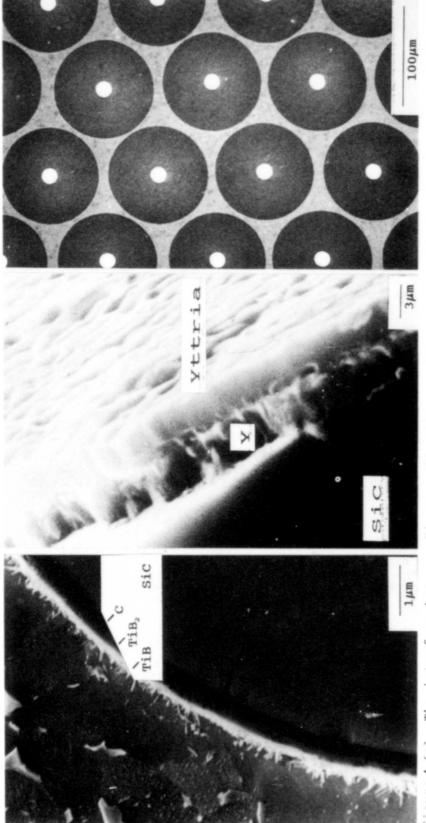




loading and (b) under transverse loading, (c) heat treated 26hr at 865C under axial loading and (d) under Figure 6. Poisson plots for Ti-6Al-4V-32\$SiC(C-TiB₂) monofilament composites (a) as fabriated under axiál transverse loading.

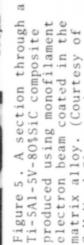
Figure 7. Measured properties of Ti-6Al-4V-35\$SiC(C-TiB,) monofilament plotted as a function of the thickness of the brittle layer formed at the interface.

Fig.7





controlled oxidising conditions. subsequent heat treatment in The duplex yttrium-yttria coating was produced by



P.G.Partridge (25). C.M.Ward Close and

CONTINUOUSLY REINFORCED TITANIUM BASED MMC'S

PRODUCED BY THE MATRIX COATED FIBRE PROCESS

C.M.Ward-Close, and P.G.Partridge,

Materials and Structures Department, Royal Aerospace Establishment, DRA, Farnborough, GU14 6TD, UK.

Abstract

A process has been developed for the production of titanium based fibre reinforced MMC's, where the reinforcing fibre is pre-coated with a thick layer of the matrix alloy, using high rate physical vapour deposition (PVD). The coated fibres are then consolidated either by vacuum hot pressing, or hot isostatic pressing (HIPping), to produce a fully dense composite. No further matrix material is introduced.

This paper describes the application of this process to the production of SIC reinforced titanium based MMC's. Different product forms will be described, including a filament wound tube. Recent developments will be described which exploit the unique features of the coated fibre process to produce novel composite materials with enhanced mechanical properties.

Comparisons are made with alternative titanium alloy based MMC fabrication methods.

Introduction

Advanced composite materials based upon continuous SiC fibres in titanium alloy [1] or titanium aluminide [2] matrices can lead to significant improvements in specific strength and stiffness of components at ambient and elevated temperatures [3]. For example up to 75% weight saving is predicted [2, 4] when a conventional Ti-alloy is replaced by Ti - alloy composite in a gas turbine compressor disc and spacer assembly. Composites are therefore of particular interest for the next generation of airframes, space vehicles and power plants.

Composites based on low melting point or non-reactive matrices are usually made by melt infiltration of fibre bundles. Reactive matrices, such as those based on titanium alloys, are limited to solid state processing at relatively low temperatures (~1000°C). Various fabrication methods are under development for titanium based MMC's, the most widely known being the foil/fibre (F-F) layup process [2], (Fig.1). Other methods have used plasma spraying or alloy powder to introduce the matrix material prior to hot pressing. However, these processes can present major problems associated with matrix selection, fibre distribution and product quality, which may adversely affect mechanical properties and limit the potential application of the composites for critical components in gas turbines. There are a number of other potential composites, both metallic and non-metallic, which like Ti-based materials may be very difficult to fabricate. Many of these disadvantages are avoided by a composite fabrication process that involves coating of SiC fibres with a thick layer of the matrix by physical vapour deposition (PVD) prior to consolidation.

Titanium '92 Science and Technology Edited by F.H. Froes and I. Caplan The Minerals, Metals & Materials Society, 1993

The Matrix Coated Fibre (MCF) Process

A new MMC fabrication process has theen developed [5] which uses electron beam evaporation and vapour deposition (EBED) to pre-coat SiC fibres with a thick layer of matrix alloy (Fig.1) prior to consolidation into a finished composite. The matrix material is provided entirely by the coating, thus avoiding expensive alloy product forms such as foil, powder or wire required for the other processes. In addition to these obvious benefits, the matrix coated fibre (MCF) process offers many advantages that are not available with other composite fabrication methods.

A range of different Ti-alloys of various thicknesses have been coated on SiC monofilament from an EB evaporation source, and composites produced by hot pressing or HiPing [5]. A scanning electron microscope (SEM) fractograph of a SiC fibre after coating with alloy Ti-5AI-5V, and fractured in bending is shown in Fig.2. The coating microstructure consisted mainly of columner grains typical of an alloy vapour deposited at a low fraction of its mothing temperature. The coatings were found to adhere well to the fibre, and the coated fibres could be handled and bent round relatively small radii without any apparent damage, or loss of strength. Tensile tests on single matrix-coated fibres (140µm SCS6 coated with 25µm Ti-6AI-4V), which had previously been wound on a 20mm diameter spool, gave failure loads in the range 59-70 N, compared with 51-64 N for uncoated fibre. No evidence was found for chemical reaction taking place between the fibre and the matrix alloys during the coating process. Matrix oxygen level was about 2600ppm (by weight).

Matrix coated fibres are particularly suited to net shape technology which permits the direct production of the final component shape and dimensions, and filament winding is a good example of an efficient fabrication method for composite components. An example of a circumferentially reinforced titanium alloy tube made from MCF is shown in Fig.3. This was produced by winding four layers of Ti-6Al-4V coated SiC fibre onto a 20mm diameter tube and inserting this tube into another tube before sealing, evacuating and consolidating by hot isostatic pressure (HIP).

Since each fibre is completely surrounded by matrix material, the fibre is protected during handling and the likelihood of damage to the fibre is reduced. Furthermore, the volume fraction (Vf) of SiC fibre in the finished MMC is determined only by the thickness of the fibre coating. Consequently, with coated fibres it is possible to obtain MMC's with up to Vf = 80 vol% SiC fibre. Compared with the alternative processes the consolidation of MCF is less damaging to the fibres, with no risk of contamination from organic binder, and the spacing of the fibres can be exceptionally uniform, with no fibres touching. The interfibre spacings for the composite shown in Fig.3 are presented in histogram form in Fig.4, together with the results of a similar analysis of composites produced by other methods (taken from Ref. 2). In the MCF composite no fibre spacing was less than 20µm, whereas in the composites made by other techniques a significant proportion of fibres were either touching or were less than 10µm separation.

Another important advantage of the MCF process is relatively small amount of contraction associated with the consolidation; stage. Volume change during consolidation can affect not only the external dimensions, but also the local stresses imposed on the fibres. These stresses may cause fibre displacement (swimming), compression buckling or tension failure of the fibres. For most vacuum hot pressing or HiPing configurations displacement is only allowed in one direction normal to the fibres. In the foll/fibre lay-up process, the green void volume depends on VI, foll thickness and fibre packing geometry given by ratio R = h/w, where h and ware the vertical and horizontal distances between fibres. This is illustrated in Fig.5 which shows the reduction required along the normal direction with increasing VI. For a fixed R in the range 0.7-1.3 the displacement reaches a maximum of between 19% and 31%. A typical F-F composite with VI=0.35 would have a consolidation contraction of 20-25%, depending on the lay-up geometry. Conversely, for a close packed unidirectional fibre array of matrix coated fibres, a reduction in thickness of 9.3% will lead to complete void closure and full density for any fibre volume fraction.

Matrices Suitable for Physical Vapour Deposition (PVD)

An important feature of electron beam evaporation and vapour quenching is the very rapid equivalent cooling rates that are obtained. Highly supersaturated and metastable alloys can be produced and processed to give novel microstructures with exceptionally uniform nanometre scale grain microstructures which may be impossible to produce by any other means.

The rate of evaporation from an electron beam heated source is dependent on EB gun power, source temperature and the vapour pressure of the element or on the fugacity of the elements during co-evaporation of alloys. Co-evaporation from a single source, with continuous alloy feed to the bath, is only possible if the vapour pressures of the alloying elements are within about two orders of magnitude of each other at the evaporation temperature. However, the use of multiple evaporation sources (either EB or radiant heat) and vapour mixing allows the deposition of almost any alloy combination. For example, in the present study, titanium alloys containing both high vapour pressure additions, such as Mg or Ca, and low vapour pressure additions, such as B or Mo, have been produced by the vapour mixing route. Provided the vapour flux rates are not exceptionally high, the mean free paths of atoms evaporated from separate sources are sufficiently long for overlapping vapour streams to mix completely. Typical deposition rates from the vapour are 100-400µm/min on a stationary substrate.

The evidence indicates that a very wide range of materials may be physical vapour deposited with a nanometre grain size directly on to fibres. One of the major advantages of a nanometre grain size is the exceptionally high tensile ductility combined with low flow stress that such materials exhibit at relatively low temperatures [6]. This ductility applies to metallic, non-metallic and ceramic materials. It is therefore expected that consolidation of fibres coated with these materials will be possible at much lower temperatures and stresses than the same materials in the bulk.

Composite Toughening

Increased longitudinal strength and stiffness is usually associated with composites. However, the toughness depends on the matrix. Compared with the unreinforced state, composites with metal matrices have much lower toughness and composites with brittle matrices (aluminides and ceramics) have slightly higher toughness but, in all composites, toughness values are much lower than the minimum values considered acceptable for critical structural components.

A major advantage of the MCF technique when applied to such composites may therefore prove to be the ability to manufacture a graded matrix composition to minimise thermal stresses or a microlaminated matrix for toughness. For example, a titanium and yttrium microlaminate coating on a continuous SiC fibre is shown in Fig.6(a). After consolidation an MMC with a laminated matrix of titanium and yttria is obtained (Fig.6(b)). Confirmation of crack deflection and delamination by the microlayers during fracture of a composite is shown in Fig.6(c). These microstructures could allow better control over fibre/matrix interface strengths and specific toughening mechanisms (e.g. ductile or brittle fracture) to be selected and optimised for the matrix.

Cost Comparisons of MMC processing Routes

The size of the market for continuous fibre composites, as for many new materials, will be dictated by the cost /benefit balance, with a rapid reduction in cost predicted as the market increases. Isolating the critical cost factors for composites under development is very difficult since much data is proprietary, but costs will clearly depend on the particular process route and matrix chosen.

At present, costs are dominated by the cost of the fibre. BP carbon/boron protected 100µm SiC fibre (SM1240) is currently about £8-10,000/kg. However, industry estimates suggest that, for production of 5-10,00 kg/year, fibre cost could fall to as low as £1000/kg.

Both the foil/fibre process and the matrix coated fibre process involve vacuum canning and hot pressing to consolidate the composite. However, the MCF process may allow substantial cost savings in the pre-consolidation stages, since the matrix coated fibres are ideally suited for automated filament winding and hot isostatic pressing of complex shapes whereas the foil-fibre process involves labour intensive laying-up of fibre mats and foils.

Some estimates of relative costs for the MCF and F/F process routes are given in Table 1. Cost estimates for the matrix coated fibre technique are based on the RAE 45kW EB/MCF pilot plant with a 10% metal utilisation efficiency (le. 10% of the metal evaporated is collected on the fibres), and a consequent production rate, for 35% SiC coated-fibre, of 2km/hr. Such a plant would be capable of producing approximately 350kg of coated fibre per year (assuming average plant utilisation of 2.5 hours/day). Material costs are similar for both routes. For the foil-fibre process, foil cost depends critically on the alloy composition, ranging from about £600/Kg for 75µm Ti-6AI-4V, to over £3000/Kg for titanium aluminide foil.

The additional costs associated with the MCF process are mainly those associated with the capital and running costs of the PVD plant. These are estimated to add about £900/Kg to the cost of the MMC (based on the RAE pilot plant). Composite consolidation costs are particularly difficult to estimate because of the variety of operations involved. However, at present, in the foil/fibre process, about 12% of MMC cost is attributed to fibre cost and 88% to foil and consolidation costs (including plant, labour, profit, etc.). The foil/fibre process costs shown in Table.1 are derived from the current commercial price for BP Ti-6AI-4V/35% SiC laminate. Fabrication costs for the MCF route are likely to be less than for the fibre/foil route, but by how much is unknown at present, as indicted in Table.1. An additional factor that might be taken into account in comparisons is the potential for more sophisticated matrices with the MCF process; this could justify greater expenditure on MCF plant.

Conclusions

For the consolidation of close packed MCF, the deformation required is much smaller and less matrix is required to move shorter distances compared with the consolidation of F-F lay-ups. This should significantly reduce the possibility of matrix/fibre interface damage and fibre breakage in MCF composites.

Improvements in the mechanical properties of advanced continuous fibre reinforced composites will require research focused not only on the fibre/matrix interface but also on the matrix microstructure and consolidation techniques.

A production process based on in-line multi-stage coating of fibre by PVD could offer a wide range of options and precise process control for the manufacture of continuous fibre composites. With oxidation stages, or local partial pressure gaseous environments the production of metallic or non-metallic matrices could be combined with a laminated microstructure for toughness. The PVD technology exists. Although, plant and up-front costs are high, the products have great potential. It remains to be seen whether the market will be considered sufficient for the investment required.

References

- J.M.Yang, S.M.Jeng and C.J.Yang, "Fracture Mechanisms of Fibre-Reinforced Titanium Alloy Matrix Composites, Part I:Interfacial Behaviour", <u>Mater Sci Eng.</u> A138 (1991), 155-190.
- R.A.MacKay, P.K.Brindley and F.H.Froes, "Continuous Fibre-Reinforced Titanium Aluminide Composites", JOM; (May 1991), 23-29.
- G.Allen, et al., "Benefits of Advanced Materials, Structures and Aerodynamics in Future High Speed Civil Transport Propulsion Systems", in 'AIAA/AHS/ASEE Aircrit Design, Systems and Operations Conference", (Dayton, Ohio, American Institute of Aeronautics and Astronautics, 1990), 1-8.
- 4. D.Driver "High Temperature Materials for Power Engineering Part II", (1990) 883-902.
- C.M.Ward-Close and P.G.Partridge, "A Fibre Coating Process for Advanced Metal Matrix Composites", J.Mater.Sci., 25 (1990), 4315-4323.
- T.G.Nieh, J.Wadsworth and F.Wakai, "Recent Advances in Superplastic Ceramics and Ceramic Composites", Inter. Mater. Rev., 36 (1991), 146-161.
 - (c) Copyright HMSO (1992)

Table 1 Cost comparison between matrix coated fibre process and foil/fibre process

		Titanium alloy/35% SiC (£/kg MMC)		
		Matrix Coated Fibre (10% coating efficiency)	Foil/fibre	
Ma	terials			
Metal (£30/Kg) Electricity (3p/kWh) SIC fibre (£9000/Kg)		200 26 2600	160-800 - 2600	
	manufacturing osts	- · · ·	·- · · · · · · · · · · · · · · · · · ·	
a) Matrix coating plant - Labour - Plant depreciation (£750K over 5 years)		460 430	-	
b) Fabricat etc.	ion costs & profit,	x <y< td=""><td>y = 14,000-19,000</td></y<>	y = 14,000-19,000	
Total		3716+x	~17,000-22,000	

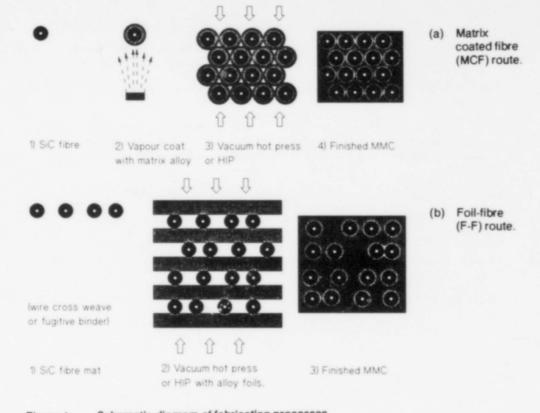


Figure 1 - Schematic diagram of fabrication processes.

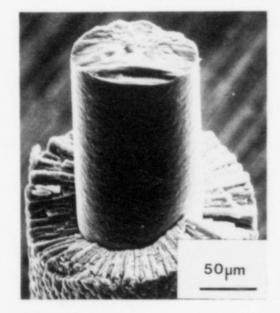


Figure 2 -

Scanning electron micrograph of SiC fibre with $35\mu m$ thick Ti-5Al-5V matrix coating made by the MCF process

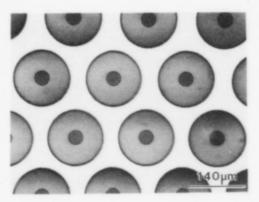


Figure 3 -

Section through wall of reinforced tube made by winding T-5AI-5V/SiC MCF and HIPing

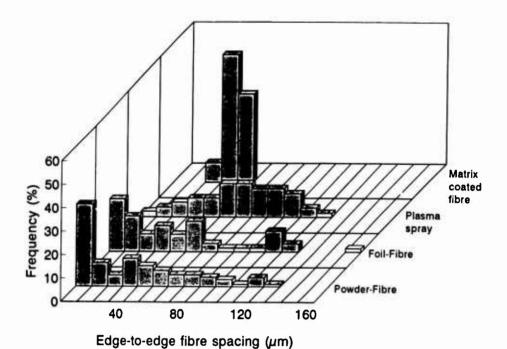


Figure 4- Frequency versus magnitude of edge to edge inter-SiC fibre spacing.

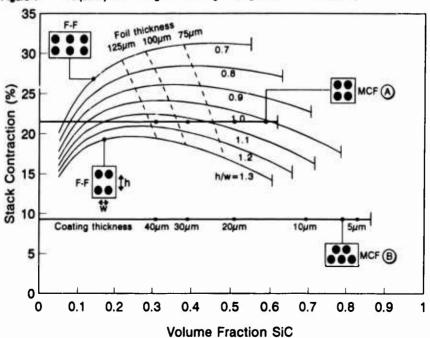
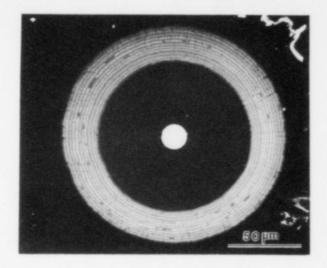
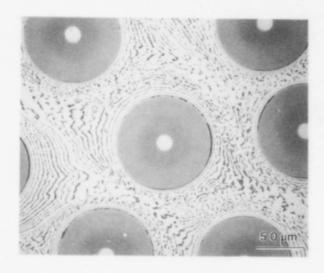


Figure 5- Contraction normal to fibre axis during consolidation of sheet (no displacement allowed in sheet plane) versus SiC vol. fraction. A and B depict vertical and close packed arrays of MCF. Effect of fibre spacing and foll thickness are also shown.

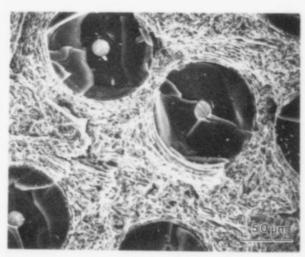
2,485



(a) Coated fibre.



(b) Microstructure of laminated matrix composite.



(c) Evidence of crack deflection in laminated matrix composite.

Figure 6-

Titanium/ Yttrium laminated matrix on SiC fibre produced by the MCF process.

MICROSTRUCTURES AND TENSILE PROPERTIES OF TITANIUM-BASED

COMPOSITES PRODUCED BY POWDER METALLURGY

Masuo Hagiwara, Satoshi Emura, Junji Takahashi Yoshikuni Kawabe and Nobuhiro Arimoto'

National Research Institute for Metals 1-2-1 Sengen, Tsukuba, Ibaraki, 305 Japan

*Osaka Titanium Manufacturing Co. 1 Higashihama-cho,Amagasaki,660 Japan

Abstract

Conventional titanium alloy matrix composites reinforced with either TiC or TiB particulates, and PREP Ti-6A1-2Sn-4Zr-2Mo matrix composites reinforced with either 30vol pct PREP Ti_3Al or 30vol pct PREP TiAl were produced using blended elemental and prealloyed P/M methods, respectively. Microstructural characterization of the particulates, matrix and reaction zone was achieved by a combination of optical and scanning microscopy. Tensile test was done in the temperature range between RT and 1123K. The elastic modulus measurement and the creep test were also performed. The results demonstrated that the dispersion of relatively large-sized particulates is a promising method for improving the performance of conventional titanium alloy.

INTRODUCTION

One of drawbacks of conventional titanium alloys is that the service temperature is limited to 600°C due to a degradation of tensile strength, creep resistance, thermal stability and environmental resistance[1]. Titanium aluminides are receiving much attention for application as high performance materials but these are intrinsically brittle, and success in improving low temperature ductility while maintaining high temperature mechanical properties has been limited. However, for future aircraft design, there is still a demand for high temperature titanium alloys having superior combinations of mechanical properties compared to the conventional counterparts in the temperature range between 600 and 1000°C[2].

Fabrication of titanium-based metal matrix composites (MMCs) creates considerable potential for improvement in various properties. There are two basic types of MMCs, i.e., long fiber reinforced and particulate reinforced. Of these, development activities are currently centered around SCS-6 fiber reinforced MMCs[3-6] but these are highly anisotropic in properties and the fabrication is complex and expensive. Interest has increased in particulate reinforced MMCs in recent years because these

Titanium '92 Science and Technology Edited by F.H. Froes and I. Caplan The Minerals, Metals & Materials Society, 1993 have isotropic characteristics and can be processed more cheaply using the conventional techniques such as ingot metallurgy[7], casting[8-9] and powder metallurgy [10-13]. However, property data available for this type of MMCs are still lacking. Particularly, high temperature tensile data and comparison with the unreinforced matrix allows have received relatively little attention.

In the present study, two different kinds of titanium alloy-based MMCs containing relatively large-sized particulate reinforcements have been produced by the powder metallurgy (P/M) route. Firstly, conventional titanium alloy matrix composites reinforced with either TiC or TiB ceramic particurates were produced using the proprietary blended elemental (BE) P/M route. Secondly, plasma rotating electrode process(PREP) Ti-6Al-2Sn-4Zr-2Mo(Ti-6242) matrix composites reinforced with PREP titanium aluminide powder(either α_2 -Ti_3Al or γ -TiAl) were produced using the prealloyed (PA) P/M route. The details of the fabrication of the composites and the results of the microstructural characterization and the high temperature tensile tests done on the composites and matrix alloys will be described in this paper.

EXPERIMENTAL PROCEDURE

The ceramic particulates reinforced BE P/N composites were made up using the processes of powder blending, cold isostatic pressing(CIP), vacuum sintering and hot isostatic pressing(HIP). As can be seen in Fig.1(a), a proprietary technique was incorporated in this BE P/M method, whereby matrix-forming powder were blended with either boron-containing powder such as FeB or carbon-containing powder such as Cr₃C₂. During sintering, these powders are dissolved in the matrix and the dissolved and diffused B or C atoms react chemically with titanium to form TiB or TiC in situ in the matrix. Two types of BE P/M composites were fabricated using this proprietary technique. One type of composites, Ti-5A1-2.5Fe containing 15 TiB (in weight pct), was made by blending extra low chlorine (ELCL) titanium powder (Cl<10 ppm, 0~1000ppm, -100mesh), Al₃Ti master alloy powder(-150mesh) and FeB powder(-325 mesh). The unreinforced Ti-5A1-2.5Fe alloy, which belongs to high strength $\alpha - \beta$ type alloy and was developed for medical application[14,15], was also made and tested to show differences from the composites. The other type of composites, Ti-5 A1-(9 \sim 13)Cr containing (7 \sim 10)TiC, was prepared using ELCL titanium powder, A1₃Ti master alloy powder and Cr₃C₂ powder(-325mesh). The Al₃Ti and FeB powders were made in our laboratory by crushing the arc-melted button ingots. The CIP'ing was done at 400MPa and vacuum sintering were performed for 14.4ks at 1573K. Sintered composites were subsequently HIP'ed for 14.4ks at 1203K and 200MPa to produce full dense composites. The oxygen content of the composites was 1450ppm.

The PREP titanium aluminides reinforced PA P/M composites were made up using the processes shown in Fig.1(b). Ti-6242 was chosen as a matrix alloy, which is most widely used high temperature titanium alloy for use up to 450°C. The Ti-6242 alloy powders were made by the PREP apparatus installed in our laboratory. These PREP Ti-6242 powders of about 200 μm in average diameter were blended with 30vol% PREP Ti_3A1(Ti-25A1-11Nb, in at.%) or 30vol% PREP TiA1(Ti-48A1, in at.%) using V-shaped blender and subsequently HIP'ed for 14.4ks at 1203K.

The high temperature tensile tests were performed in a vacuum with 3.5mm diameter by 16mm gauge length specimens at a cross head speed of 0.1mm/min and creep tests were done in air with 4.0mm diameter by 25mm gauge length specimens.

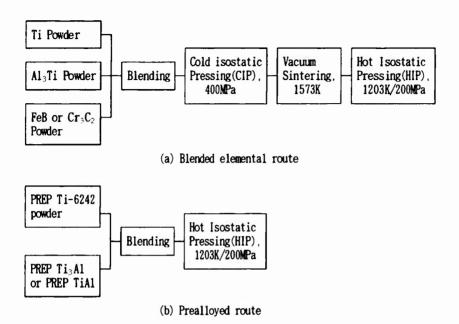


Fig.1 - Precessing steps for fabrication of titanium alloy-based P/M composites.

EXPERIMENTAL RESULTS AND DISCUSSION

Microstructure and tensile properties of the ceramic particulates reinforced BE P/M composites

The microstructure of a Ti-5A1-2.5Fe matrix alloy displays a colony microstructure of similarly aligned α -platelets with a colony size of $\sim\!150\,\mu\text{m}$ and massive α phase at the grain boundaries(FIG.2a). The Ti-5A1-2.5Fe-based composites containing 15 weight pct titanium borides result in microstructure consisting of colony matrix microstructure with both needle and globular-shaped TiB(Fig.2b). These two types of titanium borides were identified to be TiB by X-ray diffraction analysis. The structure of TiB has been reported to be of the orthorhombic FeB type with unit cell of a_0 =6.12, b_0 =3.06 and c_0 =4.56 A[13]. The reason why two types of TiB were formed is not clear at this moment. It can be seen that the TiB particulates are distributed reasonably randomly in the matrix. The morphology of α -platelets differs significantly between the unreinforced matrix alloy and composites, with aspect ratio of the α -platelets being markedly smaller in the composites. It seems that the length of each α -platelet is limited by the particulate spacing.

Titanium carbides formed in the Ti-5Al-(9~13)Cr-based composites were identified to be TiC. The X-ray analysis also revealed a matrix microstructure of primarily β phase for the Ti-5Al-13Cr-10TiC composites and $\alpha-\beta$ two phase structure for the Ti-5Al-8Cr-7TiC composites. The TiC particulates with average size of $15\,\mu\mathrm{m}$ are seen to be distributed uniformly(Fig.3). No obvious interaction zone is visible in both composites at the resolution available in optical and scanning microscopy. However, for the BE P/N Ti-6Al-4V/TiC composites, the formation of the annulus of Ti₂C arround the TiC particulate has been observed when using TEM[11].

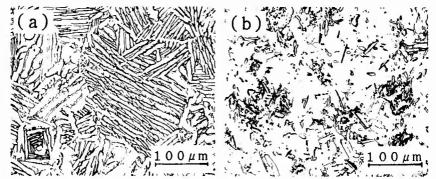


Fig.2 - Microstructures of (a) unreinforced BE P/M Ti-5Al-2.5Fe matrix alloy and (b) Ti-5Al-2.5Fe-15TiB composites.

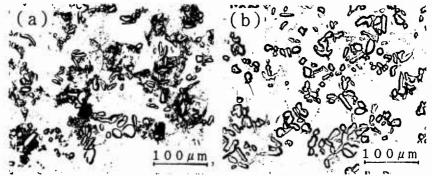


Fig.3 - Microstructures of (a) BE P/M Ti-5A1-9Cr-7TiC composites and (b) BE P/M Ti-5A1-13Cr-10TiC composites.

The Ti-5Al-2.5Fe-15TiB composites achieved remarkably higher elastic modulus at RT, 151GPa, 32pct higher than that of an unreinforced Ti-6Al-4V, 114GPa[16]. Although the Ti-5Al-13Cr-10TiC composites also showed higher elastic modulus, 125GPa, this value is considerably lower than that of the Ti-5Al-2.5Fe-15TiB composites. This result can be partly attributed to the fact that a Ti-5Al-13Cr matrix alloy is almost completely β type alloy and this type of alloy is known to exhibit lower elastic modulus[16] compared to those for α - β type alloys. The ultimate tensile strength for both types of composites were superior compared to the matrix alloys and BE P/M Ti-6Al-4V in the whole temperature range examined(Figs 4 and 5). However, the ductility of composites was significantly lower than those of the matrix alloys. At RT, both Ti-5Al-2.5Fe-15TiB and Ti-5Al-13Cr-10TiC composites failed in an brittle manner before the ultimate tensile strength was achieved. At temperature above 773K, measurable ductility (>3pct elongation) was obtained.

Irrespective of the test temperatures, the fracture surface consists of small portions of cleavage fracture with a majority of dimpled ductile fracture(Fig.6a). Optical micrograph of the cross section of tensile test specimen in the vicinity of the fracture area reveal cracking within the TiC particulates(Fig.6b). These observations indicate that the cleavage fracture seen on the fracture surface correspond to fracture of the TiC particulate. In addition, most importantly the fracture within the TiC particulate occurred prior to the dimpled fracture of the

surrounding matrix alloy. The cracking at the interface between the particulate reinforcement and matrix alloy was not observed in the present composites. This may be indicative of excellent bonding at the interface.

Alternative methods for fabricating titanium-based MMCs using the BE P/M route are possible. One technique is simply to blend the intended ceramic powder or particulates such as TiC and TiB₂ with the matrix alloy-forming powders. However, a preliminary experiment done at our laboratory and the report[10] by other researchers revealed that the commercially available very small ceramic particulates ($\sim 1 \, \mu$ m) tend to agglomerate, and the agglomerated cluster of particulates was the origin of the premature failure during the tensile test even at higher temperature. It is also said[10] that this "simple blending" technique can be limited by interfacial wettability problems, because the ceramic particulates generally have an oxide surface layer which can affect the adherence of the particulate to the matrix alloy and therefore lead to failure at the interface[10]. Our proprietary "internal reaction" technique can avoid these two intrinsic problems. As seen in Figs 2 and

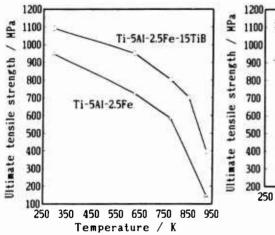


Fig.4 - Temperature dependence of the UTS of TiB reinforced BE P/N composites and matrix alloy.

Fig.5 - Temperature dependence of the UTS of TiC reinforced BE P/M composites and Ti-6A1-4V.

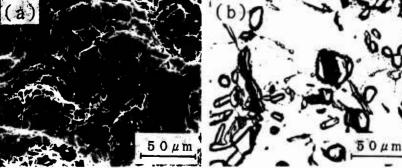


Fig.6 - Fracture surface and cross sectional area just beneath the fracture surface taken from BE P/M Ti-5Al-13Cr-10TiC composites tested at 500°C.

3, this technique enables reinforcements to be dispersed reasonably uniformly in the matrix, which means that there is no macroscopic agglomeration of the FeB or Cr_3C_2 particulates in the powder-mixing stage. In addition, because these reinforcements are formed in-situ, contamination at the reinforcement/matrix interface does not occur and hence excellent bonding at the interface can be achieved[13], which enables the sufficient load transfer from the matrix to the ceramic reinforcements. Furthermore, the ceramic particulates which were formed in-situ during the sintering process are expected to have almost no macroscopic flaws, since the ceramic formed in this manner has been reported to be single crystal[9,13]. Thus, the present BE P/M composites have three advantages,i.e., reasonably randomly dispersed particulate reinforcements, excellent bonding at the reinforcement/matrix interface and the lack of macroscopic flaws within the ceramic reinforcement, over those produced by the "simple blending" method.

Microstructure, and tensile and creep properties of the PREP titanium aluminides reinforced PAP/M composites

Both FREP Ti_3Al and PREP TiAl are seen to be dispersed quite uniformly (Figs 7 and 8). Photographs at a higher magnification show that there is almost no reaction zone seen at the interface between PREP Ti-6242 and PREP Ti_3Al . However, a massive annulus of reaction zone is clearly seen around the PREP TiAl.

The yield and ultimate tensile strength of PREP Ti-6242 matrix alloy is quite high at RT, and decreases monotonically with increasing temperature. The yield strength of PREP Ti₃A1 is lower than that of PREP Ti-6242 in the whole temperature range and thus the PREP Ti-6242 matrix composites reinforced with 30vol pct Ti₃A1 did not

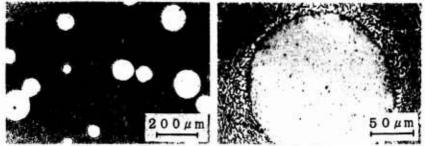


Fig. 7 - Microstructures of the PREP Ti-6A1-2Sn-4Zr-2Mo matrix composites reinforced with 30 vol.pct PREP Ti₃A1.

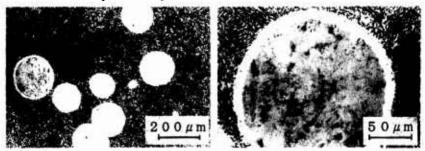


Fig.8 - Microstructures of the PREP Ti-6A1-2Sn-4Zr-2Mo matrix composites reinforced with 30 vol.pct PREP TiA1.

show any strength improvement (Fig.9). The PREP Ti-6242 matrix composites reinforced with 30vol.pct TiAl exhibit higher yield strength at temperatures above 873K, although the strength increment is not so remarkable (Fig.10). No ductility was obtained for both composites at RT, and fracture of the composites initiated within the PREP titanium aluminides.

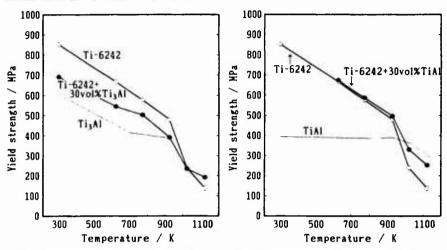
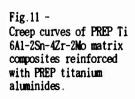


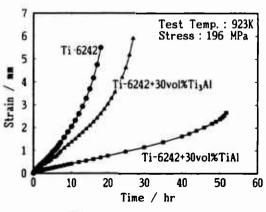
Fig. 9-Temperature dependence of YS of PREP Ti₃Al reinforced PA P/M composites and matrix alloy.

Fig. 10-Temperature dependence of YS of PREP TiAl reinforced PA P/M composites and matrix alloy.

The above indicates that titanium aluminides are not effective short time strengthening reinforcements. However, contrary to this, the creep resistance of the PREP Ti-6242 was greatly improved especially by the presence of PREP TiAl, as shown in Fig.11.

Fig.12 summarizes the creep properties of both BE and PA P/M composites, and matrix alloys obtained by the present study. It is demonstrated again that the dispersion of particulates which have higher tensile strength and/or higher elastic modulus is an effective method for improving the creep properties of conventional alloys especially in the longer time range.





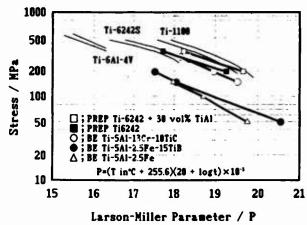


Fig.12 -Creep comparison of BE and PA P/N composites, and matrix alloys.

CONCLUDING REMARKS

The present study demonstrates that the uniform dispersion of particulates which have superior high temperature properties relative to the matrix alloys is an effective method for improving properties such as elastic modulus, and tensile and creep strength of conventional alloys. However, the composites produced in this study showed poor ductility at RT. Because the fracture initiated from the cracking within the reinforcements, it may be reasonable to consider that the size, morphology, and volume fraction of the reinforcements is mainly responsible for the performance of the composites under tensile condition. In fact, it is reported that the tensile strength of the TiC reinforced Ti composites is mostly sensitive to the size of the reinforcing particles[9]. Therefore it will be suggested that further refinement of the reinforcements through fabrication modifications such as the use of much smaller starting powder materials, may lead to additional improvement in the room temperature tensile ductility of these composites.

REFERENCES

- 1) D.Eylon, S.Fujishiro, P.J.Postans and F.H. Froes: J.Met., 36(1984), no 11, p.55
- 2) J. Wadworth and F.H. Froes: J. Met., 41 (1989), no 5, p. 12
- 3) S.F.Baumann, P.K.Brindly and S.D.Smith: Metall. Trans. A, 21A(1990), p. 1559
- 4) G.Das: Metall.Trans.A, 21A(1990), p. 1571
- 5) S.M.Russ: Metall.Trans.A.21A(1990), p. 1595
- 6) S.Jansson, H.E.Deve and A.G.Evans: Metall. Trans. A, 22A(1991), p. 2975
- 7) W. Takahashi, M. Okada, Y. Shida and M. Nakanishi: Tetsu to Hagane, 77(1991), p. 1336
- 8) A.R.C. Westwood: Metall. Trans. A, 19A(1988), p. 749
- 9) Y.Lin, R.H.Zee and B.A.Chin: Metall.Trans.A, 22A(1991), p. 859
- 10) M.L.Adams, S.L.Kampe and L.Christodoulou: Int. J. Powder Met, 26(1990), p. 105
- 11) H.H.Loretto and D.G.Konitzer: Metall.Trans.A,21A(1990),p.1579
- 12) S. Abkowitz and P. Weihrauch: Adv. Mater. Process, (1989), No 7, p. 31
- 13) L. Yuxiong, B. Jing L. Douxing and P Dehai: To be published in Proc. 92 ISONS.
- 14) J.Breme: Proc.6th World Conf.Titanium,1(1988),p.57[Societe Francaise de Metallurgie]
- 15) M. Hagiwara, Y. Kawabe, Y. Kaieda and S. Miura: Trans. ISIJ. 31(1991).p. 922
- 16) S.Lampman: Metals Handbook, Vol 2, 10th ed., (1991), p. 592[ASM]

SELECTIVE REINFORCEMENT OF INVESTMENT CAST TITANIUM COMPONENTS

VIA BICASTING

Stewart J. Veeck and Gregory N. Colvin

Howmet Corporation 1500 South Warner Street Whitehall, MI 49461-1895

Abstract

Casting experiments were conducted to evaluate the selective reinforcement of investment cast Ti-6Al-4V alloy with titanium metal matrix composite preforms. These experiments were designed to examine the effect of metal to preform area ratio relative to erosion of the preform during casting and fiber degradation as a result of the thermal exposure. The results of the casting trials revealed that significant erosion of the MMC preforms and associated fiber damage occurred at area ratios above 10 to 15. However, at area ratios below 10, the MMC preform acted like a chill within the mold cavity and no erosion of the preform was evident. Extracted fibers from these castings showed limited strength degradation only near the casting downfeed where the thermal exposure (time/temperature) was greater. Excellent metallurgical integrity was obtained at the preform/casting interface after casting and HIP processing, with only minor solid-state interactions observed at sites where machined fibers were exposed to the matrix. These experiments clearly demonstrated that bicasting can be used to selectively reinforce or stiffen investment cast titanium components.

Introduction

Components for aerospace, automotive, and similar service applications have been subjected to the ever increasing demand for improvement in one or more mechanical properties, such as tensile strength, stiffness, fatigue life, or resistance to impact damage. At the same time, the goals of maintaining or reducing component weight are targeted. (1,2) Titanium matrix composite materials have the potential to meet the mechanical property requirements of many advanced structural applications; however, these materials often are not cost effective to produce as near net-shape components. Howmet has developed a more cost effective method to selectively reinforce geometrically complex titanium investment castings using a process called bicasting.

Bicasting offers a low risk method of introducing titanium matrix composites into structural turbine engine components. It combines investment casting, which is a low cost method of producing complex shapes, with high performance metal matrix composite materials. A primary advantage of bicasting is its utilization of conventional titanium casting practice. For many operations bicast components can be post-cast processed in batches with conventional titanium castings using current production facilities.

Titanium '92 Science and Technology Edited by F.H. Froes and I. Caplan The Minerals, Metals & Materials Society, 1993 There are four major steps to bicasting: (1) mold manufacture, (2) preform fabrication, (3) casting, and (4) post-cast processing and inspection, Figure 1. Investment molds are manufactured by coating a wax replica pattern with multiple layers of ceramic slurries and subsequently removing the wax by firing. A preform is placed within the mold cavity such that it lies within the component section intended to be reinforced. The preform geometry, composition, and fabrication method can be tailored to the desired mechanical property improvements. Except for a slight modification to permit placement of the preform inside the mold cavity, bicast molds are identical to production titanium molds. Because of titanium's reactivity, melting is performed using vacuum arc remelting (VAR) of consumable electrodes into water cooled copper crucibles. The preform subsequently is surrounded by the cast metal which then solidifies, embedding it into the component. The components then are processed using conventional titanium practice including: chemical milling, hot isostatic pressing (HIP), weld repair, heat treating, and inspection.

There are several technical challenges which must be surmounted to produce a sound bicast component. For example, the preform must be fixed in place to achieve required location tolerances. Mold fill can be greatly influenced by preform position and gating design. A minimal preform/mold wall clearance is necessary to ensure that molten metal completely fills the mold. The in-rush of molten titanium into the mold cavity may shift the preform out of position and result in poor dimensional integrity or even cause surface contact of the preform. Thus, the preform must be fixtured so that it remains in position during casting. In addition, the preform must not be significantly eroded by the cast metal and the final casting must be sound (crack and inclusion free). There also must be a metallurgically sound preform-to-cast metal bond after casting and HIP processing. Lastly, the MMC preform fibers must not be damaged during casting and subsequent thermal processing. Mold gating systems are designed to minimize hot metal flow onto the preform to minimize erosion and fiber damage during casting.

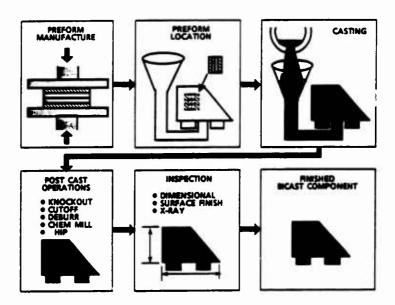


Figure 1 - Bicasting Process Schematic.

Discussion

MMC Preform Fabrication

Fabrication of metal matrix composite preforms for bicasting can be accomplished via any one of several existing processing routes, including foil/fiber/foil methods or induction plasma deposition (IPD) methods. ^[3] The final configuration of the preform will depend on the design requirements for the cast component to be reinforced. However, the preforms generally will require some degree of machining in order to fit the casting cavity.

Bicasting Process Development

Preliminary casting efforts were conducted to identify critical processing variables and establish suitable processing windows. One important variable was the erosion characteristics of the MMC preforms during casting. An experiment was designed to examine the effect of the ratio of MMC preform to cast metal cross-sectional area on preform erosion and fiber damage in an effort to establish the upper limits of the process. The experiment consisted of several duplicate molds containing 10 cm wide by 23 cm long cast slabs varying in thickness from 1.5 cm to 5.5 cm. Twenty-four ply multilayered SCS-6/Ti-6242 MMC preforms, 0.5 cm thick by 2.2 cm wide and 18.2 cm long, were HIP fabricated from 8-ply panels produced by Textron through an Air Force program (Contract F33615-89-C-5708). These preforms were placed inside the molds and the molds centrifugally cast in Ti-6Al-4V at Howmet. All the slabs were bottom gated to minimize erosion effects. The area ratio of the cast metal to MMC preform varied from 13.4 to 49.1 in the cast slabs. After casting, the individual slabs were radiographically inspected to verify the location of the preforms. The slabs then were HIP processed, and the cast metal/preform interface was examined microstructurally near the gating 2.5 cm from the bottom of the MMC preform to determine the extent of interaction. The larger cast slabs having a metal/MMC preform ratio of 49.1 showed complete dissolution of the preform, while the intermediate size slabs, having a metal/MMC preform ratio of 26.7, only showed dissolution of the first several layers of reinforcement. Erosion of the MMC was most severe in those areas adjacent to the gating in the casting mold which represents the hottest area in the cast slab. Some thermally induced porosity (TIP) also was noted in the MMC matrix adjacent to those regions where fiber dissolution occurred, as shown in Figure 2.

The cast slabs having the lowest cast metal to MMC preform area ratio (13.4) generally showed complete survival of the preform, although some solid-state interaction was evident where the fibers were exposed by machining, as shown in Figure 3. Bonding at the preform/casting interface was excellent in these cast and HIP'ed slabs as evidenced by random grain growth across the interface. The observed fiber/matrix interactions became greater as the thermal exposure experienced by the preform became more severe. However, even in the samples where the metal/MMC ratio was lowest, there was evidence of increased fiber/matrix interaction relative to the as received MMC material. At the higher metal/MMC ratios substantial fiber damage was evident, including complete fiber dissolution and the formation of TIP porosity in the matrix.

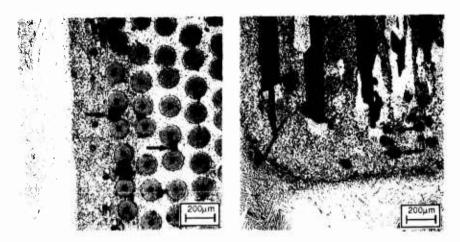


Figure 2 - Bicast slab showing partial dissolution of MMC preform. Transverse (a) and longitudinal (b) views near gating. Note the TIP porosity in the MMC matrix.

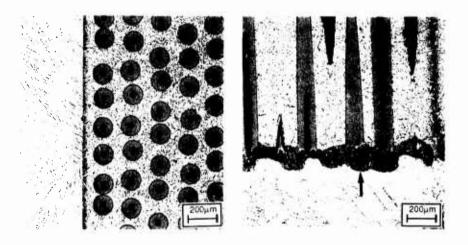


Figure 3 - Bicast slab showing minimal fiber/matrix interactions at machined surfaces only. Sound metallurgical bonding was obtained at all preform/casting interfaces.

Another group of MMC preforms, fabricated at GE using IPD processing and consisting of multiple plys of SCS-6 reinforced Ti-6242, were used in additional bicasting efforts. The preforms were held in place in specially designed molds using proprietary process methods and centrifugally cast in Ti-6Al-4V at Howmet. Following casting and conventional HIP processing at 900°C, each component was radiographically inspected

to establish the position of the preform within the component. Selective metallography subsequently was conducted on one component to examine interactions between the MMC preform and cast matrix. The results of these examinations indicate the MMC preform acted much like a chill block within the casting cavity, as shown in Figure 4, with no erosion occurring even in the regions adjacent to the downfeed gating. Moreover, positioning of the preform within the casting cavity was within 0.04 cm of centerline.

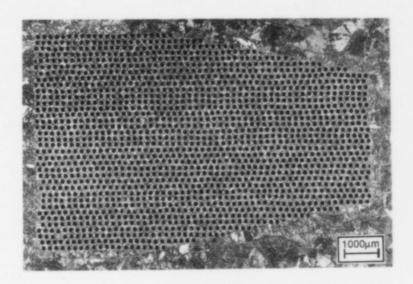
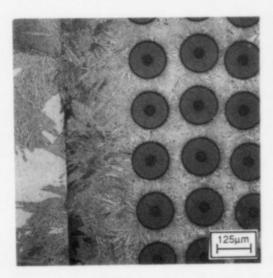


Figure 4 - Bicast component showing a machined MMC preform after casting and HIP processing. No erosion of the preform was evident.

As noted previously, there were some solid-state reactions in regions where the fibers were machined and the SiC fiber exposed. However, these interactions were minor with only small diffusion zones evident, Figure 5.



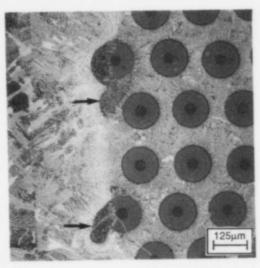


Figure 5 - MMC/casting interface after bicasting and HIP processing. Only solid-state interactions were observed where machined fibers were exposed.

As was noted previously, greater degrees of diffusion and increased fiber/matrix interactions were observed in the regions of the casting adjacent to the downfeed gating which are known to be hotter. Calculation of the metal to MMC area ratios in the component cross section showed them to range from approximately 15 near the hot end to 6 in the center of the axial length of the casting. To further clarify effects on the fiber strength, preform sections were selectively water jet cut from the casting after HIP and the matrix etched away from the fibers using an H₂O/HNO₃/HF solution. The fibers were then tensile tested by individual row (20 tests/row) and the strength of the outer rows were compared to each successive row until strength levels were uniform. One MMC sample was removed from the hottest area adjacent to the downfeed gating and another was taken from an area away from the downfeed gating. The results, shown below in Figure 6, indicate that some fiber strength degradation does occur in the hotter regions of the casting near the downfeed gating, with fiber tensile strengths being reduced by about 50%. This effect, however, was limited to only the first 4 to 5 rows of fiber in the preform. The fiber strengths in the colder regions of the casting were unaffected by the processing conditions used in this casting experiment. Testing limitations did not allow the modulus of these fibers to be determined.

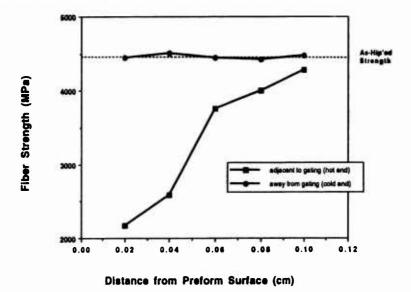


Figure 6 - Fiber strength vs. preform location in a bicast component.

Summary

A new process, called bicasting, has been developed by Howmet to selectively reinforce investment cast titanium components for turbine engine applications. Bicasting combines investment casting, which is a low cost method of producing complex shapes, with high performance MMC materials. The process is dependent on the relative ratio of the cast metal to MMC area, with high cast metal/MMC area ratios showing partial or complete dissolution of the MMC preform by the molten metal. However, at metal/MMC area ratios below 10 to 15, the process becomes very viable, with the MMC material behaving like a chill within the casting cavity and little or no fiber damage being observed. Thus, the potential to selectively stiffen or strengthen investment cast

titanium components for advanced turbine engine applications via bicasting is very promising. Efforts currently are underway to examine selective stiffening of specific turbine engine components.

References

- [1] "Developments in Metals-Forecast 1992", Advanced Materials and Processes, vol. 141, No. 1, Jan. 1992.
- [2] "S.R. Seagle, "New Titanium Developments in Products, Processes, and Applications in the USA", 1990 International Ti Conference, Oct. 5-7, 1990.
- [3] R.A. MacKay, P.K. Brindley, and F.H. Froes, "Continuous Fiber-Reinforced Titanium Aluminide Composites", <u>Journal of Metals</u>, May, 1991.

TITANIUM / CERAMIC COMPOSITES PRODUCED BY LASER PROCESSING

J.H.Abboud and D.R.F.West

Depatment of Materials

Imperial College of Science, Technology, and Medicine

London, SW7 2BP United Kingdom

ABSTRACT

An investigation has been made using high power CO₂ lasers in both continuous and pulsed modes to produce composite materials either in the form of surface layers on titanium substrates or as small pellets. In the first method the ceramic particles (i.e. TiB2 and SiC) were injected into the laser melted zone of a B Ti-15V-3Al-3Cr-3Sn alloy. The second method involved laser melting of premixed β-titanium alloy powder with 20vol.% of a ceramic (TiB₂, SiC, B₄C, or BN) or a mixture of Ti+Al+SiC. The effect of some laser processing parameters on the dimensions of the composite surface layers and pellets has been studied. Microstructural and compositional examinations of the composites showed that the ceramic particles were partially dissolved and enrichment of the melt zone with the products of the dissolution of the ceramic particles occurred; in some cases virtually complete dissolution of the ceramic particles was observed particularly with ceramic particle sizes of ~ 10 µm. The injection of TiB2 into the laser surface melted zone of Ti-15V-3Al-3Cr-3Sn alloy or laser melting of the alloy powder with 20%vol TiB₂ leads to a partial dissolution of TiB₂ and to the formation of TiB at the ceramic / matrix interfaces and in the matrix. The injection of SiC particles into the laser melted zone of B Ti alloy or laser melting of the alloy with SiC leads to the formation of TiC dendrites at the SiC / matrix interface and in the matrix, and to the enrichment of the matrix with silicon. Also laser melting of βTi alloy with B₄C leads to the formation of TiC and TiB crystals in a B Ti phase. The microhardness of the composite layers and the pellets ranged between ~ 500 and 1000Hv depending on the type of the ceramic and the extent of dissolution.

> Titanium '92 Science and Technology Edited by F.H. Froes and I. Caplan The Minerals, Metals & Materials Society, 1993

1.INTRODUCTION

The use of high power CW CO₂ lasers in producing composite surface layers has been the subject of several investigations [e.g.1-5]. Ayers et al [1,2] injected TiC particles into the laser melted zone of various titanium substrates including Ti-6Al-4V alloy and the surface hardening was interpreted as due to the partial dissolution of TiC particles and the formation of TiC dendrites in the matrix; also the wear rate decreased. Abbas and West [3] used the injection of SiC or a mixture of SiC and Stellite into mild steel to increase the surface hardeness and improve the wear resistance. Recently, the injection of SiC into the laser melted zone of commercial purity titanium and Ti-6Al-4V alloy has been investigated [4,5].SiC particles were partially dissolved and the matrix consisted of martensite (α'),Ti₅Si₃ and TiC and had a hardness of ~600Hv.

A technique developed by Weerasinghe [6] produces composites as small rapidly solidified "pellets" by placing material in powder form in a recess in a copper block, and melting using a pulsed laser. The use of mixtures of metallic and ceramic powder, with appropriate process control allows partial solution of the ceramic and the formation of composite pellets: such pellets could potentially be consolidated by a solid state processing route such as HIPing. Weerasinghe has investigated various systems, including mixtures of titanium and TiC.

The present paper is concerned with microstructural and compositional features and hardness of composites based on a β -Ti alloy (Ti-15V-3Al-3Cr-3Sn) and on a mixture of Ti-30at%Al, produced as surface layers and / or as pellets. Results are also reported on the relation between the dimensions of the processed samples and the laser processing parameters.

2. EXPERIMENTAL PROCEDURE

A 2kW and a 5kW CO_2 laser were used. Particles of TiB_2 or SiC with average particle sizes of $\sim 60\mu m$ and $150\mu m$ respectively, were blown, under a stream of argon, into the laser melted zone of β Ti alloy (Ti-15V-3Al-3Cr-3Sn) in the form of sheet of 1-3 mm thickness. An effective argon shrouding system was used. A series of single tracks were produced at different traverse speeds and powder flow rates.

A 1kW CO₂ laser was operated in pulsed mode to produce composite pellets as described above. β Ti alloy (15-3-3-3) powder with 20vol.% of either TiB₂,SiC, B₄C or BN with average particle sizes of ~10,150,40, and 10 μ m respectively, were used; also pellets were produced from a mixture of CPTi+30at%Al+20vol%SiC.The process was carried out under an atmosphere of argon.Partial solution of the ceramics was achieved with the exception of the BN; in this latter case the small particle size resulted in virtually complete solution. Transverse sections of composite surface layers and of pellets were metallographically prepared.X-ray diffractometry was carried out using Cu K α radiation. SEM-EDS analysis with a ZAF correction was used for compositional analysis. The boron and carbon contents were calculated by subtracting the total analysed proportions of other elements from 100%; the composition of the substrate before laser treatment was used as a reference standard. Thin foils from the surface layers were prepared as previously described [5]. Thin foils were also obtained by grinding relatively large pellets from both sides until ~ 150 μ m thickness was obtained, and then following the previously reported procedure [5]. Microhardness measurements were made (500g load) on the matrix of the composites.

3.RESULTS

3.1 Composites in the form of surface layers

3.1.1 B Ti alloy injected with TiB2

Fig.1 shows the structure of the β Ti alloy (Ti-15-3-3-3) injected with TiB₂ at 1.8kW laser power, 3mm beam diameter, 8.1mm/s traverse speed and 0.0546g/s powder flow rate. The laser melted zone showed a conduction limited shape and contained a reasonably uniform distribution of partially dissolved TiB₂ with a rim of a reaction product (grey in Fig.1b). The matrix had a hardness of ~ 525±25Hv and consisted of particles (grey) of plate / needle like shape in a background of a light coloured phase. X-ray diffraction data showed the presence of β -Ti phase (bcc) and TiB (orthorhombic) in addition to the undissolved TiB₂ (hexagonal). EDS analysis of the particles in the matrix and around the undissolved TiB₂ was consistent with TiB. Increasing the traverse speed from 8.1mm/s to 20mm/s led to a decrease in the zone width from 3.25 to 1.9mm and to a decrease in the thickness from 0.66 to 0.2mm.

3.1.2 B Ti alloy injected with SiC

Fig.2a shows a typical microstructure of a β -Ti alloy sample laser surface melted (3kW, 5mm, 7mm/s) without ceramic particle injection. Columnar grains have grown epitaxially from the coarse β grains in the heat affected zone. The cellular / dendritic structure, of average

cell / dendrite spacing ~ 5 to

 $10\mu m$ is indicative of cooling rates of the order of 10^3 °C/s [7]. Fig.2b shows the same alloy after injection with SiC particles at 0.15g/s. The melted zone is free from cracks and porosity; SiC segregates to the top of the melted zone. TiC dendrites nucleated at the SiC / matrix interfaces (Fig.2c). Enrichment of the matrix with respect to silicon and carbon ocurred. The upper part of the processed zone matrix contained 4wt%Si, and the structure showed a lamellar eutectic of $(\beta+Ti_5Si_3)$ with associated small TiC particles; there were some primary TiC dendrites. In the lower part of the processed zone the matrix contained only ~ 1.5wt%Si, and the structure was predominantly $\beta+TiC$; the latter occurred in dendritic and in lenticular form (Fig.2d). SADP's from the TiC were indexed as fcc crystal structure while the remainder of the structure was $\beta+\omega$. STEM analysis of the carbides showed the presence of 2wt% V. The hardness ranged from ~ 580Hv in the upper region to ~ 480Hv in the lower region. Increasing powder flow rate, while maintaining other parameters constant, led to increases in the volume of the processed layer and to the level of the enrichment with Si and C.

3.2 Composites in the form of pellets

3.2.1 B-Ti alloy

Fig 3a shows a typical nearly spherical shape of a pellet produced by laser melting of the β Ti alloy powder at 800W and 0.05s.Two diametral measurements on a pellet typically showed differences of ~ 0.1mm on a total of ~ 1.8mm. There was a trend for the number of pellets produced per pulse to increase with beam diameter and this may be due to a change in the power distribution with increasing beam diameter. Attempts to reveal the microstructure of the surface of the pellet by SEM were unsuccessful. The microstructure of a transverse section consisted of single phase β with grain sizes ranging between ~ 10 and 20 μ m; an indication of columnar growth from the pellet surface is seen. Cellular / dendritic structures were observed within the β grains; the average spacing was ~ 5 μ m suggesting a cooling rate of the order of 10^3 °C/s. The pellet size increased with increase in pulse time (Fig.3b) and the cell / dendrite spacing decreased indicating a decrease in cooling rate.

3.2.2 B Ti alloy / TiB2

The microstructure of a pellet produced from a mixture of β Ti alloy powder+20vol.%TiB₂, laser melted at 800W, 3mm, and 0.5s showed that the TiB₂ particles were partially dissolved and the microstructure of the matrix (~ 500Hv) showed needle-like crystals (identified by EDS as TiB) dispersed in β Ti phase (Fig.4a).X-ray diffraction peaks agreed with β Ti and orthorhombic TiB in addition to the hexagonal TiB₂. TEM examination showed that the TiB particles contained a high density of dislocations and stacking faults (Fig.4b).STEM analysis showed that the TiB contained ~ 10wt% of vanadium. SADP analysis showed the presence of TiB, β and ω .

3.2.3. B Ti alloy / B4C or BN

The microstructure of a pellet produced from a mixture of the β Ti alloy+20vol.% B_4 C, laser melted at 800W, 3mm, and 0.3s is shown in Fig.5a. Most of the B_4 C particles had dissolved leading to a hardness of ~ 490±10Hv. The matrix microstructure consisted of β phase containing dendrites (light grey), and faceted plates (dark grey); these dendrites and plates also formed at the interface of undissolved B_4 C particles. EDS analysis showed that the dendrites were TiC while the faceted plates were TiB, the latter containing a high proportion of V. TEM and STEM analysis showed that the TiC and the TiB contained dislocations (Fig.5b) and TiC contained V up to 2wt%, while TiB contained ~ 10wt% V.SADP analysis showed β and ω phases, fcc TiC dendrites and orthorhombic TiB.

phases, fcc TiC dendrites and orthorhombic TiB.

With the BN, and with the laser parameters used, virtually all the ceramic particles went into solution; the structure showed a mixture of Ti-dendrites (rich in nitrogen) and TiB. The hardness was ~ 1000Hv.

3.2.4 BTi alloy / SiC

The microstructure of a pellet produced from a mixture of β Ti alloy+20vol.%SiC, laser melted at 800W, 3mm, and 0.5s, is shown in Fig.6.The SiC particles were partially dissolved

and dendrites were nucleated at the SiC / matrix interface and in the matrix. The matrix (hardness ~565±10Hv) consisted of β dendrites and interdendritic regions showing a lamellar eutectic of β+Ti₅Si₃ and also particles of TiC, coexisting with the eutectic. EDS X-ray analysis data at different locations is presented in Table 1.

Table 1: EDS X-ray analysis (wt%) of BTi / SiC pellet processed at 800W, 3mm, and 0.5s.

Position	Ti	V	Cr	Al	Sn	Si	С
Matrix *	70.5	14.5	2.6	3.0	3.5	4.0	~ 2.0
Ti, dendrite **	73.5	15.0	3.0	3.5	3.5	1.5	~ 0
Eutectic region+	70.5	13.0	3.0	2.5	2.5	8.0	~ 0.5

^{*} Area analysis including Ti dendrites, eutectic regions and TiC particles, ** point analysis, + area analysis mainly, β+Ti₅Si₃

3.2.5 Ti-30at%Al / SiC

Fig.7a shows a typical structure of a pellet produced from a powder mixture of (Ti-30at%Al) +20vol.%SiC (75µm particle size), laser melted at 800W power, 3mm beam diameter, and 0.9s pulse time. The average pellet diameter was ~3mm and the SiC particles were nearly uniformly distributed.SiC particles had partially dissolved and a rim formed interpreted as consisting of a'2+TiC; enrichment of the matrix (~580Hv) with silicon and carbon had occurred.X-ray diffraction analysis showed some peaks corresponding to Ti₂Al (a₂) as reported by Goldak and Parr [8] with other peaks corresponding to TiC.TEM examination showed that the microstructure consisted of lath type martensite surrounded by a eutectic. The laths contained APB's characteristic of α2', and also a high density of dislocations; some laths contained fine precipitates of silicide. The silicide was identified by STEM as Ti₅(Si,Al)₃, containing up to ~7wt%Al.SADP data of the lath martensite were indexed as hcp crystal structure showing superlattice reflections. The eutectic regions consisted of α_2 '+ $Ti_5(Si,Al)_3+TiC$; the α_2' appears as laths, the $Ti_5(Si,Al)_3$ as rods with spacings of ~ 500nm, and the TiC as spherical particles ~1-2µm containing a high density of dislocations (Fig.7b).

4.DISCUSSION

4.1 B-Ti alloy / TiB2

This system is the simplest of those investigated since the ceramic phase contains only one additional component (namely B) as compared with the \beta alloy matrix; also the solubility of B in Ti in the solid state is very small. The binary Ti-B system contains the compounds TiB, Ti₂B₄, and TiB₂. The present observations both on the injected tracks and the composite pellets show that partial solution of the TiB₂ leads to the formation of TiB as a reaction layer around the TiB₂ and as plate / needle like primary crystals in β phase. No evidence was obtained of the formation of Ti₃B₄. The absence of Ti₃B₄ can be explained by referring to the equilibrium reactions shown on the phase diagram. At ~ 2000°C there is a peritectic reaction L+TiB2 -- Ti_3B_4 , and at a temperature only ~30°C below this a second peritectic occurs L+ Ti_3B_4 — TiB. With the rapid solidification conditions operative in the laser processing, the first peritectic reaction is unlikely to occur significantly and TiB formation is dominant. The TiB contains 10wt%V in solution resulting from the use of Ti-15V-3Al-3Cr-3Sn alloy. The small density difference between TiB₂ (~4520 kg/m³) and Ti (~4500 kg/m³) prevent the gravity segregation of undissolved ceramic particles which occurs in the case of SiC (~3200 kg/m³).

4.2 B-Ti alloy / B4C or BN

The reaction of B_AC particles with the liquid led to the formation of a three phase structure on solidification consisting of β (with some ω formed in the solid state) with a dispersion of particles of TiC + TiB. The dendritic morphology of the TiC (grey dendrites, Fig. 4a) suggests that this is the primary phase; the relatively coarse faceted crystals of TiB, which contain 10wt%V, solidified in close association with TiC. The observation can be correlated with the semi-schematic representation of the Ti-V-B-C phase diagram (Fig.8). The average

composition (*) lies on the line joining Ti-15V (neglecting the presence of Sn and Cr and Al) and B₄C. The matrix structure lies in the three phase region containing β-Ti phase +TiC+TiB. In the case of $\beta Ti / BN$, the composition of the melt pool leads to the primary phase being nitrogen-rich Ti dendrites.

4.3 B-Ti alloy /SiC

The injection of SiC into CP Ti has been previously discussed [4] in relation to the Ti-Si-C phase diagram. For the laser conditions used as also in the previous work, solution of Si and C enriched the melt pool so that TiC formed as the primary phase: TiC formed as a reaction layer around the SiC particles and also as dendrites in the matrix. Following the primary formation of TiC, a reaction involving L, β, and TiC occurred; either L → β+TiC or L+TiCβ. Finally, in the matrix of the upper part of the processed zone, which contains ~ 4.5 wt%Si, a lamellar eutectic formed of β+Ti₅Si₃ with associated TiC: the origin of this structure may either be a ternary eutectic $L \rightarrow \beta + TiC + Ti_5Si_3$ or a peritectic $L + TiC \rightarrow \beta + Ti_5Si_3$. These features are similar to those previously reported for a structure where the matrix contained ~ 3.5wt%Si [4]. In the present work the solidification sequence, allowing for the presence of 15wt%V in the β phase (which leads to its retention at room temperature) is similar to that previously discussed [4]. In the lower part of the zone, the lower silicon content of the matrix (~1.5wt%) accounts for the absence of the B+TiC+Ti₅Si₃ constituent.

4.4 CP Ti+Al+SiC

The laser melting of a mixture of CP Ti+30at%Al with SiC produced pellets in which Ti₂Al formed as a reaction product. The matrix showed similar microstructural features to those observed when B Ti is processed with SiC, with the difference that because of the high Al content of the matrix, the \(\beta \) phase formed during solidification transformed to ordered martensite α'_2 on cooling in the solid state.

5.CONCLUSIONS

- 1. Injection of TiB₂ and SiC into laser melt pools on a BTi alloy substrate can be used to produce composite surface layers. Partially dissolved TiB₂ shows a more uniform distribution than SiC; this is consistent with the small density difference between the alloy and TiB₂.
- 2. Composite pellets consisting of partially dissolved particles in a matrix based on B Ti alloy can be produced by laser melting of premixed ceramic and β Ti powder; also SiC particles in a matrix based on Ti₃Al can be produced from a mixture of Ti+Al +SiC.
- 3. Enrichment of the titanium based matrix with one or more of Si, C, B, N has been observed in all the processed samples leading to high levels of hardness.

ACKNOWLDEGMENTS

Acknowledgements are made to SERC for financial support and to IMI Titanium Ltd for supplying the metal.

REFERENCES

- 1.J.D. Ayers and R.N. Bolster "Particulate Composite Surfaces by Laser Processing," Lasers in Metallurgy, K.Mukerjee and Mazumder, eds., TMS-AIME, Warrendale, PA, 1981,115-125
- 2.J.D.Ayers and T.R.Tucker and R.C.Bowers, "A Reduction in the Coefficient of Friction for Ti-6Al-4V", Scripta Metall. 14 (1980) 549-550.
- 3.G.Abbas and D.R.F.West, "Laser Surface Cladding of Stellite and Stellite-SiC composite
- Deposite for Enhanced Hardness and Wear, Wear, 143 (1991) 353-363.
 4.J.H.Abboud and D.R.F.West, "Ceramic/ Metal Composites Produced by Laser Surface Treatment" Mat. Sci. Tech., 5 (1989) 725-728.
- 5.J.H.Abboud and D.R.F.West,"Microstructure of Titanium Injected with SiC Particles by Laser Processing" J.Mat.Sci.Lett., 10 (1991) 1149-1152. 6.V.M.Weerasinghe, to be published.
- 7.T.C.Peng, S.M.L.Sastry, and J.O'Neal, A Correlation Between Dendrite-Arm-Spacing and Cooling Rate for Laser-Melted Ti-15V-3Al-3Cr-3Sn, Lasers in Materials Processing, ed. E.A.Metzbower, ASM Conf. Proc. (1983) 241-246.
- 8.A.T.Goldak and J.Gordon Part, "The Structure of Ti3Al", Trans. AIME, 221 (1961) 639.

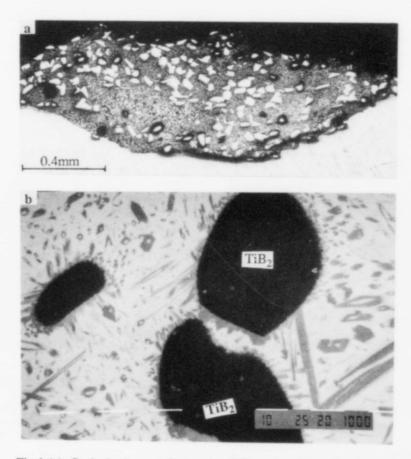


Fig.1 (a): Optical micrograph showing TiB₂ injected into Ti-15-3-3-3 alloy (b) SEM-BSI showing TiB formed around the TiB₂ and in the matrix

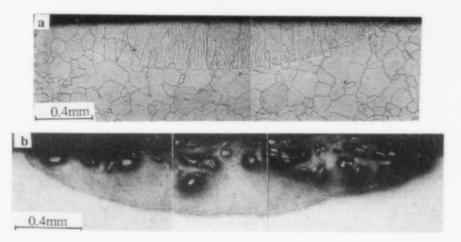
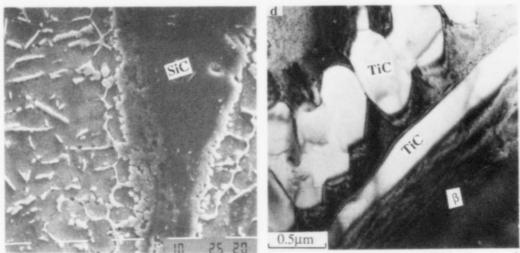


Fig.2: (a) Optical micrograph showing laser melted zone of βTi alloy (b) Optical micrograph showing SiC injected into βTi alloy



(c) SEM micrograph showing TiC around the SiC and in the matrix, (d) TEM micrograph showing TiC in β phase.

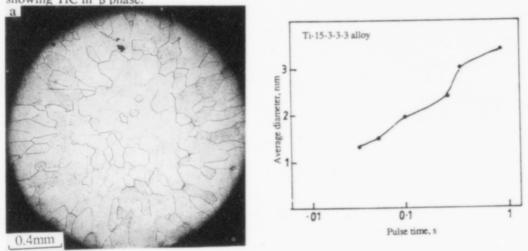


Fig.3: (a) Optical macrograph showing β Ti pellet, (b) Variation of average pellet diameter with pulse time, 800W, 3mm.

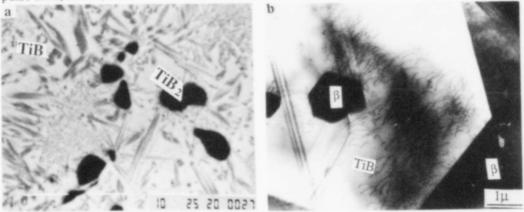


Fig.4: β Ti / TiB₂ pellet, (a) SEM micrograph showing TiB around the TiB₂ and in the matrix, (b) TEM micrograph showing TiB in β Ti.

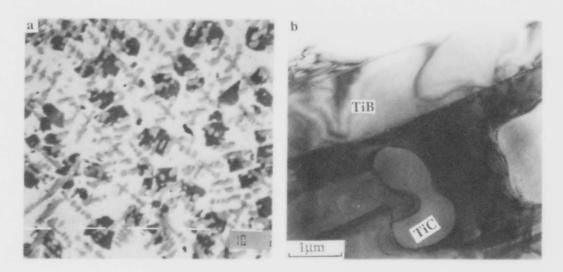
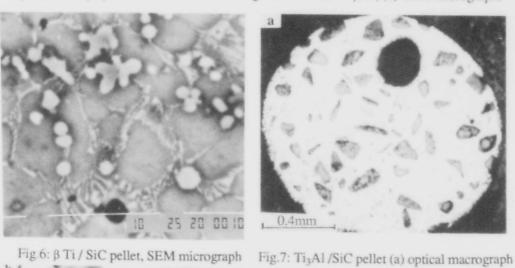
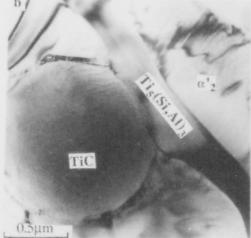
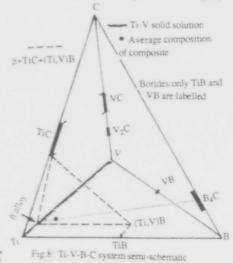


Fig.5: β Ti / B₄C pellet (a) SEM-BSI showing TiC and TiB in β Ti, (b) TEM micrograph.





(b) TEM micrograph showing α'2+Ti5(Si, Al)3+TiC



ADVANCED POWDER METAL TITANIUM ALLOY MATRIX COMPOSITES REINFORCED WITH

CERAMIC AND INTERMETALLIC PARTICLES

Stanley Abkowitz, Paul Weihrauch and Susan Abkowitz Dynamet Technology, Inc., Eight A Street, Burlington, MA 01803.

ABSTRACT

Metal matrix composites utilizing particulate reinforcements have demonstrated significant increases in the strength, modulus and use temperature of advanced structural alloys without the economic and technical drawbacks associated with continuous fiber reinforcement. Studies at Dynamet Technology involving particulate additions of ceramic or intermetallic compounds to conventional monolithic titanium alloys have resulted in several promising titanium MMC's. Based on economical powder metallurgy technology these MMC's have been fabricated both to near net component shape by the CHIP process (cold and hot isostatic pressing) and by forging and to mill product form by extrusion and rolling.

This paper describes the manufacture and properties of these MMC's with particular attention to the significant improvements in modulus and strength at both room and elevated temperatures.

Titanium '92 Science and Technology Edited by F.H. Froes and I. Caplan The Minerals, Metals & Materials Society, 1993

Introduction

Titanium base alloys offer significant opportunities for weight reduction in advanced airframe and missile structures and in gas turbine engines. However, conventional monolithic titanium alloys are limited by loss of strength and oxidation resistance to a maximum temperature of about 1000°F. Because of this temperature limitation, effort has been directed at novel approaches to titanium material development.

One such approach has involved the development of titanium materials based on intermetallic aluminide compounds, particularly Ti₃Al and TiAl. An increase in the titanium alloy use temperature of as much as 800°F has been predicted for TiAl derivative materials. The major problem with these materials is their lack of useful ductility which not only makes structural design difficult but also complicates their fabrication to mill product form and component configuration. Considerable alloying studies have been undertaken in an effort to find compositional variations which might lend enough ductility to overcome both the design and fabrication difficulties.

A second major approach to extending the use temperature of titanium alloys involves combining conventional titanium alloys or advanced titanium aluminide derivative alloys with a non-equilibrium reinforcing phase —— generally, but not always, non-metallic. These titanium metal matrix composite manufacturing development programs have emphasized the use of silicon carbide (SIC) as the stiffener addition, typically in the form of whiskers or fibers. Such technologies pose significant technical problems in fiber/matrix interreaction, performance problems in anisotropy of material properties, manufacturing problems in component shape production, as well as prohibitive material and manufacturing costs.

Other approaches develop metal matrix composites utilizing particulate additions as the reinforcing phase. Produced by casting or powder metallurgy, these materials offer significant technical improvements and an economic manufacturing technology. Dynamet has taken this latter approach, adapting its P/M CHIP (combining cold and hot isostatic pressing) manufacturing technology for monolithic titanium alloys (1) to develop a family of titanium MMC's, commercially known as CermeT (2).

P/M Processing Routes and Product Forms

The CHIP process, a powder metallurgy technology consisting of cold isostatic pressing (CIP) in reusable elastomeric tooling, and vacuum sintering followed by containerless hot isostatic pressing (HIP) (i.e., without the need for additional expensive tooling) has been recognized in recent years as a practical and economic method for the fabrication of fully dense titanium alloy components to a near-net shape. (3) This P/M method utilizes elemental cold-compactible titanium powder, which is available in both standard and extra-iow chloride grades, at reasonable prices (4). The powder is blended with other elemental or master alloy powder additions to obtain the alloy composition desired.

^{*}CermeT B is a registered trademark at the office of U.S. Patent and Trademark and is the subject of U.S. and foreign patents assigned to Dynamet Technology, Inc.

The adaptation of the CHIP process to the manufacture of titanium-matrix micro-composites overcomes many of the limitations of fiber-reinforced and other composites in a practical, cost effective way. These materials are processed essentially in the same fashion as the monolithic alloys previously described, except that a substantial amount of reinforcing particles is blended with the elemental metal powders.

Dynamet Technology has extensively evaluated CermeTi materials as a function of particle type, size and loading as well as titanium P/M matrix alloys and CHIP processing parameters. The most important factor in developing a successful CermeTi is the selection of a compatible reinforcing particle. This is demonstrated by Figure 1, which illustrates the well known but unsuccessful result of adding particulate sillcon carbide (SiC) to Ti-6AI-4V. The SiC has partially dissolved in the titanium alloy matrix at the CHIP processing temperature (2250°F maximum during sintering) resulting in a giass-brittle material. That SiC dissolution occurs during solid state sintering, far below the melting point, illustrates the problems of incorporating SiC fibers or particles in a casting.

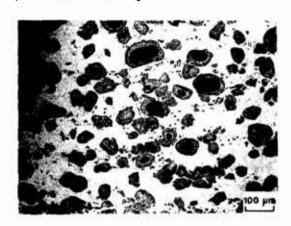


FIGURE 1. 10% SIC IN TI-6AI-6V-2Sn MATRIX PRODUCED BY CHIP PROCESS.

The initial successful CermeTi development involved the use of titanium carbide (TiC) as the particle reinforcement $^{5)}$. Since the initial work, other particulates have been successfully added including titanium diboride (TiB2) and, most recently, the intermetallic compound titanium aluminide (TiA1). A lower temperature processing route has been developed for TiA1 microcomposites to prevent particle dissolution at the normal sintering temperature (2250°F).

Most of the development work has been done with Ti-6Al-4V as the matrix alloy. However, other matrix alloys have been successfully employed including Ti-6Al-6V-2Sn (for higher strength), Ti-6Al-2Sn-4Zr-2Mo and its silicon containing variation (for elevated temperature strength) and Ti-3Al-2V (for greater machinability and workability). Furthermore, in addition to CHIP processing these composites have also been successfully fabricated by forging, extrusion and rolling of the P/M CIP plus sinter or CHIP preform.

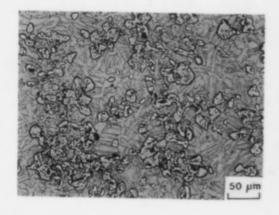
To distinguish among the various microcomposites in the CermeTi family, a generic designation system has been adopted identifying each

microcomposite as CermeTi-X-YZ, where X identifies the particulate, Y, its loading in weight percent and Z, the matrix alloy, according to the following designations:

X Designation	Particulate Type	Z Designation	Matrix Alloy
A B C	TIAI TIB ₂ TIC	A B C	Ti-6AI-4V Ti-6AI-6V-2Sn Ti-6AI-2Sn-4Zr-2Mo Ti-3AI-2V

Thus, a microcomposite consisting of a 10% addition of TiC in a Ti-6Al-6V-2Sn matrix is designated CermeTi-C-10A (the same particulate addition in a Ti-6Al-4V matrix is designated CermeTi-C-10).

Representative microstructures of CermeTi-C and CermeTi-B microcomposites are shown in Figures 2 and 3. These photomicrographs illustrate the potential for microstructural uniformity offered by the Dynamet P/M approach. In all cases the particle/matrix interfaces are clearly established having maintained the integrity of the particulate within the Ti-6Al-4V matrix. This is evident throughout the microstructure of the part and from part to part processed by this technology. The particulate is essentially homogeneously dispersed and the microcomposite has achieved virtually 100% density.



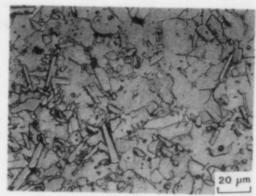


FIGURE 2.
MICROSTRUCTURE of CERMETI-C-20
MANUFACTURED BY CHIP PROCESS

FIGURE 3.
MICROSTRUCTURE OF CERMETI-B-10
MANUFACTURED BY CHIP PROCESS

An outgrowth of this technology involves alternately layering composites with monolithic alloys to create selectively reinforced components with unique properties. Since a common alloy matrix is generally used, no dilution of either phase occurs. These micro-macro composites have since been termed Common Matrix, Micro-Macro Composites or CM³Cs. Figure 5 illustrates the CM²C concept, in this instance showing a TiC reinforced CermeTi microcomposite with a monolithic titanium alloy. As a result of the self-diffusion of the titanium alloy, no discernible "bond line" exists at the original interface of the CermeTi with the titanium.

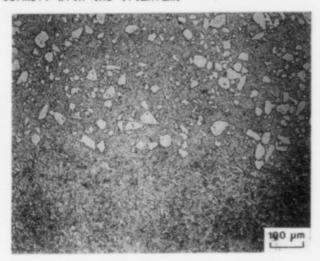


FIGURE 4.
PHOTOMICROGRAPH OF A
CERMETI-C-10 MICRO COMPOSITE (ABOVE) DIFFUSION BONDED TO MONOLITHIC TI-6AI-4V (BELOW)

The potential design flexibility offered by CM C technology is illustrated by the cross-section of the "pie extrusion" shown in Figure 5. The pie pieces consist of CermeTI-C-20 microcomposite wedges alternating with wedges of monolithic Ti-6AI-4V alloy. The CM Structure was assembled as a single billet from two powder blends and consolidated by extrusion.

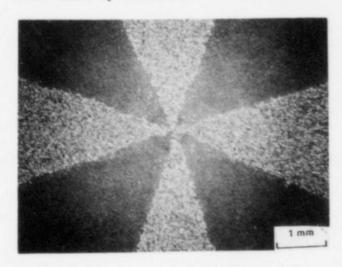


FIGURE 5. CERMETI-C-20 CM³C PIE EXTRUSION.

Mechanical Properties of CermeTi Composites

Among the family of CermeTi materials, CermeTi-C-10 (10% TiC in a Ti-6Al-4V matrix) fabricated by the CHIP process with and without subsequent forging or extrusion has been the most completely characterized. Comparison of tensile properties of CermeTi-C-10 with those of the monolithic matrix alloy indicates that the room temperature yield and tensile strengths are increased 10-15% and the strength differential is maintained to $1200^\circ F^{\{6\}}$. Reasonable engineering ductility is retained throughout the temperature range with elongation of up to 3.5 percent measured at room temperature. At 1200°F the ductilities of the composite and the matrix material do not differ significantly.

The most dramatic property improvement of the particle reinforced CermeTi-C-10 material compared to monolithic Ti-6Al-4V alloy is in the elastic modulus. Room temperature modulus values are about 15 percent higher on average than Ti-6Al-4V (Figure 7). Furthermore, the modulus advantage persists over the temperature range to 1200°F and represents as much as 600°F improvement.

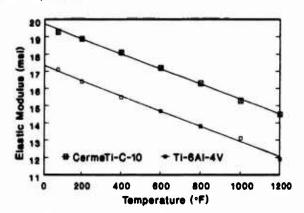


Figure 6 Dynamic (Elastic) Modulus vs. Temperature of CermeTi-C-10

Additionally, high cycle fatigue properties were found to be comparable to Ti-6Al-4V produced by the blended elemental powder metallurgy $_{(6)}$. Furthermore, fatigue fracture strength in the low cycle range (<10 6) was higher than P/M Ti-6Al-4V.

Further enhancements of strength and modulus have been obtained with higher reinforcement levels, a change in particulate type and microstructural refinement from hot working. Figure 7 shows the further improvement in elevated temperature strength of CermeTi-C-10 after beta forging (7) while Figure 8 shows the combined affects of higher particulate loading and beta forging of CermeTi-C-15(7). Other results with CermeTi-C-15 indicate fatigue properties comparable to Ti-6AI-4V castings and creep resistance considerably improved over wrought Ti-6AI-4V.

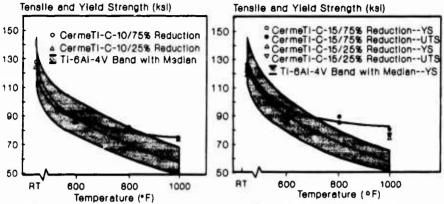
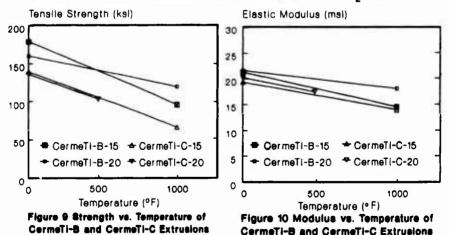


Figure 7 Tensile Properties of Forged CermeTi-C-10 and Ti-6Ai-4V as a Function of Test Temperature

Figure 8 Tensile Properties of CermeTi-C-16 and Ti-6Ai-4V as a Function of Test Temperature

The effect of changing the particulate type from TiC to TiB $_2$ is shown in Figures 9 and 10 which compare the temperature dependence of strength and modulus of extrusions containing 15 and 20 percent additions of TiC and TiB $_2$. Over the temperature range from room temperature to 1000°F, TiB $_2$ is a more effective strengthener and stiffener than TiC. However, TiB $_2$ microcomposites display lower room temperature ductility than TiC reinforced composites. Both the lower ductility and higher strength are attributed to higher oxygen introduced into the titanium alloy matrix from oxide contaminants present in commercial grades of TiB $_2$ powder.



Even with limited room temperature ductility, CermeTi microcomposites display useful levels of fracture toughness. The value of K_{1C} for CHIP processed CermeTi-C-10, estimated from 4-point bend testing of notched test bars, is about 26 ksi $\{\ln^{(5)}\}$, which is comparable to the widely used aerospace aluminum alloy 2014–T6. Reported test results for

extruded and beta annealed CermeTi-C-20 give a $K_{\rm LC}$ value of about 21 ksi fin with fatigue crack growth rate comparable to Ti-6AI-4V castings (8).

To date the TiAl reinforced microcomposites have been least characterized. Preliminary tensile data indicate higher strength and ductility than both TiC and TiB₂ microcomposites up to 1000°F. The increase in room temperature modulus is smaller but a large fraction of the room temperature value is retained at elevated temperature. An added advantage of the CermeTi-A materials is their reduced density, compared to CermeTi-B and CermeTi-C, due to the relatively lower density of the TiAl reinforcement thus resulting in further improvement in specific strength and specific modulus.

The Future of CermeTi Materials

There is still much to be done in refining the processing and charac-terizing the properties of the CermeTi family of materials. Nevertheless, just as the CHIP near-net shape P/M technology has found an important niche based on an advantageous combination of technical and economic factors, CermeTi materials are expected to find a similar place in applications where the isotropic property enhancements are necessary to meet technical requirements and the economic benefits of P/M processing can be realized. Thus, fairly large, complex parts complex parts manufactured to near-net shape either directly by the CHIP process or by forging a near-net shape P/M preform are excellent candidates for CermeTi application, since they take advantage of the inherent economics of this P/M approach. Multi-layered structures and clad components, which take advantage of the unique combinations of properties made possible by the ${
m CM}^3{
m C}$ technology, are a second area of development and application. Potential applications include forged lightweight missile fins with improved dynamic performance in the former category and composite exhaust valves for high performance automotive engines in the latter. Finally, the CermeTi materials technology will offer MMC property enhancements in mill product form by conventional low cost hot working procedures.

References:

- 1. S. Abkowitz, "Production of Complex Full Density P/M Ti Shapes by the CHIP Process," APMI Nat'l Powder Metallurgy Conf, Philadelphia, PA, 1981.
- 2. S. Abkowitz and P. Weihrauch, "Trimming the Cost of MMC's," Advanced Materials and Processes, (1989), 31-34.
- 3. S. Abkowitz, "Isostatic Pressing of Complex Shapes from Ti and Ti Alloys, "Ti-80-4th int'l Conf. on Titanium, Kyoto, Japan (1981) 2321-2330.
- 4. S. Abkowitz and D. Rowell, "Superior Fatigue Properties for Blended Elemental P/M Ti-6Ai-4V," Journal of Metals, 38 (8) (1986), 36-39.
- 5. S. Abkowitz, P. Weihrauch and S. Kraus, "Development and Evaluation of the Metallurgy and Shape Fabrication of Titanium Matrix CermeTi Composites for High Modulus, High Temperature Applications", Final Report, Navy Contract No. N69021-86C-0222, October 1988.
- 6. H. Fujli, T. Yamazaki, T. Horiya and K. Takahashi, "High Performance Ti-6Al-4V + TiC Alloy by Blended Elemental Powder Metallurgy", ^{9t} Pacific Rm international Conf. on Advanced Mat'ls, Hangzhou, China (1992)
- 7. G. Kuhiman, A. Charkrabarti and S. Abkowitz, "Properties of P/S Titanium Forgings", Aeromat Conference, Long Beach, CA, May 1990.
- 8. J. Shang, "Fracture Mechanisms in Particulate-Reinformed Metal Matrix Composites", TMS Annual Meeting, San Diego, CA, March 1992.

COMBUSTION SYNTHESIS OF TIC-Al2O3-TI CERAMIC-METAL

COMPOSITE MATERIALS: AN INITIAL PHENOMENOLOGICAL EXAMINATION

K. R. Hunter', J. J. Moore', D. Wirth2

'Department of Metallurgical and Materials Engineering Colorado School of Mines Golden, Colorado 80401

> ²Coors Ceramic Company Golden Colorado, 80401

Abstract

The initial phenomenological results are discussed for the combustion synthesis of a $TiC-Al_2O_3-Ti$ ceramic-metal composite material, based on the exothermic reaction:

$$(3 + x)TiO_2 + 3C + (4 + \frac{4}{3}x)Al \rightarrow 3TiC + (2 + \frac{2}{3}x)Al_2O_3 + xTi$$

The effect of green density, mode of combustion, and reaction stoichiometry on ignition and combustion temperatures, reaction stability and the extent of porosity are examined.

Introduction

The combustion synthesis, or Self-Propagating High Temperature Synthesis (SHS), of ceramic composite materials offers considerable potential compared with conventional routes for the synthesis and processing of advanced materials.' Combustion synthesis may be achieved by two modes of combustion. The propagating mode involves the ignition of the reactant powder mix locally, e.g. at the top surface, and the reaction front moves down through the sample. The thermal explosion or bulk mode involves heating the entire sample to the ignition temperature, Tig, thereby creating a bulk reaction in the entire sample. A major disadvantage of SHS processing is the high level of porosity, present as both micropores and long radial cracks, in the product.^{2,3}

The current research is aimed at investigating the production of ceramic-metal composites in which excess liquid metal, eg Ti, generated by the reduction of TiO₂, infiltrates these pores, thereby minimizing this inherent disadvantage. The incorporation of a ductile metal within a brittle ceramic composite has significant potential for improving both the toughness and relative density of the composite. The basic exothermic reaction investigated is:

$$(3 + x)TiO_2 + 3C + (4 + \frac{4}{3}x)Al \rightarrow 3TiC + (2 + \frac{2}{3}x)Al_2O_3 + xTi$$
 [1]

The effect of excess Ti on the enthalpy-temperature plot and $\Delta H_{\text{Reaction}}$ are given

Titanium '92 Science and Technology Edited by F.H. Froes and I. Caplan The Minerals, Metals & Materials Society, 1993 in Figures 1(a)(b): r and p refer to the reactants and products respectively for values of x = 0, 5, 10, 15, 20. The phase transformations of reactants and products are also indicated in Figure 1. Using a Tig of 1300°K in Figure 1(a) results in a Tad of 2740°K (b.p. of Al) for x=0, and a Tad of 2345°K (m.p. of Al $_2$ O $_3$) for x=20. If heat is lost from the reaction front, i.e. non-adiabatic conditions, the maximum combustion temperature, Tc, is less than Tad, as indicated in Figure 1(a). As indicated in the data in Figure 1(b), exothermicity is seen to increase and Tad decrease with increased excess Ti (xTi).

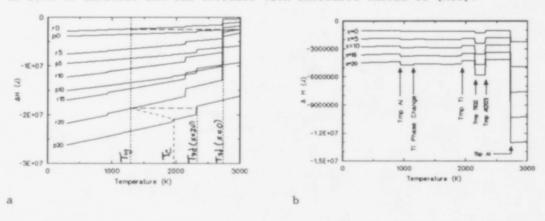


Figure 1 The effect of temperature and excess Ti on (a) enthalpy of reactants and products and (b) enthalpy change for reaction [1]

Experimental Procedure

The reactant powders (-44 μ m) were porcelain ball milled and uniaxially pressed into cylindrical pellets to various green densities and stoichiometries (x). The green pellet weights were kept constant at 3.0 grams with a diameter of 12.7 mm (0.5 in). The pellets were dried in an oven at 120°C for 1 hour and stored in a desicator to minimize moisture. The pellets were subsequently

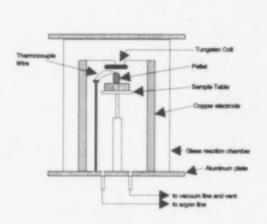


Figure 2 Schematic representation of reaction chamber

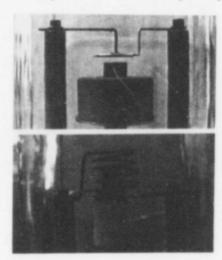


Figure 3 Coil configurations (a) propagating and (b) explosive modes

ignited using either the propagating mode with a flat tungsten wire or the thermal explosion mode using a basket-shaped coil both in an argon atmosphere in a reaction chamber. The distance between the tungsten filament and the top of each pellet was held constant in the propagating mode in order to maintain similar heating rates. At least three samples were ignited for each set of reaction parameters. A schematic representation of the reaction chamber and the flat tungsten coil position is given in Figure 2 while a photograph of both modes of ignition is given in Figure 3.

A Pt-Pt/10%Rh thermocouple and an Ircc. Mirage Two Wavelength Infrared Pyrometer, which was calibrated using a W-W/5%Re thermoccuple, were used to determine Tig and Tc respectively. The progress and stability of the reaction fronts under the propagating mode were recorded with a video camera. The composites produced were examined using optical and scanning electron microscopy (SEM) interfaced with an energy dispersive analysis by x-rays (EDAX) facility, and x-ray diffraction (XRD). Densities of the samples were determined using an immersion in water technique.

Results and Discussion

Compound	TiO ₂	С	A1	TiC	A1 ₂ O ₃	Ti
Tmp (°C)	1830	•	660	3140	2050	1660
Tbp (*C)	3000	-	2467	4820	2980	3287
Specific Gravity	4.26g/cm ³	2.25g/cm ³	2.70g/cm ³	4.93g/cm ³	3.97g/cm ³	4.54g/cm
Powder Size	-44μm	-44μm	-44 µm		-	-

Table 1 Physical properties of the reactants and products.

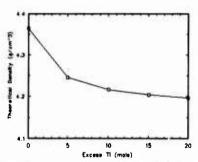


Figure 4 Theoretical density of final composite as a function of xTi.

The physical properties of the reactants and products are given in Table 1. Law of mixtures calculations indicate that the theoretical density of the final composite decreases from 4.37 g/cm³ at x=0 to 4.19 g/cm³ at x=20 (Figure 4). The volume fraction of TiC decreases from 40% at x=0 to 7% at x=15 while that of Al₂O₃ remains approximately constant at 60% for x≤20 (Figure 5).

Increasing the applied pressure above 71.6×10^6 kg/m² did not greatly increase the apparent green density of the pellet when x< 20, (Figure 6), while considerably lower green densities were achieved for reaction stoichiometries of x-20 pressed to less than 1.8×10^7 kg/m².

These green density restrictions are probably particle size dependant. Thus a relative green density of 65% was the maximum obtainable by the techniques and conditions used. The effect of relative green density and excess Ti on Tig and Tc is given in Figures 7 and 8 respectively. For the case of x=0, Tig and Tc increased as green density increased. These data correspond well with earlier research reported for this stoichiometry 4. Increasing the green density increases the thermal conductivity of the green pellet for x=0, thereby increasing heat loss from the pellet reacted under the propagation mode. This will contribute to an increased $\frac{\pi}{10}$ for x=0 and a consequent increase in T₀. Although, Tig and Tc decreased as x>0, no clear trend was apparent for the effect of green density on Tig and Tc for stoichiometries of x>0. In this reaction system, liquid Al is present below Tig and liquid Al and Ti between Tig and Tc. Liquid TiO₂ is also present in most samples between Tig and Tc (except

for x=20 at the lowest green density), whereas liquid Al_2O_3 would be expected at the reaction front for x=0 at the highest green density only.

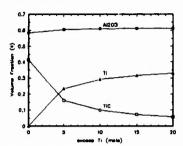


Figure 5 Volume Fractions of Componets in Final Composite as a Function of xTi.

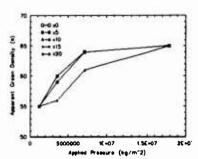


Figure 6 Green density as a function of applied load

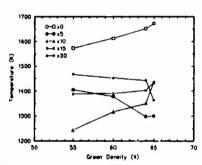


Figure 7 The effect of green density and xTi on Tig

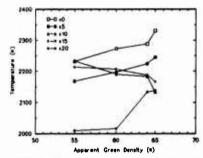


Figure 8 The effect of green density and xTi on Tc

The effect of excess Ti and volume fraction of pores (and thus green density) on the thermal conductivity of the green pellets was calculated using a law of mixtures relationship. An average thermal conductivity was calculated for a fully dense pellet and pores were considered to be a dispersed phase in a continuous matrix:

$$k = k_c \frac{1 + 2v_d(1 - k_c/k_d)/(2k_c/k_d + 1)}{1 - v_d(1 - k_c/k_d)/(k_c/k_d + 1)} \frac{[2]}{}$$

15 03 0 0.2 0.4 0.8 0.8 Present Persity (t)

Figure 9 The effect of porosity and xTi on the thermal conductivity of the green pellet

i.e. where k_c and k_d are the thermal conductivities of the continuous phase and discontinuous phase respectively and v_d is the volume fraction of the discontinuous phase. These data are presented in Figure 9. The thermal

discontinuous phase.⁵ These data are presented in Figure 9. The thermal conductivity of the green pellet decleases with increased porosity (decreased green density) and increases with xTi. Hence, a complex set of conditions exist at the rapidly moving reaction front involving solid (C, Al_2O_3) and liquid (Al, TiO_2 , Ti) reactants and products coupled with a range of thermal conductivities

green pellet the dependent reaction stoichiometry (xTi) and green Increasing the density. thermal conductivity of the green pellet will increase the heat loss from the pellet reaction front and could ahead of the result in increased Tig and Tc4. At the same time, the presence of liquids, i.e. Al, below Tig, TiO2 and Ti above Tig, will increase the heat transfer and kinetics of the combustion reaction but could decrease Tc4. As xTi is increased Al and TiO, are also increased thereby improving the reaction kinetics as well as the thermal conductivity of the green pellet.

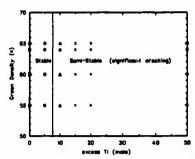


Figure 10 Stability diagram for SHS reaction

A combustion synthesis propagating wave stability diagram's was produced using examination of the slow motion video recording of the propagating combustion front. Figure 10 provides the observed data for this reaction system as a function of both excess Ti and green density. A stable combustion reaction is one in which the combustion wave propagates at a steady rate. An unstable reaction is one which quenches out, and a semistable reaction is one in which the propagating rate decreases, nearly quenches Several cycles of these rates have been observed in out and then increases. some semi-stable reactions4. Although no unstable fronts were observed, the combustion front became increasingly unstable on increasing xTi, such that at x>5 the front became semi-stable. Increasing xTi takes heat out of the system, i.e. latent heat of fusion of Al and Ti, and results in increased thermal conductivity ahead of the reaction front, until eventually the reaction is only marginally self sustaining. The condition is further exaggerated on increasing green density. For values of x>5 severe cracking was observed to occur ahead of the combustion front (Figure 11). The cracking increased with increase in The onset of cracking, e.g. x>5, was also coincidental with the onset of semi-stable propagation. A crack generated ahead of the reaction front will reduce the heat transfer from the reaction to the adjacent unreacted material, thereby reducing the stability of the reaction front resulting in the transition from stable to semi-stable propagation. Samples produced by the explosive mode were virtually crack-free with some shrinkage occurring. is most likely a result of the lower thermal gradients that are present under this mode of ignition compared with the propagating mode.

The effect of green density and xTi on wave velocity as measured from the video recording is given in Figure 12. Increased amounts of liquid Ti, Al, TiO2 will remove heat from the reaction front (latent heats of fusion) and result in a decrease in velocity 4 . Increasing green density for x=0, decreased the velocity considerably, presumably on account of the increased thermal conductivity of the green pellet and, therefore, increased heat loss from the reaction front.

XRD analysis of the products identified TiC, Al_2O_3 , and Ti only with no evidence of the reactants or other products being present (Figure 13). Typical product macrostructures produced by both modes of combustion are given in Figures 14, 15, and 16.



Figure 11 0 served cracking in green pellet ahead of the reaction front in propagating mode

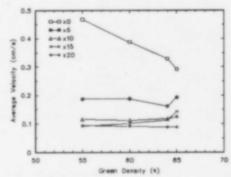
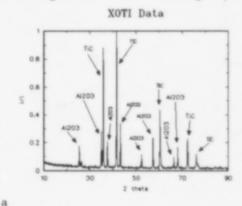


Figure 12 The effect of green density and xTi on Combustion Front Velocity

The radial cracking was found in most samples reacted under the propagating mode. Increasing Ti also produced radial cracking but resulted in a denser product. Conducting the reaction under the explosive mode eliminated the radial cracking but resulted in larger pores.



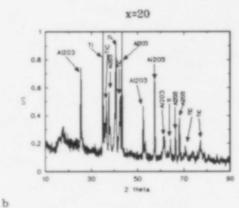


Figure 13 XRD plots for (a) x = 0 and (b) x = 20

Comparison of the product microstructure in which x=20 (Figure 17) with that in which x=0 (Figure 18) both reacted under the propagating mode clearly indicates a less porous structure for composites with increased xTi. The fine particles were identified by EDAX as TiC as was the white phase in Figure 19 for a reaction stoichiometry of x=5 reacted under the explosive mode: the dark phase (matrix) is Al_2O_3 with some excess Ti. The well dispersed TiC particles in the Al_2O_3 matrix is evident in Figure 19(b) while the permeation of the matrix (Al_2O_3 , TiC) with liquid Ti is clearly evident in Figure 20. Even though all the porosity is not filled with Ti, the reduction of porosity is significant on using the explosive mode and increasing xTi (Figure 21). It is feasible that the remaining porosity may be completely filled by increasing x, completed with the use of a small squeezing pressure applied during the combustion synthesis reaction.

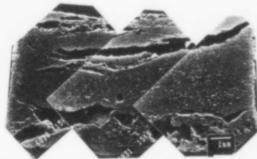


Figure 14 SEM photomicrograph of x = 0 pellet reacted by propagating mode

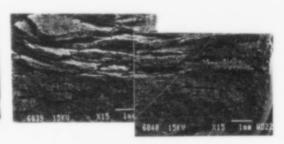


Figure 15 SEM Photomicrograph of x = 5 pellet reacted by propagation mode

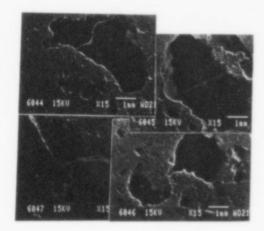


Figure 16 SEM Photomicrograph of x = 5 pellet reacted by explosive mode

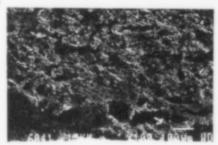


Figure 17 SEM photomicrograph of microstructure of x = 0 pellet reacted by propagation mode

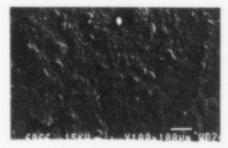


Figure 18 SEM photomicrograph of microstructure of x = 20 pellet reacted by propagation mode

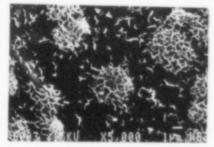
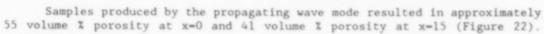


Figure 19 SEM photomicrograph of of x = 5 pellet reacted by explosive mode



Samples reacted under the explosive mode contained approximately 47 volume % porosity at x=5 and approximately 36 volume % at x=20. The propagating mode of combustion produces large temperature gradients behind and ahead of the propagating reaction front, conditions which are conducive to cracking and trapping gasses generated by the reaction, e,g, Al vapor, and which are present

in the chamber, e.g. Ar.

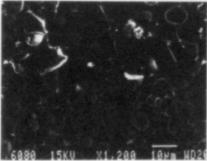


Figure 20 SEM photomicrograph microstructure of x = 15 pellet reacted by explosive mode

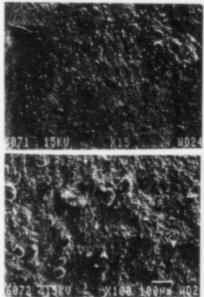
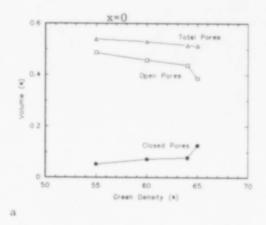


Figure 21 SEM photomicrograph of microstructure of x=50 pellet reacted by explosive mode



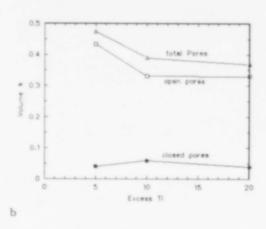


Figure 22 The effect of (a) green density for propagating mode and (b) xTi for explosive mode on volume fraction of open pores, closed pores, and total pores.

Conclusions

ullet The concept of incorporating an excess liquid metal into the combustion synthesis reaction by utilizing an in-situ reduction of a metal oxide has been shown to be successful in the synthesis of a TiC-Al₂O₃-Ti ceramic-metal composite.

- Characterization of the composites clearly revealed the required product phases, i.e. TiC, Al₂O₃, and Ti, and the effective liquid Ti infiltration of the pores in the ceramic TiC-Al₂O₃ matrix.
- Increasing x increases the exothermicity of the reaction, decreases Tad, decreases the theoretical density of the composite product and decreases the volume fraction of TiC.
- Increasing the applied pressure increased the apparent green density up to a maximum of 65% at 1.8x10⁷ kg/m². Lower apparent green densities were achieved for high values of x, e.g. x=20,.
- Increasing x and decreasing the volume fraction of pores in the green pellet increased the theoretically calculated thermal conductivity of the green pellet.
- Tig and Tc decreased in general with increased x. No clear trend was observed with respect to the effect of green density on Tig and Tc for values of x>0.
- A combustion synthesis stability diagram was constructed which established that the propagating combustion front (propagating mode) became semi-stable at values of x>5. No unstable fronts were observed for values of x≤50 for either mode.
- Cracking ahead of the propagating combustion front occurred in all samples for values of x>5 while decreased porosity and increased densities were achieved as x was increased (propagating mode). No such cracking and decreased porosity were achieved in composites produced by the explosive mode

References

- (1) Z.A. Munir, Ceramic Bull., Vol. 67, No. 2, p. 342, (1988).
- (2) J.B. Holt, Mat. Bull., October-November, 60, (1987).
- (3) H.J. Feng and J.J. Moore, <u>High Temperature Materials</u>, published by the Electrochemical Society, eds W. Johnson, R.A. Rapp, pp. 123-134.
- (4) H.J. Feng, J.J. Moore, D.G. Wirth, Met Trans 1992.
- (5) W.D. Kingery, H.K. Bowen, D.R. Uhlmann, <u>Introduction to Ceramics</u>, 2nd ed., John Wiley and Sons: New York, New York (1976) p636.
- (6) H.J. Feng, J.J. Moore, D.G. Wirth, American Ceramic Society, Cocoa Beach Conference Restricted Session.

MICROMODELLING AND METHODOLOGY OF ASSESSMENT OF FIBRE REINFORCED TITANIUM METAL MATRIX COMPOSITES USING FRACTURE MECHANICS PARAMETERS

D.C.Cardona and P.Bowen

School of Metallurgy and Materials / IRC in Materials for High Performance Applications, University of Birmingham, Edgbaston, Birmingham, B15 2TT, UK.

Abstract

Crack growth resistance of fibre reinforced composite materials has been assessed, and has been modelled using weight function methods. Many trends in observed crack growth resistance behaviour in the presence of crack bridging can be predicted accurately. The application of fracture mechanics parameters to characterise crack growth appears to be appropriate in the presence of single dominant cracks. In particular the model is used to predict the behaviour of bridged cracks subjected to remote bending and tension stresses. The effect of fibre size is also addressed.

Introduction

Titanium metal matrix based composites with continuous fibre reinforcement, have potential use in a wide range of aerospace applications, where light weight, high stiffness and good defect tolerance are required. The behaviour of these materials under cyclic loading will be critical and experimental data are now becoming more readily available (1-6). Crack growth rates in continuous fibre reinforced composites are often dependent on crack size and are controlled by fibre bridging behind the growing crack tip. An increase in crack length in the matrix is accompanied by an increase in number of fibres bridging the crack. Thus despite the increase in nominal applied stress intensity range with crack length increase (for a constant applied cyclic load amplitude) crack growth rates are generally observed to decrease, and at room temperature crack arrest is often observed (at least for tests performed in bending), i.e. cracks grow down to a "threshold" due to the influence of crack bridging by intact fibres. Fibre fracture can, however, lead to rapid local crack growth excursions in near threshold regions, and a cascade of fibre failures can promote catastrophic failure. The application of a stress intensity based approach to define crack growth resistance is made easier because it has been established experimentally that single dominant cracks can be obtained regularly (3,5,6).

Much quantitative work has been reported in the use of stress intensity based parameters for the assessment of fibre reinforced materials (4,7), and the present paper outlines a simplified approach to the characterisation of bridged cracks. The aim of this paper is to model the behaviour of stable crack growth in Ti MMC's observed experimentally, using weight function methods under nominal bending and tension stresses (8). The method is also used to predict the

effects of fibre diameter.

Weight Function Methods

Bueckner (9) introduced the concept of weight functions based on an analytical representation of elastic fields. The stress intensity factor can be obtained by solving the integration over the crack length of equations of the type:

Titanium '92 Science and Technology Edited by F.H. Froes and I. Caplan The Minerals, Metals & Materials Society, 1993

$$K = \sqrt{W} \int_0^a \sigma(x) \, m(a,x) \, dx \qquad \dots (1)$$

where m(a,x) is the weight function and $\sigma(x)$ the arbitrary crack line stress (for the uncracked body).

The strength of the method stems from the separation in equation (1) of the crack line stress $\sigma(x)$, and the cracked geometry which is completely contained in the weight function m(a,x). Wu and Carlsson have derived a new analytical approach to obtain weight functions based on the partial differentiation of the crack surface opening displacement with respect to crack length (8). The stress intensity factor for an arbitrary normalised crack line stress of $\sigma(x)/\sigma$, where σ is the nominal applied stress, on a single edge crack can be calculated from:

$$K = f \sigma \sqrt{\pi a W}$$
 (2)

where:

$$f = \frac{1}{\sqrt{2} \pi a} \int_{0}^{a} \frac{\sigma(x)}{\sigma} \sum_{i=1}^{5} \beta_{i}(a) \left(1 - \frac{x}{a}\right)^{i - \frac{3}{2}} dx \qquad \dots (3)$$

and the $\beta_1(a)$ function for single edge crack in a finite width plate may be taken directly from Wu and Carlsson (8). Equation (3) can then be integrated numerically, but care must be taken in the region of the crack tip singularity.

To use these weight functions to determine stress intensity factors it is required to know the stress distribution $\sigma(x)$ along the prospective crack line of the crack free body.

Experimental Procedure

Tests have been performed on a Ti-6Al-4V alloy matrix composite reinforced with Sigma (silicon carbide) fibres. Details are given elsewhere (5). All tests were carried out on single edge notched testpieces of dimensions 4.48mm x 1.05mm x 72mm in bending, with a span, s, to width, W, ratio of 13.3. Cracks were grown by fatigue at a single load range, ΔP , of 67N, from a slot cut to different depths of 0.22 and 1.1mm. This gives an initial unbridged crack depth, a_0 , to width ratio, a_0/W , of 0.25 and 0.05 and corresponds to initial nominal stress intensity ranges ΔK_{ap_F} , of 7.5 and 18MPa \sqrt{m} respectively. Tests were performed at a frequency of 0.5 and 10Hz respectively, and for a single stress ratio, R=0.5, (where R = σ_{min} / σ_{max} , where σ_{min} and σ_{max} are the minimum and maximum stress as applied over the fatigue cycle). A constant load range, ΔP =67N, was maintained during each test. Changes in crack length were monitored using a direct current potential difference technique (10).

Tests have also been carried out on a monolithic Ti-6Al-4V material manufactured by a processing route similar to that used for the composites under study. Further details are given elsewhere (11). In the present study it is sufficient to note that tests have been performed at low mean stress, R=0.1, and at a cyclic frequency of 0.5Hz.

In some cases, testpieces were polished metallographically after testing and examined optically to illustrate the mechanism of crack propagation.

Basis of the Model

Based on an uniform square array of fibres, of size $100\mu m$ and volume fraction of 35%, the least distance of approach between fibres is $50\mu m$. To simplify both the analyses and their interpretation greatly this is idealised to a series of plates of equivalent thickness $89\mu m$ and least distance of approach $165\mu m$. This is essential when using the weight functions method (8),

which is limited to a two dimensional elastic analysis. Perfect bonding is assumed and both a law of mixtures approach and finite element modelling studies (12) were used in order to evaluate the nominal stress partitioning between fibres and matrix so that initially a nominal applied stress intensity range of $18MPa\sqrt{m}$ was applied. To evaluate stress intensities it is clear that different stress distributions, $\sigma(x)$ are required for both fibres and matrix, and in the presence of fibre bridging, an appropriate net clamp-back stress is required.

Results

At an initial ΔK_{app} of 18MPa\m. crack growth rates observed experimentally, da/dN, are shown to failure versus total crack length in Figure 1. Crack arrest does not occur in this test, and cracks propagate to give catastrophic testpiece failure. Even so, the crack growth rate, da/dN, exhibits a periodic decrease and increase with crack length, Figure 1, prior to catastrophic fracture.

The dependence of crack growth rates observed experimentally, da/dN, are shown versus total crack length in Figure 2 for an initial ΔK_{app} value of 7.5 MPa \sqrt{m} . At this stress intensity range crack growth rates decrease with increases in fatigue crack length, until crack arrest (da/dN \leq 10-8mm/cycle) is observed. After crack arrest this testpiece was subjected to additional cycling at a higher stress intensity range of $\Delta K_{app} = 14 MPa \sqrt{m}$ and after subsequent crack growth the test was stopped prior to failure. The testpiece was polished metallographically and an optical section is shown in Figure 3. From this figure it can be seen that the micromechanism of crack growth is well characterised by initial crack growth through the matrix, with fibres bridging the crack in its wake.

The theoretical model has been fitted to the data shown in Figure 1, so that predicted crack growth rates and those observed experimentally are closely similar, see Figure 1. To achieve this an effective clamp-back stress of 400MPa was required for a fibre bridging close to at the top surface (i.e.ao/W=0) of the testpiece in bending, and assuming a linear gradient in effective clamp-back stress towards the neutral axis of the testpiece. (Such assumptions are discussed elsewhere (12)). To derive the effective crack growth rates from the local effective crack tip stress intensity range, it is necessary to have crack growth resistance curves from a monolithic alloy processed in a similar manner to the composite and this is given in Figure 4. In the present paper it is sufficient to note that the data given in Figure 4, can be well represented by a Paris-Erdogan law, da/dN=C Δ Km, for Δ K \geq 4.5MPa \sqrt m, where C and m are numerical constants and equal to 9.2×10^{-9} mm/cycle and 3.12 respectively. (It has been assumed here that there will be no effect of mean stress on data in this crack growth regime in the monolithic alloy). From Figure 1 it can be seen that the theoretical predictions are in good agreement with the experimental values.

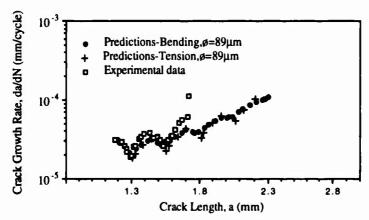


Figure 1 Crack growth resistance curves: da/dN, versus crack length. Initial $\Delta K_{app}=18MPa\sqrt{m}$, R = 0.5, a_0 / W = 0.22. Experimental data and theoretical predictions under bending and tension loading.

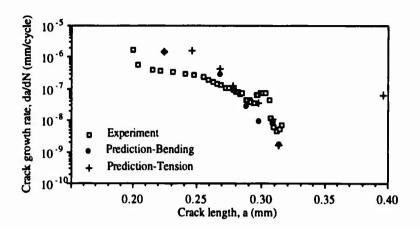


Figure 2 Crack growth resistance curves: da/dN, versus crack length. Initial ΔK_{app} =7.5 MPa \sqrt{m} , R = 0.5, a $_0$ / W = 0.05. Experimental data and theoretical predictions under bending and tension loading.

The effect of loading the testpiece in remote tension, using the same initial ΔK_{app} can be predicted, and is also shown in Figure 1. (For these predictions a constant effective clamp-back stress of 295MPa has been deduced by assuming that the clamp-back stress is directly proportional to the fibre stress). It can be seen that as the crack increases in length, the crack loaded in remote tension or bending is predicted to exhibit similar crack growth rates for the same values of crack length. This can also be seen in the near threshold regime, as shown in Figure 2, where tension and bending geometries are predicted to yield similar crack growth rates.

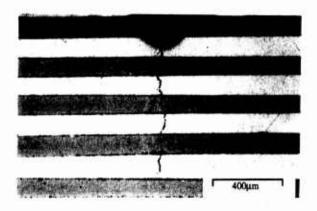


Figure 3 Representative optical micrograph showing single dominant crack bridged by intact fibres.

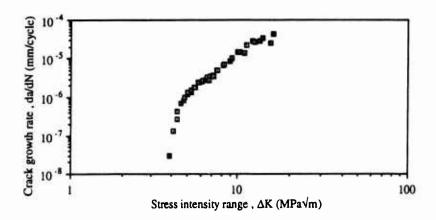


Figure 4 Crack growth resistance curves: da/dN versus ΔK for R = 0.1, υ = 0.5 Hz Monolithic Ti - 6Al - 4V alloy.

Predictions of the effects of fibre diameter is shown in Figure 5, for crack growth under an initial $\Delta K_{app} = 18MPa\sqrt{m}$, in tension, for plate diameters of 50 μ m, 89 μ m and 124 μ m. In general, "fibre diameter" is not predicted to affect crack growth behaviour of the material markedly.

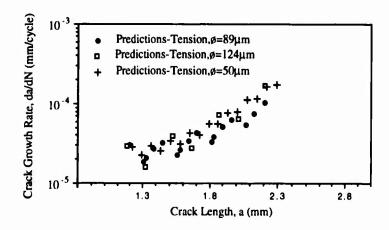


Figure 5 Crack growth resistance curves: da/dN versus crack length for initial $\Delta K_{app}=18MPa\sqrt{m}$, R = 0.5, a_0 / W = 0.22. Theoretical predictions for the effect of fibre diameter.

Discussion

Weight function methods have been used to evaluate effective stress intensity ranges and hence to model crack growth behaviour in bending in continuous fibre reinforced Ti-6Al-4V composites. Despite the limitations and simplifications inherent to the model it has enabled many experimental observations to be rationalised. (These are considered in more detail elsewhere (12)). In particular here it has been used to predict the effect of nominal tension loading compared to bending, see Figure 1 and 2, and fibre diameter for the same volume fraction of fibres, see Figure 5. In these present studies little effect of either loading condition or fibre (plate) diameter on crack growth rates has been predicted.

The model utilises two-dimensional elastic analyses to evaluate effective stress intensity solutions. Thus, it will tend to overestimate effects such as the position of the crack tip relative to the bridging fibres (modelled as plates) for the actual three - dimensional distribution of fibres. To develop a fully three - dimensional model requires experimental information about the distribution of effective stress intensity factors through - thickness. Such information is potentially becoming available based on the observations of local striation spacings (which reflect the local crack growth rates and hence by deduction local stress intensity ranges) (11). Great care is required to build a quantitative picture of crack growth rates through - thickness in

the presence of bridged fibres but early observations are encouraging.

From both experimental and theoretical modelling studies, it is clear that cra

From both experimental and theoretical modelling studies, it is clear that crack bridging by fibres can reduce crack growth rates to very low values, and provided that the fibres remain undamaged then composites possessing excellent damage tolerance under cyclic loading will be produced.

Conclusions

- 1. For the case of single dominant cracks the application of stress intensity parameters to characterise crack growth in composite materials appears to be appropriate.
- Weight function methods in bending have been used to model effective stress intensities (and hence by deduction crack growth rates) for bridged cracks in fibre reinforced titanium composites. Model predictions are in good agreement with crack growth rates observed experimentally.
- Model predictions suggest that loading the cracks in far field tension rather than bending has little effect on crack growth rates, for an equivalent initial applied stress intensity range. For the same volume fraction of fibres, it is also predicted that will be little influence of fibre diameter (plate thickness) on crack growth rates.

Acknowledgements

One of the authors (DCC) has been supported during the course of this work by a SERC research fellowship. Thanks are also due to M.V.Hartley at Rolls-Royce, plc for the provision of monolithic material used for the experimental work and many helpful discussions. The major contribution of Professors Wu and Carlsson to the development of the weight function methods used here is also recognised with gratitude.

References

- W.S.Johnson. (1989). ASTM STP 1032. Ed. W.S.Johnson, Philadelphia. pp 194-221.
- D.Walls, G.Bao and F.Zok. (1991). Conf. Proc. "Mechanical Fatigue of Advanced Materials". Eds. Ritchie et al, Santa Barbara. pp 343-356. MCE publications, Birmingham.
- 3. P. Bowen, A.R. Ibbotson and C.J. Beevers. (1991) Conf. Proc. "Mechanical Fatigue of Advanced Materials", Eds. Ritchie et al, Santa Barbara. pp 379-394, MCE publications, Birmingham.

- P.Bowen, D.C.Cardona and A.R.Ibbotson. (1991). Accepted for publication in Mat.Sci.Eng. A. Pending publication in May 1992.
- C.Barney, C.J.Beevers and P.Bowen. (March 1992). Fracture and Fatigue of Inorganic Composites, Butterworths, Oxford. Accepted for publication in Journal Composites.
- A.R.Ibbotson, C.J.Beevers and P.Bowen. (March 1992). Fracture and Fatigue of Inorganic Composites, Butterworths, Oxford. Accepted for publication in Journal Composites.
- B.N.Cox. (1991). Conf. Proc. "Mechanical Fatigue of Advanced Materials", Eds. Ritchie et al, Santa Barbara, Ca. pp 53-66. MCE publications, Birmingham.
- 8. X.R.Wu and A.J.Carlsson. (1991). Weight Functions and Stress Intensity Factor Solutions. First Edition. Pergamon Press. Oxford.
- 9. H.F.Bueckner. (1970). Angew.Math.Mech. <u>50</u>, p 529.
- P.Bowen, P.J.Cotterill and A.R.Ibbotson. (1990). Proc. Conf. "Testing Techniques for Metal Matrix Composites". Ed. N.D.R.Goddard. pp 82-96. IOPP, London.
- A.R.Ibbotson and P.Bowen. Submitted for publication to Mat.Sci.Tech. 1992.
- 12. Cardona D.C. and Bowen P. (1992). International Conference on Theoretical Concepts and Numerical Analysis of Fatigue". Birmingham, MCE Publications. Accepted for publication.

MICROMECHANICAL PREDICTION OF THE THERMAL STRESSES IN SIGMA FIBER (SIC)/β-21S TITANIUM COMPOSITE: EFFECT OF COEFFICIENT OF THERMAL EXPANSION OF THE COATING

D. Upadhyaya*, D. M. Blackketter* and F. H. Froes*

*Institute for Materials and Advanced Processes
*Department of Mechanical Engineering

University of Idaho, Moscow, ID 83843.

Abstract

The potential of using a monolithic coating layer to reduce the residual thermal stresses in a Sigma fiber $(SiC)/\beta$ -21S titanium metal matrix composite has been investigated using a two-dimensional micromechanics finite element model. The objective of this paper was to define the effects of coefficient of thermal expansion (CTE) of the coating on the residual thermal stress state of the matrix. These stresses are of concern in that they are a major cause of cracking of the matrix in many metal matrix composites. The results show that a coating with a high CTE (higher than that of matrix) allows minimization of residual thermal stresses in the matrix. Further, the effect of the coating modulus on the thermal stress state of the matrix was found to be negligible between 40 to 200 GPa range.

Introduction

Metal matrix composites (MMC's) reinforced with ceramic fibers have a high strength and stiffness-to-density ratio and are attractive for many aerospace applications where weight is of concern [1-5]. In the present facet of an on-going study, the problem of high thermal residual stresses generated in the MMC's upon cool down from fabrication, and/or high temperature use, to room temperature will be considered. The thermal residual stresses are due in part to the mismatch of the coefficient of thermal expansion (CTE) between the fiber and the matrix [6-10]. These residual thermal stresses are a major cause of micro-cracking of the matrix in many MMC's [11]. Allthough, it is recognized in a broader sense that other factors, such as reaction between the coating and the matrix, and inherent ductilities of the coating, reaction zone and matrix also enhance micro-cracking [1-4]. A conting material with an appropriate CTE can be placed between the fiber and matrix material to reduce the high residual stresses [6,7,9]. This study is a computational investigation to determine the effects of the coating CTE on the thermal residual stress state.

Many micromechanical finite element studies have been conducted in order to determine the best coating for SiC based fiber composites. Ghosen, et al. [6] performed a micromechanics analysis using a elasto-isotropic three cylinder finite element model to study the concept of a compliant layer to minimize the thermal residual stresses in the matrix using SiC and TiB, fibers in Ti-15-3, Ti₃Al and NiAl matrices. They suggested the optimum coating should have a CTE between that of the matrix and the fiber, with a relatively low modulus and a high layer thickness [6]. Doghri, et al. [10] also used a similar three cylinder model based finite element analysis in an attempt to optimize the interface layer in ceramic fiber-reinforced metal matrix composites. They concluded that a layer with sufficiently high CTE (much higher than that of the matrix) should reduce the thermal stresses in the matrix significantly. Interestingly, the conclusion of these two studies are contradictory. In the present study we have attempted to resolve this contradiction, and define the CTE effect more precisely, by employing a different finite element model to investigate the potential for using a coating to reduce the thermal stresses. Other parameters such as coating thickness and modulus will be considered, in detail, in future papers.

Materials and methodology

The Sigma fiber/ β -21S composite system was investigated in the present study. The Sigma fiber is an SiC based fiber with tungsten core [12] and the β -21S (Ti-15 Mo-2.7 Nb-3Al-.2 Si) is a β -titanium alloy [13]. The properties of the constituents, i.e., fiber, matrix and coating used to model a 30 percent fiber volume composite are tabulated in Table 1. In the present study, the upper and lower bound of the coating modulus is taken to be 200 GPa and 40 GPa, respectively. The selection of the modulus values was based on literature values [9] allowing determination of the combined effect of CTE and modulus of hypothetical metallic coating on the thermal stress state of the composite. The CTE of the β -21S titanium alloy was determined using a laser-displacement technique.

Table 1. Properties of Sigma (SiC)/β-21S titanium metal matrix composite system's constituents, 30% fiber volume.

Constituents	Modulus (GPa)	CTE 10 ⁻⁶ /°C	
Sigma fiber [12]	420	4.90	
β-21S [16,17]	80	9.30	
Coating	40, 200	2-16	

The effects of the coating CTE was evaluated using a two-dimensional micro-mechanics finite element model similar to that described by Miller and Adams [14] and Adams and Crane [15]. The model is based on a generalized plane strain finite element analysis of a typical repeating unit of matrix material containing a single fiber within a unidirectional composite (Figure 1). This model

is composed of 124 nodes and 210 axisymmetric elements and has three distinct region, namely the fiber, matrix and the coating. The model allows each region to have different mechanical and thermal properties. The temperature induced loads can be analyzed to include the effect of the different regions on the thermally induced residual stress state. For the present analysis, a temperature drop of -777°C i.e, from 800°C to room temperature, was considered in a single linear increment. Further, for simplicity, the variation of material properties with temperature is not considered in the present analysis.

Results and discussion

Figures 2-4 illustrate the spatial variation of stress in the matrix at room temperature as predicted by the analysis. Figure 2 shows the hoop stress state at a point in the matrix directly adjacent to the coating as the composite is cooled from 800°C to room temperature. It is at this location (Figure 1 and 2) that the residual stresses in the matrix are a maximum making this location the most

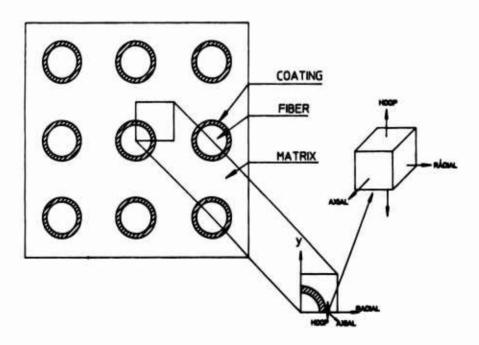


Figure 1. Square array of fibers and idealization of a unit cell.

susceptible to causing micro-cracking of the matrix. For a coating thickness of 15 micron and a modulus of 200 GPa, an increase in the coating CTE results in a significant decrease in the hoop stress i.e., from 440 MPa to 30 MPa. Further, the coating CTE has a more pronounced effect than the coating modulus on reducing the hoop stresses in the matrix. As can be seen in Figure 2, the decrease in the hoop stress for the 40 and 200 GPa coating modulus is not significantly different as the CTE is varied. This information is significant in that it shows the potential of using metallic elements as a possible coating, as the modulus of most metals is less than 200 GPa, investigated in the present study [9]. Further, coating thickness plays an important role in reducing the hoop stresses in the matrix as seen in Figure 2. When the coating thickness is increased from 5 to 15 microns, for a similar coating modulus and high CTE value, the hoop stress in the matrix is decreased by approximately 65 percent. Overall, a thicker (15 micron) coating of high CTE (higher than that of matrix) has the potential of reducing hoop stresses in the matrix.

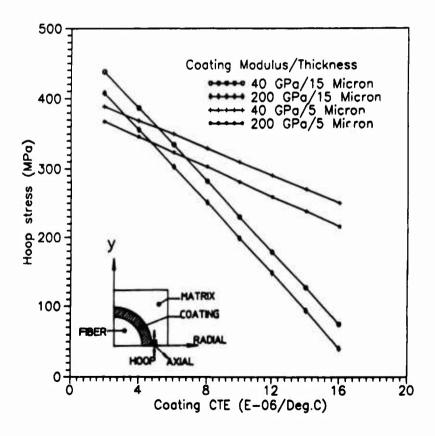


Figure 2. Hoop stress in the matrix at location adjacent to the coating as a function of the coating CTE, modulus and thickness.

A similar observation can be made for the radial stress state in the matrix at a point directly adjacent to the coating (Figure 3). These radial stresses are compressive in nature. A thick coating with high CTE has a less pronounced effect on reducing the radial compressive stresses than it has on preducing the hoop stress. Lower compressive radial stresses in the matrix are desirable as they results in a decrease in the hoop stress.

The effect of coating CTE on the axial stresses in the matrix is shown in Figure 4. The axial stress in the matrix is affected less by the coating, however, a thick, high modulus coating with a sufficiently high CTE can reduce the axial tensile stress in the matrix as seen in Figure 4. This is because, when the coating CTE, thickness, and modulus values are at an upper bound, the radial compressive stresses decrease, resulting in a significant decrease in the hoop and axial tensile stresses in the matrix.

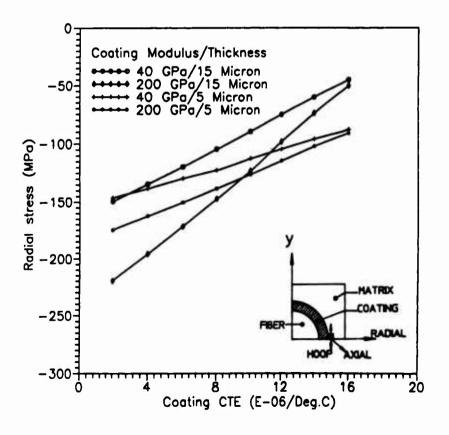


Figure 3. Radial stress in the matrix at location adjacent to the coating as a function of the coating CTE, modulus and thickness.

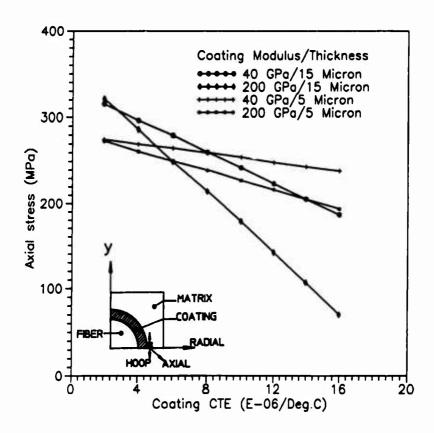


Figure 4. Axial stress in the matrix at location adjacent to the coating as a function of the coating CTE, modulus and thickness.

Conclusion

A micromechanical finite element analysis was performed to investigate the effects of coating CTE on the thermal residual stresses in the Sigma fiber (SiC)/ β -21S titanium metal matrix composite system. A coating with a sufficiently high CTE (higher than that of the matrix) has the potential of reducing the hoop stress in the matrix and hence, minimizing the tendency for matrix micro-cracking. The CTE has a more pronounced effect on reducing the hoop stress in the matrix than the coating modulus. The decrease in the hoop stress for upper and lower bound coating modulus is not significantly different as the CTE is varied. This

information is significant in that it shows the potential of using metallic elements as possible coatings.

The ultimate selection of the fiber coating will also depend on other factors such as chemical compatibility between the fiber and matrix in addition to the CTE discussed in this paper. However, the finite element analysis indicates the required coating mechanical properties. Work is continuing to broaden this micromechanics study to include parameters such as coating thickness, modulus, and the bond strength between the fiber and coating. It is also planned to construct more sophisticated models which include metallurgical variables such as the reaction between the coating and the matrix.

References

- 1. P. R. Smith and F. H. Froes, JOM, Vol.36, No.3, March, 1984, 19-25.
- 2. D. M. Blackketter and F. H. Froes, <u>Conf. Proc., High Performance Composites</u> for the 1990's, ed. S. K. Das et al., 1991, 183-193.
- 3. R. A. MacKay, P. K. Brindley and F. H. Froes, <u>JOM</u>, Vol. 43, No. 5, May 1991, 23-29.
- 4. F. H. Froes, C. Suryanarayana and D. Eliezer, <u>ISIJ International</u>, Vol. 31, No. 10, 1991, 1235-1248.
- 5. R. A. MacKey, Scripta Metallurgica et Materialia, Vol., 24, 1990, 167-173.
- 6. L. J. Ghosen and B. A. Lerch, NASA Report 102295, Aug. 1989.
- 7. S. M. Arnold, V. K. Arya and M. E. Melis, NASA Report 103204, 1990.
- 8. W. D. Brewer and J. Unnam, NASA Report 2066, 1982.
- 9. S. Jansson and F. A. Leckie, NASA Report 185302, 1990.
- 10. I. Doghri, S. Jansson, F. A. Leckie and J. Lemaitre, NASA Report 185307, 1990.
- 11. P. R. Brindley, P. A. Bartolotta and MacKay, R. A, NASA Report TM-10039, 1989.
- 12. Ward-Close, C. M, and P. G. Partridge, <u>Journal of Materials Science</u>, 25, 1990, 4315-4323.
- 13. P. Bania, Materials Edge, No. 25, June 1991, 12.
- 14. A. K. Miller and D. F. Adams, J. Comp. Mater., 11, 1977, 285-292.

- 15. D. F. Adams and D. A. Crane, Composite, 15, 1987, 88-96.
- 16. P. J. Bania and W. M. Parris, <u>Conf. Proc., Titanium Development Association</u>, Fall, 1990, 784-792.
- 17. J. Gourmann, <u>Conf. Proc., Titanium Development Association</u>, Fall, 1990, 793-802.

FIBER-MATRIX INTERFACIAL BEHAVIOR IN SIC-TITANIUM ALLOY COMPOSITES

I. Roman^a, S. Krishnamurthy^b, and D. B. Miracle^c

²School of Applied Science, Hebrew University, Jerusalem, Israel 91904

bUES, Inc., Dayton, OH 45433

CUS Air Force Wright Laboratory
Materials Directorate, WL/MLLM, Wright Patterson AFB, OH 45433

ABSTRACT

The applicability of fiber fragmentation testing to characterize the fiber/matrix interfacial region in SCS-6 SiC fiber reinforced titanium model composites was evaluated by tensile testing single fiber composite specimens with Ti-6Al-4V (wt.%) and Ti-14Al-21Nb (wt.%) matrices. The tensile tests were accompanied by continuous monitoring of the acoustic emissions produced during testing. Metallographic characterization revealed that fiber fragmentation behavior was markedly different for the two titanium alloy composites studied and this was attributed to the differences in their fiber/matrix interfacial regions. The composite specimens showed short, secondary fiber ruptures between longer primary fragments. The results of this study indicate that calculations based on a standard shear lag analysis using measured fragment lengths lead to unrealistic values of interfacial shear strength and, therefore, further understanding is required before fragmentation testing can be utilized for interfacial characterization of this class of metal matrix composites.

Titanium '92 Science and Technology Edited by F.H. Froes and I. Caplan The Minerals, Metals & Materials Society, 1993

1. INTRODUCTION

It is generally believed that the mechanical properties of composite are significantly affected by the nature of the interface between reinforcement and matrix. Consequently, as interest in continuous fiber reinforced intermetallic matrix composites (IMC) and metal matrix composites (MMC) is growing, their interfacial shear properties have become the focus of recent investigations which have employed a number of experimental techniques including fiber pull out, fiber push out, and single fiber fragmentation (SFF) tests. Published works on the employment of SFF tests for this class of materials are quite scarce and include test results for the following composite systems: W/Cu [1,2], SiC/Al 1100 and SiC/Al 6061[3], SiC/Ti-6Al-4V [4,5], and B/Ti-6Al-4V [5].

In the SFF test, a composite sample made of a single fiber embedded in a ductile matrix is subjected to tensile loading along the fiber axis. Stress transfer from the matrix to the fiber by shear causes the tensile stress along the fiber to build up. When this stress exceeds the local fiber strength, the single fiber breaks successively into smaller fragments until the fragments become too short to enable further increase in the fiber stress level.

Using arguments based on shear lag analysis, Kelly and Tyson [1] showed that the critical fiber length for load transfer, $L_{\rm C}$, is a function of the interfacial shear strength, $\tau_{\rm i}$, according to the equation

$$\tau_i = \sigma_f \cdot \frac{d}{2L_c} \tag{1}$$

where of is the tensile strength of the fiber at the critical length and d is the fiber diameter.

Recent studies have used fragmentation testing for characterizing the interfacial properties of fiber-reinforced aluminum matrix composites [3] and titanium matrix composites [4,5]. The fiber/matrix interfacial structure is markedly different in these two composite systems in that the Al based composites show very little interfacial reaction and bonding whereas significant reaction is observed in the Ti based composites. The influence of this interfacial reaction on fiber fragmentation phenomenon has not been previously addressed. The objective of the present work is to investigate this effect by studying the fiber fragmentation behavior of two different titanium based composites with significantly different interfacial structures.

2. EXPERIMENTAL APPROACH

The composites used in this study were SCS-6 SiC fiber reinforced Ti-6Al-4V and Ti-14Al-21Nb (both compositions in wt.%). The composite samples were fabricated by diffusion bonding two matrix alloy sheets with a single fiber between them. The processing method consisted of vacuum hot pressing at 925°C/5.5 MPa/30 min. followed by hot isostatic pressing at 1010°C/100 MPa/2 hr. The consolidated samples were machined into 1.50 mm thick sheet tensile specimens with 19.05mm x 6.35 mm gage sections. All samples were examined by microfocus x-ray radiography to ascertain proper alignment of fiber parallel to the tensile specimen axis. Tensile tests were conducted on a servohydraulic machine in laboratory air at ambient temperature at a nominal strain rate of 2 x 10-4 s-1 for Ti-6Al-4V/SCS-6 and of 1 x 10-4 s-1 for Ti-14Al-21Nb/SCS-6 specimens.

Acoustic emission (AE) activity during SFF tests was monitored by employing a resonant transducer with a nominal center frequency of 250 KHz which was coupled via high vacuum grease to the flat gauge section of the samples. Transducer outputs were amplified first by 40 dB using a preamplifier with a bandpass filter of 100-400 KHz and then by an additional

20 dB at the main amplifier. Some of the AE waveform parameters (peak amplitude, duration, etc.) as well as stress, strain and RMS voltage of the amplified transducer outputs, measured using an RMS voltmeter, were recorded on a computerized data acquisition system.

After testing, the samples were polished parallel to the fiber axis, and fiber fragments were examined optically and in the SEM.

3. RESULTS AND DISCUSSION

3.1 Microstructure of the Interface

Micrographs depicting the interfacial region of the two composite systems under study, i.e. Ti-6Al-4V/SCS-6 and Ti-14Al-21Nb/SCS-6, are given in Fig.1. The Ti-6Al-4V matrix showed $\alpha+\beta$ structure with equiaxed α grains (5-10 μ m grain size) and elongated β phase at α grain boundaries as well as grain interiors. The intermetallic Ti-14Al-21Nb matrix consisted of somewhat finer equiaxed α 2 grains (about 5 μ m grain size) with less elongated β phase at α 2 grain boundaries. It is evident that the two composites display a very distinct difference in the character of their matrix/fiber interface. In the case of the Ti-6Al-4V/SCS-6 system, a significant reaction product layer varying from 0.5 to 1 μ m in thickness with a very rough interface was produced due to preferential reaction between the β -phase and the outer carbonrich layer of the fiber. Much of the outer carbonrich layer was consumed by this reaction and the inner carbon-rich coating layer was also attacked by the matrix at several locations. In contrast, the Ti-14Al-21Nb/SCS-6 composite showed a relatively narrow layer of reaction products with a smooth interfacial morphology due to limited reaction between the matrix and the outer carbon-rich coating layer. However, in the Ti-14Al-21Nb/SCS-6 composite a wide (5-10 μ m) layer of β -depleted matrix was observed around the fiber.

3.2. Tensile (Fragmentation) Tests

Fig. 2 contains typical stress and AE RMS voltage vs. strain curves for the two composite systems. A distinct yield point, yield drop and Luder's band formation were observed for the Ti-14Al-21Nb material whereas continuous yielding typified the behavior of the Ti-6Al-4V system. The single-fiber composite specimens of both systems exhibit a significant amount of plastic straining. The Ti-6Al-4V samples possess both higher tensile ductility and higher strength when compared with the Ti-14Al-21Nb samples. The ductility of the Ti-14Al-21Nb composites is still quite high and is attributed to an (0001) basal texture resulting from rolling of the matrix alloy sheet material used for fabricating these specimens. This explanation is based on a previous study of a similar Ti3Al-Nb alloy with a strong basal texture which showed that a high tensile elongation (about 12%) is obtained in this material at room temperature [6]. The enhanced ductility was explained in terms of the lower average orientation factor and lower grain boundary angles enabling the slip of <a>a> type dislocations [6].

Examination of fibers in the two composite systems, which were metallographically exposed after tensile testing (Fig.3) revealed that, in all cases, the single fiber had fragmented during straining. Fiber fracture behavior was found to be distinctly different in the two composite systems studied. The fiber fragments in Ti-14Al-21Nb/SCS-6 were significantly longer than those in Ti-6Al-4V/SCS-6. In the case of Ti-14Al-21Nb/SCS-6 specimens, two different types of fiber fragments were observed: longer (>200 µm) "primary" fragments and a number of very short "secondary" fragments between the longer fragments. The secondary fragments are often lost during polishing, and are not seen in Fig. 3(b). It is supposed that the primary fragments occur when the axial stress exceeds the local fiber strength, while the secondary ruptures occur as a result of primary fiber fracture when stored elastic energy is released in the form of shock waves. Conversely, in the case of Ti-6Al-4V/SCS-6 specimens, the "primary" fragmentation caused shattering of the fiber into a number of very small fragments

and a distinction between primary and secondary fiber fragments could not be made. The distribution of fragment lengths as measured in the SEM for both the composite systems is given in Fig. 4.

3.3 Acoustic Emission (AE)

Typical AE RMS voltage vs. elongation curves for samples of the two composite systems are given in Fig.2. No AE activity occurred during elastic straining of Ti-6Al-4V samples whereas marked AE activity was noted to precede yielding in the case of Ti-14Al-21Nb. In both composite systems, a large number of sporadic high intensity AE bursts commenced with the onset of plastic deformation. These AE events clustered immediately past the yield strain and then became less frequent for the Ti-6Al-4V/SCS-6 whereas they were more evenly distributed in the case of the Ti-14Al-21Nb/SCS-6. The peak amplitude of these burst events is high (>95 dB) and their event duration ranges from 2 to 4 msec. These characteristics are significantly different from those of most of the signals detected during these SFF tests indicating the operation of a distinct mechanism. The number of these intense AE bursts was found to be similar to the number of fragments produced in the Ti-14Al-21Nb/SCS-6 composite samples. The suggestion that each intense AE burst corresponds to a fragmentation event in this material was verified by stopping a test after a given number of bursts and counting the number of fragments. However, such a correlation could not be verified in the case of Ti-6Al-4V/SCS-6 since numerous secondary ruptures followed primary fragmentation events.

The differences in the fiber fragmentation behavior of Ti-6Al-4V/SCS-6 and Ti-14Al-21Nb/SCS-6 composites can be explained in terms of the differences in their interfacial structures. As Figure 1 shows, the Ti-6Al-4V/SCS-6 composite exhibits a very rough interface due to preferential reaction between the β phase of the matrix and the SCS-6 fiber. Examination of the interfacial region shows that the outer carbon-rich coating on the fiber is fully consumed and the inner carbon-rich coating layer is also attacked in many locations. This attack probably weakened the fiber locally and contributed to the observed shattering.

If the observed average fragment length (140 μ m for Ti-6Al-4V/SCS-6 and 420 μ m for Ti-14Al-21Nb/SCS-6) is employed in Eq.1, one obtains interfacial shear strengths (1500 MPa for Ti-6Al-4V/SCS-6 and 500 MPa for Ti-14Al-21Nb, if the fiber strength is assumed to be 4000 MPa) which are abnormally higher than the τ values obtained by push-out tests as well as those estimated from the matrix yield strength. Another difficulty in interpreting the test results stems from the fact that the fragmentation process in Ti-14Al-21Nb/SCS-6 did not saturate and, therefore, the measured average fragment length cannot be directly used to calculate the critical length.

4. CONCLUDING REMARKS

The work reported here is a part of an ongoing study dealing with the role of fiber/matrix interface in the deformation and fracture of metal matrix composites. In particular, the applicability of fiber fragmentation testing to derive the fiber/matrix interfacial shear strength is being addressed. The present work has showed markedly different fiber fragmentation behavior in Ti-6Al-4V/SCS-6 and Ti-14Al-21Nb/SCS-6 single fiber composite samples arising from differences in the fiber/matrix interface. It was also shown that secondary ruptures occur in addition to primary fragmentation events. In view of these complex fiber fracture characteristics, it is concluded that direct measurement of fragment lengths along with a standard shear lag analysis for estimating L_C as has been done in previous studies would lead to erroneous values of the interfacial shear strength τ_i . A critical assessment of the assumptions involved in the analysis of SFF test specimens is needed before SFF testing can be employed unambiguously to this class of materials.

ACKNOWLEDGMENT

One of the authors (S.K.) acknowledges the support of this research by the U.S. Air Force Wright Laboratory, Materials Directorate under Contract No. F33615-92-C-5663.

REFERENCES

- 1. A. Kelly and W. R. Tyson, J. Mech. Phys. Solids, 13 (1965) pp. 329-350.
- 2. S. Ochiai and K. Osamura, Z. Metallkde., 77 (1986) pp. 255-259.
- 3. I. Roman and R. Aharonov, Acta Metall. Mater., 40 (1992) pp. 477-485.
- 4. A. Vassel, M. C. Merienne, F. Pautonnier, L. Molliex, and J. P. Favre, in <u>Sixth World Conference on Titanium</u>, ed. by P. Lacombe, R. Tricot, and G. Beranger, Les Editions de Physique, Les Ulis Cedex, France (1988) pp. 919-923.
- 5. Y. Le Petitcorps, R. Pailler, and R. Naslain, Composites Science and Technology, 35 (1989) pp. 207-214.
- 6. W. P. Hon, S. K. Wu, and C. H. Koo, Mat. Sci. and Engr., A131 (1991) pp. 85-91.

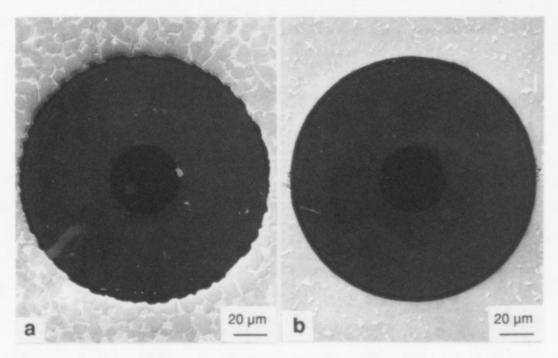


Figure 1. SEM micrographs showing the fiber/matrix interface in the two composites studied: (a) Ti-6Al-4V/SCS-6 and (b) Ti-14Al-21Nb/SCS-6.

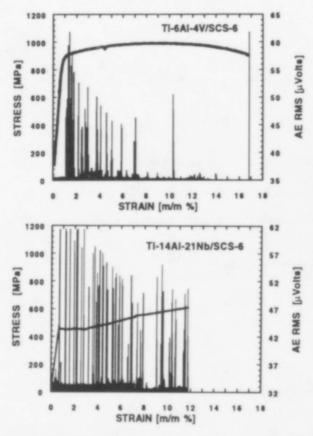


Figure 2. Typical tensile stress-strain curves and acoustic emission RMS-strain plots for the two single fiber composite systems at room temperature.

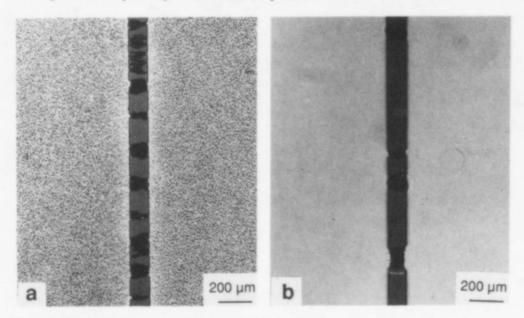


Figure 3. Optical micrographs showing a portion of the fragmented fiber in the two composites after tensile testing: (a) Ti-6Al-4V/SCS-6 and (b) Ti-14Al-21Nb/SCS-6.

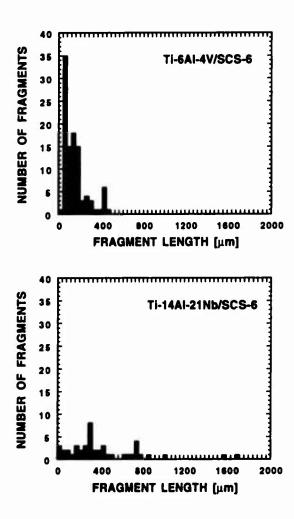


Figure 4. The distribution of fiber fragment lengths in the two composites following tensile testing at room temperature.

FIBER/MATRIX INTERFACE STRUCTURE AND FRACTURE BEHAVIOR IN

CONTINUOUS SCS-6™ REINFORCED TI 15-3-3-3

Donald E. Morel, Ph.D.

The AMT Group, Inc. 631 North Tazewell Street Arlington, Virginia 22203

ABSTRACT

This paper describes a series of experiments performed to characterize the fiber/matrix interface structure and fracture behavior of a composite fabricated using a metastable beta alloy, Ti-15V-3Cr-3Al-3Sn, for the matrix. Annealing experiments indicate that the reaction zone thickness increases linearly as a function of the square root of time at a given temperature. The activation energy for the process was calculated to be 74.7 kcal/mol versus 64.7 reported for the more commonly used Ti-6Al-4V alloy. fiber/matrix interface region was studied using scanning electron microscopy, transmission electron microscopy, and electron microprobe analysis and was observed to contain multiple layers of varying composition, comparable to what is observed in composites based on the well characterized 6Al-4V alloy. Chemical analysis of the interface region revealed the primary constituents to be titanium silicide and titanium carbide. SEM images of transverse and longitudinal tensile samples indicates that failure typically occurs at the interphase region between the reaction zone and the matrix.

INTRODUCTION

Monolithic metal alloys are being pushed to their operational limits in many demanding applications. This trend is clear in aerospace structures and propulsion systems where high specific properties coupled with the ability to operate for long times at elevated temperatures can translate directly into significant performance improvements. During the past twenty years a number of titanium matrix composites have been studied for such applications. [1-2] One of the fundamental problems facing materials engineers however is the high reactivity of titanium at temperatures required for composite fabrication. Virtually all matrix alloy/reinforcement combinations tested exhibit a reaction or "interphase" zone between the matrix and reinforcement that results in less than optimum composite mechanical properties. This zone typically consists of several intermetallic compounds with

+ Textron Specialty Materials, Lowell, MA.

Titanium '92 Science and Technology Edited by F.H. Froes and J. Caplan The Minerals, Metals & Materials Society, 1993 poor mechanical properties that reduce load transfer to the fiber and thus the effective strength of the composite. Experimental attempts to minimize the effects of the reaction zone have followed two primary approaches — i) control of matrix composition to minimize the temperature and time required for composite fabrication, or ii) coating of the reinforcing fibers with a diffusion barrier that inhibits atomic transport at the interface. To date these attempts have met with only limited success. This study was initiated to document the structure and composition of the interface zone present in SCS-6 reinforced Ti-15V-3Cr-3Sn-3Al (referred to as Ti-15-3). The matrix alloy is a metastable beta phase alloy that can be rolled into thin foils for composite fabrication at much lower cost than Ti-6Al-4V.

EXPERIMENTAL AND MATERIALS

The composite evaluated in these experiments was produced by Textron Specialty Materials, Lowell, MA, and consisted of a unidirectional panel $\{0^o\}_8$ measuring 12" x 12" x .060" fabricated via diffusion bonding. The as received panel contained 40 per cent SCS-6 fiber by volume and visual inspection showed no evidence of edge delaminations or surface defects. The growth kinetics of the reaction zone were documented by isothermal annealing experiments on composite samples enclosed in evacuated quartz tubes. Characterization of the interface was performed using a combination of optical microscopy, scanning electron microscopy with windowless EDS, and electron microprobe analysis. Tensile test were performed with a computer controlled MTS load frame at a constant strain rate of 10^{-5} s⁻¹.

RESULTS AND DISCUSSION

REACTION ZONE GROWTH KINETICS

shows an optical micrograph using contrast Figure 1 enhancement to highlight the reaction zone present at the fiber/matrix interface. The pyrolytic graphite core onto which the silicon carbide is deposited to form the final fiber is clearly visible. The fibers typically have a diameter of approximately 140 microns and are coated with a layer of Si:C of varying stoichiometry. [3] The reaction zone is clearly evident as a white ring surrounding each individual fiber with the zone thickness ranging from 1.0 to 1.5 microns. In order to document the growth kinetics of the reaction zone in this composite a set of isothermal annealing experiments were performed at temperatures of 600, 750, 875, and 950 °C (1112, 1382, 1607, and 1742 °F, respectively) for time ranging from four to ninety six hours. Figure 2 shows reaction zone thickness as a function of time for all temperatures. The data indicate that the zone thickness increases linearly with increasing square root of time as anticipated from previous measurements on 6Al-4V. [4] Constructing an Arrhenius plot (Figure 3) of ln k versus 1/T for this process allows on to calculate the activation energy for the process from the slope, -Q/R. Table 1 summarizes data from previous titanium composite systems and indicates that both the reaction constant and the activation energy are functions of the matrix composition and the fiber system used. The activation energy calculated from these experiments was 74.7 kcal/mol for Ti-15-3 versus 64.7 kcal/mol for the 6Al-4V alloy.

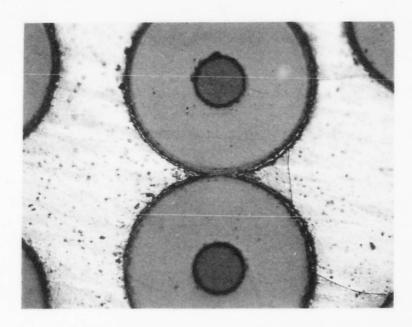


Figure 1 - Optical Micrograph using contract enhancement to highlight the reaction zone surrounding each SCS-6 silicon carbide fiber.

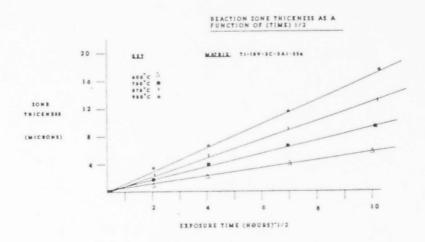


Figure 2 - Reaction zone thickness (um) as a function of the square root of time for different temperatures.

CHARACTERIZATION OF THE REACTION ZONE

Figure 4 shows a scanning electron image of a typical interface zone. Two features are of particular importance. First, a separation between the reaction zone and the matrix is observed for virtually all of the fibers across the sample cross section. This indicates a weakly bonded interface as a result of the residual stresses developed during fabrication due to the

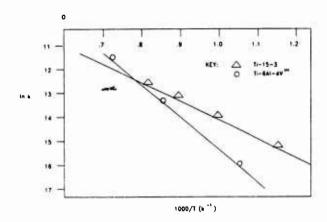


Figure 3 - Arrhenius plot of ln k (reaction constant) versus 1/T. Slope of the curve, -Q/R, yields the process activation energy, Q.

Matrix Reinforcement		Temperature.	Reaction Constant, K cm/sec +2	Activation Energy, Q kcal-mol ¹
6A1-4V(1)	SCS-6	N(N)	3.05 × 10 °	
		900	8.88×10^{-7}	64.7
		1000	3.33×10^{-6}	
$6\Delta I + 4V^{(2)}$	SiC	XIN)	4.5 × 10 °	
		900	1.27 × 10 °	59.3
		1000	3.47×10^{-6}	
Pure Tren	SiC	800	69 × 10 °	
		900	1.83×10^{-6}	56.6
		16000	4.75 × 10 °	
15-3-3-3(4)	SCS-6	750	5.7 × 10 °	
		875	9.3 × 10 °	74 7
		950	1.7 × 10 *	

NOTES: 1 Data from Whatley and Wawner, Reference [4] 2 Data from Martineau et al., Reference [7], 3. Data from this study.

Table 1 - Summary of Reaction Constant and Activation Energy Data for Selected Titanium Matrix Composites.

higher thermal expansion coefficient of the matrix. Second, a series of layers is visible as one moves from the fiber surface through the reaction zone. The outer layers (Figure 4, region 2) comprise the SCS coating deposited via CVD. Region 1 is the reaction zone that forms during the composite fabrication process.

The composition of the interface zone (region 1, Figure 4) was determined using a combination of windowless energy dispersive spectrometry and electron microprobe analysis. Corresponding composition profiles are shown in Figure 5(a-b) for the reaction zone and fiber coating, respectively. The profile shown in Figure

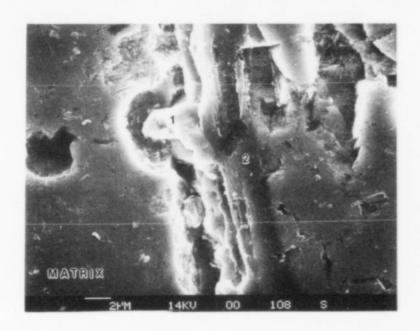


Figure 4 - Scanning electron image of the fiber/matrix interface showing the SCS coating and the reaction zone. (As received composite).

5(b) indicates the presence of titanium, carbon, and silicon in the reaction zone, probably in the form of titanium carbide and titanium silicide.

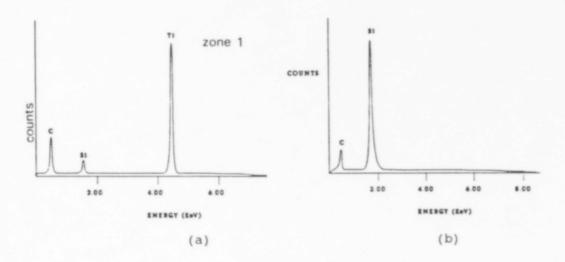


Figure 5 - EDX Spectra for the numbered regions shown in Figure 4: (a) reaction zone and (b) the SCS fiber coating.

Dissolution of the matrix was accomplished by immersing samples in solutions of 10% bromine in methanol [4] and 90% $\rm HNO_3/10\%~HF$ [5]. The bromine solution dissolved the matrix alloy leaving the reaction zone relatively intact on the fiber surface. The nitric acid/hydrofluoric acid solution also etched away the reaction zone product leaving only the fiber and coating. Figure 6 shows the structure of the fiber surface following treatment in methanol/10% $\rm Br_2$. The reaction product is visible as the nodular structure covering the lower part of the fiber. EDS analysis of the nodules (region A) shows titanium, carbon, and silicon; region B consists only of silicon and carbon.

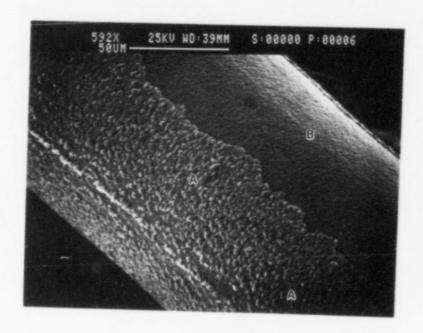


Figure 6 - Scanning electron image of the fiber surface following removal of the matrix using a 10 % bromine in methanol solution.

The presence of the reaction zone strongly affects the mechanical behavior of the composite resulting in strength values that are somewhat less than the expected strength for a unidirectional composite based on "rule of mixtures" calculations. A total of twelve samples were tested in longitudinal and transverse tension relative to the fiber orientation. The longitudinal samples had a mean failure stress of 231.2 Ksi (1.6 GPa) which is significantly lower than the value of slightly in excess of 300 Ksi (2.2 GPa) predicted by the rule of mixtures. The transverse samples where the matrix properties dominate had a mean failure strength of 36 Ksi (250 MPa). The ultimate strength of the un heat-treated, non reinforced Ti-15-3 alloy is on the order of 120/130 Ksi (830 MPa).

Two mechanisms have been proposed to account for this observed strength loss: (1) the fiber strength is degraded in the

fabrication process, [7] or (2) the reaction zone exceeds some critical size and the resulting stress concentration produces fiber fracture at lower than expected stress levels.[8] Scanning electron images of sample fracture surfaces appear to support (1) in the case of SCS-6 reinforced Ti-15-3. Figure 7 shows a scanning electron micrograph of a composite specimen stressed to failure in longitudinal tension. The SCS coating is visible on

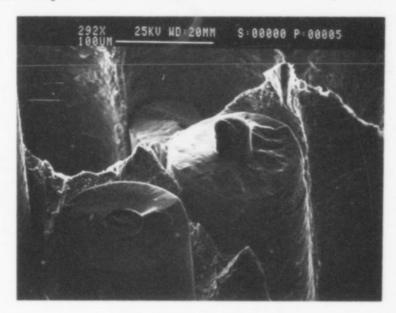


Figure 7 - Scanning electron image showing the fracture surface morphology from a longitudinal tension specimen.

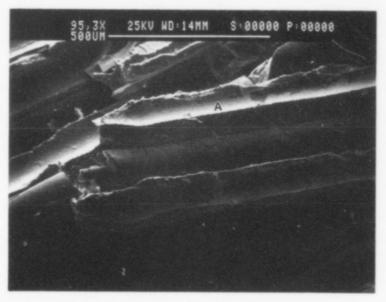


Figure 8 - Scanning electron image of the fracture surface from a transverse tension specimen.

fractured fibers protruding from the sample surface. During the failure process, the reaction zone remains bonded to the matrix and fracture proceeds along the path between the SCS coating and the reaction zone. This is confirmed by EDS analysis of areas where the fibers have been pulled away from the matrix in transverse tension. (Figure 8, point A). Titanium, silicon, and carbon are present at the surface, but no vanadium or other matrix alloying elements can be detected. Analysis of the fiber surfaces indicates no titanium is present.

CONCLUSIONS

The fiber/matrix interface zone in Ti-15-3/SCS-6 is comparable to that observed in Ti-6Al-4V and contains both titanium carbide and titanium silicide. The reaction product adheres tightly to the fiber surface, promoting fracture to occur between the zone and the matrix. EDS of the fracture surface confirms this observation as very little silicon or carbon can be detected in areas where fiber pullout has occurred. The reaction zone plays a critical role in determining the strength of the composite; longitudinal and transverse tensile failure loads were significantly less than predicted based on rule of mixtures calculations.

ACKNOWLEDGEMENTS

The assistance of Mrs. Jean Bernstein (Artech Corporation) in performing the SEM studies and the staff of the University of Maryland Microanalysis Laboratory is gratefully acknowledged.

REFERENCES

- A. G. Metcalf, in <u>Composite Materials</u>, ed. by L.J. Broutman and R.H. Crock, <u>4</u>, <u>Metal Matrix Composites</u>, Chapter 6, Academic Press, NY, NY (1974).
- 2. P.R. Smith and F.H. Froes, J. Metals, p. 19, March (1984).
- 3. X.J. Ning and P. Pirouz, J. Mat. Res., 6, 2234 (1991).
- F.E. Wawner and W.J. Whatley, J. Mat. Sci. Lett., 4, 173 (1985).
- P. Martineau, M. Lahaye, R. Pailler, R. Naslain, M. Couzi, and F. Cruege, J. Mat. Sci., 19, 2731 (1984).
- C. Jones, C.J. Kiely, and S.S. Whang, J. Mat. Res., 4(2), 327 (1989).
- 7. P.R. Smith, F.H. Froes, and J.T. Cammett, in <u>Mechanical Behavior of Metal Matrix Composites</u>, ed. by J.E. Hack and M.F. Amateau, TMS-AIME, 1983, pp. 143-168.
- 8. S. Ochai and Y. Murakami, J. Mat. Sci., 14, 831 (1979).

INTERFACIAL REACTION KINETICS IN a- AND B-TITANIUM BASED

METAL MATRIX COMPOSITES

E. N. T. Jong, H. M. Flower and D. R. F. West

Department of Materials
Imperial College of Science, Technology & Medicine
London SW7 2BP, UK

Abstract

An investigation has been made of interfacial reaction kinetics in composites using commercial purity titanium, and a 8-titanium alloy (Ti-15V-3Cr-3Al-3Sn) as matrices; particulate reinforcements investigated were TiB2, SiC and B4C. The composites were prepared by hot isostatic pressing (HIP'ing) of the matrix in powder form with 10% by volume of the particulate. HIP'ing temperatures in the range 700-900°C were used with a pressure of 103 MPa and subsequent annealing was carried out for times up to 100 hours at temperatures from 800-950°C. Structural investigations were made using electron microscopy (with x-ray energy dispersive analysis) and transmission electron microscopy, laser ionisation mass analysis and x-ray diffraction. The thicknesses of the "compact" interface reaction layers were directly proportional to the square root of the treatment time. Activation energies for the reactions involving TiB2, SiC and B4C in C.P.Ti were approximately 240, 200 and 170 kJ/mol respectively. The kinetics were slowest in the TiB₂/Ti composite (e.g. the reaction layer was 4µm thick after 100 hours annealing at 900°C) and fastest with SiC/Ti (e.g. 15µm after 100 hours at 900°C). The reaction zone thickness was significantly reduced to less than 0.1 \mu m (as-HIP'ed) by using the \(\beta-Ti \) alloy as the matrix with TiB2 and HIP'ing was successfully achieved at 700°C. The reaction zone with TiB₂ particles consisted essentially of TiB, including a region of needle-like crystals, whilst the reaction zone with B₄C particles consisted of a "compact" region of TiB+TiC phases with TiB needles growing out into the matrix. In the composite with SiC particles, the reaction zone was of a complex multi-layer nature containing TiC and titanium silicides.

> Titanium '92 Science and Technology Edited by F.H. Froes and I. Caplan The Minerals, Metals & Materials Society, 1993

1 Introduction

Interest in potential aerospace applications for titanium matrix composites has stimulated considerable research activity; previously reported work has used various titanium-based matrices^[1-2] with ceramic fibres such as boron or SiC. Among difficulties encountered were adverse effects on mechanical properties resulting from matrix-ceramic interaction producing brittle and often cracked interface layers. An important approach to overcome this difficulty is to optimise the processing parameters, particularly by reducing processing temperatures and to use high pressure in solid state powder consolidation. Also important is the selection of matrix-ceramic combinations in relation to thermodynamic and kinetic characteristics, to minimise interface reaction. The research reported here aimed to study the structural features, mechanisms and kinetics of interface reactions in C.P.Ti and a \(\beta\)-Ti alloy (Ti-15-3-3-3) with particulate dispersions of TiB₂, SiC and B₄C.

2 Experimental Procedure

Powders of 99.5% commercial purity titanium (C.P.Ti) and pre-alloyed Ti-15V-3Cr-3Al-3Sn (wt%) were used as matrices, with 10 vol% of particles of TiB₂, SiC and B₄C as the reinforcement phases; a wide range of particle sizes was involved (Table I). The powders were blended and cold pressed prior to HIP'ing in titanium capsules. HIP'ing was carried out in an argon atmosphere with standard conditions of 2 hours at 103 MPa pressure at a temperature of 900°C followed by slow cooling. Uniformity of structures of the products was checked using triplicate HIP'ing experiments. Some HIP'ing was carried out on the β-Ti alloy at 800°C and 700°C for 2 hours at 103 MPa pressure. After HIP'ing samples of the composite rod were heat-treated for times up to 100 hours at temperatures in the range 800-950°C in argon.

Standard techniques were employed for light microscopy, scanning electron microscopy (SEM) and x-ray diffraction (XRD) studies. For transmission electron microscopy (TEM) samples were mechanically dimpled and ion beam thinned. Interface reaction zones were analysed by electron probe micro-analysis (EPMA) and also by means of laser ionisation mass analysis (LIMA).

Table I Particle Size Distributions

	C.P.Ti	Ti-15-3-3-3	TiB ₂	SiC	B ₄ C
Range(µm)	10-250	2-35	2-30	10-160	2-85
Mean(µm)	150	10	7	70	10

3 Results

3.1 Metallographic Examination

3.1.1 Ti/TiB₂ The as-HIP'ed material (900°C) (Figs.1 & 2) showed TiB₂ particles ranging is, size from $^{\sim}1$ to 30μ m with some clustering of particles at the matrix grain boundaries,

and associated porosity. The matrix structure was α -Ti and there was a narrow reaction zone at the particle/matrix interface (Fig. 2). TEM examination of this zone showed a "compact" region penetrating the TiB₂ particles, with needle-like crystals of TiB (*50-300 nm in width) extending into the matrix (Fig. 3).

- 3.1.2 Ti-15-3-3-3/TiB₂ The microstructure after HIP'ing at 900°C, viewed by light microscopy was similar to that of the Ti-TiB₂ composite. SEM examination showed that the interface reaction produced a "compact" region and a network of TiB needle like crystals (Fig. 4). The matrix showed β phase with particles precipitated during cooling from the HIP'ing temperature. Fig. 5 shows features of the structure after 100 hrs annealing at 900°C including coarse TiB crystals (up to 3μ m in diameter and 25μ m in length). HIP'ing at 800°C gives rise to a discontinuous and very narrow reaction zone (<0.2 μ m thick) (Fig. 6); no TiB was observed by SEM and the matrix showed precipitated from β during cooling.
- 3.1.3 <u>Ti/SiC</u> The HIP'ed structure contained a wide range of sizes of SiC particles, uniformly distributed in the Ti matrix. There was a uniform reaction zone, 2.4 µm thick, consuming the SiC particles; some porosity was present and also some cracking of SiC particles, the latter effect being attributed to the cold compacting stage of processing. TEM observations of a region of the interfacial reaction zone extending into the SiC show particles of TiC (~10nm in diameter) and of titanium silicides in a matrix of SiC (Fig. 7). Annealing for 100 hrs at 900°C led to an increase in thickness of the reaction zone to ~15µm (Fig. 8). Within this zone, an inner region ~0.5-1µm thick is present extending into the SiC, associated with what appears to be porosity. Adjoining this region there is a region consisting mainly of TiC and Ti₅Si₃ whose extent increased with increasing annealing time and temperature; evidence of the presence of Ti₃Si was also obtained from XRD. The outermost part of the reaction zone appears to consist of a silicide and TiC. Fig. 13 shows the compositional profile across the reaction zone after 100 hrs annealing at 900°C, as determined by EPMA (C is determined by difference). During the annealing, the interaction zone originally formed by HIP'ing extended substantially into the SiC particles, whilst also growing outwards into the Ti matrix.
- 3.1.4 <u>Ti-15-3-3-3/SiC</u> HIP'ing at 900°C produced a reaction layer of only $^{-}0.4\mu m$ in thickness (cf $2.4\mu m$ with C.P.Ti); the structure within the reaction zone was similar to that in the Ti/SiC composite. Titanium-based carbide was present along the matrix grain boundaries (Fig. 9) implying considerable diffusion of carbon from the SiC. The reaction zone increased in extent on annealing for 100 hrs at 900°C and resembles that of the Ti/SiC composite except that the outermost layer of silicide was not observed and showed similar compositional profiles for Ti, Si and C to those shown in Fig. 8. The stoichiometries of the phases in the reaction zone are suggested to be mainly (Ti,V)C and (Ti,V)₅(Si,Al)₃. Lowering of the HIP'ing temperature to 800°C reduced the interface zone thickness to $0.2\mu m$ (Fig. 10); the matrix contained α phase precipitated from β during cooling. Consolidation by HIP'ing at 700°C was also successfully achieved with a further reduction in reaction zone thickness and no TiC precipitation at grain boundaries.
- 3.1.5 <u>Ti/B₄C</u> The HIP'ed material (900°C) showed a wide range of size of B₄C particles; the smaller particles tended to be clustered along the Ti grain boundaries. The reaction zones showed a compact region of $^{-}1.5\mu m$ thickness with a network of TiB crystals of needle like form, growing into the matrix. Annealing for 100 hours at 900°C increased the

thickness of the reaction zone to $^{-10}\mu m$ (Fig. 11). LIMA analysis of the reaction zone indicated the presence of TiC and TiB (Fig. 14).

3.1.6 <u>Ti-15-3-3-3/B₄C</u> The extent of the interface reaction zone ($^{\circ}$ 0.8 μ m) formed during HIP'ing was much less than in the Ti/B₄C composite; it consisted of a uniform "compact" region of TiC and TiB of very small grain size (Fig. 12).

3.2 Interface Reaction Kinetics

The thicknesses of the reaction zones after HIP'ing at 900°C and after subsequent annealing are reported as the average of ^60-100 measurements; only the thicknesses of the "compact" regions were measured. In all cases it was found that the best fit to the data was obtained by plotting reaction zone thicknesses (x) squared against annealing time (t) (eg Fig. 15) although in the case of TiB₂ at low temperatures the very limited reaction zone growth made measurements highly approximate. Data for SiC for both matrix materials is presented for annealing temperatures between 800 and 950°C in Fig. 16. Parabolic rate constants for growth of the compact reaction layers were determined and are presented in Fig. 18 as functions of temperature. Approximate activation energies were determined and are shown in Table II.

Table II Activation Energy Values, Q (kJ/mol) and Parabolic Rate Constants k at 900°C (cm²/s) for Compact Reaction Layer Growth

Matrix	7	ГіВ ₂		SiC		B ₄ C
	Q	k	Q	k	Q	k
C.P.Ti	240	2.1x10 ⁻¹³	200	5.3x10 ⁻¹²	170	2.5x-10 ⁻¹²
β -Ti	210	1.7x10 ⁻¹³	240	1.5x10 ⁻¹²	270	8.5x10 ⁻¹³

In the case of TiB₂ the low temperature rate constants are highly approximate and were not employed in the determination of the activation energy. Their relatively high values do suggest, however, the possibility that short circuit diffusion paths may be rate controlling in the low temperature regime.

4 Discussion

4.1 HIP'ing

The standard conditions of HIP'ing used, namely 2 hrs at 900°C with 103 MPa pressure were effective in producing ~100% density composites with all three of the particulate dispersions, TiB₂, SiC and B₄C. The HIP'ing map reported (Ashby)^[3] for α-titanium indicates that in the absence of ceramic particles such values of density could be achieved at a temperature of 900°C in less than 1.5 hrs at 103 MPa pressure. This is in general agreement with the present results for the composites, although where there is significant ceramic-ceramic contact, due to metal-ceramic particle size mismatch, the Ashby model will

not provide an adequate guide. The differential thermal contraction of the parent and product phases combined with the volume changes associated with the interfacial reactions gave rise to cracking where reaction zones were thick and the particles were large. The use of a ß matrix has confirmed previously reported work^[4-5] that HIP'ing temperatures can be substantially reduced (e.g. to 700° C) while still achieving the required level of density. The results show that of the three particulates studied TiB₂ offers the best prospects; in addition to achieving virtually 100% density in the composite, there is good bonding between ceramic and matrix with small interaction zones, for appropriate HIP'ing conditions temperatures between 850 and 900° C.

4.2 Structural Features of Interface Zones

In the C.P.Ti-TiB₂ interface zone, EPMA showed that the TiB adjacent to TiB₂ had the approximate composition, TiB_{0.95} while that near the titanium matrix corresponded to TiB_{0.88}; this result agrees reasonably with the limits of stoichiometry of TiB as shown in the phase diagram^[6]. However, whereas the phase diagram indicates that the Ti₃B₄ phase should be interposed between TiB₂ and TiB, no evidence of Ti₃B₄ was found in the C.P.Ti-TiB₂ composite. In contrast, x-ray diffraction data from the ß alloy-TiB₂ composite showed the presence of Ti₃B₄.

In composites containing SiC, the interface reaction zone contains titanium-based carbide and silicides. There are general similarities between the results of various investigations on SiC^[7,8] and the present work, although there are differences in detail, depending on factors such as processing temperatures. The formation of a ternary compound Ti₃SiC₂, previously reported^[9] as forming during processing at 1200°C has not been detected in the present work; the presence of a carbon-rich region on the surface of the as-received SiC particles (detected by XRD) influences the initially formed layer of TiC+SiC^[10].

In the case of B_4C (Fig. 12), the very thick reaction zone contains very fine crystals with decohesion of the B_4C from the reaction zone.

4.3 Kinetics of Interfacial Reactions

In all cases the parabolic kinetics imply that transport through the growing interface reaction products is the rate controlling step. Although diffusion data for B in Ti are lacking, the comparison of activation energies in all cases exceeds that expected for diffusion of relevant species through either α - or β -Ti. Differences in activation energies for α and β matrices may be apparent and due to the limited accuracy of the measurements. It is also possible that the changes in chemistry between the two matrices may genuinely alter the activation energy. The important role of the β alloy is that the HIP'ing temperature can be reduced to 700° C due to the fast diffusion in the β during the HIP'ing process, while the high activation energies in the reaction zone inhibits its growth.

5 Conclusions

1. C.P.titanium matrix composites with TiB_2 , SiC and B_4 C particulate reinforcements can be successfully HIP'ed to ~100% densification at 900°C with a pressure of 103 MPa for 2 hours in an argon atmosphere; the as-HIP'ed interfacial reaction zones are in the range of thicknesses ~1.5-2.5 μ m.

- 2. Fully HIP'ed β alloy (Ti-15V-3Cr-3Al-3Sn) matrix composites with TiB₂ and SiC particulates can be obtained at a temperature as low as 700°C; with TiB₂ particles, no interface zone was observed on examination by SEM.
- 3. The kinetics of interface reactions are interpreted as being controlled by diffusion through the reaction products in the "compact" interface reaction zones; this applies from 800 to 900°C, spanning the α and β ranges for C.P.Ti. It appears that the rates of growth of the interfacial reaction are too fast to achieve acceptable microstructures in all the titanium matrix composites (TMCs) studied at annealing temperatures above 900°C. Reaction rate constants (k) for TMCs with TiB₂ particles are significantly lower than those with SiC and B₄C particles.

6 Acknowledgements

Acknowledgements are made to SERC and ICI Advanced Materials, Runcorn and to HIP Ltd, Chesterfield for financial support of this research, including provision of materials, chemical analyses and HIP'ing of all TMC materials. Thanks are expressed particularly to Drs. A. M. Walker, D. R. Stanley, L. E. Tidbury and B. A. Rickinson.

7 References

- 1. A. G. Metcalfe, <u>Metallic Matrix Composites</u> (New York, NY: ed. K. G. Kreider, Academic Press, 1974), 269-318.
- 2. R. Naslain, R. Pailler, and P. Hagenmuller, Mater. Sci. Mono., 2 (1982), 766-814.
- 3. M. F. Ashby, "Operating Manual for HIP.487", Version HIP6.0, (University of Cambridge, 1990).
- 4. D. Eylon, and F. H. Froes, United States Patent No. 4822432, (April, 1989).
- 5. P. R. Smith, and F. H. Froes, United States Patent No. 4499156, (Feb., 1985).
- 6. J. L. Murray, ed., "Phase Diagrams of Binary Titanium Alloys", ASM, 1 (1986).
- 7. P. Martineau et al., "SiC filament/titanium matrix composites regarded as model composites, Part 2. Fibre/matrix chemical interactions at high 'emperatures', <u>J. Mater Sci.</u>, 19 (1984), 2749-2770.
- 8. R. Naslain, R. Pailler, and P. Martineau, in <u>Physical Chemistry of the Solid State</u>: <u>Appl. of Metals & Their Compounds</u>, (Amsterdam: ed. P. Lacombe, Elsevier Sci. Publ., 1984), 481-499.
- 9. J. J. Nickl, K. K. Schweitzer, and P. Luxenberg, "Gasphasenabscheidung im System Ti-Si-C", J. Less Common Metals, 26 (1972), 335-353.
- 10. J. M. Yang, and S. M. Jeng, "Interfacial reaction kinetics of SiC fibre-reinforced Ti₂Al matrix composites", <u>Scripta Metall.</u>, 23 (1989), 1559-1564.

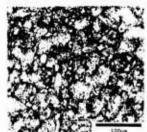


Fig. 1 TiB2-CP Ti HIP'ed 900°C 103MPa 2Hr



Fig. 2. P-M interface around a TiB2 particle



Fig. 3 TEM micrograph of P-M interface with TiBo.

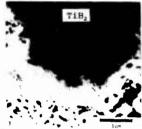


Fig. 4 TiBs-beta Ti HIP'ed 900°C 103MPa 2Hr



Fig.5 Coarsened TiB



Fig. 6 P-M interface after needles post 100 Hr 900°C HIP 800°C 103MPa 2Hr



Fig. 7 TEM micrograph of P-M interface with SiC



Fig. 8 SEM image of P-M interface with SiC post 100 Hr 900°C

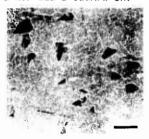


Fig.9 SiC-beta Ti HIP'ed 900°C 103MPa 2Hr



Fig. 10 SEM image of P-M interface HIP ed 800°C 103MPa 2Hr

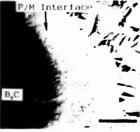
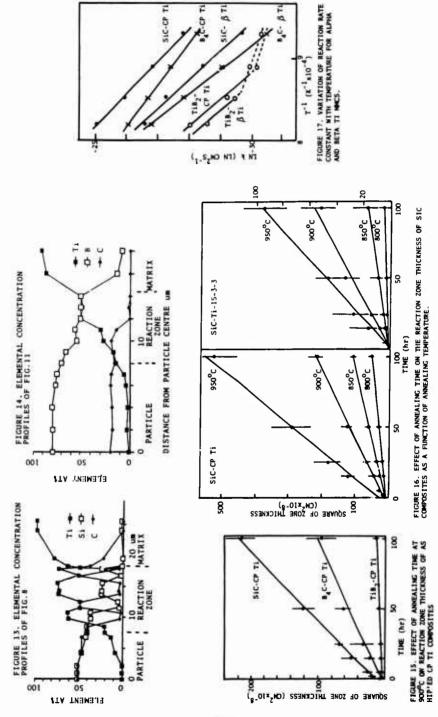


Fig. 11 SEM image of P-M interface around B₄C post interface around B₄C 100 Hr 900°C



Fig. 12 TEM image of P-M



THE USE OF PUSHOUT TESTING TO INVESTIGATE THE INTERFACIAL MECHANICAL PROPERTIES OF TI-SIC MONOFILAMENT COMPOSITES

M.C. Watson & T.W. Clyne
Department of Materials Science & Metallurgy
University of Cambridge
Pembroke Street, Cambridge CB2 3QZ, UK

Abstract

Specimens were subjected to single fibre pushout testing after various heat treatments and it is shown that a progressive increase in the interfacial shear stress for frictional sliding is observed as reaction proceeds. This increase in the resistance to frictional sliding can be correlated with a decrease in the thickness of the graphitic layer. A novel test is described in which the push-out behaviour of single fibres is measured with the simultaneous application of an equal biaxial stress in the plane of the specimen. This will in principle allow any mode mixity between pure shear and pure opening to be generated at the fibre/matrix interface. The level of residual stress will need to be established if this mixity is to be accurately known. Preliminary data for the as-fabricated composite show that a significant change in the critical shear stress required for frictional sliding is observed on introducing an opening mode stress of comparable magnitude.

1. Introduction

There is considerable interest in exploring the mechanical response of interfaces in MMCs. Significant advances have been made recently concerning stresses and fracture mechanics at bimaterial interfaces ¹⁻⁵. For interfaces which are significantly less tough than the neighbouring bulk materials, a crack (ie a debonding event) can continue to follow an interface, even though the stress intensity at the crack tip is not purely mode I (crack opening) and may have a substantial mode II (shearing) component ^{6,7}. The mixity of crack tip loading mode can vary between pure mode I and pure mode II, depending on the loading geometry and elastic properties of the two materials. This mixity is commonly characterised by the so-called phase angle, ψ , which is the angle with a tangent given by the ratio of the mode II to mode I stress intensity factors at the crack tip. This mixity is important because the toughness, for example the critical strain energy release rate, \mathcal{G}_{ic} , can vary quite markedly with ψ . A large shear component tends to result in the crack tip being shielded (particularly if the interface is geometrically rough), with more frictional work being done in the wake of the crack - leading to a larger \mathcal{G}_{ic} value.

Various tests have been devised⁸⁻¹² to measure G_{ic} . However, many of these are applicable only to planar interfaces; those suitable for fibre/matrix interfaces tend to be limited to large values of ψ (ie predominantly shear loading). Tests developed for fibre composites ¹³, such as pull-out ¹⁴⁻¹⁶ and full fragmentation ¹⁷ tests, are in general aimed at identification of critical stress levels for debonding or sliding under pure shear loading. Moreover, for many tests the specimen must be produced in a special operation which differs from the normal composite manufacturing route and may thus create different interfacial microstructures and residual stresses. One of the few tests which can be applied to normal fibrous composite material is the single fibre pushout (or push-down) test. There is therefore considerable interest in this procedure, in spite of the apparent limitation to pure shear loading (ψ =90°).

Titanium '92 Science and Technology Edited by F.H. Froes and I. Caplan The Minerals, Metals & Materials Society, 1993 Fibre pushout and push-down testing has received considerable attention recently, in terms of both experimental and theoretical work ¹⁸⁻²⁴. This has included the derivation of various shear lag-type analytical solutions to the stress field. More recently, finite element study ²⁵ and photoelastic examinations ²⁶ have shown that the variations in shear stress along the length of the fibre are less pronounced than predicted by shear lag models. Debonding is stimulated near the free surface under essentially pure shear loading. (In fact, the applied load generates a normal stress on the interface by differential Poisson expansion, and residual thermal stresses are also present, but since both effects usually generate radial compression, there is no mode I loading.) Once debonding has started, it will propagate along the length of the fibre. After the initiation of debonding, motion will be at first partly and then purely by frictional sliding at the interface. While debonding is taking place, the load may rise or fall, depending on the debonding and frictional sliding stresses. The pushout test can also be used to obtain Gic data. Analyses have been presented ^{19,27,28} of the energy balance during pushout. These depend on monitoring of the load/displacement behaviour during progressive debonding.

In the present paper, the conventional pushout test is first used to explore the effect of interfacial chemical reaction on the shear strength in the Ti-6Al-4V/SiC system. A variant of the pushout test is then proposed, in which the specimen is subjected to equal biaxial in-plane tension while an axial compressive load is applied to a fibre. This should in principle allow any value of ψ from 0° to 90° to be generated, depending on the proportion of in-plane and axial stresses (and the presence of residual stresses). Some preliminary results are presented here, obtained with a set-up giving only the peak load needed for pushout. Interfacial work of fracture data cannot be obtained without continuous load/displacement monitoring, but the results serve to demonstrate that the test procedure is viable and that an effect of the type expected was observed on changing the mode mixity.

2. Experimental

2.1 Material Production

The composite used in this investigation was supplied by BP plc in the form of 30-ply and 6-ply panels, prepared by hot isostatic pressing of Ti-6Al-4V foils and SiC monofilaments (~35% by volume). The monofilaments were W-cored, stoichiometric SiC, 100 μ m in diameter, with a duplex coating of graphitic carbon and TiB₂ (~1 μ m of each). A typical transverse section through the composite material in the as-fabricated state is shown in Fig.1.

The hot pressing operation involved a heat treatment which generated a brittle layer (initial TiB_2 coating plus any subsequent reaction product²⁹ which takes the form of TiB needles extending into the matrix) of about 2 μ m in thickness. Further heat treatments were carried out in sealed silica ampoules evacuated to about 10^{-5} torr. In view of the danger of residual oxygen penetrating along fibre/matrix interfaces³⁰, final cutting and machining operations (removing any material contaminated in this way) were carried out after the heat treatment. A treatment temperature of 865°C was selected, which is sufficiently high to cause significant changes in reaction layer thickness within relatively short periods. Treatment times ranged from 3.25 to 26 hours. Microstructures of as-fabricated and heat treated specimens are shown in Fig.2. Final reaction layer thicknesses ranged up to about 6 μ m.

2.2 Specimen Preparation

Two types of specimen were produced. For evaluation of interfacial shear strengths under pure shear loading, wedge-shaped specimens were made by careful grinding and polishing, using a special jig designed to ensure that the surfaces were flat and inclined at an angle of 3°. One of the surfaces was normal to the fibre axis. The other type of specimen, of uniform thickness, was designed to allow the interfacial shear strength to be evaluated in the presence of an applied radial tensile stress across the interface. A small specimen, 5 mm square and 2 mm

thick, was cut from a 30-ply panel, the fibres lying normal to the square surface. In order to facilitate gripping, the composite specimen was diffusion bonded into a larger panel of unreinforced Ti-alloy. This was done by stacking 6 alloy foils, each 20 mm square and 500 μ m thick and placing the composite specimen on top, after chamfering the edges to an angle of 45°. This assembly was then diffusion bonded together at 850°C for 30 minutes under about 5 10^{-4} torr., with a maintained stress of 150 MPa. The composite square became immersed in the unreinforced material during this treatment, with the fibres remaining vertical. After bonding, the specimen was cut and ground, then thinned by careful metallographic polishing to produce a 'foil' of thickness around 100 μ m.

2.3 Testing Procedures

2.3.1 Wedge-shaped Specimens

The procedure is described in detail elsewhere³¹. The arrangement is shown schematically in Fig.3. The wedge was supported on a horizontal surface, so that the fibres were lying vertical. A selected fibre was positioned over a groove approximately 250-300 µm wide and 500 µm deep. Loads were applied axially to the centre of the fibre with a pyramidal diamond indenter, using a conventional Leitz Miniload microhardness machine. Loads were progressively increased, and the fibre inspected after each loading application, until the fibre was seen to be permanently displaced. The maximum load which induced no displacement and the subsequent pushout load were then recorded for each fibre. By observing the distance of particular fibres from the end of the wedge, the aspect ratios can be calculated and the variation of pushout load with fibre aspect ratio determined. In all cases, the wedge was inverted, placed on a surface inclined at 3° to the horizontal and the testing repeated to measure the load necessary to push the fibre back. These operations confirmed that the pushout load required was determined by the shear stress for frictional sliding, rather than debonding.

2.3.2 Tensioned Pushout Testing

The procedure has been described in detail elsewhere³². The test set-up allowed biaxial loads to be applied in the plane of the specimen, whilst supported from beneath by a plinth with a hole of diameter about 200 µm, into which the fibres could be pushed - see Fig.4. Before the specimen was placed in the grips, small strain gauges were attached on the unreinforced material, parallel to the two in-plane loading directions. Readings from these were monitored during adjustment of the loads to ensure that an equal biaxial stress state was generated. Since the specimen was relatively thin, there was a danger of significant curvature arising during handling and loading - both in-plane and when indenting individual fibres. In order to compensate for the effect of this curvature on the strain gauge readings, gauges were also attached on the underside of the specimen. The applied in-plane loads could then be adjusted until the mean readings of each pair of strain gauges were the same, since this corresponded to the volume-averaged in-plane stresses being equal in the two directions. A low magnification view of a tensioned pushout specimen is shown in Fig.5.

The specimen was placed in the grip assembly, which was then moved around on the base until a selected fibre was centred in the optical imaging system of the indenter. The in-plane stress was then generated via simple screw arrangements on one half of each pair of grips. Compressive loads were then applied axially to the fibre with a conventional microhardness pyramidal indenter, the fibre being viewed after each loading operation. The applied axial load was progressively increased until pushout was seen to have occurred.

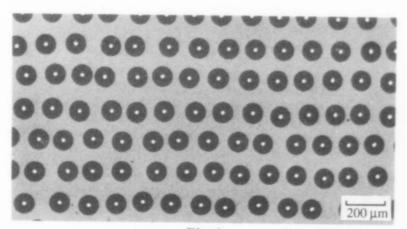
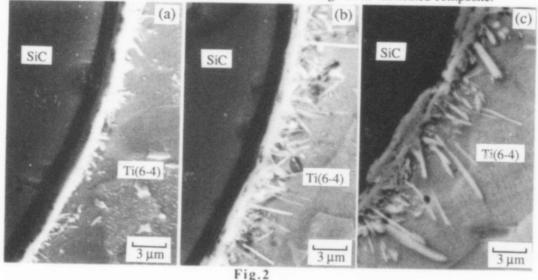


Fig. 1

SEM micrograph of a polished transverse section through an as-fabricated composite.



SEM micrographs of polished and etched specimens, showing interfacial reaction zones (a) as-fabricated, (b) after 13 hours @ 865°C and (c) after 26 hours @ 865°C.

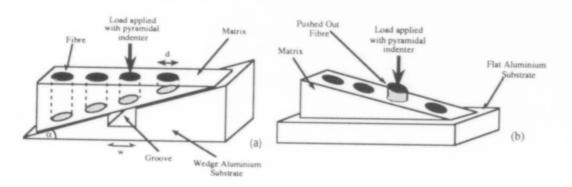


Fig. 3
Schematic illustration of the setup for (a) pushout testing and (b) pushing protruding fibres back into the matrix. The angle α was about 3°.

3. Results and Discussion

3.1 The Effect of Reaction Layer Thickness on Pushout in Pure Shear

It has been shown previously³³ that, over the range of fibre aspect ratios of interest, the pushout load in this system can be used to deduce the critical shear stress for interfacial frictional sliding, τ_{ff} . This is simply given by one quarter of the gradient of a plot of pushout stress against fibre aspect ratio (length/diameter).

$$\tau_{fr} = \frac{\sigma_{po}(s)}{A_s} \tag{1}$$

Some typical experimental data are shown in Fig.6. The linearity of the plots for each heat treatment condition is consistent with the pushout loads being determined in each case by the value of τ_{fr} . The rise in plot gradient with increasing heat treatment time indicates that τ_{fr} is raised by interfacial reaction. The initial increase in τ_{fr} is probably due to a progressive decrease in the thickness of the graphitic layer ^{33,34}. The relatively sharp increase subsequently may correspond to the interface becoming rather rough, with no remaining graphitic layer.

3.2 Tensioned Pushout Data for the As-fabricated Composite

The interpretation of results from the tensioned pushout test is described elsewhere³². Using the coaxial cylinder model^{35,36}, it was shown that the normal stress across the fibre/matrix interface, σ_r , will, for the case of this particular composite, be about 25% higher than the far field in-plane applied stress σ_1

$$\sigma_{\rm r} \sim 1.25 \, \sigma_{\rm l} \tag{2}$$

The value of the in-plane biaxial stress σ_1 is related to the strain gauge reading ϵ_s by the equation

$$\sigma_1 = \frac{E_m \, \varepsilon_s}{(1 - v_m)} \tag{3}$$

where E_m and v_m are the Young's modulus and Poisson's ratio of the matrix. The value of σ_r can therefore be calculated for any given strain gauge reading. In order to establish the actual interfacial radial stress, it will be necessary for any residual stresses to be added to this. In practice, differential thermal contraction is likely³² to have generated a compressive radial stress of the order of 200 MPa in this system.

Preliminary experimental data are shown in Fig.7, giving the experimental pushout stress, converted to an interfacial shear stress for frictional sliding, as a function of the interfacial radial tensile stress being imposed via the in-plane tension. These are preliminary data, but they do appear to indicate that a systematic trend is present in terms of applied radial tension causing a reduction in the shear stress required for frictional sliding. It will be of interest to study debonding behaviour in this test, with monitoring of load/ displacement behaviour, so as to establish the interfacial fracture toughness. This can then be evaluated as a function of the phase angle ψ , although it will be necessary to measure the thermal residual stress in order to establish ψ .

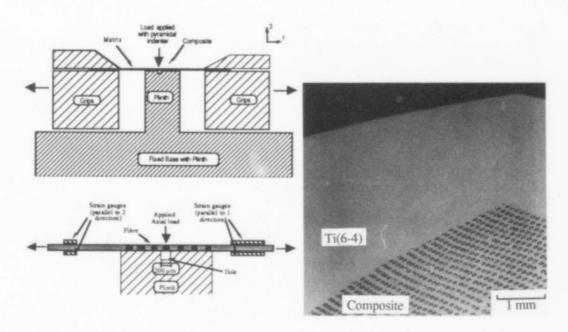


Fig.4
Schematic illustration of the set-up for tensioned pushout testing

Fig.5
SEM micrograph of a specimen ready for tensioned pushout testing

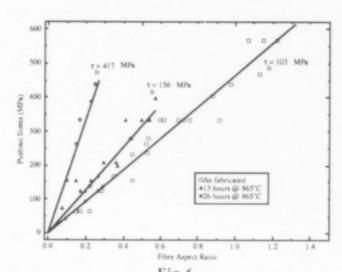
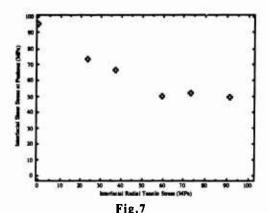


Fig.6
Single fibre pushout data for specimens subjected to different heat treatments.



Experimental pushout data from the tensioned pushout test, applied to as-fabricated Ti-6Al-4V/35%SiC, expressed in the form of interfacial shear strengths as a function of applied interfacial radial tensile stress.

4. Conclusions

The following conclusions have emerged from this work.

- (1) The reaction between C/TiB₂-coated SiC monofilaments and a surrounding Ti-6Al-4V matrix leads to progressive formation of TiB needles extending into the matrix and the consumption of the graphitic layer. These changes are accompanied by an increase in the interfacial shear stress needed to cause frictional sliding.
- (2) Preliminary studies with a new test have shown that the application of radial tensile stresses during pushout testing, causing a reduction in the phase angle of loading, leads to a reduction in the interfacial shear stress required for frictional sliding. This information, and interfacial toughness data obtained under such mixed mode loading, is important for predicting the performance of these composites when the stress axis is inclined to the fibre direction.

Acknowledgements

Thanks are due to BP for providing financial support for one of us (MCW). The assistance of C.M.Warwick and M.C.Witt, both of BP Research Centre, Sunbury, is gratefully acknowledged.

References

- 1. J.R. Rice, J. App. Mech. (Trans. ASME), vol.55, (1988) p.98-103.
- M.S. Hu, M.D. Thouless and A.G. Evans, Acta Met. et Mater., vol.36, (1988) p.1301-1307.
- 3. M. Hu, Materials Research Society Symposium, vol.130, (1989) p.213-218.
- A.G. Evans, M. Rühle, B.J. Dalgleish and P.G. Charalambides, Mater. Sci. Eng., vol. A126, (1990) p.53-64.
- 5. Z. Suo and J.W. Hutchinson, Int. J. Fract., vol.43, (1990) p.1-18.
- 6. A.G. Evans and J.W. Hutchinson, Acta Met. et Mater., vol. 37(3), (1989) p.909-916.
- 7. M.-Y. He and J.W. Hutchinson, J. Appl. Mech., vol.56, (1989) p.270-78.
- 8. C. Atkinson, R.E. Smelser and J. Sanchez, Int. J. Fracture, vol.18, (1982) p.279-291.
- 9. P.G. Charalambides, J. Lund, A.G. Evans and R.M. McMeeking, J.Appl.Mech.(Trans.ASME), vol.56, (1989) p.77-82.

- 10. H.C. Cao and A.G. Evans, Mech. Mater., vol.7, (1989) p.295-304.
- P.G. Charalambides, H.C. Cao, J. Lund and A.G. Evans, Mech. Mater., vol 8, (1990) p.269-283.
- 12. J.-S. Wang and Z. Suo, Acta Met. et Mater., vol.38(7), (1990) p.1279-1290.
- I. Verpoest, M. Desaeger and R. Keunings, in "Controlled Interphases in Composite Materials", (1990), H. Ishida (eds.), Elsevier, p.653-666.
- 14. P. Lawrence, J. Mat. Sci., vol.7, (1972) p.1-6.
- 15. P.S. Chua and M.R. Piggott, Comp. Sci. Tech., vol.22, (1985) p.33-42.
- R.R. Kieschke and T.W. Clyne, in "Interfacial Phenomena in Composite Materials", (1989), F.R.Jones (eds.), Butterworths, p.282-293.
- Y. LePetitcorps, R. Pailler and R. Naslain, Comp. Sci. & Tech., vol.35, (1989) p.207-214.
- 18. D.B. Marshall, J. Amer. Ceram. Soc., vol.67, (1984) p.C259-260.
- 19. D.B. Marshall and W.C. Oliver, J. Amer. Ceram. Soc, vol.70, (1987) p.542-548.
- T.P. Weihs and W.D. Nix, in "Metallic and Ceramic Composites", (1988), S.I. Andersen, H. Lilholt and O.B. Pedersen (eds.), Risø, Denmark, Risø National Laboratory, p.497-502.
- 21. D.K. Shetty, J.Amer.Ceram.Soc., vol.71, (1988) p.C107-109.
- 22. C.H. Hsueh, Acta Met. et Mater., vol.38, (1990) p.403-409.
- C.H. Hsueh, J.D. Bright and D.K. Shetty, J.Mat.Sci. Letts., vol.10, (1991) p.135-138.
- 24. R.N. Singh and M. Sutcu, J.Mat.Sci., vol.26, (1991) p.2547-2556.
- 25. M.N. Kallas, D.A. Koss, H.T. Hahn and J.R. Hellman, J. Mat. Sci., in press, (1991).
- 26. M.C. Watson and T.W. Clyne, Acta Met. et Mater., vol.40, (1992) p.135-140.
- 27. R.J. Kerans, R.S. Hay and N.J. Pagano, Ceram. Bull., vol.68, (1989) p.429-442.
- R.J. Kerans and T.A. Parathasarathy, J. Amer. Ceram. Soc., vol.74, (1991) p.1585-1596.
- 29. P.B. Prangnell, A.J. Reeves, T.W. Clyne and W.M. Stobbs, in "2nd European Conference on Advanced Materials and Processes, Euromat'91", (1992), T.W. Clyne and P.J. Withers (eds.), Cambridge, UK, Institute of Metals, p.215-229.
- M.V. Hartley, in "Proc. 9th Risø Int. Symp. on Mechanical and Physical Behaviour of Metallic and Ceramic Composites", (1988), S.I.Andersen, H. Lilholt and O.B. Pedersen (eds.), Roskilde, Denmark, Risø National Laboratory, p.383-390.
- 31. M.C. Watson and T.W. Clyne, Acta Met. et Mater., vol.40, (1992) p.141-148.
- 32. M.C. Watson and T.W. Clyne, The Tensioned Pushout Test for Measurement of Fibre/Matrix Interfacial Toughness under Mixed Mode Loading, submitted to Scripta. Met., (1992).
- 33. M.C. Watson and T.W. Clyne, in "2nd European Conference on Advanced Materials and Processes, Euromat'91", (1992), T.W. Clyne and P.J. Withers (eds.), Cambridge, UK, Institute of Materials, p.235-240.
- C.M. Warwick and J.E. Smith, "Metal Matrix Composites Processing, Microstructure and Properties", 12th Risø Int. Symp. on Materials Sci., (1991), N. Hansen, D.J. Jensen, T. Leffers, H. Lilholt, T. Lorentzen, A.S. Pedersen, O.B. Pedersen and B. Ralph (eds.), Risø, Denmark, Risø National Laboratory, Denmark, p.735-740.
- 35. Y. Mikata and M. Taya, J. Comp. Mats., vol. 19, (1985) p.554-579.
- 36. C.M. Warwick and T.W. Clyne, J.Mat.Sci, vol.26, (1991) p.3817-3827.

MICROMECHANISMS OF DAMAGE IN FIBRE REINFORCED TITANIUM

BASED METAL MATRIX COMPOSITES

A. R. Ibbotson, M. V. Hartley, C. J. Beevers and P. Bowen.

*School of Metallurgy and Materials / IRC in Materials for High Performance Applications,
The University of Birmingham, B15 2TT, United Kingdom.

+ Rolls Royce plc, P. O. Box 31, Derby, DE2 8BJ, United Kingdom.

Abstract

The damage tolerance of continuous fibre reinforced titanium metal matrix composites under cyclic loading has been assessed in both plane-sided testpieces and pre-cracked (notched) testpieces at ambient temperature. Lifetimes in excess of 10⁴ cycles have been obtained for an applied cyclic stress amplitude of 1200 MPa in plane sided testpieces. In pre-cracked (notched) testpieces dominant mode I cracks are produced under cyclic loading and the micromechanisms of crack growth have been well characterised. Crack growth rates are controlled primarily by intact fibres bridging in the crack wake and no unique relationship between crack growth rate and applied stress intensity range exists. Such intact bridging fibres also play a critical role in determining conditions for transitions between sub-critical crack growth and catastrophic failure. In general, such composites exhibit excellent fatigue crack growth resistance.

Titanium '92 Science and Technology Edited by F.H. Froes and I. Caplan The Minerals, Metals & Materials Society, 1993

Introduction

At present world - wide there is marked interest in the development of silicon carbide fibre reinforced titanium metal matrix composites for use in structural applications at elevated temperatures. Such materials have potential use in both air - frames (hypersonic flight) and engine components ¹. In the longer term, matrix alloys based on titanium aluminides may allow the use of such composites at temperatures of upto 900 °C, but potential applications have also been identified at lower temperatures. In these latter cases components may use conventional titanium alloys as the matrix materials, and it is possible that they will operate at relatively high stress levels. Under such envisaged conditions it is important to establish their "fitness for purpose", and thus their damage tolerance may prove to be critical. This paper considers the damage tolerance of these composites at ambient temperature under cyclic loading in both plane - sided specimens (low cycle fatigue) and pre - cracked testpieces (crack growth resistance curves).

Experimental Studies

Material

Fatigue crack propagation and low cycle fatigue tests were performed on Ti-6Al-4V / SCS 6 unidirectionally reinforced composites available commercially. Additional low cycle fatigue tests were performed on the Ti-6Al-4V / S1240 unidirectionally reinforced composite system again available commercially. The volume fraction of reinforcement was approximately 0.35 in all cases. All SCS 6 reinforced composites were eight ply, while the S 1240 reinforced composites were six ply. Further details of these systems are given elsewhere 23

Fatigue crack propagation

To date, experiments have been confined to single - edged through thickness notched test-pieces in three point bending. This testpiece geometry is well-suited for use in combination with crack growth monitoring by direct current potential difference techniques 4 . Testpiece sizes typically of nominal dimensions ($4 \times 2 \times 70$ mm 3) have been utilised, with an overall span to width ratio of 15:1. Cracks were grown by fatigue from a slot cut by electrical discharge machining typically to a depth of ≈ 1 mm, so that the initial crack depth to width ratio, a $_0$ / W, was equal to 0.25. In all tests considered here, a constant cyclic load range, $_0$ P, was used and was typically of the order of 100N. This allows the nominal applied stress intensity range, $_0$ K $_{4PF}$, to increase with increases in crack length. Load ratios of both R=0.5 and R=0.1 (where R=P $_{min}$ /P $_{max}$ and P $_{min}$, P $_{max}$ are the minimum and maximum loads applied over the fatigue cycle respectively) have been considered. The tests reported here were performed at a cyclic frequency of 0.5 Hz on an ESH servo - hydraulic testing machine fitted with a 1 kN load cell.

Low cycle fatigue

Tests were performed under tension - tension loading at a load ratio, R=0, at ambient temperature and at a cyclic frequency of 0.25 Hz. Testpiece blanks were a length of 150 mm, and a width of 12.5 mm. A reduced testpiece section with a parallel length of 30 mm, a width of 7.5 mm, and a shoulder radius of 75 mm was machined from these blanks. The testpiece thickness was either 0.8 mm (6-ply S1240 / Ti-6Al-4V composites) or 1.8 mm (8-ply SCS6 / Ti-6Al-4V composites).

Results

Low cycle fatigue

The best-fit curves shown in Figure 1 were derived from a total of fourteen tests. In all cases, testpiece failure occurred prematurely from the change in section radius and thus

exposed fibres at the end of the gauge length. Therefore testpiece lifetimes must be considered as a lower bound to the low cycle fatigue resistance of these systems. Even so, especially for the Ti-6Al-4V / S1240 composites their performance can be seen to be satisfactory with lifetimes of $\geq 10^{-4}$ cycles obtained at a cyclic stress range of 1200 MPa, see Figure 1.

Fatigue crack propagation

At ambient temperature, in all tests considered to date dominant fatigue cracks growing in the mode I crack propagation direction have been observed. Some examples are given in Figure 2 for fatigue cracks growth tests interrupted prior to catastrophic failure. For such dominant cracks the interpretation of crack growth rates, da/dN, by the use of potential difference techniques is self-evident. Crack growth resistance curves, da/dN versus applied stress intensity range, ΔK_{APP} , are shown in Figures 3,4 and 5.

These figures illustrate the effect of mean stress on crack growth resistance; initial stress intensity range ΔK_{APP} on crack growth resistance; and the reproducibility of results respectively. Also shown in all figures is the extrapolated crack growth resistance curve obtained for monolithic alloy (processed under identical conditions to the composite material), for $R=0.5, \nu=0.5$ Hz as detailed elsewhere 5 . In many cases it has been possible to detect the failure of individual fibres in - situ, and these incidences of failure are also shown (arrowed) in Figure 3, 4 and 5. It is thus possible to estimate the number of intact fibres bridging the crack as a function of crack length and such estimates are given in Table 1. In this Table they have been used to rationalise the influence of fibre bridging on stable / unstable crack growth transitions.

Discussion

It is clear that these materials may possess excellent damage tolerance under condition of both low cycle fatigue and fatigue crack propagation, see Figure 1 and Figures 3 - 5 respectively. It would appear from Figure 1 that the Ti-6Al-4V / S1240 composite system exhibits superior resistance to the Ti-6Al-4V / SCS 6 composite system under low cycle fatigue testing of smooth testpieces. From the preliminary study reported here it has not been possible to indicate the precise reason for this observation (and specimen geometry effects due to different numbers of fibre rows cannot be ruled out entirely), although work elsewhere on pre - cracked testpieces suggests that the Ti-6Al-4V / S1240 system also demonstrates improved crack growth resistance under conditions of low load ratio (R = 0.1) but inferior resistance under conditions of high load ratio (R = 0.5) to the Ti-6Al-4V / SCS 6 system 6. Such results indicate the care which may be required to compare the performance of different components under cyclic loading in a quantitative manner.

Several other characteristic features of fatigue crack growth observed in these composites to date are exemplified in Figures 3, 4 and 5. In general little effect of load ratio (Figure 3), initial applied stress intensity range, NK_{APP} (Figure 4) and individual fibre fracture (Figure 3, 4 and 5) on *stable* crack growth rates, da/dN, is observed in this mid - crack growth rate

regime (≥ 10⁻⁵ mm/cycle).

Such observations support the concept that the greater an individual fibre is stressed in tension then the greater are the bridging forces operating within the crack wake and hence an increased amount of crack - tip shielding will result provided that the fibres remains intact. This is modelled elsewhere 'a. However, most importantly it must also be recognised that as fibres are stressed more highly in tension then they are also closer to their failure stress. Indeed, all such features of increased load ratio, increased initial applied stress intensity range and fibre failure highlighted above may promote premature catastrophic testpiece fracture following either an increased sequence of fibre failure or a rapid cascade of fibre failure, see Figure 3 and 4 respectively.

One further feature of interest relates to the observed lack of rapid crack growth rate excursions following individual fibre failure, see Figures 3 and 4. This is in contrast to behaviour observed elsewhere in near crack arrest regions 3.0. In the present work they serve to illustrate that periodic crack growth excursions observed, Figure 3, are not in general related to the incidence of fibre fracture. Modelling studies elsewhere 2 suggest that such periodic variation in crack growth rates with crack length can result solely from the position of the growing crack tip relative to the position of the first row of fibres bridging behind the crack tip (consistent with a modelling approach based on discrete fibres and weight function methods).

Although the micromechanisms of fatigue crack growth appears to have been well characterised in such composites much work is still required before predictive models of behaviour can be developed fully for a system in which discrete fibre failure can be important. In this context, the growth of cracks from contained part through thickness defects is under study and is a topic of interest: through thickness interactions between fibres and matrix and hence the definition of a "sphere of influence" around a discrete fibre may provide significant challenges for both experimental and modelling approaches.

The concepts of both an unique fracture toughness and an unique relationship between applied stress intensity range, ΔK_{APP} , and crack growth rate, da/dN are inapplicable to such composites because crack growth resistance is dominated by intact bridging fibres within the crack wake. With large (twenty one) numbers of intact fibres bridging the crack wake the composite can resist overloads in nominal applied maximum stress intensity of in excess of 80 MPa \sqrt{m} , see Table 1. However, with few (eight) intact fibres bridging the crack wake, modest levels of nominal applied maximum stress intensity of approximately 39 MPa \sqrt{m} can promote catastrophic failure. It is important, therefore to ensure in service that an open (i.e. unbridged) crack cannot develop in highly stressed locations. Micromodelling studies elsewhere "have emphasised the importance of bridging scale length in this area of study. With care for specific situations, and provided that the approach is validated experimentally it may be feasible to design to ensure crack arrest (based on the development of "fully - bridged" cracks). Further work is addressing such issues at the present time.

Conclusions

Fibre reinforced titanium metal matrix composites can exhibit good damage tolerance under cyclic loading in both plane - sided testpieces and pre-cracked testpieces. Lifetimes in excess of 10 ⁴ cycles have been obtained for an applied cyclic stress amplitude of 1200 MPa in plane - sided testpieces. The micromechanisms of fatigue crack growth in pre-cracked (notched) testpieces is well characterised by initial crack growth through the matrix and which leaves fibres intact and bridging in the crack wake. These intact fibres reduce the effective stress intensity at the growing crack tip and hence control the observed crack growth rate per cycle. The transition between sub-critical crack growth and catastrophic failure will be governed primarily by the number of intact fibres within the crack wake, and this transition can be promoted by individual fibre fracture, increased load ratio and increased initial applied stress intensity range.

Acknowledgements

One of the authors (ARI) is supported by a SERC CASE award with Rolls Royce plc.

References

- 1. W. S. Johnson, ASTM STP 1032, Ed. W. S. Johnson, Philadelphia, 1989, 194 221.
- 2. P. Bowen, A. R. Ibbotson and C. J. Beevers, Conf. Proc. "Mechanical Fatigue of Advanced Materials," Ed. Ritchie et al, Santa Barbara, Ca (1991), pp. 357 377.
- 3. C. Barney, C. J. Beevers and P. Bowen, "Fracture and Fatigue of Inorganic Composites," Cambridge, (1992), to be published in J. Composites, Butterworths, Oxford.
- 4. P. Bowen, P. J. Cotterill and A. R. Ibbotson, Conf. Proc., "Test Techniques for Metal Matrix Composites," Ed. N. D. R. Goddard, (1990), pp. 82 96, IOPP, London.
- 5. D. C. Cardona, C. Barney and P. Bowen, "Fracture and Fatigue of Inorganic Composites," Cambridge, (1992), to be published in J. Composites, Butterworths, Oxford.
- 6. A. R. Ibbotson, C. Barney and P. Bowen, to be submitted for publication, (1992).
- 7. P. Bowen, D. C. Cardona and A. R. Ibbotson, Mat. Sci. Eng. A, in press, pending publication, May 1992.
- 8. D. C. Cardona and P. Bowen, "Theoretical Concepts and Numerical Analysis of Fatigue," Birmingham, May 1992, MCE publications, Birmingham.
- 9. P. J. Cotterill and P. Bowen, "Fracture and Fatigue of Inorganic Composites," Cambridge, (1992), to be published in J. Composites, Butterworths, Oxford.
- 10. A. R. Ibbotson, C. J. Beevers and P. Bowen, "Fracture and Fatigue of Inorganic Composites," Cambridge, (1992), to be published in J. Composites, Butterworths, Oxford.
- 11. B. N. Cox and C. S. Lo, Acta Metallurgica et Materialia, 40, 1992, pp. 69 80.

Number of Bridging Fibres Remaining Intact	K _{max (nominal)} (MPa√m)	Type of event
8	39	Catastrophic Failure
12	64	Catastrophic Failure
26	66	No Growth
21	80	No Growth
16	51	No Growth
7	64	Catastrophic Failure

Table 1. The importance of the number of bridging fibres intact in the crack wake on stable / unstable crack growth transitions.

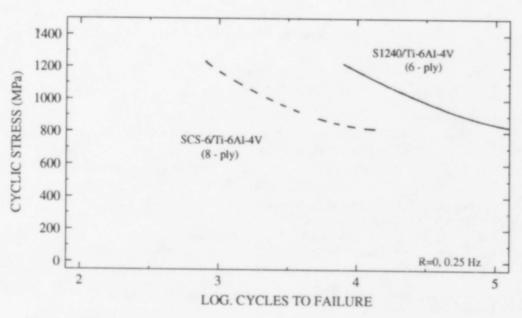


Figure 1. Number of cycles to failure versus applied cyclic stress range. Ambient temperature, R=0, v=0.25 Hz.

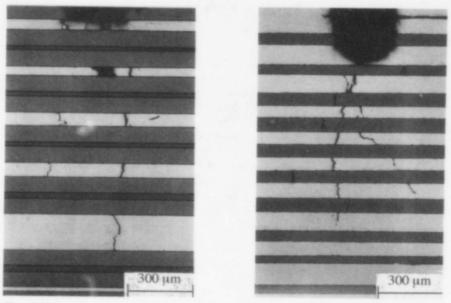


Figure 2(a) and (b). Optical micrographs of sections through interrupted fatigue crack growth, Ti-6Al-4V / SCS 6 composites.

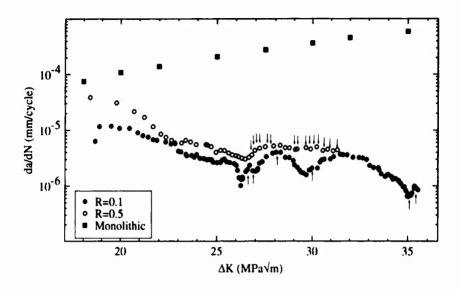


Figure 3. Effect of load ratio on crack growth resistance curves : da/dN versus ΔK_{app} . Ambient temperature, Ti-6Al-4V / SCS 6 composites, v=0.5 Hz. Positions of individual fibre failure are arrowed. Also shown is (extrapolated) data for monolithic Ti-6Al-4V.

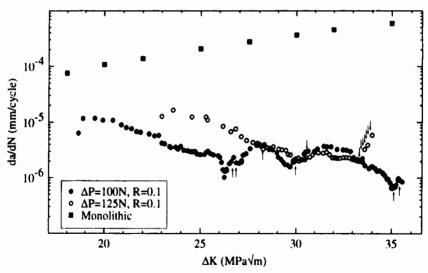


Figure 4. Effect of initial ΔK_{app} on crack growth resistance curves: da/dN versus ΔK_{app} , R=0.1, v=0.5 Hz. Ambient temperature, Ti-6Al-4V / SCS 6 composites. Positions of individual fibre fracture are arrowed. Also shown is (extrapolated) data for monolithic Ti-6Al-4V.

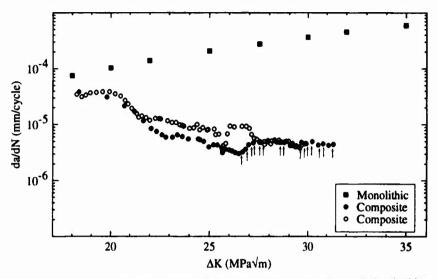


Figure 5. Crack growth resistance curves: da/dN versus ΔK_{app} , R=0.5, v=0.5 Hz. Ambient temperature, two individual tests, Ti-6Al-4V / SCS 6 composites. Positions of individual fibre fracture are arrowed. Also shown is (extrapolated) data for monolithic Ti-6Al-4V.

THE FORGING CHARACTERISTICS OF TWO Ti-6AI-4V-BASED PARTICULATE COMPOSITES

T.P. Johnson*, M.H. Loretto*, M.J. Walker**, M.W. Kearns***

- * Interdisciplinary Research Centre in Materials for High Performance Applications, The
- University of Birmingham, Edgbaston, B15 2TT, U.K.

 ** British Aerospace (Military Aircraft Division), Warton Aerodrome, Preston Lancashire, PR4
- *** IMI Titanium Ltd. PO Box 703, Witton, Birmingham, B6 7UR, U.K.

Abstract

Samples of Ti-6Al-4V, Ti-6Al-4V+ 20vol% SiC and Ti-6Al-4V+ 20vol% TiC have been isothermally forged at 950°C. It has been found that the addition of reinforcing particles leads to increases in flow stresses and decreases in strain rate sensitivity over comparable unreinforced Ti-6Al-4V alloys. Of the two composite materials the TiC-based material shows higher strain rate sensitivities, lower flow stresses and shows much lower levels of microstructural damage for the same overall strain and is therefore more suitable for forging than the SiC-based material.

The principle of adding hard, stiff fibres or particles to a metal matrix to form a composite material is very well established as a way of increasing, in particular, the specific stiffness and strength of a base material. This illustrated in Table 1, which shows values of absolute and specific stiffness in Ti-6Al-4V+SiC in the form of fibres and particles and in unreinforced Ti-6AI-4V.

TABLE 1: ABSOLUTE AND SPECIFIC YOUNG'S MODULUS

Material Y	Young's Modulus	Young's Modulus/Density
	(GPa)	(GPa/g.cm ⁻³)
Ti-6Al-4V +44vol% SiC fibres		57.7 [1]
	trans. 164	42.2 [1]
Ti-6Al-4V +20vol% SiC particl	es 146	34.7 [2]
Ti-6Al-4V	110	24.9

Much of the early work on Ti-based MMCs was concerned with fibre reinforced materials. which provide the greatest improvement in properties. However, as shown in Table 1, these are highly anisotropic. In addition to this they are also very expensive to manufacture and difficult to manipulate by subsequent forming operations. As a result of this, more attention has been focused on particulate reinforced Ti MMCs which are isotropic, somewhat cheaper to manufacture and more ameanable to subsequent processing. However, although part of the reason for the increased interest in particulate reinforced MMCs is their greater ease of processing, very little work has been published regarding the forming of these materials. Therefore, this paper will present a brief look at the subject of the forging response of two such particulate MMCs, Ti-6Al-4V+20vol% SiC and Ti-6Al-4V+20vol% TiC.

Experimental

Two composite materials and two control materials were considered in this investigation. The

Titonium '92 Science and Technology
Edited by F.H. Froes and I. Caplan
The Minerals, Metals & Materials Society, 1993 composite materials were Ti-6Al-4V+20vol% SiC and Ti-6Al-4V+20vol% TiC. The materials were manufactured by hot isostatically pressing prealloyed Ti and ceramic powders at 930°C and 100 MPa for 4 hours. The SiC powder was equiaxed and angular and had a particle size of between 40 and 20 μm and the TiC powder was rounded and equiaxed and between 25 and 10 μm in size. The as-HIPed microstructures consisted of near equiaxed α grains and discontinuous intergranular β . The α grain size was around 15 μm for the SiC-based material and 7 μm for the TiC-based material. Fig 1 shows as-HIPed microstructures of the two composite materials. The interstitial content of these materials is shown in Table 2.

TABLE 2: INTERSTITIAL ANALYSES OF COMPOSITE MATERIALS (wt ppm)

Material	Oxygen	Nitrogen	O+N
Ti-6Al-4V+20vol% SiC	4600	920	5520
Ti-6Al-4V+20vol% TiC	2800	840	3640
Ti-6Al-4V (AMS 4911)	2000 max	500 max	2500 max

This table shows that the interstitial contents of these composites is quite high. Standard grade Ti-6Al-4V (IMI 318) typically contains from 1650 to 2000 ppm oxygen and around 40 ppm nitrogen. As a rough guide, nitrogen can be regarded as having twice the alpha-stabilisation power of oxygen. This was used to indicate the level of oxygen required in the control materials in order to ensure as close a match as possible between the matrix materials and the unreinforced comparison materials. Two Ti-6Al-4V control materials were produced containing 4400ppm oxygen and

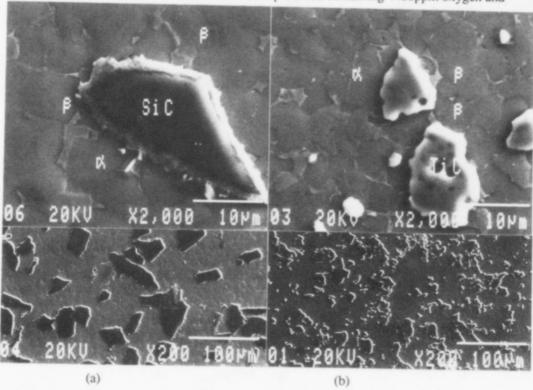


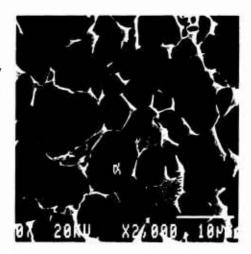
Fig 1. SEM micrographs taken in secondary electron mode showing as-HIPed microstructures of the composite materials (930°C, 4h, 100MPa)

(a) Ti-6Al-4V+20 vol% SiC;

(b) Ti-6Al-4V+20 vol% TiC

6000ppm oxygen. These were hot rolled to give an alpha plus beta structure, as shown in Fig 2. The α -grains were elongated in the rolling direction giving a grain size of around 3 μ m in the tansverse direction and up to 10μ m long in the longitudinal direction. It is important to point out

Fig 2. SEM micrograph taken in secondary electron mode showing as-received microstructure of the Ti-6Al-4V+4400ppm oxygen (transverse section)



that the unreinforced alloys should only be regarded as comparison materials, rather than as control materials, since it is impossible to reproduce the exact microstructures and solute contents of the matrices of the composites

The forging characteristics of the composite and control specimens were investigated via hot compression tests on cylinders of material 5mm in diameter and 10mm long. The specimens were compressed in vacuum between SiC plattens with BN as a parting agent. The tests were carried out at 950°C and at strain rates of between 2x10⁻⁴ and 0.1 s⁻¹. The strain rate was 'stepped' at predetermined strains throughout the tests in order to build up a series of graphs to show the variation of flow stress with strain rate for differing levels of strain up to a strain corresponding to a total reduction of 75%. The unreinforced specimens were machined with the axis of compression parallel to the rolling direction.

Results

Metallographic sections through the thickness of the forged cylinders reveal the classic shear banding in a cruciform; tensile deformation around the periphery of the specimen and two 'dead zones' forming two cones adjacent to the plattens. Fig. 3(a) shows the microstructure of the SiC-based material in the shear bands. This micrograph shows clearly that the interaction zones around the particles have been sheared away from the particles by the deformation, allowing fresh interaction zones to grow in their place. In no case could particle / matrix debonding be observed, indicating that the metal remained in intimate contact with the particles during deformation. The shearing action leads to the formation of large amounts of reaction products within the matrix, often apparently unattached to particles. Fig. 3(b) shows the microstructure around the periphery of the specimen, where tensile deformation is dominant. This has led to the fracture and debonding of many particles which have subsequently fallen out on polishing. There are many particles, however, which appear to be unfractured and well bonded to the matrix. The microstructure of the dead zone is unaffected by the deformation and differs from the parent material only in a greater thickness of the reaction zone due to the extra time at the elevated temperature.

The TiC particles in the shear regions show no evidence of the deformation that has taken place. This can be seen in Fig. 4, which shows the microstructure in a region of intense shear. It can be seen that there is no discrete interaction zone in this material. This is because the reaction zone is composed of sub-stoichiometric TiC which is coherent with the original TiC particle [3]. There is a significant amount of particle / matrix debonding and particle break up in the peripheral regions but to a lesser extent than in the SiC based material and in a very small area just underneath the outer surface of the upset specimen. The microstructure of the dead zone is

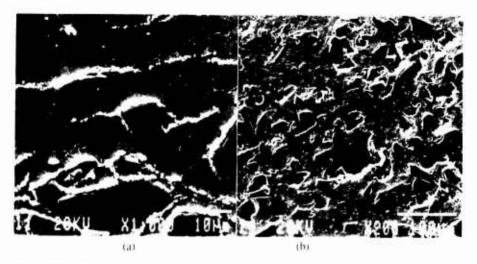
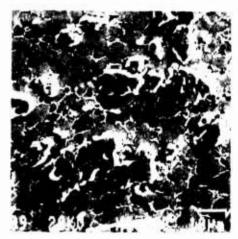


Fig 3. SEM micrographs taken in secondary electron mode showing microstructure of forged Ti-6Al-4V+20 vol% SiC;
(a) in a region of intense shear, (b) at the periphery of the specimen

Fig. 4. SEM micrograph taken in secondary electron mode showing microstructure of forged Ti-6Al-4V +20 vol/7 TiC, from a region of intense shear



virtually identical to the parent microstructure.

The shearing off of the interaction zone between the SiC particles and the matrix during deformation indicates that the particle / interaction zone bond is insufficiently strong to withstand even moderate shear. By comparison, the TiC material is very tolerant to deformation and only showed microstructural damage in areas of considerable tension. This is largely because of the absence of a discrete reaction layer, as explained above

In both materials the matrix microstructure is largely unaffected by the deformation with no substantial grain growth or refinement. Samples of the as-received materials were heated to 950°C in air before being water quenched, sectioned and polished for alpha/beta phase analysis. The matrices of the SiC based and TiC-based materials were found to contain 19.9 vol% and 35.4 vol% of beta respectively. Similarly quenched specimens of the two unreinforced control materials were found to contain 33 and 42 % beta for the high and low oxygen specimens respectively.

Flow Stress Results

Fig 5 shows a typical flow stress versus strain rate curve for the SiC-based material. The gradients of this and similar traces have been replotted to show the variation of strain rate sensitivity, 'm', with natural strain at strain rates of 6×10^{-4} and 4×10^{-3} s⁻¹. These are shown in Fig 6. The flow stress versus strain rate curves for the TiC-based materials were qualitatively similar to those for the SiC-based material and Fig 7 shows the variation of the strain rate sensitivity with natural strain for the TiC-based material at strain rates of 6×10^{-4} , 4×10^{-3} and 3×10^{-2} . Figs 6a and 6b show that the value of 'm' does not deteriorate with increasing deformation in both the SiC and TiC-based materials up to around 70% of natural strain. Indeed, at the higher strain rate, the SiC-based material shows a significant increase in 'm' with increasing deformation.

1000

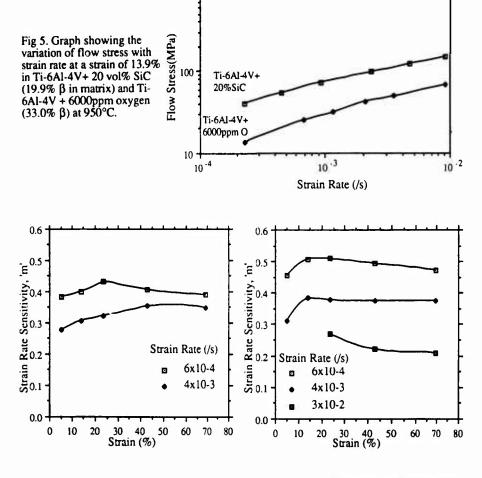
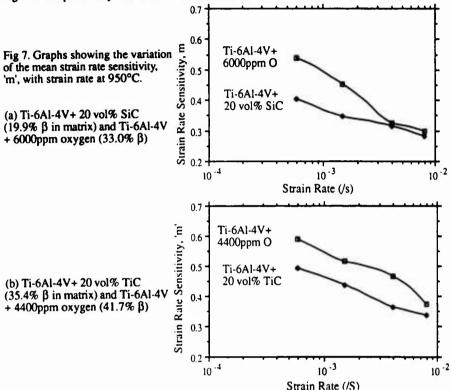


Fig 6. Graphs showing the variation of strain rate sensitivity, 'm', with natural strain at a variety of strain rates at 950°C; (a) Ti-6Al-4V+20 vol% SiC, (b) Ti-6Al-4V+20 vol% TiC.

The variation of 'm' with strain rate in the composite materials and their unreinforced comparison materials are plotted in Fig 7(a) and (b). The values of 'm' used in these plots were calculated by taking the mean value of 'm' at four different strains up to 43.1%. These figures show that although the mean value of 'm' in the composite materials is invariably lower than in

the unreinforced comparison material, the value of 'm' at low strain rates is still remarkably high. This is particulary true in the TiC-based material where the mean value of 'm' at a strain

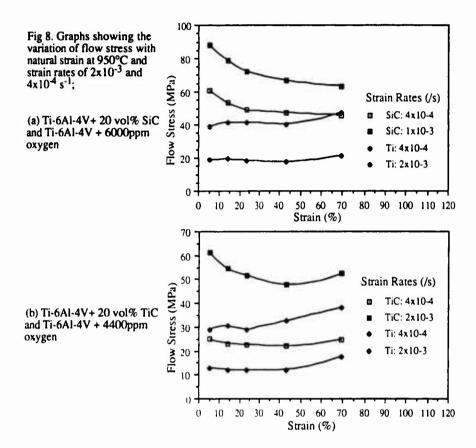


rate of $6x10^{-4}$ s⁻¹ is 0.49. This level of strain rate sensitivity is sufficiently high to enable superplastic forming operations to be used to be used on this material with a reasonable likelyhood of sucess. It can also be seen from these graphs that 'm' rises steeply with decreasing strain rate at the lower end of the graph and it seems probable that further limited increases in 'm' could be achieved by using even slower strain rates or by refining the microstructure.

From the flow stress versus strain rate data obtained at different levels of strain, true stress versus true strain curves have been constructed for both the SiC and TiC-based composites assuming constant strain rates of 2×10^{-3} and 4×10^{-4} s⁻¹, together with similar curves from the unreinforced materials (see Fig 8). This strain rate is a typical strain rate for superplastic forming and gives values of 'm' of around 0.5 for the TiC-based material and 0.4 for the SiC-based material. This shows that both the composite materials have higher flow stresses than the unreinforced control materials. However, it can be seen that in the SiC-based material the difference between the reinforced and unreinforced materials is much greater than in the TiC-based material. This greater increase in flow stress over the unreinforced material is because the strain rate sensitivity of the SiC-based composite is lower than that of the TiC-based composite.

Discussion

A comparison of the forging characteristics of the SiC-based material and the TiC-based material would seem to indicate that the TiC-based material shows the better suitability for forging. This arises from several aspects of its forging properties. Firstly, the microstructural damage caused by forging is very small compared to the SiC reinforced material. The only damage that did occur was in areas of considerable tension indicating that if large tensile forces can be avoided,



then a sound forging microstructure should be a matter of routine. It should also be noted that because TiC does not form a discrete, incoherent interaction zone with the matrix, longer times at elevated temperatures do not result in thick, deleterious reaction zones.

Secondly, the reduction in 'm' value from the unreinforced matrix at slow strain rates in the TiC-based material is less than in the SiC-based material. It may be that part of this difference between the two composite materials is a result of the smaller matrix grain size in the TiC-based material as it is well documented that larger grain sizes tend to lower the maximum 'm' values and reduce the strain rate at which this value of 'm' is reached [4,5,6]. This comparison is made more difficult when considering the unreinforced comparison materials because the grains in the unreinforced material are elongated along the axis of compression. However, in the TiC-based material, although the grains are equiaxed both the grain size and the beta content at the forging temperature are very similar to those of the unreinforced Ti-6Al-4V containing 4400ppm oxygen. Therefore, it seems reasonable to assume that this control material provides a good comparison for the TiC reinforced material. The third aspect of its forging characteristics which makes the TiC-based material more suitable for forging is that it has low flow stresses and a small increase in flow stress over the unreinforced alloy. This is a result of the higher strain rate sensitivity of the TiC-based material and is important because superplastic forming is, generally speaking, made easier by lowering the stresses involved as far as possible.

Another interesting result of this work is that both the composite materials and especially the TiC-based composite appear to have surprisingly high beta contents at the forging temperature

2,591

compared to the unreinforced Ti-6Al-4V containing comparable levels of oxygen. This would seem to suggest that less alpha-stabilisation is occurring in the two composite microstructures than might have been expected, given the presence of large sources of carbon, a powerful alpha stabilser. The reasons for this are not clear. It may be that nitrogen is less powerful as an alpha stabiliser than was assumed when deciding on appropriate levels of oxygen to add by way of comparison and that any carbon in solution in the composite matrix is simply making up the difference in alpha stabilisation. It may also be that at the forging temperature the solubility of carbon is relatively low. Clearly, this is a subject which merits closer attention.

From the results presented in this paper, it would seem that particulate-reinforced Ti-6Al-4V composites can be made which are amenable to conventional forming operations. In particular, the behaviour of the materials during isothermal forging and possibly superplastic forming appears to qualitatively very similar in the reinforced alloys compared to the unreinforced comparison materials. From this particular study TiC is clearly superior to SiC in terms of forgeability. Direct comparison of the two composites and the exact merits of each reinforcement is complicated by the differences in matrix grain size and chemical analysis in the composite materials. However, it seems certain that microstructural damage occurring through the growth and shearing-off of the interaction zones in the SiC-based material would lead to a serious degredation of composite mechanical properties.

Conclusions

- 1. Intense shear in the SiC reinforced material leads to the shearing-off of the particle / matrix interaction zone, resulting in 'stringers' of reaction products in the matrix. In contrast to this, the TiC particles shows no signs of damage in regions of equivalent shear.
- 2. Both the SiC and TiC-reinforced materials show evidence of particle fracture and debonding at the periphery of the specimen, where tensile deformation is dominant.
- 3. The addition of both SiC and TiC to Ti-6Al-4V leads to reductions in the value of 'm', the strain rate sensitivity. The extent of the reduction was greater in the SiC-based material.
- 4. The strain rate sensitivity, 'm', remains stable during deformation up to strains of around 70%.
- 5. The maximum strain rate sensitivity of the SiC and TiC-reinforced materials obtained at 950° C were 0.41 and 0.49 respectively at a strain rate of 6×10^{-4} s⁻¹. This compares with 0.54 and 0.59 in their unreinforced comparison materials at the same strain rate.

Acknowledgements

The authors would like to acknowledge British Aerospace Military Aircraft Division and British Aerospace Sowerby Research Centre for financial support and the Science and Engineering Research Council for the provision of research facilities through the Interdisciplinary Research Centre for High Performance Materials.

References

- 1 D.L. Davidson, R.M Arrowwood, J.E. Hack, G.R. Leverant, S.P. Clough, "Mechanical Behaviour of Metal Matrix Composites", 1983, 117-142, eds. J.E. Hack, M.F. Amateau, Publ. TMS/AIME
- 2. T.P. Johnson, unpublished data
- 3. D.G. Konitzer, M.H. Loretto, Acta Met., 37(2), 1989, 397-406
- 4. N.E. Paton, Ti '84, 2, 1984, 649, eds. G. Lutjering, U. Zwicker, W. Bunk
- 5. D. Lee, W.A. Backofen, Trans. AIME, 239 (1967), 1034
- 6 A.K. Ghosh, C.A. Hamilton, Met. Trans., 10A, 1979, 699

LONGITUDINAL CREEP BEHAVIOR AND DAMAGE IN

SCS-6/Ti-6AI-4V METAL MATRIX COMPOSITES

S. W. Schwenker *, D. J. Evans *, and D. Eylon b

Air Force Wright Laboratory, WL/MLLM Wright-Patterson AFB, OH 45433-6533, USA

b University of Dayton Graduate Materials Engineering, Dayton, OH 45469-0240, USA

ABSTRACT

A unidirectional SCS-6/Ti-6Al-4V composite was creep tested in air in a longitudinal orientation at temperatures between 427 to 760°C to study creep response and damage mechanisms under sustained tension loading. It is shown that after an initial transient period, the creep rate slows to an apparent steady-state creep rate which extends over most of the creep life. Evidence based on fractography and metallographic sectioning suggests that creep life at high stresses is controlled by the time-dependent redistribution of stresses resulting in eventual fiber failure by overload; while at lower stresses, it is controlled by oxidation and environmental degradation occurring on exposed edges of the composite. Although a matrix load shedding mechanism is consistent with much of the experimental evidence, it appears that additional mechanisms are required to fully explain the extensive secondary creep region observed. Strain recovery experiments were also conducted at 538°C and indicate that a large portion of the longitudinal creep strain is recoverable upon unloading at temperature.

INTRODUCTION

Titanium matrix composites (TMC) are being developed to meet the increased performance and temperature requirements of future aerospace systems. Specifically, titanium alloys reinforced with continuous silicon carbide fibers offer substantially improved performance and weight savings over unreinforced titanium alloys in a wide range of aerospace applications. Despite their potential for use at elevated temperatures, there have been only a few studies of creep in these materials [1-5]. Although there is much scatter in the data, it is clear that the reinforcement of titanium with SiC fibers can result in substantially improved creep resistance. However, as with other composite properties, such improvement is obtained only in the fiber direction. Creep studies on TMC's have also shown that they exhibit three stages of creep behavior, similar to conventional unreinforced alloys [2-4]. Despite the apparent similarity, the mechanisms of creep in continuous fiber reinforced composites are different and cannot be interpreted in terms of conventional creep theories [6]. Recent work has also shown that creep theories are different and cannot be interpreted in terms of conventional creep theories [6]. Recent work has also shown that severely degrade creep strength [3-5]. Therefore, the study of creep mechanisms and damage in these materials is essential to their development for elevated temperature aerospace applications.

To understand creep in composites, it is necessary to consider the deformation behavior of the individual components. Due to the large difference in homologous temperatures between SiC and titanium, they will deform by entirely different mechanisms. At 760° C, the homologous temperatures of the matrix and fiber are about 0.53 and 0.33 respectively. Therefore, only the matrix is above 0.4 T_m where it can readily creep by diffusion controlled processes such as dislocation climb and grain boundary sliding. On the other hand, studies on axial creep of

Science and Technology
Edited by F.H. Froes and I. Caplan
The Minerals, Metals & Materials Society, 1993

SCS-6 SiC fibers [7-10] indicate that the fibers deform elastically, with no measurable creep deformation up to temperatures of at least 800°C. In the range of 800 to 1400°C, the fibers exhibit fully recoverable anelastic creep behavior, which has been attributed to either a Zener grain boundary sliding mechanism [8] or to backstress imposed by the elastic carbon core [9]. Above 1400°C, steady-state creep in CVD SiC is apparently controlled by high temperature dislocation glide and climb mechanisms [10].

It has been suggested that the longitudinal creep response of MMC's, at temperatures where the fibers are elastic and the matrix creeps, can be described by a simple matrix relaxation model under uniaxial isostrain conditions [11-13]. In such a model, the load on the composite is initially partitioned between the fiber and matrix according to the rule-of-mixtures (ROM). However, at sufficiently high temperatures, the matrix can relax, resulting in a time-dependent redistribution of load from the matrix into the fibers. This results in additional elastic extension of the fibers at a rate dependent on the creep rate of the matrix. Such a mechanism is referred to as load shedding and predicts a decaying creep rate which asymptotically approaches zero at some critical strain $\varepsilon_C = \sigma_C / E_f$, where the matrix stress is fully transferred to the fibers.

The objectives of this work were to study the longitudinal creep response in a SCS-6/Ti-6Al-4V composite to gain a more fundamental understanding of deformation and damage mechanisms.

EXPERIMENTAL

MATERIAL

The material investigated was a 8-ply, unidirectional SCS-6/Ti-6Al-4V composite panel fabricated by Textron Specialty Materials using a foil/fiber/foil process. The continuous Textron SCS-6 fiber has a diameter of 142 μm and is produced by the chemical vapor deposition (CVD) of β -SiC onto a 37 μm carbon monofilament core. The fiber was woven into unidirectional mats with approximately 5 fibers/mm using a CP titanium ribbon interweave. The woven fiber mats and Ti-6Al-4V foils were alternately stacked and vacuum hot pressed into a 270 mm x 410 mm composite panel with a nominal fiber volume fraction of 0.35. Longitudinally orientated tensile and creep specimens, with a 30 mm long reduced gage section (Fig. 1), were machined from the panel using low-speed diamond cutting and grinding tools. Edges in the reduced section were diamond hand polished to remove transverse grinding marks.

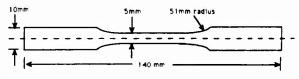


Figure 1: Longitudinal SCS-6/Ti-6AI-4V Tension and Creep Specimen.

Thickness 1 78 mm

Longitudinal tension tests were conducted in laboratory air at room temperature and 427°C on an Instron machine at a strain rate of 0.005 min-1. Longitudinal creep and creep-rupture tests were conducted under constant load in laboratory air at temperatures between 427 and 760°C. Several strain recovery tests were also performed at 538°C, where crept specimens were unloaded to a minimal load (< 30 MPa) under isothermal conditions to measure recoverable strain as a function of time. Creep tests were conducted on both lever arm and direct loaded creep machines equipped with load cells. One of the lever arm machines was also equipped with a hydraulic piston to control arm movement and provide more control over loading and unloading in the strain recovery tests. All specimens were hot gripped using bolted clamp style fixtures with precision machined grooves to maintain specimen alignment in the fixtures. Specimens were soaked at least one hour at temperature and loaded either incrementally over an interval of 90-120 seconds or, continuously at a rate of approximately 10 MPa/s. Displacement was measured using extensometry with either a single or dual LVDT's. When two LVDT's were used, the reported strain values represent the average of the two values. Temperature was controlled and monitored with type K chromel-alumel thermocouples in contact with the specimen gage section. Temperature variation over the gage length was determined to be no more than ± 5°C at 538°C. Creep testing was conducted in accordance with ASTM Standard E 139-83 where applicable.

RESULTS

The as-received microstructure of the SCS-6/Ti-6Al-4V composite is shown in Fig. 2. Extensive metallography and nondestructive testing conducted on the panel indicate that it is well consolidated and contains a relatively uniform distribution of fibers with only a limited number of fiber-to-fiber contacts (Fig. 2a). The Ti-6Al-4V matrix has a fine equiaxed alpha microstructure with average grain size of $10-12~\mu m$ (Fig. 2b). The fiber/matrix reaction zone formed during processing is approximately 3 μm thick. Although the carbon-rich outer coating on the fiber is still intact, more severe degradation to this coating, in the form of cusps, is noted where the beta phase is in contact with the coating (Fig. 2b).

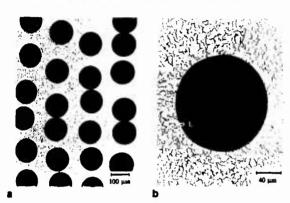


Figure 2: Microstructure of as-received SCS-6/Ti-6Al-4V [0]_B MMC panel at; (a) low and (b) high magnification.

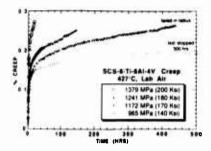
Results of room temperature and 427°C longitudinal tension tests are summarized in Table I. The average room temperature tensile strength of the composite was 1970 MPa, or 94% rule-of-mixtures (ROM), decreasing to a value of 1540 MPa at 427°C. It should be noted that there is little scatter in the data and that the strengths are high compared to other TMC's with similar fiber volume fractions [1,5]. It is believed that these strengths and lack of scatter can be attributed to the excellent fiber distribution and overall quality of the panel.

TABLE I: Longitudinal Tension of [0]a SCS-6/Ti-6Ai-4V MMC (35 volume % fiber)

Specimen	Temp °C	UTS (MPa)*	% Elongation	%_BA nil	
1	24	1972	0.16		
2	24	1958	0.19	rii	
3	427	1558	0.18	1.4	
4	427	1524	0.16	2.9	

^{*}All specimen failed before 0.2% yield strength obtained

Longitudinal creep data at 427 and 538°C is shown in Figs. 3 and 4. It should be noted that a small amount of inelastic strain was usually observed on loading the specimens and has been included in the creep strain values in Figs. 3 and 4. The inclusion of this inelastic strain results in a small positive offset in strain at zero time, but has no effect on the shape of the creep curves. Creep response at 427 and 538°C is characterized by an initial transient or primary stage where the creep rate steadily decreases with time. This is followed by a secondary stage where creep occurs at a minimum and nearly steady-state rate. Although small fluctuations in the strain rate are sometimes observed, they tend to average out over time and the composite exhibits a nearly constant rate of strain. At lower stresses, the secondary stage can extend over most of the life of the specimen. Although not shown in Fig. 4, the tests at 965 and 1034 MPa continue to exhibit constant creep rates that extend well beyond 500 hours.



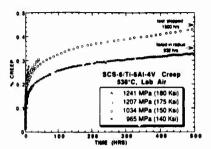
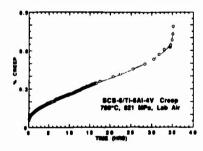


Figure 3: Longitudinal creep of SCS-6/ Ti-6Al-4V MMC at 427°C.

Figure 4: Longitudinal creep of SCS-6/ Ti-6Al-4V MMC at 538°C.

The influence of applied stress on secondary creep rate is best illustrated in Fig. 3. At the lowest stress (965 MPa) the secondary creep rate approaches a zero value as predicted by the load shedding model. However, as stress is increased, there is a pronounced increase in the secondary creep rate. In some of the tests, a short tertiary stage is also observed where creep rate rapidly accelerates just prior to final failure. A limited number of creep tests were also conducted at higher temperatures (650°C and 760°C). In general, the creep curves at higher temperatures exhibit behavior similar to those at lower temperatures except that the time spent in primary creep is shorter and the tertiary stage is more pronounced (Fig. 5). In addition, secondary creep rates at the higher temperatures are faster than at the lower temperatures in spite of the lower test stresses.



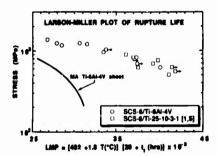


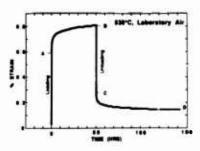
Figure 5: Longitudinal creep behavior of a SCS-6/TI-6AI-4V MMC tested in laboratory air at 760°C and 621 MPa. The specimen failed in 35 hours at a creep strain of 0.79%.

Figure 6: Larson-Miller plot of time to rupture for SCS-6/TI-6AI-4V. Data on TI-6AI-4V mill annealed sheet [14] and SCS-6/TI-25AI-10Nb-3V-1Mo [1,5] are shown for comparison.

Although the use of this material at temperatures up to 760°C will probably be limited due to the poor oxidation resistance of the Ti-6Al-4V matrix, the composite still exhibits outstanding creep strength at these temperatures. At temperatures up to 760°C, the creep lives of the SCS-6/Ti-6Al-4V composites are better than reported for SCS-6/Ti-24Al-11Nb composites [1] and are comparable to available data on SCS-6/Ti-25Al-10Nb-3V-1Mo composites [1,5]. This is demonstrated by the Larson-Miller plot in Fig. 6, where time to rupture for the SCS-6/Ti-6Al-4V composite is compared with other TMC's and the unreinforced Ti-6Al-4V matrix alloy.

Creep and strain recovery in a specimen crept for 50 hours 538°C (1034 MPa) and then unloaded at 538° are illustrated in Fig. 7. After 100 hours, 65% of the time-dependent creep strain is recovered. Most of this occurs within the first 20 hours after which the recovery rate approaches nearly zero. The same specimen was subjected to two additional loading/unloading

cycles consisting of 50 hours of creep at 538°C (1034 MPa), followed again by 100 hours of recovery at 538°C under minimal load. The amount of creep and recovered strain measured in each cycle are shown in Fig. 8. Although the amount of recovered strain remains essentially constant, the amount of creep strain decreases after the first cycle. As a result, the percentage of strain recovery increases in the second and third cycles. Loading moduli were also determined for each cycle and show no appreciable change. To evaluate the effect of longer term exposure, a specimen crept 1500 hours at 538 °C (1034 MPa) to a creep strain of 0.46% was unloaded and allowed to recover at temperature. In this case, approximately 43% of the creep strain was recovered in 70 hours, at which point no further recovery could be measured.



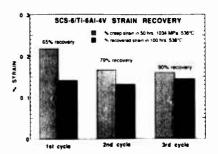


Figure 7: Longitudinal creep and recovery in Ti-6Al-4V/SCS-6 at 538°C. The specimen was crept 50 hrs (1034 MPa), f-llowed by 100 hrs of recovery at 538°C. Creep strain AB = 0.218%; recovered strain CD = 0.141%. Percent of strain recovered (CD/AB) = 0.65%.

Figure 8: Creep and strain recovery in a SCS-6/Ti-6Al-4V composite after repeated load/unload cycles at 538°C. Strain values do not include elastic or inelastic strain on loading/unloading.

SEM fractography conducted on tension tested specimens indicates that failures at both room temperature and 427°C are associated with ductile matrix failure by microvoid coalescence and limited fiber pull-out. The fracture surfaces of creep ruptured specimens are similar except that one or more brittle fracture regions are typically observed on or near the edges of the creep fracture surfaces. These regions typically extend only a few fibers layers deep into the composite. They are also more heavily oxidized than the ductile regions and appear blue when viewed under a low power optical microscope. Such oxidation would indicate that the cracks formed prior to rupture. Figs. 9a and b shows a creep fracture surface illustrating one of these brittle regions on an exposed surface edge of the composite. In this case, the crack has apparently initiated at a damaged and partially broken out fiber on the surface. It is interesting to note that no fiber pull-out is observed in the brittle region while extensive fiber pull-out is noted in fibers just outside this region. This suggests that crack bridging may slow down the growth of these cracks. Figs. 9c is a higher magnification view of the brittle matrix region showing a predominantly intergranular failure mode. This is in contrast to the ductile matrix failure observed over the rest of the fracture surface (Fig. 9d). Fractography suggests that these cracks form early on in the test, probably near broken fibers or surface defects, and continue to grow slowly during the test.

Tension tested and creep ruptured specimens were also longitudinally sectioned and polished through the fiber layers to assess damage. In the tension tested specimens, extensive transverse fiber cracking with a somewhat periodic spacing is observed near the fracture plane. Such fiber damage is also observed below the fracture surface on creep ruptured specimens (Fig. 10). In specimens tested at 538°C and above, there is also some indication of fiber breakage along the specimen edges. Although some of this damage can be attributed to specimen machining and polishing, it appears that additional surface-related cracking occurs during the creep exposure. Such damage was most evident on machined edges of the specimen where the fibers are directly exposed to the environment. The extent and depth of this surface cracking is minimal at 538°C, but appears to increase with exposure time and temperature. Several creep specimens which were interrupted during the secondary stage of creep were also sectioned to evaluate creep

damage. Although some surface related fiber cracking is observed on specimens tested at the higher temperatures, there is no evidence of any internal fiber cracking. This suggests that the fiber cracking observed near the fracture plane is associated with the final rupture event.

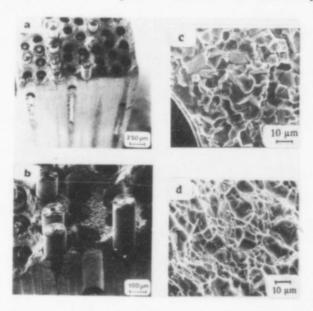


Figure 9: SEM fractography of creep specimen tested at 427°C (1241 MPa) showing; (a) creep fracture surface; (b) brittle fracture region on specimen edge; (c) higher magnification of brittle fracture region showing brittle matrix failure; and (d) ductile matrix failure away from edge showing extensive microvoid formation.

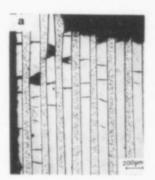


Figure 10: Longitudinal section through the first fiber layer in a creep ruptured specimen showing internal fiber cracking below the fracture plane.

DISCUSSION

A preliminary comparison of creep data with the load-shedding model by McLean [10-12], using estimated values for the Ti-6Al-4V creep constants, has shown that the model can reasonably well predict creep response at the lower creep temperatures and stresses. However, at higher stresses and temperatures, the model cannot account for the nearly constant and non-zero rate of creep observed in the secondary stage. As stress and temperature are increased, other mechanisms of deformation and/or damage must occur which are responsible for the steady-state creep region. Creep of the SCS-6 fiber is one possibility which could account for the secondary creep stage, although experimental data indicates that the fiber does not creep at these temperatures [7-9]. Another possible mechanism is the environmental related damage which is observed on the surface edges of the composite. Work is presently underway to further investigate damage mechanisms and to generate modeling parameters for the matrix using fiberless Ti-6Al-4V foil panels. This will allow a more in-depth comparison of the model with the experimental data.

The creep data obtained so far, indicates the presence of a threshold stress value for creep, as suggested by Gambone [1]. At stresses above this threshold, creep lives are short (less than 150 hours), while at stresses below this threshold they typically exceed 500 hours. At 427°C, the apparent threshold value lies between 1172 and 1241 MPa (Fig. 3), and at 538°C, between 1034 and 1202 MPa (Fig. 4). At creep stresses above this threshold, the ultimate strength of the fiber is exceeded before the matrix can fully relax; hence, creep life is comparatively short and is controlled by the creep resistance of the matrix. Below this value, the matrix is able to fully relax and redistribute the load without exceeding the tensile strength of the fiber. Therefore, the fibers can support the full applied load over extended periods of time. In this case, the creep life would be infinite if it were not for the intervention of environmentally-assisted damage processes which will ultimately limit the creep life. If such a threshold does indeed exist, then the stress carried by the fibers when the matrix is fully relaxed should be close to the ultimate tensile strength of the fiber. Assuming a threshold stress value of 1200 MPa, the calculated fiber stress based on ROM is 3430 MPa. This is very close to average tensile strength values reported for SCS-6 fibers [5].

Strain recovery has previously been reported in directionally solidified eutectic systems [11,15] and in ceramic composites [16] with elastically deforming reinforcements. Such behavior can also be explained in terms of the load shedding or stress redistribution mechanism. Upon load removal, the fibers elastically contract and develop an axial compressive stress in the matrix. If temperature is sufficiently high, the matrix can creep-relax under this compressive stress, resulting again in a time-dependent redistribution of the stresses. As a whole, the composite appears to exhibit anelastic creep behavior, but on the micromechanical level, the fibers contract elastically and the matrix contracts via high temperature creep mechanisms. In principle, if the fibers remains fully elastic, it is expected that all creep strain should be recoverable. The fact that the strain recovery is less than 100% after long term creep exposure is also an indication that some form of permanent damage, such as fiber creep or breakage has occurred. The decrease in the amount of creep strain observed after the first cycle of loading in the cyclic creep and recovery tests is not fully understood, but could be related to pre-existing defects and damaged fibers on the specimen surface. These defects can readily initiate damage during the initial creep cycle while in subsequent cycles, the damage accumulation is controlled entirely by environmental processes. In addition, if any residual stresses are present in the material, they could also contribute to additional creep strain in the first cycle.

SUMMARY AND CONCLUSIONS

Longitudinal tension, creep, and creep recovery tests were conducted in laboratory air on a Ti-6Al-4V composite containing 35 volume % SCS-6 fiber. It was found that:

- 1. The composite exhibits very high longitudinal tensile strengths and little scatter in data when tested at room temperature and 427°C.
- 2. The composite exhibits outstanding longitudinal creep strength. At temperatures up to 760°C, creep lives were as good as or better than composites based on elevated temperature titanium aluminide matrices, such as Ti-24Al-11Nb.
- 3. The load shedding model cannot entirely account for the longitudinal creep behavior. This model appears to overestimate creep resistance and cannot account for the long periods of nearly constant secondary creep observed. Although much of the primary creep probably results from load shedding, the secondary region is apparently related to another mechanism of deformation and/or damage occurring in the composites.
- 4. Creep deformation in laboratory air at 427°C and above is also associated with environmental related surface damage. Regions of brittle matrix failure and fiber cracking were observed on exposed edges of the specimen.
- 5. At 538°C, a large portion of the creep deformation can be recovered. Such recovery is attributed to the time-dependent redistribution of stresses which occurs after unloading the specimen following a creep exposure.

ACKNOWLEDGEMENTS

The authors wish to thank Mr. Dan G. Rosenthal of Textron Lycoming and Dr. Daniel B. Miracle of the Air Force Materials Directorate for their support in this project. Parts of this project were funded by Textron Lyconing.

REFERENCES

- 1. M. L. Gambone, "Fatigue and Fracture of Titanium Aluminides", Vol. II, WRDC-TR-39-4145, (1990).
- 2. D. J. Evans, "Study of Creep Damage Mechanisms and Steady-State Creep Regime in SCS-
- 6/Ti-6Al-4V Composites", M.S. Thesis, University of Dayton, (1990).

 3. M. Khobaib, "Creep Behavior of SCS-6/Ti-24Al-11Nb Composites", Titanium Aluminide Composites, Proceedings From Titanium Aluminide Composites Workshop, eds P. R. Smith,
- S. J. Balsone, and T. Nicholas, WL-TR-91-4020. (1991), 450-466.
- 4. M. Khobaib, "Damage Evolution in Creep of SCS-6/Ti-24Al-11Nb Metal Matrix Composites", Proceedings of the American Society for Composites Sixth Technical Conference: Composite Materials, Mechanics and Processing, Technomic Publishing Co., (1991), 638-647.
- 5. D. R. Schuyler, M. M. Sohi, R. L. Hollars, and J. D. Pugnale, "Feasibility of Aluminide Metal Matrix Composites (MMC) For 1400°F Applications", Naval Air Development Center Final Report No. NADC-91066-60, (1991).
- 6. O. D. Sherby and P. M. Burke, <u>Mechanical Behavior of Crystalline Solids at Elevated Temperature</u>, Progress in Materials Science, Vol. 13, Pergamon Press (1968).
 7. J. A. DiCarlo, "Thermal Stability of SCS-6 Fibers", Proceedings of the 2nd Annual HITEMP
- Review, NASA Conference Publication 10039, Cleveland, OH, (1989), 69/1-11.
- 8. J. A. DiCarlo, "Creep of Chemically Vapor Deposited SiC Fibers", J. Mater. Sci., Vol. 21, (1986), 217-224.
- 9. J. Beale, E. Lara Curzio, and S. S. Sternstein, "High Temperature Deformation Studies on CVD Silicon Carbide Fibers", Proc. of the 35th International SAMPE Symposium, (1990), 1193-1204.
- 10. C. H. Carter, Jr. and R. F Davis, "Kinetics and Mechanisms of High Temperature Creep in Silicon Carbide: II, Chemically Vapor Deposited", Journal of the American Ceramic Society, Vol. 67, No. 11, (1984), 732-740.
- 11. M. McLean, "Modelling of Creep Deformation in Metal Matrix Composites", Fifth International Conference on Composite Materials (ICCM-V), eds. W. C. Harrigan Jr., J. Strife, and A. K. Dhingra, TMS (1985), 37-52.
- 12. M. McLean, "Mechanisms and Models of High Temperature Deformation of Composites", Materials and Engineering Design: The Next Decade, eds. B. F. Dyson and D. R. Hayhurst, Inst. of Metals, London, (1989), 287-294.
- 13. M. McLean, Directionally Solidified Materials For High Temperature Service, The Metals Society, London, (1983).
- 14. R. A. Wood and R. J. Favor, Titanium Alloys Handbook, Metals and Ceramic Information
- Center, MCIC-HB-02, Battelle Columbus Laboratories, (1972).

 15. T. Khan, J. F. Stohr, and H. Bibring, "Cotac 744: "An Optimized D.S Composite for Turbine Blades", Superalloys 1980, Proceedings of the Forth International Symposium on Superalloys, ASM, (1980), 531-540.
- 16. J. W. Holmes, J. Wayne Jones, Y. Park, and C. Chiu, "Tensile Creep Behavior of Fiber Reinforced Ceramics", Proceedings of the 4th Annual HITEMP Review, Cleveland, OH, NASA Conference Publication 10082, (1991).

CYCLIC FATIGUE RESISTANCE OF FIBRE REINFORCED TITANIUM

METAL MATRIX COMPOSITES AT AMBIENT AND ELEVATED TEMPERATURE

A. R. Ibbotson, P. Bowen and C. J. Beevers

School of Metallurgy and Materials / IRC in Materials for High Performance Applications, The University of Birmingham, B 15 2TT, United Kingdom.

Abstract

The fatigue response of a continuous silicon carbide (SCS-6) fibre reinforced Ti-6Al-4V metal matrix composite in the presence of a sharp pre-crack has been studied in single edge notched testpieces in bending. Crack growth rates have been measured for different values of span to width ratio (s/W) at ambient temperature and at a test temperature of 550 °C in air by the use of a direct current potential difference technique. It was found that in most cases the observed crack growth rates initially decrease with increasing crack length (and hence increasing nominal applied stress intensity range). In general, crack growth rates are increased at 550 °C only at low frequencies, relative to the crack growth rates measured at ambient temperature. Based on observations to date it has been shown that fatigue cracks grown at a large span to width ratio propagate to failure more rapidly than cracks grown at small span to width ratios for equivalent initial nominal stress intensity ranges. Metallographic sections through the composite indicate that the improved fatigue life observed at low values of s/W ratio may be attributable to debonding at the fibre matrix interface and which is deduced to delay the onset of fibre failure.

Titanium '92 Science and Technology Edited by F.H. Froes and I. Caplan The Minerals, Metals & Materials Society, 1993

Introduction

Previous tests have been performed on Ti-6Al-4V / SCS-6 testpieces loaded in three point bending at a total span to width ratio (s/W) of 15:1'. This work has helped to demonstrate a number of points concerning the fatigue behaviour of this composite system.

First, fatigue damage in this load configuration is generally limited to a single dominant fatigue crack. Second, fibre bridging in the crack wake is a crucial factor in determining fatigue crack growth rates and is demonstrated by initial decreases in crack growth rate as the nominal stress intensity range, Δ K_{AFF}, increases with matrix crack length increase. This observation can be explained by considering the phenomenon of crack tip shielding by unbroken fibres $^{2-4}$. Also, crack bridging is important in determining the transition from stable to unstable crack growth under cyclic loading.

In general cyclic fatigue tests in bending are conducted at large span to width ratios, in order to minimise the degree of shear stresses in the material. This combined with relatively strong interfacial bond strength between the fibres and the matrix (156 - 180 MPa 34) generally lead to a dominant fatigue crack in the composite matrix at room temperature.

In service greater shear stresses may be imposed on the composite. Such increases in the applied shear stress to the fibre matrix interfaces could lead to multiple matrix cracking i.e. more distributed damage within the matrix, and therefore it is of interest to consider this situation. Indeed if fatigue crack growth rates were reduced for the case of distributed matrix damage, then this would be a powerful indication that the growth of a single dominant fatigue crack would produce conservative life estimates. Under such circumstances the use of a fracture mechanics based approach to lifing the composite system would become self-evident. Thus the primary aim of this study is to investigate the effects of total span to width ratio on fatigue crack propagation.

Experimental

All tests were performed on single edge notched bend testpieces of nominal dimensions (4 \times 1.75 \times 70 mm³). Cracks were grown by fatigue from through thickness slots cut either by electric discharge machining or by the use of a diamond saw, to a depth of approximately 1 mm. This produced an initial crack depth to width ratio, a_o/W , of 0.25. Fatigue cracks were grown perpendicular to the fibre direction and parallel to the stacking direction within a mat. All tests were carried out in three point bending. Two values of overall span to width ratio, s/W, were used for the fatigue i.e. s = 15W and s = 5W.

An ESH servohydraulic testing machine fitted with a 10 kN load cell was used at a frequency of 10 Hz. Fatigue tests were conducted at constant load ranges. In the case of s = 15W the load range, Δ P, was equal to 125N and the stress ratio, R, was equal to 0.1. In this case the stress ratio, R, is defined as $(\sigma_{\min}/\sigma_{\max})$ where σ_{\min} and σ_{\max} are the minimum and maximum applied stresses during the fatigue cycle respectively. For s = 5W, the load range was equal to 375N, with R = 0.1. In both cases of s/W the load ranges were chosen to produce an initial value of nominal applied stress intensity range, Δ Kapp, of approximately 23 MPa \sqrt{m} .

Fatigue crack growth was monitored by means of a direct current potential difference technique. The calibration curves relating normalised potential, V/V_{e} , (where V_{e} is the reference potential at a/W=0.25) to changes in normalised crack length, a/W, had been determined previously for the specimen geometry under consideration.

Fatigue tests at each value of s/W were conducted at both ambient temperature and 550° C. Testing at elevated temperature was achieved by mounting the specimens in a purpose built test jig and then heating by means of two pairs of quartz halogen furnace lamps. The temperature was monitored by means of a thermocouple attached to the testpiece surface. Once stable, the temperature was maintained to within $\pm 1^{\circ}$ C of the set temperature.

All tests were carried out on a Ti-6Al-4V alloy matrix reinforced with Textron SCS-6 silicon carbide fibres. The matrix was tested in the as received condition (i.e. solution treated at 910 ° C). The fibre diameter was 140 μ m, and the fibre volume fraction was confirmed at approximately 0.35.

Fatigue cracks were examined by one of two techniques:

- (i) testpieces containing fatigue cracks were polished and then photographed by using a light microscope.
- (ii) fracture surfaces were examined by means of a field emission gun (FEG) scanning electron microscope, operating at 45 ° tilt and 20 kV.

Results

Ambient Temperature.

Figures 1(a) and (b) show the variation of fatigue crack growth rate, da/dN, versus nominal applied stress intensity, Δ KAP, and total crack length respectively. In each case the initial value of Δ KAP was approximately 23 MPa \sqrt{m} . Initial fatigue crack growth rates are similar. However, crack growth behaviour diverged as the tests progressed. In the case of the long span testpiece (Δ P=125N, R=0.1, s=15W), the fatigue crack growth rate decreased until a at Δ KAP value of 35.5 MPa \sqrt{m} a steady growth rate of approximately 5×10^{-7} mm/cycle was achieved, and eventually resulted in catastrophic failure.

The second long span test was conducted at a frequency of 0.5 Hz. In this case it can be seen that the fatigue crack growth decreases initially but remains higher than the corresponding test at 10 Hz. It is also worth noting that the 0.5 Hz testpiece failed at a lower value of Δ K_{APP} (34.5 MPa \sqrt{m}).

The final test performed at room temperature involved reducing the total span to width ratio from s = 15W to s = 5W. This change produced a marked change in fatigue crack growth behaviour. In this case at the test frequency of 10 Hz crack growth arrested (da/dN \leq 10 $^{-8}$ mm/cycle) at a Δ K_{APT} of 36 MPa \sqrt{m} .

Figure 2 shows a metallographic section through a long span testpiece (\triangle P=125N, R=0.1, s = 15W) which was fatigue at a frequency of 10 Hz. In this case the test was interrupted before catastrophic failure occurred. From Figure 2 it can be seen that a dominant mode I fatigue crack has been produced together with some matrix cracking. Evidence of fibre matrix interface failure is also present (arrowed).

Polishing the surface of the short span testpiece revealed that similar fatigue damage had occurred in this loading configuration, see Figure 3. From this Figure it can be seen that a single dominant fatigue crack has been formed with, once again, interfacial debonding (arrowed).

It has also been observed that the surface of the fibres contain small pits, see Figure 4, which are possibly the result of a reaction between the fibre coating and the matrix. This form of surface damage will be expected to strengthen the bond between the fibre and the matrix.

Elevated Temperature (550 °C)

Fatigue crack growth rates, da/dN, are shown versus nominal Δ K_{AP} and total crack length in Figure 5(a) and (b) respectively. All tests were performed at an initial Δ K_{AP} of 23 MPa \sqrt{m} , and in all cases cracks extended until catastrophic failure occurred. Long span tests were performed at frequencies of 0.5 and 10 Hz. It was found that crack growth rates were significantly higher at the lower test frequency.

It was also noted that the initial fatigue crack growth rates of all tests performed at 550 °C were similar to those obtained at ambient temperature.

The short span test, (\triangle P=375N, R=0.1, s=5W), at a frequency of 10 Hz exhibited greatly reduced crack growth rates over most of the fatigue test. In this case crack growth rates tended to approach arrest (da/dN \le 10⁻⁸ mm/cycle) but never achieved full arrest. The period of very slow crack growth appears to have been interrupted by major fibre failure (such observations have been noted elsewhere °). The occurrence of fibre failure led to a rapid increase in crack growth rate (10⁻⁷ \rightarrow 4×10⁻⁶mm/cycle) and eventually catastrophic failure.

A striking feature of all the 550°C fatigue tests was the fact that two off-axis fatigue cracks were produced. These cracks are of very similar length and extend at angles of between 30°-45° from the mode I opening direction, see Figures 6-8.

Discussion

At large span to width ratios it has been shown that single dominant fatigue cracks are produced within the composite matrix.¹⁵. The presence of such localised damage suggests that the use of fracture mechanics parameters to characterise fatigue crack growth may be appropriate.

It must be noted that in many loading situations and in actual components multiple crack damage may result. This situation makes justification for the use of fracture mechanics parameters such as the alternating stress intensity range much more difficult. However, if it is possible to show that fatigue crack growth rates are highest under conditions which produce a single dominant crack then this data can be used as a conservative estimate of the resistance to fatigue crack growth.

In an attempt to generate more distributed damage in the matrix the span to width ratio was reduced. This has the effect of increasing the shear loading on the fibre matrix interfaces and should produce more distributed damage within the matrix in the form of debonding at the interfaces and matrix cracking. The presence of such damage at the interfaces should be reflected by changes in crack growth rates and also in the mode of crack propagation.

At room temperature Figures 2 and 3 demonstrate that production of a dominant crack within the matrix alloy is independent of the total span to width ratio under consideration here. At 550° C, it was found that two off-axis dominant cracks were produced at both span to width ratios. At both test temperatures it was observed that fatigue crack growth rates were changed significantly by reducing the total span to width ratio.

Fatigue crack growth rate data generated at ambient temperature, see Figure 1(a) and (b), illustrates that under similar initial conditions of Δ K_{APP} and also growth rate, crack growth in the short span test eventually arrests (da/dN \leq 10⁻⁸ mm/cycle).

Metallographic sections reveal the presence of debonding at the fibre matrix interfaces. Although it is difficult to make quantitative estimates of the degree of debonding it would be expected that an increase in the interfacial shear stress would promote debonding. If this were the case then it would be expected that low span to width ratios would promote debonding and reduce the probability of fibre failure close to the notch plane. This argument follows because load transfer from the matrix to the fibres is expected to be reduced locally within the debond length. Failure of the reinforcement fibres away from the crack plane allows some bridging pressure to be maintained even though fibre failure has occurred. Thus testpieces containing increased amounts of interfacial debonding would be predicted to experience lower crack growth rates.

The presence of dominant fatigue cracks within all the testpieces is reassuring from an experimental point of view, since the growth of such cracks can be measured with confidence and predictive models developed.

At 550° C two dominant off-axis fatigue cracks are produced. The formation of these cracks appears to be independent of the test span to width ratio, see Figure 6 - 8. Production of off-axis cracks is considered to be consistent with a reduction in the intrinsic interfacial strength, and greater crack deflection ". It has been determined that in similar systems compressive stresses are formed around the fibres ". It has been observed, see Figure 4, that reactions at the fibre matrix interface leads to the formation of pits in the coating. This pitting combined with compressive stresses will plausibly produce an efficient mechanical bond at ambient temperature. At 550° C the compressive stresses are almost removed ", thus reducing the efficiency of the mechanical bond. Chemical attack by atmospheric oxygen is also thought to reduce the interface strength "N.13. Both these mechanisms appear to decrease the interface strength and will promote debonding under increased shear loading.

It is interesting to note the rapid increase and decrease in da/dN observed at low growth-rates ($\leq 10^{-7}$ mm/cycle) in near arrest regions, see Figure 5(a) and (b). It is thought that these excursions are attributable to fibre failure in the crack wake (see also reference ^a).

The progress toward final arrest appears to have been interrupted by a very rapid increase in growth rate, which was possibly due to a large number of bridging fibres failures.

At 550 °C all tests to date have failed, irrespective of the test span to width ratio. This suggests that at 550 °C a combination of environmental and mechanical damage processes may lead to fibre failure after an extended number of cycles.

Conclusions

- 1. The nature of fatigue damage (i.e. dominant mode I cracks) is independent of the span to width ratio, $5 \le s/W \le 15$. However, crack arrest $(da/dN \le 10^{-8} \text{ mm/cycle})$ has been observed in short span tests, whereas cracks grew to failure in long span tests, for nominally identical initial applied stress intensity range.
- 2. At 550 °C off-axis dominant fatigue cracks are produced. This behaviour appears to be a characteristic of this system when tested in three point bending under cyclic loading. In short span tests crack arrest was not observed, consistent with fibre failure after an extended number of cycles.
- 3. The presence of dominant cracks at both ambient temperature and 550 °C appears to facilitate the use of fracture mechanics parameters in characterising fatigue crack growth.

Acknowledgements

Support for one of the authors (ARI) from a SERC CASE award with Rolls Royce is gratefully acknowledged. The support of M. V. Hartley, Rolls Royce, Derby has been particularly beneficial to the programme. Thanks are also extended to Mr J. T. Knight for his expert metallographic preparation of the testpiece surfaces.

References

- A. R. Ibbotson, P. Bowen, and C. J. Beevers, "Stable and Unstable Crack Growth Transitions Under Cyclic Loading in a Continuous Fibre Reinforced Composite," Scripta Metallurgica et Materialia, 25 (8) 1991, 1781 - 1786.
- B. N. Cox, D. B. Marshall and M. D. Thouless, "Influence of Statistical Fiber Strength Distribution on Matrix Cracking in Fiber Composites," Acta Metallurgica, 37 (7) 1989, 1933 - 1943.
- 3. D. B. Marshall and B. N. Cox, "Tensile Fracture of Brittle Matrix Composites: Influence of Fiber Strength," Acta Metallurgica, 35 (11) 1987, 2607-2619.
- D. B. Marshall, B. N. Cox and A. G. Evans, "The Mechanics of Matrix Cracking in Brittle Matrix Fiber Composites," <u>Acta Metallurgica</u>, 33 (11), 1985, 2013 2021.
 J. C. Jang, S. M. Jeng and J. -M. Jang, "Interfacial Properties Measurement for SiC Fiber Reinforced Titanium Alloy Composites," <u>Scripta Metallurgica et Materialia</u>, 24 (1990), 469 - 474.
- 6. Y. Lepetitcorps, R. Pailer and R. Naslain, "The Fibre Matrix Interfacial Shear Strength in Titanium Alloy Matrix Composites Reinforced by Silicon Carbide or Boron CVD Filaments," Composites Science and Technology, 35 (1989) 207.
- N. D. R. Goddard, ed., IOP Short Meetings Series No 28, "Test Techniques for Metal Matrix Composites," (IOP publishing ltd, 1990), 82 - 97.
- P. J. Cotterill and P. Bowen, "Fracture and Fatigue of Fibre Reinforced Metal Matrix Composites," (Paper presented at "Fatigue and Fracture of Inorganic Composites," Cambridge, UK, 31 March - 2 April, 1992 to be published.
- A. R. Ibbotson, P. Bowen, and C. J. Beevers, "Fatigue Crack Growth in Fibre Reinforced Metal Matrix Composites," Proceedings of the 2th European Conference on Advanced Materials and Processes, University of Cambridge, UK, 22 - 24 July, 2 (1991), 469 - 478.
- B. N. Cox and D. B. Marshall, "Crack Bridging in the Fatigue of Fibrous Composites," Fatigue Fract, Engng Mater. Struct., 14 (8) 1991, 847 - 861.
- 11. Y. H. Park and H. L. Marcus, "Influence of Interface Degradation and Environment

on the Thermal and Fracture Fatigue Properties of Titanium Matrix / Continuous SiC -Fibre Composites," ed. J. E. Hack and M. F. Amateau, (TMS - AIME, New York, 1983), 65

- D. Finello, Y. H. Park, M. Schmerling and H. L. Marcus, "Fractography of Metal Matrix Composites," Fractography of Ceramic and Metal Failures, ASTM STP 827, ed. J. J. Mecholsky, Jr. and S. R. Powell, Jr., (American Society for Testing and Materials, 1984), 387 - 396.
- 13. J. Gayda, Jr., T. P. Gabb, and A. D. Freed, "The Isothermal Fatigue Behaviour of a Unidirectional SiC / Ti Composite and the Ti Alloy Matrix," (NASA Technical Memorandum, TM - 101984, April 1989).

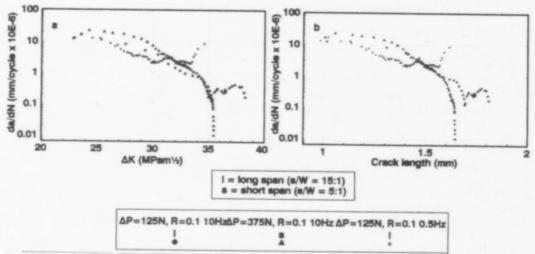


Figure 1. da/dN versus (a) ΔKAPP and (b) total crack length at ambient temperature.

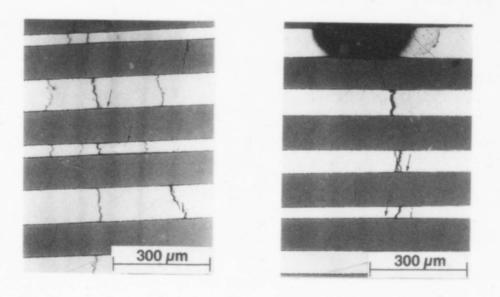


Figure 2. Metallographic section through a Figure 3. Metallographic section through a bonding (arrowed).

long span testpiece, ($\Delta P = 125N$, R = 0.1, short span testpiece, ($\Delta P = 375N$, R = 0.1, s = 15W, ambient temperature). Note the in- s = 5W, ambient temperature). Note the cidence of fibre fracture and interface de- presence of fibre fracture and debonding (arrowed).

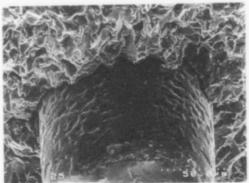


Figure 4. Micrograph showing pitting of the fibre coating after reaction with the Ti-6Al-4V matrix.

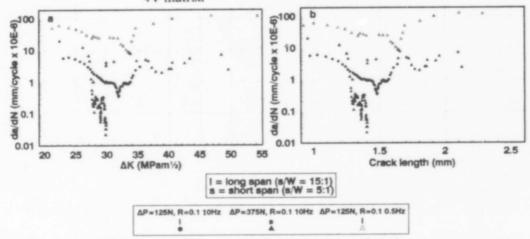


Figure 5. da/dN versus (a) Δ KAPP and (b) total crack length at the test temperature of 550 °C.

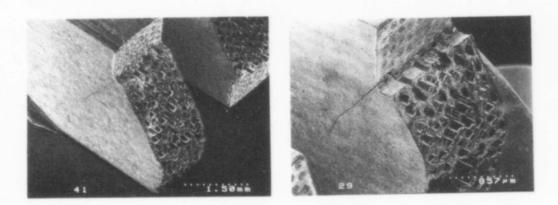


Figure 6. Off-axis fatigue cracks produced at $\Delta P = 125N$, R = 0.1, s = 15W, 0.5 Hz, 550 °C $\Delta P = 125N$, R = 0.1, s = 15W, 10 Hz, 550 °C.

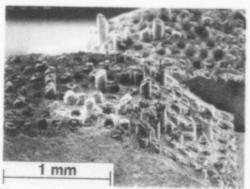


Figure 8. Off-axis fatigue cracks produced at $\Delta P = 375N$, R = 0.1, s = 5W, 10 Hz, 550 °C.

DEFORMATION MECHANISMS IN A TI-ALLOY/SIC METAL MATRIX COMPOSITE

B.S. Majumdar¹, G.M. Newaz², F.W. Brust² and J.R. Ellis³

¹Universal Energy Systems, 4401 Dayton-Xenia Rd., Dayton, Ohio 45432 ² Battelle, 505 King Avenue, Columbus, Ohio 43201 ³ NASA Lewis Research Center, Cleveland, Ohio 44135

ABSTRACT

The damage and plasticity mechanisms were evaluated for a Ti 15-3/SCS6 metal matrix composite (MMC) under tension loading at room and elevated temperatures. Experiments involved a combination of tension tests, where Poisson's ratios and unloading compliances were monitored, and detailed microstructural evaluation of tested specimens. For the 0-degree system, the primary inelastic deformation mechanism was plasticity of the matrix, although final failure occurred when a critical level of stress (or strain) was reached in the fibers. In the case of the 90-degree system, there was a three-stage deformation response, with either damage or plasticity dominating during the different stages of deformation. Reaction-zone cracks were found to play an important role in nucleating plasticity in the matrix for all ply systems, particularly during the micro-yield regime of deformation. The primary effects of elevated temperature included reduced residual stress in the MMC, and time-dependent deformation and diffused slip in the matrix. The latter was in contrast to the planar slip observed at room temperature, which was explained in terms of a very fine ω-phase detected in the microstructure of the beta-titanium matrix. The experimental results were compared with the predictions of a number of constitutive models. A finite element unit-cell model was developed, which provided best correlation with the experimental data.

INTRODUCTION

Titanium alloy based metal matrix composites have been the subject of significant research in recent years. This stems from their superior stiffness and strength-to-weight ratios and creep strengths at elevated temperatures. A deficiency of such systems is their low fracture strains, which make it imperative that inelastic deformation processes be included in any realistic design methodology. Understanding the deformation mechanisms also is important from a materials development perspective, because it can suitably guide microstructural tailoring for improved MMC properties.

In this work, monotonic tension tests were performed on a Ti 15-3/SCS6 composite. A number of ply systems were investigated: $[0]_8$, $[90]_8$, and $[\pm 45]_{28}$ systems, with primary emphasis on the 0° and 90° systems. In this paper, only the main results are discussed, and specific details are provided in references [1-4]. The results of other monotonic tension tests on this system, which are relevant to the work described here are available in references [5-7].

EXPERIMENTS

The materials tested were 8-ply Ti 15-3/SCS-6(SiC) composites, approximately 1.99 mm thick, fabricated using a foil-fiber-foil consolidation technique; the fiber volume fraction was

Titanium '92
Science and Technology
Edited by F.H. Froes and I. Caplan
The Minerals, Metals & Materials Society, 1993

approximately 0.34. The Ti 15-3 (Ti-15V-3Cr-3Al-3Sn, all in weight percent) matrix is a metastable body centered cubic (bcc) B Ti-alloy, the bcc phase being stabilized by vanadium.

Uniaxial dog-bone shaped tensile test specimens were tested in the as-fabricated condition, involving a cool-down from the HIP-ing temperature of approximately 815 C; no heat-treatment was performed prior to the testing. In addition to measuring longitudinal strains (along specimen axis), the width and thickness strains were monitored using extensometers and strain gages; such measurements provided critical information on the relative magnitudes of plasticity and damage. Experiments were performed at room temperature (RT) and at 538 C. The elevated temperature tensile and creep experiments were performed using cold grips and nucleon heating only the region between the shoulders of the specimen. The advantage of such a testing approach is that it can effectively transfer load from the grips to the fibers, through the matrix in the cold region of the sample; this is in contrast to the case of hot grips, characteristic of standard creep frames, where there are ambiguities regarding effective transfer of load from the grips to the fibers at the high testing temperatures. Following mechanical testing, specimens were examined optically and by transmission electron microscopy (TEM).

RESULTS

Mechanical Test Results [0]a MMC

The stress versus longitudinal strain data for a few of the tested [0]₈ specimens are shown in Figure 1a. The stress-strain behaviors at RT and 538 C were similar, with the unloading line being parallel to the loading line, suggesting plasticity as the dominant inelastic mechanism.

The elevated temperature deformation response differed from the RT response primarily in terms of the stresses and strains at which inelastic deformation initiated and fracture occurred. Whereas inelastic deformation at RT initiated at a "yield" strain of approximately 0.35%, it was approximately 0.35% at 538 C. The lowering of the critical strain likely reflects the lowering of the flow stress of the matrix, which was approximately 800 MPa at RT, and which was only 400 MPa at 538 C. The lowering of the strain to failure is believed to be due to less residual compression stress in the fibers at 538 C compared with that at RT. Comparisons of mechanical data with theoretical predictions will be provided later.

The dotted lines in Figure 1b represent experimental plot of ew/eL versus the total longitudinal strain (eL), where ew is the total width strain; the scatter being largely because a ratio has been plotted. The main point to note is that beyond 0.5 percent strain, the data illustrate an increase in the Poisson's ratio, rather than a decrease, suggesting plasticity as the dominant mechanism. Figure 1b also contains analytical predictions of two models: (i) the vanishing fiber diameter model (AGLPLY) of Dvorak et al. [8], and, (ii) a computational unit-cell model [9] for analyzing MMCs. The significant point here is that the models, where only plasticit accounted for all the inelastic deformation in the 0-degree MMC, predicted increasing values of ew/eL with increasing eL. Thus, the experimentally observed increasing behavior of ew/eL can indirectly be interpreted as arising from plasticity of the matrix, consistent with plasticity also being indicated by parallel loading-unloading curves.

Figure 1a also contains the stress-strain response for a specimen creep tested for four hours at 800 MPa at 538 C. The creep deformation appears to have an adverse effect on the residual tensile strength. If it is assumed that fast fracture is controlled by the attainment of a critical strain (failure strain of fibers), then the extrapolation indicated by BC in Figure 1a suggests that the loss in strength (a traditional mechanistic approach for defining damage) due to creep would be AC (approximately 150 MPa). Such large decreases in tensile strength following only four hours of creep are not observed in the case of homogeneous metals.

Although not shown here, the creep strain followed [4] a t1/n-1 relationship, where n and t correspond to the power-law creep exponent of just the matrix material and time, respectively.. A simple load-transfer formulation, somewhat similar to [10], and based only on a power-law secondary creep behavior of the matrix material, does appear to provide this relationship. It remains to be determined whether such relationships are valid for other systems.

Figure 2 shows the effect of the volume fraction of fibers on the stress-strain response of the composite. As anticipated, the figure shows that the elastic modulus of the composites increased with increasing volume fraction of fibers. Correspondingly, the fracture strains reduced slightly, likely reflecting the fact that residual compressive stresses in the fibers reduce with increasing fiber fraction. The fracture strains also may have been influenced by the greater probability of defects (such as touching fibers) in the higher volume-fraction MMC.

[90]. MMC

Figure 3a illustrates the stress-strain behavior for [90]₈ specimens at RT, 538 C, and 649 C; a few creep curves at 538 C are also included. At RT and 538 C, this lamina system had a three-stage deformation characteristic: Stages I, II, and III. The sharp decreases in stiffness in Stage II are indicative of damage. At 649 C, Stage I was absent, indicating that the residual stresses at that temperature were so small that debonding occurred immediately on loading the MMC. Note also that significant creep can occur within few hours (<4 hours) at low stresses at 538C.

Figure 3b is a plot of the instantaneous width Poisson's ratio (-dew/de_L) versus the longitudinal strain at RT, and it once again illustrates a 3-stage characteristic, similar to Figure 3a. We interpret the large decrease in Poisson's ratio in going from Stage I to Stage II as being due to damage (primarily fiber-matrix debonding), consistent with significant decreases of stiffness observed in Figure 3a. In reference [1] we have also provided microstructural evidence of debonding in Stage II. The solid lines in Figure 3b represent the results of the AGLPLY analysis [8], and the unit cell model [9]. We shall comment on the models later in this paper.

[±45]2. MMC

Figure 4 shows comparisons of the stress-strain response of the [±45]_{2s} MMC at RT and 538C. There was once again a 3-stage stress-strain response, similar to the 90° MMC, with significant stiffness decreases occurring during Stage II. We have metallographically confirmed [4] that the stiffness decrease in Stage II was due to fiber-matrix debonding. It is also notable that for the 45° MMC, the flow stress settled down to values between 450 and 500 MPa at large strains, implying in-plane shear flow strengths between 225 and 250 MPa. These numbers are well below those for the matrix material (shear strength ~ 400 MPa). We interpret the difference to be due to relative fiber-matrix sliding because of a weak interface (friction stress between 60 and 120 MPa [14,15]). If such fiber-matrix sliding is assumed, then we can indeed predict in-plane shear strengths (from 45° data) extremely well both at RT and 538 C.

MICROSTRUCTURE

Figure 5a shows the microstructure of a 0-degree MMC unloaded from a strain of 0.9 percent. This figure illustrates that there were two nucleation sites for slip bands: reaction-zone cracks (rzc), and grain boundaries (gb); the corresponding slip bands are numbered sb1 and sb2, respectively. The reaction-zone cracks formed first, followed by slip band nucleation from those cracks [2]. This type of slip occurred before the knee of the stress-strain curve. Bulk plasticity, involving slip band nucleation from gb appeared to start only after the knee.

TEM observation of the as-received material indicated that it had a reasonably low dislocation density, with dislocations being primarily long, probably being remnants from high temperature processing. Thus, residual stresses from cooling probably were not sufficient to induce large-scale plasticity in the bulk of the matrix. Figure 5b is a TEM micrograph of the matrix of the deformed 0-degree MMC, and it shows large dislocation arrays emanating from a gb. Such a dislocation structure confirms, through TEM, the plasticity that was inferred from optical observation of sb features. Analysis of diffraction patterns and dark field images indicated that a fine coherent ω-phase was present in the β-matrix. Figure 5c, taken at a high magnification, is a dark field image and shows the fine precipitate structure. The streaks in the diffraction pattern are characteristic of such a fine phase. The fine ω-phase particles would be amenable to shearing by dislocations, making the material prone to planar slip. This planar slip

character likely was responsible for making slip bands easily observable optically.

Final fracture of the 0-degree MMC was precipitated by fiber failure. Polishing of specimens unloaded from strains up to 0.9 percent failed to reveal fiber failure. Thus, the mechanism of fracture appeared to be that the fibers failed when their critical strength (or failure strain) was reached, and this was immediately followed by failure of the composite. Molybdenum ribbons, which were used to hold the fibers in place during the foil-fiber-foil consolidation, were observed to contribute to composite failure, judging from the fact that many of the critical fibers breaks occurred where the molybdenum ribbons were located.

For the 90° MMC, the microstructure of deformed samples showed fiber-matrix debonding, reaction-zone cracks, and slip bands. At large strains, the slip bands between neighboring fibers interacted, and cracks nucleated and propagated in those intense slip bands. The details on the microstructure of deformed 90° samples are provided in references [1-4]. Similar deformation processes were observed for the ±45° MMC.

COMPARISONS OF THEORY WITH EXPERIMENTS

In this section we present a preliminary assessment of how different constitutive models performed in predicting the stress-strain behavior of the [0]₈ and [90]₈ MMC. Three constitutive models were considered for comparisons: (i) the METCAN code of Chamis et al.[11-13], (ii) AGLPLY, based on the analysis of Dvorak et al.[8], and (iii) a unit-cell finite element method (FEM) model developed in this program [9].

The METCAN computer code [11-13] uses a composite micro-mechanics approach and laminate theory to model the MMC response. Although the model can account for interface damage in a limited way, by changing the mechanical properties of the interphase region (the region consisting of the reaction-zone and the interfaces), it cannot predict a priori what the interphase property should be. The AGLPLY code is based on the elastic-plastic vanishing fiber diameter model of Dvorak et al.[8]. Here too, the primary drawback is that it cannot account for debonding damage, and this once again poses a problem for off-axis systems.

The unit-cell FEM model [9] considers a 2-D fiber-matrix combination. The rectangular boundaries retain their straight faces during deformation, and generalized plane strain conditions are assumed. Additional input to the model include varying the bond strength. A bond strength of zero provided excellent correlation with RT data [1,2,4], but as will be indicated here, a higher bond strength (~ 85 MPa) appeared to be necessary at 538 C to explain the elevated temperature response of the [90]₈ MMC. In all the models that were selected here, the appropriate physical and mechanical properties of the constituents were used [1,6].

Figures 6a and 6b provide comparisons of the model predictions with experimental data for the [90]₈ MMC at RT and 538 C, respectively. At kT, the Stage I-Stage II transition was predicted reasonably well by the METCAN code. However, note that an assumption in the METCAN code was that the elastic modulus of the interphase region reduce to 2 % of the matrix modulus at the stress corresponding to the Stage I/Stage II transition. This was based on observed debonding phenomenon, and could not be predicted a priori by the code. The AGLPLY model predicted the stress-strain response reasonably well up to a strain of 0.6 percent; however here too, when the code was used, the modulus of the fibers were artificially reduced (to 3 percent of their original value) at the Stage I-Stage II transition. Without this modification, the code would not have provided good stress-strain correlation with experimental data above a strain of 0.2 percent. The unit-cell model provided best stress-strain correlation with the experimental data at RT. No assumptions were necessary regarding when debonding would occur; however, a zero bond strength was assumed in the analysis. The loading-unloading response was predicted extremely well. Figure1b and 3b show that the unit-cell model was also able to satisfactorily predict the Poisson's ratios at RT.

At 538 C, the METCAN code over-predicted the Stage I-Stage II transition of the [90]₈ MMC by approximately 50 MPa whereas the unit-cell model with zero bond strength grossly under-predicted the Stage I-Stage II transition (Figure 6b). In an effort to evaluate the reason

for under-prediction of the unit-cell model, the bond strength was varied. It was found that a bond strength of 85 MPa provided best correlation with the experimental data. A possible explanation is that the debonding phenomenon is actually a cracking process in the reaction-zone/fiber interphase region (along the axis of fibers, see our photographs in [3]), and any ductility increase of the region may increase the stress/strain required for such cracking. This explanation also is consistent with our observations of much less reaction zone cracks at 538 C compared with RT. Note that the reaction-zone essentially consists of titanium silicide and titanium carbide particles of high volume fraction in a Ti-matrix; thus any ductility improvement of the Ti-matrix with temperature could possibly lead to toughening of the interphase region.

DISCUSSION

The important objectives of this work were: to understand the mechanisms of deformation of the Ti-alloy MMC using key experiments; to evaluate the contributions of damage and plasticity to the overall deformation response; and to evaluate models based on observed longitudinal and off-axis strains. The results presented here suggest that a detailed approach is able to provide a coherent picture of the deformation mechanisms.

The effect of elevated temperature was to reduce the thermal residual stress in the MMC, and the flow stress of the matrix. Also, less reaction-zone cracks were observed at 538 C compared with RT, suggesting that the toughness of the reaction-zone region may increase with increasing temperatures. However, besides these differences, the primary mechanisms of inelastic deformation remained essentially similar at both RT and 538 C.

The modeling results showed that it is important to rigorously validate models by measuring both longitudinal strain and strains perpendicular to the loading direction. Thus, whereas the AGLPLY analysis was able to predict the stress-versus-longitudinal strain response, it was not adequate for predicting the transverse strain response. The unit cell model was able to satisfactorily predict the stress-strain and width-strain versus-longitudinal-strain response at both temperatures. However, for the 90-degree system, the model was based on the assumption of a zero bond strength at RT, although push-out tests [14,15] tend to indicate bond strengths of the order of 100 MPa at RT. We are as yet unable to reconcile such differences in the bond strengths, although for the [90]₈ MMC the debonding is perpendicular to the fiber axis, whereas in the push-out tests debonding is parallel to the fiber axis and the effects of fiber asperities become more significant.

CONCLUSIONS

The following conclusions can be drawn based on the work presented here:

- (i) Inelastic deformation of the 0-degree MMC is dominated by plasticity of the matrix at both RT and 538 C. The primary differences are lower residual stress, less reaction zone cracks and diffused slip at 538 C, compared with those at room temperature.
- (ii) An ω-phase was detected in the microstructure, and these fine precipitates likely were responsible for sharp and planar slip bands at RT.
- (iii) The 90-degree MMC shows a 3-stage deformation response, with debonding dominating in Stage II and plasticity in Stage III. Elevated temperature drastically reduced the stress at the onset of Stage II.
- (iv) For the 45° MMC, fiber-matrix sliding in shear appears to be another damage mode, and can explain the low in-plane shear strength of the MMC.
- (v) Comparisons of theoretical predictions with experimental data show that it is important to rigorously validate models, including comparisons with Poisson's ratio data, to establish whether they can adequately predict the mechanical response of the MMC.
- (vi) The microstructural examinations show that the reaction zone and fiber-matrix interface play an important role in influencing the stress-strain behavior of the MMC. From both modeling and material improvement viewpoints, there is therefore an important need to determine the physical and mechanical properties of this interphase region.

ACKNOWLEDGEMENTS

This work was supported by the NASA-Lewis Research Center, under contract NAS3-26053 through the HITEMP program. We thank Dr.B. Lerch of NASA-Lewis for many helpful discussions during this program.

REFERENCES

1. B.S. Majumdar and G.M. Newaz, Phil. Mag., Vol.66, No. 2, pp.187-212 (1992)

2. B.S. Majumdar, G.M. Newaz, and J.R. Ellis, "Evolution of Damage and Plasticity in Titanium Based Fiber Reinforced Composites", accepted in Metall. Trans. (1992)

3. B.S. Majumdar and G.M. Newaz, "Inelastic Deformation of Metal Matrix Composites: Parts I and II", NASA Contractor Reports 100937 and 100938 (1992)

4. B.S. Majumdar and G.M. Newaz, Proceedings of the ASME Winter Annual Meeting, Annaheim, MD Vol.40, ASME, NY, p.77 (1992)

5. B.A. Lerch and J.F. Saltsman, NASA Technical Memorandum 103620 (1991)

6. B.A. Lerch, M.W. Melis, and M. Tong, NASA Technical Memorandum 104470 (1991)

7. W.S. Johnson, S.J. Lubowinski, and A.L. Highsmith, Thermal and Mechanical Behavior of Metal Matrix and Ceramic Matrix Composites, ASTM STP1080, Ed. H.H. Moller and W.S. Johnson, ASTM, Philadelphia, pp.193-218 (1990)

8. G.J. Dvorak and Y.A. Bahei-El-Din, J. Appl. Mech., Vol.49, pp.327-335 (1982)
9. F.W. Brust, B.S. Majumdar, and G.M. Newaz, ASTM 11th. Symposium on Composite Materials (May, 1992), and to be published as Conference Proceedings

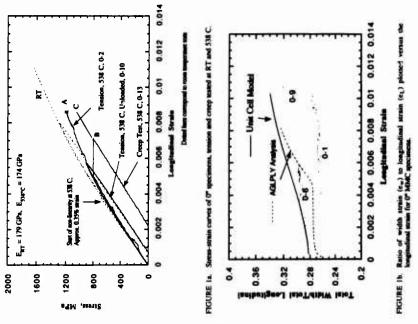
10. S. Goto and M. McLean, Acta Metall. Vol. 39, pp.153-164 (1991)

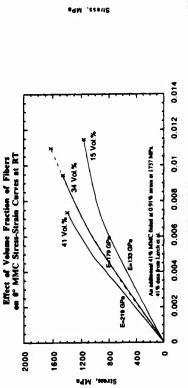
11. C.C. Chamis and D.A. Hopkins, Testing Technology of Metal Matrix Composites, Ed. P.R. Giovanni and N.R. Adsit, ASTM STP 964, pp.177-196 (1988)

12. H.J. Lee, P.L.N. Murthy, and C.C. Chamis, NASA Technical Memorandum 103682 (1991)

13. S.K. Mital and H.J. Lee, Proceedings of the 1991 HITEMP Conference at NASA Lewis, NASA Technical Publication TM10082, pp.35.1-35.9 (1991)
14. M.C. Watson and T.W. Clyne, Acta Metall., Vol.40, No. 1, pp141-148 (1992)

15. P. Kantzos, J. Eldridge, D.A. Koss, and L.J. Ghosn, Proceedings of MRS Spring Meeting, San Fransisco (1992)





90-Degree Ti 15-3/SCS6 Composite

500

400

538 C (1000 F)

300

200 100

650 C (1200 F)

1 = 1

FIGURE 3a. Streas-strain curves for 90° specimena, tension tened at RT, 538 C and 649 C. Creep curves at 538 C also included. Longitudinal Strain

0.012

0.01

0.004 0.006 0.038

0.002

538 C. Creep

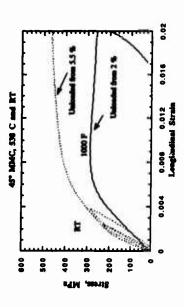


FIGURE 4. Stress-strain response for the [2457]₂₆ MIMC at RT and 538 C.

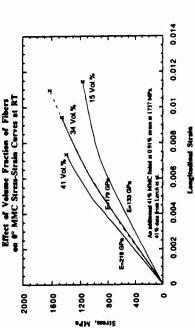


FIGURE 3b. Instantaneous Poisson's ratio (de.,/de.) versus longitudinal strain for 90° MMC.

Longitudinal Strain

0.004

0.002

90.0

[BI(BE(FECORE)

0.01

0.008

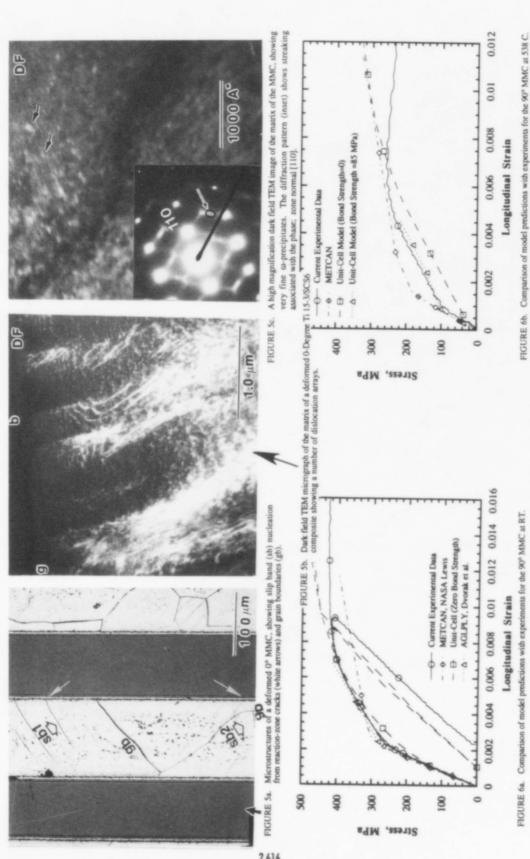
Unit Cell Mode

FIGURE 2. Suras-surais behaviors of 0-degree MIMCs, as influenced by the volume fraction of fibers.

10-Degree TI 15-3/SCS6 MMC.

0.25 0.2 0.15

Poisson's Ratio



2,616

Microstructure/Property Correlation in a Unidirectional SiC (SCS-6) Fiber-Reinforced Ti-24Al-11Nb Composite

Gopal Das

Metcut-Materials Research Group P.O. Box 33511, Wright-Patterson AFB, OH (Now at Pratt and Whitney, P.O. Box 109600 West Palm Beach, FI 33410-9600)

ABSTRACT

The tensile behavior of as-fabricated and vacuum annealed unidirectional SiC (SCS-6) fiber reinforced Ti-24Al-11Nb composites containing molybdenum wire crossweaves was evaluated at room temperature (RT) and 815°C. The stress-strain curves displayed a "two-stage" deformation behavior and the composites exhibited excellent strengths over a broad range of temperature. Specimens deformed at RT revealed a relatively flat fracture with the matrix exhibiting brittle failure. However, extensive fiber pull-out was observed at 815°C with the matrix demonstrating ductile fracture. The Mo/matrix interface failed in a brittle manner at all test temperatures. Tensile deformation of specimens at RT produced a low density of dislocations in the matrix while numerous intersecting slip bands and a high dislocation density were observed at 815°C.

INTRODUCTION

For advanced aerospace structural applications materials with low density, high strength and stiffness along with environmental resistance are required. SCS-6 fiber reinforced TigAl-based ordered titanium aluminide composites possess many of these attributes (1). When these composites are exposed to elevated temperatures, significant microstructural changes occur which may affect the mechanical properties of the composites (2,3).

The purpose of the present study was to determine the tensile behavior of asfabricated and vacuum annealed unidirectional SCS-6/Ti-24Al-11Nb composite deformed at RT and 815°C. The mechanical property of the composite is discussed in terms of the microstructure of the composite including the matrix/Mo interface.

MATERIALS AND PROCEDURES

The composite used was unidirectional SCS-6 fiber reinforced Ti-24Al-11Nb (at.%) matrix with a fiber volume fraction of 0.33 . The matrix consists of two phases: an ordered α_2 phase (DO19) and a beta phase. The SCS-6 fiber has a carbon core on which SiC is deposited by chemical vapor deposition. The composite was fabricated by the foil-fiber-foil method incorporating molybdenum wires to weave fiber mats (4, 5). A cross-section of the 8-ply composite is shown in Figure 1.

Titanium '92 Science and Technology Edited by F.H. Froes and I. Caplan The Minerals, Metals & Materials Society, 1993 Tensile tests were conducted in air at RT and 815°C with a loading rate of 100 MP_M/sec and the direction of loading parallel to the fiber axis. Some of the test specimens were vacuum annealed at 980°C/25 hr to investigate the effect of thermal treatment on tensile properties. Microstructural characterization of the composite was accomplished by optical, scanning electron microscopy (SEM), transmission electron microscopy (TEM), and electron microprobe analyzer (EMPA) methods.

RESULTS AND DISCUSSION

Composite Microstructure

Figure 2 is a typical microstructure of the as-fabricated composite showing the $(\alpha 2 + \text{beta})$ matrix, SCS-6/matrix reaction zone and a beta denuded zone. A separate reaction zone was formed at the SCS-6/Mo interface and an interface was created between the matrix and Mo wire crossweave (Figure 3). Vacuum annealing of composites at 980°C/25 hr has brought significant microstructural changes in the composite as well as growth of various interfaces and matrix grains. In the SCS-6 /matrix reaction zone TiC, (Ti,Nb,Al)5Si3, (Ti,Nb)3(Si,Al) and (Ti,Nb)3AlC have been identified (2, 6, 7). The selected area diffraction (SAD) pattern from the SCS-6/Mo reaction zone consisted of several spotted rings along with other diffracted spots (Figure 4b). The former was consistent with the Mo2C structure and the latter could presumably be due to molybdenum silicides. The SAD pattern from the Mo/matrix interface (Figure 4d) could be matched with the CsCI structure (8). The compositional analysis of the Mo/matrix interface by EMPA showed that the interface had a composition close to Ti₂(Mo,Nb)Al. Both carbon core and fiber coating showed the evidence of graphitization (Figure 5). In the carbon core bubbles were found (Figure 5a) and fine SiC precipitates were observed in the fiber outer coating (5b). Figure 6 shows the presence of an orthorhombic phase in the matrix similar to the observation made by Baneriee et al (9). A detailed description of the microstructure of SCS-6/Ti-24Al-11Nb composite containing Mo wire cross weave will be available elsewhere (7).

Tensile Behavior

Stress-strain curves of as-fabricated and vacuum annealed composites tested at RT and 815°C exhibited a two-stage deformation behavior. A typical example for vacuum annealed composite tested at RT is shown in Figure 7. An initial linear stage (Stage I) where both fibers and matrix deform elastically transitions to a non-linear stage (Stage II) which depicts the onset of plastic deformation of the matrix while the fibers continue to deform elastically. The stress at which the transition takes place is referred to as the yield stress and the corresponding strain as the yield strain. Table I presents tensile properties of all composites tested at RT and 815°C.

Table I. Tensile Properties of Ti-24Al-11Nb/SCS-6 Composite

Heat Treatment	Temp. (°C)	Yield Stress	Yield Strain	Ultimate Stress	Fracture Modulus Strain (GPa/Msi)		
		MPa/Ksi	(%)	MPa/Ksi	(%)	Stage I	Stage II
As-fabricated	RT	513/74	.30	1114/162	.74	171/25	136/20
As-fabricated	815	417/61	.31	920/134	.81	135/20	100/14
Annealed	RT	460/67	.22	1142/166	.73	209/30	133/19
Annealed	815	380/55	.23	968/137	.72	162/23	123/18

The yield stress and ultimate strength of as-fabricated and vacuum annealed composites deformed in tension at RT were higher than those for composites deformed at 815°C. This may be explained in terms of reduced yield stress and ultimate strength of the matrix at elevated temperatures. The composites exhibited good strengths over a broad temperature range, with ultimate strengths approaching 70-76% of the rule-of-mixture calculations (10). The fracture strain of composites varied from 0.72 to 0.81 which is lower than the fracture strain of the SCS-6 fibers of 0.91% (11).

The elastic moduli for Stage I for all composites varied from 78-108% of the values predicted by the rule of mixtures (ROM)¹⁰. The elastic moduli of the composites tested at RT were higher than those for composites tested at 815°C. For vacuum annealed composites tested at RT and 815°C, the elastic moduli were 20-24% higher that those of as-fabricated composites tested under similar conditions. Vacuum annealing of composites has led to microstructural changes in the fiber, matrix and reaction zones as well as growth of reaction zones, beta denuded zone and the Mo/matrix interface. All or some of these may contribute to the increased modulus of the vacuum annealed composite compared to as-fabricated condition. Since the elastic modulus of unidirectional composites is primarily fiber controlled, it is believed that changes in the fiber would primarily contribute to the increased modulus. The Stage II moduli for all composites tested at 815°C were lower than those determined at RT.

Deformation and Fracture

A low dislocation density was developed in the α_2 phase of composites deformed at RT (Figure 8). The majority of these dislocations were determined to be of the a/3 <1120> type. A similar observation has been reported for TigAl-based intermetallics (12,13). In contrast, a rather high density of dislocations was developed in the beta grains of the matrix. In addition, deformation twins were observed in the beta grains. Deformation of composites at 815°C led to the development of intersecting slip bands in the matrix, indicating that more than one slip system is active at 815°C (Figure 9). No dislocations were observed in the reaction zone.

The fracture surface at RT was relatively flat with the matrix displaying brittle failure (Figure 10). On the other hand, extensive fiber pull-out was observed at 815°C with the matrix exhibiting a ductile failure (Figure 11). The Mo wire crossweave was always present on the fracture surfaces of all composites. The Mo/matrix interface displayed a brittle failure at all test temperatures and cracks were observed at these interfaces.

Cracks were observed both in the matrix and the fibers as shown in longitudinal sections of the failed composites (Figure 12). At RT the matrix cracks were found at locations away from the overload region while cracks in the fiber were confined to the overload region. The majority of the matrix cracks appeared to have originated from the reaction zone. In addition, slip lines were observed in beta grains near the overload region. The matrix appeared to have stretched near the overload region of the vacuum annealed composite tested at 815°C as shown in Figure 13. Fewer cracks were observed in the matrix close to the overload region while cracks in fibers were observed at locations away from the overload region. Slip lines were readily observed in both α_2 and beta grains of the matrix. From these observations it may be concluded that the matrix contribution to the strain-to-failure of the composite is primarily in the form of plastic deformation at elevated temperature and mostly in the form of crack formation at RT.

REFERENCES

1. J.R. Stephens, <u>High Temperature Metal Matrix Composites for Future Aerospace Systems</u>, NASA TM-100212, 1987.

2. G. Das, presented at the TMS Annual Meeting, New Orleans, LA, Feb 1991

(unpublished)

3. G. Das and S.M. Russ, presented at the IMS International Metallography Contest,

Cincinnati, OH July, 1990

 T. Nicholas and S. M. Russ, presented at the ASM International Conference on High Temperature Aluminides and Intermetallics, San Diego, CA, Sept 1991 (unpublished).

5. M. L. Gambone, Fatigue and Fracture of Titanium Aluminides, (WRDC-TR-89-

4145, vol. 2, 1990).

- 6. S.F. Baumann, P.K. Brindley, and S.D. Smith, "Reaction Zone Microstructure in a Ti3Al + Nb/SiC Composite", Met. Trans. A, 21A, (1990) pp.1559-1569.
- 7. G. Das, "Microstructural Characterization of SiC Fiber-Reinforced Ti-24Al-11Nb Composite Containing Molybdenum Wire Crossweave", To be published in Met. Trans.

8. H. Bohm and K. Lohberg, Z. Metallk., 49, (1958) p.173.

9. D. Banerjee, A. K. Gogia, T. K. Nandy and V. A. Joshi, Acta Metall., <u>36</u>, (1988) p.871.

10. A. Kelly and G. J. Davis, Metallurgical Reviews, 10, (1965) p.1.

11. P. Soumelidis, J.M. Quenisset, R. Nasalin, and N.S. Stoloff, J. Mat. Sci. 21,

(1986) p. 895.

12. J. C. Williams and M. J. Blackburn, in <u>Ordered Alloys</u>, edited by B. H. Kear, C. T. Sims, N. S. Stoloff and J. H. Westbrook (Claitor's Publishing Division, Baton Rouge 1970) pp. 425-45.

13. S. M. L. Sastry and H. A. Lipsitt, in <u>Titanium '80. Science and Technology</u>, edited by H. Kimura and O. Izumi (TMS-AIME, Warrendale, PA 1980) pp 1231-43.

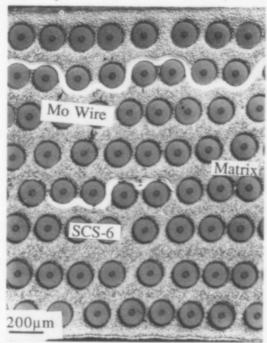


Figure 1- Cross-section of unidirectional SCS-6/Ti-24Al-11Nb composite

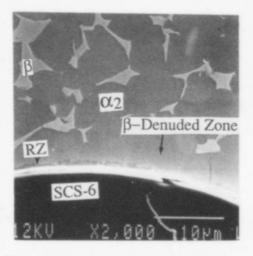


Figure 2- Microstructure of as-fabricated composite showing a2+beta matrix, SCS-6/matrix reaction zone and beta denuded zone

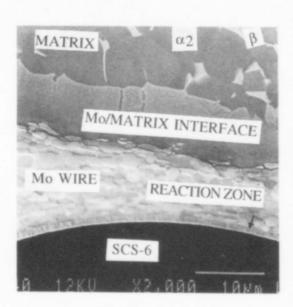


Figure 3- SCS-6/Mo reaction zone and Mo/matrix interface in as-fabricated composite

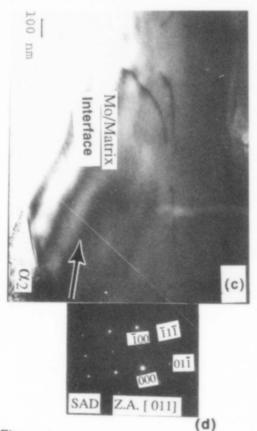


Figure 4

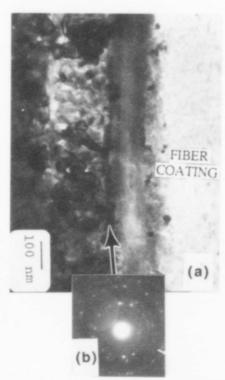


Figure 4- (a) Microstructure of SCS-6/Mo reaction zone, (b) SAD of (a), (c) Mo/matrix interface, and (d) SAD of (c) in vacuum annealed composite.

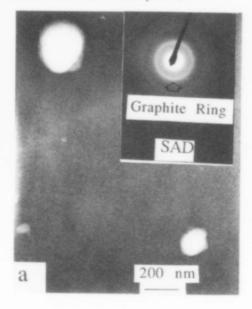
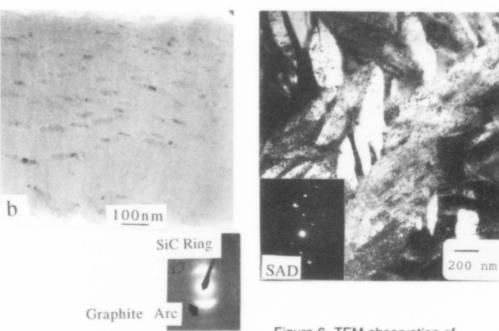


Figure 5- (a) Amorphous-to-crystalline transformation of carbon core of SCS-6 fiber in vacuum annealed composite as revealed by SAD.



SAD

Figure 5- (b) SiC precipitates in fiber coating. Diffraction arcs due to graphite in the SAD suggest that the amorphous carbon coating has undergone crystalline transformation

Figure 6- TEM observation of orthorhombic phase in the matrix of vacuum annealed composite. The SAD pattern showing both α_2 and orthorhombic phase. [11 $\overline{2}$ 0] α_2 //[100]O

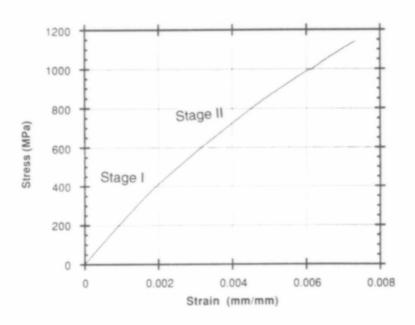


Figure 7- A typical stress-strain curve of vacuum annealed composite deformed in tension at RT showing a "two-stage" deformation behavior

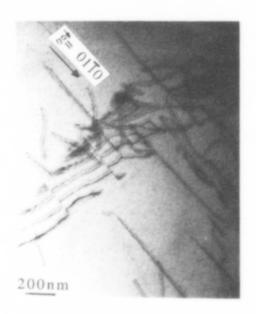


Figure 8- Dislocations in the matrix of vacuum annealed composite deformed in tension at RT. Foil plane (2110)



Figure 9- Intersecting slip bands in α2 phase of the vacuum annealed composite deformed in tension at 815°C

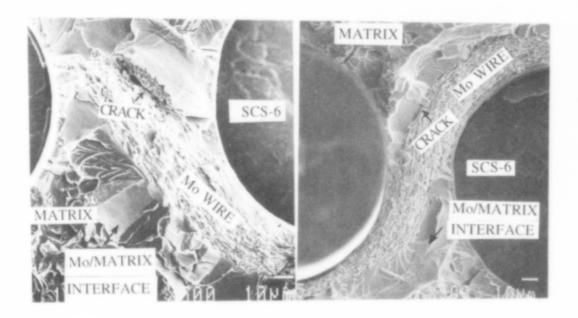


Figure 10- Fracture surface of vacuum at RT

Figure 11- Fracture surface of vacuum annealed composite deformed in tension annealed composite deformed in tension at 815°C



Figure 12- Longitudinal section of fractured vacuum annealed composite in tension at RT showing cracks in matrix and fiber



Figure 13- Longitudinal section of fractured vacuum annealed composite in tension at 815°C showing severe matrix deformation at the overload region

MICROSTRUCTURE OF UNIDIRECTIONAL SIC/Ti-24AI-11Nb COMPOSITE DEFORMED IN TENSION, FATIGUE, AND CREEP

Gopal Das

Pratt & Whitney, P.O. Box 109600 West Palm Beach, Fl 33410-9600

Stephan M. Russ Materials Directorate, WL/MLLN Wright-Patterson AFB, OH 45433-0511

Mohammad Khobaib University of Dayton Research Institute 300 College Park, Dayton, OH 45469-0128

ABSTRACT

The deformation structure of a unidirectional SiC (SCS-6)/Ti-24Al-11Nb (at%) composite tested in tension, fatigue, and creep was evaluated by transmission electron microscopy (TEM). Room temperature (RT) tensile deformation produced a low dislocation density in the matrix while deformation at 815°C yielded slip bands and a high dislocation density. Fewer dislocations were observed in the matrix adjacent to the reaction zone of composites deformed at RT and 815°C. Isothermal fatigue at 650°C revealed slip bands in the matrix and dislocation pile-ups against the reaction zone. Small cracks were observed at triple points and along grain boundaries inside the reaction zone. Creep deformation at 650°, 760°, and 815°C resulted in the formation of slip bands in the matrix and dislocation pile-ups against the reaction zone. Cracks were observed at the intersecting slip bands at 760°C and above. Voids were found in the reaction zone as well as in the matrix. In addition, voids were observed in the outer fiber coating of composites tested at 815°C in air. At 815°C, fine precipitates of unknown character were observed in the matrix adjacent to the reaction zone.

INTRODUCTION

There is an increasing demand for low density materials possessing high strength and stiffness coupled with good environmental resistance at elevated temperatures for aerospace structural applications. SiC (SCS-6) fiber-reinforced α_2 -based titanium aluminide composites are undergoing critical evaluations of various mechanical properties such as tensile, fatigue, and creep (1-6). In these investigations the microstructural characterization has primarily been confined to optical and scanning electron microscopy (SEM) levels.

The purpose of this paper is to summarize microstructural details of SCS-6/Ti-24Al-11Nb composite deformed in tension, isothermal fatigue, and creep as revealed by TEM. It is anticipated that this investigation in conjunction with optical and SEM observations will lead to a better understanding of the deformation behavior and the complex failure mechanisms

operating under the various loading modes for these composites.

MATERIAL AND PROCEDURES

The composite consists of Ti-24Al-11Nb (at%) matrix reinforced with continuous, unidirectional SCS-6 fibers with an average volume fraction of 0.33. The matrix is composed of two phases: an ordered hexagonal 02 phase (DO19) and a beta phase. The 142µm diameter SCS-6 fiber is produced by chemical vapor deposition onto a 37µm carbon core. It contains a double pass carbon coating (nominally 4 µm thick) consisting primarily of amorphous carbon with a small amount of silicon (7).

Science and Technology
Edited by F.H. Froes and I. Caplan
The Minerals, Metals & Materials Society, 1993

Composite plates, ~153 mm x 165 mm x 2 mm (eight ply), produced by the foil/fiber/foil method were used in mechanical behavior studies by Nicholas, Russ, Gambone, and Khobaib (1, 4-6). A molybdenum crossweave material was used to weave the fiber mats. A cross-section of the composite is shown in Figure 1. Mechanical tests were conducted with the loading axis parallel to the fiber direction. Specifics regarding machining and specimen geometries used for the tension, fatigue and creep studies were reported previously (5-6, 8-9). Selected tensile specimens were individually wrapped in tantalum foils, encapsulated in quartz tubes under a vacuum of ~ 10^{-5} torr, and exposed to a 980°C/25 hr to investigate the effect of thermal treatment on the tensile properties and resulting microstructure.

Tensile and fatigue tests were performed in air on an MTS servo-hydraulic test station equipped with radiant energy quartz lamps. Tensile tests were conducted at room temperature and 815°C (8-9). Isothermal fatigue tests were performed at 650°C under load control with stress levels ranged from 500 to 900 MPa, and a stress ratio (R) of 0.1 utilizing a sinusoidal wave at 3 Hz (1, 5). Creep tests were conducted at 650°C, 760°C, and 815°C at various stress

levels in laboratory air and vacuum (6).

TEM foils were prepared from the transverse sections of failed composites using ionmilling (10). TEM studies were conducted in a JEOL 2000FX transmission electron microscope equipped with a Tracor Northern-5550 EDS system and operated at 200 keV.

RESULTS AND DISCUSSION

Deformation Microstructure 1) Tensile

Results of tension tests on both as-received and heat treated unidirectional composites conducted at RT and 815°C have been reported by Das (8-9). The composite exhibited excellent strength over a broad temperature range, with ultimate strengths approaching the rule-of-mixture calculations. The strain-to-failure ranged from 0.72 to 0.81% for all tests.

In the as-received composite the matrix microstructure was characterized by α_2 and beta phases. However, heat treatment at 980°C/25 hr led to the formation of an orthorhombic phase in the matrix (8-9). A similar observation was previously made by Banerjee, et. al (11). The dislocation arrangement and distribution in the matrix were similar for both as-received and heat treated composites deformed at RT. A typical example is shown in Figure 2 for the heat treated composite. In general, a low density of long dislocation lines with few tangles was observed in the α_2 phase away from the reaction zone (Figure 2a). An application of the $g \cdot b = 0$ invisibility criterion for dislocations (where b is the Burgers vector and g is a reciprocal lattice vector normal to the reflecting planes) indicated that the Burgers vector of the majority of these dislocations was of the a/3 < 1120 > type (Figure 2b). Deformation at RT involved both basal and prism planes with dislocations predominantly arranged in a screw orientation. Similar observations have been reported for Ti₃Al based intermetallics (12-13). A rather high density of dislocations was observed in the beta grains which was expected as the beta phase is ductile at RT. In addition, deformation twins were observed in beta grains. Fewer dislocations were found in the α_2 phase adjacent to the reaction zone (Figure 3). The majority of these dislocations were found to lie on $\{10\overline{10}\}$ planes and were in a screw orientation having the $a/3 < 11\overline{20} >$ Burgers vector.

A distinctly different dislocation structure was developed in the matrix for as-received and heat treated composites deformed at 815°C. The dislocations were arranged in intense slip bands intersecting with each other, indicating that more than one slip system was active at 815°C (Figure 4). The dislocation density in the α_2 matrix adjacent to the reaction zone was

rather low. Also, no dislocations were observed in the reaction zone.

2) Isothermal Fatigue

Results of isothermal fatigue tests on as-received composite at 650°C study were presented elsewhere (1). Fractography studies indicated that cracks in the matrix initiated at edges of the specimens and propagated further into the specimen leading to failure. The matrix exhibited brittle fracture in the crack growth region and ductile dimpling in the overload region accompanied by fiber pull-out (1). It appeared that the matrix was embrittled by the test environment which may have led to crack initiation at edge locations.

Thin foils of the specimen failed after 18,777 cycles and a cumulative strain of 0.60 % at a maximum stress of 850 MPa were examined by TEM. Dislocations were arranged in slip

bands in α_2 phase away from the reaction zone, similar to the observation in tension at 815°C. However, the dislocation structure developed in the matrix adjacent to the reaction zone was significantly different. A high density of dislocations was found to pile-up against the reaction zone as shown in Figure 5. Both planar slip and tangled dislocations were observed together with dislocation loops. Fine voids were present in the reaction zone which was free of dislocations (Figure 6). Additionally, small cracks were observed at triple points as well as along the grain boundaries of the reaction zone constituents as shown in Figure 7. Apparently, the cracks were developed as a result of stress concentration due to dislocation pile-ups against the reaction zone by a mechanism proposed by Stroh (14). A small volume fraction of orthorhombic phase was also observed in the matrix resulting from extended high temperature exposure under load (Figure 8).

(3) Creep

The creep behavior of as-received SCS-6/Ti-24Al-11Nb under a constant stress of 345 MPa at temperatures of 650°C, 760°C, and 815°C in air was presented elsewhere (6). Fractographic analysis of the failed specimen revealed that in most cases cracks occurred at multiple sites. These cracks apparently initiated at surface flaws resulting from either a cut fiber, embrittled matrix, molybdenum crossweave wire exposed at the edge, or some other surface defects. However, during the creep process the linkage of cracks resulted in a single dominant crack which eventually led to the final failure of the specimen. It was concluded that stress-assisted environmental degradation played an important role in the failure of these

composites (6).

Slip bands in the matrix and dislocation pile-ups against the reaction zone were observed for specimens deformed in creep at all temperatures. However, with increasing deformation temperature the planarity of slip in the matrix was found to decrease, and the formation of dislocation tangles increased along with the formation of jogs and loops. An increased presence of dislocations with non-basal slip vectors was also noted. Cracks were observed at the intersection of slip bands at 760°C and above as shown in Figure 9. The formation of cracks is believed to be the result of stress-concentrations at the slip band intersections and can be explained by a mechanism proposed by Cottrell (15). At all test temperatures the orthorhombic phase was observed in the matrix, similar to that reported for the isothermal fatigue specimen. Creep induced void formation in the matrix was observed only in the specimen tested at 815°C as shown in Figure 10. Also evidenced in the micrograph are the dislocation pile-ups against the reaction zone. In addition, precipitates of unidentified nature were observed at the α_2 grain boundaries of the matrix in the vicinity of the reaction zone as shown in Figure 11. The EDS analysis revealed the presence of Ti, Al, and Nb and an absence of silicon in these precipitates. This leads us to believe that the precipitate is a complex carbide of Ti-Al-Nb as the detection of carbon is beyond the limits of the detector used in the spectrometer. Since these precipitates are only found near the reaction zone, it can be speculated that carbon from the outer fiber coating, under the influence of temperature and stress, diffuses into the matrix over time resulting in the formation of these precipitates. Voids were also observed in the reaction zone at all temperatures as shown in Figure 12. However, no dislocations were found in the reaction zone. At 815°C, voids and fine precipitates were also observed in the outer fiber coating, Figure 13. A similar observation of voids has previously been reported by Das and Vahldiek (16). They speculated that oxygen may be diffusing to the region of the outer fiber coating and reacting with the carbon to form CO and/or CO2, thus creating these voids. Fine precipitates in the outer fiber coating have previously been identified as SiC. Moreover, the outer amorphous carbon coating was determined to have undergone graphitization. Such graphitization of the amorphous carbon coating and SiC precipitate formation within the coating of SCS-6 fiber have been reported (17).

CONCLUSIONS

It was noted that for the composites tested in tension at RT, the deformation structure of the matrix away from the reaction zone was characterized by a low dislocation density with few dislocation tangles, while that of the matrix adjacent to the reaction zone was characterized by an even lower dislocation density. On the other hand, deformation in tension at elevated temperatures led to the formation of intersecting slip bands in the matrix suggesting that more than one slip system participated in the deformation process. However, few dislocations were observed in the region of the matrix adjacent to the reaction zone. This is in contradiction to the

model on microscopic deformation and fracture mechanisms of ductile matrix/elastic fiber

composites proposed by Pertsev et. al (18).

The dislocation substructures in the matrix away from the reaction zone in composites deformed in tension, isothermal fatigue and creep at elevated temperature were similar in that dislocations were predominantly arranged in intense slip bands. However, in contrast to the elevated temperature tension tests, a high density of dislocations was observed to pile-up in the matrix around the reaction zone in both isothermal fatigue and creep samples. Apparently the reaction zone was serving as a barrier to dislocation motion. The formation of dislocation pileups in the matrix around the reaction zone is in accordance with the models for a coherent fiber/matrix interface proposed by Stohr and Valle (19) and Goto and McLean (20). In the case of isothermal fatigue, very small cracks were observed in the reaction zone. This may be attributed to the stress concentration due to dislocation pile-ups against the reaction zone. In contrast, no cracks were observed in the reaction zone of composites deformed in creep, but voids were identified at the triple points as well as along grain boundaries, a characteristic of the creep deformation. This may also suggest that load shedding from the matrix to the reaction zone has indeed taken place. Cracks were also observed at the intersecting slip bands in the matrix of crept samples. The roles of internal cracks, as observed in the reaction zone of the isothermal fatigue samples and at the intersecting slip bands of creep samples, and other microstructural features to the failure of these composites cannot be fully established for the following reason. The test specimens used for mechanical property evaluations in this study had two edges where fiber, matrix, reaction zone, and molybdenum crossweave were directly exposed to the test environment. It has been established that cracks, originating from areas acting as stress raisers at the edges, led to failure of these composites (5-6). Thus, unless these stress raisers are removed, the deformation occurring in the various composite constituents cannot adequately explain the overall failure process of the composite, but merely highlights potential problem areas and areas for eventual engineering improvements in these composites. Also, it has been established that environment played a significant role in the failure process, especially in fatigue and creep where the composite was subjected to loads at temperature for extended periods of time (5-6). Although testing in a vacuum can eliminate the environmental effects, removal of edge effects is more difficult. In spite of these difficulties, the deformation microstructure of various constituents of the composites as determined by the present TEM studies offers a better understanding of the deformation behavior and the complex failure mechanisms operating under the various loading modes for these composites.

REFERENCES

1. T. Nicholas and S. M. Russ, "Elevated Temperature Fatigue Behavior of SCS-6/Ti-24Al-11Nb," <u>Journal of Materials Science and Engineering: Proceedings on High Temperature Aluminides and Intermetallics</u>, (Presented at the ASM International Conference on High Temperature Aluminides and Intermetallics, San Diego, CA, Sept 1991), in press.

2. P. A. Bartolotta and P. K. Brindley, High Temperature Fatigue Behavior of a SiC/Ti-24Al-11Nb Composite (NASA TM 103157, Prepared for the 10th Symposium on Composite

Materials: Testing and Design, ASTM, San Francisco, CA April 1990).

3. P. K. Brindley and P. A. Bartolotta, <u>Investigation of a SiC/Ti-24Al-11Nb Composite</u> (NASA TM 100956, Prepared for the 117th TMS-AIME Annual Meeting, Phoenix, AZ, Jan 1988).

4. M. L. Gambone, Fatigue and Fracture of Titanium Aluminides, (WRDC-TR-89-4145,

vol. 2, 1990).

5. S. M. Russ and T. Nicholas, "Thermal and Mechanical Fatigue of Titanium Aluminide Metal Matrix Composites," <u>Titanium Aluminide Composites</u> (WL-TR-91-4020, ed. P. R. Smith, S. J. Balsone, and T. Nicholas, Feb 1991) pp. 431-449.

6. M. Khobaib, "Creep Behavior of SCS-6/Ti-24Al-11Nb Composite," <u>Titanium Aluminide Composites</u> (WL-TR-91-4020, ed. P. R. Snith, S. J. Balsone, and T. Nicholas,

Feb 1991) pp. 450-466.

7. G. Das, "Microstructural Characterization of Ceramic Reinforcements for Composites," <u>Titanium Aluminide Composites</u> (WL-TR-91-4020, ed. P. R. Smith, S. J. Balsone, and T. Nicholas, Feb 1991) pp. 20-58.

3. G. Das, "Tensile Behavior of SCS-6/Ti-24Al-11Nb Composite" (Presented at the TMS

Annual Meeting, New Orleans, LA, Feb 1991)

G. Das, "Microstructure / Property Correlation in a Unidirectional SiC (SCS-6) Fiber-

Reinforced Ti-24Al-11Nb Composite," this conference.

G. Das, E. Harper, R. Omler and R. Lewis, "Metallography of Titanium Based Metal-Matrix Composites with Silicon Carbide Fibers as Reinforcement," Practical Metallography, vol 26, 1989, pp. 443-454.

D. Banerjee, A. K. Gogia, T. K. Nandy and V. A. Joshi, "A New Ordered

Orthorhombic Phase in Ti3Al-Nb Alloys," Acta Metall., vol 36 (1988) p. 871.

J. C. Williams and M. J. Blackburn, "The Structure, Mechanical Properties and Deformation Behavior of Ti-Al and Ti-Al-X Alloys," Ordered Alloys, ed. B. H. Kear, C. T. Sims, N. S. Stoloff and J. H. Westbrook (Baton Rouge. LA: Claitor's Publishing Division, 1970) pp. 425-445.

S. M. L. Sastry and H. A. Lipsitt, "Plastic Deformation of TiAl and Ti3Al," Titanium '80, Science and Technology, vol. 2, ed. H. Kimura and O. Izumi (TMS-AIME, Warrendale,

PA, 1980) pp 1231-1243.

A. N. Stroh, Advan. Phys., 6:418 (1957)

A. H. Cottrell, Trans. Amer. Inst. Mech. Engrs., April 1958, p. 192. 15.

G. Das and F. W. Vahldiek, "Effects of Elevated Temperature Oxidation on the 16. Reaction Zone of a SiC Fiber-Reinforced Ti3Al-11Nb Composite," Interfaces in Metal-Ceramic Composites, ed. R. Y. Lin, R.J. Arsenault, G. P. Martins, and S.G. Fishman (Warrendale, PA: TMS, 1990) pp. 59-73.

G. Das, "A Study of Fiber-Matrix Reaction Zone Growth Kinetics in SiC Reinforced

IMI829 by TEM," Met. Trans. A, vol 21A, June 1990, pp. 1571-1578.
N. A. Pertsev, N. D. Priemsky, A. E. Romanov and L. I. Vladimirov, "Microscopic Mechanisms of Fiber Composite Deformation and Fracture," Fracture of Composite Materials, ed. G. C. Sih and V. P. Tamuzs (Hingham, MA, Martinus Nijhoff Publishers, 1982) pp. 149-159.

19.

 J. F. Stohr and R. Valle, <u>Phil. Mag.</u>, vol 1 (1975) p. 43.
 S. Goto and M. McLean, "Role of Interfaces in Creep of Fibre-Reinforced Metal-20. Matrix Composites - I: Continuous Fibres," Acta Metall. Mater, vol. 39, No. 2 (1991) pp. 153-164.

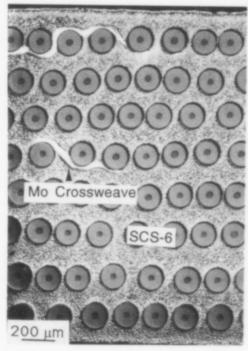


Figure 1. A typical cross-section of unidirectional, 8-ply, SCS-6/Ti-24Al-11Nb composite showing Mo wire cross-weave.

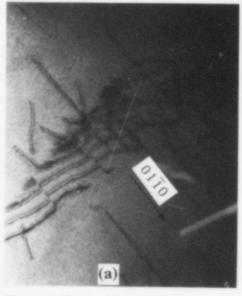


Figure 2. Dislocations in the matrix away from the reaction zone of heat treated specimen tested in tension at RT: a) dislocations are in contrast for g = 0110and b) out of contrast for g = 0002. Foil plane $(2\overline{110})$.

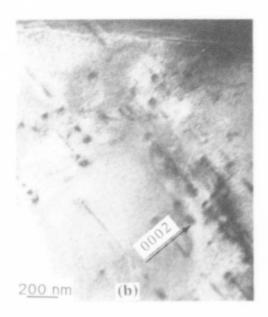


Figure 2 (b)

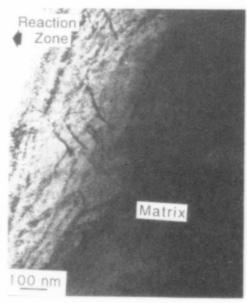


Figure 3. Dislocation structure in the matrix adjacent to the reaction zone of heat treated specimen tested in tensile at RT.

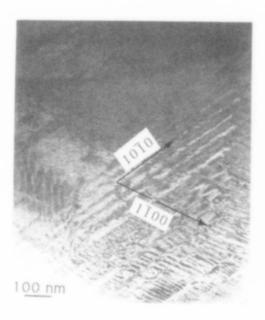


Figure 4. Intersecting $\{1010\}$ slip bands in α_2 matrix of composite tested in tension at 815° C. Foil orientation - basal.

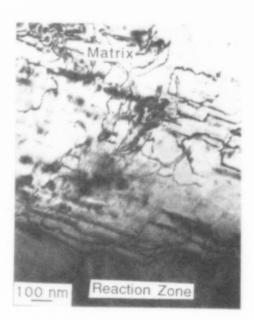


Figure 5. Dislocation pile-up against the reaction zone in fatigue specimen tested in air at 650°C/ 850 MPa to a cumulative strain of 0.6%.

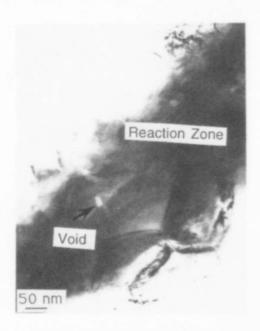


Figure 6. Observation of voids in the reaction zone of the fatigue specimen.

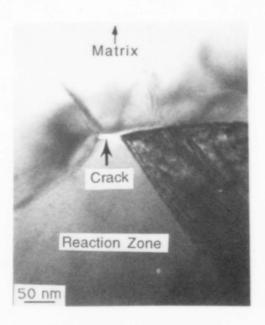


Figure 7. Crack formation at the triple point of reaction zone products of the fatigue specimen tested in air at 650°C/850 MPa to a cumulative strain of 0.6%.



Figure 8. Observation of stress-induced orthorhombic phase in the matrix of the isothermal fatigue specimen tested at 650°C.

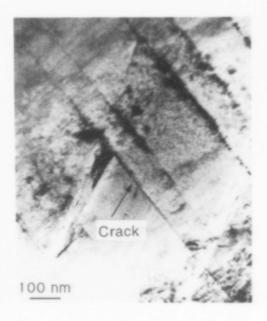


Figure 9. Observation of a crack at the intersection of slip bands in the α2 grain away from the reaction zone of the creep sample tested in vacuum at 815°C/345 MPa.

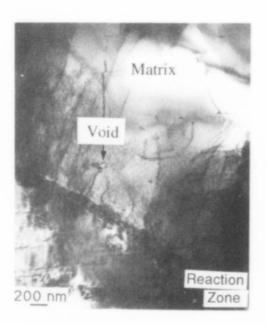


Figure 10. Dislocations in the matrix adjacent to the reaction zone of the creep sample tested in air at 815°C/345 MPa. Voids are observed in the matrix.

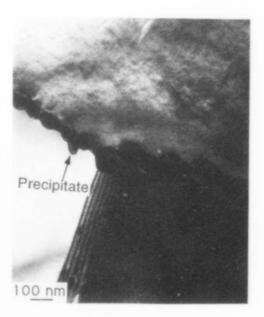


Figure 11. Precipitates at the α2 grain boundaries adjacent to the reaction zone of the creep specimen tested in air at 815°C/345 MPa

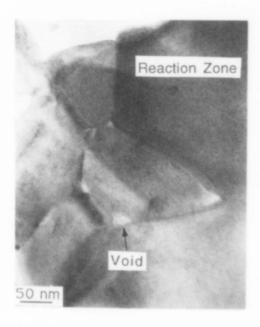


Figure 12. Voids at triple points and along grain boundaries of reaction zone products in the creep specimen tested in air at 815°C/345 MPa.

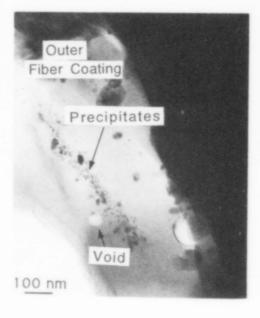


Figure 13. Voids and SiC precipitates in the outer coating of the SCS-6 fiber for the composite tested in creep in air at 815°C/345 MPa.

SIC FIBRE / TI-BASED COMPOSITES:

PROCESSING, MICROSTRUCTURE AND INTERFACE PROPERTIES

Z X Guo and B. Derby,

Oxford Centre for Advanced Materials and Composites/ Department of Materials, University of Oxford, Oxford OX1 3PH, UK.

Abstract

The present paper investigates continuous fibre-reinforced composites using TiB₂/C coated SiC monofilaments as the reinforcement, and Ti6Al4V as the matrix. A diffusion bonding technique is employed to fabricate the composites by consolidating fibre-mat and matrix foil layups. The process is analysed through the variation of the quarter contact angle between the fibre and the matrix. Effects of fabrication conditions on the microstructure of the resulting composites, including the matrix morphology and fibre/matrix interfaces, are examined. Reactions at the fibre/matrix interfaces have been found to produce TiB needles, thick TiC layer, and a mixture of TiC/Ti₅Si₃ particles, depending on the stages of the reaction involved. Interfacial bonding strength has been evaluated and correlated with the microstructure of the fabricated materials. The strength varies strongly with both bonding temperature and holding time. The results are discussed for further optimisation of processing conditions and interface properties.

Introduction

Ti-based/SiC composites are strong contenders for future air-frame and engine components. Various types of Ti alloys have been investigated as a potential matrix, e.g. $(\alpha+\beta)$ alloys [1,2], metastable β alloys [3,4], and Ti aluminides [5,6]. The fibres available for reinforcing titanium alloys are the SCS-6 SiC from Textron and the Sigma SiC from B.P. A number of papers have been devoted to the interface problems or mechanical properties of the SCS-6 SiC fibre reinforced Ti matrices, e.g. refs.[1-3,7-11]. However, the fabrication process has not yet been examined in detail. There is also a lack of systematic investigation on the processing, microstructure, and property relationships of the materials, particularly on the composite system involving the TiB₂/C coated SiC fibres.

The fabrication of Ti-based composites is confined to solid-state diffusion bonding routes, due to the restrictions of the extreme reactivity of titanium and the stability of the reinforcement at high temperature. These include Hot-Pressing, HIPing (Hot Isostatic Pressing), and VPS(Vacuum Plasma Spraying) or other types of matrix deposition techniques combined with the former two processes [12-14]. The consolidation is associated with the diffusion, creep, and (super)plastic flow of the matrix. The establishment of the matrix/fibre interface bonding involves charge transport, inter-diffusion, and mass transport [15]. Chemical reactions often take place concurrently between the matrix and the reinforcement, leading to the formation of new phases. Extensive interfacial reactions give rise to: 1) thick brittle reaction products, acting as a circumferential flaw on the fibre; 2) roughening the fibre surfaces, degrading the fibre intrinsic strength by forming easy stress concentrations; and 3) enhancing interfacial cracking and debonding [11]. It is, therefore, important to understand the relationships of processing,

Titanium '92 Science and Technology Edited by F.H. Froes and I. Caplan The Minerals, Metals & Materials Society, 1993 microstructure, and interface properties, for the design of adequate composite processing conditions. The model Ti6Al4V/SiC composite system is employed here for such investigation.

Materials and Methods

The composites were consolidated by diffusion bonding in a vacuum hot press. The procedure is schematically illustrated in Fig.1. The matrix foil is $85 \,\mu m$ in thickness; and the SiC fibre is $100 \,\mu m$ in diameter (supplied by B. P. Composites Ltd with a TiB₂ and C double-layer protective coating; the diameter of the fibre is used as a scale marker in following micrographs). First, the foils were ultrasonically cleaned. The fibres were wound into a mat with a spacing of $400 \, \text{or} \, 200 \, \mu m$, respectively, and bound using a fugitive binder. These mats were

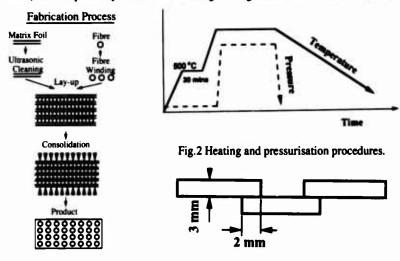


Fig. 1 Schematic of the composite fabrication process.

Fig. 3. Geometry of lap-shear specimens.

unidirectionally stacked between the cleaned foils. Such a foil/fibre assembly was then subjected to hot-pressing in vacuum at 870 °C and 970 °C under pressures of 10 - 40 MPa. The pressurisation procedure is illustrated in Fig.2, a short period dwell at 500 °C under a small pressure was carried out to drive off the fibre binder. The resulting composites have a fibre volume fraction of 18.8 % and 31.6 %, respectively for the two fibre-spacings used. Selected samples were heat-treated at temperature in a vacuum of 10-5 - 10-6 Torr for various periods of time, to evaluate the stability of the coating.

Specimens for optical and SEM examinations were lapped flat using liquid diamond slurry, down to $0.25\,\mu m$, with a light final polish to remove fine scratches. The cross-section used is perpendicular to the fibre axis direction. TEM samples were dimpled and Ion-milled to

A lap-shear method was employed to evaluate the interface strength between the fibre and the matrix after bonding at 30 MPa for 30 minutes. The specimens were produced by bonding one layer of fibre-mat between two Ti6Al4V plates, and the dimensions are illustrated in Fig.3. A double-lap specimen geometry was used to minimise bending effects during testing, as specimen bending may bias the shear results. The fibre/matrix shear strength, τ_f , is calculated by the following equation,

$$\tau_f = \frac{2}{\pi} \left[\frac{a}{d} (\tau - \tau_m) + \tau_m \right],$$

where a is the fibre spacing, d the diameter of the fibre, τ the average shear strength, and τ_{m} the

shear strength of the matrix/matrix bond. The latter was evaluated by lap-shearing testing the matrix/matrix bonds produced using the same conditions as for the matrix/fibre-mat bonds. $\tau_{\rm m}$ was 482 MPa and 511 MPa, for the bonds obtained from 870 °C and 970 °C, respectively.

Results and Discussion

Processing

Solid-state consolidation is achieved by the deformation of the matrix material to eliminate the cavities within the matrix/fibre assembly. This is usually carried out at elevated temperature under pressure. The process may be divided into a few stages, as illustrated in Fig.4. First, it involves the indentation of the fibre into the matrix once pressure is applied, Fig.4 (a), due to the instantaneous matrix plastic flow underneath the fibre surface. This is followed by matrix/matrix bridging between the fibres by continuing matrix creep and/or plastic flow, producing two main voids on both sides of a fibre, and a series of small cavities at the matrix/matrix interface due to matrix surface undulation, Fig.4(b). Further pressurisation at temperature assists the removal of the small cavities and the reduction of the main voids, Fig.4(c), through both creep flow and diffusional mass transport at the fine matrix grain boundaries and interfaces. Full consolidation is achieved when the main voids are eliminated, Fig.4(d). An example of a fully consolidated six-ply composite is presented in

To illustrate the degree of consolidation during processing, it is convenient to employ the quarter contact angle, o, as a variable with $0 \le \phi \le \pi/2$ illustrated in Fig.6. The variation of the quarter contact angle is illustrated in Fig.7 as a function of bonding time and applied pressure Here the experimental results are given as points. The curves are theoretical predictions of an analytical model, based on the constitutive plastic yielding and power-law creep functions of the matrix material, and formulated in relation to the various stages of consolidation discussed above. Details of the model are presented elsewhere [16]. The predicted consolidation behaviour generally leads to an "S" curved variation of the contact angle with time, with an initial timeindependent contact due to instantaneous fibre indentation. The rapid increase in contact angle in the middle stages corresponds to the matrix-flow process before matrix-bridging. The rate-controlling process appears to be the final reduction of the two main voids adjacent to each fibre, involving both creep flow and diffusional mechanisms. A higher pressure and / or temperature can readily

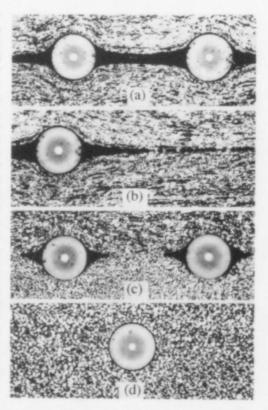


Fig. 4. Various stages of the consolidation process.

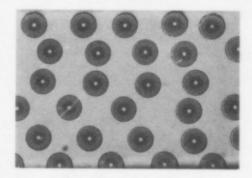
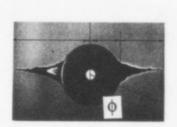


Fig. 5. Structure of a well-bonded SiC fibre/ Ti6Al4V composite.

decrease the total time required for full consolidation, as shown in Fig.7. However, an excessive uniaxial pressure may cause fibre damage [9]. A higher temperature facilitates creep and diffusion for void removal [16], but will also enhance any undesirable interfacial reactions and/or leads to unfavourable matrix microstructure [1,2], which is discussed in the next section.



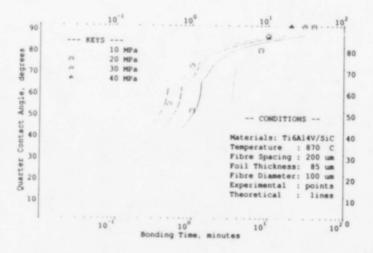
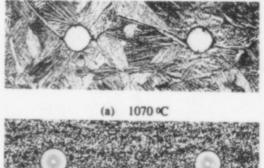


Fig.6. Illustration of a quarter contact angle, φ.

Microstructure

Ti6Al4V experiences an (α+β)/β transformation at about 995 °C. Bonding at a temperature below and above the transus leads to two different type of matrix structures after furnace cooling, as noted in Fig.8: (a) equiaxed $(\alpha+\beta)$ structure from 870 °C and (b) lamellar transformed-β structure from 1070 °C The former structure possesses good ductility and strength, whereas the latter is characterised by good creep resistance and toughness, but with poor ductility and low-cycle fatigue properties. The equiaxed structure is normally favoured for its ductility and relatively low interface reactivity. Therefore, composite processing should be conducted below the \beta transus temperature.

Fig.7. Variation of the quarter contact angle vs. bonding time at different pressures



(b) 870 °C

Fig.8. Matrix microstructure from different temperatures.

Fibre/matrix interfaces play an important role in composite properties. The microstructure at the interface need to be well understood. Fibre/matrix bonding is achieved by charge transport, diffusion, and mass transport at the interface [15]. However, due to the non-equilibrium nature of the system, interfacial chemical reaction appears to be inevitable at the consolidation temperatures. Various methods of altering the interface reaction kinetics have been investigated in the past. The most successful one is the barrier coating of stable layer(s) on fibre surface, e.g. by CVD (Chemical Vapour Deposition). The TiB₂/C coating is used for such purpose for the fibres employed here [17].

Fig.9 shows the interface microstructures of the coated fibres after two stages of reaction at 970 °C for (a) 2 and (b) 30 hours, respectively. The TiB₂ coating is noted to be unstable and readily reacts with the matrix, forming acicular needles, Fig.9(a), which are identified as TiB phases by diffraction analyses [18]. There is no distinct boundary between the needles and the original coating and a mixed TiB₂/TiB sub-layer is often noted. In the meantime, TiC particles are also introduced in the TiB₂/C interface. Once the coating is consumed, the reaction between the SiC and the matrix elements produces a mixture of titanium carbides and silicides, Fig.9(b). Similar results have been observed previously on the SiC/Ti interaction [7]. These reaction products can readily develop into large particles, and may separate into alternating sub-layers as the reaction continues [1].

A TEM micrograph with inserted SAD (Selected Area Deffraction) patterns is given in Fig.10, to illustrate the morphologies of the fibre, the C-coating, the reaction product TiC, and their interfaces. It was obtained from the same specimen as Fig.9(a). The fibre is of the β - SiC type and consists of very fine crystals. The C-coating seems to be in the form of the Turbostratic

Carbon. Its diffraction pattern is very similar to the structure of the TC coating for the core of the SCS-6 fibre [19]. This type of carbon is characterised by even weaker van de Waals bonding between the basal planes than graphite [19]. The interdiffusion at the SiC and C interface produces a thin interlayer, consisting of both of the constituent phases, as noted from the composite diffraction pattern at the interface. The reaction at the C/TiB₂ interface forms large grains of TiC, which results in a non-uniform consumption of the C-

coating, Fig. 10.

The average thickness variation of the interfacial layers is presented in Fig.11, as a function of holding time, t, at 870 and 970 °C, respectively. There is an initial increase in the TiB2/TiB layer, due to the inter-diffusion of B and Ti elements. After the disintegration of the original TiB2 coating, this layer gradually decreases upon further holding, possibly because of the diffusion of B elements into the matrix. The C-coating does not show any obvious variation until the TiB2 coating is fully disintegrated. Then the reaction is accompanied by the linear decrease of C-coating and the corresponding linear increase of TiC as a function of t1/2, indicating diffusion-controlled reaction kinetics. At the higher temperature, it is seen that the C-coating is completely consumed after about 5 hours hold. This is followed by the increase of the SiC and Ti reaction products with t1/2, in the form of TiC/Ti₅Si₃. During this period, the TiC layer shows a slight increase with time, as a result of growth after consuming the small TiC

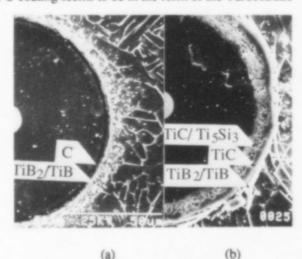


Fig.9. Interface microstructures showing the reactions at two different stages.

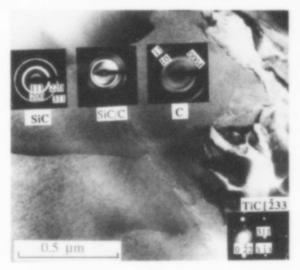


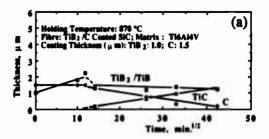
Fig.10. Morphologies of SiC, C, TiC and their interfaces under TEM.

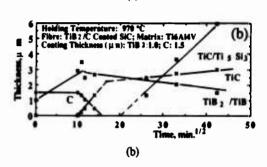
particles in the subsequent reaction products. Although the TiB_2/C coating is not as stable as expected, it has effectively produced a time-lag between the reaction of the matrix and the SiC fibre itself, particularly at the lower temperature.

Interface Properties

The interface shear strength of the coated fibre and the matrix is presented in Fig.12 as a function of total holding time at 870 and 970 °C, respectively (which includes the time for bonding the samples, 30 minutes, in these cases). Each of the data points is calculated from an average of 3 to 6 measurements. It is noted that the initial bonding strengths are relatively low in both may be for two cases, which possible reasons: (i) The matrix/fibre bonding has not been fully achieved after the short period of holding, as time is required for the removal of possible surface oxides contaminations and for interdiffusion and mass transport even after full intimate contact between the matrix and the fibre has occurred; and (ii) The bonding at the C/SiC interface is of the relatively weak van de Waals type and can be readily broken, particularly with the Ccoating being the turbostratic structure as discussed earlier. Analyses on the fibre/matrix fracture surfaces shown that fully bonded interfaces were only achieved by holding samples for a short period of time at the bonding temperature after the consolidation was completed [20]. This observation agrees with the reason (i) proposed above.

The strength increases with holding time up to a maximum value as the complete matrix/fibre bonding is progressively established, Fig. 12.





(a)

Fig.11. Thickness of the interlayers vs. time at:
(a) 870 °C; (b) 970 °C.

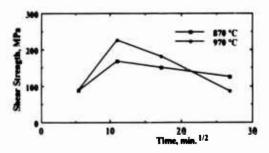


Fig.12. Fibre/matrix interfacial shear strength after various periods of heat treatment

The inter-diffusion at the weak interface, shown in Fig. 10, can also increase the bond strengths therein. The strengths decrease after about 2 hours of holding, which corresponds to the start of the consumption of the C-coating, comparing Fig. 12 with Fig. 11. A larger drop is noted for the higher temperature bonds due to a more rapid increase of the brittle, irregular TiC interlayer, which enhances debonding.

It is also clear in Fig. 12 that the strength of the higher temperature bonds is greater than that of the lower temperature bonds in the early stages of holding, but becomes lower in the later stages. This may be explained as follows. In the early stages: (1) the higher temperature leads to stronger bonding, particularly at the weak interfaces around C-coating, as a result of a

2.631

greater range of inter-diffusion; (2) possible impurities on the original matrix and fibre surfaces are more easily and extensively dissolved at the higher temperature to enhance matrix/fibre bonding; (3) cooling from the higher temperature gives rise to larger residual stresses gripping the matrix/fibre interface area, due to greater differences in thermal expansion and a greater level of matrix phase transformation (bcc β to hcp. α, which also results in matrix volume shrinkage). These influences are eventually counter-balanced by the deleterious effect of the continuing growth of the brittle reaction layers at the higher temperature, leading to a greater reduced strength in the later stages.

Summary

The consolidation process for producing continuous fibre reinforced titanium matrix composites has been examined. Among the various stages discussed, the closure of the final voids around each fibre is the rate-controlling stage, which involves the contribution of both matrix creep and diffusional mass transport from boundaries and interfaces to the void area. The processing parameters, such as temperature, pressure and time, should be optimised so that a sound matrix/fibre bonding can be established before a large scale of interfacial reaction is

introduced and without requiring too large an initial matrix/fibre contact pressure.

For the present composite system with a fibre volume fraction of 31.6%, full consolidation can be achieved after 0.5 to 1 hour at temperatures, 870 and 970 °C, under a pressure no less than 20 MPa. A short period of high temperature holding after full consolidation seems to be necessary to obtain a good bond strength, which should not result in the consumption of the C-coating. The protective TiB2 coating readily reacts with matrix at both of the temperatures studied, and, therefore, is not stable. However, it can produce a time-lag before the matrix/SiC fibre reaction takes place. This effect is greater at the lower temperature.

Both bonding temperature and interface reaction greatly influence the interfacial bonding strength of the composite. At a given holding time, the higher temperature yields a greater strength when the level of reaction is limited, while the situation is reversed after an extensive amount of reaction at the higher temperature. In both cases, the strength decreases with the increase of the reaction layer thickness, involving TiC and/or TiC/Ti₅Si₃.

Acknowledgements

The supply of the coated fibre from B.P. Research Centre is gratefully acknowledged. The work was carried out under the SERC rolling programme (Grant No. GR/F/87660) on MMCs at the Oxford Centre for Advanced Materials and Composites.

References

- 1. P. Martineau et al, "SiC Filament / Titanium Matrix Composites Regarded as Model Composites, Part II", <u>J. Mater. Sci.</u>, 19(1984), 2749-2770.
- 2. P.R. Smith and F.H. Froes, "Developments in Titanium Metal Matrix Composites", L. Metals, March (1984), 19-26.
- 3. T.M.F. Ronald, "Advanced Materials to Fly High in NASP", Adv. Mater. Proc., 5(1989), 29-37.
- 4. J.M. Yang and S.M. Jeng, "Interfacial Reactions in Titanium Matrix Composites", JOM, Nov.(1989), 56-59.
- 5. S.C. Jha, J.A. Froster, A.K. Pandey and R.G. Delagi, "MMCs via Titanium-Aluminide
- Foils", Adv. Mater. Proc., 4(1991), 87-89.

 6. J.M. Yang and S.M. Jeng, "Interfacial Reaction Kinetics of SiC Fibre-Reinforced Ti₃Al Matrix Composites", Scripta Metall., 23(1989), 1559-1564.

 7. C.G. Rhodes and R.A. Spurling, "Fibre-Matrix Reaction Zone Growth Kinetics in SiC-Reinforced Ti₆Al₄V as Studied by Transmission Electron Microscopy", Recent Advances in Reinforced Ti₆Al₄V as Studied by Transmission Electron Microscopy", Recent Advances in Reinforced Ti₆Al₄V as Studied by Transmission Electron Microscopy", Recent Advances in Reinforced Ti₆Al₄V as Studied by Transmission Electron Microscopy", Recent Advances in Reinforced Ti₆Al₄V as Studied by Transmission Electron Microscopy (Recent Advances in Reinforced Ti₆Al₄V as Studied by Transmission Electron Microscopy", Recent Advances in Reinforced Ti₆Al₄V as Studied by Transmission Electron Microscopy (Recent Advances in Reinforced Ti₆Al₄V as Studied By Transmission Electron Microscopy). Composites in the United States and Japan, ed. J.R. Vand M. Taya (Philadelphia, PA: ASTM, 1985), 585-599.
- 8. R.R. Kieschke, R.E. Somekh and T.W. Clyne, Acta Metall. Mater., 39(1991), 427-435, 437-443, 445-452.

2.639

- 9. S.J. Jeng, J.M. Yang and C.J. Yang, "Fracture Mechanisms of Fibre-Reinforced Titanium Alloy Matrix Composites" (Part I to Part III), Mater. Sci. Eng., A138(1991), 155-167, 169-180, 181-190.
- M.H. Loretto and D.G. Konitzer, "The Effect of Matrix Reinforcement Reaction on Fracture in Ti-6Al-4V Base Composites", Metall. Trans., 21A(1990), 1579-1587.
 C. Jones, C.J. Kelly, and S.S. Wang, "The Characterisation of an SCS-6/Ti-6Al-4V MMC Interface, J. Mater. Res., 4(1989), 327-335.
 T.W. Chou, A Kelly and A. Okura, "Fibre-reinforced metal-matrix composites",
- Composites, 16(3)(1985), 187-206.
- 13. C.M. Ward-Close and P.G. Partridge, "A Fibre Coating Process for Advanced Metal Matrix
- Composites ", <u>J. Mater. Sci.</u>, 25(1990), 4315-4323.

 14. D. Eylon and F.H. Froes, "Method to Produce Metal Matrix Composite Articles From Lean-Metastable β Titanium Alloys", US Patent No. 4807798, February 1989.
- 15. K. Burger, W. Mader, and M. Ruhle, "Structure, Chemistry and Diffusion Bonding of
- Metal/Ceramic Interfaces", <u>Ultramicroscopy</u>, 22(1987), 1-14.
 16. Z.X. Guo and B. Derby, "Theoretical Model for the Solid-State Consolidation of Long-Fibre Reinforced MMCs" (to be published in Acta. Metall. Mater.).
 17. C.M. Warwick and J.E. Smith, "Interfacial Reactions in Titanium Alloys Reinforced with C/TiB2-Coated Monofilament", Metal Matrix Composites- Processing, Microstructure, and Properties, ed. N. Hansen et al., (Denmark: Riso National Lab., 1991),
 27. Composites Processing Microstructure, and Properties, ed. N. Hansen et al., (Denmark: Riso National Lab., 1991),
- 18. Z.X. Guo, B. Derby, and B. Cantor, "Comparison of Ti-Based Composite Interfaces Reinforced by Uncoated and TiB2/C Coated SiC Fibres", J. Microscopy, special issue on Microscopy of Composite Materials, January-February, 1993.
- 19. X.J. Ning et al, "The Structure of Carbon in Chemically Vapour Deposited SiC Monofilaments", J. Mat. Res., 5(12)(1990), 2865-2876.
- 20. Z.X. Guo and B. Derby, "Fabrication of Long-Fibre Reinforced MMCs: What's Happening on the Microstructural Scale", J. Microscopy, special issue on Microscopy of Composite Materials, January-February, 1993.

METAL-CERAMIC COMPOSITE LAYER FORMATION ON TITANIUM SURFACES THROUGH

LASER TREATMENT

S. Mridha, H.S. Ubhi', P. Holdway', T.N. Baker, A.W. Bowen'.

Dept. of Metallurgy & Engineering Materials, University of Strathclyde, Glasgow Gl 1XN UK. *Materials and Structures Department, Defence Research Agency Aerospace Division RAE, Farnborough, Hants GUI4 6TD UK.

Abstract

SiC ceramic particles of 6 μm size, and ranging in volume fraction from 5 to 20%, have been incorporated into the surface of commercial purity titanium sheet by laser treatment and the microstructures and hardnesses produced by different processing parameters investigated. Phase identification showed the presence of TiC, Ti₂Si₃ and Ti, but there was no clear evidence for residual SiC. Metallographic examination showed that the TiC was present as globular particles ranging from 5nm to 2 μm in size. Residual stresses were tensile along, and compressive across, the laser trails which, typically, had an outside layer 100 μm deep with hardness (H $_{\nu}$) values in the range 1000–1400 H $_{\nu}$, followed by a plateau of hardness between 450 and 550 H $_{\nu}$. These large increases in hardness are attributed to the TiC produced during the glazing.

Introduction

The incorporation of ceramic particles into the surface of titanium by laser processing is an attractive means of modifying, in a controlled manner, the surface structure in specific areas, resulting in, for instance, improved wear and oxidation resistance.

Ayers and co-workers [1-3] injected hard particles of titanium carbide and tungsten carbide into laser surfaces melted zones on various substrates, and demonstrated that wear resistance improved and the friction coefficient decreased with increased volume fraction of carbide particles: injection of between 30-50 volume per cent of 0.1 mm titanium carbide particles into titanium alloys produced a hardness (H_v) of about 450 H_v. Abboud and West [4] injected 150 μm silicon carbide particles into titanium surfaces. They observed partial dissolution of the silicon carbide which lead to enrichment of the matrix with silicon and carbon; during solidification dendrites of titanium carbide formed at the silicon carbide-matrix interfaces while the matrix consisted of $\alpha/\alpha' + Ti_{s}Si_{s}$ eutectic, and the hardness of the matrix increased from 210 H_v to about 600 H_v.

In the present work, much smaller (in this case $6\mu m$) silicon carbide particles of various volume fractions were incorporated, using a range

Titanium '92 Science and Technology Edited by F.H. Froes and I. Caplan The Minerals, Metals & Materials Society, 1993 of processing parameters, into titanium surfaces by laser treatment to produce what we term a metal-ceramic composite (MCC) layer. This paper details the hardnesses and microstructures produced.

Experimental Procedure

Commercial purity (CP) titanium sheet of 3 mm thickness was used in this investigation, and silicon carbide particles of 6 μm average size were painted on the metal surface with a low temperature varnish. Most of the work was carried out using 5 and 10 vol% silicon carbide, although a few experiments were also carried out with 20 vol%. These volume fractions of silicon carbide were estimated on a hemi-spherical melt pool of 0.4 mm depth.

Laser glazing of the silicon carbide painted CPTi surfaces was carried out at Culham Laboratory, Atomic Energy Authority, Abingdon, UK, using a 10 kW CO, laser facility. Specimens were glazed using a 2.8 kW beam and a combination of 20, 30, and 50 mm defocused distances and traverse speeds of 5 and 10 mm s⁻¹ under a pure helium environment. Sections of the MCC trails produced were prepared using standard metallographic techniques and were examined by optical, scanning electron and transmission electron microscopy. X-ray diffraction analysis and residual stress measurements were also conducted. Microhardness tests were carried out on the polished sections.

Results

Microstructures

Glazing at 20 mm defocused distance produced shiny, smooth crack-free surfaces. Some agglomeration of particles occurred at the edge of trails in the 5% and 10% coatings, for both 5 and 10 mm s-1 traverse speeds. The 20% coatings, however, produced rough surfaces with a network of cracks. Glazing at 20 mm $\,\rm s^{-1}$ traverse speed resulted in a non-continuous surface layer. Agglomeration of particles was also found in the melt zone (Fig 1a), which additionally consisted of dendrites, globular, columnar and what we tentatively term thread-like features, depending on volume fraction and defocus eg the microstructure for $5 \pm SiC$, 20 mm defocus and 5mm s $^{-1}$ traverse speed is shown in Fig 1b and that for 10%SiC, 50mm defocus in Fig 1c (both at 5mm s-1 traverse speed). The globular particles appeared to be associated with coarse particles; the size of the globular particles grew larger with distance from the larger particles (S Mridha and T N Baker unpublished work). When glazed at 30 mm defocused distance, the agglomerates were observed at the surface with their frequency being higher in the 10% coatings than with 5% coatings for both 5 and 10 mm s-1 traverse speeds. The surface layer of the 10% coating was followed by a deeper zone containing the thread-like features. Increasing the defocused distance, which decreases energy density, produced a continuous surface layer in both the 5 and 10% coatings, but in the latter this was followed by a deep intermediate zone comprising dendrites and thread-like structures (Fig 1c). Coarse particles at the surface layer were again associated with globular structures.

X-ray diffraction patterns from the surface layer and approximately half way into the melt zone are shown in Figs 2a and b. While in both cases titanium, titanium carbide and titanium silicide are clearly present, the intensities of the carbide and silicide peaks are higher at the surface and diminish with distance into the melt pool while the intensities of the titanium peaks increase. Transmission electron microscopy of thin foils prepared from the melt zone showed a heavily dislocated matrix comprising α^\prime , dendritic and globular titanium carbide and lath-shaped titanium silicide (labelled in Fig 3). Microanalysis results agreed with these observations.

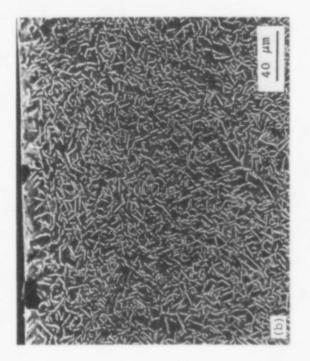
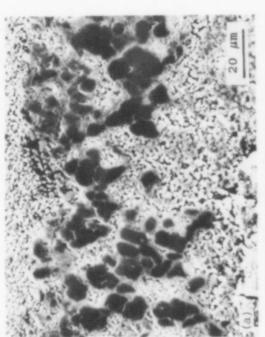
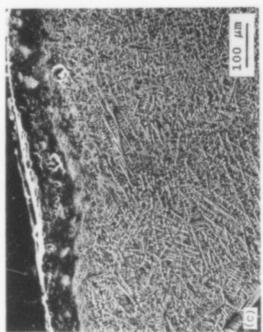
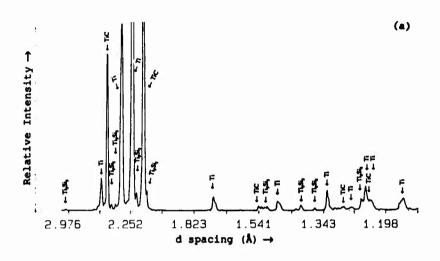


Figure 1. Scanning electron micrographs of MCC laser glazed trails showing microstructure: (a) of agglomerated particles in the melt pool; (b) after 20mm defocus and 5mm s⁻¹ traverse speed for 5% SiC; and (c) after 50mm defocus at 5mm s⁻¹ traverse speed for 10% SiC.







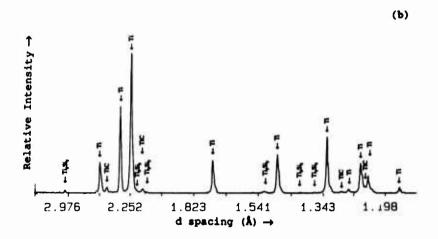


Figure 2. X-ray diffractometer traces for (a) as-glazed surface and (b) after ~250 μ m removal (Corresponding values of residual stresses are given in Table I.)

Residual stress measurements both parallel (L) and perpendicular (T) to the laser trails showed the stresses to be tensile in the former direction and almost equally compressive in the latter direction (Table I). This was also found to be true below the surface, where measurements were made after removal of the surface by grinding and polishing (preferential polishing precluded the use of electropolishing in these initial analyses). The absolute values of stress were found to vary with position within the laser trail, due to local changes in microstructure.

Table I. Residual stress values for 20mm defocus and 10mm s-1 condition

Condition	Stress (MPa) (uncorrected for material removal)	Direction
As-glazed	259±137 -244±139	L T
After removal of ~100µm	171±94 -170±83	L T
After removal of further 100µm	124±117 -99±112	L T

Hardness Profiles

The hardness profiles of the 5 mm s⁻¹ traverse speed trails given in Fig 4a show a plateau at about 500 H_v which is over 400 µm deep for both the 5% and 10% coatings glazed at 20 mm defocussed distance. A similar hardness plateau occurs when glazing at 10 mm s⁻¹ traverse speed and 10% coating (Fig 4b); however, the 5% coating gives no plateau (Fig 4b). This is consistent with the observation that at higher glazing speeds the melt depths are shallow and the microstuctures consist of a lower volume fraction of carbides due to the lower initial fraction of SiC in the coating.

Glazing at 30 mm defocused distance, 10 mm s⁻¹ and 10 % coating resulted in a profile with a thin hard layer (1400 H_{ν}) followed by a moderately hard (500 H_{ν}) plateau. The 5% coating produced high surface hardness, but a shallow profile. When glazing at the slower speed (5 mm s⁻¹), the thin hard layer was absent.

The hardness profiles produced at a 50 mm defocused distance and 5 mm s⁻¹ traverse speed but with 5 and 10 % coatings are shown in Fig 4c. The hardness plateau in the 10% coating is much deeper (650 μm), but of slightly lower mean hardness (450 H_{ν}). The 5% coating yields a lower maximum hardness (1040 H_{ν}) than the 10% coating (1400 H_{ν}).

Melt depth

The melt depths, depths of various structural zones where present in the MCC trails, and melt widths were measured. These results showed that the width of the trail increases with increasing defocused distance and decreasing traverse speed, while the total melt depth increases with both decreasing defocused distance and traverse speed. However, the 10% silicon carbide coatings resulted in higher melt depths under all conditions compared to those in 5% coatings. The very hard layer present in both the 5 and 10% coatings glazed at 50 mm defocused distance and at both glazing speeds comprise the globular microstructure, and is thicker in the 10% coating. Again the intermediate hard layer increases with decreasing speed and defocused

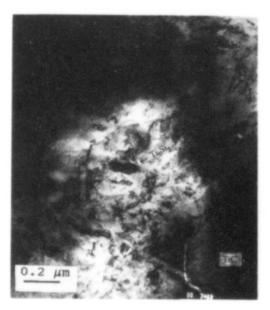
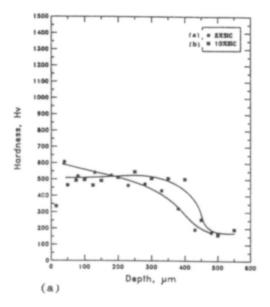
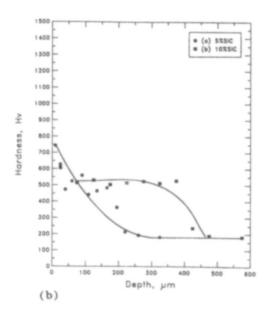


Figure 3. Transmission electron micrograph showing matrix structure, and carbide and silicide morphology.





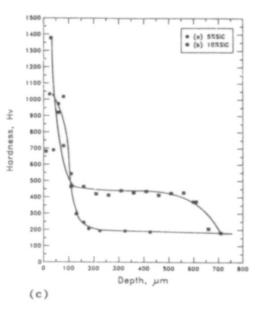


Figure 4. Hardness profiles of 5 and 10% SiC laser glazed melt trails for various defocus distances (DF) and traverse speeds (TS) (a) 20mm DF and 5mm s $^{-1}$ TS; (b) 20mm DF and 10mm s $^{-1}$ TS; and (c) 50mm DF and 5mm s $^{-1}$ TS.

distance in the 5% coating. This is opposite to that in the 10% coatings where this layer depth increased with both decreasing speed and defocused distance. This observation has not been reported previously.

Discussion

The microstructural development in the MCC trails studied under the present investigation is dominated by the reaction of the SiC particles with the molten titanium layer to form titanium carbide (dendrites, globules and "thread-like" features), titanium silicide (and α during the subsequent rapid solidification of the melt zone). Previous workers [3,4] reported that by injecting large carbide particles (100-150 μm) into the surface of titanium alloys, particles are incorporated into the melt with partial dissolution of carbides which results in the precipitation of titanium carbide dendrites at and around the surfaces of the embedded particles as well as finely dispersed carbides in the matrix. The dissolution of silicon carbide in the molten pool will be dependent on both its size and melt temperature. Since carbon has a higher affinity for titanium than for silicon, the dissolution of silicon carbide and the formation of titanium carbide and titanium silicide will take place. The shape, size and distribution of these constituents are believed to be related to the melt pool chemistry and time-temperature distribution. Glazing at 20mm defocused distance resulted in thread-like titanium carbide (Fig 1) which has a higher concentration at the surface than through the melt zone. Hardness profiles confirm this in that the highest values occur at the surface and then decrease through the melt zone (Fig 4a). After melting, dissolved or dissociated silicon carbide diffuses down through the melt pool; however, due to insufficient time and the temperature gradient of the melt, a concentration gradient is retained which, during solidification, results in the observed higher hardness and concentration of the carbide at the surface. The very high hardness observed at the surface is similarly due to the globular type of titanium carbides (Fig 1c) which also have the highest concentration at the surface. Cooper and Ayers [5] also observed that surface hardness increased from 1.1 to 2.6 times the base hardness with increased carbide injection. In actual fact, the increased hardness results in increased titanium carbide dendrite density yielding higher hardness; which is thought to be the main hardening mechanism of these surface layers, as indicated by the x-ray diffraction analysis (Fig 2a and b). The agglomerated silicon carbide in the melt zone is believed to be related to non-optimum convectional flow in the melt pool, which allowed powder clusters to remain intact in the melt pool where they subsequently became trapped on solidification. It is significant to note that in the present work hardness increments of three to four times that of the base material occurred and this value is even higher (4.3 to 9.3 times) when the hard layer consists of globular titanium carbide. Additionally, these increments are achieved by the use of lower volume fraction of fine silicon carbide particles as compared to those reported in the literature [3-5]; where hardness increments up to 1.1 to 4 times were found with very high volume percentages (25-60%) of coarse particles (45-150 μ m). This clearly indicates the advantage of finer particles, which react nearly completely to precipitate the hard titanium carbide constituent which produced the high hardnesses observed. Moreover, by varying the laser glazing parameters control of the hardness profiles is also possible.

While the load bearing capability of the present MCC trails have not yet been investigated, the very hard surface layers observed at the surface in the materials glazed is expected to increase the wear resistance and the underlying layer of intermediate hardness will contribute to an improved load-bearing ability [6,7].

Conclusions

- 1. Composites produced with 5 and 10 vol% of 6 μm silicon carbide particles, under various process variables, revealed microstructures consisting of globular, dendritic, columnar and thread-like morphologies, with some agglomerated sheet-like fragments.
- 2. The globular, dendritic and thread-like features have been identified as titanium carbide. Titanium silicide is also present in the melt zone. These phases occur through reaction of the silicon carbide particles with the molten titanium.
- 3. Production of surface layers with very high hardness, between 4.3 and 9.3 times the hardness of the base metal, and backed by a softer intermediate layer up to 400 μm deep has been demonstrated.

Acknowledgments

The authors wish to acknowledge the financial support of the DTI and MoD. © Copyright HMSO London 1992.

References

- 1. J.D. Ayers and R.N. Bolster, Abrasive wear with fine diamond particles of carbide containing aluminium and titanium alloy surfaces, <u>Wear</u>, 1984, 93, 1:3-205.
- 2. J.D. Ayers, R.T. Schaefer and W.P. Robey, A laser processing technique for improving the wear resistance of metals, \underline{J} , $\underline{\text{Met}}$., Aug 1981, 33, 19-23.
- 3. J.D. Ayers, Particulate composite surfaces by laser processing, in <u>Lasers in Metallurgy</u>, (ed K Mukherjee and J Majumdar) 1981, Warrendale, PA, The Metallurgical Society of AIME pp115-130.
- 4. J.H. Abboud and D.R.F. West, Microstructure of titanium injected with SiC particles by laser processing, <u>J. Met. Sci. Lett.</u>, 10 (1991), 1149-1152.
- 5. K.P. Cooper and J.D. Ayers, Laser melt particle injection processing, <u>Surf. Fng.</u>, 1985, 1, 4, 263-272.
- M.M. Khruschov, Resistance of metals to wear by abrasion, as related to hardness, Proc. Conf. on <u>Lubrication and Wear</u>, Inst. of Mech. Engrs., London, 1957, 655-659.
- 7. R.N. Bolster and I.L. Singer, Surface hardness and abrasive wear resistance of ivon implanted steels, <u>ASLE Trans.</u>, Vol 24, 4, 1981, 5, 526-532.

INTERFACIAL PROPERTIES AND FATIGUE CRACK PROPAGATION IN

CONTINUOUSLY REINFORCED Ti/SiC METAL MATRIX COMPOSITES.

K.M. Fox, P.J. Cotterill, M. Strangwood and P. Bowen.

School of Metallurgy and Materials / IRC in Materials for High Performance Applications, The University of Birmingham, Edgbaston, B15 2TT, U.K.

Abstract

Interfacial properties of different SiC/Ti composites have been measured using a fibre push-out technique. Three systems have been considered: Ti ß21s / SCS6 composites, Ti-15V-3Cr-3Al-3Sn / SCS6 composites and Ti-6Al-4V / SCS6 composites. The interfacial debonding shear stress was found to affect the mode of crack growth. An interfacial shear stress in the range of 90-120 MPa was measured for Ti-15-3 / SCS6 and Ti-6-4 / SCS6 systems and this was found to correlate with predominantly mode I crack growth in these materials when tested in fatigue at ambient temperature. However, the Ti ß21s / SCS6 system considered here had a lower interfacial shear stress of approximately 36 MPa, and this appeared to promote crack bifurcation during fatigue loading. A preliminary investigation into the effect of unbridged crack (notch) depth on fatigue crack propagation was also carried out in the Ti ß21s / SCS6 system and was found to have important potential implications for assessment of crack growth behaviour in these materials. Marked effects of the initial applied stress intensity range on crack growth behaviour have also been observed in the Ti-15-3 / SCS6 system.

Titanium '92 Science and Technology Edited by F.H. Fross and I. Captan The Minerals, Metals & Materials Society, 1993

Introduction

Continuously reinforced metal matrix composites (MMCs) are of interest to the aerospace industry because of their high stiffness to weight ratios and potential high temperature capabilities. Applications will include highly stressed rotating parts operating at moderate to high temperatures. Thus fatigue crack growth characterisation is of clear importance.

These composite systems have been found [1-5] to exhibit the unusual phenomenon of crack growth rates decreasing with increases in the fatigue crack length under constant cyclic load amplitude conditions, i.e. with increasing nominal applied stress intensity range, ΔK_{app} . This is due to unbroken fibres in the crack wake acting to bridge the crack and thus to reduce the effective stress intensity ΔK_{eff} at the crack tip. The amount of load bearing by the fibres is dependent on the strength of the fibre / matrix interface, and thus it would be expected that the crack growth resistance will be affected by the interfacial properties of the composite. A strong fibre / matrix interface would allow a high degree of load bearing by the fibres and means not only that fibre failure is more likely but also that the clamp back stresses in the crack wake will also be higher for unbroken fibres. Conversely a weak interface means debonding of the fibre / matrix interface is probable with reduced load transfer. This will result in a reduced risk of fibre failure, but also a reduced clamp back stress in the crack wake [6,7]. It is unclear in general which situation is preferable to prolong the life of these materials under cyclic loading and further understanding of the effect of interfacial properties on fatigue crack growth resistance in these materials is required before predictions can be made.

One technique which has been used to assess interfacial properties is that of fibre push-out testing [8,9]. This can be used to measure both the interfacial debonding shear stress and the interfacial frictional stress once the fibre has debonded from the matrix. These values will depend on:

(i) the chemical nature and thickness of fibre / matrix reaction layers;

(ii) the residual stresses set up between the fibres and the matrix set up on cooling due to differences in thermal expansion coefficient between the fibres and the matrix;

(iii) any volume changes in the matrix caused by phase transformations;

(iv) type of fibre coating.

This paper presents preliminary results from a long term programme aimed at quantifying the influence of interfacial properties on crack growth resistance in fibre reinforced metal matrix composites.

Experimental procedure

The composites considered in this work were commercially available: Ti-6Al-4V / SCS6, Ti-15V-3Cr-3Al-3Sn / SCS6 and Ti B21s / SCS6. All composites were investigated in the as processed condition and were 8-ply unidirectional lay-ups.

In order for fibre push-out tests to be carried out, slices were cut perpendicular to the fibre direction and then polished on both sides to a $1\mu m$ diamond finish and a thickness between $190\text{-}270~\mu m$. A Leitz microhardness indenter was used to obtain a value for the interfacial debonding shear stress. The specimen slices were placed on a support block so that one row of fibres was exactly above a $200~\mu m$ groove to prevent matrix deformation during indentation. The Vickers indenter was then optically positioned exactly over the centre of a fibre and the loads applied were progressively increased in increments of up to 50 g until the fibre was observed to move. The fibres were examined after testing using a Field Emission Gun Scanning Electron Microscope (SEM) both to identify the location of interfacial failure and to measure the thickness of the slices accurately .

The interfacial debonding shear stress, τ was then calculated using the equation:

$$\tau = P / (\pi d_f L_f) \tag{1}$$

where P = load applied when the fibre was observed to move, $d_f = diameter$ of fibre and $L_f = length$ of fibre (thickness of specimen).

Fatigue testing was performed on the Ti-15-3 / SCS6 and Ti B21s / SCS6 composites using single edge-notched specimens in three-point bending. The specimens were of nominal dimensions 4 x 2 x 75 mm³. A notch was cut perpendicular to the fibre direction either by electrodischarge machining or with a diamond saw of 150 μ m thickness. This allowed cracks to be grown perpendicular to the direction of fibre reinforcement and parallel to the stacking direction of fibres within the mat. All tests were carried out at a frequency of 10 Hz and at a stress ratio, R = σ_{min} / σ_{max} of 0.5 (where σ_{min} , σ_{max} are the minimum and maximum nominal stresses applied over the fatigue cycle). An ESH servo-hydraulic testing machine with a 10kN load cell was used, and a constant load range was maintained for all tests. The crack length was measured using a direct current potential difference technique.

For an investigation into the effect of changing the initial notch depth (a_0) in the Ti B21s system, notches were cut with a diamond saw to different a_0/W ratios where W is the test-piece width. The load ranges were adjusted accordingly to produce the same starting nominal applied stress intensity range ΔK_{app} .

Some of the specimens were sectioned after testing along the fibre direction normal to the notch and polished to a 1µm diamond finish to reveal the mechanism of crack growth.

Results

Fibre push out results for the various fibre / matrix systems are shown in Table I

FIBRE	MATRIX ALLOY	INTERFACIAL SHEAR STRESS / MPa
SCS6	Ti-6Al-4V	115 ± 4
SCS6	Ti-15V-3Al-3Sn-3Cr	93 ± 4
SCS6	Ti β21s	36 ± 4

Table I. Comparative interfacial shear stresses obtained using microhardness push-out tests. All values quoted are an average of at least 10 measurements on individual fibres.

Clearly there are marked differences between the composite systems. SEM observations reveal the location of interfacial failure, see Figure 1(a), (b) and (c). Fig.1(a) shows an SCS6 fibre pushed out from a Ti-6Al-4V matrix. Failure appears to be between the carbon coating layers and the fibre / matrix reaction product which has been identified to be mainly TiC [10]. Fig.1(b) shows an SCS6 fibre pushed out from a Ti-15-3 matrix. Again failure appears to be through the carbon coating layers and the fibre / matrix reaction products. Fig.1(c) shows an SCS6 fibre pushed out from a Ti \(\text{B21s matrix} \). There is very little reaction layer present around the base of the fibre and the carbon coating layers can be seen on the surface of the pushed out fibre.

The degree of interfacial shear stress also appears to dictate the mode of crack propagation, see Figure 2(a), (b) and (c). Note that crack bifurcation from the notch root is seen only in the weakly bonded Ti β 21s system. Such crack bifurcation makes a quantitative comparison of crack growth rates in this system with the other systems difficult. Nevertheless, this comparison is attempted for the Ti β 21s and Ti-15-3 systems in Figure 3. Unfortunately, the initial applied Δ Kapp values were also not identical, and in the Ti-15-3 system alone this factor is seen to have a profound effect on crack growth resistance, see Figure 3. Finally, for the Ti β 21s system the influence of initial unbridged crack length on crack growth resistance is shown in Figure 4, for identical Δ Kapp values. It can be seen that the shorter unbridged crack appears to promote more rapid failure than the deeper unbridged crack (in 45,000 cycles compared to 1,650,000 cycles respectively).

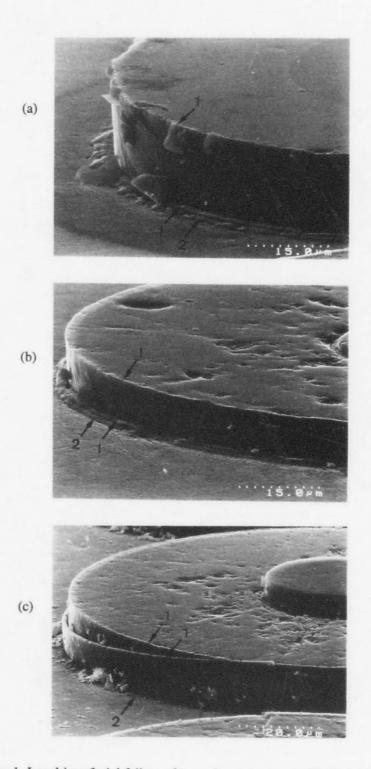


Figure 1. Local interfacial failure after push-out testing (a) Ti-15-3 / SCS6; (b) Ti-6Al-4V / SCS6 and (c) Ti β 21s / SCS6 composites. 1 indicates carbon coating layers and 2 indicates fibre / matrix reaction layer.

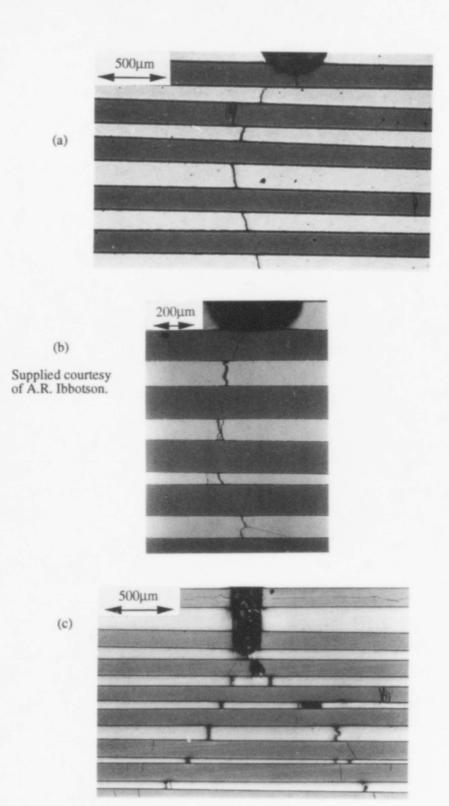


Figure 2. Optical micrographs of sections through interrupted fatigue crack growth. (a) Ti-15-3 / SCS6; (b) Ti-6Al-4V / SCS6 and (c) Ti β 21s / SCS6 composites.

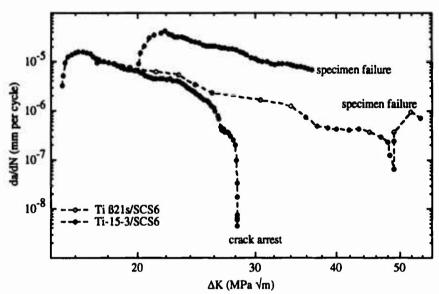


Figure 3. Crack growth resistance curves : da / dN versus ΔK_{app} for Ti-15-3 / SCS6 and Ti 821s / SCS6 composites. Ambient temperature, R=0.5, $\nu=10$ Hz

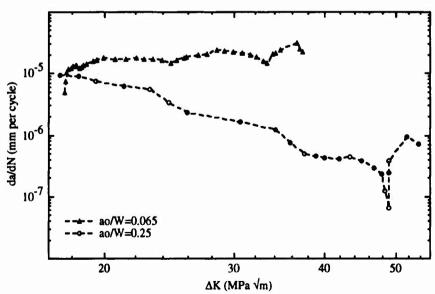


Figure 4. Effect of initial unbridged crack (notch) length on crack growth resistance curves: da/dN versus ΔK_{app} for Ti $\beta 21s$ / SCS6 composites. Ambient temperature, R = 0.5, ν = 10 Hz.

Discussion

The results from the fibre push-out testing show a considerable range in the interfacial debonding shear stress in these materials. For the systems containing SCS6 fibres, the Ti-6Al-4V and Ti-15-3 matrix have broadly similar interfacial strengths, but that of the Ti 821s is considerably lower. From the figures showing the fibre push-out specimens, it can be seen that most of the interfaces appear to have failed either between the carbon coating layers and the reaction product or within the carbon coating layers. Around the base of the fibre the remaining reaction layer can be observed, which is of similar thickness in both the Ti-6Al-4V and the Ti-15-3 composites. However in the Ti 821s system, there is very little reaction layer visible at the base of the fibre and the fibre coating layers can clearly be seen on the surface of the fibre. Therefore it seems likely that the processing of the Ti 821s was insufficient to allow the reaction layer to form and the interface is thus much weaker than in the Ti-6-4 and Ti-15-3 systems.

Optical sections through fatigue cracks after crack arrest (Figure 2 (a), (b) and (c)) show Mode I type cracks in the Ti-15-3 or the Ti-6-4 systems, which is consistent with a higher interfacial shear stress. However the Ti \(\text{B21s} \) system is prone to crack bifurcation. This can be linked directly to the low interfacial shear stress and this leads to easy fibre / matrix debonding.

It is not possible from the results in the present study to rank the relative crack growth resistance of the Ti B21s and Ti-15-3 systems, see Figure 3, because the level of initial ΔK_{app} was not held constant. Indeed, the significance of the parameter can be seen in the Ti-15-3 system, which illustrates the delicate balance that can sometimes exist between promoting crack arrest and catastrophic failure in these composites. It would appear that the increased initial ΔK_{app} value (20 MPa $^{\prime}$ m) promotes additional fibre fracture to that deduced for the lower initial ΔK_{app} value (15 MPa $^{\prime}$ m), see elsewhere [11].

For the Ti B21s system, changing the a_0/W ratio while keeping the starting nominal ΔK_{app} the same can be seen to effect the fatigue crack growth rates dramatically (see Figure 4). Although both specimens fail eventually, the specimen with the smaller initial unbridged crack fails after 45,000 cycles, compared with 1,650,000 cycles for the specimen containing the longer unbridged crack. This unusual observation is deduced to be due to increased fibre failure promoted by the higher initial mean stress (bending moment) applied to the shorter unbridged crack (to promote identical initial ΔK_{app} values). Such observations lend strong support to the importance of "bridging scale lengths" discussed elsewhere [12], and here indicate the care required to assess crack growth resistance in fibre reinforced systems. Note that if premature fibre failure does not occur in eithere case i.e.before large numbers of fibres bridge the crack, then the deeper initial unbridged crack will be more detrimental to fatigue crack growth resistance [7, 12]. Further experimental work is required to substantiate these hypotheses fully, and is currently underway.

Conclusions

Interfacial shear strengths in different commercially available Ti / SiC composites vary considerably and this effects the mode of fatigue crack propagation. Mode I cracks predominate in systems with a higher interfacial shear stress but bifurcation of cracks takes place in systems with lower interfacial shear stresses. Care is required in assessing fatigue crack growth resistance in fibre reinforced composites. Relatively modest increases in initial stress intensity range can promote catastrophic test-piece failure rather than crack arrest; and the depth of the initial unbridged crack length, for the same level of initial stress intensity range, can also influence fatigue crack growth resistance.

Acknowledgements

One of the authors (KMF) is supported by a SERC CASE award with Rolls-Royce plc, and a second (PJC) is supported by a SERC postdoctoral fellowship from the IRC in Materials for High Performance Applications. The support of Mike Hartley at Rolls-Royce plc, Derby has been particularly beneficial to the programme. Thanks are also due to A.R. Ibbotson for the provision of information with respect to this paper.

References

- [1] P.J. Cotterill and P. Bowen. Fatigue 90, Honolulu (1990), Vol. 4, pp. 2551-2556 MCE Publications, Birmingham.
- [2] P. Bowen, P.J. Cotterill and A.R. Ibbotson, Proc. Conf. "Test techniques for metal matrix composites" Ed. N.D.R. Goddard. (1990), pp. 82-96, IOPP, London.
- [3] A.R. Ibbotson, C.J. Beevers and P.Bowen. Scripta Metallurgica and Materiala, 25, (1991), pp. 1781-1786.
- [4] D. Walls, G. Bao, and F. Zok. Scripta Metallurgica et Materiala, 25, (1991) pp. 911-916.
- [5] P.J. Cotterill and P. Bowen, "Fracture and fatigue of inorganic composites", Cambridge, March 1992. To be published in J. Composites, Butterworths, London.
- [6] P. Bowen, D.C. Cardona and A.R. Ibbotson. Accepted for Mat. Sci. Eng. A, publication pending in May 1992.
- [7] D.C. Cardona and P. Bowen. "Theoretical concepts and numerical analysis of fatigue", May 1992, to be published, MCE Publications, Birmingham.
- [8] J.I. Eldridge and P.K. Brindley. Journal of Materials Science Letters, 8, (1989) pp. 1451-1454
- [9] C.J. Yang, S.M. Jeng and J.-M. Yang. Scripta Metallurgica et Materiala, 24, (1990) pp. 469-474
- [10] K.M. Fox and M. Strangwood. Submitted to Scripta Metallurgica et Materiala 1992.
- [11] B.N. Cox and C.S. Lo. Acta Metallurgica and Materiala, 40, (1992), pp. 69-80.
- [12] D.C. Cardona, C. Barney and P. Bowen. "Fracture and Fatigue of inorganic composites", Cambridge. March 1992. To be published in J. Composites, Butterworths, London.

NON-AEROSPACE APPLICATIONS

New development in application of titanium as an ecological metal = Non aerospace application / Environment and development =

Kazuo Sakai

Vice chairman of development committee of Japan Titanium Society
Tokyo, Japan

General manager(sales), Titanium division of Nippon Steel Corporation 6-3, otemachi 2-chome chiyoda-ku, Tokyo, Japan

Abstract

Titanium application is shifting from the aero to non-aero area (industrial and contruction). Though the growth of conventional Ti market seems to be moderate, recently new market is developing rapidly. Potential market are construction (architecture, civil engineering), automotive, oil and gas exploitation, sports and fashion goods.

Ti is appreciated as an economical metal for these 40 years or more. But now Ti should be evaluated as an ecological metal. Ti's superior characteristics (light weight, high elasticity, smoothness, bio-compatibility) is devoted to make more efficient machine or tools, paint and maintenance free construction. Through this, Ti contribute to prevent air pollution, water pollution or to promote safety and health.

Titanium '92 Science and Technology Edited by F.H. Froes and I. Caplan The Minerals, Metals & Materials Society, 1993

1. Preface

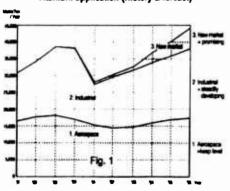
For these 40 years or more, titanium (hereafter Ti) has obtained a special position as the most economical metal for heat exchanger, electrode and chemical plant because of its excellent characteristics of anti-corrosion. But now, Ti should be evaluated as a ecological metal from the view point of environment or amenity because not only of its anti-corrosion and its light weight but also of it special and superior characteristics.

2. Change of market

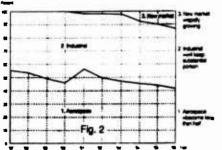
1) From serospace metal to industrial metal

For long time Ti has been mainly used in aerospace. But as the result of sudden change of world, production of military plane is losing the position, and growth of commercial plane is moderate one. We must try hard to develop the usage in the field of industry, and it seems to be possible. I made a forcast based on several information. (Fig. 1, 2)

Titanium application (history & forcast)



Change of contents



2) From special metal to popular metal

Also in the industrial field, Ti is now widely recognized and application is spreading. Especially, in these four years, construction and automotive use are in sight. Japan Titanium Society (JTS) began to classify the both usages as new items. (Fig.3)

3. Why Ti is chosen?

1) Until now

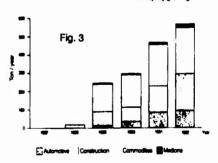
At first it may be helpful to classify the reason why Ti is used.

Application of TI at the beginning was for airplane, because of its high specific strength in medium or high temperature. Next for the chemical plant, thanks to the high corrosion resistance for chemical substance, then to the field of electrochemical anti-corrosiveness as an electrode material.

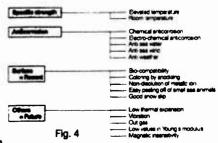
Afterward Ti's high resistance for see water attracted the intense attention for many kinds of application, and made a big success in the surface condenser for power station and desalination plant in these 15 years. (Fig.4)

Growth of new market in Japan

= Rapidly growing =



Reason of Ti application



2,660

From high or medium temperature to room temperature

Specific strength is one of the most important characteristics of Ti, and main classical application was in the atmosphere of high or middle temperature. New consumers' goods or automotive market is developing, because of its high specific strength in room temperature.

Main interest is automotive application, engine parts or body. But more popular usage as house ware or accessaries is also interesting because of its small but sure repeatness of demand.(Tab.1)

3) From special process condition to life area

Ti has been used in special process condition of chemical or electro-chemical plant. New way is along high corrosion or erosion resistance in sea water or sea wind affected zone, that is marine construction and building. (Tab.2)

4) Another characteristics

In addition to specific strength and light weight, Ti have many useful features like low heat expandability, low Young's modulus and stable surface condition. (Tab.3)

4. Ecological point of view

1) Economy and ecology

The reason why designer decided to apply Ti is now affected by the social situation. Economical feasibility may remain the most important issue to choose metal, but recently assesment of the effect by new metal (Ti for instance) must be reviewed from new view point, that is environment control and amenity.

The power condenser tubes should be appreciated from the view point of less air pollution, through higher heat transfer coefficiency. Modern application of Ti for automotive may contribute also for the same target.

Expansion of service condition-1

Tab.1 Specific strength = from Elevate of temperature to room temperature

Chara	cteristics	Aero	Marine	Automotive	Others
Elevated temperature	Movable machine parts	विधिक्षा ६०४		1	1 2 2
	Structural parts	Consulty 1			
Medium & room temperature	Movable machine parts		-Scattered		
	Structural parts				

Expansion of service condition-2

Tab.2 Anticorrosion = from Process condition to life area

Characteristics	Chemical	Power	Construction	Marine	Automotive
Chemical anticorrosion			*Factory roof *Duct		*Exhaust pipe *Tank rolley
Electro-chemical anticorrosion			*Electrode for protection		
Anti sea water		Condensers in power plants Tube sheet Desalination plants	0.48	, us	0 6 6 7 7 8 8 9
Anti weather					*Automobile outer shell *Door mirror *Muffler pipe

Utilization of special characteristics

Tab.	3 Recent	Felum
	Charcteristics	Typical application
Surface	Bio-compatibility	Watchshall Tiend Inplant material
	Non-disolution of metallic ion	Containers of liquors Thermos bottles Ultra pure water
	Slippery surface	Frons Rection group/press Rowering
	Easy peeing off of small sea animals	Screws Scoonietristinister Minesweepers Haliafetipa Management
Others	Magnetic insensitivity	• Electricis • Instrument wires
	Coloring by anodizing	Minister Minister Street signs
	Low values in young's modulas	Baltons Baltingstartytes Sparites
	Low thermal expansion	• Shopus • Shopus
	Vioration	

2) Rearrangement

Overall of these applications, it is possible to rearrange them along this point of view.

5. Air pollution

5.1 Energy

(power station, desalination plant, oil and gas exploitation)

1) Retubing

Not only in developing countries but also in industrialized countries demand for electric power is increasing. For this purpose new plant and high ratio of operation time is important. High reliability and high efficiency of TI tube is fully recognized and not only nuclear but also

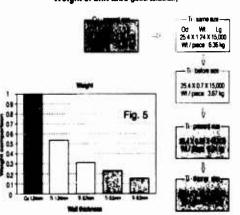
large scale thermal power station is now equipped with Ti condenser tubes. On the other hand, because of difficulty of finding new site for power station, re-powering is most popular countermeasure. In this case revamping of condenser with Ti tube is general concept. Both actions are connected with the less air pollution through improvement of fuel consumption.

Design concept and construction technique for retubing is polished to achieve less cost and shorter shut down time.

2) Thinner gauge tube

Long term experience teaches thinner gauge tubes is applicable. And 0.5mm thick tube is the most popular size for thermal or nuclear power station now. In the near future thinner gauge below 0.5mm thickness tube may be used for condenser tubes to improve efficiency and economy. (Fig.5)

Weight of unit tube (power contorner)



Ti's weak point is mainly its economy or high cost. Adopting thinner gauge it can be competitive to other metals like copper alloy. In fact in some new desalination plant, after long technical investigation and economical feasibility study to apply 0.5mm gauge Ti instead of 0.7mm, initial design was partially changed to Ti (0.5mm) from cupro-nickel(1.0mm).

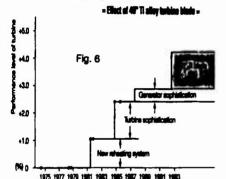
Also cell and tube type heat exchangers in merchant ships are now changing its material from copper alloy to 0.3mm thickness gauge Ti

The situation is the same with the plate type heat exchanger, adopting 0.4mm gauge sheet.

3) Ti alloy turbine blade

To utilize the longer steam turbine blade in power station is the foundamental method to increase efficiency. To encounter the centrifugal force, Ti's specific strength is advantageous. Many tests and researches were carried out and finally, three big thermal power stations were installed with the steam turbine of 40 inches long Ti alloy blade and achieved excellent efficiency improvement 1.6%, followed by less air pollution.(Fig.6)

History of improvement



4) TI cled tube sheet

To solve the cost and technical problem at once, composite material as clad, is important. In case of power condenser, how to keep high vacuum is critical facter for high performance of generation. Slow leakage along mechanical flange is most difficult problem for designer and operator.

Ti clad may be a best answer for this. Because Ti clad's base metal (steel) can be welded to steel drum easily and completely. Many condensers with Ti clad tube sheets are now operating in success. It will also contribute to minimize the accident blowing of boiler and loss of fuel. (Fig.8)

5.2 Automotive

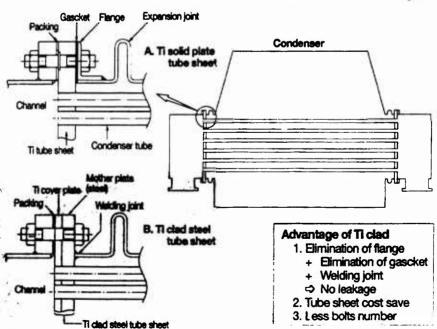
1) Most expecting field coming

From early time automotive is the target of Ti application, but nowadays not so many fruits are gained in this large market. (Tab.4)

Situation is changing now slightly and surely from the view point of environment control.

Ti clad steel as tube sheet

Fig. 8



Regulation (CAFE) is now under discussion to reduce the NOX outlet. There is two ways to attain this goal. One is to make car lighter, or make more efficient engine. For both purposes TI has many chances. (Fig. 7)

2) Engine parts

a: CAFE act may be an impact for automobile producers all over the world. Car makers and Ti rolled products makers are now cooperating to cope with the difficult theme. As the first step, racing cars and high grade sports cars is now constantly, installed with Ti engice parts (connecting rod, retainer, spring). From the view point of cost / performance, rotating or reciprocating parts are most expectable, especially power train.

 b: Automotive engine spring and under carrige spring is lighter than its specific weight ratio because of its high elasticity. In the case of spring,

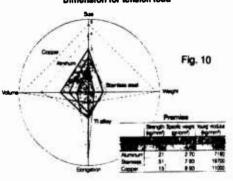
> Needs for automobile weight reduction and underlying factors.

Great impact of CATE to the transport of CATE

Ti's low young's modulus is essential to save the weight, because planner can reduce the number of turns of coil springs. (Fig.9)

c: Connecting rod made of Ti is a little bit heavier than that of aluminum, because specific strength in medium or room temperature is not superior, but Ti needs smaller space. This is a very important facter to design compact engine in limited space. (Fig.10)

Dimension for tension load



3) Outer panel and others

a: In autumn 1991, in Tokyo Motor Show, a Japanese car maker released some concept cars which have Ti side sills, aiming both light weight and anti-corrosiveness and recycling of raw materials. Technical capability (especially press formability) is checked and demonstrated for all automotive persons. (Fig.11)

Tab.4 Stage of automotive application = First step in =

	Part	Weight reduction	Racing	Concept	Limited high grade car	high grade car	Audinary car	Material	Technical theme
	Connecting rods	30% 1.1kg	- नक्ष	V : 17					Machinability Wear treatment
	Valves	40% 0.3kg	100		W/S			Ti - 6AI - 4V Ti - 1100	ibid
Engines	Valve springs	55% 0.7kg		TO NO.				Beta - C Ti - 6AI - 4V	Wear treatment
	Spring retainers	40% 0.2kg	极激	1.00				Tr 22V-4AI	Formability Wear treatment
Under- cerriage	Suspension springs	50% 5.3kg	T PIK Y	II.				Beta - C	Young's modulus Strength
Driv	e shafts	30% / 2.4kg						Beta - C	Strength Machinability
Fitting	s & others	40%				Partie	ily adopted	C/P	Thermal expension Ultrasonic transmission
Мо	otor bike		5.00			ICCCI Unde	r study	Ti - 15 - 3	Strength Wear treatment

b: Frame of car door mirror which have ultrasonic vibrating droplet cleaning system are also made of Ti for its anti-corrosiveness and suitable characteristics of vibration. (Fig.12)

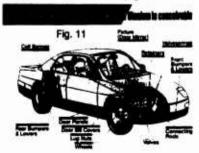


Fig. 12 Door mirror frame by Ti



Covered by water drop

Cleared by vibration

4) Development of manufacturing process

Rolling, forging, casting, extruding are general process to make Ti products, and now precision casting technique or powder metallurgy is in horizon. In Japan many Ti golf club heads are made by precision casting or super plastic forming. Powder metallurgy is advantageous process for near net shape (high yield of material and lower machining cost), is now struggling to find the proper market, its quality and cost image is becoming clear. (Fig.13)

5) Technical theme

- a: Surface hardness and anti-friction
- -- valve, spring.
- b: Good formability
 - -- connecting rod
- c: High young's modulus
 - -- pressure element, connecting rod
- d: Effective process
 - -- cast, forge, powder, extrusion super plastic

5.3 Marine

a: Dritting riser for petroleum exploitation is enjoying the high elasticity (Low YOUNG'S MODU-

LUS). A North Sea project has released the decision to apply Ti alloy for real project. In this field USA Ti people are expecting many chances and much volume of consumption, utilizing several of useful characteristics of Ti.

b: In case of screw we can expect to improve the propulsion efficient and anticavitation, because of its high elasticity and smoothness (no corrosion and emsion)

Both cases are also contributing to better environment and development.

5.4 Good snow slipperity

Ti roof is reported, after 5 years test, to have a good snow slipperity. Exact reason is not clear yet. But the continuation of smoothness of Ti roof surface must be effective. Please think of melting down method of snow, how much electric or fossil energy have been consumed.



Manifacturing method and procucts

Comples

(automotive)

Cost

Hip. Chilp

Hip. chilp

Hip. chilp

Hip. chilp

Fig. 13

Shope

Investigate Shope

American market

Fig. 13

6. Water pollution

6.1 Chlor-alkali process

For long time, in caustic acid production, coated Ti anode is the key technology to change the harmful amalgam process to ion-exchange membrane process, and contributed substancially to prevent the water pollution.

6.2 Power condenser

In case of copper alloy tube, some kind of substance is usually injected to protect condenser tubes from corrosion and sticking of small sea animals (so called fouling). Naturally this substance is also harmful for another sea animals. In case of all Ti made condensers, no injection of the anti-fouling substance is necessary, by more frequent ball cleaning system operation, compared with that of copper alloy tube which have softer surface. It is also one of the counter measures for sea water pollution.

Test in water inlet, screen, Ti shows potential material to minimize the sea animal sticking without any anti-fouling paint.

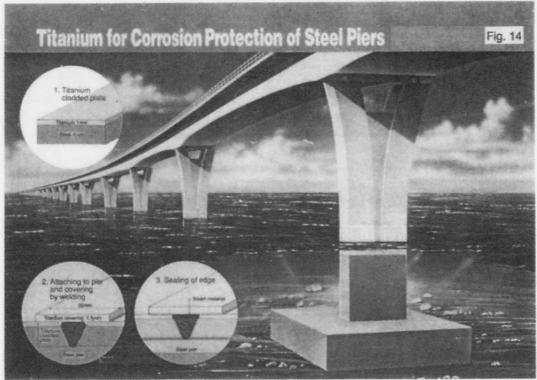
6.3 Marine construction and civil engineering

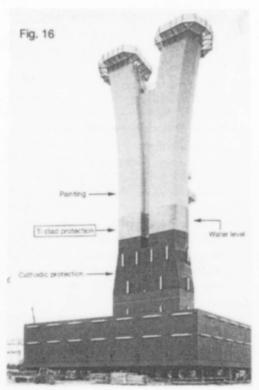
1) Bridge pier at sea

In this field long service life is one of the most important requirement. (Fig.15)

For this purpose many people come to know that Ti may be the best metal. But there were no example to assure the performance, then planner is afraid of technical problem hidden in the metal, and high initial cost. In spite of many theme to be solved, economically, technically, TTB(Trans-Tokyo-Bay) engineers decided three years ago to investigate the newly developed Ti clad covered protection system for tidal and splash zone of 12 steel piers. (Fig.14)

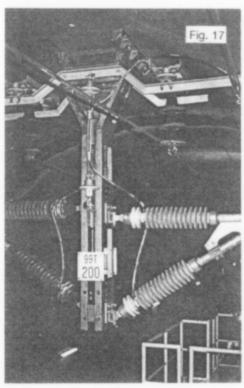
To settle and clarify all technical and economical problems such as galvanic corrosion, collision toughness, vibration toughness through test in laboratory and in site, it took one more year. Finally they decided to adopt the new method. Two giant piers were completed and now standing in the middle of Tokyo bay. We can expect more than 100 years life without maintenance. The new system attracted a world wide attention among protection engineers and marine construction engineers, as a perfect super long life protection system, at the same time gentle system to the earth. (Fig.16)





2) Railroad

In undersea tunnel, Ti hanger of trolly for high speed rail way (SHINKANSEN) is attached for the first time four years ago. After strict observation, railway men were deeply impressed and satisfied by the excellent performance compared with the conventional system, steel structure brazed and heavy coated. They are going to replace all hangers from steel to Ti. And in future, they have plan to apply it also in mountain tunnel. Next subjects of Ti in tunnel is messenger wire, in this case Ti clad (steel or copper) wire is necessary, because, Ti is inevitably handicapped by low conductivity. (Fig.17)



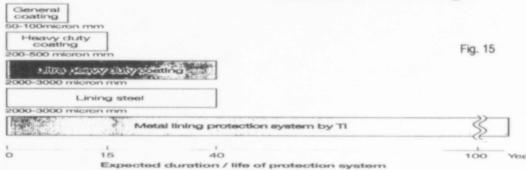
Anti-corrosive materials to protection ma terials

Before time, Ti is used as an anti- corrosive material, for cell and tube heat exchangers, plate type heat exchangers, chemical towers and vessels.

These markets are special and comparatively small. But demand for the protection system for corrosive metal as steel is much bigger. Then, my proposal is to divide the aim of Ti usage in two ways, anti-corrosive materials and protection materials. Because of its high cost, Ti as anti-corrosive materials must be limited, and we are obliged to develop the usage of Ti as protection materials.

Outline of protection system

= Expectation for Ti lining =



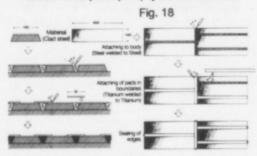
2,667

4) Method of protection

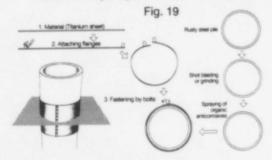
There is many kinds of method of protection by Ti. First group is direct method. Direct method means to protect steel or concrete by covering completely and separating them from sea water or air by seal weld or sealant. Second group is indirect method. Paint or resin is used usually and Ti sheet covers them to keep those organic material from mechanical damage and ultraviolet deterioration. This system is applicable for replacement of present protection system. To solve the cost problem and technical problem, thin gauge Ti and composite material(ti clad) is important. (Fig.18, 19)

- a: Titanium clad covering
 - -- Heavy duty use
- b: Titanium sheet covering
 - -- Medium duty use
- c: Titanium foil covering
 - -- Light duty or in air use

Anticorrosion (Waterproof) by titanium clad steel



Anticorrosion by using titanium sheets / Flange type



5) Development of Ti Clad production

Explosive method was dominating as the way of manufacturing clad. To get wider and longer and cheaper Ti clad, conversion method and rolling method are developing. Especially, we can get cheaper Ti clad by hot strip rolling with copper insert. It will contribute to the new devel-

opment of direct protection method. Base metal(steel) is essential as welding joint component to steel structure and toughness of outer cover.

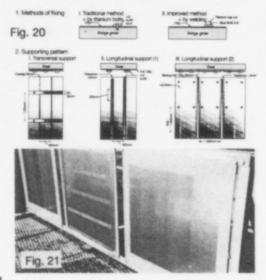
6) TI foil covering system

Painting is troublesome because of its chemical vapor and dangerous work on high foot step, and is becoming more expensive. Resin film with adhesives in rear side is used as sheet painting. Instead of resin film, we tried to use Ti foil. Thin Ti metal can completely shut out the two main deterioration factor of organics, invasion of water and ultraviolet ray attack. Theoretically, adhesives in dark, dry and not high temperature atmospher, is reported to have more than 100 years life. Ti foil with organic adhesive is of course very easy to attach to any kinds of structure. We can expect the very long life of organics, by prevention of ultraviolet ray and water or humidity. Results of test in site and laboratory is encouraging us. It will be very easy way for long life protection. (Fig.20, 21, 22)

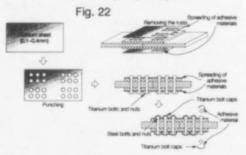
7) Economy

Of course, initial cost of Ti protection is higher than conventional method. In case of TTB project Ti system cost is about 1.3 times of that of conventional one. But as a long life cycle cost, Ti protection is more economical, and subsequently more ecological. It is not a dream to expect many steel structures are furnished with Ti protection system.

Supporting methods of titanium foils for protection



Protection of joint plate by titanium



6.4 Shipbuilding

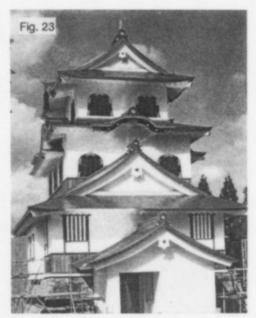
1) Double bottom tanker

Shipbuilding world is now involved in two big environment problems.

First is new regulation to use double bottom to stop the leakage of oil to sea, after sorrowful accident in North Atlantic Sea. Complicated double bottom tank is difficult to protect corrosion. Researchers are now looking for new anticorrosive steel or new protection system. For this Ti foil method is one of candi dates.

2) Restriction of harmful paint usage

Second is the sea water pollution by anti-fouling paint. To protect rapid corrosion and fouling, special paint is used for long time up to now. Recently, TBT(tri butyle tin) included in the paint is reported injurious for mankind through the



food chain. Maritime Organizationis ready to restrict the usage of TBT. Ti protection system just started, can help to solve this problem and water pollution. Of course another kind of paint is now proposed, Ti remains also fascinating material, in shape of clad, sheet or foil.

7. Paint free protection system

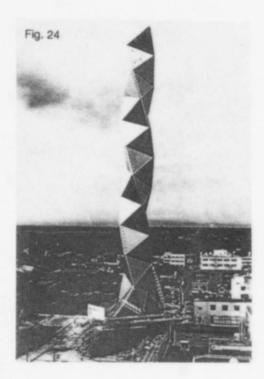
7.1 Architecture

1) Succeeding new market

As reported in last conference, in Japan many buildings are covered by Ti roof and or wall. Recently this tendency is expanding quickly and widely, obtained good reputation after many experiences. Results are of course very clear, no maintenance, no repainting, that is not harmful nor dangerous job.

2) Statistics of architectural use

Every year, JTS take statistics of Ti in building use. According to this statistics, about 40-50 buildings applying Ti as roof or wall or monument and 100-200 tons of Ti are consumed. Many roofs are made of welded system enjoy perfect watreproof with no maintenance. It is now becoming the sure market genre for Ti roll products.



3) Up date examples of building

a: Roof --aquarium, castle, private house, gymnasium long span, seaside,

b: Wall --office building

c: Exterior and interior material (Fig.23, 24)

4) Follow up research

JTS made a joint research to check the effect of Ti as a builduing use, and after that we are now surely convinced with the performance of Ti's ability of high anti-corrosiveness in any kinds of atmosphere, seaside, valcanic district, ot spring area. As for out of Japan I have no information of Ti used in this field, and I do not know the reason. They may have another philosophy or economical concept, or only technical and economical information is not enough.

5) Anodizing color

Some architects use Ti as rolled because Ti's proper color and textile is attractive. Ti can be colored by anodizing method, its tone is so natural and soft, some designers are favorable to use it as colored. Not only accessaries but some interior goods, tiles, street signs are made of colored Ti. One third of Ti roof and wall is colored. (Fig.25)



6) Economy

We haven't the clear criteria to adopt Ti as economical metal. But recent consensus to avoid difficult maintenance in high place or on sea, and to achieve free maintenance of building is wide spread, owner or architects seems to be easily and reasonably persuaded to use Ti as high grade long life material.

7.2 Tanks and pipings

Same concept and system will be applied to general tanks and piping in wide range. In isolated southern island large oil tanks are made of solid Ti, free from maintenance.

Ti bellows become perfect countermeasure for corrosive liquid, its high elastecity is much prefarable.

8. Bio-compatibility

1) Implant

Because of its lightness and non-toxicity, Ti artficial bones is replacing stainless, or Ni-Cr steel. Main technical theme is how to harden the surface of metal, and how to make the compatibility to organic cell. Pace makers and artificial teeth of Ti are also famous application.

New alloy and surface treatment is searched to avoid any potential trouble in human body.

2) Fashion goods

Frames of eye glasses, watch cases of Ti is comfortable not only of its light weight but also of its gentleness for human delicate skin. It is better to consider more factor than specific strength of material, say, space efficiency, surface hardness, bio-compatibility, or flexibility of structure. Eye glasses frame get a firm position as a material, satisfying almost all of these factors.

9. Health and safety promotion

1) Sports goods and others

Many sports goods made of Ti are now in full blossoms. New advanced technology is hired prior to general industry, for instance precision casting, super plastic forming, powder metallurgy. (Fig.26)



- a: Motor sport -- chain, valve connecting rod
- b: Cycle sport -- frame, gear
- c: Marine sport
 - -- just finished AMERICA'S CUP NIPPON CHALLENGE used many metal parts made of Ti alloy for instance chain plate, screw, rudder

2) Extention of TI electrode usage

Starting from the chlor-alkali process, Ti electrode is now expanding its application. Cathode for copper foil production roll is expelling that of stainless roll. Anode for brazing process in steel plant is now under study. Recently new type of water cleaner which produce the alkali water is widening the demand quickly, and some of the electrode is made of Ti.

10. Deep sea research

Academic research equipment for environ mental control

Long discussion (technical and economical) is now finished, Ti pressure capsule or frame and cable unit is now essential material for deep sea exploration.

2) Example

- a: Manned vehicle (Fig.27)
 - -- 6500 meter depth pressure vessel, frame
- b: Unmanned vehicle
 - -- 3300 to 10000 meter depth pressure vessel, frame, cable



11. Strategic map

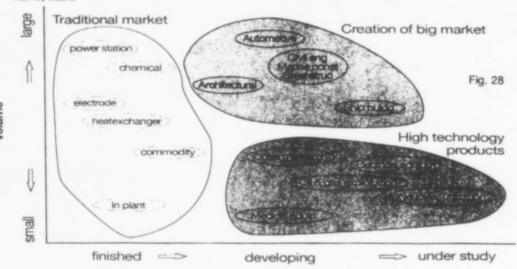
Bigger market is now developing, car, constrcution, computer, civil engineering. (Fig.28)

- a: Traditional market
 - Cost down and quality up to keep competitiveness to other metals
- b: Big developing market
 - Big cost down will response to big volume process technique is important
- c: High technology market
 - -- New alloy, high technique is necessary

12. Conclusion

Ti is not yet fully cultivated metal from view point of application. Now Ti becomes familiar metal in usual life, as a raw material of consumers' goods. Ti have many chance to jump up to major metal.

END



Development

2,671

Application of Near Beta Titanium Alloys for Turbine Blades

A. Takemura *, Y. Ashida *, H. Ohyama *, A. Morita **, S. Hattori ** K. Tani ***, A. Hasegawa ****, T. Matsumoto ***

- Materials Research Lab., Kobe Steel, Ltd. Vak i nohamacho, Chuo-ku, Kobe, 651 Japan
- Mechanical Engineering Research Lab., Kobe Steel, Ltd. Takatsukadai, Nishi-ku, Kobe, 651-22 Japan
- Engineering Dept. Steel Casting & Forging Plant, Kobe Steel, Ltd.
- Araicho Shinhama, Takasago, 676 Japan Nagoya Research Sect., Kobe Steel, Ltd. Kinjyocho, Kita-ku, Nagoya, 462 Japan

Abstract

In this study, two near beta titanium alloys, Ti-10V-2Fe-3A1 (Ti-10-2-3) and Ti-5A1-2Sn-2Zr-4Mo-4Cr (Ti-17), were investigated and compared with Ti-6A1-4V (Ti-6-4) as a blade material. Ti-10-2-3 was superior to the two other titanium alloys in strength-toughness combination, fatigue, erosion resistance and forgeability. A 20-inch Ti-10-2-3 near net shape model blade was made, which had uniform mechanical properties from root to airfoil.

Introduction

The application of Ti-6-4 for steam turbine blades has increased in recent years [1]. While Ti-6-4 is a widely used and reliable titanium alloy, higher strength and better forgeability are required to improve performance and cost efficiency of turbine blades.

Near beta titanium alloys, known to have a high strength per weight ratio and a low hot flow stress, are expected to alternate with Ti-6-4 in aerospace use[2]. In this study, two promising near beta titanium alloys, Ti-10-2-3 and Ti-17, were investigated and compared with Ti-6-4 as a blade material. The target mechanical properties were a tensile strength ≥ 115 kg/mm² and a fracture toughness≥ 150 kg/mm^{1/2}.

2. Experimental Procedure

2.1. Material

In this study two near β alloys, Ti-10-2-3 and Ti-17, and an $\alpha + \beta$ alloy, Ti-6-4, were compared. For each alloy a VAR double melted 1 ton ingot was break-down forged in the β region and forged into billets in the $\alpha + \beta$ region. These billets were used as an initial material for the following examination and blade forging. Table 1 shows the chemical composition of the three alloys.

Chemical composition of the three alloys (Weight %)

Alloy	A1	V	Fe	Zr	Sn	Mo	Cr	C	0	N
Ti-10-2-3	3. 24	9. 64	1. 99	_	-	-	-			. 0070
Ti-17	5, 08	-	. 045	2, 09	2.04	3.99	3, 98	. 005	. 101	. 0055
Ti-6-4	6. 15	4. 19	. 201	-	-	_	-	. 005	. 148	. 0058
				Titonius	192					

Science and Technology Edited by F.H. Froes and I. Caplan The Minerals, Metals & Materials Society, 1993

2.2 Heat Treatment

The tensile properties and fracture toughness of isothermally forged and heat treated pan cakes (18mm t .200mm dia.) were examined, and the appropriate heat treatment conditions were determined. Isothermal forging was done with a 400-ton isothermal forging press. Table 2 shows the isothermal forging conditions [3].

Table 2 Isothermal forging conditions

Alloy	Temperature	Strain rate
Ti-10-2-3	750 ℃	5×10 ⁻³ s ⁻¹
Ti-17	830 ℃	$5 \times 10^{-3} \text{ s}^{-1}$
Ti-6-4	900 ℃	$5 \times 10^{-3} \text{ s}^{-1}$

The investigations were carried out in the range of heat treatment conditions shown in Table 3. The tensile strength of two near β alloys varied from 115 kg/mm² to 140kg/mm² in this condition. The strength-toughness and strength-ductility combinations of each alley were compared.

Table 3 Heat treatment conditions

Alloy	Solution Treatment	Aging
Ti-10-2-3	740 ~770 °C, 1h, AC or VQ	480~525 ℃, 8h
Ti-17	800 ~840 °C, 4h, AC or VQ	600~620 ℃, 8h
Ti-6-4	Annealing: 700 °C. 1h. AC	

2.3 Evaluation

A comparison between Ti-10-2-3, Ti-17 and Ti-6-4 was done on fatigue strength, erosion resistance, damping capacity and Young's modulus. Isothermally forged pancakes heat treated under selected conditions were used. The tensile strength of Ti-10-2-3 and Ti-17 were controlled at the level of 115kg/mm^2 . The fatigue strength at room temperature in air was investigated by the axial tension method, and also in 80 °C salt water by the rotating bending method. The erosion resistance was evaluated by droplet erosion weight loss at 55 °C and the droplet velocity was 400m/sec. The damping capacity and Young's modulus were measured by an internal friction measurement apparatus at room temperature. Damping capacity was represented as a quality factor (Q -1). The effects of temperature on flow stress were investigated at a strain rate of 10^{-2} /s by the compression test.

On the basis of above results the suitable alloy for turbine blade was selected from among the three alloys and submitted to near net shape forging of model blade and evaluation.

2. 4. Manufacturing and evaluation of near net shape blades

The dimensions of the model blade were 2/5 of an actual 40-inch blade. The length of the blade was about 20inches (500mm). The near net shape forging of the blade was done with a 3000-ton isothermal forging press at the Takasago plant. The forging die was made of Ni-base super alloy. The atmosphere for heating and forging was air. Details of the forging procedure have already been reported[4]. The forged blades were heat treated and cooled in air. The surface condition (oxygen rich layer), macro and micro structures, tensile properties, and fracture toughness were examined.

3. Results

3. 1. Comparison of Ti-10-2-3, Ti-17 and Ti-6-4

Fig. 1 and 2 show the strength-toughness and strength-ductility relation of the three alloys. Ti-10-2-3 showed better strength-toughness and strength-ductility combination than Ti-17 in a tensile strength range of 115kg/mm² ~140kg/mm². The heattreatment conditions in which the target mechanical properties were attained were:

> Ti-10-2-3: ST: 770°C/1h/AC, A: 520°C/8h/AC ST: 800°C/4h/AC, A: 620°C/8h/AC

The results of fatigue at room temperature in air are shown in Fig. 3. Ti-10-2-3 demonstrated a higher fatigue strength than Ti-17 at the same tensile strength The results of fatigue at 80 °C in salt water are shown in Fig. 4. Ti-17 had a little higher fatigue strength in 80°C salt water than Ti-10-2-3 at the same tensile strength of 115kg/mm².

The result of the droplet erosion test are shown in Fig. 5. The weight loss with droplet erosion was the same level for both near β alloys' and smaller than for

The values for Young's modulus and the damping capacity are shown in Table 4. The damping capacity and Young's modulus for Ti-10-2-3 and Ti-17 were a little lower than for Ti-6-4 but the differences are small.

Table 4 Young's modulus and quality factor

Alloys	Young's modulus/ kgf/mm ²	Quality factor/Q -1
Ti-10-2-3	10.4×10^{3}	3 ×10 ⁻⁴
Ti-17	11. 1×10^{3}	2 ×10 ⁻⁴
Ti-6-4	11.2×10^{3}	4×10^{-4}

The effects of temperature on flow stress are shown in Fig. 6. Ti-10-2-3 had a lower flow stress than Ti-17 and Ti-6-4 at the same temperature but the same flow stress at a lower temperature.

Ti-10-2-3 proved superior to Ti-17 in the strength-toughness combination and forgeability, although the fatigue strength and erosion resistance were almost the same for both alloys. The Young's modulus and quality factor of Ti-10-2-3 were comparable to those for Ti-6-4.

On the basis of the above results, Ti-10-2-3 was selected from among three alloys for application for turbine blades.

3.2 Manufacturing and evaluation of the near net shape blades
Near net shape blades were formed in a single heat cycle of isothermal forging. The finished turbine blade of Ti-10-2-3 is shown in Fig. 7. No crack or any other defect was observed after shot and pickling. The surface oxygen rich layer of the blade in its forged and heat treated condition is shown in Fig. 8. The thickness of the oxygen rich layer is only $70\,\mu$ m, because of the single heat cycle of isothermal forging and the relatively low temperature of the forging and heat

Fig. 9 shows the macro structures of the root and air foil. Uniform and smooth metal flows can be observed. Fig. 10 shows the micro structures of the rootand air foil. The primary α grains of the root and air foil are almost the same in shape and distribution.

Table 5 shows the mechanical properties of the root and airfoil. The tensile strength and fracture toughness clear the target.

Table 5 Mechanical properties of Ti-10-2-3 model blade

Position	Yield Strength kgf/mm'	Tensile Strength kgf/mm ¹	Fracture Toughness kgf/m³/²
Airfoil	107	118	193 (KQ)
Root	109	118	213

4. Summary
Ti-10-2-3 is superior to Ti-17 in the strength-toughness combination and forgeability, although the fatigue strength and erosion resistance are almost the same for both alloys.

The Young's modulus and quality factor values for Ti-10-2-3 are comparable to

those for Ti-6-4. A 20-inch Ti-10-2-3 near net shape model blade was made by isothermal forging. The mechanical properties and micro structure of the Ti-10-2-3 model blade are uniform from root to airfoil.

<u>Acknowledgements</u>
This research and development was performed under the sponsorship of the Advanced Nuclear Equipment Research Institute (ANERI) under contract with the Agency of Natural Resources and Energy, Ministry of International Trade and Industry, Japan.

References

[1] R. I. Jaffee: Titanium Steam Turbine Blading, Workshop Proc., EPRI, (1988)

[2] R. R. Boyer and H. W. Rosenberg: Beta Titanium Alloys in the 80's, TMS-AIME, (1984)

[3] A. Hasegawa, S. Ishigai and T. Matsushita: Proc. 6th Int. Conf. on Titanium (1988) 1263

[4] A. Morita, S. Hattori, K. Tani, A. Takemura and Y. Ashida: ISIJ Int., 31(1991)827

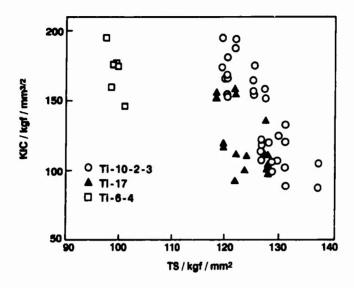


Fig. 1 Relation between tensile strength and fracture toughness

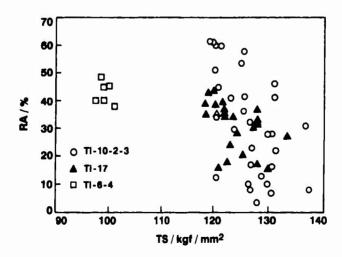


Fig. 2 Relation between tensile strength and reduction in area

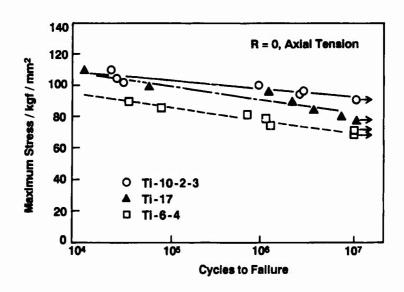


Fig. 3 S-N curves of fatigue in air

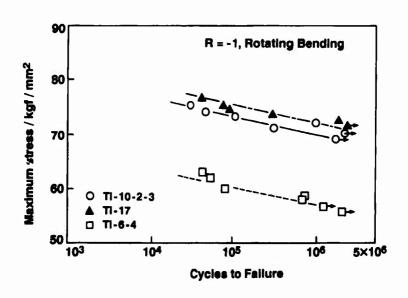


Fig. 4 S-N curves of fatigue in 80 °C salt water

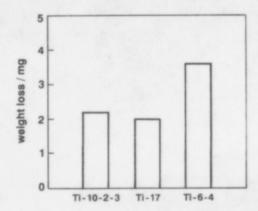


Fig. 5 Droplet erosion at 55°C droplet velocity 400m/s exposure time 30min.

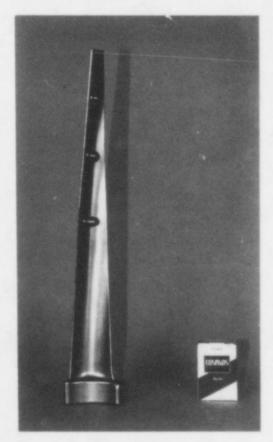


Fig. 7 Isothermallyforged 500mm Ti-10V-2Fe-3Al model blade

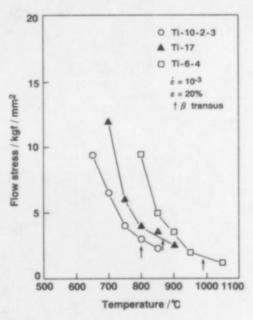
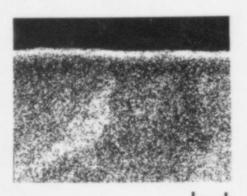


Fig. 6 Effects of temperature on flow stress



100µ yer of blade

Fig. 8 Oxygen rich layer of blade surface as forged and heat treated condition





Root

Fig. 9 Macro structure of Ti-10V-2Fe-3A1 model blade

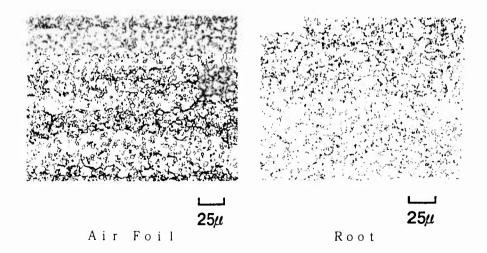


Fig. 10 Micro structure of Ti-10V-2Fe-3Al model blade

The Development of γ/α_2 Titanium Aluminides for Exhaust Valves

W.E. Dowling, Jr., J.E. Allison and A.M. Sherman

Ford Motor Company, Research Laboratory SRL Room S-2065, P.O. Box 2053 Dearborn, MI. 48121-2053

Abstract

The recent development of γ/α_2 titanium aluminides in the aerospace community have also provided an excellent material alternative for hot components in gasoline engines. The low density combined with elevated temperature strength similar to that of Ni-base superalloys make TiAl-based alloys very attractive for high performance exhaust valve applications where high temperatures preclude the use of conventional titanium alloys. Lighter weight valve train components improve performance and permit the use of lower valve spring loads thus reducing friction and increasing fuel economy. However, the difficult fabricability and a perception that TiAl alloys are high cost, low volume aerospace materials must be overcome in order to permit consideration for use in high-volume automotive applications. This paper provides a comparison of relevant material properties for exhaust valves among several alternatives. The density of TiAl alloys is lower than Ti alloys with creep and fatigue properties equivalent to IN-751, a current high performance exhaust valve Manufacturing alternatives for TiAl-based valves, and technical material. issues impeding development and implementation of TiAl-based exhaust valves are also discussed.

Introduction

The need for more fuel efficient automobile engines has lead to serious consideration of materials that are generally considered too exotic and expensive for the automotive industry. The use of γ -based titanium aluminides for exhaust valves is one example. Within certain limits, the increased cost of such components may be justifiable when measured against alternate means of achieving fuel economy improvements, reduced vehicle emissions and/or performance enhancements. One of the most promising applications of light weight materials is in the valve train, where lowering inertial weights leads directly to significant increases in fuel economy and/or performance (engine Conventional titanium alloys such as Ti-6Al-4V are widely viewed as a Likewise, elevated temperature cost-effective intake valve material (1). titanium alloys have been shown to be cost effective and durable exhaust valve However, because exhaust valves can experience temperatures materials. exceeding the normal use temperatures for traditional titanium alloys, durable exhaust valves can only be assured after significant engine testing. In some current and future engine classes exhaust valve temperatures exceed those at which conventional titanium alloys can confidently be utilized.

> Titanium '92 Science and Technology Edited by F.H. Froes and I. Caplon The Minerals, Metals & Materials Society, 1993

A strong candidate material for lightweight exhaust valves in such engines are alloys based on the γ/α_2 -titanium aluminide system. These materials can compete well with other material alternatives developed for elevated temperature valves in terms of both cost effectiveness and performance. This paper will review the benefits of TiAl-based valves, provide an overview of the design requirements such valves must meet, and compare the relevant physical and mechanical properties with other lightweight and conventional exhaust valve materials. Low-cost manufacturing and implementation issues will be described.

Lightweight Valve Benefits

In contrast to the steel valves widely employed in production automobile engines, titanium aluminide valves offer the advantages of higher operating temperature capability and lighter weight. As mentioned above, higher temperature capability makes light weight exhaust valves a possibility in applications where high temperatures preclude the use of titanium. Moreover, when manufacturing processes are fully developed titanium aluminide valves may be less expensive than currently used high temperature valves made of nickel based superalloys.

There are three benefits which may be available by the use of light weight engine valves: higher fuel economy, better performance and reduced noise and The magnitude of each has been analytically calculated and experimentally confirmed. These benefits are possible because lighter weight valvetrains require lower valve spring loads to achieve the same level of The mechanical friction which must be overcome in order to operate the valvetrain is proportional to the spring load, reductions of which thus improve engine efficiency (fuel economy). The size of this benefit is highly specific to the particular engine and valvetrain configuration. However, in valvetrains not employing roller follower mechanisms (an alternative low friction design) gains ranging between 2 and 5% have been predicted (1-2) through the use of titanium or ceramic valves both of which are about 40% lighter than steel. Titanium aluminide valves would offer at least this level of weight savings. Performance improvements involve an increase in the high speed capability of the valvetrain (ability to operate at engine rpm) and/or more aggressive valve events (faster opening and closing of the valves). improve these operating characteristics with current valvetrains requires an increase in valve spring loads. Reducing the weight of the valves can produce the same benefits. One experimental measurement (1) indicated that the high speed capability of a valvetrain increased by more than 600 rpm through the use of titanium valves. In another study (2), it was calculated that the performance improvement could be as high as a 5% increase in power output. The use of light weight valves thus produces the opportunity to trade off improved performance with better fuel economy. Finally, reduced spring loads lower the noise generated by the impact of the valves closing against the valve seats and in some designs, lighter valves reduce unbalanced shaking forces generated by the motion of the valvetrain components. The magnitude of these benefits should be proportional to the weight and spring load reductions. subjective evaluations have indicated reductions in the noise produced by engine with lighter weight valves, but due to the complex and numerous sources of noise in a running engine no definitive measurements have yet been reported.

Design Requirements

Engine exhaust valves experience severe operating conditions which include elevated temperatures, corrosive environments, cyclic and creep loading and wear. This can potentially lead to a number of failure modes illustrated in Figure 1. The determination of the suitability of a material for an exhaust

valve is complicated by the fact that exhaust valve materials are often selected based on rules of thumb and what has previously worked in similar engines (the carry-over design approach) all coupled with extensive durability testing. Thus detailed, quantitative information concerning actual valve material requirements is often difficult to obtain.

One of the most important issues in valve material selection is the valve temperature. For exhaust valves in spark ignited gasoline engines the maximum temperature occurs at the valve stem/underhead blend area (Figure 1). These maximum temperatures are highly engine dependent but typically range from 650 to 800 C, for conventional austenitic steel exhaust valves. Higher temperatures necessitate the use of more expensive Ni-base superalloy valves. A desire for higher temperature exhaust valves has provoked great interest in TiAl-based valves as a lightweight alternative for temperatures greater than the capabilities of conventional titanium alloys.

Stresses also vary with location in the valve. Under normal operating conditions, the highest stresses are in the valve underhead region (A in Figure 1) and the seat area and are in the range of 35-70 MPa. These stresses are, however, highly dependent on valve geometry, combustion gas pressure and alignment (3). Creep deformation can occur in this region if the creep strength of the material is inadequate. Fatigue can occur in the stem/blend area (location B in Figure 1) where high temperatures can also occur. Under operating conditions where the valve is properly aligned with the valve seat, stresses in this region are less than 20 MPa (4). However, when significant misalignment occurs due to such factors as seat distortion, the bending stresses can rise to 100-200 MPa (4,5).

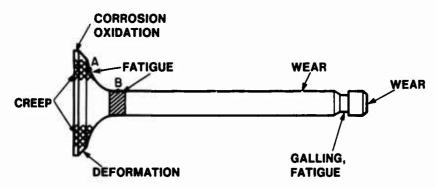


Figure 1. Potential valve failure modes.

Deformation in the valve seat region is also a serious issue. For valve material selection hot hardness is often used as a measure of valve seat peening resistance. Where hot hardness is insufficient, the application of thick hardface coatings such as Stellite or WC is an option, at an additional cost penalty. In addition the seat area is susceptible to corrosion/oxidation. Wear is an important issue in both the stem region of the valve as well as at the valve tip. This is most often solved using wear resistance coatings and hardened steel tips for steel and titanium valves.

An obvious question with regard to brittle materials like TiAl alloys is whether the low ductility of these materials precludes them from being serious valve candidates. At present, there are no firm guidelines for usage of low-ductility materials. However, there are no significant assembly deformations which necessitate high room temperature ductility and service stresses are generally not thought to be high enough to cause brittle failure in TiAl

alloys. The largest strain a valve needs to accommodate is from seating onto a misaligned and/or distorted seat. The main requirement is consistent mechanical properties from component to component. These factors combined with the extensive data base on ceramic valves (5,6) suggest that TiAl alloys are reasonable candidates for exhaust valves. However, extensive component development and durability testing will be required.

Material Property Comparison

As described previously, in order to be a promising exhaust valve candidate a material must meet many stringent physical and mechanical requirements. this section, relevant physical and mechanical properties of two common exhaust valve materials and three lightweight exhaust valve material candidates are compared. The materials are 21-2N an austenitic valve steel, IN-751, IMI-834 an example of a high temperature titanium alloy (either Ti-6242S or Ti-1100 could also be used), Si₃N₄ ceramic and the wrought TiAl alloy Ti-48Al-1V-0.2C (att) which is an early version of γ/α_2 titanium aluminide alloys. Table 1 lists the density, thermal conductivity, elastic modulus and coefficient of thermal expansion (CTE) of each material. An optimum exhaust valve material would have the following: a low density for minimum valve mass; high thermal conductivity to reduce valve temperature and temperature gradients, thereby increasing the valve operating range and decreasing thermal stresses; low CTE to reduce thermal strains; and a modulus which is low enough to enable valve sealing on a distorted seat, yet with adequate stiffness for good valve train dynamics. TiAl-based materials have a lower modulus and higher CTE than silicon nitride with a better combination of all of these physical properties than either common exhaust valve material (21-2N or IN-751) and significantly higher thermal conductivity than conventional titanium alloys.

Table 1. Physical Properties of Exhaust Valve Materials

Material	Density (g/cc)	Thermal Conduct 25 C	(W/m-K) ivity 760 C	Young's Modulus 25 C	(GPa) 760 C	CTE (70-760 C) (μπ/π/ C)
21-2N	7.7		25	200		18.4
IN-751	8.3	12	23	210	150	14.9
TiAl-based	3.9	22	28	170	145	12.2
IMI-834	4.5	7	16	114		9
S13N4	3.2	38	22	310		3.8

Mechanical properties often evaluated for valve materials are tensile and yield strength, elongation, stress for 1% creep strain in 100 h, fatigue strength and hardness from room temperature to the maximum use temperature. Table 2 shows literature values of these properties (except hardness) for the five exhaust valve materials previously described. The tensile properties are used as an initial evaluation of a candidate material. TiAl alloys have lower room temperature tensile properties than all of the other candidates except $\rm Si_3N_4$ (silicon nitride tensile strengths are an average value). However, at 815 C the tensile properties of TiAl surpass both 21-2N and IMI-834 and are similar to IN-751 and silicon nitride. However, of more relevance to use as an exhaust valve are the fatigue and creep properties of the candidate materials. γ/α_2 titanium aluminides have similar room temperature fatigue characteristics to all the other materials and superior elevated temperature creep and fatigue properties to 21-2N and IMI-834 and nearly equivalent properties to IN-751.

Table 2. Mechanical Properties of Exhaust Valve Materials

	(°C)	21-2N (7,8)	IN-751 (7,8)	TiAl-based (9,10,11)	IMI-834 (12)	Si ₃ N ₄ (13,14)
Y.S.	21	710	630	300-550	890	
(MPa)	760	280	450		280	
	815			240-400		
U.T.S.	21	1040	1170	350-600	960	524
(MPa)	760	400	550		420	
	815			300-500		510
Plastic	21	7	25	0.5-2.5	5	
Elongat- ion	760	16	10		50	
(%)	815			>25		
Smooth	21		520	275-450	425	400
Bar Fatigue	760	175			150	
Strength 10 ⁷ (MPa)	815		275	175-250		
100 Hr	732	130	330			
1% Creep (MPa)	760				55	
	815		175	150	35	

Figure 2 shows hardness as a function of temperature for 21-2N, IN-751 and three binary Ti-Al alloys (14). Hardness is used as an indicator of the resistance to valve seat peening and wear. The hardness of Ti-Al alloys is very dependent upon composition with lower aluminum contents having a higher hardness at all temperatures tested. The hardness of all the binary Ti-Al alloys examined is greater than 21-2N and the Ti-47.5Al only slightly reduced to IN-751. However, the use of Ti-Al alloys with aluminum contents as low as 45.5 at may be precluded because of significantly reduced ductilities. The physical and mechanical properties of γ/α_2 titanium aluminides are thus comparable to IN-751 and superior to IMI-834 and 21-2N for high temperature exhaust valve applications with the potential to reduce valve mass by approximately 50% relative to IN-751 and 21-2N valves.

Manufacturing Issues

Traditionally, valves are fabricated by either hot forging a complete valve blank or by inertial welding a hot forged valve head to the stem. Currently, this technology will not be suited to manufacturing of TiAl-based valves because of its poor hot forgability and the high cost of isothermal forming. Several alternative manufacturing technologies which are currently under evaluation for titanium and titanium aluminide components and that would be applicable to valves are investment casting (15,16), permanent mold casting (17) and reactively-sintered elemental powders (18). All of these processes present cost/property tradeoffs and process selection which will depend on the property requirements necessary to produce a durable valve for a given engine. Valves processed by any of these routes can be fabricated in either a one-piece

or two-piece configuration with a valve stem of TiAl-based material or some other alloy (e.g. titanium) selected on the basis of cost and performance.

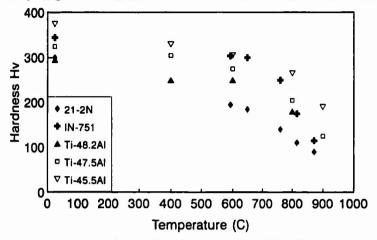


Figure 2. Hardness as a function of temperature.

The ability to routinely maintain alloy chemistry within a narrow range (46 to 48 at Al) of aluminum content may be a stumbling block in the production of high volume components. Along with chemistry maintenance a heat treatment schedule must be developed that will produce consistent properties over the range of alloy chemistries produced. A desired high ductility microstructure may necessitate heat treatment in the $\alpha + \gamma$ phase field (Figure 3) with approximately a 50/50 phase mix +/- 25%. If the heat treatment were to deviate outside these bounds, excessive grain growth, and hence poor properties could Box A in Figure 3 illustrates narrow chemistry control and the subsequent large heat treatment window available to satisfy the α/γ volume fraction constraints. Box B in Figure 3 demonstrates the much smaller heat treatment window available if the full 46 to 48 at% Al range were utilized in processing. If the alloy chemistry window were 1 at& wider it would be impossible to heat treat all components at the same temperature and stay within the phase fraction bounds outlined above. Hence, the ability to control alloy chemistry and heat treatment will be key to low/cost high volume manufacturing of valves.

Implementation Issues

From a property perspective, the material comparison above indicates that Ti-Al alloys are viable candidates for exhaust valves. However, as previously pointed out, a key technical issue which must be understood is whether brittle materials such as ceramics and TiAl can be used in high production volume engine applications. The level of tensile ductility, or perhaps more importantly, resistance to notched fatigue and impact, for successful valve applications must be determined. Analytical efforts as well as extensive durability testing will be required.

More important than performance concerns are issues related to the cost effective manufacture of high volumes of components. For a typical engine, as many as 1-2 million exhaust valves are required annually. At a weight 30 g per valve this results in approximately 80,000 kg/yr of input material (assuming a 75% material efficiency). To supply such materials and components, major investments in manufacturing process development and capital equipment are required. Because of the difficulty in obtaining long range commitments from

automotive manufacturers such investments are not often made. Despite this fact, significant commitments have been made by select members of the advanced materials community (15-18) to develop high volume manufacturing capability of titanium aluminides for the automotive market. This suggests that these material and component suppliers believe that such technology is a good investment.

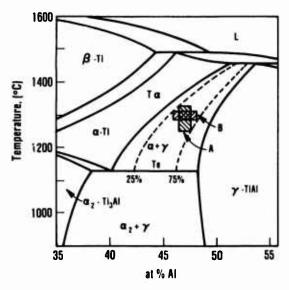


Figure 3. Ti-Al phase diagram.

It is clear that the cost of γ/α_2 titanium aluminide exhaust valves will exceed those of conventional austenitic steel valves. However, pressure for increased engine performance and enhanced fuel economy may lead to a greater demand for lightweight valves with improved temperature capability. TiAl valve technology will also have to compete with alternative means of accomplishing the performance and fuel economy improvements demanded by competitive and legislative pressures.

Summary

The physical and mechanical properties of γ/α_2 titanium aluminides make them an excellent candidate material for exhaust valves in gasoline engines. The low density combined with elevated temperature strength similar to that of Ni-base superalloys make TiAl-based alloys very attractive for high performance exhaust valve applications where high temperatures preclude the use of conventional titanium alloys. However, the low ductility, difficult fabricability and a perception that TiAl alloys are high cost, low volume aerospace materials must be overcome in order to permit consideration for use in high-volume automotive applications. Low ductility concerns can be overcome with extensive durability testing and modelling. Fabrication issues need to be addressed through commitment to develop a manufacturing process that will produce a cost effective and functional titanium aluminide for exhaust valves, rather than the best titanium aluminide at any cost.

References

 J.E. Allison, A.M. Sherman and M.R. Bapna, "Titanium in Engine Valve Systems", <u>Journal of Metals</u>, 39 (2) (1987), 14-17.

- R.Southam et al., "Analysis of Potential Improvements in Engine Behavior Due to Ceramic Valve Train Components", SAE Paper 900452, (Warrendale, PA: Society of Automotive Engineers, 1990).
- W.P. Giles, "Fundamentals of Valve Design and Material Selection", SAE Paper 660471, (Warrendale, PA:Society of Automotive Engineers, 1966).
 R.P. Worthen and D.G. Rauen, " Measurement of Valve Temperatures and
- Strains in a Firing Engine," SAE Paper 860356, (Warrendale, PA:Society of Automotive Engineers, 1986).

 5. R.R. Wills and R.E. Southam, "Ceramic Engine Valves", Ceramics Materials and Components for Engines, ed. V.J. Tennery, (Columbus, OH:ACS Inc., 1988)
- 1429-1437.

 6. R.P. Worthen and A.E. Pasto, "Ceramic Engine Components", SAE Paper 881150, (Warrendale, PA:Society of Automotive Engineers, 1986).
- 7. SAE Handbook, SAE J775 Jul80.
- 8. <u>Valve Division Handbook for Internal Combustion Engine Valves</u>, (Cleveland, OH:TRW Valve Division, 1987).

9. W.E. Dowling, W.T. Donlon, B.D. Worth and J.E. Allison, "The Effect of

- Microstructure and Carbon on the Mechanical Behavior of the γ/α₂ Alloy Ti-48Al-1V-0.2C (att)", this proceeding.
 10. W.E. Dowling, B.D. Worth, J.E. Allison and J.W. Jones, "The Influence of Microstructure on the Mechanical Behavior of γ/α₂ Titanium Aluminides",
 - Microstructure Property Relationships in Titanium Aluminides and Alloys, ed. Y-W. Kim and R.R. Boyer, (Warrendale, PA:TMS,1991) 123-134.
 11. B. London and T.J. Kelly, "A Preliminary Srudy of the Microstructure Property Relationships in Cast γ-Titanium Aluminide4 Alloys", Microstructure Property Relationships in Titanium Aluminides and Alloys, ed. Y-W. Kim and
- 12. J.E. Allison and J.V. Lasecki, unpublished research.

R.R. Boyer, (Warrendale, PA:TMS, 1991) 285-295.

- M. Masuda et al., "Fatigue Behavior of Sintered Silicon Nitride under Tension-Compression Cyclic Stress", (Paper presented at the 1988 TMS-AIME Annual Meeting).
- 14. T. Soma, M. Matsui and I. Oda, "High Temperature Tensile and Torsional Strengths of Sintered Silicon Nitride", (Paper presented at The International Workshop for Advanced Materials Technology-Ceramics II, 1987).
- S. Mitao, S. Tsuyama and K. Minakawa, "Effects of microstructure on the mechanical properties and fracture of γ-base titanium aluminides", Materials Science and Engineering, A143 (1991) 51-62.
 Y. Nishiyama et al., "Development of a Titanium Aluminide Turbocharger
- 16. Y. Nishiyama et al., "Development of a Titanium Aluminide Turbocharger Rotor", 1987 Tokyo Gas Turbine Congress, (Tokyo, 1987) 263-270.
 17. Y. Mae, "Development of Titanium Die Casting", Metallurgical Review of
- MMIJ, 8 (1) (1991), 113-118.
 18. M-S. Kim, K. Shibue and M. Kumagai, "Mechanical Properties of Reactively Sintered TiB₂/Ti-Al-Mn Composites", <u>Sixth JIM International Symposium on Intermetallic Compounds</u>, Ed. O. Izumi, (Sendai, Japan: JIM, 1991), 959-965.

BETA-TITANIUM ALLOY FOR SURGICAL IMPLANTS

S.G. Steinemann (1,3), P.-A. Mäusli (1), S. Szmukler-Moncler (1), M. Semlitsch (2), O. Pohler (3,*), H.-E. Hintermann (4), S.M. Perren (5)

(1) Institut de physique expérimentale de l'Université de Lausanne, 1015 Lausanne-Dorigny, (2) Gebrüder Sulzer, 8401 Winterthur, (3) Institut Straumann, 4437 Waldenburg, (4) CSEM Centre Matériaux et Micromécanique, 2007 Neuchâtel, (5) Laboratorium für experimentelle Chirurgie, 7270 Davos-Platz, Switzerland

Abstract

The metastable beta-type Ti15Mo5Zr3Al alloy complies well with selection criteria of a dedicated material: (i) the metal is tissue-compatible and comprises no cell-toxic component such as vanadium, (ii) it has high strength and the ratio of yield strength to elastic modulus, i.e. the admissible strain, exceeds even the quality of the natural material (bone), and (iii) it allows various fabrication routes by machining and especially by lower-cost "near-net-shape" methods.

Introduction - today's metals for surgery

National and international material standards for orthopaedic and fracture treatment implants include CrNiMo stainless steel, the cast and wrought CoCrMo(Ni) alloy, commercially pure titanium and the TiAlV alloy. Devices made from these metals in accordance with sound metallurgical practice rarely if ever show visible corrosion attack. However, the comprehensive retrieval study of Simpson et al. [1] with fracture plates made from 3 metals reveals variance. Clinical symptoms of pain, swelling and inflammation were reported for steel and cobalt alloy, but none for commercially pure (cp) Ti. Further, biopsies of the contact tissue gave high counts of vessels (capillaries, arterioles, venules) for titanium but a dense connective tissue commonly surrounded steel and cobalt alloy implants. Such findings indicate rejection reactions which even minimal corrosion rates cannot avoid [2,3].

Surgical implants transmit forces and movement, thus, wear and fretting is not an exception and produces quantities of wear particles. That enhances the corrosion reaction. Conditions are unfavorable for titanium and its oxide which are soft materials (the scratch hardness in Mohs scale is 4-5 for titanium metal

This study was supported by Schweizerischer Nationalfonds zur Förderung der wissenschaftlichen Forschung under National Program No. 19 "Materials for Tomorrow".

Science and Technology
Edited by F.H. Froes and I. Caplan
The Minerals, Metals & Materials Society, 1993

^{*} now STRATEC Medical, Waldenburg

and about 6 for its oxides, to be compared with apatite which has 5). Troublesome observations of tissue reactions with prosthetic devices are not seldom [4-7]. Their incidence is connected with the alloy comprising the highly cell-toxic vanadium. Same reactions are seen with fracture treatment implants where small movements of the screw in the hole of the bone plate are inevitable and tissue impregnation of grey colour is commonly noted. Loose vascularized tissue surrounds pure titanium while the alloy shows a prominent foreign body reaction (fig. 1). It was probably an error to adopt that material for bone surgery.

The dedicated metal

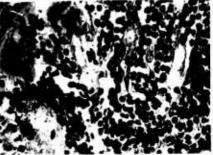
For a "2nd generation metal for implants", the surgeon rightly expects full tissue compatibility. Titanium is the reference; for it, no case of systemic and local reaction is documented. But the commercially pure metal has limited strength even in cold-worked state, and the engineer prefers the stronger alloys which further allow economic processing and fabrication methods.

In Handbooks [see 8] are listed 20 alpha, alpha-beta and beta titanium alloys. 17 of them comprise either V, Ni, Sn, Cr, elements which are known or suspected of being toxic in living tissue [9, 3]. Known alloys manifestly do not comply with an "alloy rule": No toxic component [10]. But the beta-type Ti15Mo5Zr3Al alloy is candidate for a dedicated metal.

High mechanical properties are needed for structural efficiency of surgical implants [10]. Their volume is in fact restricted by anatomic realities what require good yield and fatigue strengths of the metal. On the other hand, an implant "bridges" the forces in bone, i.e. it may reduce the normal physiological level of forces. This gives advantages to a "less-rigid" bone plate or hip prothesis. Frequently this suggestion is associated with a low elastic modulus, comparable to bone. The conjecture is misplaced; a true comparison must refer to the ratio of yield strength and Young's modulus, a dimensionless quantity of elastic strain. The engineer calls this ratio the admissible strain. It equals 0.67% for human cortical bone. Only titanium alloys can match this figure. Another concern is damage tolerance. Titanium alloys offer the good fracture toughness and ductility at much higher strength levels than the usual metals. Such gains in properties improve the safety of surgical materials.

Figure 1 - Sections from biopsies at retrieval of bone fracture plates made from cp Ti (at left) and TiAlV (at right)





Surgical implants are produced by machining, in any case the devices made from stainless steel or titanium. Economic considerations make it desirable to consider other fabrication processes, and titanium alloys provide this possibility.

Properties of Ti15Mo5Zr3Al alloy

The system was studied in the 70's by Japanese metallurgists [11, 12]. In terms of alpha-stabilizing and beta-stabilizing equivalencies [13], the specific alloy has the prototypical compositions [Al]_{eq} = 3.8 wt.% and [Mo]_{eq} = 15 wt.% and thus lies between the solute-lean Beta-III composition with equivalencies 2.5 and 11.5 wt.% respectively and the solute-rich Beta-C alloy with coordinates 3.7 and 16.8 wt.%. For these alloys, the beta phase is retained after quenching to room temperature, and for TiMoZrAl in particular, no martensite or athermal omega phase is observed. Its beta-transus temperature is $785 \pm 15^{\circ}$ C.

Corrosion resistance

Potentiokinetic tests with ground samples of the alloy were conducted in deaerated saline and in 2M hydrochloric acid and showed current densities comparable with cp Ti and high breakthrough potentials around 8V [14]. For the binary Ti16Mo alloy, corrosion currents in physiological fluids are about 11 nA/cm² [15] and in vivo measurements give 4 nA/cm² from polarization resistance [2]. Experiments in aerated 3% NaCl solution show polarization resistances of 18 Mohmcm² for the quaternary alloy and electropolished samples, independent of the metallurgical state. From that, corrosion current densities below 2 nA/cm² can be deduced, even better than that of cp titanium.

Tissue tolerance

Biological acceptance of a material is commonly referred to an implantation test. That may not be enough. Assessement of tolerance needs knowledge of hydrolysis of reaction products of corrosion and of toxicity levels for any component of an alloy [3]. Toxicity tests have been done by Gerber et al. [16] in quantifying the growth inhibition of embryonic rudiments exposed to a culture medium to which salts of metals are added. The oxides of Ti, Zr, Al have solubilities in the μ M range. Oxides of Mo (valency VI and IV) are more soluble. No growth inhibition was found for Ti, Zr, Al at saturation in the culture medium and for Mo at concentrations up to mM. The new metal is safe.

Fabrication and heat treating

The advantages of beta alloys are their high strength and toughness. In addition, the hot and cold workability of these alloys can give substantial cost savings in manufacturing. In fact, any of the interesting "fabrication routes" is feasible, namely "hot-forge at temperatures around beta-transus + age", or "solution-heat-treat + shape by cold-forming + age", or "age (evt. preceded by coldworking) + machine". Clearly, the forming operations will influence the properties of the product and any of these "routes" has its own processing window.

Mechanical properties

Tables I and II give data for TiMoZrAl, 2 other beta alloys (Beta-C, Beta-III) and several comparison materials for the use. Standardized samples served for all tensile tests. Young's modulus was obtained with ultrasonic methods (applying an averaging over directions for longitudinal and transverse modes). In the tables, SHT means solution-heat-treated, A is aged, CW is cold-worked, FOR refers to forged and numbers are temperatures in °C or cold-work in %.

Beta alloys have a tendency for tensile instability in the SHT state and for higher aging temperatures. On the other hand, the notched-tensile strength is reduced for low aging temperatures and the same metallurgical condition induces low ductility and toughness. Such properties are not desirable for surgical implants and impose strict limits for a processing window. Higher aging temperatures are favoured, contrary to recipes suggested ordinarily for beta alloys.

The TiMoZrAl alloy has good strength and ductility and compares well with other beta alloys. It is also a tough material with high fracture and notchedtensile strength. Performances exceed those of alpha-beta alloys, as expected.

Fatigue resistance

Fatigue tests of the 3 beta alloys and the comparison materials were performed on smooth, hour-glass shaped and notched specimens (small diameter 5.68 mm) in rotating-bending loading at 6000 rpm (SCHENK equipment). Test samples of beta alloys have been solution-treated or cold-worked or forged respectively, then machined and aged. Vibratory finishing and electropolishing followed for all samples and materials.

Table I - Mechanical properties of TiMoZrAl and other materials (engineering data)

		TE-ST	YI-ST	EL-FR	RE-AR	YO-MO
TiMoZrAl	SHT840	882	870	20.1	83.2	75
	SHT740	975	968	16.9	64.5	88
	SHT740-A600	1099	1087	15.3	57.5	113
	CW45-A600	1312	1284	11.3	43.8	
	FOR750-A600	1177	1173	15.0	55.0	
TiAlVCrMoZr	SHT740-A550	1120	1050	14.5	43.1	97
	CW50-A550	1420	1366	9.8	29.2	102
TiMoZrSn	A600	1010	1002	17.8	56.0	
Ti6Al4V		1076	940	14.7	40.0	110
Ti6Al7Nb		1024	921	14.0	42.0	110
Ti5Al2.5Fe		1033	914	15.6	39.0	110
cp Ti(gr.4) cold	-worked	785	692	18.3	40.0	105
316L-ESR anne	ealed	557	421	39.3	86.0	
cold	-worked	957	730	21.4	73.0	190
Unit		MPa	MPa	%	%	GPa
I amound. TT C	T is ultimate to		IL VICT	المامنية منا	atron ath	EI ED in

Legend: TE-ST is ultimate tensile strength, YI-ST is yield strength, EL-FR is elongation to fracture (gagelength/diameter = 5), RE-AR is reduction of area at fracture, YO-MO is Young's modulus.

Table II - Mechanical properties of TiMoZrAl and other materials (true data, toughness, fatigue)

		FR-ST	T-E-F	N-T-S	FR-TO	E7-FA
TiMoZrAl	SHT840	1895	178	1391		
	SHT740	1648	104	1569	145	
	SHT740-A600	1741	86	1569	77	560
	CW45-A600	1672	58	1585	31	580
	FOR750-A600	1710	80	33		640
TiAlVCrMoZr	SHT740-A550	1616	56	1550		500
	CW50-A550	1751	35	1685		610
TiMoZrSn	A600	1555	82	1482		510
Ti6Al4V		1429	51	1598	70	540
Ti6Al7Nb		1400	54	1387		540
Ti5Al2.5Fe		1424	50	1301		580
cp Ti(gr.4) cold-v	vorked	1095	51	1387		430
3161-ESR annea		2085	195	816		
cold-v	vorked	1992	131	1689		440
Unit		MPa	%	MPa	MPam ¹	/2 MPa

Legend: FR-ST is fracture stress, T-E-F is true elongation at fracture, N-T-S is notched-tensile strength (K_t =3.2), FR-TO is fracture toughness, E7-FA is endurance limit.

Table III gives representative results for beta alloys and comparison materials used in bone surgery. Data for the low-cycle and the high-cycle fatigue regime refer to service conditions. The endurance limit is certainly essential for (permanent) prosthetic devices but a (low-cycle) overload situation is in most cases at the origin of early implant failures in internal fixation of fractures (temporary splint). The beta alloy has a much higher fatigue limit than the classical metals and has some advantage compared with alpha-beta titanium alloys. The (low-cycle) fatigue strengths of beta alloys also are markedly better than those of other metals.

For the notched-fatigue tests, the specimens have been machined and no surface treatment followed. According to the table, the fatigue limits under these conditions do essentially not vary with the material, nor the metallurgical state in the case of beta alloys. The fatigue notch factor, i.e. the ratio of the fatigue strength of a smooth specimen to the fatigue strength of a notched specimen, however, does change. This factor is about equal to the stress enhancement due to the notch in the case of beta alloys but much less for the classical metals what signifies that an intrinsic strength is well "utilized" for the titanium alloy.

Figure 2 shows some interesting fatigue curves. Known materials (cold-worked stainless steel and cp Ti) are compared to the new beta alloy. The gain in strength for the high-cycle and low-cycle regime is apparent. It is further remarked that the transition from the falling (low-cycle) part in the fatigue curve to the flat portion of the S-N curve is around 1E+5 cycles for the titanium alloys but around 1E+6 cycles for steel. The sensitivity to surface effects is also shown. Electropolishing suppresses influences of roughness (curve in middle). Another factor is change of surface properties. Results are unfavourable if aging is the

Table III - Data from rotating-bending and tensile tests

		+4-FA	>7-FA	>7-NF	TE-ST	ELFR
TiMoZrAl	SHT740-A625	890	560	190	1063	17.7
	CW50-A625	900	580	200	1225	13.7
	FOR750-A625	880	649		l	
TiAlVCrMoZrAl	CW57-A600	920	610	200	1221	14.1
TiMoZrSn	CW57-A550	890	560		1240	12.1
Ti6Al4V			540		1076	14.7
Ti6Al7Nb		810	540	179	1024	14.0
cp Ti cold-worke	d	670	430	180	785	18.3
316L-ESR cold-w		820	440	210	957	21.4
Unit		MPa	MPa	MPa	MPa	%

Legend: +4-FA is low-cycle regime fatigue strength (1E+4 cycles), >7-FA is (high-cycle) fatigue limit (more than 1E+7 cycles), >7-NF is fatigue limit for notched samples ($K_t = 2.8$).

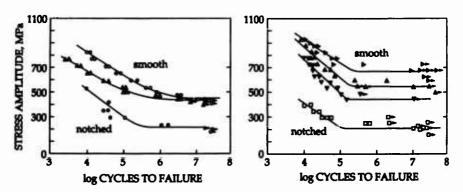


Figure 2 - Stress amplitude to number of cycles for smooth and notched specimens. Left: Stainless steel o, cpTi 4. Right: TiMoZrAl SHT740-A625 electropolished 4, aged after electropolishing ∇ , shot peened before electropolishing Φ ; notched (machined) \square .

last operation (lower curve). Oxygen and nitrogen react with titanium to form a brittle surface layer (called "alpha case") and fissures can be produced [17]. Residual stresses are a 3rd factor; shot peening has a beneficial effect (curve on top in fig. 2 at right). Altogether, the beta-type alloys react in much the same way to these factors as does Ti6Al4V [see 18].

Galling, fretting and forming

Titanium has a severe tendency to gall, a phenomenon which is connected to its high chemical reactivity. The beta alloy makes no exception. Rubbing contact occurs for surgical implants. Experiments in NaCl-solution gave friction coefficients of 0.43 to 0.53 for stainless steel, unalloyed Ti and the aged beta alloy. Wear and fretting of Ti and the beta alloy was higher than that of steel by up to a factor of 2. The only quenched beta phase has unfavourable friction (0.82) and wear (higher by factor 3). Such properties are a nuisance and require special treatments to avoid fretting fatigue, or to ease cutting operations.

Conclusion - the beta alloy has advantage

Ti15Mo5Zr3Al is a most attractive "2nd generation metallic biomaterial". Among known metals, it has lowest corrosion currents and the "unwanted reaction product (of corrosion)" is not cell-toxic or capable of reactions. The alloy is equally attractive for its good mechanical properties. Several reduced quantities are considered in table IV. A first one is yield strength which has to do with load capacity and distortion failures of surgical implants. These devices carry functional loads and the effect of a permanent deformation is self-evident; it means loss of function or anatomic reconstruction. The gain is a factor of 1.6 for beta and 1.3 for alpha-beta alloys when using figures in the table. The 2nd quantity is admissible strain. Differences for materials are large. The actual metal of fracture treatment implants has 0.38% what is about half the ratio for bone. The new metal allows reversible deformations beyond 1% what is 1.6 times the strain capacity of cortical (hard) bone. High yield and elastic strain contribute to make the alloy a "forgiving metal" in clinic; in fact, implants should have spare strength to overcome difficult fracture anatomy and lack of collaboration by the patient. The penalties associated with implant failures are always great. The following entries in the table have to do with the safety of surgical implants. The ratio of notched-tensile strength to ultimate tensile strength should exceed 1.1 and the critical crack length (for spontaneous propagation) should be inferior to shape variation and depth of (possible) surface defects on the device. The figures for the beta : !loy are favourable.

Table IV - Data for a dedicated metal

		1	YI-ST	N-T-S	2 FR-TO 2	
		YI-ST	YO-MO	TE-ST	京(YI-ST)	Z-G-E
TiMoZrAl	SHT	968	1.10	1.61	14	186
	SHT-A	1087	1.06	1.43	3.2	135
	CW-A	1284	1.14	1.18	0.4	78
TiAlV,TiAlN	lb,TiAlFe	920	0.84	1.40	4	65
cp Ti cold-v	vorked	692	0.66	1.77		67
316L-ESR co	old-worked	730	0.38	1.77		270
Unit		MPa	%		mm	%

Legend: YI-ST/YO-MO is admissible strain, N-T-S/TE-ST is ratio of notched and (smooth sample) tensile strength, $2/\pi(FR-TO/YI-ST)^2$ equals the critical crack length, Z-G-E = RE-AR/ (1-RE-AR) is the zero-gage-length elongation.

Another property derived from tensile tests has to do with fabrication; it is the zero-gage-length elongation which provides a measure of ductility that correlates with cold-forming operations (in which the gage length is very short). Elongations exceeding 100% allow cold-forming. Large reductions and complicated shapes can be imposed in the solution-heat-treated state for which the work-hardening coefficient is rather low (of same order as soft steel). The alloy has also excellent forgeability. Die or isothermal forging can be done below the beta transus, i.e. at temperatures where surface contaminations are not heavy and tooling is not expensive. Post heat-treating requirements for any secondary fabrication route are minimal; it suffices to remove some 20µm of metal by mechanical and chemical surface finishing. The new alloy for surgical implants has capabilities for fabrication which no other metal has.

References

- [1] J.P. Simpson et al., "Retrieved Fracture Plates: Implant and Tissue Analysis", Implant Retrieval: Material and Biological Analysis, ed. A. Weinstein et al. (NBS Spec. Publ. 601, 1981), 395-422.
- [2] S.G. Steinemann, "Corrosion of Titanium Alloys for Surgical Implants", <u>Titanium, Science and Technology, Proc. 5th Int. Conf. Titanium</u>, ed. G. Lütjering, U. Zwicker, W. Bunk (Oberursel: Deutsche Ges. Metallkunde, 1985), 1373-1379.
- [3] S.G. Steinemann and P.-A. Mäusli, "Titanium Alloys for Surgical Implants Biocompatibility from Physicochemical Principles", 6th World Conf. on Titanium, ed. P. Lacombe et al. (Les Ulis: Les éditions de physique, 1988), 535-540.
- [4] J. Black, "Does Corrosion matter", J. Bone Joint Surg., 70B (1988), 517-520.
- [5] J. Black et al., "Metallosis Associated with a Stable Titanium-Alloy Femoral Component in Total Hip Replacement", <u>I. Bone Joint Surg.</u> 72A (1990), 126-130.
- [6] J.D. Witt and M. Swann, "Metal Wear and Tissue Response in Failed Titanium Alloy Total Hip Replacements" J. Bone Joint Surg. 73B (1991), 559-563.
- [7] J.T. Scales, "Black Staining around Titanium Alloy Prosthesis-an Orthopaedic Enigma", <u>I. Bone Joint Surg.</u> 73B (1991), 534-536.
- [8] H.E. Boyer and T.L. Gall, eds., <u>Metals Handbook</u> Desk Edition (Metals Park, OH: American Society for Metals, 1985), 9-3.
- [9] H. Gerber and S.M. Perren, "Evaluation of Tissue Compatibility of in vitro Cultures of Embryonic Bones", <u>Evaluation of Biomaterials</u>, ed. G.D. Winter, J.L. Leroy, K. deGroot (Chichester: John Wiley & Sons, 1980), 307-314.
- [10] S.G. Steinemann and S.M. Perren, "Titanium Ailoys as Metallic Biomaterials", Titanium, Science and Technology, Proc. 5th Int. Conf. Titanium
- ed. G. Lütjering et al. (Oberursel: Deutsche Ges. Metallkunde, 1985), 1327-1334. [11] S. Ohtani and M. Nishigaki, "Effect of Al on the Various Properties of
- Ti-15Mo Base Beta Alloys (in Japanese)", <u>I. Japan Inst. Metals</u>, 36 (1972), 90-95. [12] S. Ohtani et al., "The Characteristics of Ti-Mo Beta Titanium Alloys", <u>Titanium Science and Technology</u>, ed. R.I. Jaffee and H.M. Burte (New York: Plenum Press, 1973), 1945-1956.
- [13] E.W. Collings, "Introduction to Titanium Alloy Design", <u>Alloying</u>, ed. J.L. Walter, M.R. Jackson, C.T. Sims (Metals Park OH: American Society for Metals, 1988), 257-370.
- [14] P.-A. Mäusli, S.G. Steinemann and J.P. Simpson, "Properties of Surface Oxides on Titanium and some Titanium Alloys", 6th World Conf. on Titanium, ed. P. Lacombe et al. (Les Ulis: Les éditions de physique, 1988), 1759-1764.
- [15] T.P. Hoar and D.C. Mears, "Corrosion-resistant Alloys in Chloride Solutions: Materials for Surgical Implants", <u>Proc. Roy. Soc.</u>, A294 (1966), 486-510.
- [16] H.W. Gerber, A. Moosmann and S. Steinemann, "Bioactivity of Metals", Technical Principles, Design and Safety of Implants, ed. G.H. Buchhorn,
- H.-G. Willert (Toronto: Hoogrefe & Huber, 1992), in print.
- [17] H. Becker, "Oxidation von Titan technischer Reinheit und von Titanlegierungen in Luft und über ihren Einfluss auf die Bildung von Oberflächenrissen und auf mechanische Eigenschaften", Zeits. Metallkunde, 72 (1981), 679-687.
- [18] H. Gray, L. Wagner and G. Lütjering, "Influence of Surface Treatment on the Fatigue Behaviour of Ti-alloys at Room and Elevated Temperatures", 6th World Conf. on Titanium, ed. P. Lacombe, R. Tricot, G. Béranger (Les Ulis: Les éditions de physique, 1988), 1895-1900.

LOW MODULUS, HIGH STRENGTH, BIOCOMPATIBLE TITANIUM ALLOY

FOR MEDICAL IMPLANTS

K. Wang, L. Gustavson and J. Dumbleton

Howmedica, Pfizer Hospital Products Group Inc. 359 Veterans Boulevard Rutherford, New Jersey 07070

ABSTRACT

A new beta titanium alloy, Ti-12Mo-6Zr-2Fe (TMZF) was developed for orthopaedic use. This alloy has a unique combination of properties, i.e. low modulus of elasticity, excellent mechanical strength, corrosion resistance, and formability, coupled with good wear and notch fatigue resistance. Also, no vanadium and aluminum in this alloy offer a biocompatibility advantage over the Ti-6Al-4V alloy. The processing development, metallurgical characteristics, physical and mechanical properties, and wear resistance of this new alloy are reported here.

INTRODUCTION

The most widely used orthopaedic alloy, Ti-6Al-4V, is known for its excellent corrosion resistance and good mechanical properties. It is also known for its notch fatigue sensitivity and relatively poor wear resistance. High levels of titanium, vanadium, and aluminum debris have been found in surrounding tissues under conditions of high wear. Although no toxic effect has been connected to these debris, safety concerns on vanadium and aluminum have been reported since 1980.

Due to the perceived safety concerns, two vanadium-free titanium alloys, Ti-5Al-2.5Fe and Ti-6Al-7Nb were developed in Europe in the 1980's. 1,2 Both of these alloys offer a potential biocompatibility advantage over Ti-6Al-4V due to the absence of vanadium. But in terms of mechanical properties they are quite similar to Ti-6Al-4V since they are still in the α - β alloy family.

Recent finite element studies suggest that a lower modulus (more flexible) hip prosthesis may better simulate the natural femur in distributing stress to the adjacent bone tissue.^{3,4} Animal studies also suggest that the bone resorption problem commonly experienced by hip prosthesis patients may be alleviated by a prosthesis having a lower modulus.^{5,6} These studies aroused significant interest in producing materials with a lower modulus of elasticity.

The preferred orthopedic titanium alloy should have a lower elastic modulus, a lower notch sensitivity, and a better biocompatibility than Ti-6Al-4V. In our new alloy design, beta alloys were chosen for their advantages in low modulus and lower notch sensitivity. Vanadium and aluminum were purposely avoided while more biocompatible elements, i.e. Mo, Zr, and Fe were introduced.

Titanium '92 Science and Technology Edited by F.M. Froes and I. Caplan The Minerals, Metals & Materials Society, 1993 Our recent achievement, Ti-12Mo-6Zr-2Fe, is unique in having a modulus of elasticity as low as 74 GPa, excellent mechanical strength and corrosion resistance coupled with good wear and notch fatigue resistance. As will be shown in this paper the Ti-12Mo-6Zr-2Fe alloy is successful in meeting the alloy development goals.

ALLOY PROCESSING

It is very difficult to produce a homogeneous Ti-12Mo-6Zr-2Fe ingot using the conventional vacuum arc remelting method, because Mo and Zr have a much higher melting point and density than titanium. Thus, a triple melting technique, which included two vacuum arc remelts and one electron beam or two plasma arc remelts and one vacuum arc remelt was developed for this new alloy. One 45 kg pilot lot and one 4545 kg production lot of 25.4-28.6mm diameter bars were successfully produced through the conventional forging and rolling process.

Workability of the new alloy was excellent. The hot rolled bars were cold drawn into rods of 14mm in diameter and close-die forged into hip prosthesis. In all trials, Ti-12Mo-6Zr-2Fe alloy showed excellent hot and cold formabilities.

GENERAL ALLOY MICROSTRUCTURE

Ti-12Mo-6Zr-2Fe is a metastable beta alloy. It retains an all-beta structure after rapid cooling from its beta transus temperature of 754°C or higher. The all-beta structure will precipitate fine alpha phases upon subsequent aging.

The solution-annealed single beta phase Ti-12Mo-6Zr-2Fe was chosen for orthopaedic implants for its low modulus (Figure 1).

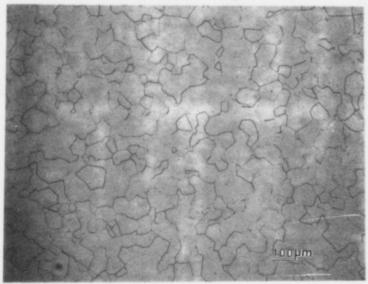


Figure 1 - Microstructure of 788°C (1450°F) solution annealed TMZF.

PHYSICAL PROPERTIES

The physical properties of Ti-12Mo-6Zr-2Fe alloy are listed in Table I.

The thermal expansion of Ti-12Mo-6Zr-2Fe alloy was measured from 25 to 900°C in accordance with ASTM E-228 (Figure 2). The thermal expansion of Ti-12Mo-6Zr-2Fe alloy is 0.884% between 25 and 900°C. The thermal expansion coefficient of Ti-12Mo-6Zr-2Fe is 8.8 x 10^{-6} /°C between 25 and 250°C; and 11.5 x 10^{-6} /°C between 525 and 900°C.

A departure from a linear response becomes evident in the range 250 to 525°C and indicates crystalline transitions of beta and alpha phases in this alloy. At temperatures above 550°C, the alpha precipitates were re-dissolved into the beta matrix.

The modulus of Ti-12Mo-6Zr-2Fe is 74-85 Gpa, which is 25% lower than that of Ti-6A1-4V. The density of this alloy is 12% higher than that of Ti-6A1-4V. The hardness of this alloy is slightly higher than the Rc 31 of Ti-6A1-4V.

Table I - Typical Physical Properties of Ti-12Mo-6Zr-2Fe Alloy

Thermal Expansion Goefficient*	x 10 ⁻⁶ /°C x 10 ⁻⁶ /°C	8.8 at 25-250°C 11.5 at 525-900°C	
Modulus*	\times 10 ⁶ psi (Gpa)	10.7 - 12.3 (74-85)	
Beta Transus	• F • C	1350 - 1390 732 - 754	
Density*	lb/cu-in gm/cu-cm	0.18 5.0	
Hardness*	Rc	34-35	

^{*}Solution treated condition

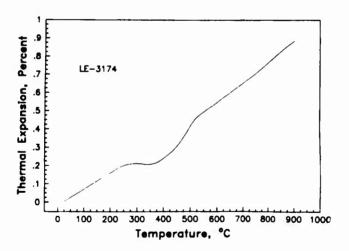


Figure 2 - Thermal expansion of TMZF alloy from 25° to 900°C

TENSILE PROPERTIES

Tensile tests were conducted on solution annealed Ti-12Mo-6Zr-2Fe bars at room temperature according to ASTM E-8. The tensile properties of Ti-12Mo-6Zr-2Fe and Ti-6Al-4V are listed in Table II. Results show that Ti-12Mo-6Zr-2Fe has a much higher yield strength and better elongation than Ti-6Al-4V. As noted in the physical property section of this report, the elastic modulus of Ti-12Mo-6Zr-2Fe alloy is lower than that of Ti-6Al-4V.

Table II - Tensile Properties of Solution Annealed Ti-12Mo-6Zr-2Fe

Alloy	YS (MPa)	UTS (Mpa)	EL (1)	RA (%)	E (Gpa)
TMZF	1000-1060	1060-1100	18 - 22	64 - 73	74 - 85
Ti-6Al-4V	850 - 900	960 - 970	10 - 15	35 - 47	110

ROTATING BEAM PATIGUE PROPERTIES

The solution annealed Ti-12Mo-6Zr-2Fe bars were subjected to smooth and notched Krouse fatigue tests. The testing modes include high cycle fatigue, rotating beam, and cantilever bending. The test loading was constant force sinusoidal at approximately 167 Hz. The test stress ratio was infinity, i.e. fully reversed. All testing was conducted at room temperature in air. Tests normally stopped when 10 million cycles were achieved. The notched samples had a stress concentration factor of Kt-1.6. For comparison purposes Ti-6Al-4V alloy bars were also tested under the same conditions.

The smooth rotating fatigue properties of Ti-12Mo-6Zr-2Fe and Ti-6Al-4V are plotted in Figure 3. The smooth fatigue strength of Ti-12Mo-6Zr-2Fe is comparable to that of Ti-6Al-4V. At 10⁷ cycles, the maximum stress of Ti-12Mo-6Zr-2Fe alloy is 585 Mpa (85ksi).

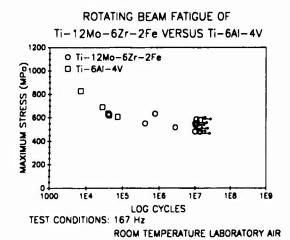
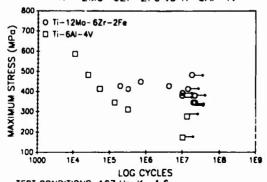


Figure 3 - Smooth rotating beam fatigue strength of TMZF and Ti-6A1-4V

The notched rotating beam fatigue properties of Ti-12Mo-6Zr-2Fe and Ti-6Al-4V are shown in Figure 4. At 10^7 cycles, the Ti-12Mo-6Zr-2Fe alloy showed a notched strength of 410 Mpa (60 ksi) at 10 million cycles (70% of its smooth fatigue strength). Under the same condition, Ti-6Al-4V showed a notched strength of 280 Mpa (45 ksi), or 53% of its smooth fatigue strength. The notched fatigue results are in keeping with the characteristic property of beta titanium alloys being less fatigue notch sensitive than alpha beta alloys such as Ti-6Al-4V alloy.

NOTCHED ROTATING BEAM FATIGUE OF



TEST CONDITIONS: 167 Hz, K_t=1.6

ROOM TEMPERATURE LABORATORY AIR

Figure 4 - Notched rotating beam fatigue strength of TMZF and Ti-6Al-4V

FRACTURE TOUGHNESS

The solution annealed Ti-12Mo-6Zr-2Fe bar samples were tested for precracking and fracture toughness at 33°C according to ASTM E399. The crack area was saturated with saline solution (0.9% NaCl) before testing. Ti-6Al-4V bar samples were also tested for comparison.

The mean toughness of Ti-12Mo-6Zr-2Fe was 90 Mpa \sqrt{m} (81.7 ksi $\sqrt{1}$ in). That of Ti-6Al-4V was 52 Mpa \sqrt{m} (47.2 ksi $\sqrt{1}$ in) (Table III). These results show that the fracture resistance of the solution annealed Ti-12Mo-6Zr-2Fe alloy is much better than that of Ti-6Al-4V.

Table III. Fracture Toughness of TM2F and Ti-6A1-4V Bar Stock (28.6 mm dia.)

Alloy	Specimen Number	Toughness.	(ksi fin)
TMZF	1 - 1	90	(81.7)
TMZF	1 - 2	88	(79.7)
TMZF	1 - 3	92	(83.7)
T1-6A1-4V	2 - 1	54	(48.8)
Ti-6A1-4V	2 - 2	51	(46.4)
T1-6A1-4V	2 - 3	51	(46.4)

CORROSION PROPERTY

Anodic polarization testing was performed on the solution annealed Ti-12Mo-6Zr-2Fe alloy specimens. Specimens were in the form of 16 mm diameter x 3 mm thick disks and 9.5 mm diameter x 12.7 mm rods. Tests were run in deaerated saline (0.9% Nacl) at 37°C. Each disc specimen was finished to a 600 grit silicon carbide immediately before testing. All rod specimens were prepared to a 600 grit silicon carbide finish followed by cleaning and passivation. Ti-6Al-4V rod samples were also tested for comparison.

ASTM G5, Standard Reference Test Method for Making Potentiostatic and Potentiodynamic Anodic Polarization Measurements was followed for the testing. The anodic polarization curves of Ti-12Mo-6Zr-2Fe and Ti-6Al-4V are shown in Figure 5. Data show excellent corrosion resistance for both alloys. As the potential increases each alloy reaches a stable passive current density. The difference in the passive current density between the two alloys is not directly related to their relative free corrosion rates in the body environment. Further increases in potential up to +1000 mv v.s. S.C.E. cause no further increase in current density for either alloy. This indicates that the protective oxide on either alloy resists breakdown equally well at this excessive polarization. Resistance to breakdown is the key result of this test.

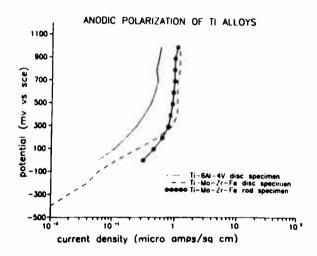


Figure 5. Anodic polarization of Ti-12Mo-6Zr-2Fe and Ti-6Al-4V

WEAR PROPERTIES

The friction and wear properties of annealed Ti-12Mo-6Zr-2Fe and Ti-6Al-4V versus Surgical Simplex® P bone cement were determined using an ISC-200 tribometer. The ISC-200 is a pin-on-disc type wear and friction measurement system. The bone cement sample was held stationary by a cantilever beam while the metal disc counterface rotated against it.

Five polished disc samples of each alloy were individually tested against a 12.7mm diameter bone cement ball at a 100 gm load, in deionized water. Tests were run at 80 cycles/min. for 1.0 x 10^3 cycles. The sliding speed for each test was 7.4 cm/sec. Wear was determined by the weight loss and surface roughness of the disc samples. The mass worn away from a ball was calculated by the radius of the worn flat spot and the density of the bone cement sample. The surface roughness of bone cement ball was 1μ m.

The friction coefficients of Ti-12Mo-6Zr-2Fe alloy and Ti-6Al-4V against bone cement are shown in Figure 6. The friction coefficient of Ti-12Mo-6Zr-2Fe is approximately 0.4 which is one half of that of Ti-6Al-4V.

After 1.0×10^5 cycles, although some light scratching was present on the rubbing surface of the Ti-12No-6Zr-2Fe samples, this did not initiate self perpetuating abrasive wear, and only bone cement debris was noted on the samples.

Severe abrasive wear of the Ti-6Al-4V discs was observed after only a few hundred cycles with subsequent scratching of the Ti-6Al-4V surface; black metal wear debris was generated.

The surfaces of all bone cement balls run against Ti-6Al-4V were covered with fine black particles. No black particles were seen on the surface of bone cement balls that rubbed against Ti-12Mo-6Zr-2Fe alloy. The wear data are shown in Table IV. Results obtained from this testing indicate that solution onnealed Ti-12Mo-6Zr-2Fe has a much better abrasive wear resistance than Ti-6Al-4V.

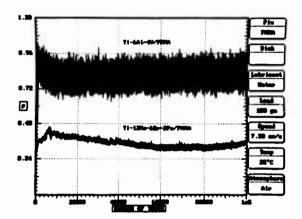


Figure 6 - Friction coefficient of TMZF and Ti-6Al-4V against bone cement.

Table IV - Results of Wear Test on TMZF and Ti-6Al-4V Against bone cement.

Sample No.	Disc Sam Surface Rough		Disc Sample Wt.loss.gm	Bone Cement Sampl Wt. Loss. mg	
	Initial	Final	(gain)		
TMZF - 1	0.02	0.07	(0,0008)	0.09	
TMZF - 2	0.02	0.08	(0,0006)	0.09	
TMZF - 3	0.02	0.03	(0,0000)	0.05	
TMZF - 4	0.05	0.09	(0.0009)	0.22	
TMZF - 5	0.07	0.09	(0.0000)	0.09	
T1-6-4 - 1	0.01	4.85	0.0129	1.04	
Ti-6-4 - 2	0.02	5.73	0.0135	1.33	
Ti-6-4 - 3	0.02	4.47	0.0176	1.04	
T1-6-4 - 4	0.06	4.13	0.0149	1.33	
Ti-6-4 - 5	0.02	6.23	0.0134	1.33	

The friction coefficients of annealed Ti-12No-6Zr-2Fe and Ti-6Al-4V versus ultra high molecular weight polyethylene (UHMWPE) pins were also measured. Two tests for each alloy were conducted in deionized water at a 500gm load and at 80 cycles/min. The sliding speed for each test was 7.3 cm/sec. The disc samples had a surface roughness of 0.02 μ m. The surface roughness of the UHMWPE pins was 2.5 μ m. The friction coefficients of Ti-12No-6Zr-2Fe and Ti-6Al-4V against UHMWPE at various distances are shown in Figure 7. The steady state friction coefficient of Ti-12No-6Zr-2Fe is 0.04 which is much lower than that of Ti-6Al-4V.

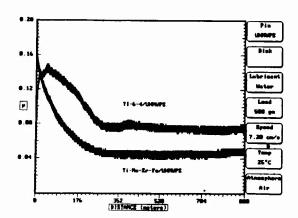


Figure 7 - Friction Coefficient of TMZF against UHMWPE

SUMMARY

A new biocompatible titanium alloy, Ti-12Mo-6Zr-2Fe has been developed. The processing and formability advantages of this alloy have been briefly reviewed. This beta titanium alloy exhibits higher yield strength, lower modulus of elasticity, higher fracture toughness and better wear resistance than Ti-6Al-4V. It also has an excellent corrosion resistance and a smooth fatigue strength similar to that of Ti-6Al-4V. With the characteristics of high strength, low modulus, biocompatibility and excellent corrosion resistance, the alloy is well suited for orthopsedic applications.

REFERENCES

- R. Zwicker, K. Buehler, R. Mueller et al., "Mechanical Properties and Tissue Reactions of a Titanium Alloy for Implant Material," <u>TITANIUM</u> <u>'80. Science and Technology Proc. 4th Int. Conf. on Titanium</u> (Kyoto, May 1980). The Met. Soc. AIME (ISBM-No. 89520-370-7); 505-514.
- M. Semlitsch, F. Staub and H. Webber, "Titanium-Aluminum-Niobium Alloy, Development for Biocompatible, High Strength Surgical Implants," <u>Biomed.</u> <u>Technik 30</u> (1985), 334-339.
- E. Cheal, M. Spector and W. Hayes, "Role of Loads and Prosthesis Material Properties on the Mechanics of the Proximal Femur After Total Hip Arthroplasty," J. Orthop Res. (1992) 10:405-422
- P. Prendergast and D. Taylor, "Stress Analysis of the Proximo-Hedial Femur After Total Hip Replacement," <u>J. Biomed.Eng.</u> (1990), Vol. 12, No. 5, 379-382.
- J.D. Bobyn, A.H. Classman, H. Goto, J. Krygier, J. Miller, and C. Brooks, "The Effect of Stem Stiffness on Femoral Bone Resorption After Canine Porous-Coated Total Hip Arthroplasty." <u>Glin. Orthop. Relat. Res.</u> (1990), 261:196-213.
- J.D. Bobyn, E.S. Mortimer, A.H Glassman, C.A. Engh, J. Miller, C. Brooks, "Producing and Avoiding Stress Shielding: Laboratory and Clinical Observation of Noncemented Total Hip Arthroplasty. Clin. Orthop. Relat. Res. (1992), 274:79-96.

THE ELECTROCHEMICAL BEHAVIOR OF A NEW TITANIUM ALLOY

WITH SUPERIOR BIOCOMPATIBILITY

Paul Kovacs and James A. Davidson

Orthopaedic Research Department Smith & Nephew Richards, Inc. 1450 Brooks Road Memphis, Tennessee 38116

Abstract

To optimize the long-term performance of metallic implants in orthopaedic applications, a new titanium alloy, which contains neither aluminum nor vanadium, has been invented at Smith and Nephew Richards Inc. The new alloy, Ti-13Nb-13Zr, has better biocompatibility than that of Ti-6Al-4V, and exhibits higher strength and lower elastic modulus which is advantageous if the load transfer to bone is desired. The improved biocompatibility of the new alloy can be directly attributed to the fact that the oxides of the alloying metals, niobium and zirconium, have very low solubilities, and tend to incorporate in the protective passive film instead of being released as dissolved metal ions into the biological environment. Furthermore, the general biocompatibility of niobium and zirconium is also superior to that of aluminum and vanadium. In this paper, the electrochemical behavior of the new alloy and the pure alloying elements during spontaneous passivation, as well as the results of biocompatibility studies, are presented and compared to those of Ti-6AI-4V. The spontaneous passivation of the mechanically polished alloys and pure metals was studied by means of electrochemical impedance spectroscopy, and the polarization behavior was determined on the basis of the potentiodynamic polarization curves. The electrolyte used in this study was lactated Ringer's solution at 37°C. The biocompatibility tests were performed according to the standard procedures for implant materials. The electrochemical measurements confirmed the higher polarization resistance of the spontaneously passivated Ti-13Nb-13Zr alloy, while the biocompatibility test results demonstrated its superior biocompatibility.

Introduction

Biocompatibility can be defined as the state of mutual coexistence between an implant material and the biological environment, in which both of them maintain adequate physical and chemical stability. The lack of sufficient physical biocompatibility may result in undesirable events such as the fracture of the implant or substantial bone loss due the stress shielding by a more rigid implant material. Insufficient chemical biocompatibility, on the other hand, may lead to unacceptably high degradation rate for the implant material and may induce intolerably severe biological effects locally and/or systemically.

The chemical biocompatibility of a metallic implant is closely related to the electrochemical behavior of the metal or alloy in the harsh biological environment [1-6]. The rate of electrochemical interactions between the implant metal and the body fluids as well as the solubility of corrosion products can have a significant bearing on biocompatibility. It has been observed that the tissue reaction is proportional to the amounts of constituent elements released by the corrosion of a pure metal or alloy. Laing et al [7] graded the tissue reaction

Titanium '92 Science and Tachnology Edited by F.H. Frose and I. Caplan The Minerals, Metals & Materials Society, 1993 according to the thickness of pseudomembranes around the implants. For an implantation duration of six months in the back muscle of rabbits, membranes up to 3 mm and more were observed in cases of severe reactions (Fe, Co, Cr, Ni, Mo, V, Mn, Incoloy), and thicknesses up to 20 µm for minor reactions (Ti, Zr, Nb, titanium alloys, cast and wrought cobalt alloys, stainless steel 316L and 17-7PH). Steinemann [3] classified the tissue reactions from a pathological point of view, in the following distinct types:

- In the case of severe reaction a "sterile abscess" is observed and, in histology, psychosis, so that this type of reaction may be termed a "toxic" response (Co, Ni, Cu, V);
- A dense, non-vascularized fibrous tissue without dead cells is a reaction which slows down metabolic exchanges, and this type may be called "capsule" (Al, Fe, Mo, Ag, Au, stainless steels, cast and wrought cobalt alloys);
- The "vital" reaction, which has an appearance of loose and vascularized fibrous tissue, and sometimes an epithelium in contact with metal (Ti, Zr, Nb, Ta, Pt, Ti alloys).

Steinemann also gave a combination of in vivo corrosion test results and histological examinations, with the general trend summarized as follows:

- 1. The "vital" reaction is possible only for the most resistant metals.
- Metals with low polarization resistances (i.e., severe corrosion), on the other hand, do
 not necessarily lead to a "toxic" reaction. For example, the severely corroding
 elements Fe, Al, Mo provoke the "capsule" type of response.
- 3. The response to stainless steel and cobalt alloys is of the intermediate (normally harmless) "capsule" type despite their very high corrosion resistance. The presence of the typically toxic elements Ni and Co in these alloys is apparently sufficient to induce a shift towards the "second best" tissue reaction.

Based on these observations, the author concluded that an alloy providing "vital" tissue behavior should not include any of the "toxic" elements, but should be based on metals in the "vital" group and have, if necessary, elements of the "capsule" group.

The results of these studies clearly demonstrate the superior biocompatibility of Ti, Nb, Zr, and Ta. It is also indicated by the results of the *in vivo* corrosion tests that the most biocompatible metals and alloys usually show the highest polarization resistance.

Due to its numerous desirable mechanical properties and excellent biocompatibility, Ti-6Al-4V has long been used in orthopaedic surgery with proven clinical success. Because the alloy is passivated by the oxides of the base metal titanium [9-10], the less than optimum biocompatibility of aluminum and vanadium does not seem to affect significantly the biocompatibility of the prepassivated alloy. However, when excessive mechanical breakdown of passivity occurs, the alloy may become a localized source of the elements aluminum and vanadium, as indicated by the results of recent ion release studies [11-16]. The replacement of these alloying elements with other metals such as Zr, Nb or Ta, the corrosion products of which have extremely low solubilities, may considerably improve the biocompatibility of the alloy in the long-term implant applications. Although these metals are well known from the literature, few attempts have been made so far to use these as alternative alloying elements alone for titanium. Custom-made orthopaedic Ti alloys Ti-6Al-7Nb [17] and Ti-11.5Mo-6Zr-2Fe [18] still contain Al, Mo, and Fe which present less than optimum biocompatibility.

This paper describes the electrochemical behavior of the new titanium alloy [19] that exhibits superior biocompatibility, both physically and chemically. The Ti-13Nb-13Zr alloy has higher strength and significantly lower modulus than Ti-6Al-4V [20,21], and shows improved chemical biocompatibility [22] due to the presence of alloying elements that contribute to the formation of a highly protective passive film on the alloy surface. For comparison, the spontaneous passivation of Ti-6Al-4V and that of pure Ti, Al, V, Nb, and Zr was also studied by using a combination of AC and DC electrochemical techniques [23,24], which had been found to provide very important information on the electrochemical behavior in case of mechanical breakdown of passivity.

Materials and Methods

Electrochemical test specimens were prepared from 1.) wrought as-quenched and 2.)cast and HIP'ed Ti-13Nb-13Zr alloy rods, from 3.)a wrought, sintered, HIP'ed Ti-6Al-4V hip s am, 4.) standard grade and 5.)ELI grade Ti-6Al-4V alloy rods, as well as from pure Ti, Al, V, Nb, and Zr. These test specimen were mechanically polished to a mirror-like finish and were immediately immersed into the test cell containing lactated Ringer's solution at 37°C.

At various time intervals during the spontaneous passivation of the polished metal surfaces, the electrochemical impedance spectra were determined. The gradually increasing time intervals between the impedance measurements (#1-#8) were: 5, 10, 20, 40, 80, 160, 320, and 360 min. The last measurement (#9) was conducted immediately after the completion of measurement #8. Following each passivation experiment, the potentiodynamic polarization curves on the spontaneously passivated samples were also recorded in order to see the polarization behavior in a broad potential range, and to make a comparison between the polarization resistance values provided by the different electrochemical methods. Under the same experimental conditions, the electrochemical behavior of carbon was also studied in order to learn more about the rate of electron exchange between the electrode material and the environment in the absence of the corrosion processes and the protective passive layers. The carbon test specimens were prepared from a high-density, non-permeable graphite electrode.

The potentiostat used in these experiments was an EG&G Princeton Applied Research Model 273 potentiostat with a Model 5210 lock-in amplifier for the high frequency impedance measurements. The reference and the counter electrodes were saturated calomel and high-density, non-permeable graphite, respectively. The experiments were conducted in a Model K47 Corrosion Cell System, which was open to air.

Results and Discussion

Both Ti alloys were subjected to numerous biocompatibility tests [22], and showed excellent biocompatibility as expected. However, there were several instances in which the cell or tissue response was considerably less for the Ti-13Nb-13Zr alloy. Examples for these are given in Figure 1, from the results of the 90-day Rabbit Intramuscular Implant Tests.

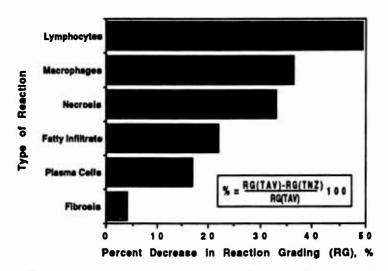


Figure 1 - Examples Showing Improved Biocompatibility of Ti-13Nb-13Zr (TNZ) Compared to Ti-6Al-4V (TAV).

2.707

In very good agreement with Zitter's and Plenk's observation [5] that the electrochemical behavior of metallic implant materials is an indicator of their biocompatibility, the reciprocal polarization resistance of the spontaneously passivated Ti-13Nb-13Zr alloy was also considerably lower than the reciprocal polarization resistance of Ti-6Al-4V. As summarized in Figure 2, the results of both the electrochemical impedance and the potentiodynamic polarization measurements demonstrate the superior electrochemical behavior of the new titanium alloy.

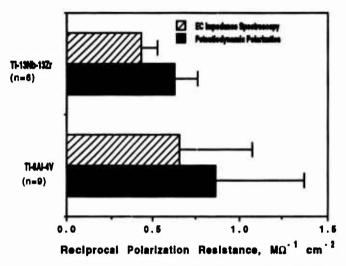


Figure 2 - 1/Rp Values for Ti-13Nb-13Zr and Ti-6Al-4V Alloys

The lower reciprocal polarization resistance represents lower current densities, and indicates the presence of a more effective passive layer on the alloy surface. In previous studies it was found [5,24] that the current densities measurable on passive orthopaedic implant alloys can be substantially affected by the electron exchange processes. Therefore, it is important to consider that the measured current densities consist of two parts:

$$i = i_{COTT} + i_{elex}$$
 (1)

where icorr and letex represent the corrosion and electron exchange current densities, respectively. In the case of extremely corrosion resistant alloys such as Ti-13Nb-13Zr and Ti-6Al-4V, ielex is usually much higher than icorr. According to these considerations, the lower reciprocal polarization resistances of the Ti-13Nb-13Zr samples indicate that the total electrochemical interaction (corrosion and electron exchange) between the passivated alloy and the environment is lower than in the case of Ti-6Al-4V.

Additionally, the improved biocompatibility of the new titanium alloy can also be the consequence of the elimination of the less biocompatible alloying elements, aluminum and vanadium. Investigating the dissolution behavior of Ti-6Al-4V, Bruneel and Helsen [11] found that the relative concentrations of the elements dissolved differ substantially from their relative presence in the alloy. Although the concentrations of aluminum and vanadium are low in the alloy, their concentration in the test solution - especially the aluminum concentration - was quite close to that of the major element titanium. Consequently, it was concluded by the authors that the Ti-6Al-4V alloy may not be underestimated as a localized source of the elements aluminum and vanadium. In contrast, as the Ti-13Nb-13Zr alloy contains only alloying elements that form oxides with extremely low solubilities, the preferential dissolution of niobium and zirconium from this alloy is highly unlikely.

To illustrate the substantially different electrochemical behavior of the various alloying elements, the potentiodynamic polarization curves of AI, V, Ti, Nb, and Zr are shown in Figure 3, which were recorded after a 20-hour exposure of the previously mechanically polished metals to the lactated Ringer's solution. The scanning rate was 1 mV/s in these experiments.

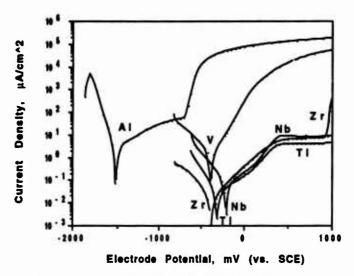


Figure 3 - Potentiodynamic Polarization Curves for Al, V, Ti, Nb, and Zr.

While aluminum and vanadium show high current densities at their corrosion potentials, titanium, niobium, and zirconium exhibit not only extremely low current densities at their open circuit potentials, but these metals also have very similar polarization behavior in a broad potential range, both cathodically and anodically. Between -750 and 0 mV (vs.SCE), which is usually the potential region for orthopaedic implant alloys, the polarization curves of aluminum and vanadium indicates transpassive dissolution, providing a plausible explanation for their preferential dissolution from the Ti-6Al-4V alloy. On the other hand, niobium and zirconium, similarly to titanium, are in the region of perfect passivity, and are not subjected to chemical breakdown of passivity even at more positive potentials. Instead of being released into the environment as dissolved metal ions, Nb and Zr contribute to the formation of the highly protective passive film on the titanium alloy.

As the biocompatibility of orthopaedic implant alloys is directly related to the protective ability of their passive surface layers, it is very important to consider that the corrosion rate of these alloy can be very high if the passive layer is partially or completely removed mechanically by the action of fretting wear processes. If this situation arises, it may become biologically significant whether the high corrosion rate can be associated primarily with a higher metal ion release rate or with a higher rate of insoluble oxide formation. Therefore, it is necessary to distinguish between the two major types of anodic corrosion processes, and interpret the corrosion rate as the sum of the rate of dissolution and the rate of protective passive layer formation [24]:

$$i_{corr} = i_{sol} + i_{ox}$$
 (2)

where isol is the rate of soluble corrosion product formation, including non-protective oxides and hydroxides, and iox is the rate of protective oxide/hydroxide formation. While i_{COTT} is mainly determined by i_{OX} in the case of Ti-13Nb-13Zr, the contribution of i_{SOI} to i_{COTT} is less negligible when the spontaneous passivation of Ti-6Al-4V takes place, resulting in the preferential release of aluminum and vanadium ions with less than optimum biocompatibility.

2,709

Although the corrosion resistance of prepassivated implant alloys has been extensively studied, the spontaneous passivation of these alloys in the chloride-containing environment has been given less attention. This is partly because of experimental difficulties in studying rapidly changing electrochemical systems such as metals or alloys undergoing spontaneous passivation in a certain electrolyte. Recent developments in electrochemical techniques, however, have made it possible to address this issue more effectively. Electrochemical Impedance Spectroscopy (EIS) offers a new experimental approach to these rapidly changing electrode systems and - in combination with classical DC polarization measurements - it can provide some fundamental information about the overall electrochemical performance of metallic implant materials [23-26]. In Figure 4, results obtained by EIS are shown, indicating the changes in the reciprocal polarization resistances during the 20-hour tests.

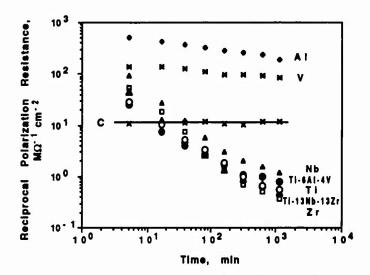


Figure 4 - EIS Results for Ti-13Nb-13Zr, Ti-6Al-4V, Al, V, Ti, Nb, Zr, and C.

The interpretation of these results requires complex electrochemical considerations, including the role of metal ion release and oxide formation in determining the overall corrosion rate, as well as the relative contribution of the rate of electron exchange to the total electrochemical interaction between the metal or alloy and the environment. As the reciprocal polarization resistance of a polished metal is proportional to the corrosion rate [23,24], the slightly higher values for the Ti-13Nb-13Zr samples indicate the higher initial reactivity of this alloy than that of Ti-6Al-4V. The higher corrosion rate, however, does not result in higher metal ion release. On the contrary, it primarily reflects the current necessary for protective passive layer formation, as neither the base metal nor the alloying elements Nb and Zr tend to dissolve preferentially. For Ti-6Al-4V, despite the apparently lower initial corrosion rate, a considerable portion of the total current density is provided by the dissolution processes of aluminum and vanadium, as the corrosion products of these two metals are much more soluble than those of titanium. While Al and V do not show effective spontaneous passivation, the titanium alloys, Ti, Nb, and Zr develop highly protective passive layers, the consequence of which is a much lower total electrochemical interaction (corrosion and electron exchange) than the electron exchange alone between carbon and the electrolyte.

In a recent editorial by J. P. Scales in the British Journal of Bone and Joint Surgery [27], the optimization of titanium alloy was discussed, concluding that "..., efforts might well be directed towards the development of transformed β-phase titanium alloys containing only such elements as niobium, tantalum, and zirconium." The Ti-Nb-Zr alloy introduced in this paper demonstrates that significant improvements in biocompatibility can be achieved in this way.

Conclusions

On the basis of the results obtained in this study, the following conclusions can be drawn:

The electrochemical behavior of Ti-13Nb-13Zr alloy is more favorable for orthopaedic implants applications than that of Ti-6Al-4V, due to the formation of a more protective passive layer on Ti-13Nb-13Zr which improves the biocompatibility of this alloy.

Additionally, less metal ion release is likely to occur during the spontaneous passivation of the Ti-13Nb-13Zr alloy because the corrosion products of the minor alloying elements Nb and Zr are less soluble than those of aluminum and vanadium, and may incorporate in the protective passive film. This difference in performance characteristics may become an issue of biological significance if the mechanical breakdown of passivity on the implant by fretting wear is excessive.

References

- 1. Hoar, T. P. and Mears, D. C., "Corrosion-Resistant Alloys in Chloride Solutions: Materials for Surgical Implants", <u>Proc. Roy. Soc.</u>, A294 (1966) 486-510
- 2. Kruger, J., "Fundamental Aspects on the Corrosion of Metallic Implants", <u>Corrosion and Degradation of Implant Materials</u>, eds. B. C. Syrett, and A. Acharya (ASTM STP 684, Philadelphia, American Society for Testing and Materials, 1979), 107-127
- 3. Steinemann, S. G., "Corrosion of Surgical Implants in vivo and in vitro Tests", Evaluation of Biomaterials, eds. G. D. Winter, J. L. Leray, and K. de Groot (John Wiley & Sons, New York, 1980) 1-34
- 4 Pourbaix, M., "Electrochemical Corrosion of Metallic Biomaterials", <u>Biomaterials</u>, 5 (1984) 122-134
- 5. Zitter, H. and Plenk Jr., H., "The Electrochemical Behavior of Metallic Implant Materials as an Indicator of Their Biocompatibility", J. Biomed. Mater. Res., 21 (1987) 881-896
- 6. Kovacs, P. and Davidson, J. A., "Chemical and Electrochemical Aspects of Implant Metal Biocompatibility" (Orthopaedic Research Report OR-90-12, Smith and Nephew Richards Inc., Memphis, TN, 1990)
- 7. Laing, P. G., Ferguson, Jr., A. B. and Hodge, E. S., "Tissue Reaction in Rabbit Muscle Exposed To Metallic Implants", J. Biomed. Mater. Res., 1 (1967) 135-149
- 8. Solar, R. J., Pollack, S. R., and Korostoff, E., "Titanium Release From Implants: A Proposed Mechanism", <u>Corrosion and Degradation of Implant Materials</u>, eds., Syrett, B. C. and Acharya, A., (ASTM STP 684, Philadelphia, American Society for Testing and Materials, 1979) 161-172
- 9. Azhar, A.A., El-Taib, F., and Gad-Allah, A. G., 'Anodic Behavior of Titanium in Aqueous Media', Corrosion. 44 (1988) 705-710
- Zhang, X. G. and Vereecken, J., "Repassivation and Stress-Corrosion Cracking of Ti-6Al-4V in Aqueous and Methanolic Solutions", Corrosion, 45 (1989) 57-62
- 11. Bruneel, N. and Helsen, J. A., "In Vitro Simulation of Biocompatibility of Ti-Al-V", J. Biomed. Mater. Res., 22 (1988) 203-214
- 12. Davidson, J. A. and Kovacs, P., "Evaluation of Metal Ion Release During Articulation of Metal and Ceramic Fernoral Heads" (Paper presented at the Eighth Southern Biomedical Engineering Conference, Richmond, Virginia. October 15-16, 1989) 33-37

- 13. Davidson, J. A., Kovacs, P., and Lanzer, W. L., "Metal Ion Release During Articulation of Ion Implanted Ti-6Al-4V Alloy Against UHMWPE" (Paper presented at the 36th Annual Meeting of the Orthopaedic Research Society, New Orleans, Louisiana, February 5-8, 1990) 460
- 14. Kovacs, P. and Davidson, J. A., "Effect of Ion Implantation on the Ion Release of Implant Metal Bearing Surfaces" (Paper presented at the 16th Annual Meeting of the Society for Biomaterials, Charleston, South Carolina, May 20-23, 1990) 127
- 15. Kovacs, P. and Davidson, J. A., "Ion Release of Implant Metal Bearing Surfaces" (Paper presented at the 16th Annual Meeting of the Society for Biomaterials, Charleston, South Carolina, May 20-23, 1990) 198
- 16. Kovacs, P. and Davidson, J. A., "Metal Ion Release Aspects of Ti-6Al-4V Bearing Surfaces in Orthopaedic Implant Applications" (Paper presented at the 1990 International Conference on Titanium Products and Applications, Orlando, Florida, October 1-3, 1990) 626-635
- 17. Semilisch, M. F., Weber, H., Streicher, R. M., and Schon, R., "Joint Replacement Components Made of Hot-Forged and Surface-Treated Ti-6Al-7Nb" (Paper presented at the 1990 International Conference on Titanium Products and Applications, Orlando, Florida, October 1-3, 1990) 653-669
- 18. Wang, K. K., Gustavson, L. J., and Dumbleton, J. H., "A New High Strength, Low Modulus, Biocompatible Beta Ti Alloy for Surgical Implants" (Paper presented at the Fourth World Biomaterials Congress, Berlin, Germany, April 24-28, 1992) 221
- 19. Davidson, J. A. and Kovacs, P., "Biocompatible Low Modulus Titanium Alloy for Medical Implants", U.S. Patent Filing, December 1989, (Ref. 61560/253)
- 20. Davidson, J. A. and Kovacs, P., "The Metallurgy, Structure, and Properties of New Low-Modulus Ti-13Nb-13Zr and Other Titanium Alloys" (Orthopaedic Research Report OR-90-01, Smith and Nephew Richards Inc., Memphis, TN, 1990)
- 21. Davidson, J. A. and Kovacs, P., "Fatigue, Strength, and Metallurgical Properties of Low-Modulus Ti-Nb-Zr Alloys for Orthopaedic Implant Applications" (Orthopaedic Research Report OR-90-05, Smith and Nephew Richards Inc., Memphis, TN, 1990)
- 22. Biocompatibility Test Reports by TOXIKON: "90-day Rabbit Implant Toxicity Tests", "In Vivo Mouse Micronucleus Tests", "Rabbit Pyrogon Tests", and "Guinea Pig Maximization Tests", 1990-91
- 23. Kovacs, P., "A Combination of AC and DC Electrochemical Techniques for Studying the Spontaneous Passivation of Orthopaedic Implant Alloy" (Paper presented at the 17th Annual Meeting of the Society for Biomaterials, Scottsdale, Arizona, May 1-5, 1991) 293
- 24. Kovacs, P., "In Vitro Studies on the Electrochemical Behavior of Orthopaedic Implant Alloys" (Paper presented at the 179th Meeting of the Electrochemical Society, Washington, D.C., May 5-10, 1991) 93
- 25. Kovacs, P., "In Vitro Studies on the Electrochemical Behavior of Pure Metals Used in Orthopaedic Implant Alloys" (Paper presented at the 180th Meeting of the Electrochemical Society, Phoenix, Arizona, October 13-17, 1991) 255
- 26. Kovacs, P., "Electrochemical Techniques for Studying the Corrosion Behavior of Metallic Implant Materials" (Paper presented at CORROSION 92, the NACE Annual Conference and Corrosion Show, Nashville, Tennessee, April 26-May 1, 1992) 214
- 27. Scales, J. P., *Black Staining Around Titanium Alloy Prostheses An Orthopaedic Enigma* (Editorial), <u>J. Bone and Joint Surg.</u> 73-B [Br] (1991) 534-535

THE DYNAMIC INTERACTION BETWEEN TITANIUM AND SNOW

M. Abe*, H. Ito*, K. Ueda**, H. Aoyagi***, and T. Nishimura****

*Department of Mechanical Engineering, Nagaoka University of Technology
**Sagamihara Machinery Works, Mitsubishi Heavy Industries,LTD
***Graduate Student, Nagaoka University of Technology
****Iron & Steel Research Laboratories,KOBE STEEL,LTD

Abstract

For structures in snowfall regions, materials like titanium, rather than the customary steel, are being used to improve performance. However, the interactions between these materials and snow, which is important for use of materials in snowfall environments, are not very well understood.

In this study, attention is directed to the dynamic properties under dynamic interaction where both of them move relative to one another. This study is the first to explain the interactions theoretically and experimentally. In this paper, the dynamic friction factor that is important practically in dynamic interactions was examined. Dynamic friction factor μ is considered to be a function of various factors, for example, snow sliding velocity V, snow temperature T, contact pressure ρ on fluid film of snow, snow density ρ , and surface roughness R_x of material.

Experiments under variations of V, T and P are discussed first. Various titanium sheets and, for comparison, stainless steel sheets, resin coated steel sheets and plastics sheets were selected for evaluation. From the results of the experiments, it has been clarified that dynamic friction resistance was strongly influenced by V, T, R_z and surface energy of material.

Moreover, considering that dynamic friction resistance is caused by resistance from surface roughness, fluid viscous resistance and shearing resistance in adhesion parts, the equations of state for expressing the interaction between various materials and snow have been derived. From the analysis of this equation, the lubrication mode between various materials and snow was made clear, and the basic theory about dynamic friction resistance has been constructed.

The results of this paper are considered to be useful for the design of structures and the selection of materials in snowfall regions.

1. Introduction

In this study, attention is directed to the dynamic properties under dynamic interactions where snow and titanium sheet etc. move relative to one another. And the interactions are explained theoretically and experimentally. In this paper, experimental results on dynamic friction resistance that is important practically in dynamic interactions are investigated, and the results of the theoretical analysis are discussed.

On the basis of the investigations of experiments, a theoretical analysis is done using the equations of state derived for expressing the interaction

Titanium '92 Science and Technology Edited by F.H. Froes and I. Caplan The Minerals, Metals & Materials Society, 1993 between snow and sheet. It must be noticed that dynamic friction factor μ to prescribe dynamic friction resistance is not constant. Therefore, μ is considered to be the function of various factors as shown in the next equation.

$$\mu = f(V, T, \rho, \rho, R_z, r, \lambda, \cdots) \tag{1}$$

where V: snow sliding velocity. T: snow temperature, p: contact pressure on fluid film of snow, p: snow density, $R_z:$ surface roughness of material, r: surface energy of material, $\lambda:$ thermal conductivity of material. In this paper, the attention is directed to V, T and p.

2. Materials and Experimental Nethods

Various sheet materials used for experiments are shown in Table I. The chemical compositions of the test sheets are shown in Table II. Table III shows the measured results of the ten point average roughness $R_{\rm II}$ of the test sheets and the contact angle θ between test sheet and water that prescribes surface energy γ . As these values on surface conditions were measured just before experiments, aging is expected. This effect is to be investigated in the future.

In the experiments, compacted snow collected from natural snow cover was used. The density was $0.3\sim0.4$ g/cm³. The experiments were conducted using testing equipment for snow-ice properties designed and made by the authors. Figure 1 shows the general view of this equipment. Friction force is measured by load cell as the force acting between snow and sheet material. An AC sarbomotor moved the sheet material. Then, snow sliding velocity V was altered by changing the moving velocity of the sheet material. V was varied to 7 levels, 0.5, 10, 20, 30, 40, 50 and 60 mm/s. On the experiments to investigate the effects of V, snow temperature T was varied to 2 levels, 0 and -4 °C. The influences of T were studied to 6 levels, 2, 0, -2, -4, -6 and -8 °C for V = 0.5 mm/s. Moreover, to investigate the effects of the contact pressure P on fluid film of snow, experiments were done to 3 levels of P, 0.4, 0.8 and 1.2 kPa for V = 0.5 mm/s, T = 0 °C.

Table I Kinds of Test Sheets

Sheet No.	Materials	Surface finish condition
Tap-1	Titanium	Annealed and pickled
Tva-2	Titanium	Vacuum Annealed
Tan-3	Titanium	Anodized
Tfl-4	Titanium	Fluoroplastics coated
SS-5	Stainless steel	Noncoated
S-6	Steel	Polyester resin coated
PC-7	Rigid polyvinyl chloride	Nonconted

Table II Chemical Compositions of Test Sheets (Weight %)

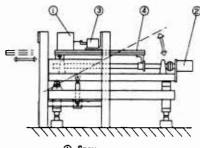
Sheet No.	С	Si	Hin	P	S	Ni	Cr	Н	0	N	Pe	Ťi
Tap-1	-	-	-	-	-	-	-	0.010	0.10	0.03	0.10	bal.
Tva-2 Tan-J	_	_	=	-	_	_	_	0.010	0.10	0.03	0.10	bal.
111-4	-	-	_	-	-	-	- 18.00-	0.010	0.10	0.03	0.10	bal.
88-5	(0.08 0.04 -	(1.00	(2.00	(0.045	(0.030	8.00 - 10.50	20.00	-	-	-	-	-
8-6	0.06	0.01	0.03	0.01	0.012	-	-	-	-	-	bal.	-

Table M Surface Conditions of Test Sheets

Chast No	R _z (μm)	θ(°)		
Sheet No.	٧٢	P	٧T	P	
Tap-1	2.87	10.93	64.5	66.7	
Tva-2	0.55	3.04	33.0	61.7	
Tan-3	3.07	6.97	52.0	54.8	
Tfl-4	1.47	4.85	70.5	65.8	
SS-5	1.89	2.18	89.0	46.5	
S-6	0.46	2.82	79.5	81.5	
PC-7	-	2.29	_	70.3	

VT: The values on test sheets used in the experiments to investigate the effect of V and T

P: The values on test sheets used in the experiments to investigate the effect of P



- ① Snow
- ② AC Sarbo-motor
- 3 Load Cell
- Sheet Material

Figure 1 - The Outline of Testing Machine of Snow-ice Property

3. Experimental Results and Discussion

3.1 Relationship between Dynamic Friction Factor and Snow Sliding Velocity

In the case of snow temperature T=-4 °C, dynamic friction factor μ decreases gradually as snow sliding velocity V increases. Polyester resin coated steel sheets show minimum value nearly regardless of V. Figure 2(a) shows the relationship for titanium sheets. As for the annealed and pickled titanium sheets and anodized titanium sheets, the decreasing ratio of μ is large when V increases. This suggests that these sheets have the advantage for snow sliding properties at high V.

In the case of T=0 °C, contrary to that of T=-4 °C, μ increases gradually as V increases. Figure 2(b) shows the relationship for titanium sheets. μ of the vacuum annealed titanium sheets, stainless steel sheets and polyester resin coated steel sheets, is small and does not increase so much with the increase of V. Although μ of the anodized titanium sheet is large, for high snow sliding velocity, the μ shows the tendency to decrease a little. This sheet seems to have the advantage on snow sliding properties at high V.

3.2 Relationship between Dynamic Friction Factor and Snow Temperature

In the case of V=0.5 mm/s, μ has the tendency to decrease a little as T increases except for anodized titanium sheet. Figure 3 shows the relationship between μ and T for titanium sheets.

3:3 Relationship between Dynamic Friction Factor and Contact Pressure on Fluid Film of Snow

In the case of V=0.5 mm/s and T=0 °C, μ has the tendency to decrease gradually as contact pressure p on fluid film of snow increases. Figure 4 shows the relationship between μ and p for titanium sheets. For the vacuum annealed titanium sheet, the decreasing ratio is large in the range of p=0.8 ~ 1.2 kPa.

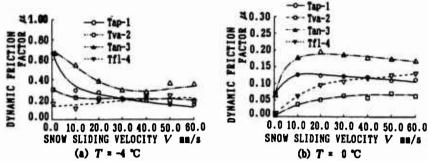


Figure 2 - The Relationship between μ and V

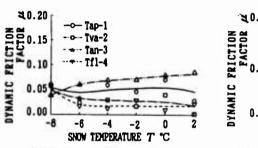


Figure 3 - The Relationship between μ and T V = 0.5 m/s

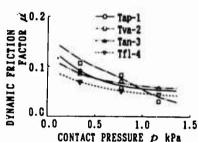


Figure 4 - The Relationship between μ and ρ $V = 0.5 \text{ ms/s}, T = 0 \text{ }^{\circ}\text{C}$

3.4 Relationship between Dynamic Friction Factor and the surface properties of materials

From the experimental results as mentioned in paragraph 3·1, 3·2 and 3·3, μ has the tendency to become larger as R_x is larger and θ is smaller. In some cases, however, μ of the titanium sheets haveing large R_x is small. So the factors except for R_x and θ will have to be investigated.

3.5 Examination of Frictional Condition by Stribeck Curve

As explained in paragraph $3\cdot 1$, $3\cdot 2$ and $3\cdot 3$, frictional conditions between snow and sheet materials are influenced by V, T and p. When water occurs by the melting of snow, the water works as the lubricant between snow and sheet material. The problem of the friction between snow and sheet material like this can be considered as a lubrication problem. So, the problem in this study will be discussed next by the Stribeck curve (1) used to indicate the lubrication mode.

On the Stribeck curve shown in Fig.5, the lubrication mode can be classified into the following 3 types.

I:Boundary lubrication, I:Mixed lubrication, I:Hydrodynamic lubrication For constant viscosity η and vertical load F_N , the relationship between μ and V can be considered to indicate the Stribeck curve. When V is constant, ρ corresponds to F_N in Fig.5 and the relationship between μ and ρ can be considered to indicate the Stribeck curve. From this viewpoint, the experimental results are investigated.

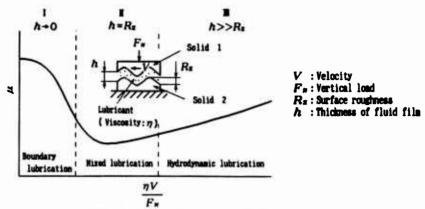


Figure 5 - Stribeck Curve and Lubrication Mode

The relationship between μ and V for T=-4 C shown in Fig.2(a) of paragraph 3·1 can be considered to correspond to region Ξ in Fig.5. The relationship for T=0 C shown in Fig.2(b) can be considered to correspond to the transition region between region Ξ and Ξ .

On the relationship between μ and T shown in Fig.3 of paragraph 3·2, the increase of T will be able to be turned into the equivalent increase of V. Therefore, if lubrication mode changes from I to I, I with the increase of T as in Fig.5, the tendency of Fig.3 can be considered to show the lubrication mode from region I to I.

The relationship between μ and ρ shown in Fig.4 of paragraph 3.3 is related to Fig.5. In Fig.4, the lubrication mode is considered to change from region π to π with the increase of ρ .

4. Theoretical Analysis

4.1 Friction Models between Snow and Sheet Material

For snow temperature $T \geq 0$ °C, the water film between snow and material occurs by the melting of snow. Therefore, taking into consideration the discussion of paragraph 3.5, it is considered that the lubrication state is the critical state between the mixed and the hydrodynamic lubrication states. Consequently, friction force F will be the resultant force of the viscous friction force F_{ν} and the sliding friction force. And, sliding friction force is considered to be the resultant force of resistance F_{μ} from surface roughness and shearing resistance F_{μ} by adhesion of the interface between snow and material. Therefore, dynamic friction factor μ and F are obtained as follows:

$$\mu = \frac{F}{w} \qquad (W: weight of snow) \tag{2}$$

$$F = F_{\bullet} + F_{A} + F_{V} \tag{3}$$

In the case of T<0°C, it is considered that friction interface is in the mixed lubrication state from the consideration by the Stribeck curve in paragraph 3.4. But water very little occurs by the melting of snow. And the amount of water generated by friction heat must be small. Therefore, F_{ν} of Eq.(3) isn't considered.

Figure 6 shows a friction analysis model by surface roughness. Here, the following assumptions are introduced.

(1) The surface roughness of material is expressed as sine curve in fig.6 and uniform to the right-angled direction of snow sliding direction.

(2) Snow is a viscoelastic material and its property is expressed by Voigt

model.

Figure 7 shows a friction analysis model by adhesion for calculating F_A . It is assumed that snow is composed of ice particles and the plastic deformation of ice particles occurs by contacting with sheet material. Figure 8 shows a friction analysis model by viscosity for calculating F_V .

4.2 Theoretical Derivation of Dynamic Friction Force

4.2.1 Sliding Friction Force (2) (3) (4). Sliding friction force, as shown in paragraph 4.1 is considered to be the resultant force of F_R and F_A .

In Fig.6, F_R is x direction's component of resistance force acting on snow from the surface unevenness and calculated from the following Eq.(4) and Eq.(5).

 F_A is obtained from Eq.(6), when the plastic deformation of snow particles occurs, by using the model in Fig.7.

$$F_{R} = m_{R}R_{z}r\left(g - \frac{R_{z}\omega^{z}}{2}\sqrt{\frac{k^{z}+c^{z}\omega^{z}}{(k-m_{z}\omega^{z})^{z}+c^{z}\omega^{z}}}\right) \quad (4)$$

$$\omega = \frac{2\pi V}{l} \tag{5}$$

$$F_A = \frac{f_i W}{p_a} \tag{6}$$

here, m_z :mass of snow, k:spring constant of snow, c:viscous damping constant of snow, l_z :the length per 1 cycle of unevenness, r:number of unevenness. Every value is for per l_z . W:weight of snow, f_z :shear strength of ice, p_z : yield pressure of ice.

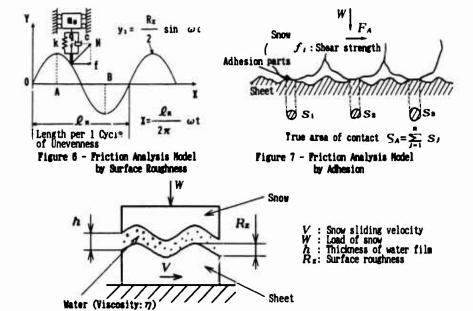


Figure 8 - Friction Analysis Hodel by Viscosity 2718

<u>4.2.2 Viscous Friction Force.</u> Viscous friction force F_{ν} of fluid is calculated from the next equation by the model shown in Fig. 8.

$$F_{V} = \eta_{f} \frac{V}{y_{f}} S_{V}, \quad S_{V} = \gamma_{f} R_{z} S_{0}, \quad y_{f} = C \theta^{f} R_{z}^{a} V^{a}$$
 (7)

Here, η_i :viscosity of fluid, r, C, l, m, n:constant values obtained from experiments, S_0 :nominal contact area between snow and sheet material and the equations of S_v and y_i are assumed on the basis of experimental results.

4.3 Comparison between Calculated Values and Experimental Values

The unevenness conditions of test sheet surfaces are shown in Table V and the various values used for the theoretical analysis are shown in Table V. As for k and c of the snow, values by Kojima $^{(5)}$ were quoted.

Figure 9(a),(b) show the comparison between the calculated values and the experimental values of titanium sheets for the relationship between dynamic friction factor μ and sliding velocity V for $T=0^{\circ}C$ and $T=-4^{\circ}C$.

For T=-4°C shown in Fig.9(a), the changing tendency of calculated values of μ to V is almost in agreement with those of experimental ones. But, for $V \ge 10 \text{mm/s}$, the calculated values are larger than the experimental values. This is possibly caused because, F_A of the interface between snow and sheet, which is one cause of sliding friction force, rigorously decreases as V increases.

For $T=0^{\circ}C$ shown in Fig.9(b), the changing tendency of μ to the change of V is almost in agreement between both calculated values and experimental ones. But experimental values of vacuum annualed titanium sheet No.Tva-2, having small surface roughness R_{π} and contact angle θ , are rather smaller than the calculated values.

On sheet materials except titanium, the tendency by theory and experiment has good agreement, too. Therefore, the dynamic friction factor μ between snow and sheet material can be predicted from the equations derived in this paper. After this, we are going to investigate the effect of V on F_A , the effect of factors except R_x and θ and to examine the effect of T in detail. And a more multilateral study on the friction resistance of snow will be conducted.

Table IV Unevenness Conditions of Test Sheets Surface

Sheet No.	l _n (m)	r	R ₂ (m)
Tap-1	25)	2000	refer to
Tva-2	100	5000	
Tan-3	250	2000	
Tf1-4	250	2000	
SS-5	500	1000	
8-6	250	2000	

Table V Various Values Used for the Theoretical Analysis

Symbols	Values
So: (cm²)	52.5
7 . (E/CB·S)	1.79×10-3
k: (dyn/cm)	7.8×107
C: (dyn-s/cm)	1.5x10*
7 :	2.0x103
C:	9.0x10-*
1:	2.6
# :	0.22
n:	0.65

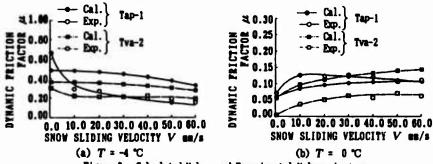


Figure 9 - Calculated Values and Experimental Values about μ

5. Conclusions

The dynamic friction resistance between snow and sheet materials has been clarified from both experiment and theory. Obtained conclusions are as follows.

- (1) Dynamic friction factor is influenced by surface roughness, contact angle between sheet and water, snow sliding velocity, snow temperature and contact pressure on fluid film of snow.
- (2) The tendency of conclusion (1) can be explained on the whole by a discussion of friction mode between snow and sheet materials based on Stribeck curve and the analytical results based on the theory established by this discussion.

The results of this research seem to be useful for the design and choice of materials for machine structures in snow fall regions.

Finally, the financial support of this study by the Ministry of Education in Japan (Scientific Research Subsidy General Research(c) in 1990 and 1991, Dynamic Interaction between Snow and Machine Structures, Subject No.02650178) is gratefully acknowledged. And the authors are very thankful to KOBE STEEL, LTD for providing us with various test sheet materials and valuable data.

References

- 1. H. Czichos, TRIBOLOGY, (Oxford, 1978), 103.
- T.He, M.Abe, H.Ito, H.Nakaya, H.Kuriyama, 'The Dynamic Interaction between Snow and Machine Structures', <u>Proceedings of Cold Region Technology Confer-</u> ence, (1989), 171-176.
- ence, (1989), 171-176.

 3. M.Abe, H.Ito, K.Ueda, H.Nakaya, T.Nishimura, 'The Relation between Priction Resistance and Slip Velocity of Snow', <u>Proceedings of 7th Japan Society for Snow Engineering</u>, (1990), 15-22.
- Snow Engineering, (1990), 15-22.
 4. F.P.Bowden and D.Tabor, The Friction and Lubrication of Solids, (Oxford, 1954).
- K.kojima, 'Visco-Elastic Property of Snow', <u>Low Temperature Science</u>, Ser. A12, (1954).

BETA TITANIUM IN THE UNITED STATES SURFACE NAVY IMPROVED WATER BRAKE

Stephen L. Opet Jr. and David F. Peters, P.E.

NAVAL AIR WARFARE CENTER, AIRCRAFT DIVISION, LAKEHURST, NJ

Abstract

This paper describes the development effort utilizing Ti 3A1-8V-6-Cr-4Mo-4Zr alloy for steam catapult water brake cylinders aboard US Navy aircraft carriers.

The prototype water brake is a one piece forging/extrusion. It measures 2.44 m in length, 45.7cm outside diameter, and possesses a 11.4cm wall thickness, which makes it the largest component formed from Beta ${\tt C}^1$ to date. The finished component has a yield strength of 1103MPa with a fracture toughness of 94MPa-m^{1/2}.



FIGURE 1 - STEAM CATAPULTS IN OPERATION ABOARD THE USS CONSTELLATION

Titanium '92 Science and Technology Edited by F.H. Froes and I. Caplan The Minerals, Metals & Materials Society, 1993

Introduction

The U.S. Navy is currently evaluating the use of titanium for several components of the steam catapult system used aboard aircraft carriers. These design programs are the first efforts by the Surface Navy to utilize titanium on major structural components. The combination of lower weight, superior marine corrosion resistance, and high strength with good fracture toughness make the Beta alloys attractive alternatives to the low alloy steels used for the last 40 years.

This paper concentrates on the redesign of the catapult's water brake by the Naval Air Warfare Center, Aircraft Division, Lakehurst. The results show that titanium can be safely substituted for alloy steels in certain applications. The initial increased cost of titanium components can be justified by life cycle cost savings.

Function of Water Brake

With the introduction of jet aircraft following World War II, the US Navy has relied on catapults to launch its air power (Figure 1). Currently, all catapults are steam driven. These catapults employ piston assemblies to convert the expansive power of steam in the launching engine cylinders to accelerate the aircraft to its power takeoff speed. The water brake, as its name implies, halts the piston assembly following release of the aircraft. It is a water filled tube which operates on the hydraulic ram principle with the piston assembly spear.

Figure 2 provides a schematic of the major components of the steam catapult.

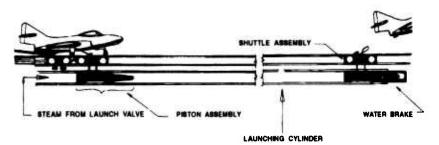


FIGURE 2 - MAJOR COMPONENTS OF STEAM CATAPULT

When the catapult is fired, high pressure steam is admitted into the launching engine cylinders and creates a force which accelerates the piston assembly. A mechanical linkage, comprised of a shuttle assembly and tow bar, is attached to the piston assembly and transmits this force to the aircraft. This linkage is such that the aircraft is freed as soon as the piston assembly decelerates.

At the end of the catapult stroke, a cam-shaped contour on the spears at the forward end of the piston assembly contacts entrained water in the water brake. As the piston assembly continues to move forward due to its own momentum, this cam-shaped contour, acting as a mandrel, penetrates the water brake cylinder and forcibly expels the water. The resultant deceleration force halts the piston assembly.

The 2176Kg piston assembly is brought from 58m/s to a halt in only 1.5m. Internal pressures of the water brake can reach 620MPa while absorbing energies up to 40,650,000 joules.

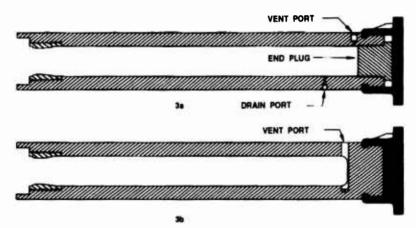


FIGURE 3 - COMPARISON OF 2 PIECE ALLOY STEEL WATER BRAKE DESIGN (3a) TO 1 PIECE TITANIUM BRAKE DESIGN (3b)

Titanium Water Brake Development Program

The water brake's operating environment plus the current use of alloy steel results in a design which is subject to corrosion damage. As a result, the Navy experiences costly overhaul repairs and periodic replacement of the current alloy steel water brake. This development program was initiated to alleviate these corrosion problems and design a new water brake to last the life of the ship, which is 40 years.

Design

Figure 3a shows the design of the existing two place alloy steel brake.

This configuration suffers corrosion damage in the crevices at the threaded connections both at the mouth and end of the brake. Corrosion damage also occurs in the bottom of the cylinder where

water tends to collect despite the drain port. To reduce the corrosion problems and eliminate potential crack initiation sites, the end plug and drain port features of the existing design were eliminated. The elimination of the end plug and the drain port redistributed stresses and resulted in the requirement for extensive FEA to confirm and optimize the design. The new design is shown in figure 3b.

The drain port was necessary in the old steel design to keep excessive water from collecting in the bottom of the cylinder and corroding it away. The new design without a drain port would require a material immune to corrosion in the water brake environment.

Material Selection

The new design presented demanding material requirements. To keep the same ultimate burst pressure of the old design this material needed a minimum ultimate tensile strength of 1103MPa. The material also had to be immune to corrosion in the water brake's environment. In operation this environment is 82 degrees C water with a maximum salinity content of .5 percent. An extensive literature survey yielded only three possible material choices. They were 38644 titanium and inconel 718 and 13-8 PH stainless steel. These materials were evaluated in a corrosion test conducted at Ocean City Research Co.

During the air/water interface corrosion susceptibility tests, the incomel 718 and titanium 38644 alloys were not affected. The 13-8 PH stainless steel pitted badly and the current alloy steel (.35 C, 3.0 Ni, 1.0 Cr, .5 Mo) pitted and suffered extensive general corrosion.

Titanium 38644 was chosen as the top candidate because of its lower weight and better thru hardening capability. The choice of titanium, however, raised some serious questions. While the required ultimate tensile strength was achievable the material has a notable decrease in fracture toughness. This necessitated a detailed finite element analysis and fracture mechanics analysis.

Finite Element Analysis

In view of the reduced fracture toughness of titanium as compared to steel and in consideration of the complexity of the water brake, the importance of an accurate structural analysis became obvious. Review of the literature revealed that there is no closed form, classical solution to analysis of this water brake design: a thick-walled pressure vessel, intersected by a transverse hole into a radius at the one closed end. Therefore, we selected finite element analysis as the method of choice.

Computer-bases performance predictions relating internal pressure in the water brake to position of the cam contour on the spears resulted in peak pressures of approximately 620MPa.

Consideration of expected high stresses at the through thickness hole formed by the vent port required a refined technique. A mesh

comprised of 24 elements, each 15 degrees of arc, was employed to provide the accuracy required for this vent port. The main portion of the water brake cylinder was modeled with two rows of elements since stresses were expected to be primarily caused by in-plane forces in this region.

Taking advantage of symmetry, only one-quarter of the brake was modelled. Figure 4 presents the finite element model employed.

Solution was obtained using the ALGOR FEA code on a 286 PC.

Figure 5 presents stresses predicted by the FEA model. The maximum stress occurs safely in the vent port region. The radius of the closed end, which is intersected by the vent port, was selected as a compromise between ease of formability, which results in a sharp radius, and structural concerns, for which a large radius is desirable.

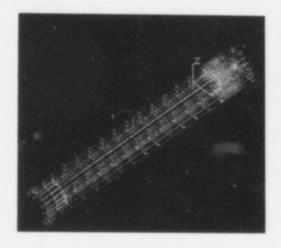


FIGURE 4 - FEA MODEL

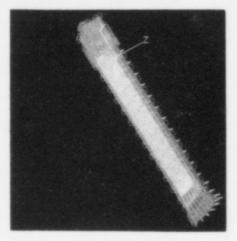


FIGURE 5 - FEA STRESS PREDICTION

Fracture Mechanics

Table I summarizes the results of the analyses. It shows that the new design configuration safely compensates for the lower fracture toughness of the titanium alloy. The one piece titanium water brake has a higher resistance to catastrophic fracture than the two piece steel brake and it will not initiate a flaw due to corrosion in the operating environment.

DESIGN	LOCATION ANALYZED	CRITICAL FLAW SIZE, Acr(mm)
2 PIECE STEEL 1 PIECE TI	DRAIN PORT IN CYLINDER BORE CYLINDER BORE VENT PORT	0.64 3.30 2.34

TABLE I - RESULTS OF FRACTURE MECHANICS ANALYSIS

Manufacturing of Prototype

The prototype was the largest piece of Beta C titanium formed to date. Fabrication was done at Cameron Forge Co. in Houston TX under contract managed by Titanium Technologies also of Houston. Figure 6 shown the sequence of operations utilized.

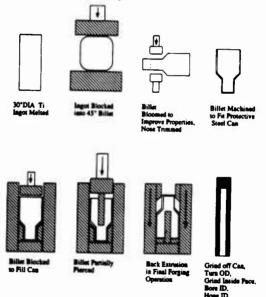


FIGURE 6 - FABRICATION SEQUENCE

The blocked billet received from the RMI Titanium Co. was pierced and extruded with excess material left on the opened end. Several rings were cut from the open end and run through heat treat operations utilizing two solution treating temperatures and four aging temperatures to provide NAWC Lakehurst the data from which to choose the treatment for the final product. Figure 7 shows the mechanical testing data which was generated from the aforementioned heat treated samples.

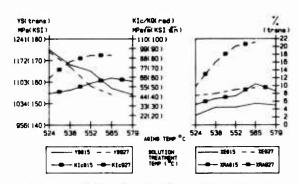


FIGURE 7 - RESULTS OF MECHANICAL TESTING

NAWC Lakehurst selected the treatment of 927 degrees C solution treatment with a 552 degree C age to optimize toughness. The heat treated cylinder was 100 percent UT inspected to a 1.93mm flat bottom hole calibration standard. The part was then final machined and shipped to Lakehurst.

Prototype Testing

The prototype cylinder was delivered to NAWC Lakehurst for testing verification. The water brake was slightly modified by drilling a port to take a pressure reading. The brake was installed in the catapults at Lakehurst and instrumented with strain gauges. It was installed at our full scale catapult next to a conventional steel brake, which allowed comparison between the two types. A series of catapult shots were run with increasing end speeds. The performance of the brake was monitored at each increment. These tests indicated that the titanium brake performed as expected: it halted the piston assembly without fracture, as did the steel brake, and within acceptable performance limits.

Current and Future Efforts at NAWC AD Lakehurst

Water Brake

NAWC is currently running a study through the Applied Research Lab at Penn State University to examine the feasibility of utilizing electron beam welding for the manufacture of the titanium water brake. This effort is to reduce the manufacturing cost of the one piece cylinder and will be completed this year. A welded construction will also allow better control in machining the closed end of the brake which proved extremely difficult during prototype manufacture. A smooth, generous radius is needed to keep stresses at a minimum as shown by the FEA.

In addition, rapid load fracture toughness testing, crack initiation tests, and crack growth rate studies will be performed in a simulated brake environment. Acoustic emission and ultrasonic testing procedures will also be developed for periodic inspections. Results of the fracture mechanics analysis will be used for establishing inspection intervals to realize a fail safe design.

Piston Assembly Barrel and Spear

New studies have just begun for evaluating the use of titanium for the barrel of the piston assembly (Figure 8). Here the decrease in weight is expected to significantly extend service life compared to the current steel alloy construction. This program is currently ongoing.

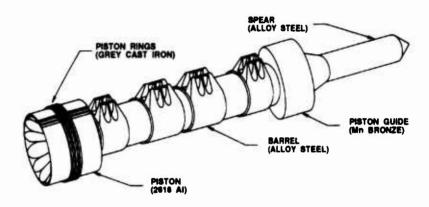


FIGURE 8 - CATAPULT PISTON ASSEMBLY

(1) Beta C is a trade mark of the RMI Titanium Company.

PRODUCTION OF TITANIUM 6A1-4V ELI ELECTRONIC BOTTLES

FOR THE CURV III SUBMERSIBLE

M.E. Wells and J.A. Sasse

Carderock Division, Naval Surface Warfare Center Annapolis, Maryland 21402-5067

Abstract

The U.S. Navy is engaged in a program to upgrade the CURV III submersible vehicle for salvage operations to 6,096 meters. This report describes the production, inspection, and testing of titanium electronic bottles for the Information is presented on the manufacture of the electronic bottles from the primary fabrication of forged billets to an evaluation of the hydrostatic performance of an electronic bottle. In brief, three titanium alloy Ti 6A1-4V ELI ingots of 83.8 cm diameter by approximately 4,536 kg were converted to billet products using a beta/alpha-beta forging procedure to produce a microstructure consisting of a mixture of elongated and equiaxed alpha and intergranular beta. The resultant mechanical properties met all strength and toughness requirements of the contract specification. However, the forged billets for the end cap components failed to meet the ultrasonic inspection requirement for detection of a 1.98 cm flat bottom hole (FBH). The billet pieces did meet a 3.18 cm FBH criteria which, with additional mechanical property test results, was considered adequate to allow acceptance. The forged billet pieces were finish-machined into externally rib-stiffened cylinders and hemispherical end caps. The components were assembled into electronic bottles, and one bottle was instrumented for hydrostatic testing. The test results indicated satisfactory performance with no evidence of creep strain at the design operating depth. After proof testing the remaining bottles, all components were delivered to the prime contractor for installation on the vehicle.

> Titanium '92 Science and Technology Edited by F.H. Froes and I. Captan The Minerals, Metals & Materials Society, 1993

Introduction

The U.S. Navy is engaged in a program to upgrade the CURV (Cable-controlled Underwater Recovery Vehicle) III submersible system for salvage operations at depths up to 6,096 m. The present CURV III system was built in 1971. With a operating depth of 1,829 m, it was one of the first successful cable-controlled undersea work vehicles commonly referred to today as an ROV or AUV. The new CURV III vehicle will have two configurations, one with a TMS (Tether Management System) for high ocean currents and depths to 2,438 m. The other configuration will be used in low current conditions and depths to 6,096 m.

The electronic equipment on the vehicle will be housed in three pressure resistant containers, known as electronic bottles, Fig. 1. The bottles were designed as cylinders with hemispherical end caps using the following material design values for Ti 6Al-4V ELI:

compressive yield stress - 758.4 MPa proportional limit stress - 606.7 MPa Young's modulus - 122.0 GPa

The cylindrical portion of each bottle was designed for a 34.3 cm inside diameter. Each cylinder is 18.1 mm thick with a length of 152.4 cm. Eighteen external frames on 7.47 cm centers are used to stiffen each cylinder, along with a "deep" frame at each end. The end caps are hemispherical shells of 19.1 mm thickness, attached to the ends of the cylinder with V-retainer coupling clamps (Marman clamps). One of each pair of end caps has six 50.8 mm diameter holes to accommodate electrical penetrators.

A total of three cylinders and six end caps were required to house the electronic equipment on the vehicle. Upon completion of the design phase, work was initiated to produce forged billets for the manufacture of the cylinder and end cap components. A second objective was to verify the structural performance of an electronic bottle by hydrostatic testing to the design operating depth of 6,096 m.

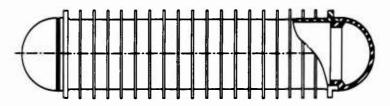


Fig. 1. Schematic of electronic bottle.

Forged billet Production and Inspection

Three heats of Ti 6Al-4V ELI were produced by double melting in an electric arc furnace. A single 83.8 cm diameter by 4,536 kg ingot was cast from each heat. Table I presents the producer's major element chemical analysis of each ingot, along with the requirements of the contract specification. The beta transus temperature (°C) of each ingot, as determined experimentally in a gradient furnace by the producer, is also provided in the table.

Table I. Chemical composition of Ti 6Al-4V ELI ingots (weight %).

Heat	Loca- tion	Al	٧	Fe	Cu	Si	Y	O DDIR	N ppm	C ppm	H ppr	Beta Transus
3454	top	5.9	3.8	0.17	<0.02	<0.03	<0.001	1000	50	100	1	974
	bottom		3.9	0.17	<0.02	<0.03	<0.001	1000	70	90	3	
3455	top	5.8	3.9	0.18	<0.02	<0.03	<0.001	1000	60	80	2	972
	bottom	5.8	3.9	0.17	<0.02	<0.03	<0.001	1000	60	100	2	
6853	top	6.3	4.0	0.18	<0.02	<0.03	<0.005	1000	50	100	6	973
	bottom	6.1	3.9	0.18	<0.02	<0.03	<0.005	900	60	80	2	
Requi	rement	5.5	3.5	0.25	0.05	0.05	0.005	800/	500	800	125	
		-6.5	-4.5	max	max	max	max	1000	max	max	max	

Cylinder Billets

The forged billets for the cylindrical components of the electronic bottles came from the ingot of heat 3454. The ingot was initially heated in a furnace to 1149 °C and upset forged to a 96.5 cm round cross section. Flat dies were used to reduce the cross section to a 76.2 cm square in a series of two reheats above the beta transus of the alloy. Air cooling was performed to increase centerline consolidation of the initial cast structure. Final forging operations were performed below the beta transus of the alloy. The piece was heated in a furnace to 927 °C and forged to a 63.5 cm square cross-section. Flat dies were then used to achieve the final shape (48 cm round) in a series of four reheats. After forging, the billet was annealed at 704 °C for two hours and air cooled. Three pieces of 48 cm outside diameter x 155 cm long were cut from the billet. The billet pieces were lath-turned and then machine-trepanned to 47 cm OD x 29.8 cm ID x 155 cm long. The interstitial content of the final billet was: oxygen-1000 ppm; nitrogen-40 ppm; carbon-180 ppm and hydrogen-45 ppm.

End Cap Billets

Billet material for the end caps was obtained from two ingots: heats 3455 and 6853. The forging procedures were the same as those used for the ingot of heat 3454. Initial breakdown of the ingots was performed above the beta transus, followed by a significant amount of metal deformation below the beta transus, high in the alpha-beta temperature field. After forging, the billets were annealed at 704 °C for two hours and air cooled. From the forged billet of heat 3455, five billet pieces of 40.1 cm diameter x 28 cm long were taken. The interstitial content of this billet was: oxygen-1000 ppm; nitrogen-80 ppm; carbon-200 ppm and hydrogen-17 ppm. One piece 40.1 cm diameter x 28 cm long was cut from the final billet product of heat 6853. The interstitial content of this piece was: oxygen-900 ppm; nitrogen-50 ppm; carbon-150 ppm and hydrogen-54 ppm. The six billet pieces were machined to 39.4 cm diameter x 26.7 cm long.

Ultrasonic Inspection

The nine billet pieces were conditioned for ultrasonic inspection by turning to a surface finish of 250 RMS. The inspection was performed in accordance with MIL-STD-271F using the longitudinal wave technique with a contract requirement for detection of a 1.98 cm diameter flat bottom hole (FBH). All three of the trepanned billet pieces from heat 3454 met the requirement for detection of a 1.98 cm diameter flat bottom hole. The six solid pieces from

heats 3455 and 6853 failed to meet the 1.98 cm criteria due to high background noise, but were acceptable to a 3.18 cm diameter flat bottom hole criterion. While the problems in obtaining good sonic penetration in thick section titanium forgings are well known (1-2), additional mechanical property tests were made on material from the center of the solid billets to ensure the quality of the end cap components. The results of these tests (Table II) were considered adequate to allow acceptance of these pieces.

Microstructure and Mechanical Properties

A test block was cut from one billet of each diameter from each heat to provide material for mechanical property and microstructural evaluation. For the mechanical property tests, one tension, one compression and one Charpy V-notch specimen were taken near the surface from two locations on the test block 90 degrees apart, in both the longitudinal (L) and circumferential (C) directions. In addition, a second set of twelve specimens of the same orientation and location were taken on material from the center of the billets from heats 3455 and 6853. Transverse specimens for microstructural examination were taken near the surfaces and center of the billets.

Microstructure

All of the billets exhibited a beta/alpha-beta processed type microstructure. Representative photomicrographs taken from the billet of heat 6853 are provided in Fig. 2. The microstructure consisted of elongated and equiaxed alpha (light) and intergranular beta (dark). The structure also showed evidence of elongated beta grain boundaries present prior to alpha-beta forging, as indicated by the arrow in Fig. 2c. Typically, a coarse plate-like alpha and intergranular beta structure is produced in thick section Ti 6A1-4V by forging in the beta temperature field and air cooling (3). The forging reductions below the beta transus were sufficient to breakup the plate-like alpha grains, resulting in a mixture of elongated and equiaxed grains of alpha. There were no indications of grain boundary alpha which can provide loci for crack initiation, or of oxygen contamination as evidenced by brightly etched massive regions of alpha phase.

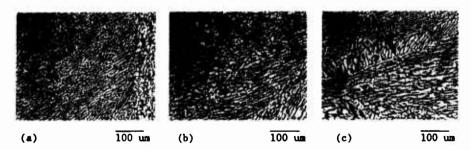


Fig. 2. Microstructure of forged billets: (a) top surface; (b) mid-thickness; (c) bottom surface.

Mechanical Properties

The mechanical properties of the forged billets are presented in Table II, along with the minimum requirements. The test results showed that all compressive and tensile specimens from the surface and mid-thickness exceeded the minimum yield strength requirements. Directional effects were

Table II. Mechanical properties of Ti 6A1-4V ELI forged billets.

Part	Location	Direc- tion	CYS MPa	Fc MPa	UTS MPa	YS MPa	E1	RA %	CVN
		19/1/3/19/5						20	40
Cylinder	Surface	L	800	717	827	758	15	32	
(#3454)		C	848	751	841	765	10	18	33
P-d ass	Surface	L	800	703	820	779	14	26	47
End cap (#3455)	Surrace	C	882	786	875	834	10	18	4:
	C	L	786	696	800	752	15	33	5
	Center	C	793	662	841	772	9	15	4
n-4	Surface	L	834	724	834	779	14	29	3
End cap (#6853)	Surrace	c	882	793	855	793	11	21	3
	Center	L	800	737	765	724	13	25	5
	Center	c	827	731	807	758	12	21	4
Minimum De	equirement		758	info.	info.	655	6	13	1

Note: Each entry is an average of two tests.

Fc - proportional limit in compression.

evident in the data, with a lower average yield strength in the longitudinal specimens compared to the circumferential specimens. Texture-dependent directional effects in titanium produce higher strength and lower ductility in the circumferential test direction (4), as was the case in this work. There was also a higher average yield strength at the surface compared to the center for specimens of the same orientation. The lower strength properties at the center are attributed to slower cooling rates and are consistent with results for other high strength, thick section titanium forgings investigated by the U.S. Navy. All impact specimens exceeded the minimum CVN requirement.

Hydrostatic Performance

Electronic Bottle

After final machining, one of the cylinders and two end caps were assembled into an electronic bottle for an instrumented hydrostatic test. Single and two-element strain gages were attached to the electronic bottle and hard wired into a Micro-Measurements System 4000 strain recording system. A photograph of the instrumented bottle is provided in Fig. 3.

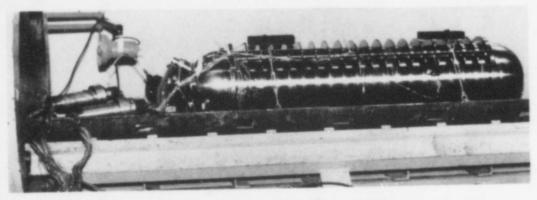
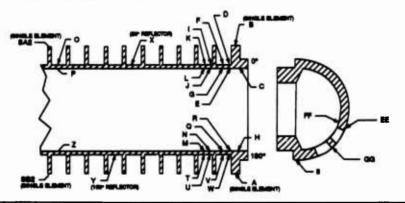


Fig. 3. Instrumented electronic bottle.

The proof test was performed in the Detachment's 1.2 meter diameter pressure test chamber. A series of three test runs were made to a maximum hydrostatic pressure of 62.3 MPa, equivalent to a depth in seawater of 6,096 meters. Pressure was applied in increments with strain measurements taken at each incremental increase. Each run also included a hold at the maximum pressure to check for creep. Stresses were calculated from the recorded strain data using the design value for Young's modulus in compression (122.0 GPa) and a Poisson's ratio of 0.3. Table III presents the experimental stresses for each test run at the maximum operating pressure of 62.3 MPa.

Table III. Experimental stresses at design operating depth.

Gage	Lo	ngitudin	al Stres	s (MPa)	Circ	unferent	ial Stre	ss (MPa
ocati	on #1	#2	#3	Average	#1	#2	#3	Average
A		no g	age		-190.3	-189.6	-189.6	-190.3
В		no g	_		-190.3	-189.6	-189.6	-190.3
С	-450.2	*	-450.2	-450.2	-475.1	-470.9	-470.2	-472.3
н	-444.7	-444.0	-440.0	-444.0	-477.8	-474.4	-473.7	-475.1
D	-416.5	-418.5	-418.5	-417.8	-447.5	-461.3	-464.7	-457.8
E	-306.8	-306.8	*	-306.8	-511.6	-508.2	*	-511.6
R	-273.7	-276.5	-277.9	-275.8	-498.5	-501.3	-504.0	-501.3
F	-578.5	*	*	-578.5	-450.9	*	*	-450.9
V	-437.8	-435.1	-434.4	-435.8	-548.8	-546.8	-546.8	-547.5
G	-213.8	-213.1	-213.8	-213.8	-555.0	-550.1	-550.1	-552.3
Q	-215.1	-239.9	-239.9	-231.7	-541.3	-548.8	-548.8	-546.1
I	-338.5	-337.9	-338.5	-338.5	-535.7	-534.4	-535.1	-535.1
U	-353.7	-353.7	-354.4	-353.7	-572.3	-570.9	-570.9	-571.6
N	-304.8	-303.4	-303.4	-304.1	-640.5	-637.8	-637.8	-638.5
K	-313.7	*	*	-313.7	-509.5	*	*	-509.5
T	-344.8	-346.1	-346.1	-345.4	-551.6	-557.1	-557.1	-550.0
X	-353.7	-350.1	-351.6	-352.3	-579.9	-580.6	-581.9	-580.6
0	-330.3	-315.1	-315.8	-320.6	-533.0	-439.2	-441.3	-470.1
P	-349.6	-281.3	-282.7	-304.8	-639.9	-476.4	-480.6	-564.7
SA2		no ga	ge		-337.9	-335.8	-335.8	-336.5
SB2		no ga	_		-348.2	-347.5	-347.5	-347.5
EE	-296.5	-297.9	-297.9	-297.2	-328.2	-327.5	-328.2	-328.2
FF	-416.5	-413.7	-413.7	-414.4	-446.1	-444.7	-446.1	-445.4
II	-110.3	*	*	-110.3	-169.6	*	*	-169.6
Maxim	um Desig	n Limit	Stress	-606.7				-606.7



Note: * (and gages W, J, L, M, Y, Z and GG) - lost due to water intrusion

The maximum average stress on the bottle at the design operating depth for all test runs was -638.5 MPa. This is slightly above the design proportional limit stress of -606.7 MPa, but was acceptable since no creep strain was observed at this location during the 1 hour hold of test run #3. Average experimental stresses at all other locations were less than the design proportional limit. In addition, all experimental calculated stresses were below the compressive proportional limits determined from tests on actual billet material, Table II.

CURV III Vehicle

After hydrostatic testing the remaining bottles, all components were installed on the CURV III in preparation for a vehicle proof test. This test was performed in the Detachment's 3 m diameter pressure test chamber, Fig. 4. A test run was made to a maximum hydrostatic pressure of 62.3 MPa to verify the operation of major vehicle subsystems, including the thrusters, hydraulic systems, electrical systems and TV units. The results indicated satisfactory vehicle performance at the design operating depth of 6,096 m.

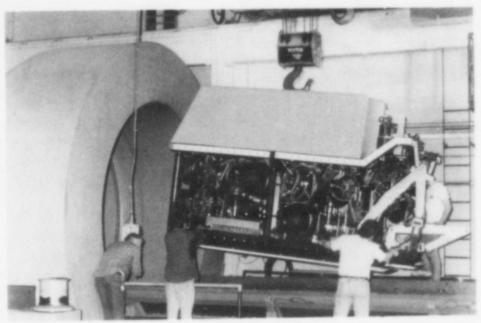


Fig. 5. CURV III on loading rack of pressure test chamber.

Work in Progress

The shallow depth configuration of the vehicle will use titanium spheres for flotation. The sphere design has an outside radius of 43.8 cm and a shell thickness of 12.95 mm. To fabricate the spheres, titanium alloy Ti-6211 disks were formed into hemispheres by hot spinning. The as-spun hemispheres were finish-machined on the inside and outside surfaces except for a 15 cm wide band around the weld joint. Welding procedures were developed for joining the hemispheres, using the buried-arc GTAW process for the root pass, and conventional GTAW cold-wire to complete the one-sided joint. Radiography of the completed welds showed that all spheres met the U.S. Navy Class I acceptance standard for welds. Upon completion of final machining of the weld band area, all spheres will undergo hydrostatic testing to the design operating depth.

Summary

The production of forged billets, mechanical property test results, and hydrostatic performance of an electronic bottle for use in the CURV III vehicle have been presented. It was determined that the cylinders and end caps accepted by the Navy either met the contract specifications or were judged acceptable after technical analysis in instances of nonconformance. Proof testing of all electronic bottles indicated satisfactory performance.

Acknowledgements

The instrumentation and pressure testing of the electronic bottles were the work of Mr. A. Hartman and Mr. J. Whitacre of the Carderock Division of the Naval Surface Warfare Center. Thanks are also given to Mr. B. Harvey of Harvey Titanium Ltd., Mr. S. Gillish of Howmet Corporation, and Mr. J. Pigg of Teledyne Allvac for the production of the titanium ingots and forged billets.

References

- K. L. Kremer et al., "Ultrasonic Inspection of Titanium Airframe Components," <u>Titanium Science and Technology</u>, Plenum Press, New York-London, 1973, 717-731.
- 2. Metals Handbook, 9th ed., Vol. 17 (Metals Park, OH: American Society for Metals, 1989), 497-498.
- 3. Metals Handbook, 8th ed., Vol. 7 (Metals Park, OH: American Society for Metals, 1974), 329.
- 4. Matthew J. Donachie, Jr., ed., <u>Titanium: A Technical Guide</u> (Metals Park, OH: American Society for Metals, 1988), 163-172.

CORROSION BEHAVIOR OF TIMETAL-21S FOR NON-AEROSPACE APPLICATIONS

J. S. Grauman

TIMET P.O. Box 2128 Henderson, Nevada 89015

Abstract

Typically, non-aerospace or industrial applications of titanium rely on its excellent corrosion resistance. Sometimes, applications also require higher strengths than C.P. grades of titanium can offer. High strength titanium alloys unfortunately do not usually possess the necessary corrosion resistance. However, a recently developed titanium alloy, TIMETAL·218 (Ti-15Mo-2.7Nb-3Al-.28i) appears to fill the void of a high-strength, corrosion resistant alloy for the CPI. The corrosion behavior of TIMETAL·218 in reducing acid environments is characterized, comparing it to other titanium alloys. In addition, hydrogen absorption under cathodic charging conditions is described. Minor compositional variations are studied with respect to effects on corrosion behavior and hydrogen uptake efficiency (HUE). Present and future non-aerospace applications are also discussed.

Introduction

Titanium and its alloys have, for roughly 30 years now, served the corrosion resistance needs of non-aerospace markets. The largest share of this service has been provided by unalloyed or commercially pure titanium. Table I lists a few of the many different non-aerospace, or industrial applications of titanium. The majority of these applications require corrosion resistance to be the primary criterion, with mechanical strength secondary. In these instances, unalloyed titanium has been used very successfully and economically. In the event commercially pure titanium does not possess sufficient corrosion resistance for a particular application, the use of ASTM grade 7 titanium (Ti-.15Pd) can usually solve the corrosion problem. The addition of palladium to C.P. titanium imparts dramatically improved corrosion resistance without altering mechanical properties. Unalloyed titanium also has attributes such as excellent weldability and formability, which make it attractive from a fabrication point of view.

The one area that unalloyed titanium does not fare well in is mechanical strength. When high temperature and/or pressure service is required, unalloyed titanium cannot always perform economically, since excessive wall thicknesses are required. High strength titanium alloys can sometimes be

Titanium '92 Science and Technology Edited by F.H. Froes and I. Caplan The Minerals, Metals & Materials Society, 1993

Table I Some Typical Non-Aerospace Applications of Titanium

Industry	Process Equipment	Titanium Alloys in Use
Chemical	Vessels, Piping, Evaporators, Distillation Columns, Exchangers	Unalloyed Ti, Grade 7 Ti, Grade 12 Ti, Ti-6Al-4V
Oil & Gas	Coolers, Overhead Condensers, Sourwater Strippers, Reboilers	Unalloyed Ti, Grade 7 Ti Grade 12 Ti
Power Plants	Condensers, Exchangers, FGD Ductwork, Service Water Piping	Unalloyed Ti, Grade 7 Ti
Orthopaedic	Joint Implants	Ti-6Al-4V and other High- Strength Ti Alloys
Pulp/Paper	Vessels, Valves, Piping, Diffusion Washer Internals, Pumps	Unalloyed Ti

used, but they typically suffer from reduced fabricability as compared to unalloyed titanium. The most common high strength titanium alloy, Ti-6Al-4V, also often times lacks the necessary corrosion resistance for a particular application. Other high strength titanium alloys possess corrosion resistance equal to or better than commercially pure titanium, but none equal the resistance of the Ti-Pd alloy.

Recently, however, a new titanium alloy, TIMETAL.21S (Ti-15Mo-2.7Nb-3Al-.2Si) was developed as an oxidation resistant material for use in metal matrix composites. The mechanical/physical property requirements necessary for use in HMC's also meet the needs of industrial applications. Namely, cold workability, weldability, and being producible in all common mill product forms. Since this is a beta titanium alloy, it readily responds to heat treatment, yielding strength levels 3-4X higher than unalloyed titanium. Finally, the high molybdenum content suggested that this alloy might have excellent reducing acid corrosion resistance analogous to other Mo-containing titanium alloys. It appeared this alloy could be well suited to serve the industrial marketplace as a high strength, corrosion resistant titanium alloy.

This paper outlines some of the properties of TIMETAL.21S, highlighting the corrosion resistance of the alloy in extremely aggressive environments. Applications of this new alloy in non-aerospace markets are also addressed.

TIMETAL + 218 Property Considerations

A comparison of mechanical properties between TIMETAL-21S and grade 2 titanium is shown in Table II. The advantage of a heat treatable alloy is that it allows the end user to be flexible in determining critical property criteria. For ease of formability, the solution treated condition would be selected. However, for high temperature or pressure service, one of the STA conditions would be preferred.

Table II Comparison of Typical Mechanical Properties Between Grade 2 Titanium and TIMETAL-21S

Alloy		UTS (MPa)	<u>YS</u> (MPa)	E1
ASTM Grade 2 Ti		483	345	28
TIMETAL 0218 ST	1	870	840	20
TIMETAL 218 STA	2	1110	1034	10
TIMETAL CLIS STA	3	1410	1310	5

1843°C, 30 Min AC.

2593°C, 8 Hr.

3482°C, 8 Hr.

TIMETAL.218 offers all the fabrication advantages of unalloyed titanium and other metastable beta titanium alloys, such as Ti-15V-3Cr-3Sn-3Al (TIMETAL.15-3). The alloy is easily produced into bar; billet, strip, and foil and can routinely pass a 1t bend test, which surpasses the cold formability of grade 2 titanium. TIMETAL.218 also has excellent weldability, again, a necessity for most industrial applications, such as heat exchangers, reactor vessels, and mixers.

Corrosion Behavior of TIMETAL - 21S

The beneficial effect of molybdenum additions on reducing acid corrosion resistance of titanium alloys has been well established. 1,2,3 Substantial improvement in corrosion resistance is first observed at about 3-4 wt.% molybdenum addition. Increasing concentrations yield correspondingly diminished corrosion rates. Thus, it was anticipated that TIMETAL.21S would have excellent resistance to reducing acids, such as hydrochloric and sulfuric. TIMETAL.21S, however, exceeds the corrosion resistance expected for a 15 wt.% molybdenum addition. This can be evidenced by comparing passive to active transition levels* for No-containing titanium alloys. Figure 1 presents several 0.127mm/yr passive to active transition levels in HCl.4 TIMETAL.21S exceeds the resistance of other 15% molybdenum alloys by, nearly a factor of two.

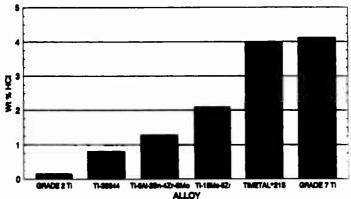


Figure 1 - Passive to active transitions (0.127mm/yr) for several titanium alloys in hydrochloric acid.

^{*}Passive to active transition level is defined here as the acid concentration (in wt.%) corresponding to a corrosion rate of 0.127mm/yr.

The driving force behind this greater than expected corrosion resistance is an additive relationship between the molybdenum and the niobium. The effect of niobium appears to remain relatively constant, whether considering a Ti-Nb binary, or Ti-No-Nb tertiary alloy. In both cases, the addition of Nb roughly halves the corrosion rate, as shown in Figure 2.5 The additive effect produces an alloy that is nearly the equal of grade 7 titanium (Ti-.15Pd), which has the greatest resistance to reducing acids of any commercially available titanium alloy. Similar results are observed in hydrochloric acid solutions. This effect carries over to crevice corrosion resistance in acidic chloride media, where TIMETAL+21S resists attack to pH levels of 0.2.6 Once again, the resistance of the alloy parallels that of grade 7 titanium.

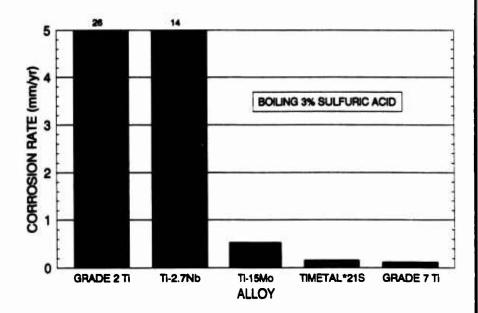


Figure 2 - Effect of Molybdenum and Niobium additions on the corrosion rate of titanium in sulfuric acid.

Hydrogen absorption is usually considered a concern when titanium is exposed to reducing acids, galvanic couples, or cathodic protection. the right conditions excessive hydrogen absorption can eventually lead to embrittlement of the titanium. TIMETAL 215 has shown a tolerance of over 3000 ppm4, or roughly ten times the acceptable tolerance level for unalloyed titanium. This extremely high tolerance level is typical for beta titanium alloys, due to high solubility of hydrogen in the beta phase. Hydrogen absorption tests which measure the hydrogen uptake efficiency (HUE) of a material demonstrate that TIMETAL.21S also resists absorption better than any currently available titanium alloy, as shown in Figure 3. The figure also illustrates the beneficial additive effect of molybdenum and niobium alloying, analogous to that observed in reducing acid environments, as described earlier. Thus, TIMETAL-21S offers the unique combination of low hydrogen absorption rates and a high tolerance, whereas all other titanium alloys have either one or the other attribute, but never both.

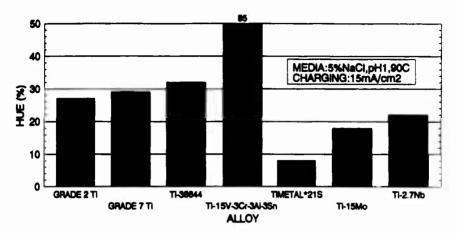


Figure 3 - Hydrogen Uptake Efficiency (HUE) of several titanium alloys.

Industrial Applications of TIMETAL - 21S

Plating

One of the first industrial applications involved the use of TIMETAL-21S strip in an electrochemical plating operation. The higher strength of the alloy in the solution treated condition was utilized for improved fatigue life and to reduce the chance of tensile overload. In addition, excellent corrosion resistance was required due to the presence of hot sulfuric acid in the process stream. Finally, TIMETAL-21S also solved a recurring problem of hydrogen embrittlement in certain areas of the process stream where galvanic corrosion was being experienced. The excellent hydrogen absorption resistance and high hydrogen tolerance has essentially eliminated the problem. In all cases, the material TIMETAL-21S replaced was unalloyed titanium.

CPI

TIMETAL. 21S is currently being tested for use in an organic acid process stream. Unalloyed titanium and to a lesser extent, Ti-Pd suffer hydrogen embrittlement in this organic acid. This is believed to be caused by an apparent weakening of the protective oxide film allowing penetration of hydrogen. It is believed TIMETAL. 21S will be better able to resist the absorption of hydrogen even if the oxide film is partially weakened. The process equipment involved is a high temperature pressurized reactor.

Fasteners

TIMETAL.21S is presently being evaluated in several non-serospace fastener studies being conducted by the Navy and a research group funded by offshore oil companies. The media for these studies is seawater, which can be effectively handled by all titanium alloys. However, unalloyed titanium does not possess the strength required to replace the current fastener material, Monel K-500. The concern for some high strength titanium alloys is SCC, and hydrogen embrittlement from cathodic protection. TIMETAL.21S is expected to be a prime candidate fastener material for seawater service due to its excellent resistance to hydrogen absorption, good strength and creep resistance, and immunity to seawater SCC (based on fracture toughness data).

Oil & Gas Production

TIMETAL.21S, and a modified version of the alloy containing palladium, have been shown to be the most promising alloys to combat the aggressive conditions in deep sour oil and gas wells. TIMETAL.21S (modified) exhibits unsurpassed SCC resistance to downhole environments, but which will be utilized as wells are drilled to deeper depths, where temperatures can exceed 250°C. The alloy also offers the possibility of using uninhibited acid solutions downhole when wells need to be cleaned for increased production capability. TIMETAL.21S is the only current candidate material capable of resisting these concentrated reducing acid solutions. 7

Summary

TIMETAL.21S appears capable of filling the void of a high strength corrosion resistant alloy for non-serospace applications. It will not replace grade 2 or even grade 7 titanium, where these materials are being utilized successfully. However, in certain applications involving high temperature reducing acid media, such as deep sour gas wells, TIMETAL.21S is being considered a viable alternative. Significant market applications will also arise for TIMETAL.21S in areas where unalloyed titanium suffers excessive hydrogen absorption, whether by detrimental galvanic couples, electrochemical charging, or corrosion.

References

- R. W. Schutz and J. S. Grauman, "Fundamental Corrosion Characterization of High Strength Titanium Alloys", <u>Industrial Applications of Titanium and Zirconium</u>, 4th Volume, STP 917, American Society for Testing and Materials, (1986), 130-143.
- 2. M. Stern and C. Bishop, <u>Transactions ASN</u>, 54, (1961), 286-298.
- N. D. Tomashov, et al., "Studies of the Alloys of the Titanium-Molybdenum-Niobium-Zirconium System With Higher Corrosion Resistance in Acid Solutions", <u>Proceedings of the 3rd International Conference on Titanium</u>, Moscow, (1976) 927-940.
- J. S. Grauman, "Beta-218: A New High Strength, Corrosion Resistance Titanium Alloy", Proceedings of the 1990 International Conference, Titanium Development Association, Dayton, OH, Vol. 1, (1990) 290-299.
- 5. Unpublished TIMET data.
- D. D. Bergman and J. S. Grauman, "The Detection of Crevice Corrosion in Titanium and Its Alloys Through the Use of Potential Monitoring", To be presented at the Seventh World Conference on Titanium, San Diego, CA, June 28-July 2, 1992.
- J. S. Grauman and E. E. Mild, "Corrosion Resistance of Titanium Alloys in Simulated Acidizing Environments", Presented at the Offshore Mechanics and Artic Engineering Conference, ASME, Calgary, Canada, June 7-11, 1992.

ANODIZING MECHANISMS IN HIGH PURITY TITANIUM

H.W. Rosenberg and M.S. Cooper

The ALTA Group RR 2 Box 710 Fombell, PA 16123

Karl Bloss

Kemkonsult Bloss 515 Squire Place Pittsburgh, PA 15237

Abstract

In common with other valve metals such as aluminum and tantalum, titanium forms an oxide film of high electrical resistivity under anodic polarization conditions. Electronic grade Ti (99.99+% metallics basis) was anodized to 100 volts or more in a variety of solutions of phosphoric acid in an aprotic solvent. The films were formed under galvanostatic conditions until a preset voltage was reached, after which the voltage was held constant. The anodization was then continued until a minimum in the current decay was reached and anodization stopped. Three regimes of electrochemical behavior were observed.

Introduction

Anodizing titanium conventionally employs aqueous electrolytes of mineral acids with impressed voltages up to 100 volts or more. Anodized titanium provides improved corrosion resistance and is decorative as well.

Titanium is a member of the family of so-called valve metals whose anodized oxides readily conduct electricity only if the substrate is made cathodic. Such films are not useful diodes, however. Tantalum and aluminum are the most important valve metals and together provide the basis for a large segment of the electrolytic capacitor industry. The superior dielectric properties of titanium oxide has not been exploited for such use because anodized titanium films are leaky at best. Residual leak rates through anodized films of itanium are still orders of magnitude larger than those attainable for tantalum and aluminum. Nevertheless, the high dielectric properties of titanium hold possibilities for miniaturization of capacitors as well as increased storage power density.

The ALTA Research Laboratory therefore embarked on a survey designed to further the understanding of the anodizing process in titanium.

Experimental

All material used for the mechanism work was 99.998% pure electrolytic titanium foil on a metallic basis. The foil analyzed about 400 ppm total gases. Electronic grade titanium was used because purity is an important factor in the performance of both tantalum and aluminum anodic films and it was thought that titanium might be an analogous case. Commercial purity titanium as well as the well known Ti-6Al-4V alloy were anodized for reference purposes but were not studied extensively and will not be reported here.

Specimens with areas of about 10 to 50 square centimeters were prepared by pickling in dilute nitric acid with just enough hydrofluoric acid to cause hydrogen evolution in a stirred solution at room temperature. This was followed by rinsing in deionized water and high purity acetone before drying. Pickling times were on the order of one minute. In all cases the specimens were kept clean and not touched until after anodizing was complete.

The ionic component of the anodizing solutions was provided by 85% orthophosphoric acid. Aprotic solvents were selected from readily available organic solvents such as propylene carbonate, gamma butyrolactone and the ethyl and methyl pyrrolidones.

The aprotic nature of a solvent is qualitatively indicated for purposes here by the lack of reaction between a 5 vol. % solution of phosphoric acid in the solvent in question and granulated ammonium carbonate. Solutions of phosphoric acid in protic solvents vigorously evolve carbon dioxide gas upon the addition of ammonium carbonate. Aprotic solvents essentially provide solutions that are poor proton doners. This is in marked contrast with aprotic solutions of the same anodizing acid.

All anodizations were done in solutions at room temperature, between 298 and 302 K. Stirring was used to ensure solution and temperature uniformity and was accomplished by magnetic stirring rods. Temperature within this range did not affect results to any measurable degree.

Anodizing solution containers were either stainless steel, where the container was the cathode, or a glass flask, in which titanium strips provided the cathodic pole. The steel container was fitted with a glass lid to facilitate observations during anodizing. Both vessels

were air tight. Solution volumes ranged from 500 ml to several liters with equivalent results obtained.

Anodizing current was provided by a power supply that allowed independent control of current and potential. A two channel chart recorder accurate to about 0.2% of full scale was used to follow electrical events during anodizing.

Anodizing experiments began under constant current, usually about one milliamp per sq cm of specimen surface. The power supply was set such that anodizing began under constant current conditions until a preset maximum voltage was reached. The voltage was then held constant for the remainder of the anodization, allowing the current to decay to a minimum where further anodization ceased. Current regulation was not perfect.

Experimental data were reduced by hand and stored on a Macintosh computer which also served as the tool for analyzing and graphing results.

Results and Discussion

Phenomenology

Film thickness calculations were based on the number of coulombs passed during anodization. The anodized film was assumed to be pure, stoichiometric TiO_2 and that the process was 100% efficient. This calculation procedure had the advantage of simplicity but was not exact. Auger sputtering time indicated that the actual film thicknesses (on the order of 2000 - 3000 Å) agreed with calculated thickness to only within about $\pm 25\%$. Also, resistivity measurements showed that electronic conduction was always present to some degree. These short circuits reduce film formation efficiency.

Film stoichiometry was not constant as shown in Table I.

Table I. Surface and Sub Surface Film Chemistries by Weight Percent.

Surface			25 nm Sub surface					
element	Ti	0	С	P	Ti	0	С	P
wt %	10.9	39.0	26.0	24.1	30.3	57.1	3.8	8.8

Depth profiling showed these changes were gradual for Ti and O. These results indicate that the film boundaries are not sharply demarked. Moreover, carbon and phosphorus were incorporated to some depth. Carbon is a common contamination in analyses such as these. On the other hand, the organic solvent is an available source of carbon and since phophorus behaves similarly, the carbon profile could well be real.

Figure 1 illustrates the initial stages of an anodization run. Stage One is designated as the region where the voltage rises linearly with time at constant current, implying the existence of a constant potential gradient across the film. The slight decrease in the current during this period is a characteristic of the power supply used. Field strengths were calculated from the applied voltage and the calculated film thickness. The voltage drop across the solution was accounted for in the calculations but no attempt was made to include the interface voltage drops. On this basis field strengths were typically about one - five MV/cm.

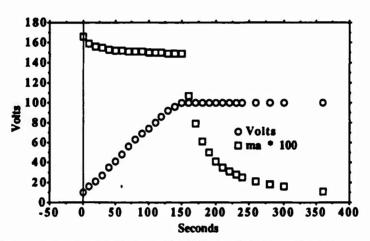


Figure 1. Initial Anodization Behavior Observed on High Purity Titanium.

The resistance of the film increases linearly with each coulomb passed. V increases as necessary to maintain the preset current flow. The film thickens in proportion to the coulombs passed. Upon reaching preset voltage, the current typically drops precipitously. Figure 2 show the resistivity time-derivative increases by roughly an order of magnitude.

In region one, I = V/R = constant, and more importantly, Et = IR, where E is the field across the film (V/cm), t is the thickness of the film (cm) I is current in amperes and r is resistance in ohms. In region two, V = IR = constant; Et = IR, as in region one.

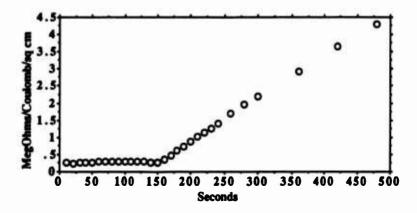


Figure 2. Transition in Film Resistivity Derivative Between Regions 1 and 2.

As one might expect, there comes a time of vanishing returns. This is region 3. Beyond about 0.475 coulombs/cm² in the example, continued anodizing provides no further gains in film formation efficiency. In figure 3 the ordinate has the dimensions of megohms per coulomb per unit specimen area. It is useful as a measure of anodization efficiency and typically reaches a maximum about the time the anodizing current bottoms out. Continued anodizing eventually causes anodizing current to increase. At that point film perforation has begun in earnest and the film forming efficiency parameter begins to fall.

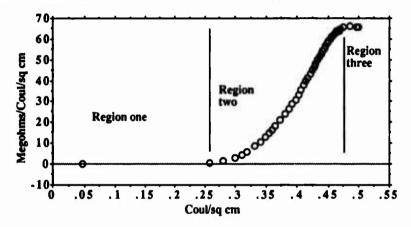


Figure 3. Illustration indicating Regions of Titanium Anodizacion.

The Mechanism

Clearly a net oxidation requires some type of ionic conduction through the film. The question is: which ions are contributing to current conduction and film formation. Mott (1) and Cabrera and Mott (2) developed an ion transport model in which the rate-limiting step for film growth is the emission of cations from the substrate. Schmidt et al (3) reported that ion size is an important factor in electrolytic rectification, which anodizing titanium amounts to. They found that the small ions Li⁺ and Na⁺ are more effective current carriers than the larger K⁺ and Rb⁺ ions having the same charge. Sato and Cohen (4) proposed a model where a layer of oxygen absorbs onto the film and exchanges places with the underlying metal atoms. Chao et. al. (5) reviewed the possible transport mechanisms and proposed a point defect model for film growth. They concluded that oxygen anions or oxide ion vacancies are essential for passive film growth.

It is useful therefore to review the force parameters observed by ions on either side of the film. This is done in Table II.

From specific force and geometric considerations, protons are the preferred charge carriers but their numbers in the substrate are insignificant and they do not in any event contribute to film formation. Titanium cations see much higher force parameters than do the hydroxyl or phosphate anions. At this stage in our research this is about all that is known. If titanium can be ionized in the metal/film interface, then cation transport should have a lower activation energy than does anion transport. Anions, of course, are already charged and ready to go. For the conditions reported here there is no apparent way to deduce unequivocally whether

Table II. Charge/Unit Area parameters influencing the possible charge carriers. (7)

Ion	Charge	Radii - Å	Area - Å ²	Charge/Unit Area
H	1	proton	proton	3x10 ⁹
TI TI	3	0.68* 0.77*	1.5 1.9	2.8 1.6
π̈	2	0.90*	2.5	0.79
π	ī	0.96*	2.9	0.35
PO ₄ OH	3	4.0**	50	0.06
OH	1	3.5**	38	0.03

ion transport is acting, and if so, which one, or whether charge transfer occurs by ion vacancy migration (6).

Auger analyses demonstrate that phosphorus is incorporated into the anodized film. While phosphorus appears to be concentrated near the surface on the solution side of the film, that fact, in itself, does not distinguish among the transport possibilities. Further work is needed on the transport mechanism.

If anion transport is controlling, the picture implied in Table II is grossly simplistic. See the discussion of solution chemistry, below. The H₃PO₄ component and its behavior in aprotic solvents is likely to be complex indeed and is not yet well understood.

At the anode, film formation consumes phosphorus containing anions, while at the cathode, hydrogen is reduced and released. Together, these two events consume the phosphoric acid component of the electrolyte.

Two types of conduction are present. They are clearly distinguished by the manner in which current depends on the applied voltage. A exponential dependence implies conduction by ion or ion vacancy diffusion or migration whereas a linear dependence implies ohmic or electronic conduction. Both types were present in results reported here. An example appears in Figure 4.

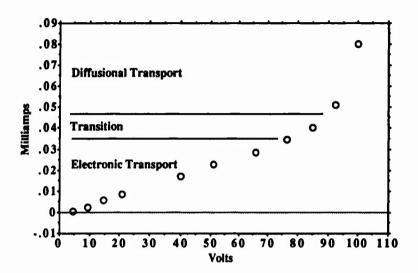


Figure 4. Conduction Regimes by mechanism.

In this example, the electronic component is larger than that typically observed.

Solution Chemistry

Most compositions of anodizing solutions have been established empirically. Except for the necessity to accommodate the right amount of 85% aqueous orthophosphoric acid for adequate ionic conductivity, the choice of aprotic solvents seems wide open. Toxicity, stability, price and other practical criteria infer constraints and preferences.

So does solution chemistry. Even in purely aqueous solutions, phosphoric acid dissociates into charge carriers other than simply three protons and a [PO₄]⁻⁻⁻ anion. At pK values of 2.12, 7.21 and 12.67 for the respective dissociation steps of orthophosphoric acid, the actual concentration of [PO₄]⁻⁻⁻ is much smaller than that of [HPO₄]⁻⁻ let alone [H₂PO₄]⁻. Nor is orthophosphoric acid the only phosphorus-containing oxy-acid behind the label "85% H₃PO₄". Usually there is a percent or so of pyrophosphoric acid around, which at pK 0.85 and 1.49 for the first and second dissociation step, is distinctly stronger than orthophosphoric acid.

In the typical anodizing solutions used here, which are combinations of aprotic solvents with a minority share of phosphoric acid and 3/17 thereof of water, association, including that to $H_4P_2O_7$, is enhanced, dissociation is subdued. A lower dielectric constant, as most organic liquids have compared to water, depresses the concentrations of the multiply charged anions further. Thus ions like $[H_3P_2O_7]^-$ or $[H_2PO_4]^-$ are likely to outnumber $[PO_4]^{--}$ by several orders of magnitude, at least per unit volume of solution. The phosphorus contents in the anodic titania films proves that phosphorus-containing anions participate in the anodizing process, but which ones do how much of what?

Turning attention to the solution cations: In aqueous media, proton hopping contributes substantially to the overall conductivity. In nominally "anhydrous" orthophosphoric acid, which contains no real H₃PO₄ molecules but about 6% real H₂O and 6% H₄P₂O₇ (partly dissociated), [H₄PO₄]⁺ and [H₂PO₄]⁻ are among the prevailing charge carriers. Proton hopping is a statistically major contributing event there too. Aminic and amidic solvents, like N-alkylpyrrolidones, accommodate protons more readily than less basic liquids, e.g. propylene carbonate, can. Yet their efficiencies as "proton floes" are hardly known.

Conclusions

High purity titanium is effectively anodized in solutions consisting of orthophosphoric acid in aprotic solvents.

Current conduction occurs by a combination of ionic and electronic transport.

References

- 1 Mott, N. F., Trans. Far. Soc., vol. 43, p 429, 1947.
- 2 Cabrera, N. and Mott N. F., Rep. Prog. Phys., vol. 12, p 163, 1948 1949.
- 3 Schmidt, P F, et. al., R. F., Phys. Chem. Solids, vol. 15, p 270, 1960.
- 4 Sato. N. and Cohen, M., J. Elec. Chem. Soc., vol. 111, p 512, 1964.
- 5 Chao, C. Y., et. al., J. Elec. Chem. Soc., vol. 126, No 6, p 1189, 1981.
- 6 Macdonald, D. D. et. al., J. Elec. Chem. Soc., vol. 139, No 1, p 172, 1992.
- 7 Lange's Handbook of Chemistry, 13th Edition, Mc Graw-Hill, 1985.

A Ti-5%Ni Alloy Electrode for Production of Electrolytic Manganese Dioxide

Kazuhiro Taki, Yasuhiro Mitsuyoshi and Hideo Sakuyama

Nippon Mining Co., Ltd 3 kurami, Samukawa-machi, Koza-gun, Kanagawa, Japan

Abstract

In the process of the production of electrolytic manganese dioxide(EMD), c.p. Ti is usually used as anodes due to its excellent corrosion resistance. However, the growth of passive film on the surface of c.p. Ti during the electrolysis causes rapid increase in bath voltage, and forces the EMD electrolysis to be made with a low current density(5 to 10 mA/cm2). Development of advanced materials has been desired for EMD anodes to suppress the growth of passive film and to make the electrolysis with a high current density.

 ${
m Ti-5\%Ni}$ alloy has recently been developed as a new EMD anode material. It is shown that the electrolysis with ${
m Ti-5\%Ni}$ allows much higher current density than that with c.p. ${
m Ti}$. Anodic polarization behaviors of c.p. ${
m Ti}$ and of ${
m Ti2Ni}$ compound are investigated and discussions are made on the mechanism of the improvement in the anodic characteristics of ${
m Ti-5\%Ni}$ alloy.

Introduction

Electrolytic manganese dioxide (EMD) as an active material of batteries is produced by electrolysis of a MnSO4+H2SO4 solution. As anodes in the electrolysis, carbon or c.p. Ti have been used. The corrosion resistance and the mechanical strength of carbon anodes are not high enough, so that the consumption rate during use is very high. This requires frequent adjustment of gaps between anodes and cathodes and causes contamination of product by carbon. Recently, c.p. Ti has been used as anodes since it has higher corrosion resistance and higher strength. The use of c.p. Ti anodes gives maintenance-free operation and good product quality. The biggest problem of c.p. Ti anode is the growth of passive film. Normal passive film of titanium is thin enough for electric current to flow through, however, when some voltage is applied to titanium, the film thickness in-

Titanium '92 Science and Technology Edited by F.H. Froes and I. Caplan The Minerals, Metals & Materials Society, 1993 creases with the voltage. It results in reduction of the anode conductivity. In the process of EMD production, galvanostatic electrolysis is generally made. Therefore, once the anode conductivity decreases due to increase in the passive film thickness, bath voltage must be increased in order to maintain the current density at a fixed level. This causes the growth of film thickness more and makes the electrolysis be stopped finally. For this reason, current density is kept at a low level, ranging from 5 to 10 mA/cm2.

Increase in the current density in EMD process provides two advantages, i.e., high productivity and possibility of finding a new type of EMD. It is expected that a unique EMD is produced by changing compositions of electrolysis solution and/or current density.

In the past, some attempts were made to obtain high current density by using an improved anode material. One of them was to use platinum-coated titanium[1]. This anode enables us to get high current density, but the coated platinum was peeled off during the collecting procedure of EMD formed on the anode surface. A Ti-Mn alloy was also tested[2]. However, this alloy also could not replace c.p. Ti due to its high production cost.

Nippon Mining has successfully developed a new titanium alloy. Ti-5%Ni, which provides high current density, good durability and reasonable price for EMD anodes. This paper reports the anodic characteristics of Ti-5%Ni and the results of investigation on the mechanism of improvement in the anodic characteristics of Ti-5%Ni compared with c.p. Ti.

Experimental

Ti-5%Ni ingots were prepared by double arc vacuum melting. A typical chemical composition is shown in Table 1. These ingots were heated to 1200 K and hot-rolled to 4 mm thick plates. These plates were heated again to 950 K for annealing, cold-rolled to 1 or 2 mm thick plates, and finally, annealed at 950 K in vacuum. Anode specimens were cut from these plates and subsequently polished or treated by sandblasting.

It has been found that H2SO4 + MnSO4 electrolyte is not suitable to examine anodic polarization behavior of Ti-5%Ni because MnO2 deposited on anode surfaces during electrolysis greatly influences anodic characteristics. Sulfuric acid solution was then used to study anodic polarization behavior of Ti-5%Ni.

	H	0	N i	Ti
C. P. Ti	0.0023	0.116	-	bal.
Ti-5%Ni	0.0013	0.141	5. 14	bal.

Table 1 Chemical Composition

Polished c.p. Ti and Ti-5%Ni anodes were investigated in a 0.35 mol/l sulfuric acid solution at an ambient temperature—using platinum as a cathode to measure change in bath voltage with time under galvanostatic electrolysis. In this electrolysis, anodes evolved oxygen gas and cathodes evolved hydrogen gas.

To study anodic characteristics in EMD production, c.p. Ti and Ti-5%Ni anodes treated by sandblasting were investigated in 0.35 mol/1 H2SO4 + 0.55 mol/1 MnSO4 solution at 95 °C using carbon cathode to measure change in bath voltage with time under galvanostatic electrolysis. The sandblasting was made to prevent deposited MnO2 from peeling off the surface of specimens. Schematic illustration of the electrolysis apparatus is shown in Fig. 1.

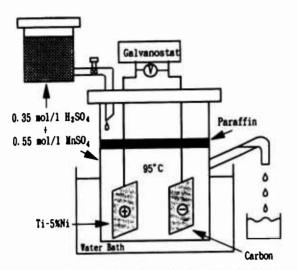


Fig. 1 Schematic Diagram of electrolysis apparatus

Results

1. Electrolysis in the sulfuric acid solution

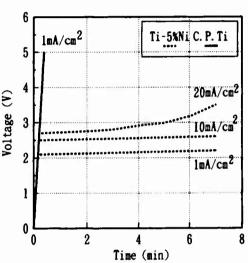
Change in bath voltage with time under galvanostatic electrolysis at current density of 1 mA/cm2, 10 mA/cm2 or 20 mA/cm2 is shown in Fig. 2. It is shown that the bath voltage for c.p. Ti increases beyond 5 v within 20 seconds at the current density of 1 mA/cm2. Whereas, Ti-5%Ni anode keeps the bath voltage at 2.1 v or 2.5 - 2.7 v in the electrolysis at 1 mA/cm2 or 10 mA/cm2, respectively. When the electrolysis is made at 20 mA/cm2, the bath voltage begins to take off after three minutes, indicating the start of passive film growth. In fact, after the electrolysis with c.p. Ti at 1 mA/cm2 and with Ti-5%Ni at 20 mA/cm2, the surfaces of anodes were discolored.

From these experimental results it is indicated that Ti-5%Ni is more excellent as EMD anodes compared with c.p. Ti.

2 Electrolysis in H2SO4 + MnSO4 solution

Figure 3 shows the change in bath voltage with time in EMD electrolysis using c.p. Ti anodes. It is found that, on each bath voltage/time curve, an incubation period until increase in the bath voltage exists and that higher

is the current density shorter is the incubation period. When the electrolysis was made at a current density of 16 mA/cm2, the incubation period was so short that it is not detected experimentally. Figure 4 shows test results with Ti-5%Ni anodes. found that the incubation period for Ti-5%Ni is much longer than at of c.p. Ti at the same current density. indicating that the growth of passive film on Ti-5%Ni is much harder than that on Accordingly, it is c. p. Ti. suggested that Ti-5%Ni anodes allow higher current density in EMD production.



 $Fig.\,2\quad Change\,\,in\,\,Bath\,\,Voltage\,\,with\,\,Time\quad in$

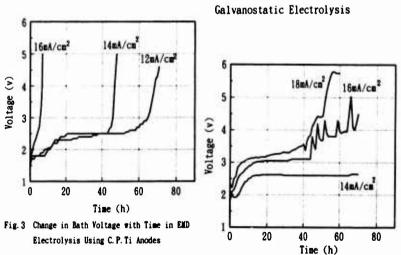


Fig. 4 Change in Bath Voltage with Time in EMD Electrolysis Using Ti-5%Ni Anodes

Discussion

Intermetallic Ti2Ni precipitates at temperatures below $oldsymbol{eta}$ transus in titanium matrix of titanium-based Ti-Ni binary alloys. Figure 5 shows a SEM image of etched Ti-5%Ni. Fine particles of Ti2Ni are observed in titanium matrix. In order to investigate the effect of Ti2Ni precipitation on the anode characteristics of Ti-5%Ni, the nature of intermetallic Ti2Ni was examined electrochemically. Ti2Ni ingots were prepared by double arc vacuum melting and were homogenized at 1050 K for 72 hours. Since the homogenized ingots are too brittle to be worked plastically, they were Microstructure of the specimens is shown in sliced directly into anodes. A small amount of α -Ti is observed in Ti2Ni matrix as shown in Due to the fluctuation of nickel concentration in an inthe photograph. got, it was impossible to prepare homogeneous Ti2Ni specimens even after the homogenization. Then, the examination was made with specimens containing the least amount of α -Ti in their microstructure.

Potentiodynamic polarization curves of c.p. Ti and Ti2Ni(containing a small amount of α -Ti) are shown in Fig. 7. The anodic polarization curve of c.p. Ti exhibited no current increase, while the anodic polarization curve of Ti2Ni exhibited rapid current increase at around 1.5 V (vs. Ag/AgCl). This current increase was confirmed to be due not to corrosion of Ti2Ni but to the evolution of oxygen gas. It is suggested from these results that passive films grow on c.p. Ti by anodic polarization and reduce of its conductivity very steeply, but that the growth of passive film does not take place on Ti2Ni in the tested range of anodic polarization.

It is estimated that, in Ti-5%Ni, the anodic current is shared by both α -Ti and Ti2Ni. At high current density, much electric current flows through Ti2Ni in order to compensate for the decrease in electric current through α -Ti. This mechanism may be the reason why Ti-5%Ni anode can keep its excellent anode characteristics in EMD production with higher current densities.



Fig. 5 SEM image of etched Ti-5%Ni White particles of Ti₂Ni are observed in α -Ti matrix



Fig. 6
Microstructure of tested ${\rm Ti}_2{\rm Ni}$ α -Ti particles were etched with a HF solution and showed black in ${\rm Ti}_2{\rm Ni}$ matrix
2,755

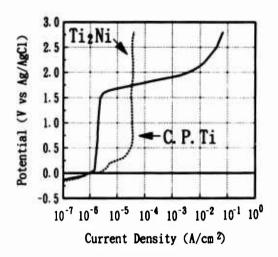


Fig. 7 Anodic Polarization Curves of C. P. Ti and Ti₂Ni in Sulfuric Acid Solution

Summary and conclusions

In the present study it has been made clear that intermetallic Ti2Ni bears high anodic current density due to its high corrosion resistance and no occurrence of the growth of passive films but that Ti2Ni itself is too brittle to be used as EMD anodes practically. As material for EMD anodes, Nippon Mining has developed Ti-5%Ni with good workability, having fine dispersion of Ti2Ni particles in titanium matrix. The foregoing studies demonstrated that, in EMD production using Ti-5%Ni anodes, the bath voltage did not tend to increase even when the electrolysis was made with high current densities. Currently, some trials have been made to use Ti-5%Ni anodes in some EMD plants, and industrial confirmation is going to be made for advantages of using Ti-5%Ni anodes.

Acknowledgments

The authors would like to thank Mr. Kuwabara of Dai-ichi carbon Ltd., for his technical advice which were helpful to starting and performing the present investigation.

References

- K. Matsuki and M. Sugawara, Progress in Batteries and Solar Cells, vol. 8 (1989)
- 2 Japan Patent S42-13938(1957)

DEVELOPMENT OF ENDOSSEOUS IMPLANTS ON THE BASE OF TITANIUM ALLOYS

WITH IMPROVED FUNCTIONALITY

J. Breme* , W. Schulte** and K. Donath***

*Universität des Saarlandes (FRG) **Universität Tübingen (FRG) ***Universität Hamburg (FRG)

Abstract

For long term implants a safe anchorage due to a bone ingrowth and a functionality of the implant as similar as possible to the natural functionality are required. Two types of endosseous implants on the basis of a TiTa30 alloy with a different surface structure were developed which both allow an ingrowth of the bone. In addition, both surface structures provide a stiffness of the implant similar to that of the bone. Subsequently, the implants behave isoelastic to the bone whereby, due to the load transfer, a new bone formation can be stimulated. The implants have been tested concerning their mechanical functionality and in animal experiments.

Introduction

For long time implants beside the use of biocompatible materials a safe anchorage due to the bone ingrowth and a functionality as similar as possible to the natural functionality are required. There is a common consense, that Titanium and its alloys are the metallic biomaterials of preference (1,2). The anchorage of implants can be improved by an enlargement of the surface. This enlargement can be achieved by different methods, e.g. by the production of a porous surface. A frequently used method is the plasma spraying of Titanium powder on the surface of implants having the disadvantage that powder particles are often detached (3,4). Another type of implant with a porous surface is produced by the powder metallurgical route. It was shown that a porosity of 50 - 100 µm allows a bone ingrowth and a stable fixation (5).

For the functionality of implants their stiffness described by the geometry and Young's Modulus is responsible. Concerning the stiffness of dental implants there exist divergent opinions.

Different theoretical calculations by the finite element method claim dental implants with an extremely high stiffness (Young's Modulus as high as possible) in order to avoid tension tips which can originate a bone resorption (6,7). In contrast to these calculations it was shown in animal experiments, that with implants with a low Young's Modulus and a high load transfer the bone resorption was avoided and a new bone formation was observed (8). Therefore, for the functionality of implants the load transfer to the bone via the implant is necessary. Such a load transfer

Titanium '92 Science and Technology Edited by F.H. Froes and I. Caplan The Minerals, Vietals & Materials Society, 1993 provides the equilibrium between the reduction and the formation of cells (8). A dynamic loading with a frequency of 1-10 Hz and 15-30 Hz, respectively, showed a favourable stimulating influence on the bone growth (9).

It was the aim of this investigation to develop dental implants with an extremely low stiffness which have an isoelastic behaviour to the bone and which provide a high load transfer.

Materials, Productions Methods

Two types of implants were developed which both allow an ingrowth of the bone and investigated. For both types an $(\alpha+\beta)-\text{alloy}$ containing 30 wt% Tantalum was chosen as base material. On the one hand, Tantalum shows a biocompatible behaviour similar to Titanium. On the other hand, the alloy TiTa30 has a high content of the $\beta-\text{phase}$ which provides, as shown in Table I, a Young's Modulus about 20 % lower than commercially pure Titanium. An additional decrease of Young's Modulus towards the modulus of the bone can be achieved by a martensitic transformation of the alloy (Table I). Fig. 1 shows the martensitic microstructure of the alloy TiTa30.

Table I Young's Modulus (N/mm²) of TiTa30 compared with cp-Ti and carticalis bone

TiTa30 $(\alpha+\beta)$ structure	TiTa30 martensicic structure	cp-Ti	carticalis bone
80000	60000	105000	20000

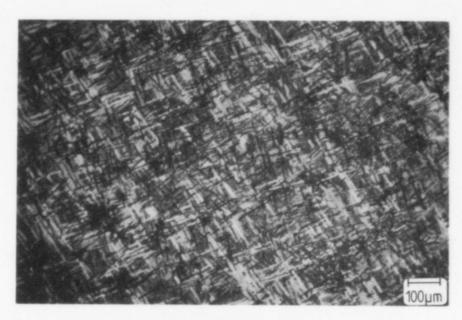


Figure 1 - Microstructure of TiTa30, martensitic after water quenching from 780 °C.

In comparison, the corticalis bone is reported to have a Young's Modulus of about 20000 N/mm. In order to provide a lower stiffness of the implant similar to that of the bone an implant was produced with a porous surface on a core of bulk material. The porosity which allows a bone ingrowth and therefore a safe fixation, was realized by sintering powder of the alloy TiTa30 on the bulk material. The powder was produced by the HDH-process. Hydrogenization was performed at 650 °C for 3 - 5 hours under a pressure of 1.5 bar. After milling the powder was dehydrogenized for 4 - 6 hours at 600 °C under vacuum. By the variation of the sintering parameters, the cold compressing pressure (500 - 1500 N/mm 2) and the sintering time (4 - 24 h), an optimization of the implants concerning their porosity, their strength porperties and their elasticity was arranged. An other implant type which was developed, allows due to its special surface structure also an osseointegration as well as a safe fixation. The surface consists of Titanium wire loops. Fig. 2 shows the design of this implant. A wire spiral of cp-Ti (300 µm diameter) was diffusion bonded with a pressure force of 5 N at 1050 °C to the surface of the bulk core consisting of TiTa. The loops had a diameter of 300 µm.

Investigation_Methods

The influence of the sintering parameters on the mechanical properties of the porous sintered implants were investigated in compression tests. For the investigation of the bond strength of the core to the porous sintered surface layerand the spiral loops, respectively, implants were embedded in a two component plastic adhesive. The core of the samples was expulsed in a compression test whereby the pressurizing force necessary for pushing out the implant core was measured. The measuring technique of these tests is schematically depicted in Fig. 3.

The functionality of the implants was investigated after embedding the implants in a two component plastic model which had the design of a jaw and a Young's Modulus similar to the bone (20000 N/mm²). The value of



Figure 2 - Loop implant design, core bulk TiTa30, loops cp-Ti.

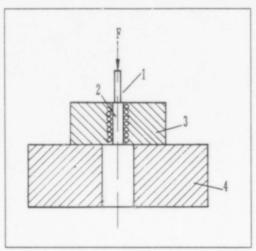


Figure 3 - Measuring technique for the bonding strength. 1 = punch, 2 = implant, 3 = embedding material, 4 = steel plate.

20000 $\rm N/mm^2$ was achieved by mixing SiO₂-powder to the plastic. In an universal testing machine the implants were loaded by pressure simulating the chewing process of a molar. The elastic deformation was

measured by strain gauges and compared with the results of implants of Al2Os and of cp-Ti as well as with the elasticity of the bone. With the implants with surface loops animal experiments were performed. After an implantation to the jaw of dogs and an exposure time between 2 and 5 months a period during which the implants were kept unloaded, histological specimen were prepared using a special cutting and grinding system for macro— and microwork with a diamond blade and a cooling unit. The thickness of the cuts is between 60 and 100 μm . A subsequent grinding to a thickness of 5 to 10 μm is possible (11).

Results and Discussion

Mechanical Properties

From the different sintering parameters the pressure: for the cold compressing has an important influence on the porosity and the mechanical properties (Fig. 4). With decreasing compressing pressure the porosity increases and Young's Modulus is diminished. For the given example with a sintering time of 16 h at a sintering temperature of 1100 °C a Modulus of similar to that of the bone can be achieved with a pressure between 400 and 600 N/mm2. Fig. 5 shows the influence of the compressing pressure and of the sintering time on the bonding strength of the porous layer to the core of the bulk material. With increasing pressure and sintering time the bonding strength increases. For a specimen which e.g. was sintered after compressing with 800 N/mm² for 8 hours at 1100 °C the was sintered after compressing with 800 N/mm bonding strength amounts to 64 N/mm². This corresponds to a force of 3200 N/mm which is necessary for the debonding. For the debonding of the loops diffusion welded to the core of the implant a force of 4700 N was are much higher than the reported highest measured. Both forces physiological force of chewing (12,13).

The stiffness of both types of implants was determined and compared with the stiffness of implants of Al203 and of cp-Ti (Fig. 6). While the Al203 implant behaves extremely stiff because of its high Young's Modulus, the

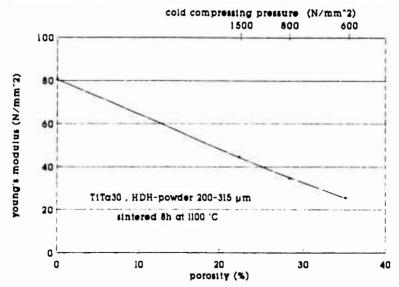


Figure 4 - Influence of cold compressing pressure on the porosity and on Young's Modulus of porous sintered implants.

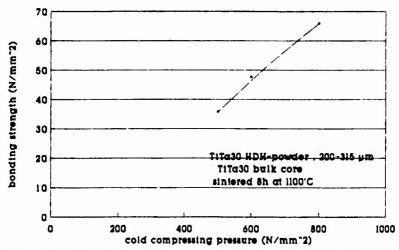


Figure 5 - Influence of the cold compressing pressure and of the sintering time on the bonding strength of porous sintered surface layers of TiTa30 to an implant core of TiTa30.

implant with the loops is the closest in its elasticity to the bone followed by the implant with the porous sintered surface. The implant with a porous sintered surface of TiTa30-powder (Young's Modulus of the porous layer = $35000 \, \text{N/mm}^4$) shows a higher elasticity than that of cp-Ti.

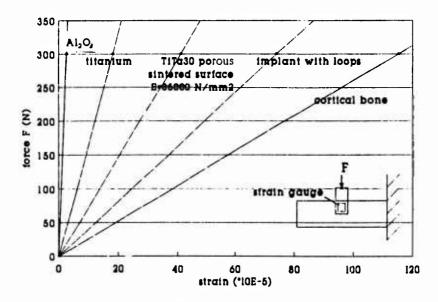


Figure 6 - Stiffness of different implants compared with the bone.

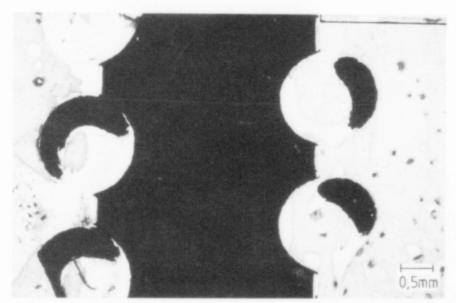


Figure 7 - Histological slice of a loop implant after an exposure time (unloaded) of 3 months in a jaw of a dog.

Animal_Experiments

Fig. 7 shows a histological slice of an implant with loops after an unloaded exposure time of 3 months. The bone is grown into all loops and in close contact to the surface of the core material. An investigation of an implant (exposure time 5 months) with the scanning electronmicroscopy

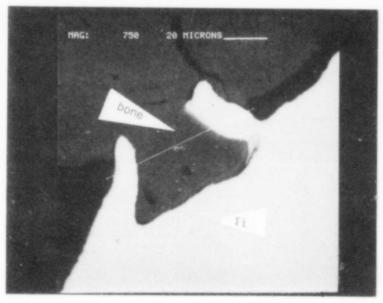


Figure 8 - Scanning electron microscopy of a histological slice of a loop implant (exposure time 5 months).

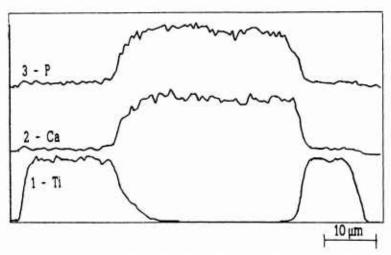


Figure 9 - Linescan of different elements on the slice of Fig. 9. 1 = T1; 2 = Ca; 3 = P.

(Fig. 8) demonstrates that the bone enters totally even small cavities or holes of about 25 µm on the surface of the loops. This surface roughness is originated by the wire production. A linescan of Ca, P (both constituents of the bone) and of Ti (Fig. 10) gives no exact information, whether a diffusion zone between the metal and the bone is existing.

Acknowledgements

The authors belong to the Sonderforschungsbereich Implantologie of the University Tübingen which is supported by the Deutsche Forschungsgemeinschaft. This support is gratefully acknowledged.

References

- 1. J. Breme, "Titanium and Titanium Alloys, Biomaterials of Preference", Révue de Métallurgie, 10 (1989) 625-637.
- R. Mericske-Stern, "Osseointegration", <u>Schweiz, Monatsschr. Zahnmed.</u>,
 (1989) 567-572.
- 3. A. Schroeder and P.D. Ledermann, "Titanimplantate", <u>Deutsche zahn-ärztliche Zeitschrift</u>, 38 (1989) 104-105.
- 4. H. Lüth and J.R. Strub, "Thickness of Plasma Flame Sprayed on Titanium Implants Exfoliated in Dogs", <u>Int. J. Oral. Maxillofac. Implants</u>, 3 (1988) 269-273.
- 5. D.D. Moyle, J.J. Klawitter and S.F. Hulbert, "Mechanical Properties of the Bone-Porous Biomaterial Interface: Elastic Behaviour", <u>Journal of Biomedical Materials Research Symposium</u>, 7 (1972) 363-382.
- 6. H. Röhrle, W. Sollbach, "Kraftflußberechnungen von Zahn- und Wurzelimplantaten", <u>Bundesministerium für Forschung und Technologie</u>, BMFG-FB-T (1985) 85.137.

- 7. D. Siegele, "Numerische Untersuchungen zur Optimierung der durch Zahnimplantate bedingten Beanspruchungen des Kieferknochens" (Dissertation, Universität Karlsruhe, 1989).
- 8. J.L. Katz, "Biomechanical Stability and Design, Stiffness and Remodeling", <u>Annals New York Academy of Sciences</u>, <u>Paper 6</u>.
- 9. T. Clinton, J. Kenneth and D.B. Steven, "Functional Strains and Cortical Bone Adaption: Epigenetic Assurance of Skeletal Integrity", <u>Journal of Biomechanics</u>, 23, Suppl. 1 (1990) 43-54.
- 10. F.J. Arendts and C. Sigolotto, "Standardabmessungen, Elastizitätskennwerte und Festigkeitsverhalten des Human-Unterkiefers, Teil I", <u>Biomedizinische Technik</u>, 34 (10) (1989) 248-255.
- 11. K. Donath, "The Diagnostic Value of the New Method for the Study of Undecalcified Bones and Teeth with Attached Tissue", Path. Res. Pract., 179 (1985) 631-633.
- 12. K. Eichner, "Messung der Kräfte bei Kauvorgängen", <u>Dtsche, Zahnärztl. Zeitschr.</u> 18 (1963) 915-924.
- 13. H. Schwickerath, "Kaukraft Kaudruck Belastbarkeit", <u>Dtsche. Zahn-ärztl. Zeitschr.</u> 31 (1976) 870-873.

Development of a New Casting Technology for Dental Applications Using Titanium

Holger Brauner', Ulrich Holzwarth" and Ulrich Zwicker"

* Dental Clinic for Prosthodontics ** Material Science Dept.2, Metals University of Erlangen-Nürnberg, Germany

Abstract

Several casting machines for casting titanium in dentistry using squeeze or centrifugal casting are commercially available, but most of the castings show an α -case with an increase of hardness in the surface area to more than 900 VHN 0.025. This hardness increase results from the reaction of the melt with ceramic crucibles, ceramic moulds or oxygen in the sourrounding area. Therefore an improved casting method was developed. In contrast to the usual centrifugal casting, where the rotation of the mould is started after pouring the liquid metal, this method pours the metal into a rotating mould. To avoid oxygen pick-up this casting machine is evacuable, using an argon-arc-system, and all parts that are in contact with liquid titanium, except the mould, are fabricated out of The moulds consist of zircon-based frontlayers completed by usual phosphate-bonded dental investments providing the needed thermal expansion. Dental crowns cast by this method exhibited a sufficient fitting, less hardness low α -case, a smoother surface and better microstructure as compared to the usual techniques.

Introduction

Commercially pure titanium and titanium alloys are the most corrosion resistant biocompatible materials used for implantation into the human body [1,2]. In recent years titanium has become an important material for dentistry too. Commercial casting systems for the production of castings for dental applications are frequently not satisfactory due to surface impurities, $\alpha\text{-}\mathrm{case}$, hardness increase, shrinkage cavities and pores. The increase in hardness in the surface area combined with a microstructural change is called " $\alpha\text{-}\mathrm{case}$ " because the increase of oxygen in this area stabilizes the $\alpha\text{-}$ phase of titanium [3]. This is the result of an oxygen-pick-up

Titanium '92 Science and Technology Edited by F.H. Froes and I. Caplan The Minerals, Metals & Materials Society, 1993

during the melting and solidifying process of the titanium metal. If the level of the oxygen content is higher than 0.5 wt.% the hardness increases to above 300 VHN compared to 150 VHN of titanium containing 0.1 wt.% oxygen [4]. From the dental point of view α -case means the weakening of prothetic frame work due to crack growth. An a-case surface cannot be highly polished, therefore leading to plague accumulation. Veneers on a-case will not exhibit the needed compound strength as well as for acrylic or ceramic veneers. These imperfections have to be minimized for the dental application of titanium. Because of this the pick-up of oxygen was investigated on titanium produced castings with different mould materials metallographic inspection and VHN 0.025 micro-hardness measurements.

Methods for minimizing oxygen pick-up in titanium castings

To minimize the oxygen pick-up in titanium castings during the melting of the titanium, the argon used for the melting procedure was more than 99.99% Ar. In the casting machine described in a former paper [5,6] the metal is molten in a copper crucible for casting hip prostheses a copper mould could be used. Each individual dental casting requires an investment supplying the thermal shrinkage in the mould. Usual phosphatebonded silicon dioxide investments provide the needed volume expansion by the crystobalite transition. Unfortunately these investments react with molten titanium. As a result frontlayer based on zircon was provided to minimize the reaction. It was shown that an increase of the number of layers of zircon from 3 to 5 layers decreases the α-case measured at a thickness of 1 mm of the casting from about 70 to 40 μ m. Because the titanium before casting was molten by an inductive method in a ceramic crucible, the melt increased its oxygen content from 0.3 wt.% to 0.4 wt.% oxygen at a casting temperature of 1760 °C [7]. This oxygen pick-up could be avoided by a copper crucible melting titanium by a tungsten electrode. To improve the isolation of the mould against the investment, up to nine layers of zircon were provided on the ceramic front.

Mould preparation

Figure 1 shows the wax model including the bus system, the zircon coated modellation, and the casting of a first molar of the lower jaw. The wax model was dipped into a suspension of zirconium dioxide and zirconium-acidester. Zirconium dioxide of greater grain size was placed over the wet model. This procedure was repeated several times depending on the number of front layers. Drying of the zirconium ceramic frontlayer lasted 10 hours at ambient temperature. This compound was embedded in a usual manner into a dental moulding system of a phosphate-bonded silica material. After annealing this investment to the producers requirements, the mould was ready for casting. To compare the zircon layer with a commercial alumina silicate

investment provided for dental titanium castings ($Titanvest^{Tm}$, OHARA) some identical crowns were cast using this technique.

Casting process:

Figure 2 shows the scheme of the inaugurated horizontal rotating casting machine working with an argon-arc system of >200 A, a copper crucible and a bent copper inlet (fig.3) for the flow of the melt. The copper crucible can be used both with and without water cooling depending on the melting time and on the weight of the titanium. After evacuating three times and argon filling of the melting chamber under an argon pressure of 40 kPa, the rotation and the ignition of the argon-arc-system started. By turning of the copper crucible, the liquid titanium was filled into the rotating casting system. The rotating speed pushes the liquid metal into the ceramic mould, fixed directly to the copper inlet. The influence on the form filling depends on rotating speed. A speed of 1100 rpm leads to an optimum casting.

Results:

Figure 4 presents one of the castings of a crown for the first molar of the lower jaw. The crown is cut in oro-lingual direction and fitted on a FrasacoTm abutment used preparation and modelling. As can be seen, the overall congruence of crown and prepared abutment is more than sufficient (<20 μ m). Problems arise with shrinkage cavities and pores, which can be polished out or concealed by veneer material according to the faces where they appear. If they are located approximately, simply accomplished by x-raying the prosthetic frame work, stability may cease. In that case the prosthetic work should be repeated. The problem of sink or blow cavities is general for dental castings, because of the complicated geometrics of dental work and not particular to titanium. However, titanium as a material is easily checked due to its x-ray transparancy. To avoid shrinkage cavities and pores the bus system as shown in figure 1 is used. Most of the shrinkage cavities and pores assemble in the tip of the riser. The relation between casting and riser system is about 1:15. Figure 5 shows the microstructure of a casting with a nine layered front based on a zircon compound. No surface treatment was used. The observed α -case is less than 10 μm . A significant improvement as compared to 100 - 300 µm of commercial castings [8,9].

The influence of the mould material on the microhardness is demonstrated in fig. 6. The hardness measurement of the cast samples was done without any etching or sandblasting of the surface. The highest microhardness of 1030 VHN 0.025 and therefore the highest oxygen concentration in the surface area was measured for the commercial alumina silicate investment castings. A single layer of zircon lowers the hardness values

at the surface to about 600 VHN 0.025 and a ninelayer compound of the same material minimizes it to 300 VHN 0.025.

Conclusion

When titanium, which is molten in a copper crucible by an argon-arc, is cast in a rotating mould via a bent copper inlet, this leads to minimization of oxygen pick-up and therefore a reduction of a-case if the mould material consists of a multilayered zircon front. Using dental investments to complete the mould controls the needed thermal expansion. The advantages of a-case free or reduced surfaces of dental skeletons are failure and plaque resistance combined with good fitting and high polishing and veneering facilities.

Acknowledgement

The authors gratefully acknowledge A. Woodfield's (GE Aircraft, Cincinnati, O) reading of this paper.

References

- [1] S.G.Steinemann, <u>Corrosion of Titanium and Titanium Alloys for Surgical Implants</u>, Proceed. of the 5.World Conference on Titanium, Munich 1984, p.1373-1380
- [2] S.G.Steinemann, <u>Titanium Alloys as Metallic Biomaterials</u>, Proceed. of the 5.World Conference on Titanium, Munich 1984, p.1327-1334
- [3] O.Miyakawa, Layered Structure of Cast Titanium Surface, Dent.Mat.J.,8,No.2, 1989, p.175-185
- [4] R.I.Jaffee, H.R.Ogden and D.I.Maykuth, <u>Alloys of Titanium with Carbon, Oxygen and Nitrogen</u>, Trans.AIME, 188 (1950), p.1261-1266
- [5] U.Zwicker and J.Breme, Evaluation of Centifugally cast TiAl5Fe2.5 Alloy for Implant Material, Proceed. of the 5.World Conference on Titanium, Munich 1984, p.171-178
- [6] H.Brauner, U.Zwicker and U.Holzwarth, <u>Verbesserung des dentalen Titangusses durch ein neues Gießverfahren</u>, 1.Int.Symposium on Titanium in Dentistry, Frankfurt 30.06./01.07.1990, Springer Berlin, (in press)
- [7] J.Schädlich.Stubenrauch, Entwicklung einer Schleuderfeingießtechnologie für kleine dünnwandige und filigrane Gußteile aus Titan und Titanlegierungen, Ph.D. RWTH Aachen, 1989
- [8] K.Krone, <u>Herstellung</u>, <u>Eigenschaften und Verarbeitung von Titanguß</u>, Metall, 30 (1976) H.6, p.556-559
- [9] Ch.Liesner, <u>Titanium Investment Casting Production</u>, <u>Properties and Applications</u>, Proceed. of the 5.World Conference on Titanium, Munich 1984, p.157-162



Fig.1: Wax model, zircon frontlayer and casting of a first molar of the lower jaw

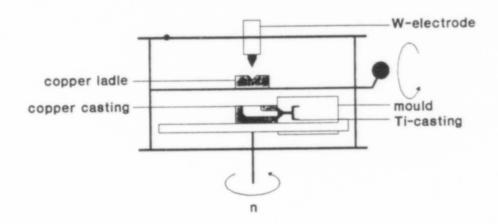


Fig.2: The horizontally rotating casting system

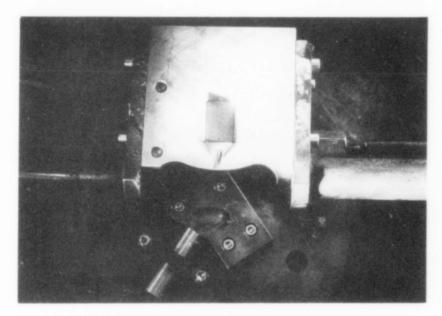


Fig.3: Copper inlet

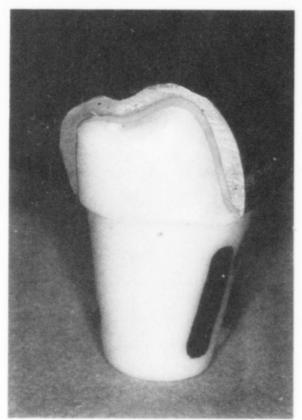


Fig.4: Cross-section of a crown for the first molar of the lower jaw fitted on abutment

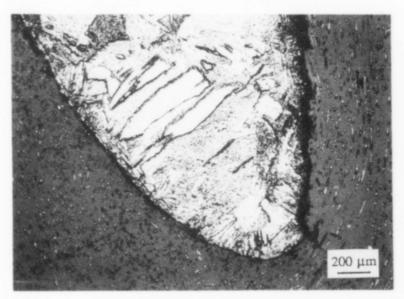
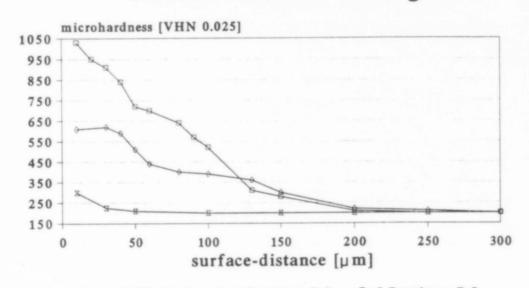


Fig.5: Microstructure of a casting produced with a nine frontlayer compound based on zircon (magn.50x)

Dental titanium castings



→ Al₂O₃SiO₂-based → 1 Frontlayer ZrO₂ → 9 Frontlayers ZrO₂ Fig.6: Microhardness versus distance of the

surface

SUPERPLASTIC FORMING OF T1-6A1-4V DENTURE BASE

Minoru Okada1), Hisashi Mitsuya2) and Isamu Katoh3)

- 1) Sumitomo Metal Ind., 1-8 Fuso-cho, Amagasaki, 660 Japan
- 2) JRCM, 1-7-2 Nishi-Shinbashi, Minato-ku, Tokyo, 105 Japan
- 3) Sankin Kogyo, 6-120-1 Kamo, Kawanishi, 666 Japan

Abstract

Titanium alloy, Ti-6Al-4V is known as biocompatible metal, and also has high strength and low density, so it seems to be the best material for denture bases. This Ti-6Al-4V can be deformed easily at the superplastic temperature between 1073 and 1173K.

This paper shows the new super-plastic forming process of Ti-6Al-4V denture bases. Ti-6Al-4V plate has been formed super-plastically on the die by argon gas pressure at 1073-1173K. Superplastically formed denture base of Ti-6Al-4V showed several merits compared with conventionally cast or cold-pressed denture bases, namely good fitness, light weight, and low producing cost because of simple manufacturing processes.

1. Introduction

Metal materials for denture use are shown in Table.1, and they all show good corrosion resistance. Titanium and titanium alloys have light weight, good corrosion resistance and good biocompatibility, so they appear to be the best materials for denture bases. Metal denture bases are now mainly manufactured by the casting of Co-Cr or Ni-Cr alloys, and titanium bases have been studied to be manufactured by cold pressing¹⁾ or casting. As titanium have low formability and low castability, it is hard to be manufactured by these processes. Alpha-beta titanium alloys show super-plasticity at high temperature of alpha-beta region²⁾³⁾. It has been reported that the large reduction of the forming cost of aerospace products have been per-

Table 1 Alloys for Dentures.

Gold Alloys
Silver Alloys
Paradium Alloys
Ni-Cr Alloys
Co-Cr Alloys
Stainless Steels
Titanium Alloys

Titanium '92 Science and Technology Edited by F.H. Froes and I. Caplan The Minerals, Metals & Materials Society, 1993 formed by super-plastic forming $^{4)-6)}$. But there have been few examples of super-plastic forming of non-aerospace products, because of its small forming rates. As denture bases need individual and precise shapes, they seem to be suitable for superplastic forming.

This paper describes the newly developed superplastic forming process of titanium alloy denture bases using argon gas pressure.

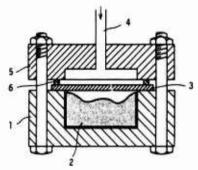
2. Materials and Methods

The effect of temperatures, strain rates and grain sizes on the superplasticity of Ti-6Al-4V was examined. The chemical composition of the material was shown in table 2.

Table 2 Chemical Composition (wt.%)

Al	٧	Fe	0	Н	N	С	Ti
6.39	4.08	0.17		0.0035		0.01	BAL

Fig. 1 shows the apparatus for super plastic forming of Ti-6Al-4V This apparatus consisted of an upper and lower pressure denture base. vessels. The forming die was set in the lower pressure vessel, and titanium alloy plate was set on the forming die. The forming die was made with phosphate, which was same as that for casting of titanium denture base. The thickness of Ti-6Al-4V alloy plate was 0.5 mm. Upper and lower pressure vessels were closed using the seal material to maintain the vacuum and the applied pressure. Forming pressure was applied by argon gas into the upper pressure vessel. Pressure vessels were made of heat resistant alloy IN 600, because they were heated to 1073-1173K. The expansion of the die from room temperature to 1173K was adjusted to be same as that of Ti-6Al-4V in order to form the denture base in the precise dimension. Fig. 2 shows the heat pattern of the forming process. After heating to superplastic temperature, the plate was formed with the gas pressure of 0.8-1.0 MPa, and kept in 1.8-3.6ks to form the denture bases.



- 1. Lower Pressure Vessel
- 2. Forming Die
- 3. Ti-6Al-4V Sheet
- 4. Gas Introduction Tube
- 5. Upper Pressure Vessel
- 6. Seal (Stainless Steel Ring)

Fig. 1 Aspects of Super-plastic Forming Apparatus.

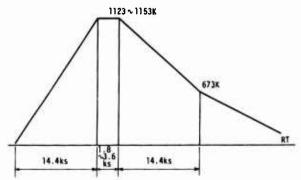


Fig. 2 Heat Pattern of Super-plastic Forming for Denture Base of Ti-6Al-4V Alloy.

3. Results and Discussions

3.1 Superplasticity of Ti-6Al-4V alloy

Fig. 3 shows the effect of strain rate and temperature on the superplastic elongation of Ti-6Al-4V alloy. Ti-6Al-4V alloy shows the superplastic elongations at the test temperatures between 1073 and 1173K and at the strain rates between $10^{-2}\,\mathrm{s}^{-1}$ and $10^{-4}\,\mathrm{s}^{-1}$. Fig. 4 shows the effect of the grain size on the super-plastic elongations of Ti-6Al-4V. The material with the initial grain diameter of 4.2µm showed the maximum elongation of 1200% at 1123K, and the strain rate of 5 x $10^{-3}\,\mathrm{s}^{-1}$. It is clear that the superplasticity of over 300% elongation is observed at the condition of the grain size under 10µm of alpha grain diameter, the temperature between 1073-1173 K and the strain rate between $10^{-2}\,\mathrm{s}^{-1}$ and $10^{-4}\,\mathrm{s}^{-1}$.

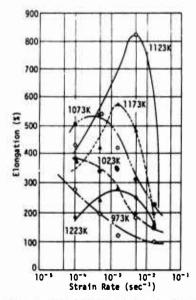


Fig. 3 The Effect of Strain Rate on the Elongation. (Ti-6Al-4V)

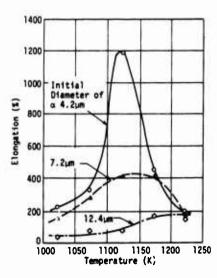


Fig. 4 The effect of Initial
Grain Size on the Elongation.
(Ti-6Al-4V)

Fig. 5 shows the temperature dependence on the flow stress in the superplastic conditions. It shows the strong dependency on the temperature. It was concluded that superplastic forming should be performed between 1073-1173K, and that the grain diameter of the material should be less than $10\mu m$.

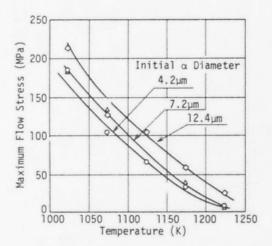


Fig. 5 The Effect of Initial α Grain Size on the Maximum Flow Stress. (Ti-6Al-4V, $\stackrel{\circ}{\epsilon}$ =5 x 10^{-3} s⁻¹)

3.2 Superplastic forming of Ti-6Al-4V alloy denture bases

Fig. 6 shows the aspect of Ti-6Al-4V denture base superplastically formed. The complex palate shape was precisely restored to the original shape. Fig. 7 shows the hardness distribution of the cross section of the denture base. Hardness increase due to oxygen absorption was not seen, even on the surface come in touch with the forming die. Fig. 8 shows the clearance measurement between the superplastically formed denture base and the master model. The mean value of the measured clearances at 3 points was about $50\mu\text{m}$, which was about 1/3 compared with those of cast or cold pressed denture base. It is clear that precise denture base can be formed by the superplastically forming process. Fig. 9 shows the comparison of the conventional forming process to the newly developed superplastic forming process of denture bases. Manufacturing process was largely simplified through

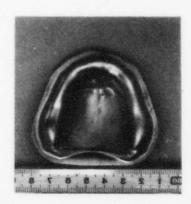


Fig. 6 Superplastically Formed Denture Base.

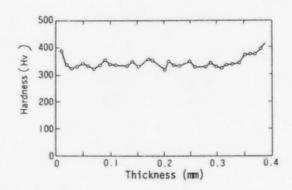


Fig. 7 Micro Vickers hardness distribution of superplastic forming.

2,776

the reduction of the number of pressings and the abbreviation of the final annealing in the developed superplastic forming process, compared with cold pressing process. Compared with that of cast denture bases, the grinding process was largely simplified because of the good surface condition in the superplastic forming process.

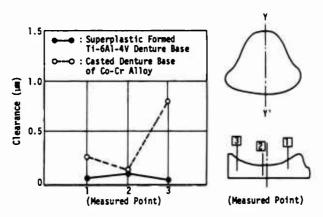


Fig. 8 The Comparison of the Fittmess between Super-plastic Formed and Casted Metal Denture Bases.

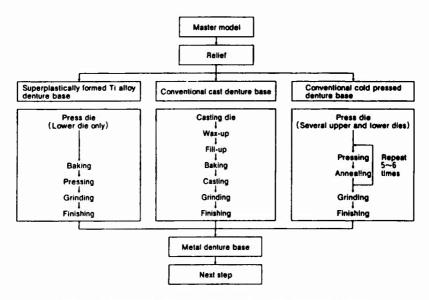


Fig. 9 Manufacturing processes of metal denture base.

Fig. 10 shows the aspect of the finished denture base. It was confirmed that titanium alloy denture bases can be formed with a good surface condition and a proper fitness by the newly developed superplastic forming process.



Fig. 10 Finished Denture Base.

4. Conclusion

- Superplastic forming process of Ti-6Al-4V denture base was newly developed.
- (2) Superplastic forming process was much simpler compared with conventional cast or cold press process.
- (3) Superplastically formed denture base has better surface condition compared with cast denture base, so grinding time can be largely reduced.
- (4) Superplastically formed denture base has better fittness than the denture bases processed by the conventional processes.
- (5) Titanium alloy denture base with light weight and biocompatible properties can be easily manufactured by this new superplastic forming process.

References

- 1) K. Iuchi, Shika-Gikoh, 12 (1984), p.1465.
- 2) S.Hori, Journal of High Temp. Society, 7 (1981), p.246.
- 3) M.Kobayashi and M.Miyagawa, Tetsu-to-Hagane, 72 (1986), p.2001.
- E.D.Weisert and G.W.Stacher, <u>Superplastic Forming of Structural Alloys</u>, (1980), p.273, AIME.
- 5) M. Inoue, Mitsubishi Juko Gihoh, 16 (1979), p.1

The Use of Titanium Chelate in Agriculture.

Huang Ming-Liang. Tang Xiao-Dong. and Liu Lu.

General Research Institute for Non-Ferrous Metals, Beijing. No 2. Xin Jie Kou Wai Dajie Beijing. 199088. China.

ABSTRACT

The effects of Ti chelate as microelement on agricultural plants, such as wheat, tomato, apple, maize, grape, water melon, straw berry, sugarcane sugar-beet, tobacco and herbage etc, were studied. Due to spraying Ti chelate on the leave of plants it can intensify the photosynthesis and increases the chlorophyli.etc, The yields of crop were increased by 5% to 20% and the quality of crops can also be improved. The toxic studies of Ti chelate showed it is practically non-toxic in agricultural application.

INTRODUCTION.

Since 1970 many papers concerned with the biological role of Ti and its application in agricultural plants have been published (1, 2, 3). The important study on this field was carried out by I. Pais. who developed Ti ascorbate to demonstrate the good effects of Ti on the growth and production of crops (4). In 1984 we began the study on the use of Ti chelate in agriculture and organisted a interdepartmental research group consisting of some agronomists, chemists and doctors to conduct the experiments on the preparation of Ti chelate, the analysis of Ti in soil and plant, the method of application, plant physiology and toxicology of Ti. the effect of Ti chelate on the yield and quality of crops, such as wheat, maize, tomato, apple, grape, water melon, strawberry, sugar-cane, sugarbeet, tobacco and herbage etc., was also studied.

EXPERIMENT

We prepared two kinds of Ti chelate, one is Ti ascorbate which contain 10% Ti in solid form or 50g/l Ti in solution (5), the other is Ti citrate, which contain 10g/l Ti in solution(6). The Ti concentration for the tests of seed dressing, seed soak and foliar spray was used at 2ppm to 500ppm. The pot-tests in green house, parcel field tests and large-scale farm tests were carried out in some provinces of our country. Some biological parameters of plant were measured. Each crop was treated with different concentration of Ti and with water as control at different growing stage. Each treatment was set with 3 or 4 repeats at random arrangement. The results of tests were made with mathemathical significant evalution. The radioactive labelled elements "N, "P and "Rb(here Rb take place of K) were used to study the effect of Ti on the absorption and the transfer of N, P and K from soil and fertilizer to plant. The best time and dose of the application for each crop was studied. The toxicological study on safety evaluation of Ti used in agriculture was also carried out.

RESULTS AND DISCUSSION.

1. The effects of Ti on the physiology role of plant.

To clarify the role of Ti in the physiology some tests on the germination, root growth and plant growth of some crops were carried out (7). By seed dressing of peanut and maize with Ti chelate solution at different concentration we observed Ti can promoted the germination of seeds (Fig 1).



Fig - 1 The test of germination for peanut(left) and maize(right)

Meanwhile, after seed dressing the seed of peanut and maize with Ti the root and plant got more strong in comparison with control(Fig 2 and Fig 3).

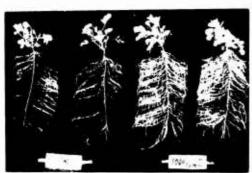




Fig - 2 The effect of Ti on the growth of peanut.

Fig - 3 The effect of Ti on the growth of maize.

The pot-test of spraying Ti chelate solution at different Ti concentration on wheat, tomato and grape showed that some parameters of root and plant were greatly increased, when the Ti concentration was used between 2ppm and 50ppm, Some inhibiting effect of Ti on growth was observed at higher Ti concentration (above 100ppm). (Table I, Table II and Table III).

Table 1 The effect of spraying Ti chelate on the root of wheat.

Treatment	Dry weight of root, g/pot	Volume of root cm³/pot	Bleeding ∎g/tiller.hr
control	1.58 ± 0.17	10.58 ± 0.49	25.25 ± 0.52
2ppm Ti	1.76 ± 0.30	10.33±0.71	28.92 ± 0.10
10pp∎ Ti	1.75 ± 0.11	11.67 ± 0.45	42.20 ± 0.79
50ppm Ti	1.75 ± 0.18	12.13±0.12	32.01 ± 3.35
100ppm Ti	1.57 ± 0.16	10.03 ± 0.47	28.30 ± 0.10
200ppm Ti	1.58 ± 0.09	10.07 ± 0.28	25.03 ± 1.36

Table II The effect of Ti on the root of tomato seedling.

						O .	
 Treatment		oot	Thick of ∎air	root	Length of main root		
		1 %	et	*	C∎	%	
control	11 ± 0.689	100	1.1±0.147	100	3.7 ± 0.213	100	
10ppm Ti	17 ± 0.516	155	2.1±+0.152	191	4.5 ± 0.254	122	
20ppm Ti	21 ± 0.718	191	1.7 ± 0.131	155	5.6 ± 0.201	151	

Table II The effect of Ti on the plant growth of grape seedling.

treatment		Plant highness cm	leaf number	leaf area cm²
	before spray	50.8	14.0	71.5
control spray with	after spray*	75.5	17.3	74.3
water	Increase	24.7	3.3	2.8
	before spray	57.1	14.7	86.4
spray with 5ppm Ti	after spray*	85.4	20.0	91.5
	increase	28.3	5.3	5.1

. Note: measured after 5 days.

As we known the chlorophyll, photosynthesis and catalase is the important factors for plant life. as seen in Table IV these parameters for some crops were increased by foliar application of Ti at low concentration (8, 9, 10).

Table IV The effect of Ti on physiology of crops.

		Crops						
parameter 	treatment	 wheat	tomato	apple	water melon	grape	straw berry	
chlorophyl	control	1.44	0.72	2.95	2.03	2.32	1.71	
content mg/g	10pp∎Ti	1.57	0.90	2.83	2.13	2.48	1.88	
photosynthesis	control	12.08	10.08	4.37	6.90	3.54		
intensity mg/dm².hr	10ppmTi	17.70	10.77	7.40	7.95	8.87		
catalase HzOz mg/g.min	control		5.34		26.02	2.0	72.11	
	10ppmTi		5.69		38.03	4.0	79.48	

Otherwise, by the radioactive labelled element **N, **P and **Rb (here Rb take place of K) we studied the effects of Ti on the absorption and transfer of **N, **P and **Rb in plant. The data collected in Table V, Table VI and Fig 4 showed that the utilization rate of **N was enhanced and Ti can promote the transfer of **N,**P and **Rb to grain.

Table V Utilization rate of N from fertilizer after spraying Ti chelate.

treatment		from fertilizer g/pot		soil /pot	utilization rate of N in fertilizer %		
	plant	plant grain		grain	plant	grain	
control	0.127	0.074	0.181	0.102	53.1	31.1	
5ppmTi	0.122	0.082	0.177	0.118*	51.5	34.3•	
10ppmTi	0.133*	0.090**	0.188	0.126**	56.6*	37.9**	
50ppmTi	0.143**	0.106**	0.198	0.142**	60.4**	44.4**	

Note: * = significant at 5% level, **=significant at 1% level.

Table VI The effect of Ti on the redistribution of "N and "P nutrient in wheat.

	the re	distrib	ution	of N	and p	in the	parts of	plant %
treatment	gr	ain	husk		stalk		leaf	
	re N seb re			≖p	72 N	≖p	16 N	≖p
control	75.83	84.27	8.13	6.38	3.41	1.30	12.63	8.00
20ppaTi	80.13	88.00	6.23	5.13	3.13	0.85	10.47	6.02
comparison	+4.3	+3.7	-1.9	-1.3	-0.3	-0.5	-2.16	-2.0

specific acctivity of ™Rb cpm/50mg of sample.

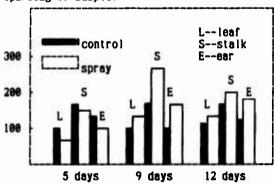


Fig - 4 The effect of spraying Ti on the absorption of *Rb for wheat

2. The effect of Ti on the yield and the quality of crops.

By the several hundred tests in green houses and on parcel field the method as well as the dosage and the time of application of Ti chelate was found. The spray concentration of Ti at 5ppm--20ppm and seed-dressing at 200ppm--250ppm proved suitable, but spraying was widely used and more efficient. The yield and increment in total demonstrative field showed that the increment of yield for crops treated with Ti was obtained by 5%--15% as compared with control (Table VI).

Table VI The yield and quality for crops treated with Ti.

05000	incr	ement	innering quality
crops	range(%)	average(%)	improving quality
spring wheat	0.717	7.9	crude protein
winter wheat	6.97.3	7.1	increase by 5%
maize	6.49.6	8.5	12%
herbage	0.620	9.8	
apple	530	13.4	more sweet and
water melon	526	15.7	Vc increase
grape	5.811	10	
straw berry	1218	15	
sugar beet	516	9.5	sugar increase by
sugar cane	8.411	9.2	0.60.8 degree
tobacco	1.56	3.8	early ripe and
tomato	815.1	11.8	good pigment

3. The titanium content in soil and plant (12).

Titanium in soil is generally bound in the form of TiO_2 or titanium silicate, so it is practically unavailable for plant, The analysis of 510 samples of soil with 0.02M EDTA + 0.5%NH4Cl as leaching solution showed that the extractable titanium content in soil is 0.3ppm--1.0ppm in average (Table WE).

Table W The titanium content in the soil of our country.

soil type	total Ti con	tent(ppm)	extractable Ti (ppm)			
Soil (ype	range	average	range	average		
cabook	120015950	5680	0.061.18	0.55		
red earth	100026253	9570	0.073.89	0.62		
loess	325019520	9971	0.080.80	0.38		
brown soil	18005940	3870	0.132.72	0.94		
terra-nera	420016130	6838	0.530.96	0.71		
chernozem	60007700	6500	0.011.28	0.30		
wet meadow	470010000	7900				

The extractable Ti content in soil not only affect by soil type and PH of soil, but also by the content of organic substance and soil-forming process. As Ti in soil is hardly absorpted by plant, The content of Ti in plant is slight. The analytical results of some crops showed the Ti concentration in root, stem and leaf was at above decade ppm, but it in grain and fruit was less than 5ppm for dry sample (Table IX).

Table IX The average content of Ti in some crops.

crop	wheat	maize	apple			lucerne	
part of plant	above ground	grain	grain	leaf		above ground	grain
Ti content ppm	29.0	<2.0	<2.0	20	5.4	<20	2.9

4. The safety of the application of Ti chelate in agricuture.

The acute toxicity tests showed the LD walue of Ti-Vc chelate for rat, mice and chicken the TLM value (the mediem talerance limit) for common fish was 1200mg/kg.b.w., 850mg/kg.b.w., 150mg/kg.b.w., and 1736-10930mg/l, respectively. It belong to non-toxicity. The test for accumulated toxicity in rat showed the accumulation coefficient was 500, known as low accumulation. Teratalogical tests on rat showed that no malformation in either appearance or internal organ of the fetus was found with dose of Ti chelate at 1g/kg.b.w.. By long term of tests we suppose acceptable daily intake of Ti for person is about 0.2mg/kg.b.w. for safety coefficient as 100%, this limit range is far exceed the possible intake for person from common foodstuff. so the harmful effect of trace titanium in agriculture application on living is almost nonexist.

CONCLUSION

The role of Ti in plant physiology showed the possibility for utilizing it in crop production is reilizable. It had found that spraying Ti chelate on plant can intensity the photosynthesis and increased the chlorophyll and the activity of catalase. The absorption and transformation of N, P and K was enhanced. The yield of crops in average was increased by 5%--15% and the quality of crops was also improved. By the toxicity tests of Ti chelate we are sure the application of Ti chelate in agriculture is safe.

REFERENCE.

- 1. Rutskaya S. I., Fiz. Blochim. Kult. rast. 8(1) (1976) 72--76.
- Kenkichi. Tsukamotb. Pat. JP 51--13677 (1978).
- 3. Joseph J. Mrowca. Pat. US 3782912 (1974).
- 4. Pals. 1. Journal of Plant Nutrition, 6.(1) (1983). 1-36.
- 5. Yu Yuxiu. Huang Mingliang. Deng Wei. Pat. CN 8507690 (1985).
- 6. Tang XiaoDong. Liu Lu and Huang MingLiang. Pat CN 8910746 (1989).
- 7. Zhu QiQing and Liu Zheng, private communication with author. (1986).
- 8. Zhang YuMei and Xu XinYu. TU RANG FEI LIAO 6. (1988) 18.
- 9. Zhang YuMei and Xu XinYu. XI YOU JIN SHU 6. (1988). 36.
- Huang WanRong and Wong Yu. <u>Journal of Beijing Agricultural College</u>. 1. (1987). 11--118.
- 11. Zhu YongYi and Cheng JingJiang. HE NONG XUE TONG BAO. 4. (1987). 12--14.
- 12. Liu Zheng. TURANGXUE JINZNAN. 19. (1) (1991). 1--7.

A NEW LOW COST TITAMIUM ALLOY

P. J. Bania, A. J. Hutt, R. E. Adams, and W. M. Parris

TIMET
P.O. Box 2128
Henderson, NV 89009

Abstract

Ti-6Al-4V (Ti-6/4) has long been established as the workhorse alloy for the titanium industry. As such, it has been the largest volume production alloy and it is produced in a variety of grades and mill product forms. However, the intrinsic cost of the alloy is sometimes too high to justify its use in some very cost sensitive non-aerospace markets such as automobile engine valves, armor plate, etc. In order to overcome this cost hurdle, a project was undertaken to develop a titanium alloy with characteristics similar to or better than Ti-6-4 but with reduced intrinsic cost. The resultant alloy (Ti-6Al-1.7Pe-.1Si, designated TIMETAL.62S) takes advantage of low cost alloying elements, thus avoiding expensive additions such as vanadium. In addition, the new alloy is designed to take full advantage of beta processing in order to lower conversion cost as well as improve product yield. It is estimated that this "6/4 equivalent" alloy will offer a 15% to 20% savings over conventional Ti-6/4 without any debit in performance.

Introduction

Titanium alloys have been used for many years in aerospace applications primarily because of their light weight and high strength at ambient to moderately elevated temperatures (up to about 550°C). In these applications the higher cost of the titanium compared to steels or other materials has been offset by the economic advantages attached to weight saving in aircraft. However, this higher cost has severely limited the use of titanium in non-aerospace high volume applications such as automobiles even though their utilization would lead to increased fuel efficiency and thus lower operating costs. Two current alloys, Ti-6Al-4V and Ti-6Al-2Sn-4Sr-2No, have been used in high performance racing engines for several years with excellent results. The former alloy is used for connecting rods and intake valves and the latter for exhaust valves. However, in these high performance applications, fuel efficiency and performance are of primary concern and material cost is secondary.

Thenium '92 Science and Technology Edited by F.H. Froes and I. Capton The Minerals, Match & Materials Society, 1993 In order for titanium alloys to make more substantial inroads into non-aerospace applications, significant cost reductions will be necessary. Some of the factors which contribute to the cost of titanium alloys, such as the cost of the base metal, cannot be changed substantially over the short-term. Others, however, can be subject to short-term cost reductions. Among these are:

- The Cost of Alloying Elements: For example, in the "workhorse"
 Ti-6Al-4V alloy the vanadium at a typical cost of approximately
 \$13.50/lb. adds about \$0.54/lb. to the cost of an ingot. Substitution of a cheaper element such as iron, at about \$0.50/lb., could save about \$0.45/lb. for an equivalent amount of beta stabilization.
 It should also be noted that the U.S. is dependent on vanadium from a foreign source, whereas iron is obviously a domestic resource.
- Increased Yield from Ingot to Final Mill Product: This could be brought about either by improvements in mill processes and/or by formulating an alloy which is more tolerant to mill processes (ie, reduced losses from surface and end cracking during forging, rolling or other metalworking procedures).

With respect to Item 2, an alloy which could achieve the desired suite of properties after being processed entirely from temperatures within its beta phase region should provide increased product yield primarily because of the higher ductility and lower flow stresses extant at these temperatures. Currently, alpha-beta alloys typically receive substantial working at temperatures within their alpha-beta phase regions. These lower temperatures, with their concomitant higher flow stresses, lead to more surface cracking and higher conditioning losses.

An alloy development program was undertaken to develop such a low cost substitute for Ti-6Al-4V, primarily for non-aerospace applications such as automobile intake valves. The principle avenue of pursuit was to remove the high cost beta stabilizer - vanadium - and replace it with a low cost beta stabilizer such as iron or chromium.

Experimental Trials

Two groups of alloy formulations were melted, processed and evaluated. All material was double vacuum arc remelted (VAR) as nominal 20-cm. dia. x 35 kg ingots. Portions of these ingots were beta processed (ie, worked by forging and/or rolling at temperatures above the beta transus temperature) to 1.2-cm dia. round rod.

Table I lists the nominal and actual chemistries melted, processed and evaluated as the first group of alloys. All ingots were melted to an aim oxygen level of .2 wt.%. The first alloy was the Ti-6Al-4V baseline alloy, added to the study to provide a proper direct comparison to the experimental alloys. The low aluminum alloy was selected to evaluate its effect on processability (ie, conversion yield) while the high aluminum alloy was selected in order to maximize the use of low cost aluminum. Iron was the principle low cost beta stabilizer used, although chromium was also evaluated in addition to iron in some heats. The silicon was added to one heat in order to assess its effect on high temperature creep properties since in some cases, such as intake valves, such an alloy could operate as high as 480°C. The yttrium was added on another heat also to assess its impact on processability.

Table I. Mominal Compositions and Actual Chemical Analyses (in wt. pct.) of the First Alloy Group Tested

Nominal Composition	Al	¥	Ze	<u>Cr</u>	<u>si</u>	Q	Ħ
T1-6A1-4V	5.96	4.10	0.055			0.18	0.002
Ti-3A1-1.5Cr-1.5Fe	2.92		1.50	1.47		0.18	0.003
Ti-6Al-2Fe	5.68		2.17			0.193	0.001
Ti-6A1-2Fe-0.1Si	5.80		1.99		0.087	0.198	0.002
Ti-6A1-2Fe-0.02Y	5.69		2.00			0.189	0.002
Ti-6Al-1Fe-1Cr	5.44		1.13	1.05		0.222	0.001
T1-8A1-2Fe	7.46		2.06			0.206	0.001

For these small heats which were forged to roughly 4-cm square then rolled to 1.2-cm round, there were no significant difference noted in processability. Table II lists the tensile properties of these alloys in a beta processed plus annealed condition. It is evident from Table II that all of the three Ti-6Al-2Fe base alloys had attempths somewhat higher than Ti-6Al-4V. Their ductilities were also slightly lower but were still very good considering the higher strengths. The data in Table II indicate that yttrium had little or no effect on the ductility of the Ti-6Al-2Fe composition. Since it also had no discernible impact on processability it was dropped from further consideration.

Table II suggests the following conclusions:

- a) Low aluminum (- 3%) results in strengths too far below the benchmark Ti-6Al-4V alloy.
- b) High aluminum (- 8%) results in a substantial penalty in ductility.
- c) While Cr can be substituted for Fe in terms of strengthening, there is no justification in terms of properties for using the higher cost Cr vs. Fe.

Table II. Tensile Properties of Table I Alloys1

Alloy Nominal Composition	Temp. C	UTS MPa	YS MPa	S RA	§ Flong.
Ti-6Al-4V	24	989	950	37.2	13.5
	150	858	795	53.0	16.5
	300	715	652	58.1	15.0
	480	650	558	60.4	18.5
Ti-3A1-1.5Cr-1.5Fe	24	863	793	41.5	17.5
	150	744	625	54.6	23.0
	300	610	479	64.0	21.0
	480	491	407	83.0	27.0
Ti-6Al-2Fe	24	1047	990	30.6	15.5
	150	922	815	39.9	15.0
	300	793	643	39.7	15.0
	480	650	547	63.7	21.0
Ti-6Al-2Fe-0.1Si	24	1059	1024	31.3	14.5
	150	950	838	36.0	15.0
	300	816	668	37.4	14.0
	480	661	562	63.9	23.0

Table II. Tensile Properties of Table I Alloys (Continued)

Alloy		UTS	YS		
Mominal Composition	Temp. C	MPa	MPa	1 RA	1 Elong.
Ti-6A1-2Fe-0.02Y	24	1019	987	31.1	15.0
	150	901	791	38.1	15.5
	300	775	626	46.8	15.5
	480	644	559	66.2	21.0
Ti-6Al-1Fe-1Cr	24	1015	969	29.1	14.5
	150	907	793	38.9	15.0
	300	769	636	40.0	14.5
	480	675	566	57.7	18.5
Ti-8A1-2Fe	24	1164	1120	5.8	4.0
	150	1072	973	10.6	5.0
	300	972	816	28.3	13.5
	480	808	687	42.8	19.5

11.2-cm dia. bar beta rolled and annealed at 700°C(2 hrs)AC.

The primary purples of the 0.1% silicon addition was to improve the creep properties of the base alloy. It had this desired effect as shown in Table III, wherein a two-fold improvement in time to .2% creep strain was obtained thru the silicon addition.

Table III. Effect of 0.1% Silicon on the Creep Properties of Ti-6Al-2Fe

Alloy	Creep Rate,	Time to 0.2% Creep,
Ti-6A1-2Fe	1.72	172
Ti-6A1-2Fe-0.1Si	1.39	331

1Creep tested at 480°C - 84 MPa.

Considering the results in Tables I thru III, it was apparent that an alloy based on the Ti-6Al-2Fe-.lSi composition would meet the desired strength goal. It was then necessary to assess the acceptable limits of the alloying elements. The aluminum level of 6% (nominal) appeared optimum, based on the indication of poor strength at low aluminum levels and poor ductility at higher levels. Silicon was also felt to be optimized at .l%, since higher levels add melting difficulties (hence cost). Thus, the iron and oxygen were selected for further study.

The chemistries melted and processed for the iron and oxygen effects are listed in Table IV. The iron ranged from 1.4 to 2.4 and the oxygen ranged from .17 to .25. The alloys were double melted as 35 kg ingots then beta processed (forged and rolled above the beta transus) to 1.2 cm dia. rod and subsequently heat treated by three processes per alloy as follows:

Heat Treat Process 1: Solution treated for 1 hour at 60°C below the beta transus followed by water quenching and aging at 540°C/8 hr.

Heat Treat Process 2: Annealed 700°C for 2 hrs.

Heat Treat Process 3: Annealed 790°C for 2 hrs.

Table IV. Alloys Melted and Processed to Study Iron and Oxygen Effects in Ti-6Al-XFe-.lSi-XO₂ Base (wt. pct)

Alloy	<u> 11</u>	Ze	<u>si</u>	<u>Q</u> 2
A	6.1	2.4	.09	.25
В	6.1	2.0	.09	.24
C	6.3	1.4	.09	.24
D	6.2	2.3	.09	.18
E	6.2	1.9	.10	.17
r	6.2	1.4	.09	.17

Tensile and creep properties of these alloys are given in Table V. The following conclusions can be drawn from this data:

Table V. Mechanical Properties of Table IV Alloys

Material Condition: Beta Rolled/Air Cooled + Solution Treated β-60°C/WO + 540°C/8/AC Age

	Tensile				Creen		
Alloy ²	Room	Temp.	900	<u>•c</u>		-	ost
							Tensile
	X5	7.89	YS	7.89	Hrs to .25	¥8	<u>■ RA</u>
A	1180	7	635	70	500	_	0
3	1055	19	595	56	740	1080	9
C	1040	17	570	52	500	1050	8
D	1115	8	610	71	330	1140	6
E	1005	19	580	72	780	1010	18
7	980	24	540	57	690	1000	17

Haterial Condition: Beta Rolled + Annealed 700°C/2 Hrs/Air Cooled

Tensile				9	Creep		
Alloy ²	Room	Temp.	900	<u>c</u>		Pe	ost
							Tensile
	YS.	7 27	YS	7_89	Hrs to .25	<u>YS</u>	7_87
A	1100	26	595	73	25	Broke	in Threads
8	1055	30	575	71	13	1060	9
C	1050	32	550	64	22	1040	12
D	1050	26	580	70	12	1030	8
E	1013	33	600	68	17	1020	5
7	980	29	540	66	26	985	16

Material Condition: Beta Rolled + Annealed 790°C/2 Hrs/Air Cooled

Tensile			Creep ²				
Alloy ²	Room	Temp.	900	<u>.</u>		P	ost
						Creep	Tensile
	<u>YS</u>	N. RA	YS	7 37	Hrs to .25	YS	7 57
A	1170	25	580	71	70	1075	3
3	1035	33	550	67	46	1060	11
С	1035	34	545	65	83	1050	10
D	980	38	565	70	24	1015	30
E	995	34	550	69	38	1015	13
P	965	39	505	67	81	980	22

¹YS = Yield Strength MPa; % RA = % Reduction in Area; Creep test run at 480°C/84 ksi for approximately 500 hrs. 2See Table IV for chemistries.

- On average, an increase of about .07 oxygen is worth about 60 MPa in strength (ie, about 8.5 MPa per .01 wt.% oxygen).
- On average, a 1% Fe change resulted in only about a 40 MPa increase in strength.
- For all heat treat conditions, the combination of high iron (2.4%) and high oxygen (.25%) resulted in unacceptable post-creep ductility.
- 4. Although annealing treatment had only a minor effect on creep properties (700°C anneal was worse than 790°C), the STA condition was substantially better than both annealed conditions.
- Post-creep ductility was maximized by the 790°C anneal, low oxygen and, in general, low iron.

In light of the above results, the following aim chemistry ranges were selected for the optimum alloy:

Element	(Wt. &	١

	VI	<u>Fe</u>	<u>si</u>	Q_2
Min	6.5	2.0	.13	.20
Aim	6.0	1.65	.10	.18
Max	5.5	1.30	.07	. 15

This alloy has been designated TIMETAL.62S.

Alloy haracterization

In order to more fully characterize the TIMETAL.62S composition, an 820 kg ingot was melted and processed to plate product. The following properties were obtained from this heat.

Physical Properties: Table VI provides a summary of physical property measurements obtained from beta processed + 790°C annealed material. With the exception of Young's Modulus, these values are very close to Ti-6Al-4V values. Of note, however, is the high modulus values obtained by testing both longitudinal and transverse directions of beta processed material. For this property, TIMETAL.62S appears to have roughly an 8-10% advantage over Ti-6Al-4V at the same density.

Table VI. Physical Property Summary

Property	Equation 1	Temp Range
Specific Heat (cal/g°C)	$c_p = .130 + 5.26 \times 10^- \text{ (T)}$	RT to 815°C
Electrical Resistivity (10-8 ohm-m)	0 = 142.0(T)	•
Thermal Conductivity (W/m-k)	$\lambda = 7.54 + .0124(T)$	•
Thermal Expansion	a = 5.678(T)	
Density (g/cc)	$\rho = 4.43$	25°C
Poissons Ratio	$\mu = .32$	**
Young's Modulus (GPa)	E = 125.5	
(Mpsi)	= 18.2	

¹Where T = °C

<u>Microstructure</u>: Figure 1 shows typical alpha-beta and beta processed structures of TIMETAL.62S. They are quite typical of Ti-6Al-4V.

100X 100X (b)

Figure 1 - Typical microstructures of TIMETAL.62S (a) alpha-beta processed and (b) beta processed conditions.

Strength: Figure 2 is a plot of strength vs. temperature for TIMETAL.62S compared to Ti-6Al-4V. As demonstrated by the smaller heats, TIMETAL.62S has a small room temperature strength advantage over Ti-6Al-4V in the annealed condition. This strength advantages diminishes with temperature such that both alloys are equivalent above roughly 250°C.

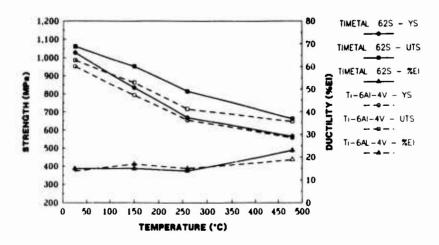


Figure 2 - Strength vs. temperature comparison of TIMETAL.62S and Ti-6Al-4V in the beta processed plus annealed condition.

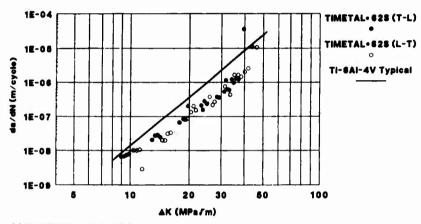
<u>Pamare Tolerance</u>: Table VII provides valid $K_{\rm IC}$ values for TIMETAL.62S in both alpha-beta and beta processed conditions. For this strength level, these values are typical of Ti-6Al-4V.

Table VII. TIMETAL. 625 Toughness Data

Condition	YS (MPa)	K_{Ic} (MPa- $m^{\frac{1}{2}}$)
Alpha Beta Forge + Rex Ann	139	45
Beta Forge + Rex Ann	138	59
Beta Forge + Hill Ann	138	55

Figure 3 shows a crack growth plot for TIMETAL.62S and again these results are quite typical of Ti-6Al-4V.

TIMETAL·62S CRACK GROWTH



ROOM TEMP.; R = 0.1, f = 20 hz BETA PROCESSED + ANNEALED MATERIAL

Figure 3 - Crack growth comparison of TIMETAL.62S with Ti-6Al-4V "typical".

Summary

A new low cost alloy, designated TIMETAL.625, has been developed which offers physical and mechanica? properties equal to or better than Ti-6Al-4V but at a substantially lower formulation cost than Ti-6Al-4V. The cost reduction is achieved primarily by substituting low cost iron for the more expensive vanadium. The primary intent of this alloy is to provide a low cost substitute for Ti-6Al-4V in cost sensitive industrial applications. Depending on product form, it is estimated that savings of 15% to 20% can be realized compared to Ti-6Al-4V.

TITANIUM TUBING EXPERIENCE IN UTILITY CONDENSERS

Peter L. Moore, Michael J. Nugent

Consolidated Edison Company of New York, Inc.

Abstract

Consolidated Edison first employed titanium tubing to replace a condenser unit that suffered severe corrosion of the tubes after only three years of brackish water service. That unit has since achieved 20 years of service with excellent reliability. Con Edison has subsequently replaced seven additional condensers with titanium tubing and has realized similar improved reliability. Overall service history, evaluation of design philosophy, installation and operational precautions with titanium tubed units are discussed. Descriptions of actual and potential failure modes of titanium tubes, including methods of Non-Destructive evaluation and corrective measures are also discussed.

System Overview

Consolidated Edison Company of New York, Inc. (Con Edison) is the primary electric, gas and steam utility serving New York City and Westchester County. The total area served is 660 sq. miles with a population of 8.1 million.

Con Edison owns and operates a steam turbine generation system capacity of approximately 7,400 MW and a steam co-generation system capable of producing 14,000 Mlbs of steam per hour. The Plant locations are shown in Figure 1. All fossil plants are located on salt/brackish water rivers. The nuclear plant is located approximately 40 miles north of Manhattan on the Hudson River. The water conditions at this site vary from fresh to brackish depending on the season.

The various steam turbine units at these facilities were originally placed into service between 1937 and 1973. The overall integrity and reliability of these units are critical for proper unit operation. The overall performance and long term reliability are crucial for unit availability.

Titophum '92

Science and Technology
Edited by F.H. Froes and I. Caplan
The Minerals, Metals & Materials Society, 1993



Figure 1: Map of the Greater New York area showing the location of the nine Con Edison Generating Stations.

First Titanium Application

Based upon the successful field test of titanium in Unit No. 2 condenser at Arthur Kill¹, a decision was made to retube Unit No. 3 condenser with titanium. As discussed in numerous publications², the main advantage of titanium is that it forms a stable, protective and strongly adherent film of TiO₂. Unit No. 3 condenser was retubed with titanium in the fall/winter of 1971 and returned to service in June 1972. The Unit No. 3 condenser was retubed with titanium. The tubesheet of aluminum bronze was left in place and no coating or cathodic protection was applied at that time. The tubes were 60 feet long and the titanium tubes were 1" diameter and 22 BWG (0.028" wall thickness). The original 13 tube support plates remained, and no additional staking/supports were installed at that time.

Based upon the successful service life of the retubed Arthur Kill Unit No. 3, Unit No. 2 was retubed in 1977. Since that time, these units have accumulated a total of 33 years of service for the 41,012 tubes. No corrosion activity has been noted in any of the tubes of these units in any of the bi-annual inspections. In total, 181 of the 41,012 tubes have been plugged either due to external mechanical damage or impingement. Subsequently, Astoria Unit No. 3 condenser was retubed with titanium tubes (%" OD - 22 BWG) in 1985. The root causes of damage and inspection techniques will be discussed later in this paper.

Rebundle Philosophy

The change in philosophy from the retubing of condensers at Arthur Kill and Astoria Unit No. 3 to the rebundling of condensers at East River Unit No. 7 and Ravenswood Unit No. 1 grew out of a need for reliability and improved performance. Essentially, the rebundling option eliminates some potentially damaging mechanisms, some of which were experienced at Arthur Kill; these include galvanic attack of the copper alloy tubesheet and subsequent coating related problems. Vibration problems are avoided due to the resizing of tube support spacings. The necessity for staking is also eliminated. Finally, state-of-the-art condenser design can now be retro-fitted into an old condenser shell for improved performance. In other words, the number and distribution of tubes, the tubesheet design and tube sizes can be upgraded to suit current requirements. An EPRI study ³ published in October 1988 highlighted these factors specifically in the case of Ravenswood Unit No. 1 and concluded that rebundling with titanium tubes was the logical and most feasible approach to replacement of this condenser for long term economy.

Ravenswood Unit No. 1 condenser, part of a 400 MW turbine-generator was rebundled in the spring of 1988 using %" OD - 22 BWG titanium tubes (ASTM B338, Grade 2), titanium tubesheets and welded tube to tubesheet joints. The unit was originally tubed with aluminum brass (%" OD - 18 BWG) tubes with 90 - 10 copper nickel in the air removal section. After 25 years of service in East River, tube pluggage reached 1,449 tubes. Chronic deterioration in its final year of operation saw over half (800) those tubes plugged.

East River Station Unit No. 7 condenser, a 185 MW turbine-generator, was rebundled in the fall of 1988 using ¾ " OD - 22 BWG titanium tubes (ASTM B338 Grade 2), titanium tubesheets and welded tube to tubesheet joints. The tube field consists of four "church" windows. Each window contains two air cooling sections and two extraction ducts that extend from tubesheet to tubesheet. Although deterioration of East River Unit No. 7 was not as dramatic as Ravenswood Unit No. 1, replacement was based on the deterioration of the tubesheets by dezincification. The unit constituted 18,350 aluminum brass tubes (1/4" OD - 18 BWG) and muntz metal tube sheets. Only 377 tubes were plugged at the time of replacement.

Further applications

Following the successful installation and operation of the modular bundles at Ravenswood and East River Stations, a Condenser Replacement Program was begun in 1990 to replace mature copper alloy condensers. Subsequently, Astoria Unit No. 4 condenser, a 383 MW turbine-generator was rebundled in the spring of 1991 using 7/6" OD - 22 BWG titanium tubing (ASTM 338 Grade 2), titanium tubesheets and welded tube to tubesheet joints. This replaced, after 28 years, the original aluminum brass tubed-unit, which had reached almost 2,000 plugged tubes out of 24,200. Astoria Station is also situated on the East River.

Replacement of Indian Point Unit No. 2 condenser, part of a 995 MW pressurized water reactor (PWR) turbine-generator, also began in early 1991 with the rebundling of one shell of a triple shell condenser. Waterboxes 21 and 22 were rebundled using %" OD - 22 BWG titanium tubes and titanium tubesheets. This was necessitated by the degradation of the arsenical admiralty brass tubes after 17 years of service. The increased emphasis of copper reduction in the PWR system also lead to the selection of titanium. The balance of the condenser is due for replacement in the near future.

Astoria Unit No. 5 condenser, part of a 383 MW Turbine-Generator, was rebundled in the spring of 1992 with a modular unit using titanium tubes, tubesheets and welded joints. Astoria Unit No. 5 is identical to Astoria Unit No. 4 and both condensers suffered similar deterioration.

SERVICE HISTORY

Galvanic Corrosion

Although the overall corrosion resistance of the titanium tubing has been exceptional, there have been specific issues, particularly with the retubed units. In the early days after retubing, particularly at Arthur Kill, galvanic corrosion between the cathodic titanium tubes and the anodic naval brass or aluminum bronze tubesheet caused significant wastage of the tubesheets. The solution to this problem was two-fold: coating the tubesheet and cathodic protection. Mixed results were encountered with both these fixes. Coatings tended to deteriorate, resulting in worse damage in the affected area and had to be replaced often, usually every other year (Figure 2). Cathodic protection requires rigorous maintenance in order to be effective. Tubesheet coatings are used at Arthur Kill Units No. 2 & No. 3 and coatings and cathodic protection are being employed at Astoria Unit No. 3. Deterioration of water boxes is also a problem. Most new waterboxes are rubber-lined carbon steel. The most effective inspection technique for this type of damage is visual examination by qualified personnel.

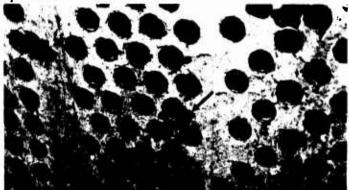


Figure 2: Tubesheet corrosion between three titanium tubes. Depth of attack approximately %" (Arrow).

Vibration

A serious problem encountered at Arthur Kill Unit No. 3 was tube to tube vibration wear resulting from mid span collisions of tubes. The root cause of this problem was inadequate tube support spacing caused by too few tube support plates. It occurred predominantly at the center spans of peripheral tubes. The tube-to-tube damage mechanism is described in Figure 3. The problem was detected by eddy current testing of the tubes in the fall of 1990 during a continuing life inspection and confirmed by a steam side inspection and subsequent metallurgical analysis. The wear was found in up to six bays at the mid-span locations.

Although no tubes suffered through wall damage, several tubes sustained 80% wall loss and were preventively plugged. The problem was mitigated by staking throughout the condenser although the damage was localized to a specific area of the bundle. The tube support spacing was about 50".

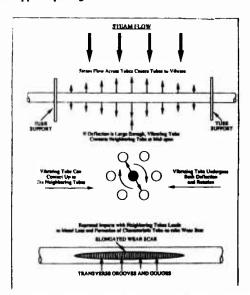


Figure 3: Tube-to-tube wear; Mechanism of scar formation and metal loss.

INSTALLATION RELATED DAMAGE/WELD SPLATTER

Retubed units

An on line tube leak in Astoria Unit No. 3 Condenser occurred in 1989 after four years of service. The tube leak was investigated with eddy current testing and the root cause was identified by laboratory examination as weld splatter damage.

During the retubing of this unit, a shroud was field welded over the air removal section resulting in weld splatter melting almost through the tube's wall in several cases, eventually (four years later) leading to a leak. Consequently all peripheral air removal section tubes in this condenser were eddy current tested to determine how widespread the problem was. Stakes were originally installed in this unit so vibration should not be a problem.

Rebundled Units

Rebundling is not always the panacea. A leaking tube was detected in the periphery of the bundle at East River Unit No. 7 condenser in 1989 and another in 1990. In the first case, the leak was eddy current tested; both cases were attributed to installation-related damage. Leaking tubes detected during the hydrotest at Indian Point Unit No. 2 on the new modular condenser were also due to installation related tube damage. In this case a hand tool was responsible.

Similarly, a hydrotest at Astoria Unit No. 4 on the new condenser detected leakage of the tubes due again to weld splatter melting through the tube wall. These tubes were on the uppermost periphery. All periphery tubes were eddy current tested and new tubes installed where damage was sustained. Two tubes sustained through wall damage (Figure 4); several others sustained partial damage.



Figure 4: Through-wall hole caused by weld splatter on titanium condenser tube, Astoria Unit No. 4.

Mill Defects

Occasionally, an original manufacturer's mill flaw is detected by eddy current testing. An example of a mill flaw in a titanium tube from Arthur Kill Unit No. 2 is shown in Figure 5; the depth of the flaw was approximately 70% through wall.

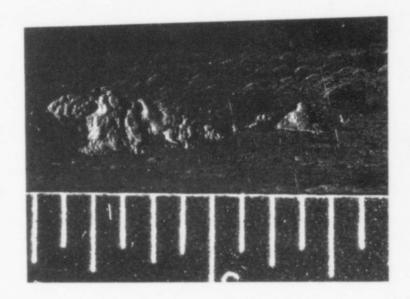


Figure 5: Mill flaw on O.D. surface of titanium condenser tube, Arthur Kill Unit No. 2.

Generally, mill defects do not propagate during service and do not lead to leaks. When they are detected, however, the tubes are usually plugged as a precautionary measure. It is important to note that in most cases of tube damage following rebundling (except East River Unit No. 7), the damage was detected by the hydrotest and corrected before the unit went on line. No subsequent cases of further damage have been reported. Ravenswood Unit No. 1 has not reported any leakage in four years of operation.

Hydriding

Although this has been a reported problem at other utilities and overseas, there has been no observed degradation of titanium tubes in Con Edison's condensers as a result of hydriding. Several uppermost tubes were removed from an older titanium condenser (Arthur Kill Unit No. 20 which was then 13 years old) in an effort to determine if hydriding was present.

Several tests were performed on the tubes, including metallography and strength; none of which indicated any problem with hydriding. For the test, a tube that had the greatest propensity for hydriding was selected. In fact, apart from a slight brownish discoloration, the tubes did not appear deteriorated at all. Titanium units are projected to provide at least 40 years of relatively maintenance free service.

Inspection

Con Edison's inspection program for titanium tubed condensers is multitiered and includes eddy current inspection of tubes on a regular basis. Incoming Quality Assurance testing was performed on sample tubes for use in Indian Point Unit No. 2 condenser to determine conformance to ASTM B338 Grade 2.

Eddy current testing is performed on a sample of tubes immediately after installation to determine a base line and also to detect installation related damage or mill flaws. Eddy current testing is then conducted in two to five years time, barring any intermediate problems, and repeated at least every five years. In addition, these units are overhauled every five to seven years for continuing life assessment. At this time, a comprehensive inspection is conducted on both the water and steam sides.

Acknowledgements

The authors would like to acknowledge the work of the Con Edison Production (Fossil Power), Engineering, and (former) Power Generation Services Departments whose work led to the selection of titanium 20 years ago. Special thanks to Icilma Thornhill for her diligence in the preparation of this manuscript.

References

- Stein, Walter "Evaluation of Experimental Condenser Tubes" Con Edison Report Met 51, April 28, 1971
- Loren Covington "Titanium Solves Corrosion Problems in Petroleum Processing" Timet Publication.
- 3. Bell, R. J. et al "Condenser Condition Assessment and Retrofit Analysis: Ravenswood Unit 10" EPRI CS-6024, October 1988.

INSPECTION, NDE, QUALITY ASSURANCE, DEFECTS

QUALITY ASSURANCE FOR TITANIUM

CRITICAL APPLICATIONS

Philippe Martin, Jean-Paul Herteman

SNECMA - Direction de la Qualité B.P. 81 91003 Evry Cedex - France

Abstract

Titanium alloys exhibit outstanding corrosion and mechanical properties that make them peerless for aerospace applications, like disks and blades of aeroengines for instance. But their fatigue behaviour is extremely sensitive to melting defects and microstructure variations. Quality control and assurance is a critical issue for safe Titanium operations and is continuously being improved.

Melting defects have been documented as Type I hard α and Type II α and β segregations. Several tenthes of potential defect origins have been identified through the whole current 3 VAR process and put under strict Q.A. specifications. As a result, defect rates detected on billets have been reduced by a factor of ten in the last 5 years. Industry wide data base (I.E.T.Q.C.) now provides a statistical knowledge of risk exposures and better opportunities for corrective actions. New melting processes, like Cold Hearth Melting, are being developed and could lead to further improvements, provided they will not be plagued by new specific defects or lack of capability of composition and microstructure control.

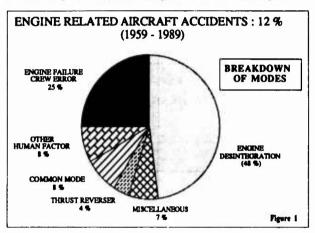
Inspection techniques, i.e. macroetching, X-Ray and, mainly, ultrasonics are being improved as well. Multifocal scanning and imaging are becoming a standard practice for Premium Quality billets and parts. In the medium term, advanced signal processing concepts, like "Time reversal self focusing" or SAFCT, could bring a capability of inspection titanium through its inherently high, microsctructure related, "grass level", achieving a major technological breakthrough.

Titanium '92 Science and Technology Edited by F.H. Froes and I. Caplan The Minerals, Metals & Materials Society, 1993

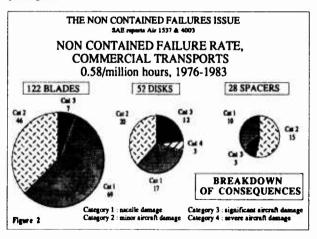
1- THE PLACE OF TITANIUM ALLOYS IN ENGINE FAILURES

The most critical applications of Titanium alloys are certainly the rotative parts of aeroengines: their Quality Assurance is, of course, driven by flight safety considerations.

Engines account for a small share of air transport accidents. A recent analysis of data has shown that they are responsible for 12 % of accidents between 1959 and 1989. However, this is not negligible, and it is clearly necessary to reduced even further [1]. Moreover, considering engines in commercial air transportation, a particular safety concern has to be addressed: uncontained failures in the engine, and their repercussions on the airframe, systems and persons carried. They are the main cause of engine-related air accidents [fig. 1].

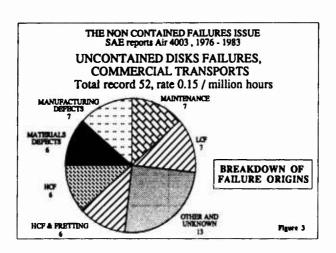


If we consider the period 1976 - 1983, and transport aircraft only, the total uncontained engine part failures is 0,58 per million flight hours. A little more than 25 % of theses failures [Fig. 2] concern discs, with a rate of 0,14 per million flight hours. For evident reasons of kinetic energy stored in disk fragments, failures of these parts have the most serious consequences. Of the 52 cases recorded between 1976 and 1983, 12 are classified category 3: significant damage to the aircraft (damage to be primary structure, rapid depressurization, fire, slight injuries to the passengers), while 3 were classified category 4: severe damage to the aircraft (crash, loss of the aircraft, serious or lethal injury to the passengers).



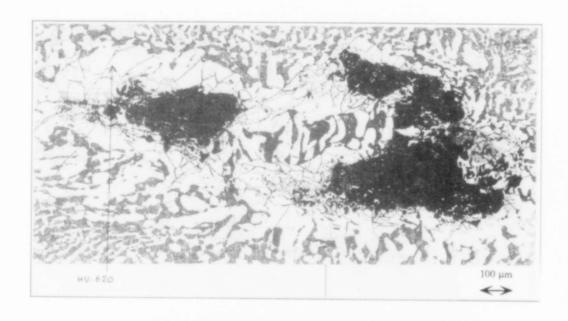
^[1] Coopération in the analysis of data and the improvement of aircraft engine safety -J-P. HERTEMAN, P. MOUTON - SNECMA - International Federation of Airworthiness - 21st IFA conference -October 1991.

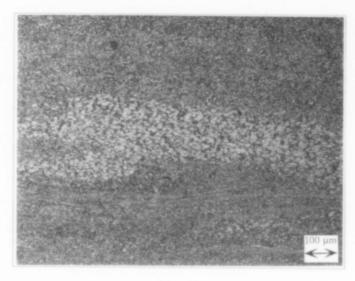
The main mechanisms involved in disk separation are usually fatigue - related, whether low cycle (induced by engine operating cycles), or high cycle (intrinsec dynamic modes of the rotor or rotor/stator interactions, sometimes of aerodynamic origin). The origin of fatigue cracking and fracture often lies in the very design of the part [Fig. 3], but fractures are also encountered as a result of maintenance fault (7 of the 52 cases recorded), machining and surface treatment faults (also 7 cases) and material defects (6 cases).



Although not the most frequent, this latter cause is of particular importance from the technical standpoint since, as they can be located anywhere in the volume of the disk, they can give rise to particularly dangerous fragments. Furthermore, from the psychological standpoint they are unacceptable as fractures of this kind can lead to a loss of confidence by the travelling public.

Titanium alloys have a significant share in the responsability of these uncontained failures. Their outstanding corrosion resistance properties and excellent ratio strengh/density make them irremplaceable in the production of high performance aeroengines: they are widely used in disks, particularly in low and high pressure compressor portions of most but all modern engines. But their fatigue behaviour is extremely sensitive to melting defects and microstructure variations. Several events during the past decades are here to recall it to us. The last one, which occured in the summer of 1989 in Sioux-City (Iowa) due to an uncontained fan disk burst, lead to the creation of the FAA "Titanium Rotating Components Review Team". This group, comprising FAA personnel, performed an extremely exhaustive and in-depth review of the cases of cracking or fracture which have occured in service since 1962, following titanium material defects, and presented its conclusions to the engine manufacturers in May 1991, and to the airlines in September 1991. It identified 25 cases of cracking or failures: 19 "Type I" defects [Fig. 4] (hard α , as with the Sioux-City disk) and 6 "Type II" [Fig. 5] (segregation without sudden rise in hardness or tearing).





- Figure 5 -

Four engine makers were concerned, which clearly shows that the problem is a widespread one, and not isolated or specific to such or such a design practice or manufacturing process. The very high chemical reactivity of liquid titanium encourages the risk of appearance of the defects mentionned earlier, throughout its working cycle (sponge manufacturing, melting, etc...). In addition, the metallurgical structure of titanium gives it a high background noise, thus making inspection of this faults by means of ultrasonic scanning of the forged blanks more delicate than with the other families of materials.

Then from the present situation, where titanium defects account for about 0.1 cracking and 0.01 uncontained failures per million flight hours, which are the opportunities of improvement for the future? Two main axis seem to contain enough potentialities to achieve a major step in adressing the issue of safer titanium operations i.e. less than 0.001 uncontained failures per million flight hour.

The first axis concerns the understanding of damage growth mechanisms, and their integration in the design. This knowledge must overpass the qualitative field, and cover quantitatively the cinetics of the different potential failure

processus, their relation with material structure and processing, as well as their sensibility to environmental factors [2]. I will not develop furthermore this axis in this presentation. Even if promising and essential, it will remain at least at short term, insufficient: some of the important damage mechanisms are still at a scientific investigation stage; furthermore, il appears sometimes very difficult to know completely and precisely the environmental parameters in which the material has to operate.

The second axis concerns the improvement of the quality of materials, by having an enhanced control of defects. In this matter, two progression ways have to be pursued: the first one, classical, of the upgrading of the non destructive testings; the other one, more global, of the control of the manufacturing processes, from the raw material to finished product. These two approaches must not be opposed to each other. They are in fact complementary. Any manufacturing process generates its own defects: the residual risk will result of the combination of both the risk of non-detection of the defect at inspections, and its occurrence rate [3]. Then it is essential to adress both issues by minimising them. Several recent and future developments offer potentialities to

2- THE CONTROL OF THE PRODUCTION AND MANUFACTURING PROCESSES OF TITANIUM ALLOYS

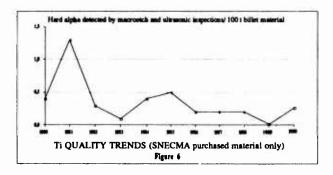
It is essential to look unceasingly for progressing in the field of generation of defects, to be more preventive, to make "right at the first time". Reliability of the final inspection is not always sufficient by itself: it is necessary to associate to it, and sometimes substitute, the reliability of the production and manufacturing processes [4]. The control of metallurgical and mechanical quality calls for a panel of coherent tools complementary between them. Their efficiency is proved and can be illustrated.

a) Statistical survey of process:

achieve these goals.

Control of processes is the constant research for the lowest possible variability of the caracteristics of the product. Therefore, it is first necessary to determine this variability, and then to survey its evolution, respecting the chronology. That necessitates to realize some measurements caracterizing the product at the significant steps of its production (it may concern non destructive testings incorporated in the processus, and non necessarely final) and the implementation of a statistical survey on these parameters (control charts, histograms of evolution, etc...).

In the case of titanium alloys, of particular interest is the follow up of melting defects for the reasons explained above. Non destructive testings directed to detect these defects are mainly the ultrasonic inspection performed on the billet before forging and on the forged disk at a premachined stage; also the macrographic inspection is realized at two steps: forged part - sonic shape - and finished disk-machined. Figure 6 shows an histogram of evolution of occurrence rate of hard α detected during these inspections. It is interesting to see the dramatic improvements accomplished during the past 10 years, allowing then to measure the impact of the quality assurance dispositions taken.



[🖾] Endommagement en fatigue oligocyclique des disques de turbomachines -

J-Y. GUEDOU, Y. HONNORAT, SNECMA - Matériaux et techniques - Janvier/février 1989.

Jes matériaux dans les problèmes de fiabilité et durabilité. Quels axes de recherche et de progrès ?

J-P. HERTEMAN - SNECMA - Entretiens Science de Défense, 1990.

^[4] La maîtrise des procédés de fabrication dans une conception de tolérance aux dommages -J.P. HERTEMAN - SNECMA - AGARD/SMP report 773.

From our experience, the "key parameters" which have driven this improvement and have to be kept under strict and constant control are:

- introduction of triple melt (1984),
- surface conditionning of electrodes, especially after primary melting,
- welding under chamber with controlled atmosphere,
- improvements in sponge process decreasing risks of fires, finer sponge size,
- reinforcement of final inspection criteria on sponge: visual inspection, contaminated particles,
- reinforcement of allowed recycled scraps, as for example interdiction of flame cut recycling,
- ultrasonic inspection by immersion,
- better control to avoid melting into stub/holder and no recycling of remaining electrode tops
- improved melting furnaces controls.

However, as shown by this histogram, the frequency of observation of the defects in question has become indeed too low for a single producer or user to be able on its own to identify significant trends. Only a world wide quality data base, such as Jet Engine Titanium Quality Comittee created after the Sioux City accident, and intended as a permanent observatory of titanium manufacturing Quality throughout industry, allows a reliable statistical evaluation of the occurrence rate of these melting defects. Its data base is designed to cover all titanium producers and currently contains 17 companies. Pooling of information for example allows identification of the areas of the ingot which present the highest risk, or quantification of the progress made, on a data base ten times greater than that which would be accessible to a single user.

b) Reliabilitation of processes:

Actions allowing to have access to it concern qualification of production equipements, and may extend up to an analysis of reliability (FMECA) of them, stability and capability study, implementation of statistical survey of pertinent operating parameters of these production equipments, and of course, an adequate preventive maintenance.

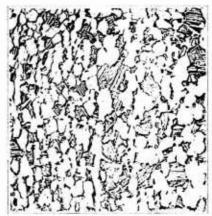
Reliability of processes governing metallurgical quality of titanium alloys is of prime concern. Experience as far as now has shown that any process has its advantages and inconvenients. Consequently, it is mandatory to gain sufficient experience in order to determine weaknesses, variability and risks associated with the process. Then, it is possible to look for the root causes of the potential defects using tools presented above, and to try to get control of them by setting for example adequate quality assurance dispositions. In order to address the hard \(\alpha \) problem, this approach has been performed recently on VAR melting process currently used. It has been clearly shown [5] than nearly 30 different causes could potentially lead to the formation of an hard or. In the same time, a study on the refining capability of the VAR process has been conducted. For the first time, starting from representative artificial defects, it has been demonstrated that the efficiency rate for eliminating hard α defects by the 3 x VAR process used for disk is approximately 92 %. It is worthwhile to note than more than 20 years of production with this process have been necessary in order to determine more appropriate and strict quality assurance specifications. Is another process more capable? This is the full intent of the Cold Hearth processes. Experience gained so far shows that Electron Beam melting has a better capability than 3 x VAR for removing LDI and HDI; but progress remains to be made to address some risks specifically related to this process: chemical homogeneity, condensate fall-in, as well as variability resulting of off-nominal conditions such as melt interruptions.

An other important metallurgical quality aspect for titanium alloys is microstructure variations, resulting both from ingot to bar/billet conversion processes and from forging processes. Relationship between microstructure (size and morphology of grains, primary and secondary phases, banding, heterogeneities, etc...) and crack initiation/propagation rate is strong. It is essential for an engine maker to control this aspect, which governs the authorized operating life of rotating parts (low cycle fatigue), and also resistance margin in high cycle fatigue. Compliance with operating life sold to airlines is a major economical goal. The cost of all the titanium, life limited, critical parts of an engine, represents 10 to 20 % of the engine maintenance cost, which ranges typically between 50 to 100 \$ per flight hour. Thus, even a 10 % variation in the certified fatigue life of these parts (typically 10.000 to 30.000 cycles) would significantly affect the life cycle cost of the engine and be a serious concern for the airline operating the engine.

Proven capability and consistency of these conversion and forging processes are then mandatory. Figure 7 illustrates an example of capability improvement made in the forging process of fan blades at SNECMA Gennevilliers, leading to an increase of 75 % of the resistance margin in high cycle fatigue.

^[5] Titanium Base Alloys Clean Melt Process Development C.E. SHAMBLEN, G.B. HUNTER - GENERAL ELECTRIC AIRCRAFT ENGINE BUSINESS GROUP -Proceedings of the 1989 Vacuum Metallurgy Conference on the Melting and Processing of Specialty Metals.





 $\label{eq:microstructure large} \begin{aligned} & \text{Microstructure l} \\ & \text{High cycle fatigue Strengh } \sigma_1 = 350 \text{ MPa} \end{aligned}$

Microstructure 2
High cycle fatigue Strengh $\sigma_2 = 620 \text{ MPa}$

- Figure 7 -

c) Total Quality Management:

Involvement of people, including operators themselves, by implementation of self-inspection in manufacturing, of Quality Improvement Teams or action groups, is a most necessary step in process control.

d) Numerical modelisation of processes:

Numerical modelisation of production (melting) and manufacturing (forging, casting, etc...) is undoubtfully a scientific tool, whose utilisation developps very quickly. Indeed, it offers potentialities to overmultiply, compared with conventional approaches by subsequent experimental iterations, industrial capabilities (i.e. at reasonnable cost and time) to:

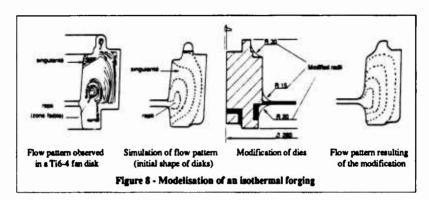
- optimize a manufacturing sequence in regards of given product specifications,
- perform studies in regards of some significant but necessarely varying, parameters of the process,
- measure impact and consequences of off-nominal conditions of the process,
- correct quickly and efficiently the process in case of trends, or occurrences of repeatable defects.

SNECMA has undertaken since about 10 years the development of modelisation programs concerning several processes such as solidification (equiaxial and directed) of superalloy turbine blades cast under vacuum, as well as forging (conventional and hot die) and heat treatment of axisymetric parts [6]. In this last case, forge 2 model from CEMEF is used. The different modelisation steps are as follows:

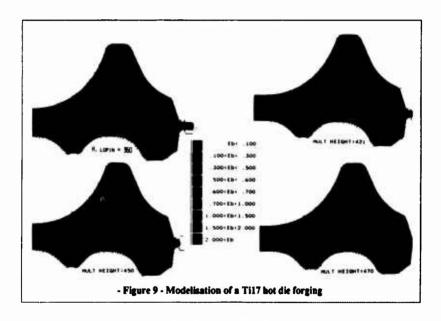
- study of the strain/flow of metal by taking as hypothesis the dimensions of the initial mult and shape of dies.
 The goal is to get a cartography showing an homogeneous strain without defects (such as lack of filling, overlap, sharp flow pattern, etc...),
- metallurgical study of the thermomechanical sequence : optimizatio) of the different parameters such as temperature, strain rate, lubricants, etc...

Figure 8 gives an example of flow pattern problem (overlap and sharp point) on a titanium forged fan disk; this has been analysed and simulated using modelisation, and could be resolved by a modification of the die radii.

^[6] La modélisation des procédés de mise en forme en Forge et Fonderie de précision – Y. HONNORAT, A. LASALMONIE SNECMA 13ème colloque Matériaux pour l'Aéronautique et l'Espace – Juin 1989, Paris.



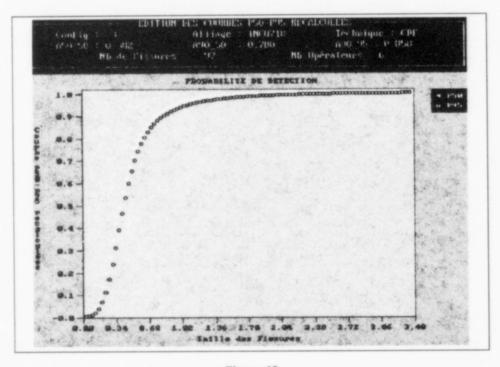
The figure 9 gives another example concerning the hot die forging of Ti17 compressor disk: the model was used to study the influence of several forging parameters (initial mult size, die shape, etc...), in a successfull attempt to assure a minimum amount of working in all areas of the part. This study is essential to evaluate dispersion of some mechanical properties within the part, such as fatigue and ductility, as they are lower in areas with less metal working, where grain size is coarser and equiaxial.



3- NON-DESTRUCTIVE TESTING

Actions to improve control of production and manufacturing processes are then essential. However, control of "defects" cannot be considered without an efficient final inspection. No existing process is perfect, and those used for melting and conversion of titanium alloys don't make exception to the rule.

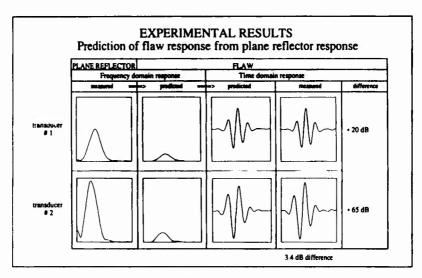
a) Improvement of inspection reliability No inspection technique provides an absolute filter. The different kinds of non-destructive testing of defects in materials, whatever is the physical process (ultrasonic, Eddy current, fluorescent penetrant, etc...) used, are all concerned. Efficiency of a non destructive testing must be analysed in statistical terms: probability of non detection of a defect with known characteristics and frequency of false calls. A considerable effort must be agreed to get access at the knowledge of effective detection performances of used techniques. This effort is already engaged concerning detection of in service defects (i.e. fatigue cracks) by fluorescent penetrant inspection, ultrasonic inspection and Eddy current inspection (figure 10).



- Figure 10 -

It will have to be pursued for detection of manufacturing defects (hard α , type II, clean voids, etc...), but probably with a different approach due to the difficulties ro obtain representative defects, and the amount of descriptive parameters of defects to take into account.

The statistical knowledge of detection performances is one thing, their improvement is another one. The first aspect of this improvement concerns inspection equipements by themselves: as defects detected are more critical, main effort is directed on ultrasonic inspection. A recent round robin campaign concerning ultrasonic response on one calibration block clearly illustrates the problem of insufficient repeatibility from one equipment to another, with difference reaching 6 dB or more. Improvements are needed on each element: US equipment, transducer, calibration block. This situation justifies the importance to identify the critical parameters of each of these elements; then, these ones can be put under control by specifying limits. Figure 11 illustrates differences of responses obtained from two transducers commonly used in the industry. Also, an important task to achieve is to establish coherent calibration conditions, by using "reference material" and generalization of Flat Bottom Hole. Another aspect of performances improvement is undoubtfully automation of inspection: more than new physical processes (infrared thermography, laser holography, ect...) which don't bring a significant gain in term of detection levels compared with current processes, decisive progresses are expected from automation.



- Figure 11 -

b) Quantify the non destructive testing

Non destructive inspection techniques have very often a nature rather qualitative (good/bad) than quantitative (characterization of the detected defect). This fact limits their ability to act as a major tool in the accession to process control, and, sometimes, reduces their efficiency to be a filter of any "mechanically inacceptable" defect.

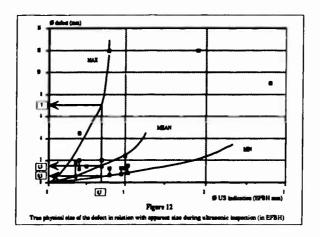
This is exactly the case concerning material defects in titanium alloys: hard α and type II segregation are typical defects resulting of the melting process, clean voids are generated during thermomechanical conversion. The nocivity of these defects depends on their physical nature, the condition of their interface with the sound matrix, the presence or not of any decohesion, and of course, their dimension and orientation. Their occurrence rate is also variable:

- < 2.10^{-6} / kg for hard α < 4.10^{-7} / kg for high density inclusion
- < 4.10 -6 / kg for clean void.

Moreover, non destructive inspections directed to detect them (very often ultrasonic) are not calibrated "in absolute", but in regards of internal references specific to each technique: for example, cylindrical hole with flat bottom perpendicular or parallel with the ultrasonic beam, of a given diameter.

Consequently, the inspection does not take into account completly all the parameters affecting the nocivity of the defects. Even on the simple side of the dimensions, the relations between the "true" physical size and its "apparent size" during ultrasonic inspection (resulting of the comparison between defect response and standard flat bottom hole) is far to be evident, as shown by figure 12 [7].

^[7] Préétude du programme d'amélioration du contrôle titane -L. BEFFY, G. MANGENET, J.M. THERET, SNECMA - Février 1991.



In this field, as for detection reliability, the development of signal processing techniques, the use of multitransducers systems, etc... let hope to considerable progress during the next decade.

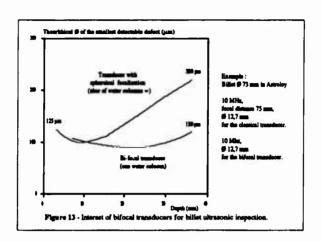
c) Improvement of titanium alloys inspection

In order to answer to the priority on titanium alloys, a specific improvement plan directed towards performances of non-destructive testing has to be pursued. The objectives settled down concern:

- better in process detection of hard α,
- better inspection of critical Ti parts, whatever process used.

At short term, some improvements are possible by using best state of the art ultrasonic techniques available: some of the possibilities have already been mentioned above concerning equipments and calibration, but are far to cover all potentialities. For example, the present status of titanium inspection reveals that two causes among others limit its performance: the noise level generated by the material structure and the curvilign shape of the entry surface. Actions have been undertaken in order to establish the correlation between billet structure and noise level. It appears that there is a strong effect of texture (arrangement of grains) and also microstructure. The optimization of thermo-mechanical processing of ingot to billet, limitation of billet size, are then largely contributing to enhance inspectability. Also, in order to avoid any distorsion of the focal spot in the billet due to the curved entry surface, the use of bi-focal transducers, for example, is capable, as shown by figure 13, to improve the performance of detection on billet.

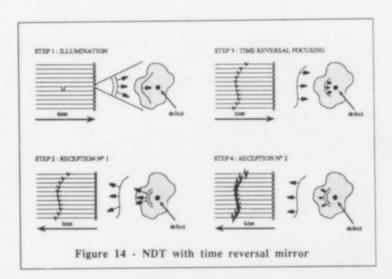
The combined impact of these actions has already resulted in a reduced noise level, but they will have to be continued in order to meet FAA recommendations.



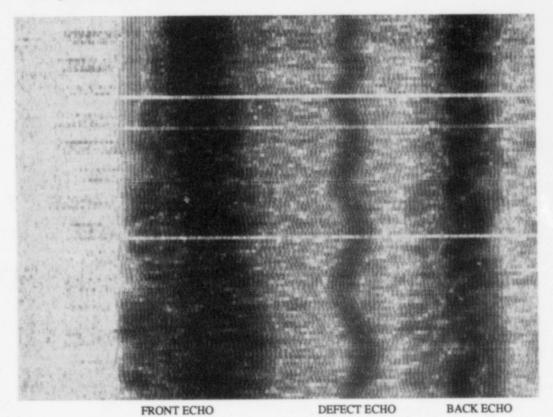
At medium term, only new technologies will be capable to bring a drastic improvement in detection performance. SNECMA has engaged beginning 1991, an important two years program on the development of a new technique: "Time Reversal Self Focusing" [8]. Focusing an ultrasonic wave on a defect of inknown shape through an inhomogeneous medium of any geometrical shape is a challenge in non destructive testing. The use of a Time Reversal Mirror (TRM) represents an original solution to this problem. It realizes in real time a focusing process matched to the defect shape to propagation medium and to the geometrical distortions and of the medium. It is a self-adaptation technique which compensates for any geometrical distortions of the mirror structure as well as for distortions due to the propagation through inhomogeneous media.

A Time Reversal Mirror is made from a 2D array of transmit-receive transducers. The process require four steps [Fig. 14]. The first step consists in transmitting a wave front from the liquid towards the solid, from the transducer array to the unknown target. The target generates a backscattered acoustic field that propagates through the solid and is distorted by refraction through the solid-liquid interface (mode conversions can occur and are involved in the process). The second step is the recording step; the scattered and refracted acoustic field is recorded as a pressure field by the transducer array. In the third step, the transducer array generates on its surface the time reversed field (i.e. the field is retransmitted in a reversal temporal chronology: last in - first out). This pressure field back propagates through the liquid-solid interface, and optimaly focuses on the defect inside the solid. During the last step, the transducer array receives the acoustic field coming from the defect which can be detected in such a way. Moreover, in case of multiple targets, the process is capable by interactive mode to focuse on the most reflective one.

^[8] Time Reversal Method to improve ultrasonic inspection of titanium alloys -Prof. M. FINK, Directeur du Laboratoire Ondes et Acoustiques de PARIS VII, J-M. THERET, Manager, Quality Technology - SNECMA.



A 128 chanel prototype has been built. Experiments on titanium samples containing different kinds of artificial defects and induced hard α demonstrating the efficiency of the technique, are in progress. An example of self-focusing on an off-axis (5 mm) hard α in Ti6-4 is presented in figure 15.



- Figure 15 -

The goal SNECMA is aiming at, is to be able to detect a 0.2 mm EFBH reflector through a 0.4 mm EFBH noise level, achieving a major technological breakthrough in detection performances.

4- CONCLUSION

Potentialities exist to achieve a major step in addressing the issue of safer titanium operations. The control of metallurgical and mechanical quality resulting of melting processes has made significant progress during the past decade, due to more appropriate and strict quality assurance specifications. New melting processes, like Cold Hearth Melting, could lead to further improvements, provided they will not be plagued by new specific defects, or lack of capability resulting of off-nominal conditions.

Whatever process used, an efficient filter in final inspection by non-destructive testing will remain a key in the control of defects. Development of new technologies, such as a "Time Reversal Self Focusing", at SNECMA, may bring a major contribution towards that goal, opening ability to act both as a tool in the accession to process control and as a filter of "mechanically inacceptable" defect.

LASER ULTRASONICS FOR LARGE

METAL STRUCTURES*

Clarence Calder

Heeyong Park

David Hiatt

Mechanical Engineering Oregon State Univ, Corvallis, OR 97331 Mechanical Engineering Univ. of Connecticut Storrs, CT 06269

Oregon Metallurgical Corp. P.O. Box 580 Albany, OR 97321

Abstract

Laser induced ultrasonics with various noncontacting and contacting sensors is being developed to detect defects in materials. The technique is being evaluated for use with large, industrial sized metals, such as ingots, billets, and other large structures common to Oregon metals industry to detect flaws such as inclusions, voids, high porosity, shrink pipe, and other irregularities. This NDT inspection would normally be done on machined surfaces by C-Scan ultrasonic methods in water or by labor intensive transducer contact. If successful, the laser method could offer significant time and cost savings over conventional C-Scan testing by allowing inspection without surface machining and a much faster scanning rate. Results indicated that strong ultrasonic stignals can be induced by pulsed laser deposition on rough, ascast, surfaces. Signal-to-noise ratio was quite limiting when using noncontact optical sensing techniques but was considerably improved when using piezoelectric pinducers with couplant on the rough surfaces.

Introduction

Stress waves induced by a pulsed laser interacting with a material surface have been used by the first author (1-4) and others (5-9) in material behavior applications and nondestructive testing (NDT) in which the unique noncontacting feature is required and/or convenient. Totally noncontact testing has been achieved by the use of laser interferometry to record the response.(1) Other optical methods such as laser speckle interferometry which do not require a specular surface might also be of interest.(10) Convenient practical application could be achieved with use of fiber optics or a rotating mirror for directing the high energy and detection laser beams. This technique should be easily adapted to large structures which may have very rough surfaces typical of as-cast and remelt surfaces without major difficulties. Laser induced ultrasonics offer some key advantages over conventional methods including

- 1. Large stress amplitude of very short duration
- 2. Remote testing convenient for severe environment and toxic samples
- 3. Test time is only a few microseconds
- 4. There are few restrictions on specimen size, configuration

Titanium '92 Science and Technology Edited by F.H. Froes and I. Caplan The Minerals, Metals & Materials Society, 1993

^{*}This work was performed as part of the Oregon Metals Initiative Program which is funded through partnership with the Oregon Economic Development Department and Oregon Lottery, the U.S. Bureau of Mines, and Oregon metals industries.

- 5. Laser excitation conveniently allows for point, line, or distributed acoustic source
- 6. Simultaneous generation of compressional, shear, and surface waves is possible
- 7. Rapid scanning of the specimen
- 8. Potentially total noncontact NDT using interferometric or other noncontact sensing

Body and surface ultrasonic waves may be simultaneously generated by pulsed laser deposition permitting inspection for either surface cracks and irregularities or subsurface flaws. Signal filtering to emphasize the desired signal will probably be necessary. Alternately, studies are currently underway to enhance the desired wave type needed (11-13).

A recent literature review has shown that significant research on laser generated ultrasonics and detection is currently being done by Wagner and Green at the NDE Center at John Hopkins University (13, 14), at Texas A & M University by Burger (15, 16), by researchers at the University of Hull in England (17, 18), at the Georgia Institute of Technology (11), and by Monchalin and co-workers at the Industrial Materials Research Institute in Canada (19,20).

Methodology

Research was conducted using facilities of the Department of Mechanical Engineering at Oregon State University. A Holobeam ruby laser, Q-pulsed with a Pockel's cell, produced light energy pulses up to 2 Joules at about 30 ns duration. Alignment and interferometry were accomplished with a Hughes 5 mW helium-neon and a Lexel 1 Watt argon ion laser. Transient data were recorded with a variety of analog and digital oscilloscopes with maximum bandwidth up to 150 MHz. All tests were conducted at energy levels sufficient to induce the ablative mode of ultrasonics as opposed to purely thermoeleastic generation.

Figure 1 shows schematic of the test arrangement using interferometry for sensing laser induced, ablation mode ultrasonic disturbances and Fig. 2 illustrates data acquisition instrumentation used for all work.

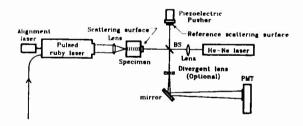


Figure 1 - Laser induced ultrasonics using interferometry sensing.

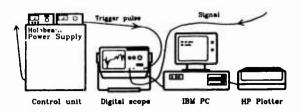


Figure 2 - Data acquisition arrangement.

Initial testing was done with aluminum samples followed by work with laser induced ultrasonics in titanium, zirconium and other metals of interest with samples reaching dimensions up to 27 inches. Michelson interferometry and piezoelectric pinducers were normally used as sensors with extensive studies carried out separately to explore various noncontacting optical techniques, particularly speckle interferometry. Wavelength (frequency) was typically determined along with propagation distances. Both spot and line focusing of the Q-pulsed ruby laser was employed using convex and cylindrical lenses, respectively. Tests were conducted to study both propagation of body and surface waves.

Laser Generated Ultrasonics Using Rough Metal Surfaces

Field application taking advantage of laser generated ultrasonics will require suitable ultrasonic wave generation on rough surfaces such as found with remelt ingots and as-cast surfaces where roughness can exceed 1 mm. Considerable effort was expended to evaluate laser ultrasonics in samples having rough to extremely rough surfaces as obtained from industry. Various optical, noncontacting, sensing means were studied including Michelson and speckle interferometry. These require a specular or reasonably smooth surfaces to give good signal to noise output and are tedious to set up. As a contacting alternative sensor, piezoelectric contact transducers called "pinducers" were studied and appear adaptable to rough surfaces and in-the-field measurements. Test results follow for individual studies completed to date.

Laser Induced Pulse Shape

The shape of the pressure pulse induced by laser deposition was studied by using a shock wave piezoelectric transducer with a 1/4" aluminum plate. This arrangement is capable of recording the actual time history of the ultrasonic pressure pulse as it is initiated by surface ablation. With propagation, the pulse begins to break up due to many influences including edge effects, grain structure, voids and inclusions, interaction with reflected waves, etc. The results of this simple test are shown in Fig. 3 and illustrate the clean, smooth shape of the initial disturbance.

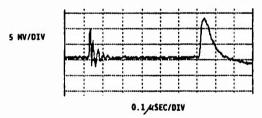
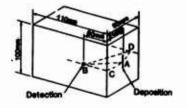


Figure 3 - Initial shape of laser induced stress pulse.

Simultaneous Generation of Longitudinal, Shear and Surface Waves

An experiment conducted on an aluminum block showed that a line deposition source produced clear ultrasonic signals travelling at longitudinal, shear, and surface (Rayleigh) wave velocities. The results of this experiment are shown in Fig. 4 where the line deposition



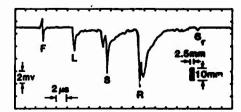
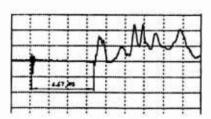


Figure 4 - Laser Induced Ultrasonics in aluminum block.

and the Michelson interferometer sensing spot are on adjacent faces of the block. The trace shows the fiducial F at the time of laser firing followed by clear signal arrivals for the longitudinal wave L and the shear wave S travelling from A to B, for the surface wave S travelling across the corner from A to C to B, and a reflected shear wave S_T travelling from A to D and reflecting to D.

Laser Induced Ultrasonics in Smooth Surface Titanium Blocks and Rods

Michelson interferometry was used to monitor laser induced ultrasonics in titanium alloy block and long rods with machined surfaces. The longitudinal wave arrival was clearly observed in the block at $6.67~\mu$ sec after the laser firing floucial as shown in Fig. 5. Laser deposition on the end of two titanium alloy rods also produced clear longitudinal signals which are shown in Fig. 6 for one rod.



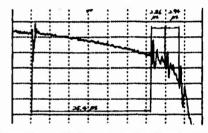


Figure 5 - P-wave in titanium block.

Figure 6 - P-wave induced in titanium rod.

As known from the Hughes method of ultrasonics in rods, the longitudinal signal in the rod is followed by successive signals arriving at times related to the shear wave velocity in the material. This information is sufficient to evaluate the elastic constants of the material which was done for each titanium rod using laser ultrasonics and conventional ultrasonics. Results compared favorably with typical published values (see Table 1).

Table I Elastic constants of titanium evaluated by laser ultrasonics, conventional ultrasonics, and compared with published values.

SPECIMEN		LASER	CONV.	PUBLISHED
RCD #1	E	15.77 Mat	15.54 Mei	15-17 Mat
	ע	0.327	0.347	0.33
ROD #2	E	16.04 Mei	17.34 Mai	15-17 Mai
		0.311	0.319	0.33

Laser Ultrasonics Induced in rough Surfaces

Laser induced ultrasonic pulses were studied using as-cast surfaces from a titanium billet about 4 inches in diameter and a 56 lb remelt segment of zirconium. The titanium billet surface was reasonably smooth but the zirconium had extremely rough surfaces in some locations. Measurements of laser-induced ultrasonic pulses was monitored in both specimens using a piezoelectric pinducer in contact with the rough surface. A drop of oil was applied for couplant. While stronger signals were obtained in the titanium, clear arrival and reflection from the far surface of the dilatational wave was found in both samples.

The pitch-catch approach was used and in some cases it was possible to also detect arrivals of shear and surface (Rayleigh) waves, especially in the titanium with its smoother surface. Measurable signals were propagated up to 5 inches in zirconium and over 20 inches in titanium. A raw data trace is shown in Fig. 7 for laser induced ultrasonics traveling across

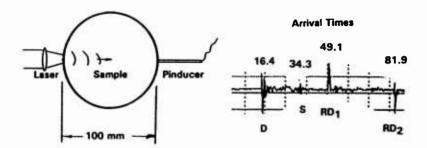


Figure 7 - Laser ultrasonics induced in 4-inch diameter titanium billet.

the 4 inch diameter of the titanium billet. The successive signals show the first arrival of the dilatation (compressive) pulse (D), a small shear wave signal (S), a strong reflected dilatation (RD_1), and a strong second reflection (RD_2) where the disturbance has now traveled five diameters or about 20 inches. Times are given in microseconds.

The piezoelectric pinducer, while a contacting transducer, shows promise for field application. Its small diameter, less than 0.1 inch, makes its use with rough surfaces more feasible than conventional ultrasonic transducers and sensitivity is about the same. Good signals were achieved with minimal attention to alignment of the pinducer to the surface and to coupling.

Use of Piezoelectric Pinducer Sensor with Rough Surface

The piezoelectric pin transducer (or pinducer) as available off-the-shelf from Valpey-Fisher, was tested as an alternative to the Michelson interferometer which seems to require moderately smooth surfaces for adequate signal to noise ratio. The outside diameter of the pinducer is about 5mm with a 2 mm diameter, 1 MHz piezoelectric crystal. The small diameter permits its use with fairly rough surfaces when a couplant is used. To test the pinducer, a 50 mm diameter aluminum disk with smooth sides was used with pulsed laser deposition on one side and pinducer sensing on the opposite side.

Many tests showed the pinducer to give strong, repeatable signals. To check a worse case application, a small gap (0.2-0.4mm) between the pinducer and specimen was intentionally set and couplant was applied. The signal was somewhat weaker than for good contact but signals were still clear enough for the accurate determination of wave arrival time. Without couplant, in any case, the signal was very weak and unacceptable. When couplant is used, the pinducer appears to be a suitable sensor for even very rough and curved surfaces.

Pulse-Echo Approach Using Pinducer and Digital Signal Processing

Effective ultrasonic NDT often employs the pitch-echo method in which the wave generation and detection are done on the same surface of specimen. In this approach, the flaw depth from the surface can be calculated using the known speed of wave propagation and the flight time of the wave reflected from the flaw. In Fig. 8, the schematic diagram is shown of a pulse-echo test using laser ultrasonics and the pinducer sensor. An artificial flaw, consisting of a threaded screw hole of 5 mm diameter, is located 12.4 mm below the surface. The laser was focused to a surface point of about 1-2 mm diameter by an optical lens at the center line of the artificial flaw. The horizontal distance of the pinducer from the flaw center line was varied for each test. When the pinducer was located 5mm from the laser beam, the reflected dilatational wave was found to have higher frequency content compared with the much stronger, superposed surface wave and could be easily detected in spite of its small amplitude. Following the surface wave were many reflected waves and noise.

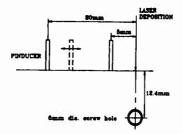


Figure 8 - Schematic for pulse-echo testing using pinducer.

Wave signals in the time domain are often noisy and superposed leading to difficulties in detecting reflected signals from a flaw. Spectrum analysis can provide useful information about the frequency characteristic of the obtained signal. Also, the desired wave can be enhanced by filtering noise and undesired frequency components. A digital filtering program with low, high, and band pass filtering capability was developed for this purpose. If a wave reflected from flaw has a specific frequency, band pass filtering could provide a powerful tool for flaw detection. Figure 9 shows an example of band pass filtering of the signal for the configuration shown in Figure 8 where the pinducer is spaced 5 mm from the laser deposition area. The high frequency content of the flaw-reflected dilatation is enhanced while the lower frequency surface waves have been filtered out.

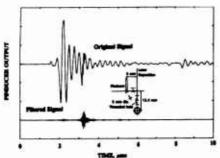


Figure 9 - Original signal with filtered signal enhancing reflected wave.

Laser Ultrasonic Generation in Remelt Zirconium Surface

Figure 10 shows test schematic for 57 lb section of zirconium remelt with the original rough surface and a machined portion. This test was conducted to determine effect of a very rough

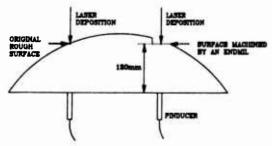


Figure 10 - Schematic of zirconium segment sample having original, rough and machined surfaces for laser deposition.

metal surface on ultrasonic generation. The laser deposition was focused to about 1 mm diameter to get sharper, stronger signals. A comparison of the signals from laser deposition on the original remelt and the machined surfaces showed very little difference. The degree of surface roughness, however, was found to change significantly along the surface. In the extreme case, voids just under the surface prevented generation of ultrasonic waves. Therefore, such surfaces would not be amenable to ultrasonic testing by any means.

CONCLUSIONS

This study has shown that ultrasonic waves suitable for non-destructive evaluation can be conveniently generated in rough metal surfaces common to the Oregon metals industry. Compressive dilatational, shear, and surface waves were all clearly induced. While laser deposition conditions can be varied to emphasize each mode, digital filtering appears to be necessary to separate out the desired information. Michelson interferometry offers noncontact sensing of ultrasonic displacements but does not appear suitable for field application due to stringent requirements on the surface condition. Speckle interferometry shows greater promise but signal-to-noise output needs to be enhanced. While requiring contact, piezoelectric "pinducers" look very promising for convenient field application with their high signal sensitivity and very small contact area.

References

- 1. Calder, C. A. and Wilcox, W. W., "Noncontact Material Testing Using Laser Energy Deposition and Interferometry," <u>Materials Evaluations</u>, 38 (1980), 86-92.
- 2. Calder, C. A. and Wilcox, W. W., "Noncontact Measurement of the Elastic Constants of Plutonium at Elevated Temperatures," <u>J. of Nuclear Materials</u>, 87 (1981), 126-136.
- 3. Calder, C. A. and Wilcox, W. W., "High Temperature Noncontact Material Testing," Characterization of Materials for Service at Elevated Temperatures, ASME Series MPC-7, (1978), 169-181.
- 4. Calder, C. A. and Cornell, R. H., "Dynamic Response of a Thin Disk Subjected to a Thermal Pulse," Experimental Mechanics, 27 (1987), 352-358.
- 5. Scruby, C. B., et. al., "Quantitative Studies of Thermally-Generated Elastic Waves in Laser-Irradiated Metals," J. Applied Physics, 51 (1980), 6210-6216.
- 6. Hutchins, D. A., et. al., "Laser Generation of Longitudinal and Shear Pulses in Metals," Proc. of the Inst. of Acoustics, (1980), 281-285.
- 7. Hutchins, D. A., et. al., Directivity Patterns of Laser-Generated Ultrasound in Aluminum," <u>Journal of Acoustical Society of America</u>, 70 (1982), 1362-1369.
- 8. Aindow, A. M., et. al., "Laser-Based Nondestructive Testing Techniques for the Ultrasonic Characterisation of Sub-Surface Flaws," NDT International, 17 (1984), 329-335.
- 9. Aindow, A. M., et. al., The Physics of Laser-Generated Surface Acoustic Waves in Metals," <u>Quantum Electronics and Electro-Optics</u>, (1983), 427-430.
- 10. Sarrafzadeh, A. and Duke, J. C., "Small In-Plane/Out-of-Plane Ultrasonic Displacement Measurement Using Laser Speckle Interferometry," <u>Experimental Techniques</u>, 10 (1986), 427-430.

- 11. Yang, et al., "Optical Fiber Phased Array Generation of Ultrasound for Non-Destructive Evaluation of Ceramic Materials," VII International Congress on Experimental Mechanics, Las Vegas, June 1992.
- 12. Machiraju, P. H., Gien, P. H., and Burger, C. P., "A Nonlinear Study of Laser Heating for NDE, VII International Congress on Experimental Mechanics, Las Vegas, June 1992.
- 13. Wagner, J. W., et al., "Modulated Laser Array Sources for Generation of Narrowband and Directed Ultrasound," J. Nondestructive Evaluation, 9 (1990), 263-270.
- 14. Wagner, J. W., et al., "Optical Detection of Ultrasound," Physical Acoustics 19 (1990), 201-266.
- 15. Burger, C. P., et al., "Laser Excitation Through Fiber Optics for NDE," L. Nondestructive Evaluation 6 (1987) 57-64.
- 16. Burger, C. P., et al., "The Use of Fiber Optic Interferometry to Sense Ultrasonic Waves," ISA Transactions, 28 (1989), 51-55.
- 17. Dewhurst, R. J., et al., "Generation of Short Acoustic Pulses from an energetic Picosecond Laser," <u>Ultrasonics</u>, 27 (1989), 262-269.
- 18. Dewhurst, R. J., et al., "High Power Optical Fibre Delivery System for the Laser Generation of Ultrasound," <u>Ultrasonics</u>, 26 (1988), 307-310.
- 19. Monchalin, J. P., "Optical Detection of Ultrasound," IEEE Trans. on Ultrasonics, V. UFFC-33, #5, Sept. 1985.
- 20. Monchalin, J. P., Heon, R., "Laser Ultrasonic Generation and Optical Detection with a Confocal Fabry-Perot Interferometer," Materials Evaluation, V. 44, pp 1231-1237, 1986.

ULTRASONIC NOISE AND ITS INFLUENCE ON FLAW DETECTABILITY IN

AIRCRAFT ENGINE ALLOYS

R. B. Thompson, J. H. Rose, F. J. Margetan, and Y. K. H. Han

Center for Nondestructive Evaluation Iowa State University, Ames, Iowa 50011

Abstract

Recent efforts to develop a quantitative relationship between backscattered ultrasonic noise, the parameters of an ultrasonic measurement system and the microstructure of a material are reported. Included is the derivation of a general model and its reduction to computation for the absolute level of the noise signals. Experimental tests of the model's ability to predict (1) the absolute signal levels in alloys of simple microstructure and (2) the general dependence of the signals on measurement parameters in alloys of more complex microstructure are presented. Included is a discussion of the use of the model to predict the detectability of small flaws such as hard-alpha inclusions.

Introduction

Ultrasonic backscattering noise, associated with reflections from microstructural inhomogeneities, can impose a fundamental limitation on the ability to detect small flaws in structural alloys. This problem is of particular importance in commercial titanium alloys, since (1) the two-phase structure can lead to noise that is both large and highly anisotropic and (2) some important classes of defects, e.g., hard-alpha inclusions, have very weak reflectivities. However, there does not presently exist a quantitative understanding of the relationship of the microstructure to the noise. Such knowledge would be of interest in both predicting the detectability of flaws in components with particular microstructures and in designing microstructures which would minimize that noise. This paper summarizes recent progress in the development of a theory that would predict these noise relationships and presents an example of its use in assessing flaw detectability.

The Noise Model

A model has been developed which predicts the rms noise level in terms of a material figure-of-merit (FOM), which is uniquely determined by the microstructure of an alloy. The noise model has two parts, one which relates the microstructure to the FOM and one which relates the FOM to the noise signals that would be observed in the laboratory with a particular measurement system. Models for each are described below.

A phenomenological model has been developed to predict the backscattered noise level for tone burst measurements in polycrystals [1,2]. This independent scattering model (ISM) assumes that the power scattered from individual grains can be added to determine the total backscattered power, i.e. the scattering is assumed to be incoherent. A measurement model [3] is utilized to quantify the relative contributions of the parameters of the measurement system and of the microstructure. The result is the following relationship for the backscattered noise seen at time t in a pulse-echo, tone-burst immersion experiment:

Titanium '92 Science and Technology Edited by F.H. Froes and I. Caplan The Minerals, Metals & Materials Society, 1993

$$N(t) = \sqrt{n} |\overline{A}| \frac{\sqrt{2} T_{\bullet|\rho_1 \nu_1}^2 e^{-2\alpha_{\bullet}(z_{\infty} - z_{\infty})}}{R_{\infty} \alpha^2 \rho_{\bullet} \nu_{\bullet} D k_1}$$

$$\left[\int \int \int |C^4| |\frac{E(t - t_o)}{E_{-\alpha_{\infty}}}|^2 e^{-4\alpha_1 z} dx dy dz \right]^{1/2}$$
(1)

Here N(t) is the rms backscattered noise (averaged over transducer location above the specimen), normalized by the amplitude of a front surface reference signal. n is the number of grains per cubic centimeter and $|\overline{A}|$ is the rms average scattering amplitude for backscatter from a single grain at the inspection frequency (A will be defined in more detail below). ρ , ν , α and k are respectively density, velocity, attenuation, and wave number, with subscript "o" referring to water and "1" referring to solid; T_{ol} and R_{oo} are liquid-solid transmission and reflection coefficients, respectively, α is the transducer radius, α is a diffraction coefficient (related to beam spread) in the reference experiment, and α is a normalized beam displacement amplitude. For the front-surface reference signal, α is the envelope of the tone burst, and has maximum amplitude α is a function of depth within the solid, and represents the time delay between the reference signal and the noise signal scattered from a grain at depth α .

Equation (1) contains two factors. The microstructure is found to be characterized by a figure-of-merit (FOM) given, for a single-phased microstructure, by the quantity $n^{1/2} \mid \overline{A} \mid$, where $\mid \overline{A} \mid$ is the rms scattering amplitude of a grain embedded in an effective medium. The scattering amplitude, A, is a fundamental quantity in elastic wave scattering theory; it relates the amplitude of a spherically scattered wave to the properties of a discontinuity, which is assumed to be illuminated by a plane wave of unit amplitude [4]. When the rms average of the scattering amplitude is evaluated for single-phase microstructures based on a related but more formally rigorous model valid only for plane waves, one finds that for hexagonal crystallites [5].

$$(F.O.M) = \frac{2\pi^{3/2} f^2}{\sqrt{3} v_1^2 (\lambda_0 + 2\mu_0)} \sqrt{\frac{\langle V^2 \rangle F_1}{\langle V \rangle}},$$
 (2)

where

$$F_1 = (192c_{11}^2 - 128c_{11}c_{13} + 48c_{13}^2 - 256c_{11}c_{33} + 32c_{13}c_{33} + 112c_{33}^2 - 256c_{11}c_{44} + 192c_{13}c_{44} + 64c_{33}c_{44} + 192c_{44}^2)/1575$$

with c_{ij} being an element of the elastic stiffness matrix of the crystallites. The same expression holds for the case of cubic symmetry, with c_{13} = c_{12} , and c_{33} = c_{11} . Above, V denotes the volume of a scatterer, and <...> denotes the ensemble average. The frequency is denoted by f, while v_1 , λ_0 and μ_0 are the longitudinal wave velocity and the two Lame parameters of the effective medium that is obtained from (the density and) the Voigt average of the elastic constants. It is thus possible to directly predict the FOM given the metallographic determination of the grain size distribution and knowledge of the single crystal elastic constants of the material, which can often be found in the literature.

The remaining factor of Eq. (1), with the exception of the attenuation constant α_1 , is essentially independent of microstructure and depends on the details of the measurement system. The primary dependence is on the beam pattern of the transducer which enters through the factor of C^4 in the integrand. This is computed using the Gauss-Hermite beam model [6,7].

Experimental Validation

The ability of the model to predict absolute noise levels for fine-grained specimens [2] is demonstrated in Figure 1. In the top portion of that figure, we display five rms noise functions observed in a single Ti-6% Al-2% Sn-4% Zn-6% Mo specimen. Five experimental trials were conducted, each using a different transducer excited with a 1- µsec duration 15-MHz tone-burst. Three of the transducers were focussed and two were planar. In the bottom portion of Figure 1 we display the rms noise functions predicted by the ISM for the five experimental trials. (The model results assume a value of 0.06 cm-1/2 for the specimen's FOM at 15 MHz, with the value being chosen to give best fit). The overall level of agreement between the measured and predicted noise levels in Figure 1 is striking.

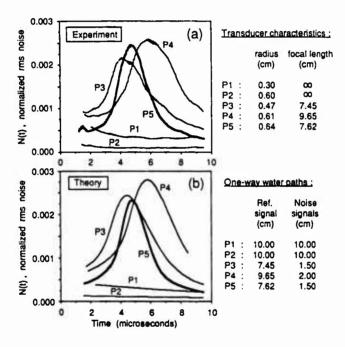


Figure 1. Measured (a) and predicted (b) normalized rms grain noise curves for one Ti-6246 specimen. Five experimental trials were performed using five different transducers.

For a given specimen, the FOM can be deduced from an experimental N(t) curve by dividing the observed noise by model values of those factors which lie to the right of $\sqrt{n} \mid \overline{A} \mid$ in Eq. (1). Since the FOM depends only upon the microstructure of the specimen, the quotient should be independent of time, and independent of the particulars of the measurement system. In Figure 2, we display the FOM values for the Ti-6246 specimen, deduced from the measured noise data of Figure 1. The scatter in the deduced FOM values is seen to be dramatically less than the variations in the raw noise curves, suggesting that, to first order, the ISM is correct and the FOM is a material property. It should be noted, however, that in strongly attenuating samples the fit is not as good, presumably due to multiple scattering effects. Further work is required to complete our understanding of such cases.

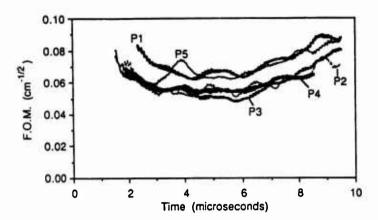


Figure 2. FOM at 15 MHz for the Ti-6246 specimen of Figure 1. The FOM has been inferred from the noise data by using the ISM (Eq. 1) to remove the influence of the measurement apparatus.

Given this direct measurement of the FOM, the next step in model validation is to compare the ultrasonically determined values to values obtained independently. For this comparison, we have chosen to make measurements on samples of randomly oriented, single-phased, equiaxed microstructures. These samples include a specimen of alpha-titanium produced using powder metallurgical techniques [8], a sample of 304 cast stainless steel, and a sample of commercially pure copper. For each of these samples, the average grain size was determined by standard metallographic analysis.

Table I presents the results of a comparison of the FOM values determined by ultrasonic noise measurements and by metallographic analysis [9]. The fourth column gives the FOM as predicted from Eq. (2), while the fifth column presents the value inferred from the ultrasonic experiments and Eq. (1). Where a range of values is indicated for the metallographic FOM, this range is a result of the uncertainty in the mean grain size inferred

Table I. Comparison of FOM Values Obtained from Ultrasonic Experiment and Metallographic Analysis.

Material	Frequency (MHZ)	Grain Diameter (Microns)	Metallographic FOM (cm ^{-1/2})	Ultrasonic FOM (cm ^{-1/2})
o-Titanium	15	64 - 112	0.021 - 0.048	0.035 - 0.042
304-Stainless	5	~ 100	~0.021	0.032 - 0.038
Copper	5	150 - 300	0.044 - 0.124	0.06 - 0.08

from micrographs. The range of values for the ultrasonically determined FOM arises from the fact that, in practice, the deduced FOM is weakly dependent on the time (or depth) at which the rms noise data is analyzed. Given these variabilities, the agreement in Table I is believed to be quite good, particularly in light of the fact that there are no adjustable parameters involved.

Although requiring more extensive validation, these results suggest that it is possible to predict the FOM for simple microstructures from first principles.

The next step is to consider the two-phased alloys that are used in actual engines. The theory is not presently available to predict the FOM's from first principles. However, some ultrasonic measurements of these parameters have been performed for commercial alloys with very interesting results. The particular set of samples studied in detail were fabricated from Ti-6% Al-2% Sn-4% Zr-6% Mo as part of an Air Force manufacturing technology program [10]. The starting point was VAR melted material, processed to an equiaxed alpha-beta microstructure at 6-inch diameter billet. Further heat treatment utilized to modify the microstructure is summarized in Table II. Note that the beta transus for this alloy is 1775° F, so that the first 3 samples were annealed below the beta transus while the fourth was annealed above the beta transus.

Table II. Further Heat Treatment of Ti-6246 Specimens.

Specimen	Anneal Temp.	Anneal Time	Cooling Method		
A1	16 7 0°F	1 Hr.	Air Cool		
A2	1745°F	1 Hr.	Air Cool		
B2	1745°F	8 Hr.	Water Quench		
C 1	1 795°F	1 Hr.	Air Cool		
	(Bet	a transus = 1775°F)			

Backscattered grain noise measurements at 15 MHz were made through three orthogonal faces of each specimen, and the noise data for each propagation direction was analyzed to extract the ultrasonic FOM [2]. The results are summarized in Figure 3 [9]. It is interesting to note that the sample processed above the beta transus had similar FOM values in each direction, while those processed below the beta transus exhibited considerable anisotropy, with the lowest values being obtained when the ultrasonic waves propagated along the axis of the billet. The origin of this anisotropy has not yet been fully identified. Micrographs indicate that the microstructure in the three orthogonal directions are quite similar, as shown in Figure 4. However, macrographs illustrate considerable anisotropy, with highly elongated regions being the dominant feature. The maximum noise signals occur when these macrostructural elements present the largest area to the ultrasonic beam, as will be discussed in detail in a subsequent publication.

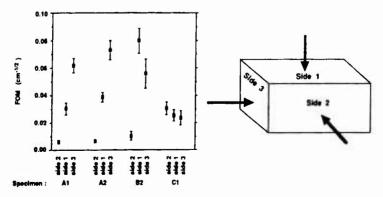


Figure 3. Figure-of-Merit for Grain Noise Severity. Values at 15 MHz for Four Ti-6246 specimens.

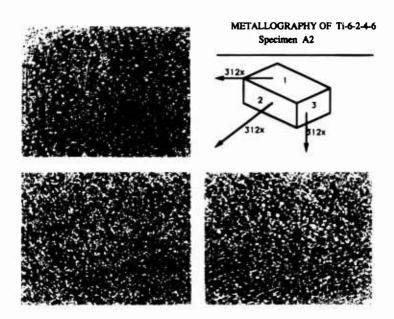


Figure 4. Micrographs of 3 orthogonal faces of Ti-6246 specimen A2.

Flaw Signal Models

Models are also available to predict the strengths of signals reflected from particular flaws, again as influenced by the parameters of the measurement system. Space constraints preclude elaboration on such models. However, it can be noted that important input parameters are the estimates of the size, shape and properties of the flaw. Particular attention has been placed on the case of hard-alpha inclusions [2,11].

Detectability Predictions

With techniques in place to predict the absolute values of the defect signals and the rms noise, it becomes possible to make quantitative predictions of the signal-to-noise ratios, an important step towards the development of a fully engineered detection capability. To illustrate this possibility, a series of calculations has been made [2]. In these simulations, three types of reflectors were compared; a flat crack oriented perpendicular to the beam, a spherical void, and a spherical hard-alpha inclusion. The latter was assumed to have ultrasonic wave speeds that were 8% greater than those of the titanium-alloy matrix and a density that was 1% less. Predictions were made for two materials. One had a FOM of 0.080 cm^{-1/2} at 15 MHz, and the other had a FOM of 0.008 cm^{-1/2}. These values were chosen to approximate the extremes of the FOM values observed in the four Ti-6246 specimens discussed in Fig. 3. In Figure 5, the performances that would be expected using a focussed probe and an unfocussed probe of similar diameter are compared. The 20 dB improvement offered by focussing for this particular case is clearly evident. Note, however, that the beam has been assumed to be focussed on the flaw rather than on the surface of the part, in contrast to a common industrial practice. Figure 6 compares the reflectivity of the three flaw types at 15 MHz. The crack and the pore are seen to produce backscattered signals of comparable amplitude, with the signal from the hypothesized hard-alpha inclusion being lower by about 40dB. Finally, Figure 7 compares the detectability of the hypothesized hard-alpha inclusion in the two materials with differing noise levels when the focussed probe is used. Whereas a 10dB signal-to-noise ratio is reached at a radius of 0.3

mm in the low-noise alloy, it has not been reached for radii as large as 1 cm in the high-noise alloy. Such calculations provide a means of quantitatively predicting the effects of microstructure on flaw detectability.

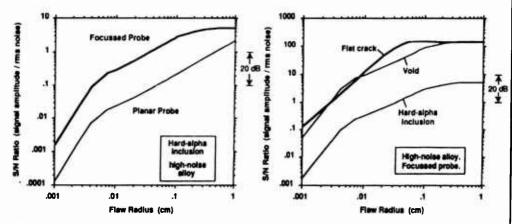


Figure 5. Comparison of detection of hypothetical hard-alpha inclusion using focussed and planar probes in high-noise, Ti-6246 alloy (15 MHz, 1-usecond toneburst). Each transducer has a 0.5" diameter; the focussed probe has a focal length in water of 3".

Figure 6.Comparison of the detection of three classes of inclusions with the focussed probe (15 MHz, 1-usecond toneburst).

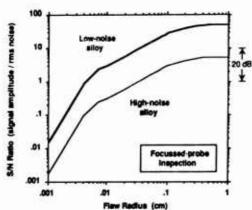


Figure 7. Comparison of the detectability of a hypothetical hard-alpha inclusion in two alloys with differing levels of microstructural noise (15 MHz, 1-usecond toneburst).

Conclusions

In our investigation of backscattered noise, we have defined a figure-of-merit (FOM) for inherent noise severity, and shown how this material property may be extracted from measured noise data. For single-phase metal specimens, including alpha-titanium, we have demonstrated that the extracted FOM is in good agreement with the value expected from a first-principals model calculation. We have also demonstrated that the rms noise level

observed in a given inspection senario can be accurately predicted if the specimen's FOM is known. Finally, we have carried out illustrative calculations of signal-to-noise ratios for hypothesized hard-alpha inclusions in titanium specimens.

Acknowledgement

This work was sponsored by the Center for Advanced Nondestructive Evaluation, operated by the Ames Laboratory, USDOE, for the Air Force Wright Aeronautical Laboratories/Materials Laboratory under Contract No. W-7405-ENG-82 with Iowa State University.

References

- F. J. Margetan, T. A. Gray and R. B. Thompson, "A Technique for Quantitatively Measuring Microstructurally Induced Ultrasonic Noise," <u>Review of Progress in Quantitative Nondestructive Evaluation</u>, Vol. 10B, D. O. Thompson and D. E. Chimenti, Eds. (Plenum Press, N.Y., 1991), pp. 1721-1728.
- 2. F. J. Margetan and R. B. Thompson, "Microstructural Noise in Titanium Alloys and its Influence on the Detectability of Hard-Alpha Inclusions", Review of Progress in Quantitative Nondestructive Evaluation, Vol. 11B, D. O. Thompson and D. E. Chimenti, Eds. (Plenum Press, New York, 1992), pp. 1717-1724.
- R. B. Thompson and T. A. Gray, "A Model Relating Ultrasonic Scattering Measurements Through Liquid-Solid Interfaces to Unbounded Medium Scattering Amplitudes," J. Acoust. Soc. Am. 74, 1279 (1983).
- J. E. Gubernatis, E. Domany, J. A. Krumhansl and Huberman, "The Born Approximation in the Theory of the Scattering of Elastic Waves by Flaws," J. Appl. Phys. 48, 2812 (1977).
- J. H. Rose, "Ultrasonic Backscatter from Microstructure", Review of Progress in <u>Ouantitative Nondestructive Evaluation</u>, Vol. 11B, D. O. Thompson and D. E. Chimenti, Eds. (Plenum Press, New York, 1992), pp. 1677-1684.
- R. B. Thompson and E. F. Lopes, "A Model for the Effects of Aberrations on Retracted Ultrasonic Fields," ibid Vol. 5A, pp. 117-125 (1986).
- B. P. Newberry and R. B. Thompson, "A Paraxial Theory for the Propagation of Ultrasonic Beams in Anisotropic Solids," J. Acoust. Soc. Am., 85, 2290-230 (1989).
- 8. L. J. Brasche, F. J. Margetan and R. B. Thompson, "Sample Preparation Techniques and Material Property Measurements of Hard Alpha Titanium Samples," <u>Review of Progress in Quantitative Nondestructive Evaluation</u>, Vol. 11B, D. O. Thompson and D. E. Chimenti, Eds. (Plenum Press, New York, 1992), pp. 1733-1738.
- R. B. Thompson, F. J. Margetan, Y. K. Han, A. J. Paxson, and C. E. Shomblem, "Relationship of Microstructure to Backscattered Ultrasonic Noise," ibid, pp. 1685-1691.
- Manufacturing Technology for Premium Ouality Titanium Alloys for Gas Turbine Engine Rotating Components, Interim Technical Report No. 4, W. H. Buttrill, G. B. Hunter, E. L. Raymond and C. E. Shamblen, Report R91AEB160, General Electric Aircraft Engines, Engineering Materials Technology Laboratory, 1991.
- R. B. Thompson, F. J. Margetan, J. H. Rose and N. K. Batra, "Effects of Interstitial Oxygen on the Ultrasonic Properties of Titanium Alloys," <u>Review of Progress in</u> <u>Ouantitative Nondestructive Evaluation</u>, Vol. 11B, D. O. Thompson and D. E. Chimenti, Eds., (Plenum, New York, 1992), pp. 1725-1731.

Confirmation Test Methods for Titanium Tube Damage

of Steam Surface Condenser

Motoharu Goto and Yukihiko Itabashi

TOSHIBA CORPORATION
Keihin Product Operations
2-4 Suehiro-cho, Tsurumi
Yokohama, 230 Japan

Abstract

Major damages on titanium condenser tube for power plant are defects occurred in tube manufacturing process, vibration crack, steam-side droplet erosion and others. Visual inspection (VT) and Eddy Current Test (ECT) are frequently applied Non-Destructive Examination (NDE) methods for the damages, but specific VT and ECT methods under the most suitable condition should be selected for each different damage form to obtain more detail information of the tube. This paper introduces special NDE techniques we usually apply and these features to confirm the titanium tube damages of power plant steam condenser.

Introduction

In recent years, thin titanium tubes have been employed for main steam condenser in the most of nuclear and large capacity fossil power plants. The titanium tubes are always exposed in sea water directly, but we have not received a report about any corrosion damage of the inside surface of the tube, because of its good corrosion resistant property.

As conventional damages of titanium tube, some kinds of weld defect generated in the longitudinal welding process and vibration crack in operation have been reported, and some countermeasures for such defects have been considered. Steam side droplet erosion, that was reported for last few years, is occurred on the tube outside surface. This type of erosion was often appeared in the nuclear plants that use copper alloy tube, but the problem on copper alloy tube is not so major until now because copper alloy tube is rather thick than most of the titanium condenser tube. However, steam erosion is serious problem for the titanium tube having very thin wall thickness.

Heavily attacked tubes are sometimes attended with many isolated deep pores, and finally, the damaged tubes may be renewed according to the erosion condition. In this case, many tube holes of support plate should be inspected to detect and remove hazardous notch and rust so as not to injure the new tubes.

Titanium '92 Science and Technology Edited by F.H. Froes and I. Caplan The Minerals, Metals & Materials Society, 1993

Damage Form of Steam Condenser Tube

(1) Defects in the tube manufacturing process

Titanium tubes used for a steam condenser in power plants are normally welded type thin tubes (0.5-0.7mm), and defects occurred in the manufacturing process sometimes give a fatal damage. As such the defects, weld defects (rounded porosity, slug inclusion, piping, incomplete penetration, etc.), material defects and physical defects in the manufacturing process are considered, but most of the tube with such defects are excluded by various inspections. Normally, the tubes are thoroughly inspected by Ultrasonic Test, ECT, VT and air leak test until the end of the manufacturing process, but some kinds of defects have been detected in some condenser tubes (especially, the tube manufactured in the early stage) during a periodic inspection.

Fig.1 shows typical weld and material defects (a porosity in the weld, inclusions in the material, a crack of the inside surface of the weld) detected by BCT of In Service Inspection. However, it is very rare to actually experience such defects, and it is not a major problem on titanium tube.

(2) Vibration crack

Very hard and thin titanium tube for heat exchanger is very good for corrosion, but it is relatively poor at physical damage. In case a continuously vibrated tube by steam flow is hit in a tube hole of support plate, longitudinal vibration cracks may be initiated. The condition for crack initiation changes with a condenser design, a tube design, a tube quality and operating period, especially foreign matter between the tube and the tube hole may accelerate crack initiation.

Fig.2 is an example of vibration crack from outside initiating point under the support plate. The crack has propagated on the peak portion produced at the bending process of titanium plate, and it is considered that bad tube ovality and unusual strong steam flow are the source of the crack initiation. Some vibration crack cases have been reported for the titanium tubes manufactured in the early times. However, today, tube ovality has been greatly improved and condenser design has been modified.

(3) Steam-side erosion 1)-5)

Steam-side droplet erosion, that occurs on the outside surface of condenser tubes after 40,000 - 50,000 hours' operation, is a newly experienced phenomenon. The eroded potions of the tube are restricted to the high speed steam flow zone and the upper side of the most outer tube of bundles. Fig.3 to Fig.5 show typical views of droplet erosion. Fig.3 is a slight droplet erosion case, Fig.4 is a slight droplet erosion but with isolated deep pores case and Fig.5 is a heavily damaged droplet erosion case

Droplet erosion is considered to progress through the following two stages; The first stage (see Fig.3) appears on the titanium tubes impinged by many droplets of steam flow in several years' exposure. The feature of the first stage tube is to show a rough sandblasted like surface. In the second stage (see Fig.4, 5), local and small deep pores are observed on the areas of the first step erosion. The droplet erosion in the second stage looks as if cavitation erosion has occurred on the tube surface, and the average diameter of the pores is about 200 - 300gm.

Inspection Methods for Tube Damages

(1) Visual inspection (VT)

Visual inspection from the outside surface of the tube that is normally not useful for detecting material defects and vibration cracks does not apply to all tube. If a doubtful indication is obtained by BCT, VT may be carried out for the limited area to verify the reason of the indication. In this case, VT from the inside surface of the tube is usually selected, because of its accessibility and cleanliness of inside tube surface.

For detecting droplet erosion, direct VT from the outside surface of the tube and palpation on the surface is a very powerful and realistic method. The indication signal of early stage droplet erosion by conventional BCT is usually very low and difficult to evaluate, but VT can easily find almost all the shape of general droplet erosion area, because the positions of eroded area are restricted to the upper side surface of the outer tubes where the inspectors can access. The eroded area is often distributed in wide area and attended with the surface color change. However, direct VT for the outer faced tube needs a large scaled inspection scaffolding and many inspectors, and it is attended with a danger of inspectors and of causing mechanical tube damage. Visual inspection with robotics and high resolution camera is indicated for visual inspection in the future.

(2) Bddy Current Test (BCT)

Inner probe BCT for titanium condenser tube is a widely used standard NDB method to detect damaged tubes and to evaluate the depth and the propagation rate of the flaw. The tubes are periodically inspected by BCT, but the interval of the inspection is not more frequently than that for copper alloy condenser tube.

Differential type bobbin probe ECT

The inner probe BCT, that can be applied from the water box side (inside the tube), is a popular NDE technique and effective for conventional defect detection of condenser tubes. The defects that can be detected by normal BCT (differential type bobbin probe BCT) are partial defects, such as crack, deposit attack, partial corrosion, etc. However, droplet erosion like defect that covers wide area and has continuously changed thickness along to the axial direction of the tube is difficult detect. The reason is that a differential type bobbin probe has neighboring two co-axial driver/pick-up coils on the same bobbin and the impedance variation between two coils is continuously measured by BCT equipment. The small partial defect affects the impedance of one of the coil, but the defect with continuous thickness change like droplet erosion makes the impedance of two coils change equally.

To detect and evaluate material defects and vibration cracks, multifrequency BCT and data processing by a computer are the most useful. The multi-frequency BCT equipment drives a normal differential bobbin coils with mixed-up two different frequency sine waves (100kHz - 1MHz in the case of thin titanium), and obtained strong support signals caused by the thin wall thickness of the tube are canceled by selecting suitable phase condition of the two frequency waves.

Consequently, vibration cracks caused under the tube hole of the support plate and foreign matter between the tube and the tube hole can be easily detected without disturbance of strong support plate signal.

Absolute type bobbin probe ECT

The absolute probe BCT that was selected from our various examination results has been proved to have good ability to detect droplet erosion. A developed absolute type probe has two special wound coils on separate probe bobbins and the impedance variation between the coil in a test tube and the other coil in a standard tube is measured. The impedance change of the coil in the test tube with droplet erosion is continuously recorded on a strip chart and a digital data recorder as a thickness variation data of the tube wall.

Fig.6 shows the shape of a real droplet erosion sample tube from an operating condenser and the test result of the absolute probe ECT and the conventional differential probe ECT. Such a grade droplet erosion (maximum depth is about half of wall thickness:0.5mm) is clearly indicated on the chart of absolute probe ECT as a wall thickness change, but not on the chart of differential probe ECT. The absolute probe ECT is now applied to all the titanium and the copper alloy condenser tube that is probable to occur droplet erosion, and its effectiveness has been proven by the results of VT and thickness measurement by sectioning at eroded areas.

Rotating probe BCT

Bddy current test with a rotating probe (Fig.7) is effective for detecting fine longitudinal and circumferential cracks and the deep pores that exists in droplet erosion area. Rotating probe BCT technique is that a small BCT probe coil, helically scanned along to the inside surface of the tube, so that sensitivity for fine cracks and small pores is very high (especially for longitudinal crack and erosion). The pick up coils set in rotating probe can be selected from various types of winding coil depending on the defect orientation and type. Fig.8 shows an example of the result of a test piece with various tube wall thickness reduction by the rotating probe BCT. However, inspection cost (probe cost and equipment cost) and inspection time (probe scanning time and data evaluation time) of rotating probe BCT is relatively high, and it has to be used only for precise inspection to investigate limited area damage.

Multi-probe BCT

Multi-probe BCT is a substitutional method for rotating probe BCT. Rotating probe has only one small coil, and probe moving speed is restricted by a helical scanning speed of the coil. The multi-probe, that has normally 6 to 8 or more small pick up coils spaced equally round the circumference, need not rotate the probe itself; it can get up moving speed to the bobbin probe speed. However, the same numbers of data acquisition and recording equipment have to be connected to each coil, and it may take long time to evaluate all coil data.

Inspection in Replacing of Condenser Tube

In case the heavily damaged titanium tube increase, those tubes should be replaced with new tubes instead of plugging. In this case, inside surface of many support plate tube holes should be smooth and free from metallic dust, deep scratches and hazardous notches generated in operation. These defects sometimes affect on the titanium tube surface during re-tubing process and in operation.

(1) Visual inspection for support plate

Fig. 9 shows a schematic figure of a VT equipment to observe the internal

surface of the support plate tube hole. The VT head consists of a high resolution CCD camera, a small mirror and micro halogen lamps. They are all assembled in a stainless tube housing and guide (24mm in outer diameter and 12m in length) to be inserted into the tube hole. Non-conformable holes to the acceptable standard are polished with a special long shaft reamer. Fig.10 shows an intentionally made small spatter detected on the inside surface of a tube hole by CCD camera.

(2) BCT for tube expansion

Renewed titanium condenser tubes are expanded and fixed at both tubesheets after tube-to-tubesheet welding. Tube expansion, that are important to prevent thin tube-to-tubesheet weld from leakage by tube stretching vibration, is inspected by inside micrometer measurement or by palpation. However, the inside diameter measurement is troublesome work for inspectors because of the amount of tubes and the similar tube arrangement, and the palpation of tube inside cannot determine expansion ratio quantitatively.

An expansion ratio checker developed using BCT technology can automatically measure and record each tube expansion ratio data quantitatively and speedy by only inserting a special probe at the end of tube inside. Fig. 11 shows a schematic probe design and a typical result of various expansion ratio tubes by the checker.

(3) BCT for Tube-to-tubesheet weld 6)

Normally, tube-to-tubesheet weld is inspected by liquid penetrant test and hydraulic test just after welding, but the main item of periodic inspection is only VT. Rotating BCT is an easy volumetric inspection method for the titanium tube-to-tubeseet that has smooth welded surface and shallow weld bead thickness; it is applied to mainly partial weld performance evaluation.

The rotating ECT probe consists of three small pencil type coils and a probe rotation mechanism. Each ECT coil is exited by different one or two mixed high frequency current (100kHz - 3MHz). One coil is used for watching the probe lift off, and other two coils are used for detecting the defect in, or on, the weld.

Conclusion

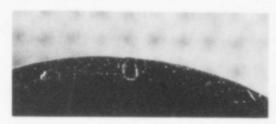
Special NDB techniques adjusted to specific physical defects on thin titanium condenser tube have been developed and applied. Biddy current tests and visual inspection techniques are very powerful weapons to detect and to evaluate the specific defects during periodic inspection. Various analyses of the defects have contributed to the improvement of condenser design. Of course, all titanium condenser has high reliability for leakage by an electro-chemical corrosion of sea water, and today, it is considerable to have the same reliability for physical attacks.

References

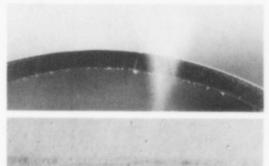
- S.W. Shor and R. Clark, "Titanium Tube Fatigue Failure from Vibration," Condenser Technology Symposium, 1988.
- 2) J.Tavast, "Steam Side Droplet Brosion of Titanium Tubes", Condenser Technology Symposium, 1983.

- 3) K.Schleithoff, and F.Schmitz, "Stainless Steel and Titanium Condenser Tubes Operational Experience and Measures for Refurbishment and Life extension," International Conference "Life Assessment and extension, 1988.
- 4) I.Multer and M.Hedstrom, "Recent Scandinavian Experience of Titanium Condensers," ASMB Joint Power Generation Conference, 1989.
- 5) N.Iwai, T.Ozeki et al., "Steam-side Condenser Tube Brosion by Droplet Impingement," International Joint Power Generation Conference, Oct. 1992
- 6) Y.Itabashi and M.Goto, "Non-destructive Examination for Titanium Tubed Condensers," 6th. World Conference on Titanium, 1988.

(a) Porosity



(b) inside surface crack



(c) inclusions



Fig.1 - Defects in the tube manufacturing process.

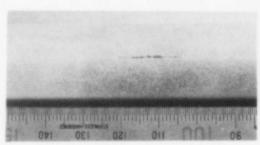


Fig. 2 - Vibration crack.

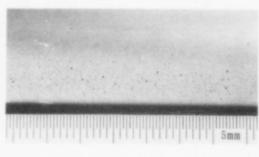


Fig.3 - Droplet erosion (1st. stage).

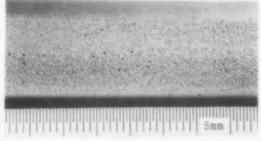


Fig.4 - Droplet erosion (1st. stage with isolated deep pores).





a) Surface view

5mm

(b) Cross sectional view

Fig.5 - Droplet erosion (2nd. stage).

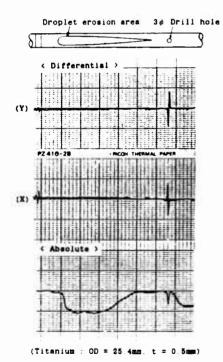


Fig.6 - Result of differential and absolute BCT for droples erosion.

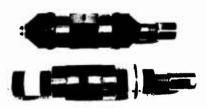
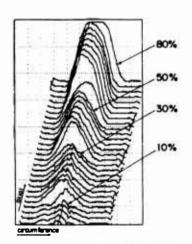


Fig.7 - Rotating ECT probes.



10% 30% 50% 80% reduction

meault of rotating BCT for test piece.

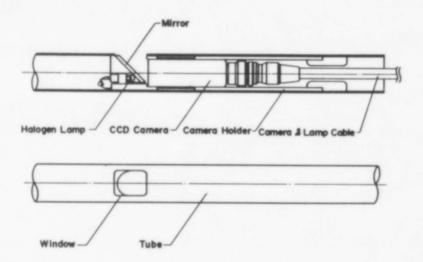


Fig.9 - Visual inspection equipment for tube hole of support plate.

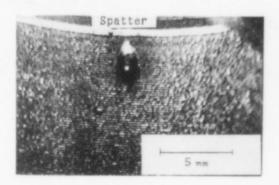


Fig.10 - Example of tube hole inside view by CCD camera.

(Test piece sample : small spatter on the hole)

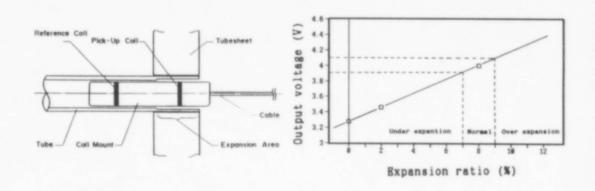


Fig.11 - Schmetic probe design and result of tube expansion test by BCT checker.

ANALYZING HIGH PURITY TITANIUM

H. W. Rosenberg and J. E. Green

The ALTA Group Fombell, Pa. 16123

Abstract

Advances in titanium product purity come only as fast as one's ability to verify that purity on the process level. Currently available analytical means to do that are reviewed. Some strengths and weaknesses of certain tools are outlined. Glow discharge mass spectrometry has become the instrument of choice for certifying metallic impurities in ultra-high purity titanium. Some problems attending chemistry certification at 99.999% metallic purity levels and higher are discussed.

Introduction

Aerospace and industrial applications of titanium are currently and adequately supported by conventional analytical techniques such as optical emission spectroscopy, atomic absorption and the various gas extraction and fusion techniques.

Much of the driving force behind the quest for high purity titanium for electronic applications comes from the need to minimize ohmic heating at the highest levels of circuit integration. Ohmic heating, of course, arises in part from impurities in metal conductors.

No single method analyzes all elements effectively.

Table 1 illustrates typical analytical ranges available in general, on a metal basis, for the various techniques.

Electronic applications require titanium with impurities certified in the range from low parts per million to high parts per trillion. Certain advanced electronic applications now specify less than ten ppm total metallic impurities along with less than 200 ppm total gases. Conventional gas analytical techniques have kept pace and are still adequate.

Titanium '92 Science and Technology Edited by F.H. Froes and J. Caplan The Minerals, Metals & Materials Society, 1993 Table 1 Listing of Techniques by typical detection limits, DL.

DL <= 0.1 - 100 ppm

Atomic absorption / furnace atomic absorption, AA - FAA Conventional quantometer, Quant Direct current plasma, DCP (Becoming obsolete) Inductively coupled plasma, ICP

DL <= 0.01 - 1 ppm Inductively coupled plasma mass spectrometer, ICPMS

DL <= 0.01 - 10 ppb Glow discharge mass spectrometer, GDMS Spark source mass spectrometer, SSMS (Becoming obsolete)

The same is true of AA or ICP for a few specific metallics. For most metallics, however, conventional means have given way to mass spectrometry.

Wet chemical techniques have several advantages, economy being high on the list. There are inherent problems that limit their sensitivities, however. Important examples are the dilutions required and the interferences that arise. Using ultra-pure reagents does not remove the interferences that arise from the reagents themselves.

Nevertheless, wet analytical methods remain quite useful for specific elements and for process control. Wet methods also provide a calibration base for mass spectrometry.

AA, the premier absorption method, is quite useful for the alkalis, alkaline earths and many non-refractory transition metals. Incidental contamination from glassware and reagents is a particular problem in the case of sodium. The non-linear relationship between signal and impurity concentration is a complication to some degree. Molecular background is high for many elements. Use of a furnace instead of a lame enhances sensitivity in many cases. Precision auto samplers with computer data reduction have made FAA a method of choice for many trace analyses. Molecular background for FAA is best removed by Zeeman corrections.

Optical emission spectroscopy via ICP or DCP complements absorption methods in that it does a better job on refractory materials. Emission line intensity is a linear function of impurity concentration over several orders of magnitude, which simplifies standardization. Molecular background exists but can be minimized to a degree by selecting the plasma field to be analyzed. Short and long term stabilities of the instrument are critical features when working near detection limits. Internal standards are helpful in this regard. Frequent calibrations before and after analyses coupled with computer correction for drift are also quite useful. Most instruments will do somewhat better than their manufacturers guarantee. For electronic grade titanium, however, that usually is not enough.

The next step up in sensitivity is provided by coupling a plasma source with a mass spectrometer. Intermediate detection limits are obtained this way. The mass spectrometer is not bothered by optical background of molecular or other origin. However, if the MS section of an ICPMS is a quadrupole, there are numerous isotope interferences that the instrument cannot resolve. In any case, the method still suffers

from the dilution required to take a sample into solution. Nevertheless ICPMS is often the method of choice when dealing with high purity solutions.

Mass spectrometry has two distinct advantages: 1) a solid sample is used so the signal is strong and 2) background is virtually non-existent. Magnetic focusing provides the mass dispersion necessary to remove most but not all isotopic interferences. Molecular ions of titanium combined with argon are known sources of interferences, particularly for Ca, Sc, Rb, Sr and Y. In these cases one has the option of using SSMS with the attendant losses in accuracy and precision. SSMS is inherently less stable than GDMS, usually requires photometric reading of a photographic plate and moreover samples less material. Neither mass spectrometry technique is any better than its calibration. Calibration was a significant problem when GDMS units were first introduced but is now largely history. Another drawback is the very small sample volumes analyzed. Not all samples are both representative and homogeneous.

Using mass spectrometry for product certification is not as straight forward as it might appear. A second aspect of certifying chemistry in ultra-pure materials is that of representative samples. One needs to be able to separate the variances arising from sampling from those of the instrument. That is not always straight forward.

Cross contamination is also a typical problem for commercial laboratories that necessarily must analyze a variety of materials in the course of their work. Counting statistics and source stability are rarely limiting but come into play at the detection limits. Uncertainty owing to counting statistics can be reduced by extending counting time. That comes at a price in both cost and time. It is nevertheless useful in order to sort out the instrumental variance. This may relate to excitation stability for example. Inhomogeneous impurities are manifest by drift. Iron is a particular offender in this regard because it tends to micro segregate during ingot solidification (1).

Certain experience in certifying ultra-high purity titanium is presented in what follows.

Discussion

In most cases, tracing material contamination at ppm levels is straight forward. At ppb levels, the problem is less tractable. Part of the reason for this is that a material can be well within specification for every individual element yet be out of specification in their total. Casual inspection, even control charting, may fail to turn up the cause.

One option is to review the raw data from GDMS and extend counting time if the analyses of interest crowd their detection limits. Another is to repeat the analyses to the point where one can calculate standard errors with confidence. This has the advantage of pointing out any outliers in the data. With these measures it still may not be obvious where the contamination is coming from, especially if only a few lots are available. More sophisticated approaches are called for.

Table 2 presents one approach to this problem. For this illustration, impurity data from 28 heats of high purity titanium were collected and analyzed. Every element analyzed between 10 ppt and 20 ppm in every heat. GDMS data for 28 elements were collected and a correlation matrix was calculated between every element pair as in a factor analysis(2, 3). The original matrix consisted of 378 independent correlations. A type one error of 0.01 was selected for the initial survey. This requires a coefficient to be 0.48 or larger for significance. On a random basis, one would expect perhaps three or four coefficients among 378 correlations to be as large as 0.48. Instead, 24 were found,

Table	2	Correlation Coefficients for 28 Ingots Analyzed by GDMS									
	Al	As	Ca	Cl	Co	Cr	Fe	Li	Mg	Mn	Мо
Al	1	.17	10	.22	02	.65	.34	04	10	.33	03
As	•	1	.13	18	.15	.17	.42	.41	.31	03	15
Ca	•	•	1	.01	.52	.06	.41	08	16	09	25
a	•	•	•	1	08	.48	03	33	24	.42	.16
Co	•	•	•	•	1	.28	.40	13	17	10	.33
Cr	•	•	•	•	•	1	.57	24	09	.53	.17
Fe	•	•		:	:	•	1	13	02	.33	.23
Li	•	•	:	•	•	:	•	1	.85	02	.10
Mg Mn	•	•	•	•	•	•			1	01 1	.07
Mo	•		•	·	•				•		.29 1
IANO	•	•	•	•	•	•	•	•	•	•	•
	Nb	Ni	P	Pb	S	Th	U	V	W	Zn	Zr
A1	01	.02	.04	.05	02	.22	13	08	.7.5	.07	.12
As	.03	.14	.01	.23	10	.59	.01	.29	.04	.42	05
Ca	03	.62	.03	17	13	.16	15	47	.03	.59	05
CI	.04	09	.07	30	.08	09	12	.17	07	20	.13
Co	07	48	.28	20	12	.20	14	32	.11	.32	08
Cr	.10	.13	.31	16	.07	.33	19	16	.29	.06	.27
Fe	.02	.52	.09	16	06	-60	20	38	.23	.64	.42
Li	.12	13	.07	.93	03	.44	<u> 59</u>	.19	.01	.22	21
Mg	.37	16	.26	85	.24	.45	<u>57</u>	.06	14	.21	04
Mn	16	.06	.04	.01	11	.05	12	02	08	02	.32
Mo	.13	06	.03	11	.14	17	13	.06	20	23	.87
	Nb	Ni	P	Pb	S	Th	U	V	W	Zn	Zr
Nb	1	07	.66	.15	.88	. 23	.13	17	13	.14	10
Ni	•	1	01	19	12	.16	21	29	.16	.26	.05
P	•	•	1	.08	.81	. 12	.15	25	04	03	.02
Pb	•	•	•	1	.02	.4	.72	.15	.08	.13	14
S	•	•	•	•	1	.04	14	14	12	05	01
Th	•	•	•	•	•	1	.4	14	.21	.63	07
U	•	•	•	•	•	•	1	01	01	.05	13
V	•	•	•	•	•	•	•	1	12	39	04
w	•	•	•	•	•	•	•	•	1	.12	06
Zn	•	•	•	•	•	•	•	•	•	1	08
Zr	•	•	•	•	•	•	•	•	•	•	1

for an incidence some seven times expectations. Moreover all were positive. If chance alone were operating, about half would be expected to be negative. Only six of the original 28 elements produced insignificant correlations with every other element. They were K, Na, B, Bi, Cu and Si and were not included in Table 2. The pairs reaching significance are shown underlined in bold face. The probability of this being a random result is essentially zero. Of the 207 remaining coefficients in Table 2, 102 were negative, of which two were 0.39 or larger. These features are consistent with random

variation. The 207 non significant pairs in Table 2 were considered to be random. The other 24 created a problem.

In calculating the correlation matrix illustrated in table 2, the analyses for every element analyzed in a series of samples was correlated pairwise with every other element analyzed throughout the series. Each correlation coefficient, r, was calculated by the method given by Walker and Lev (4) using readily available software (3).

Factor analyses are designed to illustrate which variables tend to move in concert and is a technique often used in the social sciences. It is applicable here. For example if it can be shown that Cu and Nickel repeatedly correlate positively then one might suspect that contamination from monel or a similar material might be occurring. Austenitic stainless steel provides a unique finger print as well. Although a complete factor analyses provides additional information, it turned out that the replications were unstable; the matrices alone were all that could be used.

The preliminary conclusion was that at least some impurities rose and fell together. That could be the case if the impurities all entered from the same source. Listing the correlating pairs was helpful in that regard. Table 3 presents the results. The fact that six pairs returned coefficients above 0.81 defies astronomical odds unless an assignable cause could be found. Those pairs that might have natural reasons to occur are shown in bold face. Cr/Fe and Fe/Ni pairs could arise from stainless steel sources but the low Cr/Ni coefficient, while having the correct sign, does not reach significance. Nevertheless stainless steel was an initial suspect. P and S have physico-chemical similarities and are often found together. The same is true of the Mo/Zr, Li/Mg and Co/Ni pairs.

Table 3 Correlating Impurity Pairs in Ultra-High Purity Titanium, all positive.

Correlation	Pairs
0.46 - 0.50	Cl/Cr, Co/Ni
0.51 - 0.55	Ca/Co, Ca/Zn, Cr/Mn, Fe/Ni
0.56 - 0.60	As/Th, Cr/Fe, Fe/Th, Li/U, Mg/U
0.61 - 0.70	Al/Cr, Ca/Ni, Nb/P, Th/Zn
0.71 - 0.80	AVW. Pb/U
Above 0.81	Li/Mg, Li/Pb, Mg/Pb, Mo/Zr, Nb/S, P/S

The only apparent connection between Pb and U is their radioactive pairing in nature. But that hardly explains the high 0.72 correlation. Of the remaining 16 pairs, one might assume that perhaps four could have random origins. The working conclusion was that about 12 pairs are non-random for unknown reasons in this example.

At this point it was possible to find and close some possible points of impurity entries into the process. This positive result, however, still left a mystery. Why were there so many elevated positive correlations without apparent cause?

Similar results were found in repeated analyses using independent GDMS data from the same lab and also from a separate lab on yet a third data base. Further, in each study, negative correlations among the significant coefficients were rare. Moreover, the unexplained pairs in one study rarely appeared in any of the others. It seemed likely that

features of the GDMS analyses were somehow responsible for the unexplainable pairs. This feature brought into question the accuracy and precision of GDMS.

Potential hypotheses were suggested. One was simply that the main ion beams of titanium isotopes making up most of each million counts were not being accurately calibrated relative to certain trace impurities. Each impurity has its own ion excitation efficiency and was a suspected factor. It was suggested that the detection limits, which varied with each individual analysis on a somewhat systematic fashion, contributed to the problem. Removal of results at or near the detection limits for each study removed many of the unexplained pairs while tending to leave the real signatures of Fe, Cr, Ni and other elements with atomic number less than about 40. Still some random excess remained.

That was the situation until about 1989. Since then, the commercial labs have each reduced their excess of positive correlations while agreeing better in blind comparisons. Much of this progress came from improved multiplex procedures dividing the ion beams among the Faraday cup (main titanium beam) and the ion counters seeing the impurity beams. Some progress no doubt came from the additional operator experience and availability of standards. Repeat analyses are no longer a factor of three off. Ten to thirty percent, including sampling variance is more like it.

Clearly, GDMS has come of age as an analytical tool in the ppb range. Yet a residual uncertainty remains.

GDMS and other analyses that rely on discrete quanta or particle counting are limited in their precision by the counts themselves. This uncertainty has to do with the Poisson statistics that describe the 'rare event' arrival times of each individual event representing the trace impurity being analyzed. In Poisson statistics, the standard deviation is the square root of the mean (4).

In the parlance of analytical chemistry, a quantity defined as the 'residual standard deviation', or % RSD, is used to indicate the quality of a given analysis. The % RSD is the standard deviation multiplied by 100 divided by the mean. Table 4 illustrates how this parameter relates to Poisson statistics. The % RSD is very sensitive to counts at the low end, near the detection limit.

Table 4	Relationship between % RSD and signal counts
Counts	% RSD
4	50
25	20
100	10
10000	1

Detection limits in mass spectrometry thus have natural limits relating to the count received from a given impurity.

Already we are in an era where long counts have become necessary to certify certain high purity materials.

GDMS/SSMS techniques can analyze every metallic impurity likely to be present. Mass spectrometry does not yet, however, compete with the common instrumental techniques for most of the gases. So its usefulness is primarily with metals. Even then a situation may arise where GDMS/SSMS is inadequate. An example is the radioactive alpha particle emitters, U and Th. In these cases, any U or Th present tends to segregate to grain boundaries and triple points. Rare earths in general all behave this way. A GDMS analysis, even an extended one, is likely to return values too high or too low depending on the vagaries of impurity segregation and sample erosion in the glow discharge. Alpha emission is undesirable because an alpha particle can change the state of an adjacent memory element in an integrated circuit. Errors of this type have become known as "soft errors." Since it is the alpha activity that produces the problem, it is better to determine the actual alpha decay activity directly from a large sample.

Conclusions

- 1 GDMS has rightly become the analytical method of choice for certifying high purity titanium products.
- 2 Correlation matrices are an effective too! for searching out subtle analytical problems and effects not readily evident in product control charts.
- 3 Certifying ultra-high purity titanium has begun to stretch the ability of mass spectrometry and made long analysis times necessary.

References

- 1 R. E. Adams and H. W. Rosenberg, "A Review of Titanium Solidification", Titanium and Titanium Alloys, Plenum Press, Vol. 1, p 127, 1976.
- 2 L. R. Aiken, Psychological Testing and Assessment, Allyn and Bacon, Boston, 1979, p 150.
- 3 D. Feldman et. al., "Statview SE + Graphics", V1.03, Abacus Concepts, 1988, Application software for the Macintosh Computer.
- 4 H. M. Walker and J Lev, Statistical Inference, Holt, Rinehart and Winston, NY, NY, p 424, 1953.

RADIOAUTOGRAPHY INVESTIGATION OF THE DISTRIBUTION REGULARITIES (CARBON)

IN INGOTS AS WELL AS FORGINGS OF PSEUDO-ALPHA-TITANIUM ALLOYS

E. Karasev, A. Kudrjavtsev, V. Kurapov, V. Tetjukhin, S. Ushkov, V. Urtjev, A. Trubin

Central Research Institute of Structural Materials "Prometey" Sankt-Petersburg, 193167, Russia

Abstract

In order to strengthen pseudo-alpha-titanium alloys a carbon as well as oxygen microalloying are used in the industry. Hence the carbon distribution characteristics of large ingots present significant both scientific and practical interest. We attempted to obtain these characteristics by using radio-active isotopes (carbon-14) method.

Introduction

In the commercial production of the pseudo-alpha titanium alloys the alloying by the carbon in addition to the alloying by the oxygen is applied to increase the tensile properties.

Although the hardening effect of the carbon is somewhat lower as compared to that of the oxygen, the carbon is preterable as it results in the reduction of the ductile properties though the atom size of the carbon is larger than that of the oxygen with the some content of the elements. It is related to the ordered distribution of the carbon atoms in the lattice interstitial sites, of the alpha-Ti, which is partially resulted in the reduction of the lattice damage.

Due to the low solubility of the carbon in the titanium the input of the carbon for alloying is generally limited by 0.1 % (by weight).

To produce the uniform distribution of the interstitials in the ingots they form a part of the composition of the master alloy applied to alloy the titanium alloys. To increase the carbon content in the master alloy the titanium as a carbide building element is added to carbon containing master alloys.

The homogeneity of the carbon content in the titanium alloy ingots is termed either by the homogeneity of the applied carbon containing master alloys or by the processes taking part at the time of the ingot solidification. As the carbon was not applied as an alloying element for the titanium alloys it is very important to study its distribution in the large ingots from practical and scientific view points. However, the applied analytical metho-

Titanium '92 Science and Technology Edited by F.H. Froes and I. Caplan The Minerals, Metals & Materials Society, 1993 ds to determine the carbon content of the master alloys and the titanium alloy ingots do not provide stable results and make difficulties to study the carbon distribution in the macro- and microvolumes of the ingot metal. Because of this, the radioactive isotope method (RIM) characterized by high sensitivity was used in the work.

Investigation Procedure

As an radioactive indicator the carbon isotope-14 with low β -radiation energy and electron fluence in activated metal from about the investigated surface which results in the increase of autoradiographes quality was used. The carbon isotope-14 has a large half-decay time.

The combination of the above facture is faborable for autoradiography applicating the carbon isotope-14.

The laboratory investigations allow Ti establish if the carbon isotope in the form of the titanium carbide (TiC) input is reasonable to avoid the isotope loss during the melting and to control its complete solubility during VAR, as in the carbon containing master alloys the carbon is bound in the form of the titanium carbide with the melting temperature over 3 000°C. In view of the above facts the following procedure for the isotope input is suggested: the weighted amount of the isotope in the form of the mixture of elemental carbon-14 barium carbonate containing the mentioned carbon and the fine titanium powder (1 g for the weighted amount) enclosed in an aluminium foil in the form of the tablets of 16 mm in diameter and 20 mm in height were pressed. To avoid the carbon loss during the vacuum are melting the vacuum arc melting the tablets were heat treated in the evacuated capsule at 1000°C for 10 hours, which resulted in the compound of the radioactive carbon and the titanium pressed in foil in the combination with forming the titanium carbide. The produced tablets of the radioactive compound were input at the time of pressing in each charge portion in the centre of the electrode. The total amount of the radioactive carbon input in the ingot due to safety provision while working with the metal and obtaining the contrast photos, was designed on the base of mean specific activities of the finished metal equal to 0.1 mCi/kg. To activate the ingot of 8 t 850 mCi radioactive carbon were input.

The commercial ingots of Ti-Al-V-Mo-C system activated by the carbon, were produced by vacuum-arc method in accordance with the series procedure through two remelting of the ingot of 1000 mm in diameter. The 0.08 % (by weight) carbon was input in the form of the carbon containing master alloy with 3.5 % carbon.

To investigate the ingot was out by hight on cylindrical billets of 270-300mm in height followed by autogenous cutting of the axial and diametrical templates and machining on a planer.

The autoradiographing of the templates was performed in accordance with MP-155-4-32 methodical recommendations /2/. The exposure time is 25 days. The template macrostructure was established by the chemical etching method followed by full size photography.

The microsections cut out of the templates in accordance to the procedure accepted for the titanium production were microradiographed.

The supplementary specimens were electropolished followed by liquid nuclear emulsion application which has provided the autoradiograph to be made. Light microscope observation of the radiographs of the etched, emulsion coated specimens is difficult as the established microstructure effects the autoradiographic image. Because of this the autoradiography of the etched specimens with the emulsion coating was performed only for the electron microscopy studies.

Autoradiographs were studied by MIM-8 light microscope in transmitted and reflected light with magnification of 50 - 500. The specimens for electron microscopy were cut out of the same microscotions, autoradiograph-replics

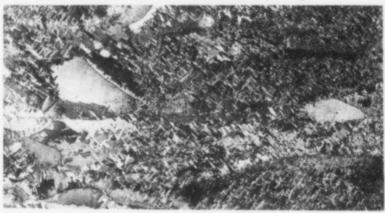
were made. The autoradiographs were studied with magnification of 5000,10000, 15000 and photographed with magnification of 10000.

The effect of procedure heating on the carbon distribution type was studied on the cast and wrought metal in accordance with the above method on the specimens cut out of the templates.

Test Results and Discussion

The developed procedure of carbon isotope-14 input in the metal provides the clear and contract autoradiographs for the full size of axial section of the ingot of 1000 mm in diameter.

The comparison of ingot's macrostructure and radiographs shows that the nature of latter is similar to the of macrostructure (Figure 1).



a)



b)

Figure 1 The macrostructural fragments (a) and autoradiographs (b) of the same portion of the diameter section of the ingots of 1000 mm in diameter (columnar crystal zone).

Autoradiographs do not show the development of the siquation zone of the carbon in the ingot volume. The socalized accumulation of the carbon in the form of inclusions also doesn't exist, which indicates the complete dissolution of the titanium carbide in combination with the radioactive carbon. Carbon isotope decorates each cast macrograin along it's perimeter and is oriented by distributed in it. The orientation of the observed ranges indicates that they are arranged along certain crystallographic planes. This vectors

rifies that the carbon redistribution in the grain volume occurs with the ingot crystallization in the beta-alpha transformation temperature range and conforms Bockstein et al. works /3/.

The arrangement of the carbon along boundaries of the cast grain can be due to their structure. The grain boundary being a hereditary biography of cast metal structure are characterized by lower density as compared to the parent metal and serves as "sinks" where the carbon is detected to decreasing the free energy of the system. In addition the higher quantity of dislocations on the grain boundary can result in interaction of the dislocations interstitials, i.e. carbon.

However, the autoradiographs doesn't allow to evaluate the intercrystalline distribution of the carbon easy, i.e. either it arranges along the subgrains or is drown to a phase; in other words, the macroautoradiographic method doesn't provide the required resolution to study microhexerogeniety. Because of this the microheterogeniety of the carbon distribution was studied. The appreciable increase of autoradiographic resolution was obtained due to the application of fine grain liquid nuclear emulsions, which allows to study the carbon distribution on microsections of the cast structure and wrought metal.

Figure 2 shows the microstructure (a) and autoradiograph (b) of the cast me-

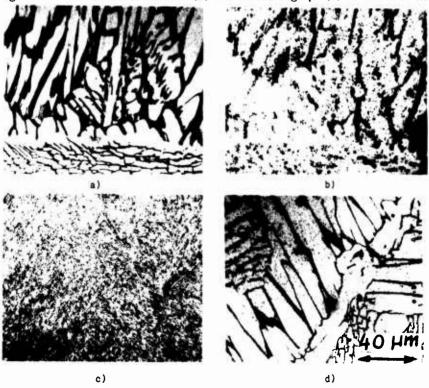


Figure 2 The microstructural fragments (a) and the autoradiographs of specimens of cast metal

b - original state

c - water quenching from 1200°C

d - slow furnace cooling after quenching.

tal specimens with magnification of 500. The carbon is arranged in the grains of the primary alpha-phase and to a great extent in the section of the decomposed beta-phase.

The investigation of the carbon distribution in the heat treated by different methods cast metal verifies the observed type of the carbon redistribution in the original metal. The heating and exposure of the metal at 1200 result in the uniform distribution of the carbon through section billet which as Figure 2 c shows is fixed by the following quenching. At the same time with the slow furnace cooling of the prequenched specimens from range the geterogenous distribution of the carbon similar to that of the cast metal without supple meutary heat treatment with boundary enrichment of individual constituents of the structure (alpha-plates, colony of unidirected, alpha-plates, beta-grain boundary) is observed. Figure 2 d indicates that alpha-phase plates are purified of the carbon, which with slow cooling process is diffusing to the boundaries, decorating them. The redistribution of the carbon may be to its solubility in alpha-phase with temperature variation. Thus , at 900, 800 and 600°C the carbon solubility amounts to 0.48%; 0.27% and 0.12% respectively /4/. Here, with the progressive solubility reduction, the diffusion process results in the carbon diffusion from the supersaturated alpha-phase to the interphase boundaries. Hence, the decorating nature of the carbon establishes the metal structure as chemical etching does.

The above mentioned relationships of the carbon redistribution in the cast metal were verified, completely on the forged rods, heat treated by different methods. The prequenched out of beta-range (1200°C) cast billets have been forged at 1100°C (exposure of 1.5 h) to square rods with side length of 16 mm and heat treated in accordance to the shidules:

1) 1000°C, 1 h, water quenching; 2) 1000°C, 1 h, furnace cooling.

Figure 3 b,d shows that in the quenched material the carbon is uniformly distributed across rod section. The slow furnace cooling results in the enrichment of the boundaries of the individual constituents, similar to the cast metal, decorating them on autoradiographs, Figure 3 c,e.

The performed electronic-microscopic investigation of the autoradiographs-replics, partially represented on Figure 4, verify the preferentiall redistribution of the carbon along the interphase boundaries and also on the subboundaries of alpha-plates and the individual structural fragments with different orientation. The observed form of the accumulations is related not to the carbon but to the large magnification (10000 times), at which the raughness of the constituents of the emulsion itself is appeared.

Conclusion

The carbon alloying of the commercial ingots of the pseudo-alpha titanium alloys amounting to 0.1 % doesn't result in appreciable evolution of microliquation process in carbon distribution. At the same time the microatuo-graphs allow to defect the microheterogeniety of carbon distribution along the interphase boundaries of the individual structural constituents: alphaplates unidirected colonies of alpha-plates, beta-grain boundaries. With slow cooling the alpha-phase is appreciably released of the carbon. Thus, the metal hardening due to carbon input can't be related to the common solid solution mechanism of the hardening only. The carbon concentration increase along the boundaries and subboundaries indicates the preterential effect of this carbon redistribution on metal hardening. The polid continuous after quenching and its sensitivity to the directed redistribution with slow cooling indicates the possible heat treatment influence on the metal properties of the pseudo-alpha alloys, alloyed by the carbon.

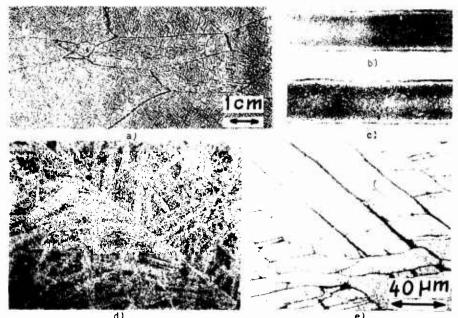


Figure 3 The autoradiographs of the original cast metal (a) and forged specimens heat treated as follows:

b, d = 1000°C, 1 h, water quenching;
c, e = 1000°C, 1 h, furnace cooling

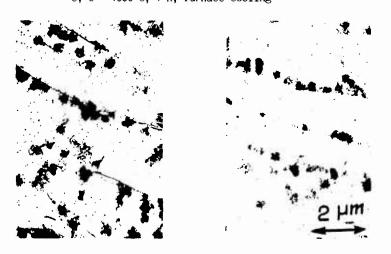


Figure 4 The fragments of the electronmicroscopic autoradiographs of the cast metal, carbon, isotope-14.

References

- 1. B.A.Kolatsev, V.A.Livanov, A.A.Buchanova, <u>Mechanical Properties of the Titanium and Its Alloys</u>, (Russia, Moscow, Metallurgia, 1974),54.
- 2. "The Preparation and the Input in the Titanium Alloy, Ingots of the Radioactive Indicators INvestigation an Inhomogeniety of the Composition", Metodicheskie recomendatsii (MP 155-4-82, Moscow, VILS, 1982).
- 3. C.Z.Bockstein, The Diffusion Processes Structural Flaws and Material Properties, (Russia, Moscow, 1972).
- 4. I.I.Kornilov, Titanium Ed.Nauka, (Russia, Moscow, 1975),205.

ULTRASONIC INSPECTION OF TITANIUM BILLETS

J. Vinot, C. Moisson and Y. Combres*

CEZUS
Av. Paul Girod
73400 Ugine Cedex France
* Centre de Recherches de CEZUS
BP 33
73400 Ugine Cedex France

Abstract

The safety of air transportation partly lies in Non Destructive Inspection. From the titanium production to final manufactured parts exploitation, the use of defect free materials has to be guaranteed. In this scope, CEZUS has run research and development on Ultrasonic Inspection of large diameter forged bars. The paper will show how, progressively, improvements of methods led to the detection of flat bottom holes, the diameter of which decreasing from 3/64" (1.2 mm) to 2/64" (0.8 mm) for the same inspected billet. The improvement of the conventional procedure was to increase the signal to noise ratio in the case of $\alpha+\beta$ type titanium alloys, which exhibit a rather high noise level. This has been obtained perfecting methodology and means in collaboration with FRAMATOME. With these new techniques, the signal to noise ratio is twice larger than the conventional one, and the detection of Flat Bottom Holes 2/64" is possible with similar confidence level. These methods, associated with the achievement of homogeneous microstructures throughout the large forged bar diameter, makes the ultrasonic inspection easy and reliable.

Introduction

To improve and to insure the metallurgical reliability of engine critical rotating parts, the american Federal Aviation Administration managed a comprehensive review and analysis to assess titanium producers practices. This review considered all pertinent design, manufacturing, quality control and inspection procedures. As a result of it, two recommendations have been underlined:

- improvement of melting practices to lower the risk of defect nucleation, which may remain; this is a driving force for the classical VAR process optimization, and the development of new melting procedures such as Cold Hearth Remelting (CHR);

The developments have been carried out in collaboration with FRAMATOME.

Titonium '92 Science and Technology Edited by F.H. Froes and I. Caplan The Minerals, Metals & Materials Society, 1993

- improvement of Non Destructive Inspection (NDI).

Of course, both improvements have to be done in parallel. Besides its fundamental and applied research on VAR & CHR, CEZUS has long invested in the NDI technique Research and Development, and has sustain its efforts. In particular, CEZUS has been driven to develop an original technique and a methodology, in collaboration with FRAMATOME. As a result, a high level of performance has been reached allowing improved control and subsequent quality of large diameter forged titanium bars and billets (dia. 250 mm to dia. 350 mm).

The objectives of the paper are to show the significant improvements that can be achieved by improving upon the conventional Ultrasonic Inspection procedure and methodology.

Material and experimental procedures

The scope of the paper is limited to Premium Quality Ti-6-4 titanium alloy (labeled hereinafter Ti-6-4 PQ). Large diameter 250 to 330 mm bars have been forged using a 2500 tons fully computerized forging press facility. Since the Ultrasonic noise level is, to a certain extent, strongly dependent on the microstructure, the computerized press insures:

- the homogeneity along the bars length and in the cross sections,
- the reproducibility from one batch to another one.

As a result of the controlled thermomechanical treatment, the macrostructure is homogeneous in the product section, as shown in figure 1 (330 mm dia. bar). The microstructure is fine homogeneous, and exhibits very few defects such as α stringer, plate-like α and banded structure. In figure 2, such a microstructure is presented with an average α grain size of approximately 20-30 μ m.

Ultrasonic Inspection of these bars is performed in immersion by reflecting ultrasonic longitudinal waves pulses. The laters are generated by an Ultrasonic device with an A-SCAN typed visualisation screen. 100% volume of the bar is scanned by the transducer longitudinal shift, while the product rotates. The probe shift rate and the billet rotation rate are adjusted, so that the sonic beam width is covered with at least 50 % efficiency.

Methodology

Conventional procedure

The conventional procedure includes first the sensitivity calibration. Before the beginning of each test, a reference line must be plotted with the required Flat Bottom Holes (FBH in short in the following), 1.2 mm in diameter (3/64"), at suitable metal depth in a standard test block. Then, a Distance-Amplitude correction curve has to be established in order to get the reflection amplitudes of the references; the correction accounts of the scanned distance. At last, signal absorption correction is performed measuring the difference between the signal due to the FBH reflector and the rotating bar, to get the same amplidude in both cases.

Improvement of the procedure

Usually, it is commonly agreed that the major difficulty encountered in ultrasonic inspection of $\alpha+\beta$ typed titanium alloys, such as Ti-6-4, is the very high noise level. Consequently, small defects may be hidden by it. Therefore, the key issue for the development of a new methodology was to increase the signal to noise ratio. This has been realized using special equipment and changes in the conventional approach.

Results

In this section, Ti-6-4 PQ (330-350 mm dia. billet) results will be presented. The macrostructure and microstructure are therefore similar to that of figures 1 and 2. In figure 3 and 4, A-SCAN plots of standard test blocks are shown. The actual records of rotating bars are presented in figures 5 and 6. The noise level is measured on the analogic record and expressed in terms of equivalent FBH diameter. The signal to noise ratio is the one between the standard test block FBH reflector and the noise level amplifications. These values appear on the figures 5 and 6.

The recent FAA recommendations for improvement of material reliability are:

- Highest standard (smallest reference) practicable for the size of part being inspected;
- Ultrasonic control detection thresholds

bars and nillets:

FBH Ø 1/64" (0.4 mm) for dia. < 5" (127 mm)

FBH Ø 2/64" (0.8 mm) for 5" (127 mm) < dia. < 10" (250 mm)

FBH Ø 3/64" (1.2 mm) for 10" (250 mm) < dia.

semi-finished disks: FBH Ø 1/64" (0.4 mm)

Since 1989, the FAA recommendation about non destructive inspection was already fulfilled with respect to the FBH 1.2 mm (3/64") detection by the conventional procedure. In figure 5, the reference level is shown. The maximum recorded noise level is 0.95 mm equivalent diameter and the signal to noise ratio is about 4 dB. Consequently, any penny shaped flaw, the size of which is larger than 1.2 mm (3/64") is detected without ambiguity.

With the new equipment, improved inspection is now possible. The signal to noise ratio is twice larger and typically of 8 dB such as in figure 6. Not only the FBH 1.2 mm (3/64") detection is enhanced, but also the one of FBH 0.8 mm (2/64") is possible with similar confidence level. For instance, in figure 6, the maximum recorded noise level is 0.5 mm equivalent FBH diameter.

Then, this on line procedure enables to get rid of smaller defects than the ones specified by the FAA guidelines. Undoubtely, this improved procedure is one step ahead the FAA requirements since FBH 0.8 mm (2/64") detection is readily achieved on bars and billets, the diameter of which exceeds 250 mm.

Conclusions

The CEZUS' facilities and methods for Non Destructive Testing by Ultrasonic Inspection, combined with performant billet production and microstructure control, enable high product quality on large diameter forged titanium bars. The control level is larger than that of conventional titanium producers state of art, and overcomes the FAA specifications. The signal to noise ratio:

- complies with the general NDT requirements for products, the diameter of which is lower than 350 mm.
- and allows the detection of FBH 0.8 mm (2/64") in diameter.

This reinforces the confidence level for the use of titanium products for compressor disks in aerospace engines. The procedure, presented here in the case of Ti-6-4 titanium alloy, is of course, extended to the other titanium alloys.

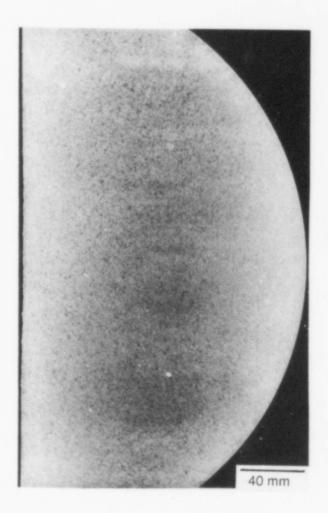


Figure 1: Typical Ø 330 mm (13" dia.) Ti-6-4 PQ macrostructure of a forged bar

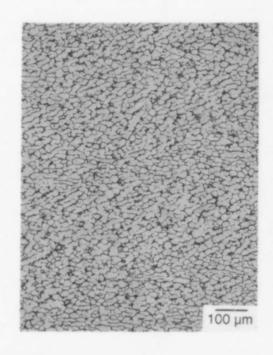


Figure 2: Typical Ø 330 mm (13" dia.) Ti- PQ microstructure of a forged bar

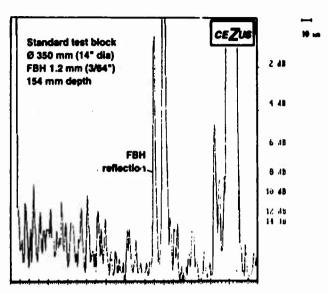


Figure 3: Standard test block Ø 350 mm (14" dia.): FBH 1.2 mm (3/64") A-SCAN at 154 mm depth.

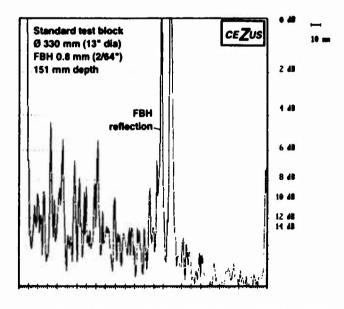


Figure 4: Standard test block Ø 330 mm (13" dia.): FBH 0.8 mm (2/64") A-SCAN at 151 mm depth.

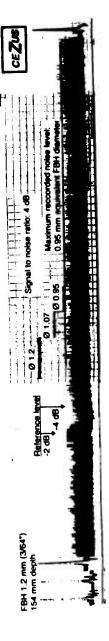


Figure 5: Conventional procedure: detection of FBH 1.2 mm (3/64") at 154 mm depth on Ø 350 mm (14" dia.) bar reccording.



Figure 6: Improved procedure: detection of FBH 0.8 mm (2/64") at 151 mm depth on Ø 330 mm (13" dia.) bar recording.

THE ROLE OF MELT RELATED DEFECTS

IN FATIGUE FAILURES OF Ti-Al-4V

K.R. Clark*, A.B. Dillard, B.C. Hendrix, J.K. Tien†, and T. Denda‡

Strategic Materials R&D Laboratory, ETC II 8.102, The University of Texas, Austin, TX 78712-1063 Abstract

Engine experience compiled by the FAA shows hard-alpha, i.e., high interstitial defects (HID), and high density inclusions (HDI) to be deleterious to lives of titanium rotating components. This study seeks to quantify the reduction of fatigue life caused by HID's and HDI's in titanium alloy Ti-6Al-4V. Titanium nitride and tungsten carbide were added to the feedstock of the master melt to induce HID and HDI defects, respectively. The material was double vacuum-arc remelted and received the conventional Ti-6Al-4V thermomechanical processing. Positive strain fatigue tests were conducted at ambient temperature. Defects can decrease the fatigue life by over an order of magnitude, depending on defect morphology and position.

Introduction

The fatigue life of most rotating, titanium gas turbine components is predicted based on the assumption that the material is free of melt defects. However, if a melt defect is present, premature cracking can lead to a catastrophic failure. The FAA has reported 25 cases since 1962 of disk bursts or premature cracking in service that can be attributed to melt-related defects [1]. In spite of the dangerous and sometimes lethal effect of these defects, little systematic research on the effects of these defects has been published. Although considerable industry effort is now focused on clean melt techniques to eliminate all defects from titanium alloy ingots, there is still a sizable quantity of double and triple melt material still in service that has not benefited from the processing/inspection changes introduced since the early seventies.

One of the most common types of defects is the high interstitial defect (HID). These defects are extremely brittle and quite difficult to locate by nondestructive inspection methods. From the center of the defect to the unaltered material [2], the hardness can vary from Rockwell C hardness of ~80 to 32. Ultrasonic inspection is the most heavily relied upon method for

105, Japan

Science and Technology Edited by F.H. Froes and I. Caplan The Minerals, Metals & Materials Society, 1993

currently at B. F. Goodrich Aerospace, 3414 S. 5th St., Phoenix, AZ 85040

[†] late of Strategic Materials R&D Laboratory, The University of Texas at Austin currently at Nippon Mining Co., Ltd., 10-1, Toranomon 2-chome, Minato-ku, Tokyo Vitonium '92

detection of HID's [3]. This inspection technique relies on the presence of a void or crack to provide a surface that will reflect/deflect the inspecting wave. Although a void is often associated with a HID [4], there have been no systematic studies to establish the void formation mechanism. Since the presence of a void cannot be assured, defects can easily go undetected.

The effect of high density inclusions (HDI's) was also studied, though they are less commonly seen than HID's. HDI's are often brittle and also represent a stress concentration, but they are more easily found with current inspection methods. These defects are consistently found during X-ray inspection because their density is much higher than the surrounding titanium matrix. However, increasing the rate of recycling Ti scrap increases the likelihood of such defects occurring. Since attempts to reduce costs may increase recycling, the incidence of HDI's could rise. It is therefore necessary to understand their behavior in light of defect free assumptions in life prediction practices.

The present study was undertaken to provide data defining the effect of hard alpha and HDI's on fatigue properties of titanium alloy Ti-6Al-4V (Ti 6-4). We will also seek to define the relationship between property degradation and defect type, and location.

Experimental Procedure

Two types of Ti 6-4 were tested. The first lot was triple vacuum melted (TVM) material purchased as 28.5 mm (1.125 in.) bar stock. The second lot was seeded with defects and double vacuum arc remelted. Two, rather than the current industry standard of three melt operations, were chosen to increase the probability of retaining defects in the material. The initial furnace charge of 907 kg (2000 lb..) contained compacts of master alloy, elemental aluminum and elemental vanadium, 5% recycled Ti 6-4 scrap, 1.8% nitrided titanium sponge (about 40 seeds/kg), and 0.079% tungsten carbide tool bit inserts (about 0.02 seeds/kg). The 400 mm (16 in.) diameter double melt ingot was beta forged to 203 mm (8 in.) diameter, and the top 1/8th of the ingot was alpha/beta forged to 76 mm diameter according to conventional practices [5].

The titanium nitride seeds were produced by nitriding virgin Ti sponge at 950°C (1750°F) for 24 hours, building on a practice developed by TIMET [6]. The nitrided sponge was crushed and screened between 3 to 6 mm (+1/8 in. -1/4 in.). The nitrided seeds contained 11 weight percent nitrogen and the balance titanium. X-ray analysis revealed the presence of both TiN and Ti₂N in the nitrided seeds. The seeds were very friable and were encased in titanium foil to prevent crushing during feed stock compaction.

The tungsten carbide tool bit inserts were introduced as received from the manufacturer. Although these inserts contain cobalt, the resultant concentration would be about 4 ppm, and insufficient to cause significant changes in the material.

The 76 mm diameter barstock was solution heat treated at 898°C (1816°F) for one hour and then water quenched. The beta transus (T_b) was determined metallographically to be 1019°C (1866°F) in the seeded material and was 1005°C (1842°F) in the TVM material. The solution temperature was set to 28°C (50°F) below T_b. This was followed by overaging for two hours at 649°C

(1200°F), then air cooling to room temperature. The resultant alloy microstructure was a primary alpha phase dispersed in a very fine transformed beta structure as shown in Figure 1. The primary alpha content was determined optically to be ~50%, and the nominal transformed beta structure platelet thickness is ~0.5 mm. The analyzed chemistry of the ingot is given in Table 1, which shows the very high nitrogen content that resulted from the high seeding rate.

Table 1. Analyzed chemistry of Ti-6Al-4V (wt.%).

Material	Al	V	Fe	0	N	C	Н
Seeded	6.19	3.97	0.01	0.07	0.13	0.004	0.0006
TVM	6.43	4.27	0.21	0.18	0.01	0.025	0.0038

The fatigue and tensile bars were machined with the longitudinal axis of the test bar parallel with that of the barstock. A 10 mm (0.4") diameter smooth fatigue bar with a 54 mm (2.25") gage length was used to maximize the probability of having defects in the gage section. The gage section was low stress ground and longitudinally polished.

Three ambient temperature tensile tests were performed to determine whether the basic mechanical behavior of the seeded material had been altered by the defects or the increased nitrogen concentration. A strength increase was observed, but the ductility remained nearly the same (Table 2). The strength difference seen may be attributed to the marked increase of nitrogen and/or the very fine transformed beta structure.

Table 2. Ambient temperature tensile properties of seeded Ti-6Al-4V.

Material	UTS (MPa)	0.2%Y.S. (MPa)	Elongation (%)	R.A. (%)
Seeded	1128	1094	14.3	40.8
TVM	1034	959	14.0	42.1
Standard [7]	972	855	15	43.0

All fatigue tests were performed using a servo-hydraulic load frame in axial total strain control; test control and data acquisition were automated. Strain was monitored using a 25 mm (1") gage length extensometer. The tests were performed at room temperature since the character of the fatigue behavior is similar up to 204°C (400°F), a typical upper limit for the use of Ti 6-4 in gas turbine engines. The fatigue tests were run under a sinusoidal wave form at a frequency of 1 Hz at $R_E=0$ and with $\Delta E=1\%$ or $\Delta E=0.8\%$. $\Delta E=1\%$ tests were performed on the specimens with the smallest visible surface defects. Hysteresis loops were observed during shake down to establish cyclic hardening or softening behavior. After shake down, loops were taken at an appropriate interval to monitor plastic strain levels.

The fracture surface of each fatigue specimen was examined using optical and scanning electron microscopy to characterize the initiation site and to correlate crack path features with changes in behavior induced by a defect. The

2 849

fatigue fractures were then cross-sectioned perpendicular to the fracture surface to reveal the microstructure adjacent to the initiation site [8]. Where a defect was seen to initiate a fracture, several Knoop microhardness measurements were made in and near the defect using a 200g load.

Results and Discussion

The initiation sites of the fatigue cracks of all of the specimens from TVM material occurred at the surfaces of the specimens. Of the seeded specimens tested, two initiated fatigue cracks from the surface with no apparent defects while defects where found at the fracture initiation sites of the remaining specimens. The fatigue life results are summarized in Figures 2 and 3 for $\Delta \epsilon$ =1% and $\Delta \epsilon$ =0.8% respectively. For $\Delta \epsilon$ =1%, the specimens with defects had lives approximately an order of magnitude shorter than specimens with no defects. There is no statistical difference between the lives in the standard TVM and the seeded material in the case where the seeded material did not initiate a crack at an inclusion. For $\Delta \epsilon$ =0.8%, all of the specimens from the seeded material initiated at defects, and their lives were less than an order of magnitude less than the lives of the triple melted material.

Figure 4 shows the origin of a typical fracture surface. This fractograph shows initiation at a HID which has an associated void. The first few hundred microns of crack growth are characterized by a significant amount of cleavage type fracture as shown in Figure 5. The next region of fracture is characterized by striated crack growth which is followed by microvoid coalescence in the final fracture region. This sequence of fracture morphology is found in both defect initiated fractures and surface initiated fractures. Striation counts from SEM fractographs show little variation from specimen to specimen within a single strain range.

Cross-sectional metallography of the defect initiated fractures was used to verify the presence of HID and HDI defects. Figure 6 shows an internal cavity associated with a HID. This cavity was surrounded by stabilized alpha phase. This stabilized alpha was significantly harder than the bulk alpha, as measured by Knoop microhardness. The microstructure directly beneath the defect in this figure shows evidence of anisotropic flow.

Specimen C had a tungsten-rich area at the crack initiation. Standardless EDS determined the rough chemistry of the defect to be 78wt% W, 18wt% Ti and 3wt% Al.

Although there was some variation in size and location among the defects, no simple correlation with life could be drawn.

Conclusions

The data in this study begins to quantify the reduction in fatigue life caused by melt-related defects.

- 1) Based on these tests, HID and HDI defects can reduce fatigue life by an order of magnitude.
- 2) Holding size and hardness constant, HID's and HDI's cause similar reductions in fatigue life.

3) Comparison of striation densities as a function of crack length suggest Stage II crack growth is independent of whether or not the crack was initiated from a defect.

In order to improve the reliability of rotating, titanium-based gas turbine components, many parameters related to the behavior of these defects must be understood. This study is continuing to gain a quantitative understanding of the effect of defects on fatigue life in different loading conditions.

Acknowledgments

The authors would like to thank Nippon Mining Corporation and Allied Signal for their support.

References

- 1. "Titanium Rotating Components Review Team Report", United States of America, Federal Aviation Administration, Aircraft Certification Service, Engine and Propeller Directorate, December 14, 1990, p. 5.K.2.
- 2. E. W. Grala, "Characterization of Alpha Segregation Defects in Ti-6Al-4V Alloy", AFML Report: AF-7351, Contract F33615-67-C-1737.
- 3. F. J. Vicki, "Non-destructive Inspection of Titanium Jet Engine Disks", Titanium Science & Technology, 1973, p. 733.
- 4. C. E. Shamblen & G. B. Hunter "Titanium Base Alloys Clean Melt Process Development", Electron Beam Melting and Refining State of the Art 1976, Ed. R. Bakish, p. 50.
- F. Shimizu, T. Yano, Y. Umemoto, T. Denda, K. R. Clark and J.K. Tien, "Test Melting of TiN and WC Seeded Ti 6-4 and Resulting Properties-A Progress Report", Electron Beam Melting and Refining-State of the Art 1991, R. Bakish ed., Bakish Materials Corp., 1991.
- 6. E. R. Poulsen & W. M. Paris "Development of Seeds for Reproducible LDI's in Titanium Melting Tests", Electron Beam Melting and Refining State of the Art 1986, Ed. R. Bakish, p. 347.
- 7. R. A. Sprague, D. L. Ruckle, & M. P. Smith, "The Effect of Microstructure on the Low Cycle Fatigue Behavior of Ti-6Al-4V", Titanium Science & Technology, 1977, p. 2069.
- 8. W. R. Kerr, D. Eylon, and J.A. Hall, "On the Correlation of Specific Fracture Surface and Metallographic Features by Precision Sectioning in Titanium Alloys", Metall. Trans., Vol. 7A, September. 1976, p. 1477.

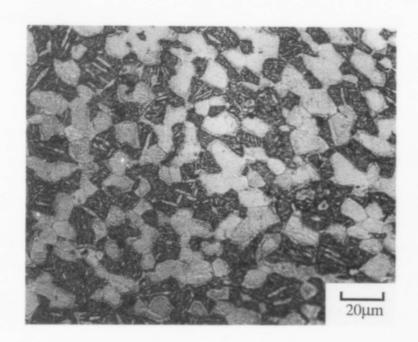


Figure 1. Ti 6Al-4V STOA Microstructure of 76.2 mm (3 in.) Barstock on the Transverse Plane

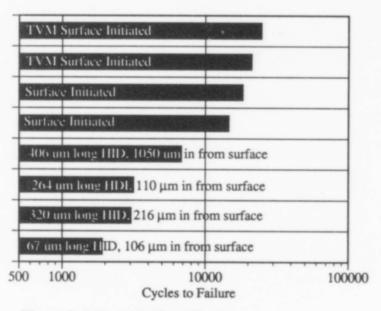


Figure 2. Life at 1% Total Strain.

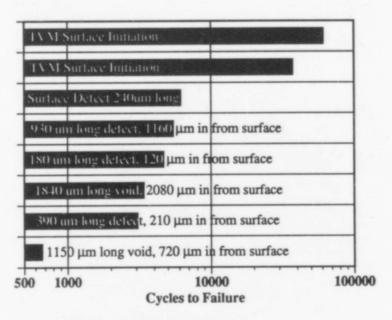


Figure 3.Life at 0.8% Total Strain.

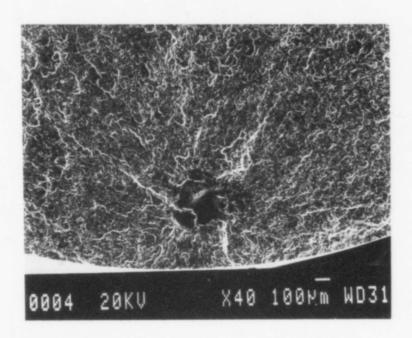


Figure 4. Cavity and HID at Origin of Specimen tested at 1% Total Strain

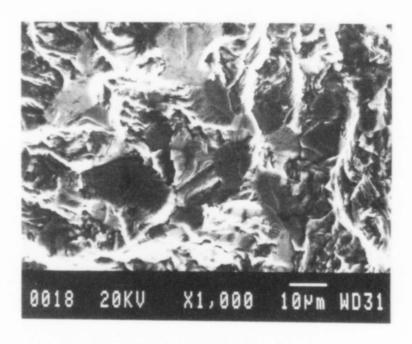


Figure 5. Cleavage Fracture Near the Initiation of One of the Specimens which had a Surface Initiated Failure.

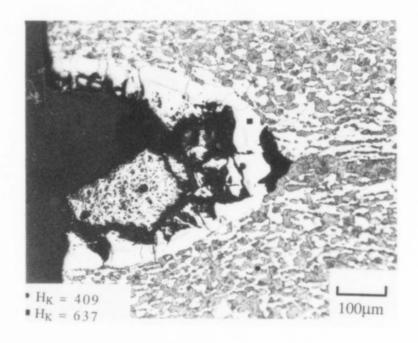


Figure 6. Microstructure of an HID with an associated void which initiated the fatigue crack in one of the 1% Total Strain Tests.

AEROSPACE APPLICATIONS

APPLICATIONS OF TI ALLOYS IN THE EUROPEAN AEROSPACE INDUSTRY

P.-J. Winkler*, M.A. Däubler** and M. Peters***

*MBB - Messerschmitt-Bölkow-Blohm, Munich, Germany
**MTU - Motoren- und Turbinen-Union, Munich, Germany
***DLR - German Aerospace Research Establishment, Cologne, Germany

Abstract

The requirements for aerospace materials are primarily spurred by improved specific-strength and elevated-temperature capabilities; these requirements confer a key role on titanium alloys.

The paper will review major Ti-alloy developments and applications in the European aerospace industry. Emphasis is placed on new alloys as well as advanced manufacturing technologies. Ongoing and future activities will be outlined for civil and military projects, mainly in airframe and engine component production.

Activities relating to future hypersonic vehicles, such as Hermes, Sänger and Hotol, have led to research and development programs concerning Ti aluminides, as well as titanium and intermetallic matrix composites.

Titanium '92 Science and Technology Edited by F.H. Froes and I. Caplan The Minerals, Metals & Materials Society, 1993

Introduction

There is probably no other metal system which is more relevant to aerospace applications than Ti alloys. With only about half the density of steels or superalloys, Ti alloys yield an excellent strength-to-weight ratio. Their corrosion resistance is excellent, their abundance essentially unlimited. However, the reduction technology to reduce the ores to metal is energy and cost-intensive, the prime reason for their relatively high price. In summary, all these technical factors make Ti alloys prime candidates for aerospace applications. Therefore it is not surprising that - despite great efforts by industry to increase the market share of general industrial applications - most of the titanium alloys used to date go into aerospace. About 7% of civil structural aircraft weight and as much as 20 to 25% of the structural weight of modern military aircraft is accounted for by titanium, with gas turbine engines consuming a substantially higher portion than airframes relative to their weight [1].

The following chapters will outline the present application of Ti alloys in the European aerospace industry, and recent developments will be stressed as well as future-oriented applications.

Producers and Users

Most of the titanium sponge needed in Europe has to be imported, mainly from the former Soviet Union and Japan. The three main titanium producers in Europe are IMI Titanium in the United Kingdom, CEZUS in France and Deutsche Titan in Germany. A full range of titanium semi-products for the aerospace industry is fabricated all over Europe with the main companies again located in France, Germany, and the United Kingdom [2].

Certainly the biggest European airframe manufacturer is Airbus Industrie. Today the four partners Aérospatiale, British Aerospace, CASA and Deutsche Airbus produce the A300, A310 and A320, with the A330/340 and A321 to be put into service soon. Smaller transport and commuter aircraft built in Europe include the BAe 146, the Fokker F50 and F100, the Aérospatiale/Alenia ATR42/72, the Saab 340 and 2000, the Dornier 228/328, the Shorts 330/360, the BAe Jetstreams and the Dassault/Breguet Falcons.

The multi-role combat aircraft Tornado is built jointly by British Aerospace, Alenia and MBB. With the proposed Eurofighter (EFA/J90), this military alliance, including CASA, will extend into the next century. Other major national military aircraft include the Mirage, Rafale (Dassault/Breguet), Harrier (British Aerospace), and Viggen (Saab-Scania). Eurocopter (Aérospatiale/MBB) and Westland are the main European companies to produce helicopters.

With Rolls-Royce, one of the three leading engine manufacturers is based in Europe. The other two, General Electric and Pratt & Whitney, USA, have established close ties to Europe through Snecma (CFM International) and MTU, respectively. Recently, Rolls-Royce teamed with BMV to form BMV Rolls-Royce Aero Engines. Other national engine manufacturers include Turbomeca, KHD Luftfahrttechnik, Fiatavio and Volvo Flygmotor. Rolls-Royce, MTU and Fiat partner International Aero Engines to produce the V2500. They also build the RB199 and - jointly with ITP - the EJ200.

Future developments in civil aviation in Europe will possibly include the extension of the Airbus family in the shape of an Ultra High Capacity Aircraft (UHCA) in the 600-800-seat range. The consortium is anticipating launching the programme in the 1995-97 period, with service to begin not before the next decade. A European industry team - Euroflag (European

Future Large Aircraft Group) - including Aérospatiale, Alenia, British Aerospace, CASA and Deutsche Airbus has started a pre-feasibility study on a Future Large Aircraft (FLA), which is slated to enter service in the next decade as a multi-role military airlifter.

Preliminary studies on a second-generation supersonic civil aircraft as a successor to Concorde are under way. British Aerospace and Aérospatiale teamed to combine their efforts, which had so far separately involved the British AST (Advanced Supersonic Transport) and the French ATSF (Avion de Transport Supersonique Futur).

During the first decade of the new millennium, the European Space Agency (ESA) plans to launch its first manned flight with the Hermes reusable spaceplane. The Ariane 5 has to be further developed to provide the necessary dispensable rocket technology. National hypersonics technology programs like Sanger in Germany or Hotol in the UK are aiming at fully reusable winged space transportation systems.

Applications in Airframes and Space Structures

Ti alloys meanwhile are well established as engineering materials for fuselage and space applications in the European aerospace industry. An Airbus study on the development of the material distribution of airframe materials for today's and future airplanes in figure 1 demonstrates relatively low variations in the use of titanium between about 4 and 7%. The titanium content of military aircraft exhibits a greater variation and a higher share of up to 20%, depending on the special strategic configurations.

Materials distribution on Airbus aircraft

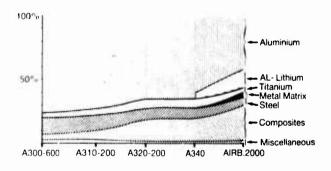


Figure 1 - Material distribution in the Airbus family.

A unique combination of mechanical properties - such as excellent specific strength and corrosion resistance together with good fatigue behaviour as well as sufficient fracture toughness values for many applications - is the main reason for using Ti alloys for airframes and space applications. Up to now the advantage offered by the good high-temperature properties of Ti alloys has hardly been exploited for fuselage applications. This may change due to the development and introduction of supersonic and hypersonic transport airplanes. Excellent compatibility between Ti alloys and CFRP

materials will increase the importance of titanium alloys for future airframe applications.

The main limitations for use in airframes are the relatively low elastic modulus of Ti alloys and in particular the high price. Consequently, particle-reinforced aluminium alloys (MMCs) have the potential to partly replace Ti alloys under certain conditions for stiffness-critical applications.

Ti6Al4V is still the airframe and space Ti alloy in Europe. Its combination of properties together with the availability of an almost unlimited data base and fabrication experience fulfill the requirements for structural applications. In most cases it is used in an annealed, i.e. stress-relieved condition; only for special weight requirements, mainly for use in space, is the heat-treated condition preferred.

In contrast to aero engines, the motivation to choose new Ti alloys for fuselage applications is relatively low and limited to special applications such as Ti3Al2.5V for hydraulic tubings, Ti10V2Fe3Al for forgings with higher strength and fatigue requirements, and Ti 1100, a sheet material for future hypersonic applications. In the UK IMI 550 is quite often used, particularly for forged parts.

Instead, the high price of Ti alloys has intensified the development of near-net-shape production techniques with the objective of better material usage and reduced assembly effort. The amount of parts made by machining from plates is reduced in favour of investment casting, net-shape forging and superplastic forming with and without diffusion bonding.

The Tornado wing box is an impressive example of the use of Ti6Al4V plates with extensive NC milling. The single parts are joined by EB welding. The dimensions are $3550 \, \text{mm} \times 1025 \, \text{mm} \times 580 \, \text{mm}$, the final weight is 438 kg, the weight of raw material 2200 kg with a machining degree of about 83%. Figure 2 shows the completely assembled Tornado wing box.

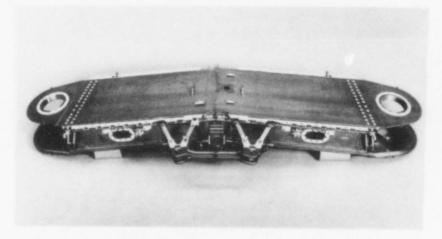


Figure 2 - Tornado wing box.

Forging technology is still dominant in producing titanium semi-products for fuselage and space applications. Their machining degree is mostly lower in comparison to plates, and the potential for taking further advantage of reducing this by a consequent development of isothermal forging technologies has not yet been exhausted. Tooling materials for temperatures higher than 900°C and tooling costs are the main restraints for extensive isothermal forging. Typical examples of aerospace forgings are hemispheres

for satellite tanks, helicopter rotor hubs, main structural parts for Airbus pylons, flap tracks and slat tracks, fittings for different applications and of different sizes, and many other parts. Figure 3 shows as an example the complete rotor system of the BO 105 and BK 117 helicopters, which is produced from Ti6Al4V forgings by Böhler. A development program conducted by Westland Helicopters and Otto Fuchs Metallwerke aims at using Ti10V2Fe3Al for a helicopter rotor hub. Higher strength and fatigue values offer distinct weight savings in comparison to Ti6Al4V.

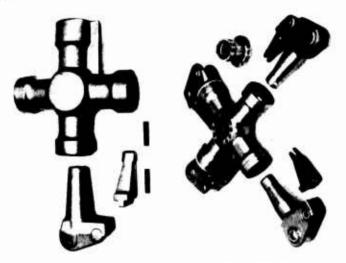


Figure 3 - Forged rotor hub of the BO 105 and BK 117 helicopters.

The developments in <u>powder metallurgy</u> concerning Ti alloys in Europe during the last decade with the objective of reducing costs by producing near-net-shape products with less or no further machining failed. Only the production of PM parts without further machining pared costs, but this could not be realized for most of the parts.

The highest potential for reducing cost through near-net-shape production is offered by investment casting technology. Other advantages are high dimensional accuracy, good surface finish, and in the meantime highly reproducible mechanical properties. Over the last decade tangible improvements in this technology have been realized. Up to now many different parts have reached production status, for instance various fittings, knots, engine nacelle structures, and flaps. Figure 4 demonstrates the advantages of this technology and shows a highly complicated rudder fitting for the EFA/J90.

The share of Ti6Al4V sheets has clearly increased in conjunction with the successful developments in superplastic forming and superplastic forming/diffusion bonding over the last decade. This technology has now reached production status of a very high level at all European aerospace companies. Impressive examples have been in production at Aérospatiale, Alenia, BAe, CASA, Dassault, Deutsche Airbus, Dornier, and MBB for different projects. Typical examples are jack cans, wing access panels, tail cones, maintenance panels, slat track cans, fin structures, canards, flaperons, foreplanes, keel structures, heat exchanger ducts, rear fuselage structures, after and middle after keels, fire bulkheads, fire floors, and satellite tank

hemispheres. Two typical parts have been selected as examples in figures 5 and 6. Figure 5 shows an Airbus SPF/Ti6Al4V maintenance panel, which is produced at MBB with cost savings of about 30% in comparison with the aluminium multi-part structure; figure 6 demonstrates the high status of SPF/DB in Europe, showing the Mirage 2000 leading edge slat produced by Dassault Aviation.

Titanium tubings meanwhile have replaced steel tubings in most new airplanes, such as the EFA/J90 and Airbus A320/340. The alloy Ti3A12,5V has been chosen because of the good compromise it offers between strength and formability. Joining is done by orbit welding (EFA) or, using a more conventional technique, by swaging (Airbus).

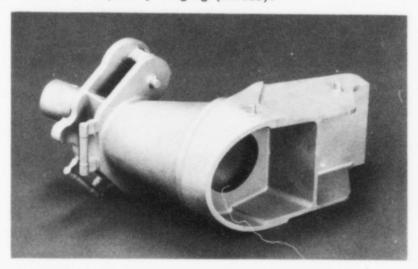


Figure 4 - EFA/J90, Ti6Al4V, rudder fitting, made by investment casting.

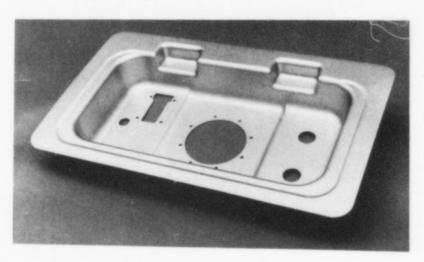


Figure 5 - SPF/Ti6Al4V maintenance panel for Airbus A340 (MBB).

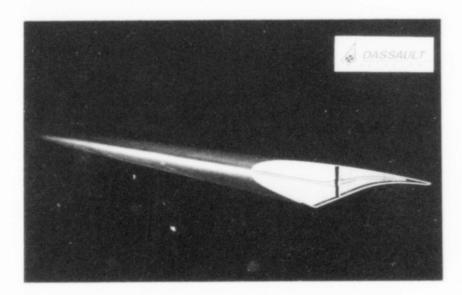


Figure 6 - SPF/DB Ti6Al4V Mirage 2000 leading edge slat (Dassault).

Applications in Aero Engines

In aero engines Ti alloys always compete with Ni-base superalloys; the use of new Ti alloys is of greater importance compared to airframes.

The low density of titanium offers the advantage of weight savings and consequently a potential for improving the efficiency of modern jet engines [3]. To realize better engine performance, the temperatures at which titanium alloys must operate have continuously been increased. Figure 7 demonstrates the improvements in yield strength and creep resistance versus temperature in the following sequence: Ti-64, Ti-6242, IMI 685, IMI 834 and Ti_3Al base alloy. The application of high-temperature Ti alloys in relation to turboshaft engines is illustrated in figure 8 in a similar order. Compressor wheels (impellers) are the main application of Ti alloys in these turboshafts.

The compressors of engines developed in the seventies (ARRIEL, ADOUR, ...) were composed of one or multiple axial stages followed by one centrifugal compressor. In more recent engines (MTR 390, ...), this configuration tends to replace single or bi-centrifugal compressors. Since the pressure ratio and the rotation speed tend to increase, the operating temperatures and the stresses are consistently rising. The high-temperature strength of alloys such as Ti-6242 and Ti-6246 allow them to be used up to 450 - 500°C. These alloys are sufficient for engines which have completed development.

For newer engines, temperature capabilities up to 600°C will be necessary. Alloys such as IMI 834 or Ti-1100 might have this capability, but the required high-temperature strength combined with surface stability might possibly reach or exceed their limits. Therefore development of high-temperature, high-strength alloys (maybe Ti aluminides) is vital.

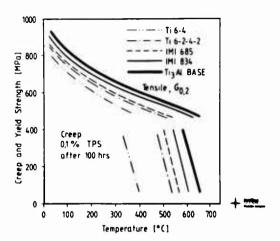


Figure 7 - Yield strength and creep resistance versus temperature for different Ti alloys.

Titanium Alloys in Turboshafts

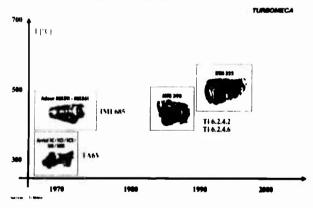


Figure 8 - Ti alloys in turboshaft applications (Turbomeca).

As pressure ratio and service temperature increase, different aspects become more and more critical and therefore urgently need to be assessed, for instance: oxidation resistance, fire resistance, hot salt corrosion, erosion resistance, foreign-object impact resistance, multiaxial fatigue sensitivity, surface finish sensitivity.

Ti alloys are also being used increasingly in jet engine compressors. Typical parts are discs, blades, bliscs (bladed disc), and casings. Some examples are illustrated in <u>figure 9</u> for the RB 199 jet engine in the low, intermediate, and high-pressure compressor, respectively. In more recent designs, as depicted in <u>figure 10</u> for EJ 200, the compressor consists of a low and high-pressure (LPC, HPC) part only. The LPC is built entirely of Ti alloys, but the all-titanium rotor is still a challenge for the HPC. The highest envisaged operating temperatures are currently around 600°C. IMI 834 has been chosen for disc application up to that temperature. How to obtain optimized mechanical properties through thermomechanical and heat

treatments has been described recently [4]. The cooperative work between INI and MTU as titanium producer and applicant, respectively, yielded important inputs towards this end.

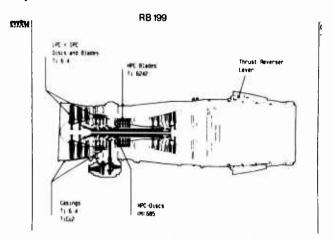


Figure 9 - Titanium parts in the RB 199 jet engine.

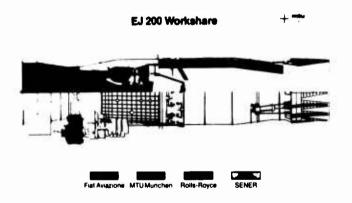


Figure 10 - EFA/EJ 200 workshare.

Future Applications of Advanced Ti Alloys

Most of the future-oriented aerospace applications, such as super- and hypersonic vehicles as well as advanced engine concepts, have stressed the need to further increase the present temperature barrier of Ti alloys well beyond 600°C as well as to increase the stiffness of Ti alloys.

The realization of Sänger, the reference concept for the German Hypersonics Technology Programme for a future space transportation system, depends on the existence of materials and structures which satisfy the high thermomechanical requirements of the mission [5]. Today the structural concept of major parts of the fuselage, the wings and stabilizers of the first stage is based on an unprotected hot structure. Even under the most extreme flight conditions before stage separation, about 80% of the outer

2,885

skin will experience temperatures lower than $600\,^{\circ}\text{C}$ and can therefore be realized with Ti-1100 or IMI 829, or even Ti6Al4V sheets. Figure 11 shows a development part for a wing leading edge structure, a Ti alloy sandwich design, developed at Deutsche Airbus.

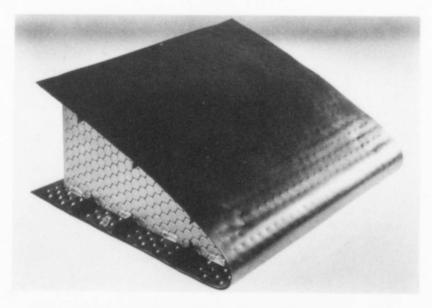


Figure 11 - Wing leading edge structural part.

Ti aluminides and metal matrix composites have to be used to meet higher temperature or stiffness requirements, provided that development is finished early enough.

As far as aero engines are concerned, a further increase in temperature capability is expected of Ti aluminides. Figure 12 indicates the areas of possible applications in the high-pressure compressor and low-pressure turbine (LPT). Typical parts are discs, blades, vanes and casings.

Research work in Europe on Ti aluminides first concentrated on ${\rm Ti}_3{\rm Al}$, then on TiAl. In the eighties most activities were conducted on a national research basis. In Germany an extensive programme on TiAl is running as part of the government-funded "National Materials Research Programme" (MATFO). A 4-year programme started in 1990 involving a total amount of about 10 mill. \$., which is subdivided into the 3 topics "Sheets and foils for hypersonic vehicles", "Turbine components", and "Motor components". Partners in this cooperative programme come from universities, research institutes, and producer and user companies. TiAl blade and vane prototype castings (Figure 13) have been produced in this programme by Tital for MTU. These castings exhibited excellent fatigue properties (HCF), sufficient creep strength, and room-temperature fracture toughness up to 30 MPa $\sqrt{}$ m despite tensile ductility values around 2 to 3 per cent [6].

Numerous efforts have been expended on the thermomechanical processing of Super Alpha Two [7]. Its bi-modal microstructure (equiaxed primary α_2 in lamellar $\alpha_2+\beta_2$ matrix) in comparison to IMI 834 was found to be superior in fatigue (HCF) and creep properties [8]. With a potential application temperature of 650°C, Super Alpha Two is suitable for blades and possibly for discs in the last stages of high-pressure compressors (HPC). Similar temperatures also prevail in the last stages of low-pressure turbines

(LPT), but the decisive difference is the hostile turbine environment. The exhaust gas carries oxygen, nitrogen, sulphur and other corrosion-supporting elements. Corrosion attack may therefore be one of the most limiting factors with respect to the application of Ti aluminides in turbine atmosphere.

In France, Onera conducted both fundamental research [9] and alloy development relating to Ti aluminides [10], partly in close cooperation with the aerospace industry. In the United Kingdom, research activities at universities are loosely coordinated by the Interdisciplinary Research Centre, while governmental contracts are monitored by DRA. Alloy developments relating to aluminides are being performed [11] as well as studies on joining intermetallics [12]. Recently, the ECC commenced funding projects on Ti aluminides conducted as part of joint European projects.

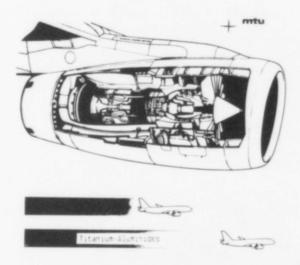


Figure 12 - Possible TiAl applications in the high-pressure compressor and low-pressure turbine of an aeroengine.

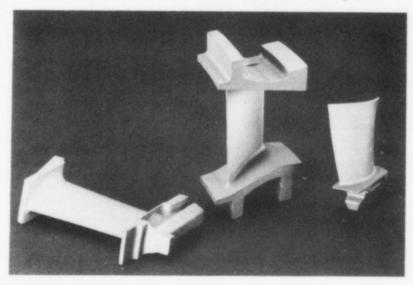


Figure 13 - TiAl vane prototype castings (Tital).

In addition to increased strength and temperature capabilities, MMC's offer the possibility of tailoring stiffness or thermal expansion. Work - mainly based on ceramic SiC fibres - included fundamental studies on the micromechanical behaviour of single fibres [13], fibre-matrix interface phenomena [14], coating of fibres [15], as well as on manufacturing components [16]. While Ti6Al4V was used initially as a matrix material, efforts are now devoted to advanced elevated-temperature Ti alloys and Ti aluminides. Pack rolling has been successfully applied to manufacture relatively ductile foils from Ti₃Al [17]. The advantage of weight saving if composite rings are being used instead of conventional discs was pointed out recently by Rolls-Royce [18]. MTU has now introduced an integrally bladed disc (blisc) made from conventional high-temperature titanium alloy. Studies are under way on how to replace such modern blisc by a bladed composite ring (bling).

MMC's in hypersonic propulsion engines can only withstand the extremely high temperatures if engine surfaces are actively cooled, e.g. by liquid hydrogen, to keep the material's temperature down. Figure 14 illustrates a possible hybrid design for an actively cooled nozzle wall structure. The T-profiled SiC/Ti composite carries the mechanical load on top, whereas the bottom structure has to withstand the hot gas.



Figure 14 - Hybrid design for an actively cooled nozzle wall structure.

Conclusion

The application and development status of Ti alloys in the European aerospace industry has been outlined for fuselages, space structures, and aero engine components. The current situation concerning producers and users has also been reviewed.

A unique combination of the properties of existing Ti alloys ensures a slight increase in the use of of Ti alloy in aerospace applications. Future-oriented aerospace applications such as super- and hypersonic vehicles as well as idvanced engine concepts will further increase the Ti-alloy share. The excellent compatibility between Ti alloys and CFRP materials, together with the trend toward building an Ultra High Capacity Aircraft, are further arguments for increasing Ti-alloy shares in the future.

Ti6Al4V is still the main Ti alloy for airframe applications. The motivation to choose or develop new airframe alloys is relatively low. Development activities are successfully aiming at near-net-shape technologies such as investment casting, isothermal forging, and superplastic forming with and without diffusion bonding. For aero engine applications, alloy development aiming at increasing service temperature is much more important in order to realize better engine performance. The spectrum of alloys includes Ti-6242, IMI 685, IMI 834 and Ti-1100. New design concepts abandon the medium intermediate-pressure compressor; an all-titanium high-pressure compressor is the goal to go for. Research work in Europe is concentrating on Ti aluminides and, with a lower priority, on metal matrix composites for higher temperature and stiffness requirements.

Acknowledgements

The authors would like to acknowledge the support provided by Y. Barbaux, Aerospatiale; J. Bottomley, British Aerospace; M. Brun, Turbomeca; H. Clemens, Metallwerke Plansee; J. Diaz Garcia, CASA; G. Fischer, Otto Fuchs; H. Folkers, Tital; D. Griffiths, BP; J. Koshorst, Airbus Industrie; H. Lajain, Deutsche Airbus; C. Liesner, Tital; M. Hansbridge, British Aerospace; F.D. Hestral, Turbomeca; P.G. Partridge, DRA; J.A. Peters, Sulzer-Innotec; H. Puschnik, Böhler; K.-H. Rendigs, Deutsche Airbus; B. Rolland, Aviation Marcel Dassault; K.F. Sahm, Dornier; D. Sauer, Otto Fuchs; H. Sibum, Deutsche Titan; G. Terlinde, Otto Fuchs; P.L. Threadgill, TWI; A. Vassel, Onera; C.M. Ward-Close, DRA; M.R. Winstone, DRA; K. Wurzwallner, Böhler. Thanks are also due to many colleagues at MBB, MTU and DLR for the helpful information and assistance they gave during the preparation of this review.

References

- [1] M. Peters, H. Buhl, J. Kumpfert, C.H. Ward, "Titanium Alloys and Aluminides" in: "Advanced Aerospace Materials", 58-83, H. Buhl (ed), Springer, Berlin/Heidelberg/New York, 1992
- [2] B. de Gelas, "Overview of Titanium Production and Applications in Western Europe" in "Titanium 1990", 9-19, TDA, Dayton, OH, USA 1990
- [3] M.A. Däubler, D. Helm, "Development of High Temperature Ti-Base Disc Haterials in Competition to Ni-Base Superalloys" in "High Temperature Materials for Power Engineering 1990", E. Bachelet et al. (eds), 1717-1726, Kluwer Academic Publishers, Dordrecht/Boston/London, 1990
- [4] M.A. Däubler, D. Helm, R.F. Neal, "Application of IMI 834 in Aeroengines - A Collaborative IMI/MTU Programme" in "Titanium 1990", 78-87, TDA, Dayton, OH, USA, 1990
- [5] H. Kuczera, P. Krammer, P. Sacher, "Sänger and the German Hypersonics Technology Programme", JAF-91-198, 42nd Congress of the Int. Astronautical Federation (JAF), Montreal, Canada, Oct. 1991
- [6] W. Smarsly, "TiAl as Alternative to Ni-Base Superalloys in Aero Engines" (in German), in "Intermetallics for High Temperatures", F.J. Bremer, (ed), 31-40, Forschungszentrum Jülich, 1991
- [7] J. Kumpfert, C.H. Ward, Y.T. Lee, M. Peters, "Improvement of Ductility and Strength of Super Alpha 2 by TMT, these proceedings

- [8] G. Lütjering, et al., "Microstructure and Mechanical Properties of Super Alpha 2", Proc. JIMIS-6, 537-541, Sendai, Japan, 1991
- [9] N. Thomas, A. Vassel, "c slip in Ti₃Al", Phil. Hag. A59 (1989) 1013-1026
- [10] A. Vassel, I. Ehrhart, M. Thomas, "Microstructure-Ductility Relationships in a Ti₃Al Base Alloy", in "Titanium 1990", 131-139, TDA, Dayton, OH, USA, 1990
- [11] M.R. Winstone, private communication, 1992
- [12] P.L. Threadgill, V.A. Besslack, III, "Metallurgical Aspects of Joining Titanium Aluminide Alloy", Proc. JIMIS-6, 1021-1025, Sendai, Japan, 1991
- [13] A. Vassel, F. Pautonnier, M.H. Vidal-Setif, "A Single Fibre Test Technique for Titanium HMC's", Proc. "Test Techniques for Metal Matrix Composites", London, 1990
- [14] H.-J. Dudek, "Titanium-Hatrix Composites", in "Advanced Aerospace Haterials", 125-139, H. Buhl (Editor), Springer, Berlin/Heidelberg/-New York, 1992
- [15] C.H. Ward-Close, P.G. Partridge, "A fibre coating process for advanced metal-matrix composites", J. Mat. Sci. 25(1990)4315-4323
- [16] R. Leucht, H.-J. Dudek and G. Ziegler, "Laboratory scale processing of SiC - Ti-6Al-4V composites", in "Fibre Reinforced Composites", 279-282, IMechE, 1990
- [17] C. Bassi, J.A. Peters, M. Blank-Beversdorff, "Titanium Aluminide an Important Aerospace Material", Sulzer Technical Review 1/1991, 1-9
- [18] D. Driver, "Materials and Process Directions for Advanced Aeroengine Design", in "High Temperature Materials for Power Engineering 1990", E. Bachelet et al. (eds), 883-902, Kluwer Academic Publishers, Dordrecht/Boston/London, 1990

TITANIUM APPLICATION IN AVIATION INDUSTRY OF CHINA

Chenggong Li and Jimin Ma

Institute of Aeronautical Materials P.O.Box 81, Beijing, 100095 China

Abstract

After more than thirty years intensive research and development work, titanium application in the aviation industry of China is growing up with the increasing titanium industry of China. The application of both wrought and cast titanium alloys in aircrafts and aeroengines is described and future developments are indicated.

Introduction

As a critical structural material being served, titanium and its alloys have been widely used in serospace industry. Since titanium possesses better performance than conventional structural materials, such as strength-to-weight ratio, corrosion resistance, heat resistance etc., the application of large-scale fan blades in aircraft jet engine becomes possible, owing to which the high thrust engine and the high mach number aircraft can be realized. It can be said without any exaggeration that development aviation industry has been advanced by making substantial progress in titanium alloys and their technology.

Since IMI 315 titanium alloy blades were used in the British Avon engine in 1954, the application of titanium in the aviation industry has been unceasingly expanded, the manufacturing technology is growing up and the quality control is being gradually improved. So far, scores of titanium alloys have been developed. Having been successfully developed in the U.S.A. during the early period, Ti-6Al-4V alloy became a universal structural material. By studying Si additions, the U.K. has made an outstanding contribution to developing a series of titanium alloys bearing silicon. For example, IMI 550(Ti-4Al-2Sn-4Mo-0.5Si) alloy allows the service temperature to rise up to 425°C, while its strength is 10% higher than that of Ti-6Al-4V alloy. With the further studying of beta processing it has been found out that beta processing can provide higher creep strength and fracture toughness and less fatigue crack propagation rate than alpha+beta processing alloys, and can be used in long term service at 520°C, such alloys as IMI 685(Ti-6Al-5Zr-0.5Mo-0.25Si) and Ti5621S(Ti-

Titanium '92 Science and Technology Edited by F.H. Froes and I. Caplan The Minerals, Metals & Materials Society, 1993 5Al-6Sn-2Zr-0.8Mo-0.25Si). It has been noticed that the induced fatigue initiation always occurs in alpha phase, but for beta processing alloys it is located in grain boundary alpha or alpha colony of prior beta grain. Concerning IMI 829(Ti-5.5Al-3.5Sn-3Zr-1Nb-0.3Mo-0.3Si) alloy, on the one hand, it is fully considered that its creep-resistance can be improved by alloying, and on the other hand, beta grain size of final forging should be restricted as far as possible so that its maximum working temperature is increased up to 580°C and it can be used in jet engine. Chinese scientists also have developed advanced titanium alloys such as ZT3 (Ti-5Al-5Mo-2Sn-0.25Si-0.02Ce) titanium cast alloy, which is contains rare-earth cerium, with service temperature of 500°C and a new alloy, which contains neodymium and can be used at 550°C temperature. Both alloys have been successfully used in aircraft engines of China.

Applications of wrought titanium alloys in aviation industry of China

The early stage of using titanium in China's aircraft engines was in the fifties to the sixties. In 1965 Ti-6Al-4V alloy was successfully used for the first, sixth, seventh, eighth and ninth stage rotor blades and disks of an early model jet engine compressor, owing to which the weight of 32 kg was saved for each engine. Since then, the application of titanium alloys such as Ti-6Al-4V, Ti-6.5Al-2Zr-3.5Mo-0.25Si (TC11) and Ti-5Al-2.5Sn have been expanded in various model jet engines and turbofan engines in succession.

Since the eighties, titanium alloy components including the third, fourth, fifth, sixth, seventh and eighth stage compressor rotor baldes and disks as well as corresponding stator baldes are fully used in the new generation of jet engines. In addition, the second to seventh stage four compressor cases made of titanium alloys such as Ti-6Al-4V alloy and ZT3 alloy bearing rare-earth cerium, the ring-shaped components and sheetmetal parts made of Ti-5Al-2.5Sn alloy and Ti-6Al-4V alloy fasteners (See Figs 1 and 2) are used for the above mentioned jet engine.

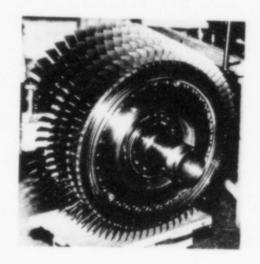


Fig.1 Titanium alloy compressor rotor



Fig.2 Titanium alloy compressor case assembly

Alpha+beta type heat-resistant titanium alloy of Ti-Al-Mo-Zr-Si system, titanium alloy possesses excellent properties of heat-resistance and thermal stability at 500°C. During the process of research and development of this alloy, the formation and varying rule of new beta grain has been explored and the alternative high-low temperature forging technology (AHLT) has been developed to improve the homogeneity of large-size forging structure. The isothermal forging of titanium alloy disks and the precision forging of titanium alloy blades (Fig.3) are widely used technologies in aircraft engine manufacture.

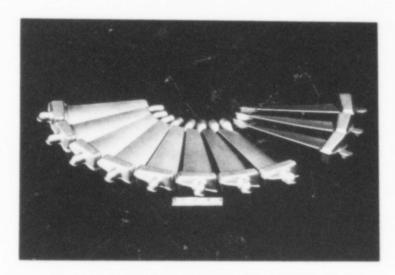


Fig.3 Precision forging titanium alloy (TC11) blades

Ti-6Al-4V alloy and Ti-10-2-3 alloy are used for some important load-bearing components such as aircraft frames and beams in order to save structure weight of modern model fighters. (See Fi .4). A Chinese forging

company has already become a titanium forging supplier for Boeing Co., which provides Ti-6Al-4V alloy closed-die forgings in batch process used in Boeing 747 aircraft.

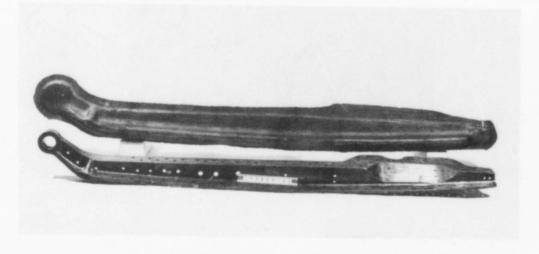


Fig. 4 Ti-6Al-4V alloy aircraft forging

The theoretical study and technical development of titanium alloy superplastic forming-diffusion bonding (SPF/DB) has also begun to be used in important structure components, e.g. aircraft cabin doors, frames etc. as shown in Fig.5.

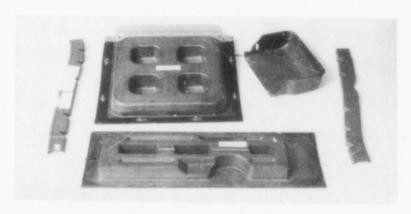


Fig. 5 Titanium alloy SPF/DB aircraft components

Ti₃Al-based alloy(Ti-25Al-10Nb-3V-1Mo, at %), which is studied by Beijing Institute of Aeronautical Materials, is manufactured as forging bar, rolled bar, rolled ring, closed-die forging, sheet and foil. Their alloying compositions are uniform, the forging microstructure is fine and the mechanical properties are quite good e.g. room temperature tensile strength is 1050 MPa and elongation is 4-8 %. As shown in Fig.6, a turbine guide plate and a turbine connector ring made of Ti-25Al-10Nb-3V-1Mo alloy have been conducting in an engine test run for 30 hrs.

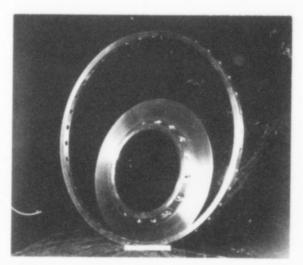


Fig.6 Ti₃Al-based alloy turbine guide plate and turbine connector ring

Status of titanium alloy casting technology in aviation industry of China

It is well known that molten titanium can react with almost all conventional refractory materials due to its very high chemical activity. Therefore its molding technology is an important key of the foundry industry. The titanium casting industry of China has successfully cast the sophisticated compressor casting case of a turboprob engine with both graphite machined mold and economic and effective rammed graphite mold. (See Fig.7) Each integral case, which consists of two castings of about 20 kg, can save over 300 welding seams and over 1000 manhour. Fig.8 shows a graphite shell mold of investment casting of a turbocharger impeller. In the eighties, the ceramic shell mold titanium investment casting technology was developed. A great number of titanium alloy casting such as the landing gear wheel hub of a hydrobomber, brake torsion tubes, the critical structural components of missile and satellite (See Fig.9 and 10) etc. have been studied and manufactured.

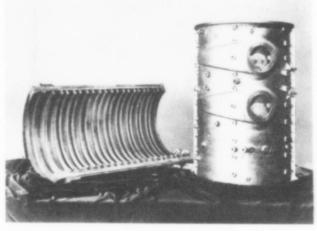


Fig.7 Titanium alloy compressor casting case of turboprob engine



Fig.8 Titanium alloy casting turbocharger impeller

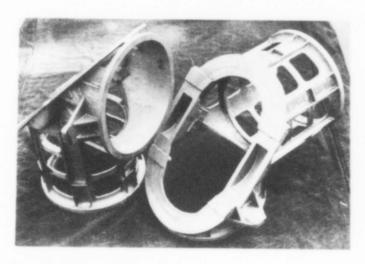


Fig.9 Man-made satellite camera cabinet of titanium alloy investment casting

ZT3 is a China made high temperature titanium cast alloy bearing rareearth cerium capable of long term service at 500°C. Internal oxidation, which is caused by cerium in the alloy, refines beta grain boundries and improves the thermal stability and heat resistance of the alloy. Thus, ZT3 titanium cast alloy compressor cases have been srccessfully applied to new generation jet engines.

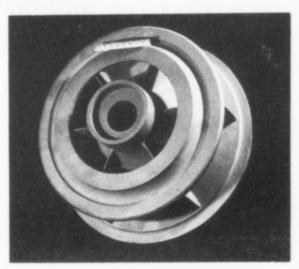


Fig. 10 Helicopter impeller of titanium alloy investment casting

Conclusions

It is very important for the development of the aerospace industry to further promote research and development as well as application of titanium technology. In recent years, research areas has focused such as the effect of overloading ratio on Ti-6Al-4V alloy fatigue crack growth, estimating of service life, the influence of microstructure on low-cycle fatigue etc. Investigations of phase transformations, the dynamic rectystallization and beta brittleness have lead to developing some advanced technology, such as beta heat treatment and so on. The study of hot isostatic pressing (HIP) technology and hydrogen treatment of titanium castings plays a positive role in improving titanium casting structure and properties.

Over thirty years of experience of titanium application in the aviation industry of China has proved that it is essential to enhance the study on material service performance, such as fatigue fracture and failure analysis, to pay more attention to fundamental study on technological processes and quality control in order to guarantee that aviation products have high quality and good stability along with satisfactory technical and economic effect.

ULTRA HIGH STRENGTH TITANIUM ALLOY FOR PASTENERS

P. J. Bania, A. J. Hutt, and R. E. Adams

TIMET
P.O. Box 2128
Henderson, Nevada 89009

Abstract

A new high strength titanium alloy has been developed primarily intended for fastener applications. While Ti-6Al-4V is used extensively as a fastener alloy in the aerospace industry, its shear strength allowable is limited to 655 MPa (95 ksi). For higher shear strength requirements, various steels or nickel-based alloys are used up to 860 MPa (125 ksi) shear strength, but with the attendant density penalty. This new alloy is intended to provide the 860 MPa shear strength at roughly a 40% weight savings. After screening various alloy systems, the optimum chemistry has been selected as follows: Ti-6.0V-6.2Mo-5.7Fe-3Al. In light of its 125 ksi shear strength goal, the alloy has been designated TIMETAL-125.

Introduction

Titanium alloys have been used extensively in the aerospace industry as fasteners, with Ti-6Al-4V being the most commonly used alloy. There are, however, two primary limitations suffered by Ti-6Al-4V which led to the development of an improved alloy. First, Ti-6Al-4V is limited to a quaranteed shear strength level of 655 MPa (95 ksi shear) which translates into a tensile strength minimum of about 1140 MPa (165 ksi). Secondly, because of its limited hardenability, it is often difficult to obtain such properties in fasteners on the order of 19mm (.75") diameter and beyond. When higher strength or larger diameter fasteners are required, occasionally other high strength titanium alloys such as Ti-6Al-6V-2Sn are employed. More often, however, other iron or nickel based alloys such as A-286, H-11 or IN718 are required. While these fastener alloys provide the desired strength and section size requirements, albeit with difficulty at times, they do so at an accompanying weight penalty of about 40% over the titanium. This weight penalty could be recouped with a titanium alloy capable of providing 860 MPa (125 ksi) shear at section sizes up to roughly 32mm (1.25°) in diameter. This translates to roughly 1585 MPa (230 ksi) average tensile strength. The goal ductility is at least 7 to 8% elongation, which is what fastener producers require in order to be able to

> Titonium '92 Science and Technology Edited by F.H. Froes and I. Caplan The Minerals, Metals & Materials Society, 1993

roll threads onto a fastener <u>after</u> solution treating and aging. Thus, the first tier typical properties for the goal alloy were established as follows:

Shear Strength: ≥ 860 MPa (125 ksi)
Yield Strength: ≥ 1520 MPa (220 ksi)
Tensile Strength: ≥ 1580 MPa (230 ksi)
Ductility (% El): ≥ 7%

Technical Approach

The first phase of the program concentrated on producing small heats of existing high strength alloys such as Ti-6Al-6V-2Sn (Ti-6/6/2), Ti-10V-2Fe-3Al (Ti-10/2/3), Ti-15V-3Cr-3Sn-3Al (Ti-15/3), Ti-3Al-8V-6Cr-4Zr-4Mo (Ti-38644, Beta C) and Ti-6Al-2Sn-4Zr-6Mo (Ti-6246) as well as various modifications thereof. Each heat was processed to 12.5mm (.5") dia. bar, solution treated plus aged to a wide range of strengths and then tensile tested at room temperature.

The resultant tensile data was then analyzed by regression analysis to establish the following general equation for each alloy (ie, baseline alloy or modification thereof):

$$\bullet \ \, \mathbf{E1} \, = \, \mathbf{A} \, + \, \mathbf{B} \, \, (\mathbf{UTS}) \tag{1}$$

This equation was then used to calculate the expected ductility at 1586 MPa (230 ksi) tensile strength. Table I provides a summary of the expected 'best' alloy from each group. Considering these results, it was clear that a new alloy base chemistry was required.

Table I Expected Ductility (% El) From Best Composition at 1586 MPa

Alloy Group	Elongation 1
Ti-6246	54
Ti-15/3	3.5%
Ti-10/2/3	41
Ti-38644	41
Ti-6/6/2	5%

¹Expected values are from 'beet' modification of given alloy group and not necessarily from the specific alloy cited.

Based on some earlier work at TIMET, an alloy based on Ti-V-Mo-Fe-Al was selected for the next phase. While each of the beta stabilizers (V, Mo, Fe) was originally felt to be optimized at roughly the 5% level, little work had been conducted to define optimum levels. Thus, a series of 18-kg (40-lb) heats were melted as outlined in Table II. Alloys A and F had one beta stabilizer at the 'low' level (- 4.5%) while Alloys B, C, and D had at least two of the beta stabilizers low. Alloy E, however, had all three beta stabilizers at the 'high' (-6%) level.

Table II Ti-V-Mo-Fe-Al Series With High and Low Levels of Beta Stabilizers 1

Alloy	¥	Mo	Ze.	PT	<u>02</u>	<u>Ti</u>
λ	4.5	5.8	5.7	3.0	.13	Bal
В	4.5	5.8	4.5	3.0	.13	Bal
C	4.3	4.8	5.7	2.7	.13	Bal
D	4.3	4.8	4.5	2.7	.13	Bal
E	6.2	6.2	5.7	2.7	.13	Bal
F	6.2	6.0	4.5	2.7	.13	Bal

¹All chemistries cited in Wt. %.

The Table II alloys were processed to 12-mm dia. rod and solution treated plus aged to various strength levels. Again, the data was analyzed by regression analysis and the results are given in Table III. This data clearly shows that the best ductility is obtained when all three beta stabilizers are at the high (> 5%) level. It also shows that when at least two of the three beta stabilizers are low (< 5%) the expected ductility at the 1586 MPa strength level is no better than the initial series of alloys (Table I). A graphic illustration of the advantage of Alloy E over the other formulations is shown in Figure 1.

Table III Results of Regression Analysis of Tensile Data from Table II ${\tt Alloys}^1$

	Regression	Coefficients2	Calculated & El
Alloy	δ	B	At 1586 MPa UTS2
λ	31.55	0161	6.03
3	42.64	0243	4.09
C	38.21	0211	4.68
D	42.74	0240	4.68
I	34.35	0167	7.84
7	34.71	0184	5.56

¹All material was finish rolled from 75mm square to 12mm round 30°C below its beta transus then solution treated 15 to 30°C below its transus and aged at various temperature/time combinations.

²Based on Equation (1) in text.

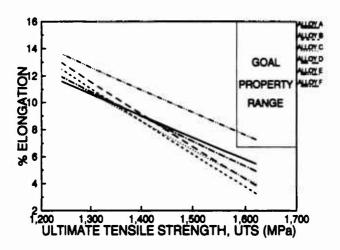


Figure 1 - Plot of Regression Curves for Data in Tables II and III.

Having established the optimum beta stabilizer content and successfully meeting the good ductility at 1586 MPa UTS, it was then decided to check the effects of the alpha stabilizers (Al and oxygen). Table IV lists the alloys melted for this portion of the study and Table V provides the calculated ductility at the 1586 MPa strength level. From these tables, it is seen that the aluminum equivalence effect is very strong, and as shown in Figure 2, there is a critical (high) level which must be maintained in order to reach the goal ductility. It should also be noted that although oxygen is shown to substitute effectively for aluminum (compare Alloys G and J, Tables IV and V) low aluminum levels are impractical because of the of the necessity to use V-Al and Mo-Al master alloys in formulating this chemistry. Figure 2 also suggests that an aluminum equivalence of about

Table IV Ti-V-No-Fe-A. Series Melted with Varying Aluminum and Oxygen Levels1

Alloy	¥	Mo	Ze	Al	02	Ti	Al_Eq2
G	6.1	6.2	5.7	3.2	.13	Bal	4.5
H	5.2	5.5	5.2	2.7	.13	Bal	4.0
I	5.0	5.1	5.0	1.5	.14	Bal	2.9
J		5.2	5.1	1.6	.31	Bal	4.7

¹All chemistries cited in Wt. %.

 $^{^{2}}$ Al Eq = Aluminum Equivalence = % Al + 10 (% $^{\circ}$ 02)

Table V Results of Regression Analysis of Tensile Data from Table IV Alloys¹

	Regression	Coefficients ²	Calculated & El
Alloy	Δ	B	at 1586 MPa UTS2
G	48.45	0261	6.92
H	49.64	0277	5.65
I	85.27	0534	0.60
J	37.79	0196	6.73

¹Material melted and processed similar to Table IV material.

²Based on Eqn (1) in text.

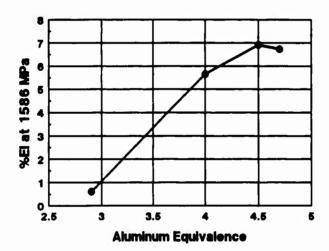


Figure 2 - Calculated Ductility of Table IV Alloys at 1586 MPa UTS as a Function of Aluminum Equivalence.

4.5 might be optimum.

In light of the above results, the selected chemistry for scale-up evaluation was: Ti-6.0V-6.2Mo-5.7Fe-2.7Al-.18O2.

An 820 kg (1800-lb) x 457mm (18-inch) diameter ingot of the above chemistry was melted. There were two primary reasons for immediately scaling to this ingot size:

- a) It provided enough material to enable hot rolling of coil stock on a production mill. This, it was felt, would allow processing to a finer grain size than with the smaller heats.
- b) It would provide a large enough ingot to evaluate segregation tendencies.

The ingot was forged to 89mm (3.5-inch) diameter as input stock for rolling to small diameter coil. Since several pieces were cut at this size, slices were taken at positions representing various positions along the ingot length and chemistry samples were taken at center and outside edge locations of each slice. These samples were analyzed for major chemistry variations in order to assess the macrosegregation tendency for this formulation. As the results of Table VI indicate, the chemistry variation was very small, thus indicating that scale-up to a full sized ingot is feasible. Of course, the degree of segregation is a function of the melt practice employed. Also, microsegregation tendency is not assessed by this technique.

Table VI Chemical Analysis of 820 kg Heat Chemistry, Wt. &

Location1	¥	Mo	£	Al	<u>o</u> x
21/0	5.47	6.02	5.25	2.53	.186
2%/C	5.42	5.95	5.27	2.52	.197
25%/0	5.78	6.43	5.27	2.60	.200
25%/C	5.58	6.19	5.34	2.56	.179
75%/0	5.69	6.30	5.51	2.58	.190
75%/C	5.61	6.29	5.43	2.57	.220
90%/0	5.72	6.34	5.32	2.59	.196
90%/C	5.79	6.42	5.52	2.61	.178
Overall Avg	5.63	6.24	5.36	2.57	. 193
Outside Avg	5.67	6.27	5.34	2.57	.193
Center Avg	5.60	6.21	5.39	2.57	.194

1% values correspond to approximate distance from ingot top; 'O' refers to outside edge of sample slice; 'C' refers to center.

The beta transus was 749° C (1380°F) for this heat. The density was measured as 4.852 gm/cm^3 .

The ingot was forged and hot rolled to 9.5mm diameter rod. A series of solution and age heat-treatments were performed on the material. The solution temperature was 710°C (1310°F) and the age temperatures ranged from 482°C to 593°C (900°F to 1100°F) for 2 to 24 hours. These heat treatments resulted in ultimate tensile strengths from 1004 to 1373 MPa below the desired level of 1586 MPa.

In order to increase the strength level, another series of heat treatments were performed utilizing a solution and duplex aging (STDA) cycle. The material was solution treated at 710°C, pre-aged at 427°C 4 or 8 hours, and final aged at 468°C or 482°C 16 hours. These heat treatments generally resulted in higher strengths. The over 1586 MPa ultimate tensile strength specimens contained 1475 MPa to 1493 MPa yield strength and 6.0 to 8.0% elongation. The highest strengths were produced by a STDA heat treatment -710°C 2 hr/fan air cool plus 427°C/8hr/air cool plus 468°C/16hr/air cool. Table VII contains the results of the six highest tensile strengths.

Table VII Tensile Test Results from STDA1 Material

		.2% YS		
Sample	UTS (MPa)	(MPa)	% RA	% Elong
1	1617	1493	11.8	6.0
2	1616	1492	12.2	7.5
3	1609	1491	10.0	7.0
4	1599	1473	12.5	7.0
5	1594	1473	14.4	8.0
6	1587	1475	13.1	8.0

1710°C 2 hr/fan air cool plus 427°C/8hr/air cool plus 468°C/16hr/air cool.

The balance of the approximately 160 tensile tests are not listed and show generally lower strengths and concomitant increasing ductility at the 482° C age temperature. However, some of the elongation values were unexpectedly low.

The double shear results from 46 tests from the 9.5mm rod heat treated at $710^{\circ}\text{C/2hr/fan}$ air cool plus 427°C/8hr air cool plus $468^{\circ}\text{C/16hr/air}$ cool are 837 MPa on average and 868 MPa at the maximum. The average shear values are less than the goal of 862 MPa on average but it was obtained in some cases. It is felt that a more optimum processing schedule to produce a finer grain sized product will provide the 862 MPa strength goal.

The microstructure of the STDA (710°C 2 hr/fan air cool plus 427°C/8hr/air cool plus 468°C/16hr/air cool) material is typically a very fine-grained alpha precipitate in a beta matrix. (See Figure 3).

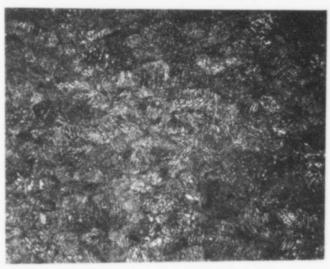


Figure 3 - Microstructure of aged rod. 200X, L.

The results of general corrosion tests (1) of beta rolled sheet and comparison with CP grade 2 and Ti-6Al-4V in various environment; are shown in Table VIII.

Table VIII General Corrosion Rates (MM/Year)

Environ	<u>nent</u>	TIMETAL - 125	CP Grade 2	T1-6A1-4V
H ₂ SO ₄ , 1%,		.094	17.4	2.5
HC1, 1%,	Boiling	.475	1.8	.845
HNO3, 40%,	Boiling	.470	. 5	

Conclusions

- a) An ultra-high-strength titanium alloy is being developed which shows potential for fasteners requiring 860 MPa shear strength, and 1520 MPa yield strength 1586 MPa tensile strength with elongation greater than 7%.
- b) The required properties were obtained except for the 1520 MPa yield strength without cold working the bar prior to aging. The heat treatment was optimized at 710°C 2hr/fan air cool plus 427°C/8hr/air cool plus 468°C/16 hr/air cool.
- c) The general corrosion rates of the ultra-high strength titanium alloy in several environments are better than Ti-6Al-4V and CP grade 2.

Summary

Since no existing class of titanium alloys showed the potential of meeting the requirements of an ultra-high strength fastener alloy, an alloy development program was initiated. After evaluating the existing alloys Ti-6/2/2, Ti-10/2/3, Ti-15/3, Ti-38644 and Ti-6246 and modifications there of, the alloy development program resulted in the alloy, Ti-6.0V-6.2Mo-5.7Fe-2.7Al. General corrosion tests indicate that corrosion rates are less than those for Ti-6Al-4V and CP grade 2.

Reference

 Bergman, D. D., "HTL Monthly Progress Report for April 1992", TIMET Henderson Technical Lab.

APPLICATIONS OF TITANIUM ALUMINIDES IN

GAS TURBINE ENGINE COMPONENTS

- P J Postans*, M T Cope*, S Moorhouse* and A B Thakker*
- * Rolls-Royce plc, PO Box 31, Derby, DE24 8BJ, UK
- * Rolls-Royce Inc, 2849 Paces Ferry Road, Atlanta, GA 30339-3769, USA

Abstract

Titanium aluminide for the last two decades have offered the prospect of significant weight savings in gas turbine engines by the replacement of Ni base superalloys. As yet they have failed to deliver despite significant R&D effort. However, recent advances in chemistry and processing capabilities have now resulted in Ti aluminides standing on the threshold of commercial engine utilisation.

For this class of material to make the transition from research curiosity to a 'real' engine material the key property requirements must first be identified. Only then can the material be tailored to meet the engineering need.

To identify key properties targets for titanium aluminides, a series of design studies have been carried out for civil, military and helicopter gas turbine engines using current gamma and alpha2 material properties.

Gamma blades in the low pressure turbine of civil engines save over 100kg per engine compared to current cast nickel blades. The key requirements here are specific stiffness coupled with adequate tensile strength and resistance to damage and defects. Other attractive applications are compressor stator vanes and simple, non critical structures where conventional titanium can not be used because of the risk of titanium fires. Compressor blading is a further possibility. Large complex static structures and high integrity parts lifed by fracture mechanics are unsuited to current alloys.

Alpha2 alloys were for a long time the front runners for engine applications compared to gamma Ti aluminides. However their poor fire and environmental resistance has proved their Achilles' heel.

Further understanding is still required on the long term effect of operating environment on mechanical properties for titanium aluminides. In addition the effect of local stress concentrations, ie, defects or damage, on life particularly for the more brittle gamma alloys, need to be assessed. The applications for alpha2 would be significantly increased if its fatigue crack growth rate could be slowed down to that of conventional titanium, allowing its use as critical discs provided environmental resistance is adequate.

Titanium '92 Science and Technology Edited by F.H. Froes and I. Caplan The Minerals, Metals & Materials Society, 1993

Introduction

'Find out what the customer wants - then supply it' is the recipe for success in any business. Applied to titanium aluminides it should ensure the materials and manufacturing processes developed have the widest industrial application and benefit.

The present paper identifies key areas where improvements are required, based on recent Rolls-Royce design studies for civil, military and helicopter engines. The conclusions provide a good indication of general aeroengine industry needs, although there will be some detailed variations between different companies due to different engine operating conditions, technology base and personal opinion.

Titanium aluminide capabilities

Design studies identifying component applications and key materials and process properties are iterative with materials and process development. A first step is to assess current materials and process capability (Figures 1 and 2) and estimate likely future improvements (1)(2)(3)(4)(5).

There are also some basic conditions which a gas turbine engine material must meet. They are described below in no particular order since all are essential.

Material must be available in the right timescales

Maximum benefit from a new material or process accrues when it is designed into a component from the start, rather than being substituted within an existing engine configuration. Such design opportunities only occur every few years.

The engineering advantage must be high enough to justify development costs and any increase in component cost

When a new material or process allows the engine to be thermodynamically more efficient, ie, operate hotter or at higher pressure ratio, the benefit is usually greater than if it just saves weight. A general rule for civil gas turbine engines is that a reduction of 1kg in component weight saves £650 in direct operating costs (mainly fuel) over the life of an engine (2). Veight assumes more importance in military combat and space vehicle components.

The risk of unexpected component failure must be acceptably low

Components are divided into several categories, dependent on the consequence of failure. The most critical must have a very low risk of premature failure; it can increase somewhat for components where failure affects efficiency but not safety.

Component design studies for civil, military and helicopter gas turbine engines

The results of these studies are summarised in Figure 3, with more detail in Table 1 for gamma and Table 2 for alpha2.

Both gamma and alpha2 are also potential matrices in composite materials. Since materials and process requirements for matrices, are likely to be significantly different they are not considered here.

Compressor aerofoils

The requirements for all 3 types of engine are broadly similar despite differences in component size and cost/weight benefit.

Aluminides offer no benefit to the engine thermodynamic cycle as temperatures are limited by available disc materials.

Stator blades in gamma offer weight savings of 50% approx compared to steel or nickel. The risk of component failure is lower for stators compared to rotors as the likelihood of impact from foreign objects in the gas stream is low. Stators held at both the inner and outer annulus are expected to remain in place even if cracked.

Rotor blades in gamma offer little advantage compared to conventional titanium, improved fire resistance being offset by increased risk of foreign object damage. As a replacement for nickel the weight savings depend on allowable crushing stress, hence blade root design. A heavier disc rim could easily cancel the 45% reduction in blade weight.

Alpha2 is of little use unless its fire resistance can be markedly improved.

Turbine aerofoils

Many turbine aerofoils, including all those in military combat engines, run too hot for gamma aluminide. Those at suitable temperatures are civil engine low pressure turbine, LPT, aerofoils and helicopter engine power turbine aerofoils. The latter will probably demand low cost in preference to low weight and hence remain in nickel.

Civil LPT blades, offer no engine cycle advantage due to gamma but weight savings of 45% are expected by replacing nickel. Since civil LPT blades can be over 35cm long this translates to a saving of 80-120kg on a large turbofan engine. Reduced blade weight facilitates lighter discs and casings, saving an additional 30%, ie 70kg. As a result Rolls-Royce consider civil LPT rotor blades are the most important application for gamma aluminide, see Figure 4. It is understood other gas turbine engine companies share this view.

Civil LPT nozzle guide vanes, ie static aerofoils, show no engineering benefit in gamma since their key requirement is high strength.

Alpha2 has some application in civil LPT blades but its lower temperature capability and lower modulus (influencing vibration) make it less useful than gamma.

Engine structures

Applications for titanium aluminides are limited. Many casings require high 'plasticity' for containment of failed blades, which precludes gamma, and fire resistance, which precludes alpha2. Spoked engine support structures require neither of these properties but their complex shape is often beyond current titanium aluminide manufacturing capability. Military engine nozzles and some combustor casings are more promising.

Discs

In recent years there has been a move away from disc lives based on fatigue initiation. The Alternative is fracture mechanics life based on a typical initial defect size and fatigue crack growth rate.

For both gamma and alpha2, it is likely that high lives to crack initiation can be obtained on 'defect free' material but both have a fairly fast crack growth rate which results in low fracture mechanics lives.

It is unlikely that fatigue crack growth rate can be slowed down sufficiently for either gamma or alpha2 to make them suitable for long life discs. Applications will therefore be limited to short life discs eg missile or some military engines, or certain turbine discs which are required to withstand a high overspeed criteria, hence tensile strength is the main requirement and fatigue stresses are relatively low.

Conclusions

Gamma has wider potential application than alpha2 due primarily to its fire resistance and reasonable temperature capability. Key areas for improvement are plasticity, both improving defect tolerance without detriment to other key properties and/or learning to effectively use material with limited plasticity; environmental stability; tensile strength and manufacturing capability.

Alpha2 alloys have limited application due to their lack of fire resistance and poor environmental resistance. Key areas for improvement are surface protection to improve temperature capability and ways of slowing fatigue crack growth rate. These would enable alpha2 to fill a useful, though small niche between conventional titanium and nickel alloys.

References

- 1 Y W Kim and D M Dimiduk, JOM, August 1991, 40-47
- 2 Rolls-Royce plc unpublished data
- 3 J C Chesnutt, J C Williams, Metals and Materials, August 1990
- 4 N J Rogers and P Bowen, 'Effects of microstructure on toughness in a gamma titanium aluminide', (Paper presented at Euromat '91, Cambridge, 1991)
- 5 Y Nishiyama et al, 'Development of titanium turbocharger rotors' Published in High Temp Aluminide and Intermetallics, Gd SH Whang et al, Minerals and Metals Society, 1990, 557-584
- 6 H A Lipsitt, D Schechtman and R E Schafrick, Met Trans A, 11A, August 1990 1369-1375.

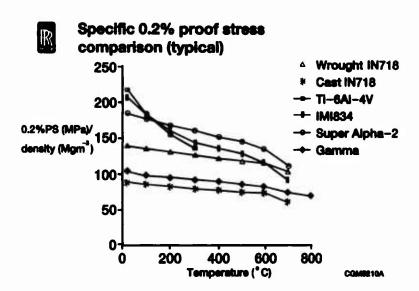


Figure 2

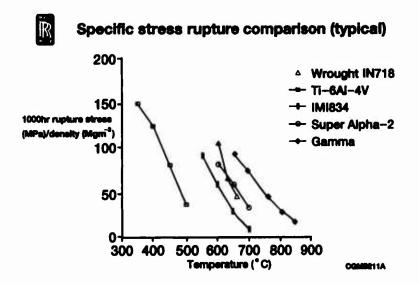


Figure 3

Potential applications of titanium aluminides in a large civil turbofan engine

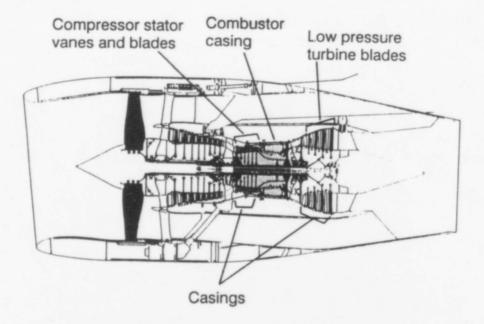


Figure 4



Table 1 Key Design Requirements for Gamma Titanium Aluminides

				211010101010101010101010101010101010101	מיני ברינו לי מומנים		2	
	Rotors	Stators	Rotors	Rotors Stators(NGVs)			improvement/research	research
Tensile Strength	`	\	`	ı	I	\	8	Note 1
Creep Strength	\	`	/	Ħ	I	۲۰		
Plasticity	H	`	н	`	н	Ç.	1	Note 2
Modulus	`	`	'	_	'	`		
Fracture Toughness	`	,	\	`	_	`		
Crack Propagation	80	กล	na	กล	н	н	7	Note 3
Fire Resistance	`	'	'	,	`	กล		
Environmental Stability	\	_	H	ı	н	`	8	Note 4
Castability	_	/	`	`	#	PC	9	Note 5
Forging/Extrusion	_	_	`	\	٥.	٥.		
Sheet	æ	na	na	na	I	na na		
Machining	`	\	'	`	c .	<i>c.</i>	2	
Welding/Bonding	æ	٥.	na	¢.	٥.	C -	4	Note 6
Engineering benefit of current or near-future material	Moderate /Low	Moderate	High	None	Low	None		

/-Acceptable in current or near future material I-Significant improvement required ?-Don't know more information Note 4 - Aim 850 to 950°C Note 5 - Imorovements needed for large complex structures Note 6 - Cooling rate critical for fusion welds Note 1 - Need to improve to nickel strength levels Note 2 - Need to learn how to design with limited Note 3 - Unlikely to achieve rates similar to conventional titanium plasticity material needed na-Not applicable

Table 2 Key Design Requirements for Alpha2 Titanium Aluminides

Design Requirement	Compressor Aerofoils	Aerofoils	Turbine	Turbine Aerofoils	Structures Discs	Discs	Priority for
	Rotors	Stators	Rotors	Stators (NGVs)			improvement/research
Tensile Strength	`	'	`	`	`	`	
Creep Strength	`	`	`	¢.	¢.	\	
Plasticity	`	'	`	`	`	`	
Modulus	_	'	`	`	`	`	
Fracture Toughness	_	`	`	`	`	`	
Crack Propagation	20	80	па	na en	н	H	2
Fire Resistance	H	H	н	Ħ	н	BU	Note 2
Environmental Stability	ı	H	н	Ħ	H	н	1 Note 1
Castability	6	na	BU	¢.	¢.	na	
Forging/Extrusion	_	/	`	`	_	`	
Sheet	80	na	en.	ยน	`	กล	
Machining	_	`	`	`	¢-	c -	
Welding/Bonding	80	¢.	na	<i>c-</i>	٥.	c -	m
Engineering benefit of current or near future material	None	None	Low	None	Low	Low/ Moderate	

[?] Don't know - more information needed Increased fire resistance would extend applications but it is unlikely to be feasible na Not applicable Note 1 Base alloy unlikely to be improved - need surface coating Note 2 Increased fire resistance would extend applications but it Acceptable in current or near future material I Significant improvement required

The Titanium Investment Casting Technology

K.-D. Folkers

Titan-Aluminium-Feinguß GmbH 5780 Bestwig GERMANY

Abstract

Today, the technology for casting titanium has advanced greatly and allows the production of precise, highly complicated castings with high quality surface finish and with excellent properties. This development can be easily shown on the example of a structural aircraft part. The mechanical properties of the high temperature alloy IMI 834 in the cast condition are discussed.

Introduction

For a long time titanium as well as titanium alloys were used as forging material in the aerospace and as corrosion-resistant material for the chemical industry.

In the lost wax investment casting process lost models and lost moulds are being used. The models are produced with thermoplastic. This happens by wax injectioning special pattern wax in tools. Very often these tools are divided/folded and separable/dismountable, in order to remove the wax from the tool. This process allows more design freedom for the components.

The main advantage of investment castings is the fact that structural components can be manufactured with considerable cost savings and considerable less machining. Using castings offers the advantage of a high dimensional accuracy, excellent surface finish, and high min. values of the mechanical property.

Thus, the investment casting process renders it possible to produce complicated components at low costs. Compared to conventional made parts this process can be considered as good alternative.

Titanium '92 Science and Technology Edited by F.H. Frose and I. Caplon The Minerals, Metals & Materials Society, 1993

Melting Practice

The traditional melting process for the production of titanium castings is the scull procedure which has been developed in the mid-fifties from the Bureau of Mines/Albany, Oregon. During research work at that time it was recognized that while melting titanium with a vacuum arc furnace the liquid pool had surprising depth. This led to the development of a casting furnace with a tiltable water-cooled crucible. The fact that there are only small evaporation losses makes this process ideal for the production of high quality investment castings (Ref 1).

Shell Moulds for Titanium Castings

At present there exists no moulding material that does not react with liquid titanium. The question of moulding system reactions plays an important role in the production of titanium investment castings. Such reactions include above all the pickup of oxygen. However, there are also other components of the moulding system that entail a hardening increase of surface areas. Normally, the penetration depth of the in-diffusing elements is between 0.05 and 0.3 mm. The thickness of this layer depends to a high degree on the contact time between solidifying titanium and moulding material at high temperature. The hardened surface area of the castings will be removed by etching. The necessary etching will be considered as machining allowance during the tool construction.

The HIP-Process

The HIPping process /Hot Isostatic Pressing) offers an excellent possibility to repair defects in the structure such as micro shrinkage or bubbles in titanium castings. HIPping for Ti-6Al-4V takes place at temperatures of 920°C and 102 MPA over two or several hours in argon. Above all the HIP-process improves the dynamic values.

Weld Repair

Titanium is fully weldable allowing repair whenever necessary. Weldments have excellent tensile and fatigue properties sometimes exceeding those of the base metal.

Therefore, weld repair is a common practice for filling gas porosity and shringkage pores exposed by chemical milling, post-HIP surface depressions, or cold shuts in connection with special welding equipment. Inert gas tungsten arc welding is typically used.

Heat Treatment

Since titanium castings are slow-cooled in insulating moulds in a vacuum, subsequent thermal treatment is mormally unnecessary since the castings are virtually "annealed" while still in the moulds. Stresses induced by welding can be relieved by a simple stress relief cycle at 750°C for 2 hours. This takes place in a special vacuum furnace under static argon atmosphere.

Aerospace Applications

Investment castings in titanium have found wide application areas in aircraft and aerospace industry because they have many advantages. For example high strength to weight ratio, dimensional accuracy, wall thicknesses down to 2 mm and excellent surface finish. As it can be seen in figure 1 TITAL produce different castings, the so called knots, for a new europeen civil aircraft the DO 328.

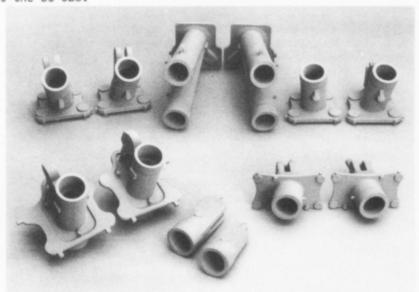


Figure 1 - Different Casting Knots

The casting knots are part of the engine suspension system manufactured by Dornier/Germany. The whole suspension system is illustrated in figure 2.

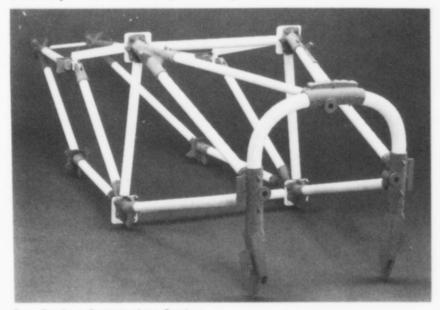


Figure 2 - Engine Suspension System

Structure and Properties of cast IMI 834

The near alpha alloy IMI 834 was developed for gas turbine aero-engine components operating at temperatures up to 600° C. Although it is a wrought alloy, no difficulties were experienced by TITAL when casting the alloy.

Chemical Analyses

The ingot material for the test program was supplied by IMI Titanium. The chemical composition of the castings can be seen in table ${\rm I.}$

Table I Casting Analyses

Element	Percent
Al	5.82
Sn	4.04
Zr	3.50
Nb	0.70
Mo	0.54
Si	0.32
C	0.05
Fe	0.018
0	1250 ppm

wt. %

HIPping and Heat Treatment

Hot Isostatic Pressing was carried out below the beta transus temperature at 965°C for 2 hours at 103 MPA to seal internal shrinkage porosity.

After this the castings were beta solution heat treated at 1075°C and 0.5 hours to avoid excessive grain growth. Finally the testing material was aged at 700°C and 2 hours.

Micro Structure

The prior beta grainsize in a 12.5 mm thick section after thermal treatment was between 1 and 2 mm.

The microstructure of cast IMI 834 consists wholly of acicular alpha and beta transformation product as can be seen in figure 3.

Beta processed alloys are typified by good creep resistance at moderate strength levels (Ref 2).



Figure 3 - Microstructure of IMI 834 in the as-cast condition

Mechanical Properties

As shown in table II the room temperature tensile properties meet the specification of wrought products, although due to the coarser grain of the cast material, at slightly lower levels of ductility.

Table II Room temperature tensile properties of cast IMI 834

condition	0.2% PS MPA	U.T.S. MPA	EL %	RA %
(1 + 3) HIP	944	1071	5	7
+ STA	966	1072	5	9
specification wrought product	910	1030	6	15

IMI-data (Ref 3)

At higher temperatures, for excample 600° C, the tensile properties of cast material are excellent with a little debit in ductility.

The high temperature tensile properties obtained in the test program are listed in table III.

Table III High temperature tensile properties of cast IMI 834

condition	0.2% PS MPA	U.T.S. MPA	EL %	RA %
(1 + β) HIP	526	663	6	16
+ STA	515	669	10	22
specification wrought product	480	585	9	20

test temperature: 600°C

IMI-data (Ref 3)

Creep performance plays an important role for the application of titanium alloys in modern gas turbine engines.

In its cast form IMI 834 exhibits superior creep performance, again due to the acicular micro structure, normally achieved after beta processing (Ref 4).

A summary of the creep data is given in table IV.

Table IV Creep data at 600°C/125 MPA of cast IMI 834

condition	% T.P.S. 100 hrs	% T.P.S. 310 hrs
(L + B) HIP + STA	0.033 0.025 0.030 0.028	0.061 0.056 0.056 0.052

IMI-data (Ref 3)

Conclusion

The state of the art of titanium casting technology has been reviewed and the possibilities for the manufacture of structural parts in the aircraft industry were shown.

This technology in combination with high temperature alloys like IMI 834 makes it possible to produce castings that offer certain advantages for the application in gas turbine engines.

Acknowledgements

The author wishes to thank Terry Green (representative of TITAL in the U.K.) and Dr. Mike Kearns (IMI).

References

- A.R. Beall, J.O. Borg and F.W. Wood, "A study of consumable electrode arc melting", <u>Report 5144</u>, U.S. Bureau of Mines, 1955
- M.T. Cope, M.J. Hill
 "The influence of ageing temperature on the mechanical properties
 of IMI 834", Proceedings of the sixth world conference on titanium,
 Cannes (1988), 153-158
- M. Kearns, Private communication with author, IMI Titanium, Birmingham, 1992
- D. Eylon, S. Fujishiro, P.J. Postans and F.H. Froes
 "High-temperature titanium alloys a review"
 <u>Titanium technology: Present status and future trends</u>,
 <u>Published by the Titanium Development Association</u>, Dayton, 1985

TIMETAL-1100 SHEET PROPERTIES

A. J. Hutt and W. M. Parris

TIMET
P.O. Box 2128
Henderson, Nevada 89015

Abstract

This report covers some mechanical and physical properties of alpha-beta and beta processed TINETAL·1100 (nominally Ti-6Al-2.78n-4Ir-.4Mo.458i-.0702 weight percent) sheet. Mechanical properties for TINETAL·1100 were developed from beta rolled, beta annealed, and alpha-beta rolled sheet from a range of thicknesses from several heat lots. Creep and stress rupture properties were enhanced by beta annealing or beta rolling but at the expense of ductility. The beta annealing temperature should be kept as low as possible in order to retain maximum ductility. Depending upon the requirements of the application, the appropriate processing route can be specified.

Introduction

Although TIMETAL·1100 was developed primarily for forging applications, as in the case of its predecessor Ti-6242S (Ti-6Al-2Sn-4Zr-2Mo-.1Si), there are numerous sheet metal applications which could benefit from its properties. Such applications include gas-turbine-engine afterburner structure and hot skin and substructure applications as found on ultrahigh-speed vehicles such as the NASP. While some applications could use TIMETAL·1100 sheet in an alpha-beta processed condition, most would probably require a beta-processed microstructure.

There are two methods for producing beta processed sheet - beta rolling and beta annealing. This paper reviews the properties associated with these approaches and identifies critical limits for beta-anneal temperatures. It also reviews a limited amount of data on alpha-beta processed sheet material. Part 1 lists the mechanical properties and Part 2 describes the development of the beta annealing and stabilization treatments.

Part 1 - Physical and Mechanical Properties of TIMETAL-1100 Sheet

TIMETAL·1100 is a near-alpha titanium alloy developed by TIMET for high-temperature applications where creep resistance is required. The beta transus is in the range of 1000 to 1015° C. The density is 4.49 gm/cm³.

Titanium '92 Science and Technology Edited by F.H. Froes and I. Caplan The Minerals, Metals & Materials Society, 1993

Material Processing

Beta Rolled Sheet. TIMETAL-1100 beta-rolled sheet was produced by alphabeta cross-rolling 75mm thick slab to 5.4mm at 982°C and unidirectional rolling at 1038°C to final gage above the beta transus (1000 to 1015°C) on a conventional rolling mill. Appropriate controls and reduction sequences were employed to refine the macro/micro-structure.

After hot rolling, the sheet was annealed at 954° C/15 minutes/AC (air cooled). Then, the sheet was finished by belt grinding which insured removal of alpha-case and surface defects.

<u>Beta Annealed Sheet</u>. Beta annealed sheet was produced from 75mm slab alpha-beta cross-rolled at 982°C/954°C roughing/finishing passes to nominal .5 to 3.7mm sheet, annealed at 1038°C/10 min/AC, and stabilized at 593°C/2 or 8 hr/AC. Then, the sheet was finished by belt grinding.

<u>Alpha-Beta Sheet</u>. Alpha-beta sheet was produced from 7.5° cm slab alpha-beta cross-rolled to nominal .5 to 3.7mm sheet from 982°C/954°C roughing/finishing passes, and annealed at 954°C/10 min/AC. Then, the sheet was finished by belt grinding.

Testing Procedures

Tensile tests were performed according to ASTM E8 and fatigue-crack-growth testing of center-cracked tension specimens according to ASTM E647-88 on various thicknesses of sheet. The crack-growth tests were conducted in room temperature laboratory air at 58 to 61% relative humidity and an R ratio of .10 and a frequency of 20 Hz sinusoidal. The tensile results in Part 1 of this report are the average of at least two tensile tests performed transverse and longitudinal to the final rolling direction.

Elevated-temperature creep and stress-rupture testing was done on samples machined into the same configuration as the tensile samples. Elevated-temperature tensile testing, stress-rupture and creep testing were conducted in air.

Tensile Results. Table I lists the results for .45 to 1.6mm sheet. Table II lists the tensile results for 2.7 to 3.17mm sheet tested parallel to (L) and perpendicular to (T) the final rolling direction. A slight drop in tensile ductility at 593°C occurred in the beta annealed material stabilized at 593°C/2 hr versus the 8 hour stabilization cycle. All other tensile properties were similar with stabilization cycles of 2 or 8 hours.

The tensile results indicate that the alpha-beta rolled material is lower strength but higher ductility than the beta annealed or the beta rolled material. The beta rolled material shows more directionality than the beta annealed material. In beta annealed sheet, the 2.7 to 3.17mm sheet contains higher ductility than the .45 to 1.6mm sheet. The lower ductility in the thinner sheets is believed to be caused by the fewer number of grains through the thickness of the sheet as compared to the thicker sheet.

<u>Crack Growth Rate Results</u>. The center-crack fatigue crack growth tests were performed on sheet which was alpha-beta rolled and then beta annealed at 1038°C/10 min/AC and stabilized at 593°C/8 hr/AC. Sheet gages of .8mm and 1.6mm thick were tested. Two samples of each were tested to cover a wide range of stress intensities. (See Figure 1).

Table I Tensile Properties of .45mm to 1.6mm Sheet (Average of Two Tests)

Condition	Temp. (°C)	Dir.	UTS (MPa)	.28 YS (MPa)	E1. (%)
B Rolled1	21	L	986	873	10.1
B Rolled1	21	T	1081	941	9.8
B Rolled1	593	L	626	528	10.5
ß Rolled ¹	593	T	725	588	8.5
B Annealed2	21	L	1038	907	9.0
B Annealed2	21	T	1017	921	11.0
ß Annealed2	593	L	681	578	7.0
B Annealed2	593	T	684	539	9.0
B Annealed3	21	L	1067	920	8
ß Annealed3	21	T	1063	883	9
ß Annealed3	204	L	878	712	12
ß Annealed3	204	T	877	720	13
ß Annealed3	315	L	804	619	12
ß Annealed3	315	T	797	633	12
B Annealed3	427	L	762	599	12
B Annealed3	427	T	771	606	12
ß Annealed3	538	L	755	578	9
B Annealed3	538	T	741	576	10
ß Annealed3	593	L	710	537	11
ß Annealed3	593	T	681	531	11
B Annealed3	649	L	647	519	10
ß Annealed ³	649	T	662	515	9
$\alpha + \beta$ Rolled ⁴	21	L	873	805	18
$\alpha + \beta$ Rolled ⁴	21	T	870	801	18
$\alpha + \beta$ Rolled	538	L	603	473	25
$\alpha + \beta$ Rolled ⁴	538	T	605	472	25
a + B Rolled4	593	L	603	487	27

^{1 954°}C/15 min/AC

Table II Tensile Properties of 2.7 to 3.17mm Sheet

Condition	Temp. (°C)	Dir.	UTS (MPa)	.24 YS (HPa)	<u>E1. (8)</u>
B Annealed1	21	L	1041	952	12
B Annealed1	593	L	692	558	12
B Annealed1	593	T	691	567	12
$\alpha + \beta \text{ Rolled}^2$	21	L	909	838	18.8
$a + B Rolled^2$	21	T	897	829	20.4
$\alpha + \beta \text{ Rolled}^2$	593	L	571	451	26
$\alpha + \beta \text{ Rolled}^2$	593	T	557	449	27.8

^{1 1038°}C/10 or 15 min/AC + 593°C/2 hr/AC

^{21038°}C/10 min/AC + 593°C/2 hr/AC

^{31038°}C/10 min/AC + 593°C/8 hr/AC

^{4 954°}C/15 min/AC

^{2 954°}C/15 min/AC

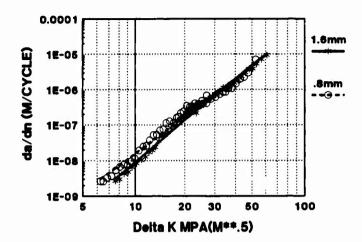


Figure 1 - Fatigue-crack-growth plot of beta annealed sheet at room temperature. R = .10, Frequency = 20 Hz.

Figure 1 shows a somewhat higher crack-growth rate for the .8mm sheet at the lower stress intensity range. However, the crack growth rate is virtually identical for stress intensities above 20 MPa $\,\mathrm{m}^{-5}$

Stress Rupture and Creep Results. The results of the creep testing (time to .2% elongation) are shown in Figure 2. These times are significantly greater for beta annealed or beta rolled sheet than for alpha-beta rolled sheet. The Larson-Hiller parameter is .6 to .7 higher for the beta annealed or beta rolled sheet than alpha-beta processed sheet. This translates into about a 26 to 31°C advantage for the beta annealed or beta rolled sheet. There are no significant differences between the beta rolled and the beta annealed sheet.

Stress rupture results are shown in the Larson-Miller plot in Figure 3. There are no significant differences between the beta rolled and the beta annealed sheet. However the Larson-Miller parameter is .6 to 1 greater for the beta annealed or beta rolled sheet compared to alpha-beta processed sheet. This translates into a 26°C to 44°C advantage for the beta annealed or beta rolled sheet.

Part 1 Conclusions

- a) The alpha-beta-rolled and annealed sheet has much better ductility but lower strength than the beta-annealed or beta-rolled sheet.
- b) The beta-rolled sheet contains more directionality than the beta annealed sheet.

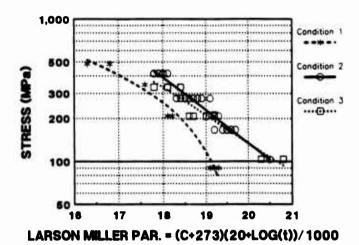


Figure 2 - Larson-Miller plot of creep to .2% total elongation of alpha beta or beta annualed sheet. Condition 1 is alpha + beta rolled + 954°C/15Min/AC. Condition 2 is alpha + beta rolled + 1038°C/10Min/AC + 593°C/2 or 8 Hrs, and Condition 3 is beta

rolled + 593°C/8Hr/AC.

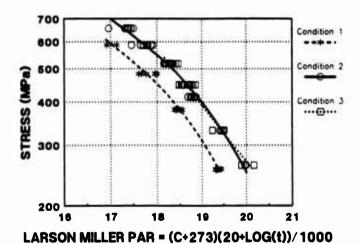


Figure 3 - Larson-Miller plot of stress-rupture of alpha-beta rolled, beta rolled, or beta annealed sheet. The conditions are the same as in Figure 2.

c) The thinner gauges show a lower ductility in the beta annealed sheet than the thicker sheet. d) Stress rupture and creep results indicate a significant advantage (26 to 44°C) in creep or stress rupture strength in beta-annealed or beta rolled sheet over alpha-beta processed sheet.

Part 2 Beta Annealing and Stabilizing Temperatures

The effect of beta annealing temperature was investigated on both alphabeta and beta rolled sheet. Two temperatures, 1038 and 1093°C, were used. Two tensile tests were run for each longitudinal and transverse to the final rolling direction and the results were averaged.

Table III is a list of the tensile results from .45 to 1.6mm sheet which was either alpha-beta rolled or beta rolled at 1038°C prior to beta annealing at 1039°C or 1093°C.

Table III Room Temperature Tensile Properties of .45 to 1.6mm Sheet Alpha-Beta or Beta Roll and 1038°C vs. 1093°C Anneal

Stabilizing Temp. (°C)	Dir.	UTS (MPa)	.29 YS (MPa)	El. (%)
593	L	1070	943	8
593	T	1082	978	9
593	L	1058	1058	2
593	T	1124	1083	4
593	L	1059	1001	3.1
593	T	1077	985	4.1
593	L	1114	1052	3.0
593	T	1128	1080	3.0
	Temp. (°C) 593 593 593 593 593 593 593 593	Temp. (°C) Dir. 593 L 593 T 593 L 593 T 593 L 593 T 593 L 593 L	Temp. (°C) Dir. UTS (MPa) 593 L 1070 593 T 1082 593 L 1058 593 T 1124 593 L 1059 593 T 1077 593 L 1114	Temp. (°C) Dir. UTS (MPa) .2% YS (MPa) 593 L 1070 943 593 T 1082 978 593 L 1058 1058 593 T 1124 1083 593 L 1059 1001 593 T 1077 985 593 L 1114 1052

¹Alpha-beta rolled

The 1093°C anneal cycle significantly degrades the ductility in alpha-beta rolled sheet as compared to the 1038°C anneal cycle. Ductility is low in both cases for the beta rolled material.

The effect of the stabilization cycle in alpha-beta rolled sheet which was beta annealed at 1038 or 1093°C was determined next. Sheet 2.54mm thick was given three separate 8 hour stabilization treatments at 593°C, 649°C, or 704°C. The results are given in Table IV.

Table IV Effect of Stabilization Temperature in 2.54mm Sheet

Stabilizing Temp. (°C)	UTS (MPa)	.28 YS (MPa)	E1. (3)
593	1118	990	4.8
649	1114	998	5.0
704	1107	939	4.0
593	1097	1008	2.3
649	1082	1031	1.5
704	1058	970	1.5
	593 649 704 593 649	Temp. (*C) UTS (MPa) 593 1118 649 1114 704 1107 593 1097 649 1082	Temp. (*C) UTS (MPa) .2% YS (MPa) 593 1118 990 649 1114 998 704 1107 939 593 1097 1008 649 1082 1031

²Beta rolled

There is little difference among the three 8 hour stabilization temperatures at 593°C, 649°C, or 704°C in either the 1093°C or the 1038°C beta annealed sheet. But again, the 1093°C beta anneal is shown to significantly reduce the ductility compared to the 1038°C anneal. Note that the 2.54mm sheet in the 1038°C/30 min/AC + 593°C/8 hr/AC condition contains a significantly lower ductility than the .45 to 1.6mm sheet. Currently, there is no explanation for the drop in ductility in the thicker sheet. Grain size was not significantly different and therefore was not a factor.

Part 2 Conclusions

- a) This data suggests that the preferred method to make creep resistant sheet would be to alpha-beta roll, beta anneal at 1038°C/15 min/AC in sheet less than 6mm and stabilize at 593°C/8 hr/AC.
- Beta annealing at 1093°C after alpha-beta rolling significantly reduced ductility.

Summary

Mechanical properties for TIMETAL+1100 sheet were developed. Creep and stress rupture properties are enhanced by beta annealing or beta rolling but at the expense of ductility. In order to retain maximum ductility in beta annealed material, the annealing temperature should be kept as low as is practical. Depending upon the requirements of the application, the appropriate processing route can be specified.

^aG A Fitzpatrick and ^bJ M Cundy Rolls-Royce plc, Aerospace Group, UK

^aP.O. Box 3 Barnoldswick, Colne Lancs BB8 5RU UK bP.O. Box 31 Derby DE2 8BJ

Abstract

Rolls-Royce has designed and developed a unique, highly efficient lightweight fan for civil engine applications in the thrust range 22000 lbs to over 90000 lbs. These wide chord fan designs are hollow and snubberless, and have applied innovative metal forming, metal joining and inspection techniques.

First generation wide chord fan blades entered service in the RB211-535E4 powered Boeing 757 in 1984. The technology has since been applied to the IAE V2500 engine for the Airbus Industries A320 and the McDonnell Douglas MD90 aircraft, and the RB211-524 G/H powerplants for Boeing 747 and 767 aeroplanes. This fan design utilises a fabrication of two external titanium alloy panels and an internal titanium alloy honeycomb core joined by Activated Diffusion Bonding.

The design and corresponding manufacturing technologies for larger fans in the higher thrust Trent series of aeroengines have now evolved to enable Rolls-Royce to specify an even lighter fan blade with enhanced cost and quality control advantages by exploiting solid-state diffusion bonding for joining the fabrication and superplastic forming to develop the supporting internal core. These second generation wide chord fan blades have been subjected to intensive pre-certification integrity and durability tests which have verified design and mechanical integrity and, most importantly have demonstrated the maturity of the manufacturing processes.

1. Introduction

The fan in modern "high by-pass ratio" civil turbofan engines must deliver a high level of performance over a wide range of operating conditions. Its primary design requirement is to minimise fuel consumption by maximising the propulsive force generated from the power supplied by the turbine. Weight, cost, noise, foreign object impact resistance and mechanical integrity under fatigue conditions are other essential design considerations.

Titonium '92
Science and Technology
Edited by F.H. Froes and I. Caplan
The Minerals, Metals & Materials Society, 1993

Conventional fan blades are manufactured from solid titanium alloy forgings and are designed with mid-span snubbers to counteract aerodynamic instability (Figure 1a). However, the snubbers impede the supersonic airflow causing a loss in aerodynamic performance with corresponding penalties in fuel consumption. Rolls-Royce has, therefore, removed the snubber from the fan to provide the most aerodynamically efficient aerofoil, increased its chord for natural stability, and reduced the number of blades per assembly by approximately a third (Figure 1b). This has been achieved at reduced weight by designing a hollow wide chord fan blade with an internal supporting core which can satisfy severe operational requirements. (References 1,2)

Its position at the front of the engine demands that the fan is capable of developing sufficient power for aircraft safety after suffering impacts, predominantly by birds, during take-off. Certification regulations require an engine to be capable of ingesting groups of lib birds with subsequent continual running at a minimum of 75% power. Also, an engine must be capable of a safe shut-down after the ingestion of 41b birds. Fan blades are subjected to low cycle fatigue stresses during every flight and to high cycle fatigue stresses from air intake disturbances at specific flight conditions. Stresses within the component have, therefore, to be maintained within established limits in order to guarantee adequate fatigue life.

To satisfy these design criteria, Rolls-Royce has developed hollow wide chord fan blades with low density cores for enhanced aerodynamic efficiencies as well as component lightness and mechanical integrity. The constructions of the designs are shown schematically in Figure 2. For both fabrications, the external titanium alloy skins are separated and supported by an internal titanium alloy core. Panel/panel joints and core/panel joints must exhibit parent material properties to withstand the effects of impact and fatigue. In the latest design, the established honeycomb core is superseded by a superplastically formed corrugation which allows the production of a lighter construction with reduced manufacturing costs.

2. Wide Chord Fan Manufacturing Technologies

Innovative metal forming, metal joining and inspection techniques have been developed by Rolls-Royce for the manufacture of its wide chord fan blades. First generation designs have been manufactured as a fabrication of external titanium alloy panels and an internal titanium alloy honeycomb core joined by a liquid-phase diffusion bonding process, Activated Diffusion Bonding (reference 3). The latest designs and corresponding manufacturing methods for Trent fan blades have now evolved to exploit solid-state diffusion bonding for joining the fabrication and superplastic forming for the development of the internal corrugated core.

The Trent wide chord fan blade is manufactured as a fabrication of three sheets of the titanium alloy, Ti-6Al-4V. An inhibiting compound is applied to the mating faces of the external panels in a pattern derived from the developed design for the internal corrugated core. Diffusion bonding can then occur at all surfaces which are not coated with the inhibitor. The three-piece

fabrication is selectively joined in a custom-built high temperature pressure vessel under computer control. Appropriate process control guarantees the generation of diffusion bonds with parent material mechanical properties (reference 4) and develops the microstructure shown in Figure 4.

The manufacturing sequence then exploits the inherent superplasticity of these fine-grained titanium alloys. The cavity of the diffusion bonded construction is inflated at elevated temperature between appropriately contoured metal dies using an inert gas to expand the core by superplastic forming whilst simultaneously developing accurately the blade's external aerodynamic profile in terms of radial bow, axial camber and aerofoil twist. This process is carried out in customised presses in a computer-controlled operation to guarantee the strict tolerances necessary for component temperature distribution as well as the strain-rate of the internal core.

Considerable experimentation has been carried out to establish diffusion bonding and superplastic forming as viable manufacturing technologies for critical hollow aeroengine component designs. Second generation wide chord fan blades also benefit significantly from reduced manufacturing costs due to their simplified manufacturing sequence.

To satisfy the stringent product assurance standards required for the service environment, all hollow wide chord fan blades are critically inspected for component integrity using a variety of sophisticated non-destructive techniques supplemented by conventional methods. In particular, Rolls-Royce has specifically developed and refined ultrasonic and radiographic techniques for the assessment of solid-state diffusion bonds and structures developed by superplastic forming. This in turn has enabled the manufacturing processes to be fully understood and matched with the requirements of the design specification.

Rolls-Royce has commissioned a unique manufacturing module with special-to-product plant and equipment for the production of wide chord fan blades (Figure 3). The operation also benefits from the implementation of systems engineering principles for the effective manufacture of high quality components.

3. Wide Chord Fan Integrity

First generation wide chord fans have been in service since 1984 and have accumulated over five million hours of Rolls-Royce exclusive operational experience. Second generation wide chord fan blades for the Trent series of aeroengines have now been subjected to intensive engine and rig component tests which have verified the design and associated manufacturing technologies. These test programmes have been successfully completed, and have confirmed metallurgical integrity as well as the maturity of the enabling manufacturing processes, diffusion bonding and superplastic forming.

A series of single-arm and bladed rotor bird ingestion tests has been carried out using Trent demonstrator wide chord fan blades. This programme has demonstrated that the airworthiness requirements have been significantly exceeded. Figure 5 demonstrates the 81b bird

ingestion capability of the second generation wide chord fan design at maximum climb ratings. Impact damage is confined to local distortion in the strike area with no metal loss.

Diffusion bonded and superplastically formed Trent wide chord fan blades have been subjected to fatigue testing in both low cycle and high cycle modes. Groups of components have been repeatedly accelerated to maximum speed in a large vacuum rig until failure is induced to determine low cycle fatigue endurance. Fan blade behaviour under high cycle conditions has been measured on a static flap vibration rig to stress levels determined from engines subjected to severe cross wind conditions. This fatigue test programme has demonstrated that the second generation fan design exceeds the capability of the initial design standard with its established integrity and service record.

4. Summary

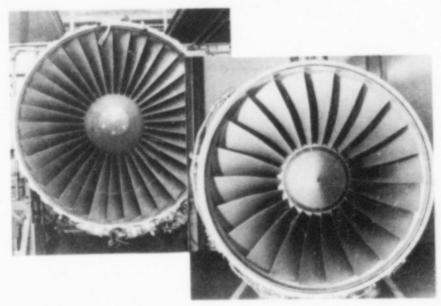
First generation wide chord fan designs have demonstrated reduced fuel consumption and increased resistance to component and engine damage over five million hours of Rolls-Royce exclusive operational experience. Second generation wide chord fans have now been specified for the higher thrust-rated Trent aeroengines with inherent weight and cost advantages. This latest design exploits diffusion bonding and superplastic forming, and has successfully completed component integrity and durability testing. The Trent series of powerplants has been launched for Airbus Industries A330 and the Boeing 777. They are also available to power the McDonnell Douglas, MD12.

References

- R E Dawson, D G Pashley, J E Melville. "Technology of the Wide Chord Fan Blade", <u>American Institute of Aero-nautics and Astronautics/ASME/SAE/ASEE</u>, 22nd Joint Propulsion Conference, Huntsville, Alabama, USA, June 1986.
- D J Nicholas. "The Wide Chord Fan Blade a Rolls-Royce first", Eighth International Symposium on Air Breathing Engines, Cincinnatti, Ohio, USA, June 1987.
- G A Fitzpatrick, T Broughton. "The Rolls-Royce Wide Chord Fan Blade", <u>International Conference on Titanium Products and Applications</u>, <u>San Francisco</u>, <u>California</u>, <u>USA</u>, October 1986.
- G A Fitzpatrick, T Broughton. "The Diffusion Bonding of Aeroengine Components", Sixth World Conference on Titanium Cannes, France, June 1988.

Acknowledgements

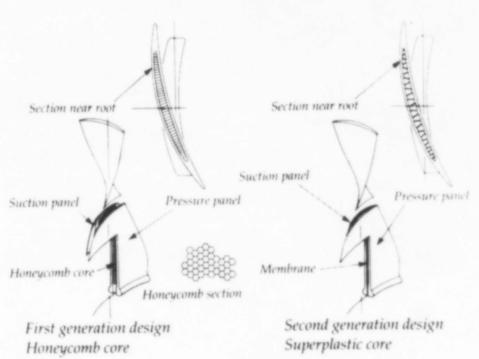
The authors wish to thank Rolls-Royce plc for permission to publish this paper. They would also like to recognise the contributions made by many colleagues at Barnoldswick and Derby to the developments reported.



(a) RB211-535C Snubbered Fan

(b) RB211-535 E4 Wide Chord Fan

Figure 1 - Fan Blade Designs



Pigure 2 - Construction of Rolls-Royce Wide Chord Fan Blades

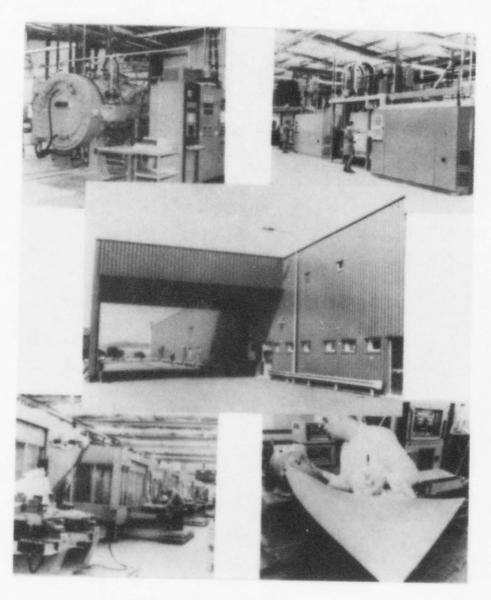
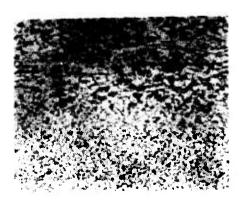


Figure 3 - Wide Chord Fan Blade Manufacturing Module



Joint Line

0,2mm

Figure 4 - Solid State Diffusion Bond Ti-6Al-4V

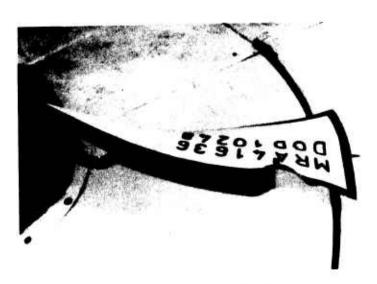


Figure 5 - Trent Fan Blade after 81bs Bird Ingestion Test

ADDENDUM

PRESSURE WELDING PROCESS WINDOW FOR TI-6AL-4V

R.E. Sundell*, M.F.X. Gigliotti*, and L. Hellemann**

*General Electric Corporate Research and Development, Schenectady, NY
**General Electric Aircraft Engines, Evendale, OH

ABSTRACT

A process window for pressure welding Ti-6Al-4V fan airfoils to forged hubs was determined by sub-scale tests in a Gleeble Model 1500 equipped with a vacuum chamber and an imaging infrared pyrometer. This work was part of a United States Air Force Manufacturing Technology Program directed toward fabrication of integrally bladed rotors for the fan components of advanced aircraft propulsion systems. Test matrices evaluated the effect of weld interface temperature, weld upset, and weld upset-rate on weld quality. Process temperatures included all-beta welding, through-transus welding, and alpha-plus-beta welding.

Charpy V-notch impact energy and metallographic results were used to evaluate weld quality. Tensile behaviors were uniformly equivalent to the base metal average and were not useful for process window definition. No statistically significant trend of Charpy energy with upset velocity was noted for upset velocities extending from 0.1 to 10 inch/sec (0.25 to 25 cm/sec). The only process parameter that had a statistically significant effect on weld Charpy values was the weld interface temperature. A preferred process weld temperature range was identified and weld microstructures were correlated with process parameters and weld quality.

This work was carried out under U.S. Air Force Contract F33615-85-C-5014.

Introduction

The use of integrally bladed rotors (IBRs) in the fan components of advanced aircraft propulsion systems will offer significant advantages over conventional blade-disk configurations in terms of efficiency and weight. However, to apply this technology presently requires time-consuming and costly manufacturing methods. In addition, an industrial base does not exist for cost-effective production of such components in large quantities.

This work, as part of the Air Force Manufacturing Technology Program to establish costeffective manufacturing technologies, was directed toward joining Ti-6Al-4V fan airfoils to
forged hubs by the pressure welding (or upset welding) process. This solid-state welding
process is described in Reference 1. The work was carried out under Air Force Contract
F33615-85-C-5014. The particular objectives were to determine the process window for
full-scale pressure welds to be made at General Electric Aircraft Engines (GEAE) and to
relate weld quality to weld microstructure.

Titanium '92 Science and Technology Edited by F.H. Froes and I. Caplan The Minerals, Metals & Materials Society, 1993 A finite element model of the pressure welding process has been developed at the General Electric Research and Development Center (GE-CRD) as described in Reference 2. The results of this experimental program were used to validate this model (See Ref. 2).

Experimental Procedure

Weld tests were conducted using rectangular specimens of Ti-6Al-4V with cross section 1.750×0.250 inches (4.45×0.635 cm) in order to simulate at subscale the blade-to-hub attachment collar geometries. The cross-sectional dimensions were approximately 1/4 scale. The 1.500 inch (3.81 cm) long specimens were cut from a forged titanium bar along the rolling direction. The finish on the weld surfaces was 20 to 30 μ -inch (0.51 to 0.76 μ m).

A micrograph of the base material is shown in Figure 1. The microstructure is typical of a material forged above the beta transus with a small amount of further work just below the beta transus (3). The beta transus temperature for the base material was experimentally determined to be approximately 1815 °F (990 °C). The orientation of the Charpy and tensile specimens relative to the parent stock is the same as for the welded samples. The mean and standard deviation(σ) of the Charpy and tensile values for the parent stock are shown on the Charpy and tensile plots for the welded samples.

Before bonding, the samples were cleaned by acid pickling in a solution of nitric and hydrofluoric acid with water. The samples were then rinsed with deionized water.

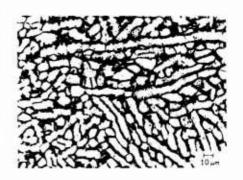


Figure 1. Ti-6Al-4V base material.

Welds were made at a vacuum level of 5×10^{-5} torr using a Gleeble Model 1500 System (4). A unique imaging infrared pyrometer described in Reference 5 was used to measure temperatures over the top surface of the weld specimens. Two test matrices were completed that evaluated the effect of weld interface temperature, weld upset, and weld upsetrate. These are specified as Test Matrix 1 and 2. A different welding cycle was used for each test matrix as described below. In addition, a small test series was conducted using parent material with a microstructure more typical of forgings used for IBR fabrication.

Tensile specimens, Charpy V-notch specimens, and metallurgical sections perpendicular to the bond surface were machined for each test point. Before being cut up, all samples were heat-treated for two hours in an air furnace at 1300 °F (704 °C) and then furnace-cooled to relieve stresses. The Charpy and the tensile test pieces were subsize (Charpy = 1.0×0.61 cm cross section). Mechanical tests were conducted at room temperature.

Test Matrix 1

The Gleeble welding cycle used for Test Matrix 1 is shown in Figure 2. The post-weld cooldown rate was controlled at 3.7 °F/sec (2.0 °C/sec). Preliminary tests with a rapid post-weld cooldown rate of 60 °F/sec (33 °C/sec) produced a martensitic structure in the bond region.

The statistically designed test matrix for Test Matrix 1 included weld interfacial temperatures ranging from 1600 °F (871 °C) to 2100 °F (1149 °C), weld upset-rates of 0.1 to 10

Upset is defined here as the ram stroke as a percentage of the sample thickness (t = 0.250 in.)

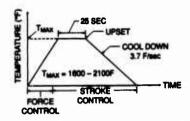


Figure 2. Gleeble welding cycle for Test Matrix 1.

inch/sec (0.25 to 25 cm/sec) and weld upsets of 50 and 100%. Upset-rate test scans were conducted both above and below the beta transus temperature (at 1900 and 1700 °F, respectively) to determine if high upset velocities enhance bond quality. Two specimens were welded at each test condition.

Results

<u>Tensile Results</u>. Tensile results for this series show little variation for the range of parameters tested and are approximately the same as the base material as indicated in Figure 3.

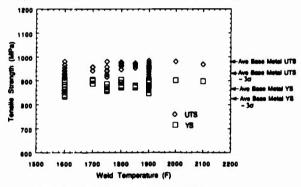


Figure 3. Tensile results for Test Matrix 1.

Charpy V-notch Results. The Charpy V-notch results are shown in Figure 4. The results show a maximum between 1850 °F (1010 °C) and 1950 °F (1066 °C) and a rapid decline below 1800 °F (982 °C). The statistical "F-Test" (6) was used to test for any trend of Charpy impact energy with weld upset or upset-rate. No statistically significant trend was indicated.

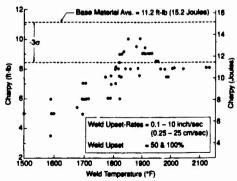


Figure 4. Charpy V-Notch impact energy for Test Matrix 1 welds.

Microstructure. Metallographic sections were taken perpendicular to the bond surface in order to correlate Charpy energies with weld microstructures. Figures 5 and 6 show microstructures for samples welded at temperatures ranging from 1600 °F (871 °C) to 2100 °F (1149 °C) with the bond line oriented vertically in the center of each photograph. The structures of samples welded at 1600 °F (871 °C) and 1700 °F (927 °C) show a large volume fraction of primary alpha grains. The grains appear continuous and aligned in the bond region in a direction consistent with the plastic deformation which occurs during upset. The continuous and aligned alpha grains may create a fracture plane resulting in the low Charpy impact energies as noted on the figure. The microstructure at 1800 °F (982 °C) shows less primary alpha but still contains some aligned alpha grains that may again be related to the low Charpy impact energy for this weld.

For the samples welded above the beta transus (Figure 6), the micrographs show transformed beta in the bond region. The prior beta grains increase in size as the weld temperature increases from 1900 °F (1038 °C) to 2100 °F (1149 °C). Here the Charpy impact energies are higher. Fracture, in this case, generally depends on the orientation of the prior beta grains and grain boundaries. Irregular orientation of the beta grains usually results in irregular fracture patterns and high Charpy toughness. Microstructures containing very large prior beta grains may, however, show more scatter in Charpy toughness depending on the relative orientation of the grains and grain boundaries and the notch on the Charpy specimen.

Test Matrix 2

The Charpy results from Test Matrix 1 showed that weld interface temperatures should be above 1800 °F (982 °C). Since the weld zone will then generally exceed the beta transus temperature of 1815 °F (990 °C) because of operating tolerances, the welding cycle for Test Matrix 2 was chosen to break up and distort the large prior beta grains that exist at these welding temperatures. This microstructure was expected to reduce scatter in Charpy impact toughness and enhance fatigue properties of the weld.

The Gleeble welding cycle used for Test Matrix 2 is shown in Figure 7. The upset for this test series occurred over the cooldown time from T_{max} to 1780 °F (971 °C) (i.e., during cooldown to below the beta transus). This upset process is designated "beta forging." Below 1780 °F, a controlled cooldown rate of 3.7 °F/sec (2 °C/sec) was maintained.

Test Matrix 2 included weld interfacial temperatures (T_{max}) ranging from 1750 °F (954 °C) to 2150 °F (1177 °C) and weld upsets from 30 to 100%. This matrix was designed to establish temperature limits for the process window. Two specimens were welded at each test condition. Mechanical tests were conducted as in Test Matrix 1.

Results

<u>Tensile Results</u>. Tensile results for this test series again show little variation for the range of parameters tested and are approximately equal to the base material values as indicated in Figure 8.

Charpy Results. As shown in Figure 9, the results from Test Matrix 2 also show a decline in Charpy toughness below 1800 °F (982 °C). Charpy values at lower temperatures (i.e., below 1700 °F) would continue to decrease as in Test Matrix 1 since the weld cycles for T_{max} below the beta transus were identical for Test Matrix 1 and 2. Above 1800 °F, the majority of the points were within the 3σ limit of the base material value. No trend of Charpy value with weld upset was noted.

<u>Microstructure</u>. As with Test Matrix 1, metallographic sections were taken to correlate Charpy impact energy with weld microstructure. Again, the weld cycle is identical for Matrix 1 and 2 for T_{max} below the beta transus, and the microstructures for the samples

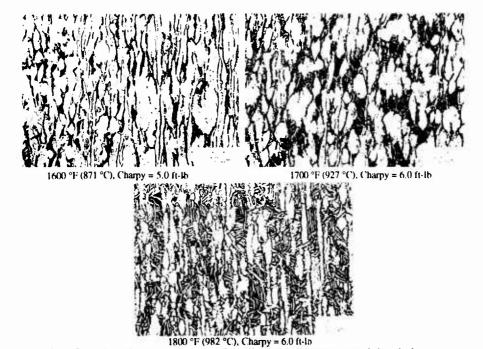


Figure 5. Comparison of weld microstructures for different interface temperatures below the beta transus. Upset = 100%.

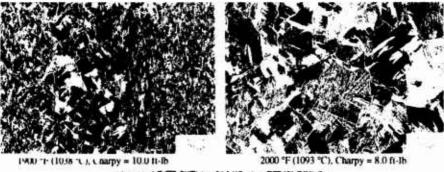




Figure 6. Comparison of weld microstructures for different interface temperatures above the beta transus. Upset = 100%

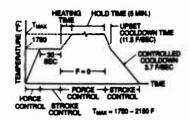


Figure 7. Gleeble welding cycle for Test Matrix 2 and STOA test series.

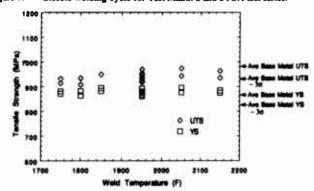


Figure 8. Tensile results for Test Matrix 2.

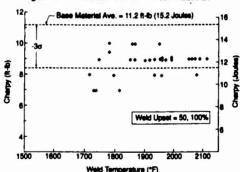
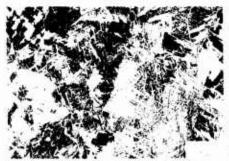


Figure 9. Charpy V-Notch impact energy for Test Matrix 2.

welded below 1815 °F are similar to those at the same temperatures in Matrix 1. The structure of samples welded at 1950 °F (1066 °C) in Figure 10 shows the effect of beta forging on the prior beta grains. In comparing 30 and 100% upset in the figure, it is evident that the greater upset increased the distortion and the breakup of the prior beta grains. High Charpy values were measured for each structure.

STOA Test Series

The Ti-6Al-4V base material used in this program had a different microstructure (i.e., a high volume fraction of alpha plates) than typically used in the forgings for actual IBR fabrication. This base metal microstructure (see Figure 1) is associated with the textured lamellar grain structure observed in some welds. This textured grain structure was oriented in the



1950 °F (1066 °C), Charpy = 9.0 ft-lb, 30% Upset, Beta Forged



1950 °F (1066 °C), Charpy = 9.0 ft-lb, 100% Upset, Beta Forgod

Figure 10. Microstructure of beta-forged welds with 30 and 100% upset.

direction of the plastic "flow lines" in regions of the weld zone that did not exceed the beta transus temperature. The textured structure may be associated with a failure mode. Therefore, a small test series was conducted using Ti-6Al-4V base material with the same microstructure to be used in actual hardware.

Base Material

To obtain material with an acceptable microstucture, bars of the original Ti-6Al-4V base material were "solution-treated/overaged" (STOA) in-house to eliminate the high volume fraction of alpha plates. The STOA heat treatment consisted of 1770 ± 10 °F (965 °C) for two hours, followed by a water quench and a further age at 1110 °F ± 20 °F (600 °C) for four hours. The resulting STOA microstructure is shown in Figure 11. This microstructure consists of a much lower volume fraction of discrete primary alpha in a transformed beta matrix.

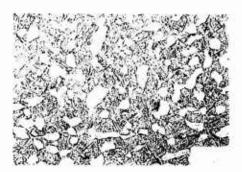


Figure 11. STOA microstructure.

Charpy Results

The test matrix for this series included weld temperatures ranging from 1850 °F (1010 °C) to 2050 °F (1121 °C) and weld upsets from 50 to 100%. The Charpy impact results for the STOA material are shown in Figure 12 along with the results for Test Matrix 2 for comparison. Charpy values for the welded STOA material are generally higher than those for welds made with the original material. Also, the STOA Charpy values show less scatter.

Conclusions

- The Charpy and metallographic results indicate that it would be desirable to choose a beta forging welding process with a temperature window extending from 1850 °F (1010 °C) to 2050 °F (1121 °C). An acceptable window on upset extends from 50 to 100%.
- No statistically significant trend of Charpy impact energy with upset-rate has been noted for upset-rates extending from 0.1 to 10 inch/sec (0.25 to 25 cm/sec) and no trend of Charpy impact energy with percent upset (30 to 100%) was noted.

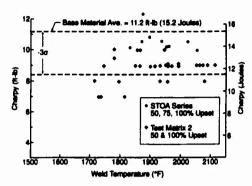


Figure 12. Charpy impact results for the STOA material and Test Matrix 2.

- Metallography showed that beta forging distorted and broke up the large prior beta grains. This microstructure is desired for high impact energies and good fatigue properties.
- 4. Tensile results were equivalent to the base material value.
- Charpy impact energies for welds made using STOA Ti-6Al-4V material are higher and show less scatter than the energies for welds made with non-STOA material.

Acknowledgments

The authors wish to acknowledge the technical and programmatic support of M.H. McLaughlin (GE/CRD) and of G. Wiggs and J. Kelley (Manufacturing Technology Laboratory/GE Aircraft Engine (MTL/GEAE)) who sponsored this work. Also, the authors cite the contribution of G. Dyson (MTL/GEAE) who did statistical analyses on the data. S. Godwin (GE/CRD) assisted in the Gleeble tests and R. Lillquist (GE/CRD) developed the imaging pyrometer which was vital in determining local temperatures on samples during the welding process. He was granted U.S. patent 4,687,344, August 18, 1987 for this invention.

References

- (1). W.H. Kearns, ed., Welding Handbook, 7th ed., vol. 3, (American Welding Society, 1980), 76.
- (2). H.A. Nied, "Finite Element Simulation of the Upset Welding Process," (Paper 91-GT-230 presented at the Int. Gas Turbine and Aeroengine Congress, Orlando, FL, June 3-6, 1991 and accepted for publication in Transactions of the ASME).
- M.J. Donachie, Jr., ed., Titanium and Titanium Alloys Source Book, (Metals Park, OH: American Society for Metals, 1982), 39, Plate 2723.
- H. Ferguson, "Metalworking Process Simulations Save Production Headaches," Metal Progress, Sept. 1986, 37-40.
- (5). R.D. Lillquist, "Imaging Pyrometer," U.S. Patent 4,687,344, April 18, 1987, assigned to General Electric Company.
- (6). G.E. Box, W.G. Hunter, and J.S. Hunter, Statistics for Experimentors, (John Wiley and Sons, 1978).

SUBJECT INDEX

A	Airbus, 2,873
α-Base Titanium Alloys, 2,081-2,086,	Aircraft Application
2,222-2,117	Landing Gear, 821
(α+β) Titanium Alloy (VT9), 1,955,	Weight Comparisons with
1.956	Steel, 821
Microstructure, 1,957	Aircraft Engine Alloys, 2,827
Silicon and Silicides, 1,956-1,959	Alloy Classification, 548
Low Cycle Fatigue, 1,955	Alloy Development, 16, 821, 828
	Alloy Theory, 27
Creep-Fatigue Interaction	Alloy
at RT, 1,956	IMI 318, 770
0T4-1 Alloy, 149	IMI 685, 770
5Al-2.5Sn-ELI Titanium, 121, 697,	IMI 829, 770
698, 700-702, 704	Alloying Elements, 643-650, 1,891,
β Phase, 697-704	1,895-1,897
α+β Type Titanium Alloys	Alloying, 547
Ti-6A1-4V, 853-860	Alloys
Ti-5A1-2.5Fe, 853-860	IMI 834, 311-318, 1,636-1,638
α+β Working, 1,934-1,936	Super Alpha, 1,638, 1,639
β Working, 1,934-1,936	Super Alpha 2, 1,187-1,194
Solution Treatment, 1,934-1,936	Ti-6Al-4V, 311-318, 1,636, 1,638
α-Widmanstatten, 1,843, 1,848	Ti-6242, 1,637
α ₂ Alloy, 1,163	
α+β Ti Alloy, 813, 814, 816	Ti-14Al-20Nb-3.2V-2Mo,
α+β Titanium Alloy, 247	1,187-1,194 Ti CALAV 1 007 1 004
α ₂ Alloys, 343	Ti-6Al-4V, 1,827-1,834
α ₂ Phase, 1,777, 1,778	Low Oxygen Content, 1,828,
α ₂ ,γ, 20, 21	1,829
Absorbed Oxygen, 2,426, 2,427	Microstructure, 1,829
Accicular Alpha, 113, 115, 118	Primary Alpha Grain,
Acoustic Emission, 2,548	_ 1,829, 1,833
Activation Energy, 683-688	Texture, 1,832
of Deformation, 979, 980,	Alpha + Beta Titanium Alloy, 1,387
983-985	Aplha-2, 1,971
Adiabatic Shear Failure, 1,939	Design Requirements for Gas
Aero Engine, 41	Turbine Engines, 2,907
Aerospace	Effect on Properties Ti Al-Sn-Zr
Applications, 2,843, 2,877, 2,916	Alloys, 83
Europe, 2,877	Gas Turbine Engine, 2,907
Properties, 2,805	Gas Turbine Engine Drives, 2,907
Age-Hardenable, 185	Aerofoils, 2,907
Aging, 824, 825	Phase, 1,147-1,150
Curves, 643-650	Titanium Aluminide, 367, 2,907
Isothermal Aging, 701-703	Alpha Case, 11
Kinetics, 643-650	Alpha Morphology, 643-650
Response Curves, 826	Alpha or Near Alpha Alloys, 82
Response Microstructures, 827	Microstructure /Properties, 82-85
ו וספףטוופס וזווטוטפווטטנעוספ, סבו	

Alpha Precipitation, 643-650	β-Titanium Alloy, 217
Alpha-Beta Alloys	B2 Phase, 837, 839-843, 845, 847,
Microstructure/Properties, 81-86, 88	851, 852, 903, 904, 908, 1,672, 1,673, 1,675
Titanium Alloy, 1,371	B4C, 2,561-2,568
ALPID, 4 Aluminum Equivalent, 2,903	Back Scattered Ultrasonic Noise,
	2,827 Beta Titanium Alloys, 2,209
Amorphous Phase, 938 Analytical Techniques, 2,843	Beta 21S, 153, 161-163, 447-454,
	2,088, 2,177, 2,179-2,183, 2,185-
Anisotropy, 497-504, 1,813, 1,814 γ Value, 1,911	2,192, 2,209, 2,212, 2,213, 2,214,
	2,192, 2,209, 2,212, 2,213, 2,214,
Grain Shape, 1,908, 1,909	-•
Annealing, 524	See Also: Ti-15Mo-2.7Nb-3Al- 0.2Si
Anodic Behavior, 2,217, 220, 2,221	*·=*·
Anodic Polorization, 2,743, 2,744,	Beta Alloys, 77-81, 86-88
2,747	Beta C, See: Ti-3Al-8v-6Cr-4Mo-4Zr
Applications	Beta Cez, 643, 650 See Also: Ti-5Al-2Sn-4Zr-2Cr-1Fe
Aerospace, 1,435 Automotive, 1,435	Beta Cez Titanium Alloy, 1,347
Centrifuges, 1,357, 1,362	Beta Cez, Beta 21S, SP700, BTT-1,
Chemical Processing, 1,357	BTT-3, Alloy C, 22
General Engineering, 1,435	Casting, 23
Heat Exchanger, 1,356, 1,357,	Fire Resistance, 22
	Medical, 22
1,362 Hydrocarbon Exploration, 1,357	MMC, 24
Offshore, 1,357, 1,435	Beta Grain Size, 77-81
Petroleum Industry, 1,357	
Arc Plasma Melting	Beta Isomorphous, 557 Beta Phase, 643-650
Plasma Flame, 2,407-2,414	Beta Stabilizers, 550, 822-825, 828,
Molten Titanium, 2,407-2,414	2,901
Arc Slag Remelting, 2,429, 2,430	Beta Titanium Alloy, 185
Artificial Intelligence, 5	Ti-15V-3Cr-3Sn-3Al, 580-586
As-Solidified Microstructure	Cold Strips, 586
Ti-52Al, 1,093, 1,094, 1,096	Beta Transus, 823
Athermal Decomposition, 643-650	Beta-C Titanium Alloy, 505
Athermal Omega, 643-650	Beta-C, 2,087, 2,088
Athermal Process, 706, 711	Beta-C™ Titanium, 2,095, 2,096, 2,098
Atomization, 8, 988	Beta-C [™] , 263, 415
Atomization, 0, 500	Beta-Ti Solid Solution Alloys, 1,779
	Beta Titanium Alloy
	Ti-15V-3Cr-3Sn-3Al, 482-488
Bling, 2,888	Bias Voltage, 2,119-2,124
β-21S, 161	Billet, 1,851, 1,852, 1,854-1,858
β-Cez Alloy, 89, 91, 95, 96, 97, 105,	Bimodal Microstructure, 129, 131
105, 110, 1,339	Blended Elemental, 794
β-Fleck, 523-515, 517-521	Bonding Strength, 1,609
β-Processing	
Microstructures, 281, 282	BT 3-1 Alloy, 603-605, 863

BT 5-1 Alloy, 603-605	Compact Tension (CT), 1,867, 1,868
BT 6 Alloy, 603-605	Component Cost, 8
BT 16 Alloy, 865, 862	Composite Toughening, 2,481
_	Composites, 2,467, 2,519
C —	Fibre Coating, 2,636-2,639
C-Curve, 559	In-Situ Strengthening, 407-411,
C.P. Ti, 2,751-2,752	413
Ca Ti F ₆ , 2,393, 2,396, 2,398	Metal Matrix Composites, 2,577,
Carbon Distribution 2,851, 2,855	2,578
Case Assembly, 2,893	Metal-Metal Matrix, 407-409
Case Depth, 10	SiC Fibre, 2,633, 2,634, 2,635,
Casting Mold, 10	2,637,2,638, 2,639
Casting Shell, 10	Titanium/Ceramic, 2,503 Ti-6Al-4V/SCS6, 2,578
Casting Shrink Defects, 12	Ti-6Al-4V/S1240, 2,578
Casting, 1,503, 2,756, 2,767, 2,769,	Ti6Al15V Matrix, 2,633-2,635,
2,895	2,638
Hot Isostatic Processing, 1,319-	Computer Aided Design, 4
1,328	Computer Aided Manufacture, 4
Investment Casting, 1,503	Computer Simulation, 1,387, 1,388,
Moulding Methods, 1,319-1,328	1,907
Mechanical Properties, 1,319-	Finite Element Method, 1,907,
1,328	1,911
Near Net Shape, 1,503	Material Model, 1,907-1,914
Quality, 1,319-1,328	Condensate, 2,425
Techniques, 1,319-1,328	Condenser Tube, 2,835, 2,836
Thermochemical Processing,	Condenser, 2,795-2,802
1,331-1,335, 1,337	Constituitive Modeling, 2,611-2,612
Castings, 10, 61, 801, 802 Caustic Resistance, 2,097	Constituting Model, 979
Cavity, 2,319, 2,320, 2,322	Constitutive Relations, 7
Shrinkage Cavity, 2,318, 2,320	Contaminants, 46
Shrinkage Cavity, 2,313, 2,320 Shrinkage Cavity Line, 2,320	Continuous Mill, 1,543
CCT Diagrams, 643-650	Cooling Diagram, 560
Centrifugal Casting, 2,756	Cooling Rates, 1,027, 1,028, 1,030
Ceramic Coated Tool, 2,027	Cooling Rate Effects
Ceramic Reinforcement, 2,468	Creep Properties, 314, 317, 318
Charpy Impact Energy, 1,875-1,878	Microstructure, 312, 313
China, 2,891	Corona 5 - See Ti-4.5A1-5Mo-1 5Cr
Cleavage Fracture, 327, 328, 331,	Corrosion
333, 1,155	Galvanic, 2798
Coating Properties, 2,537-2,544	Properites, 2,805
Coatings, 48	Resistance 2,737, 2,739, 2,740,
Cold Hearth, 59	2,087, 2,095, 2,104, 2,143, 2,145,
Melting, 2,363, 2,364, 2,365	2,157, 2,158
Refining, 2,347	Cost, 793
Cold-Rolled Titanium, 497-504	Crack Bridging, 2,529
Combustion Synthesis, 895, 896,	Crack Closure
2,519, 2,523	Plasticity Induced, 1,920, 1,921

Measurement, 1,920	Dislocations, 1,848-1,850
Load Ratio Effects, 1,921,	Twins, 1,848, 1,849
1,922	Strain, 1,845-1,848
Notch Root Plasticity, 1,921,	
1,922	D
Crack Growth Experiments, 1,075	da/dn, See: Fatigue Crack Growth
Crack Growth Rate, 1,869	Rate
See Fatigue Crack Growth Rate	Damping capacity, 2,675
Crack Growth Resistance, 1,155,	Titanium Aluminide, 2,681, 2,682
2,529, 2,531, 2,532, 2,533	Debonding, 2,611
Crack Opening Displacement, 1,073	Decomposition of b-Phase, 643-650
Crack Propagation, 331-333-Fatigue-	Deep Drawing, 1,859
Cracking, 2,025, 2,055	Defective Particles, 2,288, 2,289
Creep, 306, 1,251, 1,256, 1,257,	Defects, 2,806
1,653, 1,654, 1,656-1,658	Hard, 2,806
Testing, 1,717, 1,719, 1,723	Soft, 2,806
Bending, 1,718, 1,719	Statistics, 2,809
Equipment and Procedures	DEFORM, 4
to Minimize Bending, 1,718,	Deformation Behavior, 1,733-1,738
1,719	Deformation Induced Transformation
Creep Behavior, 439, 441	Martensite, 1,835, 1,841
Creep Crack Growth Behavior, 353	Twins, 1,835, 1,841
Creep Life, 328-331	Deformation, 683-688
Creep Properties, 2,790	Damage, 2,609-2,613
Creep Properties, 83, 84, 320-322,	Inelastic, 2,609, 2,610, 2,613,
466, 1,346, 1,593, 1,595-1,599, 1,774,	2,614
1,778	Mechanisms, 2,609, 2,613
Ti-6.2Al-2.7Sn-4Zr- 4Mo45Si,	Modeling, 2,612
83, 84	Plasticity, 2,609-2,611, 2,613
Ti-5.8AI 4Sn-3.5Zr7Nb5Mo-	Dendrite, 823
.35Si06C, 83, 84	Dental Application, 2,756
Creep Resistance, 343, 391	Denture Base, 2,773, 2,776, 2,777
Creep Rupture Strength, 1,060	Denuded Zone, 2,618, 2,620
Creep Rupture Tests, 2,594	SiC Fibers, 2,617
Creep Strengthening Mechanism,	Ti-24Al-11Nb, 2,617
1,709	Deoxidation, 1,211-1,218
Creep Test, 371, 1,123, 1,124, 1,128,	Descaling
2,594	Chemical Reaction, 2,153
Crevice Corrosion, 2,157, 2,158,	Molten Alkaline Bath, 2,149-2,150
2,193	NaNo3 Content, 2,149, 2,150
Cryogenic Mechanical Properties,	Oxidizing Bath, 2,149
121, 122	Pickling, 2,150
Cryogenic Temperatures, 1,827-1,829	Thermo-Mechanical Effect,
Crystallographic Texture, 1,812	2,152-2,153
CURV III Submersible Vehicle, 2,729	Densification, 9
Cyclic Fatigue, 2,601	Diffusion Barrier, 2,163
Cyclic Oxidation, 1,972, 1,975	Diffusion Bonding, 1,437-1,439,
Cyclic Softening, 1,843, 1,847	1,445, 1,451

Joint Formation	Electrochemical Charging, 2,010
Deformation-Time	Electrode, 2,303, 2,334, 2,751
Parameters, 1,445-1,450	Consumable Electrode, 2,317,
Alloy Structure, 1,447, 1,448	2,318, 2,322
Alloy Composition, 1,449	Electrolytic Manganese Dioxide,
Joint Configuration, 1,450	2,751-2,756
Multi-Sheet Structures,	Electromagnetic, 2,290
1,319-1,328	Electron Beam Cold Hearth Melting
Super Alpha-2, 1,629, 1,630	Condensate, 2,345
Bonding Variables, 1,628-1,630	High Density Inclusion(HDI),
Modelling, 1,626-1,628	2,341
Diffusion Welds, 1,453, 1,454	High Interstitial Defect (HID),
Dilatometric Studies, 755-757	2,341
DilatometricTests, 739	Maximelt, 2,339
Directional Solidification	Mold, 2340
Ti-52Al, 1.091, 1,098	Spatter, 2,345
Disk Failures, 2,807	ritanium Slab, 2,340
Dispersion Strengthening, 927	Electron Beam Melting, 59
Dispersoids, 431-438	Electron Beam Remelting, 2,345
Coarsening, 431-438	Electronic Bottle, 2,729, 2,733
Restraint of Grain Growth,	Electronic Grade Ti, 2,743
431-438	Electroplating
Rare Earth, 431-438	Titanium Electroplating, 1,997,
DOSS Process, 2,234, 2,265	1,998, 2,000, 2,001, 2,004
Drip Melting, 2,347	Pulse Electroplating, 2,000, 2,001
Drop Forging, 359	Metallograph of Titanium Coating
Ductility, 643-650	2,000, 2,004
Duplex Aging, 1,883	Electroslag, 2,377
Effect on Properties	Electroslag-Remelting, 2,331, 2,333
Ti-3Al-8V-6Cr-4Mo-4Zr, 79,	Electrowinning, 2,439, 2,441
80, 86, 87	Elevated Temperature Data, 2,063,
Ti-15V-3Cr-3Al-3Sn, 79, 80	2,607
Dynamic Friction Factor, 2,713-2,716	Elimination of Inclusion-Type Defects,
Dynamic Grain Growth, 8	2,416
Dynamic Tear Test, 233, 239	Embrittlement, 643-650, 2,081-2,086
Dynamic 16ai 16st, 255, 255	Endosseous Implants, 2,757
_	Energy Transition Temperature, 1,877
EB Evaporation, 651, 652	Engine Accidents, 2,806
Economics, 2,227	Engines, 2,833, 2,892
Eddy Current Test 2,835, 2,837	Environmental Cracking, 2,074
Effect of Alloying Elements, 2,081-	Environmentally Assisted Cracking,
2,086	_2,201, 2,209-2,215
Effect of Beta Stabilizers, 2,111-2,117	Environment
Electrical Beam Melting, 2,273	Fatigue, 1,221
Electrical Resistivity, 2,273, 2,743,	Oxidation, 1,221
2,746	Vacuum, 1,221
Electrolytic Refining, 2,273	Equiaxed Alpha, 113
Flectro Refining 2 371	Exhaust Valves, 2,681, 2,683

Expert Systems, 5	K _{MAX} , 1,197, 1,201		
Explosive Welding, 1,611	Low Cycle Fatigue, 2,578-2,579,		
Extrusion, 1,049, 1,100	2,582		
	Mechanism, 1,231		
F	Oxidation, 1,221, 1,222		
Failure Modes	Properties, 113, 118, 119		
Alpha/Beta Interface Cracking,	Resistance, 505		
1,698	R Ratio, 1,197, 1,200, 1,201		
Facetting, 1,771	Static Modes, 1,197		
Rooftop1,697, 1,770	Strength, 132, 1,831, 1,832		
Fan Frame, 11	Stress Intensity Factor Range,		
Fasteners, 1,559, 2,899	1,837, 1,839, 1,841		
Fatigue, 84-87, 1,852, 1,854-1,858	Temperature, 1,221		
Crack, 1,741-1,748	Tension-Tension, 2,578		
Crack Formation, 1,742,	Testing, 972 Three Boint Bonding, 2 579		
1,743, 1,745	Three Point Bending, 2,578 Ti-6Al-4V, 84-86		
Crack Growth, 1,803, 1,195-	Ti-6Al-2.7Sn-4Zr4Mo45Si, 85,		
1,198, 1,743, 1,744, 1,746-	86		
1,748, 1,819, 1,822	Ti-5.8Al-4Sn-3.5Zr7Nb.5Mo-		
Short Cracks, 1,741-1,748	.35Si06C, 85		
Threshold, 1,743, 1,744	Ti-3Al-8V-6Cr-4Mo-4Zr, 86, 87		
Crack Growth Rate, 84-88	Vacuum. 1,221, 1,222		
Ti-3Al-8V-6Cr-4Mo-4Zr, 86, 87	Fatigue Strength, 1,835		
Ti-6Al-4V, 84, 85	Fatigue Crack Propagation,		
Crack Closure, 1,835, 1,837-	1,835-1,841		
1,839, 1,841	Crack Closure, 1,835, 1,837-		
Crack Growth Resistance, 1,227	1,839, 1,841		
Crack Propagation, 1,376	Stress Intensity Factor Range,		
Crack Threshold, 85, 86	1,837, 1,839, 1,841		
Cyclic Loading, 1,237	Fatigue Crack Proagation, 2,578		
Elevated Temperature, 1,198	2,579, 2,583-2,584		
Environment, 1,221, 1,222	Fiber-Matrix Sliding, 2,611		
Fracture, 497-504	Fibre Push-Out Testing		
Failure, 2,867	Ti/SiC Fibre Composites, 2,650		
Frequency, 1,222	Ti-6Al-4V/SCS6, 2,650		
Grain Propagation	Ti-15-3/SCS6, 2,650		
a ₀ /w, 2,654	Ti β21s/SCS6, 2,650		
Bifurcation, 2,653	Fibre Reinforced Composites,		
Initial ∆K _{app} , 2,651	2,529-2,535		
Ti/SiC Fibre Composites,	Micromodeling, 2,529-2530, 253		
2,650	Crack Growth Resistance,		
Growth Rates, 1,751-1,755	2,531-2,534		
Small Cracks, 1,751-1,755	Fracture Mechanics Parameters		
Long Cracks, 1,751-1,755	2,529-2,530, 2,534		
Transitional ΔK 1,751-1,753,	Weight Function Analysis, 2,529		
1,755	2,530, 2,534		
Static Effects, 1,755	Fibre Reinforced, 2,529		

Fibre Reinforcement, 2,471	Ductile Fracture, 527-530
Finite Element Analysis, 4, 2,537-	Secondary Tored Cracks, 527-536
2,544, 2,724	Fracture Toughness, 77-82, 113, 115,
Principal Stresses, 1,792, 1,793	125, 217, 222, 343, 353, 371, 391,
Effective Stresses, 1,792, 1,793	466, 821, 825, 1,061, 1,180, 1,181,
Hydrostatic Stresses, 1,792,	1,374, 1,611, 1,614, 1,791, 1,852,
1,793	1,854-1,856, 1,875, 1,876, 2,676,
Finite Element Formulation, 1,439,	2,721
1,440	Ti-6-22-22, 1,649, 1,650
Finite Element Model, 1,403, 1,404,	Fretting Fatigue, 50
2,531	Fretting Test, 2,066
Forging on Microstructure, Effect	Friction Contact Adhesion, 2,006
of, 244	Friction, 2,006, 2,007
Forging Superalpha 2, 980	Fused Salt
Forging, 4, 1,387, , 996, 1,100, 1,101,	NaCl-KCl Fused Salt, 1,997,
1,107-1,109, 1,390	1,998
Open-Die Forgings, 1,357	Titanium Electroplating on Fused
Heavy Wall Thickness, 1,356,	Salt, 1,997, 1,998, 2,000, 2,001
1,357, 1,359, 1,362	Titanium Electrochemical Process
Low-Alloy Titanium, 1,355	in Fused Salt, 1,997, 1,998,
Hot-Forming, 1,358	1,999, 2,003
Forging Route, 1,358	1,000,000
Forging Facilities, 1,357, 1,358	0
Forming Pressure Profile, 6	γ, 48
Forming Process	Gamma Alloys, 383
Flow Forming, 1,430	Gamma TiAl, 1,091-1,098
Flow Forming at Elevated	As-Solidified Microstructure,
Temperature, 1,431	1,093, 1,094, 1,096
Forming Parameters, 1,430	Directional Solidification, 1,091-
Fractography, 126, 1,680, 2,598,	
2,599	1,098
Fracture	Hydrogen Effects, 1,092, 1,096,
Alpha-2 Alloys, 1,171-1,178	1,097
Intercrystalline Fracture, 730	Hypoperitectic Composition,
Transcrystalline Fracture, 730	1,091, 1,097
Ti-25Al-10Nb-3V-1Mo, 1,171-	Microprobe Analysis, 1,095, 1,096
1,178	Gamma Titanium Aluminide, 1,115-
Micromechanisms, 1,179	1,122, 2,907
Cleavage, 1,180	Casting, 1,487
Fracture Analysis, 1,474-1,476	Creep, 1,267-1,274
Fracture Behavior, 1,049, 1,050	Design Requirements for Gas
Fracture Mechanics, 2,725	Turbine Engines, 2,908
Fracture Mechanism, 105	Fracture Toughness, 1,267-1,274
	Gas Turbine Engine Aerofoils,
Fracture Surface, 2,051, 2,052	2,907
Fracture Topography	Gas Turbine Engine Drives, 2,907
Brittle Fracture, 527-530	Gas Turbine Engine Structures,
Cleavage Crack, 527-530	2.907

Microstructures, 1,267-1,274 Grain Size, Beta, 77-81 Mechanical Properties, 1,267-Effect on Strength, Ductility and 1,274 Toughness, 77-81 Ti-15V-3Cr-3Al-3Sn, 77-81 Properties, 1,492 Tensile, 1,267-1,274 Ti-3Al-8V-6Cr-4Mo-4Zr, 78-80 XD™, 1,487 Ti-10V-2Fe-3Al, 79 Gas Nitriding, 1,980 Beta Alloys, 77-81 Gas Nitro-Carbonizing, 1,980 Gravimetric Separation, 2,281 Gas Tungsten-Arc Welding, 1,116, Green Density, 2,522 1,117 Grindability, 1,617-1,623 Gas Turbine Engine, 2,907 GTA Welding, 1,470, 1,472 Design Requirements, 2,908 Titanium Aluminide Aerofoils. 2.907 Hardenability, 643-650 Titanium Aluminide Structures, Hardness, 643-650, 825, 826, 1,884-2,902. Titanium Aluminide Drives, 2,910 HDH Process, 919, 922 Gaseous Hydrogen Medium, 2,049, Hearth Melt Technology, 2,451 2.050 Heat Treatment (Treating) Glass-on-Aluminide Coating, 2,185 Effect on Properties, 1,648-1,652 Golf Club Heads, 61 Heat Treatment, 643-650 Grade 1 Ti, 2,194 Aging, 1,883-1,890 Grade 2 Ti, 2194 β Solution Treatment, 459-462 Grain Boundary, 826 Cold-Working, 1,883-1,890 Alpha (GBa), 643-650, 1,515 Cooling Rate, 460-462 Effect on Properties, 77 Duplex-Aging, 1,883, 1,884 Pinning, 774 Phase Transformation, 456, 457 Grain Diameter, 636 High Cycle Fatigue (HCF), 131-139, Grain Growth, 457, 635, 770-784, 824 303, 306, 307, 971-977, 1,375, Abnormal, 668, 673, 773,774 1.827 Activation Energy, 770-772, High Density Defects (HDD), 2,234 777-784 High Density Inclusion (HDI), 2,234, Critical Strain Level, 670-674 2867, 2,868 Effect of Phase Transformations, High Intersticial Defect, 2,867, 2,868 668, 670, 672, 674 High Pressure Hydrogenation (HPH), Grain Boundary Migration, 671-879, 882 674 High Purity Titanium, 56, 2,459, 2,464, Growth Order, 777-784 2,843, 2,847 Grain Growth Rate, 770-776 High Temperature X-Ray Diffraction, Kinetics, 643-650, 668, 588, 590, 592, 593, 596 670, 672 Hot Bar Rolling, 1,543, 1,545 Treatment in the β Temperature Hot Extrusion, 895, 896 Range, 668, 671 Hot Isostatic Pressing (HIP), 10, 383, Grain Size, 7, 643-650, 777-784, 824, 1,503 998, 1,617, 1,623, 1,902-1,904 Effect on Microstructure, 1,503, Grain Refinement, 456, 459 1,505, 1,506 Substructure,460, 461 Effect on Tensile Properties

1,503, 1,505, 1,506 Effect of Temperature 1,503, 1,505, 1,506 Effect of Pressure, 1,505, 1,506 Hot Rolling, 996 Hydride, 619-625 Hydriding, 2,801 Hydrogen Absorption, 2,087, 2,088, 2,089, 2,090, 2,093, 2,094, 2,100 Hydrogen Solubility in Ti, 2,153 Prevent from Absorption, 2,153 NaNO₃ Effect. 2.153 Bath Temperature Effect, 2153-2154 Descaling Time Effect, 2154 Sheet Thickness Effect, 2155 Hydrogen Assisted Stress Cracking, 2,055, 2,056 Hydrogen Effects, on. As-Solidified Microstructure. 1.096,1,097 Directionally Solidified Ti-52Al, 1,092, 1,096, 1,097 Hydrogen Embrittlement, 1,283, 1,867, 1,285, 2,049 Hydrogen Plasticization, 861 Hydrogen, 2,025, 2,055, 2,163 Hydrogen Modification, 1,694 Strain-Time Behaviour, 1,696 Fatigue Life, 1,694-1,696 Hydrovac Treatment (HVC), 871-873, Hypoperitectic TiAl Composition, 1,091, 1,097

Ilmenite, 2,247
IMI 550 Superplasticity
β-Phase Proportion, 1,532,
1,533
Deformation Variables,
1,529-1,531
Elongation to Failure, 1,531,
1,532
Grain Growth, 1,530, 1,531
IMI 829, See: Ti-6.1AI-3.2Zr-3.3Sn-1Nb-0.5Mo-0.32Si

IMI-834, 19, 42, 44, 46, 48, 295-298, 2.915, 2.917 Alloying Additions, 2,038 Kinetics, 2,039 Oxidation, 2,037 See: Ti-5.8Al-4Sn-3.5Zr-.7Nb-.5Mo-.06C Impurity Content, 1,031 In Vacuum, 497-504 In-Site Composite, 2,469 Inclusion Removal HDI Dissolution, 2,259 LDI, 2,257, 2,261 Inclusions, 2,401, 2,402 Induction Slag Process, 2,393, 2,396 Inert Gas, 1,026, 1,027 Ingot Metallurgy, 821, 1,049 Ingot Quality, 2,415, 2,416 Ingot Cast Ingot, 2,318, 2,319, 2,323 Melt Pool Depth, 2,320, 2,321 Initial Material Composition, 2,419 Interface Properties Fibre/Matrix Bonding, 2,633, 2.637-2.639 Interface Strength, 2,634, 2,638, 2.639 Interface Zone, 2,556 Interfacial Properties Crack Bifurcation, 2.653 Debonding Shear Stress, 2,651 Reaction Products, 2,651 Ti-6Al-4V/SC S6, 2,650 Ti-15-3/SC S6, 2,650 Ti B215/SC S6, 2,650 Intergranular Failure, 351 Intermetallic Alloy Powders, 1,026-1.032 Intermetallic Alloy, 1,61 Intermetallic Compound, 933, 1,123, Intermetallic Matrix Composites (IMC). 1,131, 2,546 Fatigue, 1,139-1,146 Crack Growth Rates, 1,139-1,146 Microstructure, 1,139-1,146

Lamellar Orientation, 1,142-1,144

riacture roughness, 1,135-1,140	Minerics of Aging, 045-050
Test Piece Orientation, 1,140	of Alpha Precipitation, 643-650
Lamellar Orientation, 1,141,	of Grain Growth, 643-650
1,142	Kroll Process, 55, 2,309
Ti-48Al Microstructure, 1,141	111011 1 100000, 00, 2,000
	•
Intermetallics, 733, 797	
Internal Heating, 497-504	Laser Nitriding, 1,980
Investment Cast Titanium	Laser Treatment, 554, 555
Ti-6 Al-4 V, 2,495, 2,497, 2,498	Commercial Purity Ti, 2,641-2,64
Bicasting, 2,495-2,501	Hardness Profiles 2,641-26,48
Selective Reinforcement, 2,495,	Melt Profile, 2,641-2,648
2,496, 2,500, 2,501	Metal-Ceramic Composite, 2,641
Investment Casting, 11, 415, 879,	
1,065, 1,495, 1,511, 1,519,	2,648
2,915	Microscopy, 2,641-2,648
Gamma Titanium Aluminide,	Microstructures, 2,641-2,648
	Reaction Products, 2,641-2,648
1,267-1,274	Residual Stress, 2,641-2,648
Mechanical Properties, 1,267-	SiC Particles, 2,641-2,648
1,274	TiC, 2,641-2,648
Microstructures, 1,267-1,274	Ti ₅ Si ₃ , 2,641-2,648
lodide Process, 2,459-2,464	X-Ray Diffraction, 2,641-2,648
lodide Refining, 2,273	Laser Ultrasonics 2,819, 2,820, 2,821
Ion Beam Treatment, 2,163	2,825
Ion Implantation, 2,103-2,108	
Ion Implantation, 2,103-2,108	Laser
Iron, 821-823	Cast, 1,395-1,402
	Near Shape, 1,395-1,402
Isostatic Diffusion Bonding	Titanium Alloys, 1,395, 1,398,
Modelling, 1,626-1,628	1,400, 1,402
Super Alpha-2, 1,629, 1,630	Sponge Fines, 1,396-1,401
Isothermal Decomposition, 643-650	Lattice Parameter, 2,122, 2,123, 2,12
Isothermal Fatigue, 2,625, 2,626	Leaching, 805, 807, 808, 2,247
Iscthermal Forging, 399, 979, 2,674,	Load Shredding, 2,594, 2,599, 2,628
2,812	Loading Test, 2,019
Characteristics, 1,319-1,328	Longitudial Tension, 2,559
Equipment, 1,319-1,328	
	Lost Wax Process, 1,519
Modelling, 1,319-1,328	Low Alloy Titanium 0.3Mo-0.8Ni
Isothermal Omega, 643-650	Application, 1,355, 1,356
Isothermal Process, 707, 712	Corrosion Resistance, 1,355,
Isotropic Softening, 1,762	1,356
	Mechanical Properties, 1,356
J	Design Allowables, 1,356
Joint Quality	Low Cycle Fatigue Life (N _I), 513, 518
	The state of the s
Mechanical Properties, 1,448-	520, 521
1,450, 1,452	Low Cycle Fatigue (LCF), 44, 131-
S::_cture, 1,447	139, 304, 307, 468, 469, 971-977,
	1,376, 1,757, 1,955, 1,956
K	$\alpha+\beta$ Titanium Alloy VT9, 1,955,
Kinematic Softening, 1,762	1,956
Timomatic Cottoming, 1,702	

Fatigue Life, 1,955, 1,958,	1,669, 1,686, 1,688, 1,709, 1,725,
1,960, 1,961	1,891-1,895, 1,947, 1,950, 2,073,
Cyclic Softening, 1,958	2,144, 2,185, 2,187-2,192, 2,201,
Tensile Hold, 1,955, 1,960, 1,961	2,472, 2,685, 2,733, 2,791, 2,805,
Coffin-Manson Plot, 1,955, 1,958-	2,891, 2,919, 2,923-2,925, 962, 965
1,960	Crack Nucleation, 1,636,
.,000	1,638
M	Crack Propagation, 1,636
Magnetic Seperation, 2,281	Creep, 284, 285, 1,637, 1,638
Manufacture	Creep Properties, 314, 317, 318
Forging Route, 1,358	Ductility, 1,891, 1,893-1,898
Melting, 1,357	Ductility, Reduction in Area,
Pressing, 1,358	Fatigue, 1,636-1,638
Sample Integrated, 1,357, 1,358	Fracture Toughness, 284, 285,
Upset Forging, 1,358	1,1771, 637-1,639
Martensite, 643-650	Hardness, 1,461-1,468
Master Alloy, 2,445	High Strength, 1,891, 1,893
Material, 1,851, 1,852, 1,854-1,858	KCV Impact Test, 1,461-1,468
Ti-6A1-4V, 1,931, 1,934-1,936	Small Cracks, 1,637, 1,638
Materials Distribution, 2,879	Strength-Ductility Balance, 1,891,
Materials, 1,923-1,927, 1,929, 1,930	1,894-1,897
Ti-6Al-4V, 1,923, 1,925, 1,926,	Structure, 1,461-1,468
1,929, 1,930	Tensile, 283, 284
Matrix Coated Fibre Process, 2,479,	Tensile Ductility, 1,172-1,177
2,480	Tensile Properties, 313, 314
Mean Stress Effects	Tensile Strength, 1,172, 1,893,
Load Ratio, 1,916-1,921	1,895-1,898
Maximum Stress Intensity,	Tensile Tests, 1,461-1,468
1,921	Toughness, 1,461-1,468
Stress Range, 1,921	Mechanical Testing, 297, 1,594
Mean Stress, 1,751-1,755	Melting Capacity, 58
Load Ratio, 1,751-1,755	Melting Furnances, 57
Fracture Surface, 1,754,	Melting, 57, 59, 60, 2,355, 2,357,
1,755	2,377
Temperature, 1,751-1,755	Gamma Ti, 2,300
Mechanical Alloying, 793, 798, 829-	IMI 834, 2,293
834, 903, 904, 908, 909, 927, 933,	Plasma Torch, 1,026, 1,027
940	Skull Melting Techniques, 1,026,
Mechanical Behavior, 431-438, 959	1,027
Creep Strength, 431-438	Super α ₂ , 2,299
Creep Life, 431-438	Metal Loss
Creep Rate, 431-438	Bath Temperature Effect, 2,154
Tensile Strength, 407-413, 431-	Effect of NaNo3 Content, 2,153
438	Metal Matrix Composites (MMC), 447
	2,467, 2,479, 2,511, 2,512, 2,518,
Mechanical Properties, 177, 423, 429,	2,529, 2,537-2,544, 2,546, 2,561,
447, 462, 473, 478-480, 505, 535, 554, 643, 650, 816, 928, 1, 209	2,593, 2,601, 2,609
554, 643-650, 816, 928, 1,299, 1,206, 1,555, 1,559, 1,574, 1,501	CermeTi, 2,512-2,518
1,306, 1,555, 1,558, 1,574, 1,591,	

CermeTi-A, 2 514, 2,518 CermeTi-B, 2,514, 2,517, 2,518 CermeTi-C, 2,514-2,516, 2,518 Erosion Behavior, 2,496-2,497 Mechanical Properties, 2,487-2,489, 2,491, 2,493-2,494 Powder Metallurgy, 2,487-2,494 Particulates Reinforced, 2,487-2,491, 2,493-2,494 SiC Fiber Strength, 2,500 SiC/Ti-6,242, 2,497 Metallic Magnesium, 2,426 Metallography, 643-650 Metastable-Beta Titanium Alloy, 643-650, 1,469, 1,947 Micro-hardness, 2,010 Microcracking, 1,665 Micromechanism, 1,155, 1,156 Microprobe Analysis As-Solidified Ti-52Al, 1,095, 1,096 Microradiographed, 2,853 Microstructural Stability, 161 Microstructure and Properties Metallurgical Properties, 243, 244 Microstructure Development, 5, 431-438 Beta Grain Growth, 431-438 Colony Alpha, 431-438 Microstructure Modelling, 7 Microstructure Properties/ Relationships, 77-88, 643-650 Microstructure, 497-504, 823, 824, 827, 1,470-1,473, 1,725, 1,741-1,748, 1,852, 1,853, 1,855-1,858 Basketweave, 456, 460, 462 Bi-Modal, 313 Colonized, 456, 460 Effects on Crack Growth, 1,742-1.748 Primary Alpha, 1,741-1,748 Transformed Beta, 1,742-1,748 Equiaxed α, 854-856, 858-860 Grain Boundary a, 856 Primary α Plates, 457, 458, 460 Lamellar, 312-314, 455, 456 Lath-Like, 457, 460 α-Platlet, 455, 460 **B-Interlayer**, 455, 460

Widmanstatten a, 854-856, 858-860 Microstructures, 643-650, 1,030, 1,117-1,122 Bi-Modal, 1,189, 1,190, 1,636-1,639 Dendrites, 2,641-2,648 Effect on Properties, 1,648-1,650 Elongated α , 1,836 Equiaxed α, 1,836 Globular, 2.641-2.648 Grain Growth, 1,911-1,913 Grain Shape, 1,908, 1,909 Grain Size, 1,908, 1,909 Interface Microstructure, 2,636, 2.637 Interface Reaction, 2,633, 2,636, 2,637, 2,639 Lamellar, 1,189, 1,191, 1,636-1.638 Matrix Microstructure, 2,636 Retained Metastable β, 1,835, 1.841 TiB Needle, 2,637 TiC particles, 2,637, 2,639 Ti-25Al-10Nb-3V-1Mo, 1,171-1,178 Ti₅Si₃, 2,637, 2,639 Ti-6-22-22, 1,648-1,650 Tread Life, 2,641-2,648 Microvoid Geometry, 1,437 MMC, 161, 2,467, 2,569 Fiber Coating, 2,471 Reaction Zone, 2,468 Reinforcement, 2,468 Thermodynamics, 2,468 Mechanical Properties, 2,472 Modelling, 2,812 Modulus, 824 Monofilament Composite, 2,569 Morphology, 601

N

Nanocrystalline Material, 903 Nanostructure Material, 793, 799, 800 Nanostructure, 903 NDE, 2,812, 2,814 Near Alpha Alloys

Mechanical Properties, 289, 293	P
Near Beta Titanium Alloys	Particle Reinforcements
Ti-10-2-3, 2,673	SiC, 2,512, 2,513
Ti-17, 2,673	TiAl, 2,512-2,414, 2,518
Nickel Aluminide, 1,131	Ti ₃ AI, 2,512
Nitrogen Flow Rate, 2,120-2,124	TiB ₂ , 2,513, 2,514, 2,517, 2,518
Non-Consumable Electrode, 2,355,	TiC, 2,513-2,518
2,356	Particle Size Distribution, 1,029
	Particulate Composite, 2,469
0 ———	Particulate Reinforcement, 2,561
Observations	Peritectic Solidification
Microstructures, 484-487	Ti-52Al, 1,091, 1,098
As-Deformed Microstructures,	Peritectoid Decomposition, 1,993
484-486	Phase Diagram, 35, 556
Post-Aging Microstructures,	Phase Equilibria, 563, 566, 675, 691,
483-485	713, 1,259, 1,262
Omega Phase, 225, 228, 229, 558,	Phase Morphology, 643-650, 845, 847
643-650	Phase Stability, 1,243
Omega, Effect on Crack Growth Rate	Phase Transformation, 27, 588, 590,
Ti-3Al-8V-6Cr-4Mo-4Zr, 86,87	591, 593, 597, 600, 601, 643-650,
Ordering Transformation, 785, 788-	705, 759, 941, 943, 945, 1,569-
790	1,573, 1,687
Orthogonal Tests, 874	α ₂ -Phase, 729, 731, 733
Orthorhombic Phase Alloys, 343, 344,	Dissolution, 600
359, 837, 838, 840-843, 845, 847,	Intermetallic, 733
849, 1,004-1,006, 1,008, 1,148,	Precipitation, 600, 601
1,262, 1,263, 1,669, 1,671, 1,675	Phase Transitions, 547
Orthorhombic Symmetry, 721	Phases
Oxidation Behavior, 22	Athermal ω, 697, 698, 701, 704
Oxidation (by Thermal Exposure), 83,	Orthorhombic Martensite α ,
84	697-704
Oxidation Resistance, 1,891, 1,892,	ω_{r} , 697, 700-702, 704
1,895-1,897	ω _s , 697, 700-704
Oxidation: Weight Gain	Photometric, 2,287, 2,291
IMI 125, 2,037	Physical Properties, 431-438, 2,684
Super Alpha 2, 2,037	Crystallographic Texture, 431-438
Ti-48Al-2Nb-2Mn, 2,037	Density, 2,698, 2699
Oxide Coatings, 2,005	Hardness, 2,698, 2,699
Oxygen Content Effect on Toughness	Modulus of Elasticity, 2,698, 2,699
Ti-6Al-4V, 81 Oxygen Diffusion Coefficient	Thermal Expansion, 2,698, 2,699
IMI 125, 2,040	Transus Temperature, 2,699 Young's Modulus, 431-438
Super Alpha 2, 2,040	Physical Vapor Deposition, 2,479,
Oxygen Isotope, 2,424-2,427	2,481
Oxygen Isotope, 2,424-2,427	Physico-Mechanical Properties, 1,811,
Analysis, 823	1,812, 1,817
Effects of, 821, 822, 825, 828	Plain Strain Fracture Toughness,
2110013 01, 02 1, 022, 020, 020	1 155

Plasma Arc Melting, 1,107, 1,235-	Precipitation, 643-650
1,237, 1,239 Plasma Cold Hearth Furnace, 2,363	Alpha, 824, 825
Plasma Cold Hearth Melting, 2293	Precision Forging, 2,893 Preferred Orientation, 2,119, 2,124
Plasma Melting, 60, 1,309, 2,301	Pressure Nitriding, 1,979
Plasma Nitriding, 1,980, 2,127, 2,128,	Pressure Welding Process, 1,941
2,133	Primary α_2 , 980, 981, 985
Plasma Welding	Primary Alpha Phase, 643-650
Butt Welding in Flat Position,	
1,461-1,468	Prior β Grains, 643-650 Processing Treatments
Fit-Up Tolerances, 1,461-1,468	Forming Temperatures,
General, 1,461-1,468	1,924-1,928, 1,930
Horizontal, 1,461-1,468	0xidation Removal, 1,925, 1,929,
Protection of the Weld,	1,930
1,461-1,468	Processing Window, 2,235
Vertical, 1,461-1,468	Processing, 1,937, 1,938
Plasma Spraying, 1,980	Cold Drawn 2, 2,698
Plastic Behavior, 1,859	Composite, 2,633-2,640
PM Parts, 9	Consolidation, 2,633-2,635, 2,639
Poisson's Ratio, 2,609	Creep, 2,633, 2,635, 2,636, 2,639
Postweld Heat Treatment, 1,470-	Deformation Processing,
1,473	407-410, 412, 413
Potentiodynamic Polarization, 2,104	Diffusion Bonding, 2,633-2,635
Powder Metallurgy, 8, 431-438, 793,	Extrusion, 409
794, 813, 919, 1,073, 1,083, 2,511-	Forging 2, 2,698
2,514, 2,516, 2,518	Ingot & Powder Metallurgy, 1,275,
Alloying Advantages, 821	1,276
Atomizer, 431-438	Microstructure, 1,275-1,282
Blended Elemental Method,	Properties, 1,275-1,282
887-894	Rolling 2, 2,698
Mechanical Properties, 887-894	Swaging, 409
Microstructure, 887-889, 891-893	Product Development, 16
Consolidation Processing, 431-	Product Form, 1,851, 1,852, 1,854-
438	1,858
Extrusion, 2,511, 2,513, 2,515,	Billet, 1,931-1,936, 1,938
2,516, 2,517	Forging, 1,931-1,933,
Forging, 2,511, 2,513, 2,516,	1,935-1,938
2,518	Sheet, 1,923, 1,925
Gas Atomization, 280, 822	Properties, 1,852-1,858
Hot Isostatic Pressing (HIP),	Close-Tolerance, 1,433, 1,435
2,511, 2,512	Roundness, 1,433
Mechanical Properties, 431-438	Straightness, 1,433
Microstructure, 281	Crack Growth, 1,924-1,928, 1,930
Particle Distributions, 823	Fatigue, 1,924-1,928, 1,930,
Powder Microstructure, 431-439	1,932-1,938, 2,693-2,694
Prealloyed Powder, 795 Sintering, 2,513	Homogenous Stress Distribution, 1,433
	Microstructure, 1,928-1,930

Symmetrical, 1,433, 1,435	Rolls-Royce, 2,878 Room Temperature Data, 2,603, 2,606
Tensile Properties, 1,924-1,927, 1,930, 1,932, 1,934, 1,935,	Hoom temperature Data, 2,603, 2,606
1,937, 1,938, 2,691-2,694	\$
Toughness, 2,692	Salt Bath Nitriding, 1,980
Young's Modulus, 2,692	Scrap, 62
Protective Coating, 1,971	SCS-6 Fiber, 2,545, 2,546
Push Out Testing, 2,569-2,572	SCS-6 [™] Reinforced, 2,553, 2,554
PVD, 1,980	Secondary α ₂ , 981, 985
	Segregation, 2,318, 2,320
Q	Beta Freaks, 2,320, 2,322
Quality Assurance, 2,805, 2,809	Macro Segregation, 2,320, 2,321
,,	Self Propagating High Temperature
R	Synthesis (SHS), 895, 896, 2,519
Radioactive Isotope 2,851, 2,852	Separators, 2,290, 2,291
Radioactivity, 55	Shape Casting, 68
Radioautography, 2,851-2,853	Casting, 67
Rapid Solidification, 431-438, 796,	Impurity Content, 68
821, 1,725	Ship's Bell, 69
Consolidation Processing,	Ship, 72
431-438	Shape Memory Alloy, 611, 897, 895
Mechanical Properties, 431-438	Shear Lag Analysis, 2,545, 2,546
Rare Earth Elements, 1,725	Shot Peening, 45
Rare-Earths, 2,892	SiC Reinforced, 2,479
Reaction Zone, 2,553, 2,555, 2,611	SiC, 2,561-2,568, 2,570 Silicides in Ti-6.1Al-3.2Zr-3.3Sn-1Nb-
Reaction-Zone Cracks, 2,611	0.5Mo-0.32Si, 82
Reactive Sputtering, 2,163	Silicon Carbide Fiber, 2,537-2,544
Rebundle, 2,795-2,802	Silicide, 1,777, 1,778
Recovery, 611, 614 Recrystallization, 1,203-1,210, 1,704	Single Fiber Fragmentation Test,
Compression, 1,203-1,210	2,546
Grain Size, 582-586	Skull
Isothermal Annealing, 582	Furnace, 822
Non-Isothermal Annealing, 583	Melting, 2,415-2,422
Continuous Annealing, 585	Sliding Friction Force, 2,718
Static Recrystallization,	Small Cracks
1,203-1,210	Fatigue Crack Growth, 1,750-
TiAl, 1,203-1,210	1,755, 1,916-1,921
Reliability, 2,810	Crack Shapes, 1,919, 1,921
Resistivity	Effect of Temperature, 1,751- 1,755
Composition Dependence, 699	Fracture Surface, 1,754, 1,755
Temperature Dependence,	Notches, 1,916-1,921
697-700	Stress Intensity, 1,75 i -1,755,
Resistivity-Temperature Curve, 697, 698, 700-703	1,916-1,918, 1,921
Ripple Load, 2,169, 2,170, 2,171	Snow Sliding Velocity, 2,715-2,716
Rolled Rod, 603	Solid Solubility, 659
Rolling Texture, 1,795	Solid Solution, 651, 739-741
Training Toniara, 11.00	Solidification Modelling, 11
	2,963

Solidification, 571, 572, 576, 577 Solidification Structure, 2,317- 2,323 Solidification Line, 2,319, 2,323	Triaxial Stress State, 527 Strain Hardening Rate, 1,163, 1,166 Strain Rate Sensitivity, 979, 980, 983-985, 1,163, 1,166
Solidification Temperature, 2,320	Strain Rate, 683-688, 979-981, 985
Solidification Phenomena, 2,320	Strain Recovery, 2,593, 2,596
Solidus, 12	Strength-Ductility Relationships, 77-82
Solution Treatment Temperature,	Ti-15V-3Cr-3Al-3Sn, 77-81
643-650	Ti-15Mo-2.7Nb-3Al-0.2Si, 78, 79
Solutionizing Treatment, 375	Ti-3Al-8V-6Cr-4Mo-4Zr, 78
Sorting, Automated, 2,287	Ti-10V-2Fe-3AI, 79, 80
SP-700 Titanium Alloy - 141, 143,	Ti-11.5Mo-6Zr-4.5Sn, 80
144, 146, 147, 148	Ti-10V-2Fe-5Zr-3Al, 80
Span to Width Ratio, 2,601-2,604	Ti-5Al-2Sn-4Zr-4Mo-2Cr-1Fe, 81
Spectroscopic Analysis	Ti-4.5Al-5Mo-1.5Cr, 81, 82
Intensity of Spectral Line, 2,408,	Ti-6.1Al-3.2Zr-3.3Sn-1Nb0.5Mo-
2,411	.32Si, 82
Local Thermal Equilibrium, 2,411,	Strength, 553, 1,647-1,652
2,414 Spectrospec 2,407, 3,408	Strength-to-Weight Ratio, 2,878
Spectroscope, 2,407, 2,408, 2,411	Strength/Toughness Relationships, 77-82
SPF/DB, 2,891	Ti-15V-3Cr-3Al-3Sn, 77, 78
Spinodal Decomposition, 722	Ti-3Al-8V-6Cr-4Mo-4Zr, 79, 80
Sponge Capacity, 54	Ti-5Al-2Sn-4Zr-2Mo-2Cr-1Fe,
Sponge: Production Statistics, 2,228,	81, 82
2,229	Ti-4.5Al-5Mo-1.5Cr, 81, 82
Spontaneous Reaction Synthesis	Strengthening
(SRS), 895, 896	Mechanism of Strengthening,
Spray Forming, 987, 991	244-246
Spray Reaction, 805, 806, 308	Boundary Layer
Sputter Ion Plating	Strengthening, 241, 244-246
Ti-6-4, 2,117	Strengthening Process, 241-246
Ti(CP), 2,117	Stress Corrosion Cracking, 2,074-
Stabilization Heat Treatment, 1,507	2,080, 2,097, , 2,111-2,117, 2,169,
Effect on Microstructure, 1,507,	2,170, 2,171, 2,172, 2,174-2,175
1,508	Stress Intensity Factor, 353, 1,804,
Statistical Process Control	1,805, 1,869, 2,529, 2,530
Automatic Exception Detection, 2,325-2,329	Stress-Induced Transformation, 643-650
Steady State Creep Rate, 1,251,	Stress-Rupture Strength, 383
1,256, 1,257, 2,593	Stress-Strain Response, 1,662, 1,664,
Strain and Fracture	1,665
Crack Propagation, 527	Structural Strengthening, 539, 540
Critical Resolved Shear Stress,	Structure, 683-688
527	Cast Stucture, 2,318, 2,319,2,322
H.C.P. Cell Orientation, 527, 528	Dendrite Stucture, 2,321
Slip System, 527	Macrostructure, 2,853, 2,852
Tensile Opening Crack in Plane Strain, 527	Microstructure, 2,852, 2,854

Solidification Structure, 2,318,	TA6V Alloy, 473, 474
2,319, 2,322	TA6V4, 747
Super α ₂ , 1,669, 1,670, 1,672, 1,675	TA6Zr5D, 627, 633
Super Alpha-2, 979, 980, 985, 986	TCP, 551, 793, 799, 801, 802
Alloying Additions, 2,039	Temperature Measurement
Diffusion Bonding, 1,629, 1,630	Emissivity, 2,407, 2,408, 2,410,
Modelling, 1,626-1,628	2,412
Kinetics, 2,040	Radiation Thermometer,
Oxidation, 2,037	2,407-2,414,
Super Dislocations, 1,148	Surface Temperature,
Super Partials, 1,148	2,407-2,414
Super Plastic Forming, 6, 202, 1,403,	Temperature of Titanium Vapor,
1,404, 1,651, 1,652	2,407, 2,408, 2,411, 2,414
Design, 1,319-1,328	Thermocouple, 2,407, 2,410,
Equipment, 1,319-1,328	2,412
Ti-6-22-22, 1,651, 1,652	Temperature, 979-981, 985
Super Plasticity, 1,899-1,904, 2,773,	Tensile1,852-1,858
2,775, 2,777	Tensile Behavior, 1,678, 1,679
β-Phase Proportion, 1,532, 1,533	Tensile Properties, 117, 145, 146,
Deformation Variables, 1,529-	180, 306, 319-322, 495, 643-650,
1,531	1,011-1,013, 1,058, 1,104, 1,346,
Elongation to Failure, 1,531,	1,374, 1,593, 1,595-1,599, 1,787,
1,532	1,790, 1,861, 1,949, 2,674, 2,789
Grain Growth, 1,530, 1,531 Material Model, 1,907-1,914	Tensile Strength, 124, 217, 220, 1,831, 1,832, 1,877, 1,885-1,889
Strain Hardening, 1,913, 1,914	Tensile Testing, 1,074
Strain Rate Sensitivity, 1,913,	Tensile Tests, 297, 304, 371, 515,
1,914	613, 1,780, 1,790, 1,899-1,902,
Tensile Stability, 1,913, 1,914	2,049, 2,594
Superplastic Behavior, 871, 1,421,	Tension Tests, 2,594
1,422	Testing Techniques
Surface Oxidation Layer, 1,775	Tension-Torsion, 1,765-1,767
Surface Oxidation, 42	Dwell, 1,766, 1,767
Surface Properties, 2,716	Tests
Surface Treatment, 41	Beta Ti Alloy, 2,697-2,704
Surface	Charpy Impact Test, 1,877-1,880
Anodic Oxide, 2,135-2,141	Transition Curve, 1,878
Dielectric Constant, 2,135-2,141	Fracture Surface, 1,879,
Electrical Impedance,	1,880
2,135-2,141	Chemical Composition, 1,358-
Electrical Resistivity, 2,135-2,141	1,360, 1,431
Oxide Film, 2,135-2,141	CMA, 2,318
Polarization Resistance,	Commercial Purity Titanium,
2,135-2,141	1,581-1,586
_	Compression, 1,702, 1,909, 1,910
7	Corrosion Resistance, 2,702
T40, Alloy, 473-475	Creep Tests, 1,191
T60 Alloy, 473, 474	Creep Resistance, 1,188
T-T-T Diagram, 559	965
Ζ,	70.7

Delamination, 1,963, 1,966 Ductility, 487 Elongation, 2,700 Etchant, 2,318, 2,321, 2,322 Etching Condition, 2,322 Etch Pit, 2,318, 2,319, 2,320 Flattening Test, 1,434 Fracture Toughness, 1,192-1,194, 2,517 Fretting Fatigue, 1,963-1,968 High Cycle Properties, 1,829-1,831 Crack Initiation Site, 1,831-1,833 Internal Initiation, 1,830-1,834 Subcrack, 1,831-1,833 Fatigue Strength, 1,831 S-N Curves, 1,830, 1,831 Impact, 730 Texture, 271-278, 1,000, 1,636, 1,859 α-Based Alloys, 271-278 Electron Back Scattered Patterns, 271-278 Procedure, 280 Measurements, 281 Orientation Distribution Functions (ODF), 271-278 Pole Figures, 271-278, 283 Quantitative Texture Analysis, 271-278 Texture, Effect on Properties Ti-6Al-4V, 84-86 Thermal Analysis (CDTA), 596 Thermal Analysis, 588, 590 591, 593 Thermal Conductivity, 2,522 Thermal Residue Stress, 2,537-2,544
Elongation, 2,700 Etchant, 2,318, 2,321, 2,322 Etching Condition, 2,322 Etch Pit, 2,318, 2,319, 2,320 Flattening Test, 1,434 Fracture Toughness, 1,192-1,194, 2,517 Fretting Fatigue, 1,963-1,968 High Cycle Properties, 1,829-1,831 Crack Initiation Site, 1,831-1,833 Internal Initiation, 1,830-1,834 Subcrack, 1,831-1,833 Fatigue Strength, 1,831 S-N Curves, 1,830, 1,831 Electron Back Scattered Patterns, 271-278 Fractor, (Kearns), 271-278 Procedure, 280 Measurements, 281 Orientation Distribution Functions (ODF), 271-278 Pole Figures, 271-278, 283 Quantitative Texture Analysis, 271-278 Texture, Effect on Properties Ti-6Al-4V, 84-86 Thermal Analysis (CDTA), 596 Thermal Analysis, 588, 590 591, 593 Thermal Conductivity, 2,522
Etchant, 2,318, 2,321, 2,322 Etching Condition, 2,322 Etch Pit, 2,318, 2,319, 2,320 Flattening Test, 1,434 Fracture Toughness, 1,192-1,194, 2,517 Fretting Fatigue, 1,963-1,968 High Cycle Properties, 1,829-1,831 Crack Initiation Site, 1,831-1,833 Internal Initiation, 1,830-1,834 Subcrack, 1,831-1,833 Fatigue Strength, 1,831 S-N Curves, 1,830, 1,831 Facility Condition, 2,322 Fractor, (Kearns), 271-278 Procedure, 280 Measurements, 281 Orientation Distribution Functions (ODF), 271-278 Pole Figures, 271-278, 283 Quantitative Texture Analysis, 271-278 Texture, Effect on Properties Ti-6Al-4V, 84-86 Thermal Analysis (CDTA), 596 Thermal Analysis, 588, 590 591, 593 Thermal Conductivity, 2,522
Etching Condition, 2,322 Etch Pit, 2,318, 2,319, 2,320 Flattening Test, 1,434 Fracture Toughness, 1,192-1,194, 2,517 Fretting Fatigue, 1,963-1,968 High Cycle Properties, 1,829-1,831 Crack Initiation Site, 1,831-1,833 Internal Initiation, 1,830-1,834 Subcrack, 1,831-1,833 Fatigue Strength, 1,831 S-N Curves, 1,830, 1,831 Factor, (Kearns), 271-278 Procedure, 280 Measurements, 281 Orientation Distribution Functions (ODF), 271-278 Pole Figures, 271-278, 283 Quantitative Texture Analysis, 271-278 Texture, Effect on Properties Ti-6Al-4V, 84-86 Thermal Analysis (CDTA), 596 Thermal Analysis, 588, 590 591, 593 Thermal Conductivity, 2,522
Etch Pit, 2,318, 2,319, 2,320 Flattening Test, 1,434 Fracture Toughness, 1,192-1,194, 2,517 Fretting Fatigue, 1,963-1,968 High Cycle Properties, 1,829-1,831 Crack Initiation Site, 1,831-1,833 Internal Initiation, 1,830-1,834 Subcrack, 1,831-1,833 Fatigue Strength, 1,831 S-N Curves, 1,830, 1,831 Fracture Toughness, 1,192-1,194, Orientation Distribution Functions (ODF), 271-278 Pole Figures, 271-278, 283 Quantitative Texture Analysis, 271-278 Texture, Effect on Properties Ti-6Al-4V, 84-86 Thermal Analysis (CDTA), 596 Thermal Analysis, 588, 590 591, 593 Thermal Conductivity, 2,522
Flattening Test, 1,434 Fracture Toughness, 1,192-1,194, 2,517 Fretting Fatigue, 1,963-1,968 High Cycle Properties, 1,829- 1,831 Crack Initiation Site, 1,831-1,833 Internal Initiation, 1,830-1,834 Subcrack, 1,831-1,833 Fatigue Strength, 1,831 S-N Curves, 1,830, 1,831 Fracture Toughness, 1,192-1,194, Orientation Distribution Functions (ODF), 271-278 Pole Figures, 271-278, 283 Quantitative Texture Analysis, 271-278 Texture, Effect on Properties Ti-6Al-4V, 84-86 Thermal Analysis (CDTA), 596 Thermal Analysis, 588, 590 591, 593 Thermal Conductivity, 2,522
Fracture Toughness, 1,192-1,194, 2,517 Fretting Fatigue, 1,963-1,968 High Cycle Properties, 1,829- 1,831 Crack Initiation Site, 1,831-1,833 Internal Initiation, 1,830-1,834 Subcrack, 1,831-1,833 Fatigue Strength, 1,831 S-N Curves, 1,830, 1,831 Crack Initiation Distribution Functions (ODF), 271-278 Pole Figures, 271-278, 283 Quantitative Texture Analysis, 271-278 Texture, Effect on Properties Ti-6Al-4V, 84-86 Thermal Analysis (CDTA), 596 Thermal Analysis, 588, 590 591, 593 Thermal Conductivity, 2,522
2,517 Fretting Fatigue, 1,963-1,968 High Cycle Properties, 1,829- 1,831 Crack Initiation Site, 1,831-1,833 Internal Initiation, 1,830-1,834 Subcrack, 1,831-1,833 Fatigue Strength, 1,831 S-N Curves, 1,830, 1,831 Fretting Fatigue, 1,963-1,968 Pole Figures, 271-278 Quantitative Texture Analysis, 271-278 Texture, Effect on Properties Ti-6Al-4V, 84-86 Thermal Analysis (CDTA), 596 Thermal Analysis, 588, 590 591, 593 Thermal Conductivity, 2,522
Fretting Fatigue, 1,963-1,968 High Cycle Properties, 1,829- 1,831 Crack Initiation Site, 1,831-1,833 Internal Initiation, 1,830-1,834 Subcrack, 1,831-1,833 Fatigue Strength, 1,831 S-N Curves, 1,830, 1,831 Fretting Fatigues, 271-278, 283 Quantitative Texture Analysis, 271-278 Texture, Effect on Properties Ti-6Al-4V, 84-86 Thermal Analysis (CDTA), 596 Thermal Analysis, 588, 590 591, 593 Thermal Conductivity, 2,522
High Cycle Properties, 1,829- 1,831 Crack Initiation Site, 1,831-1,833 Internal Initiation, 1,830-1,834 Subcrack, 1,831-1,833 Fatigue Strength, 1,831 S-N Curves, 1,830, 1,831 Guantitative Texture Analysis, 271-278 Texture, Effect on Properties Ti-6Al-4V, 84-86 Thermal Analysis (CDTA), 596 Thermal Analysis, 588, 590 591, 593 Thermal Conductivity, 2,522
1,831 271-278 Crack Initiation Site, 1,831-1,833 Texture, Effect on Properties Internal Initiation, 1,830-1,834 Ti-6Al-4V, 84-86 Subcrack, 1,831-1,833 Thermal Analysis (CDTA), 596 Fatigue Strength, 1,831 Thermal Analysis, 588, 590 591, 593 S-N Curves, 1,830, 1,831 Thermal Conductivity, 2,522
1,831 Crack Initiation Site, 1,831-1,833 Internal Initiation, 1,830-1,834 Subcrack, 1,831-1,833 Fatigue Strength, 1,831 S-N Curves, 1,830, 1,831 271-278 Texture, Effect on Properties Ti-6Al-4V, 84-86 Thermal Analysis (CDTA), 596 Thermal Analysis, 588, 590 591, 593 Thermal Conductivity, 2,522
Internal Initiation, 1,830-1,834 Subcrack, 1,831-1,833 Fatigue Strength, 1,831 S-N Curves, 1,830, 1,831 Ti-6Al-4V, 84-86 Thermal Analysis (CDTA), 596 Thermal Analysis, 588, 590 591, 593 Thermal Conductivity, 2,522
Subcrack, 1,831-1,833 Thermal Analysis (CDTA), 596 Fatigue Strength, 1,831 Thermal Analysis, 588, 590 591, 593 S-N Curves, 1,830, 1,831 Thermal Conductivity, 2,522
Subcrack, 1,831-1,833 Thermal Analysis (CDTA), 596 Fatigue Strength, 1,831 Thermal Analysis, 588, 590 591, 593 S-N Curves, 1,830, 1,831 Thermal Conductivity, 2,522
Fatigue Strength, 1,831 Thermal Analysis, 588, 590 591, 593 S-N Curves, 1,830, 1,831 Thermal Conductivity, 2,522
S-N Curves, 1,830, 1,831 Thermal Conductivity, 2,522
impact, 730 Internal residue Stress, 2,537-2,544
Impact Energy, 526 Thermal Simulation of Weld HAZ,
Ingot Hardness, 1,359 1,116-1,121
Low-Cycle Fatigue, 730, 731 Thermal Stability, 1,773, 1,775, 1,777
Mechanical Properties, 1,432, Thermal Treatments
1,434, 2,516-2,518 Cooling Rate, 1,933, 1,934
Mechanical Properties at Room Deformation Rate, 1,933-1,936
Temperature, 1,360, 1,361 Thermo-Mechanical Treatments
Microstructure, 1,361 Cold-Rolling, 482
Modulus (Elastic), 2,516-2,518 Working, 482, 483
Roughness Measurement, 1,432 Warm-Rolling, 482
Strain Path Changes, 1,580-1,586 Thermochemical Analysis, 2,310-
Strain Rate Jump Test, 1,909, 2,312
1,910 Thermochemical Processing, 793,
Strength, 487 799, 801, 802, 834, 835, 2,009
Stress-Strain Curves, 1,703, Dehydrogenation, 853-860
2,700, 2,701 Hydrogenation, 853-860
Tensile Properties, 484, 487, 488, Thermochemical Treatment, 879,
526, 1,880-1,882, 2,699, 2,700 1,979
Elongation, 1,880-1,882 Thermodynamic Properties, 27, 336
Reduction of Area, 1,880- Thermoelectric, 2,288, 2,289, 2,290,
1,882 2,291
Stress-Strain Curve, 1,881 Thermogravimetric Analysis, 2,179
Tensile Tests, 1,189, 1,191 Thermohydrogenous Treatment,
Tension, 1,909, 1,910 549, 941
Ti-I0V-2Fe-3Al, 1,963-1,968 Thermomechanical Processing
Ultrasonic Behaviour, 1,361 (TMP), 193, 209, 210, 399, 431-438,
Uniaxial Tensile Properties, 1,581 627, 628, 630, 633, 1,034, 1,035,
Wear Properties, 2,702, 2,703, 1,371, 1,372, 1,551
$(\alpha+\beta)$ Processing, 457-461
Work-Hardening Behaviour, β-Processing, 457-461
1,582, 1,583

Ti-0.2Pd, 2,217 Extrusion, 431-438 Heat Treatment, 431-438 Ti-0.3Mo-0.8Ni, 2,217 HIP, 431-438 Ti-10-2-3, 463-466 Pseudo-α Processing, 457-461 Ti-10V-2Fe-3Al, 79, 80, 255, 1,851, Strain, 457-460 1,852, 1,854-1,858 Ti-1100 - See Ti-6Al-2.7Sn-4Zr-.4Mo-Strain Rate, 457-46 Thermomechanical Treatments, 89. .45Si Fatigue Crack Growth Behavior, 489, 490, 1,795, 1,685, 1,686 Cooling Rate, 1,636-1,638 2.043 Fracture Morphologies, 2,045 Effect on Properties, 79-82, 84-86 Final Heat Treatment, 1,638, Ti-13V-11Cr-3Al, 1,895, 2,201 1.639 Ti-14Al-21Nb, 785, 1,453, 1,456, Intermediate Annealing, 1,637, 1,457, 2,545 1.638 Ti-15-3, 177, 761-765 1,875-1,877, Ti-15V-3Cr-3Al-3Sn, 79-81 1,881, 1,883, 1,884, 1,887-1,890, 1,892, 1,895-1,898, 2,209-2,215 Ti-5Al-2Sn-4Zr-4Mo-2Cr-1Fe. Isothermal Transformation. 81,86 Ti-4.5Al-5Mo-1.5Cr, 81, 82 761-765 Ti-6Al-2.7Sn-4Zr-4Mo-.45Si, Phase Transformation, 761-765 84-86 Ti-15Mo-2.7Nb-3Al-0.2Si, 1, 78, 79, Ti-5.8Al-4Sn-3.5Zr-.7Nb-.5Mo-153, 2,737, 2,738, 2,177, 2,185 .35Si-.06C, 84 Ti-15Mo-2.7Nb-3Al-0.2Si-0.150, 2,209 Ti-6Al-4V, 84-86 Ti-15Mo-3Nb-3Al-0.2-Si, 161 Thickness Prediction, 6 Ti-15V-3Cr-3Al-3Sn, 77-80, 87, 169, 217, 1,511, 1,867-1,869, 1,873, Three-Stage Deformation, 2,609 2,169, 2,170, 2,172, 2,175, 2,553, Ti 15-3 Alloy, 2,609-2,610 Ti 17, 463-466, 1,339 2,554, 2,557, 2,558, 2,561 Ti 6242, 463-466 Ti-16V, 1,947, 1,948 Ti 6242-0.1Si, 1,717-1,723 Ti-17, 2,452, 2,453 Effects of Solution Annealing Ti-19V, 705, 707, 708 Temperature, 1,719-1,723 Ti-20Al-11Nb-0.5Si, 1,005, 1,007 Primary, 1,720-1,722 Ti-20Al-11Nb-0.9Si, 1,005, 1,007 Recovery, 1,721, 1,722 Ti-20Al-11Nb-1.2Si, 1,005, 1,007 Steady State, 1,720, 1,722 Ti-22Al-27Nb, 344, 345 Ti 6246, 1,757 Ti-23Nb-11Al, 185, 186, 189 Ti-23V, 705, 708-711 Ti Aluminide, 1,235, 1,236 Ti-24.5Al-12.5Nb-1.5Mo, 367 TIG Welding, 1,601 Timetal 62S, 2,781, 2,792-2,794 Ti-24.5Al-10.5Nb-1.5Mo, 1,163-1,169 Ti-24.6A1-23.4Nb, 344, 345 Timetal 125, 2,899 Timetal 21S, 2,201, 2,203, 2,204, Ti-24Al-11Nb, 1,593-1,600 2,205, 2,194, 2,737, 2,738 Ti-24Al-11Nb, 996, 1,251, 1,252, Ti metal 1100, 2,923 1,254, 1,331-1,335, 1,337, 2,445, Ti metal 38644, 2,194 2.625 Ti N, 2,127, 2,128, 2,133 Fatigue, 2,625 Ti Powder, 805, 809 Tension, 2,625 Ti Sheet, 1,601, 1,602 Ti-24Al-IINb, 351, 359, 439-442, Ti-Ta30 Alloy, 2,757, 2,759-2,761 903-909

Ti-25Al-10Nb-3V-1Mo, 375, 837-840, 843, 845, 847-852, , 971, 972, 0.2Si, 1,709 1,235, 1,331-1,335, 1,337, 1,593-Ti-6242, 42, 46, 48, 319, 320, 1,453, 1,600, 1,669, 1,677, 1,679, 1,682, 1,456-1,458 1,683, 1,685-1,687 Ti-6242S, 295-298 Ti-26Al-21Nb, 1,147 Ti-6246, 2,452, 2,453, 2,830, 2,831, Ti-27 mol% Al, 1,123, 1,124, 1,127 2,832 Ti-3Al-8V-6Cr-4Zr-4Mo, 2,095, 2,096 Ti-662, 489, 490 Ti-6Al-1.7Fe-0.1Si, 2,787, 2,789 Ti-3Al-4.5Mo-4.5V, 862, 86 Ti-3Al-8V-6Cr-4Mo-4Zr, 78-80, 86, 87, Ti-6Al-2.7Sn-4Zr-0.4Mo-0.45Si, 83, 84, 263, 415, 505, 2,721 Ti-3AR, 2,143 Ti-6Al-2.7Sn-4Zr-0.4Mo-0.45Si-Ti-4.5Al-5Mo-1.5Cr, 81, 82 $0.07O_2$, 2,923 Ti-6Al-2Mo-2Cr, 755 Ti-40 at %AI, 571, 572, 574, 577 Ti-6Al-2Sn-2Zr-2Cr-2Mo-0.25Si, 201 Ti-45.5 Ni 54.5, 611 Ti-6Al-2Sn-2Zr-2Mo-2Cr, 1,647-1,652 Ti-48Al, 1,107-1,109, 1,309-1,316 Ti-6Al-2Sn-2Zr-2Mo-2Cr-0.25Si, 193, Ti-48Al-1.5Cr, 1,048, 1,057, 1,052 210 Ti-48Al-1V, 1,661-1,664, 1,665-1,667 Ti-6Al-2Sn-4Zr-2Mo, 319, 320, 2,787, Ti-48Al-2.5Nb-0.3Ta, 1,074 2,789 Ti-48Al-2Cr, 1,041-1,047 Ti-6Al-2Sn-4Zr-2Mo-0.1Si, 1,453 Ti-48Al-2Cr-2Nb, 1,065, 1,083-1,089, Ti-6Al-3Mo, 755 1,099, 1,102-1,105, 1,499, 1,500 Ti-6Al-3Mo-V, 755 Ti-48Al-2Mn-2Nb, 1,033, 1,035, Ti-6Al-4V Alloy, 1,379-1,386, 5, 17, 81, 1,107-1,109, 1,309-1,316 81, 84-86, 89-93, 96, 113, 129, 130, Ti-48Al-2Nb-2Cr, 399 141, 145-147, 201,202,206,207, 225-Ti-48Al-3Cr, 1,041-1,047 228, 619, 777-784, 879, 882, 949, Ti-48Al-1V-0.2C, 423 952, 1,421-1,423, 1,543-1,549, 1,587, Ti-4Wt%Mg, 651 1,592, 1,617, 1,787, 1,819, 1,820, Ti-5% Ni, 2,751, 2,752, 2,753, 2,754-1,827, 1,828, 1,830, 1,831, 1,833, 2,756 1,843-1,845, 1,867, 1,868, 1,899-Ti-5.5Al-2V-2Zr, 234 1,901, 1,939, 1,941, 1,943, 1,946, Ti-5.5Al-1Mo-2Zr, 234 2,128, 2,169, 2,170, 2,172, 2,173, Ti-5.8Al-4Sn-3.5Zr-.7Nb-.5Mo-.35Si-2,217, 2,451-2,453, 2,472, 2,545, .06C, 83-85 2,570, 2,729, 2,773-2,778, 2,787, Ti-52Al, 988-992, 1,309-1,316 2,789, 2,867-2869, 2,941, , 2,982 Ti-53Al-1Nb, 1,653-1,656 Flow Instability, 1,379-1,386 Ti-5Al-2Sn-4Zr-4Mo-2Cr-1Fe, 81, 82, Forged Bars, 1,835-1,838, 1,841 97, 105, 106 Rolled Plates, 1,835, 1,836, Ti-5Al-4.5Mo-4.5V-1Cr-1Fe, 1,569 1,839-1,841 Ti-6-22-22S, 193, 201, 202, 206, 207, Stress-Strain Behavior, 209-212, 1,371, 1,372 1,379-1,386 Ti-6-2222, Ti-10-2-3, Ti-15-3-3-3 Beta Ti-6Al-4V/SiC, 2,601, 2,602 C, IMI550, 16 Ti-6Al-5Mo-5V-ICr-IFe, 755 Ti-6-4 Alloy, 988-992, 1,403, 1,404, Ti-6Al-6V-2Sn, 489, 490, 1,551-1,553, 1,437, 2,860 2,899 Surface Hardening, 2,009 Ti-7Cr, 1,947, 1,948 Ti-6.1Al-3.2Zr-3.3Sn-1Nb-0.5Mo-Ti-7Mo-16Al, 185 0.32Si, 82

Ti-6.5Al-2.2Sn-1.2Zr-2.0Mo-2.2Nb-

Ti-8Al-1Mo-1V, 2,170, 2,172, 2,174 Ti-Al Equilibrium Diagram, 1,291, 1,295 Ti-Al System, 547-552 Ti-Al, 548, 552 Ti-Al-Mo-Ni, 2,143 Ti-Al-Mo-Zr Alloy, 233 Ti-Al-Nb Alloy, 1,259, 1,260, 1,264 Ti-Al-Sn-Zr Alloys - 83 Ti-Al-Sn-Zr-Nb-Si, 335 -337	TiAl, 933, 938, 959, 960, 965, 1,017, 1,057, 1,203-1,218, 1,653 Alloying Effects, 961 Applications, 967 Cold-Rolling, 964 Compression1,203-1,210 Deformation, 963 Dynamic Recrystallization, 1,203-1,210
Ti-Al-Ta System, 713-718	Environmental Effects, 8, 9
Ti-Al-V-Zr Alloy, 233	Flow Behavior, 1,203-1,210
Ti-Aluminides, 987, 1,163	Lamellar Structure, 961
γ-TiAl, 1,275-1,282	Microstructure Types, 961
Microstructure, 1,275-1,277	Recrystallization, 962
Properties, 1,275-1,282 Ti-C-N, 689	Static Recrystallization,
Ti-Ca Alloy, 651-653	1,203-1,210
Ti-Hf-N, 678, 675	TiAl/Ti ₃ Al Alloy, 1,299-1,306 TiB ₂ , 2,561-2,568
Ti-IOV-2Fe-3AI, 531-537, 871-873	Timetal 21S, 153-160
Ti-II00, 295-298, 303	TiN, 2,163, 2,165
Ti-Mg Alloy, 651-653, 659	Titanium
Ti-Mn Alloys, 1,733, 1,734	Air Pollution, 2,662
Ti-Mo, 539-541	Anodizing Color, 2,670
Ti-Mo, Ti-Al, 31	Applications, 1,998, 2,660
Ti-Mo-Al System, 927	Articles, 914-916
Ti-N, 675, 677	Automotive, 2,663, 2,664, 2,665
Ti-Nb, 539-541	Bio-Compatibility, 2,670
Ti-Ni-(Pd, Ru)-Cr alloy, 2,157, 2,158,	Buildings, 2,669
2,159-2,161	Chronoamperometry Study,
Ti-V, 539-541	1,999, 2,003
Ti-V-Fe-Al Alloy, 531-537	Clad Steel 2,663
Ti-V-N, 747	Cold Hearth Melting, 2,231
Ti-Zr 1 Alloy, 743	Control, 2,402-2,405
Ti-Zr 2 Alloy, 743 Ti-Zr 3 Alloy, 743	Corrosion, 2,661
Ti-Zr-N, 678, 675	Cyclic Voltammetry Study, 1,999,
Ti ₂ NbAl, 1,259	2,003
Ti ₃ Al, 1,195, 1,243	Ecolgical Metal, 2,659, 2,661
Crack Growth, 1,197	Electrolytic, 911-916
Effect on Environment, 1,221,	Foil, 2,668 Gas-Saturated Inclusions, 2,401
1,222	
Fatigue, 1,220-1,222	History, 2,660 Low-Grade Spongy, 911, 915
Fatigue Props, 1,197	Market, 2,660
Fracture Toughness, 1,220	Mechanochemical, 911-916
Tensile Props, 1,20, 1,196	Non-Aerospace Applications,
Titanium Aluminide, 1,195	2,659
Ti ₃ Al-Nb Alloy, 785-790	Piers, 2,666
	Processing 911 2 401

Powders, 911, 916 Ti-15Mo-5Zr-3Al, 2,689-2,696 Quality, 2,403-2,405 Ti-Nb Alloys, 697, 698, 703 Railroad, 2,667 Ti-13Nb-13Zr, 2,705 Reduction, 2,401 Ti-V Alloys, 698 Separation, 2,402, 2,403, 2,404 Ti-15Mo-5Zr-3Al, 1,876 Shipbuilding, 2,669 Ti-15V-3Cr-3Sn-3Al, 1,876-1,882, Sponge, 2,227 1,891, 1,892 Sponging, 2,401-2,405 Titanium Aluminide Foils, 995 Sports, 2,670 Titanium Aluminides, 30, 301, 343, Ti-Cu Alloy, 408-410, 413 375, 391, 563, 566, 571, 572, 587, ri-Mo Alloy, 408-411, 413 595, 600, 601, 713, 793, 797, 829, Ti-Y Alloy, 408, 409, 411-413 831-835, 837, 838, 845, 959, 960, Temple, 2,669 965, 971, 1,003, 1,009, 1,017, Titanium Electrode Process, 1,033, 1,041, 1,065, 1,073, 1,083, 1,997, 1,998, 1,999 1,099, 1,131, 1,155, 1,283-1,289, Ultra-High Purity, 2,230 1,309, 1,453, 1,495, 1,499, 1,503, Vacuum Arc Remelting, 2,233 1,593, 1,971, 2,445 Titanium Alloy Grade 2, 5, 9, 12, 2,087 Acoustic Emission, 1,174 Titanium Alloys Ingots 2,851, 2,852 Alpha-2, 1,172-1,178 Titanium Alloy, 1,741, 1,742, 1,811, α2 Phase, 595, 600, 601 1,817, 2,318, 2,511-2,513, 2,515, Fracture Toughness, 1,177 2,517 Microstructure, 1,172, 1,173 Beta Alloy, 1,876, 1,877 Near-y Titanium Aluminides. Beta Grain Size, 1,877, 1,878 1.503 Beta Titanium, 1,891, 1,892, Investment Cast, 1,503 1,897 Ti-48Al-2Nb-2Cr Alloy, 1,503 Beta-Type Alloy, 2,689-2,696 Tensile Properties, 1,172-1,177 Bio-Compatibility, 2,705 Ti-25Al-IINb, 595 Electromechanical Impedence Ti-48Al-2Nb-2Mn, 588, 593 IMI685, 455, 456, 460 TiB2, 588, 589, 593 Medical Application, 2,689-2,696 Ti₃Al, 1,179, 1,227 Microstructure, 524, 525 Ti-25Al-10Nb-3V-1Mo, 1,171 Near-Alpha, 1,741 Titanium Application, 65, 66, 68 Crack Growth in, 1,741-1,748 Chemical Use, 66 IMI 834, 1,741 Military Use, 66 Near-α Alloy, 455, 456 Titanium Consumption, 66 Orthopedic Application, 2,705 Titanium Cast, 3 Oxygen Content, 1,877-1,879 Titanium Chelate Rolling, 524 Acute Toxicity, 2,785 Spectroscopy, 2,710 Application in Agriculture. Texture, 525 2,779-2,786 Tissue Tolerance, 2,689-2,696 Catalaze Enzyme, 2,782 Toxicity, 2,689-2,696 Chlorophyll, 2,782 Ti-3Al-2V, 2,513, 2,514 Germination of Seeds, 2,780 Ti-4Al Alloy, 523, 524 Physiology Role, 2,780 Ti-6Al-4V, 2,513, 2,514-2,518 Photosynethesis, 2,782 Ti-6Al-6V-2Sn, 2,513, 2,514 Safety, 2,785 Ti-6Al-2Sn-4Zr-2Mo, 2,513, 2,514 Ti Content in Soil and Plant, Ti-Mo Alloys, 698, 700

2,784

Yield and Quality of Crops, 2,784	Thickness Reduction.
Yields of Crop, 2,784	1,364-1,366
Titanium Clad Steel, 1,609	Ti-10V-2Fe-3Al (Ti-10-2-3) Alloy,
Titanium Fire, 48	1,363
Titanium Grade 2, 2,055, 2,056,	Transformation Kinetics, 643-650,
2,057, 2,058, 2,059	739, 1,017
Titanium Grade 5, 2,055-2,058, 2,061	Transgranular Fracture, 375
Titanium Grade 12, 2,055-2,058,	Transverse Tension, 2,559
2,060	Tribological Parameters, 2,034
Titanium Ingots, 53, 2,377	Tribologically Transformed Structure,
Titanium Market, 2,243	2,065, 2,066, 2,067, 2,068, 2,069-
Titanium Metallurgy, 67, 68	2,071
Bleaching Tower, 67	Trobotechnical Characteristics, 2,006
Brazing, 71	Trobotechnical Properties, 2,006
Food and Wine, 67	TTT Diagrams, 643-650, 758, 1,344
Sports equipment, 67	Tubes
Welding, 71	Seamless, 1,429, 1,430
Titanium Mono-Nitride, 1,989	Thin-Walled, 1,433
Titanium Process Modelling, 3	TiAl6V4, 1,430
Titanium Requirements, 2,239	Tubing
Titanium Sheet, 2,333	Retube, 2,795-2,802
Titanium Silicides	Tube, 2,795-2,802
Composition, 290, 291	Tubing, 2,795-2,802
Effect on Properties, 289, 293	Turbine Blades, 1,587, 1,588, 2,673
Microstructure, 290	Two-Phase Titanium Alloy
Titanium Sponge, 53, 2,287, 2,288,	TC4 Titanium Alloy, 241-244
2,289, 2,290, 2,309, 2,401, 2,423	
Titanium Tetrachloride, 2,425	U
Titanium Turnings, 2,265, 2,281	UAR, 53, 59
Titanium Weld, 1,787	Ultimate Tensile Strength, 824, 825,
Titanium Welding, 71	828
Corrosion resistance, 65	Ultrasonic Inspection, 2,729, 2,731,
Surgery, 70	2,859
Medicine, 65	Unalloyed Titanium, 2,073-2,076,
TMT, See: Thermomechanical	2,077, 2,078, 2,079
Treatment	Undermatched Weldments
Topography, 2,027, 2,029	Contact Strengthening, 1,790,
Tornado, 2,830	1,791
Torsion	Joint Strength, 1,790
Stress-Strain Criteria, 1,767,	Fracture Toughness Properties,
1,768	1,791
Toughness, See: Fracture Toughness	Tensile Properties, 1,790
TQM, 2,811	Unit-Cell Model, 2,610, 2,612
Trade Studies, 821	Utility, 2,795
Trans-Beta Hot Die Forging, 1,363	, L,, vo
Die Temperature, 1,363-1,367	V
Hot Die Forging, 1,363	
Stock Temperature, 1,363, 1,364	Vacuum Annealing, 845-848, 850
	Vacuum Arc Furnace, 2355

Vacuum Arc Remelting, 399, 1,235-1,237, 1,239 Vapor Quenching, 659 VAR, 2,317, 2,318, 2,320 Void Growth, 255, 256 VT 3-1 Alloy, 547, 554, 1,445 VT 6 Alloy, 1,445, 1,448-1,450 VT 16 Alloy, 1,560-1,563, 1,565 VT 19 Alloy, 1,560-1,565 VT 22 Alloy, 1,445, 1,449, 1,569-1,576 VT 23 Alloy, 248, 1,560-1,563, 1,565 VT 35 Alloy, 1,560-1,565

W

Water Brake, 2,721-2,727 Wear Behavior, 2,020 Wear Resistance, 2,005, 2,006 Wide Chord Fan, 2,981-2,983 Wrought Processing, 1,099

X-Ray Diffraction
Diffraction Profile, 701-703
Phase Constitution, 699

Y₂O₃ Dispersion, 813-819 Yield Strength, 824, 825, 828, 1,877, 2,721

AUTHOR INDEX

Abboud, J.H., 2,503 Abkowitz, S., 2,511 Ablitzer, D., 2,347 Adamesku, R.A., 603, 1,811 Adams, R.E., 2,787, 2,899 Albert, D.E., 1,251 Albrecht, J., 1,187, 1,635 Aleksandrovsky, S.V., 2,423 Allison, J.E., 295, 391, 423, 2,681 Amato, R.A., 279, 431 Ameyama, K., 169 Andreev, A.E., 2,401 Andres, C., 311 Andrienko, S.Y., 2,377 Angelier, C., 643 Ankem, S., 1,733 Anokhin, V.M., 911 Anoshkin, N.F., 383, 1,445 Aoyagi, H., 2,713 Apgar, L.S., 837, 845, 1,331, 1,593 Arcella, F.G., 1,395 Arimoto, N., 2,487 Arrell, D.J., 1,003 Ashida, Y., 2,673 Audrerie, P., 1,347 Austin, C.M., 1,065 Azkarate, I., 2,055

Baccino, R., 927
Bache, M.R., 1,693, 1,765
Bachmann, V., 303
Badami, S.A., 149
Baeslack, III, W.A., 1,115, 1,453, 1,469, 1,477
Baker, T.N., 455, 2,641
Banerjee, D., 1,259, 1,147
Bania, P.J., 153, 2,227, 2,787, 2,899
Bannadi, R.K., 149
Barbaux, Y., 611
Barbis, D.P., 415, 1,469
Barbosa, R.A.N.M., 1,701

Barnes, K., 473 Bars, J.P., 1,989 Bartz, A., 1,291 Bashir , S., 319 Baudin, T., 89 Bauer, J., 675, 747 Bayles, R.A., 2,169 Bechet, J., 643 Beevers, C.J., 1,179, 1,227, 1,741, 2,577, 2,601 Beil, T., 2,127 Bellet, M., 1,403 Bellot, J.P., 2,347 Beranger, A.S., 1,757 Berata, W., 1,819 Bergman, D.D., 2,193 Berztiss, D., 1,971 Bin, Y., 1,363 Binder, S., 689 Bingnan, L., 1,891 Bird, R.K., 2,185 Blackketter, D.M., 447, 2,537 Blanchard, P., 2,065 Blenkinsop, P.A., 15 Bliss, R.C., 201 Bogar, F.D., 2,073 Bogensperger, M.L., 263 Bondarev, B.I., 383 Boucher, C., 1,461 Bouchet, B., 1,819 Bourcier, R.J., 1,661 Bowen, A.W., 271, 473, 659, 1,795 2,641 Bowen, P., 1,139, 1,179, 1,195, 1,219, 1,227, 2,529, 2,577, 2,601, 2,649 Boyer, R.R., 77, 1,511, 1,647 Braga, H.C., 1,701 Brauner, H., 2,765 Breme, J., 1,701, 2,757 Brenet, D., 927 Bribiesca, S.L., 2,247, 2,439 Bridges, P.J., 1,319 Bristow, B.M., 1,717

Broderick, T.F., 1,453 Brooks, J.W., 979, 1,319 Broszeit, E., 2,017 Brun, M.Y., 1,387 Brust, F.W., 2,609 Buchillier, T., 2,135 Bunge, M.J., 473 Burilla, C.T., 1,091 Buttinelli, D., 505 Buttrill, W.H., 2,363, 2,451 Bykova, L.A., 1,387

C

Caddey, A.F., 1,647 Cai, X.Z., 2,143, 2,149 Calder, C., 2,819 Campagnac, M.H., 611 Canova, G., 473 Cao, C., 1,677 Caplan, I.L., 233, 2,073 Cardona, D.C., 2,529 Chakrabarti, A.K., 209, 1,371 Chamberlain, R.A., 1,579 Champin, B., 105, 813 Chang, C.P., 879 Chaudhury, P.K., 595 Chave, R.A., 1,179, 1,227 Chaze, A.-M., 105, 1,347 Chen, G.-H., 903 Chen, Z., 1,235 Cheneau, N., 473 Chesnutt, J.C., 1,099 Chinnis, W.R., 2,363 Choudhury, A., 2,331 Chuanxi, H., 1,773, 1,891 Chumbley, L.S., 407 Cianci, M.S., 1,495 Clark, K.R., 2,867 Clark, R.K., 2,177, 2,185 Clavel, M. 611, 1,757 Clevenger, E.M., 571 Clunlei, W., 871 Clyne, T.W., 2,467, 2,569 Colvin, G.N., 1,495, 2,495 Combres, C., 105 Combres, Y., 2,859

Côme-Dingremont, N., 667, 1,347 Contreras, E.S., 2,247, 2,439 Cooper, M.S., 2,743 Cope, M.T., 1,033, 1,195, 1,219, 2,907 Cormier, B., 643 Corsini, C., 1,403 Cotterill, P.J., 2,649 Cullinan, J., 1,971 Cundy, J.M., 2,931

D

Da Silva, M., 949 Dadkhah , M.S., 1,073 Daeubler, M.A., 41 Dai, Y., 1,803 Dajno, D., 1,347 Dary, F.C., 375 Das, G., 2,617, 2,625 Das, S., 713 Dassargues, P., 2,385 Däubler, M.A., 1,187, 2,877 Davidson, J.A., 2,705 Davies, D.P., 1,851, 1,923, 1,931 Dawson, P.R., 1,907 Dean, T.A., 1,107, 1,235 Debuigne, J., 675, 739, 747, 1,519 Del Barrio, A., 2,055 Denda, T., 2,867 Dennies, D.P., 121 Denguin, A., 1,017 Derby, B., 2,633 Dewes, R., 1,107 Dickson, J.I., 1,803 Dillard, A.B., 2,867 Dimiduk, D.M., 1,041 Dolgov, V.V., 1,559 Donath, K., 2,757 Dong, L., 785 Donlon, W.T, 295, 423 Dowling, W.E., Jr., 423, 2,681 Dowling, W.E., 391 Dowson, A.L., 1,741 Driver, J., 473 Drozdenko, V.A., 911 Duan, S., 1,997

Dubinsky, I.N., 2,377 Duffy, L.B., 1,527 Dumas, G., 105 Dumbleton, 2,697 Durjagin, V., 2,049

E -

Ehrhart, I., 1,009
Elagin, D.V., 383
Ellis, J.R., 2,609
Ellis, T.W., 407
Emura, S., 2,487
Entrekin, C.H., 2,339
Eschenbach, R.C., 2,301
Esling, C., 473, 1,795
Etchessahar, E., 739, 1,989
Ettmayer, P., 675, 689
Evans D.J., 1,593, 2,593
Evans, W.J., 1,693, 1,749, 1,765, 1,915
Eylon, D., 415, 837, 845, 1,083, 1,331, 1,503, 1,511, 1,593, 2,593

E.

Fayeulle, S., 2,065 Feaugas, X., 1,757 Fedorovskii, B.B., 2,429 Felli, F., 505 Festa, G.B., 505 Fischer, D., 1,355 Fisher, G.T., 2,393 Fisher, R.L., 2,239, 2,265 Fitzpatrick, G.A., 2,931 Fladischer, J., 131 Flower, H.M., 531, 705, 1,003, 2,467, 2,561 Foerch, R., 2,043 Folkers, K.-D., 2,915 Fontana, A., 2,385 Fox, K.M., 2,649 Fox, S.P., 287, 769 Franz, H., 2,017 Fraser, H.L., 1,453 Freedman, A.S., 2,415 Frefer, A., 933 Frey, N., 2,135

Froes, F.H., 3, 447, 793, 829, 903, 933, 2,537
Frommeyer, G., 1,299
Fuchs, G.E., 1,275
Fujiwara, K., 1,211
Fukada, N., 2,317
Fukasawa, E., 919
Fukumoto, M., 217
Furushiro, N., 635

a

Gaillard, F., 1,461 Galeev, I., 2,005 Gan, F.X., 2,217 Ganesh, R., 149 Gangloff, R.P., 2,209 Gaochao, W., 871 Gautier, E., 627, 667, 1,347 Gavart, A., 627 Gegel, H.L., 3 Gelman, A.A., 1,445 George, W., 2,325 Gerling, R., 1,025 Ghonem, H., 2,043 Ghosh, A.K., 995, 1,203 Gibeling, J.C., 121 Gigliotti, M.F.X., 279, 431, 2,941 Gil, F.J., 777, 1,843 Gill, S.J., 2,169 Gilmore, C.J.651 Gittos, M.F., 1,601 Glazunov, S.G., 547 Godavarti, P.S., 971 Goldfine, V., 2,005 Golubev, A.A., 2,287 Gong, B., 853 Gorynin, I., 65, 1,811 Goto, M., 2,835 Goulding, A., 1,749, 1,915 Grabowski, L., 1,741 Grauman, J.S., 2,193, 2,737 Graves, J.A., 1,073 Gray, III, G.T., 225, 1,163 Green, J.E., 2,371, 2,843 Grosman, F., 755

Gu, X., 1,997 Guanjun, Y., 1,725 Guillard, S., 587 Guillou, A., 747 Guliakin, A.I., 2,401, 2,423 Gunbina, O., 729 Guo, Z.X., 455, 2,633 Guoliang, C., 1,709 Guozhen, L., 1,725, 1,859 Gustavson, L., 2,697 Gysler, A., 311, 1,635

H -

Hagiwara, M., 887, 2,487 Hall, E.L., 1,259 Hall, J.A., 77, 971 Hamilton, C.H., 3 Hammond, C., 1,413, 1,535 Han, B.-Q., 1,899 Han, Y.K., 2,827 Hanada, S., 1,947 Harada, I., 217 Harbison, L.S., 1,661 Hardwick, D.A., 161 Harker, H.R., 2,339 Hartley, M.V., 2,577 Hasegawa, A., 2,673 Hassan, M.A., 1,413, 1,535 Hattori, S., 2,673 Hauert, R., 2,027 Haun, R.E., 2,301 Hayakawa, H., 2,317 Hayes, R.W., 1,653 Hellemann, L., 2,941 Helm, D., 41, 1,187 Hendrix, B.C., 2,867 Henri, A., 97 Herr, W., 2,017 Herteman, J.P., 2,805 Hesin, Y., 2,111 Heuze, J.L., 1,461 Hiatt, D., 1,717, 2,819 Hill, M.J., 813 Hintermann, H.-E., 2,689 Hirai, K., 169

Hirota, K., 169

Holdway, P., 2,641, 659 Holzwarth, U., 2,765 Hong, S.I., 1,163 Honglin, G., 1,709 Hongoh, M., 1,803 Honriorat, Y., 1,339 Horiya, T., 1,875 Hou, K.H., 1,477 Hsu, S.E., 879, 895 Hu, Y.J., 2,143 Hua, W., 523 Huang, C.L., 1,235 Huang, M.-L., 2,779 Huang, S.C., 1,065 Hughes, J.R., 431 Hülse, K., 1,355 Hunter, G.B., 2,451 Hunter, K.R., 2,519 Hurley, J., 1,477 Hutt, A.J., 2,787, 2,899, 2,923 Hyun, Y.T., 1,203

Ibbotson, A.R., 2,577, 2,601 Ignatov, V., 2,005 Igolkin, A., 2,081, 2,111 Ikeda, M., 697 llyn, A.A., 547, 941 lmam, M.A., 177 Imamura, Z., 2,459 Inaba, T.169 Inoue, S., 497 Ishigai, S., 113, 1,587 Ishikawa, K., 1,827, 1,875 Ishikawa, M., 141 Ishikawa, S., 489 Ishikawa, Y., 1,779 Ishunkina, T.V., 1,569 Isiyama, S., 1,947 Islam, M.F., 1,625 Itabashi, Y., 2,835 Ito, H., 2,713 Ito, Y., 1,827 Itoh, G., 987 Ivanova, L.A., 2,111 Ivasishin, O.M., 247, 721

Jacobs, M.H., 1,107 Jaffee, R.S., 131 James, A.W., 1,139 Jardy, A., 2,347 Jelenak, H., 1,429 Jensen, J.A., 407 Jewett, T.J., 713 Jezioro, M., 1,033 Jialong, X., 1,709 Jing, Z., 785 Jinxu, Z., 1,709 Jinyou, W., 1,363 Johnson, T.J., 2,035 Johnson, T.P., 2,585 Jones, I.P., 979, 1,309 Jones, J.W., 391 Jones, P.E., 1,503 Jong, E.N.T., 2,561 Ju, D., 1,725 Judy, R.W., Jr., 233, 2,073 Juhas, M.C., 1,453

..

Kagohashi, W., 919 Kaieda, Y., 887 Kako, Y., 489 Kaku, K., 489 Kamei, K., 697, 1,617 Kametani, H., 805 Kamimura, T., 217 Kao, H.P., 895 Kao, S.G., 879 Karasev, E., 2,851 Kassner, M.E., 1,717 Kato, H., 635 Kato, M., 217 Katoh, I., 2,773 Kawabe, Y., 887, 2,487 Kawanami, T., 1,609 Kearns, M.W., 2,293, 2,035, 2,585 Keller, D.A., 2,027 Kelly, T.J., 1,065, 1,115, 1,503 Kempf, B., 2,163 Kempf, J.M., 627 Kerry, S., 1,003, 1,179, 1,227

Kexiu, C., 1,709 Khan, T., 813, 1,017, 1,243, 1,669 Khobaib, M., 351, 439, 2,625 Khulman, G.W., 1,371 Kobayashi, T., 853, 1,835 Koch, M., 1,429 Koizumi, M., 2,317 Kolachev, B.A., 861, 941 Komatsu, S.-Y., 697 Kondratenko, L.K., 539 Kong, Y., 1,997 Konitzer, D.G., 407, 1,259 Kopylov, V.N., 683 Korobov, O.S., 1,569 Kosenko, N.S., 721 Koss D.A., 185, 1,661 Kovacs, P., 2,705 Kremser, T., 1,299 Krishnamurthy, S., 2,545 Krivitskiy, B., 683 Kubo, K., 217 Kuboyama, O., 141 Kudrjavtsev, A., 1,811, 2,851 Kudryashov, V.G., 1,569 Kuhlman, G.W., 3, 209 Kulkov, A.D., 2,287 Kumagai, N., 1,617 Kumpfert, J., 1,685 Kupperman, D.S., 1,131 Kurapov, V., 2,851

L

Lacagne, O., 643
Lai, D., 1,757
Larsen, D.E., 587
Larsen, Jr., D.E., 1,267, 1,487
Larsen, M., 1,259
Lasecki, J.V., 295
Lawson, A.C., 225
Lê, V.-D., 2,135
Lee, Y.T., 303, 1,203, 1,685
Lengauer, W., 675, 689
Leurquin, B., 2,385
Levaillant, C., 1,347
Levin, U.S., 2,287

Lhermitte, M., 643

Li, P.Q., 2,149, Li, C., 523 Li, C., 1,677, 2,891 Liang, Y.M., 761, 1,963 Lin, Z.-R., 1,899 Lipschutz, M.D., 971 Lipsitt, H.A., 1,041, 1,291 Liu, G.Z., 2,143 Liu, J., 619 Liu, L., 2,779 Liu, P.S, 1,477, 1,469 Liying, X., 1,859 Lobanov, V.S., 2,401 London, B., 1,267, 1,487 Long, M., 595 Loretto, M.H., 987, 1,235, 2,035, 2,585 Loria, E.A., 2,445 Lozhko, A.N., 1,387 Ishansky, V.M., 1,387 Ludwig, N., 2,331 Lugovoy, V.E., 2,401 Lunde, L., 2,087 Lütjering, G., 131, 311, 1,187, 1,635

M -

Ma, J., 2,891 Madsen, A., 2,043 Maeda, T., 705, 1,057 Mahoney, M.W., 161 Majumdar, B.S., 2,609 Maksimov, A.P., 2,377 Malkin, G.Z., 1,387 Malkov, A.V., 861 Mallory, L.C., 1,115 Malshin, V.M., 2,287, 2,401 Mamonov, A.M., 941 Manero, J.M., 1,843 Marchand, N., 1,803 Margetan, F.J., 2,827 Margolin, H., 255 Markovsky, P.E., 247 Marnier, N., 1,339 Marquardt, B.J., 367, 1,163 Martin, P., 2,805 Martin, P.L., 161, 399, 1,653 Marty, M., 1,669

Matsumoto, T., 113, 1,587, 2,673 Mäusli, P.-A., 2,689 McCarron, R.L., 1,971 McQuay, P.A., 1,041 Medina-Perilla, J.A., 473 Medovar, B.I., 2,429 Medovar, L.B., 2,429 Meier, G.H., 1,971 Meier, M., 1,421 Meng, X.K., 241 Messager, F., 1,461 Meyer, L.W., 1,939 Meyer, M., 2,017 Meyn, D.A., 2,169 Millett, J.C.F., 979 Minarski, P., 1,979 Miracle, D.B., 2,545

Mishurda, J.C., 563 Mitchell, A., 2,257 Mitin, A.V., 861 Mitsuya, H., 2,773 Mitsuyoshi, Y., 2,751 Miura, S., 887 Moisson, C., 2,859 Molinari, A., 473 Moll, J.H., 3

Molotkov, A.V., 383 Montheillet, F., 1,347 Moore, J.J, 2,519 Moore, P.L., 2,795 Moorhouse, S., 1,033, 2,907 Morel, D.E., 2,553 Moret, F., 927 Moriga, M., 1,543 Morinaga, M., 217

Morita, A., 2,673
Morris, C.E., 225
Morton, P.H., 2,127
Mosher, D.A., 1,907
Mosser, P.E., 1,339
Mridha, S., 2,641
Mukherjee, A.K., 1,421
Mukhopadhyay, D.K., 829
Muraleedharan, K., 1,259
Muranaka, S., 113
Murayama, R., 919
Musatov, M.I., 2,415

Pao, P.S., 2,169 Park, H., 2,819 Nagai, K., 1,827, 1,875 Park, N.K., 1,203 Nagane, T., 2,407 Parris, W.M., 153, 2,787, 2,923 Nagata, K., 2,407 Partridge, P.G., 651, 659, 2,479 Nagesh, R.V.S., 2,309 Paton, B.E., 2,429 Naka, S., 813, 1,017, 1,243, 1,669 Pavlov, V.M., 1,445 Nakamura, M., 2,273 Penelle, R., 27, 89 Nakasa , K., 619 Penton, R.J.T., 1,195, 1,219 Nakazawa, S., 335 Perepezko, J.H., 563, 571, 713 Neal, D.F., 287, 813 Perkins, R.A., 1,971 Nesterova, E., 729 Perocchi, L.C., 431 Newaz, G.M., 2,609 Perren, S.M., 2,689 Nied, H.A., 1,437 Peters, D.F., 2,721 Niikura, M., 141 Peters, M., 303, 1,685, 2,877 Niinomi, M., 853, 1,835 Petit, J., 1,819 Nishimura, T., 113, 481, 579, Petrunko, A.N., 2,287 1,827, 2,713, Phelps, H.R., 193 Niwa , N., 1,883 Philippe, M.J., 473, 1,795, 473 Noda, N., 489 Phillips, D., 1,115 Notkin, A.B., 383 Phillips, P., 1,453 Nozue, A., 1,867 Pilling, J., 1,625 Nugent, M.J., 2,795 Piper, K.-E., 2,355 Nwobu, A.I.P., 531 Pishko, R., 209 Nyborg, R., 2,087 Planell, J.A., 777, 1,843 Plänker, E., 1,429 Pohler, O., 2,689 Ogata, T., 1,827 Polkin, I.S., 547, 1,559, 1,569 Ohno, K., 335 Pera, J., 1,403 Ohtsuka, M., 1,123 Porter, W.J., 1,503, 1,511, 1,593 Ohyabu, Y., 853 Postans, P., 1,033, 2,907 Ohyama, H., 481, 579, 1,123, Poulose, P.K., 177 1,779, 2,673 Preisser, F., 1,979 Oishi, T., 1,211, 2,273 Prigent, S., 1,519 Okabe, T.H., 1,211, 2,273 Proske, G., 1,187 Okada, M., 1,057, 1,551, 2,773 Prozorov, V.M., 911 Okubo, T., 1,867 Puschnik, H., 131 Oliver, B.F., 1,091 Omlor, R., 1,291

2,979

Qiao, Z., 1,997

Quan, H., 1,859

Quesne, C., 89

Quattrocchi, L.S., 185

Rack, H.J., 587, 595, 1,379

Ono, K., 1,211, 2,273

Onodera, H., 335

Opet, Jr., S.L. 2,721

Orsborn, L.M., 821

Ouchi, C., 141

Pak, S.J., 25

Radchenko, V.N., 2,377 Rama Rao, K.V., 2,309 Ramachandra, C., 1,955 Ramanujan, R.V., 1,107, 1,309 Ramesh, K.T., 949 Rao. S., 2,309 Rasuvaeva, I.N., 683, 729 Rath, B.B., 177 Recio, A., 2,055 Reissner, J., 2,027 Rengi, Z., 1,773 Repechenko, A., 2,049 Rhodes, C.G., 399 Riabinin, V.A., 2,429 Ridley, N., 1,527, 1,625 Roberts, W.T., 1,579 Rodinov, V.L., 1,569 Rohde, K.A., 1,371 Roman, I., 1,171, 2,545 Rome, C., 2,385 Rose, J., 2,827 Rosenberg, H.W, 2,371, 2,743, 2.843 Rothenflue, L., 1,291 Roumagnac, P., 611 Rowe, R.G., 343, 1,147, 1,259 Rtitsheva, L., 2,049 Rüdinger, K., 2,355 Russ, S.M., 2,625 Russell, A.M., 407 Rybin, V., 729

Saenko, V.Y., 2,429
Saigal, A., 1,131
Saita, Y., 1,867
Sakai, H., 805
Sakai, K., 2,659
Sakamaki, H., 1,867
Sakuyama, H., 2,751
Salehi, M., 2,127
Sample, V.M., 209
Samusik, E.D., 2,287
Saqib, M., 837, 845, 1,291, 1,331, 1,503, 1,593
Sasse, J.A., 2,729
Sastry, S.M.L., 1,049

Satake, T., 497 Satoh, H., 2,103, 2,119, 2,157 Satoh, T., 1,587 Schaeffer, J.C., 1,971 Schimansky, F.P., 1,025 Schley, J.R., 1,469 Schlienger, M.E., 2,301 Schnecke, H., 2,355 Scholz, H., 2,331 Schüler, P., 2,355 Schulte, W., 2,757 Schurmann, H., 303 Schutz R.W., 2,095 Schwartz, F., 813 Schwarzer, R., 473 Schwenker, S.W., 2,593 Scott, M.M., 1,601 Scully, J.R., 2,201 Seagle, S.R., 2,265 Sears, J.W., 987, 1,309, 2,293 Segawa, A., 1,609 Segers, L., 2,385 Seki, M., 1,779 Semiatin, S.L., 1,041 Semlitsch, M., 2,689 Serghat, M., 473, 1,795 Servant, C., 27, 89 Sevillano, J.G., 473 Shamblen, C.E., 2,451 Shamray, V.F., 539 Shaoxuan, G., 785 Sharma, S.C., 149 Sheenkov, V.A., 1,559 Shen, G.Q., 761, 1,963 Shepelev, V.V., 2,429 Sherman, A.M., 2,681 Shida, Y., 1,057 Shigenaga, M., 1,543 Shih, D.S., 1,099 Shihmakov, A.S., 603 Shimizu, Y., 2,459 Shimokawa, A., 1,835 Shirasuna, S., 1,609 Shirogane, S., 1,609 Shuqi, Z., 1,859 Shutey, J.J., 2,429

Sibum, H., 1,429 Sieniawski . J., 755 Simon, A., 627, 667, 1,347 Singh, A.K., 1,955 Singh, V., 1,955 Smarsly, W.G., 1,669 Snow, D.B., 1,091 Snow, J.G., 971 Soboyejo , W.O., 1,049, 359 Sohn, Y.-U., 1,989 Spence, S.H., 1,749, 1,915 Staskewitsch, E., 1,939 Steinemann, S.G., 2,135, 2,689 Stephen, 1,319 Strangwood, M., 2,649 Stroshkov, A.N., 1,569 Suchentrunk, R., 2,017 Sugano, M., 497 Sugimoto, T., 697 Sugizaki, Y., 2,103, 2,119, 2,157 Sukhorosov, B.N., 2,415 Sun, F., 1,677 Sun, W.P., 879 Sundell, R.E., 2,941 Suryanarayana, C., 447, 829, 903, 933 Susa, M., 2,407 Suzuki, H., 1,875 Suzuki, H.G., 2,317, 489 Sytshikov, V.I., 2,049 Szmukler-Moncler, S., 2,689

T

Takahashi, J., 2,487
Takahashi, Y., 1,543
Takatori, H., 1,883
Takayama, Y., 635
Takemura, A., 481, 579, 2,673
Taki, K., 2,751
ſamamoto, S., 53
Tanaka, Y., 1,617
Tang, J.L., 513
Tang, S.-D., 2,779
Tani, K., 2,673
Tao, L., 1,725

Tarín, P., 777 Tarlov, O.V., 2,377 Täubler, R., 675 Tavafoghi, M., 1,955 Tavera, F.J., 2,247, 2,439 Tetjukhin, V., 2,851 Thakker, A.B., 2,907 Thiehsen, K.E., 1,717 Thomas, M., 1,243, 1,669 Thomas, M.C., 319 Thompson, A.W., 375, 1,155, 1,171, 1,251, 1,283 Thompson, R.B., 2,827 Threadgill, P., 1,453 Thun, S.T., 879 Tien, J.K., 2,867 Tokizane, M., 169 Tomari, H., 2,119 Tomita, A., 2,407 Toth, L.S., 473 Tozawa, T., 635 Traut, D.E., 2,393 Trautmann, K.-H., 303 Tripp, D.W., 2,257 Trubin, A.N., 2,851

Ubhi, H.S., 473, 2,641 Ueda, K., 2,157, 2,713 Ueki, T., 2,273 Uginet, J.F., 463, 627 Umakushi, Y., 635 Umezawa, O., 1,827 Upadhyaya, D., 2,537 Upadhyaya, D., 447 Urtjev, V., 2,851 Ushkov, S., 683, 729, 2,005, 2,049, 2,081, 2,111, 2,851 Ustinov, V.S., 911

V

Van Houtte, P., 473 Vannes, A.B., 2,065 Vassel, A., 97, 793, 1,009 Veeck, S.J., 2,495 Verma, R., 995 Vernin, P., 2,385 Vijayshankar, M.N., 1,733 Vincent, L., 2,065 Vinot, J., 2,859 Vogt, R.G., 1,495 Voleinik, V.V., 911 Volodin, V.A., 861 Vornbyov, I.A., 861 Vorobyev, I.A., 1,559

W

Wagner, F., 1,795 Wagner, R., 1,025 Walker, M.J., 2,585 Wallace, T.A., 2,177, 2,185 Wang, A., 1,379 Wang, K., 2,697 Wang, S.H., 1,963, 761 Ward, C.H., 303, 1,171, 1,685 Ward-Close, C.M., 651, 659, 2,479 Watson, M.C., 2,569 Weaver, M.J., 813 Weihrauch, P., 2,511 Weiss, I., 837, 845, 1,503, 1,593 Weiss, T., 1,331 Wells, M.E., 1,787, 2,729 West, D.R.F., 531, 2,503, 2,561 Wheeler, D.A., 1,267, 1,487 Wiedemann, K.E., 2,177, 2,185 Wilhelmsen, W., 2,087 Williams, J.C., 1,171 Winand, R., 2,385 Winkler, P.-J., 2,877 Wirth, D., 2,519 Wise, M.L.H., 1,107 Wood, J.R., 193, 263, 415, 1,469 Woodfield, A.P., 279, 431, 1,259 Worth, B.D., 391, 423 Wu, T.I., 2,009 Wunderlich, W., 1,299

V

Yamada, N., 489 Yamagata, T., 335 Yamaguchi, M., 959 Yamazaki, M., 335 Yao, L.-A., 2,217 Yashiki, T., 2,119 Yasunaga, T., 2,103 Yeh, M.T., 895 Yiqing, W., 1,859 Yoder, G.R., 2,169 Yolton, C.F., 821, 1,083, 1,331 Yoshimura, Y., 2,459 Young, J.M., 1,309, 2,293 Young, Jr., G.A., 2,201 Young, L.M., 2,209 Young, R., 2,281 Yu, H.Q., 241, 513, 327 Yueqin, Z., 1,725 Yuri, T., 1,827 Yuxio, C., 871

Z

Zakharevich, A.A., 2,423 Zefferer, S., 473 Zeng, W.D., 513 Zhang, X.D., 1,107, 1,309 Zhang, Y.Q., 2,149 Zhao, Y.X., 2,217 Zheng, H.H., 2,149 Zhifang, Z., 871 Zhongquan, D., 871 Zhou, Y., 327 Zhou, Y.G., 241, 327, 513 Zwicker, U., 2,765